Studies of Ambient and Chamber Aerosol Composition using the Aerosol Mass Spectrometer

Thesis by

Jill Suzanne Craven

In Partial Fulfillment of the Requirements

for the Degree of

Doctor of Philosophy

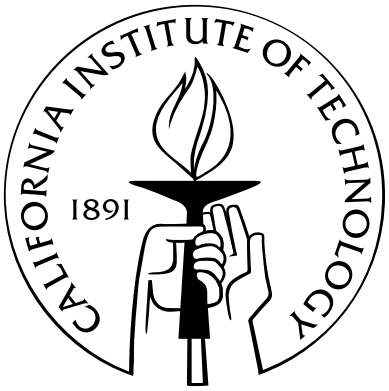

California Institute of Technology

Pasadena, California

2013

(Submitted April 11, 2013)

To my parents, Carl and Heather Craven.

Acknowledgments

I extend thanks to the many people I have encountered over the past five years while at Caltech, in lab, at field campaigns, and at conferences. I am extremely grateful to be a part of the atmospheric science community.

I would like to thank my advisor, John Seinfeld, for providing me the opportunity to study atmospheric aerosols in many ground and airborne based field campaigns, as well as in the laboratory. In addition, I appreciate his guidance and support for my enthusiasm for teaching, as well as research.

I would also like to thank my co-adivsor, Rich Flagan, who I am looking forward to working with more during my postdoc at Caltech. When I went on my first field campaign, Rick's advice from past field experiences were invaluable. I also appreciated being able to talk to Rick about anything, from dealing with an injured leg while on a campaign to kayaking on the Kern river.

Early on in my PhD experience I had an immense amount of help from older students and postdocs who I would like to thank: Puneet Chhabra patiently trained me how to use the aerosol mass spectrometer, even though the first time I touched the instrument I broke vacuum with all of the high voltages on. He was always available and helped me explore the seemingly bottomless pit of analysis involved with AMS mass spectra. Shane Murphy, the senior student in my office, gave advice on how to juggle all of the research projects that were expected from me. He also was supportive even after leaving Caltech, answering emails, and frantic phone calls from me on my first field campaign. Andrew Metcalf helped me build a DMA to bring into the field, accompanied me to my first campaign, and was always around to help troubleshoot instrument issues in the lab and in the field. Beth Kautzman was a postdoc in our

group when I joined and was always available for scientific and emotional support.

Special thanks to the aerosol mass spectrometer community, who had an enormous impact on my growth as a scientist. The AMS clinics and user meetings provided me a place for not only learning about an instrument, but also to gain confidence as a researcher, practice technical public speaking, programming skills, research collaboration, teaching, and friendship. Thank you to the many scientist at CU Boulder CIRES and Aerodyne for sponsoring it every year. The scientists at Aerodyne were incredible to work with. Specifically, I would like to thank Bill Brooks and John Jayne for being available for many phone conversations and emails about instrument repair and upgrades. Thank you to Donna Sueper and Joel Kimmel who helped me with Squirrel/PIKA analysis and DAQ software questions. I also would like to thank Sally Ng and Manjula Canagaratna for their contributions with the alkane project and chamber PMF analysis and interpretation. Also, thanks to Jose Jimenez and Roya Bhareini, alumni of the Caltech program, who were also extremely helpful when I had questions about the AMS.

Thanks to Bob Yokelson who lead the SLOBB aircraft campaign and opened up the opportunity for me to study aerosol formation in a wildfire plume, a subject of study I am eager to continue for future work. I would also like to acknowledge Sheryl Akagi, Johnny Taylor, and Gavin McMeeking for their support during the campaign.

Thank you to the CIRPAS crew, especially aircraft mechanic Greg Cooper, for helping me install the AMS into the Twin Otter on both the CalNex and EPEACE field campaigns. Also, thank you to the members of the USFS who helped with the integration during the SLOBB campaign, and for the smoke-jumper pilot who kept us safe as we were flying through the heart of a wildfire plume.

I would like to thank Jean Chen for her friendship during our two months living together for our summer campaign in Monterey. We had a lot of fun doing science and cooking and eating together.

Thanks to Paul Ziemann, who met with Lindsay Yee and I on more than one occasion to discuss details of the alkane chemical mechanism and mass spectrometry results.

I would also like to thank my current officemates who feel like brothers and sisters to me: Lindsay Yee, who is my graduate school sister, for staying up late before AAAR, trying to make sense of our data; Joey Ensberg who helped me learn about the modeling world and how important the tiny details of your instrument collection can be to atmospheric models; and Matt Coggon who is so productive and positive, and is a kayaking machine. I could not have asked for a better person to train and leave the AMS to.

I would like to thank the Women Mentoring Women program at Caltech. When I started, Felicia Hunt was in charge, and although she has moved offices, I still value her support and encouragement as a fellow woman in academia. I'd like to thank Portia Harris for her support in starting the Married/Partnered Women's group. Through the Women Mentoring Women I have met Anne Laraia, who I have had the pleasuring of mentoring the past three years, and who I would also like to thank for her friendship and support.

Thanks to my chemical engineering 1st year class Mandy Grantz, Christine Loza, Artemis Ailianou, Han Han, Nick Hoh, Yashodhan Bhawe, Larry Dooling, Jason Goodpaster and Rui Wang. We celebrated every birthday during our first year, and had many potlucks in between. You guys made first year fun. Special thanks to Christine Loza for staying up with me well past midnight to finish homework sets, and for the continued relationship I have had with her in the laboratory.

I would like to thank the National Science Foundation for the NSF graduate research fellowship which funded my first three years of graduate school.

I would also like to thank the many teachers and professors I have had that encouraged me to pursue a career in science and engineering. Especially I would like to thank three professors from the University of Arizona. Two of them were my chemical engineering undergraduate professors, Dr. Paul Blowers and Dr. Anthony Muscat. Their creative ways of teaching me the fundamentals of chemical engineering helped motivate me to follow the professor career path. They were also helpful when discussing graduate schools and helped me prepare my application. The third person at Arizona I would to thank is my undergraduate research advisor Dr. Sergio Mendes.

For four years, he was so patient with me in the lab and helped me go through nearly all of the processes of research to “test the waters" before I applied to graduate school. It was in Sergio’s lab that I started my first research project and jumpstarted the trajectory I’m currently on.

My acknowledgments would not be complete without recognizing my incredibly supportive and loving family. My parents, Carl and Heather Craven, have been my constant emotional support. Thanks to my dad, a chemical engineer himself, who helped guide me and encourage me to pursue my PhD in chemical engineering. Thanks to my siblings, Bryan Craven and Celeste Lombardi for listening to me talk about my research and for your support and visiting me during my graduate studies. I have to make a special thanks to my uncle, Bill Craven, who was so supportive of me going to Caltech that he accompanied me to visit the department before I even applied. If it wasn’t for my uncle, I probably would not have applied to Caltech. I also want to thank my grandma Craven who was encouraging and told me stories of her adventures with chemistry when she was a young adult and for telling me stories of my grandpa Craven who got his PhD in physical chemistry. I also want to thank my grandpa Kimble for his support and interest in both mine and Devin’s research as we progressed in our doctorate work.

Lastly, I would like to thank my husband, Devin Wiley. Through thick and thin we have made it through this process together. I appreciate our ability to support each other’s research lifestyles and witness each other’s joys and more often our challenges in research. More importantly, I appreciate and value our life away from research on our many outdoor adventures. I am glad to have you by my side through our continued life journey.

Abstract

This thesis presents composition measurements for atmospherically relevant inorganic and organic aerosol from laboratory and ambient measurements using the Aerodyne aerosol mass spectrometer. Studies include the oxidation of dodecane in the Caltech environmental chambers, and several aircraft- and ground-based field studies, which include the quantification of wildfire emissions off the coast of California, and Los Angeles urban emissions.

The oxidation of dodecane by OH under low NO conditions and the formation of secondary organic aerosol (SOA) was explored using a gas-phase chemical model, gas-phase CIMS measurements, and high molecular weight ion traces from particle-phase HR-TOF-AMS mass spectra. The combination of these measurements support the hypothesis that particle-phase chemistry leading to peroxyhemiacetal formation is important. Positive matrix factorization (PMF) was applied to the AMS mass spectra which revealed three factors representing a combination of gas-particle partitioning, chemical conversion in the aerosol, and wall deposition.

Airborne measurements of biomass burning emissions from a chaparral fire on the central Californian coast were carried out in November 2009. Physical and chemical changes were reported for smoke ages $0-4$ h old. CO_2 normalized ammonium, nitrate, and sulfate increased, whereas the normalized OA decreased sharply in the first 1.5 - 2 h, and then slowly increased for the remaining 2 h (net decrease in normalized OA). Comparison to wildfire samples from the Yucatan revealed that factors such as relative humidity, incident UV radiation, age of smoke, and concentration of emissions are important for wildfire evolution.

Ground-based aerosol composition is reported for Pasadena, CA during the sum-

mer of 2009. The OA component, which dominated the submicron aerosol mass, was deconvolved into hydrocarbon-like organic aerosol (HOA), semi-volatile oxidized organic aerosol (SVOOA), and low-volatility oxidized organic aerosol (LVOOA). The HOA/OA was only 0.08–0.23, indicating that most of Pasadena OA in the summer months is dominated by oxidized OA resulting from transported emissions that have undergone photochemistry and/or moisture-influenced processing, as apposed to only primary organic aerosol emissions. Airborne measurements and model predictions of aerosol composition are reported for the 2010 CalNex field campaign.

Contents

List of Figures

List of Tables

Chapter 1

Introduction

Atmospheric aerosols have an important role in climate radiative forcing. Of all of the factors that contribute to the earth's overall energy balance, aerosol formation and the impact of aerosols on cloud formation have the greatest level of uncertainty in past climate radiative forcing [IPCC 2007].

An atmospheric aerosol is a suspension of fine solid or liquid particles suspended in a gas. Particles can be can be directly emitted from natural sources, such as wildfires, or anthropogenic sources, such as fossil fuel combustion, and these are called primary organic aerosols (POA). Aerosols are also formed when a volatile organic compound (VOC) becomes oxidized and forms a semi-volatile organic compound (SVOC). This SVOC can then participate in gas-particle partitioning, and the resulting aerosol is called a secondary organic aerosol (SOA). SOA can come from thousands of compounds in the atmosphere, and the pathways by which SOA are formed are not fully understood.

Three of the main techniques for studying aerosol are field measurements, environmental chamber experiments, and modeling. Field measurements provide spatial and diurnal patterns of aerosol properties. The aerosol properties discovered in the field provide motivation for further study in the chamber laboratory, and also lay a foundation for comparison with modeling results. The chamber laboratory is a controlled environment in which the chemical mechanism and yield (particulate mass measured/amount of hydrocarbon reacted) of the aerosol can be thoroughly understood for one hydrocarbon under specific oxidation conditions. Modeling of at-

mospheric aerosols employs known properties or processes of aerosol formation and applies them to a specific application that can range from studying the evolution of a single hydrocarbon growing onto an existing particle distribution (simulating a chamber experiment) to studying aerosol formation at a global scale.

This thesis focuses on composition analysis of both field and laboratory-generated aerosol using measurements made by the Aerodyne aerosol mass spectrometer (AMS). The AMS enables fast online measurements of aerosol size and composition. The fast data acquisition is especially critically for aircraft campaigns that sample plumes of pollution that may only last for seconds. The two primary instruments used in this thesis are the compact time-of-flight (C-TOF) and high-resolution time-of-flight (HR-TOF) AMS.

Knowledge of the composition of the aerosol is important for understanding how the aerosol is formed, and the source of the aerosol. The composition also determines its ability to uptake water, its volatility, and how it will scatter light. All of these properties are necessary to understand how aerosols affect climate radiative forcing.

A summary of the aerosol mass fraction field measurements presented in this thesis are shown in Figure 1.1. The main components of atmospheric aerosol are sulfate, nitrate, ammonium, chloride, and organic [Zhang et al. 2007]. Organic aerosol (OA) tends to dominate the mass fraction of submicron atmospheric aerosol mass. While the inorganic aerosol formation come from a few known reactions, organic aerosol formation is initiated from thousands of compounds.

The organic portion of the aerosol is further described with the application of positive matrix factorization (PMF) to AMS organic mass spectra. PMF elucidates the source of the organic aerosol, or, when the source is known, is used to quantify the amount of oxidation that the aerosol has undergone in the atmosphere. PMF is classified as a factor analysis receptor model, and more specifically is a bilinear unmixing model that constrains the elements of the resulting factors to be positive. The model output is a linear combination of factors that contain a constant mass spectral profile and a time-varying scalar value of that mass spectrum to the total AMS signal.

In chapters 2 and 3, the chemical mechanism of dodecane oxidation under low NO conditions in the Caltech environmental chambers is presented. In chapter 2, important tracer ion fragments are proposed for peroxyhemiacetal compounds hypothesized to be components of the aerosol. The PMF model, which is traditionally used for ambient aerosol datasets, was utilized in Chapter 3 to explore the variation in the aerosol composition and aerosol mass in the oxidation of dodecane under low NO conditions. The potential processes regarding aerosol formation and aging in the chamber experiments are visualized in Figure 1.2. The PMF results unveiled three factors, which are correlated with particle-phase and gas-phase molecular traces from two chemical ionization mass spectrometers (CIMS). The factors support the hypothesis that condensation of increasingly oxidized products and chemical conversion in the particle-phase are both important, but generally overlooked elements in aerosol chemical formation.

Chapters 4–9 present field studies that utilized the C-TOF-AMS. In Chapter 4, the evolution of an isolated wildfire plume during the 2009 San Luis Obispo Biomass Burning Experiment (SLOBB) was studied and compared to previously reported wildfire studies. Aerosol emission ratios are calculated using the initial wildfire emissions. Chapter 5 describes the aerosol measurements made during the 2009 Pasadena Aerosol Characterization Observatory Experiment (PACO). Ambient aerosol composition for Pasadena, CA was reported, and the organic portion was further characterized using PMF. Organic aerosol was characterized as hydrocarbon-like organic aerosol (HOA), semi-volatile oxidized organic aerosol (SVOOA), and low-volatility oxidized organic aerosol (LVOOA). Size resolved chemical composition was utilized with hygroscopicity measurements to calculate κ_{org}, a water uptake parameter for organic aerosol. Chapters 6–9 report the major findings for the 2010 California Nexus: Research at the Nexus of Air Quality and Climate Change (CalNex) campaign in Los Angeles. The black carbon mass concentrations, coating thickness, and coating composition measured onboard the CIRPAS Twin Otter aircraft are reported in Chapter 6. Chapter 7 summarizes the regional modeling of inorganic and black carbon in the Los Angeles Basin using the CMAQ model; the model simulations are compared to data from two

aircraft platforms and a ground-based site. An overview of the airborne aerosol measurements made onboard the Twin Otter aircraft platform are given in Chapter 8. A detailed analysis of the airborne organic aerosol composition is provided in Chapter 9.

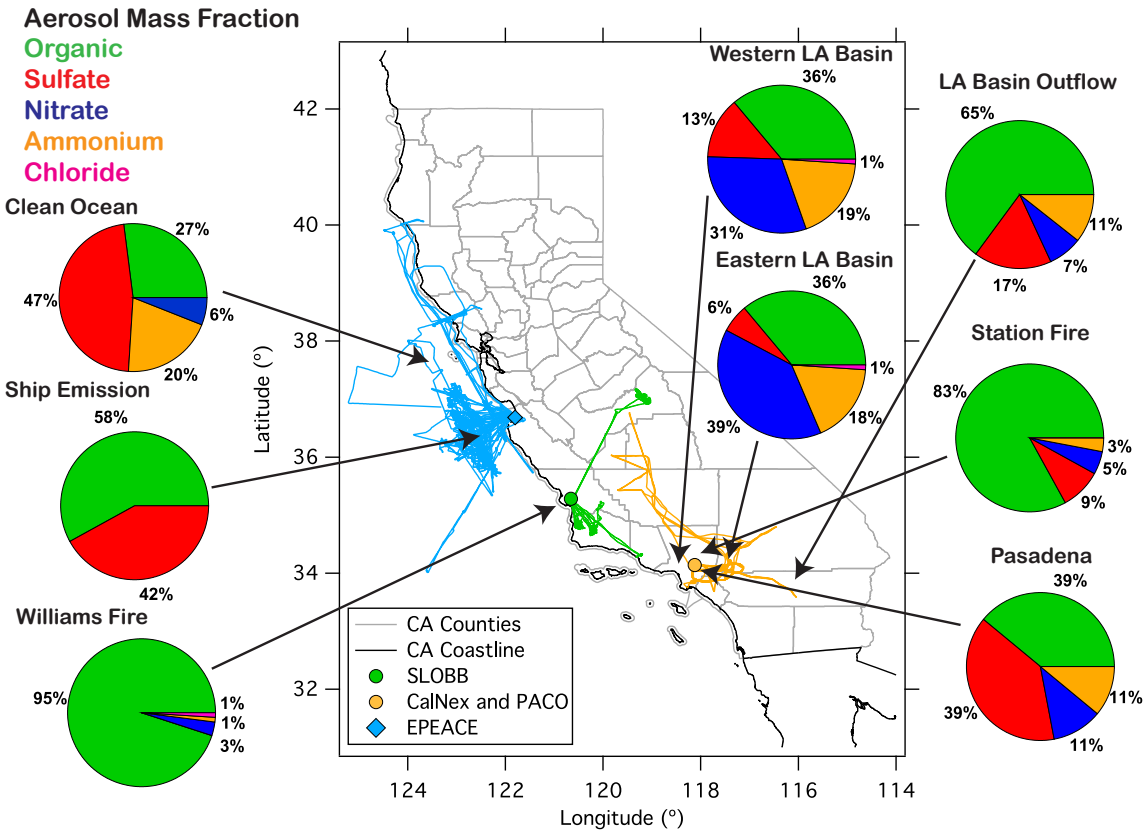

Figure 1.1: Summary of the location and aerosol composition measurements made in the field using the Aerodyne aerosol mass spectrometer.

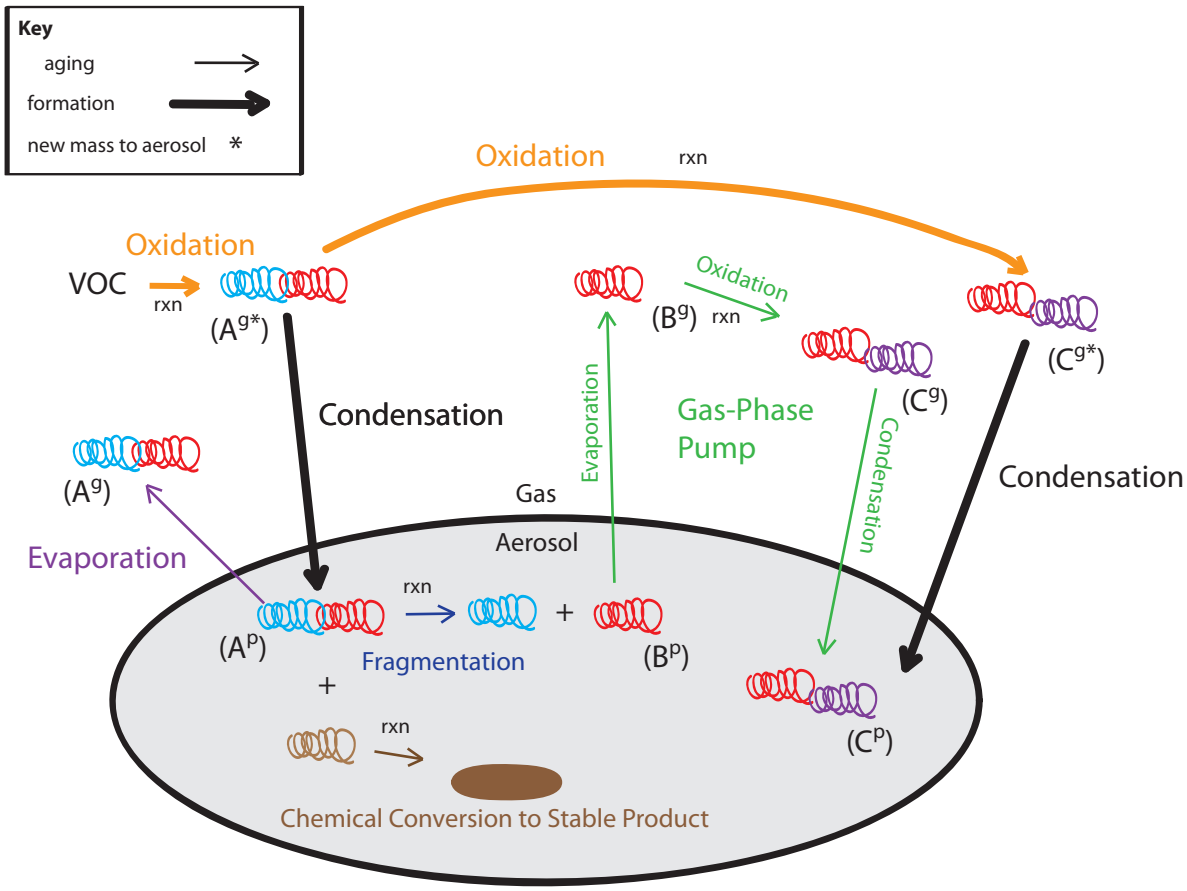

Figure 1.2: Schematic of SOA formation and aging. The red/blue compound represents an oxidized product (A^{g*}), that can either partition into the aerosol (A^{p}) or become oxidized to the red/purple compound (red since it retains some of its original form, but oxidation has added new functionality to it, (C^{g*})), and then condenses into the aerosol phase (C^{p}). Both of these processes are considered SOA formation. In some cases, the red/blue compound can evaporate back to the gas phase (B^{g}) once the initial red/blue has reacted away (gas-phase pump). Or, the compound can fragment in the aerosol, pieces of which can then react further (B^{p}) or evaporate and become more oxidized (A^{g}). Additionally, the red/blue compound can undergo phase transition to ultra low volatility and remain in the the aerosol (the brown). These remaining processes are considered as aging.

Chapter 2

Secondary Organic Aerosol Formation from Low-NOx Photooxidation of Dodecane: Evolution of Multigeneration Gas-Phase Chemistry and Aerosol Composition[1]

[1]This chapter is reproduced by permission from "Secondary Organic Aerosol Formation from Low-NOx Photooxidation of Dodecane: Evolution of Multigeneration Gas-Phase Chemistry and Aerosol Composition" by Lindsay D. Yee, Jill S. Craven, Christine L. Loza, Katherine A. Schilling, Nga Lee Ng, Manjula R. Canagaratna, Paul J. Ziemann, Richard C. Flagan, and John H. Seinfeld, *Journal of Physical Chemistry A*, 116, 6211 – 6230, dx.doi.org/10.1021/jp211531h, 2012.

THE JOURNAL OF PHYSICAL CHEMISTRY A

Article

pubs.acs.org/JPCA

Secondary Organic Aerosol Formation from Low-NO_x Photooxidation of Dodecane: Evolution of Multigeneration Gas-Phase Chemistry and Aerosol Composition

Lindsay D. Yee,[†] Jill S. Craven,[‡] Christine L. Loza,[‡] Katherine A. Schilling,[‡] Nga Lee Ng,[§] Manjula R. Canagaratna,[∥] Paul J. Ziemann,[⊥] Richard C. Flagan,[†,‡] and John H. Seinfeld*[,†,‡]

[†]Division of Engineering and Applied Science, California Institute of Technology, Pasadena, California 91125, United States

[‡]Division of Chemistry and Chemical Engineering, California Institute of Technology, Pasadena, California 91125, United States

[§]School of Chemical and Biomolecular Engineering and School of Earth and Atmospheric Sciences, Georgia Institute of Technology, Atlanta, Georgia 30332, United States

[∥]Aerodyne Research, Inc., Billerica, Massachussets 01821, United States

[⊥]Air Pollution Research Center, Department of Environmental Sciences and Environmental Toxicology Graduate Program, University of California, Riverside, California 92521, United States

Supporting Information

ABSTRACT: The extended photooxidation of and secondary organic aerosol (SOA) formation from dodecane ($C_{12}H_{26}$) under low-NO_x conditions, such that RO_2 + HO_2 chemistry dominates the fate of the peroxy radicals, is studied in the Caltech Environmental Chamber based on simultaneous gas and particle-phase measurements. A mechanism simulation indicates that greater than 67% of the initial carbon ends up as fourth and higher generation products after 10 h of reaction, and simulated trends for seven species are supported by gas-phase measurements. A characteristic set of hydroperoxide gas-phase products are formed under these low-NO_x conditions. Production of semivolatile hydroperoxide species within three generations of chemistry is consistent with observed initial aerosol growth. Continued gas-phase oxidation of these semivolatile species produces multifunctional low volatility compounds. This study elucidates the complex evolution of the gas-phase photooxidation chemistry and subsequent SOA formation through a novel approach comparing molecular level information from a chemical ionization mass spectrometer (CIMS) and high m/z ion fragments from an Aerodyne high-resolution time-of-flight aerosol mass spectrometer (HR-ToF-AMS). Combination of these techniques reveals that particle-phase chemistry leading to peroxyhemiacetal formation is the likely mechanism by which these species are incorporated in the particle phase. The current findings are relevant toward understanding atmospheric SOA formation and aging from the "unresolved complex mixture," comprising, in part, long-chain alkanes.

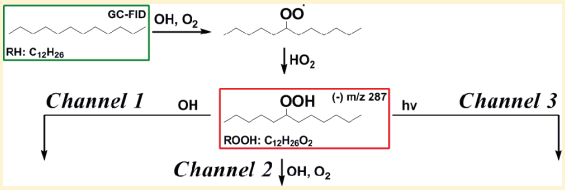

INTRODUCTION

Atmospheric chemical transformations occur through mechanisms involving free radical reactions, sunlight, and reactions in or on condensed media.[1] The formation of secondary organic aerosol (SOA) involves the multigeneration oxidation of a parent organic molecule leading to product molecules that partition between the gas and particle phases. As the parent organic is consumed, usually by reaction with the hydroxyl (OH) radical, subsequent products may also react with OH, giving rise to an evolving product distribution. As products become more functionalized with oxygen-containing moieties, their volatility decreases, and their propensity to partition into the particle phase increases.[2] In the gas-phase chemical cascade, both functionalization and fragmentation (C−C bond scission) reactions occur, and the interplay between these two general types of reactions, together with the progressive decrease in volatility accompanying the addition of oxygen atoms to the parent backbone, defines the SOA formation process for a particular parent organic.[3] As the SOA formation process evolves, a competition ensues between the rate of production of lower volatility species with increasing oxygen-to-carbon (O:C) atomic ratio and the increase in the SOA mass; as the mass of SOA increases, the partitioning of gas-phase products with somewhat higher volatility and somewhat lower O:C ratio is enhanced. The mass of SOA can, in some cases, reach a maximum and decrease as gas-phase fragmentation reactions convert lower volatility species into higher volatility species, leading to evaporation of the lower volatility particle-phase species in an attempt to maintain gas-particle equilibrium. In

Special Issue: A. R. Ravishankara Festschrift

Received: November 30, 2011
Revised: March 16, 2012
Published: March 16, 2012

   dx.doi.org/10.1021/jp211531h | J. Phys. Chem. A 2012, 116, 6211−6230

short, the rate at which oxygens are added via successive gas-phase reactions, the relative importance of fragmentation versus functionalization reactions, and the specific decrease in volatility attending the formation of oxidized species govern the evolution of the SOA mass.

Long-chain alkanes represent an especially important class of organics with respect to SOA formation. The so-called unresolved complex mixture (UCM) is likely an important source of unaccounted for SOA formation in the atmosphere,[4] and alkanes are a major component of that mixture.[5,6] Low-volatility vapors from the UCM are a source of "untraditional" SOA, as they evaporate from primary organic aerosol emissions upon dilution and undergo subsequent oxidation to form SOA.[4] Quantifying the SOA formation from long-chain alkanes will undoubtedly aid in closing the gap between observed atmospheric organic aerosol and that predicted by atmospheric models based on traditional biogenic and anthropogenic SOA precursors. SOA formation from alkane photooxidation has received study.[7−12] Alkane−OH reaction kinetics[13,14] and gas-phase chemistry in the presence of NO_x exhibit a product distribution that can lead to highly oxidized products.[7,9,10] Studies of alkane oxidation under low-NO_x conditions have also been carried out.[15] Importantly, owing to the relatively long lifetimes against OH reaction at typical ambient OH concentrations (on the order of 12 h to several days) and to a relatively rich information base on the kinetics and mechanisms of alkane oxidation reactions, long-chain alkanes represent an especially important class of compounds with respect to SOA formation. Finally, it is crucial to develop detailed chemical databases on the explicit pathways of SOA formation for classes of parent organics, which can serve as benchmarks for evaluation of empirical/statistical models of SOA formation.

The present work represents the first report on a comprehensive series of laboratory chamber experiments on SOA formation from long-chain alkanes. We focus here on SOA formation from dodecane under low-NO_x conditions. The low-NO_x regime of atmospheric chemistry is particularly important in the regional to remote atmosphere and is especially relevant to the chemical aging that is intrinsic to SOA formation. The key to atmospheric photooxidation chemistry is the fate of the alkyl peroxy radical (RO_2) formed after OH attack and O_2 addition. RO_2 can react with HO_2, RO_2, or NO_x, the distribution of which is critical for understanding radical propagation and sinks, as well as the pathways that lead eventually to SOA.[16,17] In atmospheric regions of low NO_x levels, the RO_2 radical will react preferentially with HO_2 and RO_2. In such regions, HO_2 concentrations are on the order of 10^9 molecules cm^{-3},[18−20] and the RO_2−HO_2 reaction is competitive with the reaction of RO_2 with NO_x. Generally, under such atmospheric conditions, the RO_2−HO_2 reaction, which leads to hydroperoxides, dominates over RO_2 self-reaction. We present here the first experimental study of SOA formation from dodecane oxidation in the regime in which the fate of the dodecane peroxy radical is dominated by the RO_2 + HO_2 regime of alkyl peroxy radical chemistry. The particular focus of the present work is the multigeneration gas-phase chemistry of dodecane oxidation that leads to SOA formation. We employ chemical ionization mass spectrometry (CIMS) to track the evolution of the gas-phase oxidation products. We develop a gas-phase mechanism to describe the low-NO_x regime of chemistry. The mechanism is used to explicitly simulate four generations of gas-phase chemistry. By combining CIMS and high-resolution time-of-flight aerosol mass spectrometer (HR-ToF-AMS) measurements, we are able to simultaneously track several semivolatile oxidation products in the gas and particle phases. Together, these measurements provide evidence of particle-phase formation of peroxyhemiacetals (PHAs).

EXPERIMENTAL SECTION

Instrumentation. Experiments were conducted in the dual 28 m^3 Teflon reactors in the Caltech Environmental Chamber described elsewhere.[21,22] The reactors are flushed with clean, dry air for 24 h before a new experiment. A suite of online gas- and particle-phase instruments was used to monitor the development of the chemistry from dodecane photooxidation. The dodecane decay was monitored by taking hourly samples at 0.13 LPM of chamber air over 10 min (1.3 L total sample volume) onto a Tenax adsorbent. This was then loaded into the inlet of a gas chromatograph with flame ionization detection (GC/FID, Agilent 6890N), desorbed, and then injected onto an HP-5 column (15 m × 0.53 mm ID × 1.5 μm thickness, Hewlett-Packard). Desorption was at 270 °C for 15 min onto the column held at 30 °C. Next the oven was ramped from 30 to 280 °C at 10 °C/min and held at 280 °C for 5 min. The mass response of the detector was calibrated by spiking the Tenax cartridges with 0.5 μL of standard solution and analyzing them following the previously described method. Standard solutions of 25 mL volume each with concentrations ranging from 1 mM to 11 mM of dodecane in cyclohexane were prepared for these calibrations. The O_3 and NO_x were monitored using a standard UV absorption O_3 analyzer (Horiba, APOA 360) and a chemiluminescence NO_x analyzer (Horiba, APNA 360). During the injection period and before lights on, the temperature was around 293−294 K. After lights on, the temperature for all experiments ranged between 296 and 298 K, and relative humidity levels remained <5%.

The gas-phase chemistry was tracked using measurements from a CIMS, consisting of a modified Varian 1200 quadrupole mass spectrometer to accommodate a custom ionization region. The general operation and details of the instrument have been discussed previously.[23−25] In negative mode operation, the use of CF_3OOCF_3 reagent gas makes the instrument ideal for measuring hydroperoxide containing compounds and acidic species, as described in studies of CF_3OOCF_3 chemistry.[26] For a more strongly acidic species [H·X], the transfer product is formed during ionization $[H{\cdot}X{\cdot}F]^-$, resulting in a nominal mass-to-charge ratio, m/z, of $[M+19]^-$, where M is the molecular weight of the analyte. For less acidic species and hydroperoxides [R], the cluster product forms $[R{\cdot}CF_3O]^-$, or $m/z = [M+85]^-$. Carboxylic acids such as acetic and formic acids tend to have equal contributions to the transfer and cluster product, in which case the overall signal of a compound is considered as the sum of the two product channels. In positive mode operation, an analyte R can undergo proton transfer reaction generating an ion of the form $[R{\cdot}H]^+$ and/or react with n positively charged water clusters to form a cluster in the form of $[(H_2O)_n{\cdot}R{\cdot}H]^+$. Hydroperoxide species tend to undergo dehydration after protonation, and are thus monitored at nominal $m/z = [M-17]^+$.[27] Unfortunately, due to mass tuning shifts midproject, the positive mode m/z's reported do not reflect the expected m/z from the clustering theory, but use of this mode of the CIMS was essential for tracking less polar compounds such as the carbonyl and, in some instances, where product m/z's were out of range for the mass scan in negative

Table 1. Dodecane Low-NO_x Experiments

expt date	hrs of photooxidation	initial HC (ppb)	$[NO]_0$ (ppb)	$[NO_x]_0$ (ppb)	$[O_3]_0$ (ppb)	initial seed vol. ($\mu m^3 cm^{-3}$)	ΔHC (ppb)	peak organic[a] ($\mu g\ cm^{-3}$)
1/16/2011	18	34.2 ± 1.6	<LDL	<LDL	2.7	9.1 ± 0.3	32.0 ± 2.1	54.6
3/13/2011	36	34.9 ± 1.6	<LDL	<LDL	2.6	11.4 ± 1.5	33.6 ± 2.1	62.8
3/16/2011	18	33.0 ± 1.6	<LDL	<LDL	3.3	12.0 ± 1.2	32.3 ± 2.1	51.3

[a]Not corrected for particle wall loss.

mode operation. The positve mode m/z's are reported as monitored during the experiment, but suggested assignments were made using a back calibration of the shift of m/z, generally upward by five atomic mass units (amu) in the m/z range of interest from 200 to 220. While the CIMS is capable of measuring a diverse array of chemical species, specificity is challenged when isomers or different compounds with the same nominal MW contribute to the same m/z signal, which has unit mass resolution. In this study, many isomers are formed because there are many possible locations of hydroxyl radical attack on the starting chain. The CIMS signal at one m/z represents the summed contribution of all the isomers. Isomeric compounds in this study were mostly problematic for distinguishing the acids, in that one cannot fully distinguish the difference between a C_n peracid, C_n hydroxycarboxylic acid, and a C_{n+1} hydroperoxide, as discussed in the results section on acid formation.

Particle size distribution and number concentration measurements are made with a cylindrical differential mobility analyzer (DMA; TSI Model 3081) coupled to a condensation particle counter (TSI Model 3010). A logarithmic scan from a mobility diameter of 10 nm to 1 μm is completed every 90 s. Sheath and excess flows of 2.5 LPM were used, with a 5:1 flow rate ratio of sheath-to-aerosol (i.e., a resolving power of 5). An Aerodyne HR-ToF-AMS,[28−30] hereafter referred to as the AMS, continuously measured submicrometer nonrefractory aerosol composition at 1 min resolution switching between the higher resolution, lower sensitivity W mode and the lower resolution, higher sensitivity V mode. A detailed discussion of the AMS method for the automated m/z calibration, mass accuracy, mass resolution of V and W modes, the high-resolution ion fitting algorithm, and ion signal integrations at the same integer mass is presented in previous work.[29] The AMS ions (organic) are reported with a relative ionization efficiency of 1.4.[30]

Experimental Protocols. To maximize total OH exposure, a set of experiments was designed following phased instrument sampling protocols similar to those used in the work of Loza et al.[31] to capture 36 h of total photooxidation while preserving reactor volume. In this study, the 36 h time series is achieved by combining data from an 18 h experiment during which all instruments are online and a 36 h experiment during which all instruments but the AMS are offline during the first 20 h of oxidation. Relative humidity and temperature were monitored for the full 36 h. Thus, the concatenated time series for many instruments (i.e., the CIMS, DMA, NO_x, and O_3 analyzers) is that of the 18 h experiment and the last 16 h of the 36 h experiment. A list of the experiments used for this study are in Table 1. The March experiments used another DMA with a lower total effective flow rate. General consistency between the AMS and CIMS measurements across the two 18 h experiments is observed (see Supporting Information, Figure S1). In the 18 h January experiment, CIMS traces for negative mode ions at m/z > 300 were included; the mass scan was reduced to $m/z \leq 300$ in the March experiments. The January experiment also provided evidence for supporting alternate positive mode m/z's used for monitoring select hydroperoxide species in the March experiments, which would otherwise be best monitored by the negative mode in the m/z range >300 (see Supporting Information, Figure S2).

Injection protocols were the same for all experiments. Two-hundred eighty microliters of a 50% by weight solution of hydrogen peroxide in water was measured using a glass syringe and injected into a glass trap. The trap was submerged in a warm water bath (~35−38 °C) while 5 LPM of the purified injection air flowed through the trap and into the chamber evaporating the hydrogen peroxide over approximately 90 min. This results in an approximate starting hydrogen peroxide concentration of 4 ppm. Next a 0.015 M aqueous ammonium sulfate solution was atomized into the chambers providing ~11 $\mu m^3/cm^3$ volume concentration of seed prior to lights on, as measured by the chamber DMA. Finally, 9 μL of dodecane (Sigma-Aldrich, 98% purity) was injected into a glass bulb and connected within six inches to a reactor injection port via 1/4″ o.d. polytetrafluoroethylene (PTFE) tubing. This led to a 10 inch line of 1/4″ o.d. PTFE internal to the reactor from the injection port to ensure injection would not be directly to the reactor wall. Using a heat gun with gentle heat, the dodecane evaporated into a flow of 5 LPM of purified injection air going into the chamber. This injection method was performed as close to the chamber as possible to prevent losses of the parent hydrocarbon during line transfer. The resulting dodecane concentration in the chamber was about 34 ppb. Each experiment's starting concentration is listed in Table 1. After loading the reactors, an hour period elapsed to allow for mixing. Then, the blacklights were turned on initiating generation of the OH radical from H_2O_2 photolysis.

Experimental Controls. A thorough discussion on characterizations of the particle-phase wall loss for longer experiments in the Caltech Environmental Chamber appears elsewhere.[31] For this study, we estimate that by 18 and 36 h of oxidation, approximately 15% and finally 28% of the particle volume has been lost to the walls when comparing DMA suspended volume and wall loss corrected particle volume. A diagnostic dark vapor-phase wall-loss experiment was performed by injecting 60 ppb 2-dodecanone into the chamber and monitoring its decay in the dark over 22 h. Although there was an observed loss of 14% CIMS dodecanone signal over 22 h from its initial signal after injection, one cannot eliminate the possibility of immediate wall-loss or transfer loss during the injection and mixing period (~75 min total). Because handling of the standard proved difficult for establishing a confident calibration curve for the CIMS, this could not be verified. No appreciable formation of > C_3 acids and hydroperoxide species above the background noise from the CIMS measurements was observed, and no aerosol volume above the limit of detection (~0.6 $\mu m^3\ cm^{-3}$) was produced by 22 h as measured by the DMA. Further investigation would be necessary for the goal of mass closure. In order to verify the fragmentation pattern of

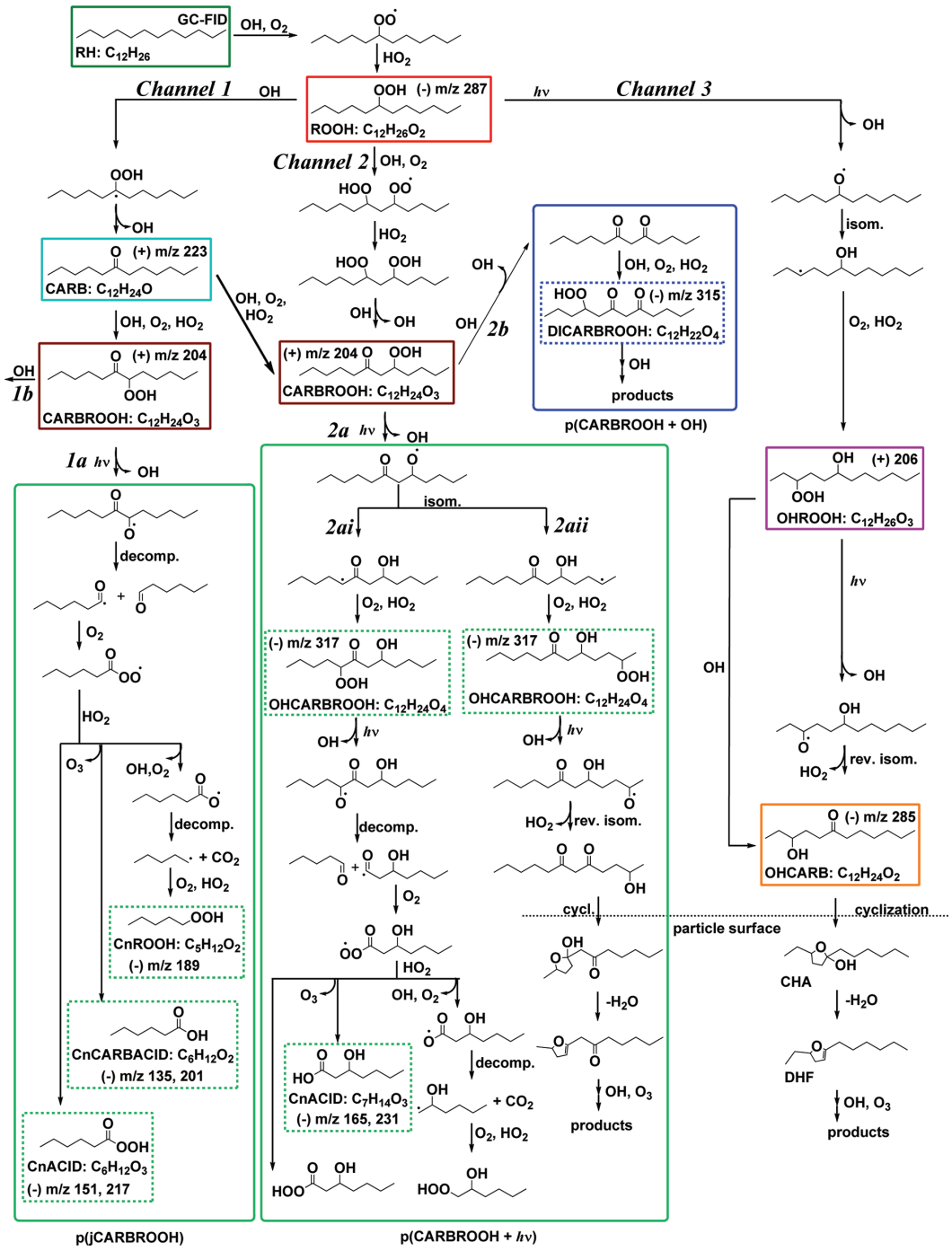

Figure 1. Dodecane low-NO_x mechanism. This scheme explicitly shows OH attack at the C_6 position; however, abstraction of other hydrogens on secondary carbons can also occur. Reaction of dodecane with OH forms a hydroperoxide (ROOH). The hydroperoxide undergoes successive reactions to generate the carbonyl hydroperoxide (CARBROOH, Channel 1 and Chanel 2) or photolyzes to form the hydroxy hydroperoxide (OHROOH, Channel 3). The solid colored boxes indicate compounds or reaction pathways photochemically simulated. CIMS monitored species have m/z noted. Dashed colored boxes indicate compounds monitored by CIMS, but not explicitly simulated in the photochemical mechanism. The gray dashed line denotes a gas−particle interface where 1,4-hydroxycarbonyl (OHCARB)-like compounds reactively uptake onto the particle and cyclize to form a cyclic hemiacetal (CHA).

dx.doi.org/10.1021/jp211531h | J. Phys. Chem. A 2012, 116, 6211−6230

Table 2. Reactions Included in the Gas-Phase Photochemical Model

rxn #	reaction	k	ref.
1	$H_2O_2 + h\nu \rightarrow 2OH$	$j_{H_2O_2} = 2.87 \times 10^{-6}$ s^{-1}	JPL[37] + chamber irradiance data
2	$H_2O_2 + OH \rightarrow HO_2 + H_2O$	$k_1 = 1.8 \times 10^{-12}$ cm^3 molecule^{-1} s^{-1}	JPL[37]
3	$RH + OH \rightarrow RO_2 + H_2O$	$k_2 = k_{OH} = 13.2 \times 10^{-12}$ cm^3 molecule^{-1} s^{-1}	Atkinson, 1997[14]
4	$RO_2 + RO_2 + M \rightarrow pRO_2RO_2 + M$	$k_3 = 5 \times 10^{-15}$ cm^3 molec^{-1} s^{-1}	Atkinson, 1997[14]
5	$RO_2 + HO_2 \rightarrow ROOH + O_2$	$k_4 = 2.16 \times 10^{-11}$ cm^3 molecule^{-1} s^{-1}	MCM 3.2
6	$HO_2 + HO_2 \rightarrow H_2O_2 + O_2$	$k_5 = 1.5 \times 10^{-12}$ cm^3 molec^{-1} s^{-1}	JPL[37]
7	$OH + HO_2 \rightarrow H_2O + O_2$	$k_6 = 1.1 \times 10^{-10}$ cm^3 molecule^{-1} s^{-1}	JPL[37]
8	$OH + OH \rightarrow H_2O_2$	$k_7 = 6.28 \times 10^{-12}$ cm^3 molec^{-1} s^{-1}	JPL[37]
9	$ROOH + OH \rightarrow CARB$	$k_8 = 7.4 \times 10^{-12}$ cm^3 molecule^{-1} s^{-1}	JPL[37]
10	$ROOH + h\nu \rightarrow RO + OH$	$j_{ROOH} = 2.30 \times 10^{-6}$ s^{-1}	MCM 3.2 + chamber irradiance data
11	$RO + O_2 \rightarrow OHRO_2$	$k_9 = 2.59 \times 10^{-6}$ cm^3 molecule^{-1} s^{-1}	MCM 3.2
12	$OHRO_2 + HO_2 \rightarrow OHROOH + O_2$	$k_{10} = k_4$	MCM 3.2
13	$CARB + OH \rightarrow CARBRO_2 + H_2O$	$k_{11} = 1.49 \times 10^{-11}$ cm^3 molecule^{-1} s^{-1}	MCM 3.2
14	$CARBRO_2 + HO_2 \rightarrow CARBROOH$	$k_{12} = k_4$	MCM 3.2
15	$CARB + h\nu \rightarrow pjCARB$	$j_{CARB} = 3.32 \times 10^{-7}$ s^{-1}	MCM 3.2 + chamber irradiance data
16	$CARBROOH + OH \rightarrow p(CARBROOH + OH)$	$k_{13} = 9.10 \times 10^{-11}$ cm^3 molecule^{-1} s^{-1}	MCM 3.2
17	$CARBROOH + h\nu \rightarrow p(jCARBROOH)$, aka $p(CARBROOH + h\nu)$	j_{ROOH}	MCM 3.2 + chamber irradiance data
18	$OHROOH + OH \rightarrow OHCARB$	$k_{14} = 4.97 \times 10^{-11}$ cm^3 molecule^{-1} s^{-1}	MCM 3.2
19	$OHROOH + h\nu \rightarrow pjOHROOH$	j_{ROOH}	MCM 3.2 + chamber irradiance data
20	$pjOHROOH \rightarrow OHCARB + HO_2$	$k_{15} = 2.83 \times 10^{7}$ cm^3 molecule^{-1} s^{-1}	MCM 3.2
21	$RO_2 + NO \rightarrow 0.56\ RO + 0.44\ pRONO_2$	$k_{16} = 9.04 \times 10^{-12}$ cm^3 molecule^{-1} s^{-1}	MCM 3.2
22	$OHRO_2 + NO \rightarrow 0.176\ OHRO + 0.824\ pOHRONO_2$	$k_{17} = k_{16}$	MCM 3.2
23	$CARBRO_2 + NO \rightarrow CARBRO$	$k_{18} = k_{16}$	MCM 3.2
24	$OHRO_2 + RO_2 \rightarrow pOHRO_2RO_2$	$k_{19} = k_3$	MCM 3.2
25	$CARBRO_2 + RO_2 \rightarrow pCARBRO_2RO_2$	$k_{20} = k_3$	MCM 3.2
26	$RO_2 + NO_2 \rightarrow pRO_2NO_2$	$k_{21} = 9.0 \times 10^{-12}$ cm^3 molecule^{-1} s^{-1}	JPL[37]
27	$OHRO_2 + NO_2 \rightarrow pOHRO_2NO_2$	$k_{22} = k_{21}$	JPL[37]
28	$CARBRO_2 + NO_2 \rightarrow pCARBRO_2NO_2$	$k_{23} = k_{21}$	JPL[37]

hydroperoxide species in the AMS spectrum, a seeded photooxidation experiment was run with a target injection of 300 ppb octadecane ($C_{18}H_{38}$) using the experimental protocols discussed earlier. The first generation hydroperoxide ($C_{18}H_{38}O_2$) immediately partitions to the particle-phase, and a distinct AMS ion at nominal m/z = 253 ($C_{18}H_{37}^+$) appeared after lights on, suggesting that hydroperoxide species fragment to form ions of the form $[M\text{-}33]^+$, where M is the molecular weight of the hydroperoxide species.

DODECANE LOW-NO_x GAS-PHASE MECHANISM

The OH-initiated photoxidation of *n*-alkanes has been studied previously, providing a framework of well-known chemical reactions under varying NO_x conditions[14,15] that can be extended to the case of dodecane. Such reactions are also included in the Master Chemical Mechanism 3.2 (MCM 3.2) via Web site: http://mcm.leeds.ac.uk/MCM.[32,33] The reactions proposed in such previous studies in conjunction with gas-phase measurements from this study afforded the development of a mechanism for the photoxidation of dodecane under low-NO_x conditions where $RO_2 + HO_2$ chemistry dominates (see Figure 1). Reaction pathways past the carbonyl hydroperoxide (CARBROOH) along Channel 1a and Channel 2b are not included in the MCM 3.2 for dodecane. For clarity, colored boxed molecules with simple labels are those that were explicitly simulated in the photochemical mechanism and are represented in the reactions of Table 2, consistent with the color scheme comparing CIMS measurements and simulated output in Figure 2 (RH, ROOH, CARB, CARBROOH, OHROOH, and OHCARB). In some cases, a group of products was not modeled explicitly, so a reaction pathway is boxed and labeled (p(jCARBROOH), p(CARBROOH + hν), and p(CARBROOH + OH)). Boxed molecules with a dashed border indicate those that have been monitored by the CIMS including the m/z that was monitored, but they were not explicitly modeled in the photochemical mechanism (CnROOH, CnCARBACID, CnACID, OHCARBROOH, and DICARBROOH). Reaction channels are noted with alphanumeric labels, and the labels for molecules or product channels of interest are referred to throughout the text. OH attack is explicitly shown at the C_6 carbon, although it is expected that any of the hydrogens on secondary carbons will be similarly vulnerable to abstraction by the OH radical. Using estimated structure activity relationship reaction rate constants,[34] OH abstraction of the hydrogens on the primary carbons would only represent two percent of the overall reaction rate of dodecane with OH. Five generations of chemistry are represented in the reaction pathways of Figure 1, with a generation defined as the OH-initiated or photolysis reaction of a stable (nonradical) compound. The mechanism provides an overview of the types of products generated from the alkyl peroxy radical RO_2 exclusively reacting with HO_2 to generate hydroperoxides, which then react with OH or undergo photolysis. While a wide variety of compounds are included in the mechanism shown in Figure 1, this mechanism is by no means exhaustive of all possible compounds formed in terms of functional group placement and molecular structure.

Low-NO_x Conditions. Under conditions in which $[HO_2] \gg [RO_2]$, and in which NO_x levels are very low, RO_2 can be expected to react exclusively with HO_2. For the experimental conditions, the HO_2 is calculated by a photochemical model. The HO_2 concentration ($\sim 1 \times 10^{10}$ molecules cm^{-3}) exceeds

dx.doi.org/10.1021/jp211531h | J. Phys. Chem. A 2012, 116, 6211–6230

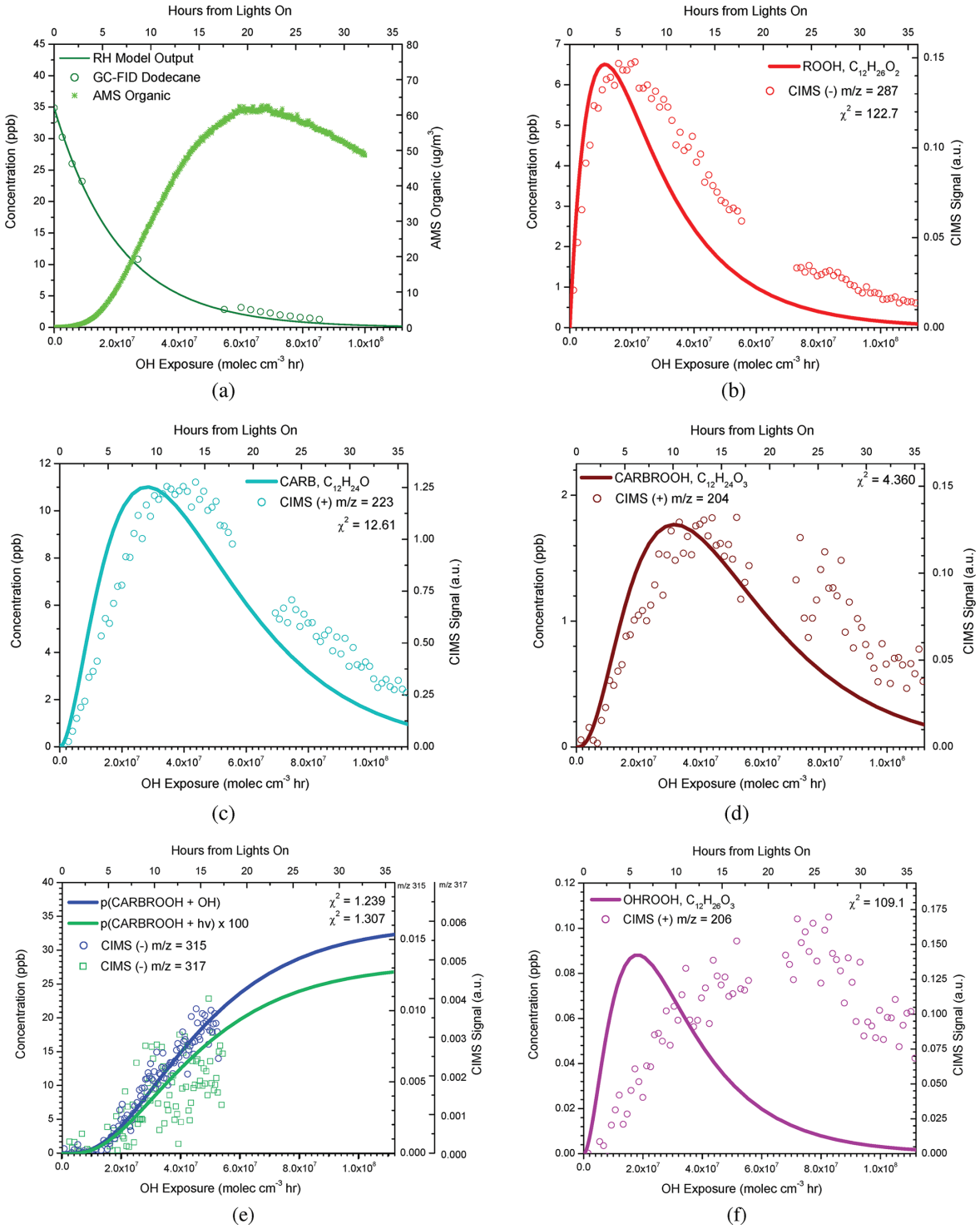

Figure 2. continued

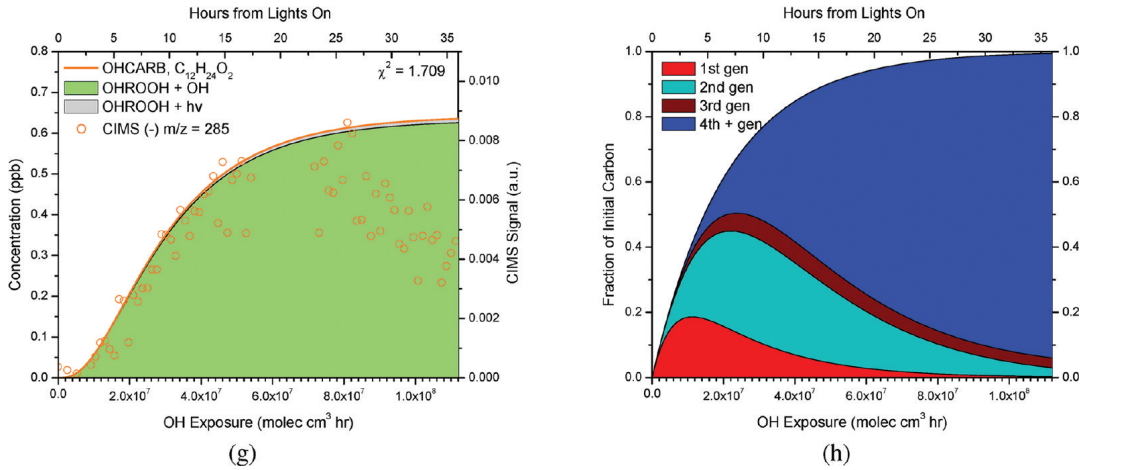

Figure 2. Simulated (curves) and observed (open circles) time evolutions of various gas-phase species from OH-initiated photoxidation of dodecane. Colors used match species outlined in the gas-phase mechanism. (a) Decay of dodecane parent hydrocarbon with suspended organic growth. (b) First-generation formation of the hydroperoxide (ROOH) monitored at (−) m/z 287. (c) Second-generation formation of the ketone (CARB) monitored at (+) m/z 223. (d) Third-generation formation of the carbonyl hydroperoxide (CARBROOH) monitored at (+) m/z 204. (e) Simulated output of remaining carbon from further oxidation of the carbonyl hydroperoxide p(CARBROOH + OH) as (−) m/z 315 or photolysis p(CARBROOH + hν) as (−) m/z 317. (f) Photolysis of the hydroperoxide (ROOH) leads to formation of a hydroxy hydroperoxide (OHROOH) monitored at (+) m/z 206. (g) Formation of the hydroxycarbonyl (OHCARB) from two sources: (1) photolysis of the hydroxy hydroperoxide (OHROOH + hν) and (2) OH reaction with the hydroxy hydroperoxide (OHROOH + OH). (h) Simulated fraction of initial carbon in the gas-phase by generation over the course of the experiment.

that of RO_2 (~1 × 10^8 molecules cm^{-3}) by 2 orders of magnitude. The dominant route of RO_2 chemistry is reaction with HO_2 to form hydroperoxide compounds. It is important to note that what determines low-NO_x or high-NO_x conditions is not merely dependent on the HO_2 concentration iteslf; rather, the conditions are defined by the dynamics of NO and RO_2 and the various reaction rate constants. For example, the reaction rate constants for CH_3O_2 with HO_2, CH_3O_2, NO, and NO_2 at 298 K are 5.2 × 10^{-12} cm^3 $molecule^{-1}$ s^{-1}, 3.7 × 10^{-13} cm^3 $molecule^{-1}$ s^{-1}, 6.5−7.8 × 10^{-12} cm^3 $molecule^{-1}$ s^{-1}, and 3.9 × 10^{-12} cm^3 $molecule^{-1}$ s^{-1}, respectively.[14] On the basis of these rate constants, CH_3O_2 lifetime against reaction with these species increases in the order of NO, HO_2, NO_2, and CH_3O_2. However, sufficient concentrations of HO_2 and/or CH_3O_2 as compared with NO would shift the conditions to an effectively low-NO_x regime of chemistry, in which the relative concentrations of HO_2 and CH_3O_2 would then determine whether the low-NO_x regime is dominated by CH_3O_2 + HO_2 or shared with CH_3O_2 + CH_3O_2.

Without any addition of NO_x, a small amount of NO_x, presumably from residual nitrogen-containing acids (e.g., HONO or HNO_3) on the chamber walls, is generated upon irradiation. This phenomenon of "NO_x offgasing"[35] is a common observation among environmental chambers.[35,36] In the chamber experiments to be described, the NO concentration is below the limit of detection (~ 5 ppb), and the NO_2 generated is <5 ppb. While the total generated NO_x is primarily in the form of NO_2, NO_2 cannot be calibrated directly with this technique, and there are fewer calibration points at this lower range leading to some uncertainty in the measurement. Low-NO_x conditions in the chamber are further verified by CIMS measurements of HO_2NO_2 pernitric acid (PNA), the formation of which is highly sensitive to the HO_2:NO_2 ratio. Using the CIMS sensitivity to PNA,[24] the PNA concentration generated upon lights on is <350 pptv. As discussed in the work of Paulot et al.,[24] it is likely that the sensitivity to PNA is overestimated due to ligand exchange of H_2O_2 with the reagent ion. Using the expected HO_2 concentration generated upon irradiation, and the equilibrium constant for HO_2 + NO_2 ⇌ HO_2NO_2, 1.6 × 10^{-11} cm^3 $molec^{-1}$,[37] the predicted NO_2 residual concentration is <1.2 ppb.

To explore possible effects of residual NO_x, the chemistry was simulated with initial concentrations of NO at 0.1 ppb, 2 ppb, and constant NO at 0.1 ppb, using all reactions in Table 2. Under these varying NO_x conditions, we estimate that <1%, < 10%, and <19%, respectively, of the dodecane reacts via RO_2 + NO_x reactions. Relative lifetimes of RO_2 against reaction with RO_2, HO_2, NO, and NO_2 for these varying NO_x conditions are provided in the Supporting Information, Table S1. The two species, the 1,4-hydroxycarbonyl (OHCARB, Figure 1) and the hydroxy hydroperoxide (OHROOH, Figure 1) that would be most affected by the presence of NO_x are shown based on NO concentration and provided in the Supporting Information, Figure S3. At NO concentration greater than 0.1 ppb, the delay seen in the CIMS measurement of the 1,4-hydroxycarbonyl is not reproduced (Supporting Information, Figure S3a). The 1,4-hydroxycarbonyl is an important intermediate in SOA formation in the presence of NO_x,[12,38] so the presence of NO should enhance its production and contribute to initial organic growth. The observed delay in the organic growth as measured by the AMS is consistent with the absence of any appreciable NO_x in the system. Further, the presence of NO should accelerate formation of the hydroxy hydroperoxide (OHROOH) (Supporting Information, Figure S3b), causing the simulations to further deviate from the observed gas-phase measurements. These analyses support the fact that residual NO_x does not play a significant role in the overall chemistry represented and that the majority of alkoxy radical formation is not a result of RO_2 + NO chemistry. In addition, CIMS spectra show no evidence of nitrate compounds formed. Thus, the

photochemical mechanism used in the remainder of this study excludes the presence of NO_x.

Hydroperoxide Photolysis. The OH-initiated reaction of dodecane results in the formation of the peroxy radical which, upon reaction with HO_2, rapidly produces the hydroperoxide ($C_{12}H_{26}O_2$, ROOH in Figure 1). The hydroperoxide can undergo further reaction with OH or photolyze. In the absence of an explicit photolysis rate, following MCM 3.2, the methyl hydroperoxide photolysis rate is used as a proxy for the photolysis rate of hydroperoxide species. Using absorption cross sections and quantum yields for methyl hydroperoxide (CH_3OOH)[39,40] with the actinic flux calculated from spectral irradiance measurements in the chamber using a LICOR spectroradiometer, the expected photolysis rate constant of methyl hydroperoxide is calculated to be $j = 2.30 \times 10^{-6}$ s^{-1}. Under these experimental conditions, the C_{12} hydroperoxide is simulated in the mechanism to react with OH and undergo photolysis in branching ratios of 86% and 14%, respectively. The most likely route of photolysis is to sever the O−OH bond rather than the C−OOH bond in the hydroperoxy group,[41] resulting in the formation of an alkoxy radical. In the domain of $RO_2 + HO_2$ chemistry, alkoxy radicals can be generated only via photolysis of a hydroperoxy group; there is no formation of simple alcohols, which is the same when NO_x is present.[9,11,14,15] Along Channel 3 of the mechanism in Figure 1, the hydroperoxide photolyzes to generate the alkoxy radical. Due to the length of the carbon chain, isomerization through a 1,5-hydride shift will occur,[9,11,15] generating a hydroxy group and leaving a radical on a secondary carbon. Reaction of this radical with O_2 followed by reaction with HO_2 leads to the hydroxy hydroperoxide ($C_{12}H_{26}O_3$) referred to as OHROOH in Figure 1, which can undergo photolysis or further reaction with OH. Under photolysis, the same reverse isomerization of the resulting hydroxy alkoxy radical occurs to form a 1,4-hydroxycarbonyl ($C_{12}H_{24}O_2$)[9,11] referred to as OHCARB in Figure 1. On the basis of the calculated photolysis rate constant of methyl hydroperoxide as a proxy and the OH concentration lumped reaction rate constant, $k_{OH} = 9.94 \times 10^{-5}$ s^{-1}, generation of the 1,4-hydroxycarbonyl (OHCARB) via reaction with OH is the preferred pathway. The 1,4-hydroxycarbonyl is estimated to react with OH and undergo photolysis in branching ratios of 98% and 2%, respectively, according to the photochemical simulation. In the case of reaction with OH, the positions of the carbonyl and hydroxy groups would be switched from what is shown in the mechanism. This formation mechanism of the 1,4-hydroxycarbonyl (OHCARB) is also distinct from the predominant reverse isomerization mechanism when in the presence of NO_x.[9,11,14,15] Still, an even quicker route of formation is through alkyl peroxy radical isomerization with an extrapolated isomerization rate constant of 0.03 s^{-1} at 298 K, which is applicable to the conditions of $[RO_2] < 6 \times 10^{12}$ molecules cm^{-3} and $[NO] < 3 \times 10^9$ molecules cm^{-3}.[15,42,43] Since the NO concentration is only confidently known to be <5 ppb or 1×10^{11} molecules cm^{-3} (the lower detection limit of our NO_x analyzer), the alkyl peroxy radical isomerization route is unconfirmed.

Hydroperoxide + OH. The hydroperoxide primarily reacts with OH, in which abstraction of the hydrogen from the hydroperoxy-containing carbon is favored.[41] This leads to decomposition of the hydroperoxy group to form a carbonyl ($C_{12}H_{24}O$), resulting in recycling of OH radical (Channel 1, CARB in Figure 1). In the case in which the OH attacks another secondary carbon along the hydroperoxide chain, a dihydroperoxide, $C_{12}H_{26}O_4$, (Channel 2 in Figure 1) may be formed. Reaction of the carbonyl or the dihydroperoxide with OH would generate the third-generation carbonyl hydroperoxide (CARBROOH), with chemical formula $C_{12}H_{24}O_3$. OH reaction with the carbonyl generally favors attack at a carbon beta from the existing carbonyl group;[34] however, a small fraction could occur at the α position. Depending on the relative positions of the carbonyl and hydroperoxy group, fragmentation or functionalization will occur. In the case of Channel 1, the carbonyl and hydroperoxy groups are on adjoining carbons, such that when photolysis of the hydroperoxy group generates the alkoxy radical, scission of this C−C bond is favored. Products along Channel 1a are referred to as p(jCARBROOH) in reaction 17 of Table 2. Decomposition of the carbonyl alkoxy radical leads to an acyl radical and an aldehyde. The eventual fate of the acyl radical is reaction with O_2 to generate an acyl peroxy radical, which reacts with HO_2 to generate acids (Channel 1a, CnCARBACID and CnACID) and eventually a shorter chain hydroperoxide (Channel 1a, CnROOH). While the formation of aldehydes and acids is reliant upon the formation of a less abundant form of the carbonyl hydroperoxide and its photolysis, Channel 1a serves an important role in generating aldehydes in a system with hydroperoxide species. These aldehydes can react in the particle phase to form PHAs, to be discussed later in the paper.

In the case of the carbonyl and hydroperoxy groups located beta to one another (Channel 2), photolysis (Channel 2a) or reaction with OH (Channel 2b) leads to more highly functionalized compounds than if the C_{12} backbone is fragmented as in Channel 1a. Products along Channel 2a are collectively referred to as p(CARBROOH + hν) in reaction 17 (Table 2), and products along Channel 2b are referred to as p(CARBROOH + OH) in reaction 16 (Table 2). In chemistry analogous to the photolysis route (Channel 3) of the initial hydroperoxide (ROOH), functionalization is achieved by gain of a hydroxy group through isomerization, leading to a multifunctional compound containing carbonyl, hydroxy, and hydroperoxide groups (Channel 2a). Again, the relative positions of these functional groups lead to hydroxy acids formation through photolysis (Channel 2ai, CnACID) or a 1,4-hydroxycarbonyl with an additional keto group (Channel 2aii). Consecutive OH reaction with the carbonyl hydroperoxide (CARBROOH) would lead to multiple keto groups forming from the previous hydroperoxide group (Channel 2b). However, the competitive photolysis of hydroperoxy groups leads to the variety in functionalization as in Channel 2a. Although the fate of the carbonyl hydroperoxide (CARBROOH) is likely to channel more carbon through reaction with OH (pCARBROOH + OH), (Channel 2b), the gas-phase chemistry in Channel 1a becomes important for SOA growth and will be discussed subsequently.

COMPARISON OF GAS-PHASE MECHANISM AND MEASUREMENTS

The dodecane−OH mechanism derived from the MCM 3.2[32,33] (Table 2) was used to simulate the first four generations of chemistry. The simulated hydrocarbon decay agrees with GC-FID measurements of dodecane in Figure 2a. The photolysis rate for H_2O_2 was calculated using the absorption cross section and quantum yield[39,40] with the chamber actinic flux, analogous to the calculation done for hydroperoxide species. The simple labels for compounds in Figure 1 are also used in the legend entries for the photochemical mechanism

and CIMS measurements comparisons throughout Figure 2. CIMS traces are referred to with a polarity as "(+)" or "(−)" preceding the m/z solely to indicate the ionization mode used, positve or negative, respectively. Table 3 provides a summary of the monitored CIMS ions and their suggested assignments.

Table 3. Signals Monitored by CIMS and Their Suggested Assignments

mode	m/z (s)	assignment	molecular formula
(−)	287	ROOH	$C_{12}H_{26}O_2$
(+)	223	CARB	$C_{12}H_{24}O$
(+)/(−)	204/301[a]	CARBROOH	$C_{12}H_{24}O_3$
(+)/(−)	206/303[a]	OHROOH	$C_{12}H_{26}O_3$
(−)	285	OHCARB	$C_{12}H_{24}O_2$
(−)	315[a]	DICARBROOH	$C_{12}H_{22}O_4$
(−)	317[a]	OHCARBROOH	$C_{12}H_{24}O_4$
(−)	187	C5CARBACID	$C_5H_{10}O_2$
(−)	135/201	C6CARBACID	$C_6H_{12}O_2$
(−)	149/215	C7CARBACID	$C_7H_{14}O_2$
(−)	163/229	C8CARBACID	$C_8H_{16}O_2$
(−)	177/243	C9CARBACID	$C_9H_{18}O_2$
(−)	191/257	C10CARBACID	$C_{10}H_{20}O_2$
(−)	205/271	C11CARBACID	$C_{11}H_{22}O_2$
(−)	203	C5ACID/C6ROOH	$C_5H_{10}O_3/C_6H_{14}O_2$
(−)	151/217	C6ACID/C7ROOH	$C_6H_{12}O_3/C_7H_{16}O_2$
(−)	165/231	C7ACID/C8ROOH	$C_7H_{14}O_3/C_8H_{18}O_2$
(−)	245	C8ACID/C9ROOH	$C_8H_{16}O_3/C_9H_{20}O_2$
(−)	193/259	C9ACID/C10ROOH	$C_9H_{18}O_3/C_{10}H_{22}O_2$

[a]Denotes negative mode ions at m/z > 300 monitored in the January 18 h experiment. All other m/z's were monitored in the January and March experiments.

The mechanism was used primarily for evaluating time profiles of expected products in the CIMS measurements. The scales for the CIMS signal and the simulated output have been adjusted for peak matching to compare the trends in Figure 2. Reduced χ^2 values are given for the fit of the simulated trace and the CIMS measurements using the maximum value for the first 18 h as the normalization parameter. The χ^2 for the simulated and measured 1,4-hydroxycarbonyl (OHCARB) is for the first 18 h since the measurement decays, but the simulation does not include a reactive sink. Vapor-phase wall loss is not treated here in the photochemical model or in correcting the gas-phase observations (for reasons described in the Experimental Section), although it is likely to play a role affecting the more highly oxidized lower volatility products formed as in other chamber studies.[44,45] While the gas-phase chemistry represented in the mechanism generally describes the gas-phase CIMS trends for many species such as the hydroperoxide (ROOH), carbonyl (CARB), and carbonyl hydroperoxide (CARBROOH), the hydroxy hydroperoxide (OHROOH) may be subject to greater vapor-phase wall loss, contributing to some of the discrepancy between the simulated and measured trace in the begininng of the experiment. This effect is discussed further in the following section.

Mechanism and Measurement Comparison of Hydroperoxide + OH. Mechanism predictions of the hydroperoxide (ROOH) capture the trend of the CIMS measurements for the hydroperoxide (−) m/z = 287 (Figure 2b). At its peak, the hydroperoxide is simulated to represent about 20% of the initial carbon. While the hydroperoxide production rate is captured by the ROOH photochemical mechanism, the simulated loss is overestimated. The loss processes for the hydroperoxide include ROOH + OH and ROOH + hν. As noted, the MCM 3.2 gives an explicit reaction rate constant for a C_{12} hydroperoxide with OH, but utilizes the photolysis rate of CH_3OOH as a general photolysis rate for all hydroperoxide species. Extrapolating the photolysis rate from a C_1 to a C_{12} hydroperoxide is a source of uncertainty in the simulated trace. The simulated chemistry is more rapid than the measurements, consistent with a faster than measured production rate of the carbonyl.

The MCM 3.2 mechanism for dodecane does not include explicit reactions for formation of the dihydroperoxide (Channel 2), although evidence exists in the CIMS data at (−) m/z = 319 (CF_3O^- cluster) that suggests formation. The possibility of alkyl peroxy radical isomerization[46] was also considered, but this is unlikely under these experimental conditions because the [HO_2] and [OH] are not low enough to extend the lifetime of the alkyl peroxy radical for it to isomerize. Because the carbonyl (CARB) is not sufficiently polar to be detected in the negative mode ionization, it was monitored in positive mode at (+) m/z = 223. The carbonyl measurements also track the mechanism simulations, although with a slight lag (Figure 2c). The carbonyl (CARB) forms quickly, simultaneously with the hydroperoxide generation, so its peak just after 10 h represents almost a third of the initial carbon. The carbonyl hydroperoxide (CARBROOH) monitored at (+) m/z = 204 also times well with the model output during growth, but the gas-phase concentration remains low overall because of its many reactive sinks.

Owing to the complexity of the many later generation products, these are not represented explicitly in the mechanism, and the simulation terminates with the remaining carbon represented in further reaction of the carbonyl hydroperoxide. This includes three possible routes as discussed previously and seen in Figure 1: (1) photolysis and subsequent decomposition if the carbonyl and hydroperoxy group are vicinal (Channel 1a), (2) photolysis of the hydroperoxy group beta to the carbonyl (Channel 2a), and subsequent decomposition products (Channel 2ai) or C_{12} retaining products (Channel 2aii), and (3) continued OH reaction and functionalization of the C_{12} molecule (Channel 2b). The respective photolysis of the α-carbonyl hydroperoxide (Channel 1a) and the β-carbonyl hydroperoxide photolysis (Channel 2a) or reaction with OH (Channel 2b) are represented in the mechanism scheme in Figure 1. However, the MCM 3.2 makes no distinction between reaction rates for isomers of the carbonyl hydroperoxide, so the sum of the α-carbonyl hydroperoxide (Channel 1) and the β-carbonyl hydroperoxide (Channel 2) are implemented in the photochemical simulation as (CARBROOH). Thus, the subsequent photolysis product from the α-carbonyl hydroperoxide (Channel 1a) and the β-carbonyl hydroperoxide (Channel 2a), respectively, will produce the same time trend from the photochemical simulation (Table 2, Reaction 17), although we distinguish the alpha photolysis products (Channel 1a) as p(jCARBROOH) and the beta photolysis products (Channel 2a) as p(CARBROOH + hν) for relevant discussion on a distinct set of products formed from photolysis of each isomer. That is, acid formation (Figures 3b and 4b) is considered as p(jCARBROOH), and the multifunctional formed via Channel 2a is considered as p(CARBROOH + hν) in Figure 2e.

Note that photolysis of the β-carbonyl hydroperoxide (Channel 2ai) produces a hydroxy carbonyl hydroperoxide

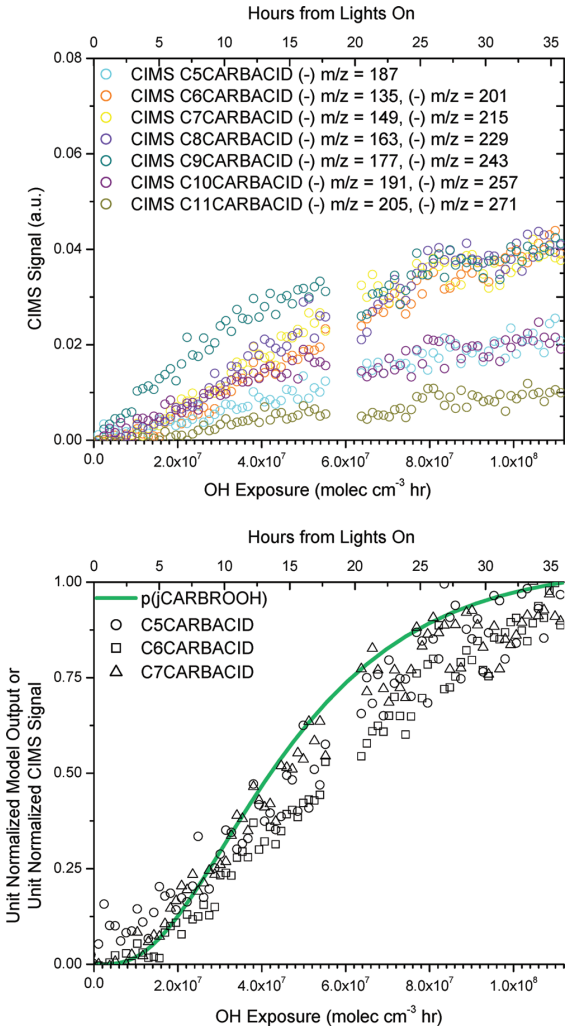

Figure 3. Carboxylic acids. (a) Series of suggested C_5 through C_{11} carboxylic acid traces and the ions measured in CIMS negative mode ionization. (b) Representative C_5 through C_7 carboxylic acid traces on a unit normalized scale trend with modeled results for photolysis of the carbonyl hydroperoxide.

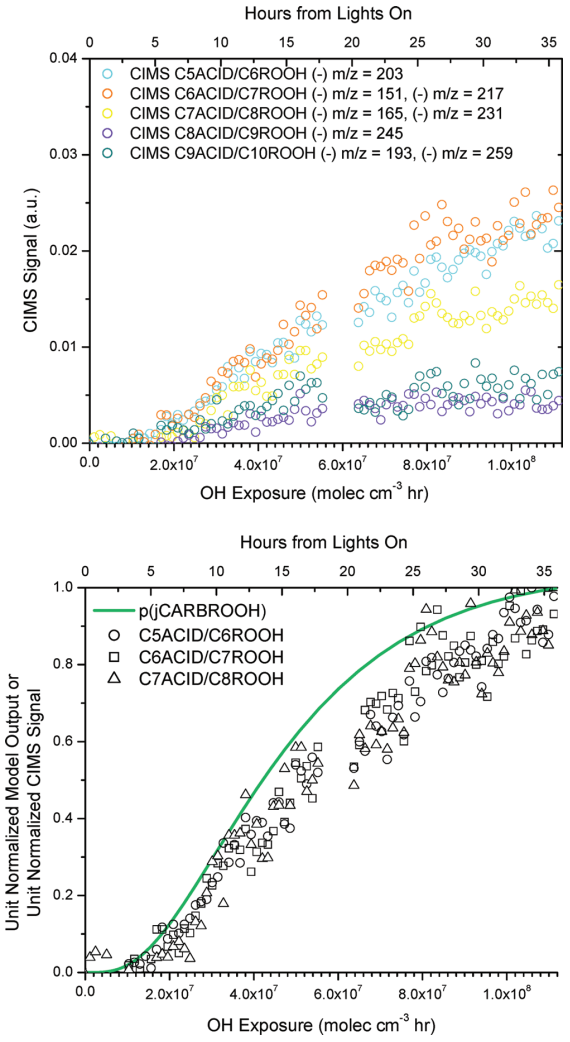

Figure 4. Acids (hydroxycarboxylic/peracid) or hydroperoxides. (a) Series of suggested C_5 through C_9 peracid and hydroxy carboxylic acid, and C_6 through C_{10} hydroperoxide traces. Since the peracid and hydroxy carboxylic acid are the same molecular weight as a hydroperoxide with one additional carbon, the ions measured by the CIMS may have contributions from all three species. (b) Example unit normalized trends of C_5 through C_7 peracids and hydroxycarboxylic acids, and C_6 through C_8 hydroperoxides that trend with the product of carbonyl hydroperoxide photolysis from the mechanism.

(OHCARBROOH) with the carbonyl and hydroperoxide groups vicinal. Photolysis of this multifunctional compound shows a parallel decomposition route to Channel 1a leading to hydroxy acids. Channel 2aii retains the C_{12} backbone, because, although it also starts with a hydroxy carbonyl hydroperoxide (OHCARBROOH), the carbonyl and hydroxy functional groups are nonvicinal to the −OOH group. Analogous to the treatment of the two carbonyl hydroperoxide (CARBROOH) isomers, these two hydroxy carbonyl hydroperoxide (OHCARBROOH) isomers are also not distinguished in the photochemical simulation; they are shown as p(CARBROOH + hν). That is, Figure 2e compares the simulated output of p(CARBROOH + hν) to the CIMS measured ion suggested for the multifunctional compound (presumably OHCARBROOH, $C_{12}H_{24}O_4$) at (−) m/z = 317 to represent Channel 2a. Products of the continued OH oxidation of the β-carbonyl hydroperoxide (Channel 2b) are simulated under p(CARBROOH + OH), which has a distinct output from that of the carbonyl hydroperoxide photolysis, represented identically in p(CARBROOH + hν) and p(jCARBROOH). Production of a possible dicarbonyl hydroperoxide (presumably DICARBROOH, $C_{12}H_{22}O_4$), monitored at (−) m/z = 315, represents this channel in the mechanism (Channel 2b). Note that the signals at (−) m/z = 317 and (−) m/z = 315 do not extend the full 36 h because they were not monitored for a full 36 h as described in the Experimental Section. More detailed treatment of Channel 1a is discussed subsequently relative to acid formation.

Mechanism and Measurement Comparison of Hydroperoxide Photolysis. The hydroxy hydroperoxide measurements exhibit the largest deviation of all CIMS traces from the simulated hydroxy hydroperoxide (OHROOH) (Figure 2f). While we cannot fully account for this discrepancy at the present time, it could be possible that (1) the hydroxy hydroperoxide formation is in fact slower than predicted by using the photolysis rate of a C_1 hydroperoxide for the C_{12} hydroperoxide and (2) the hydroxy hydroperoxide (OHROOH) has sufficiently low volatility that it may be lost to the chamber walls more quickly than other gas-phase compounds. We observe that the chemistry in general is actually slower than the simulation. That is, the simulated hydroperoxide (ROOH) exhibits a faster decay than that of the measurement (Figure 2b) and subsequent products (CARB, CARBROOH, and OHROOH) are simulated to rise more quickly than their individual measurements (Figure 2c,d,f). Hence, we do expect that OHROOH's actual rise will come later than that simulated. If gas-to-wall partitioning is responsible for the discrepancy, the walls may first act as a reservoir but subsequently release the hydroxy hydroperoxide back to the gas-phase as it is removed by secondary reactions, shifting the trend of the gas-phase measurement from the simulated trend. We return to the hydroxy hydroperoxide sinks in the SOA Growth section.

The 1,4-hydroxycarbonyl (OHCARB, Figure 2g) is generated from the hydroxy hydroperoxide (OHROOH, Figure 2f) in greater concentration than its precursor. As discussed earlier, the 1,4-hydroxycarbonyl may be formed via photolysis of the hydroxy hydroperoxide (OHROOH + hν) or via hydroxyl radical reaction with the hydroxy hydroperoxide (OHROOH + OH). The relative contributions from these sources to 1,4-hydroxycarbonyl (OHCARB) formation are shown in Figure 2g. The CIMS measurement of the 1,4-hydroxycarbonyl at (−) m/z = 285 follows the simulated production despite discrepancy in the simulation and measurement for its precursor, the hydroxy hydroperoxide (OHROOH). This may suggest that the true time profile for OHROOH is not captured by the measurement. The vapor pressure of OHROOH is about 2 orders of magnitude lower than OHCARB, so one hypothesis is that the early losses of OHROOH are due to vapor-phase wall loss to the reactor walls and reaction with OH to form OHCARB. Mass closure is needed to confirm whether the measurements match the expected OHROOH distribution among losses to the wall and its oxidation to OHCARB, but it is possible that if the OHROOH is converted quickly to OHCARB via reaction with OH (lifetime ∼ 2.8 h), then the trend in the CIMS measurement for OHCARB would still agree with the simulation early on as observed (Figure 2g). Although there is no explicitly simulated sink for the 1,4-hydroxycarbonyl (OHCARB), the measurement peaks sometime after 18 h. It is expected that from the difference between the gas-phase and mechanism trends, roughly 0.3 ppb of it exists in this sink.

Mechanism and Measurement Comparison of Acid Formation. Acidic species are expected to form from photolysis of a hydroperoxy group that is vicinal to another oxygen containing carbon. Photolysis of the hydroperoxy group results in an alkoxy radical vicinal to another oxygen containing carbon so decomposition ensues (see Figure 1, Channels 1a and 2ai). Depending on where in the molecule the C−C bond is severed, varying carbon length carboxylic acids (Channel 1a, CnCARBACID, $C_nH_{2n}O_2$), peracids (Channel 1a, CnACID, $C_nH_{2n}O_3$), hydroxycarboxylic acids, (Channel 2ai, CnACID $C_nH_{2n}O_3$), and hydroxyperacids (Channel 2ai) result. Such compounds in the CIMS may appear as both the transfer (m/z = $[M + 19]^-$) and the cluster product (m/z = $[M + 85]^-$), so the traces shown are the sum of these two ions (see Figure 3 and Figure 4). In some cases, like the C_5 carboxylic acid, there were additional contributions to the cluster product ion (m/z = 253), so it is omitted. The C_9 carboxylic acid likely has contributions from an unidentified mass interferent since its time profile is slightly different than the others. The overall time profiles and their relative abundances are consistent with expectations that C_{11} acid production is least likely to form, as tertiary H abstraction at the end carbons is slower.[34] Still, distribution by carbon number would need to be confirmed after full mass quantification. When unit normalized, the carboxylic acid traces (CnCARBACID) collapse to a distinct time profile consistent with the modeled trace representing the photolysis products of the carbonyl hydroperoxide p(jCARBROOH) in Figure 3b.

The formation of a peracid (Channel 1a, CnACID) of the same carbon number as a hydroxy carboxylic acid (Channel 2ai, CnACID) is difficult to discern, as they are isomers. Thus, these two types of acids have been referred to generally as CnACID, and this is separate from the carboxylic acids referred to as CnCARBACID. Other isomers include a hydroperoxide (Channel 1a, CnROOH) with an additional carbon. Hence, the ions monitored are generally assigned as a C_n acid or a C_{n+1} hydroperoxide in Figure 4. Still, it is more likely that the majority initial contribution to these ions stems from the peracid, as the hydroxycarboxylic acid (Channel 2ai, CnACID) is a higher generation product. Further, resulting branching ratios for the products of the acyl peroxy radical reaction with HO_2, as discussed in Hasson et al.[47] for the case of acetyl peroxy radical ($CH_3C(O)O_2$), would tend to favor peracid (via $R(O)O_2 + HO_2 \rightarrow R(O)OOH$) and carboxylic acid formation (via $R(O)O_2 + HO_2 \rightarrow R(O)OH + O_3$) routes over generation of another alkoxy radical (leading to the eventual < C_{12} hydroperoxides of Channel 1a in the dodecane case). Again, on a unit normalized basis, these ion traces collapse onto the unit normalized mechanism prediction for the products of carbonyl hydroperoxide photolysis, p(jCARBROOH), consistent with this identification as peracids accompanying carboxylic acid formation (Figure 4b). While the decomposition products (i.e., acyl radical and aldehyde) in Channel 1a preceding acid formation are not explicitly modeled, the reaction of the acyl radical with O_2 is considered instantaneous, and the lifetime of an acyl peroxy radical with HO_2 is expected to be 3.7 s under low-NO_x conditions. Thus, comparison of the acid traces with p(jCARBROOH) is sufficiently close for comparison to the trend in the gas-phase measurements. While the aldehydes could not be explicitly monitored by the CIMS, the acid traces are confirmation of aldehyde formation in the gas-phase. The aldehyde will be seen to be an important gas-phase intermediate, for its role in PHA formation.

Carbon Balance. Now we discuss the fate of the initial mass of dodecane distributed among the various reaction channels in the mechanism and compare to the gas-phase measurements. More reactions are represented in the mechanism scheme of Figure 1 than are implemented in the photochemical simulation (Table 2). While the distinct product distribution from photolysis of the two isomers of the carbonyl hydroperoxide (CARBROOH) matters for the gas-phase chemistry and SOA formation, the alpha isomer is not

considered in MCM 3.2, although reactions along Channel 2a including the formation and fate of a hydroxy carbonyl hydroperoxide (OHCARBROOH) are included. As is, the photolysis rates of the carbonyl hydroperoxide (CARBROOH) isomers would be treated the same, so p(jCARBROOH) and p(jCARBROOH + hν) are simulated to be the same (Table 2, Reaction 17). This prevents further explicit extension of the photochemical simulation for products along Channel 1a without further approximation of reaction rate coefficients. For carbonyl hydroperoxide (CARBROOH) reaction with OH, MCM 3.2 ends with production of the carbonyl hydroperoxy radical ($CARBRO_2$ in reactions 13 and 14 of Table 2); $CARBRO_2$ then goes back to the carbonyl hydroperoxide (CARBROOH) after reaction with HO_2 for these experimental conditions. That is, MCM 3.2 does not suggest further oxidation of CARBROOH to a dicarbonyl or to a thrice-functionalized chain (DICARBROOH), as supported by the CIMS trace monitored at (−) m/z = 315 (DICARBROOH). Effectively, this route (Channel 2b) becomes a large carbon sink without further explicit treatment of the products. With the limitation of measurable gas-phase species beyond this point, extension of the photochemical simulation is not attempted, although the further extent of oxidation is of interest, as it will play a role in the volatilities of products and contribution to particle growth.

The simulated fraction of initial carbon over time in the various generations of products is shown in Figure 2h. After sufficient time, the majority of the carbon resides in fourth and later generation products. While fourth and later generation products represent over half of the initial carbon, the major development of this chemistry becomes apparent after the third and earlier generations peak around 2.3×10^7 molecules cm^{-3} h of total OH exposure (~10 h). This would correspond to almost a day of atmospheric aging, assuming an ambient OH concentration of $\sim 10^6$ molecules cm^{-3}. Thus, dodecane and other alkanes that have similarly long OH-reactive lifetimes have the potential for generating multifunctional semivolatile species over the course of a few days.

Although CIMS sensitivities to each individual compound could not be determined (see Experimental Section), we used previously determined sensitivities for compounds with similar functionality as proxies for the sensitivity of species in this mechanism. We used the previously measured sensitivity of methyl hydroperoxide (CH_3OOH)[23] for the C_{12} hydroperoxide monitored at (−) m/z = 287, and the previously measured sensitivity of hydroxyacetone ($C_3H_6O_2$)[48] for the acids and multifunctional compounds. At the end of 18 h, it is estimated that roughly 13 ppb within a factor of 2 of the simulated 31 ppb of dodecane reacted is accounted for by the CIMS negative mode ions measured. All CIMS traces shown in Figure 2 were included, except the carbonyl (CARB, Figure 2c), as it could only be monitored in positive mode, and signal intensities of this mode are not comparable to that of negative mode. Although the carbonyl hydroperoxide (CARBROOH, Figure 2d) and the hydroxy hydroperoxide (OHROOH, Figure 2f) are tracked in positive mode over 36 h, we used the signals at (−) m/z = 301 and (−) m/z = 303, respectively, from the 18 h January experiment for a rough carbon balance at 18 h. The acid traces shown in Figure 3a and Figure 4a were also included, although there is likely a great deal of carbon still unaccounted for in < C_5 acids. Other remaining carbon not accounted for by the CIMS measurements include vapor-phase wall loss (though it is expected to be small), aldehyde formation from Channel 1a of the mechanism, and the many later generation products along Channel 2 that are not explicitly monitored by the CIMS.

SOA GROWTH

Organic growth as measured by the AMS is shown versus the dodecane decay in Figure 2a. The AMS organic trace is not corrected for particle wall-loss. The onset of growth occurs coincident with the peak of the hydroperoxide, indicating aerosol formation from higher generation oxidation products. The total suspended particle organic peaked at approximately 63 $\mu g\ m^{-3}$ around hour 20, consistent with the development of fourth-generation gas-phase chemistry. Peak particle diameter grew from 58 nm (seed diameter) to 190 nm at the point of maximum concentration, and then to 200 nm by the end of the experiment as measured by the DMA. Further analyses and consideration of heterogeneous chemistry provide more insight into the dynamics of the aerosol growth.

Vapor Pressure Estimation. To better constrain the expected aerosol chemical makeup, vapor pressures at 298 K were estimated for an array of compounds listed in Table S2 of the Supporting Information section using the EVAPORATION (Estimation of Vapor Pressure of ORganics, Accounting for Temperature, Intramolecular, and Nonadditivity effects) method.[49] The method predicts the (subcooled) liquid pure compound vapor pressure, p^0, taking into account intramolecular effects from the positions of functional groups on a compound. For example, the predicted p^0 for the α-carbonyl hydroperoxide is 6.58×10^{-8} atm, more than twice that of the β-carbonyl hydroperoxide, $p^0 = 2.45 \times 10^{-8}$ atm. Conversion of the pure component liquid vapor pressure to a value of C_i^o in units of $\mu g\ m^{-3}$ (also in Table S2, Supporting Information) can be used to classify compounds according to previously defined volatility classes.[50] These classes in order of increasing volatility include extremely low volatility organic compounds (ELVOCs) with $C_i^* < 3 \times 10^{-4}\ \mu g\ m^{-3}$, low volatility organic compounds (LVOCs) with $3 \times 10^{-4} < C_i^* < 0.3\ \mu g\ m^{-3}$, semivolatile organic compounds (SVOCs) with $0.3 < C_i^* < 300\ \mu g\ m^{-3}$, intermediate volatility organic compounds (IVOCs) with $300 < C_i^* < 3 \times 10^6\ \mu g\ m^{-3}$, and finally volatile organic compounds (VOCs) with $C_i^* > 3 \times 10^6\ \mu g\ m^{-3}$. These volatility regimes are provided for reference in Figure 5. Note that the calculated values presented here are not the conventionally used C_i^*, since values for the activity coefficients, γ_i, are not estimated and experimental volatility measurements were not made. C_i^* is related to C_i^o through the activity coefficient, $C_i^* = \gamma_i C_i^o$.[50]

O:C Values. The O:C values for each molecule are included in the Supporting Information section, Table S2. To view the progression of the oxidation, each compound is shown in the O:C versus log C_i^o space (Figure 5). The marker colors indicate the gas-phase generation of the compound. Black markers are reserved specifically for those compounds that may participate in heterogeneous chemistry. Each compound has a letter assigned label, corresponding to the key used in Table S2. A general upward trend to the left indicates lower volatility and increasing oxygenation over time. Exceptions do occur where there is formation of second generation compounds, like the hydroxy hydroperoxide and the dihydroperoxide, of a higher O:C and lower volatility compared to later generation products. AMS measurements show that within the first 10 h of early growth, the O:C stabilizes at 0.22, after which it steadily increases to 0.30 by the end of the experiment. O:C measurements are estimated to have an uncertainty of 30%,[51]

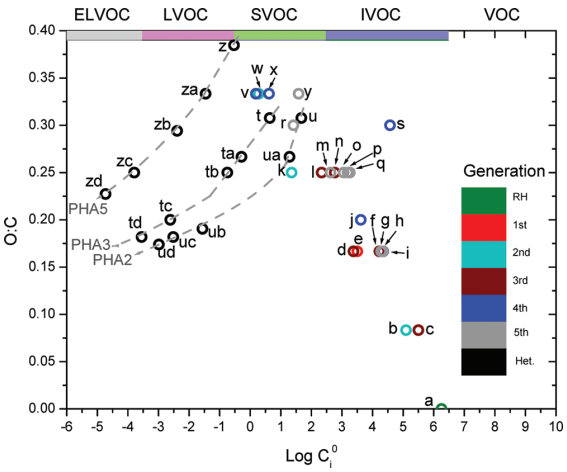

Figure 5. Span of O:C values versus log of the pure subcooled liquid vapor pressures in units of μg m^{-3} (C_i^o) for predicted compounds from dodecane low-NO$_x$ photooxidation. Colored markers indicate the product generation, and black markers indicate compounds thought to participate in heterogeneous chemistry. Letter data labels correspond with the compounds listed in Table S2. Regions of volatility previously defined[50] are denoted along the top axis for reference. The overall progression is upward to the left; vapor pressure drops from the starting dodecane, "a", at log(C_i^o) = 6.3 to log(C_i^o) = 0.19 for $C_{12}H_{24}O_4$, "v", and O:C increases to a max at 0.33. AMS measured O:C of 0.22−0.30 during the experiment. The gray dashed lines indicate the progression of increasing carbon length on the aldehyde that reacts with a hydroperoxy compound to form PHAs. PHA2 represents formation of the carbonyl hydroperoxide (CARBROOH) derived PHA, γ-keto-α-alkyl-α'-hydroxyalky peroxide (KAHAP); PHA3 the hydroxy hydroperoxide (OHROOH) derived PHA, δ-hydroxy-α-alkyl-α'-hydroxyalky peroxide (HAHAP); and PHA5 the hydroxycarbonyl hydroperoxide derived PHA, ε-hydroxy-γ-keto-α-alkyl-α'-hydroxyalky peroxide (HKAHAP). Increasing carbon length leads to convergence to a lower O:C and lower vapor pressure approaching the ELVOC region.

and the species shown in Figure 5 fall within the measured O:C range. The fifth-generation compounds in gray markers represent an increase in vapor pressure, owing to the formation of the hydroxy acids (Channel 2ai) and conversion of hydroperoxy groups to carbonyl groups. Only C_{10} acids are shown to condense the space and represent the bulk aerosol character. With estimated volatilities of expected gas-phase products and the measured O:C range, we investigate further the role of the semivolatiles on SOA growth.

Peroxyhemiacetal Formation. Many of the semivolatiles in Figure 5 are hydroperoxide species including (1) the second-generation hydroxy hydroperoxide (OHROOH, Channel 3; Figure 5 "k"), (2) the third-generation carbonyl hydroperoxide (CARBROOH, Channels 1 and 2; Figure 5 "n" and "l"), (3) the fourth-generation hydroxycarbonyl hydroperoxide (OH-CARBROOH, Channel 2a; Figure 5, "v" and "x"), and (4) the fifth-generation dicarbonyl hydroperoxide (DICARBROOH, Channel 2b; Figure 5, "y"). Once these semivolatiles have partitioned into the particle phase, reaction with aldehydes generated from decomposition of the photolyzed α-carbonyl hydroperoxide (Channel 1a) can occur to form PHAs. A general mechanism summarizing some possible reactions for the current system is shown in Figure 6. If the first-generation hydroperoxide (ROOH) reacts with an aldehyde, an α-alkyl-α'-hydroxyalky peroxide (hereafter referred to as AHAP) will be generated. If the β-carbonyl hydroperoxide (CARBROOH) reacts with an aldehyde, a γ-keto-α-alkyl-α'-hydroxyalky peroxide is formed (hereafter referred to as KAHAP). Similarly, if a hydroxy hydroperoxide (OHROOH) reacts with an aldehyde, a δ-hydroxy-α-alkyl-α'-hydroxyalky peroxide (hereafter referred to as HAHAP) will be formed. If a dicarbonyl hydroperoxide (DICARBROOH) reacts with an aldehyde, a ε-γ-diketo-α-alkyl-α'-hydroxyalky peroxide is formed (hereafter referred to as DKAHAP). Finally, if a hydroxycarbonyl hydroperoxide (OHCARBROOH) reacts with an aldehyde, a ε-hydroxy-γ-keto-α-alkyl-α'-hydroxyalky peroxide is formed (hereafter referred to as HKAHAP). There is also the possibility of cyclization of the KAHAP, DKAHAP, or HKAHAP because of the carbonyl groups, similar to the mechanisms proposed in previous studies,[52−54] although being isomers the cyclic and noncyclic forms would be hard to distinguish. Of course, alternative functional group placement on the compounds presented in Figure 6 is expected, and the compounds shown are examples.

PHA volatility will depend on the length of the aldehyde that originally reacted with the particle-phase incorporated hydroperoxide. Progression of the O:C and volatility of three select PHAs with increasing length of the aldehyde is marked by the series of "t" through "td" markers for HAHAP, "u" through "ud" for KAHAP, and "z" through "zd" for HKAHAP in Figure 5. The gray dotted lines are intended to guide the eye along these progressions toward lower O:C and lower vapor pressure, labeled "PHA2" for the KAHAP, "PHA3" for the HAHAP, and "PHA5" for the HKAHAP for visual clarity. PHA formation effectively converts semivolatiles into lower volatility products that approach the ELVOC region.

Evidence of PHA Formation Comparing Gas-Phase and Particle-Phase Mass Spectra. PHA formation is complex, as it involves reaction of a fourth-generation aldehyde (of varying carbon length) with second- to fifth-generation but lower vapor pressure hydroperoxy compounds at/in the particle. Figure 7 shows that aerosol growth follows after gas-phase formation of the carbonyl hydroperoxide (CARBROOH, Channels 1 and 2), but more importantly it is delayed until photolysis of the carbonyl hydroperoxide, p(jCARBROOH). The aldehydes could not be measured directly with CIMS because of their nonpolar nature, but the simulated p(jCARBROOH) can be used as a proxy for their expected formation according to Channel 1a in the mechanism. The aldehydes would precede acid formation, which is very quick after photolysis of the carbonyl hydroperoxide, when comparing the C_6CARBACID trace with the p(jCARBROOH) trace in Figure 7. From the trends presented in Figure 7, it appears that aerosol growth is timed with aldehyde formation, making PHA formation a potential mechanism for aerosol growth. This is further supported in species-specific comparisons of the CIMS and AMS.

Comparisons of the gas-phase mechanism predictions and CIMS traces were made with selected ion fragments from the HR-ToF-AMS mass spectra. The AMS utilizes vaporization and electron impact (EI) ionization resulting in fragmentation of aerosol species, but the prevalence of high amu (m/z > 100) in the spectra suggests that some stable high MW ions retain more of the original backbone and functionality of the initial product molecule. The selected ions discussed are those that would result from a PHA severed at either C−O bond of the peroxide RC_1-OO-C_2R. Scission at C_1-O results in the ion RC_1^+.

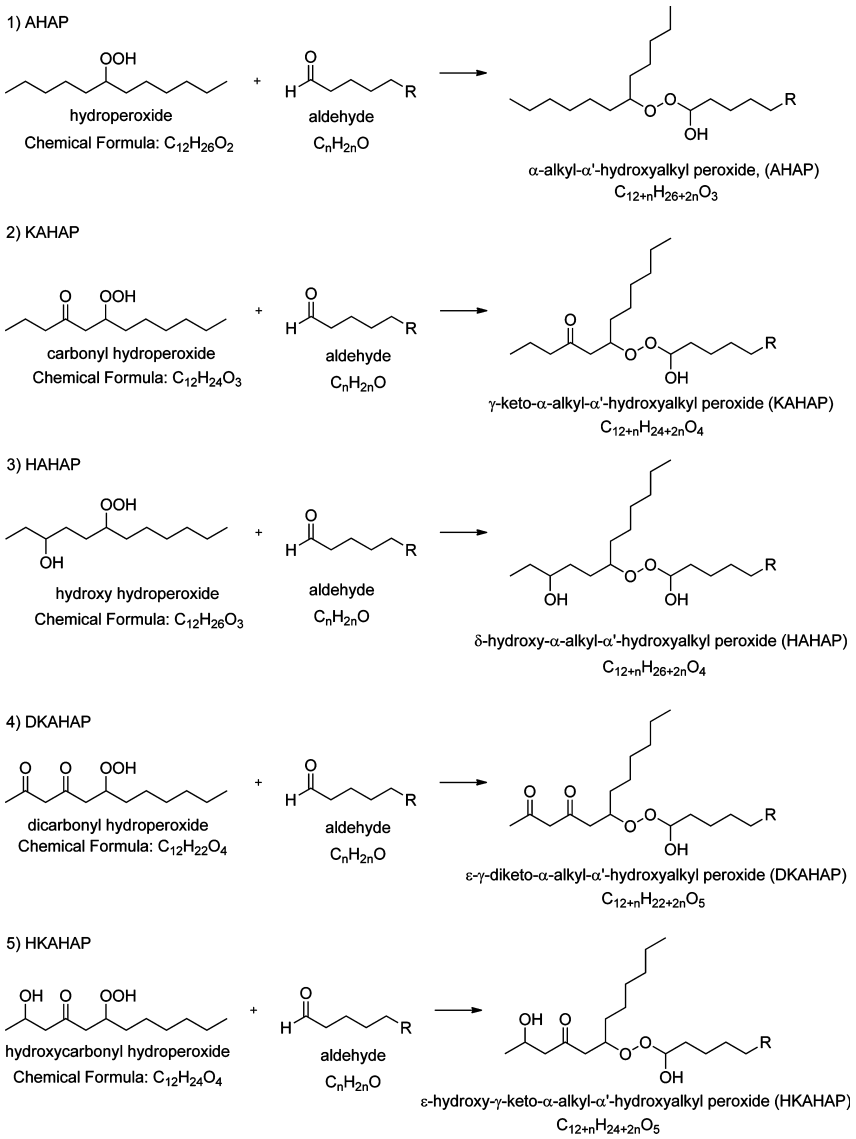

Figure 6. Scheme for forming five types of PHAs from reaction of an aldehyde of carbon length *n*, with various hydroperoxy compounds. (1) Reaction with a hydroperoxide generates an AHAP. (2) Reaction with a *β*-carbonyl hydroperoxide forms a KAHAP. (3) Reaction with a hydroxy hydroperoxide generates a HAHAP. (4) Reaction with a dicarbonyl hydroperoxide forms a DKAHAP. (5) Reaction with a hydroxycarbonyl hydroperoxide forms a HKAHAP.

Scission at C_2−O results in the ion RC_1OO^+, 32 amu greater than the RC_1^+ ion. The RC_1^+ ion was observed in previous studies of *α*-substituted hydroperoxide-derived PHAs,[52,55] although not the RC_1OO^+, which we propose for the PHAs in this study. The hydroperoxides we discuss in this study are not *α*-substituted, which may be cause for the different fragmentation pattern. Note that the RC_1^+ ion would be the equivalent ion generated from a hydroperoxide compound, RC_1−OOH, by loss of the hydroperoxy group to generate the $m/z = [M\text{-}33]^+$ ion, where M = mass of the hydroperoxide, also previously observed.[52,55] This fragmentation pathway was observed in identifying the C_{18} hydroperoxide during the standard experiment described previously in the Experimental section. Examination of $[M\text{-}33]^+$ ions and their exact masses from this fragmentation pathway alone suggests incorporation of the gas-phase carbonyl hydroperoxide (CARBROOH), hydroxy hydroperoxide (OHROOH), and other multifunctional long chains (OHCARBROOH, DICARBROOH) into the aerosol phase. However, the predominance of their respective RC_1^+ ions trending closely with their respective RC_1OO^+ ions strongly supports that these compounds are incorporated into the aerosol phase via PHA formation. The following discussion focuses on the pairing of $m/z < 200$ ions and their $m/z > 200$ (+ 32 amu) counterparts. For simplicity, we refer to the nominal mass of an ion rather than its exact

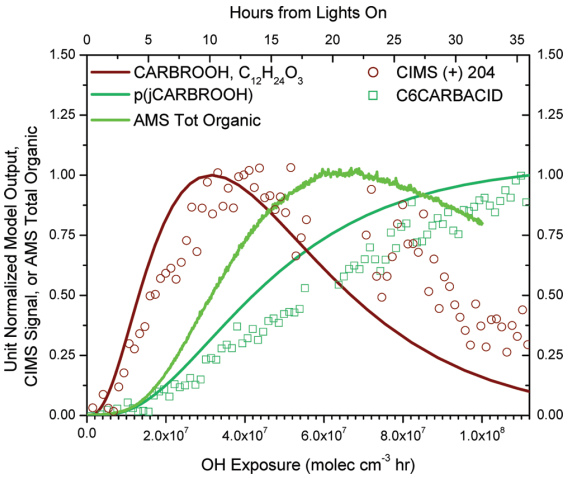

Figure 7. Aerosol growth occurs between formation of the carbonyl hydroperoxide (CARBROOH) and the onset of acid formation (observations in teal squares and simulated result, p(jCARBROOH), in teal) in the gas-phase. It is likely that initial aerosol growth can be supported by PHA formation since hydroperoxide containing species in the gas phase form within 5 h of lights on, and aldehyde formation will precede acid formation after photolysis of the carbonyl hydroperoxide.

mass, but the exact mass was used to obtain the chemical formula of the ion.

The AMS ions at m/z = 183 ($C_{12}H_{23}O^+$) and m/z = 215 ($C_{12}H_{23}O_3^+$) dominate the early SOA growth, suggesting that they may be characteristic fragments of the carbonyl hydroperoxide (CARBROOH)-derived PHA (KAHAP in Figure 6). Comparison of the simulated and measured gas-phase carbonyl hydroperoxide and AMS ions m/z = 183 and m/z = 215 is shown in Figure 8a along with the simulated gas-phase trend for photolysis of the carbonyl hydroperoxide, p(jCARBROOH) in Channel 1a. The growth of these ions in the aerosol phase is delayed from the onset of the carbonyl hydroperoxide formation in the gas phase until aldehyde formation begins, as proxied by the simulated p(jCARBROOH) trace in teal representing Channel 1a of the mechanism in Figure 1. As further reactions of the carbonyl hydroperoxide dominate, the gas-phase trace peaks and decays, followed as well by a decrease in these characteristic ions in the AMS mass spectrum. An analysis of the dynamics of the particle-phase AMS spectra will be addressed in a subsequent study.

AMS ions consistent with hydroxy hydroperoxide (OHROOH)-derived PHAs (HAHAP in Figure 6) at m/z = 185 ($C_{12}H_{25}O^+$) and m/z = 217 ($C_{12}H_{25}O_3^+$) grow in similarly with m/z = 183 and m/z = 215, although they peak later with their corresponding gas-phase trace (See Figure 8a and Figure 8b). Again, the appearance of these hydroxy hydroperoxide-derived PHA ions are contingent upon aldehyde formation as represented by the simulated p(jCARBROOH) trace in Figure 8b. If gas-to-particle partitioning was partially responsible for the simulated versus measured discrepancy for hydroxy hydroperoxide (OHROOH) Figure 2f, we would expect to see the m/z = 185 ion grow into the aerosol-phase before m/z = 217 and before aldehyde formation. That is, m/z = 185 growing in earlier to the aerosol-phase would indicate uptake of the hydroxy hydroperoxide (OHROOH) itself without conversion to PHA. With little SOA at this time and no aldehyde formation, partitioning of the hydroxy hydroperoxide early on is unlikely to account for this model-measurement discrepancy. It is possible that the hydroxy hydroperoxide lingers in the gas phase before aldehyde formation and undergoes vapor-phase wall loss as discussed previously.

The incorporation of the dicarbonyl hydroperoxide (DICARBROOH, $C_{12}H_{22}O_4$) into the particle phase is tracked with the AMS ion fragment at m/z = 197 ($C_{12}H_{21}O_2^+$) paired with m/z = 229 ($C_{12}H_{21}O_4^+$) in Figure 8c but after aldehyde formation. Note that, on a unit normalized scale, the p(jCARBROOH) overlaps the p(CARBROOH + OH) trend. This implies that dicarbonyl hydroperoxide (DICARBROOH) formation is practically simultaneous with aldehyde formation, although not necessarily in the same amount. The other thrice-functionalized chain, a hydroxycarbonyl hydroperoxide (OHCARBROOH, $C_{12}H_{24}O_4$) is tracked with AMS ion fragments m/z = 199 ($C_{12}H_{23}O_2^+$) and m/z = 231 ($C_{12}H_{23}O_4^+$). The ion trace at m/z = 199 is within the variation of the noisy CIMS marker at (−) m/z = 317 (Figure 8d).

Thus far, we observe that in the progression of increasing oxygenation (decreasing volatility) of the starting hydroperoxide there is less time between the gas-phase formation of a species and its incorporation into the particle phase. For example, there are a few hours between carbonyl hydroperoxide (CARBROOH) formation in the gas-phase measured by the CIMS at (+) m/z = 204 and the growth of the derived PHA AMS ions at m/z's 183 and 215 (Figure 8a). This is partially due to the delay in aldehyde formation. Still, once aldehyde is present, this time is significantly reduced for the delay between the hydroxy hydroperoxide (OHROOH) growth in the gas-phase measurement and its derived PHA ions (Figure 8b). While this also holds for the dicarbonyl hydroperoxide (DICARBROOH) in Figure 8c and the hydroxycarbonyl hydroperoxide (OHCARBROOH) in Figure 8d, there is a delay in the appearance of the AMS ions expected from their derived PHAs. That is, even though aldehyde is present and the thrice multifunctional compounds have been produced in the gas-phase, their incorporation as PHAs to the aerosol-phase is not timed with aldehyde formation as is the case for CARBROOH- and OHROOH-derived PHAs. This lag may be due to limiting reactant effects. That is, although the unit normalized simulations in Figure 8c suggest that DICARBROOH and aldehyde formation are practically simultaneous, it may be that the aldehyde produced is in lower quantity than the stoichiometric amount needed for reaction compared to the total semivolatile hydroperoxides available. Another possibility may be decreased reactivity of the dicarbonyl hydroperoxide (DICARBROOH) with another aldehyde since it already contains two carbonyl groups that may compete for or deactivate reaction with the hydroperoxy group, depending on their placement. Cyclization of carbonyl containing α-substituted hydroperoxides via intramolecular reaction of the carbonyl with the hydroperoxy group has been observed, setting up potential competition between cyclization and PHA formation.[52] Further study would be required to test for deactivation effects. Steric effects due to intramolecular hydrogen bonding[56] may also play a role for compounds like the hydroxy carbonyl hydroperoxide (OHCARBROOH). A previous study on the kinetics of α-hydroxy peroxides (RCH(OH)OOR) in solution noted that tetralin hydroperoxide is more reactive to acetaldehyde over cumene

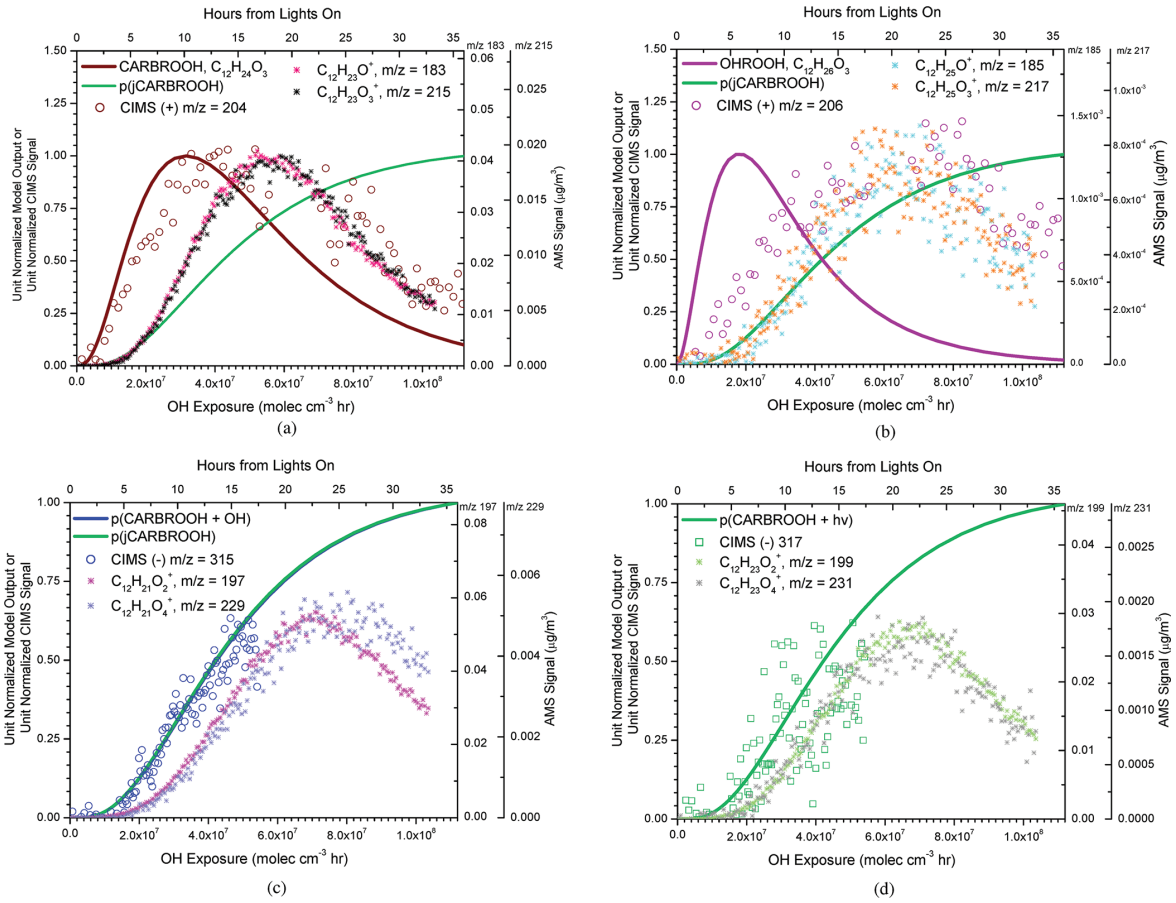

Figure 8. (a) AMS high-resolution fragments at m/z = 183 and m/z = 215 are possible characteristic fragments of the carbonyl hydroperoxide (CARBROOH)-derived PHA. (b) AMS high-resolution fragments at m/z = 185 and m/z = 217 are possible characteristic fragments of the hydroxy hydroperoxide (OHROOH)-derived PHA. (c) AMS high-resolution fragments at m/z = 197 and m/z = 229 are possible characteristic fragments of a multifunctional compound, dicarbonyl hydroperoxide (DICARBROOH)-derived PHA. (d) AMS high-resolution fragments at m/z = 199 and m/z = 231 are possible characteristic fragments of a multifunctional compound, hydroxycarbonyl hydroperoxide (OHCARBROOH) and its derived PHA.

hydroperoxide and other hydroperoxides because the peroxy group is surrounded by α-hydrogens.[56]

We note that the m/z = 183 and m/z = 185 (Figure 8a,b) ion fragments may be derived from other molecules containing similar functionalities to the carbonyl hydroperoxide (CARBROOH) and hydroxy hydroperoxide (OHROOH). For example, the fourth-generation hydroxycarbonyl hydroperoxide multifunctional (OHCARBROOH, Channel 2a) shares two of its functional groups with the carbonyl hydroperoxide (CARBROOH) and two with the hydroxy hydroperoxide (OHROOH), suggesting that there may be contributions to these ion signals from later incorporation of this multifunctional compound into the particle. This is similar to the case of the dicarbonyl hydroperoxide (DICARBROOH, Channel 2b) sharing two functionalities with the carbonyl hydroperoxide (CARBROOH), so it may contribute to the signal at m/z = 183. However, because the m/z = 183 and m/z = 185 ions are distinct and dominant components of the initial organic growth, and since their trends do not deviate from their respective +32 amu ion partners (m/z = 215, m/z = 217) with later incorporation of the suggested ions for the multifunctionals (m/z's 197, 199, 229, and 231), they are still likely representative ion fragments from the carbonyl hydroperoxide-derived PHA (KAHAP) and the hydroxy hydroperoxide-derived PHA (HAHAP).

Particle-Phase Peroxyhemiacetal Formation. The surface matrix of an aerosol particle probably enhances PHA generation by lowering energetic barriers or chemically catalyzing the reaction at the surface,[55] similar to dihydrofuran (DHF) formation.[38] Still, a lower energy barrier was not sufficient to see evidence of AHAP formed from the second-generation hydroperoxide (ROOH) in the AMS spectra. Its higher vapor pressure, further reaction with OH or photolysis, as well as the delay to aldehyde formation are all likely reasons why the fate of the ROOH is purely gas-phase oxidation. The nature of the particle interface and bulk are difficult to establish when considering such heterogeneous processes in the current study, but some insights into the chemistry behind PHA formation come from the study by Antonovskii and Terent'ev.[56] First, they find that aldehydes are more likely than ketones to participate in α-hydroxy peroxide formation because they exhibit greater polarity and polarizability in their

dx.doi.org/10.1021/jp211531h | J. Phys. Chem. A 2012, 116, 6211–6230

C═O containing π bond. Hence, PHA formation from the second-generation carbonyl is not considered for this discussion. Second, they observed that the forward reaction to α-hydroxy peroxide dominated over backward dissociation when run in polar solvents (chloroform, diisopropyl ether, or hexanol). Considering earlier discussion on the characteristic of the aerosol chemistry, PHA formation may be hindered if the aerosol matrix is not sufficiently polar, as there is a large mass fraction of organic described by CH family ions. Lastly, Antonovskii and Terent'ev observed stable α-hydroxy peroxides at 20 and 40 °C, but they note that α-hydroxy peroxides are less thermally stable than the hydroperoxide. This could mean the peroxides do not survive well through the thermal vaporization (600 °C) and ionization process in the techniques here. This may possibly explain the small mass concentrations for the characteristic PHA ions relative to the total organic mass. Still, in this study we keep in mind that the aldehyde formation relies on photolysis of a well-positioned α-carbonyl hydroperoxide. So, concentration, timing, and chemistry of the aerosol all have to be in harmony to facilitate PHA formation.

Cyclic Hemiacetal Formation. The 1,4-hydroxycarbonyl (OHCARB) has been theorized[38] and found experimentally to heterogeneously react, isomerizing to a cyclic hemiacetal (CHA) in the particle[9,11] or on chamber walls in an acid-catalyzed process.[15] These heterogeneous reactions have been found to happen within a time frame of approximately 1 h.[9,11,15] Conversion of the CHA to a DHF is sensitive to water vapor;[57] under low relative humidity environments, it will dehydrate to form a higher vapor pressure DHF compound that can partition back to the gas-phase and undergo further reaction with OH or O_3. A summary of these reactions is shown in Channel 3, Figure 1. Higher relative humidity conditions will slow the dehydration process, and OH reaction with the 1,4-hydroxycarbonyl (OHCARB) will more likely be its fate.[58] Under the current experimental conditions, DHF reaction with O_3 is expected to dominate after 2.5 h of irradiation when O_3 produced over time surpasses 5 ppb, the limit at which reaction with O_3 is competitive with reaction of the available OH radical ($\sim 2 \times 10^6$ molecules cm^{-3}). This is based on reaction rate coefficients available in the literature on 4,5-dihydro-2-methylfuran, using $k_{DHF-OH} = 2.18 \times 10^{-10}$ molecules cm^{-3} s^{-1} and $k_{DHF-O_3} = 3.49 \times 10^{-15}$ molecules cm^{-3} s^{-1}.[59] This provides an interesting problem to consider when thinking of the true lifecycle of the starting alkane and its ultimate generation of a higher vapor pressure unsaturated compound susceptible to oxidation and relevant for further SOA formation. Kinetic study of this heterogeneous conversion under OH radical initiated photoxidation of $C_{11}-C_{17}$ alkanes in the presence of NO_x suggests that the conversion to the CHA is fast in dry air, while the dehydration of the CHA to the DHF occurs on the order of ~15 min.[12]

CHA formation may be possible via the photolysis of the hydroperoxide (ROOH) in Channel 3 or through a fifth-generation multifunctional commpound analogously cyclizing (Channel 2aii), though the resulting CHA has an extra carbonyl group as seen in Figure 1. Sufficient evidence does not exist to confirm CHA formation for this study despite low relative humidity experimental conditions. If the CHA is formed as $C_{12}H_{24}O_2$, an AMS fragment at m/z = 183 ($C_{12}H_{23}O^+$) generated from loss of the −OH group[9] is possible. However, this fragment is more appropriately assigned as a characteristic ion of the carbonyl hydroperoxide (CARBROOH)-derived PHA instead as discussed earlier. In experiments carried out in the presence of NO_x, which are not reported here, the m/z = 183 ion is observed distinctly and does not pair with m/z = 215, making the current assignment consistent with the expected gas-phase mechanism under low-NO_x conditions. Since a distinct time trend indicating formation of the CHA in the particle-phase is not yet fully distinguished from the nominal mass at m/z = 183, the kinetics under the current experimental conditions cannot be modeled. On another note, the nature of the particle acidity is different than that of previous studies, as it is thought that adsorbed HNO_3 on the particle surface catalyzed the heterogeneous conversion to the DHF.[11,12] Under these low-NO_x conditions, HNO_3 formation is not considered. While the particle character shows enhancement of acidity as tracked by the AMS ion CO_2^+ at m/z = 44, there is still a large mass fraction described by the CH family ions, consistent with the many reduced fragments that could be derived from these long chain products. Considering that the simulated production of the 1,4-hydroxycarbonyl is only around 0.6 ppb in the gas-phase (without sinks) and the unclear nature of the particle acidity, if the cyclization and dehydration to the DHF does occur, the amount that formed was probably small, indiscernible in the AMS signal.

Heterogeneous Chemistry versus Gas-Phase Oxidation. We have currently considered two routes to formation of SOA through heterogeneous reactions. We see evidence of PHA formation derived from many semivolatile hydroperoxide species formed in all reaction channels, but we cannot confirm formation of the CHA from the 1,4-hydroxycarbonyl (OHCARB) at this time. Furthermore, the contributions to the SOA mass from pure gas-particle partitioning and heterogeneous chemistry of the hydroperoxide compounds to the SOA mass are unclear. To explore this, we roughly estimate the mass contributions of organic from five select semivolatiles that have been highlighted in a previous discussion: (1) carbonyl hydroperoxide (CARBROOH), (2) hydroxy hydroperoxide (OHROOH), (3) hydroxycarbonyl hydroperoxide (OHCARBROOH), (4) dicarbonyl hydroperoxide (DICARBROOH) and (5) 1,4-hydroxycarbonyl (OHCARB). Using the roughly estimated gas-phase concentrations of these species as monitored by the CIMS, the subcooled pure component liquid vapor pressure estimates (C_i^o), and the organic mass concentration from the AMS (as shown in Figure 2a), we assume that gas-particle equilibrium is established quickly so that the instantaneous contribution of each compound in the particle-phase is calculated by eq 1:

$$C_{pi} = \frac{C_{org} C_{gi}}{\gamma_i C_i^0} \quad (1)$$

where C_{pi} is the mass concentration of species i in the particle phase [μg m^{-3}], C_{org} is the mass concentration of organic aerosol in [μg m^{-3}], C_{gi} is the mass concentration of species i in the gas phase [μg m^{-3}], γ_i is the activity coefficient of species i in the bulk aerosol solution (assumed as 1 here), and C_i^0 = the subcooled pure component liquid vapor pressure of species i [μg m^{-3}].

The result of this analysis is presented in Figure 9. Note that we estimate the organic mass only up to 18 h because we utilized species monitored at $m/z \geq 300$, available only from the January experiment. We see that just under 10 μg m^{-3} of organic is expected each from the dicarbonyl hydroperoxide (DICARBROOOH), carbonyl hydroperoxide (CARBROOH),

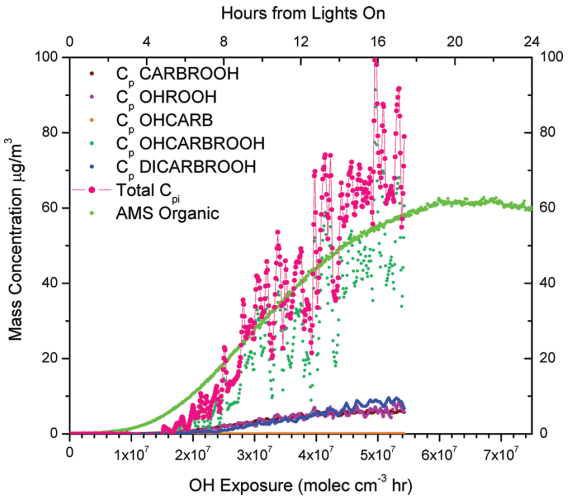

Figure 9. Rough estimate of total organic mass attributed to gas-to-particle phase partitioning from select semivolatiles (pink circles with line) as compared to the AMS organic trace (bright green). Individual contributions from each species are shown: (1) carbonyl hydroperoxide (CARBROOH, wine-colored circles), (2) hydroxy hydroperoxide (OHROOH, purple circles), (3) 1,4-hydroxycarbonyl (OHCARB, orange circles), (4) hydroxycarbonyl hydroperoxide (OHCARBROOH, teal circles), and (5) dicarbonyl hydroperoxide (DICARBROOH, blue circles).

and the hydroxy hydroperoxide (OHROOH). The 1,4-hydroxycarbonyl (OHCARB) makes negligible mass, and this is consistent with the small amount expected to form from the gas-phase chemistry and the absence of an AMS ion for the CHA. The hydroxycarbonyl hydroperoxide (OHCARBROOH) is expected to make up the majority of the organic mass ($\sim$ 60 μg m^{-3}). The total contributions of these species to organic mass is $C_{ptot} = \sum_i C_{pi}$. Thus, partitioning from just four semivolatile hydroperoxides could explain the majority of the organic growth observed after 5 h of irradiation. However, a small amount of organic was formed previously and is not fully described by equilibrium partitioning of these semivolatiles.

The uncertainty in the estimated gas-phase concentrations could resolve the appearance of organic growth prior to significant contributions from partitioning, but based on the well-paired m/z < 200 and m/z > 200 ions that differ by 32 amu, it is overwhelmingly likely that the fragments come from the same compound (their respective PHA). These ions also begin to appear prior to 5 h with aldehyde formation in the case of the carbonyl hydroperoxide (CARBROOH) and the hydroxy hydroperoxide (OHROOH) (see Figure 8a,b). So the early gap between the measurement and estimated organic mass may be due to PHA formation initiating aerosol growth. In light of the AMS measurements of characteristic PHA ions and the estimated mass from partitioning of the same hydroperoxide semivolatiles, it is difficult to tell whether these semivolatiles would be completely in the particle-phase as PHAs or in molecular form. In addition, later more functionalized compounds may partition in without conversion to PHA formation right away, as in the lag between gas-phase aldehyde formation and PHA ion appearance observed for the hydroxycarbonyl hydroperoxide (OHCARBROOH) and for that of the dicarbonyl hydroperoxide (DICARBROOH). However, since aldehyde formation is fairly coincident with most of the higher generation multifunctionals (OHCARBROOH, DICARBROOH) in the gas-phase, PHA formation as a mechanism for their incorporation into the particle phase cannot be ruled out. Full treatment of the kinetics of the heterogeneous chemistry require mass closure on the contribution of PHA mass to the organic present. While the AMS ions presented support PHA formation, their mass concentration signals do not account for the total mass of the derived PHA in the particle phase. Recall that the ions discussed do not include the side of the molecule that contains varying carbon lengths from the aldehyde that reacted with the hydroperoxide species. This provides a multitude of possible PHA structures. Second, being such a large molecule, PHA mass would certainly be distributed in the AMS spectrum among many possible fragmentation pathways. To truly understand these aspects, synthesis of these compounds would be required as an AMS standard to understand the full spectrum distribution.

■ ATMOSPHERIC IMPLICATIONS

Presented here is the first experimental study of SOA formation from the long-chain alkanes under low-NO_x conditions, such that RO_2 + HO_2 chemistry dominates the fate of the RO_2 radical. This regime of chemistry is typical of a region relatively isolated from NO_x sources and where trace VOC concentrations are too low to sustain RO_2 self-reaction. It is a challenge to simulate this chemistry in most laboratory chambers under atmospherically pristine conditions at which NO_x levels are typically tens to low hundreds of pptv. The gas-phase measurements of this study are consistent with chemistry expected for NO_x levels toward this range. Further, a regime of "slow" chemistry that lengthens the RO_2 lifetime sufficiently to allow for alkyl peroxy radical rearrangement through a 1,6-H shift is relevant to pristine conditions (ppt levels of NO_x, HO_2, and low [OH] $\sim 1.2 \times 10^5$ molecules cm^{-3}).[46] Achieving such conditions further challenges the design of environmental chamber studies. Although many challenges remain in simulating and spanning the range of "atmospherically relevant" conditions using environmental chambers, fundamental studies such as that described here address the fundamental chemistry in a regime relevant for closing the gap in the VOC and SOA budgets.

A myriad of compounds is formed in long-chain alkane photooxidation via functionalization and fragmentation pathways in the gas phase. For dodecane, 19 gas-phase species were monitored by the CIMS, and many compared well to a simulation with an abbreviated chemical mechanism based on the MCM 3.2. The gas-phase mechanism generally captures the observations only using four generations of explicit chemistry. Further work on empirical quantification and branching ratios of the gas-phase routes in the mechanism is needed, but was hindered for this study due to the lack of available standards and difficulties associated with experimental handling. Nonetheless, this study fundamentally captures the chemical framework representative of low initial organic loading of a longer-lived species (in terms of reaction with OH) while in the relative absence of NO_x that can be extended to alkanes of different lengths and structures. Current work is ongoing to understand the chemistry of SOA formation from other C_{12} alkanes of branched and cyclic conformations.

Mechanisms of particle formation emerge from comparison of the gas-phase mechanism and known heterogeneous chemistry. While there is evidence supporting the formation

of PHAs, confirmation of the heterogeneous conversion of the 1,4-hydroxycarbonyl to the CHA is lacking, but the amount that formed was probably small. A powerful approach to confirming direct partitioning of specific gas-phase compounds is through comparison of CIMS gas-phase time trends and corresponding characteristic ion fragments from the AMS. The paired (32 amu difference) high m/z > 100 AMS fragments identified were instrumental in deriving more molecular structure information in support of PHA formation. Comparisons of time trends provide insight into the chemistry of the partitioning, as seen, for example, with the decreasing delay between appearance of characteristic AMS ions and gas-phase product growth with increasing oxidation of the parent molecule. A rough estimate shows that much of the organic growth can be described by theoretical partitioning estimates of select semivolatile hydroperoxides. Still, better mass closure on the semivolatiles in the system in the gas and particle-phases could provide greater insight into the kinetic and equilibrium effects on SOA formation from dodecane.

The degree of generational development in the gas-phase photooxidation of this long-chain alkane over the extended chamber experiments is quite remarkable. While the majority of the gas-phase product distribution (almost two-thirds of the carbon) is developed within the first 20 h of photoxidation, SOA formation clearly involves the further oxidation of the third-generation carbonyl hydroperoxide, which peaks about 8 h earlier. This chemical development occurs much later than typical experimental time scales for chamber experiments, which highlights the need for simulating extended oxidation to truly capture the SOA formation process.

While the chemical composition of the gas and aerosol phases was well resolved with the techniques used in this study, challenges still exist in understanding the nature of the particle phase, as this can have profound effects on the further chemical aging of the particles.[60] This aging could be manifested in the formation of alkane-derived PHAs. In regards to time scale, the current work focuses on oxidative processes in the gas phase affecting the chemical development of the particle phase, although the possibility of photolysis or reactions with OH of the aerosol products may become more important under extended photoxidation time scales. A better understanding of these and other factors that potentially affect SOA chemical evolution might address issues such as the observed "glassy" nature of some SOA.[61,62] Extrapolating the present study to the atmosphere suggests that (1) hydroperoxide and PHA species are likely to be in the particle phase for alkane-derived aerosol under low-NO_x conditions, and (2) with the possibility of viscous phases that affect further chemical aging in the aerosol phase, the lifetimes of these products could be extended, lending themselves to long-range transport and a more complicated assessment of the SOA life cycle.

■ ASSOCIATED CONTENT

Supporting Information

The Supporting Information includes (1) A table with calculated lifetimes of RO_2 with RO_2, HO_2, NO, and NO_2 under varying NO_x conditions, (2) table of O:C and volatility, (3) figures on AMS and CIMS measurements across all experiments, (4) alternative positive mode ions for CIMS negative mode ions, and (5) simulations of varying NO concentration. This information is available free of charge via the Internet at http://pubs.acs.org.

■ AUTHOR INFORMATION

Corresponding Author

*E-mail: seinfeld@caltech.edu.

Notes

The authors declare no competing financial interest.

■ ACKNOWLEDGMENTS

This work was supported by the Office of Science (Biological and Environmental Research), U.S. Department of Energy Grant (DE-SC 0006626), and National Science Foundation Grants AGS-1057183 and ATM-0650061. We acknowledge John D. Crounse and Jason M. St. Clair for helpful discussions on CIMS data analysis, Reddy L. N. Yatavelli and ManNin Chan for useful discussions, and Andreas Zuend, Xuan Zhang, and Steve Compernolle for assistance with the vapor-pressure estimations. L.D.Y., J.S.C., and C.L.L. were supported by National Science Foundation Graduate Research Fellowships.

■ REFERENCES

(1) Ravishankara, A. R. *Chem. Rev.* **2003**, *103*, 4505−4508.
(2) Jimenez, J. L.; Canagaratna, M. R.; Donahue, N. M.; Prevot, A. S. H.; Zhang, Q.; Kroll, J. H.; DeCarlo, P. F.; Allan, J. D.; Coe, H.; Ng, N. L.; et al. *Science* **2009**, *326*, 1525−1529.
(3) Kroll, J. H.; Donahue, N. M.; Jimenez, J. L.; Kessler, S. H.; Canagaratna, M. R.; Wilson, K. R.; Altieri, K. E.; Mazzoleni, L. R.; Wozniak, A. S.; Bluhm, H.; et al. *Nat. Chem.* **2011**, *3*, 133−139.
(4) Robinson, A. L.; Donahue, N. M.; Shrivastava, M. K.; Weitkamp, E. A.; Sage, A. M.; Grieshop, A. P.; Lane, T. E.; Pierce, J. R.; Pandis, S. N. *Science* **2007**, *315*, 1259−1262.
(5) Schauer, J. J.; Kleeman, M. J.; Cass, G. R.; Simoneit, B. R. T. *Environ. Sci. Technol.* **1999**, *33*, 1578−1587.
(6) Schauer, J. J.; Kleeman, M. J.; Cass, G. R.; Simoneit, B. R. T. *Environ. Sci. Technol.* **2002**, *36*, 1169−1180.
(7) Presto, A. A.; Miracolo, M. A.; Kroll, J. H.; Worsnop, D. R.; Robinson, A. L.; Donahue, N. M. *Environ. Sci. Technol.* **2009**, *43*, 4744−4749.
(8) Presto, A. A.; Miracolo, M. A.; Donahue, N. M.; Robinson, A. L. *Environ. Sci. Technol.* **2010**, *44*, 2029−2034.
(9) Lim, Y. B.; Ziemann, P. J. *Environ. Sci. Technol.* **2005**, *39*, 9229−9236.
(10) Lim, Y. B.; Ziemann, P. J. *Environ. Sci. Technol.* **2009**, *43*, 2328−2334.
(11) Lim, Y. B.; Ziemann, P. J. *Aerosol Sci. Technol.* **2009**, *43*, 604−619.
(12) Lim, Y. B.; Ziemann, P. J. *Phys. Chem. Chem. Phys.* **2009**, *11*, 8029−8039.
(13) Talukdar, R. K.; Mellouki, A.; Gierczak, T.; Barone, S. *Int. J. Chem. Kinet.* **1994**, *26*, 973−990.
(14) Atkinson, R. *J. Phys. Chem. Ref. Data* **1997**, *26*, 215−290.
(15) Atkinson, R.; Arey, J.; Aschmann, S. M. *Atmos. Environ.* **2008**, *42*, 5859−5871.
(16) Tyndall, G. S.; Cox, R. A.; Granier, C.; Lesclaux, R.; Moortgat, G. K.; Pilling, M. J.; Ravishankara, A. R.; Wallington, T. J. *J. Geophys. Res.* **2001**, *106*, 12157−12182.
(17) Kroll, J. H.; Seinfeld, J. H. *Atmos. Environ.* **2008**, *42*, 3593.
(18) Lelieveld, J.; Butler, T. M.; Crowley, J. N.; Dillon, T. J.; Fischer, H.; Ganzeveld, L.; Harder, H.; Lawrence, M. G.; Martinez, M.; Taraborrelli, D.; et al. *Nature* **2008**, *452*, 737−740.
(19) Ren, X.; Olson, J. R.; Crawford, J. H.; Brune, W. H.; Mao, J.; Long, R. B.; Chen, Z.; Chen, G.; Avery, M. A.; Sachse, G. W.; et al. *J. Geophys. Res.* **2008**, *113*, D05310.
(20) Wolfe, G. M.; Thornton, J. A.; Bouvier-Brown, N. C.; Goldstein, A. H.; Park, J.-H.; McKay, M.; Matross, D. M.; Mao, J.; Brune, W. H.; LaFranchi, B. W.; et al. *Atmos. Chem. Phys.* **2011**, *11*, 1269−1294.
(21) Cocker, D. R.; Flagan, R. C.; Seinfeld, J. H. *Environ. Sci. Technol.* **2001**, *35*, 2594−2601.

(22) Keywood, M. D.; Varutbangkul, V.; Bahreini, R.; Flagan, R. C.; Seinfeld, J. H. *Environ. Sci. Technol.* **2004**, *38*, 4157−4164.
(23) St Clair, J. M.; McCabe, D. C.; Crounse, J. D.; Steiner, U.; Wennberg, P. O. *Rev. Sci. Instrum.* **2010**, *81*, 6.
(24) Paulot, F.; Crounse, J. D.; Kjaergaard, H. G.; Kroll, J. H.; Seinfeld, J. H.; Wennberg, P. O. *Atmos. Chem. Phys.* **2009**, *9*, 1479−1501.
(25) Crounse, J. D.; McKinney, K. A.; Kwan, A. J.; Wennberg, P. O. *Anal. Chem.* **2006**, *78*, 6726−6732.
(26) Huey, L. G.; Villalta, P. W.; Dunlea, E. J.; Hanson, D. R.; Howard, C. J. *J. Phys. Chem.* **1996**, *100*, 190−194.
(27) Crutzen, P.; Williams, J.; Pöschl, U.; Hoor, P.; Fischer, H.; Warneke, C.; Holzinger, R.; Hansel, A.; Lindinger, W.; Scheeren, B.; Lelieveld, J. *Atmos. Environ.* **2000**, *34*, 1161−1165.
(28) Jayne, J. T.; Leard, D. C.; Zhang, X.; Davidovits, P.; Smith, K. A.; Kolb, C. E.; Worsnop, D. R. *Aerosol Sci. Technol.* **2000**, *33*, 49−70.
(29) DeCarlo, P. F.; Kimmel, J. R.; Trimborn, A.; Northway, M. J.; Jayne, J. T.; Aiken, A. C.; Gonin, M.; Fuhrer, K.; Horvath, T.; Docherty, K. S.; et al. *Anal. Chem.* **2006**, *78*, 8281−8289.
(30) Canagaratna, M.; et al. *Mass Spectrom. Rev.* **2007**, *26*, 185−222.
(31) Loza, C. L.; Chhabra, P. S.; Yee, L. D.; Craven, J. S.; Flagan, R. C.; Seinfeld, J. H. *Atmos. Chem. Phys. Disc.* **2011**, *11*, 24969−25010.
(32) Jenkin, M. E.; Saunders, S. M.; Pilling, M. J. *Atmos. Environ.* **1997**, *31*, 81−104.
(33) Saunders, S. M.; Jenkin, M. E.; Derwent, R. G.; Pilling, M. J. *Atmos. Chem. Phys.* **2003**, *3*, 161−180.
(34) Kwok, E. S.; Atkinson, R. *Atmos. Environ.* **1995**, *29*, 1685−1695.
(35) Carter, W. P.; Cocker, D. R. I.; Fitz, D. R.; Malkina, I. L.; Bumiller, K.; Sauer, C. G.; Pisano, J. T.; Bufalino, C.; Song, C. *Atmos. Environ.* **2005**, *39*, 7768−7788.
(36) Wang, J.; Doussin, J. F.; Perrier, S.; Perraudin, E.; Katrib, Y.; Pangui, E.; Picquet-Varrault, B. *Atmos. Meas. Tech.* **2011**, *4*, 2465−2494.
(37) Sander, S. P.; Abbatt, J.; Barker, J. R.; Burkholder, J. B.; Friedl, R. R.; Golden, D. M.; Huie, R. E.; Kolb, C. E.; Kurylo, M.; Moortgat, G. K.; et al., Chemical kinetics and photochemical data for use in atmospheric studies, Evaluation No. 17. JPL Publication 10-6, 2011; http://jpldataeval.jpl.nasa.gov.
(38) Dibble, T. S. *Chem. Phys. Lett.* **2007**, *447*, 5−9.
(39) Vaghjiani, G.; Ravishankara, A. *J. Geophys. Res.* **1989**, *94* (D3), 3487−3492.
(40) Vaghjiani, G. L.; Ravishankara, A. R. *J. Chem. Phys.* **1990**, *92*, 996−1003.
(41) Baasandorj, M.; Papanastasiou, D. K.; Talukdar, R. K.; Hasson, A. S.; Burkholder, J. B. *Phys. Chem. Chem. Phys.* **2010**, *12*, 12101−12111.
(42) Atkinson, R. *J. Phys. Chem. Ref. Data, Monogr.* **1994**, *2*, 1−216.
(43) Atkinson, R.; Arey, J. *Chem. Rev.* **2003**, *103*, 4605−4638.
(44) Matsunaga, A.; Ziemann, P. J. *Aerosol Sci. Technol.* **2010**, *44*, 881−892.
(45) Loza, C. L.; Chan, A. W. H.; Galloway, M. M.; Keutsch, F. N.; Flagan, R. C.; Seinfeld, J. H. *Environ. Sci. Technol.* **2010**, *44*, 5074−5078.
(46) Crounse, J. D.; Paulot, F.; Kjaergaard, H. G.; Wennberg, P. O. *Phys. Chem. Chem. Phys.* **2011**, *13*, 13607−13613.
(47) Hasson, A. S.; Tyndall, G. S.; Orlando, J. J. *J. Phys. Chem. A* **2004**, *108*, 5979−5989.
(48) Spencer, K. M.; Beaver, M. R.; Clair, J. M. S.; Crounse, J. D.; Paulot, F.; Wennberg, P. O. *Atmos. Chem. Phys. Disc.* **2011**, *11*, 23619−23653.
(49) Compernolle, S.; Ceulemans, K.; Müller, J.-F. *Atmos. Chem. Phys.* **2011**, *11*, 9431−9450.
(50) Donahue, N. M.; Kroll, J. H.; Pandis, S. N.; Robinson, A. L. *Atmos. Chem. Phys. Disc.* **2011**, *11*, 24883−24931.
(51) Aiken, A. C.; DeCarlo, P. F.; Jimenez, J. L. *Anal. Chem.* **2007**, *79*, 8350−8358.
(52) Ziemann, P. J. *J. Phys. Chem. A* **2003**, *107*, 2048−2060.
(53) Matsunaga, A.; Docherty, K. S.; Lim, Y. B.; Ziemann, P. J. *Atmos. Environ.* **2009**, *43*, 1349−1357.
(54) Kern, W.; Spiteller, G. *Tetrahedron* **1996**, *52*, 4347−4362.
(55) Tobias, H. J.; Ziemann, P. J. *Environ. Sci. Technol.* **2000**, *34*, 2105−2115.
(56) Antonovskii, V. L.; Terent'ev, V. A. *J. Org. Chem. U.S.S.R. (Engl. Transl.)* **1967**, *3*, 972.
(57) Holt, T.; Atkinson, R.; Arey, J. *J. Photochem. Photobiol., A* **2005**, *176*, 231−237.
(58) Aschmann, S. M.; Arey, J.; Atkinson, R. *J. Atmos. Chem.* **2003**, *45*, 289−299.
(59) Martin, P.; Tuazon, E. C.; Aschmann, S. M.; Arey, J.; Atkinson, R. *J. Phys. Chem. A* **2002**, *106*, 11492.
(60) Ziemann, P. J. *Faraday Discuss.* **2005**, *130*, 469−490.
(61) Virtanen, A.; Joutsensaari, J.; Koop, T.; Kannosto, J.; Yli-Pirila, P.; Leskinen, J.; Makela, J. M.; Holopainen, J. K.; Poschl, U.; Kulmala, M.; et al. *Nature* **2010**, *467*, 824−827.
(62) Vaden, T. D.; Imre, D.; Beránek, J.; Shrivastava, M.; Zelenyuk, A. *Proc. Natl. Acad. Sci. U. S. A.* **2011**, *108*, 2190−2195.

Chapter 3

Analysis of Secondary Organic Aerosol Formation and Aging Using Positive Matrix Factorization of High-resolution Aerosol Mass Spectra: Application to the Dodecane Low-NOx System[1]

[1]This chapter is reproduced by permission from "Analysis of Secondary Organic Aerosol Formation and Aging Using Positive Matrix Factorization of High-resolution Aerosol Mass Spectra: Application to the Dodecane Low-NOx System" by J. S. Craven, L. D. Yee, N. L. Ng, M. R. Canagaratna, C. L. Loza, K. A. Schilling, R. L. N. Yatavelli, J. A. Thornton, P. J. Ziemann, R. C. Flagan, and J. H. Seinfeld, *Atmospheric Chemistry and Physics*, 12, 11795 –11817, doi:10.5194/acp-12-11795-2012, www.atmos-chem-phys.net/12/11795/2012/, 2012.

Atmos. Chem. Phys., 12, 11795–11817, 2012
www.atmos-chem-phys.net/12/11795/2012/
doi:10.5194/acp-12-11795-2012

Atmospheric Chemistry and Physics

Analysis of secondary organic aerosol formation and aging using positive matrix factorization of high-resolution aerosol mass spectra: application to the dodecane low-NO_x system

J. S. Craven[1], L. D. Yee[2], N. L. Ng[6], M. R. Canagaratna[3], C. L. Loza[1], K. A. Schilling[1], R. L. N. Yatavelli[4,*], J. A. Thornton[4], P. J. Ziemann[5], R. C. Flagan[1,2], and J. H. Seinfeld[1,2]

[1]Division of Chemistry and Chemical Engineering, California Institute of Technology, Pasadena, California, USA
[2]Division of Engineering and Applied Science, California Institute of Technology, Pasadena, California, USA
[3]Aerodyne Research, Inc., Billerica, Massachusetts, USA
[4]Department of Atmospheric Sciences, University of Washington, Seattle, Washington, USA
[5]Air Pollution Research Center, Department of Environmental Sciences, and Environmental Toxicology Graduate Program, University of California, Riverside, California, USA
[6]School of Chemical and Biomolecular Engineering and School of Earth and Atmospheric Sciences, Georgia Institute of Technology, Atlanta, Georgia, USA
[*]current address: Cooperative Institute for Research in Environmental Sciences (CIRES), University of Colorado, Boulder, Colorado, USA

Correspondence to: J. H. Seinfeld (seinfeld@caltech.edu)

Received: 7 June 2012 – Published in Atmos. Chem. Phys. Discuss.: 6 July 2012
Revised: 26 October 2012 – Accepted: 4 December 2012 – Published: 17 December 2012

Abstract. Positive matrix factorization (PMF) of high-resolution laboratory chamber aerosol mass spectra is applied for the first time, the results of which are consistent with molecular level MOVI-HRToF-CIMS aerosol-phase and CIMS gas-phase measurements. Secondary organic aerosol was generated by photooxidation of dodecane under low-NO_x conditions in the Caltech environmental chamber. The PMF results exhibit three factors representing a combination of gas-particle partitioning, chemical conversion in the aerosol, and wall deposition. The slope of the measured high-resolution aerosol mass spectrometer (HR-ToF-AMS) composition data on a Van Krevelen diagram is consistent with that of other low-NO_x alkane systems in the same O : C range. Elemental analysis of the PMF factor mass spectral profiles elucidates the combinations of functionality that contribute to the slope on the Van Krevelen diagram.

1 Introduction

The processes by which the atmospheric oxidation of volatile organic compounds (VOCs) leads to low volatility products that partition into the aerosol phase, forming Secondary Organic Aerosol (SOA), are complex and not thoroughly understood. Gas-phase oxidation processes are key in SOA formation, but there is increasing evidence that chemistry occurring in the particle phase, as well, may be important in producing the low-volatility, oxygenated compounds that characterize SOA. Laboratory chamber studies are essential to understand the lifecycle of organics involved in the formation of SOA. In such chamber experiments, measurements of both gas- and particle-phase chemical composition provide a window into the complex chemistry of SOA formation. While measurement of the complete suite of compounds involved in SOA formation is generally not feasible, key observations can provide considerable insight into the nature of the multi-generation gas-phase oxidation that characterizes SOA formation. High-Resolution Time-of-Flight

Aerosol Mass Spectrometer (HR-ToF-AMS) measurements of aerosol composition enable derivation of a number of key SOA properties; these include the atomic oxygen-to-carbon and hydrogen-to-carbon ratios (O : C and H : C), from which one can infer the overall oxidation state of the aerosol. The full HR-ToF-AMS spectrum, over the course of SOA formation and evolution, comprises a large number of mass-to-charge ratios (m/z), which contain time-dependent information on the overall processes occurring. Positive Matrix Factorization (PMF) has proved to be a powerful procedure for analyzing HR-ToF-AMS spectra in terms of the evolution of major mass spectral factors (Lanz et al., 2007; Ulbrich et al., 2009; Aiken et al., 2009; Ng et al., 2010; Hersey et al., 2011; Fry et al., 2011). The factor profile extracts the contributions from a number of masses that are co-correlated, providing information on the time evolution of the aerosol composition that is not immediately evident from the complex aerosol spectrum. We present here the first application of PMF to HR-ToF-AMS spectra obtained in a laboratory chamber investigation of SOA formation.

The present study is part of a comprehensive investigation of SOA formation from large alkanes. Historically, alkanes have been considered a significant atmospheric component of the unresolved complex mixture (UCM) of organics (Schauer et al., 2001, 2002). With the advent of a recently developed soft ionization gas chromatography technique, the unresolved complex mixture has been characterized at the molecular level to contain *n*-alkanes, cycloalkanes, bicycloalkanes, tricycloalkanes, and steranes (Isaacman et al., 2012). Pye and Pouliot (2012) predict from the Community Multiscale Air Quality (CMAQ) model the SOA yield from alkanes and PAHs to be 20 to 30 % of that from anthropogenic hydrocarbons. In particular, the linear alkane is predicted to dominate the SOA yield for the C_{12} alkanes. This first phase of the comprehensive investigation of alkanes focuses on high-resolution HR-ToF-AMS spectra of dodecane ($C_{12}H_{26}$) SOA. In conjunction with Chemical Ionization Mass Spectrometer (CIMS) measurements, and Micro-Orifice Volatilization Impactor Coupled to a Chemical Ionization Mass Spectrometer (MOVI-HRToF-CIMS), the application of PMF provides insight into the multi-generational and multi-phase processes involved in SOA formation and aging.

2 Experimental

Experiments were carried out in the Caltech environmental chamber facility, which is comprised of dual 28 m^3 teflon chambers (Table 1, Cocker et al., 2001). Experiments were carried out in a low-NO_x environment with hydrogen peroxide (H_2O_2) photolysis as the OH source. For each experiment, 280 µl of 50 % wt aqueous H_2O_2 solution was evaporated into the chamber, followed by atomization of 0.015 M aqueous ammonium sulfate (AS) solution for seed particles, which were subsequently dried. Finally, the specific volume of liquid dodecane necessary to achieve the desired gas-phase concentration was evaporated into the chamber. The oxidant, seed, and hydrocarbon mixed for 1 h prior to irradiation.

2.1 High-resolution time-of-flight aerosol mass spectrometer

In the Aerodyne high-resolution time-of-flight aerosol mass spectrometer (HR-ToF-AMS), aerosol is sampled at atmospheric pressure through an aerodynamic lens into a particle time-of-flight chamber, at the end of which the particles impact a 600 °C heater and 70 eV filament assembly where they are vaporized and ionized. The aerosol ion fragments are then orthogonally extracted into the ion time-of-flight chamber where they are sampled in either V (higher signal) or W (higher resolution) mode. For these experiments, both modes were utilized at a 1 min sequential sampling rate. The V-mode was utilized for PMF analysis, as the higher m/z values exhibit a more favorable signal-to-noise ratio; the W-mode was used for ion identification, clarification, and elemental analysis. The V-mode and W-mode can be set to measure bulk aerosol composition in which all of the particles within the transmission of the instrument (60–600 nm with 100 % transmission efficiency) are measured. This is commonly referred to as mass spec.-mode (MS-mode). The HR-ToF-AMS can also measure size-resolved chemistry by employing the particle time-of-flight-mode (PTOF-mode) in which the aerosol beam is chopped in the particle time-of-flight chamber and single particles are sized and sampled. All HR-ToF-AMS data were processed with "Squirrel", the ToF-AMS Unit Resolution Analysis Toolkit (http://cires.colorado.edu/jimenez-group/ToFAMSResources/ToFSoftware/index.html), in Igor Pro Version 6.22A (Wavemetrics, Lake Oswego, OR). Adjustments to the fragmentation table were made to correct for air interferences based on measurements made at the beginning of each experiment with a particle filter in-line with the chamber sample line and the HR-ToF-AMS (Allan et al., 2004). The ToF-AMS High Resolution Analysis software tool PIKA (Peak Integration by Key Analysis) was employed for high-resolution analysis (DeCarlo et al., 2006). Elemental ratios were calculated using the technique outlined by Aiken et al. (2008) and Chhabra et al. (2010).

2.2 Chemical Ionization Mass Spectrometer

A Chemical Ionization Mass Spectrometer (CIMS) was employed for the measurement of gas-phase photooxidation products, including key intermediates contributing to the particle phase. The CIMS consists of a Varian 1200 triple quadrupole mass spectrometer that has been modified to accommodate a custom ionization region. Sample air from the environmental chamber flows at 190 sccm into a glass flow

Table 1. Experimental conditions for dodecane low-NO_x photooxidation.

Exp #	duration (h)	initial hydrocarbon conc. (ppb)	seed type	initial seed volume ($\mu m^3\ cm^{-3}$)	HR-ToF-AMS mode
1	18	34	AS	9.1	MS-mode, (V and W)
2	34	34	AS	11.4	(MS-mode (V and W)
3	18	33	AS	12.0	(MS-mode (V and W)
4	18	50	AS	14.1	MS-mode (V and W), PTOF-mode (V)
5	18	300	AS	34.7	MS-mode (V and W), turned heater off

tube, where it is diluted by a factor of nine with N_2 gas. It then enters the chemical ionization region. The CIMS uses CF_3OOCF_3 reagent gas, generating cluster products at $[X.CF_3O]^-$ and fluoride transfer products at $[X.F]^-$, where X is the analyte. Hydroperoxide-containing species are detected as a cluster product, and strongly acidic species are primarily detected as the transfer product. More weakly acidic species can be detected as both a cluster and transfer product. In these experiments, such products were tracked with the CIMS as discussed previously (Yee et al., 2012). Additional details of the instrument and its general operation have been described elsewhere (St. Clair et al., 2010; Paulot et al., 2009; Crounse et al., 2006).

2.3 Micro-orifice volatilization impactor coupled to a high-resolution time-of-flight chemical ionization mass spectrometer

A micro-orifice volatilization impactor coupled to a high-resolution time-of-flight chemical-ionization mass spectrometer (MOVI-HRToF-CIMS) was employed. Analysis in the MOVI-HRToF-CIMS is a two-step cycle in which (i) gas-phase compounds are measured by the high-resolution TOFMS while aerosols are collected, and (ii) collected aerosols are then thermally vaporized with composition measured by the spectrometer. Chemical ionization (CI) preserves the parent ion in most cases, which, when combined with a high-resolution TOF analyzer, allows determination of the elemental composition of the molecular ions in the mass range of 17–550 m/z with a mass resolution of 4500 for mass to charge > 100 (Yatavelli and Thornton, 2010; Yatavelli et al., 2012).

2.4 Positive Matrix Factorization (PMF)

Positive Matrix Factorization (PMF) has emerged as a powerful technique for source apportionment of HR-ToF-AMS measurements of ambient aerosol (Paatero and Tapper, 1994; Jimenez et al., 2009; Lanz et al., 2007; Ulbrich et al., 2009; Aiken et al., 2009; Hersey et al., 2011; Ng et al., 2010; Allan, 2003; Zhang et al., 2011). Here, the application of PMF to HR-ToF-AMS spectra to investigate SOA formation in a laboratory chamber is reported for the first time. The factors are groups of ions (or fractions of ions) that vary together in time. For chamber experiments, this variation could result from processes such as gas-particle partitioning, chemical conversion in the aerosol, or wall loss of either individual molecules, or more likely a group of molecules with similar chemical character, such as the gas-phase products from a specific generation of gas-phase oxidation. Gas-phase measurements support and the dodecane low-NO_x mechanism predicts the multi-generation production of increasingly oxidized gas-phase products, which are expected to condense at different times. The AMS-PMF time series results are compared with molecular level detail of the CIMS gas-phase and MOVI-HRToF-CIMS aerosol-phase measurements, linking the HR-ToF-AMS high time-resolution electron impact ion information to the complex aerosol molecular level composition. The PMF results are explored using the PMF Evaluation Tool Version 2.04 in Igor Pro (http://cires.colorado.edu/jimenez-group/wiki/index.php/PMF-AMS_Analysis_Guide, Ulbrich et al., 2009). The details of implementing PMF are given in the Appendix A.

3 Results

SOA formation and aging comprise a number of atmospheric processes: (1) gas-phase reactions involving the primary organic and its oxidation products that involve functionalization and fragmentation; (2) gas-particle partitioning of lower volatility products; (3) chemical reactions in the aerosol phase that can lead to even lower volatility compounds or, in some cases, fragmentation and return to the gas phase. In interpreting the results of laboratory chamber experiments, one must also consider the effect of deposition of gases and particles to the chamber walls. In the present study we seek, via a combination of HR-ToF-AMS and CIMS measurements, to evaluate both gas- and particle-phase routes to formation of oxidized compounds.

3.1 Elemental ratios

Figure 1 shows the evolution of total organic aerosol mass during the longer experiment (Table 1). The O : C and H : C elemental ratios of the aerosol provide information on the bulk chemical evolution over the course of the experiment.

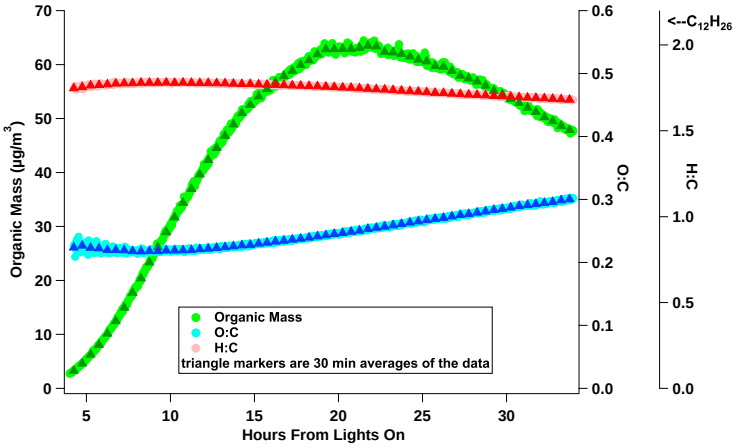

Fig. 1. Total organic aerosol mass and O : C and H : C elemental ratios for experiment 2. The $C_2H_4^+$ ion has been removed from the mass spectra due to its interference with the large signal from the N_2^+ ion. The triangles are 30 min averages of the data.

The first reliable O : C measurement yields a value near 0.22, which is consistent with the predicted early aerosol product, the C_{12} carbonyl hydroperoxide (product formula of $C_{12}H_{24}O_3$, O : C of 0.25). Upon further OH exposure, the O : C ratio grows to about 0.3. The H:C ratio is initially at 1.7, reflecting the oxidized nature of the aerosol composition at a relatively early stage of formation. The H : C ratio then increases after early growth to 1.79 and then decreases to 1.69 at 34 h. Dodecane itself has an H : C of 2.17 and an O : C of 0, so the initially high H : C and low O : C reflect the early oxidation stage of aerosol. The $C_2H_4^+$ ion was removed from the mass spectra owing to large interference with the N_2^+ ion, but with little effect on the absolute value and time trend of the elemental ratios. Individual high resolution ions provide further information on those masses in the spectrum that are driving the evolution of the aerosol chemical composition.

3.2 High-resolution ion analysis

The higher mass ions ($> m/z$ 100) in the HR-ToF-AMS spectrum provide key information regarding the low-volatility SOA constituents. Owing to the fragmentation caused by electron impact ionization, numerous ion combinations contribute to each nominal mass; the larger the mass, the greater the potential information regarding molecular detail, but the greater challenge in extracting that information. An explicit chemical mechanism of dodecane oxidation is critical in identifying individual ions, as well as patterns in the HR-ToF-AMS spectrum. A simplified schematic of the low-NO_x mechanism presented by Yee et al. (2012) is shown in Fig. 2.

At early growth, m/z 183 and m/z 215 dominate the signal for $m/z > 100$ (Figs. 3 and 4). At the outset, the only apparent ion at m/z 183 is $C_{12}H_{23}O^+$, but by the end of oxidation, $C_{10}H_{15}O_3^+$ has clearly grown in as a "left-side" neighbor to the original ion. This same type of behavior occurs for m/z 215 and, indeed, for almost all of the other masses in the spectrum. These developing patterns allow for a systematic identification of the ions at each mass. In each case, the later neighboring ion(s) have fewer carbons and more oxygens, as expected from continuous multi-generation oxidation. The unit mass resolution signals of m/z 183 and m/z 215, shown in Figs. 3 and 4, emphasize the difference in information between the unit mass and high-resolution analysis. The high resolution ions well past m/z 100 provide ion trend information (see Sect. 3.3), even if these ions do not influence the overall H : C and O : C ratios owing to small mass contributions.

3.3 Varying time trends for C_{12} ion fragments

The ions at higher m/z provide unique time traces from which inferences about the aerosol composition can be drawn. For example, the time series of C_{12} fragments in Fig. 5 shows distinct maxima during the course of the experiment. Since the parent hydrocarbon is a C_{12} molecule, the fragments shown in Fig. 5 are close to molecular level detail. The steady increase in signal of the less oxidized ion $C_{12}H_{23}O^+$ at m/z 183, followed by the increase of $C_{12}H_{21}O_2^+$ at m/z 197, and then $C_{12}H_{19}O_3^+$ at m/z 211 reflect the incorporation of increasingly oxidized products to the aerosol. The processes by which each ion reaches a maximum and then decreases are more challenging to infer. Deposition of aerosol to the chamber walls will cause the ion

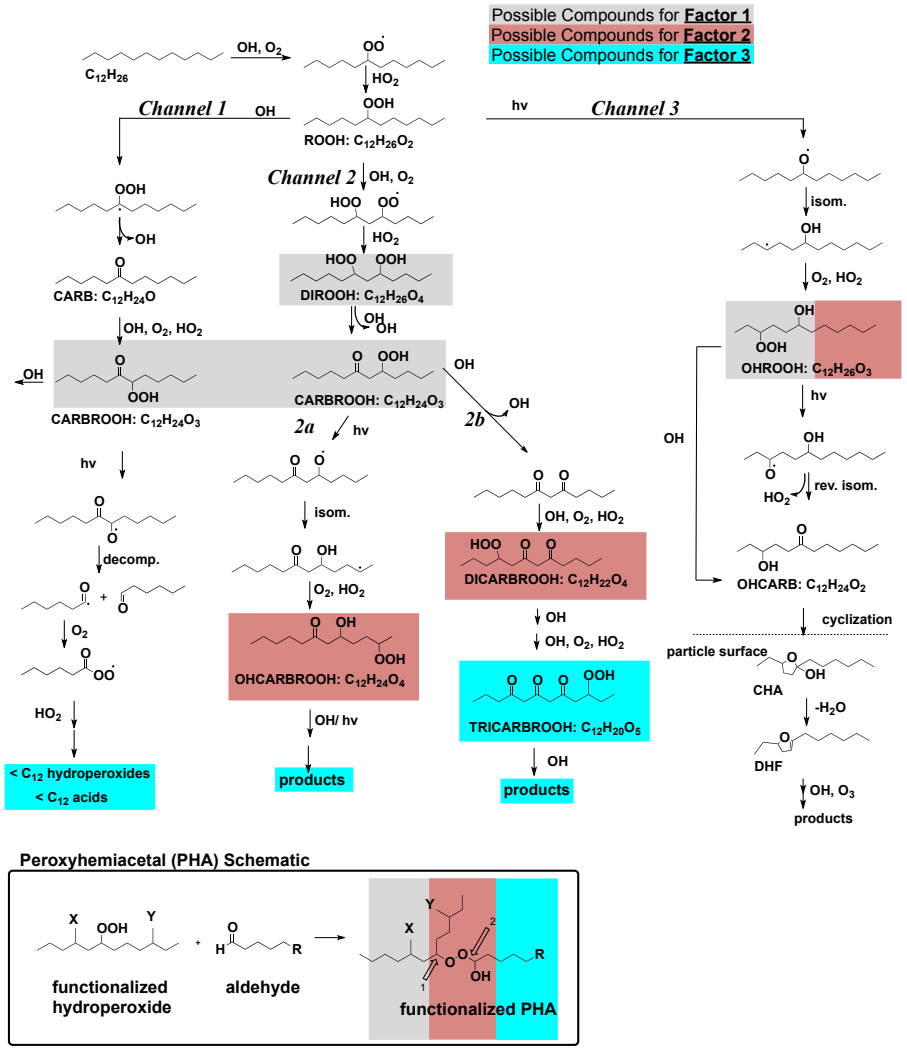

Fig. 2. Simplified chemical mechanism for dodecane photooxidation under low-NO_x, adapted from Yee et al. (2012). Shaded portions of the mechanisms are possible assignments for the PMF factors 1, 2 and 3, as discussed in Sects. 3.4 and 3.5.

signals to decrease (Sect. 3.6). A decreasing trend could also be the result of partitioning of products back to the gas-phase as their gas-phase equivalent reacts. Then, upon further oxidation in the gas-phase, the product re-condenses as a more oxidized species. Chemical conversion of the condensed products would provide another explanation for some ions to be decreasing, at the same time other ions are increasing. In electron impact ionization a particular ion fragment can be produced from two different compounds. This effect is magnified in the smaller m/z's, for example, the $C_2H_3^+$ ion at m/z 27, which is dominant throughout the entire experiment and a common fragment for alkyl molecules.

The ions identified in the HR-ToF-AMS spectra are a linear combination of the molecules in the aerosol; positive matrix factorization is well suited for long-duration chamber experiments, especially with ions that have unique time trends. The PMF results are an attempt to rebuild the molecular trend information that is lost from electron impact ionization in the HR-ToF-AMS. The less harsh ionization methods of both the heating mode of the MOVI-HRToF-CIMS and gas-phase measurements from the CIMS provide molecular

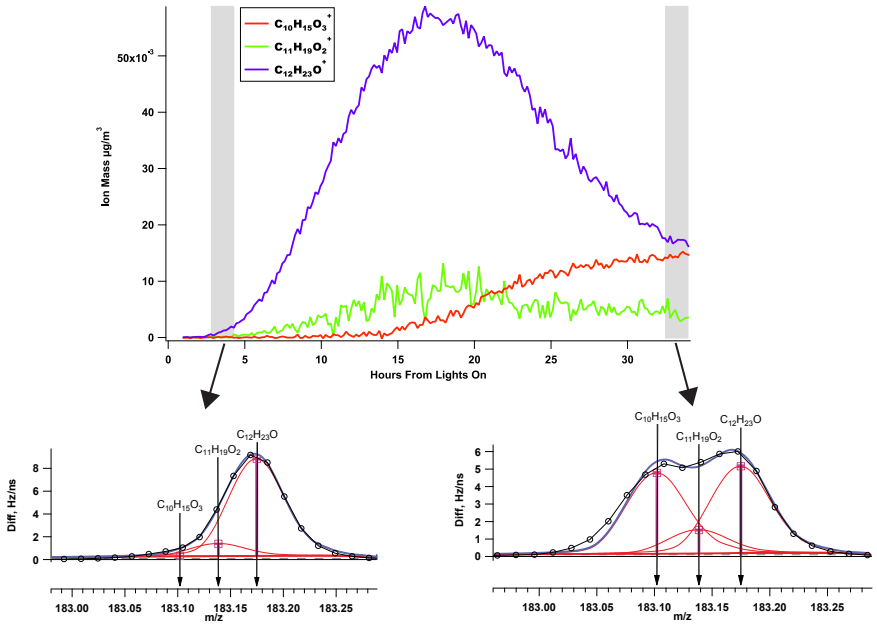

Fig. 3. Time series of ions and the raw data for "early growth" and "most oxidized growth" for m/z 183.

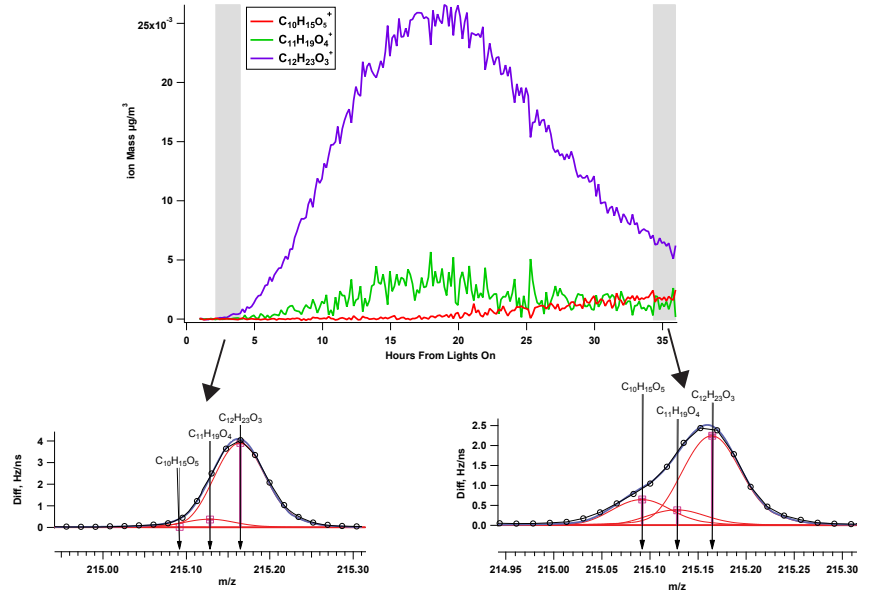

Fig. 4. Time series of ions and the raw data for "early growth" and "most oxidized growth" for m/z 215.

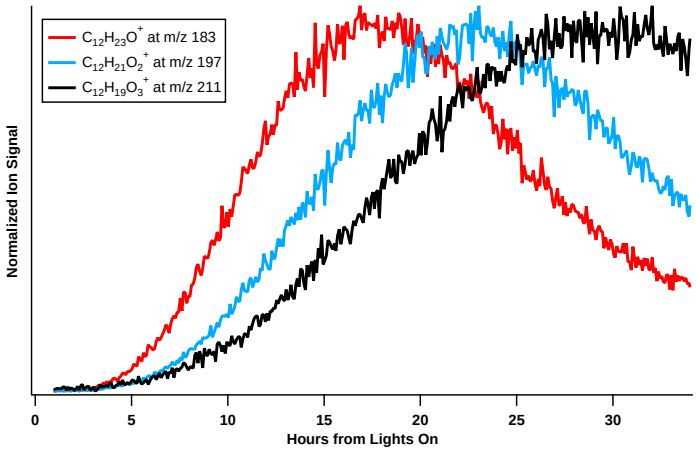

Fig. 5. C_{12} backbone ions with varying contributions of oxygen have distinct time trends over the duration of the experiment.

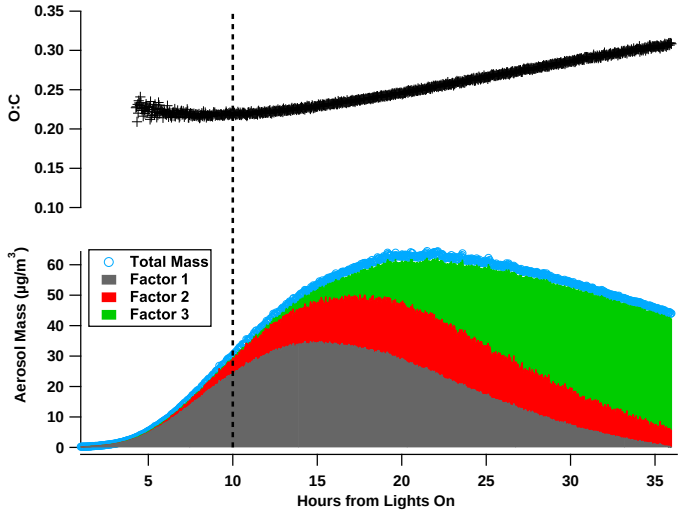

Fig. 6. Three-factor PMF solution, total organic mass, and O : C ratio. The dashed line denotes the point at which factor 3 grows in and the O : C begins to rise appreciably.

level information that the HR-ToF-AMS is unable to obtain, but to which the PMF results show similarity. From this comparison, molecular information can be inferred about the HR-ToF-AMS spectra, and how compounds fragment in the HR-ToF-AMS. Moreover, PMF results can be applied to obtain insight into the partitioning of the populations of oxidized molecules and the aerosol composition that evolves with continued oxidation.

3.4 Three-factor PMF solution

The PMF results for low-NO_x SOA formation from dodecane oxidation exhibit three distinct time traces with their correlating factor mass spectral profiles (Figs. 6 and 7) . The three factor time series, shown in Fig. 6, are overlaid with the total organic loading to emphasize the relationship of each factor to the total SOA mass. The O : C ratio traces the overall oxidation state in the aerosol, and the PMF factors help explain that behavior. Factor 1, in grey, is dominant in the early aerosol growth and contains the least oxidized ions

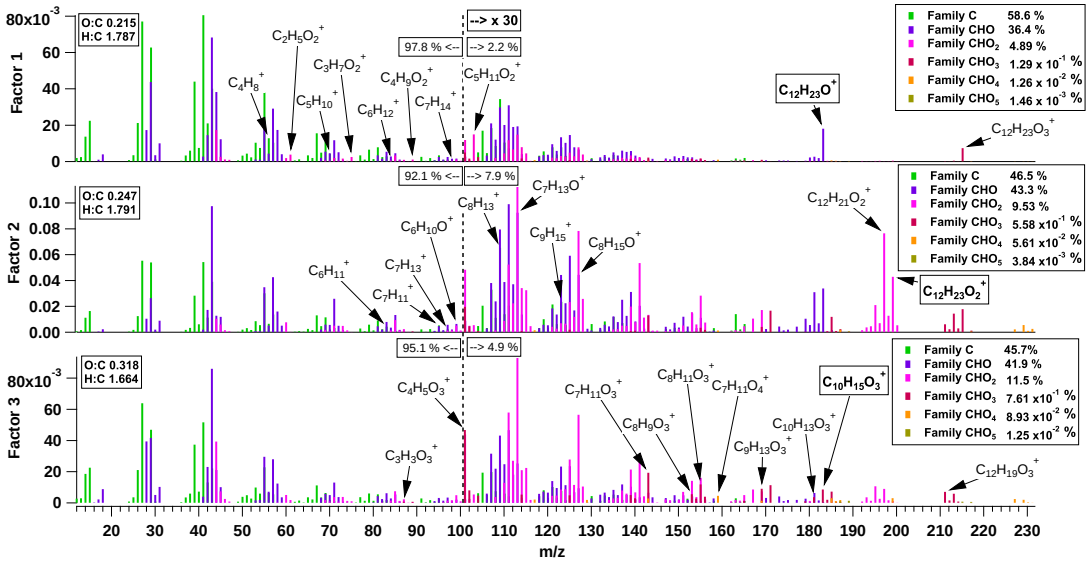

Fig. 7. The 3-factor mass spectra profiles in terms of their families. The ions past m/z 100 are multiplied by 30 to amplify signal strength.

(has the highest H:C ratio) of the factors. Factor 2 grows in next, peaks after factor 1, and then decreases. Factor 3 contains the highest contribution to the CO^+ and CO_2^+ ions and other O_2, O_3, O_4, and O_5 – containing ions, explaining the steady increase in O:C over the course of the experiment. The CO_2^+ ion is the tracer for carboxylic acid in the HR-ToF-AMS (Aiken et al., 2008), which could explain the increase in O : C; however, the existence of the > 2 oxygen ion fragments indicates the O : C ratio increase could also be due to highly functionalized compounds, and not solely carboxylic acids, an observation supported by the chemical mechanism (Fig. 2) and the Van Krevelen Diagram (Sect. 3.7).

The mass spectral profiles of the factors are presented in Fig. 7, in which ions with different oxygen contents (different ion families) are highlighted by different colors. The mass percentage of each family to the total factor is presented in each factor's legend. Each factor profile has distinct, unique masses in the $> m/z$ 100 range. While it is difficult to identify an ion unique to one factor, certain ions have a higher contribution to one factor than another. Pearson's r correlation of each ion in the spectrum to each factor time series was used to identify which unique ions contribute the most to each factor. The 10 ions with the highest correlation in time with the factor profiles are tagged in the figure, with the top ion surrounded by a box. These are also listed in Table 3. The time trends of the top 3 ions correlating with each factor are displayed in Fig. 8. These ions provide the basis for identifying HR-ToF-AMS tracer ions for different generations of oxidation products. The interpretation of these factor time series and mass spectral profiles is aided by a chemical mechanism of dodecane oxidation, as well as comparison of time series to CIMS and MOVI-HRToF-CIMS data and individual HR-ToF-AMS ions.

3.5 Chemical interpretation of PMF solution

Factor 1 mass spectra and time series correlations with CIMS (Fig. 10) and MOVI-HRToF-CIMS (Fig. 11) ion time traces suggest that factor 1 could be C_{12} carbonyl hydroperoxide or C_{12} dihydroperoxide gas-to-particle partitioning (CARBROOH or DIROOH, Fig. 2, see grey shaded box) and possibly peroxyhemiacetal formation (see inset from Fig. 2). A $C_{18}H_{38}$ low-NO_x photooxidation experiment was carried out to produce a hydroperoxide standard and to understand the hydroperoxide fragmentation pattern in the HR-ToF-AMS (Fig. 9 and Table 4). The first product from $C_{18}H_{38}$ low-NO_x photooxidation is the hydroperoxide, which because of its long carbon chain, is expected to condense immediately onto the aerosol. Removal of HO_2 from the C_{18} hydroperoxide is supported by the $C_{18}H_{37}^+$ ion in the HR-ToF-AMS spectrum; this ion is considered a tracer for the C_{18} hydroperoxide. Fraser et al. (1970) also saw alkyl ions with 70 eV electronic impact ionization mass spectrometry measurements of alkyl hydroperoxides and attributed these peaks to HO_2 elimination from the hydroperoxide. The $C_3H_7O_2^+$ ion is also considered to be a tracer for the hydroperoxide-like compound since it has the highest percent difference between the $C_{18}H_{38}$ condensation spectrum before irradiation and the mass spectrum immediately after irradiation.

For dodecane, we do not expect the C_{12} hydroperoxide to partition to the particle phase, but we do expect the C_{12}

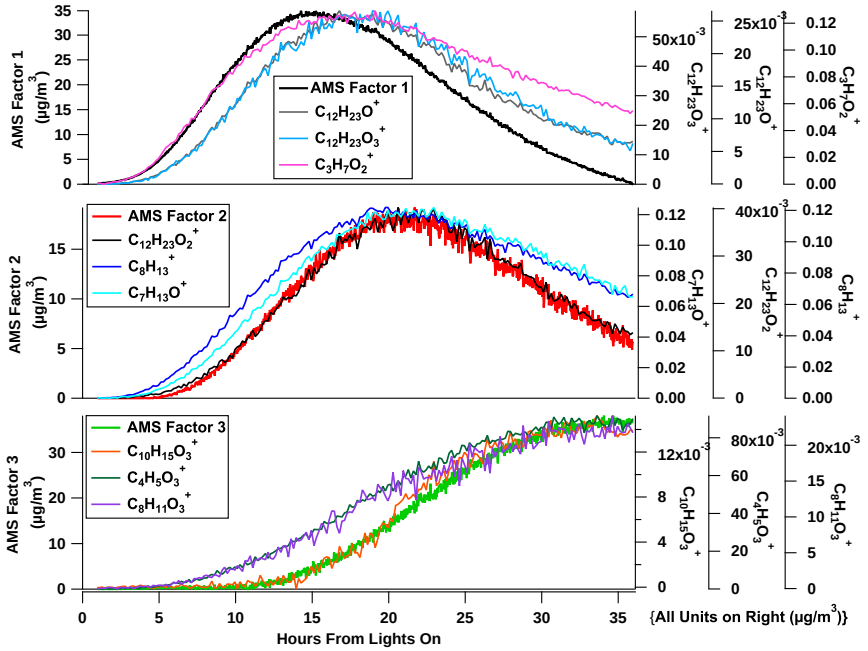

Fig. 8. Factor time series with the top three highest Pearson's r correlating HR-ToF-AMS ions.

Table 2. Ion fragments.

m/z	Ion	possible identification
169	$C_{12}H_{25}^+$	hydroperoxide, hydroperoxide-peroxyhemiacetal
201	$C_{12}H_{25}O_2^+$	hydroperoxide-peroxyhemiacetal
185	$C_{12}H_{25}O^+$	hydroxy hydroperoxide, hydroxy hydroperoxide-peroxyhemiacetal
217	$C_{12}H_{25}O_3^+$	hydroxy hydroperoxide-peroxyhemiacetal
183	$C_{12}H_{23}O^+$	carbonyl hydroperoxide, carbonyl hydroperoxide-peroxyhemiacetal
215	$C_{12}H_{23}O_3^+$	carbonyl hydroperoxide-peroxyhemiacetal
197	$C_{12}H_{21}O_2^+$	dicarbonyl hydroperoxide, dicarbonyl hydroperoxide-peroxyhemiacetal
229	$C_{12}H_{21}O_4^+$	dicarbonyl hydroperoxide-peroxyhemiacetal
199	$C_{12}H_{23}O_2^+$	hydroxy carbonyl hydroperoxide, hydroxy carbonyl hydroperoxide-peroxyhemiacetal
231	$C_{12}H_{23}O_4^+$	hydroxy carbonyl hydroperoxide-peroxyhemiacetal
211	$C_{12}H_{19}O_3^+$	tricarbonyl hydroperoxide, tricarbonyl hydroperoxide-peroxyhemiacetal
243	$C_{12}H_{19}O_5^+$	tricarbonyl hydroperoxide-peroxyhemiacetal

carbonyl hydroperoxide to partition (Yee et al., 2012). The presence of ion fragment $C_{12}H_{23}O^+$ at m/z 183 supports this explanation (Fig. 3). The $C_{12}H_{23}O_3^+$ ion at m/z 215 (a 32 m/z and O_2^+ difference from the carbonyl hydroperoxide ion) trends with the $C_{12}H_{23}O_3^+$ ion with a Pearson's r of 0.986 and is the ion with the highest correlation in the entire spectrum to $C_{12}H_{23}O^+$. A possible assignment of $C_{12}H_{23}O_3^+$ in correlation with $C_{12}H_{23}O^+$ is the peroxyhemiacetal corresponding to the carbonyl hydroperoxide (possible fragmentation at site 2 of peroxyhemiacetal, see inset in Fig. 2). Although the fragmentation of a peroxyhemiacetal standard in the HR-ToF-AMS can not be confirmed, the chemical mechanism prediction of aldehyde formation in the gas-phase and evidence for hydroperoxides in the gas- and particle-phase

Table 3. HR-ToF-AMS ions with highest Pearson's r values for $f_{peak} = 0.2$ solution.

Pearson's r with factor 1	Ion Formula	Ion Mass ($\mu g\,m^{-3}$)	Pearson's r with factor 2	Ion Formula	Ion Mass ($\mu g\,m^{-3}$)	Pearson's r with factor 3	Ion Formula	Ion Mass ($\mu g\,m^{-3}$)
0.888964	$C_{12}H_{23}O$	183.175	0.992157	$C_{12}H_{23}O_2$	199.17	0.978408	$C_{10}H_{15}O_3$	183.102
0.858995	$C_{12}H_{23}O_3$	215.165	0.975248	C_8H_{13}	109.102	0.970308	$C_4H_5O_3$	101.024
0.854958	$C_3H_7O_2$	75.0446	0.973654	$C_7H_{13}O$	113.097	0.95434	$C_8H_{11}O_3$	155.071
0.851494	C_6H_{12}	84.0939	0.973188	C_7H_{13}	97.1017	0.953511	$C_5H_7O_3$	115.039
0.835077	$C_5H_{11}O_2$	103.076	0.972338	$C_8H_{15}O$	127.112	0.949821	$C_9H_{13}O_3$	169.087
0.830188	$C_4H_9O_2$	89.0603	0.972216	C_7H_{11}	95.0861	0.947504	$C_7H_{11}O_3$	143.071
0.83002	C_5H_{10}	70.0782	0.970214	$C_{12}H_{21}O_2$	197.154	0.94481	$C_{12}H_{19}O_3$	211.133
0.819021	C_7H_{14}	98.1096	0.969585	C_9H_{15}	123.117	0.943721	$C_{10}H_{16}O_3$	184.11
0.812879	$C_2H_5O_2$	61.0289	0.969189	C_6H_{11}	83.0861	0.941672	$C_{10}H_{13}O_3$	181.087
0.775934	C_4H_8	56.0626	0.968232	$C_6H_{11}O$	99.081	0.939138	$C_3H_3O_3$	87.0082

suggest that peroxyhemiacetal formation or other oligomerization processes are possible.

Figure 8 shows the PMF factor time series with the top 3 correlating HR-ToF-AMS ions. The $C_3H_7O_2^+$ ion at m/z 75, which is a suggested hydroperoxide tracer (Table 4), nearly overlaps factor 1 for the first 15 h, after which the time trend of $C_3H_7O_2{}^+$ decays more slowly than factor 1; this is because the hydroperoxide functionalization could also have a contribution to factor 2, or later generations of oxidation products. $C_{12}H_{23}O^+$ at m/z 183 and $C_{12}H_{23}O_3^+$ at m/z 215 also have a high correlation, although these ions grow in slightly after the hydroperoxide ion at m/z 75. The difference between the individual ions trends and the PMF time trace is expected since the PMF factor represents the bulk variation of the aerosol composition over time and is not necessarily expected to exactly overlap with individual ion trends. Additionally, due to the fragmentation in the HR-ToF-AMS, single ions can contribute to multiple factors. The top 10 ions with the highest Pearson's r values for each factor show this effect (Fig. A1). The chemical interpretation of factor 1 is also supported by comparison to the CIMS gas-phase measurement of positive mode m/z 204, the suggested product being the carbonyl hydroperoxide (Fig. 10, Yee et al., 2012) as well as the MOVI-HRToF-CIMS heating-mode measurement of the $C_{12}H_{21}O_3{}^+$ ion, which is likely the chemical ionization product of a C_{12} dihydroperoxide (Fig. 11).

HR-ToF-AMS, CIMS, and MOVI-HRToF-CIMS measurements suggest that factor 2 represents the gas-phase partitioning of tri-functionalized products and their corresponding peroxyhemiacetals (see pink shaded boxes in Fig. 2). Factor 2 correlates highly with HR-ToF-AMS ion $C_{12}H_{23}O_2^+$ at m/z 199, which is the suggested ion tracer for the hydroxy carbonyl hydroperoxide (OHCARBROOH). Factor 2 also correlates well with the CIMS gas-phase positive mode m/z 219, which is the suggested dicarbonyl hydroperoxide product (Fig. 10) and the MOVI-HRToF-CIMS heating-mode ion $C_9H_{15}O_4^+$ (Fig. 11). The MOVI-HRToF-CIMS ion has higher oxygen content than ions trending with factor 1, which could suggest an additional functional group from further oxidation.

Factor 3 is likely the gas-particle partitioning of multifunctional (4 or more functional groups) products, as indicated by HR-ToF-AMS ion $C_{10}H_{15}O_3^+$ at m/z 183 and $C_{12}H_{19}O_3^+$ at m/z 211 (Fig. 7), which could be the tricarbonyl hydroperoxide product (TRICARBROOH). MOVI-HRToF-CIMS data also support the addition of a highly oxidized product to the aerosol with the ion $C_{10}H_{15}O_3^+$ trend (Fig. 11). Although the CIMS did not measure in the high m/z range necessary for identifying greater than trifunctionalized gas-phase products, the CIMS gas-phase C_8 carboxylic acid trace shows continual increase. This is consistent with factor 3 growth, the potential for acid formation in the chemical mechanism, and HR-ToF-AMS CO_2^+ ion, which could be from either acid formation or multifunctional products (Fig. 10). These results support factor 3 containing highly functionalized compounds, and acidic compounds, either from gas-to-particle partitioning of highly oxidized products or possibly from condensed chemical conversion from products in factors 1 and 2.

Factors 1 and 2 both exhibit a maximum with respect to time. A decrease after the maximum owing to wall deposition alone, addressed in Sect. 3.6, does not fully explain the decrease of these factors. The extent of evaporation of aerosol products is difficult to interpret from the gas-phase data. Other processes, such as cyclization or peroxyhemiacetal oligomerization, are possible (Tobias and Ziemann, 2000; Ziemann, 2003) but cannot be established unequivocally from HR-ToF-AMS data, as the fragments resulting from oligomerization are not unique. Masses greater than m/z 300 are observed in the MOVI-HRToF-CIMS spectra, which although difficult to assign exact elemental formulas, may suggest that products greater than C_{12} exist in the aerosol. Chemical conversion likely contributes to the decrease in factors 1 and 2 and increase in factor 3 (although gas-phase partitioning of highly oxidized compounds could also be contributing to the increase in factor 3). The percentages of mass greater than m/z 100 for factors 2 and 3 are

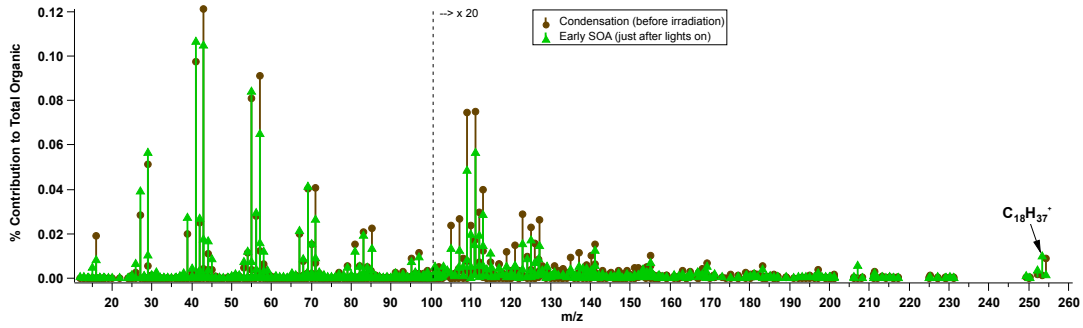

Fig. 9. Mass spectrum of octadecane condensing onto the seed before irradiation, and the relative mass spectrum just after lights on. The hypothesized octadecane-equivalent hydroperoxide fragment is marked at m/z 253.

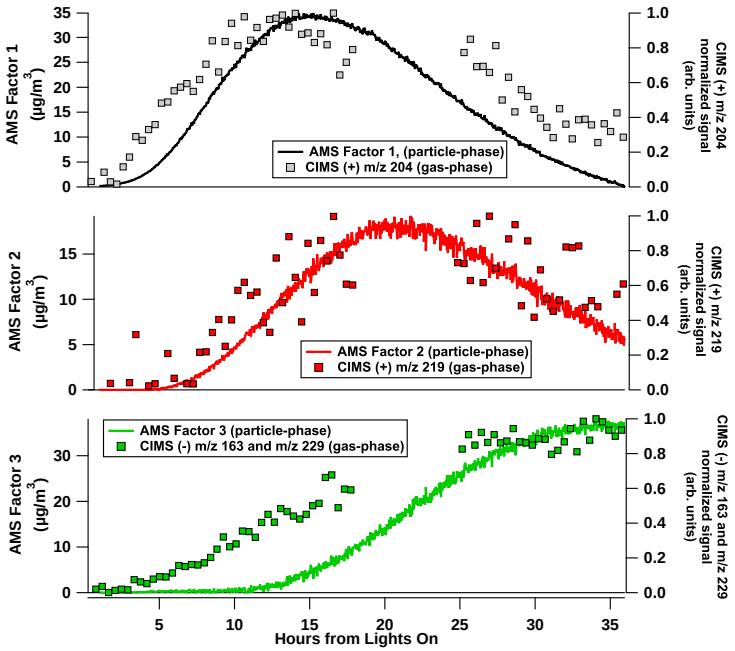

Fig. 10. Particle-phase HR-ToF-AMS factor time series with gas-phase CIMS time traces.

8 % and 5 %, respectively. The decrease of mass concentration of ions correlating with factor 2 may be a result of fragmentation in the aerosol. Molecular level identification of individual species from further MOVI-HRToF-CIMS analysis would be necessary to confirm this.

Other HR-ToF-AMS ions with 32 m/z difference that support a C_{12} functionalized hydroperoxide reacting with an aldehyde to form peroxyhemiacetal are listed in Table 2. Other 32 m/z pairs with fewer than 12 carbons exist, and may come from hydroperoxide formation in Channel 1 of the mechanism containing fragmentation of carbon chains fewer than 12.

The proposed peroxyhemiacetal tracer ions behave differently under reduced HR-ToF-AMS temperature. In experiment 5 in Table 1, the HR-ToF-AMS 600 °C heater was turned off and only ionization (no vaporization) was used to sample the aerosol. During the time when the heater was turned off, the bulk of the organic ions decreased, since the ionization of the aerosol is contingent upon its vaporization. However, signal generated by the ions for the hypothesized

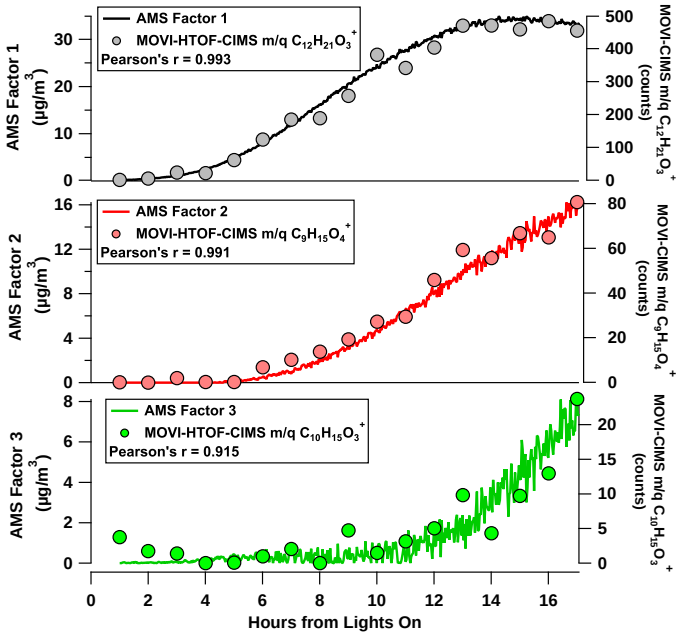

Fig. 11. Factor time series with MOVI-HRToF-CIMS heating-mode, aerosol-phase traces. Only the first 18 h of data is available for the MOVI-HRToF-CIMS data.

peroxyhemiacetal actually increased (Fig. 12). Since peroxyhemiacetals are unstable at high temperature, the decrease in temperature would stabilize peroxyhemiacetal, allowing the molecules to be more available for ionization.

It is important to note that the latter half of experiment 2 provides useful information in interpreting the chemistry of the aerosol. In the first 17 h, all of the factors show only an increase (see Figs. 11 and A1). The time trends of factors 2 and 3 look very similar in the first 17 h, but distinction becomes possible in the latter half of the experiment in which factor 2 decreases and factor 3 increases (Fig. 6). This explains perhaps why in a shorter experiment, two factors explain the data better (see Appendix A for further explanation on the effect of PMF on different lengths of experiment).

3.6 Chamber processes

Deposition of aerosol to the chamber walls decreases the suspended aerosol mass. PTOF-mode data are not available for the 34 h experiment discussed above. Experiment 4 was carried out, with a similar initial dodecane concentration, to explore the contribution from wall loss to the decrease in mass of the PMF factor time series. As expected, the average diameter of the aerosol mass distribution grew with increasing OH exposure (Fig. 13 and panel a1, a2 and a3 in Fig. 14). Since the wall loss rate is a function of diameter (Fig. 13, Loza et al., 2012), the size of the aerosol and composition at that size are important for factor dependent wall-loss corrections. Panel b of Fig. 14 shows the PMF factors (only 2 for a shorter experiment, see Sect. A2) as a function of time. "Time 1" is early in the experiment when the mass distribution is expected to have a major contribution from factor 1. "Time 2" is at maximum growth in time of factor 1 and a large contribution from factor 2, and "Time 3" is when factor 2 has passed factor 1 in overall mass. The PMF results for the mass distributions (diameter is the independent variable now instead of time) are shown with the overall organic mass distribution to emphasize the contribution from factors 1 and 2 to each size bin (panel a1, a2, and a3 with b on Fig. 14). Since factor 1 is the first to condense onto the aerosol, some of its mass is lost more rapidly than factor 2, which condenses later onto larger particles (which are lost by deposition at a slower rate). The mass fractions of factors 1 and 2 were calculated for each size bin for 12 mass distributions; this information was used to adapt the wall deposition calculations carried out by Loza et al. (2012) for individual factor wall loss corrections.

Even with wall loss correction, factor 1 shows a decrease, while factor 2 shows an increase; the cumulative mass loss by wall deposition for factor 1 at the end of the experiment is 18 µg m^{-3}, which accounts for approximately 50 % of the decrease in mass from the peak of factor 1 (panel c from Fig. 14). These results further support the hypothesis that the mass in the aerosol is undergoing chemical conversion. It is

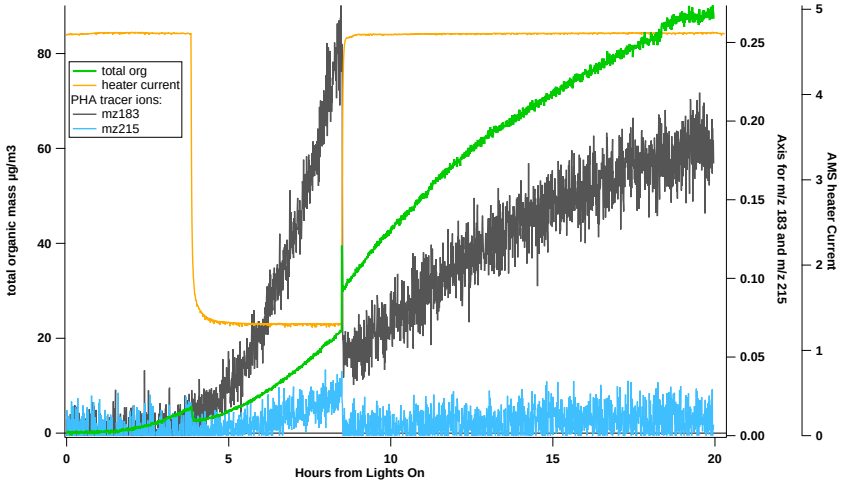

Fig. 12. Tracer ions for the carbonyl hydroperoxide increase while the bulk organic trace decreases when the 600 °C HR-ToF-AMS heater is turned off.

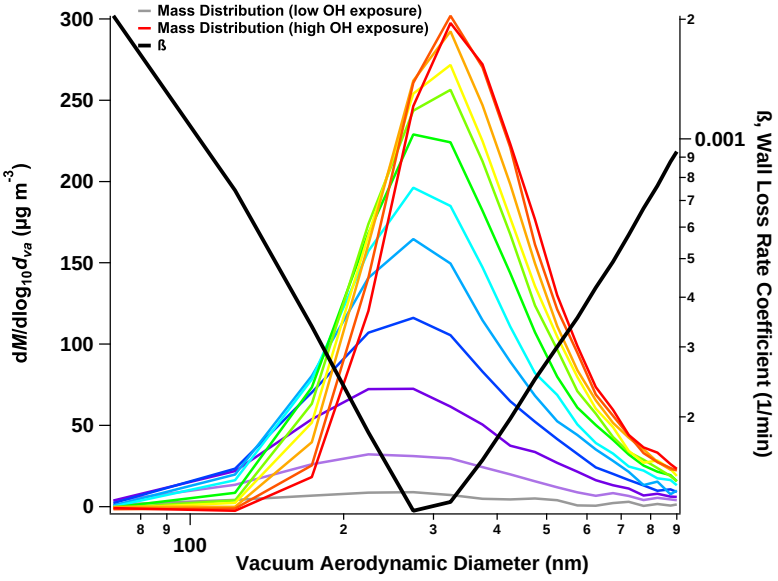

Fig. 13. The aerosol mass distribution grows from smaller diameter sizes to larger diameter sizes with increasing OH exposure (purple is low OH exposure, red is high OH exposure). The wall deposition rate coefficient is overlaid for comparison.

also important to note that the effects of wall loss on factors 1 and 2 differ as a result of the size distribution of the aerosol when the factor emerges.

3.7 Van Krevelen diagram

The Van Krevelen diagram has been used to represent the evolution of HR-ToF-AMS elemental ratios, H : C vs. O : C, for both ambient and chamber-generated organic aerosols (Heald et al., 2010; Ng et al., 2011; Chhabra et al., 2011; Lambe et al., 2011, 2012). A slope of 0 on the diagram is

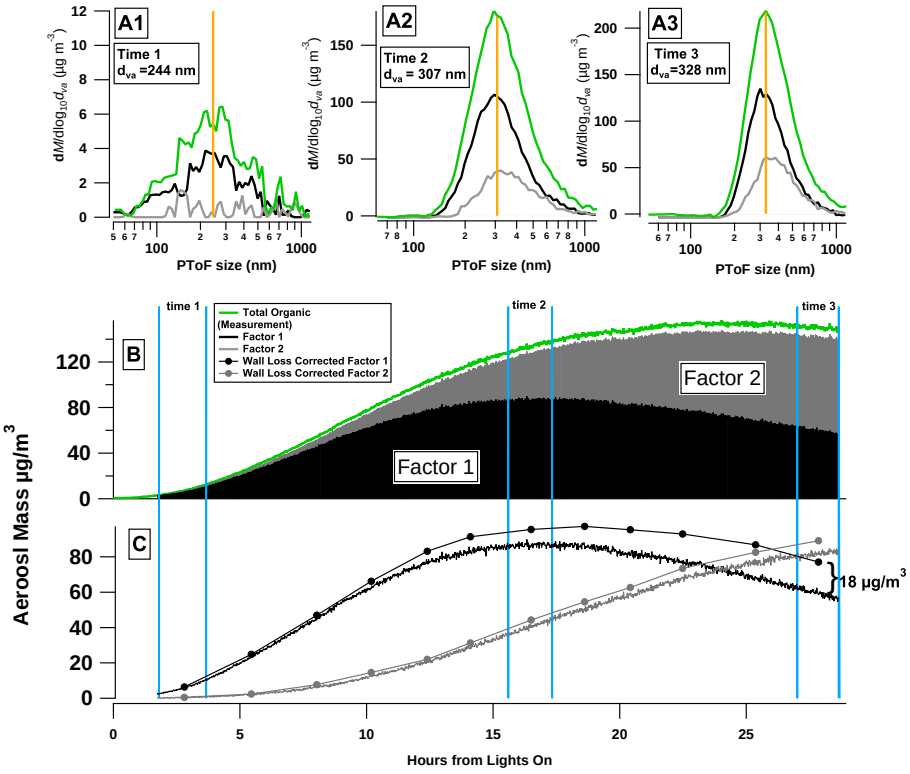

Fig. 14. Mass distributions (**A1**, **A2** and **A3**) and time series **(B)** of total organic mass (green) broken down into 2 factors (black and grey). The average diameter for each mass distribution is highlighted by the yellow bar, and the time associated with each distribution is outlined with the two blue bars on the time series graphs. The wall-loss corrected versions of the individual factor time series are also shown **(C)**.

consistent with peroxide or alcohol functionalization without carbon chain fragmentation. A slope of -1 is consistent with carboxylic acid or ketone/aldehyde and alcohol addition on the same carbon chain, and a slope of -2 is consistent with ketone/aldehyde addition (Van Krevelen, 1950; Heald et al., 2010). Lambe et al. (2012) report the slopes for low-NO_x photooxidation of long chain alkanes (C_{10}, C_{15}, and C_{17}) in a PAM reactor in two regimes in terms of the O : C ratio. For O : C < 0.3, the slope is relatively steep (-1.3 ± 0.2), while for O : C > 0.3 the slope becomes less negative (-0.7 ± 0.1). Lambe et al. (2012) attribute this change in slope to a transition from functionalization to fragmentation dominated reactions. The dodecane aerosol composition data presented here lie primarily in the regime where O : C < 0.3, with a slope of -1.16 that is consistent with Lambe et al. (2012) in this O : C range.

As discussed by Ng et al. (2011) and Lambe et al. (2012), the slope on a Van Krevelen diagram can represent a combination of several functionalities and generally requires molecular level information for further interpretation. The PMF analysis links the HR-ToF-AMS aerosol spectrum to molecular level detail when compared to measurements from CIMS and MOVI-HRToF-CIMS. Concurrent with our chemical understanding, over 34 h of oxidation, the dodecane low-NO_x system is characterized by the addition of peroxides and ketone/aldehyde functionalization, as opposed to solely carboxylic acid formation. PMF factor 1 (black marker in Fig. 15) overlaps the bulk composition data (grey markers) near the initial growth at low OH exposure. Factor 2 (red marker in Fig. 15) has a similar H : C ratio as factor 1, but higher O : C ratio. The slope between factors 1 and 2, $m_{12} = 0.12$, is characteristic of either hydroxy or peroxide addition. We have already shown that factor 2 describes the gas-phase partitioning of hydroperoxide species (Sect. 3.5). The addition of hydroperoxide functional groups is not obvious from the bulk H : C and O : C ratios (slope $= -1.16$), but only from the PMF factor elemental ratios. The H:C and O : C ratios of factor 3 (green marker in Fig. 15) overlaps the data (grey markers) at the end of the experiment. The slope from factor 2 to 3, $m_{23} = -1.78$, is characteristic of

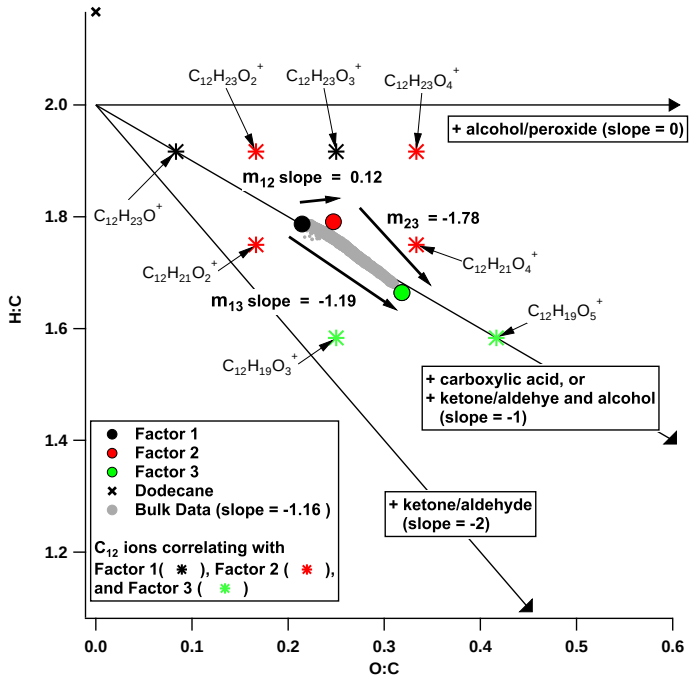

Fig. 15. Van Krevelen diagram for low-NO_x photooxidation of dodecane. HR-ToF-AMS bulk composition data are indicated by the grey markers and PMF factors 1–3 are shown by the black, red, and green circle markers. C_{12} ions, which are the ions retaining the most molecular-level detail, with high correlation to each factor are also displayed by the black, red, and green star markers.

the addition of products with carbonyl or ketone functionalization. The slope between factor 1 and 3, $m_{13} = -1.19$, is consistent with either carboxylic acid formation or ketone/aldehyde and alcohol addition to a product in factor 1. The slopes between the factor elemental ratios help indicate the combinations of functionality in the aerosol, with more clarity than one slope from the bulk elemental analysis. The C_{12} ion fragments correlating the highest with each factor and hypothesized to be mono-, di-, or tri- functionalized C_{12} hydroperoxides and/or functionalized peroxyhemiacetals are also displayed on Fig. 15.

4 Conclusions

In the present work, PMF has been applied to high-resolution chamber HR-ToF-AMS mass spectra to deduce the chemical and physical processes associated with low-NO_x dodecane SOA formation and aging. PMF untangles some of the complexity of SOA mass spectra by providing a mass spectral signature, with ion tracers, associated with a group of molecules at a distinct oxidation level. Factor 1 represents the gas-phase partitioning of initial oxidation products with two functional groups, factor 2 is the further oxidized, tri-functionalized products incorporating into the particle phase, and factor 3 is the partitioning of extended oxidation products quadruply functionalized. All three factors could also include oligomerization processes and contributions from wall-loss.

An octadecane low-NO_x photooxidation experiment was conducted to develop a hydroperoxide standard for the HR-ToF-AMS, from which the alkyl-ion $C_{18}H_{37}^+$ at m/z 253 and $C_3H_7O_2^+$ at m/z 75 were identified as hydroperoxide ion tracers. With the PMF factor results, in combination with the SOA mechanism, CIMS, and MOVI-HRToF-CIMS measurements, the peroxyhemiacetal ion tracers were proposed, such as the $C_{12}H_{23}O^+$ at m/z 183 and $C_{12}H_{23}O_3^+$ at m/z 215 for the carbonyl hydroperoxide-peroxyhemiacetal.

The Van Krevelen diagram of the data, supported by the chemical interpretation of the dodecane low-NO_x oxidation, is consistent with the addition of peroxides and ketone/aldehyde functionalization rather than solely carboxylic acids. While the bulk experimental elemental ratios exhibit a slope of -1.16, the change in H : C and O : C ratios from factors 1 to 2 reveals a slope of 0.12, strongly indicating hydroperoxide addition to the aerosol. The elemental ratios between factors 2 and 3 have a slope of -1.78, indicating adding of aldehyde/carbonyl functionalization, and the slope between factor 1 and 3 is -1.19, indicating either

Table 4. Distinct ions present in early C_{18} SOA formation.

Ion Formula	Exact Mass	% Difference from C_{18} Condensation MS*	Mass Fraction in SOA Spectrum
$C_3H_7O_2$	75.0446	0.99	0.0005
CO	27.9949	0.99	0.0007
CO_2	43.9898	0.99	0.0007
C	12.0000	0.99	0.0006
C_2H_2O	42.0106	0.99	0.0017
CHO_2	44.9977	0.99	0.0006
CH	13.0078	0.99	0.0006
CH_3	15.0235	0.99	0.0048
C_5H_3	63.0235	0.99	0.0006
$C_{18}H_{37}$	253.2900	0.98	0.0005
C_5H_7O	83.0497	0.98	0.0024
C_4H_9O	73.0653	0.98	0.0014
C_2H_3O	43.0184	0.97	0.0174
C_6H_6	78.0470	0.96	0.0014
CH_3O	31.0184	0.95	0.0027
C_2H_2	26.0156	0.95	0.0066
C_3H_7O	59.0497	0.95	0.0036
C_2H_5O	45.0340	0.94	0.0084
C_3H	37.0078	0.94	0.0008
C_4H_2	50.0157	0.94	0.0009
C_3H_3O	55.0184	0.94	0.0072
CHO	29.0027	0.93	0.0103
C_4H_4	52.0313	0.93	0.0012
$C_2H_5O_2$	61.0289	0.93	0.0007
C_3H_6O	58.0419	0.93	0.0118
C_3H_4O	56.0262	0.93	0.0010
C_5H_5O	81.0340	0.92	0.0010
C_4H_5	53.0391	0.92	0.0074
C_3H_4	40.0313	0.92	0.0041
$C_5H_{10}O$	86.0732	0.92	0.0005
$C_5H_{11}O$	87.0810	0.92	0.0005
C_9H_7	115.0550	0.92	0.0006
C_4H_6O	70.0419	0.92	0.0019
C_2H_4O	44.0262	0.92	0.0167
C_6H_8	80.0626	0.92	0.0013
C_3H_2	38.0157	0.91	0.0020
C_2H_3	27.0235	0.91	0.0390
C_5H_5	65.0391	0.91	0.0020
$C_6H_{11}O$	99.0810	0.91	0.0015
C_4H_7O	71.0497	0.91	0.0089
C_3H_3	39.0235	0.91	0.0271
C_4H_3	51.0235	0.91	0.0016
C_3H_5O	57.0340	0.90	0.0158

* Early Oxidation MS-Condensation MS)/Condensation MS

carboxylic acid formation or aldehyde/ketone and alcohol addition. With the aid of the PMF results, the experimental data displayed on the Van Krevelen diagram can be broken down into contributions from different types of functionality.

Size-dependent composition was utilized to determine the extent of wall-loss deposition affecting factors 1 and 2. The wall deposition contributed differently to each factor, but does not entirely explain the factor mass decrease; the decrease unexplained by wall loss deposition is attributed to chemical aging of the aerosol.

The chamber photooxidation HR-ToF-AMS PMF results facilitate the interpretation of SOA chemical and physical processes by linking the bulk AMS aerosol composition data to molecular level information provided by CIMS and MOVI-HRToF-CIMS measurements.

Appendix A

SOA formation from a single source in a laboratory is characterized by smooth aerosol growth (Fig. A1); the well-behaved nature of ion signals and their associated errors is ideal for application of PMF. The size of the organic signal input matrix for PMF of experiment 2 in Table 1 is 1050×325. The columns of the matrix correspond to individual identified ions. High resolution stick intensities for identified ions at fractional m/z's from 12–300 were used. AMS ion identification in the m/z 101–300 range was aided by the dodecane low-NO_x chemical mechanism, CIMS gas-phase measurements, and MOVI-CIMS aerosol measurements. Not all of the individual ions identified were included in PMF analysis, due to S/N constraints.

The ions included in PMF analysis and the solution justification are discussed here. The organic matrix was calculated using PIKA's "Open" minus "Closed" option for high-resolution ions with an average signal-to-noise ratio (S/N) greater than 0.2. Signals with a S/N between 0.2 and 2 were down-weighted by a factor of 3, as recommended by Paatero and Hopke (2003). The error matrix was calculated in PIKA in the standard way using "Open" minus "Closed" errors. The errors (σ) normalize the residuals (e) for the minimization function routine of PMF, Q; therefore, good quantification of errors is needed. For an input matrix of $n \times m$, the PMF minimization function from Ulbrich et al. (2009), is:

$$Q = \sum_{i=1}^{n} \sum_{j=1}^{m} (e_{ij}/\sigma_{ij})^2 \quad \text{(A1)}$$

Careful consideration was given when choosing the ions for PMF. Even though the ion may appear to be present in the ion fitting window in PIKA, sometimes the time trend of this ion is too noisy for PMF. Noisiness in the time trend can be introduced when there are: (a) ions that are in the shoulder of a larger ion at the same nominal mass (i.e., $C_3H_3O_5^+$ is in the shoulder of the much larger ion $C_8H_7O^+$ at m/z 119), (b) ions that are in the valley of two larger ions at the same nominal mass (i.e., the $C_3H_7^+$ ion is in-between $C_3H_3O_3^+$ and $C_4H_7O_2^+$ at m/z 87), (c) ions that exhibit a strong signal in the closed spectra, but only a small signal in the difference spectra (i.e., $C_{10}H_7^+$ at m/z 127), and/or (d) an ion is coincident with another ion that is expected to be there (i.e., the isotope of N_2^+ ion and CHO^+ ion are extremely close in exact mass). If ions like the ones mentioned above are included in PMF, then there is considerable noise in the time trend

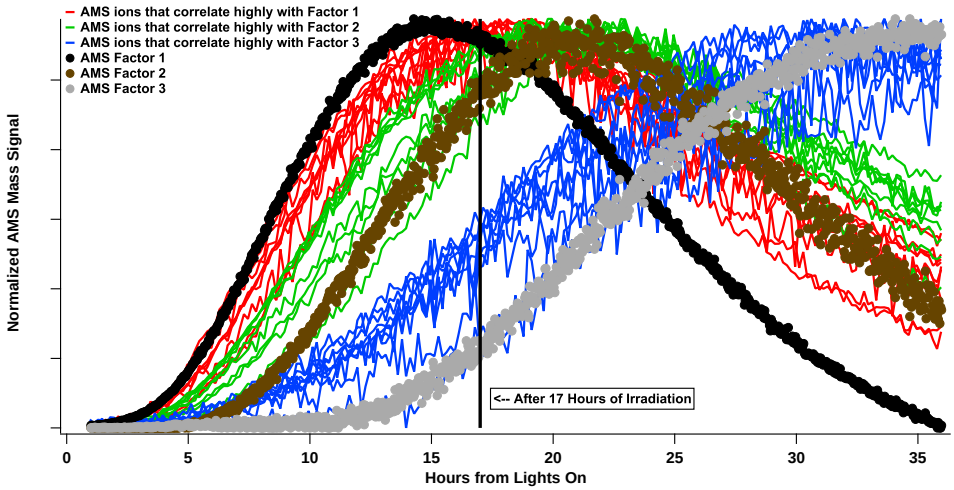

Fig. A1. Normalized mass signals from the AMS PMF factor time series are plotted with the AMS ions that have the highest correlations with those factors (ions listed in Table 3).

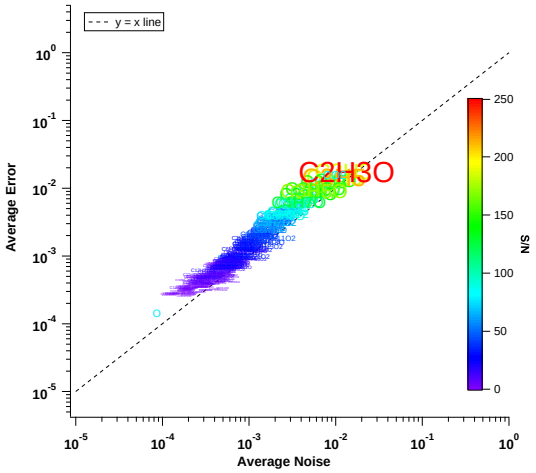

Fig. A2. Average error vs. the average noise for each ion is plotted along with the y = x line. The marker is labeled by the ion it represents and is colored and sized by the S/N ratio of that ion. If the marker lies directly on the y = x line, this means the calculated errors have captured the noise in the ion signal, which is critical for PMF analysis.

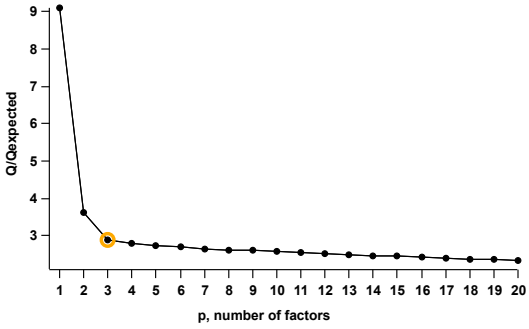

Fig. A3. Q/Q_{exp} vs. p, number of factors. The solution chosen is highlighted by the yellow circle.

of Q/Q_{expected}. This noisiness results from peak fitting ions that experience large interference from other (often larger) ions, and should not be considered for PMF. An effective diagnostic to determine which ions to exclude from PMF is to calculate the S/N of each ion using the errors generated in PIKA (S/N_{error}), and then compare that to the S/N using the observed noise (S/N_{noise}). The observed noise is calculated by smoothing the data using the binomial smoothing function in Igor (order of smoothing is chosen by user) and then subtracting the data from the smoothed data at each time point. Since the equation for errors in PIKA does not consider noise introduced by ion fitting (in the a., b., c., and d. scenarios described above), the S/N_{noise} is a good way to asses how well the ion is quantified. If S/N_{error} is much different than the S/N_{noise}, then either the ion should not be fit because it is a minor ion, or it is an ion described by a., b., c., or d. above, and should be removed from PMF analysis. Figure A2 shows the time-averaged error vs. time-averaged noise for each ion. The marker is labeled by the ion it represents and is sized and colored by its S/N. A marker lying on the y = x line means that the calculated errors in PIKA captured the noisiness of

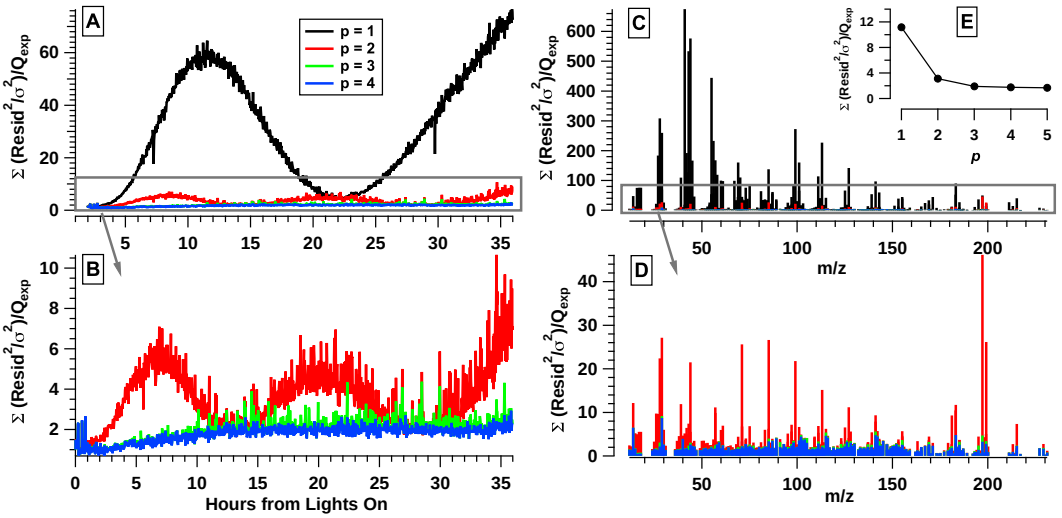

Fig. A4. The ratio of Q/Q_{expected} for $p = 1$, 2, 3, and 4 is used as a diagnostic in determining the number of factors in PMF analysis. Time series trend of Q/Q_{expected} for $p = 1$ through $p = 4$ solutions **(A)** and **(B)** clearly show that at least three factors are needed to describe the solution. The difference between the $p = 3$ and 4 solutions is minor, with the $p = 4$ solution having the same trend as the $p = 3$, but with less noise. The Q/Q_{expected} at each m/z for $p = 1$ through $p = 4$ solutions and **(C)** and **(D)** show similar results, just for the m/z dependence. The overall time trend and m/z contributions to the Q/Q_{expected} at each factor are also presented **(E)**.

the ion, which is essential for PMF analysis. The noisiness in the Q/Q_{expected} time trend results from some noisy ions that were selected to remain in the input PMF analysis because the time trend of the ions, albeit noisy, appears to contain useful time trend information. This must be decided by the user for each system analyzed with PMF. No smoothed or averaged data were used for PMF, albeit averaging is recommended for future chamber PMF studies (Paatero, 2012).

The optimization function, Q, for PMF involves the minimization of the scaled residual at each mass over time (Ulbrich et al., 2009). Figure A3 shows the initial decrease in Q/Q_{expected} with the addition of one factor from $p = 1$ to $p = 2$, which is expected for any data set with enough variability to run PMF. And then there is a slight decrease between $p = 2$ and $p = 3$. After $p = 3$, the decrease in Q/Q_{expected} is small and continues to decrease by the same amount with each increase in p and never flattens out. At $p = 3$, the solution has reached a point at which no additional information is gained in adding another factor. It is useful to remember that in PMF, the factor mass spectral profiles are constant, and so one has to assume that the same is true for the actual SOA. The numerous processes associated with continuous oxidation of the gas and aerosol phase may invalidate this assumption, and so this may be why the Q/Q_{expected} never flattens out. This behavior can make it difficult to select a solution. A good strategy is to examine how both specific ions and the majority of the ions are reconstructed by the factorization and if individual high m/z ions (tracer ions) trend with each factor time series (see Fig. 8).

The time series of the sum of the residuals and the Q/Q_{expected} is also useful in determining a solution. Any major structure in either of these parameters would suggest that additional factors are needed to describe the data. Figure A4 shows these two parameters for the $p = 1$, $p = 2$, $p = 3$ and $p = 4$ solution for the all ion iteration of PMF. There is clear structure in both the $p = 1$ and $p = 2$ solutions, whereas the $p = 3$ and $p = 4$ solutions have a flat sum of residuals and a relatively flat and small Q/Q_{expected}. There is little difference between the $p = 3$ and $p = 4$ solutions, so the addition of another factor would not enhance the information learned from the factorization from a residual point of view. The reason why the Q/Q_{expected} has a slightly curved shape for both the $p = 3$ and $p = 4$ solutions arises from variability in the mass spectra that is beyond what is explained by the input noise. This may be a consequence of the composition of the aerosol becoming more complex, combined with the assumption of PMF that the factor must have a constant mass spectral profile (which does not hold with these systems).

Map plots were made for the $p = 2$ and $p = 3$ solutions (Figs. A5 and A6). In these plots, a red dot indicates the $\text{residual}_{ij} > \text{error}_{ij}$, a blue dot is where $\text{residual}_{ij} < -\text{error}_{ij}$, and a white dot is where $-\text{error}_{ij} < \text{residual}_{ij} < \text{error}_{ij}$. For a two factor solution (Fig. A5) there is clearly a non-random

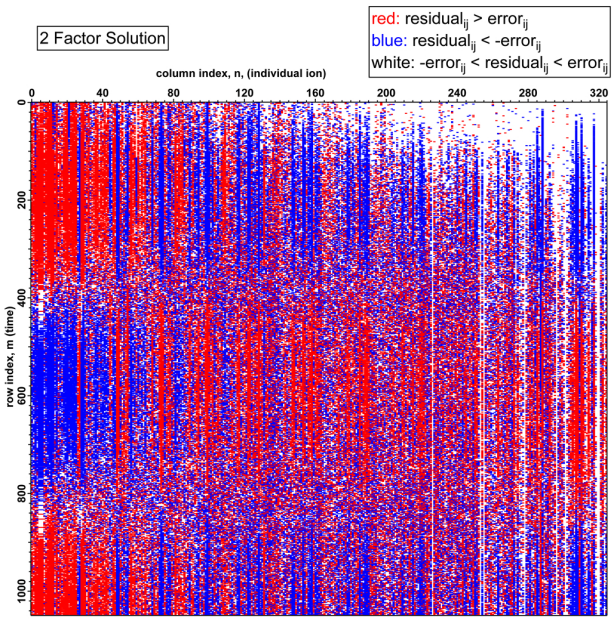

Fig. A5. The map plot for the two factor solution displays a red dot where the residual$_{ij}$ > error$_{ij}$, a blue dot where residual$_{ij}$ < −error$_{ij}$, and a white dot where −error$_{ij}$ < residual$_{ij}$ < error$_{ij}$. For a two-factor solution there is clearly a non-random pattern, indicating two factors do not adequately describe the data.

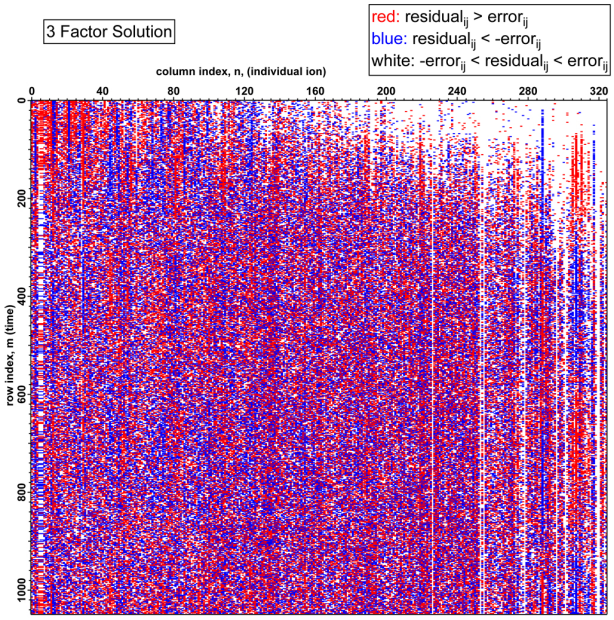

Fig. A6. The map plot, as described in Fig. A5 is shown for 3 factors. The pattern is random, indicating 3 factors describe the data variation well.

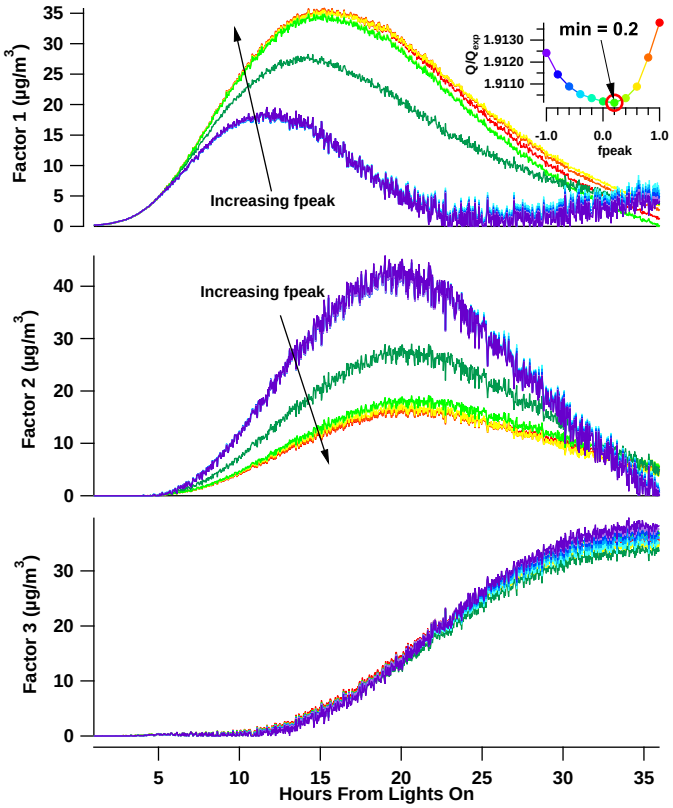

Fig. A7. The change in f_{peak} affects factors 1 and 2 more than factor 3. The increase in factor 1 explains the decrease in factor 2 when f_{peak} changes from 0 to 1. The same effect occurs when the f_{peak} changes from 0 to -1. There is a small change in factor 3, but overall trend and magnitude remain the same for factor 3. The minimum in Q is associated with an f_{peak} of 0.2.

pattern, whereas for the 3 factor solution (Fig. A6), the pattern is random. This further supports a three factor solution.

The solution was chosen by running several iterations of PMF on the same dataset. As explained by Ulbrich et al. (2009), the PMF solution can be systematically explored by varying p, the factor number, and two other parameters, the seeds and the f_{peaks}. The 3-factor solution was uniform across many seeds, but not across f_{peaks}. Figure A7 shows the effect of f_{peak} for the three factor solution. Factor 3 shows little difference for varying solutions, however factors 1 and 2 seem to trade off mass between the different types of solutions. The minimum of $Q/Q_{expected}$ which occurs at $f_{peak} = 0.2$ (see inset of Fig. A7) was chosen as the solution. This solution had good agreement with the time series comparison with high m/z HR-ToF-AMS molecular ion tracers (Fig. 8) and with the CIMS and MOVI-HRToF-CIMS measurements (Fig. 10). However, as emphasized by Ulbrich et al. (2009), f_{peak} does not explore all possible rotations (Paatero et al., 2002). In the current experiment, it is possible that factor 1 time trend goes to zero, however, as indicated by the positive f_{peaks} (Fig. A7), the factor 1 decrease could also taper toward the end of 34 h and perhaps not reach zero. A longer experiment may have clarified this ambiguity, and/or comparison with aerosol molecular-level information out at this time range. If an external comparison (i.e. MOVI-CIMS molecular trace) for factor 1 did not go to zero, then it would be necessary to pull up the last few elements of the time trend of factor 1. If the increase in factor 1 at the end of the experiment did not increase Q too intensely, then the desired rotation would have been found (Paatero, 2012). Although not reported here, a full exploration of rotational ambiguity requires induced rotations, such as the example just described, by explicitly pulling individual factor elements in desired directions. For PMF2, this is described in Paatero et al. (2002).

The solution of PMF will only be as descriptive as the data matrix itself. In a chamber experiment, the initial mass spectra reflect the chemistry of early aerosol formation and are not necessarily the same as those later in the oxidation.

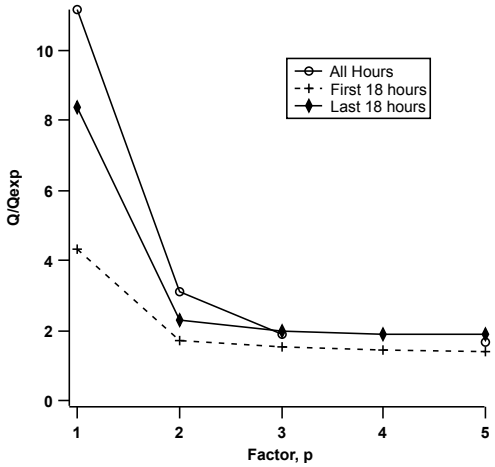

Fig. A8. Q/Q_{exp} vs. p for 3 types of solutions.

Figure A8 shows the Q/Q_{expected} versus factor number, p, for the 1 seed solution from experiment 2 for "all h", "first 18 h", and the "last 18 h". For the 1 factor solution ($p = 1$), the "first 18 h" solution has the lowest Q/Q_{expected}, the "all h" solution has the highest Q/Q_{expected}, and the "last 18 h" is in between. This trend is the same for $p = 2$. The first 18 h solution is lower than the last 18 h because chemically the mass spectra are less complex at the beginning of the experiment, and $p = 1$ or $p = 2$ describes much of the data (there is less variability earlier on, in comparison to the full 34 h solution). As the oxidation progresses, the aerosol composition becomes more complex, as higher m/z oxygen-containing ions appear in the mass spectra, in addition to those observed at initial aerosol growth. For the same Q/Q_{expected} value, the last 18 h (and all h) requires more factors to describe the data to the same degree as the "first 18 h". Three factors best describe the "all h" solution and the "last 18 h" solution since the third factor grows in at about 18 h. The "first 18 h" solution, would not "see" this third factor (since it covers only the first 18 h), so only 2 factors are necessary to describe the variability in the input data matrix.

Acknowledgements. This work was supported by US Department of Energy grant DE-SC 000 6626. Analysis of the MOVI-HRToF-CIMS data is supported by a grant to J. A. T. from the US Department of Energy (DOE-ER65318).

Edited by: M. C. Facchini

References

Aiken, A. C., DeCarlo, P. F., Kroll, J. H., Worsnop, D. R., Huffman, J. A., Docherty, K. S., Ulbrich, I. M., Mohr, C., Kimmel, J. R., Sueper, D., Sun, Y., Zhang, Q., Trimborn, A., Northway, M., Ziemann, P. J., Canagaratna, M. R., Onasch, T. B., Alfarra, M. R., Prevot, A. S. H., Dommen, J., Duplissy, J., Metzger, A., Baltensperger, U., and Jimenez, J. L.: O/C and OM/OC Ratios of Primary, Secondary, and Ambient Organic Aerosols with High-Resolution Time-of-Flight Aerosol Mass Spectrometry, Environ. Sci. Technol., 42, 4478–4485, 2008.

Aiken, A. C., Salcedo, D., Cubison, M. J., Huffman, J. A., DeCarlo, P. F., Ulbrich, I. M., Docherty, K. S., Sueper, D., Kimmel, J. R., Worsnop, D. R., Trimborn, A., Northway, M., Stone, E. A., Schauer, J. J., Volkamer, R. M., Fortner, E., de Foy, B., Wang, J., Laskin, A., Shutthanandan, V., Zheng, J., Zhang, R., Gaffney, J., Marley, N. A., Paredes-Miranda, G., Arnott, W. P., Molina, L. T., Sosa, G., and Jimenez, J. L.: Mexico City aerosol analysis during MILAGRO using high resolution aerosol mass spectrometry at the urban supersite (T0) – Part 1: Fine particle composition and organic source apportionment, Atmos. Chem. Phys., 9, 6633–6653, doi:10.5194/acp-9-6633-2009, 2009.

Allan, J. D.: Quantitative sampling using an Aerodyne aerosol mass spectrometer 1. Techniques of data interpretation and error analysis, J. Geophys. Res., 108, 4090, doi:10.1029/2002JD002358, 2003.

Allan, J. D., Delia, A. E., Coe, H., Bower, K. N., Alfarra, M. R., Jimenez, J. L., Middlebrook, A. M., Drewnick, F., Onasch, T. B., Canagaratna, M. R., Jayne, J. T., and Worsnop, D. R.: A generalised method for the extraction of chemically resolved mass spectra from Aerodyne aerosol mass spectrometer data, J. Aerosol Sci., 35, 909–922, 2004.

Chhabra, P. S., Flagan, R. C., and Seinfeld, J. H.: Elemental analysis of chamber organic aerosol using an aerodyne high-resolution aerosol mass spectrometer, Atmos. Chem. Phys., 10, 4111–4131, doi:10.5194/acp-10-4111-2010, 2010.

Chhabra, P. S., Ng, N. L., Canagaratna, M. R., Corrigan, A. L., Russell, L. M., Worsnop, D. R., Flagan, R. C., and Seinfeld, J. H.: Elemental composition and oxidation of chamber organic aerosol, Atmos. Chem. Phys., 11, 8827–8845, doi:10.5194/acp-11-8827-2011, 2011.

Cocker, D. R., Flagan, R. C., and Seinfeld, J. H.: State-of-the-Art Chamber Facility for Studying Atmospheric Aerosol Chemistry, Environ. Sci. Technol., 35, 2594–2601, 2001.

Crounse, J. D., McKinney, K. A., Kwan, A. J., and Wennberg, P. O.: Measurement of Gas-Phase Hydroperoxides by Chemical Ionization Mass Spectrometry, Anal. Chem., 78, 6726–6732, 2006.

DeCarlo, P. F., Kimmel, J. R., Trimborn, A., Northway, M. J., Jayne, J. T., Aiken, A. C., Gonin, M., Fuhrer, K., Horvath, T., Docherty, K. S., Worsnop, D. R., and Jimenez, J. L.: Field-Deployable, High-Resolution, Time-of-Flight Aerosol Mass Spectrometer, Anal. Chem., 78, 8281–8289, 2006.

Fraser, R. T. M., Paul, N. C., and Phillips, L.: Mass spectrometry of some alkyl peroxides, J. Chem. Soc. B, 1970, 1278–1280, doi:10.1039/J29700001278, 1970.

Fry, J. L., Kiendler-Scharr, A., Rollins, A. W., Brauers, T., Brown, S. S., Dorn, H.-P., Dubé, W. P., Fuchs, H., Mensah, A., Rohrer, F., Tillmann, R., Wahner, A., Wooldridge, P. J., and Cohen, R. C.: SOA from limonene: role of NO_3 in its generation and degradation, Atmos. Chem. Phys., 11, 3879–3894, doi:10.5194/acp-11-

3879-2011, 2011.

Heald, C. L., Kroll, J. H., Jimenez, J. L., Docherty, K. S., DeCarlo, P. F., Aiken, A. C., Chen, Q., Martin, S. T., Farmer, D. K., and Artaxo, P.: A simplified description of the evolution of organic aerosol composition in the atmosphere, Geophys. Res. Lett., 37, L08803, doi:10.1029/2010GL042737, 2010.

Hersey, S. P., Craven, J. S., Schilling, K. A., Metcalf, A. R., Sorooshian, A., Chan, M. N., Flagan, R. C., and Seinfeld, J. H.: The Pasadena Aerosol Characterization Observatory (PACO): chemical and physical analysis of the Western Los Angeles basin aerosol, Atmos. Chem. Phys., 11, 7417–7443, doi:10.5194/acp-11-7417-2011, 2011.

Isaacman, G., Chan, A. W. H., Nah, T., Worton, D. R., Ruehl, C. R., Wilson, K. R., and Goldstein, A. H.: Heterogeneous OH Oxidation of Motor Oil Particles Causes Selective Depletion of Branched and Less Cyclic Hydrocarbons, Environ. Sci. Technol., 46, 10632–10640, 2012.

Jimenez, J. L., Canagaratna, M. R., Donahue, N. M., Prévôt, A. S. H., Zhang, Q., Kroll, J. H., DeCarlo, P. F., Allan, J. D., Coe, H., Ng, N. L., Aiken, A. C., Docherty, K. S., Ulbrich, I. M., Grieshop, A. P., Robinson, A. L., Duplissy, J., Smith, J. D., Wilson, K. R., Lanz, V. A., Hueglin, C., Sun, Y. L., Tian, J., Laaksonen, A., Raatikainen, T., Rautiainen, J., Vaattovaara, P., Ehn, M., Kulmala, M., Tomlinson, J. M., Collins, D. R., Cubison, M. J., E., Dunlea, J., Huffman, J. A., Onasch, T. B., Alfarra, M. R., Williams, P. I., Bower, K., Kondo, Y., Schneider, J., Drewnick, F., Borrmann, S., Weimer, S., Demerjian, K., Salcedo, D., Cottrell, L., Griffin, R., Takami, A., Miyoshi, T., Hatakeyama, S., Shimono, A., Sun, J. Y., Zhang, Y. M., Dzepina, K., Kimmel, J. R., Sueper, D., Jayne, J. T., Herndon, S. C., Trimborn, A. M., Williams, L. R., Wood, E. C., Middlebrook, A. M., Kolb, C. E., Baltensperger, U., and Worsnop, D. R.: Evolution of Organic Aerosols in the Atmosphere, Science, 326, 1525–1529, 2009.

Lambe, A. T., Onasch, T. B., Massoli, P., Croasdale, D. R., Wright, J. P., Ahern, A. T., Williams, L. R., Worsnop, D. R., Brune, W. H., and Davidovits, P.: Laboratory studies of the chemical composition and cloud condensation nuclei (CCN) activity of secondary organic aerosol (SOA) and oxidized primary organic aerosol (OPOA), Atmos. Chem. Phys., 11, 8913–8928, doi:10.5194/acp-11-8913-2011, 2011.

Lambe, A. T., Onasch, T. B., Croasdale, D. R., Wright, J. P., Martin, A. T., Franklin, J. P., Massoli, P., Kroll, J. H., Canagaratna, M. R., Brune, W. H., Worsnop, D. R., and Davidovits, P.: Transitions from Functionalization to Fragmentation Reactions of Laboratory Secondary Organic Aerosol (SOA) Generated from the OH Oxidation of Alkane Precursors, Environ. Sci. Technol., 46, 5430–5437, 2012.

Lanz, V. A., Alfarra, M. R., Baltensperger, U., Buchmann, B., Hueglin, C., and Prévôt, A. S. H.: Source apportionment of submicron organic aerosols at an urban site by factor analytical modelling of aerosol mass spectra, Atmos. Chem. Phys., 7, 1503–1522, doi:10.5194/acp-7-1503-2007, 2007.

Loza, C. L., Chhabra, P. S., Yee, L. D., Craven, J. S., Flagan, R. C., and Seinfeld, J. H.: Chemical aging of *m*-xylene secondary organic aerosol: laboratory chamber study, Atmos. Chem. Phys., 12, 151–167, doi:10.5194/acp-12-151-2012, 2012.

Ng, N. L., Canagaratna, M. R., Zhang, Q., Jimenez, J. L., Tian, J., Ulbrich, I. M., Kroll, J. H., Docherty, K. S., Chhabra, P. S., Bahreini, R., Murphy, S. M., Seinfeld, J. H., Hildebrandt, L., Donahue, N. M., DeCarlo, P. F., Lanz, V. A., Prévôt, A. S. H., Dinar, E., Rudich, Y., and Worsnop, D. R.: Organic aerosol components observed in Northern Hemispheric datasets from Aerosol Mass Spectrometry, Atmos. Chem. Phys., 10, 4625–4641, doi:10.5194/acp-10-4625-2010, 2010.

Ng, N. L., Canagaratna, M. R., Jimenez, J. L., Chhabra, P. S., Seinfeld, J. H., and Worsnop, D. R.: Changes in organic aerosol composition with aging inferred from aerosol mass spectra, Atmos. Chem. Phys., 11, 6465–6474, doi:10.5194/acp-11-6465-2011, 2011.

Paatero, P.: Interactive comment on Atmos. Chem. Phys. Discuss., 12, 16647, 2012.

Paatero, P. and Hopke, P. K.: Discarding or downweighting high-noise variables in factor analytic models, Anal. Chim. Acta, 490, 277–289, 2003.

Paatero, P. and Tapper, U.: Positive Matrix Factorization – a Nonnegative Factor Model with Optimal Utilization of Error-Estimates of Data Values, Environmetrics, 5, 111–126, 1994.

Paatero, P., Hopke, P. K., Song, X. H., and Ramadan, Z.: Understanding and controlling rotations in factor analytic models, Chemometr. Intell. Lab., 60, 253–264, 2002.

Paulot, F., Crounse, J. D., Kjaergaard, H. G., Kroll, J. H., Seinfeld, J. H., and Wennberg, P. O.: Isoprene photooxidation: new insights into the production of acids and organic nitrates, Atmos. Chem. Phys., 9, 1479–1501, doi:10.5194/acp-9-1479-2009, 2009.

Pye, H. O. T. and Pouliot, G. A.: Modeling the Role of Alkanes, Polycyclic Aromatic Hydrocarbons, and Their Oligomers in Secondary Organic Aerosol Formation, Environ. Sci. Technol., 46, 6041–6047, 2012.

Schauer, J. J., Kleeman, M. J., Cass, G. R., and Simoneit, B. R. T.: Measurement of Emissions from Air Pollution Sources. 3. C1–C29 Organic Compounds from Fireplace Combustion of Wood, Environ. Sci. Technol., 35, 1716–1728, 2001.

Schauer, J. J., Kleeman, M. J., Cass, G. R., and Simoneit, B. R. T.: Measurement of Emissions from Air Pollution Sources. 5. C1–C32 Organic Compounds from Gasoline-Powered Motor Vehicles, Environ. Sci. Technol., 36, 1169–1180, 2002.

St. Clair, J. M., McCabe, D. C., Crounse, J. D., Steiner, U., and Wennberg, P. O.: Chemical ionization tandem mass spectrometer for the in situ measurement of methyl hydrogen peroxide, Rev. Sci. Instrum., 81, 094102, doi:10.1063/1.3480552, 2010.

Tobias, H. J. and Ziemann, P. J.: Thermal Desorption Mass Spectrometric Analysis of Organic Aerosol Formed from Reactions of 1-Tetradecene and O_3 in the Presence of Alcohols and Carboxylic Acids, Environ. Sci. Technol., 34, 2105–2115, 2000.

Ulbrich, I. M., Canagaratna, M. R., Zhang, Q., Worsnop, D. R., and Jimenez, J. L.: Interpretation of organic components from Positive Matrix Factorization of aerosol mass spectrometric data, Atmos. Chem. Phys., 9, 2891–2918, doi:10.5194/acp-9-2891-2009, 2009.

Van Krevelen, D. W.: Graphical-statistical method for the study of structure and reaction processes of coal, Fuel, 24, 269–284, 1950.

Yatavelli, R. L. N. and Thornton, J. A.: Particulate Organic Matter Detection Using a Micro-Orifice Volatilization Impactor Coupled to a Chemical Ionization Mass Spectrometer (MOVI-CIMS), Aerosol Sci. Tech., 44, 61–74, 2010.

Yatavelli, R. L. N., Lopez-Hilfiker, F. D., Wargo, J., Kimmel, J. R., Cubison, M. J., Bertram, T. H., Jimenez, J., Gonin, M., Worsnop, D. R., and Thornton, J. A.: Analysis of Gas and Particle-phase

Organic Matter Using a Chemical Ionization High-Resolution Time-of-Flight Mass Spectrometer (HTOF-CIMS) Coupled to a Micro Orifice Volatilization Impactor (MOVI), Aerosol Sci. Tech., 46, 1313–1327, doi:10.1080/02786826.2012.712236, 2012.

Yee, L. D., Craven, J. S., Loza, C. L., Schilling, K. A., Ng, N. L., Canagaratna, M. R., Ziemann, P. J., Flagan, R. C., and Seinfeld, J. H.: Secondary Organic Aerosol Formation from Low-NO_x Photooxidation of Dodecane: Evolution of Multi-Generation Gas-Phase Chemistry and Aerosol Composition, J. Phys. Chem. A, 116, 6211–6230, 2012.

Zhang, Q., Jimenez, J. L., Canagaratna, M. R., Ulbrich, I. M., Ng, N. L., Worsnop, D. R., and Sun, Y.: Understanding atmospheric organic aerosols via factor analysis of aerosol mass spectrometry: a review, Anal. Bioanal. Chem., 401, 3045–3067, 2011.

Ziemann, P. J.: Formation of Alkoxyhydroperoxy Aldehydes and Cyclic Peroxyhemiacetals from Reactions of Cyclic Alkenes with O_3 in the Presence of Alcohols, J. Phys. Chem. A, 107, 2048–2060, 2003.

Chapter 4

Evolution of Trace Gases and Particles Emitted By a Chaparral Fire in California[1]

[1]This chapter is reproduced by permission from "Evolution of Trace Gases and Particles Emitted By a Chaparral Fire in California" by S. K. Akagi, J. S. Craven, J. W. Taylor, G. R. McMeeking, R. J. Yokelson, I. R. Burling, S. P. Urbanski, C. E. Wold, J. H. Seinfeld, H. Coe, M. J. Alvarado, and D. R. Weise, *Atmospheric Chemistry and Physics*, 12, 1397–1421, www.atmos-chem-phys.net/12/1397/2012/, doi:10.5194/acp-12-1397-2012, 2012.

Atmos. Chem. Phys., 12, 1397–1421, 2012
www.atmos-chem-phys.net/12/1397/2012/
doi:10.5194/acp-12-1397-2012

Atmospheric Chemistry and Physics

Evolution of trace gases and particles emitted by a chaparral fire in California

S. K. Akagi[1], J. S. Craven[2], J. W. Taylor[3], G. R. McMeeking[3,*], R. J. Yokelson[1], I. R. Burling[1], S. P. Urbanski[4], C. E. Wold[4], J. H. Seinfeld[2], H. Coe[3], M. J. Alvarado[5], and D. R. Weise[6]

[1]University of Montana, Department of Chemistry, Missoula, MT, USA
[2]California Institute of Technology, Division of Chemistry and Chemical Engineering, Pasadena, CA, USA
[3]University of Manchester, Centre for Atmospheric Science, Manchester, UK
[4]United States Forest Service, Fire Sciences Laboratory, Missoula, MT, USA
[5]Atmospheric and Environmental Research (AER), Lexington, MA, USA
[6]USDA Forest Service, Pacific Southwest Research Station, Forest Fire Laboratory, Riverside, CA, USA
[*]now at: Department of Atmospheric Science, Colorado State University, Fort Collins, USA

Correspondence to: R. J. Yokelson (bob.yokelson@umontana.edu)

Received: 2 June 2011 – Published in Atmos. Chem. Phys. Discuss.: 8 August 2011
Revised: 27 December 2011 – Accepted: 20 January 2012 – Published: 7 February 2012

Abstract. Biomass burning (BB) is a major global source of trace gases and particles. Accurately representing the production and evolution of these emissions is an important goal for atmospheric chemical transport models. We measured a suite of gases and aerosols emitted from an 81 hectare prescribed fire in chaparral fuels on the central coast of California, US on 17 November 2009. We also measured physical and chemical changes that occurred in the isolated downwind plume in the first ∼4 h after emission. The measurements were carried out onboard a Twin Otter aircraft outfitted with an airborne Fourier transform infrared spectrometer (AFTIR), aerosol mass spectrometer (AMS), single particle soot photometer (SP2), nephelometer, LiCor CO_2 analyzer, a chemiluminescence ozone instrument, and a wing-mounted meteorological probe. Our measurements included: CO_2; CO; NO_x; NH_3; non-methane organic compounds; organic aerosol (OA); inorganic aerosol (nitrate, ammonium, sulfate, and chloride); aerosol light scattering; refractory black carbon (rBC); and ambient temperature, relative humidity, barometric pressure, and three-dimensional wind velocity. The molar ratio of excess O_3 to excess CO in the plume ($\Delta O_3/\Delta CO$) increased from $-5.13\ (\pm 1.13) \times 10^{-3}$ to $10.2\ (\pm 2.16) \times 10^{-2}$ in ∼4.5 h following smoke emission. Excess acetic and formic acid (normalized to excess CO) increased by factors of 1.73 ± 0.43 and 7.34 ± 3.03 (respectively) over the same time since emission. Based on the rapid decay of C_2H_4 we infer an in-plume average OH concentration of $5.27\ (\pm 0.97) \times 10^6$ molec cm^{-3}, consistent with previous studies showing elevated OH concentrations in biomass burning plumes. Ammonium, nitrate, and sulfate all increased over the course of 4 h. The observed ammonium increase was a factor of 3.90 ± 2.93 in about 4 h, but accounted for just ∼36 % of the gaseous ammonia lost on a molar basis. Some of the gas phase NH_3 loss may have been due to condensation on, or formation of, particles below the AMS detection range. NO_x was converted to PAN and particle nitrate with PAN production being about two times greater than production of observable nitrate in the first ∼4 h following emission. The excess aerosol light scattering in the plume (normalized to excess CO_2) increased by a factor of 2.50 ± 0.74 over 4 h. The increase in light scattering was similar to that observed in an earlier study of a biomass burning plume in Mexico where significant secondary formation of OA closely tracked the increase in scattering. In the California plume, however, $\Delta OA/\Delta CO_2$ decreased sharply for the first hour and then increased slowly with a net decrease of ∼20 % over 4 h. The fraction of thickly coated rBC particles increased up to ∼85 % over the 4 h aging period. Decreasing OA accompanied by increased scattering/particle coating in initial aging may be due to a combination of particle coagulation and evaporation processes. Recondensation of species initially evaporated from the particles may have contributed to the subsequent slow rise in OA. We compare our results to observations from other plume aging studies

and suggest that differences in environmental factors such as smoke concentration, oxidant concentration, actinic flux, and RH contribute significantly to the variation in plume evolution observations.

1 Introduction

Biomass burning (BB) is the largest global source of primary, fine carbonaceous particles; the second largest source of trace gases; and a key element of the carbon cycle (Crutzen and Andreae, 1990; Fearnside et al., 1993; Bond et al., 2004; Akagi et al., 2011). Globally, dry season deforestation and savanna fires in the tropics are the most dominant, and most studied, type of open burning (Yokelson et al., 2003a; van der Werf et al., 2010). However, the comparatively smaller amount of BB that occurs year-round in the contiguous US is a prominent domestic source of gas and particle emissions. These fires may be prescribed or ignited naturally. Prescribed burning is a significant fraction of US BB and it is used to restore or maintain the natural, beneficial role of fire in many terrestrial ecosystems; reduce fire risk by consuming accumulated wildland fuels under preferred weather conditions; and accomplish other land management objectives (Biswell, 1989; Hardy et al., 2001; Carter and Foster, 2004; Wiedinmyer and Hurteau, 2010). These burns are often recurrent, sometimes near populated areas, and despite being controlled may occasionally have negative air quality impacts. Together, wild and prescribed fires are thought to produce about one-third of the total $PM_{2.5}$ (particle mass with aerodynamic diameter $<2.5\,\mu m$) in the US (Watson, 2002; Park et al., 2007). The particles can impact local to regional air quality, health, and visibility (McMeeking et al., 2006). In addition, fires can influence regional levels of ozone (O_3), which is an air toxic (Pfister et al., 2006). Large areas of the US commonly have O_3 mixing ratios not far below the US national ambient O_3 air quality standard (75 ppb 8-h average). Thus, in these areas even modest production of O_3 in a smoke plume can potentially lead to O_3 levels that exceed air quality criteria. Because fire has both benefits and drawbacks, the optimum amount and timing of prescribed fire is an area of active research and better information on the initial chemistry and evolution of BB emissions is a major need (Haines and Cleaves, 1999; Sandberg et al., 2002; Yoder et al., 2003; Kauffman, 2004; Stephens et al., 2007; Akagi et al., 2011).

Next we summarize the limited amount of data available on the emissions and downwind chemical evolution of trace gases and particles from BB in the contiguous US. Ground-based measurements of prescribed fire emissions from various temperate fuel types in the US were carried out by Hardy and Teesdale (1991). Hardy et al. (1996) measured smoke emissions from chaparral fires in southern California (CA) and reported emission factors (EF, g compound emitted per kg dry biomass burned) for PM (total PM, $PM_{2.5}$, PM_{10}), CO, CO_2, CH_4, and non-methane hydrocarbons by combustion process (i.e. flaming or smoldering). Prescribed fire emissions have also been measured from airborne platforms (Cofer III. et al., 1988; Radke et al., 1990; Yokelson et al., 1999). Ward et al. (1993) compiled the first extensive inventory of particulate matter and trace gas EF for prescribed fires in the US, which estimated EF based on combustion efficiency from field and laboratory measurements for the different classes of biomass consumed. Numerous laboratory studies of the initial emissions from burning temperate ecosystem fuels have been conducted (e.g. Yokelson et al., 1996, 1997; Goode et al., 1999; McMeeking et al., 2009; Veres et al., 2010; Burling et al., 2010; Hosseini et al., 2010). The studies discussed above focused on measuring fresh smoke emissions, which can help properly initialize models that predict the evolution of BB smoke as it ages downwind. However, they did not directly observe post-emission photochemical and heterogeneous processes. Recently, several laboratory studies investigated the post emission processing of smoke from temperate fuels (Grieshop et al., 2009; Heringa et al., 2011; Hennigan et al., 2011; Cubison et al., 2011), but the aging of smoke from real fires is difficult to reproduce in a laboratory. The behavior and fate of these emissions are important, as air pollutants from fires can remain in the atmosphere for many days and they can also be transported thousands of kilometers (Lee et al., 2005; Yokelson et al., 2007a; Warneke et al., 2009). The $PM_{2.5}$ emissions interact with trace gases via heterogeneous chemistry and gas-particle interconversion processes as smoke plumes age (Mühle et al., 2007; Phuleria et al., 2005). The gas-particle interactions can increase or decrease the amount of $PM_{2.5}$ and also change the aerosol mixing state and lifetime (Petters et al., 2009). Some trace gases in BB smoke are rapidly depleted post-emission via reaction with the hydroxyl radical (OH), while others (e.g. O_3, HCHO) are created from oxidation of non-methane organic compounds (NMOC). Most previous field studies of smoke aging focused on major biomass burning regions such as the tropics (Reid et al., 1998; Hobbs et al., 2003; Yokelson et al., 2009), where ∼70–80 % of biomass burning is thought to occur (Crutzen and Andreae, 1990; van der Werf et al., 2010). The only field study that tracked the evolution of an isolated aging plume from a fire in temperate fuels that we know of followed the evolution of the plume from the Quinalt prescribed fire in the US Pacific Northwest for only 30 min (Trentmann et al., 2003). Thus, more field measurements of plume evolution in temperate ecosystems are needed to improve our understanding of the trade-offs between air quality and ecosystem health and between wild and prescribed fires (Sandberg et al., 2002).

Two plume evolution processes are especially important, both domestically and globally, but are poorly understood: (1) secondary organic aerosol (SOA) formation, and (2) O_3 formation. The atmospheric influence of pollution sources is studied by modeling the dispersion and chemical evolution

of the emissions with local to global scale models (e.g. Alvarado and Prinn, 2009; Byun and Schere, 2006; Heald et al., 2005). Recently, numerous studies in urban plumes have observed rapid production of SOA in amounts up to ten times the original emissions of primary organic aerosol (POA), which greatly exceeds the predictions of standard aerosol modules in atmospheric chemistry models (de Gouw and Jimenez, 2009). This has spurred the development of new, largely empirical modeling approaches that can cope with the large increases (Robinson et al., 2007). In contrast, measurements of organic aerosol (OA) evolution in biomass burning smoke are rare and have thus far shown smaller and variable SOA formation compared to urban plumes. In an airborne study of a BB plume in Mexico (Yokelson et al., 2009) and a laboratory study of wood smoke (Grieshop et al., 2009) the OA/POA ratio increased to greater than two in about 1 and 3 h, respectively. Capes et al. (2009) did not observe evidence of SOA formation in African BB emissions on the time scale of several days. Cubison et al. (2011) observed modest SOA formation that averaged about 25 % of POA in boreal BB smoke. The laboratory study of Hennigan et al. (2011) observed OA/POA between 0.7 and 2.9 in BB smoke aged for 3–4.5 h, while Heringa et al. (2011) found that OA/POA rose to 4.1 ± 1.4 after 5 h for wood smoke aged in a smog chamber. We also note that biomass burning is known to emit species that are precursors for aqueous phase SOA such as glycolaldehyde and phenol (Yokelson et al., 1997; Perri et al., 2009; Lim et al., 2010) and that a large fraction of the organic gases emitted by BB are still unidentified (Karl et al., 2007; Warneke et al., 2011) and may play a role in several types of SOA formation. Many more measurements of OA evolution in BB plumes are needed to determine the relative importance of the different OA/POA outcomes at various time scales and to understand the factors driving the variability.

A second major issue is understanding O_3 production in biomass burning plumes. O_3 production is evidently the norm in tropical BB plumes, but both production and destruction of O_3 occurs in boreal BB plumes and little is known about O_3 chemistry in temperate BB plumes (Akagi et al., 2011). The few available time-resolved observations of O_3 formation in isolated plumes have proven difficult to reproduce even in specialized photochemical models (Trentmann et al., 2005; Alvarado and Prinn, 2009). Additional measurements of the O_3 formation rate in various plume environments are needed to further develop the specialized models and ultimately guide the implementation of reasonably accurate O_3 formation mechanisms into air quality models currently in wide use, such as CMAQ (Byun and Schere, 2006).

Here we report new field measurements that address the issues discussed above. We acquired the measurements during the San Luis Obispo Biomass Burning (SLOBB) experiment, which was carried out in November 2009 primarily in midcoast California. The main goal of SLOBB was to study the emissions and the evolution of gases and particles produced by prescribed burns on US Department of Defense lands. We measured many new emission factors for US prescribed fires during SLOBB and related field studies as detailed by Burling et al. (2011). In addition, a prescribed fire near Buellton, CA named the Williams Fire proved particularly opportune for the study of gas-phase photochemistry and particle transformations in a smoke plume. These processes are difficult to simulate in a laboratory and frequently inaccessible even for airborne platforms. The Williams Fire produced a long, clearly-identifiable, isolated plume above the boundary layer where the smoke evolved without influence from factors such as clouds, mixing with plumes from other pollution sources, or complex meteorology. Thus, the measurements provide an ideal case study to test the chemical mechanism of a smoke model. To our knowledge the Williams Fire is the first temperate zone fire for which the evolution of numerous trace gases and aerosol species in the plume was continuously tracked for smoke ages of more than one-half hour. Extensive particle and trace gas measurements in fresh and aged smoke (for ages up to 4.5 h old) were performed to quantify the changes in NMOC, O_3, NO_x, PAN, NH_3, light scattering, inorganic and organic aerosol, refractory black carbon (rBC), and the rBC mixing state. We describe and discuss these measurements in detail in the following sections.

2 Experimental details

2.1 Instrument details

2.1.1 Airborne Fourier transform infrared spectrometer (AFTIR)

The University of Montana AFTIR system and the instruments described below were deployed on a US Forest Service (USFS) Twin Otter. The AFTIR was used to measure 21 gas-phase species: water vapor (H_2O), carbon dioxide (CO_2), carbon monoxide (CO), methane (CH_4), nitric oxide (NO), nitrogen dioxide (NO_2), ammonia (NH_3), hydrogen cyanide (HCN), nitrous acid (HONO), peroxy acetyl nitrate (PAN), ozone (O_3), glycolaldehyde ($HCOCH_2OH$), ethylene (C_2H_4), acetylene (C_2H_2), propylene (C_3H_6), formaldehyde (HCHO), methanol (CH_3OH), furan (C_4H_4O), phenol (C_6H_5OH), acetic acid (CH_3COOH), and formic acid (HCOOH). Ram air was directed through a halocarbon-wax coated inlet and into a Pyrex multipass cell. The IR beam was directed into the cell where it traversed a total path length of 78 m and was then focused onto an MCT detector. The cell exchange time was about ten seconds when the flow control valves were open and IR spectra were collected at 1 Hz. "Grab samples" of air were selected by closing the valves for 1–2 min to temporarily stop system flow to allow signal averaging on the smoke or background samples. The IR spectra were analyzed to identify and quantify all detectable compounds (Sect. 2.4.1). More details of the AFTIR system are

given by Yokelson et al. (1999, 2003a). In this project, upgrades to the spectrometer electronics, transfer optics, and multipass cell led to a factor of three increase in sensitivity compared to the original system.

2.1.2 Aerosol mass spectrometer (AMS)

An Aerodyne compact time-of-flight (CToF) aerosol mass spectrometer (herein referred to as AMS) measured aerosol chemical composition in a repeating cycle for 4 out of every 12 s during flight, including within the smoke plume. An isokinetic particle inlet sampling fine particles with a diameter cut-off of a few microns (Yokelson et al., 2007b) supplied the AMS and a single particle soot photometer (SP2, Sect. 2.1.3). The AMS and SP2 do not measure super-micron particles, so the inlet transmission should not have affected our results. In addition, particles smaller than 1 µm diameter account for nearly all the fine particle mass emitted by biomass fires (Radke et al., 1991; Reid et al., 2005b), so our composition analyses for fine particles should not be affected by the lack of sensitivity to super-micron particles. The AMS collected sub-micron particles via an aerodynamic lens into a high vacuum particle sizing chamber. At the end of the particle sizing chamber, the particles impact a 600 °C vaporizer and filament assembly where they are vaporized and ionized by electron impact. The resulting molecular fragments are then extracted into an ion time-of-flight chamber where they are detected and interpreted as mass spectra. The AMS has been described in great detail elsewhere (Drewnick et al., 2005; Canagaratna et al., 2007). A collection efficiency of 0.5 (Huffman et al., 2005; Drewnick et al., 2003; Allan et al., 2004) was applied to the AMS data, which were processed with the ToF-AMS Analysis Toolkit in Igor Pro 6 (Wavemetrics, Lake Oswego, OR) to retrieve the mass concentration at standard temperature and pressure (µg sm^{-3}, 273 K, 1 atm) for the major non-refractory particle species: OA, non-sea salt chloride, nitrate, sulfate, and ammonium, with <36 % uncertainty. Adjustments to the default AMS unit mass resolution (UMR) fragmentation table were made for sulfate and nitrate concentrations. For instance, nitrate was corrected for organic interference at the nitrate peak at *m/z* 30 based on the results of Bae et al. (2007).

2.1.3 Single particle soot photometer (SP2)

Refractory black carbon (rBC, µg sm^{-3}) was measured using a single particle soot photometer (SP2) (Stephens et al., 2003). The isokinetic particle inlet that supplied the AMS was followed by a three-way splitter and also supplied the SP2 with carefully matched flow rates. Particles were then drawn through a 1064 nm Nd:YAG laser cavity where light scattered by the particles was measured by two avalanche photodiode detectors. Sufficiently light-absorbing particles (at 1064 nm) were heated and eventually vaporized when passing through the beam. The emitted incandescent light was detected by two photomultiplier tubes with optical filters to measure light over two wavelength ranges. The incandescence signal was related linearly to the mass of rBC, regardless of the presence or type of rBC coating (Moteki and Kondo, 2007). The sample flow into the SP2 was diluted with filtered air at a ratio of 7:1 for smoke plume samples near the source with high concentrations of particles. A dilution of 0.35:1 or no dilution was used for the less concentrated downwind samples. Information on the rBC mixing state was inferred from the time delay between the peak of the scattering and incandescence signals, which is a proxy for the time taken for coatings to evaporate before incandescence can occur (Schwarz et al., 2006). Particles with long time delays were considered "thickly coated", while those with shorter delays were "thinly coated" following Shiraiwa et al. (2007). The critical delay time needed for classification was based on the observed minimum in the bimodal frequency distribution of delay times for the rBC particles between 120 and 315 nm volume equivalent diameter and was 1.1 µs. The SP2 data products were collected at >1 Hz and later averaged as needed to match the sampling rates of the other instruments.

2.1.4 Other simultaneous measurements

A 25 mm i.d. forward facing elbow "fastflow" inlet, co-located with the isokinetic and AFTIR inlets, fed air to a Radiance Research Model 903 nephelometer fit with a 2.5 µm cut-off cyclone that measured the dry particle light scattering coefficient (b_{scat}) at 530 nm at 0.5 Hz. The b_{scat} was converted to b_{scat} at STP and then to a mass of $PM_{2.5}$ (µg sm^{-3}) using a conversion factor (for fresh smoke) of 208 800 µg sm^{-2} (equivalent to a mass scattering efficiency of ~4.8 sm^2 g^{-1}) obtained by a gravimetric calibration of the type described by Trent et al. (2000). The nephelometer inlet also supplied air to a non-dispersive infrared instrument (NDIR, LiCor model 6262), which measured CO_2 at the same time as b_{scat}. Since the AFTIR also measured CO_2, this allowed the $PM_{2.5}$ measurements to be normalized to the trace gas data as described in detail below. A second NDIR (LiCor model 7000) measured CO_2 (at 0.5 Hz) from the third channel on the isokinetic particle inlet that also supplied the AMS and SP2 allowing the data from the latter instruments to be coupled to the trace gas data. Measurements of the ambient three-dimensional wind velocity, temperature, relative humidity, and barometric pressure at 1-Hz were obtained with a wing-mounted Aircraft Integrated Meteorological Measuring System probe (AIMMS-20, Aventech Research, Inc.). Details of the AIMMS-20 probe and a performance evaluation are provided by Beswick et al. (2008). A chemiluminescence instrument measured ozone at 0.5 Hz.

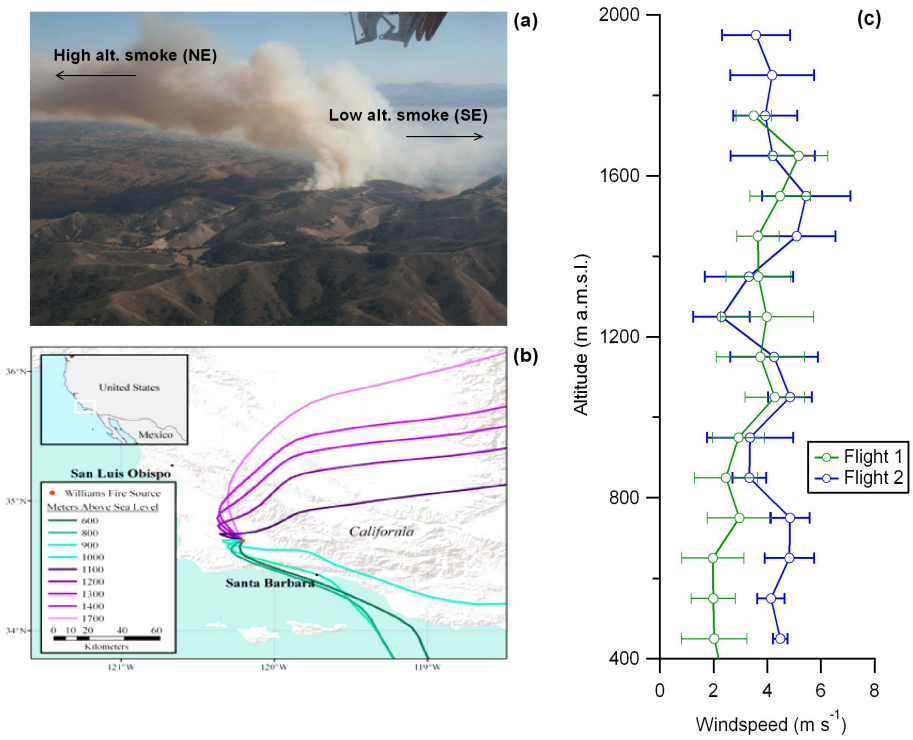

Fig. 1. **(a)** Photograph of the high- and low-altitude smoke plumes from the Williams Fire taken at 12:20 LT on 17 November 2009 from the USFS Twin Otter. **(b)** HYSPLIT forward trajectories starting at 11:00 LT at the Williams Fire (Draxler and Rolph, 2010; Rolph, 2010). Eight 24 h trajectories show air at 600–1000 m a.m.s.l. (green) drifting SE and air at 1100–1700 m a.m.s.l. (purple) drifting NE. **(c)** Vertical profile of windspeeds from Flights 1 (green) and 2 (blue).

2.2 Vegetation and fire development

The Williams prescribed fire was carried out on 17 November 2009. The 81 hectare site (∼10 km north of Buellton, California; 34°41′45″ N, 120°12′23″ W) covered several hillsides with various aspects. The land cover can be classified as chaparral and the vegetation burned consisted of scrub oak woodland understory and coastal sage scrub, which is a mixture of California sagebrush (*Artemisia californica*) with coyote brush (*Baccharis pilularis*), black sage (*Salvia mellifera*), and California buckwheat (*Eriogonum fasciculatum*). Dead fuel moisture ranged from 9 to 15 % with higher moisture in the larger diameter fuels. Live fuel moisture was 70 %, which is below average compared to normally observed values. Ground level winds were light and variable at 2–8 km h^{-1}. Ground level relative humidity (RH) ranged from 26–11 % between 09:00–13:00 LT (PST, UTC-8). Surface temperature ranged from 19 °C at 09:00 LT to 24 °C at 12:20 LT. Skies were clear all day. (Fuels and surface weather information, J. McCarty, personal communication, Santa Barbara County Fire Department, 2009.) Ignition of the Williams Fire began at approximately 09:57 LT. The plume built up gradually and most of the smoke rose to ∼1200–1336 m above mean sea level (m a.m.s.l.) and then drifted northeast. Some smoke detrained at lower altitudes (below ∼600 m a.m.s.l.) and drifted southeast, settling into nearby valleys (Fig. 1a). Our visual observations were consistent with air parcel forward trajectory simulations using HYSPLIT (NOAA Air Resources Laboratory, http://ready.arl.noaa.gov/HYSPLIT.php), which shows low-altitude trajectories (600–1000 m a.m.s.l., Fig. 1b) originating at the source traveling southeast, while higher altitude trajectories (1100–1700 m a.m.s.l.) traveled northeast (Fig. 1b). The upwind vertical profiles of temperature and water vapor mixing ratio from the AIMMS-20 (Supplement Fig. S1) showed that the top of the boundary layer was located at ∼800 m a.m.s.l. (∼450 m above ground level, or a.g.l.) and the AIMMS-20 wind direction data confirmed the shift in wind direction modeled by HYSPLIT at 1100 ± 100 m a.m.s.l. The bulk of the smoke was sufficiently buoyant to penetrate the temperature inversion and rose to ∼1200 m a.m.s.l. where it encountered an average

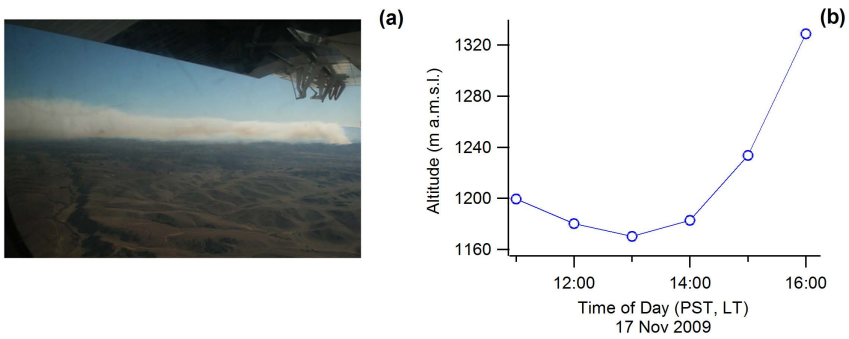

Fig. 2. (a) Side view of the Williams Fire high altitude plume at 12:40 LT from ∼58 km downwind. **(b)** HYSPLIT trajectory for source air starting at 11:00 LT and 1200 m a.m.s.l. No significant altitude gain is modeled in the first ∼4 h since emission.

windspeed of $\sim 5\,m\,s^{-1}$ (Fig. 1c). Low-altitude smoke dispersed slowly ($\sim 2.5\,m\,s^{-1}$ was the average windspeed at altitudes <1200 m a.m.s.l. during Flights 1 and 2) and tended to collect in low-lying areas as discussed further in Sect. 3.5.

The high altitude plume that drifted northeast from the source was isolated from other pollution sources and unimpeded by topography as seen in the photograph taken from ∼58 km downwind (Fig. 2a). The high altitude plume gradually rose from ∼1200 m a.m.s.l. at the source to ∼1800 m a.m.s.l. at ∼58 km (4.5 h) downwind, but HYSPLIT trajectories starting at 1200 m a.m.s.l. failed to capture this observed behavior, showing no substantial altitude gain/loss for at least 4 h following fire ignition (Fig. 2b). The observed rise might have been due to self lofting since the high levels of O_3 and black carbon in the plume would readily absorb significant amounts of solar energy. By 14:30 LT the fire had transitioned to mainly smoldering combustion with minimal plume rise.

2.3 Flight details

Two flights (mid-morning and afternoon) were conducted onboard the Twin Otter aircraft to sample initial emissions and aged smoke. Table 1 summarizes the times, locations, and meteorological conditions for AFTIR samples taken during both flights. For every plume sample on both flights we also collected a background sample at similar altitude just outside the plume.

Flight 1 occurred from 10:29–13:10 LT. We arrived at the site of the fire approximately 30 min after initial ignition, at which time the fire was beginning to produce a large plume of thick, white and brown smoke. From 10:50–12:19 LT we collected ten samples of "nascent" smoke (smoke "just created" or "emerging from another form") (Samples 1–6, 8, 10–12 in Table 1). The source samples were collected ∼600–1300 m a.m.s.l. at the center and top portions of the single updraft core. After 12:30 LT we concentrated on sampling the smoke downwind at ∼1200 m a.m.s.l., making perpendicular plume transects in an "S" shaped pattern and sampling the smoke eight times 4.5–16.1 km from the source (see flight path and AFTIR smoke sample locations in Fig. 3).

Flight 2 was conducted from 14:20–15:47 LT and sampled the high altitude plume at 1200–1900 m a.m.s.l. and 27–58 km from the source. From 14:45–15:16 LT we collected 10 grab samples of aged smoke 2.4–4.5 h old. We obtained estimated emission times by first calculating the average windspeed for incremental altitude bins of 100 m a.m.s.l. The smoke sample distance from the plume source was then divided by the average windspeed at the sample altitude. Estimated times since emission, or smoke "ages", were calculated for all the downwind samples from both flights (Table 1) using this methodology. This method implies that the oldest smoke sample had aged approximately 4.5 h. In addition, based on the estimated emission time of each downwind sample: 14 of the 18 downwind samples from the two flights were likely emitted during the time we were sampling the source (10:50–12:19 LT) and the other 4 downwind samples were emitted within 20 min of our source sampling period, supporting that the data are pseudo-Lagrangian. The Williams Fire plume was visible in GOES images and the position of the plume in the last daytime image (∼16:45 LT, acquired after Flight 2) is indicated in yellow in Fig. 3. Our measurements covered ∼70 % of the distance the plume traveled the first day.

2.4 Data processing and synthesis

2.4.1 FTIR spectral analysis

We use nonlinear least squares, multi-component fits to regions of the IR spectra with the HITRAN spectral database (Rothman et al., 2009) and reference spectra from the Pacific Northwest National Laboratory (Sharpe et al., 2004; Johnson et al., 2006, 2010) to obtain mixing ratios in both the smoke and background spectra for most compounds (Griffith, 1996; Burling et al., 2010). For these compounds the

Table 1. Smoke samples from the Williams Fire obtained during Flights 1 and 2.

Sample	Time (LT)	Latitude (° N)	Longitude (° W)	Altitude (m a.m.s.l.)	Pressure (hPa)	Relative Humidity (RH %)	Outside Air Temperature (°C)	Distance From Fire Source (km)	Time Since Emission (h:min:s)	Estimated Emission Time (LT)
Flight 1										
1	10:51:13	34°41′40″	120°12′13″	817	923.0	13.0	16.6	0.31	0:02:04	10:49:09
2	10:55:45	34°41′41″	120°12′18″	819	919.2	14.0	17.3	0.21	0:01:25	10:54:20
3	11:02:01	34°41′42″	120°12′18″	871	918.0	12.4	17.3	0.16	0:01:05	11:00:56
4	11:07:39	34°41′42″	120°12′23″	676	938.8	14.2	17.2	0.12	0:00:59	11:06:40
5	11:11:54	34°41′42″	120°12′28″	748	925.9	15.9	17.9	0.18	0:00:58	11:10:56
6	11:20:47	34°42′4″	120°12′11″	1336	865.3	11.2	15.4	0.65	0:03:05	11:17:42
7	11:31:55	34°46′35″	120°10′59″	1230	877.6	15.5	15.3	9.21	0:37:27	10:54:28
8	11:55:25	34°42′39″	120°12′41″	1196	882.3	13.4	15.2	1.71	0:07:35	11:47:50
9	11:59:58	34°43′42″	120°10′35″	1192	881.8	16.8	15.3	4.55	0:20:08	11:39:50
10	12:08:08	34°41′44″	120°12′30″	621	938.7	26.3	17.8	0.18	0:01:23	12:06:45
11	12:15:24	34°41′45″	120°12′23″	624	936.3	25.9	18.3	0.00	0:00:00	12:15:24
12	12:18:55	34°42′6″	120°12′33″	901	911.4	23.6	16.5	0.68	0:04:17	12:14:38
13	12:30:30	34°45′28″	120°9′22″	1198	880.3	15.4	15.5	8.28	0:36:38	11:53:52
14	12:34:01	34°46′40″	120°11′48″	1202	879.9	15.0	15.7	9.15	0:37:13	11:56:48
15	12:38:50	34°49′28″	120°9′58″	1195	879.9	15.6	15.4	14.8	1:05:26	11:33:24
16	12:44:57	34°52′18″	120°10′44″	1196	879.9	14.4	15.6	19.7	1:27:21	11:17:36
17	12:47:56	34°50′50″	120°6′26″	1210	884.0	12.5	15.8	19.1	1:17:44	11:30:12
18	12:55:27	34°48′21″	120°10′57″	1163	888.6	16.3	15.9	12.4	0:55:03	12:00:24
Flight 2										
19	14:45:06	34°55′28″	120°6′15″	1259	879.9	14.7	15.4	27.1	3:17:12	11:27:54
20	14:49:08	35°4′34″	120°6′40″	1744	825.8	12.4	14.0	43.2	3:03:30	11:45:38
21	14:50:06	35°6′31″	120°7′33″	1790	821.2	15.3	12.7	46.5	3:17:35	11:32:31
22	14:52:41	35°8′16″	120°5′52″	1898	810.1	13.7	12.9	50.2	3:20:17	11:32:24
23	14:56:11	35°9′40″	120°2′56″	1899	813.2	13.5	12.7	53.7	3:34:29	11:21:42
24	14:56:48	35°10′52″	120°3′42″	1882	813.3	14.3	12.2	55.6	3:41:56	11:14:52
25	14:59:48	35°11′56″	120°2′37″	1979	801.2	13.1	12.3	57.9	4:29:44	10:30:04
26	15:07:59	35°5′18″	120°6′7″	1423	867.7	14.2	13.9	44.7	2:26:20	12:41:39
27	15:12:00	34°57′51″	120°3′46″	1377	864.7	20.3	13.9	32.6	2:43:56	12:28:04
28	15:16:26	34°57′28″	120°4′13″	1376	864.3	16.6	13.9	31.7	2:39:22	12:37:04

excess mixing ratio for any species "X" (denoted ΔX) is the mixing ratio of species "X" in the plume sample minus its mixing ratio in the background air. For HCN, NO, and NO_2 we determine the excess mixing ratios directly from absorbance spectra via spectral subtraction or peak integration (Yokelson et al., 1997). The absorbance spectra are made using background spectra acquired at nearly the same pressure. The NO detection limit is ∼25 ppb and all excess mixing ratios below this concentration were omitted. The detection limit for the other compounds reported here is 1–10 ppb.

2.4.2 Estimation of excess mixing ratios, normalized excess mixing ratios (NEMR), emission ratios (ER), and emission factors (EF)

The procedure to calculate excess mixing ratios for the AFTIR data is given above. Excess mixing ratios can also be calculated from the continuous data (SP2, CO_2, b_{scat}) and repetitive discrete samples (AMS). In both these cases, we compute the background value from the average of a large number of points at the plume altitude (but outside the plume) and then subtract that background from the values obtained in the plume.

The normalized excess mixing ratio (NEMR) is obtained by dividing ΔX by the excess mixing ratio of another species (ΔY) measured at the same time and location; usually a fairly long-lived plume "tracer" such as ΔCO or ΔCO_2. For the Williams Fire, the NEMRs for all species (except ΔNH_3 referenced to ΔCO or ΔCO_2) measured at the source of the fire did not vary greatly as the fire progressed through the available fuels. We incorporated the ten measurements of the source NEMR into an estimate of the fire-average initial molar emission ratio (ER) as described below. The ER has two important uses: (1) Since the CO or CO_2 tracers dilute at the same rate as the other species, differences between the ERs and the NEMRs measured downwind allow us to quantify post-emission gas-phase chemistry and gas-particle

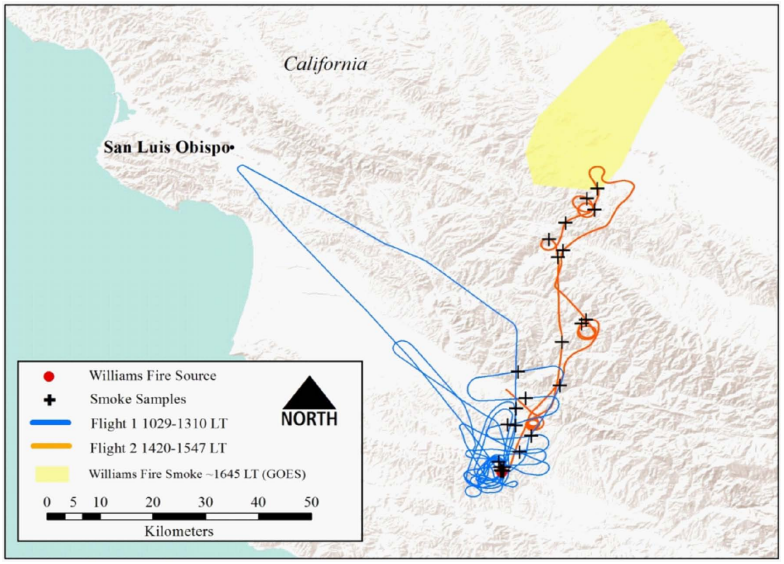

Fig. 3. The flight paths and the location of smoke samples for Flight 1 (blue) and Flight 2 (orange). The approximate position of the densest smoke in the Williams Fire plume (yellow) during the last daytime GOES image (~16:45 LT) captured after our second flight on 17 November 2009. The overlay shows that our measurements probed most of the daytime plume evolution that occurred on 17 November (plume image from http://www.firedetect.noaa.gov).

partitioning; and (2) The ER can be used to calculate emission factors (EF) as described below.

The measurement of a NEMR is most accurate when both species were measured simultaneously on the same instrument (e.g. two gases in the AFTIR cell or two particle species on the AMS). When comparing NEMR that were determined using data from two different instruments, error can be introduced due to the different time responses of the instruments. However, this error can be largely eliminated for continuous instruments by deriving the NEMR from a comparison of the integrals over the whole plume sample. In addition, in the dispersed, downwind plume, the excess mixing ratios tended to vary slowly in time and space compared to measurement frequency. In this work, we most often use NEMR relative to ΔCO since CO has a lifetime of several months at ~35° N in November, low background variability, and there were no other major sources of CO noted in the vicinity. In some cases we show downwind NEMR to CO_2 since that was the relevant co-measured species.

We computed fire-average initial emission ratios as our best estimate of the starting conditions in the plume using our ten source samples as follows. For grab samples we take the fire-average ER as the slope of the linear least-squares line with the intercept forced to zero when plotting ΔX against ΔY (Yokelson et al., 1999). For example, the slope of the plot of ΔX vs. ΔCO yields the initial molar emission ratio for compound "X" to CO and the uncertainty is the 1σ standard error in the slope (Fig. 4a, b). The intercept is forced to zero since the background concentration is typically well known and variability in the plume can affect the intercept if it is not forced. This method heavily weights the large values that may reflect more intense combustion and were collected with higher signal-to-noise. Smoke samples collected more than 1.8 km from the source showed signs of aging (O_3 formation) and were not used to derive the initial ER. We obtained initial mass emission ratios for the AMS species, rBC, and $PM_{2.5}$ to CO_2 since CO_2 was measured on the same inlet. These ratios were computed by comparing the integrated excess amounts as the aircraft passed through the nascent smoke as mentioned above. For the set of passes through the fresh smoke we plot the integrals of the excess values from the AMS and continuous instruments versus the integrals of excess CO_2 and obtain the ER from the slope, analogous to the grab sample plots (Fig. 4c, d). To test the robustness of our integral-based AMS ERs to CO_2, we compared them to ER obtained by plotting the excess values from the 4 s discrete samples versus the values of ΔCO_2 measured during the same 4 s interval. In nearly all cases we obtained agreement within 5 %, except for sulfate, which was reconstructed based on samples of smoke with low levels of organic loading where the AMS fragmentation table gave reasonable results. The major sulfate fragments in the AMS spectrum are *m/z* 48 (has minor organic interference based on unpublished high resolution data of a similar fuel type), *m/z* 64, *m/z* 80, *m/z* 81 and *m/z* 98. The ratios of *m/z* 64, *m/z* 80, *m/z* 81 and *m/z* 98 to m/z 48 were calculated for low smoke levels

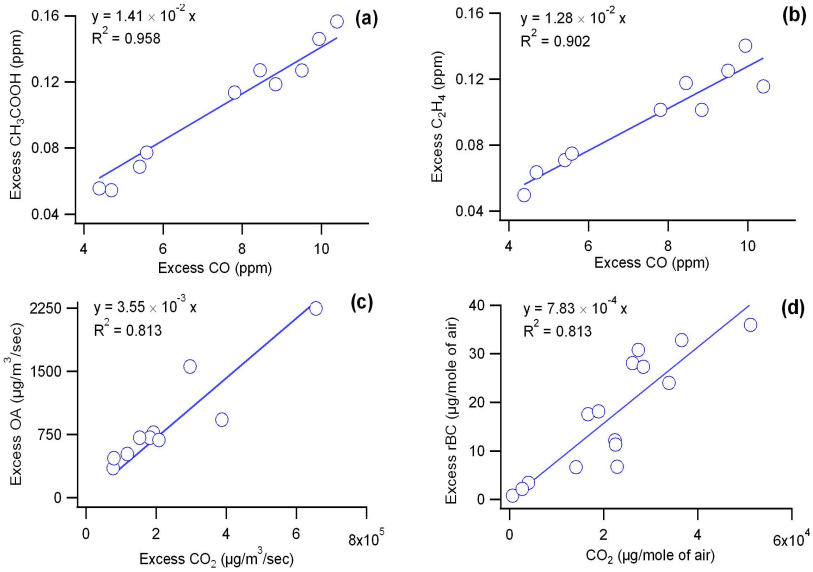

Fig. 4. Emission ratio plots for **(a)** $\Delta CH_3COOH/\Delta CO$ and **(b)** $\Delta C_2H_4/\Delta CO$ measured by AFTIR. **(c)** $\Delta OA/\Delta CO_2$ measured by AMS and NDIR. **(d)** $\Delta rBC/\Delta CO_2$ measured by SP2 and NDIR.

where organic interference at these masses is low, and were then applied to the higher loading smoke samples. The issues related to calculating inorganic aerosol concentrations from UMR AMS data during episodes of high organic loading is an active area of research and will be presented in future work.

For any carbonaceous fuel, the source ERs can be used to calculate emission factors (EF) expressed in grams of compound emitted per kilogram of biomass burned (on a dry weight basis) using the carbon mass-balance method (as explained in Yokelson et al., 1996, 1999). The carbon mass balance method is most accurate when the fraction of carbon in the fuel is precisely known and all the burnt carbon is volatilized and detected. Based on carbon content analysis of about 50 chaparral vegetation samples during a companion study (Burling et al., 2010) and literature values for similar fuels (Susott et al., 1996; Ebeling and Jenkins, 1985), we assumed a carbon content of 50 % by mass on a dry weight basis for the fuels that burned in the Williams Fire. The actual fuel carbon percentage likely varied from this by less than a few percent. EF scale linearly with the assumed fuel carbon fraction. Total C in this study was determined from the sum of the C from AFTIR species, rBC, and an organic carbon (OC) value based on the assumption that OA/OC was 1.6 in fresh smoke (Yokelson et al., 2009). This sum could underestimate the total carbon by 1–2 % due to unmeasured C. That would lead to a slight, across the board overestimate of our calculated EF by a factor of 1–2 % (Akagi et al., 2011).

3 Results and discussion

3.1 Initial emissions compared to other chaparral fires

The fire-average molar emission ratios for the Williams Fire (computed as described in Sect 2.4.2) are presented in Table 2. A detailed comparison of the Williams Fire initial emissions (ER and EF) to the emissions from other chaparral fires sampled during SLOBB and chaparral fires sampled in other studies is presented by Burling et al. (2011). Here we simply note that the Williams Fire had similar ERs, EFs, and modified combustion efficiency (MCE, 0.933) to those reported in the literature for other chaparral fires (Radke et al., 1991; Hardy et al., 1996; Burling et al., 2011). The one exception is that Radke et al. (1991) reported a study-average EF($PM_{2.5}$) ($15.93 \pm 6.88\,g\,kg^{-1}$) that is significantly higher than our EF($PM_{2.5}$) or the literature average (Burling et al., 2011, $\sim 8\,g\,kg^{-1}$), which likely reflects that they sampled more of the smoldering phase near the end of the fires, as smoldering normally produces higher EF(PM) (Ferek et al., 1998). Radke et al. (1991) note that their spot measurements of particle EF increased by as much as a factor of three as the fraction of smoldering combustion increased. Rather than measure samples of smoldering combustion as the fire died down, we focused first on characterizing the emissions that were produced by the bulk of the fuel consumed and then on the evolution of those emissions in the downwind plume.

3.2 Plume evolution

Many chemical and physical changes can affect nascent smoke as it begins to mix with ambient air. These changes include photochemical transformations, mixing with biogenic and/or anthropogenic pollutants, cloud processing, coagulation, and gas-to-particle conversion (Reid et al., 1998). The complexity of the aging scenario can vary greatly, depending on factors such as temperature, dispersion altitude, time of day, humidity, cloud cover, the initial emissions, and the proximity of other emission sources. In this study, the Williams Fire produced an isolated, nearly "undisturbed" plume, which provides a rare, valuable opportunity to test the mechanism of a photochemical model. A companion paper will use our observations of the Williams Fire to test and evaluate an advanced smoke plume chemistry model (Alvarado and Prinn, 2009).

The evolution of the reactive species we could measure over the course of 4 h following emission is summarized in Table 2. To illustrate photochemical changes in the plume it is useful to have a best estimate of the starting NEMR and uncertainty to compare to downwind NEMR. We use the slope-based fire-average ER as our best estimate of the likely starting NEMR for primary species measured in any individual smoke parcel downwind. Sloped based initial NEMRs were also calculated for secondary species such as ozone and PAN (shown in Table 2) though the concept of an ER does not strictly apply to these species. We use the standard deviation in the mean of the ten source NEMRs as our best estimate of the uncertainty in the starting NEMR for all species with downwind data (also shown in Table 2). Stable species that did not change significantly for 4 h after emission and species that dropped below our detection limit in that time are also included in Table 2 just to provide a more complete reference. The uncertainty in the ER shown for these species is the standard error in the slope and no downwind data is shown except for rBC. Absolute uncertainties in the ERs and NEMRs have a component from random and systematic instrumental errors, sampling representativeness, and other issues; but many of these errors should not greatly impact the study of plume evolution. As an example we note that downwind smoke was only sampled in the high altitude plume and the low-altitude source samples could potentially represent smoke that instead detrained in the low elevation plume. However, the source ERs were not significantly dependent on altitude. In a few cases we will illustrate this by comparing the downwind NEMRs to an alternate ER based solely on the high altitude source samples and show that the impact of this was small.

At this point it should be clear that fires do not produce "ideal" plumes. Instead there is some temporal and spatial fluctuation about the average ER and smoke parcels mix with both background air and other parts of the plume, which explains some of the variation in the downwind NEMRs. We fit the evolution of the NEMRs to various "best fit" functions to estimate the final NEMR at the age of the last measurement (4–4.5 h time since emission), to assist in discerning differences between the final downwind NEMR and the ER, and to estimate lifetimes. We report the final downwind NEMR and estimated uncertainty for the measured reactive species in Table 2. The uncertainty shown for the final NEMR is the uncertainty in individual downwind samples, but the uncertainty in whether a trend is occurring is smaller than shown by these uncertainties. We note that the functions used were selected empirically based on how well they fit the data and cannot necessarily be rigorously derived from the complex, sometimes unknown, underlying chemistry. Nor do we assume that these fits describe the behavior beyond the time since emission measured here. We show relative growth factors that compare the downwind and initial NEMRs (or ERs) over this time period to summarize the magnitude of species evolution that occurred in this photochemically active plume. Detailed discussions of these changes are presented in the remainder of this section.

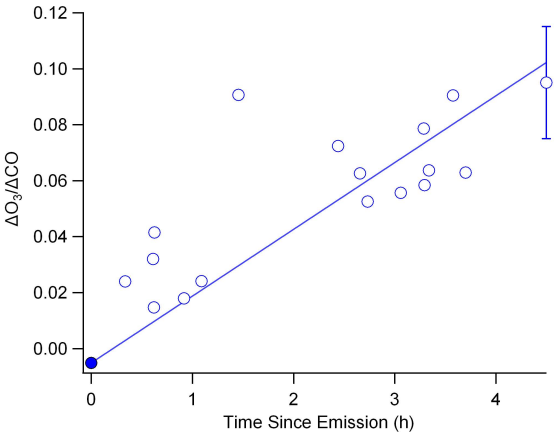

Fig. 5. $\Delta O_3/\Delta CO$ vs. time since emission (h). Individual source samples are not shown and we instead show the initial negative $\Delta O_3/\Delta CO$ NEMR (solid circle). The error bar reflecting the standard deviation in the mean of the ten source measurements is too small to be visible. The downwind error bar is an estimate of the uncertainty in the oldest individual downwind sample.

3.2.1 Ozone

Ozone is an important secondary product formed in biomass burning smoke. Figure 5 shows the $\Delta O_3/\Delta CO$ NEMR tracked over the course of estimated times since emission of 0 h to ~4.5 h. The initial $\Delta O_3/\Delta CO$ NEMR (solid circle) is negative because the background air contained ~50 ppb of ozone that was quickly destroyed by fast reaction with NO emitted by the fire. Negative initial $\Delta O_3/\Delta CO$ NEMRs are common when sampling fresh smoke (Yokelson et al., 2003a). The y-intercept of a linear trendline was forced to the

Table 2. Emission ratios (ER), initial and downwind NEMR for the Williams Fire.

	ER (mol mol^{-1}) or initial NEMR	Uncertainty[a]	Downwind NEMR (4–4.5 h since emission)	Uncertainty[b]	Factor Change after 4–4.5 h	Uncertainty
	Ratioed to ΔCO_2					
CO	7.13×10^{-2}	5.50×10^{-3}				
	Ratioed to ΔCO					
Methane (CH_4)	8.72×10^{-2}	2.40×10^{-3}				
Acetylene (C_2H_2)	2.72×10^{-3}	2.10×10^{-4}				
Propylene (C_3H_6)	4.80×10^{-3}	8.00×10^{-5}				
Phenol (C_6H_5OH)	1.48×10^{-3}	1.70×10^{-4}				
Furan (C_4H_4O)	1.46×10^{-3}	8.00×10^{-5}				
Methanol (CH_3OH)	1.67×10^{-2}	7.00×10^{-4}				
Hydrogen Cyanide (HCN)	1.30×10^{-2}	1.10×10^{-3}				
Nitrous Acid (HONO)	4.00×10^{-3}	6.10×10^{-4}				
Ethylene (C_2H_4)	1.28×10^{-2}	1.10×10^{-3}	6.01×10^{-3}	7.15×10^{-4}	0.47	0.07
Glycolaldehyde ($HCOCH_2OH$)	1.87×10^{-5}	1.18×10^{-5}	2.52×10^{-3}	2.12×10^{-3}	135	142
Formic Acid (HCOOH)	6.59×10^{-4}	1.53×10^{-4}	4.84×10^{-3}	1.65×10^{-3}	7.34	3.03
Acetic Acid (CH_3COOH)	1.41×10^{-2}	1.19×10^{-3}	2.45×10^{-2}	5.69×10^{-3}	1.73	0.43
Formaldehyde (HCHO)	1.65×10^{-2}	2.59×10^{-3}	2.42×10^{-2}	4.74×10^{-3}	1.47	0.37
Ammonia (NH_3)	3.84×10^{-2}	9.69×10^{-3}	1.91×10^{-2}	2.65×10^{-3}	0.50	0.14
Ozone (O_3)	-5.13×10^{-3}	1.13×10^{-3}	1.02×10^{-1}	2.16×10^{-2}	N/A	N/A
	Ratioed to ΔCO_2					
Peroxy Acetyl Nitrate (PAN)	4.75×10^{-5}	2.04×10^{-5}	5.10×10^{-4}	1.21×10^{-4}	10.74	5.27
Nitric Oxide (NO)	8.21×10^{-4}	1.17×10^{-4}				
Nitrogen Dioxide (NO_2)	1.64×10^{-3}	9.00×10^{-5}				
NO_x (as NO)	2.30×10^{-3}	3.62×10^{-4}	4.60×10^{-4}	2.30×10^{-4}	0.20	0.10
$PM_{2.5}$ (light scattering)[c,d]	5.15×10^{-3}	1.33×10^{-3}	1.29×10^{-2}	1.89×10^{-3}	2.50	0.74
OC[c]	2.22×10^{-3}	5.36×10^{-4}				
OA[c]	3.55×10^{-3}	8.57×10^{-4}	2.83×10^{-3}	2.52×10^{-4}	0.80	0.21
Sulfate (SO_4^{2-})[c]	3.58×10^{-6}	3.28×10^{-6}	6.72×10^{-6}	2.42×10^{-6}	1.88	1.85
Nitrate (NO_3^-)[c]	9.61×10^{-5}	7.09×10^{-5}	3.87×10^{-4}	1.39×10^{-4}	4.03	3.30
Ammonium (NH_4^+)[c]	6.00×10^{-5}	3.95×10^{-5}	2.34×10^{-4}	8.42×10^{-5}	3.90	2.93
Chloride (Cl^-)[c]	4.97×10^{-5}	2.15×10^{-5}	1.33×10^{-5}	4.79×10^{-6}	0.27	0.15
rBC[c]	7.83×10^{-4}	3.48×10^{-4}	7.30×10^{-4}	1.51×10^{-4}	0.93	0.46
fTC rBC[e]	0.54	0.07	0.85	0.01	1.57	0.20

[a] Error calculated as the standard error in the slope when no downwind NEMR data shown. Otherwise, uncertainty was calculated as the standard deviation in the mean of the source measurements collected.
[b] Downwind errors shown are an estimate of the uncertainty in individual downwind samples. The uncertainty in whether a trend is occurring is smaller.
[c] Reported as a mass ratio.
[d] Converting light scattering to $PM_{2.5}$ with constant mass scattering efficiency not valid for aged smoke, see Sect. 3.3.
[e] Fraction of "thickly coated" rBC particles. All numbers reported as fractions.

initial slope-based $\Delta O_3/\Delta CO$ NEMR at time $t = 0$ h and the individual source measurements are not shown. The downwind error bar is an estimate of the uncertainty in the oldest individual downwind sample. As shown, $\Delta O_3/\Delta CO$ increased from $-5.13\ (\pm 1.13) \times 10^{-3}$ to $10.2\ (\pm 2.16) \times 10^{-2}$ in ∼4.5 h since smoke emission. Ozone production in a temperate forest BB plume in the Pacific Northwest of the US was noted previously by Hobbs et al. (1996), who reported that $\Delta O_3/\Delta CO$ reached 1.5×10^{-2} in 30 min. Akagi et al. (2011) assessed the literature on O_3 measurements in BB plumes and concluded that O_3 formation is ubiquitous in tropical BB plumes, but O_3 formation or destruction can occur in extratropical BB plumes. Global models consistently conclude that BB is a major global source of tropospheric O_3 (Fishman et al., 2003; Sudo and Akimoto, 2007). However, detailed plume scale studies find that reproducing detailed observations of O_3 formation is difficult (Trentmann et al., 2005; Alvarado and Prinn, 2009). The data we report here provides a rare opportunity to test the photochemical mechanism in a model with low uncertainty in transport (M. Alvarado, personal communication, 2012).

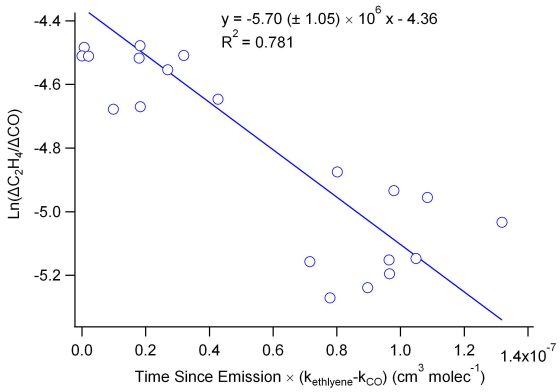

Fig. 6. Ln(Δethylene/ΔCO) vs. time since emission (h) × ($k_{\text{ethylene}} - k_{\text{CO}}$). Average OH in the plume from ∼10:30–15:16 LT is initially estimated from the absolute value of the slope ($5.70 \pm 1.05 \times 10^6$ molec cm^{-3}) and then corrected for O_3 oxidation (see Sect. 3.2.2).

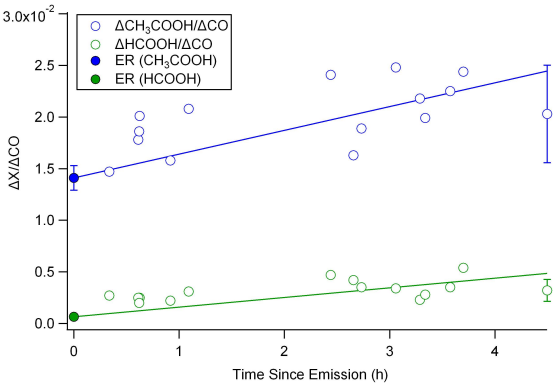

Fig. 7. Increase in $\Delta CH_3COOH/\Delta CO$ (blue) and $\Delta HCOOH/\Delta CO$ (green) vs. time since emission (h). Individual source samples are not shown and we instead show ERs (solid blue and solid green circles, respectively) with an error bar reflecting the standard deviation in the mean of the ten source measurements. The ER(HCOOH) error bar is too small to be visible. Downwind error bars are an estimate of the uncertainty in the oldest individual downwind samples.

3.2.2 Alkenes and estimated OH

Propylene mixing ratios dropped to levels near our detection limits within ∼30 min due to oxidation and dilution. The low signal-to-noise for C_3H_6 in the aged smoke made it difficult to quantify the decay rate. We also observed a rapid, but readily quantifiable, decrease in $\Delta C_2H_4/\Delta CO$ (Fig. 6). We estimate the average OH concentration in the plume by considering both main oxidation processes for C_2H_4. Reaction with OH is the primary removal process ($k_{\text{ethylene}} = 8.32 \times 10^{-12}$ cm^3 molec^{-1} s^{-1}; Sander et al., 2006). Ozone oxidation is a competing reaction, but the loss of C_2H_4 is relatively small (∼7.6 %) given the lower rate constant ($k_{\text{ozone}} = 1.7 \times 10^{-18}$ cm^3 molec^{-1} s^{-1}; Sander et al., 2006) and the typical O_3 levels (∼100 ppb) measured in the plume. As a first step, following the procedure derived by Hobbs et al. (2003), we fit a line to the decay of $\ln(\Delta C_2H_4/\Delta CO)$ versus (time since emission) × ($k_{\text{ethylene}} - k_{\text{CO}}$), where $k_{\text{CO}} = 1.74 \times 10^{-13}$ cm^3 molec^{-1} s^{-1} (Sander et al., 2006) (Fig. 6). The slope in the plot implies an average OH concentration of 5.70 ($\pm$1.05) $\times 10^6$ molec cm^{-3}. We reduce this average OH by 7.6 % to account for the ethylene lost via the O_3 oxidation channel resulting in a corrected OH estimate of 5.27 ($\pm$0.97) $\times 10^6$ molec cm^{-3}. If we use only the high-altitude source samples it raises the initial $\Delta C_2H_4/\Delta CO$ by ∼12 % and that would also raise the OH estimate. The OH and O_3 were unlikely to be constant in the plume and the background CO was as high as 22 % of total CO in the most dilute sample. However, omitting the 2–4 most dilute samples or the oldest samples had only a small effect on the OH retrieval. Thus, we use the O_3 corrected OH concentration of 5.27 ($\pm$0.97) $\times 10^6$ molec cm^{-3} as a reasonable estimate of average OH in this plume.

The OH levels largely govern the lifetime of VOCs and semi-volatile organic compounds (SVOCs) and the rate of formation of soluble or less volatile secondary products (Seinfeld and Pandis, 2006). Other oxidants such as HO_2 and RO_2 are also likely elevated in high OH environments (Mason et al., 2001). Similarly high concentrations of OH, some greater than 10^7 molec cm^{-3}, have been inferred or measured in African and Mexican biomass burning plumes within the first hour of plume processing (Hobbs et al., 2003; Yokelson et al., 2009). The Williams Fire OH was likely lower than that in the African and Mexican plumes largely because of less intense solar radiation that would occur in mid-November at ∼35° N (Tables 3.7 and 3.9 in Finlayson-Pitts and Pitts, 2000). However, the Williams Fire OH is by no means depleted and likely contributes to the O_3 production described above and many of the additional rapid post-emission changes described in the following sections.

3.2.3 Organic acids and aldehydes

The aging plots for AFTIR and AMS species from this point forward (Fig. 7–11) show the ER of $\Delta X/\Delta CO$ or $\Delta X/\Delta CO_2$ at an estimated time since emission of $t = 0$ h with the y-intercept of a best-fit trendline forced to the initial slope-based, fire-average ER, shown in Table 2. The uncertainty in the ER is an estimate of source variability from the 1σ standard deviation in $\Delta X/\Delta CO$ in the ten source samples (described in Sect. 3.2). The uncertainty shown for the downwind samples is an estimate of the uncertainty in individual downwind samples.

We measured formation of both acetic acid and formic acid over the course of 4.5 h (Fig. 7). The $\Delta CH_3COOH/\Delta CO$ ratio increased from 1.41 ($\pm$0.119) $\times$ 10^{-2} to 2.45 ($\pm$0.569) $\times$ 10^{-2} over 4.5 h, a factor of $\sim 1.73 \pm 0.43$ (Table 2). Over the same aging period $\Delta HCOOH/\Delta CO$ increased from 6.59 ($\pm$1.53) $\times$ 10^{-4} to 4.84 ($\pm$1.65) $\times$ 10^{-3}, a factor of 7.34 ± 3.03. Organic acids are a major component of biomass burning plumes and their post-emission behavior in BB plumes is summarized in Yokelson et al. (2009). The increase in acetic acid in the Williams Fire plume was slower than the rapid increase in $\Delta CH_3COOH/\Delta CO$ to $\sim$0.09 in less than 1 h seen in African savanna fire plumes (Yokelson et al., 2003a). However, formic acid did not increase downwind of those savanna fires. In the Williams Fire plume, and many other studies, the post-emission increases in organic acids were greater than the amount of known precursors, which suggests that organic acids may be the oxidation products of currently unidentified co-emitted NMOC (Yokelson et al., 2009). At higher RH, heterogeneous reactions may also be a source of formic acid (Tabazadeh et al., 1998).

The glycolaldehyde NEMR to ΔCO increases by a small total amount downwind, but with a high uncertainty (Table 2). Glycolaldehyde is a major product of cellulose pyrolysis (Richards, 1987; Radlein et al., 1991) and smoldering combustion (Yokelson et al., 1997), and also a known byproduct of hydroxyl initiated oxidation of ethylene and isoprene. Being highly water soluble, aqueous-phase reactions of glycolaldehyde may be important in the formation of secondary organic aerosol (Perri et al., 2009) via the formation of lower volatility compounds. Formaldehyde can be produced post-emission in plumes from the oxidation of NMOC, but also lost by photolysis and reaction with OH or HO_2. HCHO photolysis is an important source of OH (Mason et al., 2001). In the Williams Fire plume, $\Delta HCHO/\Delta CO$ increased during the first hour after emission and then leveled off (Table 2, graph not shown).

3.2.4 Gas-particle conversion and formation of reservoir species: nitrogen-containing compounds

Fitting an exponential decay to the molar ratio of $\Delta NH_3/\Delta CO$ (not shown) implies that roughly half of the initial NH_3 was lost in $\sim$4.5 h. Much of the decrease between the downwind NEMRs and the ER occurs in the first hour following emission, suggesting rapid, initial NH_3 removal by chemical and physical aging. In Fig. 8 we compare the decrease in the molar ratio of $\Delta NH_3/\Delta CO_2$ (derived from AFTIR data) to the molar increase in $\Delta NH_4^+/\Delta CO_2$ (measured by the AMS and NDIR) over 4 h, which is the approximate time since emission of the oldest AMS sample. The fit implies a significant decay in $\Delta NH_3/\Delta CO_2$ along with a clear increase in $\Delta NH_4^+/\Delta CO_2$ (Fig. 8a and b, respectively). We note the apparent high variability in the source measurements for NH_3 and emphasize that this is an artifact arising from compression to "time zero" of all

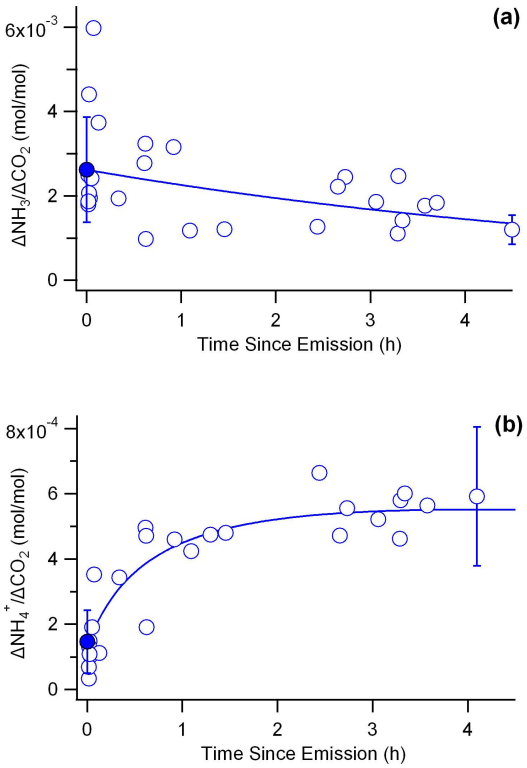

Fig. 8. **(a)** $\Delta NH_3/\Delta CO_2$ molar ratio vs. time since emission (h). The decay in $\Delta NH_3/\Delta CO$ vs. time since emission is slightly better correlated, but we show $\Delta NH_3/\Delta CO_2$ here for direct comparison to the AMS data in Fig. 8b. Points were fit to an exponential trendline. **(b)** $\Delta NH_4^+/\Delta CO_2$ molar ratio vs. time since emission (h). Note difference in y-scale. Points were fit to a logarithmic trendline. For both **(a)** and **(b)**, ERs (solid circles) are shown with an error bar reflecting the standard deviation in the mean of the ten source measurements. We retain all source samples to show the inherent variability in source measurements. Downwind error bars are an estimate of the uncertainty in the oldest individual downwind samples.

the $\Delta NH_3/\Delta CO_2$ ER samples, which increased in monotonic fashion from the beginning to end of the source sampling period. The $\Delta NH_4^+/\Delta CO_2$ ratio increases post emission by a factor of 3.90 ± 2.93 (Table 2), with this growth accounting for a fraction of 0.36 ± 0.31 of the gaseous ammonia lost on a molar basis. NH_3 reacts quickly with HNO_3 to form solid NH_4NO_3 and NH_3 may also react with organic acids to form other ammonium compounds in both the solid and liquid phases (though the low RH in the Williams Fire plume favors reactions in the solid phase, see below). However, since only about one-third of the ammonia lost was detected as ammonium, other loss processes must be considered. Ammonia removal pathways competing with

ammonium formation include the oxidation of NH_3 by OH (Dentener and Crutzen, 1994), but this reaction proceeds at a relatively slow rate at typical plume concentrations ($k = 1.6 \times 10^{-13}$ cm^3 molec^{-1} s^{-1}; Sander et al., 2006) and would not significantly reduce the amount of free ammonia over the course of 4 h. No precipitation or even clouds impacted the plume so wet deposition was not a factor, but a plausible loss process was the dry deposition of NH_3 since it is a "sticky" molecule known to adhere on surface sites (Yokelson et al., 2003b) and undergo dry deposition readily (Seinfeld and Pandis, 2006). Dry deposition of NH_3 to any water coating that could be present on the surface of aerosol particles can remove ammonia from the gaseous state (Asman et al., 1998), however, over 99 % of gaseous ammonia absorbing into the liquid phase would exist as ammonium and be detected by the AMS. Dry particles can also provide surface sites for ammonia adsorption to occur. However, NH_3 adsorbed to particles would also likely be detected by the AMS as ammonium, since particulate ammonium fragments to *m/z* 17, 16, and 15, following vaporization and ionization. Thus, it is not likely that dry deposition accounts for the majority of the observed NH_3 loss.

Other plausible fates of NH_3 may have involved the formation of new ammonium nitrate particles at the plume temperatures of 12–15 °C or condensation of ammonium nitrate onto existing particles that, in either case, are outside the most efficient detection range of the AMS (50–800 nm). Due to the low RH environment of the Williams Fire, nascent particles were probably not water coated and grew very slowly. While Semuniuk et al. (2007) observed rapid hygroscopic growth of fresh smoke particles in the range of 55–100 % RH, the Williams Fire RH range of ∼11–26 % is much lower, and also lower than the deliquescence and efflorescence points of most common salts (>60 %) (Tang and Munkelwitz, 1993, 1994a, b). Thus, new particle formation and condensation on those particles could have been occurring without being detected if particles were growing slow enough to evade AMS detection even after several hours since emission. We also can not discount the possibility that ammonium nitrate was incorporated in particles that were larger than 800 nm.

We roughly compare the Williams Fire observations with those in a Yucatan BB plume in a 70–100 % RH environment where ammonium formation accounted for roughly 32 % of the estimated starting NH_3 in just 1.4 h (Yokelson et al., 2009). Ammonium formation accounted for only ∼13 % of the measured initial NH_3 over 1.4 h in the Williams Fire plume. Faster ammonium formation accounting for more of the initial ammonia may have occurred in the Yucatan due to increased deposition to wetter particles, faster particle growth, or faster HNO_3 formation under tropical photochemical conditions.

Figure 9 shows the decrease in $\Delta NO_x/\Delta CO_2$ (blue) and corresponding increases in both $\Delta NO_3^-/\Delta CO_2$ (green) and $\Delta PAN/\Delta CO_2$ (light blue) during 4 h after emission. Processes that remove NO_x from the plume or transfer it to reservoir species such as PAN or alkyl nitrates are important, as NO_x is a precursor for O_3 formation. A major NO_x loss process is the association reaction of OH with NO_2 to form HNO_3, which can condense to form particle nitrate. At the average temperature and pressure of the Williams Fire plume, the NO_2 association reaction occurs with a pseudo second order rate constant of 1.04×10^{-11} cm^3 molec^{-1} s^{-1} (Sander et al., 2006) and a pseudo first order rate constant (using our derived average OH concentration from Sect. 3.2.2) of 5.47×10^{-5} s^{-1} for an NO_2 lifetime of ∼5.1 h. Thus, in the 4 h that we monitored the plume this reaction would be expected to convert roughly 54 % of the initial NO_x to HNO_3 (and potentially nitrate). Gas-phase nitric acid was not measured in the Williams Fire plume, however other studies have reported that there was no measureable enhancement of gas-phase HNO_3 in any of the BB plumes measured (Yokelson et al., 2009; Alvarado et al., 2010). The reason for this is likely because HNO_3 can react rapidly with NH_3 to form NH_4NO_3 (as discussed above), and HNO_3 (or NH_4NO_3) have high deposition velocities to wet and dry surfaces. In the Williams Fire, all these processes could theoretically remove HNO_3 from the plume, but loss by deposition to wet surfaces is unlikely due to the low RH.

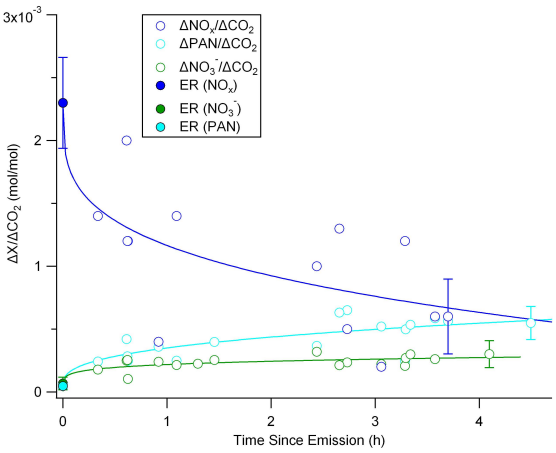

Fig. 9. ΔNO_x (blue), ΔPAN (light blue), and ΔNO_3^- (green) ratioed to ΔCO_2 (molar) vs. time since emission (h). Corresponding emission ratios (ER) are shown as solid blue, light blue, and green circles, respectively. ER error bars show the standard deviation in the mean of the ten source measurements. The ER(PAN) error bar is too small to be visible. Downwind error bars are an estimate of the uncertainty in oldest individual downwind samples. Points were fit to logarithmic trendlines.

The $\Delta NO_3^-/\Delta CO_2$ molar ratio was initially very low, but secondary formation of nitrate occurred rapidly as can be seen from the logarithmic trendline in Fig. 9 (green). The trend in $\Delta NO_3^-/\Delta CO_2$ is similar to that of $\Delta NH_4^+/\Delta CO_2$,

suggesting an initial burst in these inorganic particle species in the first hour since emission. After 4 h, AMS-detected nitrate accounted for only ∼22 % of the HNO_3 (molar basis) predicted to form based on our derived average OH concentration. The unaccounted for HNO_3 comprises ∼42 % of the initial NO_x. Some of the missing HNO_3 could have been present in the plume as nitrate in particles that dissociated in the AMS inlet. However, inlet losses in the AMS due to evaporation probably did not significantly affect our measurements given the modest temperature increase within the aircraft (3–11 °C) and the inlet residence time of ∼2.5 s. Huffman et al. (2009) outfitted their airborne AMS inlet with a thermodenuder and measured nitrate evaporation rates of $\sim 0.2\,\% \, C^{-1}\, s^{-1}$. As mentioned above, it is plausible that NH_3 and HNO_3 formed new (or condensed on existing) particles that were outside the AMS size detection range. Missing HNO_3 ratioed to missing ammonium (∼1.3) does suggest that small or large particles containing ammonium nitrate could account for substantial undetected signal due to both ions, but that some gas phase HNO_3 may have also been present that we were unable to measure with the instruments onboard the Twin Otter. The possible importance of ammonium nitrate in small particles in fresh BB plumes is further supported by the observations of Yokelson et al. (2009). In that study, 49 ± 16 % of HNO_3 expected to form from the reaction of NO_2 and OH was observed as nitrate in a high RH BB plume after 1.4 h since emission. Further, HNO_3 was measured, but not elevated above background in the plume. Thus, in that high RH environment (70–100 %), particle growth could have been approximately six times faster than in the Williams Fire, but still slow enough that half the nitrate mass was in particles too small to detect with the AMS.

Formation of reservoir species such as PAN also causes NO_x to decrease from its initial level (Seinfeld and Pandis, 2006; Alvarado et al., 2010). PAN ratioed to CO_2 shows rapid initial growth (Fig. 9, light blue) similar to nitrate and ammonium. Overall, $\Delta PAN/\Delta CO_2$ increases by a factor of 10.7 ± 5.3 in 4 h since emission (Table 2) and accounts for 22 ± 6 % of initial NO_x on a molar basis after 4 h. Thus, the total NO_x decrease due to the observed PAN formation plus the calculated NO_x loss via reaction with OH is 76 %, which agrees remarkably well with the observed total NO_x decrease of ∼80 % seen in Fig. 9. However, the uncertainties are high enough that formation of other reservoir species such as gas-phase HNO_3, alkyl nitrates, or other peroxy nitrates could also be significant. The decrease in $\Delta NO_x/\Delta CO_2$ over 4 h shows how NO_2, which is available for photolysis and O_3 formation in the fresh plume, was quickly converted to PAN, which can then be transported considerable distances before thermally decomposing and releasing NO_2 for O_3 production far from the source (Val Martin et al., 2006). After 4 h since emission, the excess PAN is roughly double the excess NO_3^-. Alvarado et al. (2010) also observed a PAN/nitrate ratio of 2 in boreal forest fire plumes of qualitatively similar time since emission. In the case of the Williams Fire, we are hesitant to interpret the PAN/nitrate ratio as a measure of the $\Delta PAN/\Delta HNO_3$ branching ratio since the nitrate fails to account for all the NO_x calculated to be converted to HNO_3. Smoke plume simulation studies by Mason et al. (2001) found that PAN formation becomes increasingly dominant over HNO_3 formation further downwind. While we cannot account for all NO_x lost to the HNO_3 channel, we do observe that the $\Delta PAN/\Delta NO_3^-$ ratio grew by a factor of ∼2 over the course of 4 h since emission.

3.2.5 Evolution of sulfate and chloride

The $\Delta SO_4^{2-}/\Delta CO_2$ mass ratio steadily increased nearly two-fold from 3.58 $(\pm 3.28) \times 10^{-6}$ to 6.72 $(\pm 2.42) \times 10^{-6}$ in 4 h since emission (Table 2, Fig. 10a). The high uncertainty reported is due to the large variability in the source measurements, but a clear increasing trend with time since emission is evident. Unlike the rapid initial formation of nitrate and ammonium, the sulfate growth is gradual. This is expected since OH reacts relatively slowly with SO_2 ($8.8 \times 10^{-13}\, cm^3\, molec^{-1}\, s^{-1}$, Sander et al., 2006), and the plume was too dry for aqueous sulfate formation to be significant. In a Yucatan BB plume characterized by high initial emissions of SO_2 and high RH, Yokelson et al. (2009) observed that $\Delta SO_4^{2-}/\Delta CO$ increased by a factor of 8.8 ± 2.7 in just 1.4 h. This suggests that the higher RH, OH, and initial SO_2 contributed to much faster sulfate formation in the Yucatan plume. In addition, Yokelson et al. (2009) observed ΔNH_4^+ to be about equal to the sum of twice the ΔSO_4^{2-} plus the ΔNO_3^- (on a molar basis) in that plume. Additionally, sulfate had accounted for ∼60 % as much negative charge as nitrate. For the Williams Fire, a graph of ΔNO_3^- vs. ΔNH_4^+ on a molar basis (Fig. 10b) yields a slope of 0.466 ± 0.010 ($R^2 = 0.95$), which is almost identical to the ratio observed in the Yucatan plume, but the Williams Fire ΔNO_3^- to ΔSO_4^{2-} molar ratio was >100. This suggests sulfate was not a significant counter-ion for ammonium in this plume and that the particle ammonium was pairing with negative ions other than nitrate and sulfate.

The $\Delta Cl^-/\Delta CO_2$ ratio decreases with time since emission in a well correlated fashion (Fig. 10c), except for one sample collected during Flight 1. Chloride may decrease because it is replaced by other anions such as nitrate as they form (Posfai et al., 2003; Li et al., 2003) although nitrate formation greatly exceeds chloride losses. The fate of the chloride released from the particles is unknown, but it is unlikely that most of the released chloride constitutes a rapid source of Cl atoms. The Cl atom has an appreciable rate coefficient with C_2H_2 (Tabazadeh et al., 2004), and we did not observe a change in $\Delta C_2H_2/\Delta CO$ over 4.5 h since emission. In any case, the amount of ΔCl^- is insufficient to pair with a significant fraction of the ΔNH_4^+ during the later stages of plume evolution (Fig. 10d) and the total charge from measured inorganic anions (Cl^- + twice sulfate + nitrate) is only sufficient

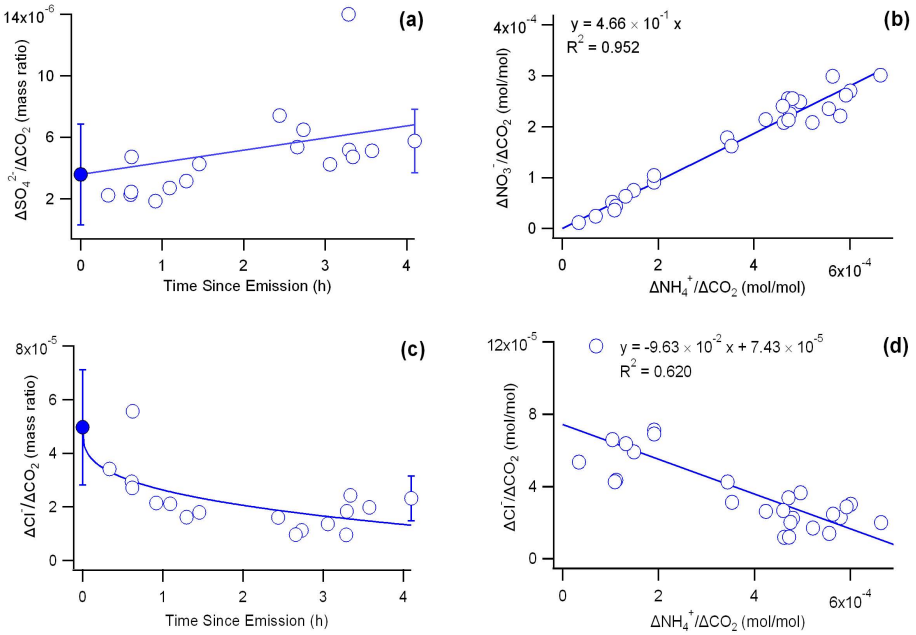

Fig. 10. (a) $\Delta SO_4^{2-}/\Delta CO_2$ mass ratio vs. time since emission (h). **(b)** $\Delta NO_3^-/\Delta CO_2$ vs. $\Delta NH_4^+/\Delta CO_2$ on a molar basis. **(c)** $\Delta Cl^-/\Delta CO_2$ mass ratio vs. time since emission (h) fit to a power curve. **(d)** $\Delta Cl^-/\Delta CO_2$ vs. $\Delta NH_4^+/\Delta CO_2$ on a molar basis. In both **(a)** and **(c)** individual source samples are not shown and we instead show ERs (solid circles) with an error bar that is the standard deviation in the mean of the ten source measurements. Downwind error bars are an estimate of the uncertainty in oldest individual downwind samples.

to pair with ∼50 % of the ammonium suggesting that the latter may also be pairing with unmeasured organic anions such as formate or acetate. The possible significance of organic anions is further supported by the fact that ammonium is not the only significant cation in BB plumes. For instance high levels of K^+ are normally reported in BB plumes and it is often used as a tracer for BB (Zhang et al., 2010).

3.3 Evolution of light scattering and organic aerosol

The trends in light scattering and organic aerosol (OA) were similar when we used source ER based on all the source samples or only those obtained at high altitudes. In general, Δb_{scat} (or Δlight scattering)/ΔCO_2 increased by a factor of 2.50 ± 0.74 (Table 2) and $\Delta b_{scat}/\Delta CO$ increased by a similar factor of 2.45 ± 0.55 over the course of 4 h. If we assume a constant conversion factor with time since emission (208 800 µg sm^{-2}, Sect. 2.1.4) between scattering (at 530 nm wavelength) and $PM_{2.5}$, then this implies a factor of ∼2.50 increase in $\Delta PM_{2.5}$ (ratioed to ΔCO_2) as shown in Fig. 11. This increase is comparable to the 2.6 ± 1.5 growth factor in Δlight scattering/ΔCO seen in ∼1.4 h in an isolated BB plume in the Yucatan (Yokelson et al., 2009). In the case of the Yucatan plume, the particle growth inferred from increased scattering (derived using the same methodology as above) was confirmed by a growth factor of ∼2.4 in the sum of species measured by AMS ratioed to ΔCO. The growth in AMS species was driven mostly by significant secondary OA (SOA) formation in the Yucatan plume, with an increase in $\Delta OA/\Delta CO$ of 2.3 ± 0.85 in 1.4 h (Yokelson et al., 2009).

However, in the Williams Fire, although light scattering increased significantly with time since emission, $\Delta OA/\Delta CO_2$ dropped initially, followed by a slow increase after ∼1.5–2 h. The net result was a decrease in $\Delta OA/\Delta CO_2$ by a factor of 0.80 ± 0.21 when assessing all samples up to 4 h since emission (Table 2). In addition, the assumption of a constant ratio between light scattering and particle mass would imply that $\Delta OA/\Delta PM_{2.5}$ decreased from 0.69 ± 0.24 to 0.22 ± 0.04 after 4 h since emission. This is inconsistent with the change in OA normalized by the sum of the species measured by the AMS, which decreased from a fraction of 0.94 to 0.82 over this 4 h time period (where the sum of the measured AMS species should account for approximately 0.8–0.9 of $PM_{2.5}$ mass). Thus it seems unlikely that the relationship between light scattering and $PM_{2.5}$ was constant with aging. We therefore cannot determine changes in $PM_{2.5}$ over the 4 h following emission using a constant conversion factor.

Next we describe a plausible physical model to rationalize both the Yucatan and Williams Fire observations. It is possible that the increased light scattering in the Yucatan

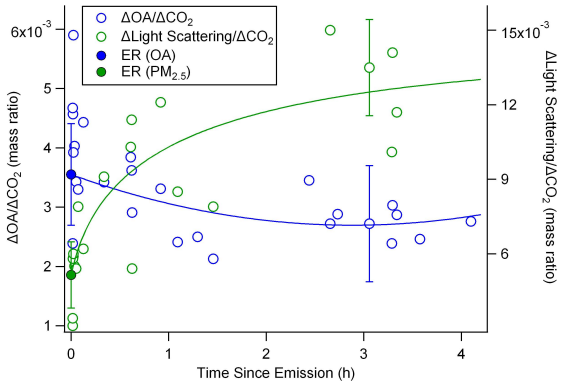

Fig. 11. ΔLight scattering/ΔCO_2 (green) and $\Delta OA/\Delta CO_2$ (blue) mass ratios are shown vs. time since emission (h). ER($PM_{2.5}$) (solid green circle) and ER(OA) (solid blue circle) are shown with error bars depicting the standard deviation in the mean of the ten source measurements. We show all the source samples to illustrate the variability in the source measurements. The log-normal (Δlight scattering/ΔCO_2) and second order polyfit ($\Delta OA/\Delta CO_2$) trendlines shown best correlate with the data. Error bars shown on downwind samples are an estimate of the uncertainty in individual downwind samples. ΔLight scattering/ΔCO_2 is shown converted to the mass ratio $\Delta PM_{2.5}/\Delta CO_2$ under the assumption that the ratio between b_{scat} and $PM_{2.5}$ is constant with time since emission. The assumption that the conversion between b_{scat} and $PM_{2.5}$ is constant with smoke age would imply an unrealistic $\Delta OA/\Delta PM_{2.5}$ of $<25\,\%$ at a plume age of 4 h. The increase in light scattering during the first 1.5 h since emission is probably due to particle growth via coagulation and then chiefly by condensation soon thereafter (Sect. 3.3).

plume was due to growth in the average particle diameter towards the measurement wavelength. The diameter growth could have occurred by both condensation and coagulation and the mass growth confirmed by the AMS in the Yucatan plume implies that condensation dominated over evaporation and coagulation. The similar increase in light scattering and the AMS mass may have been coincidental. In contrast, the increased scattering in the Williams Fire plume could have been caused by growth in average particle diameter mainly due to coagulation while, in contrast to the Yucatan plume, evaporation of organics initially exceeded condensation. A simple polydisperse coagulation scenario can explain the Williams Fire observations. We start by assuming that, at the source, there are many more particles in the 50–100 nm diameter range (which do not contribute substantially to the measured scattering) than particles in the 100–300 nm diameter range. Collisions between the small and large particles then decrease the small particle number (without reducing scattering), but increase the average diameter of the larger particles towards the measurement wavelength (530 nm in this case), thus increasing scattering efficiency according to Mie theory. Coagulation may also account for most of the increase in the fraction of thickly coated rBC particles we observed in the Williams Fire plume (discussed in the next section). At the same time, ∼20–30 % of the OA could have evaporated causing the small decrease in OA that is observed. We note that this explanation invokes the presence of large quantities of small (∼50–100 nm) particles in the fresh smoke. Particles ∼30–50 nm in diameter dominated the number distribution in some laboratory BB studies (Hosseini et al., 2010; Chakrabarty et al., 2006), but there are no airborne measurements of particles in this size range in BB plumes to our knowledge.

We also note that the probability of observing fast, initial coagulation was much higher in the Williams Fire plume. The Yucatan plume was from a small fire and the freshest sample was at an altitude of 1700 m a.g.l. when the smoke was already 10–30 min old and the ΔCO reading on a fast 1-s instrument was 823 ppb. We did not have 1-s CO instrumentation during the Williams Fire, but our 2-s CO_2 instrument observed a maximum ΔCO_2 of 390 ppm. The ΔCO_2 maximum multiplied by the fire-average $\Delta CO/\Delta CO_2$ ratio (0.0713, Table 2) for the Williams Fire implies a maximum ΔCO in our freshest smoke of at least 28 ppm. Thus, the smoke at the beginning of the aging sequence observed in the Williams Fire plume was about 34 times more concentrated than at the beginning of the observations for the Yucatan plume and coagulation would likely have been about 1000 times faster.

We point out that the decrease in $\Delta OA/\Delta CO_2$ in the Williams Fire plume continues only to the samples collected around ∼1.5–2 h following emission. After this time, $\Delta OA/\Delta CO_2$ increases at about the same rate as scattering suggesting that some of the organics that initially evaporated from the particles may have undergone homogeneous oxidation in the gas-phase leading to products with lower vapor pressure that then recondensed on the particles (Robinson et al., 2007). In any case, condensation is evidently dominating over evaporation from 1.5–2 h onward.

The OA evolution observed in the Yucatan plume is more likely to be the norm for most global biomass burning than the OA evolution observed in the Williams Fire plume since the Yucatan observations were made in the tropical boundary layer where most of the global smoke evolution occurs. However, the difference in OA evolution between the Yucatan and Williams Fire plume presents an opportunity to better understand the factors controlling OA evolution in smoke plumes. Here, we propose that the different balance between evaporation and condensation in the Yucatan plume and the Williams Fire plume could be rooted partly in the respective ambient conditions. In the case of the Williams Fire, the smoke penetrated above the boundary layer and diluted in the free troposphere where there was low RH (∼11–26 %, Table 1). In the Yucatan, the plume diluted in the boundary layer at 70–100 % RH, where particles would be more likely to have thick aqueous coatings. Hennigan et al. (2008)

found that particle water soluble organic carbon (WSOC, a surrogate for SOA) may substantially increase upon reaching a threshold RH of ∼70 % (though particle liquid water content may be strongly affected by particle hygroscopicity and not just RH). Furthermore, aqueous phase SOA formation results in a higher OA/OC ratio than straight gas-phase SOA formation and the high OA/OC in the Yucatan plume is consistent with some of the SOA being formed in the aqueous phase (Lim et al., 2010; Yokelson et al., 2009). The concentration of the hydroxyl radical in the plume should also affect how fast the gas-phase organic precursors for SOA are oxidized. In the Yucatan plume, the measured OH concentration was nearly twice our estimate of the OH in the Williams Fire plume. Both higher OH and the higher light intensity expected for the tropical (Yucatan) plume should speed up SOA formation in both the gas phase and aqueous phase. This speculation is further supported when comparing the rate of ozone formation: $\Delta O_3/\Delta CO$ increased ∼4 times faster in the Yucatan plume than in the Williams Fire plume (Sect. 3.2.1). Thus, conditions in the Yucatan were significantly more favorable for the formation of SOA.

We have not ruled out the possibility that the different OA evolution observed between the Williams Fire and Yucatan plumes could be partly due to the different fuels and/or different volatilities of the initial POA. In a laboratory study of aging BB smoke Hennigan et al. (2011) observed the most SOA formation (growth factor of almost three) for black spruce fuel and minimal SOA formation for white spruce fuel. Thus, nominally similar fuels sometimes gave widely different outcomes in an experiment where the environmental variables were monitored, but not fixed to a narrow range. In assessing global SOA production from biomass burning it may be significant that the Yucatan plume evolved under conditions with more light, more OH, and more chemical pathways for SOA formation than the Williams Fire plume and substantially more SOA was formed. Finally, we point out that the large increase in light scattering with plume age observed in both the Williams Fire and Yucatan plumes has important implications for visibility impacts and climate forcing regardless of the underlying mechanism (McMeeking et al., 2006; Reid et al., 2005a). More research would be useful to determine if the optical properties of moderately aged smoke are better suited for assessing the visibility and climate impacts of biomass burning.

3.4 Evolution of the black carbon mixing state

A fraction of 0.54 ± 0.07 of the initially emitted rBC particles are "thickly coated" as shown in Fig. 12 (solid circle, see Table 2). The remaining particles are classified as either "thinly coated" or "not coated" at the time of emission. However, the fraction of thickly coated (fTC) particles grew quickly and a fraction of $\sim 0.70 \pm 0.10$ of rBC particles were thickly coated within the first hour following emission. The fraction of thickly coated rBC particles for both

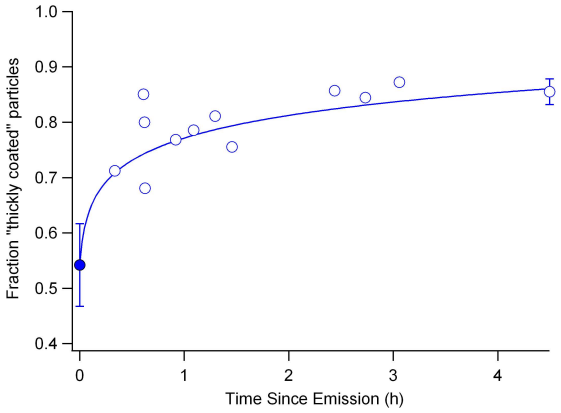

Fig. 12. Fraction of "thickly coated" (fTC) rBC particles vs. time since emission (h). Individual source sample fTC fractions are not shown and we instead show the mean fraction of source samples at $t = 0$ h (solid circle) with an error bar reflecting the standard deviation of the mean. The downwind error bar is an estimate of the uncertainty in the oldest individual downwind sample. Points were fit to a logarithmic trendline.

the fresh and 1 h old emissions was higher than in SP2 measurements from urban sources and the rate of increase in the Williams Fire plume was also faster than was observed in those urban plumes (McMeeking et al., 2011b). Schwarz et al. (2008) also found a higher fraction of rBC particles were thickly coated in BB plumes when compared to urban plumes that they measured nearby. Kondo et al. (2011) used an alternative analysis to show that rBC coatings in boreal BB plumes increased over several days, in some cases leading to increases in the volume of the coatings by a factor of two.

Similar coating development most likely also occurs on the nascent inorganic and organic particles. The coating formation on the rBC particles (a flaming product) likely formed in large part due to coagulation with OA particles produced by smoldering combustion. In addition, since ammonium and nitrate exhibit rapid initial increases, the coatings likely contain some inorganic material from gas-particle conversion involving precursors produced both by flaming (NO_x) and smoldering (NH_3). Kondo et al. (2011) speculated that OA could be redistributed from non-rBC-containing particles as the plume aged through evaporation and recondensation and they also showed that coagulation alone can lead to substantial increases in rBC coatings.

Regardless of the exact mechanism, as the rBC (and other) particles become coated they may scatter light more efficiently due mostly to size increases, but also due to changes in the index of refraction of the particle surface layer. Thus, the observed increase in rBC coatings is consistent with the observed increase in Δlight scattering/ΔCO_2 (Sect. 3.3). The evolution of the BC mixing state is also important

because the addition of organic coatings can increase the mass absorption efficiency of the BC particles, though the magnitude of this effect may be lower if the coatings absorb light (Lack and Cappa, 2010). In addition, coating formation with salts and soluble organics increases the hygroscopicity of the particles (Petters et al., 2009; McMeeking et al., 2011a; Zhang et al., 2008) and this likely increases their contribution to indirect effects on clouds (Koch et al., 2011) as well as decreasing their lifetime and availability for long range transport to sensitive snow/ice covered regions (Petters et al., 2009). Finally, black carbon affects human health and visibility, and contributes both to warming due to its ability to absorb light and decrease surface albedo (Ramanathan and Carmichael, 2008), and cooling due to indirect effects on clouds (Koch et al., 2011). Our observations in the Williams Fire plume suggest that the evolution of the BC mixing state could significantly affect the overall impact of black carbon emitted by biomass fires.

3.5 Dispersion of the low altitude plume

Our measurements of the high-altitude (1200–1900 m a.m.s.l.) plume generated by the Williams Fire detail the evolution of the bulk of the emissions produced by the fire and these emissions would contribute to the burden on the regional air shed along with many other sources. As discussed earlier (Sect. 2.2); a small fraction of the smoke from the Williams Fire detrained below 600 m a.m.s.l., drifted southeast, and settled into low lying areas (Fig. 2). We observed that this smoke was noticeably whiter in color and was probably more dominated by smoldering emissions, which implies a significant difference in chemical composition (Bertschi et al., 2003). Flight safety considerations prevented us from sampling this low-lying smoke. Thus, we examined data collected by county health departments (http://www.arb.ca.gov/aqmis2/aqdselect.php) for possible signatures of the low altitude Williams Fire plume. The nearest air quality station southeast of the Williams Fire was in Santa Ynez, but only O_3 was monitored there and no clear influence of the Williams Fire was evident. The next closest station was in Santa Barbara where PM_{10}, $PM_{2.5}$, and O_3 were monitored. A possible influence of the Williams Fire low-altitude plume was evident only in the nighttime $PM_{2.5}$ maxima; which were 20, 29, and 13 $\mu g\,m^{-3}$ for 16, 17, and 18 November, respectively. The modest increase in $PM_{2.5}$ the night after the Williams Fire (17 November) may have been partly attributable to the fire, but the peak was below the air quality standard. In contrast, an extreme peak in PM_{10} (118 $\mu g\,m^{-3}$) on the night of 18 November that was not accompanied by an increase in $PM_{2.5}$ was almost certainly due to non-combustion sources. A comprehensive network of ground-based samplers would have been needed to quantify the dispersion and chemistry of the low-altitude smoke and determine the contribution of the Williams Fire to pollution levels on the ground. The expected post-emission transport of smoke is already a critical factor when choosing prescribed burn locations and times in the US (Hardy et al., 2001). This case study illustrates that air quality predictions could benefit from research that elucidates both the rate of smoke production and the distribution of injection altitudes as a function of time.

4 Conclusions

In this work we describe detailed pseudo-Lagrangian measurements of the chemical evolution of an isolated biomass burning plume generated by a prescribed fire in a temperate chaparral ecosystem. Despite occurring approximately one month before the winter solstice, the plume was photochemically active and significant amounts of ozone formed within a few hours. Rapid formation of organic acids was also observed with the precursors likely being unidentified NMOC species. The measured decay in ethylene was consistent with an in-plume average OH of 5.27 ($\pm$0.97) $\times 10^6$ molec cm^{-3}. This is a factor of two or more lower OH than some observations in tropical BB plumes, but sufficiently high to affect large changes in plume chemistry within several hours. The calculated loss of NO_x due to the reaction of NO_2 with OH ($\sim$54 %) and the observed formation of PAN (22 ± 6 % of initial NO_x) accounted for all the observed NO_x loss (80 ± 10 %) within the measurement uncertainty. Roughly half of the gas-phase NH_3 was also lost within the 4 h since emission. While both particle ammonium and nitrate increased rapidly in the aging plume, the amount of the increase was significantly smaller than that required to balance the loss of the associated gas-phase precursors. We speculate that much of the "missing" ammonium and nitrate could have been present in small particles that grew slowly due to the low RH (11–26 %) and were thus too small to be detected efficiently by the AMS. In addition, a charge balance suggests that perhaps $\sim$40 % of the ammonium was pairing with organic anions that were also not measured. In contrast to the rapid initial growth in some particle inorganic species, evaporation of OA dominated condensation for the first 1.5–2 h since emission. Thereafter OA increased slowly, but overall $\Delta OA/\Delta CO_2$ decreased by a factor of 0.80 ± 0.21 over 4 h. In contrast, in an isolated tropical BB plume, rapid SOA formation was observed. We speculate that drivers for the higher SOA formation in the tropical plume include: higher OH, higher incident UV radiation, and higher RH (70–100 %) where the latter would promote more SOA formation pathways. The sum of the excess values of the species measured by the AMS normalized to excess CO_2 decreased slightly over 4 h, suggesting a net loss of particulate matter. However, Δlight scattering/ΔCO_2 increased by a factor of $\sim$2.50 over 4 h, which may have been due to mostly to rapid, initial coagulation-induced increases in particle diameter. The increase in scattering has implications for climate forcing and visibility even if it accompanied a decrease in particulate

matter. We found that as much as 85 % of the BC particles may have been thickly coated after 4 h following emission; most likely with a mix of organic and inorganic species. The coatings are likely to strongly influence the BC radiative forcing, increase the BC hygroscopicity and cloud impacts, and reduce the BC lifetime.

Supplementary material related to this article is available online at: http://www.atmos-chem-phys.net/12/1397/2012/acp-12-1397-2012-supplement.pdf.

Acknowledgements. We thank our pilot Scott Miller and the USFS Region 4 Twin Otter management and support team. We thank Jason McCarty and the Santa Barbara County Fire Department for carrying out the burn, fuels and weather information, and coordination with our airborne team. We thank Jose Jimenez, Doug Worsnop, and Chuck Kolb for useful discussions regarding this manuscript and Holly Eissinger for help in preparation of selected figures. Satellite imagery and analysis were provided by Mark Ruminski, NESDIS, Satellite Analysis Branch. Research modifications to the Twin Otter, specialized inlets, and upgrades to AFTIR were funded by NSF grant ATM-0513055. S. A., G. M., and R. Y. were supported in whole or part by NSF grant ATM-0936321. R. Y., J. C., I. B., and the Twin Otter flight hours were supported by the Strategic Environmental Research and Development Program (SERDP) projects SI-1648 and SI-1649 and administered through Forest Service Research Joint Venture Agreement 08JV11272166039, and we thank the sponsors for their support. Participation of the SP2 was made possible in part by a travel grant from the Royal Society and support from the UK Natural Environment Research Council.

Edited by: R. Cohen

References

Akagi, S. K., Yokelson, R. J., Wiedinmyer, C., Alvarado, M. J., Reid, J. S., Karl, T., Crounse, J. D., and Wennberg, P. O.: Emission factors for open and domestic biomass burning for use in atmospheric models, Atmos. Chem. Phys., 11, 4039–4072, doi:10.5194/acp-11-4039-2011, 2011.

Allan, J. D., Delia, A. E., Coe, H., Bower, K. N., Alfarra, M. R., Jimenez, J. L., Middlebrook, A. M., Drewnick, F., Onasch, T. B., Canagaratna, M. R., Jayne, J. T., and Worsnop, D. R.: A generalized method for the extraction of chemically resolved mass spectra from Aerodyne aerosol mass spectrometer data, J. Aerosol Sci., 35, 909–922, 2004.

Alvarado, M. J. and Prinn, R. G.: Formation of ozone and growth of aerosols in young smoke plumes from biomass burning: 1. Lagrangian parcel studies, J. Geophys. Res., 114, D09306, doi:10.1029/2008JD011144, 2009.

Alvarado, M. J., Logan, J. A., Mao, J., Apel, E., Riemer, D., Blake, D., Cohen, R. C., Min, K.-E., Perring, A. E., Browne, E. C., Wooldridge, P. J., Diskin, G. S., Sachse, G. W., Fuelberg, H., Sessions, W. R., Harrigan, D. L., Huey, G., Liao, J., Case-Hanks, A., Jimenez, J. L., Cubison, M. J., Vay, S. A., Weinheimer, A. J., Knapp, D. J., Montzka, D. D., Flocke, F. M., Pollack, I. B., Wennberg, P. O., Kurten, A., Crounse, J., Clair, J. M. St., Wisthaler, A., Mikoviny, T., Yantosca, R. M., Carouge, C. C., and Le Sager, P.: Nitrogen oxides and PAN in plumes from boreal fires during ARCTAS-B and their impact on ozone: an integrated analysis of aircraft and satellite observations, Atmos. Chem. Phys., 10, 9739–9760, doi:10.5194/acp-10-9739-2010, 2010.

Asman, W. A. H., Sutton, M. A., and Schjorring, J. K.: Ammonia: emission, atmospheric transport and deposition, New Phytol., 139, 27–48, 1998.

Bae, M.-S., Schwab, J. J., Zhang, Q., Hogrefe, O., Demerjian, K. L., Weimer, S., Rhoads, K., Orsini, D., Venkatachari, P., and Hopke, P. K.: Interference of organic signals in highly time resolved nitrate measurements by low mass resolution aerosol mass spectrometry, J. Geophys. Res., 112, D22305, doi:10.1029/2007JD008614, 2007.

Bertschi, I. T., Yokelson, R. J., Ward, D. E., Babbitt, R. E., Susott, R. A., Goode, J. G., and Hao, W. M.: Trace gas and particle emissions from fires in large diameter and belowground biomass fuels, J. Geophys. Res., 108, 8472, doi:10.1029/2002JD002100, 2003.

Beswick, K. M., Gallagher, M. W., Webb, A. R., Norton, E. G., and Perry, F.: Application of the Aventech AIMMS20AQ airborne probe for turbulence measurements during the Convective Storm Initiation Project, Atmos. Chem. Phys., 8, 5449–5463, doi:10.5194/acp-8-5449-2008, 2008.

Biswell, H.: Prescribed Burning in California Wildlands Vegetation Management, University of California Press, 1989.

Bond, T. C., Streets, D. G., Yarber, K. F., Nelson, S. M., Woo, J.-H., and Klimont, Z.: A technology-based global inventory of black and organic carbon emissions from combustion, J. Geophys. Res., 109, D14203, doi:10.1029/2003JD003697, 2004.

Burling, I. R., Yokelson, R. J., Griffith, D. W. T., Johnson, T. J., Veres, P., Roberts, J. M., Warneke, C., Urbanski, S. P., Reardon, J., Weise, D. R., Hao, W. M., and de Gouw, J.: Laboratory measurements of trace gas emissions from biomass burning of fuel types from the southeastern and southwestern United States, Atmos. Chem. Phys., 10, 11115–11130, doi:10.5194/acp-10-11115-2010, 2010.

Burling, I. R., Yokelson, R. J., Akagi, S. K., Urbanski, S. P., Wold, C. E., Griffith, D. W. T., Johnson, T. J., Reardon, J., and Weise, D. R.: Airborne and ground-based measurements of the trace gases and particles emitted by prescribed fires in the United States, Atmos. Chem. Phys., 11, 12197–12216, doi:10.5194/acp-11-12197-2011, 2011.

Byun, D. and Schere, K. L.: Review of the governing equations, computational algorithms, and other components of the Models-3 Community Multiscale Air Quality (CMAQ) modeling system, Appl. Mech. Rev., 59, 51–77, doi:10.1115/1.2128636, 2006.

Canagaratna, M. R., Jayne, J. T., Jimenez, J. L., Allan, J. D., Alfarra, M. R., Zhang, Q., Onasch, T. B., Drewnick, F., Coe, H., Middlebrook, A., Delia, A., Williams, L. R., Trimborn, A. M., Northway, M. J., DeCarlo, P. F., Kolb, C. E., Davidovits, P., and Worsnop, D. R.: Chemical and microphysical characterization of ambient aerosols with the Aerodyne aerosol mass spectrometer, edited by: Viggiano, A., Mass Spectrom. Rev., 26, 185–222,

2007.

Capes, G., Murphy, J. G., Reeves, C. E., McQuaid, J. B., Hamilton, J. F., Hopkins, J. R., Crosier, J., Williams, P. I., and Coe, H.: Secondary organic aerosol from biogenic VOCs over West Africa during AMMA, Atmos. Chem. Phys., 9, 3841–3850, doi:10.5194/acp-9-3841-2009, 2009.

Carter, M. C. and Foster, C. D.: Prescribed burning and productivity in southern pine forests: a review, Forest Ecol. Manag., 191, 185–197, doi:10.1016/j.foreco.2003.11.006, 2004.

Chakrabarty, R. K., Moosmuller, H., Garro, M. A., Arnott, W. P., Walker, J., Susott, R. A., Babbitt, R. E., Wold, C. E., Lincoln, E. N., and Hao, W. M.: Emissions from the laboratory combustion of wildland fuels: Particle morphology and size, J. Geophys. Res., 111, D07204, doi:10.1029/2005JD006659, 2006.

Cofer III., W. R., Levine, J. S., Riggan, P. J., Sebacher, D. I., Winstead, E. L., Shaw Jr., E. F., Brass, J. A., and Ambrosia, V. G.: Trace gas emissions from a mid-latitude prescribe chaparral fire, J. Geophys. Res., 93, 1653–1658, 1988.

Crutzen, P. J. and Andreae, M. O.: Biomass burning in the tropics: Impact on atmospheric chemistry and biogeochemical cycles, Science, 250, 1669–1678, 1990.

Cubison, M. J., Ortega, A. M., Hayes, P. L., Farmer, D. K., Day, D., Lechner, M. J., Brune, W. H., Apel, E., Diskin, G. S., Fisher, J. A., Fuelberg, H. E., Hecobian, A., Knapp, D. J., Mikoviny, T., Riemer, D., Sachse, G. W., Sessions, W., Weber, R. J., Weinheimer, A. J., Wisthaler, A., and Jimenez, J. L.: Effects of aging on organic aerosol from open biomass burning smoke in aircraft and laboratory studies, Atmos. Chem. Phys., 11, 12049–12064, doi:10.5194/acp-11-12049-2011, 2011.

De Gouw, J. and Jimenez, J. L.: Organic aerosols in the Earth's atmosphere, Environ. Sci. Technol., 43, 7614–7618, 2009.

Dentener, F. J. and Crutzen, P. J.: A three-dimensional model of the global ammonia cycle, J. Atmos. Chem., 19, 331–369, 1994.

Draxler, R. R. and Rolph, G. D.: HYSPLIT (HYbrid Single-Particle Lagrangian Integrated Trajectory) Model access via NOAA ARL READY Website: http://ready.arl.noaa.gov/HYSPLIT.php, last access: 4 August 2011, NOAA Air Resources Laboratory, Silver Spring, MD, 2010.

Drewnick, F., Schwab, J. J., Hogrefe, O., Peters, S., Husain, L., Diamond, D., Weber, R., and Demerjian, K. L.: Intercomparison and evaluation of four semi-continuous $PM_{2.5}$ sulfate instruments, Atmos. Environ., 37, 3335–3350, 2003.

Drewnick, F., Hings, S. S., DeCarlo, P., Jayne, J. T., Gonin, M., Fuhrer, K., Weimer, S., Jimenez, J. L., Demerjian, K. L., Borrmann, S., and Worsnop, D. R.: A new Time-of-Flight Aerosol Mass Spectrometer (TOF-AMS) – instrument description and first field deployment, Aerosol Sci. Tech., 39, 637–658, 2005.

Ebeling, J. M. and Jenkins, B. M.: Physical and chemical properties of biomass fuels, T. ASAE, 28, 898–902, 1985.

Fearnside, P. M., Leal Jr., N., and Fernandes, F. M.: Rainforest burning and the global carbon budget: biomass, combustion efficiency, and charcoal formation in the Brazilian Amazon, J. Geophys. Res., 98, 16733–16743, 1993.

Ferek, R. J., Reid, J. S., Hobbs, P. V., Blake, D. R., and Liousse, C.: Emission factors of hydrocarbons, halocarbons, trace gases, and particles from biomass burning in Brazil, J. Geophys. Res., 103, 32107–32118, doi:10.1029/98JD00692, 1998.

Finlayson-Pitts, B. J. and Pitts Jr., J. N.: Chemistry of the Upper and Lower Atmosphere, Academic Press, San Diego, USA, 969 pp., 2000.

Fishman, J., Wozniak, A. E., and Creilson, J. K.: Global distribution of tropospheric ozone from satellite measurements using the empirically corrected tropospheric ozone residual technique: Identification of the regional aspects of air pollution, Atmos. Chem. Phys., 3, 893–907, doi:10.5194/acp-3-893-2003, 2003.

Goode, J. G., Yokelson, R. J., Susott, R. A., and Ward, D. E.: Trace gas emissions from laboratory biomass fires measured by open-path Fourier transform infrared spectroscopy: Fires in grass and surface fuels, J. Geophys. Res., 104, 21237–21245, 1999.

Grieshop, A. P., Logue, J. M., Donahue, N. M., and Robinson, A. L.: Laboratory investigation of photochemical oxidation of organic aerosol from wood fires 1: measurement and simulation of organic aerosol evolution, Atmos. Chem. Phys., 9, 1263–1277, doi:10.5194/acp-9-1263-2009, 2009

Griffith, D. W. T.: Synthetic calibration and quantitative analysis of gas-phase FTIR spectra, Appl. Spectrosc., 50, 59–70, 1996.

Haines, T. K. and Cleaves, D. A.: The legal environment for forestry prescribed burning in the south: Regulatory programs and voluntary guidelines, South J. Appl. For., 23, 170–74, 1999.

Hardy, C. C. and Teesdale, D. R.: Source characterization and control of smoke emissions from prescribed burning of California chaparral, CDF Contract No. 89CA96071, California Department of Forestry and Fire Protection, Sacramento, CA, 1991.

Hardy, C. C., Conard, S. G., Regelbrugge, J. C., and Teesdale, D. R.: Smoke emissions from prescribed burning of southern California chaparral, Res. Pap. PNW-RP-486, US Department of Agriculture, Forest Service, Pacific Northwest Research Station, Portland, OR, 1996.

Hardy, C. C., Ottmar, R. D., Peterson, J. L., Core, J. E., and Seamon, P.: Smoke management guide for prescribed and wildland fire: 2001 edition, available at: http://www.treesearch.fs.fed.us/pubs/5388, last access: 4 August 2011, National Wildfire Coordination Group, Boise, ID, 2001.

Heald, C. L., Jacob, D. J., Park, R. J., Russell, L. M., Huebert, B. J., Seinfeld, J. H., Liao, H., and Weber, R. J.: A large organic aerosol source in the free troposphere missing from current models, Geophys. Res. Lett., 32, L18809, doi:10.1029/2005GL023831, 2005.

Hennigan, C. J., Bergin, M. H., Dibb, J. E., and Weber, R. J.: Enhanced secondary organic aerosol formation due to water uptake by fine particles, Geophys. Res. Lett., 35, L18801, doi:10.1029/2008GL035046, 2008.

Hennigan, C. J., Miracolo, M. A., Engelhart, G. J., May, A. A., Presto, A. A., Lee, T., Sullivan, A. P., McMeeking, G. R., Coe, H., Wold, C. E., Hao, W.-M., Gilman, J. B., Kuster, W. C., de Gouw, J., Schichtel, B. A., J. L. Collett Jr., Kreidenweis, S. M., and Robinson, A. L.: Chemical and physical transformations of organic aerosol from the photo-oxidation of open biomass burning emissions in an environmental chamber, Atmos. Chem. Phys., 11, 7669–7686, doi:10.5194/acp-11-7669-2011, 2011.

Heringa, M. F., DeCarlo, P. F., Chirico, R., Tritscher, T., Dommen, J., Weingartner, E., Richter, R., Wehrle, G., Prévôt, A. S. H., and Baltensperger, U.: Investigations of primary and secondary particulate matter of different wood combustion appliances with a high-resolution time-of-flight aerosol mass spectrometer, Atmos. Chem. Phys., 11, 5945–5957, doi:10.5194/acp-11-5945-2011, 2011.

Hobbs, P. V., Reid, J. S., Herring, J. A., Nance, J. D. Weiss, R. E., Ross, J. L., Hegg, D. A., Ottmar, R. D., and Liousse, C.: Particle and trace-gas measurements in the smoke from prescribed burns of forest products in the Pacific northwest, in: Biomass Burning and Global Change, vol. 2, edited by: Levine, J. S., MIT Press, Cambridge, Mass., 697–715, 1996.

Hobbs, P. V., Sinha, P., Yokelson, R. J., Christian, T. J., Blake, D. R., Gao, S., Kirchstetter, T. W., Novakov, T., and Pilewskie, P.: Evolution of gases and particles from a savanna fire in South Africa, J. Geophys. Res., 108, 8485, doi:10.1029/2002JD002352, 2003.

Hosseini, S., Li, Q., Cocker, D., Weise, D., Miller, A., Shrivastava, M., Miller, J. W., Mahalingam, S., Princevac, M., and Jung, H.: Particle size distributions from laboratory-scale biomass fires using fast response instruments, Atmos. Chem. Phys., 10, 8065–8076, doi:10.5194/acp-10-8065-2010, 2010.

Huffman, J. A., Jayne, J. T., Drewnick, F., Aiken, A. C., Onasch, T., Worsnop, D. R., and Jimenez, J. L.: Design, modeling, optimization, and experimental tests of a particle beam width probe for the aerodyne aerosol mass spectrometer, Aerosol Sci. Technol., 39, 1143–1163, 2005.

Huffman, J. A., Docherty, K. S., Aiken, A. C., Cubison, M. J., Ulbrich, I. M., DeCarlo, P. F., Sueper, D., Jayne, J. T., Worsnop, D. R., Ziemann, P. J., and Jimenez, J. L.: Chemically-resolved aerosol volatility measurements from two megacity field studies, Atmos. Chem. Phys., 9, 7161–7182, doi:10.5194/acp-9-7161-2009, 2009.

Johnson, T. J., Masiello, T., and Sharpe, S. W.: The quantitative infrared and NIR spectrum of CH_2I_2 vapor: vibrational assignments and potential for atmospheric monitoring, Atmos. Chem. Phys., 6, 2581–2591, doi:10.5194/acp-6-2581-2006, 2006.

Johnson, T. J., Profeta, L. T. M., Sams, R. L., Griffith, D. W. T., and Yokelson, R. J.: An infrared spectral database for detection of gases emitted by biomass burning, Vib. Spectrosc., 53, 97–102, 2010.

Karl, T. G., Christian, T. J., Yokelson, R. J., Artaxo, P., Hao, W. M., and Guenther, A.: The Tropical Forest and Fire Emissions Experiment: method evaluation of volatile organic compound emissions measured by PTR-MS, FTIR, and GC from tropical biomass burning, Atmos. Chem. Phys., 7, 5883–5897, doi:10.5194/acp-7-5883-2007, 2007.

Kauffman, J. B.: Death rides the forest: perceptions of fire, land use, and ecological restoration of western forests, Conserv. Biol., 18, 878–882, 2004.

Koch, D., Balkanski, Y., Bauer, S. E., Easter, R. C., Ferrachat, S., Ghan, S. J., Hoose, C., Iversen, T., Kirkevåg, A., Kristjansson, J. E., Liu, X., Lohmann, U., Menon, S., Quaas, J., Schulz, M., Seland, Ø., Takemura, T., and Yan, N.: Soot microphysical effects on liquid clouds, a multi-model investigation, Atmos. Chem. Phys., 11, 1051–1064, doi:10.5194/acp-11-1051-2011, 2011.

Kondo, Y., Matsui, H., Moteki, N., Sahu, L., Takegawa, N., Kajino, M., Zhao, Y., Cubison, M. J., Jimenez, J. L., Vay, S., Diskin, G. S., Anderson, B., Wisthaler, A., Mikoviny, T., Fuelberg, H. E., Blake, D. R., Huey, G., Weinheimer, A. J., Knapp, D. J., and Brune, W. H.: Emissions of black carbon, organic, and inorganic aerosols from biomass burning in North America and Asia in 2008, J. Geophys. Res., 116, D08204, doi:10.1029/2010JD015152, 2011.

Lack, D. A. and Cappa, C. D.: Impact of brown and clear carbon on light absorption enhancement, single scatter albedo and absorption wavelength dependence of black carbon, Atmos. Chem. Phys., 10, 4207–4220, doi:10.5194/acp-10-4207-2010, 2010.

Lee, S., Baumann, K., Schauer, J. J., Sheesley, R. J., Naeher, L. P., Meinardi, S., Blake, D. R., Edgerton, E. S., Russell, A. G., and Clements, M.: Gaseous and particulate emissions from prescribed burning in Georgia, Environ. Sci. Technol., 39, 9049–9056, 2005.

Li, J., Posfai, M., Hobbs, P. V., and Buseck, P. R.: Individual aerosol particles from biomass burning in southern Africa: 2. Compositions and aging of inorganic particles, J. Geophys. Res., 108, 8484, doi:10.1029/2002JD002310, 2003.

Lim, Y. B., Tan, Y., Perri, M. J., Seitzinger, S. P., and Turpin, B. J.: Aqueous chemistry and its role in secondary organic aerosol (SOA) formation, Atmos. Chem. Phys., 10, 10521–10539, doi:10.5194/acp-10-10521-2010, 2010.

Mason, S. A., Field, R. J., Yokelson, R. J., Kochivar, M. A., and Tinsley, M. R.: Complex effects arising in smoke plume simulations due to inclusion of direct emissions of oxygenated organic species from biomass combustion, J. Geophys. Res., 106, 12527–12539, 2001.

McMeeking, G. R., Kreidenweis, S. M., Lunden, M., Carrillo, J., Carrico, C. M., Lee, T., Herckes, P., Engling, G., Day, D. E., Hand, J., Brown, N., Malm, W. C., and Collett Jr., J. L.: Smoke-impacted regional haze in California during the summer of 2002, Agr. Forest Meteorol., 137, 25–42, 2006.

McMeeking, G. R., Kreidenweis, S. M., Baker, S., Carrico, C. M., Chow, J. C., Collet Jr., J. L., Hao, W. M., Holden, A. S., Kirchstetter, T. W., Malm, W. C., Moosmüller, H., Sullivan, A. P., and Wold, C. E.: Emissions of trace gases and aerosols during the open combustion of biomass in the laboratory, J. Geophys. Res., 114, D19210, doi:10.1029/2009JD011836, 2009.

McMeeking, G. R., Good, N., Petters, M. D., McFiggans, G., and Coe, H.: Influences on the fraction of hydrophobic and hydrophilic black carbon in the atmosphere, Atmos. Chem. Phys., 11, 5099–5112, doi:10.5194/acp-11-5099-2011, 2011a.

McMeeking, G. R., Morgan, W. T., Flynn, M., Highwood, E. J., Turnbull, K., Haywood, J., and Coe, H.: Black carbon aerosol mixing state, organic aerosols and aerosol optical properties over the United Kingdom, Atmos. Chem. Phys., 11, 9037–9052, doi:10.5194/acp-11-9037-2011, 2011b.

Moteki, N. and Kondo, Y.: Effects of mixing state of black carbon measurements by laser-induced incandescence, Aerosol Sci. Tech., 41, 398–417, 2007.

Mühle, J., Lueker, T. J., Su, Y., Miller, B. R., Prather, K. A., and Weiss, R. F.: Trace gas and particulate emissions from the 2003 southern California wildfires, J. Geophys. Res., 112, D03307, doi:10.1029/2006JD007350, 2007.

Park, R. J., Jacob, D. J., and Logan, J. A.: Fire and biofuel contributions to annual mean aerosol concentrations in the United States, Atmos. Environ., 41, 7389–7400, 2007.

Perri, M. J., Seitzinger, S., and Turpin, B. J.: Secondary organic aerosol production from aqueous photooxidation of glycolaldehyde: Laboratory experiments, Atmos. Environ., 43, 1487–1497, 2009.

Petters, M. D., Carrico, C. M., Kreidenweis, S. M., Prenni, A. J., DeMott, P. J., Collett, J. L., and Moosmüller, H.: Cloud condensation nucleation activity of biomass burning aerosol, J. Geophys. Res., 114, D22205, doi:10.1029/2009jd012353, 2009.

Pfister, G. G., Emmons, L. K., Hess, P. G., Honrath, R., Lamarque,

J.-F., Val Martin, M., Owen, R. C., Avery, M. A., Browell, E. V., Holloway, J. S., Nedelec, P., Purvis, R., Ryerson, T. B., Sachse, G. W., and Schlager, H.: Ozone production from the 2004 North American boreal fires, J. Geophys. Res., 111, D24S07, doi:10.1029/2006JD007695, 2006.

Phuleria, H. C., Sheesley, R. J., Schauer, J. J., Fine, P. M., and Sioutas, C.: Roadside measurements of size-segregated particulate organic compounds near gasoline and diesel-dominated freeways in Los Angeles, CA, Atmos. Environ., 41, 4653–4671, 2007.

Posfai, M., Simonics, R., Li, J., Hobbs, P. V., and Buseck, P. R.: Individual aerosol particles from biomass burning in southern Africa: 1. Compositions and size distributions of carbonaceous particles, J. Geophys. Res., 108, 8483, doi:10.1029/2002JD002291, 2003.

Radke, L. F., Lyons, J. H., Hobbs, P. V., Hegg, D. A., Sandberg, D. V., and Ward, D. E.: Airborne monitoring and smoke characterization of prescribed fires on forest lands in western Washington and Oregon, Gen. Tech. Rep. PNW-GTR-251, Portland, OR, US, Dept. of Agriculture, Forest Service, Pacific Northwest Research Station, 1990.

Radke, L. F., Hegg, D. A., Hobbs, P. V., Nance, J. D., Lyons, J. H., Laursen, K. K., Weiss, R. E., Riggan, P. J., and Ward, D. E.: Particulate and trace gas emissions from large biomass fires in North America, Global biomass burning – Atmospheric, climatic, and biospheric implications, MIT Press, Cambridge, MA, 209–224, 1991.

Radlein, D., Piskorz, J., and Scott, D. S.: Fast pyrolysis of natural polysaccharides as a potential industrial process, J. Anal. Appl. Pyrolysis, 19, 41–63, 1991.

Ramanathan, V. and Carmichael, G.: Global and regional climate changes due to black carbon, Nat. Geosci., 1, 221–227, doi:10.1038/ngeo156, 2008.

Reid, J. S., Hobbs, P. V., Ferek, R. J. , Martins, J. V., Blake, D. R., Dunlap, M. R., and Liousse, C.: Physical, chemical, and radiative characteristics of the smoke dominated regional hazes over Brazil, J. Geophys. Res., 103, 32059–32080, 1998.

Reid, J. S., Eck, T. F., Christopher, S. A., Koppmann, R., Dubovik, O., Eleuterio, D. P., Holben, B. N., Reid, E. A., and Zhang, J.: A review of biomass burning emissions part III: intensive optical properties of biomass burning particles, Atmos. Chem. Phys., 5, 827–849, doi:10.5194/acp-5-827-2005, 2005a.

Reid, J. S., Koppmann, R., Eck, T. F., and Eleuterio, D. P.: A review of biomass burning emissions part II: intensive physical properties of biomass burning particles, Atmos. Chem. Phys., 5, 799–825, doi:10.5194/acp-5-799-2005, 2005b.

Richards, G. N.: Glycolaldehyde from pyrolysis of cellulose, J. Anal. Appl. Pyrolysis, 10, 251–255, 1987.

Robinson, A. L., Donahue, N. M., Shrivastava, M. K., Weitkamp, E. A., Sage, A. M., Grieshop, A. P., Lane, T. E., Pierce, J. R., and Pandis, S. N.: Rethinking organic aerosols: Semivolatile emissions and photochemical aging, Science, 315, 1259–1262, 2007.

Rolph, G. D.: Real-time Environmental Applications and Display sYstem (READY) Website (http://ready.arl.noaa.gov, last access: 27 January 2012), NOAA Air Resources Laboratory, Silver Spring, MD, 2010.

Rothman, L. S., Gordon, I. E., Barbe, A., Benner, D. C., Bernath, P. F., Birk, M., Boudon, V., Brown, L. R., Campargue, A., Champion, J. P., Chance, K., Coudert, L. H., Dana, V., Devi, V. M., Fally, S., Flaud, J. M., Gamache, R. R., Goldman, A., Jacquemart, D., Kleiner, I., Lacome, N., Lafferty, W. J., Mandin, J. Y., Massie, S. T., Mikhailenko, S. N., Miller, C. E., Moazzen-Ahmadi, N., Naumenko, O. V., Nikitin, A. V., Orphal, J., Perevalov, V. I., Perrin, A., Predoi-Cross, A., Rinsland, C. P., Rotger, M., Simecková, M., Smith, M. A. H., Sung, K., Tashkun, S. A., Tennyson, J., Toth, R. A., Vandaele, A. C., and Vander Auwera, J.: The HITRAN 2008 molecular spectroscopic database, J. Quant. Spectrosc. Ra., 110, 533–572, 2009.

Sandberg, D. V., Ottmar, R. D., Peterson, J. L., and Core, J.: Wildland fire on ecosystems: effects of fire on air, Gen. Tech. Rep. RMRS-GTR-42-vol. 5, Ogden, UT, US, Department of Agriculture, Forest Service, Rocky Mountain Research Station, 2002.

Sander, S. P., Finlayson-Pitts, B. J., Friedl, R. R., Golden, D. M., Huie, R. E., Keller-Rudek, H., Kolb, C. E., Kurylo, M. J., Molina, M. J., Moortgat, G. K., Orkin, V. L., Ravishankara, A. R., and Wine, P. W.: Chemical kinetics and photochemical data for use in atmospheric studies, Evaluation Number 15 (JPL Publication 06-2), Jet Propulsion Laboratory, Pasadena, CA, 2006.

Schwarz, J. P., Gao, R. S., Fahey, D. W., Thomson, D. S., Watts, L. A., Wilson, J. C., Reeves, J. M., Darbeheshti, M., Baumgardner, D. G., Kok, G. L., Chung, S. H., Schulz, M., Hendricks, J., Lauer, A., Karcher, B., Slowik, J. G., Rosenlof, K. H., Thompson, T. L., Langford, A. O., Loewenstein, M., and Aikin, K. C.: Single-particle measurements of midlatitude black carbon and light-scattering aerosols from the boundary layer to the lower stratosphere, J. Geophys. Res., 111, D16207, doi:10.1029/2006JD007076, 2006.

Schwarz, J. P., Gao, R. S., Spackman, J. R., Watts, L. A., Thomson, D. S., Fahey, D. W., Ryerson, T. B., Peischl, J., Holloway, J. S., Trainer, M., Frost, G. J., Baynard, T., Lack, D. A., de Gouw, J. A., Warneke, C., and Del Negro, L. A.: Measurement of the mixing state, mass, and optical size of individual black carbon particles in urban and biomass burning emissions, Geophys. Res. Lett., 35, L13810, doi:10.1029/2008GL033968, 2008.

Seinfeld, J. H. and Pandis, S. N.: Atmospheric chemistry and physics: From air pollution to climate change, John Wiley & Sons, Inc., US, 2006.

Semuniuk, T. A., Wise, M. E., Martin, S. T., Russell, L. M., and Buseck, P. R.: Hygroscopic behavior of aerosol particles from biomass fires using environmental transmission electron microscopy, J. Atmos. Chem., 56, 259–273, 2007.

Sharpe, S. W., Johnson, T. J., Sams, R. L., Chu, P. M., Rhoderick, G. C., and Johnson, P. A.: Gas-phase databases for quantitative infrared spectroscopy, Appl. Spectrosc., 58, 1452–1461, 2004.

Shiraiwa, M., Kondo, Y., Moteki, N., Takegawa, N., Miyazaki, Y., and Blake, D. R.: Evolution of mixing state of black carbon in polluted air from Tokyo, Geophys. Res. Lett., 34, L16803, doi:10.1029/2007gl029819, 2007.

Stephens, M., Turner, N., and Sandberg, J.: Particle identification by laser-induced incandescence in a solid-state laser cavity, Appl. Opt., 42, 3726–3736, 2003.

Stephens, S. L., Martin, R. E., and Clinton, N. E.: Prehistoric fire area and emissions from California's forests, woodlands, shrublands, and grasslands, Forest Ecol. Manag., 251, 205–216, 2007.

Sudo, K. and Akimoto, H.: Global source attribution of tropospheric ozone: Long-range transport from various source regions, J. Geophys. Res., 112, D12302, doi:10.1029/2006JD007992, 2007.

Susott, R. A., Olbu, G. J., Baker, S. P., Ward, D. E., Kauffman, J. B., and Shea, R. W.: Carbon, hydrogen, nitrogen, and thermogravimetric analysis of tropical ecosystem biomass, in: Biomass Burning and Global Change, edited by: Levine, J. S., MIT Press, Cambridge, 350–360, 1996.

Tabazadeh, A., Jacobson, M. Z., Singh, H. B., Toon, O. B., Lin, J. S., Chatfield, R. B., Thakur, A. N., Talbot, R. W., and Dibb, J. E.: Nitric acid scavenging by mineral and biomass burning aerosols, Geophys. Res. Lett., 25, 4185–4188, 1998.

Tabazadeh, A., Yokelson, R. J., Singh, H. B., Hobbs, P. V., Crawford, J. H., and Iraci, L. T.: Heterogeneous chemistry involving methanol in tropospheric clouds, Geophys. Res. Lett., 31, L06114, doi:10.1029/2003GL018775, 2004.

Tang, I. N. and Munkelwitz, H. R.: Composition and temperature dependence of the deliquescence properties of hygroscopic aerosols, Atmos. Environ., 27A, 467–473, 1993.

Tang, I. N. and Munkelwitz, H. R.: Water activities, densities, and refractive indices of aqueous sulfates and sodium nitrate droplets of atmospheric importance, J. Geophys. Res., 99, 18801–18808, 1994a.

Tang, I. N. and Munkelwitz, H. R.: Aerosol phase transformation and growth in the atmosphere, J. Appl. Meteorol., 33, 792–796, 1994b.

Trent, A., Davies, M. A., Fisher, R., Thistle, H., and Babbitt, R.: Evaluation of optical instruments for real-time, continuous monitoring of smoke particulates, Tech. Rep. 0025 2860 MTDC, USDA Forest Service, Missoula Technology and Development Center, Missoula, MT, USA, 38 pp., 2000.

Trentmann, J., Andreae, M. O., and Graf, H.-F.: Chemical processes in a young biomass-burning plume, J. Geophys. Res., 108, 4705, doi:10.1029/2003JD003732, 2003.

Trentmann, J., Yokelson, R. J., Hobbs, P. V., Winterrath, T., Christian, T. J., Andreae, M. O., and Mason, S. A.: An analysis of the chemical processes in the smoke plume from a savanna fire, J. Geophys. Res., 110, D12301, doi:10.1029/2004JD005628, 2005.

Val Martin, M., Honrath, R. E., Owen, R. C., Pfister, G., Fialho, P., and Barata, F.: Significant enhancements of nitrogen oxides, black carbon, and ozone in the North Atlantic lower free troposphere resulting from North American boreal wildfires, J. Geophys. Res., 111, D23S60, doi:10.1029/2006JD007530, 2006.

van der Werf, G. R., Randerson, J. T., Giglio, L., Collatz, G. J., Mu, M., Kasibhatla, P. S., Morton, D. C., DeFries, R. S., Jin, Y., and van Leeuwen, T. T.: Global fire emissions and the contribution of deforestation, savanna, forest, agricultural, and peat fires (1997–2009), Atmos. Chem. Phys., 10, 11707–11735, doi:10.5194/acp-10-11707-2010, 2010.

Veres, P., Roberts, J. M., Burling, I. R., Warneke, C., de Gouw, J., and Yokelson, R. J.: Measurements of gas-phase inorganic and organic acids from biomass fires by negative-ion proton-transfer chemical-ionization mass spectrometry, J. Geophys. Res., 115, D23302, doi:10.1029/2010JD014033, 2010.

Ward, D. E., Peterson, J., and Hao, W. M.: An inventory of particulate matter and air toxic emissions from prescribed fires in the USA for 1989, Air and Waste Management Assoc. Annual Meeting, Denver, CO, 14–18 June 1993, 93-MP-6.04, 1993.

Warneke, C., Bahreini, R., Brioude, J., Brock, C. A., de Gouw, J. A., Fahey, D. W., Froyd, K. D., Holloway, J. S., Middlebrook, A., Miller, L., Montzka, S., Murphy, D. M., Peischl, J., Ryerson, T. B., Schwarz, J. P., Spackman, J. R., and Veres, P.: Biomass burning in Siberia and Kazakhstan as an important source for haze over the Alaskan Arctic in April 2008, Geophys. Res. Lett., 36, L02813, doi:10.1029/2008GL036194, 2009.

Warneke, C., Roberts, J. M., Veres, P., Gilman, J., Kuster, W. C., Burling, I., Yokelson, R. J., and de Gouw, J. A.: VOC identification and inter-comparison from laboratory biomass burning using PTR-MS and PIT-MS, Int. J. Mass Spectrom. Ion Proc., 303, 6–14, doi:10.1016/j.ijms.2010.12.002, 2011.

Watson, J. G.: Visibility: Science and regulation, J. Air Waste Manage., 52, 628–713, 2002.

Wiedinmyer, C. and Hurteau, M. D.: Prescribed fire as a means of reducing forest carbon emissions in the Western United States, Environ. Sci. Technol., 44, 1926–1932, 2010.

Yoder, J., Tilley, M., Engle, D., and Fuhlendorf, D.: Economics and prescribed fire law in the United States, Applied Economic Perspectives and Policy, 25, 218–233, doi:10.1111/1467-9353.00055, 2003.

Yokelson, R. J., Griffith, D. W. T., and Ward, D. E.: Open path Fourier transform infrared studies of large-scale laboratory biomass fires, J. Geophys. Res., 101, 21067–21080, doi:10.1029/96JD01800, 1996.

Yokelson, R. J., Ward, D. E., Susott, R. A., Reardon, J., and Griffith, D. W. T.: Emissions from smoldering combustion of biomass measured by open-path Fourier transform infrared spectroscopy, J. Geophys. Res., 102, 18865–18877, 1997.

Yokelson, R. J., Goode, J. G., Ward, D. E., Susott, R. A., Babbitt, R. E., Wade, D. D., Bertschi, I., Griffith, D. W. T., and Hao, W. M.: Emissions of formaldehyde, acetic acid, methanol, and other trace gases from biomass fires in North Carolina measured by airborne Fourier transform infrared spectroscopy, J. Geophys. Res., 104, 30109–30126, doi:10.1029/1999JD900817, 1999.

Yokelson, R. J., Bertschi, I. T., Christian, T. J., Hobbs, P. V., Ward, D. E., and Hao, W. M.: Trace gas measurements in nascent, aged, and cloud-processed smoke from African savanna fires by airborne Fourier transform infrared spectroscopy (AFTIR), J. Geophys. Res., 108, 8478, doi:10.1029/2002JD002322, 2003a.

Yokelson, R. J., Christian, T. J., Bertschi, I. T., and Hao, W. M.: Evaluation of adsorption effects on measurements of ammonia, acetic acid, and methanol, J. Geophys. Res., 108, 4649, doi:10.1029/2003JD003549, 2003b.

Yokelson, R. J., Karl, T., Artaxo, P., Blake, D. R., Christian, T. J., Griffith, D. W. T., Guenther, A., and Hao, W. M.: The Tropical Forest and Fire Emissions Experiment: overview and airborne fire emission factor measurements, Atmos. Chem. Phys., 7, 5175–5196, doi:10.5194/acp-7-5175-2007, 2007a.

Yokelson, R. J., Urbanski, S. P., Atlas, E. L., Toohey, D. W., Alvarado, E. C., Crounse, J. D., Wennberg, P. O., Fisher, M. E., Wold, C. E., Campos, T. L., Adachi, K., Buseck, P. R., and Hao, W. M.: Emissions from forest fires near Mexico City, Atmos. Chem. Phys., 7, 5569–5584, doi:10.5194/acp-7-5569-2007, 2007b.

Yokelson, R. J., Crounse, J. D., DeCarlo, P. F., Karl, T., Urbanski, S., Atlas, E., Campos, T., Shinozuka, Y., Kapustin, V., Clarke, A. D., Weinheimer, A., Knapp, D. J., Montzka, D. D., Holloway, J., Weibring, P., Flocke, F., Zheng, W., Toohey, D., Wennberg, P. O., Wiedinmyer, C., Mauldin, L., Fried, A., Richter, D., Walega, J., Jimenez, J. L., Adachi, K., Buseck, P. R., Hall, S. R., and Shetter, R.: Emissions from biomass burning in the Yucatan, Atmos. Chem. Phys., 9, 5785–5812, doi:10.5194/acp-9-5785-2009,

2009.

Zhang, R. Y., Khalizov, A. F., Pagels, J., Zhang, D., Xue, H., and McMurry, P. H.: Variability in morphology, hygroscopicity, and optical properties of soot aerosols during atmospheric processing, P. Natl. Acad. Sci. USA, 105, 10291–10296, 2008.

Zhang, X., Hecobian, A., Zheng, M., Frank, N. H., and Weber, R. J.: Biomass burning impact on $PM_{2.5}$ over the southeastern US during 2007: integrating chemically speciated FRM filter measurements, MODIS fire counts and PMF analysis, Atmos. Chem. Phys., 10, 6839–6853, doi:10.5194/acp-10-6839-2010, 2010.

Chapter 5

The Pasadena Aerosol Characterization Observatory (PACO): Chemical and Physical Analysis of the Western Los Angeles Basin Aerosol[1]

[1]This chapter is reproduced by permission from "The Pasadena Aerosol Characterization Observatory (PACO): Chemical and Physical Analysis of the Western Los Angeles Basin Aerosol" by S. P. Hersey, J. S. Craven, K. A. Schilling, A. R. Metcalf, A. Sorooshian, M. N. Chan, R. C. Flagan, and J. H. Seinfeld, *Atmospheric Chemistry and Physics*, 11, 7417–7443, www.atmos-chem-phys.net/11/7417/2011/, doi:10.5194/acp-11-7417-2011, 2011.

Atmos. Chem. Phys., 11, 7417–7443, 2011
www.atmos-chem-phys.net/11/7417/2011/
doi:10.5194/acp-11-7417-2011

Atmospheric Chemistry and Physics

The Pasadena Aerosol Characterization Observatory (PACO): chemical and physical analysis of the Western Los Angeles basin aerosol

S. P. Hersey[1], **J. S. Craven**[2], **K. A. Schilling**[2], **A. R. Metcalf**[1], **A. Sorooshian**[3], **M. N. Chan**[1], **R. C. Flagan**[1,2], **and J. H. Seinfeld**[1,2]

[1]Division of Engineering and Applied Science, California Institute of Technology, Pasadena, CA, USA
[2]Division of Chemistry and Chemical Engineering, California Institute of Technology, Pasadena, CA, USA
[3]Department of Chemical and Environmental Engineering, University of Arizona, Tucson, AZ, USA

Received: 3 February 2011 – Published in Atmos. Chem. Phys. Discuss.: 18 February 2011
Revised: 16 June 2011 – Accepted: 25 June 2011 – Published: 1 August 2011

Abstract. The Pasadena Aerosol Characterization Observatory (PACO) represents the first major aerosol characterization experiment centered in the Western/Central Los Angeles Basin. The sampling site, located on the campus of the California Institute of Technology in Pasadena, was positioned to sample a continuous afternoon influx of transported urban aerosol with a photochemical age of 1–2 h and generally free from major local contributions. Sampling spanned 5 months during the summer of 2009, which were broken into 3 regimes on the basis of distinct meteorological conditions. Regime I was characterized by a series of low pressure systems, resulting in high humidity and rainy periods with clean conditions. Regime II typified early summer meteorology, with significant morning marine layers and warm, sunny afternoons. Regime III was characterized by hot, dry conditions with little marine layer influence. Regardless of regime, organic aerosol (OA) is the most significant constituent of nonrefractory submicron Los Angeles aerosol (42, 43, and 55 % of total submicron mass in regimes I, II, and III, respectively). The overall oxidation state remains relatively constant on timescales of days to weeks (O:C = 0.44 ± 0.08, 0.55 ± 0.05, and 0.48 ± 0.08 during regimes I, II, and III, respectively), with no difference in O:C between morning and afternoon periods. Periods characterized by significant morning marine layer influence followed by photochemically favorable afternoons displayed significantly higher aerosol mass and O:C ratio, suggesting that aqueous processes may be important in the generation of secondary aerosol and oxidized organic aerosol (OOA) in Los Angeles. Online analysis of water soluble organic carbon (WSOC) indicates that water soluble organic mass (WSOM) reaches maxima near 14:00–15:00 local time (LT), but the percentage of AMS organic mass contributed by WSOM remains relatively constant throughout the day. Sulfate and nitrate reside predominantly in accumulation mode aerosol, while afternoon SOA production coincides with the appearance of a distinct fine mode dominated by organics. Particulate NH_4NO_3 and $(NH_4)_2SO_4$ appear to be NH_3-limited in regimes I and II, but a significant excess of particulate NH_4^+ in the hot, dry regime III suggests less SO_4^{2-} and the presence of either organic amines or NH_4^+-associated organic acids. C-ToF-AMS data were analyzed by Positive Matrix Factorization (PMF), which resolved three factors, corresponding to a hydrocarbon-like OA (HOA), semivolatile OOA (SV-OOA), and low-volatility OOA (LV-OOA). HOA appears to be a periodic plume source, while SV-OOA exhibits a strong diurnal pattern correlating with ozone. Peaks in SV-OOA concentration correspond to peaks in DMA number concentration and the appearance of a fine organic mode. LV-OOA appears to be an aged accumulation mode constituent that may be associated with aqueous-phase processing, correlating strongly with sulfate and representing the dominant background organic component. Periods characterized by high SV-OOA and LV-OOA were analyzed by filter analysis, revealing a complex mixture of species during periods dominated by SV-OOA and LV-OOA, with LV-OOA periods characterized by shorter-chain dicarboxylic acids (higher O:C ratio), as well as appreciable amounts of nitrate- and

Correspondence to: J. H. Seinfeld
(seinfeld@caltech.edu)

sulfate-substituted organics. Phthalic acid was ubiquitous in filter samples, suggesting that PAH photochemistry may be an important SOA pathway in Los Angeles. Aerosol composition was related to water uptake characteristics, and it is concluded that hygroscopicity is largely controlled by organic mass fraction (OMF). The hygroscopicity parameter κ averaged 0.31 ± 0.08, approaching 0.5 at low OMF and 0.1 at high OMF, with increasing OMF suppressing hygroscopic growth and increasing critical dry diameter for CCN activation (D_d). An experiment-averaged κ_{org} of 0.14 was calculated, indicating that the highly-oxidized organic fraction of aerosol in Los Angeles is appreciably more hygroscopic than previously reported in urban areas. Finally, PACO will provide context for results forthcoming from the CalNex field campaign, which involved ground sampling in Pasadena during the spring and summer of 2010.

1 Introduction

Over half the world's population lives in urban areas, and that fraction is expected to increase in coming decades (Bremner et al., 2009). There have been a number of recent coordinated studies focused on characterizing particulate air quality in major urban areas, such as Pittsburgh, PA (Pittsburgh Air Quality Study, PAQS; e.g., Pekney et al., 2006; Bein et al., 2006; Wittig et al., 2004; Cabada et al., 2004; Modey et al., 2004), Los Angeles, CA (Southern California Air Quality Study, SCAQS; e.g., Eldering et al., 1994; Watson et al., 1994; Chow et al., 1994; Turpin and Huntzicker, 1991; Southern California Ozone Study 1997, SCOS97-NARSTO; e.g., Croes and Fujita, 2003; Liu et al., 2000; Pastor et al., 2003; Hughes et al., 2002; Secondary Organic Aerosol in Riverside, SOAR; e.g., Docherty et al., 2008; Eatough et al., 2008; Denkenberger et al., 2007), Mexico City, Mexico (Megacity Initiative: Local and Global Research Observations, MILAGRO; e.g., DeCarlo et al., 2008; Stone et al., 2008; Aiken et al., 2009), and Beijing, China (Campaign of Air Quality Research in Beijing, CAREBEIJING; e.g., Matsui et al., 2009; Yue et al., 2009; van Pinxteren et al., 2009).

The Los Angeles metropolitan area, with a population of over 17 million people, has long been considered a laboratory for air quality. Once the quintessential example of classic photochemical smog, the Los Angeles area has, as a result of decades of aggressive emission controls, reached a point where 8-h US National Ambient Air Quality Standard ozone exceedances have decreased from over 200 days/year in the 1980s to 120 in 2008 (AQMD, 2010). Nonetheless, this area remains one in which particulate matter levels continue to regularly exceed air quality standards, with annual $PM_{2.5}$ averages exceeding the national standard every year from 2000–2008 in Los Angeles County (CARB, 2010).

The Los Angeles Basin is generally characterized as source-rich in its western area, with prevailing west and southwest winds transporting emissions downwind toward the east and northeast (Lu and Turco, 1995). Three major coordinated studies have been undertaken to characterize Los Angeles air quality, in addition to ongoing work to describe facets of Los Angeles aerosol (Table 1). The majority of previous studies in the Los Angeles Basin have been centered in the downwind, eastern part of the basin, roughly 60 km east of downtown Los Angeles. The aerosol in this region is predominantly aged, with local contributions as well.

A major source of gaseous and particulate pollution in the Los Angeles area is mobile source emissions. The Los Angeles aerosol undergoes dramatic evolution from nighttime/morning periods to the photochemically active afternoon, characterized by changes in both its microphysical properties and composition. Overall, the submicron aerosol is dominated by organic aerosol (OA), which is predominantly secondary in origin (SOA), and nitrate (Docherty et al., 2008), with smaller amounts of sulfate and a minor chloride contribution. Primary marine and secondary sulfate aerosol are expected to contribute a relatively uniform loading of sulfate across the Los Angeles Basin (Watson et al., 1994). Marine sulfate is expected to be contributed by natural primary processes (biological, sea spray, bubble bursting), with anthropogenic shipping-related emissions contributing a varied and often significant loading of sulfate (Ault et al., 2010).

The Pasadena Aerosol Characterization Observatory experiment (PACO) was conducted from May–August 2009 in Pasadena, CA, in the north-central/north-western portion of the Los Angeles Basin, 16 km NE of downtown Los Angeles. Aerosol physics, composition, and hygroscopicity were measured during 54 days that spanned three distinct regimes of the annual meteorological cycle. A major forest fire occurred at the end of the sampling period, starting on 26 August and consuming over 160 000 acres of the Angeles National Forest before containment on 16 October. Named the "Station Fire", its southernmost extent was roughly 8 km from the sampling site, and emissions from the fire impacted the sampling site with periodic heavy smoke, soot, and ash. Results from PACO sampling during the Station Fire will be presented in subsequent work.

PACO represents the first prolonged experiment aimed at characterizing the aerosol near the source-rich western/central part of the Los Angeles basin; comparisons with previous studies in downwind areas will help determine the rate of aerosol generation from Los Angeles sources, as well as the nature of aerosol transformations with downwind transport. Further, the PACO study was well-timed to precede the 2010 CalNex field campaign (http://www.esrl.noaa.gov/csd/calnex/).

This paper presents an overview of the PACO experiment. Aerosol number and volume distributions measured by a differential mobility analyzer (DMA) exhibit distinct diurnal patterns, and composition data from an Aerodyne Compact-Time-of-Flight Aerosol Mass Spectrometer (C-ToF AMS)

Table 1. Previous Los Angeles air quality studies and major findings relative to particulate matter.

Study	Date	Major aerosol findings
Southern California Air Quality Study (SCAQS)	Summer/ fall 1987	- SOA/OA $\sim$ 40 % in summer afternoon (Turpin and Huntzicker, 1991) - Primary vehicle exhaust is the major aerosol component near PACO sampling site (Watson et al., 1994) - 20- 32 % of PM_{10} is SO_4^{2-} and NO_3^- (Watson et al., 1994)
Southern California Ozone Study (SCOS97-NARSTO)	Summer 1997	- Submicron organic mode evolves during periods of intense photochemistry, coincident with maximum O_3 (Pastor et al., 2003) - NH_4NO_3 and organics added to submicron aerosol with photochemical age (Pastor et al., 2003) - NH_3 sources in eastern basin enhance particulate NH_4NO_3 (Hughes et al., 2002)
Secondary Organic Aerosol in Riverside (SOAR-1, 2)	Aug, Nov 2005	- Significant diurnal changes in organic aerosol, with species more reduced in the morning and more oxidized in the afternoon (DeCarlo et al., 2006) - Oligomers detected in aged, acidic particles (Denkenberger et al., 2007) - SOA/OA = 70- 90 % at midday and $\sim$ 45 % during morning commute; SOAR average = 74 % (Docherty et al., 2008)
Individual studies	1999, 2001- 2002	- Complex, multi-modal GF data in Pasadena (Cocker et al., 2001) - SOA $>$ 50 % of total $PM_{2.5}$ in eastern basin (Sawant et al., 2004; Na et al., 2004)

indicate that these patterns are associated largely with the production of semivolatile oxidized organic species during photochemically active daytime periods. AMS-based Positive Matrix Factorization (PMF) results indicate that the character of OA in Los Angeles is overwhelmingly oxidized and secondary, and the high time resolution data allow for investigation of the daily evolution of OA components. Ultra Performance Liquid Chromatography/Electrospray Ionization Time-of-Flight High-Resolution Mass Spectrometry (UPLC/ESI-TOFMS) analysis of high-volume filter samples provides further evidence for diurnal changes in the character of OA, while thermal-optical analysis of low-volume, denuded filter samples reveals the magnitude of organic and elemental carbon in morning versus afternoon sampling periods. A particle-into-liquid sampler with offline ion chromatography analysis (PILS-IC) provides quantitative water-soluble inorganic ion composition during PACO, while a PILS coupled with online total organic carbon analysis (PILS-TOC) measured total water soluble organic carbon measurements during the third regime. Finally, trends in aerosol hygroscopicity indicate the degree to which changes in the magnitude and character of OA affect particle water uptake. PACO results are compared with previous aerosol characterization experiments in the Los Angeles Basin, with major differences attributed to regional variations in both source profiles and degree of aging.

2 Methods

Sampling was conducted on the Caltech campus in Pasadena, at 34.138° N, 118.124° W. Caltech is located in the western/central portion of the Los Angeles Basin, 8 km south of the San Gabriel Mountains and 16 km NE of downtown Los Angeles in the San Gabriel Valley. The 210 freeway is located 1.5 km north of the site, with heavy traffic between the hours of 08:00 and 09:00 LT, and then again between 15:00 and 19:00 LT. Prevailing daytime winds are from the W or SW, minimizing the impact of primary emissions from the 210 freeway at the sampling site, but overnight NW winds occasionally bring freeway emissions to Caltech. Other than this periodic impact from local primary emissions, the Pasadena aerosol is representative of transported urban particulate pollution from near the source-rich downtown area of the Los Angeles Basin.

PACO sampling took place between May and August of 2009, spanning the transition from spring to summer meteorological regimes. PACO was separated into three distinct analysis periods on the basis of meteorology, as summarized in Table 2.

2.1 Meteorology

Hourly meteorological data were downloaded from the Remote Automatic Weather Stations (RAWS) archive from the Western Regional Climate Center at the Desert Research Institute (DRI, Reno, Nevada). Data are from the Santa Fe Dam station, approximately 16 km east of the sampling site in the San Gabriel Valley, and are available online: http://www.raws.dri.edu/cgi-bin/rawMAIN.pl?caCSFD.

Table 2. PACO sampling regimes (2009).

Regime	Dates	Characteristics
Springtime meteorology	22 May to 12 Jun	- Basin impacted by a series of low pressure systems - Cutoff low brought rare springtime precipitation and cleaner atmosphere - Persistent cloudcover, unstable atmosphere - Low daytime temperatures, high RH, and limited photochemistry - High visibility with low O_3
Early summer/ marine influence	18 Jun to 7 Jul	- Limited impact from low pressure systems - Morning marine layer eroded several hours after sunrise - Higher daytime temperatures, slightly lower RH, and photochemically active afternoons - Hazy afternoons with increased O_3
Photo-chemically active	10 Jul to 4 Aug	- Semi-permanent high pressure over Southern California - Little marine moisture and infrequent, quickly-eroded marine layer - High daytime temp. (often exceeding 35 °C), very low daytime RH ($\leq$ 15 %), photochemically active days - Decreased visibility, high afternoon O_3

2.2 Gas-phase data

Hourly O_3, NO_x, and CO data were obtained from the California Air Resources Board's Pasadena (South Wilson) monitoring site located on the Caltech campus. Data are available online at http://www.arb.ca.gov/adam/hourly/hourly1.php.

2.3 Differential mobility analyzer

Particle size distribution measurements were performed with a cylindrical scanning differential mobility analyzer (TSI Model 3081) upstream from a condensation particle counter (TSI Model 3760). A logarithmic scan from a mobility diameter of 15 nm to 815 nm was completed every 237 s. The sheath and excess flows of 2.5 l min^{-1} were used, with a 10 : 1 flow rate ratio of sheath-to-aerosol.

2.4 Aerosol mass spectrometer

An Aerodyne compact time-of-flight aerosol mass spectrometer (C-ToF-AMS; Drewnick et al., 2005; Canagaratna et al., 2007) measured aerosol composition and size information for 54 days during PACO. The AMS collects sub-micron particles via an aerodynamic lens into a particle sizing chamber, after which particles are vaporized and ionized by a heater and filament assembly. Aerosol fragments are then orthogonally extracted into an ion time-of-flight chamber where they are detected and interpreted as mass spectra. Adjustments to the AMS fragmentation table were made regularly, based on 21 filter sample periods over the course of PACO (Allan et al., 2004b). Additionally, thirteen ionization efficiency calibrations were made using ammonium nitrate solutions. The AMS sulfate measurement was compared to sulfate concentrations from the PILS-IC, resulting in an AMS collection efficiency (CE) of 0.5. This CE is in agreement with previous ambient studies (Huffman et al., 2005; Drewnick et al., 2003; Allan et al., 2004a). AMS data were processed with the ToF-AMS Analysis Toolkit in Igor Pro 6 (Wavemetrics, Lake Oswego, OR).

2.5 Positive matrix factorization analysis

The dominant fraction of submicron nonrefractory aerosol is organic in most urban areas (Zhang et al., 2007). OA comprises a multitude of compounds, such that characterization by identification of each component is not currently possible (Schauer et al., 1996). Positive Matrix Factorization (PMF) has been used to deconvolve AMS mass spectra in order to identify classes of organic compounds that constitute OA (Paatero and Tapper, 1994; Paatero, 1997; Ulbrich et al., 2009). PMF solutions represent linear, positive combinations of mass spectra that describe variability in data, and AMS-based PMF results from most sites resolve factors whose mass spectra have characteristics of hydrocarbon-like OA (HOA) and oxygenated OA (OOA), with other factors such as biomass burning OA (BBOA) occurring in some areas (Zhang et al., 2007). OOA can often be further deconvolved into low-volatility OOA (LV-OOA) and semivolatile OOA (SV-OOA), broadly representing aged, transported, and highly oxidized OA and fresher, local, and less oxidized OA, respectively (Ng et al., 2010). AMS measurements, in conjunction with PMF analysis, allow for investigation of the diurnal evolution of OA and rapid changes in OA occurring during photochemically intense periods. Further, the combination of PMF solutions with analysis of the relative abundance of mass-to-charge (*m/z*) ratios 43 and 44 can be used as an aerosol aging diagnostic that allows comparison between locations (Ng et al., 2010).

For the PACO dataset, bulk AMS organic aerosol was prepared and then processed using the PMF2.exe algorithm (Paatero and Tapper, 1994). Solutions from the PMF algorithm were compared to meteorological variables and chemical tracers, as well as previously published mass spectra, using the PMF Evaluation Tool (PET Ulbrich et al., 2009). The strategic procedure for probing the PMF solution space is provided in Appendix A.

2.6 PILS-IC

A particle-into-liquid sampler coupled with off-line ion chromatography (PILS-IC, Sorooshian et al., 2006) sampled during 4-h periods (07:00–11:00 and 15:00–19:00 LT), providing quantitative measurements of inorganic and organic ions. The PILS samples ambient air through a 1 µm cut size impactor and three denuders (URG and Sunset Laboratory) designed to remove inorganic and organic gases that might bias aerosol measurements. Sampled air is then exposed to high water supersaturation in a steam chamber, where particles grow sufficiently large to be collected by inertial impaction before being delivered to vials held on a rotating carousel. Samples were collected every 30 min, and were stored at 2 °C until analysis by a dual IC system (Dionex ICS-2000). PILS-IC data from PACO are used primarily to determine collection efficiency corrections for the AMS and are not presented in detail here.

2.7 PILS-TOC

Water-soluble organic carbon (WSOC) was quantified during 12-h periods (07:00–19:00 LT) using a PILS (Brechtel Manufacturing Inc.) coupled to a Sievers Model 800 Total Organic Carbon (TOC) Analyzer (PILS-TOC). Details of this technique are described in detail by (Sullivan et al., 2004, 2006). Briefly, particles smaller than 2.5 µm in diameter are sampled by the PILS and passed immediately through an organic carbon denuder (Sunset Laboratory Inc.) to remove organic vapors. Particles are grown into droplets, collected by inertial impaction, and delivered to a TOC analyzer for quantification of WSOC, with data reported every 6 min. To account for dilution of the PILS liquid wash flow to the TOC analyzer owing to collected drops and condensation on the PILS droplet impactor, a constant dilution factor of 1.15 is assumed. This factor is based on measurements with an independent PILS system coupled to ion chromatography, a technique that can more precisely quantify the dilution factor. The reported WSOC levels are the difference between the measured and background concentrations. Contamination in the MQ water was the main component of the background levels, which were assumed to be constant between periodic background measurements. The overall measurement uncertainty is estimated to be approximately 10 %. The PILS-TOC was employed during the final, photochemically active regime of PACO, from 10 July to 4 August.

2.8 Filter sampling

Both high- and low-volume filter samples were collected during 4-h sampling periods (07:00–11:00 and 15:00–19:00 LT). High-volume ($1250\,\mathrm{l\,min^{-1}}$) samples were collected with a Tisch TE-6001 sampler fitted with a $PM_{2.5}$ fractionater, using Whatman Quartz Microfibre Filters (cat. #1851-865). Low volume ($15.9\,\mathrm{l\,min^{-1}}$) samples were collected on 47 mm PALL Life Sciences Pallflex membrane filters, downstream from a Sunset Laboratory parallel-plate carbon filter denuder. Sampling was carried out according to the IMPROVE_A protocol, except that oven limitations forced filters to be pre-baked at 300 °C before sampling. Despite the lower pre-baking temperature, subsequent analysis of pre-baked filters revealed ≤ 0.01 µg of organic carbon (OC) and elemental carbon (EC). After sampling, filters were wrapped in two layers of aluminum foil and stored at −20 °C until analysis.

Low- and high- volume samples were analyzed for OC and EC via thermal-optical analysis (TOA) with a Sunset OC-EC TOA analyzer, following the IMPROVE_A temperature and calibration protocols. High volume quartz filters were also analyzed by Ultra Performance Liquid Chromatography/Electrospray Ionization Time-of-Flight High-Resolution Mass Spectrometry (UPLC/ESI-TOFMS). One-eighth of each filter was extracted with high-purity methanol under ultrasonication for 45 min. Filter extracts were filtered through a PALL Life Sciences Acrodisc CR 25-mm syringe filter (PTFE membrane, 0.2-mm pore size) into a scintillation vial. The filtered extracts were blown dry under a gentle nitrogen stream at ambient temperature. The residue was reconstituted with 50 : 50 v/v methanol with 0.1 % acetic acid and water. Blank filters were extracted and treated in the same manner as the field samples. Extracts were analyzed by a Waters ACQUITY ultra performance liquid chromatography (UPLC) system, coupled with a Waters LCT Premier TOF mass spectrometer equipped with an electrospray ionization (ESI) source, allowing for accurate mass measurements (i.e., determination of molecular formulas) to be obtained for each observed ion. Extracts were analyzed by UPLC/ESI TOFMS operated in both negative and positive ion modes. Details of operation protocols, including column information and chromatographic method for the UPLC/ESI-TOFMS are given by Surratt et al. (2008).

2.9 Hygroscopicity

Hygroscopicity measurements were carried out with the Differential Aerosol Sizing and Hygroscopicity Spectrometer Probe (DASH-SP, Brechtel Mfg), which is described by Sorooshian et al. (2008). Briefly, ambient particles pass through a nafion dryer before size-selection by a cylindrical, single-classification differential mobility analyzer (DMA). The resulting monodisperse aerosol is split into five separate flows – one providing a redundant measurement of total

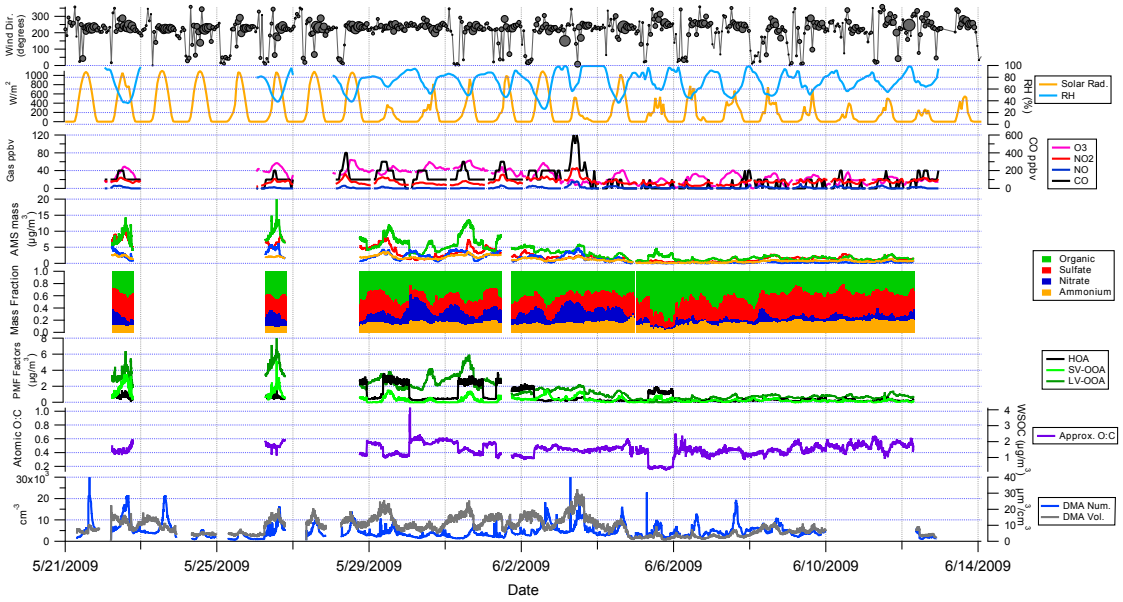

Fig. 1a. Regime I (wind direction marker size proportional to wind speed; max size = 20 km h^{-1}).

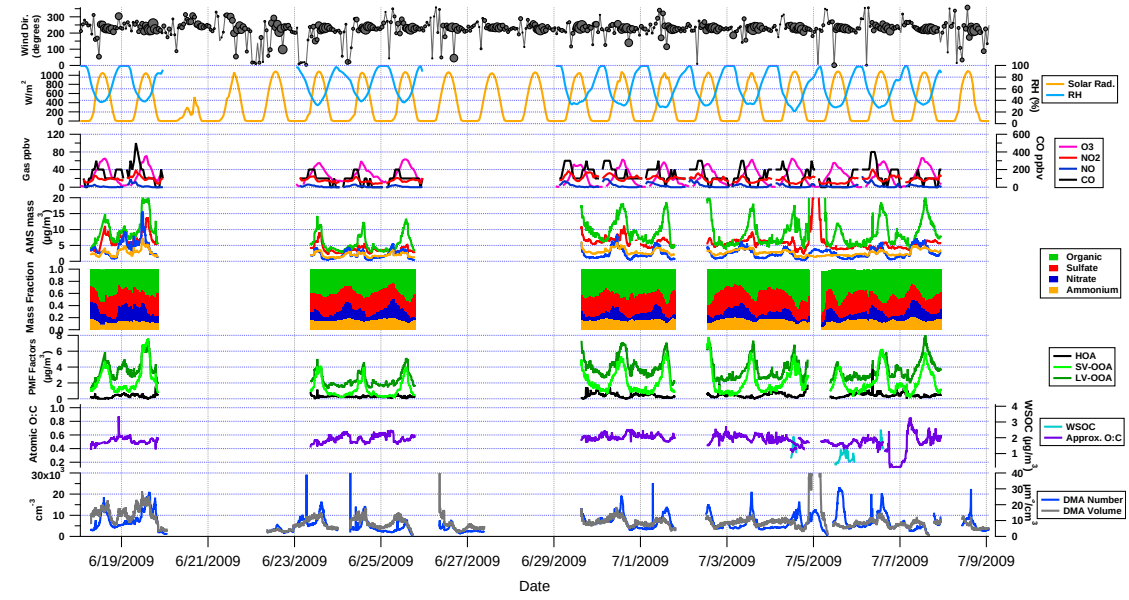

Fig. 1b. Regime II (wind direction marker size proportional to wind speed; max size = 20 km h^{-1}).

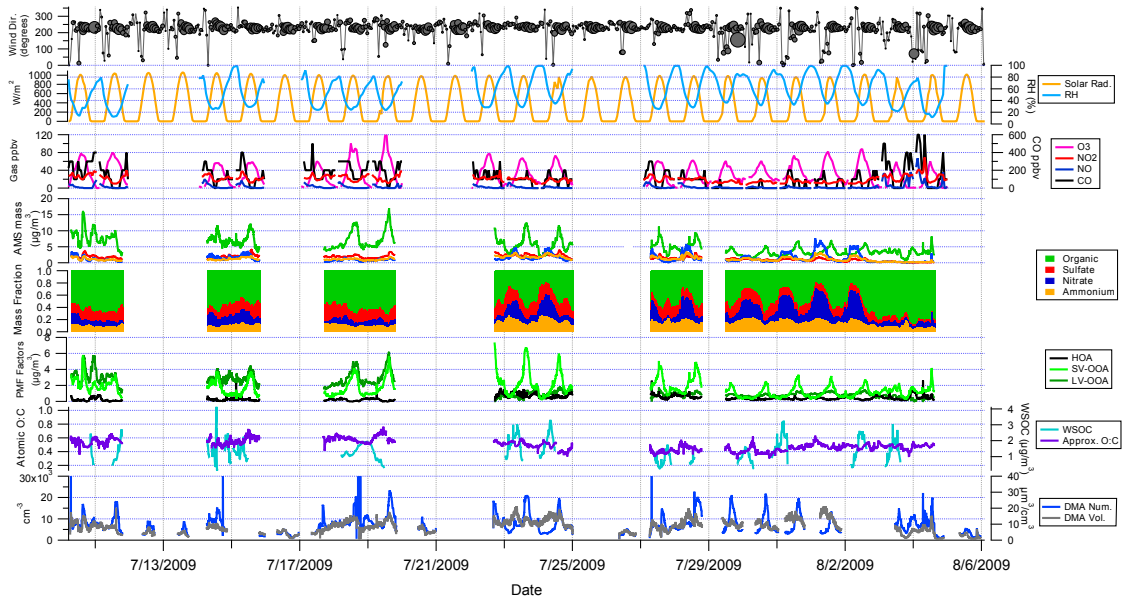

Fig. 1c. Regime III (wind direction marker size proportional to wind speed; max size = 20 km h^{-1}).

particle concentration at the DMA-selected size with a water condensation particle counter (TSI Model 3831), and the remaining four channels consisting of parallel nafion humidification chambers (Perma Pure, LLP, Model MD-070-24FS-4), followed by correspondingly humidified custom optical particle counters (OPCs). In the OPC sample volume, particles pass through a focused laser beam ($\lambda = 532$ nm, World Star Technologies, Model TECGL-30) and scatter light in proportion to size (D_p) and refractive index (RI). Forward-scattered light is collected and focused on a photomultiplier tube, and the resulting electrical pulse is recorded by a high-speed data acquisition computer. An iterative data processing algorithm, based on laboratory calibrations with salts of known refractive indices, is used to determine the best fit on a solution surface relating electrical pulse height, size, and refractive index. The hygroscopic growth factor ($GF = D_{p,wet}/D_{p,dry}$) is corrected for the RI change caused by particulate liquid water at elevated RH.

In the current study, the DASH-SP sampled for 4-h periods (07:00–11:00 and 15:00–19:00 LT). Hygroscopicity was measured at dry sizes corresponding to $D_{p,em}$ of 150, 175, 200, and 225 nm. Multiple RH sensors in the nafion tubes and OPCs controlled RHs to dry (≤ 8 %), 74 %, 85 %, and 92 %, with RH uncertainty of 1.5 %. Because calculated RI varied little during sampling periods, GF calculations were made with a single RI for each sampling period, representing the average RI calculated for the entire period. The error introduced by this assumption is small, as light scattering in the DASH is far more sensitive to size than RI. Overall uncertainty in GF calculations is calculated to be 4.5 %.

3 Results and discussion

3.1 Atmospheric conditions

Figure 1a–c is a compilation of meteorological data, as well as gas- and aerosol-phase composition for regimes I, II, and III, respectively. Wind speed and direction display distinct diurnal patterns, with stagnant or very light winds from the N/NE in the overnight to early morning hours (20:00–06:00 LT) changing direction to come from the W/SW shortly after sunrise (06:00–07:00 LT). Between 06:00 and 16:00 LT, wind speed increases from 3–4 km h^{-1} to 13–15 km h^{-1} out of the W/SW before decreasing back to very light or stagnant out of the N/NE by 20:00 LT. One effect of these wind patterns is to allow local emissions to build up in the Los Angeles Basin during the nighttime and early morning hours, leading to significant carryover of aged aerosol in the background Los Angeles air, as proposed by (Blumenthal et al., 1978). When sea breezes develop, fresh emissions in source-rich areas are gradually transported from the Western Los Angeles Basin toward downwind areas in the E/NE. Situated 16 km from downtown Los Angeles, Pasadena can be considered as a receptor site that first receives transported pollution between 10:00 and 11:00 LT, after roughly 4–5 h of transport. During the afternoon hours

(13:00–18:00 LT), the sampling site receives a steady influx of air from the W/SW with photochemical age of 1–2 h. There are no significant freeways or point sources of particulate pollution in close W/SW proximity to the sampling site, and so it is expected that air sampled during PACO is representative of transported urban air in Los Angeles. A major freeway with significant diesel and gasoline mobile sources is located 1.5 km to the north of the sampling site, and so overnight N/NE winds may have periodically impacted the site with primary particulate emissions. Daytime variation in gas- and aerosol-phase composition is expected to result from three sources: (1) temporal changes in emissions from source-rich areas, (2) diurnal variations in the intensity of photochemistry, and (3) the age of transported pollution.

A clear diurnal trend is observed in RH and solar radiation, with RH increasing to near 100 % on most nights and remaining at or near saturation until sunrise. The incidence of nighttime and morning marine cloudcover was common during regimes I and II, while regime III was typically drier, with clear nighttime skies more common. Periods of more significant marine layer influence are indicated by longer periods of saturated RH and more gradual decrease in RH (and slower increase in solar radiation) after sunrise. Regime I has been classified as "springtime meteorology" due to the impact of several low pressure systems in Southern California, bringing periodic drizzle and leading to several days of cloudcover and significantly diminished solar radiation (i.e. 6 to 12 June). Daytime RH rarely fell below 50 % during regime I. Regime II exhibited the strongest summertime marine layer influence, with heavy cloudcover persisting until late morning (10:00 to 12:00 LT) nearly every day before making way for sunny, hazy afternoons with daytime RH between 25 and 40 %. Regime III observed the least marine layer influence, with many mornings of clear skies and daytime RH typically between 10 and 30 %. Despite differences in meteorology, the diurnal wind patterns described above were robust, with stagnant morning winds giving way to afternoon sea breezes and pollutant transport from the W/SW.

Gas-phase data give a sense of the atmospheric chemical environment during sampling. O_3 exhibits a strong diurnal pattern correlated with solar radiation and serves as a tracer for photochemical activity. During periods of relatively dry atmospheric conditions, the O_3 concentration peak increases in magnitude over subsequent days (see 17 to 19 July and 27 July to 2 August in regime III), suggesting that either pollutants accumulate or photochemical activity increases during periods of consistent, stable atmospheric conditions, resulting in photochemical episodes. CO and NO_x display more random behavior, exhibiting periodic peaks in concentration indicative of plumes of fresher emissions.

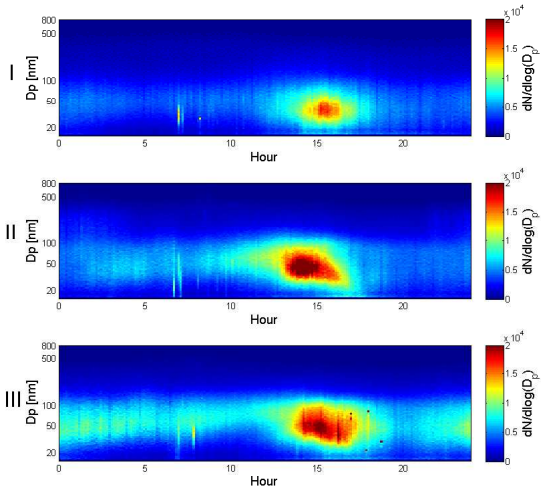

Fig. 2. Average diurnal DMA number concentrations (cm^{-3}) for regimes I, II, and III.

3.2 Aerosol composition

OC and EC mass concentrations, in addition to OC:EC ratios from representative days in each regime, are presented in Table 3. OC is higher in afternoon periods when compared with mornings in each regime (27, 18, and 4 % higher in regimes I, II, and III, respectively), while EC is lower during afternoons (7, 35, and 22 % lower in regimes I, II, and III, respectively). Further, OC:EC ratios are significantly higher during afternoon periods. These diurnal trends in OC are expected, given the importance of photochemical SOA production, and the percentage increase in OC mass between morning and afternoon periods is similar to that observed by the AMS (15, 17, and 10 % higher in regime I, II, and III, respectively). Discrepancies may arise due to the different size ranges measured by the AMS and filter sampling (upper limits of measurement are 1.0 and 2.5 µm for the AMS and filters, respectively), in addition to potential volitalization of semivolatile organics relating to the thermo-optical OC/EC analysis technique. The modest increase in OC between morning and afternoon periods during the photochemically intense regime III may indicate that significant OC existed in the background aerosol during this period. The decrease in EC observed between morning and afternoon periods suggests that primary organics are a more significant portion of the Los Angeles aerosol in the mornings, and the relatively low concentrations of EC suggest that the dominant source of organic aerosol in Los Angeles is secondary.

DMA data are presented in panel 8 of Fig. 1a–c. Diurnal patterns are evident in both DMA volume and number in all regimes. DMA volume tends to reach a maximum in the mid-to-late morning (10:00, 11:00, 08:00 LT in regime I, II, and

Table 3. OC/EC concentrations ($\mu g\,m^{-3}$) for representative days from each regime.

	OC		EC		OC:EC	
Regime	AM	PM	AM	PM	AM	PM
I	3.88 ± 0.32	4.92 ± 1.18	0.43 ± 0.02	0.40 ± 0.27	9.1	12.4
II	4.24 ± 0.46	5.01 ± 1.62	0.80 ± 0.31	0.52 ± 0.40	5.3	9.6
III	6.16 ± 1.40	6.41 ± 1.44	0.83 ± 0.47	0.65 ± 0.22	7.4	9.9

III, respectively), when RH is still high and particles have presumably undergone cloud processing. The early maxima in regime III underscore the absence of significant marine layer influence persisting into the late morning. On average, DMA number concentration reaches a maximum between 14:00 and 15:00 LT during each regime, roughly 3 h after transported pollution is expected to first arrive at the sampling site (Fig. 2). This indicates that increases in fine particle mass at the PACO sampling site are not the result of transport alone, but also affected by photochemical production in transported, polluted air from source-rich areas. There was no significant difference in wind patterns between regimes, so the slightly earlier peak in DMA number in regime II suggests that marine moisture and aqueous-phase processes (most prevalent in regime II) may hasten secondary aerosol production. Figure 2 indicates that appreciable concentrations of fine particles (< 100 nm) are present in late nights and early mornings (particularly in regimes II and III), possibly comprised of fresh emissions, nighttime-generated NO_3^-, or fine particle carryover residing in a shallow mixed layer.

With the exception of a high-volume filter sampler located outdoors on the roof, instruments sampled from inlets connected to a main sampling line drawing in ambient air at a 16 l per minute ($l\,min^{-1}$) laminar flow rate. Sample flow to each instrument was supplemented with pumps to be isokinetic with flow in the main sampling line, and sample lines were designed to draw from the center of flow through the main line. Ambient air was dried by nafion driers upstream of each instrument.

The third and fourth panels of Fig. 1a–c show time traces of bulk AMS aerosol mass concentration and mass fraction, respectively, while the sixth panel shows a time trace of approximate O:C ratio, based on Aiken et al. (2008), as well as WSOC concentration from the PILS-TOC (regime III). Organics dominated the aerosol sampled during PACO, and except for short episodes in regime I, the approximate O:C ratio remained relatively constant during each regime (0.44 ± 0.08, 0.55 ± 0.05, and 0.48 ± 0.08 during regimes I, II, and III, respectively). Organic aerosol in regime II appears to be more oxidized than I and III, suggesting that the marine moisture and presumed aqueous processing may enhance the rate of organic oxidation in Los Angeles. From bulk AMS time traces it is evident that organics increase in both magnitude and mass fraction each afternoon, particularly during the more photochemically active regimes II and III. It is noteworthy that there are no distinct trends in approximate O:C between mornings and afternoons (morning approximate O:C = 0.44 ± 0.08, 0.54 ± 0.08, and 0.49 ± 0.07 for regimes I, II, and III, respectively, while afternoon approximate O:C = 0.44 ± 0.08, 0.53 ± 0.06, 0.50 ± 0.08 for regimes I, II, and III, respectively). This suggests that there is little change in overall oxidation state of Los Angeles aerosol, even on timescales of weeks. It is unlikely that all organics are uniformly oxidized at all times in Los Angeles, but rather that there exists a continuum of OA oxidation, with more reduced and more oxidized ends of that continuum maintaining a relatively constant ratio for extended periods of time.

Trends in aerosol mass fraction are presented in Fig. 4. Organics dominate the Los Angeles submicron aerosol, contributing 42, 43, and 55 % of aerosol mass in regimes I, II, and III, respectively. Diurnal trends are evident in Fig. 4, with organic mass fraction increasing significantly from morning (07:00–11:00 LT) to midday (11:00–15:00 LT) to afternoon (15:00–19:00 LT) in each regime. Sulfate is a significant component in marine/moisture-influenced regimes I and II, and is a more minor component in regime III, suggesting that cloud processing and marine influence may be an important source of sulfate aerosol in Los Angeles. Nitrate contributes equal mass fractions in each regime, with a minimum in the afternoon and a maximum in the morning. Ammonium contributes a remarkably constant mass fraction to the aerosol, despite significantly less inorganic sulfate in regime III, suggesting an ammonium surplus for aerosol sampled in regime III. The significant peak in AMS masses during the early morning of 5 July (regime II) corresponds to a total submicron mass of over 200 $\mu g\,m^{-3}$, and resulted from a myriad of fireworks displays in the area surrounding the sampling site. This plume has been removed from further analysis. Diurnal trends in bulk composition are highlighted in the top panel of Fig. 3. It is noteworthy that during the significantly marine-layer-impacted regime II, bulk organic, sulfate, nitrate, and ammonium masses are all enhanced. This is further evidence that aqueous processing associated with marine layer influence may be an important factor in generating aerosol mass in Los Angeles. Typically, organics increase in magnitude to a maximum near 14:00–15:00 LT in each

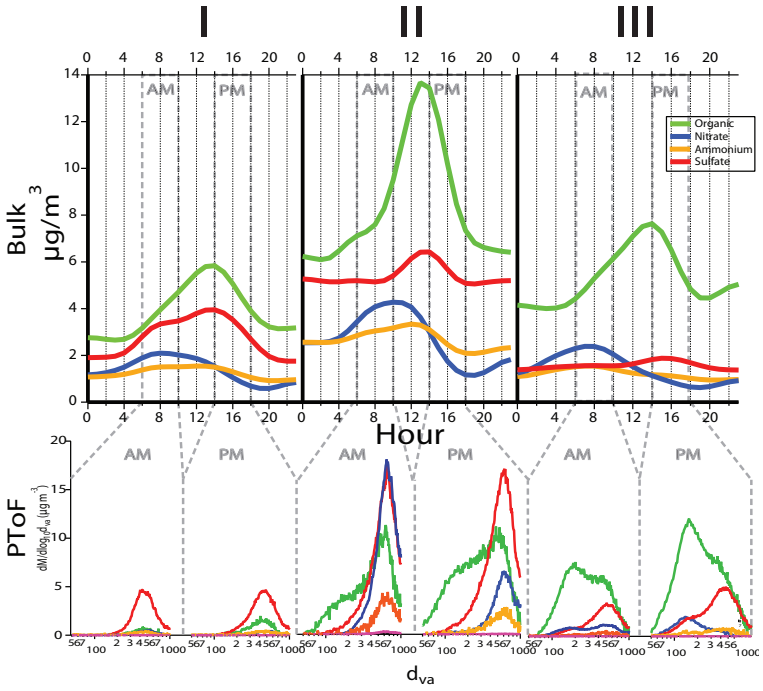

Fig. 3. Bulk AMS diurnal mass averages for regimes I, II, and III. Bottom panel shows size-resolved PToF AMS data for a representative morning and afternoon period in each regime, where morning = 07:00–11:00 LT and afternoon = 15:00–19:00 LT.

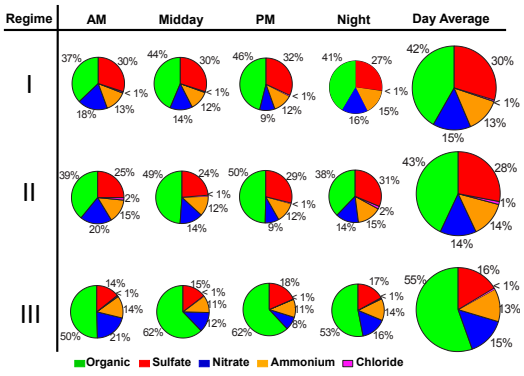

Fig. 4. AMS bulk mass fractions for AM (07:00–11:00 LT), midday (11:00–15:00 LT), PM (15:00–19:00 LT), and night (19:00–07:00 LT) for regimes I, II, and III.

regime, corresponding to a maximum in ozone, solar radiation, and DMA number – evidence of photochemical SOA production. Sulfate exhibits slight enhancements during periods of peak photochemical activity in all three regimes, but as suggested by Kleeman et al. (1999), it appears to be predominantly a background marine species. Nitrate mass is highest in the nighttime and morning periods, likely resulting from ozone-NO_x production of HNO_3 at night and HO_x-NO_x production of HNO_3 after rush hour in the mornings. As mentioned in Sect. 3.1, there were periods of high O_3 observed during PACO, and during several of these periods there also appeared to be significantly elevated levels of aerosol nitrate during nighttime sampling (e.g. 30 July to 3 August). Further, morning peaks in aerosol nitrate varied significantly in magnitude, suggesting that there may be significant variation in the amount of gas-phase HNO_3 production from day to day.

Ammonium mass generally follows the combined trends of SO_4^{2-} and NO_3^-, but appears to be in excess in regime III. Defining an ammonium ratio as:

$$\frac{\text{(moles of } NH_4^+ \text{ measured by AMS)}}{\text{(moles of } NH_4^+ \text{ required to neutralize } SO_4^{2-} \text{ and } NO_3^-)}, \quad (1)$$

aerosol sampled in regimes I and II was found to be generally neutralized (average ammonium ratio $= 0.96 \pm 0.21$ and 0.94 ± 0.17 for regimes I and II, respectively), while aerosol from regime III was characterized by significant ammonium excess (ammonium ratio $= 1.28 \pm 0.30$). These

results suggest that aerosol phase NH_4NO_3 was ammonia-limited during regimes I and II, but ammonia may have been in excess during regime III. Investigating molar ratios of inorganic species, it is apparent that the role of SO_4^{2-} is significantly diminished in regime III, corresponding to the absence of marine layer influence. The ratio of NO_3^- to NH_4^+ remains relatively constant across regimes (0.32, 0.29, and 0.34 in regimes I, II, and III, respectively), while the ratio of SO_4^{2-} to NH_4^+ exhibits a marked decrease in regime III (0.42, 0.41, and 0.24 in regimes I, II, and III, respectively). The AMS has difficulty distinguishing whether NH, NH_2, and NH_3^+ (*m/z* 15, 16, and 17, respectively) are contributed by inorganics or organic amines. One explanation for these trends is that ammonium may be chiefly inorganic during the moister, marine-layer-influenced regimes I and II, serving primarily to neutralize SO_4^{2-} and NO_3^-, while there may be an influence from organic amines in the absence of marine layer influence during regime III. While particulate amines have been observed in the particle phase, it is unclear why they would appear to be more prevalent in regime III, as amines are typically associated with cooler, moister environments. Another explanation is that the "excess" NH_4^+ may be associated with organic anions. An enhancement in acidic organic species, which would not be unexpected in a hot, dry, photochemically active regime, may lead to a corresponding enhancement in neutralizing NH_4^+. Since the AMS does not specifically quantify organic anions, such an enhancement in both organic acids and associated NH_4^+ would lead to an increased ammonium ratio.

The bottom panel of Fig. 3 shows size-resolved PToF-AMS composition for a representative morning and afternoon period in each regime, with 9 June, 19 June, and 19 July representing regimes I, II, and III, respectively. Size-resolved data indicate that aerosol in regime I is typically internally-mixed, with the mode centered at $\sim$ 400–500 nm. Afternoon PToF data from regime I indicate that photochemical organic production typically results in organics condensing on existing accumulation mode aerosol. Regime II is characterized by significantly higher aerosol mass and more complex size distributions. While there is a significant internally-mixed accumulation mode present and centered at $\sim$ 600–700 nm, there is also significant aerosol mass at sizes smaller than 300 nm in both morning and afternoon sampling periods, though the mass at smaller sizes does not comprise a distinct mode. Afternoon PToF data from regime II indicate that a fine mode appears coincident with photochemistry, suggesting that fine mode aerosol is predominately comprised of secondary species. Nitrate, sulfate, and ammonium are generally confined to accumulation mode aerosol in regime II. Regime III PToF data reveal an aerosol that is dominated by organics at all sizes and is distinctly bimodal. In addition to an internally mixed accumulation mode centered at $\sim$ 500–600 nm, distributions from regime III also reveal a significant fine mode centered at $\sim$ 100–200 nm. The accumulation mode tends to be comprised of sulfate, nitrate, and ammonium (in addition to organics) in the morning periods, with less nitrate in afternoons. Afternoon PToF data from regime III, like those from regime II, reveal fine-mode aerosol growth resulting from production of secondary organic species. Numerous studies have shown that the critical species for new particle formation in the atmosphere is H_2SO_4. The extent to which the observed fine mode aerosol might have originated from the nucleation of gas-phase species during PACO is unclear. However, given the relatively large amount of pre-existing aerosol surface area, as well as the relatively low concentration of SO_2, the precursor to H_2SO_4, it is unlikely that new particle formation by nucleation is an important process in Los Angeles. Instead, the growth of fine-mode organics is proposed to occur by condensation of SOA on existing ultrafine primary aerosol. This tentative conclusion is contrasted with results from Pittsburgh, in which Stanier et al. (2004) found new particle formation to be an important process, strongly correlated with SO_2 concentrations. Whether condensing on nucleated sulfate or existing ultrafine primary aerosol, growth of fine mode particles in Los Angeles is predominantly due to SOA.

Figure 5 shows the hourly average for WSOC mass (top panel, representing WSOC organic mass) and % of AMS organic accounted for by WSOC (bottom panel) for regime III. A factor of 1.8 was used to convert water soluble carbon (WSOC) mass to water soluble organic mass (WSOM), within the range of factors presented by Turpin and Lim (2001), and matching the factor used by Docherty et al. (2008) for aerosol in the Los Angeles Basin. Averaged hourly data reveal a trend in WSOM, increasing from a minimum in the late evening and early morning to a maximum at 15:00 LT, corresponding to maxima in O_3 concentration, solar radiation, AMS organic, and DMA number concentration. This suggests that photochemical production of SOA in air transported from source-rich areas is a significant source of WSOM in the Los Angeles Basin. While there is a diurnal trend in WSOM, the fraction of AMS organic accounted for by WSOM is relatively constant at 0.44 ± 0.16 during regime III, with a slight enhancement between 15:00 and 19:00 LT. This suggests that while significant WSOM is photochemically generated during the course of a day, water soluble organics comprise a relatively constant percentage of organic aerosol in Los Angeles. WSOC has been found to correlate well with oxidation state of organic aerosol (e.g., Kondo et al., 2007). Given the relatively constant approximate O:C ratio observed in regime III and steady afternoon influx of polluted air on the order of 1–2 h old, the constant WSOM:AMS organic ratio is not unexpected.

3.3 PMF results

AMS data from PACO were combined into a single continuous dataset for analysis by the PMF method. PMF produced several non-unique solutions that were compared with known

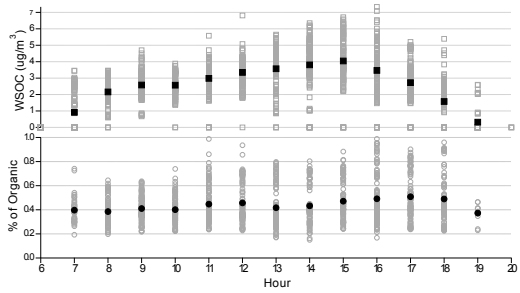

Fig. 5. WSOC magnitude (squares) and % of AMS organic (circles). Black markers represent the average over regime III.

mass spectra and external time traces in order to choose final solutions. Figure 6 presents a summary of PMF factors, while panel 6 of Fig. 1a–c represents time traces for PMF factors for regimes I, II, and III, respectively. Details of the PMF method and solution selection are presented in Appendix A.

Three factors were resolved from the PMF method, and comparisons with previously published spectra indicate that they correspond to a hydrocarbon-like organic aerosol (HOA) and semivolatile- and low-volatility-oxygenated organic aerosol (SV-OOA and LV-OOA, respectively). PMF analysis was also performed on each regime separately, to determine the sensitivity of solutions to the assumption that OA is comprised of factors with constant mass spectra. In each case (HOA, SV-OOA, and LV-OOA), the factors resolved in the bulk analysis displayed a high degree of correlation (Pearson's R generally on the order of 0.94–0.99 for LV-OOA, SV-OOA, and HOA) with those resolved in analysis of individual regimes. The HOA factor is closely correlated with previously published spectra from periods dominated by reduced, primary organics (Zhang et al., 2005; Lanz et al., 2007; Ulbrich et al., 2009), and has significant signal at *m/z* 41 and 57. The LV-OOA factor is closely correlated with previously-published OOA-1 factors and OOA-like factors observed in highly oxidizing environments (Zhang et al., 2005; Lanz et al., 2007; Ulbrich et al., 2009; Alfarra et al., 2004). The SV-OOA factor is also correlated with previously-published OOA factors, but has a higher degree of correlation with previously-published factors expected to represent less-aged, less-oxidized, semivolatile oxygenated organic aerosol, or SV-OOA (Zhang et al., 2005; Lanz et al., 2007; Ulbrich et al., 2009; Bahreini et al., 2005; Alfarra et al., 2004). The LV-OOA factor has a larger ratio of *m/z* 44 to *m/z* 43, an indication of a more aged, oxidized organic component (Ng et al., 2010). The SV-OOA factor, on the other hand, has a smaller *m/z* 44 to *m/z* 43 ratio. PACO PMF factors correlated closely with "standard" HOA, SV-OOA, and LV-OOA factors reported by Ng et al. (2011), based on an average of results from 15 sites.

As seen in Fig. 1a–c, the HOA factor has the character of a periodic plume source, with low background concentrations punctuated by sudden, significant increases in concentration that remain high for several hours at a time. These increases in HOA concentration occurred primarily during regime I and are typically correlated with or just following peaks in CO concentration (panel 3 in Fig. 1a–c), though the low time- and concentration-resolution of CO measurements made statistical analysis difficult. HOA is typically associated with primary organic aerosol (POA) (e.g., Ulbrich et al., 2009; Ng et al., 2010), and the only significant local source of POA is expected to be the 210 freeway, 1.5 km north of the sampling site. There appears to be a trend of HOA plumes coinciding with or immediately following periods of light winds out of the N, which suggests that the HOA-like factor may represent primary freeway emissions. It is unclear why this HOA factor does not appear during every period of light winds out of the N. Low correlation between the HOA factor and ozone ($Pr = 0.39$) suggests that HOA production is not a photochemical process, and low correlations with inorganic AMS traces ($Pr = 0.18$, 0.15, 0.21, and 0.02 for sulfate, nitrate, ammonium, and chloride, respectively) suggest that HOA production is independent of formation of inorganic aerosol, and that HOA may comprise an externally mixed mode, separate from the accumulation mode aerosol that is typically comprised of inorganic constituents.

The more dominant LV-OOA factor is most significantly correlated with inorganic AMS traces ($Pr = 0.75$, 0.46, 0.65, and 0.46 for sulfate, nitrate, ammonium, and chloride, respectively). As discussed in Sect. 3.2, inorganics are most prevalent in accumulation mode aerosol (rather than fine mode), and their loadings appear to be associated with significant marine layer influence in the Los Angeles Basin (e.g., regimes I and II). The high degree of correlation between LV-OOA and inorganic constituents suggests that the LV-OOA factor represents an organic component that typically resides in accumulation mode aerosol and may be associated with marine layer/cloud processing influence. The correlation between LV-OOA and ozone is relatively low ($Pr = 0.39$), indicative of an aged background organic species, as opposed to a rapidly-produced photochemical product that exhibits a distinct diurnal trend. Examining time traces for LV-OOA in Fig. 1a–c reveals that the LV-OOA factor exhibits relatively high background levels in the mornings and at night, while periodically showing moderate increases in magnitude during midday periods of photochemistry. These periodic photochemical trends in LV-OOA correspond to periods of intense photochemistry (e.g., 18–19 July), characterized by midday ozone concentrations near 80–100 ppb. This suggests that while LV-OOA appears to be the major constituent of the aged background aerosol discussed in Sect. 3.2, it can be photochemically produced on relatively short timescales during periods of intense photochemical activity. Its strong correlation with SO_4^{2-}, consistent presence during humid overnight and morning hours, coincidence

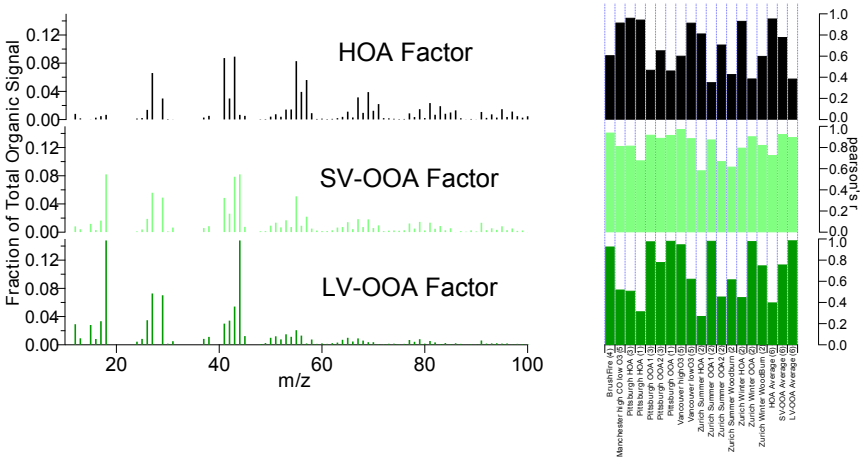

Fig. 6. Mass spectra for the three factors identified in PMF analysis (HOA, SV-OOA, and LV-OOA; left) and Pearson's R correlations of those solution mass spectra with previously reported mass spectra (1, 2, 3, 4, 5, 6: Zhang et al., 2005; Lanz et al., 2007; Ulbrich et al., 2009; Bahreini et al., 2005; Alfarra et al., 2004; Ng et al., 2011, respectively).

with accumulation mode aerosol, and greater prevalence in moisture-impacted regimes I and II suggest that there may be significant aqueous processing sources for LV-OOA in Los Angeles.

Figure 1a–c show a regular diurnal trend in SV-OOA, with overnight minima increasing to maximum concentrations daily at approximately 14:00–15:00 LT, correlating with maxima in solar radiation, AMS organic, and DMA number concentration. The SV-OOA factor exhibits a reasonable degree of correlation with ozone (Pr = 0.53), suggesting that semivolatile organics are products of short-timescale photochemical oxidation of VOCs. Correlations with inorganic traces are lower than those for LV-OOA (Pr = 0.42, 0.31, 0.45, and 0.19 for sulfate, nitrate, ammonium, and chloride, respectively). As discussed in Sect. 3.2, aerosol size distributions exhibit significant enhancements in fine mode aerosol in afternoon periods, with the fine mode comprised almost entirely of organics (particularly in regimes II and III). Further, SV-OOA correlates strongly with DMA number concentration (Pr = 0.62, vs. 0.00 and 0.33 for HOA and LV-OOA, respectively). The regular, significant enhancements in SV-OOA during peak photochemical periods, high correlation with DMA number concentration combined with lower correlations with inorganics (which typically comprise accumulation mode aerosol), and the regular appearance of fine organic modes during afternoons suggests that the SV-OOA factor is comprised of early-generation photochemical products that are chiefly responsible for the growth of fine-mode aerosol in the afternoons. Based on wind patterns discussed in Sect. 3.1, SV-OOA is proposed to consist of secondary organic products on the order of 1–2 h old, based on the transport time from source-rich areas near downtown to the sampling site.

Traditional PMF analysis correlates LV-OOA with sulfate, since SO_4^{2-} is essentially nonvolatile, and SV-OOA with nitrate since NO_3^- is more volatile. These correlations are not necessarily based on mechanistic chemistry, but rather a similarity in volatilities. So there is no reason, on a fundamental chemical basis, that NO_3^- should correlate better with SV-OOA than with LV-OOA. That is, the routes by which semivolatile organics and NO_3^- reach the particle phase are distinctly different chemically. In the Los Angeles aerosol, these distinct pathways result in a relatively poor correlation between SV-OOA and NO_3^-. A better correlation between inorganics and LV-OOA suggests that the pathways by which they reach the aerosol phase are more similar than for SV-OOA in transported Los Angeles Aerosol.

Ng et al. (2011) applied a simple method for making real-time estimates of OA components, based on an empirical scaling factor that relates HOA and OOA (further segregated as SV-OOA and LV-OOA) to signal at fragments *m/z* 57 and *m/z* 44. HOA is estimated by $b \times (C_{57} - 0.1 \times C_{44})$, where b for PACO was found to be 14.0, compared with 13.4 (range = 8.5 – 19.2) for Ng et al. (2011). PACO OOA (combined SV-OOA and LV-OOA) is estimated by $c \times C_{44}$, where c was found to be 8.1 for PACO, compared with 6.6 (range = 2.9 – 9.0) by Ng et al. (2011). The PACO SV-OOA and LV-OOA factors are estimated by $3.3 \times C_{44}$ and $4.8 \times C_{44}$, respectively.

Figure 7 shows the mass fraction of organic accounted for by each organic component during each regime. OA in Los Angeles is overwhelmingly oxidized in nature, with LV- and

SV-OOA combined contributing 77, 92, and 86 % of OA during regimes I, II, and III, respectively. HOA contributed the largest fraction to OA during regime I, in large part due to episodically high HOA concentrations during May and early June. HOA is a minor factor during regimes II and III. SV-OOA is a major constituent of OA during periods of photochemistry, with the hot, dry, photochemically intense regime III seeing the most significant contribution of SV-OOA to OA. LV-OOA dominates in regimes I and II, which were both periods of significant marine/moisture influence and cloud processing.

3.4 Filter analysis

PMF factors are mathematical solutions that return constant mass spectra that are combined linearly to describe variability in AMS data, and it is important to compare PMF results to physical, independent characterizations of OA. For PACO, UPLC-ESI-(+ and −)-MS analysis of high-volume filter samples was performed on 9 selected filters representing periods of high HOA, SV-OOA, and LV-OOA concentrations, in order to distinguish chemical profiles associated with the PMF factors. Periods distinguished as "high SV- and LV-OOA" were chosen such that those species were the single, dominant component of OA. PACO filter sampling did not include any periods in which HOA was the isolated, dominant species, as periods distinguished as "high HOA" were also impacted by high background levels of LV-OOA.

Functional groups of interest in UPLC-ESI-(+)-TOF-MS analysis were basic nitrogen groups (i.e. amines, imines) as well as oxygen-containing moieties (i.e. carbonyls, alcohols, ethers). The complexity of the samples made complete speciation by this technique difficult, but it was possible to identify the majority of the base peaks. Non-oxygenated nitrogenous compounds likely to be amines were detected in significant concentrations and with some variety of carbon chain-length (C8–C16) in the high HOA + LV-OOA periods, as well as during morning periods in which background LV-OOA dominated the organic fraction. This suggests that amines may be an important class of organic compounds in aged, background Los Angeles aerosol. The most prominent class of compounds in all filters was oxygenated organic species, with increased variety of oxygenated species during periods of significant photochemical organic production.

UPLC-ESI-(−)-TOF-MS offered better mass spectral resolution and more complete identification of base peaks than (+)-mode, allowing for more complete chemical profiles. Phthalic acid is ubiquitous in appreciable quantities in the extractable fraction of Los Angeles OA. Phthalic acid has been identified as a significant product of poly-aromatic hydrocarbon (PAH) photochemistry (Kautzman et al., 2010), so this result suggests that PAHs may be a significant class of precursor VOCs to OA in Los Angeles. The high HOA + LV-OOA samples were characterized by appreciable quantities of nitrogen- and sulfur-containing organics (> 10 % of the extractable, identifiable fraction), which is unique to periods in which both HOA and LV-OOA were high in magnitude. Carboxylic acids were significant during both SV- and LV-OOA periods (> 15 % of extractable, identifiable fraction), though the carboxylic acids identified during SV-OOA periods tended to be longer-chain (C7-C10, as opposed to C4-C9 for LV-OOA periods). Additionally, aerosol in LV-OOA periods tended to have a more complex chemical profile, with no single class of compounds dominating the extractable fraction identified by UPLC. This suggests that while the SV- and LV-OOA periods contain many of the same chemical compounds, LV-OOA tends to be characterized by smaller organic acids (higher O:C ratio), as well as a more complex profile of organonitrates, organosulfates, and oxidized acids. As explained in Ulbrich et al. (2009), aerosol partitioning with a bilinear PMF model is inherently limited in fitting a dynamic organic component. With a dataset as large as that represented by PACO, it is not unexpected that the organic component undergoes numerous and significant changes over the course of a single regime. Thus, two unique, constant mass spectra used to describe variability in a bilinear model may be more accurately viewed as two points on a continuum of volatility, rather than two distinct components of differing volatility. This hypothesis is supported by the commonality of compound classes identified by UPLC analysis for SV- and LV-OOA periods. The continuum of oxygenation is further illustrated in Fig. 8, a plot of *m/z* 44 (CO_2^+) vs. *m/z* 43 (mostly $C_2H_3O^+$) proposed by Ng et al. (2010) as a mass spectral diagnostic for the age of organic aerosol. It is hypothesized that LV-OOA components tend to have a higher ratio of *m/z* 44 to *m/z* 43 and represent a lower-

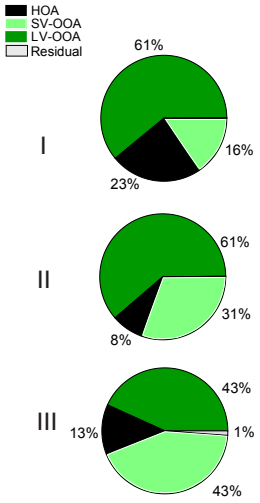

Fig. 7. Mass fraction of total organic accounted for by each PMF factor during regimes I, II, and III.

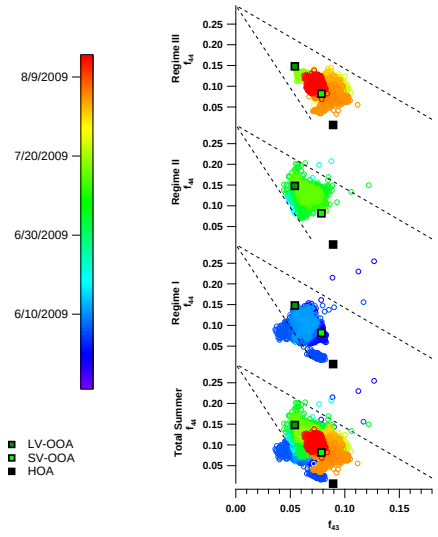

Fig. 8. f_{44} vs. f_{43} for PACO, with color scale corresponding to date. Square markers represent values for HOA, SV-OOA, and LV-OOA factors identified in PACO.

volatility, more-aged organic component with a higher degree of oxidation. Results from PACO indicate that the organic component of Los Angeles aerosol produces a continuum of f_{44} values during each regime and that the most aged organic fraction may actually be characterized by a predominance of longer-chain, oxidized monoacids, complex amines, and nitrate- and sulfate- containing organics. It is concluded that for the Los Angeles aerosol, a bilinear PMF model, with mass spectra assumed to be constant over an entire regime, is helpful in qualitatively assessing the degree of aging of the organic component, but represents a broad simplification of a dynamic organic fraction of aerosol.

3.5 Hygroscopicity

The intensity of scattered light is a strong function of particle diameter (D_p), and since aerosol water uptake largely determines particle size, it is a major variable determining the interaction of particles with radiation. Urban aerosol tends to be dominated by organic material, which is often hydrophobic, leading to overall growth factors (GFs, $D_{p,wet}/D_{p,dry}$) that are smaller than those for pure inorganic aerosol. At RH above the deliquescence RH of common inorganic aerosol constituents, the comparatively low hygroscopicity of organics tends to result in an inverse correlation between organic mass fraction and overall aerosol hygroscopicity (Shinozuka et al., 2009; Quinn et al., 2005; Hersey et al., 2009).

Because urban aerosol is, in part, an external mixture of organic and inorganic components, hygroscopic behavior is often complex, with several GF modes observed (e.g., Cocker et al., 2001; Massling et al., 2005, 2009; Swietlicki et al., 2008; Meier et al., 2009; Tiitta et al., 2010; Rose et al., 2010). The optical sizing method utilized by the DASH-SP provides rapid measurements on timescales suitable for aircraft studies, but does not allow resolution of more than two modes (a nonhygroscopic and hygroscopic mode). During PACO, two modes were typically distinguishable: a nonhygroscopic mode ($1 < GF < 1.15$ at 92 % RH) identified during morning sampling (≤ 30 % of aerosol), decreasing to very minor significance in the afternoon, in addition to a dominant hygroscopic mode that will be the focus of the rest of this section. This suggests that aerosol sampled in the morning included an appreciable fraction of nonhygroscopic particles, with afternoon photochemistry and SOA production resulting in an aerosol of more uniform, unimodal hygroscopicity. Since it was not possible to resolve multiple growth modes, GF data represent the overall subsaturated water uptake behavior for hygroscopic particles.

The DASH-SP measured GF at dry particle sizes of 150, 175, 200, and 225 nm. There was no statistically significant difference between GF at these dry sizes, and so data were averaged to give GFs representative for particles between 150 and 225 nm dry diameter. Particles sampled during morning periods (07:00–11:00 LT) were significantly more hygroscopic at 74 and 92 % than those sampled during afternoon periods (15:00–19:00 LT); morning GF averaged 1.14 ± 0.13, 1.37 ± 0.10, and 1.97 ± 0.45 at 74, 85, and 92 % RH, respectively, while afternoon GF averaged 1.06 ± 0.04, 1.37 ± 0.07, and 1.74 ± 0.20 at 74, 85, and 92 % RH, respectively. Suppressed GF at 74 and 92 % during afternoon sampling but constant GF at 85 % suggests that the hygroscopic growth curve (GF vs. RH) for morning-sampled aerosol is one with a higher GF at lower RHs, combined with a steep ascending section at RH > 85 %, suggestive of a predominantly inorganic aerosol with a small hygroscopic organic component and little nonhygroscopic aerosol.

These GF values are significantly higher than those measured during the 1987 SCAQS study in the eastern Los Angeles Basin (1.23 ± 0.08 for 200 nm particles at 90 ± 3 % RH; Zhang and McMurray, 1993), and are more consistent with the most hygroscopic mode measured in Pasadena in 1999 (1.6 at 89 % RH; Cocker et al., 2001).

Figure 9 shows GF at 74, 85, and 92 % plotted against organic mass fraction (OMF), with markers colored by sampling date and time. PACO data show a clear trend of suppressed GF with increasing organic mass fraction ($Pr = -0.56$, -0.78, -0.71 for 74, 85, and 92 %, respectively). The lowest GFs and highest values of organic mass fraction occur late in PACO, during the dry and photochemically intense regime III characterized by significant photochemical production of SV-OOA.

An increasingly popular representation of aerosol hygroscopicity is the κ parameter, developed by Petters and Kreidenweis (2007). As outlined in Shinozuka et al. (2009), one

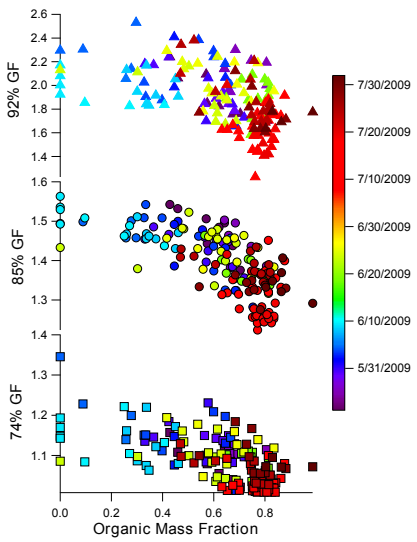

Fig. 9. GF at 74, 85, and 92 % RH plotted against organic mass fraction, with color scale corresponding to date.

can use size-resolved GF data at sub-saturated RH to solve the equation:

$$S(D) = \frac{D^3 - D_d^3}{D^3 - D_d^3(1-\kappa)} \exp\left[\frac{4\sigma M_w}{RT\rho_w D}\right] \quad (2)$$

for κ, where S is the saturation ratio over an aqueous droplet (0.74, 0.85, or 0.92), D and D_d are the humidified and dry diameters, respectively, σ is the surface tension at the interface of air and pure water (0.072 J m^{-2}), M_w is the molecular weight of water (18 g mol^{-1}), R is the gas constant (8.3 J mol^{-1}K^{-1}), T is the temperature (298 K), and ρ_w is the density of water (1 g cm^{-3}). Because the effect of organics on surface tension is not explicitly accounted for in this model, the κ here may be regarded an "effective hygroscopicity parameter", which includes both solute-induced water activity changes and surface tension effects (Petters and Kreidenweis, 2007; Rose et al., 2010).

Using the calculated κ values, one may estimate critical dry diameter (D_d), or the diameter above which aerosol particles activate as cloud consenation nuclei (CCN) at a given saturation ratio (S), using the following equations:

$$\kappa = \frac{4A^3}{27 D_d^3 \ln^2 S} \quad (3)$$

where:

$$A = \frac{4\sigma M_w}{RT\rho_w} \quad (4)$$

Following Shinozuka et al. (2009) and assuming a supersaturation (S_c) of 0.2 %, the relationship between κ and D_d becomes:

$$D_d = \kappa^{(-1/3)} \cdot 70\,\text{nm} \quad (5)$$

Values of κ and critical dry diameter at 0.2 % supersaturation were calculated based on GFs at 85 % RH and dry particle diameter of 200 nm. Uncertainties are estimated to be 25 %, based on sizing uncertainties in the DASH-SP and RH variation in the instrument (Sorooshian et al., 2008). Figure 10 shows κ (left axis) and critical dry diameter (right axis; D_d) plotted against organic mass fraction (OMF), colored by time and date. Kappa values range from 0.15 to 0.51, with an average of 0.31 ± 0.08, while critical diameters ranged from 87 to 131 nm, with an average of 105 ± 10 nm. As with GF data, there is a clear trend of decreasing κ and increasing critical dry diameter with increasing organic mass fraction, with the lowest hygroscopicity and CCN activity occurring during regime III. Earlier periods characterized by more marine influence and higher RH exhibited more hygroscopic behavior. At low values of organic mass fraction, κ approaches that of nitrate and sulfate salts (0.53–0.67), while approaching 0.1 at high organic fracion. Cubison et al. (2008) found that CCN concentrations in eastern Los Angeles were best modeled by treating organics (including the oxidized fraction) as nonhygroscopic. GF- and CCN- derived κ values for hygroscopic organics range from 0.01 to 0.5 (Petters and Kreidenweis, 2007), with only the most hygroscopic organics (i.e. malonic acid) approaching the high end of that range. Results from PACO suggest that organics are moderately hygroscopic, with κ values on the lower end of the range cited by Petters and Kreidenweis (2007).

Shinozuka et al. (2009) presented paramaterizations for calculating as a function of organic mass fraction for 100 nm D_p, dry aerosol in Central Mexico and the North American West Coast ($\kappa = 0.34$–$0.20 \cdot \text{OMF}$ and $\kappa = 0.47$–$0.43 \cdot \text{OMF}$, respectively), and these parameterizations are shown in Fig. 10. Overall, aerosol sampled during PACO are more hygroscopic at a given OMF than those presented in Shinozuka et al. (2009), and are parameterized as $\kappa = 0.50 - 0.29 \cdot \text{OMF}$. This suggests that the organic fraction measured by Shinozuka et al. (2009) inhibits hygroscopicity significantly more than in Los Angeles. It is possible that the organics measured in Central Mexico and off the N. American West Coast exhibit more surface-active behavior, inhibiting hygroscopic activity, or that those organics are predominantly nonhygroscopic. In order to further investigate the hygroscopicity of organics, κ calculations were combined with AMS data giving mass fractions of individual aerosol species in order to estimate a κ value for organics, κ_{org}. If the overall hygroscopicity parameter, κ is given by:

$$\kappa = \sum_{i=1}^{n} \kappa_i \cdot \chi_i, \quad (6)$$

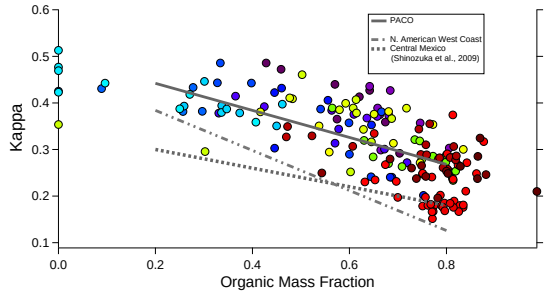

Fig. 10. κ and critical dry diameter plotted against mass fraction organic, with color scale corresponding to date; lines represent empirical parameterizations from PACO, Central Mexico, and N. American West Coast.

where n is the number of chemical constituents, i, with mole fraction χ_i and hygroscopicity parameter κ_i, then the organic hygroscopicity parameter, κ_{org} can be estimated by:

$$\kappa_{\text{org}} = \frac{\kappa - \sum_{i=1}^{n_{\text{inorg}}} \kappa_i \cdot \chi_i}{\chi_{\text{org}}}, \quad (7)$$

where n_{inorg} is the number of inorganic constituents, i, with hygroscopicity parameter κ_i and mole fraction χ_i, and χ_{org} is the mole fraction of organics in the aerosol. Previous publications have assumed κ_{org} of 0.1 for "hygroscopic" organics, and 0 for "nonhygroscopic" organics (Dusek et al., 2010; Wang et al., 2010; Wex et al. , 2010). Assuming κ_i for inorganics to be 0.6 and κ_i for sea salt to be 1.3 (Wex et al. , 2010), Eq. (7) gives κ_{org} of 0.16 for urban background aerosol transported to the PACO sampling site. Assuming κ_i for inorganics to be 0.7 (Dusek et al., 2010) gives κ_{org} of 0.12. Taking a median κ_{org} of 0.14, it is clear that the organics measured during PACO are significantly more hygroscopic than those previously measured in urban areas. This is not unexpected, given the consistently high O:C ratios of organics and the dominance of SV-OOA and LV-OOA during all three regimes of PACO. Further, the PACO sampling site is relatively free from the influence of local sources of primary aerosol, which would have the effect of reducing κ_{org}. Given that organics dominate aerosol in most urban areas, it is potentially significant to find that organics in an important urban center such as Los Angeles would have a value of κ_{org} appreciably higher than previously calculated for urban aerosol.

4 Conclusions

A major ambient sampling experiment was conducted at a site in Pasadena, CA positioned to sample a constant afternoon influx of transported Los Angeles pollution with a photochemical age of roughly 1–2 h and generally free from the influence of local point sources. Sampling spanned 4 months during the summer of 2009, and was characterized by three distinct meteorological regimes: a "springtime" period characterized by clean conditions coincident with low pressure systems (regime I), a typical early-summer period characterized by significant morning marine layer followed by warm, photochemically active afternoons (regime II), and a late-summer period characterized by little marine layer influence, hot and dry conditions, and elevated photochemical activity (regime III).

Chemical analysis of aerosol revealed that OC dominates particulate carbon in Los Angeles (OC:EC average of 8.04), and is enhanced relative to EC by an average of 47 % in the afternoon, suggesting significant SOA production. High RH during marine-layer-influenced morning sampling periods resulted in aqueous processing of aerosol particles and high aerosol volume, while drier afternoon periods saw increased aerosol number and volume due to SOA production. Maxima in aerosol volume occured in the mid-late morning, reflecting a balance between RH-induced hygroscopic growth and SOA production. Maxima in aerosol number tended to occur near 14:00–15:00 LT, indicating that daytime photochemistry tended to generate a fine aerosol mode.

Organics are the most significant constituent of transported Los Angeles aerosol, contributing an average of 42, 43, and 55 % of total submicron mass in regimes I, II, and III, respectively. Interestingly, there was no significant difference between morning and afternoon O:C ratios, suggesting that the constant influx of 1–2 h old aerosol results in an overall organic oxidation state at the sampling site varying little despite significant SOA production. Regime II, characterized by significant morning marine layer influence followed by photochemically active afternoons, displayed significantly higher aerosol mass and 15–25 % higher average O:C ratio, suggesting that aqueous processes may be important in the generation of secondary aerosol and OOA in Los Angeles. Afternoons during regime II and III are characterized by the appearance of a fine organic mode, suggesting that SOA contributes significantly to growth of fine particles. It is unclear whether these fine particles are the result of sulfate nucleation and subsequent SOA growth or SOA condensation on existing primary aerosol.

Water soluble organic mass (WSOM) reaches maxima near 14:00–15:00 LT, coincident with markers for photochemistry and suggesting significant SOA contribution to WSOM. Sulfate is predominantly an accumulation mode constituent, and its magnitude appears to depend on the degree of marine influence. Nitrate is similarly a predominantly accumulation mode species, reaching maxima after morning

rush hour periods. Nighttime nitrate production is observed during periods in which maximum ozone levels indicated significant photochemical events. An ammonium ratio, defined as the moles of ammonium measured divided by the moles of ammonium required to neutralize sulfate and nitrate as $(NH_4)_2SO_4$ and NH_4NO_3, respectively, revealed that ammonia limits particulate $(NH_4)_2SO_4$ and NH_4NO_3 in regimes I and II. An ammonium ratio of 1.28 ± 0.30 in regime III suggests that ammonium was in excess and that organic amines may have been an important constituent of submicron aerosol during this hot, dry, photochemically intense sampling period with reduced marine sulfate influence.

PMF analysis of C-ToF-AMS data resolved three factors, corresponding to HOA, SV-OOA, and LV-OOA, and correlating well with the "standard" factors presented in Ng et al. (2011). The HOA factor appears to be a periodic plume source, generally appearing during or shortly after peaks in CO concentration. SV-OOA displays a strong diurnal pattern, correlating strongly with ozone and the appearance of a fine mode (< 100 nm) in the aerosol size distribution, suggesting that these SOA products are generated on timescales of 1–2 h and tend to comprise a fine aerosol mode. LV-OOA is correlated with inorganic nitrate and sulfate and appears to be an aged carryover organic component that resides in accumulation mode aerosol, but may be generated on short timescales (1–2 h) under extremely oxidizing conditions. Its prevalence during humid overnight and morning hours and enhanced importance in moisture-influenced regimes I and II suggest that there may be significant aqueous-phase sources for LV-OOA. Overall the organic fraction of Los Angeles aerosol is overwhelmingly oxidized, with LV- and SV-OOA contributing 77, 92, and 86 % of OA in regimes I, II, and III, respectively.

Filter analysis by both (+) and (−) mode UPLC-ESI-TOF-MS reveals a complex mixture of organic compounds dominated by oxygenated species. Long (C8-C16), non-oxygenated nitrogenous compounds likely to be amines are detected during periods impacted by high concentrations of background LV-OOA, suggesting that amines may be an important constituent of aged organic aerosol in Los Angeles. Phthalic acid represents a ubiquitous, appreciable fraction of extractable OA, suggesting that PAH photochemistry may be an important pathway for SOA production in Los Angeles. Organo-nitro-sulfate species are observed during periods when aerosol appears to be a mixture of aged background species and freshly emitted particles. Carboxylic acids appear to be major contributers to both SV- and LV-OOA, with LV-OOA tending to be associated with shorter (C4-C9) carboxylic acids and thereby higher O:C ratio.

The organic fraction of transported Los Angeles aerosol is dynamic and undergoes numerous and significant changes on timescales of days to weeks, despite exhibiting consistency in the overall degree of oxidation. Many compounds are common to periods identified as distinct by PMF analysis, and PACO data suggest that Los Angeles OA is best described as a complex, dynamic mixture of compounds that represent a continuum of oxidation. Thus, a bilinear PMF model that assumes constant mass spectra representative of classes of OA is a useful tool in qualitatively assessing the degree of OA aging and oxidation, but is a dramatic simplification of a complex organic fraction.

Finally, aerosol water uptake characteristics measured by the DASH-SP indicate that a bimodal distribution becomes more unimodal during periods of photochemical SOA production. The degree of hygroscopicity of the main hygroscopic mode is highly anti-correlated with organic mass fraction, as indicated by decreasing GF and κ, as well as increasing critical diameter with increased organic fraction. Values for κ averaged 0.31 ± 0.08, approaching 0.5 at low OMF and 0.1 at high OMF. It appears that organics in Los Angeles inhibit hygroscopicity less than those measured in Central Mexico and off the N. American West Coast, potentially owing to less surface-active behavior or an organic fraction comprised of more water soluble species.

PACO represents the first major aerosol characterization in the Western Los Angeles Basin, and comparison with SOAR will help identify spatial variation in Los Angeles aerosol and determine the nature of aerosol evolution as it is transported from source-rich (western) to downwind (eastern) parts of Los Angeles. Further, its timing will serve to contextualize and compare forthcoming results from the CalNex field campaign, part of which involved ground sampling at the PACO site.

Appendix A

PMF analysis

PMF was initiated using 50 seed values, and then again using a range of fpeak values from -1 to 1 varying by 0.1. Figures A1 and A2 show the Q/Q_{expected} values for the different solutions. The PMF results were sorted by regime, number of factors, and seed (only where it caused the solution to vary) and compared to previously published mass spectra in the AMS online Spectral Database explained in Ulbrich et al. (2009). Table A1 shows Pearson's r values comparing the PMF mass spectral profile solutions to existing mass spectra. Table A2 shows Pearson's r values comparing the PMF time series solutions to gas phase tracers, AMS inorganic tracers, PILS tracers, and WSOC. Figure A3 shows total residuals of all masses over time for solutions with different factor numbers. Figure A4 shows the scaled residuals at each mass for the presented 3 factor solution. The 2 and 4 factor solution profiles and time series contributions are shown in Figs. A5a, b.

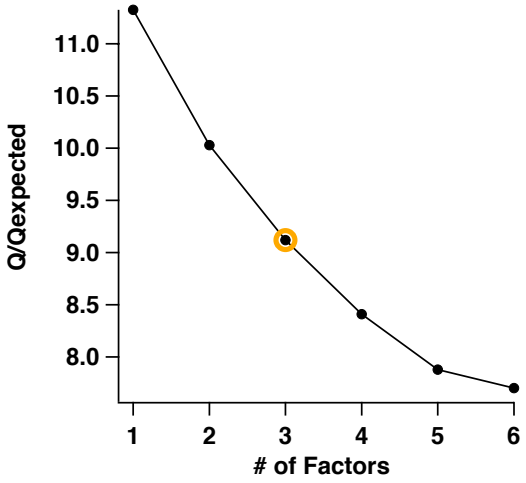

Fig. A1. Q/Q_{exp} values for varying number of factors (p values). The circled marker is the presented solution.

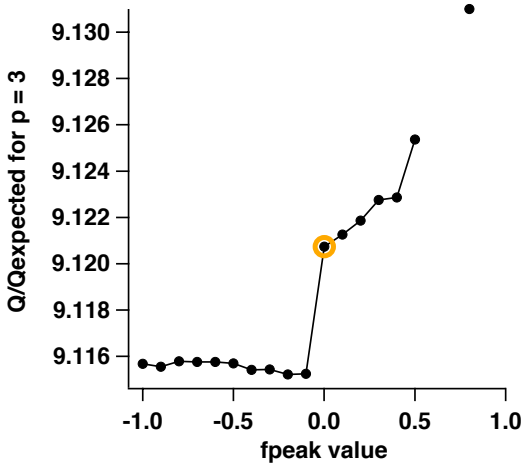

Fig. A2. Q/Q_{exp} for varying fpeak values for $p = 3$. The circled marker is the presented solution.

The difference in the total residuals was noticeable between the 1 and 2 factor solution and the 2 and 3 factor solution, but negligible between the 3 and 4 factor solution. In the 2 factor solution there is evidence of an HOA-like factor and OOA-like factor from the mass spectral comparison, but the when compared to the 3 factor solution, the time series correlations with AMS inorganic and certain gas phase tracers is improved. In the 3 factor case, 3 solutions were explored, and were representative of the 50 possible solutions from the PMF results. Regarding the mass spectral profile, the seed¯6 solution was chosen since it has very strong correlations with the real mass spectra, and each of the profiles are least similar to one another (see the right hand side of Table A2) when compared to the two other 3 factor solutions. When considering the time series comparison, the seed = 6 LV-OOA like factor (factor 1) has the highest correlation with the AMS inorganic species. The p-ToF data suggests the organic profile of LV-OOA has similar particle size distributions to the AMS inorganic species (this was investigated in areas of known LV-OOA like factor and low SV-OOA like factor, since PMF was not performed on pToF data). When the afternoon sun reaches a maximum, there is another, smaller mode that is believed to be SV-OOA, without the strong inorganic signal. Also, the seed = 6 SV-OOA factor correlates best with ozone when compared to the two other solutions. The tracers for HOA were limited in this study since the resolution for the CO and NO_x were poor and the r values are very low. However, when comparing the seed = 6 and seed = 1 solutions, the correlations of the HOA-like factor to CO and NO_x are slightly larger. Additionally, the HOA-like factor was compared to *m/z* 57, which is higher for the seed = 6 solutions. The HOA correlations for the seed = 4 solutions are slightly higher than in the seed = 1 and seed = 6 solutions, but this solution is not as strong mass spectrally, and when comparing the tracers for the two other factors. The four factor situation provided two different solutions, representative of the 50 seeds. In addition to the residuals not changing dramatically, in the mass spectral comparison, for both solutions, two of the factors have very similar r values (factor 1 and 4 for seed 1 and factor 2 and 4 for seed 4). Also, the time series correlations are worse in the four factor solutions, when compared the the presented 3 factor solution.

Table A1. Mass spectral comparison of several PMF solutions.

Mass Spectra Comparison																					
Factor Number (p)	Seed	Brushfire (4)	Manchester high CO low O3 (5)	Pittsburgh HOA (3)	Pittsburgh HOA(1)	Pittsburgh OOA I (3)	Pittsburgh OOA II (3)	Pittsburgh OOA (1)	Urban Vancouver high O_3 (5)	Urban Vancouver low O_3 (5)	Zurich Summer HOA (2)	Zurich Summer OOA I (2)	Zurich Summer OOA II (2)	Zurich Summer Wood burning (2)	Zurich Winter HOA (2)	Zurich Winter OOA (2)	Zurich Winter Wood burning (2)	Factor 1	Factor 2	Factor 3	Factor 4
1	1	0.96	0.68	0.68	0.51	0.97	0.85	0.97	0.99	0.77	0.44	0.95	0.58	0.64	0.66	0.97	0.81				
1	1	0.94	0.55	0.54	0.35	0.98	0.80	0.98	0.96	0.65	0.30	0.98	0.47	0.62	0.50	0.98	0.76		0.64		
2	1	0.77	0.94	0.97	0.91	0.67	0.78	0.66	0.78	0.96	0.78	0.57	0.76	0.51	0.90	0.61	0.73	0.64			
1	1	0.92	0.50	0.49	0.29	0.98	0.77	0.98	0.94	0.60	0.25	0.98	0.44	0.61	0.42	0.98	0.74		0.56	0.56	
2	1	0.74	0.91	0.95	0.88	0.63	0.73	0.62	0.74	0.93	0.76	0.53	0.71	0.51	0.88	0.56	0.69	0.56		0.94	
3	1	0.74	0.95	0.97	0.93	0.63	0.79	0.63	0.76	0.97	0.79	0.54	0.75	0.48	0.92	0.58	0.70	0.56	0.94		
1	4	0.93	0.66	0.66	0.49	0.93	0.79	0.93	0.93	0.73	0.42	0.89	0.56	0.64	0.55	0.92	0.81		0.92	0.57	
2	4	0.92	0.51	0.50	0.30	0.98	0.78	0.98	0.95	0.61	0.26	0.99	0.45	0.61	0.44	0.98	0.74	0.92		0.39	
3	4	0.59	0.93	0.97	0.96	0.46	0.67	0.45	0.61	0.93	0.83	0.35	0.72	0.39	0.95	0.38	0.58	0.57	0.39		
1	6	0.93	0.52	0.51	0.32	0.98	0.78	0.98	0.95	0.62	0.27	0.98	0.46	0.62	0.45	0.98	0.75		0.41	0.90	
2	6	0.61	0.92	0.96	0.95	0.47	0.65	0.46	0.60	0.92	0.81	0.35	0.71	0.43	0.93	0.39	0.60	0.41		0.73	
3	6	0.94	0.81	0.82	0.68	0.92	0.89	0.92	0.97	0.89	0.58	0.88	0.67	0.62	0.80	0.91	0.82	0.90	0.73		
1	1	0.94	0.57	0.56	0.37	0.98	0.81	0.98	0.97	0.67	0.32	0.98	0.49	0.63	0.54	0.98	0.76		0.89	0.49	0.93
2	1	0.90	0.60	0.59	0.43	0.89	0.74	0.89	0.87	0.66	0.37	0.84	0.54	0.65	0.43	0.87	0.80	0.89		0.53	0.86
3	1	0.61	0.92	0.96	0.94	0.48	0.67	0.48	0.63	0.93	0.81	0.38	0.68	0.41	0.94	0.41	0.58	0.49	0.53		0.56
4	1	0.93	0.69	0.66	0.51	0.95	0.86	0.94	0.96	0.75	0.46	0.92	0.62	0.58	0.60	0.95	0.82	0.93	0.86	0.56	
1	4	0.90	0.60	0.59	0.43	0.89	0.74	0.89	0.87	0.66	0.37	0.85	0.54	0.65	0.43	0.88	0.80		0.89	0.53	0.87
2	4	0.94	0.57	0.56	0.37	0.98	0.81	0.98	0.97	0.67	0.32	0.98	0.49	0.63	0.54	0.98	0.76	0.89		0.49	0.93
3	4	0.61	0.92	0.96	0.94	0.48	0.67	0.48	0.63	0.93	0.81	0.38	0.68	0.41	0.94	0.41	0.58	0.53	0.49		0.56
4	4	0.93	0.69	0.66	0.51	0.95	0.87	0.94	0.96	0.76	0.46	0.92	0.63	0.58	0.60	0.95	0.82	0.87	0.93	0.56	

(1) Zhang, et al., 2005; (2) Lanz et al., 2007; (3) Ulbrich, et al., 2009; (4) Bahreini et al., 2005; (5) Alfarra et al., 2004

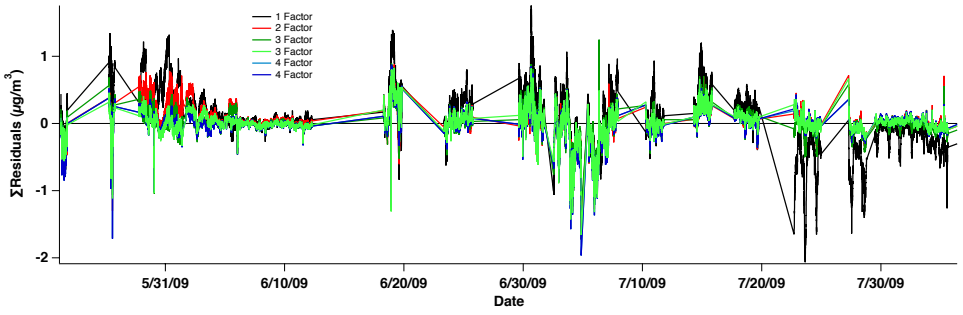

Fig. A3. Sum of the residuals for 1, 2, 3, and 4 factor solutions.

Table A2. Time series comparison of several PMF solutions.

		Gas Phase Tracers			AMS Inorganic Tracers				Organic Tracers		PILS Tracers						
Factor Number (p)	Seed	Ozone	CO	NO_x	SO_4	NO_3	NH_4	Chl	WSOC	org57	NH_4	NO_3	SO_4	Factor 1	Factor 2	Factor 3	Factor 4
1	1	0.51	0.38	0.24	0.66	0.45	0.63	0.35	0.58	0.79	0.70	0.67	0.76				
1	1	0.46	0.33	0.14	0.73	0.45	0.64	0.43	0.53	0.54	0.74	0.69	0.79		0.51		
2	1	0.41	0.34	0.30	0.37	0.31	0.44	0.12	0.30	0.91	0.56	0.56	0.63	0.51			
1	1	0.47	0.33	0.16	0.71	0.44	0.63	0.42	0.56	0.53	0.73	0.68	0.79		−0.02	0.73	
2	1	−0.06	0.15	−0.03	0.23	0.18	0.24	0.06	−0.39	0.61	0.22	0.22	0.20	−0.02		0.00	
3	1	0.51	0.34	0.30	0.43	0.32	0.47	0.18	0.50	0.77	0.60	0.59	0.67	0.73	0.00		
1	4	0.07	0.12	−0.14	0.22	0.29	0.30	0.02	−0.19	0.22	0.10	0.25	0.14		−0.19	−0.02	
2	4	0.47	0.32	0.19	0.66	0.39	0.58	0.40	0.58	0.54	0.71	0.66	0.77	−0.19		0.64	
3	4	0.42	0.35	0.30	0.42	0.31	0.45	0.15	0.36	0.93	0.59	0.58	0.65	−0.02	0.64		
1	6	0.39	0.31	0.09	0.75	0.46	0.65	0.46	0.47	0.49	0.76	0.73	0.81		0.05	0.60	
2	6	0.39	0.17	0.04	0.18	0.15	0.21	0.02	−0.29	0.70	0.16	0.17	0.14	0.05		−0.08	
3	6	0.53	0.31	0.28	0.42	0.31	0.45	0.19	0.56	0.62	0.60	0.58	0.67	0.60	−0.08		
1	1	0.43	0.30	0.15	0.71	0.39	0.58	0.43	0.53	0.52	0.73	0.66	0.79		−0.14	0.26	0.56
2	1	0.01	0.15	−0.07	0.16	0.29	0.26	0.01	−0.22	0.07	0.03	0.20	0.04	−0.14		0.06	−0.18
3	1	0.24	0.29	0.22	0.28	0.19	0.30	0.04	0.16	0.94	0.43	0.43	0.46	0.26	0.06		0.44
4	1	0.51	0.28	0.27	0.31	0.34	0.44	0.13	0.39	0.58	0.57	0.58	0.66	0.56	−0.18	0.44	
1	4	0.01	0.15	−0.07	0.16	0.29	0.26	0.01	−0.23	0.07	0.02	0.20	0.04		−0.15	0.06	−0.18
2	4	0.43	0.30	0.15	0.70	0.39	0.58	0.43	0.54	0.52	0.73	0.66	0.79	−0.15		0.26	0.56
3	4	0.24	0.29	0.22	0.27	0.19	0.30	0.04	0.16	0.94	0.43	0.43	0.46	0.06	0.26		0.43
4	4	0.51	0.28	0.27	0.31	0.34	0.44	0.13	0.39	0.58	0.57	0.58	0.66	−0.18	0.56	0.43	

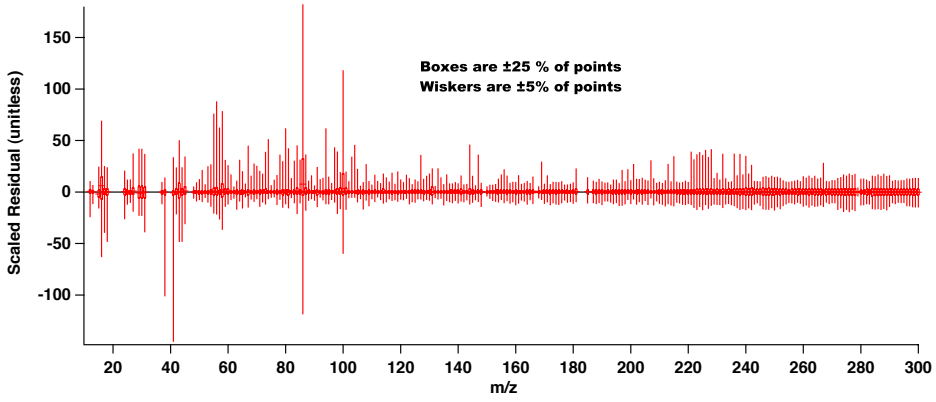

Fig. A4. Scaled residuals for the 3 factor solution (seed = 6).

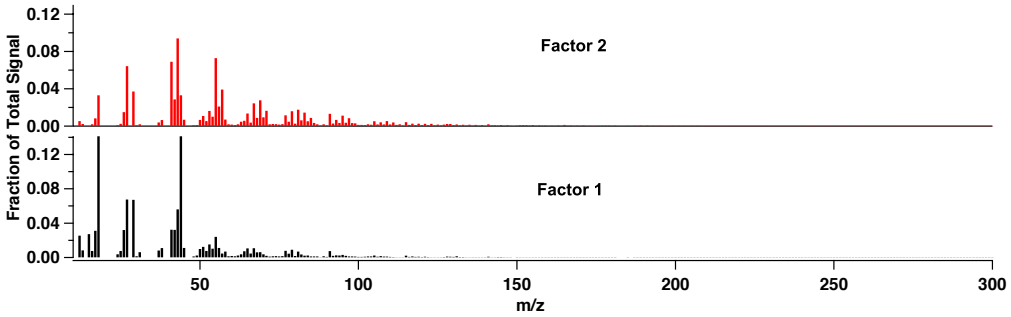

Fig. A5a. Mass spectral profiles for the 2 factor solution.

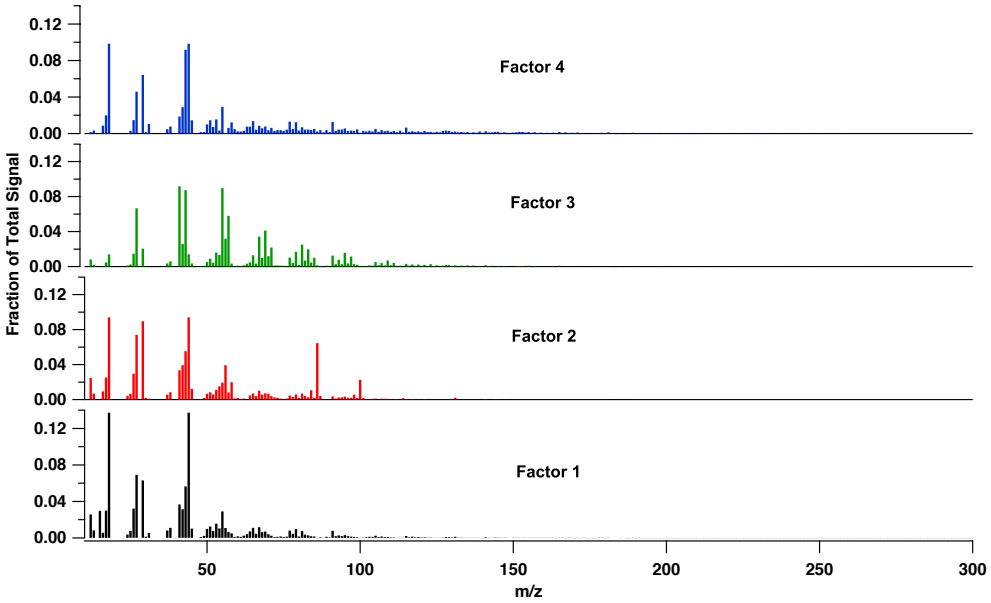

Fig. A5b. Mass spectral profiles for the 4 factor solution.

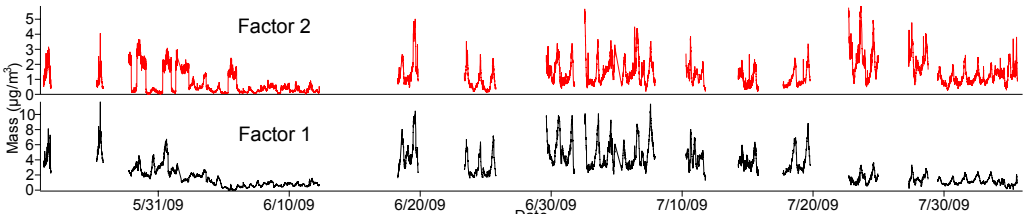

Fig. A6. Time series contributions for the 2-factor solution.

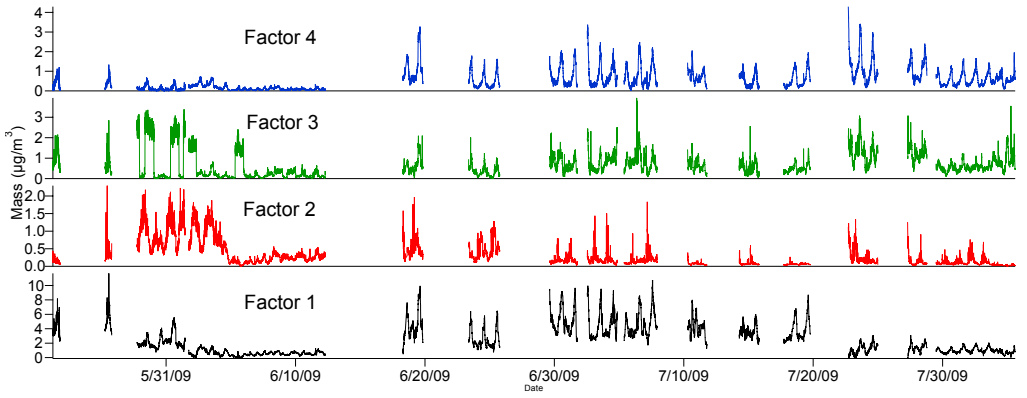

Fig. A7. Time series contributions for the 4-factor solution.

Acknowledgements. Funding was provided by the Electric Power Research Institute. The authors would like to thank Jason Surratt for his helpful comments and direction. We would also like to thank Eric Edgerton and the SEARCH network for guidance on high-volume filter sampling and for the use of a sampler during PACO.

Edited by: M. C. Facchini

References

Aiken, A. C., DeCarlo, P. F., Kroll, J. H., Worsnop, D. R., Huffman, J. A., Docherty, K. S., Ulbrich, I. M., Mohr, C., Kimmel, J. R., Sueper, D., Sun, Y., Zhang, Q., Trimborn, A., Northway, M., Ziemann, P. J., Canagaratna, M. R., Onsach, T. B., Alfarra, M. R., Prevot, A. S. H., Dommen, J., Duplissy, J., Metzger, A., Baltensperger, U., and Jimenez, J. L.: O/C and OM/OC ratios of primary, secondary, and ambient organic aerosols with high-resolution time-of-flight aerosol mass spectrometry, Environ. Sci. Technol., 42, 4478–4485, 2008.

Aiken, A. C., Salcedo, D., Cubison, M. J., Huffman, J. A., DeCarlo, P. F., Ulbrich, I. M., Docherty, K. S., Sueper, D., Kimmel, J. R., Worsnop, D. R., Trimborn, A., Northway, M., Stone, E. A., Schauer, J. J., Volkamer, R. M., Fortner, E., de Foy, B., Wang, J., Laskin, A., Shutthanandan, V., Zheng, J., Zhang, R., Gaffney, J., Marley, N. A., Paredes-Miranda, G., Arnott, W. P., Molina, L. T., Sosa, G., and Jimenez, J. L.: Mexico City aerosol analysis during MILAGRO using high resolution aerosol mass spectrometry at the urban supersite (T0) – Part 1: Fine particle composition and organic source apportionment, Atmos. Chem. Phys., 9, 6633–6653, doi:10.5194/acp-9-6633-2009, 2009.

Alfarra, M., Coe, H., Allan, J., Bower, K., Boudries, H., Canagaratna, M., Jimenez, J., Jayne, J., Garforth, A., Li, S., and Worsnop, D. R.: Characterization of urban and rural organic particulate in the Lower Fraser Valley using two aerodyne aerosol mass spectrometers, Atmos. Environ., 38, 5745–5758, 2004.

Allan, J., Bower, K., Coe, H., Boudries, H., Jayne, J., Canagaratna, M., Millet, D., Goldstein, A., Quinn, P., Weber, R., and Worsnop, D.: Submicron aerosol composition at Trinidad Head, California, during ITCT 2K2: its relationship with gas phase volatile organic carbon and assessment of instrument performance, J. Geophys. Res. Atmos., 109, D23S24, doi:10.1029/2003JD004208, 2004a.

Allan, J., Delia, A., Coe, H., Bower, K., Alfarra, M., Jimenez, J., Middlebrook, A., Drewnick, F., Onasch, T., Canagaratna, M., Jayne, J., and Worsnop, D.: A generalised method for the extraction of chemically resolved mass spectra from aerodyne aerosol mass spectrometer data, J. Aerosol Sci., 35, 909–922, doi:10.1016/j.jaerosci.2004.02.007, 2004b.

Ault, A. P., Gaston, C. J., Wang, Y., Dominguez, G., Thiemens, M. H., and Prather, K. A.: Characterization of the single particle mixing state of individual ship plume events measured at the port of Los Angeles, Environ. Sci. Technol., 44(6), 1954–1961, 2010.

AQMD: Historic ozone air quality trends, available at: http://www.aqmd.gov/smog/o3trend.html, last access: August 2010, 2010.

Bahreini, R., Keywood, M., Ng, N., Varutbangkul, V., Gao, S., Flagan, R., Seinfeld, J., Worsnop, D., and Jimenez, J.: Measurements of secondary organic aerosol from oxidation of cycloalkenes, terpenes, and m-xylene using an Aerodyne aerosol mass spectrometer, Environ. Sci. Technol., 39, 5674–5688, 2005.

Bein, K. J., Zhao, Y. J., Pekney, N. J., Davidson, C. I., Johnston, M. V., and Wexler, A. S.: Identification of sources of atmospheric PM at the Pittsburgh Supersite – Part II: Quantitative comparisons of single particle, particle number, and particle mass measurements, Atmos. Environ., 40, S424–S444, 2006.

Blumenthal, D., White, W., and Smith, T.: Anatomy of a Los Angeles smog episode: pollutant transport in the daytime sea breeze regime, Atmos. Environ., 12, 893–907, 1978.

Bremner, J., Haub, C., Lee, M., Mather, M., and Zuehlke, E.: World Population Highlights: Key Findings From PRB's 2009 World Population Data Sheet, Population Reference Bureau, available at: www.prb.org, 2009.

Cabada, J. C., Rees, S., Takahama, S., Khlystov, A., Pandis, S. N., Davidson, C. I., and Robinson, A. L.: Mass size distributions and size resolved chemical composition of fine particulate matter at the Pittsburgh supersite, Atmos. Environ., 38, 3127–3141, 2004.

Canagaratna, M., Jayne, J., Jimenez, J., Allan, J., Alfarra, M., Zhang, Q., Onasch, T., Drewnick, F., Coe, H., Middlebrook, A., Worsnop, D. R., and Jimenez, J. L.: Chemical and microphysical characterization of ambient aerosols with the aerodyne aerosol mass spectrometer, Mass Spectrom. Rev., 26, 185–222, 2007.

CARB: iADAM Air Quality Data Statistics, California Air Resources Board, available at: http://www.arb.ca.gov/adam/, 2010.

Chow, J. C., Fujita, E. M., Watson, J. G., Lu, Z. Q., Lawson, D. R., and Asbaugh, L. L.: Evaluation of filter-based aerosol measurements during the 1987 Southern California-Quality Study, Environ. Monit. Assess., 30, 49–80, 1994.

Cocker, D. R., Whitlock, N. E., Flagan, R. C., and Seinfeld, J. H.: Hygroscopic properties of Pasadena, California aerosol, Aerosol Sci. Technol., 35, 637–647, 2001.

Croes, B. E. and Fujita, E. M.: Overview of the 1997 Southern California Ozone Study (SCOS97-NARSTO), Atmos. Environ., 37, S3–S26, 2003.

Cubison, M. J., Ervens, B., Feingold, G., Docherty, K. S., Ulbrich, I. M., Shields, L., Prather, K., Hering, S., and Jimenez, J. L.: The influence of chemical composition and mixing state of Los Angeles urban aerosol on CCN number and cloud properties, Atmos. Chem. Phys., 8, 5649–5667, doi:10.5194/acp-8-5649-2008, 2008.

DeCarlo, P. F., Kimmel, J. R., Trimborn, A., Northway, M. J., Jayne, J. T., Aiken, A. C., Gonin, M., Fuhrer, K., Horvath, T., Docherty, K. S., Worsnop, D. R., and Jimenez, J. L.: Field-deployable, high-resolution, time-of-flight aerosol mass spectrometer, Anal. Chem., 78, 8281–8289, 2006.

DeCarlo, P. F., Dunlea, E. J., Kimmel, J. R., Aiken, A. C., Sueper, D., Crounse, J., Wennberg, P. O., Emmons, L., Shinozuka, Y., Clarke, A., Zhou, J., Tomlinson, J., Collins, D. R., Knapp, D., Weinheimer, A. J., Montzka, D. D., Campos, T., and Jimenez, J. L.: Fast airborne aerosol size and chemistry measurements above Mexico City and Central Mexico during the MILAGRO campaign, Atmos. Chem. Phys., 8, 4027–4048, doi:10.5194/acp-8-4027-2008, 2008.

Denkenberger, K. A., Moffet, R. C., Holecek, J. C., Rebotier, T. P., and Prather, K. A.: Real-time, single-particle measurements of oligomers in aged ambient aerosol particles, Environ. Sci. Technol., 41, 5439–5446, 2007.

Dusek, U., Frank, G. P., Curtius, J., Drewnick, F., Schneider,

J., Kürten, A., Rose, D., Andreae, M. O., Borrmann, S., and Pöschl, U.: Enhanced organic mass fraction and decreased hygroscopicity of cloud condensation nuclei (CCN) during new particle formation events, Geophys. Res. Lett., 37, L03804, doi:10.1029/2009GL040930, 2010.

Docherty, K. S., Stone, E. A., Ulbrich, I. M., DeCarlo, P. F., Snyder, D. C., Schauer, J. J., Peltier, R. E., Weber, R. J., Murphy, S. M., Seinfeld, J. H., Grover, B. D., Eatough, D. J., and Jimenez, J. L.: Apportionment of primary and secondary organic aerosols in Southern California during the 2005 Study of Organic Aerosols in Riverside (SOAR-1), Environ. Sci. Technol., 42, 7655–7662, 2008.

Drewnick, F., Schwab, J., Hogrefe, O., Peters, S., Husain, L., Diamond, D., Weber, R., and Demerjian, K.: Intercomparison and evaluation of four semi-continuous $PM_{2.5}$ sulfate instruments, Atmos. Environ., 37, 3335–3350, doi:10.1016/S1352-2310(03)00351-0, 2003.

Drewnick, F., Hings, S., DeCarlo, P., Jayne, J., Gonin, M., Fuhrer, K., Weimer, S., Jimenez, J., Demerjian, K., Borrmann, S., and Worsnop, D.: A new time-of-flight aerosol mass spectrometer (TOF-AMS) – instrument description and first field deployment, Aerosol Sci. Tech., 39, 637–658, doi:10.1080/02786820500182040, 2005.

Eatough, D. J., Grover, B. D., Woolwine, W. R., Eatough, N. L., Long, R., and Farber, R.: Source apportionment of 1 h semi-continuous data during the 2005 Study of Organic Aerosols in Riverside (SOAR) using positive matrix factorization, Atmos. Environ., 42, 2706–2719, 2008.

Eldering, A., Cass, G. R., and Moon, K. C.: An Air monitoring network using continuous particle-size distribution monitors – connecting pollutant properties to visibility via mie scattering calculations, Atmos. Environ., 28, 2733–2749, 1994.

Hersey, S. P., Sorooshian, A., Murphy, S. M., Flagan, R. C., and Seinfeld, J. H.: Aerosol hygroscopicity in the marine atmosphere: a closure study using high-time-resolution, multiple-RH DASH-SP and size-resolved C-ToF-AMS data, Atmos. Chem. Phys., 9, 2543–2554, doi:10.5194/acp-9-2543-2009, 2009.

Huffman, J., Jayne, J., Drewnick, F., Aiken, A., Onasch, T., Worsnop, D., and Jimenez, J.: Design, modeling, optimization, and experimental tests of a particle beam width probe for the aerodyne aerosol mass spectrometer, Aerosol Sci. Tech., 39, 1143–1163, doi:10.1080/02786820500423782, 2005.

Hughes, L. S., Allen, J. O., Salmon, L. G., Mayo, P. R., Johnson, R. J., and Cass, G. R.: Evolution of nitrogen species air pollutants along trajectories crossing the Los Angeles area, Environ. Sci. Technol., 36, 3928–3935, 2002.

Kautzman, K. E., Surratt, J. D., Chan, M. N., Chan, A. W. H., Hersey, S. P., Chhabra, P. S., Dalleska, N. F., Wennberg, P. O., Flagan, R. C., and Seinfeld, J. H.: Chemical composition of gas- and aerosol-phase products from the photooxidation of naphthalene, J. Phys. Chem. A, 114, 913–934, 2010.

Kleeman, M., Hughes, L., Allen, J., and Cass, G.: Source contributions to the size and composition distribution of atmospheric particles: Southern California in September 1996, Environ. Sci. Technol., 33, 4331–4341, 1999.

Kondo, Y., Miyazaki, Y., Takegawa, N., Miyakawa, T., Weber, R. J., Jimenez, J. L., Zhang, Q., and Worsnop, D. R.: Oxygenated and water-soluble organic aerosols in Tokyo, J. Geophys. Res., 112, D01203, doi:10.1029/2006JD007056, 2007.

Lanz, V. A., Alfarra, M. R., Baltensperger, U., Buchmann, B., Hueglin, C., and Prévôt, A. S. H.: Source apportionment of submicron organic aerosols at an urban site by factor analytical modelling of aerosol mass spectra, Atmos. Chem. Phys., 7, 1503–1522, doi:10.5194/acp-7-1503-2007, 2007.

Liu, D. Y., Prather, K. A., and Hering, S. V.: Variations in the size and chemical composition of nitrate-containing particles in Riverside, CA, Aerosol Sci. Technol., 33, 71–86, 2000.

Lu, R. and Turco, R.: Air pollutant transport in a coastal environment – II. Three-dimensional simulations over Los Angeles Basin, Atmos. Environ., 29, 1499–1518, 1995.

Massling, A., Stock, M., and Wiedensohler, A.: Diurnal, weekly, and seasonal variation of hygroscopic properties of submicrometer urban aerosol particles, Atmos. Environ., 39, 3911–3922, 2005.

Massling, A., Stock, M., Wehner, B., Wu, Z. J., Hu, M., Bruggemann, E., Gnauk, T., Herrmann, H., and Wiedensohler, A.: Size segregated water uptake of the urban submicrometer aerosol in Beijing, Atmos. Environ., 43, 1578–1589, 2009.

Matsui, H., Koike, M., Kondo, Y., Takegawa, N., Kita, K., Miyazaki, Y., Hu, M., Chang, S. Y., Blake, D. R., Fast, J. D., Zaveri, R. A., Streets, D. G., Zhang, Q., and Zhu, T.: Spatial and temporal variations of aerosols around Beijing in summer 2006: model evaluation and source apportionment, J. Geophys. Res. Atmos., 114, D00G13, 2009.

Meier, J., Wehner, B., Massling, A., Birmili, W., Nowak, A., Gnauk, T., Brüggemann, E., Herrmann, H., Min, H., and Wiedensohler, A.: Hygroscopic growth of urban aerosol particles in Beijing (China) during wintertime: a comparison of three experimental methods, Atmos. Chem. Phys., 9, 6865–6880, doi:10.5194/acp-9-6865-2009, 2009.

Modey, W. K., Eatough, D. J., Anderson, R. R., Martello, D. V., Takahama, S., Lucas, L. J., and Davidson, C. I.: Ambient fine particulate concentrations and chemical composition at two sampling sites in metropolitan Pittsburgh: a 2001 intensive summer study, Atmos. Environ., 38, 3165–3178, 2004.

Na, K., Sawant, A. A., Song, C., and Cocker, D. R.: Primary and secondary carbonaceous species in the atmosphere of Western Riverside County, California Atmos. Environ., 38, 1345–1355, 2004.

Ng, N. L., Canagaratna, M. R., Zhang, Q., Jimenez, J. L., Tian, J., Ulbrich, I. M., Kroll, J. H., Docherty, K. S., Chhabra, P. S., Bahreini, R., Murphy, S. M., Seinfeld, J. H., Hildebrandt, L., Donahue, N. M., DeCarlo, P. F., Lanz, V. A., Prévôt, A. S. H., Dinar, E., Rudich, Y., and Worsnop, D. R.: Organic aerosol components observed in Northern Hemispheric datasets from Aerosol Mass Spectrometry, Atmos. Chem. Phys., 10, 4625–4641, doi:10.5194/acp-10-4625-2010, 2010.

Ng, N. L., Canagaratna, M. R., Jimenez, J. L., Zhang, Q., Ulbrich, I. M., and Worsnop, D. R.: Real-time methods for estimating organic component mass concentrations from aerosol mass spectrometer data, Environ. Sci. Technol., 45, 910–916, doi:10.1021/es102951k, 2011.

Paatero, P.: A weighted non-negative least squares algorithm for three-way "PARAFAC" factor analysis, Chemom. Intell. Lab. Syst., 38, 223–242, 1997.

Paatero, P. and Tapper, U.: Positive matrix factorization – a nonnegative factor model with optimal utilization of error-estimates of data values, Environmetrics, 5, 111–126, 1994.

Pastor, S. H., Allen, J. O., Hughes, L. S., Bhave, P., Cass, G. R., and Prather, K. A.: Ambient single particle analysis in Riverside, California by aerosol time-of-flight mass spectrometry during the SCOS97-NARSTO, Atmos. Environ., 37, S239–S258, 2003.

Pekney, N. J., Davidson, C. I., Bein, K. J., Wexler, A. S., and Johnston, M. V.: Identification of sources of atmospheric PM at the Pittsburgh Supersite, Part I: single particle analysis and filter-based positive matrix factorization, Atmos. Environ., 40, S411–S423, 2006.

Petters, M. D. and Kreidenweis, S. M.: A single parameter representation of hygroscopic growth and cloud condensation nucleus activity, Atmos. Chem. Phys., 7, 1961–1971, doi:10.5194/acp-7-1961-2007, 2007.

van Pinxteren, D., Bruggemann, E., Gnauk, T., Iinuma, Y., Muller, K., Nowak, A., Achtert, P., Wiedensohler, A., and Herrmann, H.: Size- and time-resolved chemical particle characterization during CAREBeijing-2006: different pollution regimes and diurnal profiles, J. Geophys. Res. Atmos., 114, D00G09, doi:10.1029/2008JD010890, 2009.

Quinn, P., Bates, T., Baynard, T., Clarke, A., Onasch, T., Wang, W., Rood, M., Andrews, E., Allan, J., Carrico, C., Coffman, D., and Worsnop, D. R.: Impact of particulate organic matter on the relative humidity dependence of light scattering: a simplified parameterization, Geophys. Res. Lett., 32(22), L22809, doi:10.1029/2005GL024322, 2005.

Rose, D., Nowak, A., Achtert, P., Wiedensohler, A., Hu, M., Shao, M., Zhang, Y., Andreae, M. O., and Pöschl, U.: Cloud condensation nuclei in polluted air and biomass burning smoke near the mega-city Guangzhou, China – Part 1: Size-resolved measurements and implications for the modeling of aerosol particle hygroscopicity and CCN activity, Atmos. Chem. Phys., 10, 3365–3383, doi:10.5194/acp-10-3365-2010, 2010.

Sawant, A. A., Na, K., Zhu, X., Cocker, K., Butt, S., Song, C., and Cocker III, D. R.: Characterization of $PM_{2.5}$ and selected gas-phase compounds at multiple indoor and outdoor sites in Mira Loma, California, Atmos. Environ., 38, 6269–6278, 2004.

Schauer, J. J., Rogge, W. F., Hildemann, L. M., Mazurek, M. A., and Cass, G. R.: Source apportionment of airborne particulate matter using organic compounds as tracers, Atmos. Environ., 30, 3837–3855, 1996.

Shinozuka, Y., Clarke, A. D., DeCarlo, P. F., Jimenez, J. L., Dunlea, E. J., Roberts, G. C., Tomlinson, J. M., Collins, D. R., Howell, S. G., Kapustin, V. N., McNaughton, C. S., and Zhou, J.: Aerosol optical properties relevant to regional remote sensing of CCN activity and links to their organic mass fraction: airborne observations over Central Mexico and the US West Coast during MILAGRO/INTEX-B, Atmos. Chem. Phys., 9, 6727–6742, doi:10.5194/acp-9-6727-2009, 2009.

Sorooshian, A., Brechtel, F., Weber, R., Corless, A., Flagan, R., and Seinfeld, J.: Modeling and characterization of a particle-into-liquid sampler (PILS), Aerosol Sci. Technol., 40, 396–409, 2006.

Sorooshian, A., Hersey, S., Brechtel, F., Corless, A., Flagan, R., and Seinfeld, J.: Rapid, size-resolved aerosol hygroscopic growth measurements: differential aerosol sizing and hygroscopicity spectrometer probe (DASH-SP), Aerosol Sci. Technol., 42, 445–464, 2008.

Stanier, C., Khlystov, A., and Pandis, S.: Nucleation events during the Pittsburgh Air Quality Study: description and relation to key meteorological, gas phase, and aerosol parameters special issue of aerosol science and technology on findings from the fine particulate matter supersites program, Aerosol Sci. Technol., 38, 253–264, 2004.

Stone, E. A., Snyder, D. C., Sheesley, R. J., Sullivan, A. P., Weber, R. J., and Schauer, J. J.: Source apportionment of fine organic aerosol in Mexico City during the MILAGRO experiment 2006, Atmos. Chem. Phys., 8, 1249–1259, doi:10.5194/acp-8-1249-2008, 2008.

Sullivan, A., Weber, R., Clements, A., Turner, J., Bae, M., and Schauer, J.: A method for on-line measurement of water-soluble organic carbon in ambient aerosol particles: results from an urban site, Geophys. Res. Lett., 31, L13105, doi:10.1029/2004GL019681, 2004.

Sullivan, A., Peltier, R., Brock, C., De Gouw, J., Holloway, J., Warneke, C., Wollny, A., and Weber, R.: Airborne measurements of carbonaceous aerosol soluble in water over Northeastern United States: method development and an investigation into water-soluble organic carbon sources, J. Geophys. Res., 111, 1–14, 2006.

Surratt, J., Gomez-Gonzalez, Y., Chan, A., Vermeylen, R., Shahgholi, M., Kleindienst, T., Edney, E., Offenberg, J., Lewandowski, M., Jaoui, M., Maenhaut, W., Claeys, M., Flagan, R. C., and Seinfeld, J. H.: Organosulfate formation in biogenic secondary organic aerosol, J. Phys. Chem. A, 112, 8345–8378, 2008.

Swietlicki, E., Hansson, H., Hameri, K., Svenningsson, B., Massling, A., McFiggans, G., McMurry, P., Petaja, T., Tunved, P., Gysel, M., Topping, D., Weingartner, E., Baltensperger, U., Rissler, J., Wiedensohler, A., and Kulmala, M.: Hygroscopic properties of submicrometer atmospheric aerosol particles measured with H-TDMA instruments in various environments – a review, Tellus B, 60, 432–469, 2008.

Tiitta, P., Miettinen, P., Vaattovaara, P., Joutsensaari, J., Pet, T., Virtanen, A., Raatikainen, T., Aalto, P., Portin, H., Romakkaniemi, S., Kokkolab, H., Lehtinena, E. J., Markku, K., and Laaksonena, A.: Roadside aerosol study using hygroscopic, organic and volatility TDMAs: characterization and mixing state, Atmos. Environ., 44, 976–986, 2010.

Turpin, B. J. and Huntzicker, J. J.: Secondary formation of organic aerosol in the Los-Angeles Basin – a descriptive analysis of organic and elemental carbon concentrations, Atmos. Environ. A, 25, 207–215, 1991.

Turpin, B. J. and Lim, H.-J.: Species contributions to $PM_{2.5}$ mass concentrations: revisiting common assumptions for estimating organic mass, Aerosol Sci. Technol., 35, 602–610, 2001.

Ulbrich, I. M., Canagaratna, M. R., Zhang, Q., Worsnop, D. R., and Jimenez, J. L.: Interpretation of organic components from Positive Matrix Factorization of aerosol mass spectrometric data, Atmos. Chem. Phys., 9, 2891–2918, doi:10.5194/acp-9-2891-2009, 2009.

Ulbrich, I. M., Lechner, M., and Jimenez, J. L.: AMS Spectral Database, available at: http://cires.colorado.edu/jimenez-group/AMSsd/, 2009.

Wang, J., Cubison, M. J., Aiken, A. C., Jimenez, J. L., and Collins, D. R.: The importance of aerosol mixing state and size-resolved composition on CCN concentration and the variation of the importance with atmospheric aging of aerosols, Atmos. Chem. Phys., 10, 7267–7283, doi:10.5194/acp-10-7267-2010, 2010.

Watson, J. G., Chow, J. C., Lu, Z. Q., Fujita, E. M., Lowenthal, D. H., Lawson, D. R., and Ashbaugh, L. L.: Chemical mass-balance source apportionment of $PM_{(10)}$ during the Southern California Air-Quality Study, Aerosol Sci. Technol., 21, 1–36, 1994.

Wex, H., McFiggans, G., Henning, S., and Stratmann, F.: Influence of the external mixing state of atmospheric aerosol on derived CCN number concentrations, Geophys. Res. Lett., 37, L10805, doi:10.1029/2010GL043337, 2010.

Wittig, A. E., Anderson, N., Khlystov, A. Y., Pandis, S. N., Davidson, C., and Robinson, A. L.: Pittsburgh air quality study overview, Atmos. Environ., 38, 3107–3125, 2004.

Yue, D. L., Hu, M., Wu, Z. J., Wang, Z. B., Guo, S., Wehner, B., Nowak, A., Achtert, P., Wiedensohler, A., Jung, J., Kim, Y. J., and Liu, S.: Characteristics of aerosol size distributions and new particle formation in the summer in Beijing, J. Geophys. Res. Atmos., 114, D00G12, doi:10.1029/2008JD010894, 2009.

Zhang, X. and McMurray, S.: Mixing characteristics and water content of submicron aerosols measured in Los Angeles and at the Grand Canyon, Atmos. Environ. A, 27, 1593–1607, 1993.

Zhang, Q., Alfarra, M., Worsnop, D., Allan, J., Coe, H., Canagaratna, M., and Jimenez, J.: Deconvolution and quantification of hydrocarbon-like and oxygenated organic aerosols based on aerosol mass spectrometry, Environ. Sci. Technol., 39, 4938–4952, 2005.

Zhang, Q., Jimenez, J. L., Canagaratna, M. R., Allan, J. D., Coe, H., Ulbrich, I., Alfarra, M. R., Takami, A., Middlebrook, A. M., Sun, Y. L., Dzepina, K., Dunlea, E., Docherty, K., DeCarlo, P. F., Salcedo, D., Onasch, T., Jayne, J. T., Miyoshi, T., Shimono, A., Hatakeyama, S., Takegawa, N., Kondo, Y., Schneider, J., Drewnick, F., Borrmann, S., Weimer, S., Demerjian, K., Williams, P., Bower, K., Bahreini, R., Cottrell, L., Griffin, R. J., Rautiainen, J., Sun, J. Y., Zhang, Y. M., and Worsnop, D. R.: Ubiquity and dominance of oxygenated species in organic aerosols in anthropogenically-influenced Northern Hemisphere midlatitudes, Geophys. Res. Lett., 34, L13801, doi:10.1029/2007GL029979, 2007.

Chapter 6

Black Carbon Aerosol Over the Los Angeles Basin During CalNex[1]

[1]This chapter is reproduced by permission from "Black Carbon Aerosol Over the Los Angeles Basin During CalNex" by A. R. Metcalf, J. S. Craven, J. J. Ensberg, J. Brioude, W. Angevine, A. Sorooshian, H. T. Duong, H. H. Jonsson, R. C. Flagan, and J. H. Seinfeld, *Journal of Geophysical Research*, 117, D00V13, doi:10.1029/2011JD017255, 2012. An edited version of this paper was published by AGU.

JOURNAL OF GEOPHYSICAL RESEARCH, VOL. 117, D00V13, doi:10.1029/2011JD017255, 2012

Black carbon aerosol over the Los Angeles Basin during CalNex

A. R. Metcalf,[1] J. S. Craven,[2] J. J. Ensberg,[2] J. Brioude,[3] W. Angevine,[3] A. Sorooshian,[4,5] H. T. Duong,[4] H. H. Jonsson,[6] R. C. Flagan,[1,2] and J. H. Seinfeld[1,2]

Received 1 December 2011; revised 13 March 2012; accepted 14 March 2012; published 20 April 2012.

[1] Refractory black carbon (rBC) mass and number concentrations were quantified by a Single Particle Soot Photometer (SP2) in the CalNex 2010 field study on board the Center for Interdisciplinary Remotely-Piloted Aircraft Studies (CIRPAS) Twin Otter in the Los Angeles (LA) Basin in May, 2010. The mass concentrations of rBC in the LA Basin ranged from 0.002–0.530 μg m^{-3}, with an average of 0.172 μg m^{-3}. Lower concentrations were measured in the Basin outflow regions and above the inversion layer. The SP2 afforded a quantification of the mixing state of rBC aerosols through modeling the scattering cross-section with a core-and-shell Mie model to determine coating thickness. The rBC particles above the inversion layer were more thickly coated by a light-scattering substance than those below, indicating a more aged aerosol in the free troposphere. Near the surface, as the LA plume is advected from west to east with the sea breeze, a coating of scattering material grows on rBC particles, coincident with a clear growth of ammonium nitrate within the LA Basin and the persistence of water-soluble organic compounds as the plume travels through the outflow regions. Detailed analysis of the rBC mixing state reveals two modes of coated rBC particles; a mode with smaller rBC core diameters (~90 nm) but thick (>200 nm) coating diameters and a mode with larger rBC cores (~145 nm) with a thin (<75 nm) coating. The "weekend effect" in the LA Basin results in more thickly coated rBC particles, coinciding with more secondary formation of aerosol.

Citation: Metcalf, A. R., J. S. Craven, J. J. Ensberg, J. Brioude, W. Angevine, A. Sorooshian, H. T. Duong, H. H. Jonsson, R. C. Flagan, and J. H. Seinfeld (2012), Black carbon aerosol over the Los Angeles Basin during CalNex, *J. Geophys. Res.*, *117*, D00V13, doi:10.1029/2011JD017255.

1. Introduction

[2] Black carbon is an important atmospheric constituent owing to its role in both air pollution and climate. Refractory black carbon (rBC), alternatively referred to as elemental carbon, light-absorbing carbon, or simply black carbon, is emitted from a variety of incomplete combustion sources, including diesel and gasoline-burning vehicles, residential fuel use, ships, and biomass burning. rBC refers to the strongly light-absorbing component of soot, which may contain other constituents such as polycyclic aromatic hydrocarbons, aliphatic hydrocarbons, and other volatile compounds. rBC, as defined here, is the quantity reported in emission inventories [*Dentener et al.*, 2006] and simulated in regional air quality models [*Binkowski and Roselle*, 2003]. While the majority of atmospheric particulate chemical constituents primarily scatter sunlight, producing an overall cooling effect on climate, rBC absorbs strongly in visible and ultraviolet wavelengths and is the dominant component of light-absorbing atmospheric aerosol. A significant presence of rBC in ambient aerosol can lead to heating of the atmosphere, with effects on atmospheric transport and cloud dynamics [e.g., *Jacobson*, 2002; *Menon et al.*, 2002; *Chung and Seinfeld*, 2005; *Bond*, 2007; *Ramanathan et al.*, 2007; *Ramanathan and Carmichael*, 2008; *Bauer et al.*, 2010; *Ramana et al.*, 2010; *Jones et al.*, 2011].

[3] After emission, rBC particles generally become coated by inorganic and organic (non-absorbing) components via coagulation with other particles and condensation of vapors [e.g., *Riemer et al.*, 2004]. Fresh urban-emitted rBC has typically been shown to be thinly coated with secondary material, while rBC in aged air masses tends to be more thickly coated [*Johnson et al.*, 2005; *Moteki et al.*, 2007; *Shiraiwa et al.*, 2007, 2008; *Schwarz et al.*, 2008a; *Subramanian et al.*, 2010]. In addition, rBC at higher altitudes is found to be more thickly coated than that near the ground [*Schwarz et al.*, 2008b]. Layers of rBC above reflective clouds have an increased radiative forcing per unit

[1]Division of Engineering and Applied Science, California Institute of Technology, Pasadena, California, USA.
[2]Division of Chemistry and Chemical Engineering, California Institute of Technology, Pasadena, California, USA.
[3]Chemical Sciences Division, NOAA Earth System Research Laboratory, Boulder, Colorado, USA.
[4]Department of Chemical and Environmental Engineering, University of Arizona, Tucson, Arizona, USA.
[5]Department of Atmospheric Sciences, University of Arizona, Tucson, Arizona, USA.
[6]Center for Interdisciplinary Remotely-Piloted Aircraft Studies, Naval Postgraduate School, Monterey, California, USA.

0148-0227/12/2011JD017255

Table 1. Urban Black Carbon Measurement Studies

Region	Dates	BC Levels[a] (μg m^{-3})	Measurement Method	Reference
Asia				
Sapporo, Japan	1982	5.1 (2.3–8.0)	ground, filter	*Ohta and Okita* [1990]
Nagoya, Japan	1984–1986	5.3–34.4	ground, filter	*Kadowaki* [1990]
Uji, Japan	1989–1999	2.6	ground, filter	*Hitzenberger and Tohno* [2001]
Sapporo, Japan	1991–1992	3.9 (2.25–6.93)	ground, filter	*Ohta et al.* [1998]
Seoul, Korea	1994	7.6 (4.86–9.86)	ground, filter	*Kim et al.* [1999]
Kaohsiung City, Taiwan	1998–1999	2.2–5.2	ground, filter	*Lin and Tai* [2001]
Mumbai, India	1999	7.5–17.5	ground, filter	*Venkataraman et al.* [2002]
Seoul, Korea	1999	8.4	ground, filter	*Park et al.* [2001]
Beijing, China	1999–2000	6.3–11.1	ground, filter	*He et al.* [2001]
Bangalor, India	2001	0.4–10.2	ground, aethalometer	*Babu et al.* [2002]
Guangzhou, China	2004	7.1 (3.1–19.4)	ground, filter	*Andreae et al.* [2008]
Kanpur, India	2004	6–20	ground, aethalometer	*Tripathi et al.* [2005]
Nagoya, Japan	2004	0.5–1.1	aircraft, SP2	*Moteki et al.* [2007]
Europe				
Orleans, France	1985	2.9	ground, filter	*Del Delumyea and Kalivretenos* [1987]
Paris, France	1985	7.9	ground, filter	*Del Delumyea and Kalivretenos* [1987]
Clermont, France	1985	2.4	ground, filter	*Del Delumyea and Kalivretenos* [1987]
Strasbourg, France	1985	2.9	ground, filter	*Del Delumyea and Kalivretenos* [1987]
Görlitz, Germany	1988–1990	1.3–11.8	ground, filter	*Zier* [1991]
Halle, Germany	1988–1990	1.6–12.0	ground, filter	*Zier* [1991]
Kap Arkona, Germany	1988–1990	0.4–3.5	ground, filter	*Zier* [1991]
Neuglobsow, Germany	1988–1990	0.6–5.2	ground, filter	*Zier* [1991]
Neuhaus, Germany	1988–1990	0.5–3.5	ground, filter	*Zier* [1991]
Potsdam, Germany	1988–1990	1.0–12.3	ground, filter	*Zier* [1991]
Radebeul, Germany	1988–1990	1.4–12.6	ground, filter	*Zier* [1991]
Dushanbe, Russia	1989	4–20	ground, filter	*Hansen et al.* [1993]
Vienna, Austria	1989–1999	2.8	ground, filter	*Hitzenberger and Tohno* [2001]
Arnhem, Netherlands	1994	2.95	ground, filter	*Janssen et al.* [1997]
Po Valley, Italy	1996	1.0 (0.5–1.5)	ground, filter	*Zappoli et al.* [1999]
Paris, France	1997	13.6	ground, filter	*Ruellan and Cachier* [2001]
Thessaloniki, Greece	1997	3.3	ground, filter	*Ruellan and Cachier* [2001]
Thessaloniki, Greece	1997	3.5–8.9	ground, filter	*Chazette and Liousse* [2001]
Liverpool/Manchester, England	2008	0.3	aircraft, SP2	*McMeeking et al.* [2010]
Barcelona, Spain	2009	1.7 (0.7–3.8)	ground, absorption	*Reche et al.* [2011]
Bern, Switzerland	2009	3.5 (1.3–7.1)	ground, absorption	*Reche et al.* [2011]
Huelva, Spain	2009	0.7 (0.1–2.3)	ground, absorption	*Reche et al.* [2011]
London, England	2009	1.9 (0.8–3.4)	ground, aethalometer	*Reche et al.* [2011]
Lugano, Switzerland	2009	1.8 (0.6–3.6)	ground, absorption	*Reche et al.* [2011]
Santa Cruz de Tenerife, Spain	2009	0.8 (0.1–2.6)	ground, absorption	*Reche et al.* [2011]
Paris, France	2010	1.66	ground, aethalometer	*Healy et al.* [2012]
North America				
Akron, Ohio	1985	2.6	ground, filter	*Del Delumyea and Kalivretenos* [1987]
Chicago, Illinois	1985	4.6	ground, filter	*Del Delumyea and Kalivretenos* [1987]
Norfolk, Virginia	1985	3.0	ground, filter	*Del Delumyea and Kalivretenos* [1987]
Chicago, Illinois	1994–1995	0.19–0.45	ground, filter	*Offenberg and Baker* [2000]
Baltimore, Maryland	1997	0.53–2.60	ground, filter	*Brunciak et al.* [2001]
Atlanta, Georgia	1999	1.5 (0.5–3.0)	ground, filter	*Modey et al.* [2001]
Mexico City, Mexico	2003, 2005	0.5–3.0	ground, SP2	*Baumgardner et al.* [2007]
Dallas/Houston, Texas	2006	0.7 (0.65–0.74)	aircraft, SP2	*Schwarz et al.* [2008a]
Mexico City, Mexico	2006	0.276–1.100	aircraft, SP2	*Subramanian et al.* [2010]
South America				
Santiago, Chile	1991	30.6 (11–75)	ground, filters	*Didyk et al.* [2000]

[a]BC levels are campaign average values (and/or range) depending on availability.

mass relative to those below cloud [*Zarzycki and Bond*, 2010].

[4] Available data indicate that a high fraction of atmospheric rBC particles are mixed with other species [*Pósfai et al.*, 1999; *Park et al.*, 2004; *Seinfeld and Pandis*, 2006; *Schwarz et al.*, 2008a; *Huang et al.*, 2011]. A coating of non-absorbing components onto rBC increases the light scattering and absorption cross sections of these mixed-phase particles [*Fuller et al.*, 1999; *Schnaiter et al.*, 2005; *Bond et al.*, 2006; *Mikhailov et al.*, 2006; *Lack and Cappa*, 2010]. The overall single scattering albedo (the fraction of total light extinction due to scattering) of an internally mixed rBC and non-absorbing aerosol population (all particles of a given size have the same composition) is smaller than that of an externally mixed aerosol population (no mixing of species in individual particles) of the same overall composition and concentration, resulting in a net increase in light absorption by the internally mixed aerosol population. In addition, the mixing state of atmospheric aerosols affects the hygroscopic properties of those aerosols, cloud formation, and atmospheric lifetime by wet deposition [*Weingartner et al.*, 1997; *Jacobson*, 2006]. In short, the extent to which rBC is mixed with non-absorbing aerosol components, such as sulfate, nitrate, and organics, exerts a strong influence on its interaction with radiation and water [*Stier et al.*, 2007; *Cubison et al.*, 2008].

Table 2. California Black Carbon Measurement Studies

Region	Dates	BC Levels[a] (μg m^{-3})	Measurement Method	Reference
Bakersfield area				
Edison	July–September, 1990	2.95	ground, filter	*Chow et al.* [1996]
Caliente	July–September, 1990	3.33	ground, filter	*Chow et al.* [1996]
Bakersfield	May, 2010	0.050 (0.040–0.072)	aircraft, SP2	this study
San Joaquin Valley				
Academy	July–September, 1990	1.43	ground, filter	*Chow et al.* [1996]
Buttonwillow	July–September, 1990	1.86	ground, filter	*Chow et al.* [1996]
San Joaquin Valley	May, 2010	0.041 (0.014–0.087)	aircraft, SP2	this study
Long Beach area				
Long Beach	Jan–Dec, 1982	3.75	ground, filter	*Gray et al.* [1986]
Long Beach	Jun–Sep, 1987	0.99	ground, filter	*Chow et al.* [1994]
Long Beach	May, 2010	0.126 (0.010–0.467)	aircraft, SP2	this study
West Los Angeles Basin				
Lennox	Jan–Dec, 1982	4.51	ground, filter	*Gray et al.* [1986]
Downtown LA	Jan–Dec, 1982	4.87	ground, filter	*Gray et al.* [1986]
West Los Angeles	Jan–Dec, 1982	3.61	ground, filter	*Gray et al.* [1986]
Lennox	Jul–Sep, 1984	1.7	ground, filter	*Turpin et al.* [1991]
Downtown LA	Jun–Sep, 1987	2.37	ground, filter	*Chow et al.* [1994]
Hawthorne	Jun–Sep, 1987	0.70	ground, filter	*Chow et al.* [1994]
Diamond Bar	Jan, 1995–Feb, 1996	3.08	ground, filter	*Kim et al.* [2000]
Downtown LA	Jan, 1995–Feb, 1996	3.81	ground, filter	*Kim et al.* [2000]
West LA Basin	May, 2010	0.175 (0.029–0.526)	aircraft, SP2	this study
Pasadena area				
Azusa	Jan–Dec, 1982	3.30	ground, filter	*Gray et al.* [1986]
Burbank	Jan–Dec, 1982	5.04	ground, filter	*Gray et al.* [1986]
Pasadena	Jan–Dec, 1982	3.95	ground, filter	*Gray et al.* [1986]
Duarte	Jan–Dec, 1983	4.35	ground, filter	*Pratsinis et al.* [1988]
Azusa	Jul–Sep, 1984	4.1	ground, filter	*Turpin et al.* [1991]
Pasadena	Jul–Sep, 1984	2.5	ground, filter	*Turpin et al.* [1991]
Azusa	Jun–Sep, 1987	2.64	ground, filter	*Chow et al.* [1994]
Burbank	Jun–Sep, 1987	2.21	ground, filter	*Chow et al.* [1994]
Pasadena	May, 2010	0.179 (0.097–0.381)	aircraft, SP2	this study
East Los Angeles Basin				
Upland	Jan–Dec, 1982	3.14	ground, filter	*Gray et al.* [1986]
Rubidoux	Jan–Dec, 1982	3.03	ground, filter	*Gray et al.* [1986]
Upland	Jul–Sep, 1984	2.8	ground, filter	*Turpin et al.* [1991]
San Bernardino	Jul–Sep, 1984	1.4	ground, filter	*Turpin et al.* [1991]
Claremont	Jun–Sep, 1987	1.92	ground, filter	*Chow et al.* [1994]
Rubidoux	Jun–Sep, 1987	1.73	ground, filter	*Chow et al.* [1994]
Fontana	Jan, 1995–Feb, 1996	3.49	ground, filter	*Kim et al.* [2000]
Rubidoux	Jan, 1995–Feb, 1996	3.25	ground, filter	*Kim et al.* [2000]
Riverside	Feb–May, 2001	0.5–2.7	ground, aethalometer	*Fine et al.* [2004]
Rubidoux	Jun–Aug, 2001	0.8–3.8	ground, aethalometer	*Fine et al.* [2004]
Claremont	Oct, 2001–Mar, 2002	0.3–5.2	ground, aethalometer	*Fine et al.* [2004]
East LA Basin	May, 2010	0.179 (0.047–0.445)	aircraft, SP2	this study

[a]BC levels are campaign average values (and/or range) depending on availability.

[5] Extensive measurements of rBC in urban locations around the globe exist (see Table 1). Wide variability exists in rBC concentrations owing to proximity to emission sources, the environment into and time of year during which the rBC is emitted, the type of combustion source, and the measurement technique used. The extent to which sulfate, nitrate, organics and other species are co-mixed in rBC particles depends on many factors. Sulfate is the dominant secondary component with rBC in many of the locations in which measurements are available. Mexico City and Riverside, CA are two locations, for example, in which nitrate dominates sulfate as the companion species. Regardless of the total concentrations of rBC and other components, the fraction of rBC particles mixed with some amount of secondary material tends to be appreciable in all regions where data are available.

[6] While California has well-documented air quality problems, the state has also taken a leading role in efforts to address air quality and climate change issues. California has ambitious programs to control emissions of pollutants despite the challenges of increased population and demands for goods and services. Studies of the Los Angeles (LA) area are exemplary in terms of the evolution of our understanding of particulate matter in the atmosphere, from the quantification of the contribution of primary emissions from vehicles (diesel and gasoline) [*Schauer et al.*, 1996], to establishing the importance of secondary aerosol formation [*Turpin and Huntzicker*, 1995; *Zhang et al.*, 2007]. Many studies (see Table 2) have measured rBC levels at various locations in California. The first 3D modeling study to treat size-resolved internal mixing of rBC suggested that aerosols containing rBC in LA led to a decrease in daytime surface temperatures but increased nighttime temperatures to a greater extent, causing a net warming [*Jacobson*, 1997]. In the LA Basin, rBC particles are emitted directly from a variety of sources into a rich background of inorganic and organic airborne gaseous and particulate species. Understanding the evolution of rBC-containing particles as they undergo atmospheric

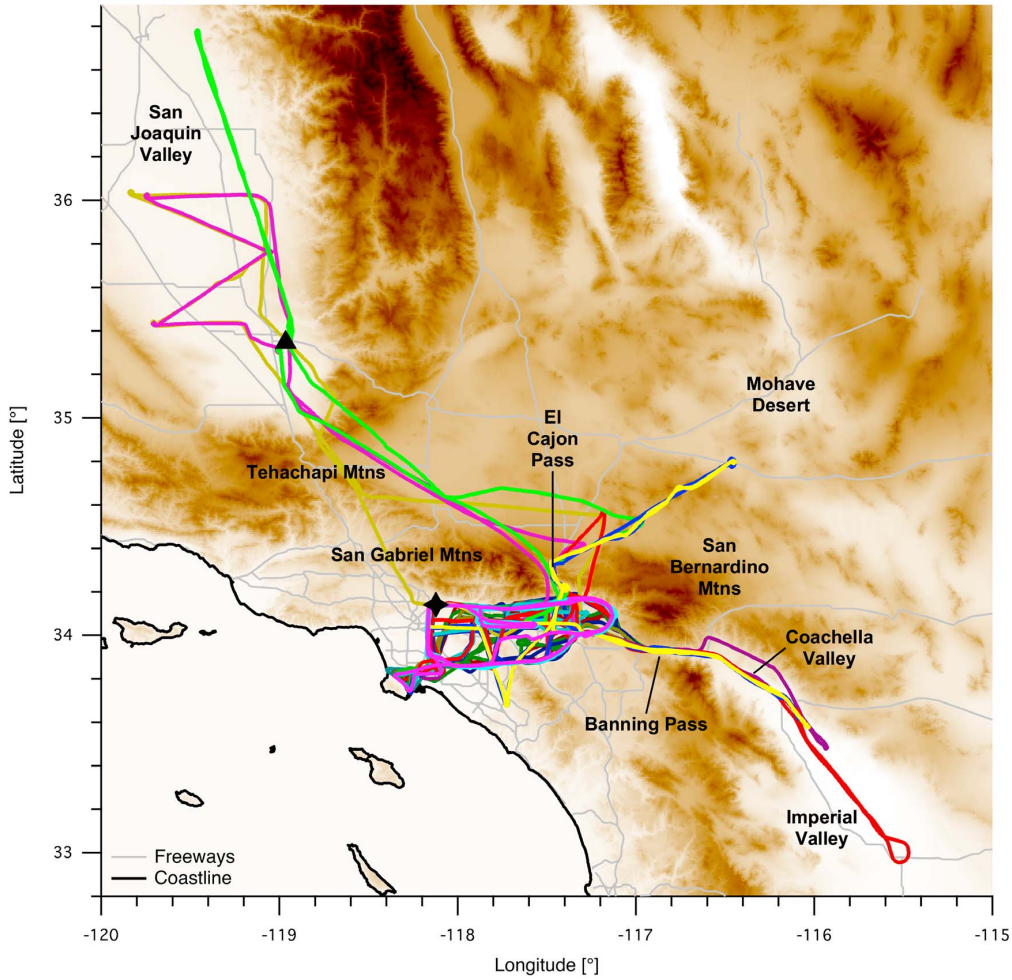

Figure 1. All flight paths (colored lines) of the CIRPAS Twin Otter during CalNex. The star denotes the location of the CalNex LA ground site at Caltech and the triangle denotes the CalNex ground site at Bakersfield. Terrain is shaded brown, with darker colors indicating higher elevation.

aging in this important region provides a unique window on atmospheric gas and particle phase processes.

2. CalNex 2010

[7] The California Research at the Nexus of Air Quality and Climate Change (CalNex) study is a multiagency collaboration aimed at tackling problems related to both air quality and climate change in California (www.esrl.noaa.gov/csd/calnex/). The CalNex study was conducted May–July 2010 in the Los Angeles Basin and southern San Joaquin Valley, involving the NOAA WP-3D aircraft, the CIRPAS Twin Otter aircraft, the NOAA Twin Otter aircraft, the NOAA R/V Ronald H. Brown ship, and two ground-based super-sites, one in Pasadena (34.1405°N, 118.1225°W) on the campus of the California Institute of Technology and one near Bakersfield (35.3463°N, 118.9654°W) in the southern San Joaquin Valley. We report here comprehensive airborne measurements of rBC-containing aerosols in the Los Angeles Basin during May 2010 on the CIRPAS Twin Otter aircraft. Particular focus is paid to rBC concentrations in the Basin, in its outflow regions, and above the inversion layer, as well as the extent to which rBC-containing particles are coated with other species and how this degree of coating varies with location in the Basin and altitude above the surface. The present work is devoted to the actual rBC measurements; subsequent work will address comparison of model predictions and data.

2.1. Climatology of the Los Angeles Basin

[8] The Los Angeles Basin, with a population of about 18 million people, exhibits unique air pollution characteristics and dynamics. Because of the mountainous terrain surrounding the Basin (see Figure 1), airborne species occupy an area of about 1300 km^2, confined near the ground by a relatively shallow day-time mixed layer under 1 km deep [*Robinson*, 1952; *Edinger*, 1959; *Neiburger*, 1969]. The typical daytime sea breeze from the southwest advects emissions toward the north and northeast, exiting the Basin through passes in the

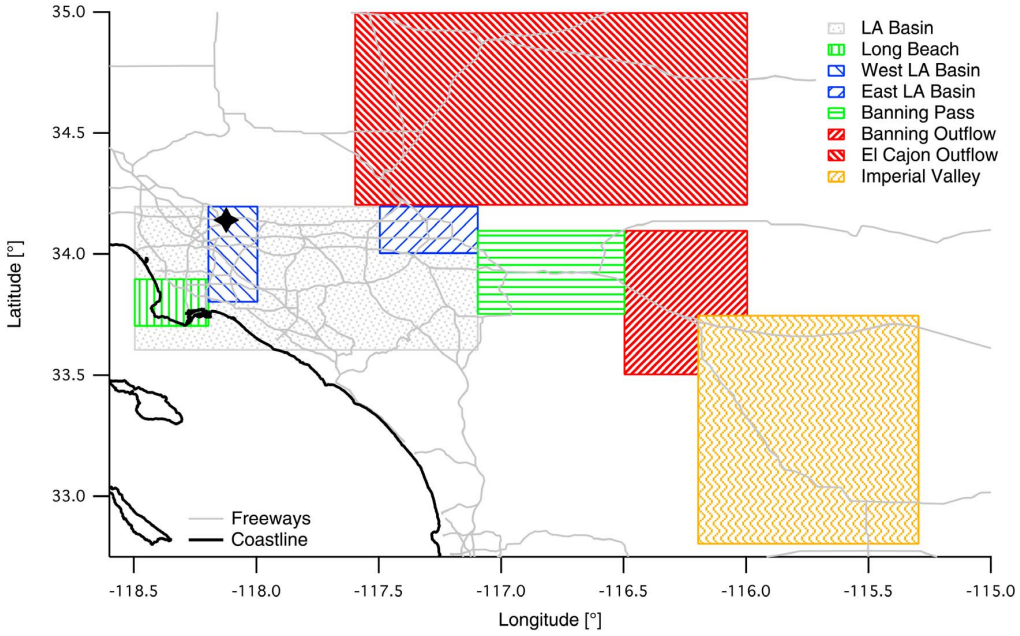

Figure 2. Regional definitions used in Table 4 and elsewhere in the text. Only measurements below the inversion layer are considered.

San Gabriel and San Bernardino mountain ranges to the high desert regions [*Lu and Turco*, 1995]. The two main eastern outflows, the El Cajon and Banning (San Gorgonio) Passes, and one less prominent northern outflow, the Tejon (Newhall) Pass, are not sufficient to completely drain the Basin of its atmospheric contents each day, leading to some degree of carry-over from one day to the next [*Harley et al.*, 2005]. In addition, mountain-flow circulations coupled to the sea breeze can produce multiple layers of pollution in and above the temperature inversion; such layers may mix down to the surface on subsequent days as the boundary layer deepens during its diurnal cycle [*Blumenthal et al.*, 1978; *Wakimoto and McElroy*, 1986; *Moore et al.*, 1991; *Lu and Turco*, 1994, 1995; *Collins et al.*, 2000] or may be subject to long-range transport [*Jaffe et al.*, 1999; *Liu et al.*, 2003; *Liang et al.*, 2004]. Thus, barring a precipitation event, the atmosphere sampled in the LA Basin on any given day contains a mix of fresh and aged material.

[9] For the analysis presented in this work, we have defined several regions of interest in and around the LA Basin (see Figure 2). Given the climatology of the region, we expect the Long Beach and West LA Basin regions to be near major sources of fresh emissions and the Banning Pass and Outflow regions to contain the "LA plume" that has been transported from west to east during the daytime hours.

2.2. FLEXPART Modeling

[10] To track the origins of the specific air masses sampled in the Los Angeles basin during CalNex, a modified version of the FLEXPART Lagrangian particle dispersion model [*Stohl et al.*, 2005] is used to calculate back trajectories of air masses based on advection and turbulent mixing processes. FLEXPART has been used extensively to quantify the impacts of meteorological processes on pollution transport [e.g., *de Foy et al.*, 2006; *Palau et al.*, 2006; *Brioude et al.*, 2009; *Ding et al.*, 2009; *Langford et al.*, 2012]. The main modification for this work consists of using time-averaged winds from the Weather Research Forecasting (WRF version 3.3) meteorology model instead of snapshot winds to improve mass consistency within the FLEXPART model [*Nehrkorn et al.*, 2010]. The WRF output has a spatial grid of 4 km × 4 km, with a temporal resolution of 30 min and 60 vertical levels. In reverse mode, FLEXPART releases virtual tracer particles at receptors, in this case at the instantaneous spatial and temporal location of the Twin Otter aircraft, and integrates their trajectories backward in time using predicted wind fields combined with random turbulent motion. FLEXPART computes the average residence time of the particles in each grid cell (8 km × 8 km) every 2 h over a 24-h period. Surface level contributions to air masses are determined by averaging the residence times of particles between the surface and 200 m altitude.

[11] Figures 3 and 4 present FLEXPART back-trajectory analysis results from three representative flights, May 14 and 15 in Figure 3, and May 25 in Figure 4. In Figure 3, the 12-h integrated residence times reveal the surface history of the air masses sampled in the chosen locations within the LA Basin. The model results for locations on both the western side (Figures 3a and 3b) and the eastern side (Figures 3c and 3d) of the Basin indicate that the dominant airflow in the Basin is the daytime southwesterly sea breeze that advects air masses from Long Beach and downtown LA toward the northeast side of the Basin. FLEXPART results from other LA Basin flights (not shown) paint a similar picture of airflow throughout the LA Basin during the CalNex flights.

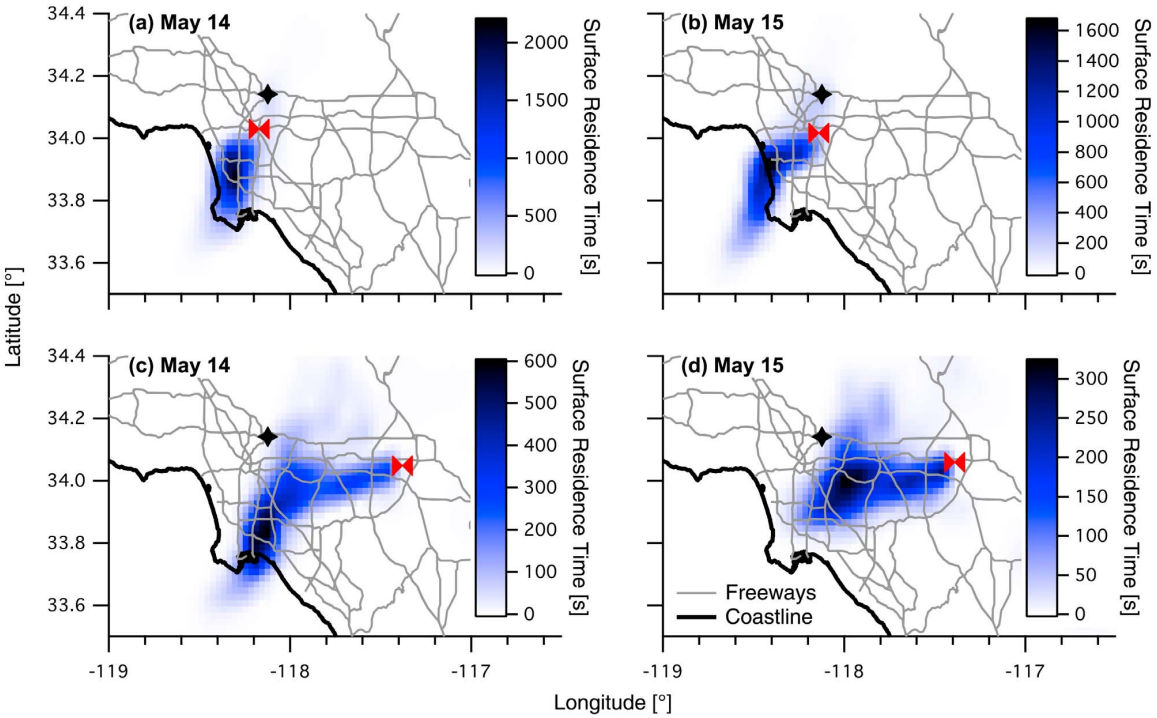

Figure 3. The 12-h integrated surface residence times from FLEXPART during (a and c) the Friday, May 14 flight and (b and d) the Saturday, May 15 flight. Figures 3a and 3b are points on the western side of the LA Basin; Figures 3c and 3d are points on the eastern side of the LA Basin. The red bow-ties denote the location of the Twin Otter aircraft and the stars denote the CalNex LA ground site at Caltech.

[12] Figure 4 displays the FLEXPART results for several locations on the May 25 flight. The left panels are the surface residence times at 4 h prior to sampling and the right panels are the 12-h integrated surface residence times. Figures 4a and 4b show a location approximately halfway between the El Cajon Pass and the farthest sampling point in the El Cajon Outflow region. The surface contribution clearly tails back toward the El Cajon Pass, showing the connection between the LA Basin and the El Cajon Outflow. Figures 4c and 4d show the farthest sampling point in the El Cajon Outflow. At this farthest point from the El Cajon Pass, the tail back toward the Pass is faint, showing that, for this particular day, it takes longer than 12 hours for LA Basin air to reach this location. Figures 4e and 4f show back-trajectories for a location in approximately the center of the Banning Outflow region. The 4-h residence times (Figure 4e) clearly show a connection to the Banning Pass and LA Basin. The 12-h integrated residence times (Figure 4f) show this connection in addition to a smaller circulation within the Coachella Valley. The FLEXPART results for the Imperial Valley sampling location, in Figures 4g and 4h, show no connection to the LA Basin, with both the 4-h (Figure 4g) and 12-h integrated (Figure 4h) back-trajectories indicating flow from the southeast.

2.3. Twin Otter Flights

[13] The Center for Interdisciplinary Remotely-Piloted Aircraft Studies (CIRPAS, Naval Postgraduate School, Monterey, CA, USA) Twin Otter conducted a total of 18 research flights during the month of May, 2010 as part of the CalNex field campaign. Figure 1 shows all 18 Twin Otter flight tracks during CalNex, and Table 3 gives a brief synopsis of each flight. All flights originated from the Ontario International Airport (Ontario, CA, USA). Most sampling was performed at an altitude of about 300 m above ground level at an airspeed of about 50 m s^{-1}. Exceptions were the transits over the San Gabriel and Tehachapi Mountains on the way to the CalNex Bakersfield ground site and the southern San Joaquin Valley. All measurements presented in this work are from instruments inside the unpressurized cabin of the Twin Otter. All instruments are serviced by a two-stage diffusion inlet with a transmission efficiency near unity for particle diameters up to about 3.5 μm [*Hegg et al.*, 2005]. Sampling lines inside the cabin are kept reasonably uniform to all instruments, so further corrections for diffusional losses in these lines have not been made. Owing to a hardware adjustment on the SP2 after the second flight, only data from the final 16 of 18 flights during CalNex are presented here.

[14] A typical flight in the LA Basin consisted of two or three counter-clockwise loops around the Basin, beginning in Ontario and traveling west to Pasadena (passing over the CalNex-LA ground site at Caltech) between the 10 and 210 freeways, then heading south to Long Beach along the 710 freeway to do a loop of missed approaches at the Long Beach and Torrance Airports, then east along the 91 freeway

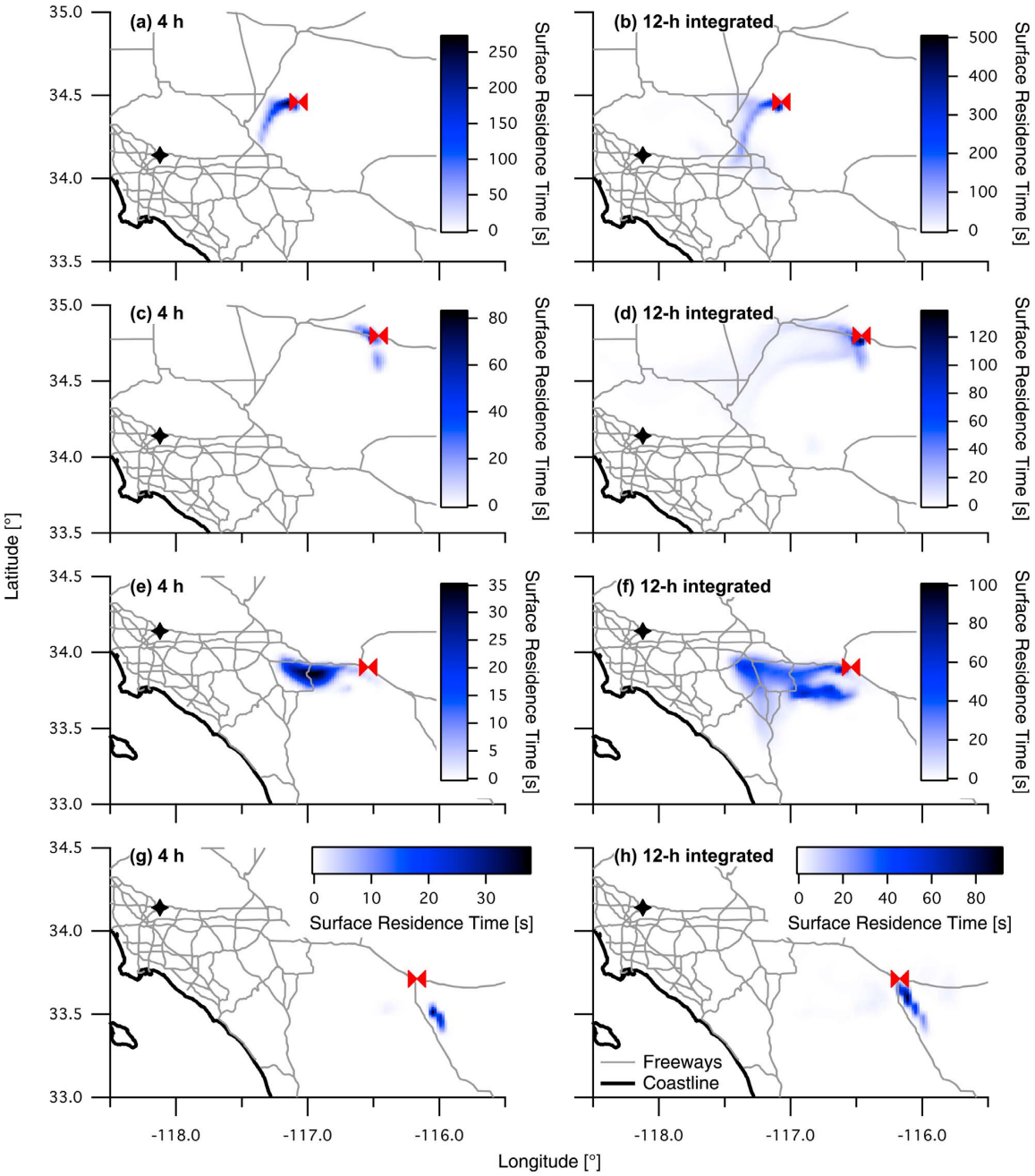

Figure 4. Surface residence time back-trajectories from FLEXPART for the May 25 flight at various regions in the flight: (a and b) midway between the El Cajon Pass and the farthest sampling location in the El Cajon outflow, (c and d) the farthest sampling location in the El Cajon Outflow, (e and f) the Banning Outflow, and (g and h) the Imperial Valley. Figures 4a, 4c, 4e, and 4g are surface residence times at 4 h, showing where the sampled air mass was 4 h prior to sampling. Figures 4b, 4d, 4f, and 4h are 12-h integrated surface residence times, showing the surface contributions for the previous 12 h to the sampled air mass. The red bow-ties denote the location of the Twin Otter aircraft and the stars denote the CalNex LA ground site at Caltech.

Table 3. Summary of CIRPAS Twin Otter Flights During CalNex 2010[a]

Date	Day of Week	Sampling Time (Local Time[b])	Region Sampled
May 4	Tues	11:01–14:23	LA Basin, missed approaches[c]
May 5	Wed	11:04–15:10	LA Basin, missed approaches[c]
May 6	Thu	12:06–15:59	LA Basin
May 7	Fri	11:02–14:57	LA Basin
May 10	Mon	12:00–16:05	LA Basin, western edge
May 12	Wed	10:56–15:08	LA Basin, Imperial Valley
May 13	Thu	11:05–14:54	LA Basin, Imperial Valley
May 14	Fri	10:59–15:01	LA Basin
May 15	Sat	11:13–15:13	LA Basin
May 18	Tue	11:59–15:53	San Joaquin Valley
May 19	Wed	11:40–15:45	LA Basin
May 20	Thu	11:33–15:58	San Joaquin Valley
May 21	Fri	10:57–15:05	LA Basin, outflow regions
May 22	Sat	11:01–15:12	San Joaquin Valley
May 24	Mon	11:01–15:03	LA Basin, outflow regions
May 25	Tue	11:27–15:31	LA Basin, outflow regions
May 27	Thu	10:59–14:45	LA Basin
May 28	Fri	10:58–15:03	LA Basin

[a]The month of May, 2010, in particular, was slightly cooler than normal with a relatively strong coastal marine layer present much of the time. The average high temperature in downtown LA for the month was 19°C, with a maximum high of 24°C on May 29. The average low was 12°C, with the lowest minimum of 10°C on May 25. There were three days (May 17, 18, and 27) with measurable precipitation in downtown LA totaling just 0.11 inches of rain; these days had a particularly strong marine layer leading to measurable drizzle. One day (May 10) had a weak offshore flow, but all others exhibited the typical day-time sea-breeze from the southwest.

[b]Local time is 7 hours behind UTC time.

[c]The missed approaches on the first two flights took place at various small airports scattered throughout the LA Basin. Beginning with May 6 flight, we performed missed approaches only at the Long Beach and Torrance Airports.

to Riverside, turning west along the 210 freeway just before the San Bernardino mountains. During the first two flights, missed approaches were carried out at additional airports throughout the Basin, including Fullerton, Corona, Riverside, Flabob, Banning, Redlands, San Bernardino, Rialto, Cable, Brackett, and El Monte, but these were deemed unnecessary, as little variation in concentrations between an altitude of 15 m and 300 m above ground level were found. Several flights included north–south tracks in order to sample the interior of the Basin, and several flights probed the two main eastern outflows, the El Cajon Pass and the Banning Pass, into the Mohave Desert and Coachella Valley, respectively (see Figure 1).

3. Refractory Black Carbon Measurement

3.1. Single Particle Soot Photometer

[15] rBC mass measurements were made onboard the Twin Otter aircraft with a Droplet Measurement Technologies (DMT, Boulder, CO, USA) Single Particle Soot Photometer (SP2). The SP2 affords measurements of both the particle-by-particle rBC mass as well as the thickness of non-rBC coating on each particle [*Stephens et al.*, 2003; *Baumgardner et al.*, 2004; *Schwarz et al.*, 2006; *Moteki and Kondo*, 2007; *Slowik et al.*, 2007]. The theory of operation and setup of similar SP2 instruments are detailed elsewhere [*Stephens et al.*, 2003; *Schwarz et al.*, 2006, 2010]. Briefly, for each particle traversing the optical cavity of the SP2, 36 μs of signal at 0.2 μs resolution on four detectors, two incandescence and two scattering, are saved for offline analysis. The two incandescence channels detect refractory black carbon mass by measuring the thermal emission from single rBC-containing particles heated to their boiling point when passing through the intense intracavity Nd:YAG laser beam (λ =1064 nm). The two scattering channels detect the scattering cross-section of each particle and are used to determine the mixing state of rBC-containing particles, as detailed below. Note that throughout this work, the rBC volume-equivalent diameter (VED) is calculated from the detected rBC mass by assuming this mass is compacted to a spherical particle with a density of 1.8 g cm^{-3} [*Bond and Bergstrom*, 2006].

[16] Appendix A details the calibration of the Twin Otter SP2. Briefly, the incandescence signals were calibrated with Aquadag (Aqueous Deflocculated Acheson Graphite, Acheson Colloids Company, Port Huron, MI, USA) using the density given by *Gysel et al.* [2011]. The detection range of single-particle rBC mass is 0.48–317 fg (80–696 nm VED). We estimate the uncertainty in mass determination to be ~40%, based largely on the uncertainty in Aquadag mass during calibration, which translates to a ~12% uncertainty in VED. These uncertainties were determined in a similar fashion to previous SP2 studies [*Schwarz et al.*, 2008b; *Shiraiwa et al.*, 2008]. Other rBC standards were tested and the results presented in Appendix A; however, Aquadag is used here because the density is known and samples of Aquadag have been distributed to most SP2 users by DMT, facilitating the inter-comparison of SP2 instruments. Recent results suggest that the SP2 may be up to 40% more sensitive to Aquadag than to ambient rBC particles [*Moteki and Kondo*, 2010; *Laborde et al.*, 2012], but no attempt has been made to correct for this potential bias because it is not yet known how Aquadag relates to ambient rBC particles in the LA Basin. A three-point inter-comparison of the Twin Otter SP2 with the NOAA SP2, which was calibrated with well-characterized Fullerene soot, found that the Twin Otter SP2 response yielded a 12% smaller mass measurement than the NOAA instrument (A. E. Perring, personal communication, 2012). With this potential bias, the mass concentrations reported in this work may be lower than the true ambient values, but the number concentrations are unaffected by this artifact.

[17] The scattering channels were calibrated with dioctyl sebecate (DOS, refractive index = 1.45-0.0*i*), and scattering cross-sections were related to the SP2 signal using Mie theory, as detailed below. For purely scattering ambient particles, we assume a refractive index of 1.5-0.0*i*, in the middle of observed ambient values [*Ensor et al.*, 1972; *Stelson*, 1990; *Stolzenburg et al.*, 1998] and consistent with coating material refractive indices used in this work. The detection range of optical diameter with these assumptions is 169–600 nm. The estimated uncertainty in retrieved scattering amplitude is ~22%, which propagates through Mie theory to an uncertainty of ~5% in optical diameter for purely scattering particles.

3.2. Mixing State Determination

[18] Figure 5 shows the time traces of signal on the four measurement channels of the SP2 for three single particles: an uncoated rBC particle (Figure 5a), a purely scattering particle (Figure 5b), and a coated rBC particle (Figure 5c).

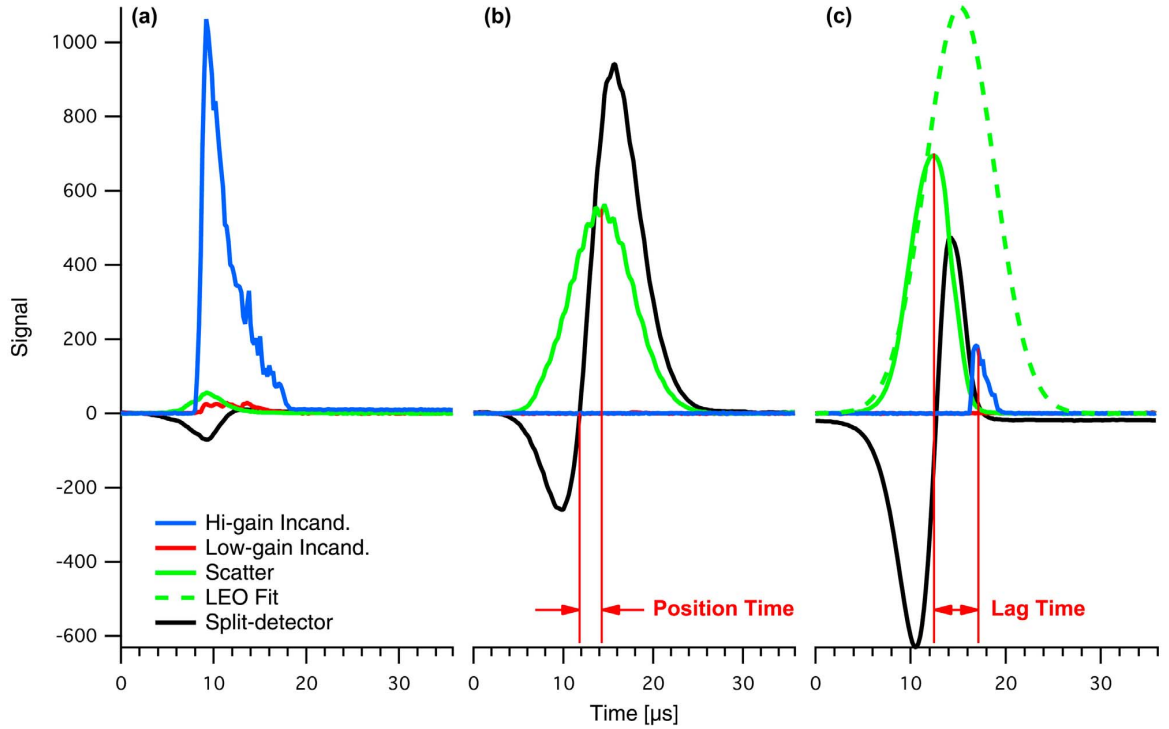

Figure 5. Raw spectra of three single particles measured by the SP2: (a) a 149 nm VED uncoated rBC particle, (b) a 286 nm optical diameter purely scattering particle, and (c) an 83 nm VED rBC core coated by a 237 nm thick layer of a purely scattering substance. "Position Time" labeled in Figure 5b is the time between the zero-crossing of the split-detector signal and the peak of the scatter signal and is used to determine the position of the scatter peak for particles evaporating in the laser beam. "Lag Time" labeled in Figure 5c is the distance between the detected scatter peak and incandescent peak and is used to assess the coating thickness on rBC particles. See the text for a description of the LEO Fit calculation.

An uncoated rBC particle has little or no discernible signal on the scattering channel and, if present, the scattering peak coincides with the incandescent peak, indicating that the scattering arises from the rBC particle itself. A purely scattering particle has no incandescent signal whatsoever, and the scattering signal has the shape of a Gaussian curve. A coated rBC particle exhibits both scattering and incandescing signals.

[19] Typically, as a coated rBC particle heats up in the laser beam of the SP2, the coating material will evaporate, causing the scattering signal to peak and decrease before the onset of the incandescent signal. A parameter often used to describe the coating thickness is the lag time between the peak scattering signal and the peak incandescent signal (labeled in Figure 5c) [*Schwarz et al.*, 2006; *Moteki and Kondo*, 2007]. Previous studies have classified a thickly coated rBC particle as one with a lag time $\geq$2 μs [*Moteki et al.*, 2007]. In this study, we will classify a thickly coated particle as one with a lag time $\geq$1.8 μs, a shift of one data point, or time step, in the single-particle data (Figure 5). This shift is made to reflect the observation (not shown) that there are two distinct populations of lag time in the single-particle data for CalNex, similar to the two populations shown by *Moteki et al.* [2007, Figure 3]. A lag time of 1.8 μs is the point that most clearly separates these two populations in our data set.

[20] Because the coating on rBC particles evaporates before the particle passes through the entire laser beam, the scattering signal is not a true Gaussian shape, as in Figure 5b, and is smaller in amplitude than it should be for the full, unperturbed coated rBC diameter (see the difference in Figure 5c). To retrieve an accurate scattering cross-section and, therefore, optical size for this particle, we use the leading-edge only (LEO) part of the scattering signal to fit the scattering data to the calibration, as outlined by *Gao et al.* [2007]. Figure 5c shows a LEO fit compared to the raw signal, which clearly would have under-sized this coated rBC particle had this correction not been made. Appendix A provides more details of how LEO fitting was calibrated and implemented for the Twin Otter SP2.

3.3. Mie Scattering Model

[21] For purely scattering particles detected by the SP2, we calculate scattering cross-section with Mie theory for a given particle diameter and refractive index, for which we have adapted a version of BHMIE [*Bohren and Huffman*, 1998]. This adaptation involves integrating the scattering function over the solid angles subtended by the SP2

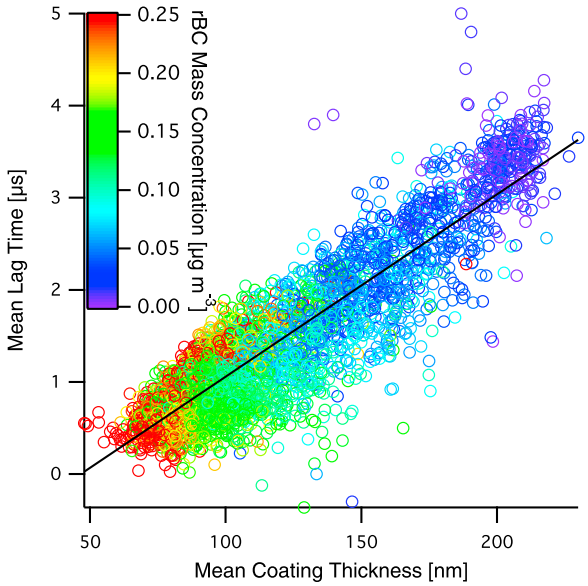

Figure 6. Mean lag time versus mean coating thickness for all 1-min average measurements during CalNex. Marker color indicates rBC mass concentration. Coating thickness is the diameter increase from the rBC VED. The solid black line is a linear fit to the data ($R^2 = 0.797$).

avalanche photodiodes (APDs) to calculate the differential scattering cross-section specifically detected by those APDs rather than the total scattering cross-section. To calculate scattering cross-section for coated rBC particles, we have replaced the scattering coefficients with those for stratified spheres from *Toon and Ackerman* [1981] to create a core-and-shell Mie model. Because the rBC mass is detected with the SP2 incandescence channels, the VED from this mass, with assumed rBC refractive index of 1.95-0.79*i* [*Bond and Bergstrom*, 2006] is treated as a known quantity in the core-and-shell Mie model. An assumed coating refractive index of 1.5-0.0*i*, consistent with earlier published works [*Schwarz et al.*, 2008a, 2008b], leaves coating thickness diameter as the only unknown when comparing measured scattering cross-sections to core-and-shell Mie model scattering cross-sections. The measurements are then fit to the core-and-shell Mie calculations to determine coating thickness diameters. Given an uncertainty in retrieved scattering amplitude of ~22% and an uncertainty in rBC VED of ~12%, uncertainties in coating thicknesses are ~40%, with uncertainty decreasing with increasing coating thickness. For the 1-min average SP2 data, in addition to reporting mean coating thicknesses, the Mie model-derived total coated rBC particle diameter is used to calculate the total particle volume, from which we calculate the coating-only volume by subtracting the calculated rBC core volume.

[22] Previous SP2 studies have emphasized lag time as a way of presenting rBC mixing state [e.g., *Subramanian et al.*, 2010]. Figure 6 relates mean lag times to mean coating thicknesses for all measurements taken during CalNex. The black line is a linear fit of the data ($R^2 = 0.797$; the actual slope and intercept are unimportant) showing a strong correlation between these two variables, as expected. Both measurements are reported because both suffer from limitations. Interpretations of lag times to infer coating thicknesses rely on the aerosol to follow a core-and-shell physical model and for all coatings to evaporate in the SP2 laser at equal rates such that time is related to thickness only and not to coating material as well. Mean coating thicknesses calculated with Mie theory suffer from limited detection range, additional uncertainties in extracting the true scattering peak signal from an evaporating particle, and, again, relies on the core-and-shell physical model to apply.

3.4. The rBC Number and Mass Concentrations

[23] Histograms of single-particle rBC mass onto 500 logarithmically-spaced mass bins between 0.48 and 398 fg (80–750 nm VED) were made for every 1-min of single-particle data. Accumulation mode rBC particle size distributions in the atmosphere have been observed to be single lognormal in nature [*Pueschel et al.*, 1992; *Clarke et al.*, 2004; *Moteki et al.*, 2007; *Schwarz et al.*, 2008a, 2008b]; thus, a single lognormal function is fit to each 1-min number distribution to determine the full distribution over the range of 9.4×10^{-7} to 942 fg (1–1000 nm VED). The fitted mass distributions are implied from the fitted number distributions.

[24] Figure 7 shows examples of typical number and mass distributions measured and fitted for various regions. At very large rBC masses (>300 nm VED), the measurements deviate from the fitted distribution, because at these large masses a single count becomes a significant differential mass (dM) in the distribution. This potential error illustrates the importance of fitting the number distribution to a lognormal, rather than the mass distribution, in order to avoid biasing the fit of the mass distribution. The rBC mass median diameter (MMD) is the VED at the peak of the mass distribution.

[25] The bulk number and mass concentrations are found by integrating each distribution over all sizes and dividing by the sampled volume of air for that 1-min period. The bulk

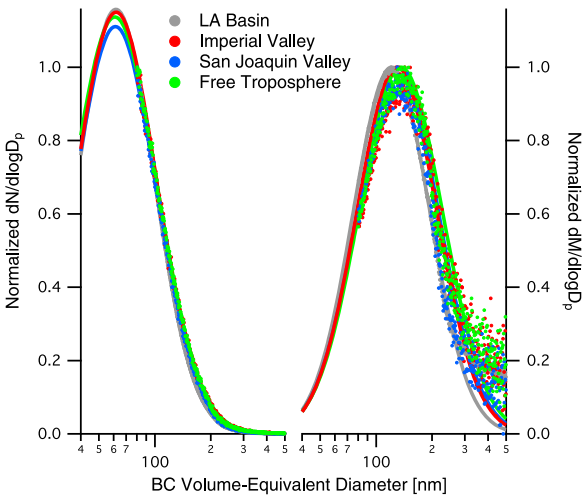

Figure 7. Campaign-average rBC number (left trace) and mass (right trace) distributions by region. Solid lines denote single lognormal fits to the data.

Table 4. Summary of SP2 Measurements Broken Down by Region[a]

Region[b]	rBC Number Concentration (cm^{-3})	rBC Mass Concentration ($\mu g\ m^{-3}$)	Mean Coating Thickness (nm)	Percent Thickly Coated (%)	rBC Mass Fraction (%)	rBC Mass Median Diameter (nm)
LA Basin	267 (288 ± 136)	0.154 (0.167 ± 0.0828)	99 (20)	37 (11)	2.4 (1.3)	122 (7)
Long Beach	187 (199 ± 121)	0.112 (0.126 ± 0.0777)	99 (23)	38 (13)	2.8 (0.9)	130 (7)
Pasadena	289 (321 ± 109)	0.164 (0.179 ± 0.0647)	94 (14)	29 (9)	2.8 (1.2)	120 (3)
West LA Basin	280 (309 ± 149)	0.159 (0.175 ± 0.0873)	93 (20)	32 (10)	2.4 (1.0)	123 (7)
East LA Basin	274 (295 ± 119)	0.159 (0.179 ± 0.0782)	102 (20)	41 (10)	2.1 (1.2)	122 (4)
Banning Pass	162 (162 ± 77)	0.0907 (0.0954 ± 0.0445)	135 (29)	55 (13)	2.0 (1.0)	126 (6)
Basin Outflows	136 (165 ± 104)	0.0792 (0.0978 ± 0.0619)	138 (33)	47 (15)	4.5 (2.3)	127 (7)
Banning Outflow	129 (136 ± 71)	0.0703 (0.0690 ± 0.0265)	144 (28)	54 (15)	4.9 (1.7)	130 (10)
El Cajon Outflow	130 (173 ± 110)	0.0868 (0.105 ± 0.0662)	136 (34)	52 (13)	4.4 (2.3)	129 (7)
Imperial Valley	93 (107 ± 61)	0.0616 (0.0671 ± 0.0293)	156 (17)	65 (8)	5.3 (2.6)	141 (10)
San Joaquin Valley	60 (67 ± 33)	0.0408 (0.0414 ± 0.0143)	153 (20)	58 (13)	1.0 (0.6)	130 (8)
Bakersfield	86 (82 ± 19)	0.0472 (0.0502 ± 0.0102)	145 (14)	52 (6)	1.3 (0.5)	127 (5)
Free Troposphere	14 (54 ± 90)	0.0167 (0.0346 ± 0.0454)	188 (31)	76 (13)	1.7 (2.8)	161 (41)

[a]The concentrations are campaign medians (mean ± 1σ); all other values are campaign-average values (±1σ).
[b]Region definitions are given in Figure 2.

values reported here are derived from the fitted distributions. Uncertainties in the bulk concentrations are dominated by the single-particle mass uncertainty; thus, additional uncertainties due to flow fluctuations are negligible. Because the fitted range captures a wider diameter range than the detection limits of the SP2, the calculated rBC number and mass concentrations are higher than those corresponding to the strict detection range of the instrument. The number concentration nearly doubles because of this adjustment, while the mass concentration is about 15–20% larger.

4. Results and Discussion

4.1. Regional Variability in rBC Aerosol

[26] Over the entire monthlong campaign, rBC mass concentrations in the LA Basin varied from 0.002 to 0.530 $\mu g\ m^{-3}$, with smaller values measured in regions outside of the Basin (see Table 4). rBC-containing particle number concentrations ranged from as low as 3 cm^{-3} up to 1180 cm^{-3}. Figure 8 shows rBC mass concentrations for 12 flights in the LA Basin. On the May 28 flight (Figure 8l), the spikes in mass concentration on the southeast corner of the sampling pattern are the result of flying through a dense smoke plume from a tanker truck fire on the 91 freeway. These spikes have been removed for the calculated values in Tables 2 and 4. The anomalously low concentrations on the southern side of the LA Basin on May 6 (Figure 8a), in the central Basin on May 15 (Figure 8g), and on the northeast corner of the Basin on May 21 (Figure 8i) are a result of sampling above the inversion layer; all other measurements were made at ~300 m above ground level. Figure 9 shows a typical flight contrasting the measurements between the LA Basin and its two eastern outflow regions.

[27] From Figure 8, together with Figure 9a, a pattern of higher rBC mass concentrations occurring on the north side of the Basin emerges. These larger concentrations to the north are the result of a southwesterly sea breeze during the day (see Figure 3) that transports rBC emissions up against the San Gabriel mountains, where the terrain and typically shallow mixed layer collect the air mass prior to exiting the Basin. One might expect enhanced emissions from the Port of Long Beach and the industries (refineries) in the area; however, except for a few spikes in the data near Long Beach, this region is generally characterized by lower concentrations of rBC as compared with the northern side of the LA Basin (see also Table 4).

[28] Table 4 presents a detailed regional breakdown of the SP2 measurements during CalNex. Except for the free troposphere, all measurements are from below the inversion layer, with region definitions given in Figure 2. Within the LA Basin, rBC concentrations are fairly uniform throughout, because the region definitions do not distinguish north and south Basin as discussed above. The rBC mass concentrations in the LA Basin are higher than in the outflow regions (Figure 9a). The mean coating thickness and percent thickly coated both increase from west to east, indicating that the rBC particles are becoming more thickly coated. Moving into the outflows, the rBC continues to become more thickly coated, with the thickest coatings (except for the free troposphere) occurring at the farthest points from the LA Basin (see also Figures 9c and 9d). rBC mass fraction increases in the outflows, despite a decrease in rBC number and mass concentrations, owing to the evaporation of volatile species from the aerosol as the plume is diluted over the desert regions.

[29] Minor differences exist in the mass median diameter of the rBC core aerosol between regions (see Figures 7 and 9b). The MMD is the smallest in the LA Basin, at about 122 nm, indicating the rBC in the Basin is characteristic of fresh urban emissions that tend to have smaller rBC cores [e.g., *McMeeking et al.*, 2010; *Schwarz et al.*, 2008a]. The MMD is smaller by 30–70 nm than most other urban measurements found in the literature [see *McMeeking et al.*, 2010, Table 5]. Most comparable to the Los Angeles values observed are those of fresh rBC emissions at Cranfield airfield in England, which exhibited values near 130 nm [*McMeeking et al.*, 2010], and of the Tokyo, Japan outflow, which exhibited values of 145–150 nm [*Shiraiwa et al.*, 2007]. The MMD of rBC in the Imperial Valley is larger than that in the LA Basin and its outflow regions, indicating an air mass of a different origin. Figures 4g and 4h support this conclusion, showing that the air mass originates from the southeast of its sampling location.

4.2. Secondary Aerosol Chemical Composition

[30] Particle mass and composition measurements were made by an Aerodyne compact time-of-flight aerosol mass spectrometer (C-ToF-AMS, Aerodyne Research, Inc.,

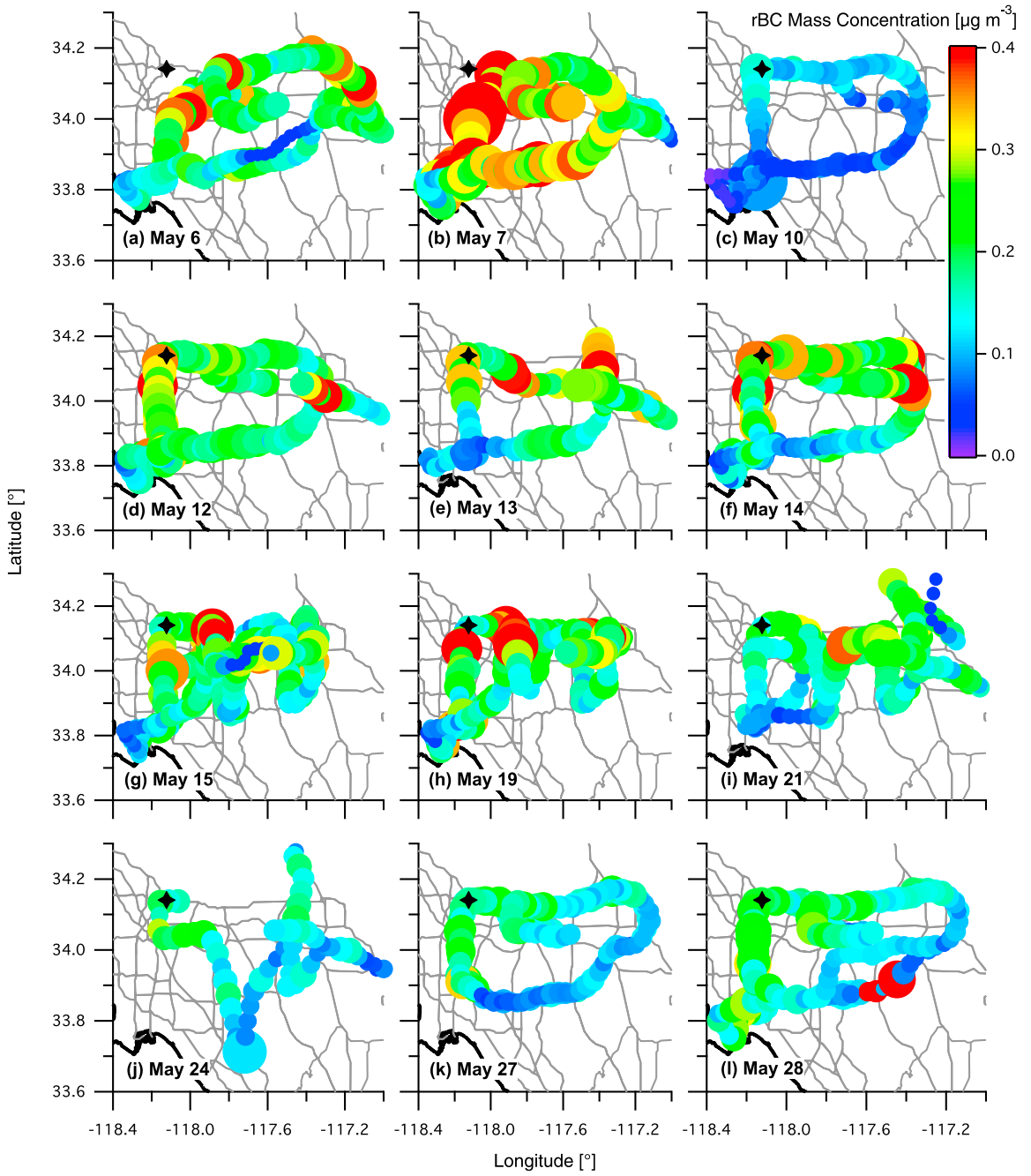

Figure 8. All rBC mass (marker color) and number (marker size) concentrations observed in the LA Basin during CalNex, with the exception of the May 25 flight, which can be found in Figure 9a. The stars denote the CalNex LA ground site at Caltech.

Billerica, MA USA) [*Drewnick et al.*, 2005; *Murphy et al.*, 2009] that was deployed on the final nine Twin Otter flights. The AMS measures sub-micron, non-refractory size-resolved aerosol composition over the diameter range 60 to 600 nm (with unit transmission efficiency) [*Jayne et al.*, 2000]. For the purposes of comparison to SP2 measurements, bulk composition AMS data are averaged to 1-min time intervals. Water-soluble organic carbon (WSOC) was quantified by a particle-into-liquid sampler (PILS; Brechtel Manufacturing, Inc., Hayward, CA) coupled to a Total

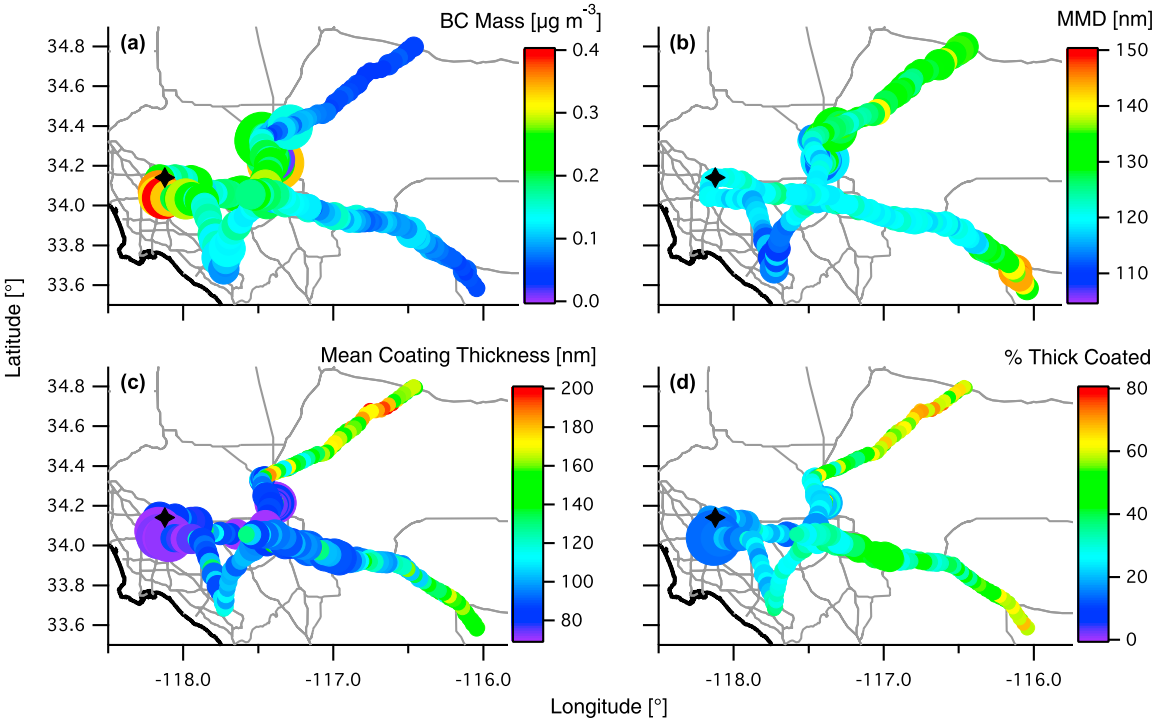

Figure 9. The 1-minute average SP2 data from Research Flight 16 on May 25, 2010: (a) rBC mass (marker color) and number (marker size) concentrations, (b) mass-median diameter of rBC cores (marker color) and width of the mass distributions (marker size), (c) mean coating thickness on rBC particles (marker color) and total volume concentration of the coating on rBC particles in SP2 detection range (marker size), and (d) percent of mixed-phase rBC particles thickly coated (marker color) and number concentration of coated rBC particles in SP2 detection range (marker size). The stars denote the CalNex LA ground site at Caltech.

Organic Carbon (TOC) Analyzer (Sievers Model 800) [*Sullivan et al.*, 2006]. The major findings on the nature of WSOC in Los Angeles during CalNex have been presented elsewhere [*Duong et al.*, 2011]. The WSOC data presented here have been converted to water-soluble organic mass (WSOM) by applying a correction factor of 1.7, which is within range of previous measurements made in Southern California [*Turpin and Lim*, 2001; *Docherty et al.*, 2008; *Wonaschütz et al.*, 2011].

[31] Figure 10 presents the region-averaged ratios of the mass concentration of various chemical species to the rBC mass concentration during the May 25 flight. The regions are ordered from west to east, which coincides with the direction of the general LA airflow; thus, for daytime sampling, plume age increases from left to right on Figure 10 with the exception of the Imperial Valley, which Figures 4g and 4h show to be isolated from the LA Basin for at least the 12 hours prior to measurement. Within the LA Basin, the rBC mass concentration decreases slightly from west to east and decreases sharply in the Banning Outflow and Imperial Valley regions, largely due to dilution of the air mass with the cleaner, desert air. In the absence of any major rBC sources over the desert, rBC can be considered a tracer for the LA plume and the mass ratios reveal the occurrence of secondary formation of these chemical species as the LA plume ages.

[32] The overall mass ratio of measured chemical species to rBC increases from west to east within the LA Basin and is at a maximum in the Banning Pass region, reflecting the build-up of secondary aerosol species, particularly nitrate and organics, relative to rBC. The Banning Pass is a relatively narrow mountain pass on the east side of the LA Basin (see Figures 1 and 2) where the LA plume is advected through this region and out of the Basin by the daytime sea breeze. Figure 9c shows the mean coating thicknesses and Figure 9d shows the percent thickly coated (defined using single-particle lag times) for this flight. Mean coating thicknesses for this flight do not show much increase within the Basin, much like the campaign-average values in Table 4; however, percent thickly coated shows an increase from west to east within the LA Basin with an area of larger percentages in the Banning Pass region. Figure 10 indicates that these more thickly coated particles in the Banning Pass region are likely a mix of ammonium nitrate and organics. A previous study found that coating materials on rBC in Nagoya, Japan were likely ammonium sulfate and secondary organic compounds formed during transport away from the urban center

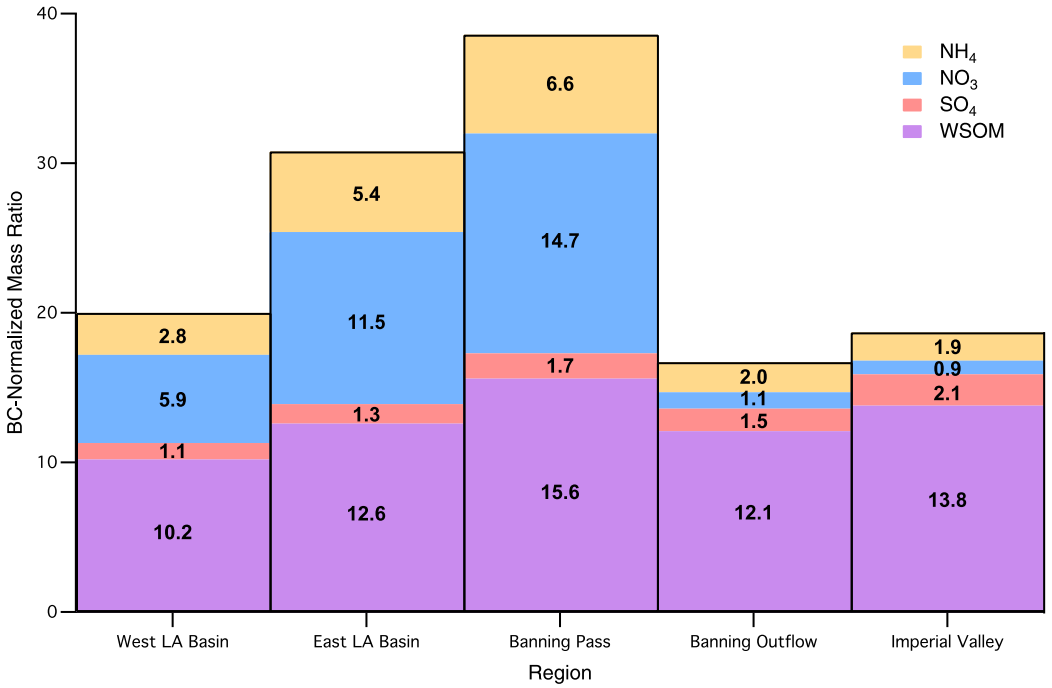

Figure 10. The rBC mass-normalized concentration ratios of aerosol chemical compounds broken down by region from west to east in and near the Los Angeles Basin for the May 25 flight. See text for details on the calculation of water-soluble organic mass (WSOM) and Figure 2 for region definitions.

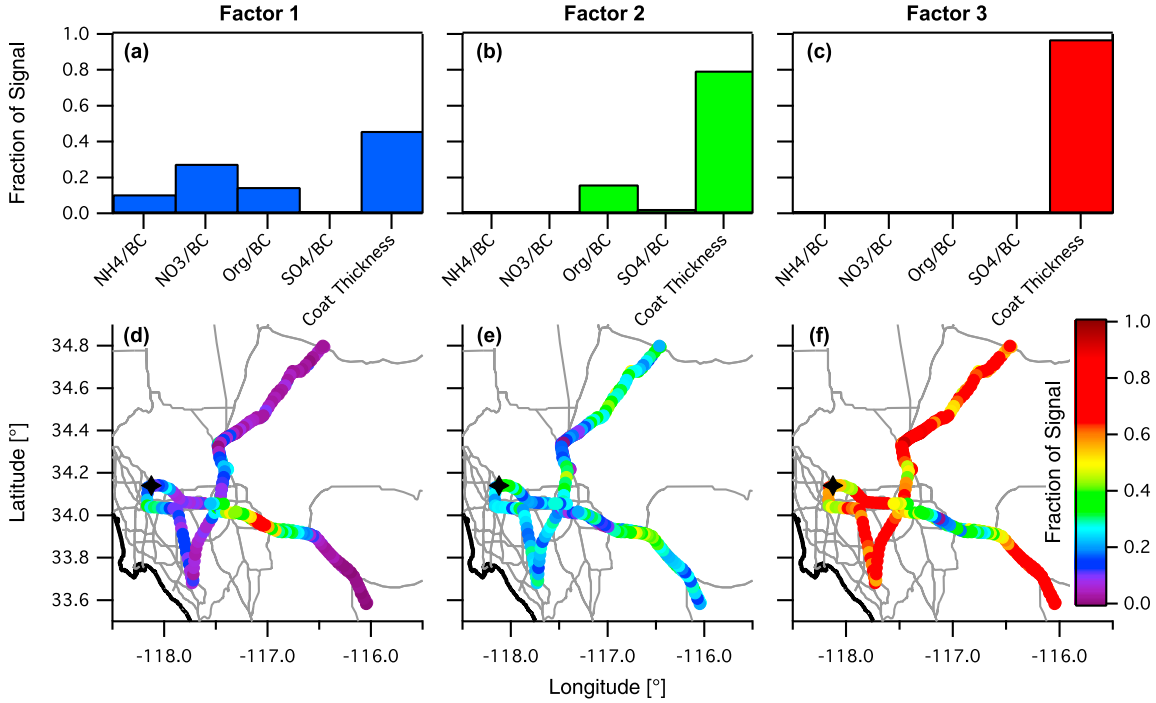

Figure 11. (a, b, and c) Fraction of total signal contributions to each PMF input parameter for each factor of the three-factor PMF model and (d, e, and f) fraction of total signal contributions from each factor to the total signal for the May 25 flight.

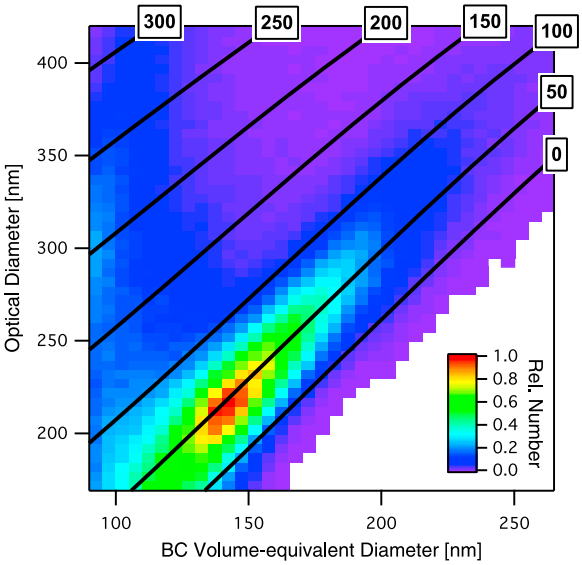

Figure 12. The 2-D histogram of all particles detected in the West LA Basin region as defined in Figure 2. Optical diameter is calculated with a Mie model (assuming a refractive index of 1.5-0.0*i*) fit to the scattering cross-section detected by a LEO fit of these particles' scattering signal. The solid lines denote the results of a core-and-shell Mie model forced with the rBC core diameters on the *x* axis and fit to the equivalent scattering cross-sections on the *y* axis. The numbers denote the shell thickness diameters in nm.

[*Moteki et al.*, 2007]. In the LA Basin, sulfate is a minor constituent of the secondary aerosol relative to nitrate.

[33] In the Banning Outflow region, the overall mass ratio is the smallest, reflecting loss of the volatile species from the aerosol, particularly ammonium nitrate, relative to rBC. For comparison, the Imperial Valley region data are also shown; however, as mentioned above, the timescales over which LA Basin air may mix into this region are unknown. Figures 9c and 9d both show that rBC coating thicknesses increase at the farthest sampling points outside of the LA Basin in both the Banning Outflow and El Cajon Outflow regions. The more noticeable increase in coating thicknesses occurring outside the LA Basin may be due to the timescales necessary for the coatings to grow on rBC. *Moteki et al.* [2007] found that rBC particles become internally mixed on a timescale of about 12 h in urban plumes. Figure 4f shows a sampling location during the May 25 flight in the Banning Outflow region in which the 12-h integrated surface history of the air mass shows a clear link to the eastern LA Basin. The data in Figure 10 show that the water-soluble organics continue to remain high relative to rBC in both the Banning Outflow and Imperial Valley regions and, therefore, likely contribute to any coatings on rBC particles in these regions.

[34] To explain the variation in rBC coating thicknesses, we used Positive Matrix Factorization (PMF) [*Paatero and Tapper*, 1993; *Paterson et al.*, 1999; *Ulbrich et al.*, 2009] with input parameters of mean rBC coating thickness and AMS masses normalized by rBC mass for the May 25 flight. Although Figure 10 shows the presence of two dominant species available as coating materials, nitrate and organics, we used a three-factor PMF model in order to compare with similar previous studies [*Shiraiwa et al.*, 2007, 2008]. The predicted parameters (ammonium/rBC, nitrate/rBC, organics/rBC, sulfate/rBC, and mean rBC coating thickness) by the PMF model agree well with the measured values (R^2 = 0.934, 0.999, 1.000, 0.625, and 1.000, respectively), indicating that the PMF model sufficiently describes the variance in the data. The three factors are shown in Figures 11a–11c. The fraction of signal is the contribution of each parameter to the overall signal and is, thus, weighted by the relative abundances of each parameter over the entire May 25 flight. Thus, the ammonium and sulfate fractions are small, because they have small loadings compared to the nitrate, organics, and mean coating thickness signals. If we look at the average fraction of measured signal accounted for by each factor, Factor 1 (Figure 11a) describes ~90% of the measured nitrate/rBC signal, ~28% of the organics/rBC, but only ~9% of the mean coating thickness. Factor 2 (Figure 11b) describes ~57% of the organics/rBC and ~22% of the mean coating thickness, while Factor 3 (Figure 11c) describes ~15% of the organics/rBC and ~69% of the mean coating thickness. Factors 2 and 3 each only describe ~5% of the nitrate/rBC signal. The cumulative explained fraction of measured signal by the PMF model of nitrate/rBC, organics/rBC, and mean coating thickness are 1.008, 0.999, and 1.000, respectively.

[35] Figures 11d–11f show the spatial pattern of the fraction of total signal contributed by the three factors on the May 25 flight. Factor 1 (Figure 11d) has the largest contribution to the signal in the Banning Pass, coincident with the largest loadings of nitrate measured on this flight. Although the overall explained signal of mean coating thickness for the entire flight is small for this factor, the dominance of the total factor signal in this region means that the coatings are likely nitrate and organics within the Banning Pass. Factor 2 (Figure 11e) has a more highly variable pattern throughout the flight; however, there are noticeable local maxima in several locations, particularly downwind of the Banning Pass in the Banning Outflow region, where this factor makes up ~50% of the total signal. The areas of high Factor 2 signal are characterized by a largely organic rBC coating, consistent with the ammonium nitrate having largely evaporated in this region (Figure 10). Factor 3 (Figure 11f) is dominant, by far, over most of the flight, with the exception of the two areas mentioned above. Because Factor 3 is essentially mean coating thickness by itself (Figure 11c), this factor is, in essence, the residual variation in mean coating thickness not described by Factors 1 and 2. Given its importance over most of the flight, it is clear that the PMF model does not contain enough parameters that vary with mean coating thickness to fully describe, in a physical interpretation, the cause for the variation in coating thickness in most regions. However, in the Banning Pass and Outflow regions, the PMF results support the conclusions from Figure 10 that the available coating materials are largely nitrate and organics, especially in regions where these compounds have relatively high loadings.

4.3. The rBC Mixing State

[36] Figure 12 presents a 2D histogram of all particles measured in the West LA Basin region (see Figure 2) during

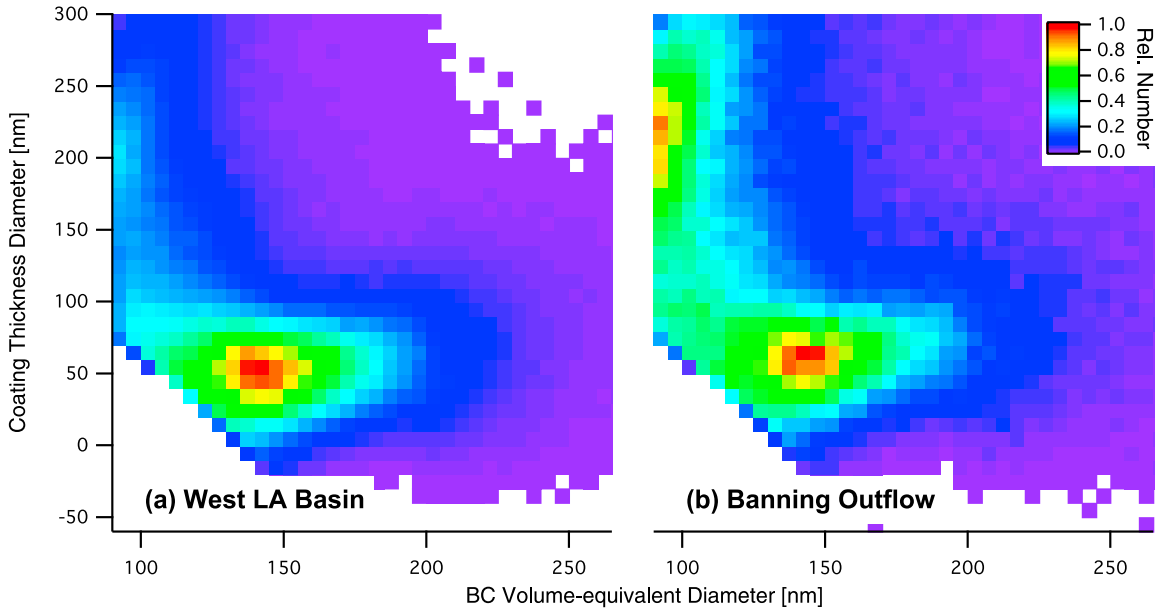

Figure 13. The 2-D histogram of all particles detected in (a) the West LA Basin region and (b) the Banning Outflow region, defined in Figure 2. Coating thickness is derived from a core-and-shell Mie model fit with the detected scattering cross-section by a LEO fit of the scattering signal.

CalNex. rBC core diameters (VED) from 90–260 nm are binned according to their optical diameter (175–410 nm) determined with the LEO method. Optical diameter, calculated using Mie theory assuming that the particle is purely scattering with a refractive index of 1.5-0.0*i*, is used instead of scattering cross-section in this figure for convenience of relating the scattering signal to particle diameter. Given the assumed rBC core sizes of these particles in Figure 12, solid lines representing a core-and-shell Mie model have been overlaid with the shell thickness diameters given in nm. Presented this way, the x- and y-axes limits on Figure 12 are the limits of detection for coated rBC of the Twin Otter SP2. As shown earlier, the MMD peaks below 130 nm for much of the measurements during CalNex, and Figure 12 clearly shows that one cannot determine the mixing state of the majority of these particles unless they have a coating thickness greater than 50 nm in diameter.

[37] Despite these limitations, we can examine how the behavior of coated rBC particles within the detection range of the SP2 change with region. To simplify the presentation of these data, Figure 13a is calculated directly from Figure 12 by re-binning the 2D histogram in terms of the core-and-shell Mie model scattering cross-sections to put the measurement in terms of coating thickness diameter. Figure 13a again shows the limits of detection at small rBC core sizes, as the major mode of coated rBC particles is cut off in the lower-left corner of the plot.

[38] Of particular interest is the evolution of the mixing state of the rBC aerosol as it is transported into the outflow regions. Figures 13a and 13b demonstrate this evolution from the source-rich area of the western LA Basin to the more aged Banning Outflow region. Figure 13 clearly shows that a second mode of particles at small rBC VED's but with thick (≥150 nm) coatings become more important relative to the main mode of more thinly-coated, larger rBC in the outflows. In the source-rich region of the western LA Basin, this second mode is barely visible as compared to the main mode of thinly coated rBC, indicating a dominance of thinly coated rBC particles, largely outside the detection range of the SP2.

4.4. Variability of rBC Levels With Altitude

[39] Figure 14a shows the 1-min resolution rBC mass concentration for all research flights as a function of altitude with single soundings presented in Figures 14b and 14c. In general, rBC mass concentration decreases with altitude, with the smallest concentrations measured in the free troposphere. In contrast, the mean coating thickness increases with altitude, with a dramatic increase above the inversion layer. The trend of lower rBC concentrations with increasing coating thickness is also shown in Figure 6. That the more thickly coated rBC particles lie in the free troposphere is consistent with a more aged aerosol, on which secondary species have condensed. A dramatic shift in MMD occurs above the inversion layer, indicating the rBC cores themselves are larger in the free troposphere. The characteristic time for coagulation by rBC-containing particles only in the free troposphere is about 82 days, but that of all particles in this region is about 7 days (using a coagulation coefficient $K = 6.41 \times 10^{-9}$ cm^3 s^{-1} calculated from the measurements) [*Seinfeld and Pandis*, 2006]. While this seems excessively long for the rBC particles, it is likely that rBC concentrations were much higher at their source, meaning

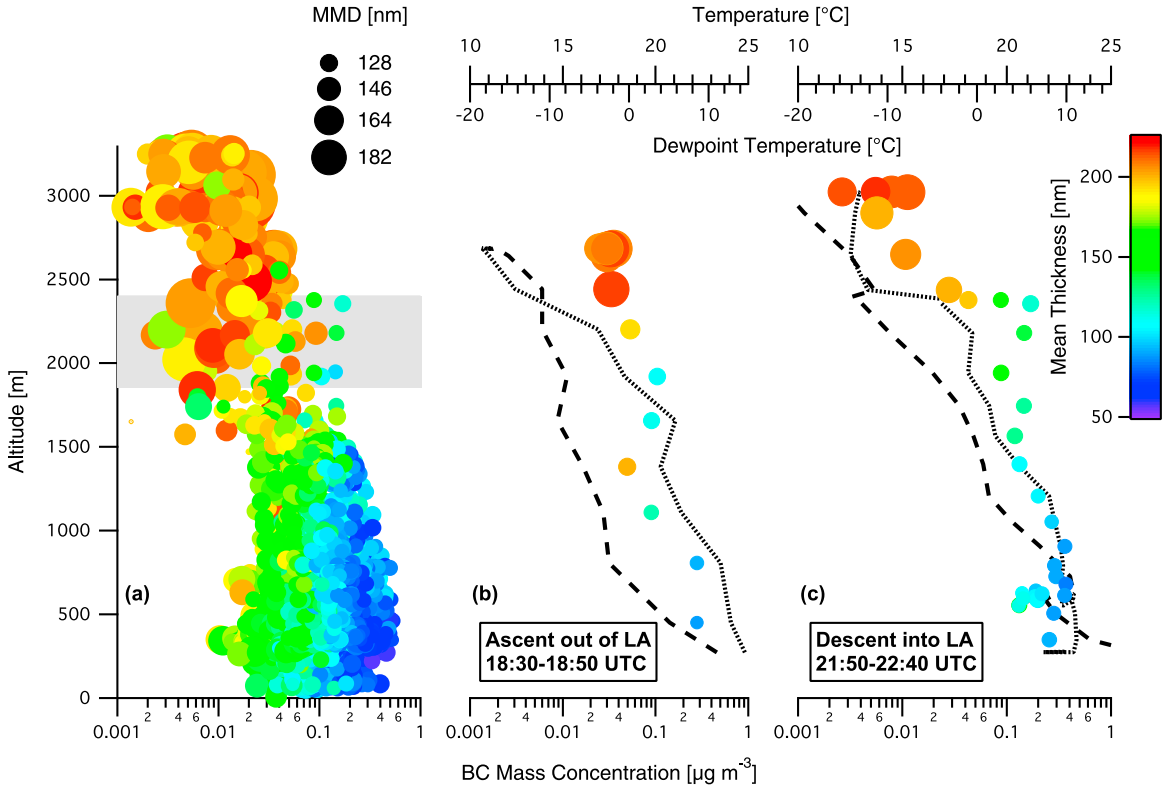

Figure 14. Vertical distribution of (a) all SP2 measurements, (b) ascent out of LA on May 20, and (c) descent into LA 3 h later. Each marker is a 1-min average data point indicating rBC mass concentration (x axis), mean coating thickness on rBC particles (marker color), and MMD (marker size). The gray shaded region in Figure 14a denotes the range of inversion layer altitudes observed during CalNex. The dashed lines in Figures 14b and 14c are the ambient temperature profiles and the dotted lines are the dew point temperature profiles.

coagulation would have proceeded much faster initially before being transported above the inversion. Another possible explanation is that the rBC above the inversion layer is from a different combustion source (biogenic vs. anthropogenic) than for the fresh rBC particles in the Basin, which may have caused larger rBC core sizes to begin with [*Schwarz et al.*, 2008a].

[40] Figures 14b and 14c show single soundings out of and back into the LA Basin on May 20. These soundings are for the same time periods as those presented in Figure 5 of *Duong et al.* [2011]. The ascent took place before noon local time on the east side of the LA Basin near the El Cajon Pass, and the temperature profile indicates the presence of a weak inversion layer ($\Delta T = \sim 0.5°C$ at ~1800 m) and a layer of elevated rBC levels (an increase of ~0.05 $\mu g\ m^{-3}$) around the same level. The decrease in dew point temperature (6.4°C) over this same layer is more dramatic and continues to decrease above this layer, indicating a much drier air mass aloft. Three hours later, on the descent into the LA Basin, again near the El Cajon Pass, rBC levels below the inversion layer are higher overall, especially near the base of the inversion layer ($\Delta T = \sim 1.6°C$ at ~2400 m). Again, the dew point temperature profile shows a sharp decrease (9.3°C) indicating a much drier air mass aloft. Although *Raga et al.* [2001] argue that the presence of an absorbing aerosol layer just above the temperature inversion helps to strengthen the inversion layer near Mexico City, we do not have enough soundings at sufficiently high resolution to evaluate this for the LA Basin. In fact, the data show that the rBC mass concentrations on this flight are higher below the inversion, especially later in the afternoon. Figures 14b and 14c also show the presence of rBC layers with different mean coating thicknesses. On the ascent out of the LA Basin, there is a layer of rBC at ~1400 m altitude with a mean coating thickness of ~200 nm surrounded above and below by rBC layers with mean coating thicknesses of ~115 nm. On the descent into the LA Basin later in the day, just below the inversion layer, at ~2350 m altitude, the local maxima in rBC mass concentration (an increase of ~0.08 $\mu g\ m^{-3}$) coincides with a mean coating thickness of ~115 nm with surrounding layers >160 nm in coating thickness. The descent also records the presence of a second inversion ($\Delta T = \sim 2.4°C$) much closer to the surface (~600 m altitude) in which a layer of rBC with mean

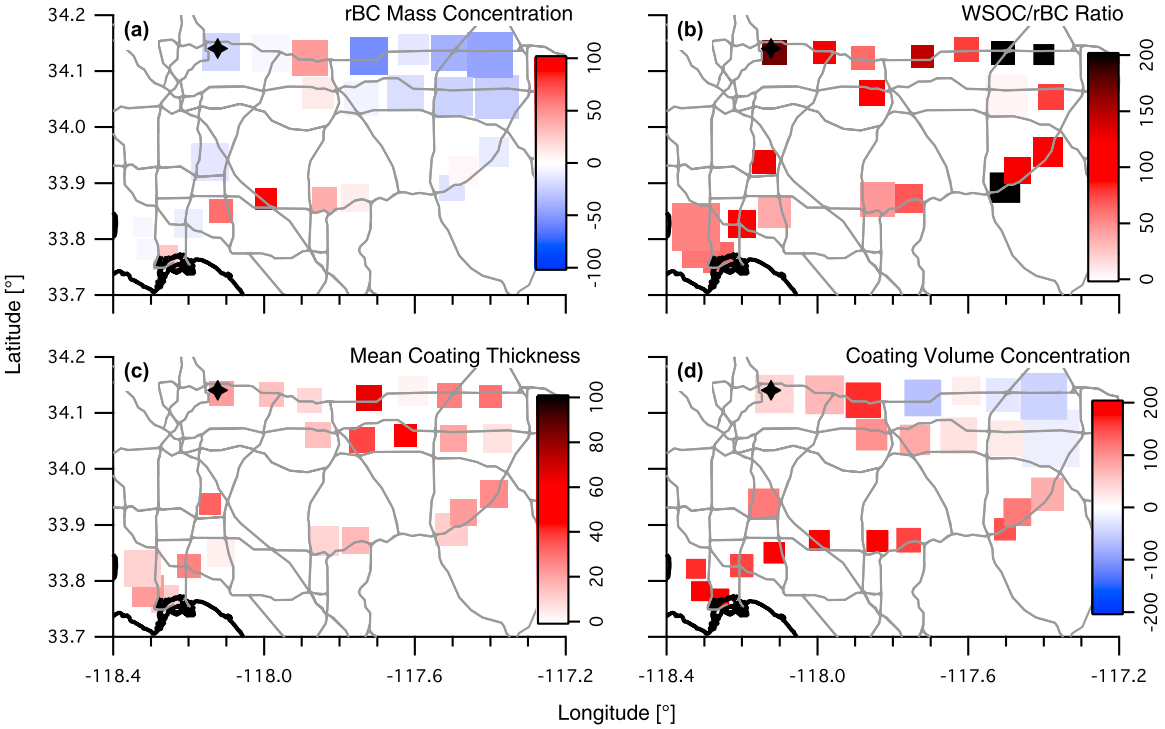

Figure 15. Percent change between Friday, May 14 and Saturday, May 15 measurements displayed as percent change from the May 14 values (marker color) for: (a) rBC mass concentration, (b) WSOC/rBC ratio, (c) mean coating thickness, and (d) coating volume concentration. The SP2 measurements are averaged over a grid spacing of 0.12° longitude by 0.1° latitude. The size of the markers in each plot is proportional to the May 14 measurement value. The stars denote the CalNex LA ground site at Caltech.

coating thickness ~150 nm is surrounded by layers with coating thicknesses of ~105 nm. The complicated vertical structure in Figures 14b and 14c is likely the result of the "mountain-chimney effect" described by *Lu and Turco* [1994, 1995]. In both soundings, the rBC just above the inversion layer is dramatically different than below; the rBC is much more thickly coated and the mass median diameters are much larger.

4.5. Case Study: "Weekend Effect" on rBC Aerosol

[41] Ozone levels in the LA Basin are subject to the well-documented weekday-weekend effect [e.g., *Marr and Harley*, 2002; *Pollack et al.*, 2012]. This so-called "weekend effect" is a result of the dramatically reduced amount of heavy-duty truck traffic (diesel truck emissions decrease by 60–80%), as reflected primarily in NO_x levels [*Harley et al.*, 2005].

[42] To examine the possible effects on rBC in the LA Basin as a result of the weekend effect, Figure 15 presents the percent change of several measurements from Friday, May 14 to Saturday, May 15. We define the percent change referenced to the measurements from May 14; thus, positive values denote measurements that are higher on the weekend flight of May 15. The size of the markers is proportional to the measured values on May 14, revealing the weekday pattern of larger values in the Basin. Figure 15a shows rBC mass concentration changes in the Basin (see Figures 8f and 8g for actual measurements). By flight average, there is virtually no change in rBC levels from May 14 to 15 (+0.01%), but there are regions within the Basin of increase and decrease. Figure 15b shows change in the WSOC/rBC ratio, which is indicative of secondary organic aerosol (SOA) formation, increasing everywhere in the Basin by a large percent. This observation is consistent with previous observations that the highest levels of SOA formation in the LA Basin occur on weekends [*Turpin and Huntzicker*, 1991, 1995]. Figure 15c shows that mean coating thicknesses also increase everywhere on May 15 throughout the LA Basin. Finally, Figure 15d shows that in the far northeast corner of the LA Basin the coating volume concentration is smaller on May 15, in contrast to the rest of the Basin which has more coating volume on this particular Saturday. While this may seem to conflict with Figure 15c, note that mean coating thickness is a particle-by-particle average, which gives the mean state of single rBC particles, whereas coating volume concentration is a bulk measurement that reflects total number concentration as well as average coating thickness. Thus, on Friday, May 14, there were more particles in the LA Basin, and thus more total coating volume on rBC in the northeast corner of the Basin, where pollution accumulates,

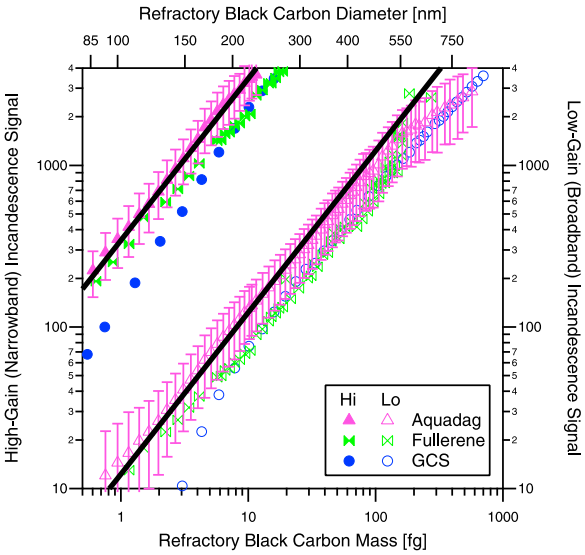

Figure A1. Calibration data for the high-gain (upper-left trace) and low-gain (lower-right trace) incandescence channels. The rBC mass (bottom x axis) is calculated from the selected mobility diameter with mobility density for Aquadag and Fullerene from *Gysel et al.* [2011] and density = 1.4 g cm^{-3} for glassy carbon spheres (GCS). rBC diameter (top x axis) is volume-equivalent diameter (VED) calculated as for ambient particles, assuming a spherical particle with a density = 1.8 g cm^{-3}. The solid line is the calibration curve used in this study, calculated from the Aquadag data only.

despite the fact that per rBC particle, there was a thinner coating of material.

5. Summary

[43] The present work reports rBC measurements during May 2010 as part of the CalNex 2010 field experiment in California. The measurements were carried out onboard the CIRPAS Twin Otter aircraft during 18 research flights, using the Single Particle Soot Photometer. The dominant feature controlling the regional variability of rBC aerosol in the LA Basin is the daytime southwesterly sea breeze. The sea breeze advects the fresh LA plume inland, where mountain ranges and a shallow inversion layer collect the pollution before exiting the Basin through two narrow mountain passes. While rBC mass concentrations remain fairly uniform west-to-east within the Basin, there is clear growth of secondary organics and ammonium nitrate as the LA plume is advected eastward in the Basin. This secondary growth coincides with an increase in the coating thickness on rBC particles from west to east. In the outflow regions, the volatile ammonium nitrate largely evaporates, leaving WSOC as the most abundant secondary material available to contribute to the growing mean rBC coating thicknesses. Detailed analysis of the rBC mixing state reveals two modes of coated particles, one with an rBC VED ~145 nm with a coating that grows from ~50 nm to ~70 nm from the western LA Basin to the Banning Outflow region and one with an rBC VED ~90 nm, on the edge of the SP2 detection range, with a coating that grows from <100 nm (out of detection range) to >200 nm. In general, rBC mass concentrations decrease with altitude, while the coating thickness increases dramatically above the inversion layer, consistent with a more aged aerosol in the free troposphere. The "weekend effect" on rBC resulted in more thickly coated rBC particles on a Saturday versus the preceding Friday everywhere in the LA Basin, coinciding with higher WSOC/BC ratios, indicating more secondary formation of aerosol on Saturday.

Appendix A: Calibration of the SP2

A1. The rBC Mass Calibration

[44] The SP2 has two incandescence channels, a broadband (λ = 350–800 nm) and a narrowband (λ = 630–800 nm) channel. The Twin Otter SP2 was additionally configured such that the broadband incandescence channel was set to a higher gain setting than the narrowband channel, to increase the total range of detectable refractory black carbon mass. Figure A1 presents the incandescence calibration for the two channels, showing the clear overlap in signal ranges and deviation of the signal from the linear fit at larger particle masses. A comparison is made to other rBC aerosol standards, Fullerene soot (stock #40971, lot #G25N20, Alfa Aesar, Ward Hill, MA, USA) and glassy carbon spheres (GCS, Type II, stock #38008, lot #C14K07, Alfa Aesar). The mass of generated Fullerene particles is calculated using the relation from *Gysel et al.* [2011]; however, we note that our batch of Fullerene is different from that used in their study. GCS mobility diameter is converted to mass using the manufacturer-reported density of 1.42 g cm^{-3}. The Fullerene and GCS calibration slopes are both ~37% larger than the Aquadag slope, meaning that these calibrations would yield larger rBC masses. When more data becomes available relating these three rBC standards to ambient rBC in the LA Basin, corrections to the calibration can be made.

[45] The SP2 incandescence channels were calibrated with Aquadag by nebulizing a solution of Aquadag and milliQ water through a differential mobility analyzer (DMA, TSI Model 3081) used to classify the mobility of the generated particles. The mass of those particles was calculated from the mobility diameter using the relation from *Gysel et al.* [2011], who showed that Aquadag mobility density is independent of production batch and specific aerosol generation procedures. We have chosen to use Aquadag as our calibration standard because of this published density and because the different production lots of Aquadag have been distributed to most SP2 users by DMT; thus, providing a means to inter-relate the many SP2 instruments. Recent work by *Laborde et al.* [2012] instead recommend the use of Fullerene soot, as has been recommended previously [*Moteki and Kondo*, 2010]. However, the mobility density of Fullerene soot is not consistent across different production lots and may vary by up to 14% between specific batches [*Laborde et al.*, 2012]. For this study, we did not have access to a particle mass analyzer and, therefore, could not verify the mobility density of our batch of Fullerene.

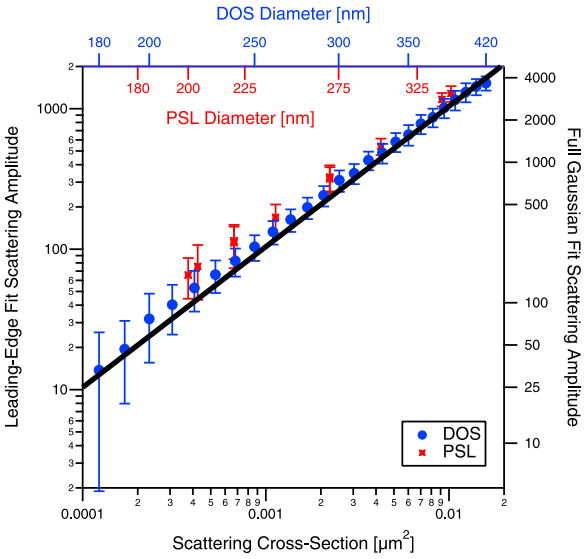

Figure A2. PSL and DOS scattering calibration data. Each data point is the median of about 10,000 particles, and the error bars indicate one standard deviation. For reference, both the full Gaussian and the leading-edge only fits are shown, but operationally, only the leading edge fits are used to determine an optical diameter.

[46] It has been previously shown that the incandescence response of the SP2 is linear up to particle masses of 10 fg and independent of particle shape or mixing state [*Moteki and Kondo*, 2007, 2010; *Slowik et al.*, 2007]. We have found a linear response over a slightly larger range, up to at least a 50 fg particle (see Figure A1), before surface area effects lead to a power law dependence in the signal. The coefficients of determination (R^2 = 0.993, 0.996, and 0.997 for Aquadag, Fullerene, and GCS, respectively) clearly demonstrate the linearity in the response of the SP2 to rBC mass. We have chosen to fit both incandescence channels with a linear function and note that errors will be greatest at the extreme large end of the rBC mass spectrum, where few particles were detected in this study. The detection limit of the high-gain broadband incandescence channel was 0.48–11.1 fg rBC per particle (80–227 nm VED) and of the low-gain narrowband incandescence channel was 3.66–317 fg rBC per particle (157–696 nm VED).

A2. Scattering Calibration

[47] The SP2 has two scattering channels, a high-gain and a low-gain channel, which are filtered to detect scattered light at λ = 1064 nm. The Twin Otter SP2 was configured with a split-detector on the high-gain scatter channel, which is used to obtain particle position information for use in a leading-edge only (LEO) fit of the scattering data on the low-gain channel [*Gao et al.*, 2007]. The scattering channels were calibrated with both dioctyl sebecate (DOS, refractive index = 1.45-0.0i) and polystyrene latex spheres (PSL, refractive index = 1.59-0.0*i*) size-selected by a DMA. Figure A2 shows the results of the calibration for a full Gaussian fit to the scattering signal and for the LEO fits to the scattering signal, detailed below. A Mie scattering model is used to relate diameter and refractive index to the scattering cross-section. In Figure A2, each data point represents the median of a sample of about 10,000 particles. The error bars are one standard deviation of the LEO fit amplitude, indicative of the spread in the data for each size. The linear fit was found by forcing a zero intercept, but very little change in slope occurs if this criterion is relaxed. The data used to generate the linear fit were the DOS data only. Both DOS and PSL calibration curves demonstrate the linearity of the scattering response of the SP2 to scattering cross-section (R^2 = 0.996 and 0.999, respectively). Uncertainty in the full Gaussian fit amplitude is ~14%.

A3. LEO Fitting

[48] We desire to use only the leading-edge of the scattering signal so that coated rBC particles, which have a scattering signal that begins as a Gaussian shape but then is perturbed as the coating evaporates, may be sized according to their full, unperturbed diameter. We have chosen the criterion for determining the last point in the leading-edge signal consistent with *Gao et al.* [2007]; that is, an amplification factor of 30, which means signals up to the point where the signal is 3.33% of the maximum observed signal for that particle are used in the LEO fit.

[49] In addition to using only a limited portion of the scattering signal for each particle, we simplify the Gaussian fit based on calibration results. The Gaussian-shaped scatter signal, S, as a function of time, t, on the low-gain scatter channel is written as

$$S(t) = a\exp\left[-4\ln 2\left(\frac{t-b}{c}\right)^2\right] + d \qquad \text{(A1)}$$

where a is the height of the peak, b is the position of the center of the peak, c is the full width at half maximum, and d is the baseline or offset. Owing to the constant flow rate and width of the laser in the instrument, purely scattering particles of all sizes exhibit the same full width at half maximum (c) and peak position (b) relative to the zero-crossing of the split-detector (labeled as "Position Time" on Figure 5) [*Gao et al.*, 2007]. Thus, equation (A1) can be simplified to

$$S(t) = aX(t) + d \qquad \text{(A2)}$$

where $X = \exp\left(-4\ln 2\left(\frac{t-b}{c}\right)^2\right)$ can be calculated directly from calibration data and S, a, and d are defined above. In fitting equation (A2), we do not restrict the value of d, the signal baseline, but keep it as a free parameter and compare the fitted d to the baseline value estimated as the minimum average of the first or last 20 signal data points on the single-particle time trace (Figure 5). This comparison ensures that the fit to the scattering data yields realistic values for a. Due to fluctuations in sample flow and laser profile, LEO fitting increases uncertainty in the retrieved scattering amplitude to ~22%.

[50] To validate the LEO method of fitting, we compared the full Gaussian fit amplitude to the leading-edge fits for the

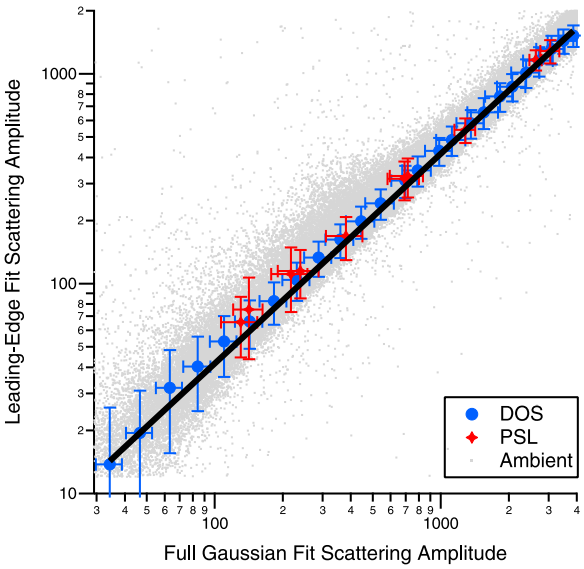

Figure A3. Comparison of the leading-edge only (LEO) fit amplitudes to the full Gaussian fit amplitudes for purely scattering particles. DOS ($R^2 = 0.998$) and PSL ($R^2 = 0.999$) calibration data are shown, as well as purely scattering ambient particle data from one of the flights during CalNex.

DOS and PSL calibration data as well as for a subset of purely scattering particle data from several of the research flights. The results are given in Figure A3. For clarity, the fits from a segment of only one of the flights is shown, but all flights gave similar results. Although the slope between the two methods is not ideally unity, the linearity of the plot (R^2 = 0.998 and 0.999 for DOS and PSL, respectively) validates this as an effective method for sizing particles.

[51] **Acknowledgments.** This work was supported by NOAA grant NA09OAR4310128. The authors wish to thank Greg Kok at DMT and Anne Perring and Joshua (Shuka) Schwarz at NOAA for their guidance on data analysis and calibration. We also acknowledge the entire CIRPAS crew for their professionalism and assistance during the campaign.

References

Andreae, M., O. Schmid, H. Yang, D. Chand, J. Zhen Yu, L. Zeng, and Y. Zhang (2008), Optical properties and chemical composition of the atmospheric aerosol in urban Guangzhou, China, *Atmos. Environ.*, *42*, 6335–6350, doi:10.1016/j.atmosenv.2008.01.030.

Babu, S. S., S. K. Satheesh, and K. K. Moorthy (2002), Aerosol radiative forcing due to enhanced black carbon at an urban site in India, *Geophys. Res. Lett.*, *29*(18), 1880, doi:10.1029/2002GL015826.

Bauer, S. E., S. Menon, D. Koch, T. C. Bond, and K. Tsigaridis (2010), A global modeling study on carbonaceous aerosol microphysical characteristics and radiative effects, *Atmos. Chem. Phys.*, *10*, 7439–7456, doi:10.5194/acp-10-7439-2010.

Baumgardner, D., G. L. Kok, and G. Raga (2004), Warming of the Arctic lower stratosphere by light absorbing particles, *Geophys. Res. Lett.*, *31*, L06117, doi:10.1029/2003GL018883.

Baumgardner, D., G. L. Kok, and G. B. Raga (2007), On the diurnal variability of particle properties related to light absorbing carbon in Mexico City, *Atmos. Chem. Phys.*, *7*, 2517–2526, doi:10.5194/acp-7-2517-2007.

Binkowski, F. S., and S. J. Roselle (2003), Models-3 Community Multiscale Air Quality (CMAQ) model aerosol component: 1. Model description, *J. Geophys. Res.*, *108*(D6), 4183, doi:10.1029/2001JD001409.

Blumenthal, D., W. White, and T. Smith (1978), Anatomy of a Los Angeles smog episode: Pollutant transport in the daytime sea breeze regime, *Atmos. Environ.*, *12*(4), 893–907, doi:10.1016/0004-6981(78)90028-8.

Bohren, C. F., and D. R. Huffman (1998), *Absorption and Scattering of Light by Small Particles*, John Wiley, New York.

Bond, T. C. (2007), Can warming particles enter global climate discussions?, *Environ. Res. Lett.*, *2*(4), 045030, doi:10.1088/1748-9326/2/4/045030.

Bond, T. C., and R. W. Bergstrom (2006), Light absorption by carbonaceous particles: An investigative review, *Aerosol Sci. Technol.*, *40*(1), 27–67, doi:10.1080/02786820500421521.

Bond, T. C., G. Habib, and R. W. Bergstrom (2006), Limitations in the enhancement of visible light absorption due to mixing state, *J. Geophys. Res.*, *111*, D20211, doi:10.1029/2006JD007315.

Brioude, J., et al. (2009), Effect of biomass burning on marine stratocumulus clouds off the California coast, *Atmos. Chem. Phys.*, *9*, 8841–8856, doi:10.5194/acp-9-8841-2009.

Brunciak, P. A., J. Dachs, T. P. Franz, C. L. Gigliotti, E. D. Nelson, B. J. Turpin, and S. J. Eisenreich (2001), Polychlorinated biphenyls and particulate organic/elemental carbon in the atmosphere of Chesapeake Bay, USA, *Atmos. Environ.*, *35*(32), 5663–5677, doi:10.1016/S1352-2310(01)00222-9.

Chazette, P., and C. Liousse (2001), A case study of optical and chemical ground apportionment for urban aerosols in Thessaloniki, *Atmos. Environ.*, *35*(14), 2497–2506, doi:10.1016/S1352-2310(00)00425-8.

Chow, J. C., J. G. Watson, E. M. Fujita, Z. Lu, D. R. Lawson, and L. L. Ashbaugh (1994), Temporal and spatial variations of $PM_{2.5}$ and PM_{10} aerosol in the Southern California Air Quality Study, *Atmos. Environ.*, *28*(12), 2061–2080, doi:10.1016/1352-2310(94)90474-X.

Chow, J. C., J. G. Watson, Z. Lu, D. H. Lowenthal, C. A. Frazier, P. A. Solomon, R. H. Thuillier, and K. Magliano (1996), Descriptive analysis of $PM_{2.5}$ and PM_{10} at regionally representative locations during SJVAQS/AUSPEX, *Atmos. Environ.*, *30*(12), 2079–2112, doi:10.1016/1352-2310(95)00402-5.

Chung, S. H., and J. H. Seinfeld (2005), Climate response of direct radiative forcing of anthropogenic black carbon, *J. Geophys. Res.*, *110*, D11102, doi:10.1029/2004JD005441.

Clarke, A. D., et al. (2004), Size distributions and mixtures of dust and black carbon aerosol in Asian outflow: Physiochemistry and optical properties, *J. Geophys. Res.*, *109*, D15S09, doi:10.1029/2003JD004378.

Collins, D. R., H. H. Jonsson, H. Liao, R. C. Flagan, J. H. Seinfeld, K. J. Noone, and S. Hering (2000), Airborne analysis of the Los Angeles aerosol, *Atmos. Environ.*, *34*(24), 4155–4173, doi:10.1016/S1352-2310(00)00225-9.

Cubison, M. J., B. Ervens, G. Feingold, K. S. Docherty, I. M. Ulbrich, L. Shields, K. Prather, S. Hering, and J. L. Jimenez (2008), The influence of chemical composition and mixing state of Los Angeles urban aerosol on CCN number and cloud properties, *Atmos. Chem. Phys.*, *8*, 5649–5667, doi:10.5194/acp-8-5649-2008.

de Foy, B., J. Varela, L. Molina, and M. Molina (2006), Rapid ventilation of the Mexico City basin and regional fate of the urban plume, *Atmos. Chem. Phys.*, *6*, 2321–2335, doi:10.5194/acp-6-2321-2006.

Del Delumyea, R., and A. Kalivretenos (1987), Elemental carbon and lead content of fine particles from American and French cities of comparable size and industry, 1985, *Atmos. Environ.*, *21*(7), 1643–1647, doi:10.1016/0004-6981(87)90325-8.

Dentener, F., et al. (2006), Emissions of primary aerosol and precursor gases in the years 2000 and 1750 prescribed data-sets for AeroCom, *Atmos. Chem. Phys.*, *6*, 4321–4344, doi:10.5194/acp-6-4321-2006.

Didyk, B. M., B. R. T. Simoneit, L. A. Pezoa, M. L. Riveros, and A. A. Flores (2000), Urban aerosol particles of Santiago, Chile: Organic content and molecular characterization, *Atmos. Environ.*, *34*(8), 1167–1179, doi:10.1016/S1352-2310(99)00403-3.

Ding, A., et al. (2009), Transport of north China air pollution by midlatitude cyclones: Case study of aircraft measurements in summer 2007, *J. Geophys. Res.*, *114*, D08304, doi:10.1029/2008JD011023.

Docherty, K. S., et al. (2008), Apportionment of primary and secondary organic aerosols in Southern California during the 2005 Study of Organic Aerosols in Riverside (SOAR-1), *Environ. Sci. Technol.*, *42*(20), 7655–7662, doi:10.1021/es8008166.

Drewnick, F., et al. (2005), A new time-of-flight aerosol mass spectrometer (TOF-AMS)–Instrument description and first field deployment, *Aerosol Sci. Technol.*, *39*(7), 637–658, doi:10.1080/02786820500182040.

Duong, H. T., et al. (2011), Water-soluble organic aerosol in the Los Angeles Basin and outflow regions: Airborne and ground measurements during the 2010 CalNex field campaign, *J. Geophys. Res.*, *116*, D00V04, doi:10.1029/2011JD016674.

Edinger, J. G. (1959), Changes in the depth of the marine layer over the Los Angeles Basin, *J. Meteorol.*, *16*, 219–226, doi:10.1175/1520-0469(1959)016<0219:CITDOT>2.0.CO;2.

Ensor, D. S., R. J. Charlson, N. C. Alhquist, K. T. Whitby, R. B. Husar, and B. Y. H. Liu (1972), Multiwavelength nephelometer measurements in

Los Angeles smog aerosol. I. Comparison of calculated and measured light scattering, *J. Colloid Interface Sci.*, *39*(1), 242–251, doi:10.1016/0021-9797(72)90159-2.

Fine, P. M., S. Shen, and C. Sioutas (2004), Inferring the sources of fine and ultrafine particulate matter at downwind receptor sites in the Los Angeles Basin using multiple continuous measurements, *Aerosol Sci. Technol.*, *38*(S1), 182–195, doi:10.1080/02786820390229499.

Fuller, K. A., W. C. Malm, and S. M. Kreidenweis (1999), Effects of mixing on extinction by carbonaceous particles, *J. Geophys. Res.*, *104*(D13), 15,941–15,954, doi:10.1029/1998JD100069.

Gao, R. S., et al. (2007), A novel method for estimating light-scattering properties of soot aerosols using a modified single-particle soot photometer, *Aerosol Sci. Technol.*, *41*(2), 125–135, doi:10.1080/02786820601118398.

Gray, H. A., G. R. Cass, J. J. Huntzicker, E. K. Heyerdahl, and J. A. Rau (1986), Characteristics of atmospheric organic and elemental carbon particle concentrations in Los Angeles, *Environ. Sci. Technol.*, *20*(6), 580–589, doi:10.1021/es00148a006.

Gysel, M., M. Laborde, J. S. Olfert, R. Subramanian, and A. J. Gröhn (2011), Effective density of Aquadag and fullerene soot black carbon reference materials used for SP2 calibration, *Atmos. Meas. Tech.*, *4*, 2851–2858, doi:10.5194/amt-4-2851-2011.

Hansen, A. D. A., V. N. Kapustin, V. M. Kopeikin, D. A. Gillette, and B. A. Bodhaine (1993), Optical absorption by aerosol black carbon and dust in a desert region of Central Asia, *Atmos. Environ., Part A*, *27*(16), 2527–2531, doi:10.1016/0960-1686(93)90025-T.

Harley, R. A., L. C. Marr, J. K. Lehner, and S. N. Giddings (2005), Changes in motor vehicle emissions on diurnal to decadal time scales and effects on atmospheric composition, *Environ. Sci. Technol.*, *39*(14), 5356–5362, doi:10.1021/es048172+.

He, K. B., F. M. Yang, Y. L. Ma, Q. Zhang, X. H. Yao, C. K. Chan, S. Cadle, T. Chan, and P. Mulawa (2001), The characteristics of $PM_{2.5}$ in Beijing, China, *Atmos. Environ.*, *35*(29), 4959–4970, doi:10.1016/S1352-2310(01)00301-6.

Healy, R. M., et al. (2012), Sources and mixing state of size-resolved elemental carbon particles in a European megacity: Paris, *Atmos. Chem. Phys.*, *12*, 1681–1700, doi:10.5194/acp-12-1681-2012.

Hegg, D., D. Covert, H. Jonsson, and P. Covert (2005), Determination of the transmission efficiency of an aircraft aerosol inlet, *Aerosol Sci. Technol.*, *39*(10), 966–971, doi:10.1080/02786820500377814.

Hitzenberger, R., and S. Tohno (2001), Comparison of black carbon (BC) aerosols in two urban areas—Concentrations and size distributions, *Atmos. Environ.*, *35*(12), 2153–2167, doi:10.1016/S1352-2310(00)00480-5.

Huang, X.-F., et al. (2011), Black carbon measurements in the Pearl River Delta region of China, *J. Geophys. Res.*, *116*, D12208, doi:10.1029/2010JD014933.

Jacobson, M. Z. (1997), Development and application of a new air pollution modeling system—Part III. Aerosol-phase simulations, *Atmos. Environ.*, *31*(4), 587–608, doi:10.1016/S1352-2310(96)00201-4.

Jacobson, M. Z. (2002), Control of fossil-fuel particulate black carbon and organic matter, possibly the most effective method of slowing global warming, *J. Geophys. Res.*, *107*(D19), 4410, doi:10.1029/2001JD001376.

Jacobson, M. Z. (2006), Effects of externally-through-internally-mixed soot inclusions within clouds and precipitation on global climate, *J. Phys. Chem. A*, *110*(21), 6860–6873, doi:10.1021/jp056391r.

Jaffe, D., et al. (1999), Transport of Asian air pollution to North America, *Geophys. Res. Lett.*, *26*(6), 711–714, doi:10.1029/1999GL900100.

Janssen, N. A. H., D. F. M. Van Mansom, K. Van Der Jagt, H. Harssema, and G. Hoek (1997), Mass concentration and elemental composition of airborne particulate matter at street and background locations, *Atmos. Environ.*, *31*(8), 1185–1193, doi:10.1016/S1352-2310(96)00291-9.

Jayne, J. T., D. C. Leard, X. Zhang, P. Davidovits, K. A. Smith, C. E. Kolb, and D. R. Worsnop (2000), Development of an aerosol mass spectrometer for size and composition analysis of submicron particles, *Aerosol Sci. Technol.*, *33*(1–2), 49–70, doi:10.1080/027868200410840.

Johnson, K. S., B. Zuberi, L. T. Molina, M. J. Molina, M. J. Iedema, J. P. Cowin, D. J. Gaspar, C. Wang, and A. Laskin (2005), Processing of soot in an urban environment: Case study from the Mexico City metropolitan area, *Atmos. Chem. Phys.*, *5*, 3033–3043, doi:10.5194/acp-5-3033-2005.

Jones, G. S., N. Christidis, and P. A. Stott (2011), Detecting the influence of fossil fuel and bio-fuel black carbon aerosols on near surface temperature changes, *Atmos. Chem. Phys.*, *11*, 799–816, doi:10.5194/acp-11-799-2011.

Kadowaki, S. (1990), Characterization of carbonaceous aerosols in the Nagoya urban area. 1. Elemental and organic carbon concentrations and the origin of organic aerosols, *Environ. Sci. Technol.*, *24*(5), 741–744, doi:10.1021/es00075a020.

Kim, B. M., S. Teffera, and M. D. Zeldin (2000), Characterization of $PM_{2.5}$ and PM_{10} in the South Coast Air Basin of Southern California: Part 1–Spatial variations, *J. Air Waste Manage. Assoc.*, *50*(12), 2034–2044.

Kim, Y. P., K.-C. Moon, J. H. Lee, and N. J. Baik (1999), Concentrations of carbonaceous species in particles at Seoul and Cheju in Korea, *Atmos. Environ.*, *33*(17), 2751–2758, doi:10.1016/S1352-2310(98)00313-6.

Laborde, M., P. Mertes, P. Zieger, J. Dommen, U. Baltensperger, and M. Gysel (2012), Sensitivity of the single particle soot photometer to different black carbon types, *Atmos. Meas. Tech. Discuss.*, *5*, 663–690, doi:10.5194/amtd-5-663-2012.

Lack, D. A., and C. D. Cappa (2010), Impact of brown and clear carbon on light absorption enhancement, single scatter albedo and absorption wavelength dependence of black carbon, *Atmos. Chem. Phys.*, *10*, 4207–4220, doi:10.5194/acp-10-4207-2010.

Langford, A. O., J. Brioude, O. R. Cooper, C. J. Senff, R. J. Alvarez II, R. M. Hardesty, B. J. Johnson, and S. J. Oltmans (2012), Stratospheric influence on surface ozone in the Los Angeles area during late spring and early summer of 2010, *J. Geophys. Res.*, *117*, D00V06, doi:10.1029/2011JD016766.

Liang, Q., L. Jaeglé, D. A. Jaffe, P. Weiss-Penzias, A. Heckman, and J. A. Snow (2004), Long-range transport of Asian pollution to the northeast Pacific: Seasonal variations and transport pathways of carbon monoxide, *J. Geophys. Res.*, *109*, D23S07, doi:10.1029/2003JD004402.

Lin, J. J., and H.-S. Tai (2001), Concentrations and distributions of carbonaceous species in ambient particles in Kaohsiung City, Taiwan, *Atmos. Environ.*, *35*(15), 2627–2636, doi:10.1016/S1352-2310(00)00444-1.

Liu, H., D. J. Jacob, I. Bey, R. M. Yantosca, B. N. Duncan, and G. W. Sachse (2003), Transport pathways for Asian pollution outflow over the Pacific: Interannual and seasonal variations, *J. Geophys. Res.*, *108*(D20), 8786, doi:10.1029/2002JD003102.

Lu, R., and R. P. Turco (1994), Air pollutant transport in a coastal environment. Part 1: Two-dimensional simulations of sea-breeze and mountain effects, *J. Atmos. Sci.*, *51*(15), 2285–2308, doi:10.1175/1520-0469(1994)051<2285:APTIAC>2.0.CO;2.

Lu, R., and R. P. Turco (1995), Air pollutant transport in a coastal environment–II. Three-dimensional simulations over Los Angeles Basin, *Atmos. Environ.*, *29*(13), 1499–1518, doi:10.1016/1352-2310(95)00015-Q.

Marr, L. C., and R. A. Harley (2002), Spectral analysis of weekday–weekend differences in ambient ozone, nitrogen oxide, and non-methane hydrocarbon time series in California, *Atmos. Environ.*, *36*(14), 2327–2335, doi:10.1016/S1352-2310(02)00188-7.

McMeeking, G. R., et al. (2010), Black carbon measurements in the boundary layer over western and northern Europe, *Atmos. Chem. Phys.*, *10*, 9393–9414, doi:10.5194/acp-10-9393-2010.

Menon, S., J. Hansen, L. Nazarenko, and Y. Luo (2002), Climate effects of black carbon aerosols in China and India, *Science*, *297*(5590), 2250–2253, doi:10.1126/science.1075159.

Mikhailov, E. F., S. S. Vlasenko, I. A. Podgorny, V. Ramanathan, and C. E. Corrigan (2006), Optical properties of soot–water drop agglomerates: An experimental study, *J. Geophys. Res.*, *111*, D07209, doi:10.1029/2005JD006389.

Modey, W. K., Y. Pang, N. L. Eatough, and D. J. Eatough (2001), Fine particulate ($PM_{2.5}$) composition in Atlanta, USA: Assessment of the particle concentrator-Brigham Young University organic sampling system, PC-BOSS, during the EPA supersite study, *Atmos. Environ.*, *35*(36), 6493–6502, doi:10.1016/S1352-2310(01)00402-2.

Moore, G. E., S. G. Douglas, R. C. Kessler, and J. P. Killus (1991), Identification and tracking of polluted air masses in the South-Central Coast Air Basin, *J. Appl. Meteorol.*, *30*(5), 715–732, doi:10.1175/1520-0450(1991)030<0715:IATOPA>2.0.CO;2.

Moteki, N., and Y. Kondo (2007), Effects of mixing state on black carbon measurements by laser-induced incandescence, *Aerosol Sci. Technol.*, *41*(4), 398–417, doi:10.1080/02786820701199728.

Moteki, N., and Y. Kondo (2010), Dependence of laser-induced incandescence on physical properties of black carbon aerosols: Measurements and theoretical interpretation, *Aerosol Sci. Technol.*, *44*(8), 663–675, doi:10.1080/02786826.2010.484450.

Moteki, N., et al. (2007), Evolution of mixing state of black carbon particles: Aircraft measurements over the western Pacific in March 2004, *Geophys. Res. Lett.*, *34*, L11803, doi:10.1029/2006GL028943.

Murphy, S. M., et al. (2009), Comprehensive simultaneous shipboard and airborne characterization of exhaust from a modern container ship at sea, *Environ. Sci. Technol.*, *43*(13), 4626–4640, doi:10.1021/es802413j.

Nehrkorn, T., J. Eluszkiewicz, S. C. Wofsy, J. C. Lin, C. Gerbig, M. Longo, and S. Freitas (2010), Coupled Weather Research and Forecasting–Stochastic Time-Inverted Lagrangian Transport (WRF-STILT) model, *Meteorol. Atmos. Phys.*, *107*, 51–64, doi:10.1007/s00703-010-0068-x.

Neiburger, M. (1969), The role of meteorology in the study and control of air pollution, *Bull. Am. Meteorol. Soc.*, *50*(12), 957–965.

Offenberg, J., and J. Baker (2000), Aerosol size distributions of elemental and organic carbon in urban and over-water atmospheres, *Atmos. Environ.*, *34*(10), 1509–1517, doi:10.1016/S1352-2310(99)00412-4.

Ohta, S., and T. Okita (1990), A chemical characterization of atmospheric aerosol in Sapporo, *Atmos. Environ., Part A*, *24*(4), 815–822, doi:10.1016/0960-1686(90)90282-R.

Ohta, S., M. Hori, S. Yamagata, and N. Murao (1998), Chemical characterization of atmospheric fine particles in Sapporo with determination of water content, *Atmos. Environ.*, *32*(6), 1021–1025, doi:10.1016/S1352-2310(97)00347-6.

Paatero, P., and U. Tapper (1993), Analysis of different modes of factor analysis as least squares fit problems, *Chemom. Intell. Lab. Syst.*, *18*(2), 183–194, doi:10.1016/0169-7439(93)80055-M.

Palau, J. L., G. Pérez-Landa, J. Meliá, D. Segarra, and M. M. Millán (2006), A study of dispersion in complex terrain under winter conditions using high-resolution mesoscale and Lagrangian particle models, *Atmos. Chem. Phys.*, *6*, 1105–1134, doi:10.5194/acp-6-1105-2006.

Park, K., D. B. Kittelson, and P. H. McMurry (2004), Structural properties of diesel exhaust particles measured by transmission electron microscopy (TEM): Relationships to particle mass and mobility, *Aerosol Sci. Technol.*, *38*(9), 881–889, doi:10.1080/027868290505189.

Park, S. S., Y. J. Kim, and K. Fung (2001), Characteristics of $PM_{2.5}$ carbonaceous aerosol in the Sihwa industrial area, South Korea, *Atmos. Environ.*, *35*, 657–665, doi:10.1016/S1352-2310(00)00357-5.

Paterson, K. G., J. L. Sagady, D. L. Hooper, S. B. Bertman, M. A. Carroll, and P. B. Shepson (1999), Analysis of air quality data using positive matrix factorization, *Environ. Sci. Technol.*, *33*(4), 635–641, doi:10.1021/es980605j.

Pollack, I. B., et al. (2012), Airborne and ground-based observations of a weekend effect in ozone, precursors, and oxidation products in the California South Coast Air Basin, *J. Geophys. Res.*, *117*, D00V05, doi:10.1029/2011JD016772.

Pósfai, M., J. R. Anderson, P. R. Buseck, and H. Sievering (1999), Soot and sulfate aerosol particles in the remote marine troposphere, *J. Geophys. Res.*, *104*(D17), 21,685–21,693, doi:10.1029/1999JD900208.

Pratsinis, S. E., M. D. Zeldin, and E. C. Ellis (1988), Source resolution of the fine carbonaceous aerosol by principal component-stepwise regression analysis, *Environ. Sci. Technol.*, *22*(2), 212–216, doi:10.1021/es00167a013.

Pueschel, R. F., D. F. Blake, K. G. Snetsinger, A. D. A. Hansen, S. Verma, and K. Kato (1992), Black carbon (soot) aerosol in the lower stratosphere and upper troposphere, *Geophys. Res. Lett.*, *19*(16), 1659–1662, doi:10.1029/92GL02478.

Raga, G., T. Castro, and D. Baumgardner (2001), The impact of megacity pollution on local climate and implications for the regional environment: Mexico City, *Atmos. Environ.*, *35*(10), 1805–1811, doi:10.1016/S1352-2310(00)00275-2.

Ramana, M. V., V. Ramanathan, Y. Feng, S.-C. Yoon, S.-W. Kim, G. R. Carmichael, and J. J. Schauer (2010), Warming influenced by the ratio of black carbon to sulphate and the black-carbon source, *Nat. Geosci.*, *3*(8), 542–545, doi:10.1038/ngeo918.

Ramanathan, V., and G. Carmichael (2008), Global and regional climate changes due to black carbon, *Nat. Geosci.*, *1*(4), 221–227, doi:10.1038/ngeo156.

Ramanathan, V., M. V. Ramana, G. Roberts, D. Kim, C. Corrigan, C. Chung, and D. Winker (2007), Warming trends in Asia amplified by brown cloud solar absorption, *Nature*, *448*(7153), 575–578, doi:10.1038/nature06019.

Reche, C., et al. (2011), New considerations for PM, black carbon and particle number concentration for air quality monitoring across different European cities, *Atmos. Chem. Phys.*, *11*, 6207–6227, doi:10.5194/acp-11-6207-2011.

Riemer, N., H. Vogel, and B. Vogel (2004), Soot aging time scales in polluted regions during day and night, *Atmos. Chem. Phys.*, *4*, 1885–1893, doi:10.5194/acp-4-1885-2004.

Robinson, E. (1952), Some air pollution aspects of the Los Angeles temperature inversion, *Bull. Am. Meteorol. Soc.*, *33*(6), 247–250.

Ruellan, S., and H. Cachier (2001), Characterisation of fresh particulate vehicular exhausts near a Paris high flow road, *Atmos. Environ.*, *35*(2), 453–468, doi:10.1016/S1352-2310(00)00110-2.

Schauer, J. J., W. F. Rogge, L. M. Hildemann, M. A. Mazurek, G. R. Cass, and B. R. T. Simoneit (1996), Source apportionment of airborne particulate matter using organic compounds as tracers, *Atmos. Environ.*, *30*(22), 3837–3855, doi:10.1016/1352-2310(96)00085-4.

Schnaiter, M., C. Linke, O. Möhler, K. Naumann, H. Saathoff, R. Wagner, U. Schurath, and B. Wehner (2005), Absorption amplification of black carbon internally mixed with secondary organic aerosol, *J. Geophys. Res.*, *110*, D19204, doi:10.1029/2005JD006046.

Schwarz, J. P., et al. (2006), Single-particle measurements of midlatitude black carbon and light-scattering aerosols from the boundary layer to the lower stratosphere, *J. Geophys. Res.*, *111*, D16207, doi:10.1029/2006JD007076.

Schwarz, J. P., et al. (2008a), Measurement of the mixing state, mass, and optical size of individual black carbon particles in urban and biomass burning emissions, *Geophys. Res. Lett.*, *35*, L13810, doi:10.1029/2008GL033968.

Schwarz, J. P., et al. (2008b), Coatings and their enhancement of black carbon light absorption in the tropical atmosphere, *J. Geophys. Res.*, *113*, D03203, doi:10.1029/2007JD009042.

Schwarz, J. P., et al. (2010), The detection efficiency of the single particle soot photometer, *Aerosol Sci. Technol.*, *44*(8), 612–628, doi:10.1080/02786826.2010.481298.

Seinfeld, J. H., and S. N. Pandis (2006), *Atmospheric Chemistry and Physics: From Air Pollution to Climate Change*, 2nd ed., John Wiley, Hoboken, N. J.

Shiraiwa, M., Y. Kondo, N. Moteki, N. Takegawa, Y. Miyazaki, and D. R. Blake (2007), Evolution of mixing state of black carbon in polluted air from Tokyo, *Geophys. Res. Lett.*, *34*, L16803, doi:10.1029/2007GL029819.

Shiraiwa, M., Y. Kondo, N. Moteki, N. Takegawa, L. K. Sahu, A. Takami, S. Hatakeyama, S. Yonemura, and D. R. Blake (2008), Radiative impact of mixing state of black carbon aerosol in Asian outflow, *J. Geophys. Res.*, *113*, D24210, doi:10.1029/2008JD010546.

Slowik, J. G., et al. (2007), An inter-comparison of instruments measuring black carbon content of soot particles, *Aerosol Sci. Technol.*, *41*(3), 295–314, doi:10.1080/02786820701197078.

Stelson, A. W. (1990), Urban aerosol refractive index prediction by partial molar refraction approach, *Environ. Sci. Technol.*, *24*(11), 1676–1679, doi:10.1021/es00081a008.

Stephens, M., N. Turner, and J. Sandberg (2003), Particle identification by laser-induced incandescence in a solid-state laser cavity, *Appl. Opt.*, *42*(19), 3726–3736, doi:10.1364/AO.42.003726.

Stier, P., J. H. Seinfeld, S. Kinne, and O. Boucher (2007), Aerosol absorption and radiative forcing, *Atmos. Chem. Phys.*, *7*, 5237–5261, doi:10.5194/acp-7-5237-2007.

Stohl, A., C. Forster, A. Frank, P. Seibert, and G. Wotawa (2005), Technical note: The Lagrangian particle dispersion model FLEXPART version 6.2, *Atmos. Chem. Phys.*, *5*, 2461–2474, doi:10.5194/acp-5-2461-2005.

Stolzenburg, M., N. Kreisberg, and S. Hering (1998), Atmospheric size distributions measured by differential mobility optical particle size spectrometry, *Aerosol Sci. Technol.*, *29*(5), 402–418, doi:10.1080/02786829808965579.

Subramanian, R., et al. (2010), Black carbon over Mexico: The effect of atmospheric transport on mixing state, mass absorption cross-section, and BC/CO ratios, *Atmos. Chem. Phys.*, *10*, 219–237, doi:10.5194/acp-10-219-2010.

Sullivan, A. P., R. E. Peltier, C. A. Brock, J. A. de Gouw, J. S. Holloway, C. Warneke, A. G. Wollny, and R. J. Weber (2006), Airborne measurements of carbonaceous aerosol soluble in water over northeastern United States: Method development and an investigation into water-soluble organic carbon sources, *J. Geophys. Res.*, *111*, D23S46, doi:10.1029/2006JD007072.

Toon, O. B., and T. P. Ackerman (1981), Algorithms for the calculation of scattering by stratified spheres, *Appl. Opt.*, *20*(20), 3657–3660, doi:10.1364/AO.20.003657.

Tripathi, S. N., S. Dey, V. Tare, and S. K. Satheesh (2005), Aerosol black carbon radiative forcing at an industrial city in northern India, *Geophys. Res. Lett.*, *32*, L08802, doi:10.1029/2005GL022515.

Turpin, B. J., and J. J. Huntzicker (1991), Secondary formation of organic aerosol in the Los Angeles basin: A descriptive analysis of organic and elemental carbon concentrations, *Atmos. Environ., Part A*, *25*(2), 207–215, doi:10.1016/0960-1686(91)90291-E.

Turpin, B. J., and J. J. Huntzicker (1995), Identification of secondary organic aerosol episodes and quantitation of primary and secondary organic aerosol concentrations during SCAQS, *Atmos. Environ.*, *29*(23), 3527–3544, doi:10.1016/1352-2310(94)00276-Q.

Turpin, B. J., and H.-J. Lim (2001), Species contributions to PM2.5 mass concentrations: Revisiting common assumptions for estimating organic mass, *Aerosol Sci. Technol.*, *35*(1), 602–610, doi:10.1080/02786820119445.

Turpin, B. J., J. J. Huntzicker, S. M. Larson, and G. R. Cass (1991), Los Angeles summer midday particulate carbon: Primary and secondary aerosol, *Environ. Sci. Technol.*, *25*(10), 1788–1793, doi:10.1021/es00022a017.

Ulbrich, I. M., M. R. Canagaratna, Q. Zhang, D. R. Worsnop, and J. L. Jimenez (2009), Interpretation of organic components from positive matrix factorization of aerosol mass spectrometric data, *Atmos. Chem. Phys.*, *9*, 2891–2918, doi:10.5194/acp-9-2891-2009.

Venkataraman, C., C. K. Reddy, S. Josson, and M. S. Reddy (2002), Aerosol size and chemical characteristics at Mumbai, India, during the INDOEX-IFP (1999), *Atmos. Environ.*, *36*(12), 1979–1991, doi:10.1016/S1352-2310(02)00167-X.

Wakimoto, R. M., and J. L. McElroy (1986), Lidar observation of elevated pollution layers over Los Angeles, *J. Clim. Appl. Meteorol.*, *25*(11), 1583–1599, doi:10.1175/1520-0450(1986)025<1583:LOOEPL>2.0.CO;2.

Weingartner, E., H. Burtscher, and U. Baltensperger (1997), Hygroscopic properties of carbon and diesel soot particles, *Atmos. Environ.*, *31*(15), 2311–2327, doi:10.1016/S1352-2310(97)00023-X.

Wonaschütz, A., S. P. Hersey, A. Sorooshian, J. S. Craven, A. R. Metcalf, R. C. Flagan, and J. H. Seinfeld (2011), Impact of a large wildfire on water-soluble organic aerosol in a major urban area: The 2009 Station Fire in Los Angeles County, *Atmos. Chem. Phys.*, *11*, 8257–8270, doi:10.5194/acp-11-8257-2011.

Zappoli, S., et al. (1999), Inorganic, organic and macromolecular components of fine aerosol in different areas of Europe in relation to their water solubility, *Atmos. Environ.*, *33*(17), 2733–2743, doi:10.1016/S1352-2310(98)00362-8.

Zarzycki, C. M., and T. C. Bond (2010), How much can the vertical distribution of black carbon affect its global direct radiative forcing?, *Geophys. Res. Lett.*, *37*, L20807, doi:10.1029/2010GL044555.

Zhang, Q., et al. (2007), Ubiquity and dominance of oxygenated species in organic aerosols in anthropogenically-influenced Northern Hemisphere midlatitudes, *Geophys. Res. Lett.*, *34*, L13801, doi:10.1029/2007GL029979.

Zier, M. (1991), Mass concentrations of total dust and soot in the near surface air in East Germany, *J. Aerosol Sci.*, *22*(S1), S597–S600, doi:10.1016/S0021-8502(05)80172-7.

W. Angevine and J. Brioude, Chemical Sciences Division, NOAA Earth System Research Laboratory, 325 Broadway, Mail Stop R/CSD4, Boulder, CO 80305, USA.

J. S. Craven, J. J. Ensberg, R. C. Flagan, A. R. Metcalf, and J. H. Seinfeld, Division of Chemistry and Chemical Engineering, California Institute of Technology, 1200 E. California Blvd., Mail Code 210-41, Pasadena, CA 91125, USA. (metcalf@caltech.edu; seinfeld@caltech.edu)

H. T. Duong and A. Sorooshian, Department of Chemical and Environmental Engineering, University of Arizona, PO Box 210011, Tucson, AZ 85721, USA.

H. H. Jonsson, Center for Interdisciplinary Remotely-Piloted Aircraft Studies, Naval Postgraduate School, Monterey, CA 93943, USA.

Chapter 7

Inorganic and Black Carbon Aerosols in the Los Angeles Basin During CalNex[1]

[1]This chapter is reproduced by permission from "Inorganic and Black Carbon Aerosols in the Los Angeles Basin During CalNex" by J. J. Ensberg, J. S. Craven, A. R. Metcalf, J. D. Allan, W. M. Angevine, R. Bahreini, J. Brioude C. Cai, H. Coe, J. A. de Gouw, R. A. Ellis, J. H. Flynn, C. L. Haman, P. L. Hayes, J. L. Jimenez, B. L. Lefer, A. M. Middlebrook, J. G. Murphy, J. A. Neuman, J. B. Nowak, J. M. Roberts, J. Stutz, J. W. Taylor, P. R. Veres, J. M. Walker, and J. H. Seinfeld, *Journal of Geophysical Research*, In Press. An edited version of this paper was published by AGU.

JOURNAL OF GEOPHYSICAL RESEARCH: ATMOSPHERES, VOL. 118, 1–27, doi:10.1029/2012JD018136, 2013

Inorganic and black carbon aerosols in the Los Angeles Basin during CalNex

J. J. Ensberg,[1] J. S. Craven,[1] A. R. Metcalf,[2] J. D. Allan,[3,4] W. M. Angevine,[5,6] R. Bahreini,[7] J. Brioude,[5,6] C. Cai,[8] H. Coe,[3] J. A. de Gouw,[5,6] R. A. Ellis,[9] J. H. Flynn,[10] C. L. Haman,[10] P. L. Hayes,[5,11] J. L. Jimenez,[5,11] B. L. Lefer,[10] A. M. Middlebrook,[6] J. G. Murphy,[12] J. A. Neuman,[5,6] J. B. Nowak,[5,6] J. M. Roberts,[6] J. Stutz,[13] J. W. Taylor,[3] P. R. Veres,[14] J. M. Walker,[15] and J. H. Seinfeld[1,15]

Received 22 May 2012; revised 4 December 2012; accepted 10 December 2012.

[1] We evaluate predictions from the Community Multiscale Air Quality (CMAQ version 4.7.1) model against a suite of airborne and ground-based meteorological measurements, gas- and aerosol-phase inorganic measurements, and black carbon (BC) measurements over Southern California during the CalNex field campaign in May/June 2010. Ground-based measurements are from the CalNex Pasadena ground site, and airborne measurements took place onboard the Center for Interdisciplinary Remotely-Piloted Aircraft Studies (CIRPAS) Navy Twin Otter and the NOAA WP-3D aircraft. BC predictions are in general agreement with observations at the Pasadena ground site and onboard the WP-3D, but are consistently overpredicted when compared to Twin Otter measurements. Adjustments to predicted inorganic mass concentrations, based on predicted aerosol size distributions and the AMS transmission efficiency, are shown to be significant. Owing to recent shipping emission reductions, the dominant source of sulfate in the L.A. Basin may now be long-range transport. Sensitivity studies suggest that severely underestimated ammonia emissions, and not the exclusion of crustal species (Ca^{2+}, K^{+}, and Mg^{2+}), are the single largest contributor to measurement/model disagreement in the eastern part of the L.A. Basin. Despite overstated NO_x emissions, total nitrate concentrations are underpredicted, which suggests a missing source of HNO_3 and/or overprediction of deposition rates. Adding gas-phase NH_3 measurements and size-resolved measurements, up to 10 μm, of nitrate and various cations (e.g. Na^{+}, Ca^{2+}, K^{+}) to routine monitoring stations in the L.A. Basin would greatly facilitate interpreting day-to-day fluctuations in fine and coarse inorganic aerosol.

Citation: Ensberg, J. J., et al. (2013), Inorganic and black carbon aerosols in the Los Angeles Basin during CalNex, *J. Geophys. Res. Atmos.*, *118*, doi:10.1029/2012JD018136.

All Supporting Information may be found in the online version of this article.

[1]Division of Chemistry and Chemical Engineering, California Institute of Technology, Pasadena, California, USA.
[2]Now at the Combustion Research Facility at Sandia National Laboratories, Livermore, California, USA.
[3]National Centre for Atmospheric Science, University of Manchester, Manchester, UK.
[4]School of Earth, Atmospheric and Environmental Sciences, University of Manchester, Manchester, UK.
[5]Cooperative Institute for Research in Environmental Sciences, University of Colorado Boulder, Boulder, Colorado, USA.

Corresponding author: J. H. Seinfeld, Division of Chemistry and Chemical Engineering, California Institute of Technology, Pasadena, California, USA. (seinfeld@caltech.edu)

2169-897X/13/2012JD018136

[6]Chemical Sciences Division, Earth System Research Laboratory, NOAA, Boulder, Colorado, USA.
[7]Now at the Department of Environmental Sciences University of California, Riverside, Riverside, California, USA.
[8]Planning and Technical Support Division, Air Resources Board, California Environmental Protection Agency, Sacramento, California, USA.
[9]Now at Harvard University, Cambridge, Massachusetts, USA.
[10]Department of Earth and Atmospheric Sciences, University of Houston, Houston, Texas, USA.
[11]Department of Chemistry and Biochemistry, University of Colorado, Boulder, Colorado, USA.
[12]Department of Chemistry, University of Toronto, Toronto, Ontario, Canada.
[13]Department of Atmospheric Sciences, University of California, Los Angeles, California, USA.
[14]Now at the Max Planck Institute for Chemistry in Mainz, Germany.
[15]Division of Engineering and Applied Science, California Institute of Technology, Pasadena, California, USA.

1. Introduction

[2] The Los Angeles mega-city has consistently experienced among the highest particulate matter levels in the United States and the highest ozone levels (http://www.stateoftheair.org/2012/city-rankings/most-polluted-cities.html). Several measurement campaigns have focused on characterizing particulate air quality in the Los Angeles Basin (e.g. *Appel et al*. [1982]; *Turpin and Huntzicker* [1991]; *Chow et al*. [1994]; *Watson et al*. [1994]; *Eldering et al*. [1994]; *Liu et al*. [2000]; *Hughes et al*. [2002]; *Pastor et al*. [2003]; *Croes and Fujita* [2003]; *Neuman et al*. [2003]; *Jacob et al*. [2010]; *Docherty et al*. [2011]), and in other urban areas, such as Pittsburgh, PA (Pittsburgh Air Quality Study, PAQS; e.g. *Wittig et al*. [2004]; *Cabada et al*. [2004]; *Modey et al*. [2004]; *Pekney et al*. [2006]; *Bein et al*. [2006]), Mexico City, Mexico (Mega-city Initiative: Local and Global Research Observations, MILAGRO; e.g. *Salcedo et al*. [2006]; *DeCarlo et al*. [2008]; *Querol et al*. [2008]; *Molina et al*. [2010]), Houston, Texas (2006 TexasAir Quality Study, TexAQS; e.g. *Parrish et al*. [2009]; *Nowak et al*. [2010]; *Washenfelder et al*. [2010]), and Beijing, China (Campaign of Air Quality Research in Beijing, CAREBEIJING; e.g. *van Pinxteren et al*. [2009]; *Yue et al*. [2009, 2010]; *Ianniello et al*. [2011]; *Zheng et al*. [2011]). Many studies have used data gathered during these field campaigns to evaluate the fidelity of three-dimensional atmospheric chemical transport models (CTMs) (e.g. *Sarwar and Bhave* [2007]; *Fountoukis and Nenes* [2007]; *Nolte et al*. [2008]; *Matsui et al*. [2009]; *Fountoukis et al*. [2009]; *McKeen et al*. [2009]; *Fast et al*. [2009]; *Foley et al*. [2010]; *Renner and Wolke* [2010]; *Zhang and Ying* [2010]; *Karydis et al*. [2010]; *Kelly et al*. [2010]; *Lee et al*. [2011]; *Huang et al*. [2011]; *Pfister et al*. [2011]).

[3] The California Research at the Nexus of Air Quality and Climate Change (CalNex) study was conducted during May–June 2010 to address both air quality and climate change through coordination and collaboration between several government agencies, such as the California Air Resources Board (CARB), the National Oceanic and Atmospheric Administration (NOAA), and academic institutions (www.esrl.noaa.gov/csd/calnex/). During CalNex, state-of-the-art airborne, ship-based, and ground-based measurements of atmospheric species, and of their transport over and off the coast of California, were conducted with the goal of understanding the impact of airborne pollutants on air quality and climate.

[4] The motivation for the present work is to evaluate the extent to which we understand the observed behavior of inorganic aerosols in the Los Angeles airshed, one of the world's most important urban areas from the point of view of air quality. The suite of ground-level and airborne measurements made during CalNex represent, by far, the most complete characterization of Los Angeles air quality yet carried out. Such a complex suite of measurements, gas and particle, surface and aloft, can only be placed in a unified context through the integration of chemistry and physics provided by a state-of-the-science atmospheric chemical transport model, driven by appropriate meteorology for the days of the experiment and operating on the emissions inventory of the region assembled by the relevant governmental agencies. In many respects, the current work can be seen as a parallel to the Mexico City MILAGRO study [*Molina et al*., 2010].

[5] To evaluate the extent to which predictions of a state-of-the-science CTM, driven by current emission inventories and resolved meteorological fields, agree with measured concentrations, we employ the Community Multiscale Air Quality (CMAQ) model version4.7.1 (http://www.cmaq-model.org/, *Foley et al*. [2010]) to simulate the three-dimensional distribution of aerosols and gases over Southern California during the CalNex field campaign. Predictions are compared to a suite of airborne and ground-based meteorological measurements, gas- and aerosol-phase inorganic measurements, and black carbon (BC) measurements over Southern California during the CalNex field campaign. Airborne measurements took place onboard the Center for Interdisciplinary Remotely-Piloted Aircraft Studies (CIRPAS) Navy Twin Otter aircraft (hereafter referred to as the Twin Otter) and the NOAA WP-3D (hereafter referred to as the P3) aircraft during May and June 2010. A Lagrangian particle dispersion model, FLEXPART (http://transport.nilu.no/flexpart, *Stohl et al*. [2005]), is used to track the origins of measured and predicted species in the Los Angeles Basin during CalNex by calculating back trajectories based on advection and turbulent mixing processes. Our goal is to identify the major sources of measurement/model disagreement for BC and various inorganic aerosol species and to suggest additional measures that address these sources of error. The organic component of the particulate matter will be addressed in a future study.

2. Model description and application

2.1. CMAQ

[6] In this study, we use CMAQ version 4.7.1 [*Foley et al*., 2010] on a domain that includes a large portion of Southern California as well as parts of Mexico (Figure 1), covering the area from (31.83°N, 121.43°W) to (35.69°N, 114.43°W) with 4 km by 4 km horizontal grid cells (102 x 156 grid points). Simulations cover the time period of May 2010. All simulations include a minimum spin-up period of four days to mitigate the influence of initial conditions, except for the P3 flight during 4 May 2012 which included only three days of spin up due to lack of MM5 meteorology for 30 April 2010. The meteorological fields used to drive the model were generated by the 5th generation Penn State/National Center for Atmospheric Research Meso-scale Model (MM5 version 3.7.4; *Grell et al*. [1995]). Three nested grids, with horizontal resolutions of 36, 12, and 4 km, were used to generate meteorological fields at the desired resolution (Figure S1). Nesting is the process by which a model simulation is run over a certain domain (the parent domain) at a given resolution. From the predicted concentrations within the parent domain, boundary conditions are extracted and used to drive a separate finer-resolution model simulation that is run over a portion of the parent domain (the nested domain). The MM5 model was initialized from NARR analysis data (http://nomads.ncdc.noaa.gov/data/narr/) with analysis nudging option, but observational nudging was not used. The 36 km and 12 km grids were first run together, via two-way nesting, using the Grell cumulus, simple ice microphysics, NOAH soil scheme, MRF PBL, and RRTM radiation options. The 4 km grid was then run, via one-way nesting, using boundary conditions derived from the 12 km grid with all options identical to the coarse domain simulations, except that the cumulus parameterization was turned off since the sufficiently fine horizontal

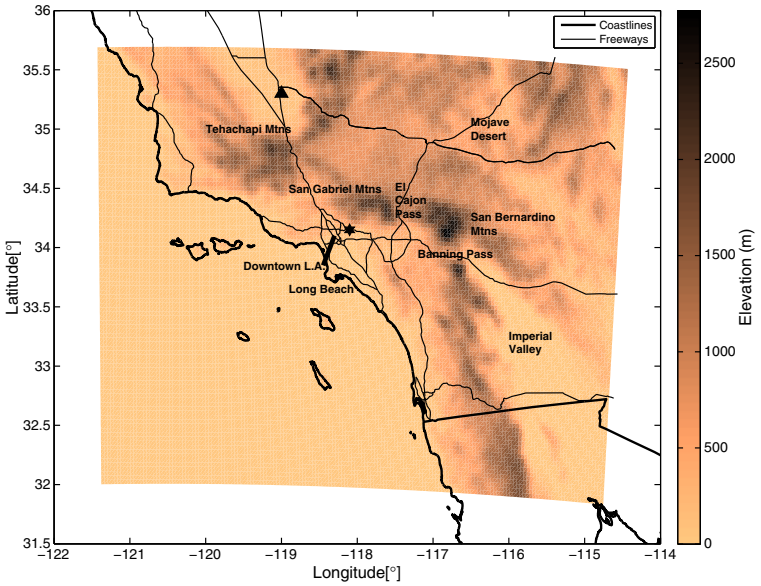

Figure 1. CMAQ modeling domain (colored area) used for simulations during the CalNex Field Campaign. The domain covers the area from (31.83°N, 121.43°W) to (35.69°N, 114.43°W) with 4 km x 4 km horizontal grid cells (102 x 156 grid points). The star represents the Pasadena ground site and the triangle represents Bakersfield.

resolution of the 4 km grid is expected to capture the smaller cloud scale atmospheric motions. CMAQ-compatible meteorological fields were then generated by processing MM5 output using the Meteorology-Chemistry Interface Program (MCIP) version 3.6 [*Otte and Pleim*, 2010]. Vertically, the meteorological fields extend from the surface to 100 mb (∼18 km above sea level) using 30 layers. This vertical resolution is typical for regional-scale and meso-scale modeling studies such as this. For instance, *Kelly et al.* [2010] configured CMAQ to use 30 vertical layers for the coast of Florida. Similarly, *Foley et al.* [2010] tested CMAQ4.7 over the eastern United States using 12, 24, and 34 vertical layers. In the present study, there are 11 layers in the lowest 1000 m, and the surface layer is ∼30 m deep.

[7] The emission inventory used in this study is a modified version of the day-specific ARCTAS-CARB inventory from June 2008. The modification consists of averaging June emissions to produce emissions for one representative week-day and one representative weekend-day for use during May 2010. In so doing, it is implicitly assumed that emissions did not change appreciably from 2008 to 2010. This assumption may be in question due to the recent emissions control programs, such as the diesel truck rules and ocean going vessel (OGV) fuel regulations (http://www.arb.ca.gov/msprog/operators.htm). As a result, emissions of BC and sulfur containing compounds may have decreased significantly from 2008 to 2010 [*Dallmann et al.*, 2011; *Lack et al.*, 2011]. The CARB recognizes this limitation and is working toward releasing a newer version of the emission inventory. Daily total emission rates for each species are given in Tables S4 and S5, and the emission inventory used in this study is available from the authors upon request. The limitations of the current CARB inventory are expected to impact agreement between observations and predictions of anthropogenic BC and sulfur containing compounds, but not sea-salt emissions of SO_4^{2-} which are modeled interactively in CMAQ [*Gong*, 2003; *Sarwar and Bhave*, 2007; *Kelly et al.*, 2010]. All meteorological fields and gridded emission inventories were prepared and provided by CARB.

[8] Gas-phase predictions are based on a modified version of the Statewide Air Pollution Research Center (SAPRC) chemical mechanism (version SAPRC07TC, *Carter* [2010]) implemented in CMAQ with the Rosenbrock numerical solver. The main modification consists of using an updated isoprene photooxidation mechanism based on *Paulot et al.* [2009a, 2009b]. Atmospheric mass distributions of particulate matter by size are represented in CMAQ as the superposition of three log-normal distributions, referred to as modes. These are the Aitken mode (typical D_p range is 20 nm to 90 nm), the accumulation mode (typical D_p range is 90 nm to 1-2.5 μm), and the coarse aerosol mode (typical D_p range is 1-2.5 to 10 μm) [*Binkowski and Roselle*, 2003]. Each mode is defined by its geometric standard deviation, geometric mean diameter, and the magnitude of mass within the mode. All particles are assumed to be spherical and each mode is assumed to be internally mixed chemically. Aerosol processes such as evaporation, condensation, coagulation, nucleation, advection, and wet and dry deposition affect the total number of particles, total surface area, and total mass within each mode. The majority of primary $PM_{2.5}$ emissions (99.9% by mass), including BC, are assigned to the accumulation mode, and a small fraction (0.1% by mass) is assigned to the Aitken mode according to section 1.3 of *Binkowski and Roselle* [2003].

[9] The thermodynamic model ISORROPIA-II [*Fountoukis and Nenes*, 2007] is used in CMAQ to compute the thermodynamic equilibrium of the NH_4^+-Na^+-SO_4^{2-}-NO_3^--Cl^--H_2O aerosol system. The assumption of thermodynamic equilibrium between fine inorganic particulate nitrate and ammonium with gas-phase nitric acid and ammonia is commonly invoked in atmospheric CTMs. The validity of this assumption for fine particles (D_p typically < 2.5 μm) was confirmed on the basis of data obtained during the 1999 Atlanta Supersite Experiment [*Zhang et al*., 2002]. *Karydis et al*. [2010] used the PMCAMx model with ISORROPIA-II to model inorganic aerosol measured during the Mexico City MILAGRO campaign. They concluded that explicitly treating mass transfer to and from coarse aerosol as a dynamic process is essential for capturing the competition between small and large particles for condensible inorganic vapors. To account for this competition, CMAQ partitions mass between the gas and aerosol phases according to the hybrid method [*Capaldo et al*., 2000], in which instantaneous equilibrium is assumed between the gas and aerosol phases in the two fine modes, and dynamic mass transfer governs the coarse aerosol mode. Since ISORROPIA-II is capable of simulating aerosol systems that include K^+-Ca^{2+}-Mg^{2+}, we conduct an additional sensitivity simulation on the impact of dust emissions and crustal species on inorganic aerosol concentrations in the L.A. Basin.

2.2. GEOS-Chem

[10] Dynamic chemical boundary conditions (1-h temporal resolution) used in the CMAQ simulations were generated from the GEOS-Chem global chemical transport model (version 9-01-01, http://acmg.seas.harvard.edu/geos/) via one-way nesting. GEOS-Chem was used to simulate global gas- and aerosol-phase concentrations at 2° latitude x 2.5° longitude horizontal resolution, with 47 vertical levels. Boundary conditions were extracted from the global simulation and used to drive a nested GEOS-Chem simulation over North America at 0.5° latitude x 0.667° longitude horizontal resolution, with 47 vertical levels. Finally, CMAQ-consistent boundary conditions were then extracted from the nested GEOS-Chem simulations for the domain shown in Figure 1. All three domains are shown on a single map in Figure S2. The coarse GEOS-Chem parent grid simulation spin-up period was 1 year, and the spin-up period for the nested GEOS-Chem grid simulation was 4 months (Jan-Apr 2010). Goddard Earth Observing System (GEOS-5) assimilated meteorological data from the NASA Global Modeling and Assimilation Office (GMAO) were used for all GEOS-Chem model simulations, which included ozone-NO_x-hydrocarbon chemistry [*Bey et al*., 2001] coupled with sulfate-nitrate-ammonium aerosol chemistry [*Park et al*., 2004]. Outside North America, global emissions used in the coarse simulations are from the Emissions Database for Global Atmospheric Research (EDGAR) inventory [*Olivier and Berdowski*, 2001]. Anthropogenic emissions data for the United States, used in GEOS-Chem, were from the EPA National Emissions Inventory (NEI) 2005, scaled to the simulation period according to trends in the EPA Acid Rain Program (http://camddataandmaps.epa.gov/gdm/) and the NEI Air Pollutant Emissions Trends Data (http://www.epa.gov/ttn/chief/trends/). The nested GEOS-Chem simulation also includes aircraft, biofuel and natural emissions of inorganic aerosol precursors, as described by *Park et al*. [2004].

[11] Since the nested GEOS-Chem horizontal grid resolution of 0.5° latitude x 0.667° longitude (~55 km x ~60 km at latitude 33°N) is considerably coarser than the 4 km x 4 km resolution of CMAQ, and the domain shown in Figure 1 is relatively small compared to the North American continent, the potential double-counting of species in the L.A. Basin was taken into consideration. Coarse resolution acts to smooth concentration gradients via dilution, thereby reducing peak values within the region and increasing species concentrations at the boundaries. These species can then partially reenter the L.A. Basin as boundary conditions, while simultaneously being emitted within the L.A. Basin via the ARCTAS-CARB emission inventory, which is physically unrealistic. However, it is possible for species emitted in the L.A. Basin to be transported outside the domain (Figure 1), and then reenter via recirculation. To determine the impacts of both of these potential issues, additional sensitivity simulations have been conducted with CMAQ using two sets of boundary conditions: (1) one set is derived from a nested GEOS-Chem simulation over North America that includes emissions in the L.A. Basin, and (2) one set is derived from the same nested GEOS-Chem simulation over North America with emissions in the domain shown in Figure 1 set to zero (the latter set was used in the results to be presented). The results (not shown) indicate that the impact of turning off emissions in the L.A. Basin in the nested GEOS-Chem simulation has virtually no impact on black carbon concentrations, and only a very slight impact on the boundary inflow of sulfate. Therefore recirculation and the potential double-counting of species are not issues in the current model configuration, although this may not be true for modeling configurations with different domain sizes and different grid-cell sizes, or if there are significant emissions sources near the boundaries of the nested domain.

2.3. FLEXPART

[12] To trace the origins of measured and predicted species during CalNex, a modified version of the FLEXPART Lagrangian particle dispersion model [*Stohl et al*., 2005] is used to calculate back trajectories of air masses. FLEXPART has been used extensively to quantify the impacts of meteorological processes on pollution transport (e.g., *de Foy et al*. [2006]; *Palau et al*. [2006]; *Ding et al*. [2009]; *Brioude et al*. [2009]). A detailed description of the FLEXPART model used in this study can be found in the Supplementary Material.

3. Observations

3.1. Pasadena Ground-Site Data

[13] Planetary boundary layer (PBL) heights were measured at the Pasadena ground site with a Vaisala Ceilometer CL31, which uses the minimum-gradient method to determine aerosol backscatter profiles [*Emeis and Schafer*, 2006; *Schafer et al*., 2004]. Observed PBL heights are compared to predicted PBL heights in Figure 2. Previous studies have shown overall agreement between this technique as compared to radiosonde and sonic detection and ranging estimates of PBL height [*Haman*, 2011; *van der Kamp et al*., 2010; *Martucci et al*., 2007; *Münkel et al*., 2006]. For this study, the average PBL height uncertainty and the minimum detection limit are ±5m and ~80 m, respectively. A detailed description of the instruments and settings used in this study can be found in *Haman* [2011].

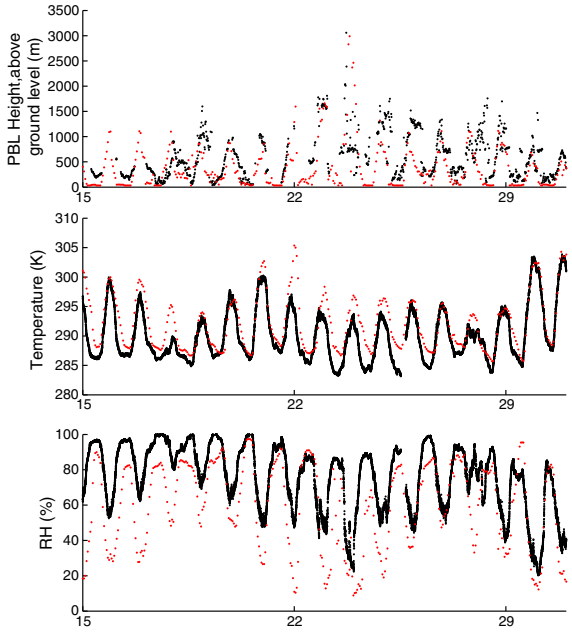

Figure 2. Observed (black) and predicted (red) planetary boundary layer (PBL) heights, temperature, and relative humidity (RH) at the Pasadena ground site from 15 May–31 May 2010.

[14] Refractory black carbon (BC) aerosol mass was measured at the Pasadena ground-site with a Droplet Measurement Technologies (DMT, Boulder, CO, USA) Single Particle Soot Photometer (SP2). Briefly, the SP2 detects refractory BC mass by measuring the incandescence signal emitted from single BC-containing particles heated to their boiling point when passing through an intense Nd:YAG laser beam (λ =1064 nm). BC volume-equivalent diameter (VED) is calculated from the detected mass assuming a spherical particle with density of 1.8 g cm^{-3} [*Bond and Bergstrom*, 2006]. The SP2 incandescence channels were calibrated in the same way as described in Section 2 of the Supplemental Material to *McMeeking et al*. [2010], with the main difference being that Alfa Aesar glassy carbon spheres were used instead of Aquadag. The data have been corrected for mass above and below the detection limit of the instrument by fitting a log-normal distribution to the primary mode in the BC mass distribution and another log-normal distribution to the residual of this fit (i.e. a secondary mode). The two fits were then added together, and the fraction of the fits above and below the SP2 detection limit were calculated as 8.0% of BC mass below the detection limit and 1.9% above. The measured BC mass concentrations have been divided by (1- 0.099). Based on *Shiraiwa et al*. [2008] and *Schwarz et al*. [2008b], the uncertainty in the determination of the mass of a single BC particle measured at the Pasadena ground site is estimated to be ~30%. All BC measurements from the Pasadena ground site are shown in Figure 3.

[15] Inorganic aerosol measurements were made by the University of Colorado-Boulder Aerodyne high-resolution time-of-flight aerosol mass spectrometer (Aerodyne HR-ToF-AMS, Aerodyne Research, Inc., Billerica, MA USA, [*DeCarlo et al*., 2008]) at the CalNex Pasadena ground site. The inlet is designed to transmit particles with vacuum-aerodynamic diameters (D_{va}) of 60 to 600 nm with unit transmission efficiency, although particles with D_{va} above 600 nm are also detected [*Canagaratna et al*., 2007; *DeCarlo et al*., 2004]. A composition-dependent collection efficiency (CE) was applied to the AMS data based on

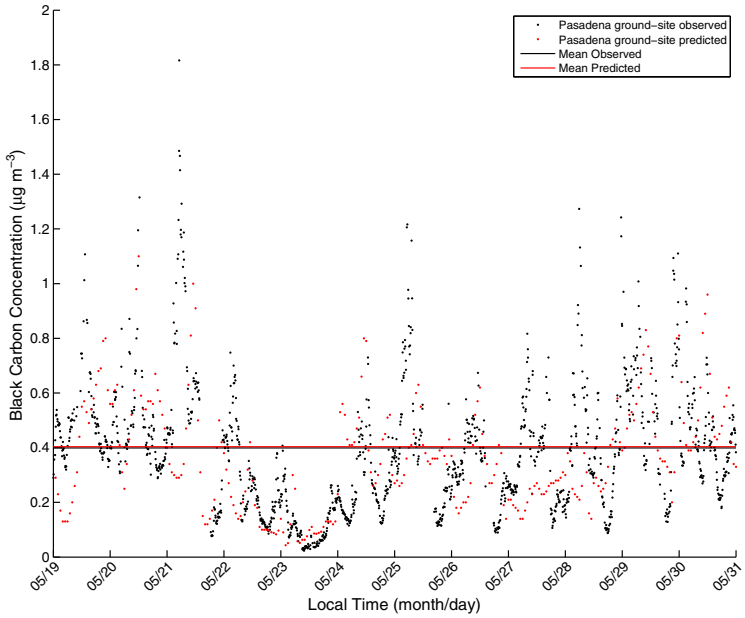

Figure 3. Measured (black dots) and predicted (red dots) BC concentrations at the Pasadena ground site from 19 May – 31 May 2010.

recent work [*Middlebrook et al*., 2012]. The composition based method for collection efficiency addresses the issue of particle bounce in the AMS and that particle bounce is a function of particle phase. The technique presented by *Middlebrook et al*. [2012] encompasses the four main factors influencing particle phase: relative humidity in the sampling line, acidity/neutralization of the sulfate content, ammonium nitrate content, and organic liquid content. For this data set, there were several instances where ammonium nitrate dominated the aerosol mass, and as shown in Figure 3 in *Middlebrook et al*. [2012], when the ammonium nitrate fraction exceeds 0.4, the CE for the aerosol increases from 0.45 to 1. Using a constant CE value during these periods would cause an overprediction of aerosol mass. The ground-site AMS measurements are reported as 5-min averages and have an uncertainty <30%. NH_3 was measured at 1 Hz by quantum cascade tunable infrared laser differential absorption spectroscopy (QC-TILDAS from Aerodyne Inc.) with an overall uncertainty during the CalNex campaign of 10% + 0.42 ppbv. [*Ellis et al*., 2010]. HNO_3 measurements were made with the acetate ion CIMS described by *Roberts et al*. [2010]. Data were acquired every 10 seconds, and were averaged to one minute. The calibrations were performed with permeation tubes calibrated as described by [*Neuman et al*., 2002]. The time constant for transmission of HNO_3 through the inlet was found to be several minutes. The overall uncertainty of the HNO_3 measurement was 34% + 0.05 ppbv. SO_2 mixing ratios were measured at the Pasadena site with a commercial pulsed fluorescence detector (Model 43i-TL, Thermo Electron Corp) operated as described in *Luke* [1997]. All inorganic species measurements from the Pasadena ground site are shown in Figure 4. Hourly measurements of NO_x and SO_2 at three ground sites in the L.A. Basin are also reported by the CARB ground network (http://www.arb.ca.gov/aqmis2/aqmis2.php) and shown in Figure 5.

3.2. CIRPAS Twin Otter

[16] BC aerosol mass was measured onboard the Twin Otter aircraft with a Droplet Measurement Technologies (DMT, Boulder, CO, USA) Single Particle Soot Photometer (SP2). The major findings from this SP2 during CalNex, including calibration of the instrument, are detailed elsewhere

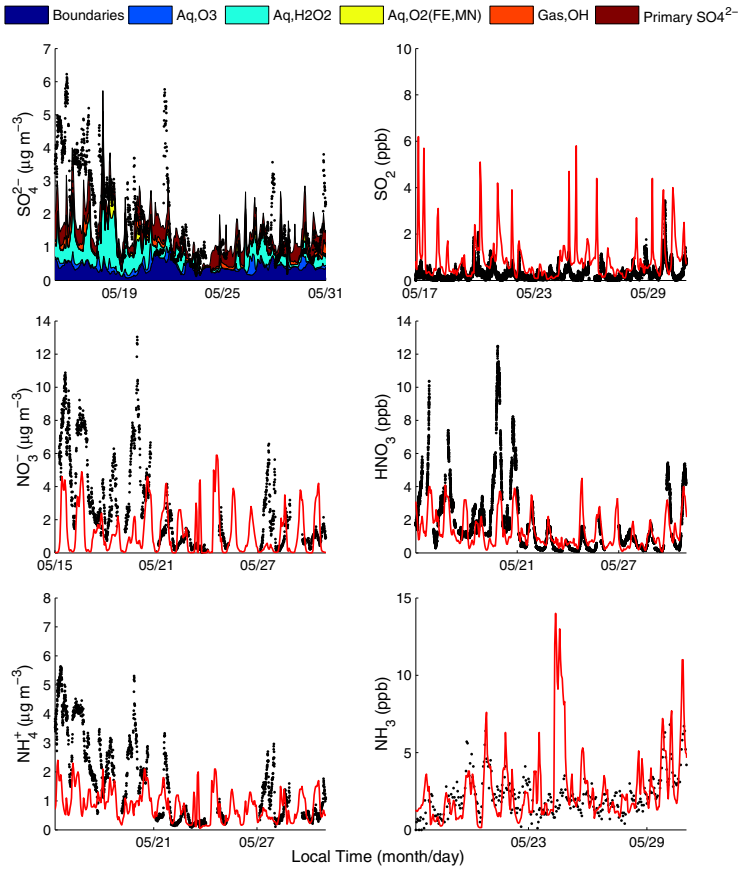

Figure 4. Observed (black) and predicted (red) particulate sulfate, nitrate, ammonium, sulfur dioxide, nitric acid, and ammonia concentrations from the CalNex Pasadena ground site. In the legend, "Boundaries" refers to sulfate attributable to boundary conditions, "(Aq,Gas),OX" refers to secondary sulfate produced by aqueous-phase (Aq) or gas-phase (Gas) oxidation of SO_2 by oxidant OX. "Primary SO_4^{2-}" refers to sulfate emitted within the basin.

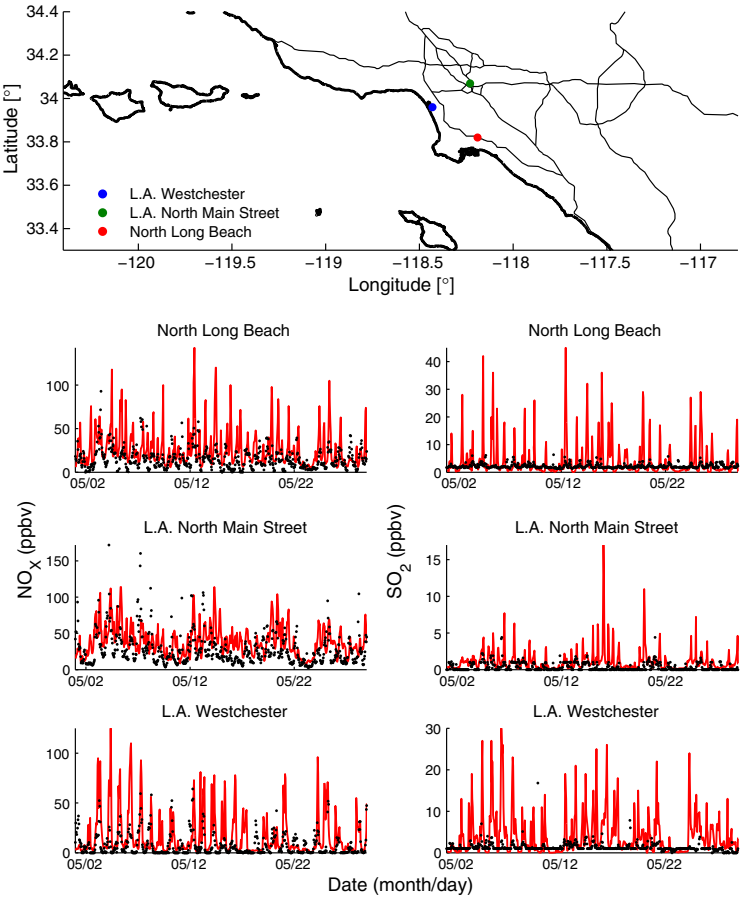

Figure 5. Measured (black) and predicted (red) NO_x and SO_2 mixing ratios for May 2010 at three locations in the Los Angeles Basin. Gaseous measurements were taken from the Air Quality and Meteorological Information System (AQMIS, http://www.arb.ca.gov/aqmis2/aqmis2.php).

[*Metcalf et al*., 2012]. In *Metcalf et al*. [2012], 1-min average data are reported, but in this study, we have re-sampled the dataset at 1 Hz to take advantage of the highest time-resolution available. To account for the BC mass outside the SP2 detection range, a single log-normal function is fit to each 1-s histogram of single-particle BC mass between 0.48 and 290 fg (50-675 nm VED, assuming a spherical particle density of 1.8 g cm^{-3}), and integrated to give bulk BC mass concentrations. Unlike the SP2 measurements at the Pasadena ground site, a single log-normal mode is sufficient to adjust the measured BC size distributions for mass above and below the Twin Otter SP2 detection limits [*Metcalf et al*., 2012]. As discussed in *Metcalf et al*. [2012], this adjustment increases bulk BC mass concentrations by 15–20%. Based on the calibration standards available, uncertainty in single-particle BC mass determination and bulk mass concentrations is estimated to be ~40%.

[17] Non-refractory particle mass and composition measurements were made by an Aerodyne compact time-of-flight aerosol mass spectrometer (C-ToF-AMS, Aerodyne Research, Inc., Billerica, MA USA) [*Drewnick et al*., 2005; *Murphy et al*., 2009]. The AMS onboard the Twin Otter measures sub-micron, non-refractory, size-resolved aerosol composition. The inlet and collection efficiency of the AMS onboard the Twin Otter were similar to those of the AMS at the Pasadena ground site. In an effort to measure aerosol mass distributions, the AMS onboard the Twin Otter was periodically run in particle-time-of-flight (PToF) mode. Due to relatively low aerosol loadings, the signal-to-noise ratio was not of sufficient quality for a meaningful comparison to size distributions predicted by CMAQ. Instead, we focus on bulk particulate ammonium (NH_4^+), particulate nitrate (NO_3^-), and particulate sulfate (SO_4^{2-}) mass concentrations reported as 10-s averages. We note that due to the attempted size-resolved measurements, narrow plumes may have been missed by the AMS onboard the Twin Otter.

[18] All Twin Otter measurements reported here are from instruments inside an unpressurized cabin. All instruments sampled downstream of a two-stage diffusion inlet with a transmission efficiency near unity for particle diameters up to about 3.5 μm [*Hegg et al*., 2005]. Sampling lines inside the cabin are kept reasonably uniform to all instruments, so further corrections for diffusional losses in these lines have not been made. The Twin Otter conducted 18 research

flights from Ontario, CA between 4 May and 28 May 2010 during CalNex. The AMS was onboard during 8 of the flights, three of which were to San Joaquin Valley, which is outside the domain shown in Figure 1. Therefore, this analysis makes use of 5 Twin Otter flights during which inorganic aerosol concentrations were measured within the L.A. Basin.

3.3. NOAA P3

[19] The P3 aircraft conducted 18 research flights from Ontario, CA between 4 May and 20 June 2010 during CalNex 2010 (esrl.noaa.gov/csd/calnex/). This study uses daytime measurements from 5 P3 flights that focused on sampling L. A. Basin emissions and the resulting photochemical products. NH_3, HNO_3, NH_4^+, NO_3^-, and SO_4^{2-}, and various meteorological parameters were measured onboard the P3 aircraft. NH_3 was measured at 1 Hz (equivalent to 100 m spatial resolution) by chemical ionization mass spectrometry (CIMS) with typical uncertainties of (30% + 0.2 ppbv) and a 1σ imprecision of 0.08 ppbv [*Nowak et al*., 2010]. HNO_3 was measured at 1 Hz by a separate CIMS instrument with an uncertainty of (15% + 0.040 ppbv) and a 1σ imprecision of 0.012 ppbv [*Neuman et al*., 2012]. CO measurements were made by a vacuum ultraviolet fluorescence instrument with ±5% uncertainty and 1 ppbv imprecision [*Holloway et al*., 2000]. SO_4^{2-}, NH_4^+, and NO_3^- were measured from a pressure-controlled region downstream of a low turbulence inlet using a compact time-of-flight aerosol mass spectrometer (Aerodyne, Billerica, Massachusetts) [*Bahreini et al*., 2009]. The AMS data are reported as 10-s averages with 2σ uncertainty (1-σ imprecision) of 34% (0.06 μg m^{-3}), 34% (0.01 μg m^{-3}), and 36% (0.01 μg m^{-3}) for ammonium, nitrate, and sulfate, respectively. BC measurements in the size range of 95-720 nm VED (still assuming a BC void-free density of 1.8 g cm^{-3}) were made by an SP2 similar to that used onboard the Twin Otter [*Schwarz et al*., 2006]. As with the SP2 measurements onboard the Twin Otter, a single log-normal function is sufficient to account for mass above and below the P3 SP2 detection limits, and this adjustment increases bulk BC mass concentrations by 10–25%. As described in detail in *Metcalf et al*. [2012], due to differences in calibration, measurements from the SP2 onboard the Twin Otter are potentially biased low by ∼12%, as compared to those from the SP2 onboard the P3 (e.g. if the P3 measurement is 1 μg m^{-3}, the Twin Otter measurement would be 0.88 μg m^{-3}).

[20] The AMSs used in this study, both ground-based and airborne, measured only particles with vacuum aerodynamic diameters between 60 nm and 600 nm diameter with 100% efficiency. Particles with aerodynamic diameters above 600 nm were also measured, but with reduced collection efficiency. However, since the predicted Aitken, accumulation, and coarse aerosol modes are expressed in CMAQ in terms of log-normal functions, each mode is defined for particle diameters ranging from zero to infinity. Therefore, all aerosol predictions are adjusted to match the transmission efficiency of the AMS based on the following piece-wise defined transmission function:

- 0% transmission below D_{va} = 40 nm;
- linear increase in transmission vs ln(D_{va}), from 0% at D_{va} = 40 nm to 100% at D_{va} = 100 nm;
- 100% transmission from D_{va} = 100 nm up to D_{va} = 550 nm;
- linear decrease in transmission vs ln(D_{va}), from 100% at D_{va} = 550 nm to 0% at D_{va} = 2 μm.
- 0% transmission above D_{va} = 2 μm;

[21] This transmission function is an average of the transmission curves used in several AMS studies as described in *Knote et al*. [2011] and references therein, and is applied to all inorganic aerosol predictions (CMAQ) that are compared to AMS measurements from the Pasadena site, the Twin Otter aircraft, and the P3 aircraft. We note that due to variation between specific aerodynamic lenses in different instruments, the exact transmission efficiencies of the AMS at the Pasadena site, onboard the Twin Otter, and onboard the P3 will be slightly different than the one used in this study. Appendix B presents the equations used to modify CMAQ predictions based on the AMS transmission window and efficiencies, and a derivation of these equations is given in the Supplemental Material. Measured BC concentrations from all platforms, adjusted for mass above and below the SP2 detection limits, are compared directly to the unmodified predicted BC concentrations in all results to be presented.

4. Results and Discussion

[22] The Aerosol Modeling Testbed analysis toolkit [*Fast et al*., 2011] was used to map three-dimensional CMAQ meteorological parameters, predicted gas-phase concentrations, and predicted aerosol-phase concentrations onto each flight path (as well as for various ground sites). The temporal resolution of the CARB emission inventory and MM5 meteorology is 1 h. In this work, CMAQ predicted species concentration fields, averaged over the previous hour, are compared to observations according to observational time-stamps (i.e. observational points with time-stamps of 12:20 and 12:40 would both be compared to predictions averaged between the hours of 12:00-13:00). The discrepancy between measured and simulated species concentration fields and meteorological parameters is quantitatively assessed using the following four statistical metrics:

$$ME = \frac{1}{N}\sum_{i=1}^{N}|P_i - M_i| \text{(mean error)} \quad (1)$$

$$MB = \frac{1}{N}\sum_{i=1}^{N}(P_i - M_i) \text{(mean bias)} \quad (2)$$

$$NME = \frac{\sum_{i=1}^{N}|P_i - M_i|}{\sum_{i=1}^{N}M_i} \text{(normalized mean error)} \quad (3)$$

$$NMB = \frac{\sum_{i=1}^{N}(P_i - M_i)}{\sum_{i=1}^{N}M_i} \text{(normalized mean bias)} \quad (4)$$

where N, P, and M stand for the number of data points, predicted quantity, and measured quantity, respectively.

4.1. Meteorological Variables

4.1.1. Ground Site

[23] Observed and predicted temperature, relative humidity (RH), and planetary boundary layer (PBL) height from the Pasadena ground site are shown in Figure 2 and statistical metrics are given in Table 1. Overall, the agreement

between observed and predicted PBL height in Pasadena has a 15-day average bias of -80 m (-9%). Agreement between observed and predicted temperature has a 15-day average bias of 1.06°C. The agreement between observed and predicted RH has a 15-day average bias of -10.3%. The discrepancies in RH are most likely a combination of underpredicted water vapor mixing ratios and of the exponential dependence of saturation-vapor pressure on errors in temperature (1°C temperature error leads to approximately 5% RH error). Additional ground-site comparisons of predicted and observed meteorology are given in the Supplemental Material. The results show that temperature and RH are consistently overpredicted and underpredicted, respectively, during the first week of May, with much better agreement during the last three weeks. Predicted wind speeds and wind directions agree to within 2 m/s and 60°, respectively, at all surface sites.

Table 1. Statistical Metrics Based on Measurements and Predictions at the Pasadena Ground Site During May 2010

Parameter	N	ME	MB	NME	NMB
PBL Height (m)	1179	129	-80	0.14	-0.09
Temperature (k)	24697	1.88	1.06		
RH (%)	24697	11.6	-10.3		
BC ($\mu g\ m^{-3}$)	3918	0.19	0.03	0.48	0.07
SO_4^{2-} ($\mu g\ m^{-3}$)	1860	0.93	-0.36	0.44	-0.17
NO_3^- ($\mu g\ m^{-3}$)	1860	2.15	-1.50	0.72	-0.50
NH_4^+ ($\mu g\ m^{-3}$)	1860	1.07	-0.76	0.35	-0.25
SO_2 (ppbv)	22491	0.72	0.64	2.50	2.01
HNO_3 (ppbv)	22761	0.98	-0.38	0.85	-0.38
NH_3 (ppbv)	366	1.51	0.45	0.74	0.22

ME = Mean Error, MB = Mean Bias, NME = Normalized Mean Error, NMB = Normalized Mean Bias. N is the number of data points collected during May 2010.

4.1.2. Twin Otter and P3

[24] The Twin Otter and P3 flight paths and altitudes are shown in Figures 6–11 and Appendix A Figures A1, A2, A3, A4. Temperature and relative humidity (RH) measurements from the Twin Otter and P3 flights are compared to

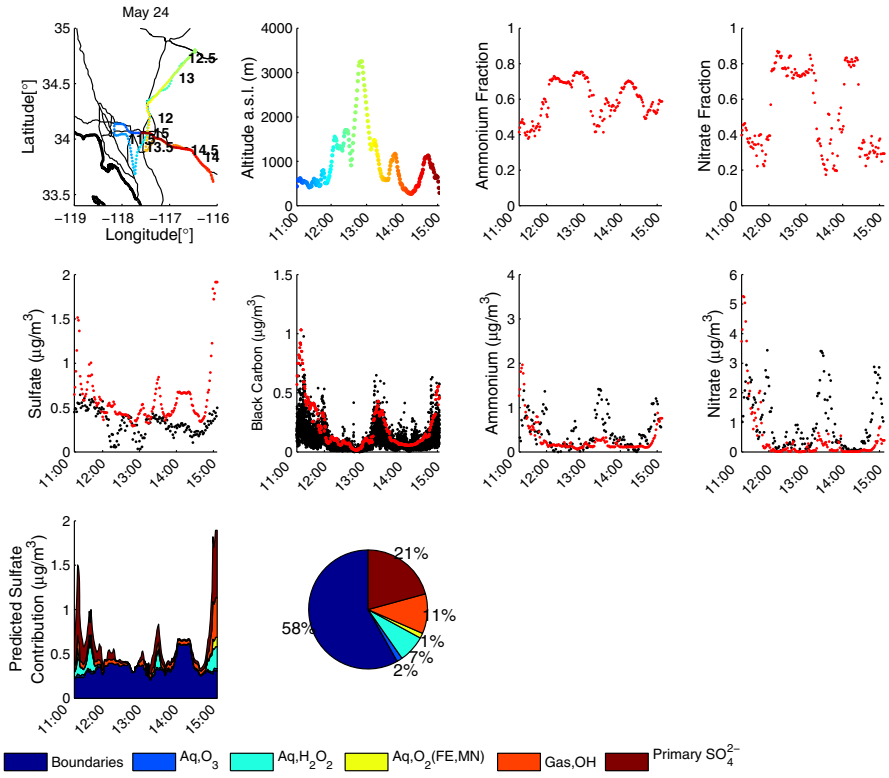

Figure 6. From left to right and top to bottom: Twin Otter aircraft flight path for May 24, Twin Otter altitudes (with respect to sea level) with the flight track and altitude trace are colored by the time (Pacific Standard Time) of day and time-stamps printed along each flight path in 30 min increments, Fraction of predicted particulate ammonium within the AMS transmission window, Fraction of predicted particulate nitrate within the AMS transmission window, predicted (red) and observed (black) sulfate concentrations, predicted (red) and observed (black) black carbon concentrations, predicted (red) and observed (black) nitrate concentrations, predicted (red) and observed (black) ammonium concentrations, predicted sulfate source apportionment, Pie chart indicating the relative contribution from routes to sulfate averaged over a given flight. In the bottom legend, "Boundaries" refers to sulfate attributable to boundary conditions, "(Aq,Gas),OX" refers to secondary sulfate produced by aqueous-phase (Aq) or gas-phase (Gas) oxidation of SO_2 by oxidant OX. "Primary SO_4^{2-}" refers to sulfate emitted within the basin.

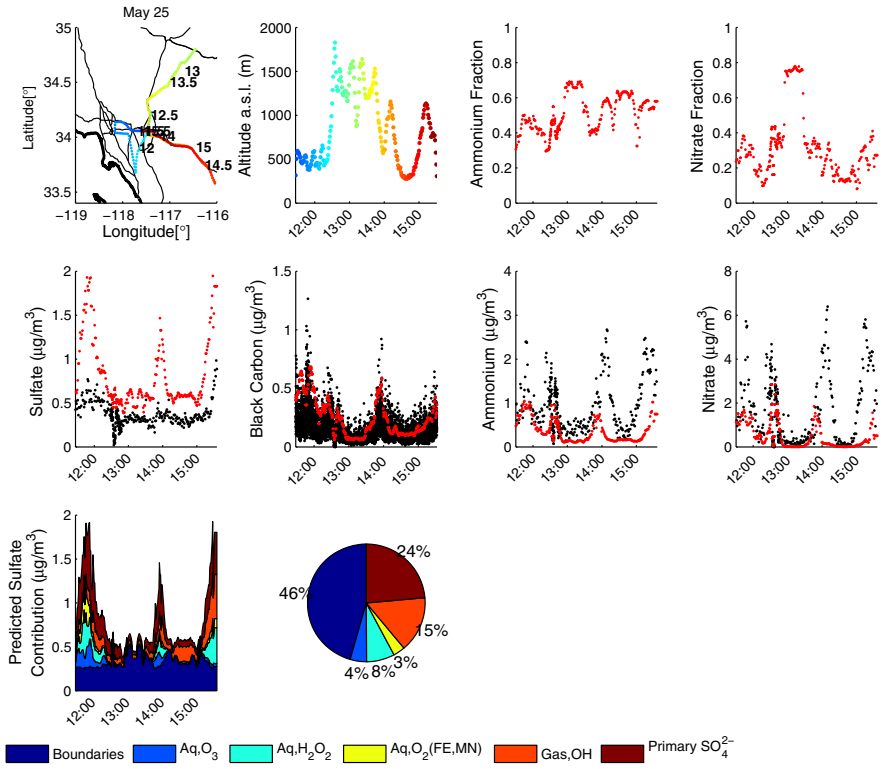

Figure 7. Same as Figure 6, but for the Twin Otter May 25 flight.

MM5 predictions in Table 2. Observed and predicted temperatures (averaged over each flight) typically agree to within 4°C, while observed and predicted RH (averaged over each flight) typically agree to within 15%. *Zhang et al.* [2006] evaluated MM5 meteorology coupled with CMAQ against measurements taken during the Southern Oxidants Study, and found similar levels of agreement between predicted and observed temperature and RH. In the present study, the largest disagreement occurred during the 21 May Twin Otter flight and the 14 May P3 flight, during which predicted RH was biased low by 26.6% and 22.1%, respectively. Wind speed and wind direction measurements onboard the Twin Otter and the P3 are shown in Table 3. Predicted and observed wind speeds generally agree to within ~50% when averaged over each flight. Although the mean discrepancy between predicted and observed wind direction ranges between 22-65°, the average predicted and observed wind direction is that of the daytime southwesterly sea breeze which advects emissions towards the north and northeast, exiting the Basin through passes in the San Gabriel and San Bernardino mountain ranges [*Lu and Turco*, 1995]. However, it is difficult to quantify errors in species concentrations attributable to discrepancies between measured and observed wind vectors.

4.2. Black Carbon

4.2.1. Pasadena Ground Site

[25] Measured and predicted BC concentrations at the Pasadena ground site are shown in Figure 3. The overall agreement between predicted and observed BC concentrations is very good, with a CalNex-average NME and NMB of 47.8% and 6.6%, respectively (Table 1). This NME of 47.8% is slightly higher than the measurement error inherent to the SP2 (~30–40%) owing mostly to large missing peaks in predicted BC on specific days (e.g. 27 and 28 May). Because predicted BC is chemically inert, the Pasadena ground-site is fixed, and all weekday emissions are assumed to be identical, day-to-day variations in BC predictions at the Pasadena ground site can only be caused by variations in the predicted meteorological fields (e.g. wind fields). For instance, May 20 and May 27 were both Thursdays. However, the 1-h average BC predictions on 27 May did not get above 0.4 μg^{-3}, while BC predictions on 20 May were up to 1.1 μg^{-3}. Since the predicted PBL heights on these days were comparable (Figure 2), variation in the predicted wind fields is the primary cause of the day-to-day variation in predicted BC concentrations. Therefore, if the differences between the predicted and observed wind fields on any given day are comparable to the day-to-day differences in the predicted wind fields, large errors in BC predictions may occur at any given point (e.g. Pasadena ground site). However, the overall agreement between predicted and observed BC at the Pasadena ground site (NMB = 6.6%) suggests that on average, both wind fields and upwind BC sources are represented well by CMAQ.

4.2.2. Twin Otter and P3

[26] Measured and predicted BC concentrations from the Twin Otter flights and the P3 flights during May 2010 are shown in Figures 6–11 and Figures A1, A2, A3, A4. The illusory differences in noise levels of the Twin Otter BC

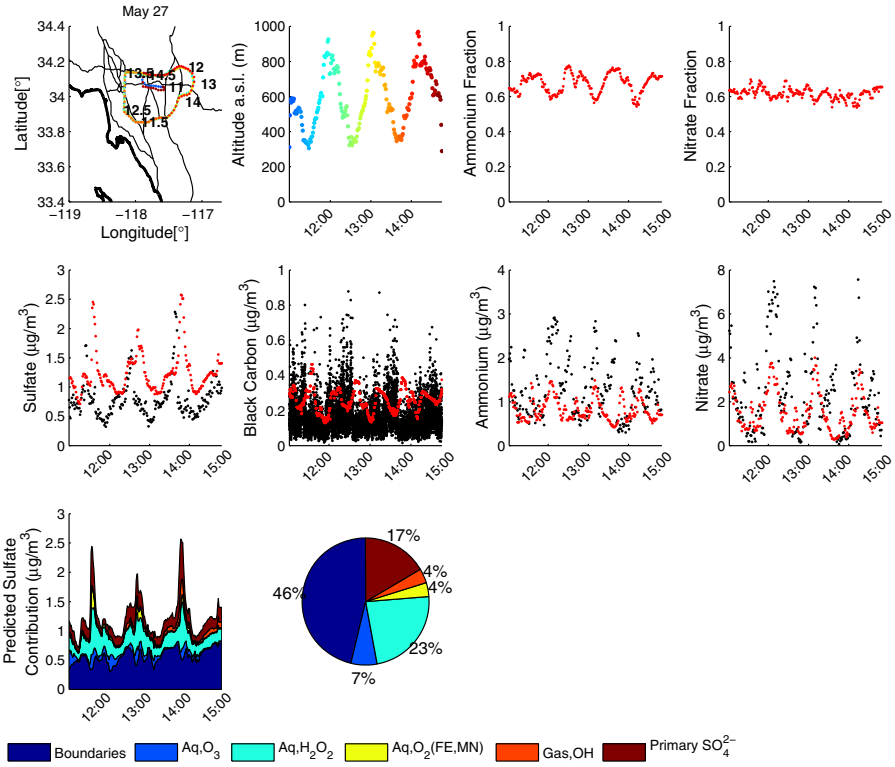

Figure 8. Same as Figure 6, but for the Twin Otter May 27 flight.

measurements and the P3 BC measurements exist because (1) the P3 aircraft transitioned between high and low altitudes many times during each flight, which creates the appearance of less noise due to very low BC concentrations at high altitudes, and (2) the average P3 flight was roughly 1.5 times longer than the average Twin Otter flight, but the x-axes in all time-series plots are the same length. Therefore, the P3 time-series are more compressed and the true level of noise in the measurements is somewhat obscured. To illustrate this, all measurements from both aircraft made above 1000 m a.s.l. have been removed and the resulting data-set is plotted as a function of data-point number, as opposed to time, so that the series plots are continuous (Figure S3). In addition, the x-axis limits for all subplots in Figure S3, regardless of the length of the flight, are identical. Figure S3 shows that the actual noise for both instruments is essentially comparable during most flights.

[27] A statistical comparison, at all altitudes and below 1000 m above sea level (a.s.l.) where local emissions influence BC concentrations most, between BC predictions and observations is given in Table 4. Although the extent of agreement between observations and predictions varies from flight to flight, the overall agreement (i.e. the 5-flight average) indicates that predicted BC concentrations have a slight positive bias (19.2%) when compared to P3 measurements below 1000 m a.s.l., and a significant positive bias (78.2%) when compared to Twin Otter measurements. Visual inspection of Figures 6–11 and Figures A1, A2, A3, A4 suggests that the CMAQ predictions capture the spatial distribution of BC during many flights, although the predicted concentration range is biased by 53 to 116% as compared to Twin Otter measurements below 1000 m a.s.l., and biased by -27% to 52% as compared to P3 measurements below 1000 m a.s.l. FLEXPART back trajectory analyses indicate that highest predicted BC concentrations exist in air masses influenced by emissions in the Long Beach industrial area. For example, the trajectory paths shown in Figure S4 suggest that during the 24 May flight, both observed and predicted concentrations of BC, at 11:21 (downtown Los Angeles) and 14:59 (Fontana), occurred in air masses that were influenced by emissions near Long Beach and downtown Los Angeles. We note that since WRF meteorological fields were used to drive FLEXPART, whereas MM5 meteorological fields were used to drive CMAQ, potential inconsistencies may exist between between the two sets of meteorology. Nevertheless, both the FLEXPART back trajectories and the extent of agreement between observed and predicted BC concentrations from both aircraft suggests that the locations of the BC sources are accurately accounted for in the CARB BC inventory used in this study.

[28] As mentioned previously, the calibration of the SP2 onboard the Twin Otter biased BC measurements low by 12% as compared to those of the SP2 onboard the P3 [*Metcalf et al.*, 2012]. Since the normalized statistical metrics used in this study are nonlinear functions of observed concentrations, the 12% measurement bias will cause higher than 12% bias when compared to predictions. As an example, in a 1-point data set, if the predicted BC concentration is 1 μg m^{-3} and the observed BC concentration is 0.568 μg m^{-3}, the NMB

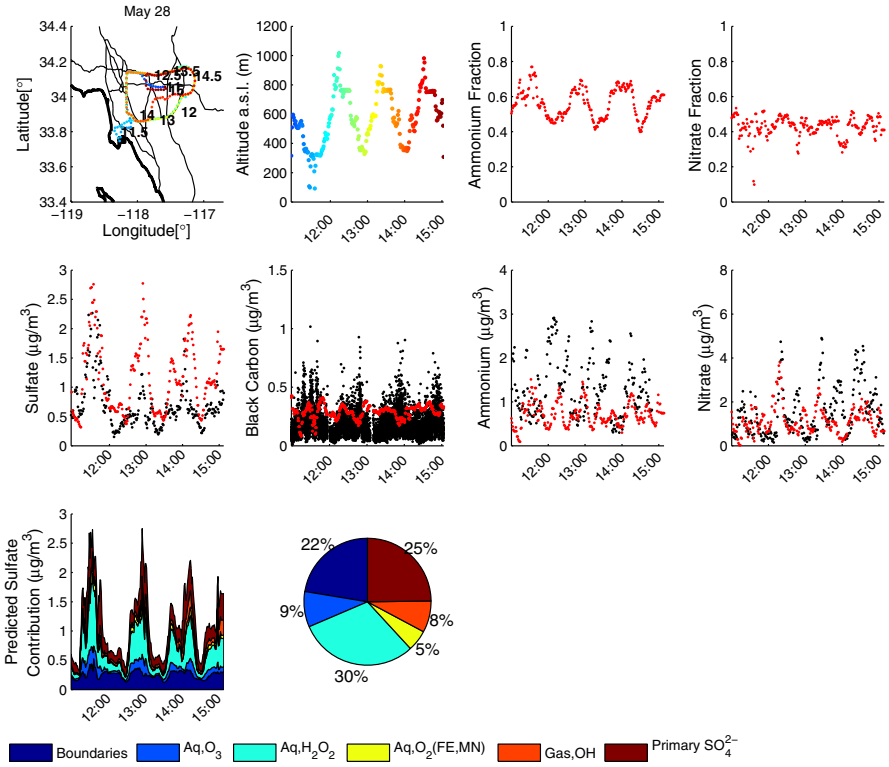

Figure 9. Same as Figure 6, but for the Twin Otter May 28 flight.

will be 76.1%. However, if the measured concentration is reduced to 0.5 μg m^{-3} due to the 12% instrument bias (88% of 0.568 is 0.5), the NMB becomes 100%, which is a difference inNMB of 23.9%. Taking this difference into account brings the NMBs from several of the Twin Otter flights into closer agreement with the higher NMBs from the P3 flight. For instance, dividing all Twin Otter measurements by 0.88 reduces the NMBs from the May 25, 27, and 28 Twin Otter flights (below 1000 m a.s.l.) to 56.5%, 34.6%, and 40.6%, respectively, making them comparable to the NMBs measured during the May 8 and 16 P3 flights, which are 52.3% and 39.5%, respectively. The precise reason for Twin Otter observations being a factor ~2 lower than predictions during the May 21 and 24 flights cannot be pinpointed at this time.

[29] Additional results showing measured and predicted CO mixing ratios (available only for P3 flights), as well as predicted and observed ΔBC/ΔCO ratios (Figure S5), are included in the Supplemental Material. For the comparison shown in Figure S5, ΔBC/ΔCO values are calculated by subtracting the minimum BC and CO measurements (background values) below 1000 m a.s.l. from all BC and CO measurements, respectively, below 1000 m a.s.l. Data points for which ΔCO < 1 ppbv are also removed. Note that, owing to data points lying on top of each other in Figure S5, the average ΔBC/ΔCO ratios (horizontal lines) can appear lower than the spread of individual data points may suggest. Since the accuracy of the ARCTAS-CARB CO emissions has already been established by *Wunch et al*. [2009], using measured and observed ratios of ΔBC/ΔCO reduces the impact of inaccuracies in meteorology at locations other than Pasadena. As shown in Figure S5, the comparisons of ΔBC/ΔCO are in general agreement with observations, with ratios being overpredicted during the May 8 and 16 flights, and underpredicted during the May 4, 14, and 16 flights. The agreement between surface measurements and the P3 measurements suggests that no systematic bias exists in the ARCTAS-CARB emission inventory, or the MM5 meteorology used in this study.

4.3. Sulfate

[30] To characterize the sources of the predicted sulfate, the CMAQ sulfate tracking system was employed, in which separate tracers are used to keep track of the sulfate contributions from the formation pathways listed in Table S1. Due to the transmission window of the AMS, the mass contributions from the Aitken mode and the coarse mode sulfate are a negligible fraction of the total predicted sulfate aerosol mass (< 1%) in the applicable size range and are not shown in Figure 4. Sulfate predicted to be formed by aqueous-phase oxidation by methyl hydrogen peroxide (MHP) and peroxyacetic acid (PAA) is also predicted to be negligible. However, *Stein and Saylor* [2012] show that the relative contributions of sulfate formation pathways depend critically on the chemical mechanism used. Specifically, during the ICARTT 2004 campaign, up to 30% of the sulfate in certain locations is attributable to the aqueous-phase oxidation of MHP when using CMAQv4.6 with the CBIV mechanism, and very little sulfate is attributable to PAA oxidation. However, this is likely

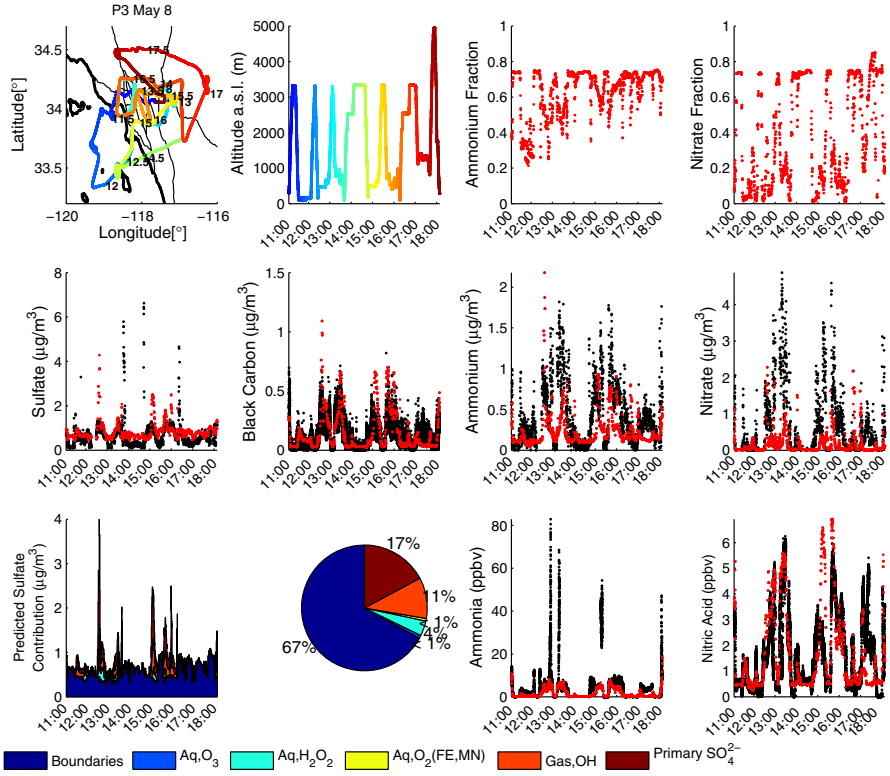

Figure 10. From left to right and top to bottom: P3 aircraft flight path for May 8, P3 altitudes (with respect to sea level) with the flight track and altitude trace are colored by the time (Pacific Standard Time) of day and time-stamps printed along each flight path in 30 min increments, Fraction of predicted particulate ammonium within the AMS transmission window, Fraction of predicted particulate nitrate within the AMS transmission window, predicted (red) and observed (black) sulfate concentrations, predicted (red) and observed (black) black carbon concentrations, predicted (red) and observed (black) nitrate concentrations, predicted (red) and observed (black) ammonium concentrations, predicted sulfate source apportionment, Pie chart indicating the relative contribution from routes to sulfate averaged over a given flight. In the bottom legend, "Boundaries" refers to sulfate attributable to boundary conditions, "(Aq,Gas),OX" refers to secondary sulfate produced by aqueous-phase (Aq) orgas-phase (Gas) oxidation of SO_2 by oxidant OX. "Primary SO_4^{2-}" refers to sulfate emitted within the basin.

an overestimation since the MHP concentrations were overpredicted by an order of magnitude with that mechanism. Furthermore, when using the CB05 or SAPRC99 mechanisms, very little sulfate is attributable to MHP oxidation, and up to 20% is attributable to PAA oxidation. However, this is also likely an overestimation since the PAA was overpredicted by up to a factor of 4 when using the CB05 or SAPRC99. We are not aware of any sulfate tracking assessments based on the SAPRC07 mechanism combined with the ARCTAS-CARB inventory. Although Fe^{3+} and Mn^{2+} are not model-predicted species in CMAQv4.7.1 (although they are in CMAQv5.0), prescribed background concentrations of 0.01 μg m^{-3} Fe^{3+} and 0.005 μg m^{-3} Mn^{2+} still lead to a small, but non-negligible, portion (up to 5%) of accumulation mode sulfate forming via these routes [*Walcek and Taylor*, 1986; *Chang et al.*, 1987]. The predominant predicted accumulation mode sulfate comes from four sources (no particular order): the inflow of sulfate from the boundaries (e.g. Asian inflow [*Lin et al.*, 2012]), aqueous-phase oxidation of S(IV) by H_2O_2 and O_3, gas-phase photooxidation of SO_2, and direct sulfate emission.

4.3.1. Pasadena Ground Site

[31] Observed and predicted sulfate and sulfur dioxide concentrations from the CalNex Pasadena ground site are shown in Figure 4, and statistical metrics are given in Table 1. In addition, ground-site SO_2 measurements from three locations within the L.A. Basin, taken from the CARB AQMIS are compared to CMAQ predictions in Figure 5. As at the Pasadena ground site, SO_2 mixing ratios are over-predicted at all locations within the L.A. Basin.

[32] Despite over-predictions in SO_2, predicted sulfate concentrations are actually biased low compared to sulfate measurements at the Pasadena ground site, mostly due to underestimations during the first few days of comparison. The relative sulfate contributions are listed in Table 5. Few clouds are present during daylight hours, but an MM5 predicted nighttime coastal marine layer facilitates aqueous-phase conversion of S(IV) to S(VI) in CMAQ. The predicted

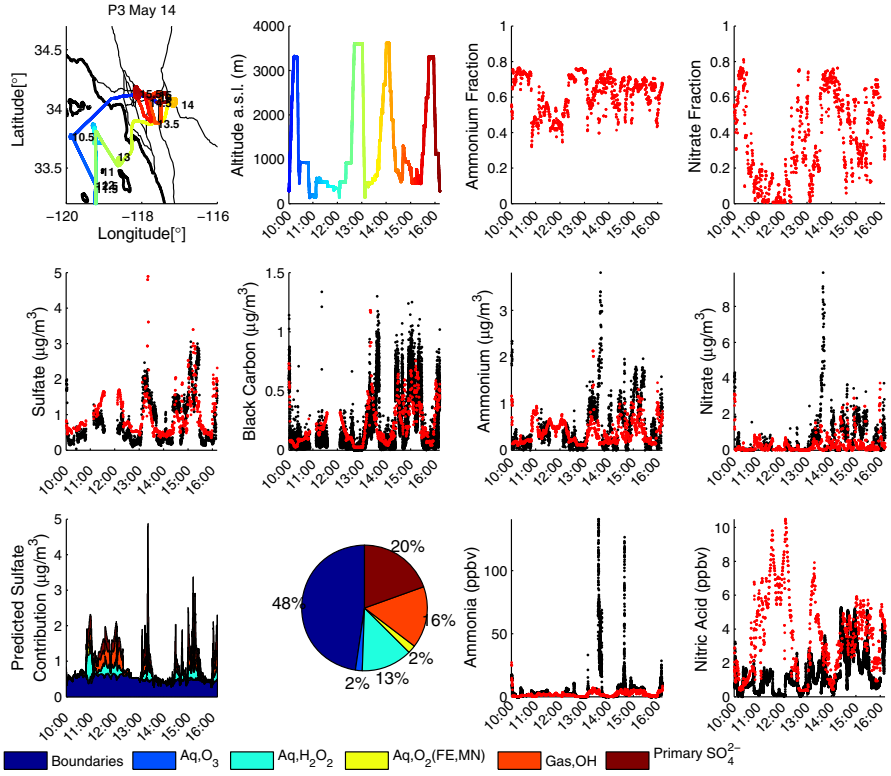

Figure 11. Same as Figure 10, but for the P3 May 14 flight.

marine layer evaporates during the day, but the cloud-processed sulfate remains airborne. At the Pasadena ground-site, enhancements in the relative sulfate contributions from aqueous-phase oxidation of SO_2 are not directly proportional to over-predictions in SO_2 emissions owing partially to the nonlinear pH dependence of the rate of S(IV) oxidation by O_3. More specifically, the second-order reaction rate constant for the S(IV)-O_3 reaction varies by up to four orders of magnitude for aerosol pH ranging from 1 to 6 [*Seinfeld and Pandis*, 2006]. Production of sulfate via this reaction lowers the pH and slows down the reaction. In addition, if the oxidants H_2O_2 and O_3 are the limiting reactants, the impacts of overestimated SO_2 emissions will also be lessened. Sulfate formation via gas-phase oxidation of SO_2 should respond more linearly to increases in SO_2 concentrations. However, the lifetime of SO_2 against the hydroxyl radical is relatively long (~1 week, *Seinfeld and Pandis* [2006]) and only represents 7% of the average predicted sulfate at the Pasadena ground site. Long-range transport of sulfate is predicted (CMAQ) to account for 26% of the sulfate measured at the Pasadena ground-site.

4.3.2. Twin Otter and P3

[33] Observed and predicted sulfate concentrations from the Twin Otter and P3 flights are shown in Figures 6–11 and Figures A1, A2, A3, A4. A statistical comparison between sulfate predictions and observations is given in Table 6. The average predicted sulfate concentration is biased high by 55% to 268% as compared to Twin Otter measurements, and biased by 0% to 71% as compared to P3 measurements

Table 2. Statistical Metrics Based on Measured and Predicted Temperature and Relative Humidity for Twin Otter and P3 Flights During May 2010

Flight Date	N	ME [°C]	MB [°C]
Temperature (Twin Otter)			
21	189	3.89	3.88
24	167	3.33	3.32
25	334	2.21	2.21
27	219	1.55	-1.23
28	239	0.75	-0.23
Temperature (P3)			
4	17219	2.12	0.60
8	25439	2.10	1.60
14	22258	3.77	3.33
16	27899	2.17	0.92
19	24239	1.67	0.71
Flight Date	N	ME [%]	MB [%]
Relative Humidity (Twin Otter)			
21	189	26.7	-26.6
24	167	9.99	-9.13
25	334	5.76	-5.12
27	219	10.5	5.67
28	239	7.16	-0.33
Relative Humidity (P3)			
4	17219	12.3	-0.47
8	25439	14.6	-1.00
14	22258	24.9	-22.1
16	27899	16.1	-7.91
19	24239	8.89	-2.49

ME = Mean Error, MB = Mean Bias. N is the number of data points collected during a given flight.

Table 3. Statistical Metrics Based on Measured and Predicted Wind Magnitudes and Directions for Twin Otter and P3 Flights During May 2010

Flight Date	N	ME [m/s]	MB [m/s]	NME	NMB
Wind Magnitudes (Twin Otter)					
21	180	1.89	1.19	0.38	0.23
24	167	1.79	-0.61	0.36	-0.12
25	334	1.89	0.49	0.37	0.10
27	219	2.04	0.98	0.56	0.27
28	239	2.00	2.11	0.55	0.52
Wind Magnitudes (P3)					
4	17219	2.33	-0.48	0.48	-0.10
8	25439	2.15	1.06	0.27	0.14
14	22258	1.69	0.57	0.55	0.19
16	27899	2.10	-0.26	0.41	-0.05
19	24239	4.03	-2.63	0.48	-0.31
Flight Date	N	ME [deg]	$\bar{\theta}_{obs}$ [deg]	$\bar{\theta}_{mod}$ [deg]	
Wind Directions (Twin Otter)					
21	180	23.8	242	254	
24	167	40.7	228	253	
25	334	28.8	209	223	
27	219	36.9	225	242	
28	239	22.5	240	246	
Wind Directions (P3)					
4	17219	64.0	263	239	
8	25439	24.2	263	276	
14	22258	65.1	203	206	
16	27899	54.5	224	230	
19	24239	25.2	278	267	

ME = Mean Error, MB = Mean Bias, NME = Normalized Mean Error, NMB = Normalized Mean Bias, and $\bar{\theta}$ = average wind direction. N is the number of data points collected during a given flight. The wind directions θ_{obs} and θ_{mod} are the observed and modeled wind directions, respectively, in units of degrees ($0^\circ \leq \theta \leq 360^\circ$). Wind direction, θ, is defined as the direction from which the wind is blowing, and is measured in degrees clockwise from true north.

Table 4. Statistical Metrics Based on Measured and Predicted Black Carbon Concentrations, at All Altitudes and Below 1000 m Above Sea Level, for Twin Otter Flights and P3 Flights During May 2010

Flight Date	N	ME [$\mu g\ m^{-3}$]	MB [$\mu g\ m^{-3}$]	NME	NMB
Black Carbon (Twin Otter, all altitudes)					
21	8537	0.23	0.19	1.08	0.90
24	6503	0.13	0.15	1.16	1.04
25	8256	0.13	0.11	0.84	0.70
27	8133	0.12	0.09	0.73	0.53
28	8700	0.14	0.11	0.79	0.60
5-flight average	40129	0.15	0.12	0.91	0.74
Black Carbon (Twin Otter, below 1000 m a.s.l.)					
21	6794	0.27	0.25	1.20	1.09
24	4117	0.17	0.16	1.26	1.16
25	5406	0.16	0.14	0.89	0.78
27	8133	0.12	0.09	0.73	0.53
28	8656	0.14	0.11	0.80	0.60
5-flight average	33106	0.17	0.14	0.94	0.78
Black Carbon (P3, all altitudes)					
4	16923	0.07	0.00	0.58	0.01
8	25257	0.08	0.04	0.74	0.32
14	18974	0.14	0.05	0.83	0.30
16	21273	0.10	0.07	1.32	1.01
19	23610	0.08	-0.03	0.47	-0.12
5-flight average	106037	0.09	0.03	0.79	0.31
Black Carbon (P3, below 1000 m a.s.l.)					
4	3527	0.13	-0.04	0.48	-0.13
8	11184	0.13	0.09	0.75	0.52
14	10803	0.16	0.02	0.62	0.09
16	9791	0.08	0.06	0.60	0.40
19	7518	0.17	-0.12	0.40	-0.27
5-flight average	42823	0.13	0.02	0.60	0.19

ME = Mean Error, MB = Mean Bias, NME = Normalized Mean Error, NMB = Normalized Mean Bias. N is the number of data points collected during a given flight.

(Table 6). Moreover, the relative contributions predicted from each sulfate source vary considerably for both aircraft depending on the individual flight path.

[34] A significant fraction of the predicted sulfate (airborne and ground-based) comes from direct sulfate emission and boundary inflow of sulfate, both of which are independent of SO_2 concentrations (Table 5 and Figures 6–11). That direct sulfate emission contributes a significant fraction of the predicted sulfate in the L.A. Basin can be understood via analysis of the CARB sulfur emission inventory (Tables S4 and S5). The CARB sulfur emission inventory includes gas-phase SO_2 emissions, gas-phase H_2SO_4 emissions, and particle-phase SO_4^{2-} emissions (i.e. direct sulfate emission). Since, sulfuric acid is highly water-soluble and has an extremely low vapor pressure, it is assumed to enter the particle-phase immediately upon emission. Therefore, direct sulfate emissions include both direct emission of sulfate and direct emission of sulfuric acid. The ratio (by mass) of the different sulfur emissions in the CARB inventory, $(H_2SO_4 + SO_4^{2-})/(H_2SO_4 + SO_4^{2-} + SO_2)$ within the Basin is ~5%. However, since only a fraction of the SO_2 emitted is converted to sulfate, the sulfate from primary emissions will account for more than 5% of the total sulfate measured at the ground site and by the aircraft [*Dominguez et al.*, 2008]. As shown in Figure 10 and 11, sharp increases in predicted sulfate were predicted but not measured by the P3 near Long Beach (e.g. 8 May just before 13:00 and 14 May just after 13:00). Similarly, FLEXPART back trajectories suggest that during the 21 May flight (at 11:23 and 13:57, specifically), the Twin Otter intercepted air masses that had been influenced by emissions near Long Beach (Figure S6) and should have contained high concentrations of primary sulfate. Since such hot spots of primary sulfate near Long Beach were generally not observed by the Twin Otter (Figures A1, 6, and 7), one concludes that the major source of disagreement between predicted and observed sulfate is most likely attributable to the emission inventory.

[35] Sulfate concentrations measured onboard the Twin Otter were below 1 $\mu g\ m^{-3}$ on 21, 24, and 25 May and showed little spatial variation. For these three flights, the predicted sulfate attributable to the GEOS-Chem boundary conditions represents 43-58% of the total predicted sulfate and accounts for almost the entire measured sulfate. Boundary

Table 5. Relative Contributions to Predicted Sulfate Concentrations at the Pasadena Ground Site Averaged Over 15-30 May 2010

Sulfate Pathway	Predicted contribution (%)
Boundary inflow	26
Aq, O_3	6
Aq, H_2O_2	29
Aq, O_2 (FEMN)	4
Gas, OH	7
Primary SO_4^{2-}	28

"Boundary inflow" refers to sulfate attributable to boundary conditions, "(Aq,Gas),OX" refers to secondary sulfate produced by aqueous-phase (Aq) or gas-phase (Gas) oxidation of SO_2 by oxidant OX. "Primary SO_4^{2-}" refers to sulfate emitted within the basin. "FEMN" refers to catalysts Fe^{3+} and Mn^{2+}

Table 6. Statistical Metrics Based on Measured and Predicted Particulate Sulfate, Ammonium, and Nitrate Concentrations for Twin Otter and P3 Flights During May 2010

Twin Otter					
Flight Date	N	ME [μg m^{-3}]	MB [μg m^{-3}]	NME	NMB
Sulfate					
21	185	1.30	1.30	2.68	2.68
24	172	0.28	0.27	0.84	0.82
25	337	0.39	0.39	1.11	1.11
27	224	0.50	0.44	0.62	0.55
28	244	0.53	0.46	0.77	0.65
Ammonium					
21	185	0.92	-0.77	0.62	-0.52
24	172	0.29	-0.14	0.68	-0.33
25	337	0.54	-0.51	0.60	-0.56
27	224	0.59	-0.47	0.46	-0.36
28	244	0.42	-0.20	0.46	-0.22
Nitrate					
21	185	1.64	-1.47	0.73	-0.65
24	172	0.80	-0.50	0.84	-0.52
25	337	1.17	-0.94	0.72	-0.58
27	224	1.24	-0.85	0.52	-0.35
28	244	0.93	-0.37	0.61	-0.24
P3					
Flight Data	N	ME [μg m^{-3}]	MB [μg m^{-3}]	NME	NMB
Sulfate					
4	1722	0.26	0.24	0.79	0.71
8	2544	0.41	0.20	0.65	0.32
14	2226	0.47	0.16	0.59	0.20
16	2790	0.33	0.00	0.33	0.00
19	2424	0.20	0.02	0.33	0.02
Ammonium					
4	1722	0.23	-0.11	0.77	-0.36
8	2544	0.27	-0.17	0.65	-0.42
14	2226	0.33	-0.15	0.64	-0.28
16	2790	0.47	-0.38	0.65	-0.52
19	2424	0.70	-0.65	0.71	-0.65
Nitrate					
4	1722	0.50	-0.31	0.99	-0.62
8	2544	0.51	-0.38	0.93	-0.68
14	2226	0.62	-0.37	0.91	-0.55
16	2790	0.94	-0.77	0.94	-0.76
19	2424	2.03	-1.99	0.80	-0.78

inflow of sulfate affects predicted sulfate concentrations along P3 flight paths in a similar manner. That the sulfate boundary conditions exert a noticeable impact on sulfate concentrations within the basin is not totally unexpected. For instance, *Huang et al*. [2011] evaluated the inflow of sulfur oxides ($SO_x = SO_2 + SO_4^{2-}$) to the South Coast (SC) of California by comparing predictions from the STEM atmospheric chemical transport model against aircraft measurements during the ARCTAS-CARB campaign [*Jacob et al*., 2010] in June 2008. They estimated that elevated SO_x levels at altitudes between 1-4 km enhanced SO_4^{2-} surface levels by a maximum of ~0.13 ppb (0.13 ppb $SO_4^{2-} \simeq 0.5$ μg m^{-3} at 1 atmosphere and 300 K) during this time period. Despite the influence of long-range SO_x transport, *Huang et al*. [2011] found that near-surface SO_x concentrations were mostly influenced by local emissions and estimated that the 2005 CARB sulfur emissions were low by about a factor of two. This is in contrast to our findings which suggest that the 2008 CARB SO_2 emissions are overestimated (Figure 5). Since the sulfur emission inventory used in *Huang et al*. [2011] is similar to that used in this study, the most likely explanation is that SO_2 emissions have decreased from 2008 to 2010, which is consistent with sulfur emission regulations that went into effect during those two years.

[36] The CMAQ sulfate source apportionment presented in this study suggests that, with the current sulfur emission inventory based on emission factors from 2008, long-range transport of sulfate accounts for 22-82% of the sulfate in the L.A. Basin. However, if the reductions in sulfur emission factors reported by *Lack et al*. [2011] (~90%) were to be included in the simulations, unlike the results presented in *Huang et al*. [2011], the boundary inflow of sulfate would become the single largest contributor to predicted sulfate concentrations in the L.A. Basin. Future work should continue to quantify the impact of foreign and domestic emissions on Southern California air quality as this is crucial for determining the potential efficacy of emission control strategies, and establishing the necessity for international collaboration.

4.4. Ammonium and Nitrate

[37] Ammonium nitrate aerosol is semivolatile and continuously partitions between the gas- and aerosol-phase. The distributions of total ammonium ($NH_3 + NH_4^+$) and total nitrate ($NO_3^- + HNO_3$) between the gas- and aerosol-phases are sensitive to the relative concentrations of other ions such as sulfate, sodium, and chloride, as well as meteorological factors such as temperature and relative humidity.

4.4.1. Pasadena Ground Site

[38] Particulate ammonium and nitrate predictions are generally biased low at the Pasadena ground site (Table 1). Aside from the large over-prediction on 24 May, NH_3 concentrations are well predicted (average bias of 22%), and predicted HNO_3 concentrations have a 15-day average bias of -38%. *Nowak et al*. [2012] used observations from the P3 aircraft during CalNex to show that the NH_3 emissions from automobiles in the CARB inventory are fairly accurate and contribute ~60 metric tons day^{-1} to the NH_3 budget within the L.A. Basin. *Nowak et al*. [2012] also found the NH_3 emissions from dairy facilities in the eastern part of the L.A. Basin are likely understated by up to a factor of 20. Since, strictly during the daytime, the Pasadena ground site is downwind of downtown L.A., but upwind of the dairy facilities, the predicted and observed NH_3 at this location is represented well within CMAQ.

[39] Ground-site NO_x ($NO + NO_2$) measurements taken from the CARB AQMIS are compared to CMAQ predictions in Figure 5. NO_x mixing ratios are over-predicted by a factor of ~2 at the three locations (North Long Beach, L.A.Westchester, and L.A. North Main Street location). Although slight over-predictions of temperature and under-predictions of RH artificially shift particulate ammonium and nitrate to the gas-phase, both particulate nitrate and nitric acid concentrations are underpredicted from 15-20 May. Since SO_4^{2-}, HNO_3, NO_3^-, and NH_4^+ are underpredicted during the first week of comparison, but are in better agreement with predictions during the second week, and since these species have different upwind sources, it is likely that errors in predicted wind fields, as opposed to uncertainties in the CARB emission inventory, are responsible for disagreement during the first week of comparison. Uncertainties/inaccuracies in predicted sea-salt emissions may also influence the agreement between predictions and observations at the Pasadena ground site, as will be discussed in the next section.

Table 7. Statistical Metrics Based on Measured and Predicted Ammonia and Nitric Acid Mixing Ratios for P3 Flights During May 2010

P3					
Flight Date	N	ME [ppbv]	MB [ppbv]	NME	NMB
Nitric Acid					
4	17219	0.92	-0.54	0.46	-0.27
8	25439	0.86	0.15	0.56	0.09
14	22258	2.50	2.32	1.96	1.82
16	27899	0.60	0.09	0.41	0.06
19	24239	0.96	-0.31	0.46	-0.15
Ammonia					
4	17219	2.96	-2.00	0.81	-0.55
8	25439	3.37	-3.00	0.98	-0.60
14	22258	3.80	-3.11	0.72	-0.59
16	27899	2.78	-2.05	0.86	-0.63
19	24239	12.38	-12.31	0.91	-0.90
Ammonia (no dairy)					
4	17219	1.39	-0.15	0.78	-0.09
8	25439	2.17	-1.98	0.60	-0.55
14	22258	1.25	-0.83	0.47	-0.31
16	27899	0.82	-0.34	0.77	-0.32
19	24239	2.80	-2.73	0.67	-0.68

Statistical metrics based on ammonia measurements in the "no dairy" column are calculated excluding all data points east of longitude 117.7°W.

4.4.2. Twin Otter and P3

[40] Observed and predicted particulate nitrate and ammonium concentrations from the Twin Otter and P3 flights are shown in Figures 6–11 and Figures A1, A2, A3, A4. Statistical metrics for inorganic aerosol species from both aircraft are given in Table 6. The fraction of simulated mass the AMS would measure is determined by taking the ratio of predictions that have been modified to match the AMS transmission efficiency to the total, unmodified inorganic aerosol concentration predictions. As shown in Figures 6–11 and Figures A1, A2, A3, A4, application of the AMS transmission efficiency results in the removal of ∼35% of the total predicted particulate sulfate and ammonium, and 20-100% (higher removal at low altitudes where sea-salt is present) of the total predicted nitrate during all flights. Since all predicted inorganic components are assumed to be in a metastable state (i.e. an aqueous electrolyte solution), predicted coarse mode particulate nitrate forms when HNO_3 reversibly condenses onto coarse NaCl particles via solution thermodynamics [*Kelly et al*., 2010]. This causes a significant fraction of the predicted particulate nitrate to reside in the coarse aerosol mode, while ammonium and sulfate reside primarily within the accumulation mode. Since sea-salt emissions are modeled online in CMAQv4.7.1, variations in wind speed lead to fluctuations in sea-salt emissions, and therefore different distributions of nitrate between the accumulation mode and the coarse mode. As shown in Figure S7, the day-to-day differences in sodium emissions can be substantial. Therefore, the differences in the fraction of nitrate removed by the AMS transmission curve along somewhat similar flight paths is likely attributable to the amount of sea-salt emitted. For instance, the amount of predicted nitrate removed as a result of the AMS transmission efficiency curve is ∼40% on the 27 May flight and ∼55% on the 28 May flight, which is consistent with the sea-salt emissions on May 28 being much greater than on May 27 (Figure S7). Adding size-resolved sodium and nitrate measurements, up to 10 μm, at various monitoring sites in the L.A. Basin would help unravel the impacts of anthropogenic and natural emissions on inorganic aerosol formation.

[41] Gas-phase measurements of HNO_3 and NH_3 were not conducted on the Twin Otter, so one cannot determine based on that data set alone if discrepancies between particulate ammonium and nitrate observations and predictions are the result of errors in the NO_x ($NO + NO_2$) emissions, NH_3 emissions, or predictions of HNO_3 within the SAPRC07TC chemical mechanism. However, HNO_3 and NH_3 measurements were conducted onboard the P3 aircraft (Figures 10, 11 and Figures A2, A3 and Table 7). As stated previously, *Nowak et al*. [2012] estimated, via mass balance, that the NH_3 emissions from automobiles in the CARB inventory are consistent with their measurements (∼60 metric tons day^{-1}), but that the CARB inventory underestimates NH_3 emissions from dairy facilities by a factor of 3-20. By conducting a formal 3-D simulation, we not only corroborate the conclusions of *Nowak et al*. [2012], but also show that NH_3 mixing ratios can be under-predicted by factors as high as $10^2 - 10^3$ (Figure 16). Moreover, sharp increases in submicrometer ammonium and nitrate measurements downwind of dairy facilities (e.g. Figure 11 just before 14:00) can be attrib uted entirely to point-source dairy NH_3 emissions. As these sharp increases in ammonium and nitrate are consistently missed by predictions, severely underpredicted NH_3 emissions from dairy facilities is identified as the dominant source of measurement/model disagreement in the eastern L.A. Basin. Upwind of dairies, predicted NH_3 mixing ratios are in better agreement with observations (see "no dairy" metrics in Table 7). Similarly, HNO_3 mixing ratios are generally predicted well during the P3 flights (NME typically ∼0.5) with the most notable exception being 14 May between 11:00 and 12:00 when the aircraft flew off the coast. HNO_3 and NO_x contour maps (not shown) suggest that the over-predictions on 14 May are caused by overstated coastal NO_x emissions (Figure 5).

[42] Even though gas-phase measurements were not taken onboard the Twin Otter, the impact of understated ammonia emissions and underpredicted total nitrate concentrations can be seen in the particulate ammonium and nitrate measurements (Figures 6–8). For instance, as shown in Figures 6 and 7, particulate ammonium and nitrate concentrations are significantly under-predicted in the eastern part of the L.A. Basin before the Twin Otter flew into the outflow regions at 12:30 and 14:30 during the 21 May flight. These under-predictions are exacerbated by an under-prediction of RH by 26.6% (flight average, Table 2). Particulate ammonium and nitrate concentrations are also under-predicted in the eastern part of the L.A. Basin during the 24 (between 13:00 and 15:00), 25 (between 13:30 and 15:30), and 27 (just after every hour) flights. Both predicted and observed nitrate concentrations are ∼2 times higher in the eastern part of the L.A. Basin on 25 May as compared to 24 May. The differences in nitrate concentrations are potentially attributable to warmer temperatures and lower RHs (predicted and observed) that shift both predicted and observed particulate nitrate to the gas-phase during the 24 May flight.

[43] Given that surface-level NO_x concentrations are generally over-predicted (Figure 5), one might expect the total nitrate mixing ratios to be over-predicted. However, as shown in Figure S8 and given in Table S2, the predicted total nitrate mixing ratios (within the AMS transmission window) agree with observations to within 50% NME, but tend to be

Table 8. Speciation of Primary PM_{fine} and PM_{coarse} Emissions Into Ca^{2+}, K^+, and Mg^{2+}

Fine Mode Species	Reff et al. [2009]
Ca^{2+}	0.0386×A25J
K^+	0.0309×A25J
Mg^{2+}	0.00368×A25J
Coarse Mode Species	CMAQv5.0[1]
Ca^{2+}	0.0838×ASOIL + 0.0562×ACORS
K^+	0.0242×ASOIL + 0.0176×ACORS
Mg^{2+}	0.0000×ASOIL + 0.0032×ACORS

[1]ASOIL = 0.9× PM_{coarse}, ACORS = 0.1× PM_{coarse}, A25J = PM_{fine}

under-predicted. There are several potential explanations for this. (1) Since the daytime production of HNO_3 occurs via gas-phase oxidation of NO_2 ($OH + NO_2 \rightarrow HNO_3$), the predicted OH concentration, which is highly dependent on the concentrations of hydrocarbons and other oxidants, may be too low. (2) The rate of conversion of NO to NO_2, which is also highly dependent on the concentrations of hydrocarbons and other oxidants, may be limiting. (3) The nighttime heterogeneous reaction of N_2O_5 ($N_2O_5(g) + H_2O(s) \rightarrow 2HNO_3$) may be understated. (4) If the predicted particulate nitrate mass concentrations are correct, but the size distributions predicted by CMAQ are inaccurate, the amount of predicted particulate nitrate could be biased low once predictions are adjusted to match the size-dependent transmission efficiency of the AMS. (5) Inaccurate shifting of total nitrate from the particle phase to the gas phase for various potential reasons (e.g. over-predicted temperature, under-predicted RH, over-predicted SO_4^{2-} concentrations, under-predicted NH_3 emissions) may artificially enhance the removal of total nitrate from the system due to faster dry deposition rates for gas-phase HNO_3 [*Dzepina et al*., 2009]. (6) Coarse cations (either from sea-salt particles or crustal species from dust emissions) may significantly reduce HNO_3 concentrations via condensation of HNO_3 onto deliquesced particles to form non-refractory coarse nitrate [*Fountoukis et al*., 2009; *Hsu et al*., 2007; *Moya et al*., 2002; *Jacobson*, 1999].

[44] We focus on the possibilities (4) and (6) regarding total nitrate underpredictions and defer a detailed analysis regarding the extent to which the other four sources of inaccuracy/uncertainty impact the amount of total nitrate predicted as the subject of future work. We note, however, that positive temperature biases and negative RH biases (Table 2), as well as positive sulfate biases (Table 6) and negative ammonia biases (Table 7), suggest that several of these possible factors contribute to shifting of predicted particulate nitrate to the gas-phase, thereby artificially enhancing total nitrate removal via dry deposition. To examine the hypothesis that total nitrate concentrations are underpredicted during most flights due to inaccurate distribution of total nitrate between the gas-phase, the fine aerosol-phase, and the coarse aerosol-phase, we present statistical metrics for all five P3 flights (Table S2) with and without the AMS transmission curve applied to predictions. When the AMS transmission efficiency is taken into consideration, total nitrate concentrations are underpredicted during four of the five P3 flights by 0-42% (Table S2). However, when full transmission (i.e. all predicted particulate nitrate and gas-phase nitric acid) is assumed, total nitrate concentrations are still underpredicted by up to 33% during the 4, 16, and 19 May flights. Since coarse particles were not measured onboard the Twin Otter or P3, the accuracy of the coarse mode nitrate predictions cannot be assessed. However, by comparing predicted and observed concentrations of total nitrate, assuming full transmission (Table S2), we show that regardless of whether nitrate is predicted to form ammonium nitrate, nitric acid, or coarse nitrate (e.g. sodium nitrate, calcium nitrate, potassium nitrate, etc.), on most days predicted total nitrate concentrations are simply not high enough. We deduce that the two likeliest causes of this are: (1) there is a missing source of HNO_3, or (2) the inaccurate distribution of total nitrate between the gas-phase and the two aerosol modes artificially enhances the removal of nitrate via dry deposition.

4.4.3. Impact of Crustal Species on Ammonium and Nitrate

[45] Several studies have shown that crustal species (Mg^{2+}, K^+, Ca^{2+}), from both anthropogenic emissions and fugitive dust, can potentially influence the thermodynamic partitioning of ammonium and nitrate aerosol between the gas-phase and both fine and coarse aerosol modes [*Fountoukis et al*., 2009; *Moya et al*., 2002; *Jacobson*, 1999]. Dominant sources of crustal species include unpaved and paved roads, agricultural tilling, construction dust, and sand and gravel from mining and quarry operations [*Reff et al*., 2009]. Assessing the impacts of crustal species requires representation of fugitive dust emissions, anthropogenic dust emissions, and chemical speciation profiles to determine the mass fraction of crustal elements within the dust. All three of these inputs are not well constrained on regional and global scales. For example, in a modeling study of the April 2001 dust storm episode over the trans-Pacific domain, *Wang et al*. [2012] assume that 10% of emitted crustal species reside in the fine mode and 90% reside in the coarse mode based on results presented in *Midwest Research Institute*, 2005, and use a static speciation profile based on *Van Pelt and Zobeck* [2007] to map 0.10%, 0.17%, and 0.071% of fugitive dust to K^+, Ca^{2+}, and Mg^{2+}, respectively. In contrast, in CMAQv5.0, 80% of fugitive dust emissions are assumed to reside in the coarse mode and 20% in the fine mode. In CMAQv5.0, a static speciation profile is used to map 3.8%, 7.9%, and 0.0% of all windblown dust to K^+, Ca^{2+}, and Mg^{2+}, respectively (http://www.cmaq-model.org/cmaqwiki/index.php?title=CMAQv5.0_PMother_speciation), while fine mode soil dust requires source specific speciation profiles available from the EPA SPECIATE database (http://www.epa.gov/ttnchie1/software/speciate/). One concludes that simulating dust emissions of crustal species is quite uncertain. Despite this high uncertainty, the potential influence of crustal species on aerosol formation suggests that this be addressed, if only approximately.

[46] Crustal species are not represented explicitly in the standard CMAQv4.7.1 model, and the ARCTAS-CARB emission inventory does not contain speciated crustal emission rates. However, the ARCTAS-CARB emission inventory does include two species, PM_{fine} and PM_{coarse}, which represent primary, unspeciated, fine and coarse mode particulate emissions, respectively. Within CMAQv4.7.1, 90% of PM_{coarse} emissions are assigned to the inert species ASOIL, which represents all coarse-mode, soil-derived, fugitive dust emissions, and 10% are assigned to the inert species ACORS, which represents non-fugitive dust emissions from anthropogenic sources such as diesel trucks. All fine dust emissions are assigned to the unspeciated accumulation-mode species

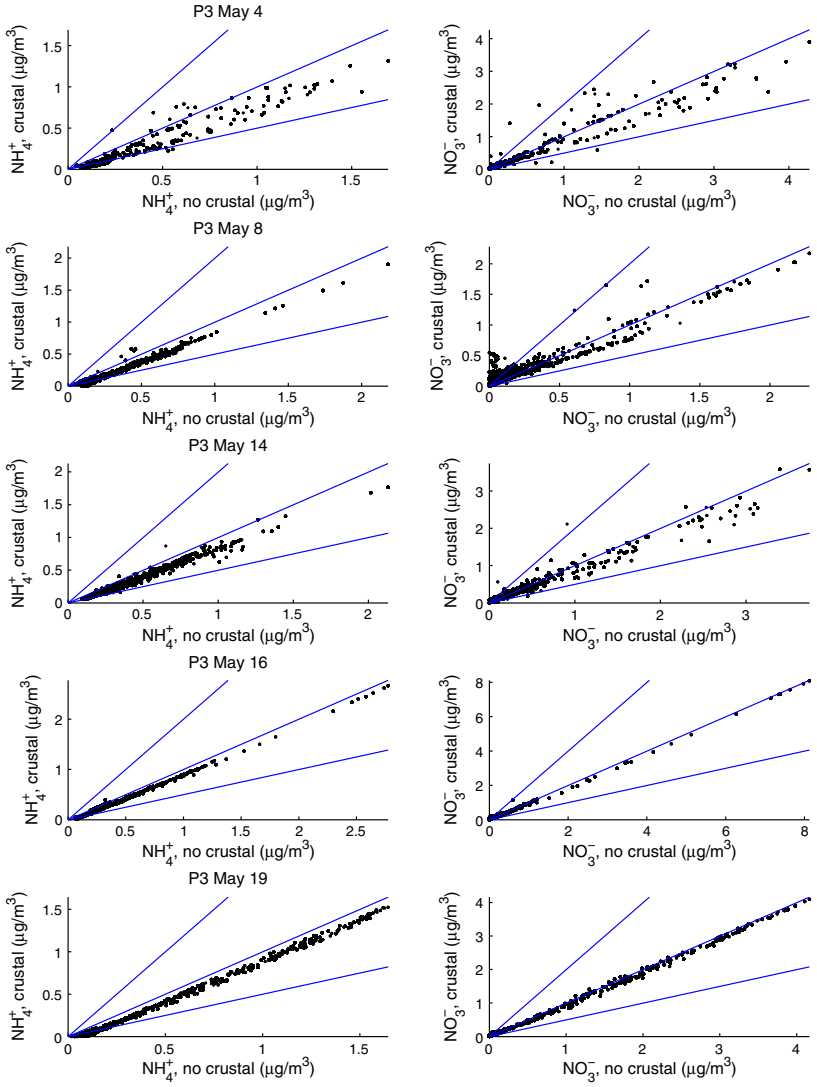

Figure 12. Scatter plots showing predicted ammonium and nitrate concentrations, with and without crustal species, along five P3 flight paths. Ammonium and nitrate predictions have been corrected to account for the transmission window of the AMS. The 1–1, 1–2, and 2–1 lines are included for reference.

A25J (A = aerosol, 25 = PM2.5, J = accumulation mode). Long-range transport of fine and coarse dust is accounted for via nested GEOS-Chem simulations of chemically inert dust species (http://wiki.seas.harvard.edu/geos-chem/index.php/Mineral_dust_aerosols).

[47] Due to a lack of information, we use static speciation profiles to assign the fractions of ACORS/ASOIL and A25J to coarse and fine mode crustal species, respectively (Table 8). Fine mode speciation profiles listed in Table 8 are taken directly from Figure 3 of *Reff et al*. [2009], and are based on average speciation profiles from the U.S. National Emission Inventory (2001). Coarse mode speciation profiles listed in Table 8 are taken directly from the static speciation profiles used in CMAQv5.0, which are based on a combination of speciation profiles from the EPA SPECIATE database. We have modified CMAQv4.7.1 to use ISORROPIAII, which allows for the inclusion of crustal species in thermodynamic calculations. We have not modified any other simulated processes (e.g. dry deposition, wet deposition, sea-salt emissions, aqueous-phase chemistry) to account for the chemical speciation of dust aerosol. As in the unmodified CMAQv4.7.1 model, mass is partitioned between the gas- and aerosol-phases according to the hybrid method [*Capaldo et al*., 2000]

[48] For the sake of brevity, we restrict our analysis of crustal species to the P3 flights. Figure 12 shows particulate (still corrected for AMS transmission window) predicted along P3 flight paths, with and without crustal species. The results suggest that, with the inclusion of crustal species, ammonium concentrations consistently decrease, while nitrate concentrations can increase, decrease, or remain virtually unchanged. *Jacobson* [1999] showed that, depending on the environment (e.g. ammonia limited, nitric acid limited),

coarse crustal species can increase, decrease, or have virtually no effect on the predicted amount of coarse-mode nitrate. Nitrate concentration increases are caused by crustal cations driving nitric acid into the particle phase to maintain charge balance. Nitrate concentration decreases are caused by crustal cations increasing mixed activity coefficients and driving ammonium nitrate aerosol into the gas phase. When these two effects roughly cancel each other, nitrate concentrations remain unchanged and ammonium also gets shifted to the gas phase, or to a different aerosol mode (e.g. coarse aerosol phase). Figure S9 shows time-series plots of Ca^{2+}, K^{+}, and Mg^{2+} concentrations predicted along the five P3 flight paths, as well as the amount of additional fine and coarse mode nitrate that could potentially be neutralized by the crustal cations. Using the speciation profile listed in Table 8, predicted coarse mode Ca^{2+} concentrations are typically higher than fine mode concentrations, fine and coarse mode K^{+} concentrations are comparable, and Mg^{2+} is present only in the fine aerosol mode. Since crustal species are predicted to be present in both fine and coarse modes, it is difficult to decouple the impacts aerosol modes have on each other. Overall, the inclusion of crustal species tends to decrease submicrometer ammonium aerosol, and increase or decrease submicrometer nitrate aerosol depending on the relative concentrations of dust. However, other than the May 4 P3 flight, the results presented in Figure 12 indicate that the impact of crustal species is not very substantial, most likely due to low crustal species concentrations predicted along the P3 flight paths. Moreover, these results would be even less pronounced if the speciation factors from *Van Pelt and Zobeck* [2007] were to be used since they are roughly an order of magnitude lower than those listed in Table 8. These results suggest that the exclusion of crustal species in thermodynamic calculations is not the dominant source of error between predicted and observed fine ammonium and nitrate concentrations. Future work should focus on acquiring chemically-resolved and size-resolved (up to 10 μm) measurements of crustal species, sea-salt, and nitrate.

5. Summary and Conclusions

[49] A detailed three-dimensional chemical transport model (CMAQ version 4.7.1), which contains state-of-the-science gas-phase chemistry and aerosol thermodynamics, was applied during the May 2010 CalNex campaign in the Los Angeles Basin. Boundary conditions were extracted from a nested global-scale GEOS-Chem model (version 9.1.1) simulation. Input meteorology and emission inventories were provided by the CARB. Inorganic and BC aerosol predictions were compared against the suite of ground-based and airborne measurements taken from various CIRPAS Twin Otter and WP-3D flights. The FLEXPART Lagrangian particle dispersion model is used to determine the trajectories of air parcels that reached the aircraft.

[50] Comparisons of predicted and observed BC measurements at the Pasadena ground site suggest that potentially large peaks in measured BC concentrations may be missed on any given day, owing most likely to inaccuracy in the predicted wind fields, but are generally represented well by CMAQ. BC predictions are consistently higher than observations onboard the Twin Otter, which is at least partially due to a systematic bias inherent to the SP2 onboard. However, predicted and observed BC concentrations and ΔBC/ΔCO ratios along P3 flight paths suggests that no systematic bias exists in the ARCTAS-CARB BC emission inventory or the MM5 meteorology.

[51] SO_2 concentrations are consistently overpredicted at surface sites, while the agreement between predicted and observed sulfate concentrations is variable. Sulfate is overpredicted by 55%-268% as compared to Twin Otter measurements, 0%-71% as compared to P3 measurements, and is actually under-predicted by 17% as compared to observations at the Pasadena ground site. The sulfate source apportionment presented in this study suggests that, with the current sulfur emission inventory based on emission factors from 2008, long-range transport of sulfate accounts for a substantial fraction (22-82%) of the sulfate in L.A. Basin. However, if the reductions in sulfur emission factors reported by *Lack et al.* [2011] ($\sim$90%) were to be included in simulations, unlike the results presented in *Huang et al.* [2011], the boundary inflow of sulfate would become the single largest contributor to predicted sulfate concentrations in the L.A. Basin.

[52] Severely underpredicted NH_3 emissions from dairy facilities are identified as the dominant source of measurement/model disagreement in the eastern L.A. Basin. By comparing predicted and observed concentrations of total nitrate, with and without applying the AMS transmission window, we show that, regardless of whether nitrate is predicted to form ammonium nitrate, nitric acid, or coarse nitrate (e.g. sodium nitrate, calcium nitrate, potassium nitrate, etc.), on most days predicted total nitrate concentrations are simply not high enough. We deduce that the two likeliest causes of this are: (1) there is a missing source of HNO_3, or (2) the inaccurate distribution of total nitrate between the gas-phase and the two aerosol modes artificially enhances the removal of nitrate via dry deposition. We estimate that, for most P3 flights, the exclusion of crustal species in thermodynamic calculations is not the dominant source of error between predicted and observed fine ammonium and nitrate concentrations. However, as stated previously, there is considerable uncertainty in all parameters used in the crustal sensitivity simulation, and we are reluctant to draw conclusions based on this study alone.

[53] This work, as part of the CalNex campaign, provides an up-to-date characterization of the inorganic and black carbon fraction of the Los Angeles Basin particulate matter. Adding gas-phase NH_3 measurements and size-resolved measurements, up to 10 μm, of nitrate and various cations (e.g. Na^{+}, Ca^{2+}, K^{+}, Mg^{2+}) to routine monitoring stations in the L.A. Basin would facilitate interpreting day-to-day fluctuations in fine and coarse inorganic aerosol greatly. Future work will focus on improving and assessing the treatment of anthropogenic and fugitive dust emissions, as well as characterizing the nature of organic aerosol formation and evolution in the Los Angeles Basin.

Appendix A: Additional Flights

[54] Appenix A contains Figures A1, A2, A3, A4.

Appendix B: AMS Transmission Efficiencies

[55] The AMS transmission curve used in this study is piece-wise defined for three diameter ranges: (a) linear increase in transmission vs ln(D_{va}), from 0% at D_{va} = 40 nm to 100% at D_{va} = 100 nm, (b) 100% transmission from D_{va} = 100 nm up to D_{va} = 550 nm, (c) linear decrease in transmission vs ln(D_{va}), from 100% at D_{va} = 550 nm to 0% at D_{va} =

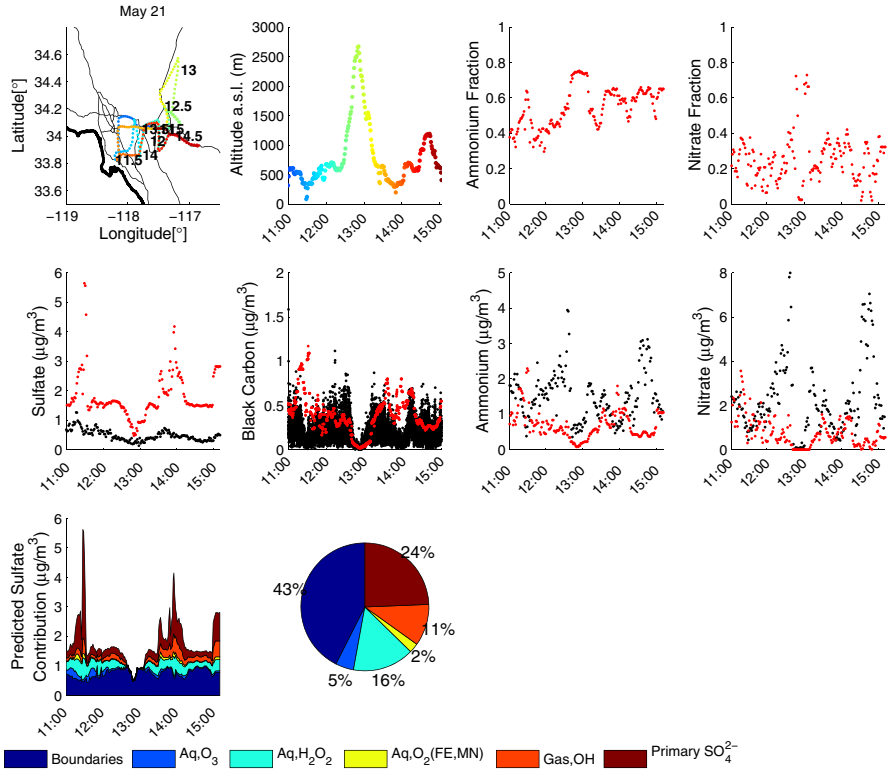

Figure A1. Same as Figure 6, but for the Twin Otter May 21 flight.

2 μm, and zero elsewhere. This transmission curve can be applied analytically to any log-normal mass distribution: 40 nm < D_{va} < 100 nm:

$$f(D_{va}) = \frac{\ln(D_{va}/40nm)}{\ln(100nm/40nm)} \tag{B1}$$

$$M(40\ nm < D_{va} < 100nm) = \tag{B2}$$

$$M(40\ nm/\rho_{dry} < D_p < 100\ nm/\rho_{dry}) =$$

$$\frac{M_{tot}}{2} \times \frac{\ln\left(\bar{D}_{pgV}^{dry}/\left(40nm/\rho_{dry}\right)\right)}{\ln(100nm/40nm)}$$

$$\times \left[erf\left(\frac{ln\left(\left(100nm/\rho_{dry}\right)/\bar{D}_{pgV}^{dry}\right)}{\sqrt{2}\times\ln\left(\sigma_{dry}\right)}\right) - erf\left(\frac{\ln\left(\left(40nm/\rho_{dry}\right)/\bar{D}_{pgV}^{dry}\right)}{\sqrt{2}\times\ln\left(\sigma_{dry}\right)}\right)\right] +$$

$$\frac{M_{tot}}{2} \times \frac{\ln\left(\sigma_{dry}\right)}{\ln(100nm/40nm)\times\sqrt{\frac{\pi}{2}}} \times \left\{ \exp\left[-\left(\frac{\ln\left(\left(40nm/\rho_{dry}\right)/\bar{D}_{pgV}^{dry}\right)}{\sqrt{2}\times\ln\left(\sigma_{dry}\right)}\right)^2\right] - \exp\left[-\left(\frac{\ln\left(\left(100nm/\rho_{dry}\right)/\bar{D}_{pgV}^{dry}\right)}{\sqrt{2}\times\ln\left(\sigma_{dry}\right)}\right)^2\right]\right\}$$

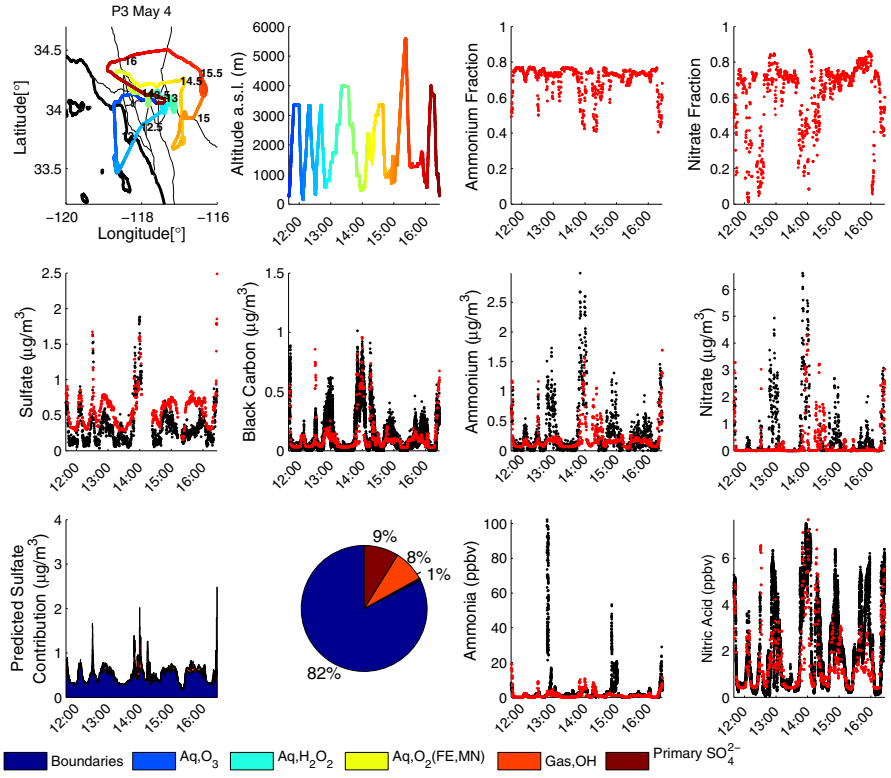

Figure A2. Same as Figure 10, but for the P3 May 4 flight.

100 nm < D_{va} < 550 nm:

$$f(D_{va}) = 1 \qquad \text{(B3)}$$

$$\begin{aligned} &M(100\ nm < D_{va} < 550\ nm) \\ &= M\left(100\ nm/\rho_{dry} < D_p < 550\ nm/\rho_{dry}\right) \\ &= \frac{M_{tot}}{2} \times \left[erf\left(\frac{\ln\left(\left(550nm/\rho_{dry}\right)/\bar{D}_{pgV}^{dry}\right)}{\sqrt{2} \times \ln(\sigma_{dry})}\right) - erf\left(\frac{\ln\left(\left(100nm/\rho_{dry}\right)/\bar{D}_{pgV}^{dry}\right)}{\sqrt{2} \times \ln(\sigma_{dry})}\right)\right] \end{aligned} \qquad \text{(B4)}$$

550 nm < D_{va} < 2000 nm:

$$f(D_{va}) = \frac{\ln(D_{va}/2000nm)}{\ln(550nm/2000nm)} \qquad \text{(B5)}$$

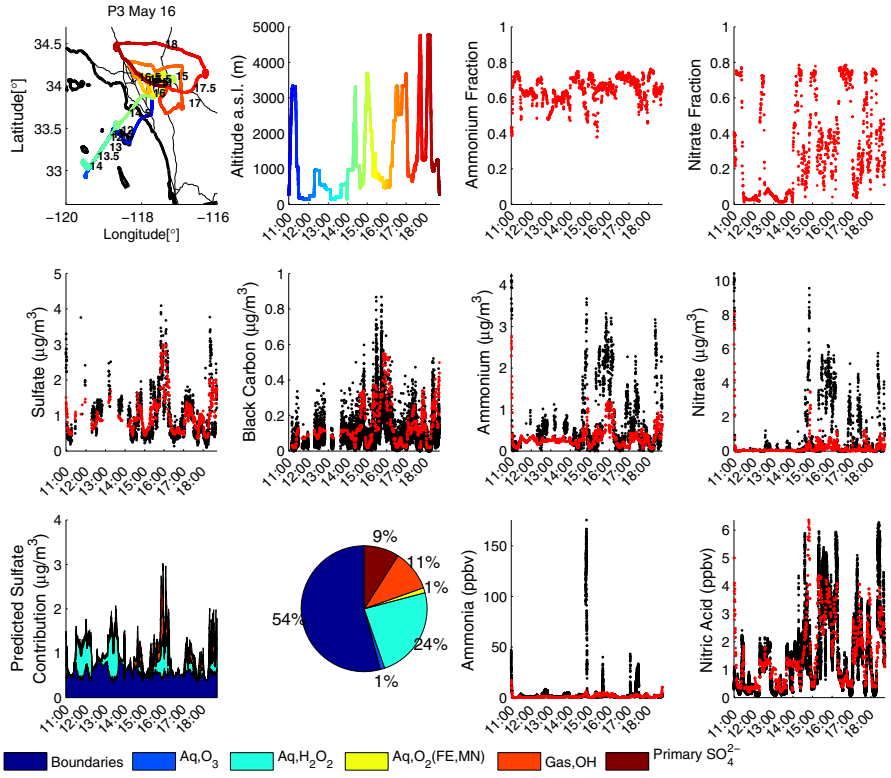

Figure A3. Same as Figure 10, but for the P3 May 16 flight.

$$M(550\ nm < D_{va} < 2000\ nm) = M\left(550\ nm/\rho_{dry} < D_p < 2000\ nm/\rho_{dry}\right) = \frac{M_{tot}}{2} \times \frac{\ln\left(\bar{D}_{pgV}^{dry}/\left(2000nm/\rho_{dry}\right)\right)}{\ln(550nm/2000nm)}$$
$$\times \left[erf\left(\frac{\ln\left(\left(2000nm/\rho_{dry}\right)/\bar{D}_{pgV}^{dry}\right)}{\sqrt{2} \times \ln(\sigma_{dry})}\right) - erf\left(\frac{\ln\left(\left(550nm/\rho_{dry}\right)/\bar{D}_{pgV}^{dry}\right)}{\sqrt{2} \times \ln(\sigma_{dry})}\right)\right]$$
$$+ \frac{M_{tot}}{2} \times \frac{\ln(\sigma_{dry})}{\ln(550nm/2000nm) \times \sqrt{\frac{\pi}{2}}}$$
$$\times \left\{ exp\left[-\left(\frac{\ln\left(\left(550nm/\rho_{dry}\right)/\bar{D}_{pgV}^{dry}\right)}{\sqrt{2} \times \ln(\sigma_{dry})}\right)^2\right] - exp\left[-\left(\frac{\ln\left(\left(2000nm/\rho_{dry}\right)/\bar{D}_{pgV}^{dry}\right)}{\sqrt{2} \times \ln(\sigma_{dry})}\right)^2\right]\right\} \quad \text{(B6)}$$

where f is the transmission efficiency as a function of D_{va}, M_{tot} is the unmodified, total amount of predicted species mass (e.g. nitrate, sulfate, ammonium) in the mode, and $M(D_{va,min} < D_{va} < D_{va,max})$ is the modified amount of species mass, within the mode, in the given vacuum-aerodynamic diameter range. The vacuum-aerodynamic diameter limits of the AMS transmission curve are converted to particle (Stokes) diameters for each data point by using $D_p = \left(\frac{\rho_o}{\rho_{dry}}\right) D_{va}$ [*DeCarlo et al.*, 2004], where D_p is the physical (Stokes) diameter of the particle, D_{va} is the vacuum-aerodynamic diameter, ρ_o is the standard density (1 g cm^{-3}), and ρ_{dry} is the density of the particle predicted by CMAQ not including water. The total mass from each mode (using this specific AMS transmission efficiency curve) is then:

$$M_{mode}^{AMS} = M(40\ nm < D_{va} < 100\ nm) + M(100\ nm < D_{va} < 550\ nm) + M(550\ nm < D_{va} < 2000\ nm) \quad \text{(B7)}$$

where M_{mode}^{AMS} is the total amount of predicted species mass in the mode that has been adjusted to match the transmission curve of the AMS. The total amount of predicted species

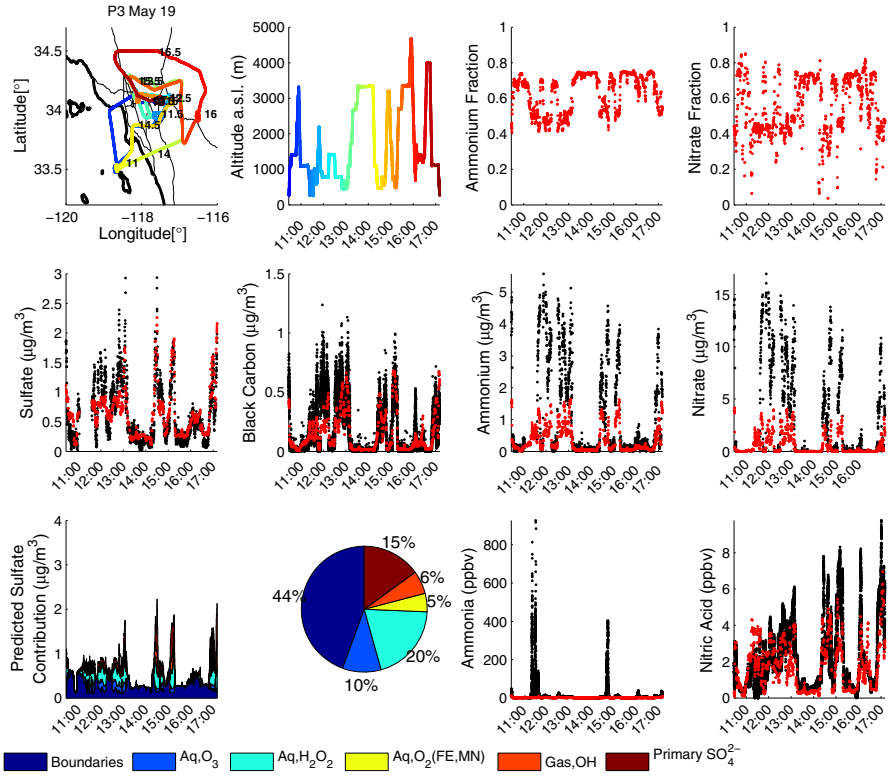

Figure A4. Same as Figure 10, but for the P3 May 19 flight.

mass that should be compared to the AMS is then the sum of all three adjusted modes ($M = M_I^{AMS} + M_J^{AMS} + M_K^{AMS}$), where I, J, and K are the Aitken mode, the accumulation mode, and the coarse mode, respectively. The derivation of the equations for transmission curve adjustment are presented in the supplementary section.

[56] **Acknowledgments.** This work was funded by NOAA grant NA09OAR4310128 and by the State of California Air Resources Board (CARB) Agreement 10-328. NOAA's Climate and Air Quality programs supported the NOAA-P3 deployment. PLH and JLJ were supported by CARB-319 and DOE (BER, ASR program) DE-SC0006035, and PLH acknowledges a CIRES Visiting Postdoctoral Fellowship. This work was supported in part by the NOAA Health of the Atmosphere Program and the NOAA Climate Goal. We acknowledge four anonymous reviewers for their thorough and insightful comments. The authors would like to thank Nehzat Motallebi, Havala O. T. Pye, and Andreas Zuend for useful discussions, Ying Xie and Rob Pinder at the Environmental Protection Agency (EPA) for providing the SAPRC07TC chemical mechanism, Anne Perring, Joshua Schwartz, and David Fahey for the use of the SP2 measurements from the NOAA P3 aircraft and for useful discussion, John Holloway at NOAA for CO measurements from the NOAA P3 aircraft, Kemal Gurer for MM5 modeled data, and Jerome Fast for providing the Aerosol Modeling Testbed analysis toolkit. The statements and conclusions in this paper are those of the researchers (contractor) and not necessarily those of CARB. The mention of commercial products, their source, or their use in connection with material reported herein is not to be construed as actual or implied endorsement of such products.

References

Appel, B., E. Hoffer, Y. Tokiwa, and E. Kothny (1982), Measurement of sulfuric-acid and particulate strong acidity in the Los-Angeles basin, *Atmos. Environ.*, *16*, 589–593, doi:10.1016/0004-6981(82)90168-8.

Bahreini, R., et al. (2009), Organic aerosol formation in urban and industrial plumes near Houston and Dallas, Texas, *J. Geophys. Res.-Atmos.*, *114*, doi:10.1029/2008JD011493.

Bein, K. J., Y. Zhao, N. J. Pekney, C. I. Davidson, M. V. Johnston, and A. S. Wexler (2006), Identification of sources of atmospheric PM at the Pittsburgh Supersite - Part II: Quantitative comparisons of single particle, particle number, and particle mass measurements, *Atmos. Environ.*, *40*, S424–S444, doi:10.1016/j.atmosenv.2006.01.064.

Bey, I., D. Jacob, R. Yantosca, J. Logan, B. Field, A. Fiore, Q. Li, H. Liu, L. Mickley, and M. Schultz (2001), Global modeling of tropospheric chemistry with assimilated meteorology, Model description and evaluation, *J. Geophys. Res.-Atmos.*, *106*, 23,073–23,095, doi:10.1029/2001JD000807.

Binkowski, F., and S. Roselle (2003), Models-3 community multiscale air quality (CMAQ) model aerosol component - 1. Model description, *J. Geophys. Res.-Atmos.*, *108*, doi:10.1029/2001JD001409.

Bond, T., and R. Bergstrom (2006), Light absorption by carbonaceous particles: An investigative review, *Aerosol. Sci. Tech.*, *40*, 27–67, doi:10.1080/02786820500421521.

Brioude, J., et al. (2009), Effect of biomass burning on marine stratocumulus clouds off the California coast, *Atmos. Chem. Phys.*, *9*, 8841–8856.

Cabada, J., S. Rees, S. Takahama, A. Khlystov, S. Pandis, C. Davidson, and A. Robinson (2004), Mass size distributions and size resolved chemical composition of fine particulate matter at the Pittsburgh supersite, *Atmos. Environ.*, *38*, 3127–3141, doi:10.1016/j.atmosenv.2004.03.004.

Canagaratna, M. R., et al. (2007), Chemical and microphysical characterization of ambient aerosols with the aerodyne aerosol mass spectrometer, *Mass SpectromRev.*, *26*, 185–222, doi:10.1002/mas.20115.

Capaldo, K., C. Pilinis, and S. Pandis (2000), A computationally efficient hybrid approach for dynamic gas/aerosol transfer in air quality models, *Atmos. Environ.*, *34*, 3617–3627.

Carter, W. P. L. (2010), Development of a condensed SAPRC-07 chemical mechanism, *Atmos. Environ.*, *44*, 5336–5345, doi:10.1016/j.atmosenv.2010.01.024, 2nd Biennial Conference on Atmospheric Chemistry Mechanisms, Air Quality Res Ctr, Davis, CA, DEC, 2008.

Chang, J., R. Brost, I. Isaksen, S. Madronich, P. Middleton, W. Stockwell, and C. Walcek (1987), A 3-dimensional eulerian acid deposition model - physics concepts and formulation, *J. Geophys. Res.-Atmos.*, *92*, 14,681–14,700, doi:10.1029/JD092iD12p14681.

Chow, J., E. Fujita, J. Watson, Z. Lu, D. Lawson, and L. Asbaugh (1994), Evaluation of filter-based aerosol measurements during the 1987 Southern California Air-Quality Study, *Env. Monit. Assess.*, *30*, 49–80, doi:10.1007/BF00546199.

Croes, B., and E. Fujita (2003), Overview of the 1997 Southern California Ozone Study (SCOS97-NARSTO), *Atmos. Environ.*, *37*, S3–S26, doi:10.1016/S1352-2310(03)00379-0.

Dallmann, T., R. Harley, and T. Kirchstetter (2011), Effects of diesel particle filter retrofits and accelerated fleet turnover on drayage truck emissions at the port of oakland, *Environ. Sci. Technol.*, *45*, 10773–10779, doi:10.1021/es202609q.

de Foy, B., J. Varela, L. Molina, and M. Molina (2006), Rapid ventilation of the Mexico City basin and regional fate of the urban plume, *Atmos. Chem. Phys.*, *6*, 2321–2335.

DeCarlo, P., J. Slowik, D. Worsnop, P. Davidovits, and J. Jimenez (2004), Particle morphology and density characterization by combined mobility and aerodynamic diameter measurements. Part 1: Theory, *Aerosol. Sci. Tech.*, *38*, 1185–1205, doi:10.1080/027868290903907.

DeCarlo, P. F., et al. (2008), Fast airborne aerosol size and chemistry measurements above Mexico City and Central Mexico during the MILAGRO campaign, *Atmos. Chem. Phys.*, *8*, 4027–4048.

Ding, A., et al. (2009), Transport of north China air pollution by midlatitude cyclones: Case study of aircraft measurements in summer 2007, *J. Geophys. Res.-Atmos.*, *114*, doi:10.1029/2008JD011023.

Docherty, K. S., et al. (2011), The 2005 Study of Organic Aerosols at Riverside (SOAR-1): instrumental intercomparisons and fine particle composition, *Atmos. Chem. Phys.*, *11*, 12, 387-12, 420, doi:10.5194/acp-11-12387-2011, 2011.

Dominguez, G., T. Jackson, L. Brothers, B. Barnett, B. Nguyen, and M. H. Thiemens (2008), Discovery and measurement of an isotopically distinct source of sulfate in Earth's atmosphere, *Proc. Nat. Acad. Sci. USA*, *105*, 12 769–12 773, doi:10.1073/pnas.0805255105.

Drewnick, F., S. Hings, P. DeCarlo, J. Jayne, M. Gonin, K. Fuhrer, S. Weimer, J. Jimenez, K. Demerjian, S. Borrmann, and D. Worsnop (2005), A new time-of-flight aerosol mass spectrometer (TOF-AMS) - Instrument description and first field deployment, *Aerosol. Sci. Tech.*, *39*, 637–658, doi:10.1080/02786820500182040.

Dzepina, K., R. M. Volkamer, S. Madronich, P. Tulet, I. M. Ulbrich, Q. Zhang, C. D. Cappa, P. J. Ziemann, and J. L. Jimenez (2009), Evaluation of recently-proposed secondary organic aerosol models for a case study in Mexico City, *Atmos. Chem. Phys.*, *9*, 5681–5709, doi:10.5194/acp-9-5681-2009.

Eldering, A., G. Cass, and K. Moon (1994), An air monitoring network using continuous particle-size distribution monitors - connecting pollutant properties to visibility via mie scattering calculations, *Atmos. Environ.*, *28*, 2733–2749, doi:10.1016/1352-2310(94)90445-6.

Ellis, R. A., J. G. Murphy, E. Pattey, R. van Haarlem, J. M. O'Brien, and S. C. Herndon (2010), Characterizing a Quantum Cascade Tunable Infrared Laser Differential Absorption Spectrometer (QC-TILDAS) for measurements of atmospheric ammonia, *Atmos. Meas. Tech.*, *3*, 397–406, doi:10.5194/amt-3-397-2010.

Emeis, S. and K. Schafer (2006), Remote sensing methods to investigate boundary-layer structures relevant to air pollution in cities, *Bound.-Lay. Meteorol.*, *121*, 377–385, doi:10.1007/s10546-006-9068-2.

Fast, J., et al. (2009), Evaluating simulated primary anthropogenic and biomass burning organic aerosols during MILAGRO: implications for assessing treatments of secondary organic aerosols, *Atmos. Chem. Phys.*, *9*, 6191–6215, doi:10.5194/acp-9-6191-2009.

Fast, J. D., W. I. Gustafson, Jr., E. G. Chapman, R. C. Easter, J. P. Rishel, R. A. Zaveri, G. A. Grell and M. C. Barth (2011), The Aerosol Modeling Testbed: A community tool to objectively evaluate aerosol process modules, *Bull. Amer. Meteor. Soc.*, *92*, 343–360, doi:10.1175/2010BAMS2868.1.

Foley, K. M., et al. (2010), Incremental testing of the Community Multiscale Air Quality (CMAQ) modeling system version 4.7, *Geosci. Mod. Devel.*, *3*, 205–226.

Fountoukis, C., and A. Nenes (2007), ISORROPIA II: a computationally efficient thermodynamic equilibrium model for K^+-Ca^{2+}-Mg^{2+}-NH_4^+-Na^+-SO_4^{2-}-NO_3^--Cl^--H_2O aerosols, *Atmos. Chem. Phys.*, *7*, 4639–4659.

Fountoukis, C., A. Nenes, A. Sullivan, R. Weber, T. Van Reken, M. Fischer, E. Matias, M. Moya, D. Farmer, and R. C. Cohen (2009), Thermodynamic characterization of Mexico City aerosol during MILAGRO 2006, *Atmos. Chem. Phys.*, *9*, 2141–2156.

Gong, S. (2003), A parameterization of sea-salt aerosol source function for sub- and super-micron particles, *Glo. Biogeochem. Cyc.*, *17*, doi:10.1029/2003GB002079.

Grell, G. A., J. Dudhia, and D. R. Stauffer (1995), A description of the fifth-generation Penn State/NCAR mesoscale model (MM5). NCAR Technical Note NCAR/TN-398+STR, Note TN398 STR, p. 138.

Haman, C. L. (2011), Seasonal and daily variability of the boundary layer and the impact of synoptic controls and micrometeorological processes on surface ozone evolution at an urban site, Ph.D. thesis, University of Houston, Texas, USA.

Hegg, D., D. Covert, H. Jonsson, and P. Covert (2005), Determination of the transmission efficiency of an aircraft aerosol inlet, *Aerosol Sci. Technol.*, *39*(10), 966–971, doi:10.1080/02786820500377814.

Holloway, J. S., R. O. Jakoubek, D. D. Parrish, C. Gerbig, A. Volz-Thomas, S. Schmitgen, A. Fried, B. Wert, B. Henry, and J. R. Drummond (2000), Airborne intercomparison of vacuum ultraviolet fluorescence and tunable diode laser absorption measurements of tropospheric carbon monoxide, *J. Geophys. Res.*, *105*(D19), 24,25124,261, doi:10.1029/2000JD900237.

Hsu, S.-C., S. C. Liu, S.-J. Kao, W.-L. Jeng, Y.-T. Huang, C.-M. Tseng, F. Tsai, J.-Y. Tu, and Y. Yang (2007), Water-soluble species in the marine aerosol from the northern South China Sea: High chloride depletion related to air pollution, *J. Geophys. Res.*, *112*, D19304, doi:10.1029/2007JD008844.

Huang, M., et al. (2011), Multi-scale modeling study of the source contributions to near-surface ozone and sulfur oxides levels over California during the ARCTAS-CARB period, *Atmos. Chem. Phys.*, *11*, 3173–3194, doi:10.5194/acp-11-3173-2011.

Hughes, L., J. Allen, L. Salmon, P. Mayo, R. Johnson, and G. Cass (2002), Evolution of nitrogen species air pollutants along trajectories crossing the Los Angeles area, *Environ. Sci. Technol.*, *36*, 3928–3935, doi:10.1021/es0110630.

Ianniello, A., F. Spataro, G. Esposito, I. Allegrini, M. Hu, and T. Zhu (2011), Chemical characteristics of inorganic ammonium salts in PM (2.5) in the atmosphere of Beijing (China), *Atmos. Chem. Phys.*, *11*, 10,803–10,822, doi:10.5194/acp-11-10803-2011.

Jacob, D. J., et al. (2010), The Arctic Research of the Composition of the Troposphere from Aircraft and Satellites (ARCTAS) mission: design, execution, and first results, *Atmos. Chem. Phys.*, *10*, 5191–5212, doi:10.5194/acp-10-5191-2010.

Jacobson, M. Z. (1999), Studying the effects of calcium and magnesium on size-distributed nitrate and ammonium with EQUISOLV II, *Atmos. Environ.*, *33*, 3635–3649, doi:10.1016/S1352-2310(99)00105-3.

Karydis, V. A., A. P. Tsimpidi, C. Fountoukis, A. Nenes, M. Zavala, W. Lei, L. T. Molina, and S. N. Pandis (2010), Simulating the fine and coarse inorganic particulate matter concentrations in a polluted megacity, *Atmos. Environ.*, *44*, 608–620, doi:10.1016/j.atmosenv.2009.11.023.

Kelly, J. T., P. V. Bhave, C. G. Nolte, U. Shankar and K. M. Foley (2010), Simulating emission and chemical evolution of coarse sea-salt particles in the Community Multiscale Air Quality (CMAQ) model, *Geosci. Mod. Devel.*, *3*, 257–273, doi:10.5194/gmd-3-257-2010.

Knote, C., et al. (2011), Towards an online-coupled chemistry-climate model: evaluation of trace gases and aerosols in COSMO-ART, *Geosci. Model Dev.*, *4*, 1077–1102, doi:10.5194/gmd-4-1077-2011.

Lack, D. A., et al. (2011), Impact of fuel quality regulation and speed reductions on shipping emissions: implications for climate and air quality, *Environ. Sci. Technol.*, *45*, 9052–9060, doi:10.1021/es2013424.

Lee, S. H., S. W. Kim, W. M. Angevine, L. Bianco, S. A. McKeen, C. J. Senff, M. Trainer, S. C. Tucker, and R. J. Zamora (2011), Evaluation of urban surface parameterizations in the WRF model using measurements during the Texas Air Quality Study 2006 field campaign, *Atmos. Chem. Phys.*, *11*, 2127–2143, doi:10.5194/acp-11-2127-2011.

Lin, M., et al. (2012), Transport of Asian ozone pollution into surface air over the western United States in spring, *J. Geophys. Res.-Atmos.*, *117*, doi:10.1029/2011JD016961.

Liu, D., K. Prather, and S. Hering (2000), Variations in the size and chemical composition of nitrate-containing particles in Riverside, CA, *Aerosol. Sci. Tech.*, *33*, 71–86, doi:10.1080/027868200410859.

Lu, R., and R. Turco (1995), Air pollutant transport in a coastal environment - II. 3-Dimensional simulations over Los-Angeles Basin, *Atmos. Environ.*, *29*, 1499–1518, doi:10.1016/1352-2310(95)00015-Q.

Luke, W. T. (1997), Evaluation of a commercial pulsed fluorescence detector for the measurement of low-level SO2 concentrations during GASIE. *J. Geophys. Res. 102*, 16, 25516, doi:10.1029/96JD03347.

Martucci, G., R. Matthey, V. Mitev, and H. Richner (2007), Comparison between backscatter lidar and radiosonde measurements of the diurnal and nocturnal stratification in the lower troposphere, *J. Atmos. Ocean. Technol.*, *24*, 1231–1244, doi:10.1175/JTECH2036.1.

Matsui, H., et al. (2009), Spatial and temporal variations of aerosols around Beijing in summer 2006: Model evaluation and source apportionment, *J. Geophys. Res.-Atmos.*, *114*, doi:10.1029/2008JD010906.

McKeen, S., et al. (2009), An evaluation of real-time air quality forecasts and their urban emissions over eastern Texas during the summer of 2006 Second Texas Air Quality Study field study, *J. Geophys. Res.-Atmos.*, *114*, doi:10.1029/2008JD011697.

McMeeking, G. R., et al. (2010), Black carbon measurements in the boundary layer over western and northern Europe, *Atmos. Chem. Phys.*, *10*, 9393–9414, doi:10.5194/acp-10-9393-2010.

Metcalf, A. R., J. S. Craven, J. J. Ensberg, J. Brioude, W. M. M. Angevine, A. Sorooshian, H. T. Duong, H. H. Jonsson, R. C. Flagan, and J. H. Seinfeld (2012), Black carbon aerosol over the Los Angeles Basin during CalNex, *J. Geophys Res.*, *117*, doi:10.1029/2011JD017255.

Middlebrook, A. M., R. Bahreini, J. L. Jimenez, and M. R. Canagaratna (2012), Evaluation of composition-dependent collection efficiencies for the Aerodyne Aerosol Mass Spectrometer using field data, *Aerosol. Sci. Tech.*, *46*, 258–271, doi:10.1080/02786826.2011.620041.

Midwest Research Institute (2005), Analysis of fine fraction of particulate matter in fugitive dust, Report to the WRAP by Midwest Research Institute, Project No. 110397.

Modey, W., D. Eatough, R. Anderson, D. Martello, S. Takahama, L. Lucas, and C. Davidson (2004), Ambient fine particulate concentrations and chemical composition at two sampling sites in metropolitan Pittsburgh: a 2001 intensive summer study, *Atmos. Environ.*, *38*, 3165–3178, doi:10.1016/j.atmosenv.2004.03.005.

Molina, L. T., et al. (2010), An overview of the MILAGRO 2006 Campaign: Mexico City emissions and their transport and transformation, *Atmos. Chem. Phys.*, *10*, 8697–8760, doi:10.5194/acp-10-8697-2010.

Moya, M., S. N. Pandis, and M. Z. Jacobson (2002), Is the size distribution of urban aerosols deter- mined by thermodynamic equilibrium?: An application to Southern California, *Atmos. Environ.*, *36*, 2349–2365, doi:10.1016/S1352-2310(01)00549-0.

Münkel, C., E. Noora, J. Räsänen, and A. Karppinen (2006), Retrieval of mixing height and dust concentration with lidar ceilometer, *Bound.-Lay. Meteorol.*, doi:10.1007/s10546-006-9103-3.

Murphy, S. M., et al. (2009), Comprehensive simultaneous shipboard and airborne characterization of exhaust from a modern container ship at sea, *Environ. Sci. Technol.*, *43*, 4626–4640, doi:10.1021/es802413j.

Neuman, J., et al. (2002), Fast-response airborne in situ measurements of HNO3 during the Texas 2000 Air Quality Study, *J. Geophys. Res.-Atmos.*, *107*, doi:10.1029/2001JD001437.

Neuman, J., et al. (2003), Variability in ammonium nitrate formation and nitric acid depletion with altitude and location over California, *J. Geophys. Res.-Atmos.*, *108*, doi:10.1029/2003JD003616.

Neuman, J. A., et al. (2012), Observations of ozone transport from the free troposphere to the Los Angeles basin, *J. Geophys. Res.-Atmos.*, *117*, doi:10.1029/2011JD016919.

Nolte, C. G., P. V. Bhave, J. R. Arnold, R. L. Dennis, K. M. Zhang, and A. S. Wexler (2008), Modeling urban and regional aerosols - Application of the CMAQ-UCD Aerosol Model to Tampa, a coastal urban site, *Atmos. Environ.*, *42*, 3179–3191, doi:10.1016/j.atmosenv.2007.12.059.

Nowak, J. B., J. A. Neuman, R. Bahreini, C. A. Brock, A. M. Middlebrook, A. G. Wollny, Holloway, J. S., Peischl, J., Ryerson, T. B., and F. C. Fehsenfeld (2010), Airborne observations of ammonia and ammonium nitrate formation over Houston, Texas, *J. Geophys. Res.-Atmos.*, *115*, doi:10.1029/2010JD014195.

Nowak, J. B., J. A. Neuman, R. Bahreini, A. M. Middlebrook, J. S. Holloway, S. A. McKeen, D. D. Parrish, T. B. Ryerson, and M. K. Trainer (2012), Ammonia sources in the California South Coast Air Basin and their impact on ammonium nitrate formation, *J. Geophys. Res.-Lett.*, *39*, doi:10.1029/2012GL051197.

Olivier, J. G. J., and J. J. M. Berdowski (2001), Global emissions sources and sinks. In: Berdowski, J., Guicherit, R. and B.J. Heij (eds.) The Climate System, pp. 33–78. A. A. Balkema Publishers/Swets and Zeitlinger Publishers, Lisse, The Netherlands., 2001.

Otte, T. L., and J. E. Pleim (2010), The Meteorology-Chemistry Interface Processor (MCIP) for the CMAQ modeling system: updates through MCIPv3.4.1, *Geosci. Model Dev.*, *3*, 243–256, doi:10.5194/gmd-3-243-2010.

Palau, J., G. Perez-Landa, J. Melia, D. Segarra, and M. Millan (2006), A study of dispersion in complex terrain under winter conditions using high-resolution mesoscale and Lagrangian particle models, *Atmos. Chem. Phys.*, *6*, 1105–1134.

Park, R., D. Jacob, B. Field, R. Yantosca, and M. Chin (2004): Natural and transboundary pollution influences on sulfate-nitrate-ammonium aerosols in the United States Implications for policy, *J. Geophys. Res.-Atmos.*, *109*, doi:10.1029/2003JD004473.

Parrish, D. D., et al. (2009), Overview of the Second Texas Air Quality Study (TexAQS II) and the Gulf of Mexico Atmospheric Composition and Climate Study (GoMACCS), *J. Geophys. Res.-Atmos.*, *114*, doi:10.1029/2009JD011842.

Pastor, S., J. Allen, L. Hughes, P. Bhave, G. Cass, and K. Prather (2003), Ambient single particle analysis in Riverside, California by aerosol time-of-flight mass spectrometry during the SCOS97-NARSTO, *Atmos. Environ.*, *37*, S239–S258, doi:10.1016/S1352-2310(03)00393-5.

Paulot, F., J. D. Crounse, H. G. Kjaergaard, J. H. Kroll, J. H. Seinfeld, and P. O. Wennberg (2009a), Isoprene photooxidation: new insights into the production of acids and organic nitrates, *Atmos. Chem. Phys.*, *9*, 1479–1501.

Paulot, F., J. D. Crounse, H. G. Kjaergaard, A. Kuerten, J. M. St Clair, J. H. Seinfeld, and P. O. Wennberg (2009b), Unexpected epoxide formation in the gas-phase photooxidation of isoprene, *Science*, *325*, 730–733, doi:10.1126/science.1172910.

Pekney, N. J., C. I. Davidson, K. J. Bein, A. S. Wexler, and M. V. Johnston (2006), Identification of sources of atmospheric PM at the Pittsburgh Supersite, Part I Single particle analysis and filter-based positive matrix factorization, *Atmos. Environ.*, *40*, S411–S423, doi:10.1016/j.atmosenv.2005.12.072.

Pfister, G. G., et al. (2011), Characterizing summertime chemical boundary conditions for airmasses entering the US West Coast, *Atmos. Chem. Phys.*, *11*, 1769–1790, doi:10.5194/acp-11-1769-2011.

Querol, X., et al. (2008), PM speciation and sources in Mexico during the MILAGRO-2006 Campaign, *Atmos. Chem. Phys.*, *8*, 111–128.

Reff, A., P. V. Bhave, H. Simon, T. G. Pace, G. A. Pouliot, J. D. Mobley, and M. Houyoux (2009), Emissions inventory of PM2.5 trace elements across the United States, *Environ. Sci. Technol.*, *43*, 5790–5796, doi:10.1021/es802930x.

Renner, E., and R. Wolke (2010), Modelling the formation and atmospheric transport of secondary inorganic aerosols with special attention to regions with high ammonia emissions, *Atmos. Environ.*, *44*, 1904–1912, doi:10.1016/j.atmosenv.2010.02.018.

Roberts, J. M., et al. (2010), Measurement of HONO, HNCO, and other inorganic acids by negative-ion proton-transfer chemical-ionization mass spectrometry (NI-PT-CIMS): Application to biomass burning emissions, *Atmos. Meas. Tech.*, *3*, 981–990, doi:10.5194/amt-3-981-2010.

Salcedo, D., et al. (2006), Characterization of ambient aerosols in Mexico City during the MCMA-2003 campaign with Aerosol Mass Spectrometry: results from the CENICA Supersite, *Atmos. Chem. Phys.*, *6*, 925–946.

Sarwar, G., and P. V. Bhave (2007), Modeling the effect of chlorine emissions on ozone levels over the eastern United States, *J. Appl. Met. Clim.*, *46*, 1009–1019, doi:10.1175/JAM2519.1.

Schafer, K., S. M. Emeis, A. Rauch, and C. Vogt (2004), Determination of mixing layer heights from ceilometer data, *Remote Sens. Clouds Atmos.*, *5571*, 248–259, doi:10.1117/12.565592.

Schwarz, J. P., et al. (2006), Single-particle measurements of midlatitude black carbon and light-scattering aerosols from the boundary layer to the lower stratosphere, *J. Geophys. Res.-Atmos.*, *111*, doi:10.1029/2006JD007076.

Schwarz, J. P., et al. (2008b), Coatings and their enhancement of black carbon light absorption in the tropical atmosphere, *J. Geophys. Res.-Atmos.*, *113*, doi:10.1029/2007JD009042.

Shiraiwa, M., Y. Kondo, N. Moteki, N. Takegawa, L. K. Sahu, A. Takami, S. Hatakeyama, S. Yonemura, and D. R. Blake (2008), Radiative impact of mixing state of black carbon aerosol in Asian outflow, *J. Geophys. Res.-Atmos.*, *113*, D24210, doi:10.1029/2008JD010546.

Seinfeld, J., and S. Pandis (2006), Atmospheric chemistry and physics: from air pollution to climate change (Second Edition), John Wiley and Sons, Inc..

Stein, A. F., and R. D. Saylor (2012), Sensitivities of sulfate aerosol formation and oxidation pathways on the chemical mechanism employed in simulations. *Atmos. Chem. Phys.*, *12*, 8567–8574, doi:10.5194/acp-12-8567-2012

Stohl, A., C. Forster, A. Frank, P. Seibert, and G. Wotawa (2005), Technical note: The Lagrangian particle dispersion model FLEXPART version 6.2, *Atmos. Chem. Phys.*, *5*, 2461–2474.

Turpin, B., and J. Huntzicker (1991), Secondary formation of organic aerosol in the Los Angeles Basin - A descriptive analysis of organic and elemental carbon concentrations, *Atmos. Environ.*, *25*, 207–215, doi:10.1016/0960-1686(91)90291-E.

van der Kamp D., and I. McKendry (2010), Diurnal and seasonal trends in convective mixed-layer heights estimated from two years of continuous ceilometer observations in Vancouver, BC, *Bound.-Lay. Meteorol.*, *137*, 459475, doi:10.1007/s10546-010-9535-7.

Van Pelt, R. S., and T. M. Zobeck (2007), Chemical constituents of fugitive dust, *Environ. Monit. Assess.*, *130*, 3–16, doi:10.1007/s10661-006-9446-8.

van Pinxteren, D., E. Brueggemann, T. Gnauk, Y. Iinuma, K. Mueller, A. Nowak, P. Achtert, A. Wiedensohler, and H. Herrmann (2009), Size- and time-resolved chemical particle characterization during CAREBeijing-2006: Different pollution regimes and diurnal profiles, *J. Geophys. Res.-Atmos.*, *114*, doi:10.1029/2008JD010890.

Wang, K., Y. Zhang, A. Nenes, and C. Fountoukis (2012), Implementation of dust emission and chemistry into the Community Multiscale Air Quality modeling system and initial application to an Asian dust storm episode *Atmos. Chem. Phys. Disc.*, http://www.atmos-chem-phys-discuss.net/12/13457/2012/acpd-12-13457-2012-discussion.html.

Walcek, C., and G. Taylor (1986), A theoretical method for computing vertical distributions of acidity and sulfate production within cumulus clouds, *J. Atmos. Sci.*, *43*, 339–355, doi:10.1175/1520-0469(1986)043<0339:ATMFCV>2.0.CO;2.

Washenfelder, R. A., et al. (2010), Characterization of NO(x), SO(2), ethene, and propene from industrial emission sources in Houston, Texas, *J. Geophys. Res.-Atmos.*, *115*, doi:10.1029/2009JD013645.

Watson, J., J. Chow, Z. Lu, E. Fujita, D. Lowenthal, D. Lawson, and L. Ashbaugh (1994), Chemical mass-balance source apportionment of pm(10) during the Souther California air-quality study, *Aerosol. Sci. Tech.*, *21*, 1–36, doi:10.1080/02786829408959693.

Wittig, A., N. Anderson, A. Khlystov, S. Pandis, C. Davidson, and A. Robinson (2004), Pittsburgh air quality study overview, *Atmos. Environ.*, *38*, 3107–3125, doi:10.1016/j.atmosenv.2004.03.003.

Wunch, D., P. O. Wennberg, G. C. Toon, G. Keppel-Aleks, and Y. G. Yavin (2009), Emissions of greenhouse gases from a North American megacity, *Geophys. Res. Lett.*, *36*, L15810, doi:10.1029/2009GL039825.

Yue, D., et al. (2009), Characteristics of aerosol size distributions and new particle formation in the summer in Beijing, *J. Geophys. Res.-Atmos.*, *114*, doi:10.1029/2008JD010894.

Yue, D. L., et al. (2010), The roles of sulfuric acid in new particle formation and growth in the mega-city of Beijing, *Atmos. Chem. Phys.*, *10*, 4953–4960, doi:10.5194/acp-10-4953-2010.

Zhang, Y., P. Liu, B. Pun, and C. Seigneur (2006), A comprehensive performance evaluation of MM5-CMAQ for the Summer 1999 Southern Oxidants Study episode - Part I: Evaluation protocols, databases, and meteorological predictions, *Atmos. Environ.*, *40*, 4825–4838, doi:10.1016/j.atmosenv.2005.12.043.

Zhang, H., and Q. Ying (2010), Source apportionment of airborne particulate matter in Southeast Texas using a source-oriented 3D air quality model, *Atmos. Environ.*, *44*, 3547–3557, doi:10.1016/j.atmosenv.2010.06.004.

Zhang, J., W. Chameides, R. Weber, G. Cass, D. Orsini, E. Edgerton, P. Jongejan, and J. Slanina (2002), An evaluation of the thermodynamic equilibrium assumption for fine particulate composition. Nitrate and ammonium during the 1999 Atlanta Supersite Experiment, *J. Geophys. Res.-Atmos.*, *108*, doi:10.1029/2001JD001592.

Zheng, J., et al. (2011), Measurements of gaseous H(2)SO(4) by AP-ID-CIMS during CAREBeijing 2008 Campaign, *Atmos. Chem. Phys.*, *11*, 7755–7765, doi:10.5194/acp-11-7755-2011.

Chapter 8

Composition and Hygroscopicity of the Los Angeles Aerosol: CalNex[1]

[1]This chapter is reproduced by permission from "Composition and Hygroscopicity of the Los Angeles Aerosol: CalNex" by S. P. Hersey, J. S. Craven, Andrew R. Metcalf, Jack Lin, Terry Lathem, Kaitlyn J. Suski, John F. Cahill, Hanh T. Duong, Armin Sorooshian, Haflidi H. Jonsson, Manabu Shiraiwa, Andreas Zuend, Athanasios Nenes, Kimberly A. Prather, Richard C. Flagan, John H. Seinfeld, *Journal of Geophysical Research*, Accepted, 10.1002/jgrd.50307. An edited version of this paper was published by AGU.

Composition and Hygroscopicity of the Los Angeles Aerosol: CalNex

Scott P. Hersey[1], Jill S. Craven[1], Andrew R. Metcalf[1,7], Jack Lin[2], Terry Lathem[2], Kaitlyn J. Suski[3], John F. Cahill[3], Hanh T. Duong[4], Armin Sorooshian[4], Haflidi H. Jonsson[5], Manabu Shiraiwa[1], Andreas Zuend[1], Athanasios Nenes[6], Kimberly A. Prather[3], Richard C. Flagan[1], John H. Seinfeld[1]

1. California Institute of Technology, Pasadena, CA

2. School of Earth and Atmospheric Sciences, Georgia Institute of Technology, Atlanta, GA

3. University of California, San Diego, La Jolla, CA

4. University of Arizona, Tucson, AZ

5. Naval Postgraduate School, Monterey, CA

6. School of Earth and Atmospheric Sciences and School of Chemical and Biomolecular Engineering, Georgia Institute of Technology, Atlanta, GA

7. Now at Combustion Research Facility, Sandia National Laboratories, Livermore, CA

Correspondence to J.H. Seinfeld (seinfeld@caltech.edu)

This article has been accepted for publication and undergone full peer review but has not been through the copyediting, typesetting, pagination and proofreading process, which may lead to differences between this version and the Version of Record. Please cite this article as doi: 10.1002/jgrd.50307

Abstract

Aircraft-based measurements of aerosol composition, either bulk or single-particle, and both sub- and supersaturated hygroscopicity were made in the Los Angeles Basin and its outflows during May 2010 during the CalNex field study. Aerosol composition evolves from source-rich areas in the western Basin to downwind sites in the eastern Basin, evidenced by transition from an external to internal mixture, as well as enhancements in organic O:C ratio, the amount of organics and nitrate internally-mixed on almost all particle types, and coating thickness on refractory black carbon (rBC). Transport into hot, dilute outflow regions leads to significant volatilization of semivolatile material, resulting in a unimodal aerosol comprising primarily oxygenated, low-volatility, water-soluble organics and sulfate. The fraction of particles with rBC or soot cores is between 27 and 51% based on data from a Single Particle Soot Photometer (SP2) and Aerosol Time of Flight Mass Spectrometer (ATOFMS). Secondary organics appear to inhibit water uptake in aged particles, while CCN activity is enhanced with photochemical age. A biomass-burning event resulted in suppression of subsaturated hygroscopicity but enhancement in CCN activity, suggesting that BB particles may be nonhygroscopic at subsaturated RH but important sources of CCN. Aerosol aging and biomass burning can lead to discrepancies between sub-and supersaturated hygroscopicity that may be related to mixing state. In the cases of biomass burning aerosol and aged particles coated with secondary material, more than a single parameter representation of subsaturated hygroscopicity and CCN activity is needed.

1. Introduction

Despite significant improvements in air quality resulting from decades of aggressive emission controls, annual $PM_{2.5}$ averages exceeded the national standard every year from 2000-2010 in the Los Angeles Basin [*AQMD*, 2012]. Several major coordinated studies have investigated air quality in Los Angeles, including the Southern California Air Quality Study (SCAQS) [*Eldering et al.,* 1994; *Watson et al.,* 1994; *Chow et al.,* 1994; *Turpin and Huntzicker*, 1991], Southern California Ozone Study 1997 (SCOS97-NARSTO) [*Croes and Fujita*, 2003; *Liu et al*., 2000; *Pastor et al*., 2003; *Hughes et al*., 2002], Secondary Organic Aerosol in Riverside (SOAR) [*Docherty et al*., 2008; *Eatough et al*., 2008; *Denkenberger et al.*, 2007], and Pasadena Aerosol Characterization Observatory (PACO) [*Hersey et al*., 2011; *Wonaschütz et al.*, 2011]. The CalNex field study (http://www.esrl.noaa.gov/csd/calnex/), conducted from May-June 2010, was aimed at addressing both air quality and climate change through multi-agency collaboration to intensively sample gas and particulate pollutants from aircraft-, ship-, and ground-based platforms in both the San Joaquin Valley and Los Angeles Basin.

A major fraction of aerosol mass in the Los Angeles Basin results from gas-phase oxidation of anthropogenic emissions, leading to condensation of secondary organics, sulfate, nitrate, and ammonium [*Docherty et al.,* 2008], with primary black carbon (rBC or soot) particles serving as condensation sites for significant amounts of secondary material [*Pratt and Prather.,* 2009; *Metcalf et al.,* 2012]. The Basin may be characterized as source-rich in the west, with prevailing W/SW winds transporting emissions primarily from motor vehicles, diesel engines, and shipping to downwind receptor sites in the east. Aerosols evolve during transport, leading to significant changes in composition and thereby affecting optical and physical properties of particles. As aerosol composition and mixing state evolve during downwind transport in the Los Angeles Basin, it is expected that subsaturated hygroscopicity and cloud condensation

nuclei (CCN) properties of the aerosol likewise undergo changes. In the current study we seek to understand: (1) regional trends in aerosol composition in the Los Angeles Basin, (2) the characteristics of aging during downwind transport, (3) the impact of aerosol composition and evolution on both sub- and supersaturated aerosol hygroscopicity, and (4) the impact of biomass burning emissions on aerosol composition and hygroscopicity. Analysis is based on measurements made onboard the Center for Interdisciplinary Remotely-Piloted Aircraft Studies (CIRPAS) Twin Otter aircraft during the CalNex field study during May 2010. With high-time-resolution measurements of composition from an Aerosol Time-of-Flight Mass Spectrometer (ATOFMS), Aerosol Mass Spectrometer (AMS), Single Particle Soot Photometer (SP2), Particle-into-Liquid Sampler with Total Organic Carbon (PILS-TOC), Differential Aerosol Sizing and Hygroscopicity Spectrometer Probe (DASH-SP) and Cloud Condensation Nuclei Counter (CCNC), we combine measurements of aerosol composition, mixing state, and sub- and supersaturated hygroscopicity in a single comprehensive study of aerosol characteristics in the Los Angeles Basin. The large area covered by measurements made onboard the Twin Otter (Figure 1) complements previous studies on aerosol composition and hygroscopicity at localized ground sites in the Los Angeles Basin, and allows for direct characterization of evolution of the Los Angeles Aerosol during downwind transport.

2. Methods

2.1 CalNex Experiment

The California Research at the Nexus of Air Quality and Climate Change (CalNex) experiment, conducted from May-July 2010 in the Los Angeles Basin and San Joaquin Valley, sought to address the impacts of anthropogenic pollutants on both air quality and climate change in California (www.esrl.noaa.gov/csd/calnex/). Sampling was conducted at two ground

sites (Pasadena, CA in the western Basin on the campus of the California Institute of Technology (34.1405°N, 118.1225°W), and near Bakersfield, CA in the San Joaquin Valley (35.3463°N, 118.9654°W)), and onboard the Center for Interdisciplinary Remotely Piloted Aircraft Studies (CIRPAS, Naval Postgraduate School, Monterey, CA) Twin Otter aircraft, the NOAA Twin Otter aircraft, the NOAA WP-3D aircraft, the NASA King Air aircraft, and the NOAA R/V Ronald H. Brown.

We report here on data collected onboard the CIRPAS Twin Otter aircraft over 18 flights during May 2010. *Metcalf et al.* [2012] outline CIRPAS Twin Otter flights in detail. The aircraft, hangared at the Ontario International Airport (Ontario, CA, USA), sampled extensively in the Los Angeles Basin, desert outflows, and southern San Joaquin Valley at an altitude of 300 m above ground level. Typical flight duration was 4 h and covered 700-800 km. We focus here on flights that circled the Los Angeles Basin and probed the outflow of the Los Angeles plume as it was transported through the Banning Pass in the eastern Basin. Regions of study in the Los Angeles Basin are identified in Figure 1, while *Metcalf et al.* [2012] show the entire CalNex study area, including the San Joaquin Valley, on a topographic map. A summary of the instruments sampling onboard the Twin Otter during CalNex, including the size ranges measured, is presented in *Metcalf et al*. [2012]. The operating dates for each instrument are described below, and mission averages described in the results refer to averages over the entire operating time of the respective instrument during CalNex. The ATOFMS and AMS split time on the Twin Otter, which is why data are available for fewer days from those instruments. Gaps in data availability from other instruments indicate that instrument malfunction prevented collection of quality data.

2.2 Aerosol Mass Spectrometer (AMS)

Chemical composition of submicrometer non-refractory aerosol was measured with an Aerodyne compact Time-of-Flight Aerosol Mass Spectrometer (C-TOF-AMS, Aerodyne Research, Inc., Billerica, MA, USA) [*Jayne et al.,* 2000; *Drewnick et al.,* 2005; *Murphy et al.,* 2009] during the final nine flights (18-22, 24-25, 27-28 May 2010) onboard the CIRPAS Twin Otter. The instrument was operated in PTOF mode during five of those flights (21, 24-25, 27-28 May 2010). Particles with vacuum aerodynamic diameters (d_{va}) 50 nm $\leq d_{va} \leq$ 800 nm, pass through a 2% chopper and are subsequently vaporized at 600° C. The chopper is operated in three modes, detecting background mass spectra, ensemble average mass spectra over all particle sizes, or size-resolved mass spectra. After vaporization, particles are ionized by 70 eV electron impact and pulsed orthogonally into a time-of-flight mass spectrometer. Mass spectral deconvolution resolves sulfate, nitrate, ammonium, chloride, and organic mass loadings. Approximate organic O:C ratios are calculated by using mass fraction of organic at m/z 44 to total organic and a parameterization presented by *Aiken et al.* [2008]. During CalNex, both bulk and size-resolved particle time-of-flight (PTOF) AMS data were collected and averaged to 1 min resolution. Comparison of PTOF-AMS to differential mobility analyzer (DMA; section 2.8) size distributions assumes density of 1.3 g cm^{-3} for organics and 1.8 g cm^{-3} for inorganic species.

2.3 Aerosol Time of Flight Mass Spectrometer (ATOFMS)

Chemical characterization of individual aerosol particles was performed *in-situ* using an aircraft-aerosol time-of flight mass spectrometer (A-ATOFMS) [*Pratt et al.*, 2009a] during the first five flights during CalNex (6-7, 10, 14-15 May 2010). The A-ATOFMS uses an aerodynamic lens [*Liu et al.*, 1995] to focus particles between 100 and 1000 nm. However,

only particles with vacuum aerodynamic diameters between 100-300 nm were included in this analysis, to correspond to the size range of hygroscopicity measurements. The particles are aerodynamically sized by measuring the time it takes for the particle to pass through two 532 nm scattering lasers positioned a known distance apart. Particle speeds are converted to aerodynamic diameters using a calibration curve created with polystyrene latex spheres of known size. The sized particles are then desorbed and ionized using a pulsed 266 nm Nd-YAG laser. Positive and negative ion mass spectra from each particle are acquired using a dual polarity time-of-flight mass spectrometer. YAADA (www.yaada.org), a toolkit for Matlab (The MathWorks, Inc.), is used to facilitate data analysis. The mass spectra are clustered based on ion peak patterns and intensities using the ART-2a neural network [*Song et al.*, 1999]. Clusters are then hand classified and grouped into particle types based on similar mass spectral characteristics. The ion peaks are labeled as the most probable ions based on previous source and laboratory studies at each mass-to-charge (*m/z*) ratio.

2.4 Single Particle Soot Photometer (SP2)

Single-particle refractory black carbon (rBC) mass, as well as the thickness of coating that is non-refractory at 4000 K on each rBC particle, was measured by a Droplet Measurement Technologies (DMT, Boulder, CO, USA) Single Particle Soot Photometer (SP2) [*Stephens et al.*, 2003; *Baumgardner et al.*, 2004; *Schwarz et al.*, 2006; *Moteki and Kondo*, 2007; *Slowik et al.*, 2007] during 15 flights (6-7, 10, 12, 14-15, 18-22, 24-25, 27-28 May 2010). In the SP2, rBC-containing particles are heated to their vaporization point as they pass through the active cavity of an Nd:YAG laser beam (λ = 1064 nm), with incandescence detected by two channels. Two scattering channels detect the scattering cross section of particles before incandescence, with Mie theory enabling determination of non-rBC coating thickness based on the scattering

signal and the assumption of a core-shell morphology. *Metcalf et al.* [2012] details the calibration of this particular SP2 and the measurement techniques applied during Twin Otter flights. The rBC mass concentrations reported here are derived from lognormal fits to the single-particle size distributions, a correction which yields ~15-20% larger mass concentration than the raw data. The SP2 was calibrated with Aquadag (Aqueous Deflocculated Acheson Graphite, Acheson Colloids Company, Port Huron, MI, USA), which recently has been shown to yield calibration factors different than ambient soot would yield (Baumgardner et al, 2012; Laborde et al 2012). As reported by Metcalf et al. 2012, total rBC mass concentrations are ~12% smaller than comparable SP2s operated during CalNex. This potential bias has not been corrected for in the data presented here because the calibration standards have not yet been definitively linked to ambient rBC in the LA Basin. In addition, coating thickness diameters reported here may also be biased high, because each optical diameter may be assigned to a smaller rBC core particle. These potential biases will not change the spatio-temporal distribution of the measurements during CalNex.

The refractory, light-absorbing fraction of combustion aerosol is referred to as either refractory black carbon (rBC) or soot, depending on whether it is detected by incandescence or thermochemical characteristics, respectively. The ATOFMS (Section 2.3) identifies soot particles as those producing mass spectra with a simple carbon pattern often extending up to C_{12}^+ [*Moffet and Prather*, 2009]. In the SP2, particles, heated to their vaporization point, incandesce as they pass through a 1 MW Nd:YAG laser [*Schwarz et al.*, 2006]. rBC particles are identified based on comparison of their ambient particle incandescence signature to those in laboratory-generated rBC particles. During CalNex, the number of soot particles detected by the ATOFMS was regionally correlated with rBC number concentration measured by the SP2,

based on comparing time averages of data from each instrument over each region (Pearson's R correlation coefficient, Pr, equal to 0.91), and the two measurements are thus considered to provide similar estimates of the regional variability in soot-type combustion particles in Los Angeles. Nonetheless, for accuracy, rBC and soot will be defined respectively as the amount of light-absorbing material that incandesces with a signature that matches that of laboratory-generated rBC particles (rBC) and as the number of particles that produce mass spectral signature with simple carbon patterns (soot).

2.5 Particle into Liquid Sampler with Total Organic Carbon (PILS-TOC)

WSOC was quantified during 16 flights, using a particle-into-liquid sampler (PILS; Brechtel Manufacturing Inc.) coupled to a Total Organic Carbon (TOC) Analyzer (Sievers Model 800) [*Sullivan et al.*, 2006; *Duong et al.*, 2011], and data are presented here for 13 flights (6-7, 10, 12, 14-15, 18-21, 25, 27-28 May 2010). Particles smaller than 2.5 μm in diameter are sampled by the PILS and passed immediately through an organic carbon denuder (Sunset Laboratory Inc.) to remove organic vapors. Particles are grown into droplets, collected by inertial impaction, and delivered through a 0.5 μm PEEK (polyetheretherketone) liquid filter prior to entering a TOC analyzer for quantification of WSOC approximately every 4 s. Reported WSOC concentrations represent the difference between the measured and background concentrations, which were obtained by passing sampled air through a high efficiency particulate air (HEPA) filter. The overall measurement uncertainty is estimated to be approximately 10%, with a minimum detection limit of 0.1 □g C m^{-3}. Synchronization of WSOC measurements with the other aircraft instrument data takes into account well-documented liquid transport delays in the PILS instrument [*Sorooshian et al.*, 2006].

2.6 Differential Aerosol Sizing and Hygroscopicity Spectrometer Probe (DASH-SP)

The Differential Aerosol Sizing and Hygroscopicity Spectrometer Probe (DASH-SP, Brechtel Mfg.) was used to measure subsaturated aerosol water uptake at 74 and 92% RH for 17 flights (4-7, 10, 12, 14-15, 18-22, 24-25, 27-28 May 2010) during CalNex. The DASH-SP was operated as described by *Sorooshian et al.* [2008], except that the 85% RH humidification channel was not functioning. Ambient particles are dried in a nafion dryer before being size-selected in a cylindrical differential mobility analyzer (DMA) to generate a monodisperse aerosol of 150, 175, 200, or 225 nm dry diameter (d_{dry}) particles. After size-selection, the flow of monodisperse aerosol is split into four separate flows, one providing a redundant measurement of particle number concentration via a condensation particle counter (CPC, TSI Model 3831), with the other three channels consisting of parallel nafion humidification chambers (Perma Pure, LLP, Model MD-070-24FS-4) operated at dry (< 10), 74, and 92% RH, followed by custom-built optical particle counters (OPCs). Within the OPCs, particles pass through a focused laser beam (λ = 532 nm, World Star Technologies, Model TECGL-30), where all forward-scattered light is collected and focused on a photomultiplier tube, and the resulting electrical pulse is recorded by a high-speed data acquisition computer. A dry refractive index is calculated from the dry OPC response to particles of known DMA size and used as an initial condition in an iterative data processing algorithm based on laboratory calibrations with salts of known refractive indices. The algorithm determines the best fit on a solution surface relating electrical pulse height, size, and refractive index, thereby accounting for the change in refractive index with particle water uptake. Temperature, pressure, and RH are monitored and controlled at several locations in the DASH-SP, ensuring that variability in these parameters does not impact growth factor measurements. RH was controlled to within 1.5%, and overall uncertainty in GF calculations is 4.5%.

Two factors may result in volatilization of semivolatile species in the DASH-SP. First, sheath gas entering the DASH-SP is filtered through a Pall Life Sciences HEPA filter (p/n 12144). The large surface area of packing material is expected to effectively scrub the sheath gas of $NH_{3\,(g)}$, but is not expected to adsorb $HNO_{3\,(g)}$ or organic gases (personal correspondence with Pall), and is therefore expected to result in volatilization of NH_4NO_3. Next, utilization of a heating element to humidify DASH sample flows results in a temperature increase of 8 ºC between the aircraft inlet and DASH optical sizing, likely resulting in volatilization of both particulate NH_4NO_3 and semivolatile organics. Volatilization is expected to be modest, due to the short residence time in the DASH-SP (7 s total), but an explicit treatment of NH_4NO_3 volatilization and its effect on calculated water uptake of the organic fraction of particles is presented in Section 3.4.

2.7 Scanning Flow Cloud Condensation Nuclei Analyzer (CCNC)

CCN measurements were made with a Droplet Measurement Technologies streamwise, thermal-gradient cloud condensation nuclei counter (CCNC) [*Roberts and Nenes*, 2005; *Lance et al.*, 2006] for 16 flights (5-7, 10, 12, 14-15, 18-22, 24-25, 27-28 May 2010). Particles are introduced into the centerline of a cylindrical tube with wetted walls on which a streamwise, linear thermal gradient is applied. Owing to the difference in diffusivity between water and air molecules, a supersaturation is generated in the column, the maximum of which is located at the centerline. Particles that activate into cloud droplets are counted and sized with an optical particle counter.

During CALNEX, the CCNC was operated as a CCN spectrometer using Scanning Flow CCN Analysis [SFCA; *Moore and Nenes*, 2009]. In SFCA operation, dynamically changing the instrument flow while maintaining constant pressure and temperature gradients produces a nearly instantaneous change in supersaturation. The instrument temperature gradient was nominally held at 10 K and the pressure maintained at 700 mb by use of a flow orifice and active flow control system, as described by *Moore et al.* [2011]. Nominal flow upscan and downscan times of 20 s were used.

Instrument supersaturation was calibrated following the procedure in *Moore and Nenes* [2009]. Multiple calibrations were performed throughout the campaign to account for the effect of ambient temperature on the flow rate range. The uncertainty in CCNC supersaturation is estimated to be ± 0.04%. The uncertainty in CCN number concentration due to counting statistics and variations in temperature, pressure, and flow rates is estimated to be ~12% for CCN concentrations above 100 cm^{-3} STP.

2.8 DMA Size Distributions

Particle size distribution measurements were made with a cylindrical scanning differential mobility analyzer (TSI Model 3081) coupled to a condensation particle counter (TSI Model 3010) for 17 flights (4-7, 10, 12, 14-15, 18-22, 24-25, 27-28 May 2010). An exponential scan from a mobility diameter of 10 nm to 800 nm is completed every 90 s. The sheath and excess flows of 2.5 liters per minute were used, with a 5:1 flow rate ratio of sheath-to-aerosol. The data are inverted following the method outlined by Collins et al. (2002), which corrects for the DMA transfer function smearing as a result of a faster-than-normal scan time at a resolution of 5. Any residual smearing of the retrieved size distributions as a result of the operating

parameters is expected to be minimal compared to the effect of sampling narrow plumes and changing air masses during flight.

3. Results and Discussion

3.1 Los Angeles Basin Meteorology

Winds tend to display distinct and predictable diurnal patterns in the Los Angeles Basin [*Blumenthal*, 1978; *Lu and Turco*, 1995; *Hersey et al.*, 2011]. Under the most frequent meteorology, stagnant or light offshore N/NE winds in the overnight hours (20:00-6:00 LT; UTC - 8 h) give way to light onshore W/SW winds shortly after sunrise as surface heating generates a pressure gradient between cool coastal and warm inland areas. As solar heating intensifies through the day, the magnitude of the ocean-land pressure gradient increases and W/SW winds correspondingly increase in velocity to near 15 km/h by 15:00-16:00 LT. After 16:00 LT, winds decrease in velocity again to become stagnant, eventually changing direction as N/NE return flow increases in overnight hours. This local diurnal meteorology results in downwind transport of air from source-rich western portions of the Los Angeles Basin to receptor sites in the eastern Los Angeles Basin [*Lu and Turco*, 1995], with eventual transport out the El Cajon and Banning Passes and into desert outflow regions. Stagnant overnight winds can lead to pollutant buildup and carryover from one day to the next, resulting in an aged background aerosol in the Basin characterized by accumulation mode particles (0.1-1.0 μm diameter) containing a significant fraction of highly oxidized organic species [*Blumenthal*, 1978; *Hersey*, 2011]. *Metcalf et al.* [2012] found that meteorological conditions during May 2010 were more characteristic of springtime than classical summer meteorology in the Los Angeles Basin, but FLEXPART modeling of air parcel histories indicates similar airmass origin and west-east transport as described previously in Los Angeles. In general, spring

meteorological conditions are characterized by similar overall patterns as the summer, but generally weaker coast-land pressure gradients and onshore winds, cooler temperatures, and less intense photochemical conditions [*Hersey et al.*, 2011]. Average ambient temperature (at flight altitude) over 18 flights during CalNex varied regionally, increasing from 16.1 ± 2.0°C in the western Basin to 18.3 ± 3.4°C in the eastern Basin and 24.3 ± 1.8°C in desert outflows (Figure 2 (k)).

Composition and hygroscopicity can vary spatially to a great extent within the Los Angeles Basin, and so discussion of trends will focus on averages over the sum of sampling hours for each respective instrument for each of 8 regions defined in Figure 1. The flight on 13 May 2010 was influenced by biomass burning emissions from a brush fire in the eastern Basin, and will be considered separately.

3.2 Aerosol Bulk Composition

Because diurnal wind patterns result in downwind transport of airborne species in the Los Angeles Basin, one may consider regional trends from west to east as representative of aerosol aging. Further aerosol aging between the Basin itself and outflow regions is expected to occur, as well as processes of dilution and volatilization. Analysis of bulk, non-refractory, submicrometer aerosol composition from the AMS (average over 9 flights; 18-22, 24-25, 27-28 May 2010), SP2 (average over 15 flights; 6-7, 10, 12, 14-15, 18-22, 24-25, 27-28 May 2010), and PILS-TOC (average over 13 flights; 6-7, 10, 12, 14-15, 18-21, 25, 27-28 May 2010), with averages comprising total sampling hours for each instrument (Figure 2 (a-k)) will focus on regional, west-to-east trends in order to highlight aerosol evolution during downwind transport and aging. Black carbon characteristics are presented by *Metcalf et al.* [2012], and a detailed

analysis of the organic fraction of aerosol (OA) by positive matrix factorization of AMS data will follow in a separate manuscript.

Total submicrometer aerosol mass (Figure 2 (a)), taken as the sum of non-refractory mass detected by the AMS and rBC mass detected by the SP2, displays distinct regional trends. Within the Los Angeles Basin, total submicrometer mass over May 2010 was relatively constant from west to east, averaging 7.7 ± 3.9 μg m^{-3} in source-rich western areas and 8.2 ± 4.6 μg m^{-3} in downwind eastern Basin receptor sites. This constant mass concentration was observed despite warmer temperatures in the eastern Basin (Fig. 2 (k); 16.1 ± 2.0°C in the western Basin, versus 18.3 ± 3.4°C in the eastern Basin) that are expected to lead to volatilization of semivolatile species and decreased aerosol mass. This suggests that as particles are transported downwind, secondary species are photochemically produced in the gas phase and condense onto particles. A sharp decrease in aerosol mass is observed from that in the Banning Pass (4.9 ± 3.8 μg m^{-3}) to that in outflow regions (1.2 ± 0.2 μg m^{-3}), as the Los Angeles plume is diluted upon transport into hot desert areas (24.3 ± 1.8°C). Because there are no significant industrial sources of rBC in outflow areas and only one freeway in the region, rBC may be considered a conservative, nonvolatile tracer in outflow areas, and one may estimate the importance of volatilization by comparing the mass fraction of rBC (rBCMF; Figure 2 (g)) in upwind versus downwind regions, according to the ratio:

$$rBC_{Enhancement} = \frac{rBCMF_{Downwind}}{rBCMF_{Upwind}}, \quad (1)$$

where $rBC_{Enhancement}$ is the enhancement in *rBCMF* between upwind ($rBCMF_{Upwind}$) and downwind ($rBCMF_{Downwind}$) sites. *rBCMF* is enhanced in outflow regions, and $rBC_{Enhancement}$ approaches 2.2 when comparing Basin aerosol with particles in outflows, underscoring the importance of volatilization during transport to outflows.

Individual non-refractory species exhibit behavior consistent with condensation of secondary material during downwind transport (Table 1, Figure 2 (b-f)). The western Basin is characterized by relatively high sulfate and chloride mass fractions (SMF and CMF, respectively), owing to their marine sources and the highest concentration of shipping and industrial SO_2 emissions occurring in the western Basin and near Long Beach. The downwind eastern Basin is significantly enhanced in nitrate and ammonium mass fraction (NMF, AMF, respectively), compared to SMF and CMF, owing to photochemical production of nitrate during downwind transport and the presence of a large concentration of bovine NH_3 emissions in the area [*Neuman et al.*, 2003; *Docherty et al.*, 2008]. The local maximum in AMF in the Long Beach region may be associated with industrial selective catalytic reduction (SCR) and selective non-catalytic reduction (SNCR) NO_x emission control strategies - both of which are associated with ammonia emissions [*Heck*, 1999]. Further, there are local maxima in sulfate mass in the Long Beach region, which would serve to drive ammonia into the particulate phase as $(NH_4)_2SO_4$ and NH_4HSO_4 and thereby enhance AMF relative to organics, nitrate, and chloride.

After traversing the narrow Banning Pass, NMF and AMF decrease quickly in outflows, as temperature increases by ~ 6°C (Fig. 2 (k)). Owing to rapid volatilization of ammonium nitrate, the resulting aerosol is enriched in OMF. Rapid volatilization of ammonium nitrate has also

been described for Los Angeles and Mexico City aerosols [*Huffman et al.*, 2009]. The mass ratio of organics to conservative, nonvolatile rBC is surprisingly constant between the Basin (131) and outflows (129), indicating that much of the secondary organic aerosol (SOA) formed in the Los Angeles Basin is relatively low in volatility, as previously reported for Los Angeles and Mexico City aerosol [*Huffman et al.*, 2009]. SMF is also enhanced in outflow regions while the ratio of sulfate to rBC does not decrease, as expected by the low volatility of sulfate species.

The relative mass fractions of non-refractory submicrometer species are compared with those reported in other megacity field experiments in Table 2. Total aerosol mass measured in the Basin during CalNex is relatively low when compared with more characteristically polluted megacities (e.g. Beijing, China; Mexico City, Mexico), and is also lower than previously reported in the Los Angeles Basin during SOAR [*Docherty et al.*, 2008; 2011] and PACO [*Hersey et al.*, 2011]. One reason for this discrepancy is that the month of May tends to be less photochemically active than months in the mid to late summer (July-September), and is associated with less production of SOA [*Hersey et al.*, 2011]. Additionally, *Metcalf et al.* [2012] noted that Twin Otter CalNex flights were carried out during atypical May meteorology in Los Angeles, which resulted in one of the least polluted months of May in the last 25 years. The mass fractions of organics and sulfate are lower during CalNex sampling, while the fractions of nitrate and ammonium are appreciably higher than previous studies, potentially owing to less intense photochemical conditions and cooler temperatures during May 2010. The results presented here, therefore, should be considered characteristic of mild springtime conditions in Los Angeles, with similar patterns to the summertime meteorology described in

Section 3.1, but weaker pressure gradients and onshore winds, cooler temperatures, and less intense photochemistry.

The nature and evolution of organic aerosol (OA) are of particular interest, owing to the prevalence of organic species in ambient particles [*Zhang et al.*, 2007] and uncertainties about their formation pathways and aging. Figures 2 (h-i) highlight the nature of OA in the Los Angeles Basin and outflows. The oxidation state of organics (O:C ratio; Figure 2 (i)) is relatively constant throughout the Basin, with regional averages between 0.38 and 0.43. The mass fraction of aerosol comprised of WSOC (WMF) is similarly relatively constant throughout the Basin (0.16-0.24), as is the ratio of WMF to total organic mass (0.06-0.08). Further transport and evolution of aerosol into the outflow regions lead to significantly higher O:C ratio (0.49-0.55), WMF (0.51-0.60), and ratio of WMF to total organic mass (0.51-0.56), and *Hanh et al.* [2012] found that the fraction of $PM_{2.5}$ consisting of WSOC is enhanced in outflows. Overall, aging of Los Angeles OA appears to be associated with an enhancement in the oxidiation state of organics, as has been reported in other studies of urban aerosol [*Alfarra et al.*, 2004; *de Gouw et al.*, 2005; *Zhang et al.*, 2007; *Aiken et al.*, 2008; *Kleinman et al.*, 2008], as well as a significant enhancement in the mass fraction of WSOC in comparison with total organic mass. *Hersey et al.* [2011] found O:C ratios ranging from 0.44 to 0.55 at the Pasadena site relatively free from influence of primary emissions, with the highest values measured during photochemically intense conditions. *Docherty et al.* [2011] reported O:C ratios between 0.28 and 0.44 in Riverside in the eastern Basin at a site 0.5 km from a major freeway, which was influenced by reduced organics from primary vehicle emissions. The O:C ratios measured during CalNex lie between those reported by *Hersey et al.* [2011] and *Docherty et al.* [2011], owing to their distribution across areas impacted by primary emissions

and those more representative of regional OA. Detailed analysis of the organic fraction of aerosol sampled onboard the Twin Otter during CalNex will follow in a subsequent manuscript.

Condensation of secondary species during aging and downwind transport is further supported by observations of significant downwind enhancement of rBC coating thickness diameter of rBC particles between 90 and 270 nm, as measured by the SP2 [*Metcalf et al.*, 2012]. Figure 2 (j) indicates that the diameter of coating on rBC aerosol increases consistently from the western to eastern Basin, and increases significantly as the Los Angeles plume passes through the Banning Pass and into outflows. The most dramatic increases in rBC coating thickness diameter occur in outflow regions, which are also the areas where bulk composition measurements indicate significant volatilization of semivolatile species and enhancement in OMF. These trends may be evidence of production and subsequent condensation of low-volatility SOA in outflow regions, and may alternately result from dilution of the Los Angeles plume with air containing aged aerosol with thick coatings on rBC cores.

In many urban areas, a smaller mode in the aerosol number distribution is dominated by OA or soot while inorganic species and OA comprise a larger mode [*Moore et al.*, 2007; *Shields et al.*, 2008; *Titta et al.*, 2010, *Sun et al.*, 2009]. In Los Angeles, fine organic modes are commonly present in morning hours and during photochemically active periods in source-rich areas [*Moore et al.*, 2007; *Hersey et al.*, 2011], and are associated with vehicle exhaust [*Shields et al.*, 2008]. Aged aerosol, such as that observed in the downwind eastern Basin, is often characterized by unimodal distributions and the presence of aged species including oligomeric compounds [*Moore et al.*, 2007; *Denkenberger et al.*, 2007]. Representative size-resolved non-

refractory AMS composition and DMA size distribution averaged over 5 flights (21, 24, 25, 27, 28 May; Figure 3) indicates that aerosol in the western Basin is characterized by a distinctly bimodal distribution, with the smaller of two modes (centered at 80-90 nm d_{va}) dominated by organics and the larger mode (centered at 500-600 nm d_{va}) dominated by nitrate in addition to containing sulfate, ammonium, and chloride. After transport to the eastern Basin, nitrate, sulfate, ammonium, and chloride still reside in the larger mode, but organics are distributed bimodally, comprising the dominant fraction of a smaller mode (60-110 nm d_{va}), as well as contributing a significant fraction to the larger mode (200-400 nm d_{va}). After transport into outflows, all species generally reside in a unimodal distribution centered at 300-400 nm d_{va}. One overall impact of the aging of Los Angeles aerosol appears to be that organics transition from comprising a largely separate fine mode to contributing to a single, larger mode, while inorganic species consistently reside in larger particles. Transition of an externally mixed aerosol to an internal mixture with photochemical age has been observed for bulk composition in Los Angeles [*Bhave et al.*, 2001], and results here suggest that such changes in mixing state are the result of size-dependent condensation of secondary species [*Alfarra et al.*, 2004].

3.3 Single Particle Composition

AMS measurements address the overall composition of an aerosol population but are limited in their ability to determine mixing state and cannot detect refractory species. The Aerosol Time-of-Flight Mass Spectrometer (ATOFMS) measures single-particle aerosol composition for both refractory and non-refractory species and provides a direct measure of both size and mixing state. In ATOFMS analysis, single particles are classified into particle types based on dominant mass spectral peaks. ATOFMS measurements detected 9 major particle types in CalNex for

particles in the size range 100-300 nm d_{va} (Table 3), whose representative mass spectra are represented in Figure 4. The major particle types detected were soot, soot-OC, biomass burning, highly processed, sea spray, biological, aged organic carbon, and ship emissions. Soot particles, most likely produced by vehicles [*Sodeman et al.*, 2005; *Toner et al.*, 2006; *Shields et al.*, 2007], contained C ion subunits, Cn^+ ($^{12}C^+$, $^{24}C_2^+$, $^{36}C_3^+$, $^{48}C_4^+$, $^{60}C_5^+$, etc.), whereas soot-organic carbon (Soot-OC) particles were mixtures of carbon ions and smaller organic carbon ions ($^{27}C_2H_3^+$, $^{43}C_2H_3O^+$) internally mixed with nitrate ($^{62}NO_3^-$). Biomass burning particles contained a large potassium ion ($^{39/41}K^+$), potassium ion clusters ($^{104}K_2CN^+$, $^{113/115}K_2Cl^+$, $^{213/215}K_3SO_4^+$), elemental carbon, and organic carbon ions [*Silva et al.,* 1999; *Pratt et al.*, 2011]. Highly processed particles produced only negative ion mass spectra primarily containing sulfate ($^{97}HSO_4^-$) and/or nitrate ($^{46}NO_2^-$, $^{62}NO_3^-$) ions. Sea spray was characterized by the presence of sodium ($^{23}Na^+$), sodium clusters ($^{46}Na_2^+$, $^{62}Na_2O^+$, $^{63}Na_2OH^+$, $^{81/83}Na_2Cl^+$) and chloride ($^{35/37}Cl^-$) and internally mixed with nitrate ($^{62}NO_3^-$) [*Gaston et al.*, 2011; *Gard et al.*, 1998]. Biological particles contained sodium ($^{23}Na^+$), potassium ($^{39}K^+$), organic nitrogen ($^{26}CN^-$, $^{42}CNO^-$) and phosphate ($^{79}PO_4^-$) ions, and some were enriched in metals ($^{24}Mg^+$, $^{40}Ca^+$, $^{56}Fe^+$ or $^{52}Cr^+$) [*Pratt et al.*, 2009b; *Russell et al.*, 2009; *Fergenson et al.*, 2003]. Aged organic carbon particles were classified based on an intense oxidized organic carbon ion ($^{43}C_2H_3O^+$) in addition to elemental and organic carbon ions [*Qin et al.*, 2012]. These particles were primarily internally mixed with sulfate ($^{97}HSO_4^-$). Ship emissions were characterized by intense vanadium ($^{51}V^+$) and vanadium oxide ($^{67}VO^+$) ions which were internally mixed with sulfate ($^{97}HSO_4^-$) [*Ault et al.*, 2010]. While soot was present in most particle types, characteristic soot peaks are not labeled in all mass spectra in Fig. 4 because their presence is often masked by high-intensity ion peaks (e.g. that of V^+ in the ship emissions spectrum).

Regional averages of the ATOFMS data are based on measurements of ~1000 particles in the smallest geographical regions in Fig. 1 (Pasadena, Long Beach, Banning Pass), and > 4000 in larger regions (western, central, and eastern Basin). ATOFMS data are available for only one flight that sampled in outflow regions, which was heavily influenced by biomass burning emissions from a brush fire in the eastern Basin (13 May 2010) and will be considered separately. Thus, average non-biomass-burning-influenced ATOFMS data are based on 5 flights for which it collected data onboard the Twin Otter (6-7, 10, 14-15 May 2010) within the Basin, with data on 13 May 2010 presented separately and including results from sampling in outflow regions.

Characteristic particle types were identified in each region of the Basin and outflows, indicating that Los Angeles aerosol is an external mixture in the sense that not every particle has the same composition. However, each particle type identified by the ATOFMS represents an internal mixture of many different species, with nitrate and organics ubiquitous as condensed secondary material in all particle types except for pure, newly-emitted soot-type particles. The areas of nitrate and organic peaks in mass spectra are enhanced in the eastern Basin relative to the western Basin, indicating that nitrate and organics become internally-mixed with all particle types during downwind transport. This finding is consistent with those from the AMS and SP2, indicating that a major characteristic of aging during downwind transport is the production and condensation of secondary organic and nitrate species.

Following trends in single-particle aerosol composition from west to east in the Basin and outflows allows analysis of the effect of aging during downwind transport on both aerosol composition and mixing state in Los Angeles (Figure 5). The influence of sea spray, sulfate,

and ship emissions all decrease from west to east and into outflows. The flight on 16 May 2012 was heavily influenced by sulfate particles throughout the Basin, and the small sample size in Pasadena resulted in a disproportionate enhancement in sulfate fraction in that region when compared with other regions, explaining the greater than expected influence of sulfate there. The soot+OC, Aged OC, and biomass burning particle types show little variation within the Basin, which suggests that these types of particles either have relatively uniform sources across the Basin or that they exist as background species that become well-mixed throughout the Basin over hours to days. Nitrate increases in influence in eastern portions of the Basin downwind of dairies, consistent with findings from the AMS and SP2. The influence of nitrate is significantly diminished in outflows, owing to volatilization of ammonium nitrate.

One would expect that soot particles become increasingly coated with secondary material during downwind transport and evolution; thus the constant fraction of particles identified as purely soot suggests relatively uniform emissions of soot-type particles in the Basin - likely from on-road fuel combustion and widespread diesel engine use. *Pratt and Prather* [2009] heated particles to volatilize semivolatile species and found that nearly 80% of particles in the eastern Los Angeles Basin contained soot cores. To determine the fraction of particles between 100 and 300 nm d_{va} possessing soot cores in the Los Angeles Basin during CalNex, single particle data were searched for soot markers in the mass spectra (m/z 12, 36, -36, -48, corresponding to C^+, C_3^+, C_3^+, and C_4^+, respectively). Particles with soot cores were defined as those containing soot markers at an absolute area of at least 50 on the mass spectrum [*Spencer et al.,* 2006], and comprised 51% of particles. This result is slightly lower than reported by *Cahill et al.* [2012], who analyzed particles collected across the Basin during the 2010 CalNex study onboard the Twin Otter aircraft and determined that 60% of particles contained soot

cores over the entire ATOFMS size range (100-1000 nm). Another estimate of the fraction of particles with rBC cores was obtained from the SP2 by comparing the number of particles with purely scattering signatures to the total number of particles detected by the instrument. Results indicate that the fraction of 100-300 nm particles containing rBC cores was 27 ± 15% across the Basin, with the discrepancy from ATOFMS likely due to the higher sensitivity of ATOFMS to soot (lower detection limit of ~50 nm soot cores, compared with 90 nm for the SP2) and the slightly narrower size range of SP2. We conclude that it is not possible to assign a single number to the fraction of particles with soot cores in the Los Angeles Basin, but instead bracket that fraction with estimates from the SP2 and ATOFMS of 27 and 51%, respectively.

3.4 Subsaturated Aerosol Hygroscopicity

Hygroscopicity is a function of chemical composition. Generally, inorganics are associated with a higher degree of water uptake and organics with suppressed water uptake [*Shinozuka et al.*, 2009; *Quinn et al.*, 2005; *Hersey et al.*, 2009; *Hersey et al.*, 2011]. Urban aerosol often exhibits complex hygroscopic behavior, with externally-mixed particles resulting in multiple hygroscopic modes with distinct water uptake characteristics [*Cocker et al.*, 2001; *Massling et al.*, 2005; *Swietlicki et al.*, 2008; *Massling et al.*, 2009; *Meier et al.*, 2009; *Tiitta et al.*, 2010; *Rose et al.*, 2010]. The optical sizing method employed by the DASH-SP during CalNex is limited in its ability to resolve multiple growth modes, and so subsaturated hygroscopic data reported here are for the main hygroscopic mode of particles, as is common in studies of aerosol hygroscopicity [*Wex et al.*, 2010]. Subsaturated data represent particles between 175 and 225 nm dry diameter (d_{dry}), and hygroscopic growth was measured at RH of 74% and 92%.

The κ single-parameter measure of aerosol hygroscopicity presented by *Petters and Kreidenweis* [2007] has been widely adopted, the value of which can be derived from measurements of either subsaturated growth factor or supersaturated CCN activation. The DASH-SP measures hygroscopic growth factor, which is the ratio of wet to dry particle diameter ($GF = d_{wet}/d_{dry}$), at a range of d_{dry} and RH values. Considering that $d_{wet} = d_{dry} * GF$, κ may be calculated from:

$$S = K \times a_w = K \frac{d_{wet}^3 - d_{dry}^3}{d_{wet}^3 - d_{dry}^3(1-\kappa)}, \quad (2)$$

where S is the equilibrium water vapor saturation above the particle (i.e. RH/100), K is the Kelvin term accounting for droplet curvature, a_w is the activity of water, and κ is the hygroscopicity parameter. The Kelvin term includes the droplet surface tension, to which subsaturated hygroscopicity measurements are relatively insensitive. Therefore, the surface tension of water was assumed for this study. There was no systematic difference between κ at 74 and 92% RH, and so κ reported here is the average of the two. Size-dependent hygroscopic behavior was not observed for particles between 175 and 225 nm during CalNex, and results here represent average hygrosopicity for particles in the DASH size range. Uncertainty in individual κ calculations is estimated to be ± 0.05, based on uncertainty in particle diameters measured by the DASH. In all regions the standard deviation (SD) in κ values is greater than propagated uncertainty and results are reported as κ ± SD.

Overall, subsaturated κ of 0.37 ± 0.10 in the Basin and 0.24 ± 0.07 in outflows during CalNex is consistent with κ of ~ 0.3 reported in other megacity studies [*Shinozuka et al.*, 2009; *Chang et al.*, 2010; *Rose et al.*, 2010; *Wex et al.*, 2010]. DASH-SP averages represented in Figure 6 indicate that subsaturated water uptake of the main hygroscopic mode decreases significantly

as Basin aerosols age during downwind transport. GF-derived κ is largest in the western Basin, where a distinctly bimodal aerosol exists and AMS and SP2 indicate that the amount of organic coating material is at a minimum. In the bimodal distribution, the separate, fine mode comprises primarily organics, while inorganic species constitute the majority of aerosol mass in the DASH-SP size range. Because DASH-SP measurements represent hygroscopicity for the main hygroscopic mode for particles between 175 and 225 nm dry diameter, and because organics appear to comprise a separate mode in the aerosol, it is expected that subsaturated κ values in the western Basin are representative of a predominantly inorganic aerosol, with a less significant contribution from condensed organic species. This characterization is consistent with an observed κ of ~ 0.41 ± 0.10 for the western Basin, assuming inorganic nitrate and sulfate species to have a representative κ between 0.45 and 0.65 and organics to be between 0 and 0.1 [*Kreidenweis et al*., 2008; *Massoli et al.*, 2009; *Duplissy et al.,* 2011].

Hygroscopicity is suppressed in the eastern Basin relative to that in the western Basin, with an average κ of 0.32 ± 0.09, corresponding to reduced SMF and CMF, condensation of significant amounts of both secondary nitrate and SOA, and a transition of much of the organic fraction to the larger mode.

As noted in Section 3.2, aerosols are transformed significantly during transport into outflow regions, where temperature is significantly higher and dilution is important. Volatilization results in particles that are enriched in low-volatility organic species, and continued aging causes particles to become unimodal and thickly coated with what AMS data indicate to be predominantly organic species. Particles measured by the SP2 are not exactly in the same size range as the DASH-SP and coating thicknesses are only measured for particles with rBC cores

(~27% of particles in CalNex). However, the processes by which secondary species condense onto rBC particles in the 90-270 nm size range of the SP2 will similarly tend to coat particles in the 175-225 nm size range of the DASH-SP. These general transformations by condensation of secondary coating material result in significant reduction in subsaturated hygroscopicity to $\kappa \sim 0.24 \pm 0.06$ in outflows.

To further investigate the hygroscopic behavior of organics in aerosol between 175 and 225 nm d_{dry}, κ values calculated from DASH-SP data were combined with representative size-resolved PTOF composition data from the AMS (Fig. 3). Assuming linearly additive water uptake of each species and no interaction between aerosol constituents and representative density of 1.77 g cm^{-3} for inorganics and 1.35 g cm^{-3} for organics, it is possible to estimate the k for organics. If the overall hygroscopicity parameter, κ is given by:

$$\kappa = \sum_{i=1}^{n} \kappa_i \chi_i \qquad (3)$$

where n is the number of aerosol constituents, i, each comprising volume fraction χ and having hygroscopicity represented by κ_i, then the organic hygroscopicity parameter, κ_{org} can be estimated by:

$$\kappa_{org} = \frac{\kappa - \sum_{i=1}^{n_{inorg}} \kappa_i \chi_i}{\chi_{org}} \qquad (4)$$

where n_{inorg} is the number of inorganic constituents, i, with hygroscopicity parameter κ_i and volume fraction χ, and χ_{org} is the volume fraction of organics in the aerosol. rBC is ignored in

Eq. 4 because its volume fraction is insignificant compared with inorganic and organic species. Assuming that ammonium is associated with nitrate and sulfate according to molar ratios (i.e. 33% as ammonium nitrate and 67% as ammonium sulfate), and assuming κ_i for ammonium nitrate, ammonium sulfate, and sea salt to be 0.67, 0.56, and 1.2, respectively, and with propagated uncertainty estimated to be ± 0.1, Eq. 4 gives κ_{org} of 0.1 ± 0.1 and 0.0 ± 0.1 for aerosol sampled in the western Basin and outflows, respectively. Eq. 4 indicates that in the eastern Basin organics suppress water uptake below what would be expected based on the assumption of additive water uptake – a result that falls outside the range of uncertainties.

Because the sheath flow is free of $NH_{3(g)}$ (Section 2.6), and the DASH operates at a temperature 8°C higher than the Twin Otter inlet, the extent to which ammonium nitrate is expected to evaporate from the particles in the form of ammonia (NH_3) and nitric acid (HNO_3) is an issue that must be addressed. Here we calculate an estimate of the volatilization of ammonium nitrate (AN) in the DASH-SP by combining predictions from the thermodynamic model AIOMFAC (Aerosol Inorganic-Organic Mixtures Functional groups Activity Coefficients) [*Zuend et al.*, 2008; 2011] and the kinetic model KM-GAP (kinetic multi-layer model of gas-particle interactions in aerosols and clouds) [*Shiraiwa et al.*, 2012]. AN volatilization is modeled as a series of two distinct stages in the DASH-SP (Figure 8): 1. A drying and sizing stage, where the partial pressure of ammonia vapor (p_{NH3}) is initially equal to zero, the partial pressure of nitric acid vapor (p_{HNO3}) is equal to ambient, RH = 10%, and 2. A humidification stage, where p_{NH3} and p_{HNO3} are modeled as in stage 1, but RH is increased to either 74 or 92%. The residence times of particles in stage 1 and 2 are 3 and 4 s, respectively. The temperature in both stages is assumed to be 28 ºC, or 8 ºC higher than the characteristic aircraft inlet temperature.

Based on AMS observations from CalNex, the particles are assumed to be 30% NH_4NO_3, 20% $(NH_4)_2SO_4$, and 50% organics in terms of dry mass fractions, with organics residing in a separate phase at all RH [*Song et al.*, 2012b]. Vapor-liquid equilibrium of ammonium nitrate is described by the relationship $K(T) = (a^{(m)}{}_{NH4+} \times a^{(m)}{}_{NO3-}) / (p_{NH3} \times p_{HNO3})$, with the temperature-dependent equilibrium constant *K(T)* taken from *Seinfeld and Pandis* [2006]. The $a^{(m)}$ are molality-based activities calculated using AIOMFAC for the aqueous salt solutions at given RH. Using D_{HNO3} = 0.120 cm^2 s^{-1} [*Durham and Stockburger*, 1986] and D_{NH3} = 0.306 cm^2 s^{-1} [*Wu et al.*, 2003] for the diffusivities in air at 28 ºC, the vapor pressure of ammonia over the salt solutions is estimated to be 6.9×10^{-4} Pa at 10 % RH, 2.9×10^{-4} Pa at 74 % RH, and 1.3×10^{-4} Pa at 92 % RH. The mass loss of NH_4NO_3 from the particles is assumed to be stoichiometrically related to the net evaporation of ammonia. The estimated equilibrium values are used as input parameters for the mass transfer simulations with KM-GAP. The surface accommodation coefficients of NH_3 and HNO_3 are assumed to be unity. The particle aqueous phase is treated as a liquid with a bulk diffusivity of 10^{-6} cm^2 s^{-1}. Based on AMS results, the initial particle mass concentration and diameter are set to be 5 μg m^{-3} of air and 300 nm, respectively.

Figure 8 shows the results of the KM-GAP simulation. The red lines indicate the particle phase mass of NH_4NO_3 normalized by the initial mass. About 8 % by mass of NH_4NO_3 is estimated to evaporate in the first stage (drying and DMA size selection) at 10% RH. Evaporation of NH_4NO_3 is diminished during stage 2 (humidification and optical sizing) because the equilibrium vapor pressure of NH_3 is inversely proportional to RH. At the outflow of stage 2, the loss of NH_4NO_3 is ~12 % for 74 % RH and ~10 % for 92 % RH, respectively. This

thermodynamic modeling of the DASH-SP does not explicitly account for potential interactions with nafion and metal tubing in the instrument, which may potentially lead to additional nitrate loss in the instrument. However, it is expected that these losses would be less significant than those associated with removal of ammonia by filtering and temperature increases in the DASH-SP.

Considering this loss of NH_4NO_3 in the DASH-SP, κ_{org} was re-calculated according to Eq. 4, giving values of 0.2 ± 0.1 and 0.1 ± 0.1 in the western Basin and outflows, respectively. Accounting for NH_4NO_3 loss, this analysis indicates that organics suppress water uptake in the eastern Basin, and this result is outside the range of uncertainty. The same result is obtained whether regional averages for GF-derived κ are based on all 17 flights or limited to the 5 flights for which PTOF AMS data are available.

Typical values for κ_{org} range from 0 to 0.1, depending on oxidation state [*Dusek et al.*, 2010; *Wex et al.*, 2010]. *Duplissy et al.* [2011] found a simple relationship between κ_{org} and the fraction of organic signal accounted for by m/z 44 in the AMS spectrum (f_{44}) in Mexico City, resulting in enhanced κ_{org} in oxidized organics with high f_{44}. Such a trend is not observed in CalNex data, with κ_{org} appearing to be independent of organic oxidation state.

While κ_{org} for the western Basin and outflows are within the range of expected values for urban OA, organics appear to inhibit water uptake into particles in the eastern Basin. Lower-than-expected hygroscopicity may arise from a number of factors, including potential unidentified instrument artifacts. One possible explanation for apparent inhibition of water uptake in the eastern Basin involves non-ideal interactions between organic and inorganic species in the

aerosol phase [*Saxena et al.*, 1995, *Clegg et al.*, 2001, *Zuend et al*., 2008] that have been associated with separation of amorphous organic-rich and aqueous electrolyte phases in particles [*Pankow*, 2003; *Erdakos and Pankow*, 2004; *Chang and Pankow*, 2006; *Marcolli and Krieger*, 2006]. Such liquid-liquid phase separations (LLPS) are, in fact, expected to be common in tropospheric aerosol at RH < 85%, with less pronounced impact as RH approaches saturation [*Zuend et al.*, 2010; *Smith et al.*, 2011; *Bertram et al.*, 2011; *Song et al.*, 2012a, *You et al.,* 2012, *Bones et al.*, 2012], and may be expected to form in aerosol like that observed in the eastern Basin - thickly coated particles comprising dissolved ammonium nitrate and ammonium sulfate with an organic fraction with relatively low O:C ratio (< ~0.4) [*Song et al.*, 2012b]. If the organic-rich phase adopts semi-solid state [*Virtanen et al.,* 2010; *Koop et al.*, 2011, *Song et al.*, 2012b, *Zuend and Seinfeld*, 2012] the rate of diffusion of water and reactive gases by several orders of magnitude, effectively isolating the aqueous electrolyte core of particles from the surrounding gas phase and inhibiting establishment of thermodynamic equilibrium on the timescale of DASH-SP humidification (4 s) [*Zobrist et al.*, 2011; *Shiraiwa et al.*, 2011, *Tong et al.*, 2011]. It is possible that the observed suppression of water uptake by organics in the eastern Basin and outflows may be the result of LLPS and kinetic limitation of water vapor accommodation, resulting in more effective suppression of hygroscopicity than predicted by models based on assumptions of internally-mixed, single-phase aerosol in a liquid, low-viscosity state.

3.5 Supersaturated (CCN) Hygroscopicity

Like subsaturated hygroscopicity, CCN behavior of a population of particles of the same size is governed by chemical composition, with inorganics enhancing CCN activity and organics suppressing it. Parallel studies of sub- and super- saturated hygroscopicity have found the two

to be correlated [e.g. *Prenni et al.*, 2001], with more hygroscopic particles measured in the subsaturated regime corresponding to a higher degree of CCN activity in the supersaturated regime.

By integrating the DMA number distribution from large to small sizes (since Köhler theory predicts that larger particles activate before smaller ones) and comparing to the measured droplet concentration in the CCNC, one may obtain a value for the critical diameter (D_{crit}) - the diameter above which particles are expected to activate. The single-parameter κ representation of Köhler theory [*Petters and Kreidenweis*, 2007] relates D_{crit} to the hygroscopicity parameter κ. Once D_{crit} is determined, κ is calculated for particles corresponding to that diameter. According to Köhler theory, given an internally-mixed aerosol, higher SS will correspond to CCN activation of smaller particles. Thus, the κ values calculated at different SS give a measure of size-dependent hygroscopicity. And because hygroscopic activity is a function of particle composition, the supersaturation-resolved D_{crit} and κ measurements provide an indirect measure of size-resolved composition.

Figure 9 displays regional averages of CCN-derived κ versus D_{crit} for each SS measured by the SFCA instrument, averaged over the 16 flights during which it collected data (5-7, 10, 12, 14-15, 18-22, 24-25, 27-28 May 2010). Gray lines represent average DMA number distributions for each region. Enhanced CCN activity may result from three sources: (1) increasing SS, (2) increasing κ (representing increased solubility), or (3) changes in mixing state (because D_{crit} is calculated by integrating a DMA distribution from large to small sizes until the integrated number matches the concentration of activated particles, an external mixture with primarily insoluble material at small sizes will result in increased D_{crit}, and thereby smaller κ). In each

region, D_{crit} decreases with increased supersaturation. Because CCN activity is a function of SS, hygroscopicity, and mixing state, the extent to which D_{crit} decreases with increased SS indicates whether an aerosol is impacted by insoluble material or an external mixture. Within the Basin, D_{crit} decreases significantly as SS increases from 0.275 to 0.375%, and the most hygroscopic particles ($\kappa \sim 0.4$-0.6) correspond to 60-70 nm particles measured at $0.425\% < SS < 0.475\%$. Further increases in supersaturation do not result in significant decreases in D_{crit}, suggesting an externally-mixed aerosol with particles smaller than 60 nm comprising nonhygroscopic material. This conclusion is consistent with previous findings in Los Angeles and Beijing that small organics behave as nonactivating or only slightly hygroscopic in CCN activity [*Cubison et al.*, 2008; *Gunthe et al.*, 2011]. Indeed, overall κ calculated for particles < 60 nm at SS > 0.475% is low in the Basin (0.2-0.3). These results are consistent with the observation of a small mode in the aerosol comprised predominantly of organics condensed onto soot particles (Sections 3.2 and 3.3). Particles that activate at SS < 0.375% in the LA Basin are significantly larger (~ 100 nm), corresponding roughly to the DASH-SP size range. CCN-derived κ of these particles is 0.2-0.4, comparing favorably with GF-derived κ (0.3-0.4). Size-resolved AMS and ATOFMS data for 100-300 nm particles indicate that these particles comprise several distinct types, including pure soot and organic-coated soot at the smallest sizes.

In the Banning Pass and outflow regions, D_{crit} similarly decreases with increased SS from 0.275 to 0.375%. Further increases in SS from 0.375 to 0.625% do not correspond to significant decreases in D_{crit}, suggesting that the majority of particles in this size range (50-70 nm) are relatively non-hygroscopic. This observation is consistent with that from PToF AMS data that a fine mode exists, comprised almost entirely of organics and with ATOFMS

evidence of an external mixture dominated by biomass burning particles in the outflow regions. Further increases in SS (> 0.625%) in outflows correspond to significant decreases in D_{crit} (approaching 30 nm) and increases in κ (approaching 0.7), suggesting an external mixture with the smallest particles containing hygroscopic inorganic material.

Figures 10 and 11 display west-east trends in CCN-derived hygroscopicity for particles that activate at 0.325% and 0.725% SS (~ 70-120 and 30-60 nm D_{crit}, respectively), as well as regionally-averaged size-resolved composition and coating thickness. As noted in Section 3.4, the size range measured by the SP2 is 90-270 nm rBC cores. While this size range does not directly compare with the CCN diameters measured at 0.325 and 0.725% SS, the processes that result in condensation of secondary coatings on these rBC particles will also result in significant coatings on particles in the CCN size range. Thus, comparison of coating thickness on rBC particles in the SP2 size range with CCN particles of 30-120 nm can provide a valuable framework for understanding the types of transitions to which these fine particles are subject during downwind transport. At 0.325% SS, there is a clear trend of increasing hygroscopicity from west to east in the Basin, corresponding to an increase in coating thickness diameter and the fraction of nitrate and ammonium on particles. Further transport and evolution into outflows correspond to decreased prevalence of nitrate, enhanced coating thickness, and suppressed CCN-derived hygroscopicity. At 0.725% SS, particles similarly increase in hygroscopicity during downwind transport from the western to eastern Basin, corresponding to an increase in coating thickness and the fraction of nitrate in small particles. Volatilization of semivolatile species, leaving low volatility organics and sulfate, translate to relatively constant hygroscopicity in outflows. These supersaturated hygroscopicity results suggest that the nitrate and organic coatings added to particles during downwind transport and evolution serve to

enhance CCN activity, despite tending to suppress subsaturated hygroscopicity (Section 3.4). Overall, CCN-derived κ averaged 0.35 ± 0.12 in the Basin and 0.38 ± 0.11 in Outflows – values that are 15-25% higher than previous studies that have suggested urban aerosol hygroscopicity may be estimated by κ ~ 0.3 [*Shinozuka et al.*, 2009; *Chang et al.*, 2010; *Rose et al.*, 2010, *Wex et al.*, 2010].

Hygroscopicity of the organic fraction (κ_{org}) was estimated for CCN particles by employing Eq. 4 and the method described in Section 3.4 and utilizing size-resolved PTOF AMS data for particles between ~30-60 nm (0.725% SS) and ~70-120 nm (0.325% SS). Results indicate that κ_{org} is independent of region for CCN-derived hygroscopicity, remaining a constant 0.1 ± 0.1 throughout the western and eastern Basin and outflows. These values are comparable to subsaturated GF-derived κ_{org} except in the eastern Basin, where organics appear to suppress water uptake in the subsaturated regime but contribute somewhat to supersaturated hygroscopicity.

3.6 Influence of Biomass Burning from a Localized Brush Fire

On 13 May 2010, a brush fire was sparked at ~ 13:30 LT in Riverside County in the eastern Los Angeles Basin, burning 500 acres before being contained later that evening. Twin Otter takeoff time on 13 May was 11:06 and landing was at 14:51 PM. The Twin Otter sampled in biomass-burning-influenced air for nearly 90 min near the end of the flight. The Twin Otter sampled within both the Basin and outflow regions and was positioned to sample both the immediate vicinity of the brush fire and the downwind, aged biomass burning aerosol. On 13 May ATOFMS data indicate that the biomass burning particle type number was enhanced by ~ 500 and 1100% in the west and east Basin, respectively, and constitute ~ 41 and 60% of

particles in the west and east Basin, respectively, as compared with ~ 7 and 5% during non-biomass-burning-influenced flights. In outflow regions on 13 May biomass burning particles represented 58% of particles between 100 and 300 nm d_{va} (Figure 12 a, b). These enhancements in biomass burning particles are associated with significant suppression of subsaturated hygroscopicity, but an enhancement in CCN concentration, CCN activation ratio (AR), and CCN-derived hygroscopicity (Table 4). Biomass burning particles have been identified as important sources of CCN [*Hennigan et al.*, 2012]. *Petters et al.* [2009] determined that biomass burning particles tend to be CCN active at the point of emissions, but subsaturated κ of particles tend to be suppressed under the influence of biomass burning [*Petters et al*., 2009; *Rose et al.*, 2010, *Dusek et al*., 2011]. *Dusek et al.* [2011] found that biomass burning influence can result in surface-active organics and phase separation of species in aerosols. This leads to discrepancies between subsaturated and CCN-derived hygroscopicity (with subsaturated κ suppressed relative to CCN κ). Under the influence of biomass burning, CCN concentrations and activation ratios tend to be enhanced by the production of new CCN-active particles, while if surface-active organic species induce phase separation, hygroscopicity is suppressed at subsaturated RH.

3.7 Comparison of GF- and CCN- Derived Hygroscopicity

One would expect sub- and super- saturated hygroscopicity to be correlated, with higher subsaturated κ tending to correspond to lower critical diameters for cloud droplet activation. Aerosols in the Los Angeles Basin are compositionally complex, with significant evolution in bulk and size-resolved composition and mixing state between source-rich and downwind areas. This evolution in composition results in complex hygroscopic behavior and discrepancies between GF- and CCN- derived hygroscopicity.

In the western and Central LA Basin, sub- and supersaturated hygroscopicity measurements display relatively good agreement when hygroscopicity is calculated for similarly-sized particles (GF-derived κ 0.3-0.4 for $D_{p,dry}$ 175-225 nm, versus 0.2-0.4 for CCN measurements at 0.275-0.375% SS and corresponding to particles ~100 nm in diameter). In the nitrate-rich eastern Basin, sub- and supersaturated hygroscopicity measurements disagree. Disagreements between sub- and super-saturated estimates of the hygroscopicity parameter κ have been noted in a number of studies and have been attributed to factors such as differences in size-resolved composition and instrument operating conditions, adsorption of gases in sampling lines, as well as non-ideal effects of solutes on water activity and surface tension [*Good et al.,* 2010; *Irwin et al.,* 2010, 2011, *Sareen et al.*, 2012]. In CalNex there is some evidence of size-dependent differences in composition between particles in the CCN and DASH size ranges – despite their residing in the same mode of the DMA distribution (Fig. 3). Also, as discussed in Section 3.2, evolution in aerosol from the western to eastern Basin is associated with a transition of the organic-soot fraction from a small mode in the aerosol to a larger, unimodal fraction. *Pratt and Prather* [2009] observed similar evidence of internally-mixed aerosols in aged plumes in the eastern Los Angeles Basin, owing to condensation of secondary species onto primary particulates. CCN measurements of hygroscopicity may be biased low in the case where aerosol exists as an external mixture with the smallest particles composed primarily of insoluble organic material. The transition from externally- to internally-mixed aerosol from west to east in the Basin and elimination of this small insoluble mode by growth and condensation of secondary material would tend to enhance CCN activity, but the condensation of organics on a unimodal aerosol comprising the main hygroscopic mode would tend to result

in suppressed subsaturated hygroscopicity as measured by the DASH-SP, thus leading to a disagreement between the two measurements.

The discrepancy between subsaturated hygroscopicity and CCN activity in areas of the eastern Basin and the disagreement between sub- and super-saturated RH estimates of κ_{org} suggests that the delay of water uptake by organics is more pronounced at RH < 100%. As discussed in Section 3.4, LLPS and the presence of an amorphous organic layer is one possible explanation for the observed suppression of subsaturated hygroscopicity evidenced by estimates of κ_{org}. *Dusek et al.* [2011] found similar disagreement between subsaturated hygroscopicity and CCN activity under the influence of LLPS, but general agreement between the two when aerosols appeared to be comprised of a single liquid phase. While results here are not conclusive evidence of LLPS, it is possible that condensation of secondary organics onto particles during aging in the Los Angeles Basin results in separate organic coating layers that form a barrier to water vapor accommodation. However, this effect is primarily observed in subsaturated measurements of hygroscopicity with short humidification residence times, as opposed to supersaturated measurements of CCN activity.

Conclusions

Aerosols age as they are transported from source-rich sites in the western Los Angeles Basin to downwind receptor sites in the eastern Basin and desert outflow regions. Within the Basin, this aging is associated with increased rBC coating thickness and increased mass of ammonium, nitrate, and organics, owing to the production and condensation of secondary species. In the relatively source-rich western areas of the Basin, the aerosol distribution comprises a small mode of predominantly organic species mixed with soot and a larger accumulation mode

consisting primarily of inorganics coated on soot-organic cores. Condensation of secondary species results in a unimodal aerosol at downwind receptor sites in the eastern Basin and outflows. With increasing age in the Basin, aerosols become internally mixed, with secondary nitrate and organics detected on most particles. Transport into desert outflow regions is associated with dilution and volatilization of semivolatile species, and the resulting aerosol consists of predominantly low-volatility, oxidized, water-soluble organics and sulfate. It is not possible on the basis of the available measurements to infer a single number for the overall fraction of particles with soot cores in Los Angeles; results from the SP2 and ATOFMS indicate a range of 27-51%.

Transformations in aerosol composition during downwind transport and aging have different effects on hygroscopicity at subsaturated and supersaturated RH. Sub- and supersaturated hygroscopicity measurements tend to agree in the western Basin, but at subsaturated RH, κ is suppressed significantly in the eastern Basin and outflows as secondary nitrate and organics condense onto particles in the 175-250 nm size range. Calculations of κ_{org} suggest that organics inhibit water uptake in the eastern Basin and are nonhygroscopic in outflows. Subsaturated water uptake appears to be inhibited by organics in the eastern Basin, and one possible explanation for this behavior is the formation of separate, organic layers that inhibit water uptake on humidification timescales similar to those in the DASH-SP. Supersaturated hygroscopicity is highest for particles on the order of 60-70 nm in the Basin, with smaller particles (identified organics mixed with soot) appearing to be nonhygroscopic. CCN-derived hygroscopicity is enhanced when rBC coating thickness increases, and CCN-derived κ_{org} is spatially invariant at 0.1 ± 0.1, suggesting that the potential inhibition of water uptake by layers of secondary organics primarily affects subsaturated water uptake. Other sources of

discrepancy between sub- and supersaturated hygroscopicity measurements include size-dependent variation in composition within the small aerosol mode, as well as the apparent conversion of externally-mixed aerosol to one that is internally-mixed, which tends to enhance CCN activity but result in suppressed subsaturated water uptake of the main hygroscopic mode.

Finally, a small brush fire in the eastern Basin on 13 May 2010 quickly (on the order of 1-2 h) and significantly enhanced the concentration of the biomass burning particle type throughout much of the Los Angeles area. Enhancements in biomass burning aerosols resulted in significant suppression of water uptake at subsaturated RH, but enhanced CCN activity, consistent with previous findings that biomass burning particles are relatively nonhygroscopic but yet are CCN-active.

Acknowledgment:

This work was supported by NOAA grant NA09OAR4310128 and CARB agreement #09-333.

References

Aiken, A. C., P. F. Decarlo, J. H. Kroll, D. R. Worsnop, J. A. Huffman, K. S. Docherty, I. M. Ulbrich, C. Mohr, J. R. Kimmel, D. Sueper, Y. Sun, Q. Zhang, A. Trimborn, M. Northway, P. J. Ziemann, M. R. Canagaratna, T. B. Onasch, M. R. Alfarra, A. S. H. Prevot, J. Dommen, J. Duplissy, A. Metzger, U. Baltensperger, and J. L. Jimenez (2008), O/C and OM/OC ratios of primary, secondary, and ambient organic aerosols with high-resolution time-of-flight aerosol mass spectrometry, *Environ. Sci. Technol., 42*, 4478–4485.

Alfarra, M. R., H. Coe, J. D. Allan, K. N. Bower, H. Boudries, M. R. Canagaratna, J. L. Jimenez, J. T. Jayne, A. A. Garforth, S. M. Li, and D. R. Worsnop (2004), Characterization of urban and rural organic particulate in the lower Fraser valley using two Aerodyne aerosol mass spectrometers, *Atmos. Environ., 38,* 5745– 5758.

Andreae, M.O. and A. Gelencsér (2006), Black carbon or brown carbon? The nature of light-absorbing carbonaceous aerosols, *Atmos. Chem. Phys., 6*, 3131-3148.

Andreae, M. O. and D. Rosenfeld (2008), Aerosol-cloud-precipitation interactions. Part 1. The nature and sources of cloud-active aerosols, *Earth Sci. Rev., 89*, 13–41.

Anttila, T. (2010), Sensitivity of cloud droplet formation to the numerical treatment of the particle mixing state, *J. Geophys. Res. Atmos., 115*, DOI 10.1029/2010JD013995.

AQMD: Historic ozone air quality trends (2012), available at: http://www.aqmd.gov/smog/o3trend.html.

Ault, A. P., C. J. Gaston, Y. Wang, G. Dominguez, M. H. Thiemens, and K. A. Prather (2010), Characterization of the Single Particle Mixing State of Individual Ship Plume Events Measured at the Port of Los Angeles, *Environ. Sci. Technol.*, *44*, 1954-1961.

Bahadur, R., L. M. Russel, and K. Prather (2010), Composition and Morphology of Individual Combustion, Biomass Burning, and Secondary Organic Particle Types Obtained Using Urban and Coastal ATOFMS and STXM-NEXAFS Measurements, *Aerosol Sci. Technol., 44*, 551-562.

Baumgardner, D., G. L. Kok, and G. Raga (2004), Warming of the Arctic lower stratosphere by light absorbing particles, *Geophys. Res. Lett.*, *31*, L06117, doi:10.1029/2003GL018883

Baumgardner, D., et al. (2012), Soot reference materials for instrument calibration and intercomparisons: a workshop summary with recommendations. *Atmos. Meas. Tech.*, *5*, 1869-1887, doi:10.5194/amt-5-1869-2012.

Bertram, A. K., S.T. Martin, S. J. Hanna, M. L. Smith, A. Bodsworth, Q. Chen, M. Kuwata, A. Liu, Y. You, and S. R. Zorn (2011), Predicting the relative humidities of liquid-liquid phase separation, efflorescence, and deliquescence of mixed particles of ammonium sulfate, organic material, and water using the organic-to-sulfate mass ratio of the particle and the oxygen-to-carbon elemental ratio of the organic component, *Atmos. Chem. Phys. Discuss., 11*, 17759–17788, doi:10.5194/acpd-11-17759- 2011.

Bhave, P. V., D. P. Fergenson, K. A. Prather, and G. R. Cass (2001), Source apportionment of fine particulate matter by clustering single-particle data: tests of receptor model accuracy, *Environ. Sci. Technol., 35*, 2060-2072.

Blumenthal, D., W. White, and T. Smith (1978), Anatomy of a Los Angeles smog episode: Pollutant transport in the daytime sea breeze regime, *Atmos. Environ., 12*, 893–907.

Bones, D.L., J.P. Reid, D.M. Lienhard, and U.K. Krieger (2012), Comparing the mechanism of water condensation and evaporation in glassy aerosol, *Proc. Natl. Acad. Sci. USA 109*, doi:10.1073/pnas.1200691109.

Cahill, J. F., K. Suski, J. H. Seinfeld, R. A. Zaveri, and K. A. Prather (2012), The mixing state of carbonaceous aerosol particles in Northern and Southern California measured during CARES and CalNex 2010, *Atmos. Chem. Phys. Disc., 12,* 18419-18457.

Chang, E. I. and J. F. Pankow (2006), Prediction of activity coefficients in liquid aerosol particles containing organic compounds, dissolved inorganic salts, and water – Part 2: Consideration of phase separation effects by an X-UNIFAC model, *Atmos. Environ., 40*, 6422–6436, doi:10.1016/j.atmosenv.2006.04.031.

Chang, R. Y., J. G. Slowik, N. C. Shantz, A. Vlasenko, J. Liggio, S. J. Sjostedt, W. R. Leaitch, and J. P. D. Abbatt (2010), The hygro- scopicity parameter (κ) of ambient organic aerosol at a field site subject to biogenic and anthropogenic influences: relationship to degree of aerosol oxidation, *Atmos. Chem. Phys., 10*, 5047– 5064, doi:10.5194/acp-10-5047-2010.

Chow, J., E. Fujita, J. Watson, Z. Lu, D. Lawson, and L. Asbaugh (1994), Evaluation of filter-based aerosol measurements during the 1987 Southern California Air-Quality Study, *Env. Monit. Assess., 30*, 49-80,doi:10.1007/BF00546199.

Clegg, S. L., J. H. Seinfeld, and P. Brimblecombe (2001), Thermodynamic modelling of aqueous aerosols containing electrolytes and dissolved organic compounds, *J. Aerosol. Sci., 32*, 713–738, 2001.

Cocker, D. R., N. E. Whitlock, R. C. Flagan, and J. H. Seinfeld (2001), Hygroscopic properties of Pasadena, California aerosol, *Aerosol Sci. Technol., 35*, 637–647.

Croes, B. and E. Fujita (2003), Overview of the 1997 Southern California Ozone Study (SCOS97-NARSTO), *Atmos. Environ., 37*, S3-S26, doi:10.1016/S1352-2310(03)003790.

de Gouw, J. A., A. M. Middlebrook, C. Warneke, P. D. Goldan, W. C. Kuster, J. M. Roberts, F.C. Fehsenfeld, D. R. Worsnop, M. R. Canagaratna, A. A. P. Pszenny, W. C. Keene, M. Marchewka, S. B. Bertman, and T. S. Bates (2005), Budget of organic carbon in a polluted atmosphere, Results from the New England Air Quality Study in 2002, *J. Geophys. Res.-Atmos., 110*, D16305, doi:16310.11029/12004JD00562.

Denkenberger, K. A., R. C. Moffet, J. C. Holecek, T. P. Rebotier, and K. A. Prather (2007), Real-time, single-particle measurements of oligomers in aged ambient aerosol particles, *Environ. Sci. Technol., 41*, 5439–5446.

Docherty, K. S., E. A. Stone, I. M. Ulbrich, P. F. DeCarlo, D. C. Snyder, J. J. Schauer, R. E. Peltier, R. J. Weber, S. M. Murphy, J. H. Seinfeld, B. D. Grover, D. J. Eatough, and J. L. Jiimenez (2008), Apportionment of Primary and Secondary Organic Aerosols in Southern California during the 2005 Study of Organic Aerosols in Riverside (SOAR-1), *Environ. Sci. Technol., 42*, 7655–7662.

Docherty, K.S., A.C. Aiken, J. A. Huffman, I. M. Ulbrich, P.F. DeCarlo, D. Sueper, D. R. Worsnop, D. C. Snyder, R. E. Peltier, R. J. Weber, B. D. Grover, D. J. Eatough, B. J. Williams,

A. H. Goldstein, P. J. Ziemann, and J. L. Jimenez (2011), The 2005 Study of Organic Aerosols at Riverside (SOAR-1): instrumental intercomparisons and fine particle composition, *Atmos. Chem. Phys., 11*, 12387-12420, doi:10.5194/acp-11-12387-2011.

Drewnick, F., et al. (2005), A new time-of-flight aerosol mass spectrometer (TOF-AMS)–Instrument description and first field deployment, *Aerosol Sci. Technol.*, *39* (7), 637–658, doi:10.1080/02786820500182040.

Duong, H. T., A. Sorooshian, J. S. Craven, S. P. Hersey, A. R. Metcalf, X. Zhang, R. J. Weber, H. Jonsson, R. C.Flagan, and J. H. Seinfeld (2011), Water- soluble organic aerosol in the Los Angeles Basin and outflow regions: Airborne and ground measurements during the 2010 CalNex field campaign, *J. Geophys. Res.*, 116, D00V04, doi:10.1029/2011JD016674.

Duplissy, J., P. F. DeCarlo, J. Dommen, M. R. Alfarra, A. Metzger, I. Barmpadimos, A. S. H. Prevot, E. Weingartner, T. Tritscher, M. Gysel, A. C. Aiken, J. L. Jimenez, M. R. Canagaratna, D. R. Worsnop, D. R. Collins, J. Tomlinson, and U. Baltensperger (2011), Relating hygroscopicity and composition of organic aerosol particulate matter, *Atmos. Chem. Phys.,* 11, 1155–1165, doi:10.5194/acp-11-1155-2011, 2011.

Durham, J. L., and L. Stockburger (1986), Nitric acid-air diffusion coefficient: Experimental determination, *Atmospheric Environment, 20*(3), 559-563.

Dusek, U., G. P. Frank, A. Massling, K. Zeromskiene, Y. Iinuma, O. Schmid. G. Helas, T. Henning, A. Wiedensohler, and M. O. Andreae (2011), Water uptake by biomass burning

aerosol at sub- and supersaturated conditions: closure studies and implications for the role of organics, *Atmos. Chem. Phys., 11*, 9519-9532.

Eatough, D. J., B. D. Grover, W. R. Woolwine, N. L. Eatough, R. Long, and R. Farber (2008), Source apportionment of 1 h semicontinuous data during the 2005 Study of Organic Aerosols in Riverside (SOAR) using positive matrix factorization, *Atmos. Environ., 42*, 2706–2719.

Eldering, A., G. Cass, and K. Moon (1994), An air monitoring network using con-tinuous particle-size distribution monitors - connecting pollutant properties to visibility via mie scattering calculations, *Atmos. Environ., 28*, 2733-2749,doi:10.1016/13522310(94)90445-6.

Erdakos, G. B. and J. F. Pankow (2004), Gas/particle partitioning of neutral and ionizing compounds to single- and multi-phase aerosol particles. 2. Phase separation in liquid particulate matter containing both polar and low-polarity organic compounds, *Atmos. Environ., 38*, 1005–1013, doi:10.1016/j.atmosenv.2003.10.038.

Fergenson, D.P., et al. (2003), Reagentless Detection and Classification of Individual Bioaerosol Particles in Seconds, *Anal. Chem., 76*, 373-378.

Gard, E.E., et al. (1998), Direct observation of heterogeneous chemistry in the atmosphere, *Science, 279*, 1184-1187.

Gaston, C.J., et al. (2011), Unique ocean-derived particles serve as a proxy for changes in ocean chemistry, *J. Geophys. Res.-Atmos., 116*, doi:10.1029/2010JD015289.

Good, N., D.O. Topping, J.D. Allan, M. Flynn, E. Fuentes, M. Irwin, P.I. Williams, H. Coe, and G. McFiggans (2010), Consistency between parameterizations of aerosol hygroscopicity and CCN activity during the RHaMBLe discovery cruise, *Atmos. Chem. Phys., 10,* 3189-3203.

Gunthe, S.S., D. Rose, H. Su, R. M. Garland, P. Achtert, A. Nowak, A. Wiedensohler, M. Kuwata, N. Takegawa, Y. Kondo, M. Hu, M. Shao, T. Zhu, M. O. Andreae, and U. Pöschl (2011), Cloud condensation nuclei (CCN) from fresh and aged air pollution in the megacity region of Beijing, *Atmos. Chem. Phys., 11*, 11023-11039.

Heck, R.M. (1999), Catalytic abatement of nitrogen oxides – stationary applications, *Catalysis Today, 53*, 519-523.

Hennigan, C.J., D. M. Westervelt, I. Riipinen, G. L. Engelgart, T. Lee, J. L. Collett, S. N. Pandis, P. J. Adams, A L. Robinson (2012), New particle formation and growth in biomass burning plumes: An important source of cloud condensation nuclei, *Geophys. Res. Lett., 39*, doi: 10.1029/2012GL050930.

Hersey, S. P., A. Sorooshian, S. M. Murphy, R. C. Flagan, and J. H. Seinfeld (2009), Aerosol hygroscopicity in the marine atmosphere: a closure study using high-time-resolution, multiple-RH DASH-SP and size-resolved C-ToF-AMS data, *Atmos. Chem. Phys.,* 9, 2543–2554.

Hersey, S. P., J. S. Craven, K. A. Schilling, A. R. Metcalf, A. Sorooshian, M. N. Chan, R. C. Flagan, and J. H. Seinfeld (2011), The Pasadena aerosol characterization observatory (PACO):

Chemical and physical analysis of the western Los Angeles Basin aerosol, *Atmos. Chem. Phys., 11*, 7417–7443, doi:10.5194/acp-11-7417-2011.

Huffman, J. A., K. S. Docherty, A. C. Aiken, M. J. Cubison, I. M. Ulbrich, P. F. DeCarlo, D. Sueper, J. T. Jayne, D. R. Worsnop, P. J. Ziemann, and J. L. Jimenez, J. L. (2009), Chemically-resolved aerosol volatility measurements from two megacity field studies, *Atmos. Chem. Phys., 9*, 7161–7182, doi:10.5194/acp-9-7161- 2009.

Hughes, L., J. Allen, L. Salmon, P. Mayo, R. Johnson, and G. Cass (2002), Evolution of nitrogen species air pollutants along trajectories crossing the Los Angeles area, *Environ. Sci. Technol., 36*, 3928-3935, doi:10.1021/es0110630.

Irwin, M., Good, N., J. Crosier, T.W. Choularton, and G. McFiggans (2010), Reconciliation of measurements of hygroscopic growth and critical supersaturation of aerosol particles in central Germany, *Atmos. Chem. Phys., 10, 11737-11752*.

Irwin, M., N. Robinson, J.D. Allan, H. Coe, and G. McFiggans (2011), Size-resolved aerosol water uptake and cloud condensation nuclei measurements as measured above a Southeast Asian rainforest during OP3, *Atmos. Chem. Phys, 11,* 11157-11174.

Jayne, J. T., D. C. Leard, X. Zhang, P. Davidovits, K. A. Smith, C. E. Kolb, and D. R. Worsnop (2000), Development of an aerosol mass spectrometer for size and composition analysis of submicron particles, *Aerosol Sci. Technol.*, *33*, 49–70, doi:10.1080/027868200410840.

Koop, T., J. Bookhold, M. Shiraiwa, and U. Pöschl, Glass transition and phase state of organic compounds: dependency on molecular properties and implications for secondary organic aerosols in the atmosphere, *Phys. Chem. Chem. Phys., 13*, 19238-19255.

Kreidenweis, S.M., M. D. Petters, and P. J. DeMott (2008), Single parameter estimates of aerosol water content, *Environ. Res. Lett., 3*, doi: 10.1088/1748-9326/3/3/035002.

Laborde, M., P. Mertes, P. Zieger, J. Dommen, U. Baltensperger, and M. Gysel (2012), Sensitivity of the Single Particle Soot Photometer to different black carbon types, *Atmos. Meas. Tech.*, *5*, 1031-1043, doi:10.5194/amt-5-1031-2012.

Lance, S., J. Medina, J. N. Smith, and A. Nenes (2006), Mapping the operation of the DMT continuous-flow CCN counter, *Aerosol Sci. Technol., 40*, 242–254, doi:10.1080/02786820500543290.

Liu, P., et al. (1995), Generating Particle Beams of Controlled Dimensions and Divergence .2. Experimental Evaluation of Particle Motion in Aerodynamic Lenses and Nozzle Expansions, *Aerosol Sci. Technol., 22*, 314-324.

Liu, D., K. Prather, and S. Hering (2000), Variations in the size and chemical composition of nitrate-containing particles in Riverside, CA, *Aerosol. Sci. Tech., 33*, 71-86,doi:10.1080/027868200410859.

Lu, R. and R. Turco (1995), Air pollutant transport in a coastal environment–II. Three-dimensional simulations over Los Angeles Basin, *Atmos. Environ., 29*, 1499–1518.

Mallet, M., J. C. Roger, S. Despiau, J. P. Putaud, and O. Dubovik (2004), A study of the mixing state of black carbon in urban zone, *J. Geophys. Res. Atm., 109*, DOI 10.1029/2003JD003940.

Marcolli, C. and U. K. Krieger (2006), Phase changes during hygroscopic cycles of mixed organic/inorganic model systems of tropospheric aerosols, *J. Phys. Chem. A, 110*, 1881–1893, doi: 10.1021/jp0556759.

Massling, A., M. Stock, and A. Wiedensohler (2005), Diurnal, weekly, and seasonal variation of hygro- scopic properties of submicrometer urban aerosol particles, *Atmos. Environ., 39*, 3911–3922.

Massling, A., M. Stock, B. Wehner, Z. J. Wu, M. Hu, E. Bruggemann, T. Gnauk, H. Herrmann, and A. Wiedensohler (2009), Size segregated water uptake of the urban submicrometer aerosol in Beijing, *Atmos. Environ., 43*, 1578–1589.

Massoli, P., A. T. Lambe, A.T. Ahern, L. R. Williams, M. Ehn, J. Mikkilä, M. R. Canagaratna, W. H. Brune, T. B. Onasch, J. T. Jayne, T. Petäjä, M. Kulmala, A. Laaksonen, C. E. Kolb, P. Davidovits, and D. R. Worsnop, D. R., Relationship between aerosol oxidation level and hygroscopic properties of laboratory generated secondary organic aerosol (SOA) particles, *Geophys. Res. Lett.,* 37**,** L24801, doi:10.1029/2010GL045258, 2010.

Meier, J., B. Wehner, A. Massling, W. Birmili, A. Nowak, T. Gnauk, E. Bruggemann, H. Herrmann, H. Min, and A. Wiedensohler (2009), Hygroscopic growth of urban aerosol particles in Beijing (China) during wintertime: a comparison of three experimental methods, *Atmos. Chem. Phys., 9*, 6865–6880.

Metcalf, A. R., J. S. Craven, J. J. Ensberg, J. Brioude, W. Angevine, A. Sorooshian, H. T. Duong, H. H. Jonsson, R. C. Flagan, and J. H. Seinfeld (2012), Black carbon aerosol over the Los Angeles Basin during CalNex, *J. Geophys. Res. Atmos., 117*, doi:10.1029/2011JD017255.

Moffet, R. C. and K. A. Prather (2009), In-situ measurements of the mixing state and optical properties of soot with implications for radiative forcing estimates, *Proc. Nat. Acad. Sci. USA, 106*, 11872-11877.

Moore, K. F., Z. Ning, L. Ntziachristos, J. J. Schauer, C. Sioutas (2007), Daily Variation in the properties of urban ultrafine aerosol - Part 1: Physical characterization and volatility, *Atmos. Environ., 41*, 8633-8646.

Moore, R. H., and A. Nenes (2009), Scanning flow CCN analysis—A method for fast measurements of CCN spectra, *Aerosol Sci. Technol., 43*, 1192–1207, doi:10.1080/02786820903289780.

Moore, R. H., R. Bahreini, C. A. Brock, K. D. Froyd, J. Cozic, J. S. Holloway, A. M. Middlebrook, D. M. Murphy, and A. Nenes (2011), Hygroscopicity and composition of

Alaskan Arctic CCN during April 2008, *Atmos. Chem. Phys., 11*, 11,807–11,825, doi:10.5194/acp-11- 11807-2011.

Moteki, N., and Y. Kondo (2007), Effects of mixing state on black carbon measurements by laser-induced incandescence, *Aerosol Sci. Technol.*, *41* (4), 398–417, doi:10.1080/02786820701199728.

Murphy, S.M., H. Agrawal, A. Sorooshian, L. T. Padro, H. Gates, S. P. Hersey, W. A. Welch, H. Jung, J. W. Miller, D. R. Cocker, A. Nenes, H. H. Jonsson, R. C. Flagan, and J. H. Seinfeld, (2009), Comprehensive simultaneous shipboard and airborne characterization of exhaust from a modern container ship at sea, *Environ. Sci. Tech., 43*, 13, 4626-4640.

Neuman, J. A., et al. (2003), Variability in ammonium nitrate formation and nitric acid depletion with altitude and location over California, *J. Geophys. Res.*, *108*(D17), 4557, doi:10.1029/2003JD003616.

Noble, C. A. and K.A. Prather (1996), Real-time measurement of correlated size and composition profiles of individual atmospheric aerosol particles, *Environ. Sci. Technol., 30*, 2667-2680.

Quinn, P., T. Bates, T. Baynard, A. Clarke, T. Onasch, W. Wang, M. Rood, E. Andrews, J. Allan, C. Carrico, et al. (2005), Impact of particulate organic matter on the relative humidity dependence of light scattering: A simplified parameterization, *Geophys. Res. Lett., 32*, 22.

Pastor, S., J. Allen, L. Hughes, P. Bhave, G. Cass, and K. A. Prather, (2003), Ambient single particle analysis in Riverside, California by aerosol time-of-flight mass spectrometry during the SCOS97-NARSTO, *Atmos. Environ., 37*, S239-S258,doi:10.1016/S13522310(03)00393-5.

Petters, M. D. and S. M. Kreidenweis (2007), A single parameter representation of hygroscopic growth and cloud condensation nucleus activity, *Atmos. Chem. Phys., 7*, 1961–1971.

Petters, M. D., C. M. Carrico, S. M. Kreidenweis, A. J. Prenni, P. J. DeMott, J. L. Collett, and H. Moosmuller (2009), Cloud condensation nucleation activity of biomass burning aerosol, *J. Geophys. Res. Atmos. 114*, doi: 10.1029/2009JD012353.

Pratt, K. A. and K. A. Prather (2009), Real-Time, Single-Particle Volatility, Size, and Chemical Composition Measurements of Aged Urban Aerosols, *Environ. Sci. Technol., 43*, 8276-8282.

Pratt, K.A., et al. (2009a), Development and Characterization of an Aircraft Aerosol Time-of-Flight Mass Spectrometer. *Anal. Chem., 81*, 1792-1800.

Pratt, K.A., et al. (2009b), In situ detection of biological particles in cloud ice-crystals, *Nature Geosci, 2*, 398-401.

Pratt, K.A., et al. (2011), Flight-based chemical characterization of biomass burning aerosols within two prescribed burn smoke plumes, *Atmos. Chem. Phys., 11*, 12549-12565.

Prenni, A., P. DeMott, S. Kreidenweis, D. Sherman, L. Russell, and Y. Ming (2001), The effects of low molecular weight dicarboxylic acids on cloud formation, *J. Phys. Chem. A., 105*, 11240–11248.

Russell, S.C. (2009), Microorganism characterization by single particle mass spectrometry, *Mass Spec. Rev., 28*, 376-387.

Qin, X., et al. (2012), Seasonal Comparisons of Single-particle Chemical mixing state in Riverside, CA, *Atmos. Environ., Accepted*.

Roberts, G. C., and A. Nenes (2005), A continuous-flow streamwise thermal-gradient CCN chamber for atmospheric measurements, *Aerosol Sci. Technol., 39*, 206–221, doi:10.1080/027868290913988.

Rose, D., A. Nowak, P. Achtert, A. Wiedensohler, M. Hu, M. Shao, Y. Zhang, M. Andreae, and U. Pöschl (2010), Cloud condensation nuclei in polluted air and biomass burning smoke near the mega- city Guangzhou, China- Part 1: Size-resolved measurements and implications for the modeling of aerosol particle hygroscopicity and CCN activity, *Atmos. Chem. Phys., 10*, 3365–3383.

Sareen, N., A. N. Schwier, T. L. Lathem, A. Nenes, and V. F. McNeill (2012), Surfactants from the gas phase may promote cloud droplet formation, *Proc. Natl. Acad. Sci. USA*, doi:10.1073/pnas.1204838110.

Saxena, P., L. M. Hildemann, P. H. McMurry, and J. H. Seinfeld (1995), Organics alter hygroscopic behavior of atmospheric particles, *J. Geophys. Res. Atmos., 100*, 18755–18770.

Schwarz, J. P., et al. (2006), Single-particle measurements of midlatitude black carbon and light-scattering aerosols from the boundary layer to the lower stratosphere, *J. Geophys. Res.*, *111*, D16207, doi:10.1029/2006JD007076.

Seinfeld, J. H., and S. N. Pandis (2006), *Atmospheric Chemistry and Physics: From Air Pollution to Climate Change*, John Wiley & Sons, pp. 469.

Shields, L.G., D.T. Suess, and K.A. Prather (2007), Determination of single particle mass spectral signatures from heavy-duty diesel vehicle emissions for PM2.5 source apportionment, *Atmos. Environ., 41*, 3841-3852.

Shinozuka, Y., A. Clarke, P. DeCarlo, J. L. Jimenez, E. Dunlea, G. Roberts, J. Tomlinson, D. Collins, S. Howell, V. Kapustin, et al. (2009), Aerosol optical properties relevant to regional remote sensing of CCN activity and links to their organic mass fraction: airborne observations over Central Mexico and the US West Coast during MILAGRO/INTEX-B, *Atmos. Chem. Phys., 9*, 6727–6742.

Shiraiwa, M., M. Ammann, T. Koop, and U. Pöschl (2011), Gas uptake and chemical aging of semisolid organic aerosol particles, *P. Natl. Acad. Sci. USA 108* (27), 11003–11008.

Shiraiwa, M., C. Pfrang, T. Koop, and U. Pöschl (2012), Kinetic multi-layer model of gas-particle interactions in aerosols and clouds (KM-GAP): linking condensation, evaporation and chemical reactions of organics, oxidants and water, *Atmos. Chem. Phys.*, *12*(5), 2777-2794.

Silva, P.J., et al. (1999), Size and chemical characterization of individual particles resulting from biomass burning of local Southern California species, *Environ. Sci. Technol.*, *33*, 3068-3076.

Slowik, J. G., et al. (2007), An inter-comparison of instruments measuring black carbon content of soot particles, *Aerosol Sci. Technol.*, *41*(3), 295–314, doi:10.1080/02786820701197078.

Smith, M. L., M. Kuwata, and S. T. Martin (2011), Secondary Organic Material Produced by the Dark Ozonolysis of α- Pinene Minimally Affects the Deliquescence and Efflorescence of Ammonium Sulfate, *Aerosol Sci. Technol., 45*, 244–261, doi:10.1080/02786826.2010.532178, http://dx.doi.org/10.1080/ 02786826.2010.532178.

Sodeman, D.A., S.M. Toner, and K.A. Prather (2005), Determination of single particle mass spectral signatures from light-duty vehicle emissions, *Environ. Sci. Technol., 39*, 4569-4580.

Song, X.H., et al. (1999), Classification of single particles analyzed by ATOFMS using an artificial neural network, ART-2A, *Anal. Chem., 71*, 860-865.

Song, M., C. Marcolli, U. K. Krieger, A. Zuend, and T. Peter (2012a), Liquid-liquid phase separation and morphology of internally-mixed dicarboxylic acids/ammonium sulfate/water particles, *Atmos. Chem. Phys., 12*, 2691-2712, doi:10.5194/acp-12-2691-2012.

Song, M., C. Marcolli, U. K. Krieger, A. Zuend, and T. Peter (2012b), Liquid-liquid phase separation in aerosol particles: Dependence on O:C, organic functionalities, and compositional complexity. *Geophys. Res. Lett. 39*, L19801, doi:10.1029/2012gl052807.

Sorooshian, A., F. J. Brechtel, Y. L. Ma, R. J. Weber, A. Corless, R. C. Flagan, and J. H. Seinfeld (2006), Modeling and characterization of a particle-into-liquid sampler (PILS), *Aerosol Sci. Tech.*, *40*, 396-409.

Sorooshian, A., S. P. Hersey, F. J. Brechtel, A. Corless, R. C. Flagan, and J. H. Seinfeld (2008), Rapid size-resolved aerosol hygroscopic growth measurements: differential aerosol sizing and hygroscopicity spectrometer probe (DASH-SP), *Aerosol Sci. Tech., 42*, 445–464.

Spencer, M.T. and K. A. Prather (2006), Using ATOFMS to determine OC/EC mass fractions in particles, *Aerosol Sci. Tech., 40,* 585-594.

Stephens, M., N. Turner, and J. Sandberg (2003), Particle identification by laser-induced incandescence in a solid-state laser cavity, *Appl. Opt.*, *42* (19), 3726–3736, doi:10.1364/AO.42.003726.

Suda, S. R., M. D. Petters, A. Matsunaga, R. C. Sullivan, P. J. Ziemann, and S. M. Kreidenweis (2012), Hygroscopicity frequency distributions of secondary organic aerosols, *J. Geophys. Res. Atm., 117*, doi: 10.1029/2011JD016823.

Sullivan, A. P., R. E. Peltier, C. A. Brock, J. A. de Gouw, J. S. Holloway, C. Warneke, A. G. Wollny, and R. J. Weber (2006), Airborne measurements of carbonaceous aerosol soluble in water over northeastern United States: Method development and an investigation into water-soluble organic carbon sources, *J. Geophys. Res., 111*, D23S46, doi:10.1029/2006JD007072.

Sun, J., Q. Zhang, M. R. Canagaratna, Y. Zhang, N. L. Ng, Y. Sun, J. T. Jayne, X. Zhang, X. Zhang, and D. R. Worsnop (2009), Highly Time- and Size-Resolved Characterization of Submicron Aerosol Particles in Beijing Using an Aerodyne Aerosol Mass Spectrometer, *Atmos. Environ., 44*, 131–140.

Swietlicki, E., H. Hansson, K. Hameri, B. Svenningsson, A. Massling, G. McFiggans, P. McMurry, T. Petaja, P. Tunved, M. Gysel, et al. (2008), Hygroscopic properties of submicrometer atmospheric aerosol particles measured with H-TDMA instruments in various environments: A review, *Tellus B, 60*, 432–469.

Tiitta, P., P. Miettinen, P. Vaattovaara, J. Joutsensaari, T. Pet, A. Virtanen, T. Raatikainen, P. Aalto, H. Portin, S. Romakkaniemi, et al. (2010), Roadside aerosol study using hygroscopic, organic and volatility TDMAs: Characterization and mixing state, *Atmos. Environ., 44*, 976–986.

Toner, S.M., D.A. Sodeman, and K.A. Prather (2006), Single particle characterization of ultrafine and accumulation mode particles from heavy duty diesel vehicles using aerosol time-of-flight mass spectrometry, *Environ. Sci. Technol., 40*, 3912-3921.

Tong, H.J., J. P. Reid, D. L. Bones, B. P. Luo, U. K. Krieger (2011), Measurements of the timescales for the mass transfer of water in glassy aerosol at low relative humidity and ambient temperature, *Atmos. Chem. Phys., 11*, 4739-4754, doi:10.5194/acp-11-4739-2011.

Turpin, B. and J. Huntzicker (1991), Secondary formation of organic aerosol in the Los Angeles Basin - A descriptive analysis of organic and elemental carbon concentrations, *Atmos. Environ., 25*, 207-215,doi:10.1016/0960-1686(91)90291-E.

Ulbrich, I. M., M. R. Canagaratna, Q. Zhang, D. R. Worsnop, and J. L. Jimenez (2009), Interpretation of organic components from Positive Matrix Factorization of aerosol mass spectrometric data, *Atmos. Chem. Phys., 9*, 2891–2918.

Virtanen, A., J. Joutsensaari, T. Koop, J. Kannosto, P.J. Yli, L. Pirilä, J.M. Mäkelä, J.K. Holopainen, U. Pöschl, M. Kulmala, D.R. Worsnop, and A. Laaksonen (2010), An amorphous solid state of biogenic secondary organic aerosol particles, *Nature*, 467, 824-827.

Wang, J., M. J. Cubison, A. C. Aiken, J. L. Jimenez, and D. R. Collins (2010), The importance of aerosol mixing state and size-resolved composition on CCN concentration and the variation of the importance with atmospheric aging of aerosols, *Atmos. Chem. Phys., 10*, 7267-7288.

Watson, J. G., J. C. Chow, Z. Q. Lu, E. M. Fujita, D. H. Lowenthal, D. R. Lawson, and L. L. Ashbaugh (1994), Chemical Mass-Balance Source Apportionment of Pm(10) during the Southern California Air-Quality Study, *Aerosol Sci. Technol., 21*, 1–36.

Wex, H., G. McFiggans, S. Henning, F. Stratmann (2010), Influence of the external mixing state of atmospheric aerosol on derived CCN number concentrations, *Geophys. Res. Lett., 37*, doi: 10.1029/2010GL043337.

Wonaschütz, A., S. P. Hersey, A. Sorooshian, J. Craven, A. R. Metcalf, R. C. Flagan, and J. H. Seinfeld (2011), Impact of a large wildfire on water-soluble organic aerosol in a major urban setting: The 2009 station fire in Los Angeles County, *Atmos. Chem. Phys.,11*, 8257–8270, doi:10.5194/acp-11-8257-2011.

Wu, J., D. L. Nofziger, J. Warren, and J. Hattey (2003), Estimating Ammonia Volatilization from Swine-Effluent Droplets in Sprinkle Irrigation, *Soil Sci. Soc. Am. J., 67*(5), 1352-1360.

You, Y., L, Renbaum-Wolff, M. Carreras-Sospedra, S.J. Hanna, N. Hiranuma, S. Kamal, M.L. Smith, X.L. Zhang, R.J. Weber, J.E. Shilling, D. Dabdub, S.T. Martin, and A.K. Bertram, A. K. (2012), Images reveal that atmospheric particles can undergo liquid-liquid phase separations, *Proc. Natl. Acad. Sci. USA, 109*, 13188-13193, 10.1073/pnas.1206414109, 2012.

Zhang, Q., M. R. Canagaratna, J. T. Jayne, D. R. Worsnop, and J. L. Jimenez (2005), Time- and size-resolved chemical composition of submicron particles in Pittsburgh: Implications for aerosol sources and processes, *J. Geophys. Res, 110*, doi:10.1029/2004JD004649.

Zhang, Q., D. R. Worsnop, M. R. Canagaratna, and J. L. Jimenez (2005), Hydrocarbon-like and oxygenated organic aerosols in Pittsburgh: insights into sources and processes of organic aerosols, *Atmos. Chem. Phys., 5*, 3289–3311.

Zhang, Q., et al. (2007), Ubiquity and dominance of oxygenated species in organic aerosols in anthropogenically-influenced Northern Hemisphere midlatitudes, *Geophys. Res. Lett., 34*, L13801, doi:13810.11029/12007GL029979.

Zobrist, B., V. Soonsin, B. P. Luo, U. K. Krieger, C. Marcolli, T. Peter, and T. Koop (2011), Ultra-slow water diffusion in aqueous sucrose glasses, *Phys. Chem. Chem. Phys, 13*, 3514-3526.

Zuend, A. and J. H. Seinfeld (2012), Modeling the gas-particle partitioning of secondary organic aerosol: the importance of liquid-liquid phase separation. *Atmos. Chem. Phys. 12*, 3857–3882, doi:10.5194/acp-12-3857-2012.

Zuend, A., C. Marcolli, B. P. Luo, and T. Peter (2008), A thermodynamic model of mixed organic-inorganic aerosols to predict activity coefficients, *Atmos. Chem. Phys., 8*, 4559–4593, doi:10.5194/acp- 8-4559-2008.

Zuend, A., C. Marcolli, A. M. Booth, D. M. Lienhard, V. Soonsin, U. K. Krieger, D. O. Topping, G. McFiggans, T. Peter, and J. H. Seinfeld (2011), New and extended parameterization of the thermodynamic model AIOMFAC: calculation of activity coefficients for organic-inorganic mixtures containing carboxyl, hydroxyl, carbonyl, ether, ester, alkenyl, alkyl, and aromatic functional groups, *Atmos. Chem. Phys., 11*, 9155-9206, doi:10.5194/acp-11-9155-2011.

Table 1: Regional averaged AMS mass concentrations and O:C ratio for 9 flights (18-22, 24-25, 27-28 May 2010).

	Total Aerosol Concentration [μg m^{-3}]	Organic Concentration [μg m^{-3}]	Sulfate Concentration [μg m^{-3}]	Nitrate Concentration [μg m^{-3}]	Ammonium Concentration [μg m^{-3}]	Chloride Concentration [μg m^{-3}]	Organic O:C Ratio
Long Beach	7.81 (± 3.02)	2.54 (± 0.74)	1.33 (± 0.64)	2.21 (± 1.36)	1.49 (± 0.69)	0.07 (± 0.06)	0.41 (± 0.10)
West Basin	7.71 (± 3.85)	2.54 (± 0.99)	0.92 (± 0.45)	2.55 (± 2.04)	1.42 (± 0.80)	0.10 (± 0.07)	0.38 (± 0.08)
Pasadena	6.96 (± 4.33)	2.38 (± 0.99)	0.68 (± 0.29)	2.41 (± 2.47)	1.24 (± 0.93)	0.08 (± 0.07)	0.39 (± 0.07)
Central Basin	7.44 (± 4.12)	2.48 (± 0.99)	0.63 (± 0.33)	2.80 (± 2.39)	1.35 (± 0.86)	0.09 (± 0.08)	0.41 (± 0.08)
East Basin	8.24 (± 4.63)	2.60 (± 0.99)	0.43 (± 0.17)	3.56 (± 2.77)	1.48 (± 0.95)	0.09 (± 0.08)	0.43 (± 0.05)
Banning Pass	4.90 (± 3.85)	1.80 (± 0.75)	0.23 (± 0.07)	1.87 (± 2.09)	0.84 (± 0.92)	0.06 (± 0.07)	0.47 (± 0.09)
Banning Outflow	1.44 (± 0.36)	0.91 (± 0.24)	0.20 (± 0.08)	0.12 (± 0.09)	0.14 (± 0.11)	0.00 (± 0.02)	0.49 (± 0.09)
Imperial Valley	0.89 (± 0.16)	0.54 (± 0.13)	0.18 (± 0.08)	0.05 (± 0.02)	0.09 (± 0.02)	0.00 (± 0.02)	0.55 (± 0.10)

Table 2: Total mass and relative mass fractions of non-refractory submicron species measured by Aerosol Mass Spectrometry in megacity studies and onboard the Twin Otter during CalNex.

Megacity Study	Total mass conc. [μg m^{-3}]	OMF	SMF	NMF	AMF	CMF
Beijing, PRC [Su et al., 2009]	71	0.35	0.25	0.22	0.16	0.01
Mexico City, Mexico [Aiken et al., 2008; DeCarlo et al., 2009]	31	0.61	0.15	0.13	0.09	0.02
Pittsburgh, PA, USA [Zhang et al., 2005]	15	0.3	0.47	0.06	0.16	0.01
Pasadena, CA (West LA Basin) [Hersey et al., 2011]	8-20	0.42-0.55	0.16-0.30	0.14-0.15	0.13-0.14	0-0.01
Riverside, CA (East LA Basin) [Docherty et al., 2008; Huffman et al., 2009]	19	0.68	0.13	0.12	0.06	0.01
W. Basin [this study]	7.7	0.35	0.13	0.3	0.18	0.01
E. Basin [this study]	8.2	0.35	0.06	0.38	0.17	0.01
Outflows [this study]	1.16	0.61	0.16	0.07	0.1	0

Table 3: ATOFMS particle types, typical sources, and commonly co-emitted species.

Type	Source	Co-emitted
Soot-OC	Combustion Sources, Fossil fuels	Soot, Semi-volatile organics, SO_2, NO_x, CO, CO_2
Soot	Combustion Sources, Fossil fuels	Soot-OC, Semi-volatile organics, SO_2, NO_x, CO, CO_2
Biomass Burning, Biomass Burning-Soot, Biomass Burning-Soot-OC	Biomass Burning	Soot, Semivolatile organics, CH_4, CO, CO_2, N_2O, NH_3, NO_x, SO_2
Biological	Ocean, Soil, Spores	Dust, Sea Salt
Ship Emissions	Ship/bunker Fuel	Soot, Semivolatile organics, SO_2, NO_x, CO, CO_2
Sea Spray	Ocean	Biological
Highly Processed-Sulfate	Secondary Aerosol	Soot, Semivolatile organics, SO_2, NO_x, CO, CO_2, NH_3
Highly Processed-Nitrate	Secondary Aerosol	Soot, Semivolatile organics, SO_2, NO_x, CO, CO_2, NH_3
Aged Organic Carbon	Secondary Aerosol	Soot, Semivolatile organics, SO_2, NO_x, CO, CO_2
Amines, Dust, Fe, unclassified spectra	Organic Nitrogen, Arid Regions	Semivolatile organics, CH_4, CO_2, H_2S, NH_3, NO_x, Biological, Metals

Table 4: Influence of Biomass Burning on subsaturated hygroscopicity, CCN concentration, and activation ratio (AR) and CCN-derived κ at 0.325% SS.

		Non-BB-influenced	13 May 2010	% change
W. Basin	**GF κ**	0.39	0.20	-0.49%
	CCN cm^{-3}	1569	1714	+ 9%
	0.325% SS AR	0.14	0.24	+ 67%
	0.325% SS κ	0.26	0.35	+ 35%
E. Basin	**GF κ**	0.32	0.18	-0.44%
	CCN cm^{-3}	2116	3064	+ 45%
	0.325% SS AR	0.29	0.47	+ 65%
	0.325% SS κ	0.33	0.78	+ 138%
Outflows	**GF κ**	0.24	0.13	-0.46%
	CCN cm^{-3}	274	1189	+ 335%
	0.325% SS AR	0.07	0.29	+ 310%
	0.325% SS κ	0.23	0.40	+ 78%

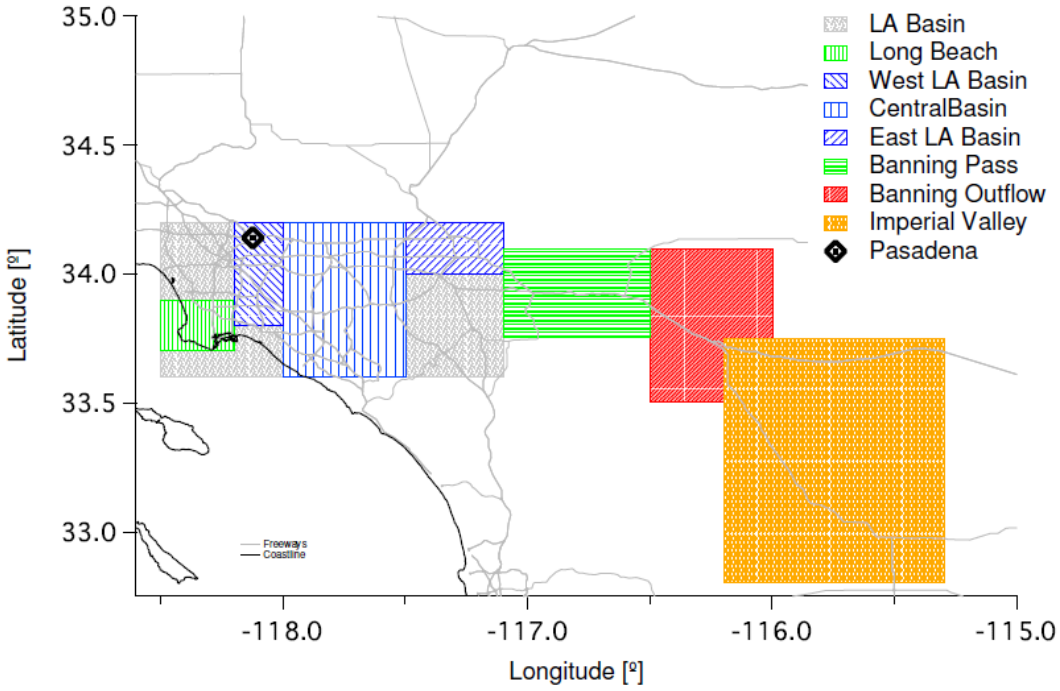

Figure 1: Definitions used in calculating regional averages of CalNex data. Only data below the boundary layer are included in analysis.

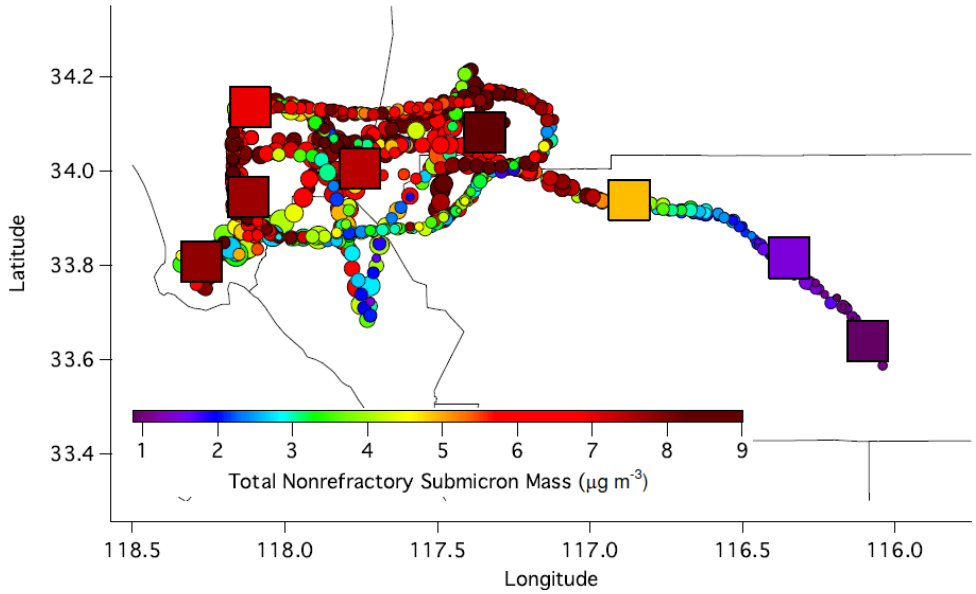

Figure 2: Bulk aerosol composition - regional trends from the AMS (average over 9 flights; 18-22, 24-25, 27-28 May 2010), SP2 (average over 15 flights; 6-7, 10, 12, 14-15, 18-22, 24-25, 27-28 May 2010), and PILS-TOC (average over 13 flights; 6-7, 10, 12, 14-15, 18-21, 25, 27-28 May 2010). Circles represent 1 min resolution data, while squares represent mission averages for the entirety of each instrument's operating period (Sec. 2.2-2.8) for each region. For clarity, color scales for mass fraction are different for each species.

(a) Total Mass

(b) Organic Mass Fraction

(c) Sulfate Mass Fraction

(d) Nitrate Mass Fraction

(e) Ammonium Mass Fraction

(f) Chloride Mass Fraction

(g) Refractive Black Carbon Mass Fraction

(h) WSOC Mass Fraction

(i) Organic O:C Ratio

(j) Refractive Black Carbon Coating Thickness

(k) Surface Temperature

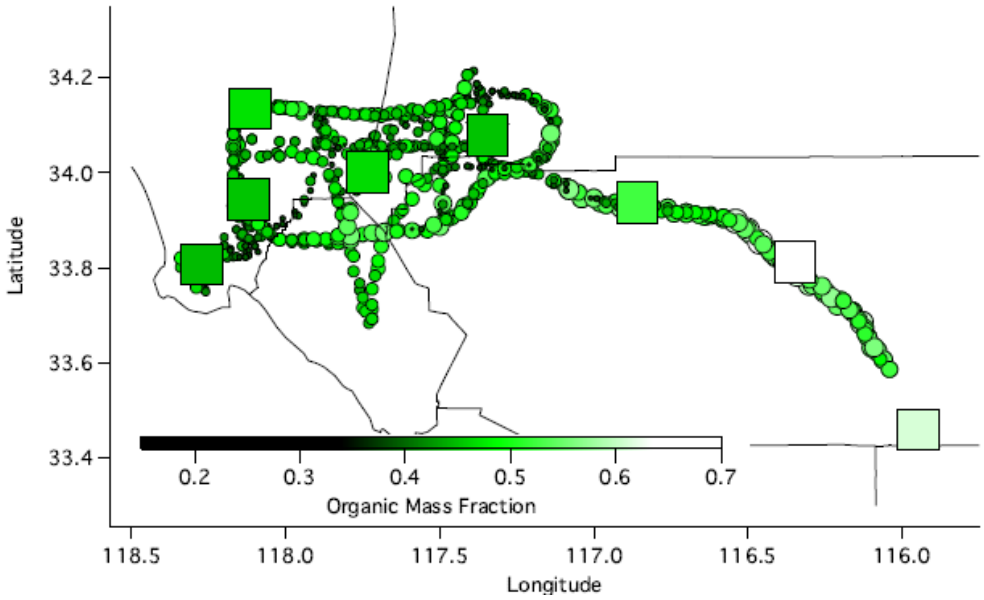

Figure 2. (continued)

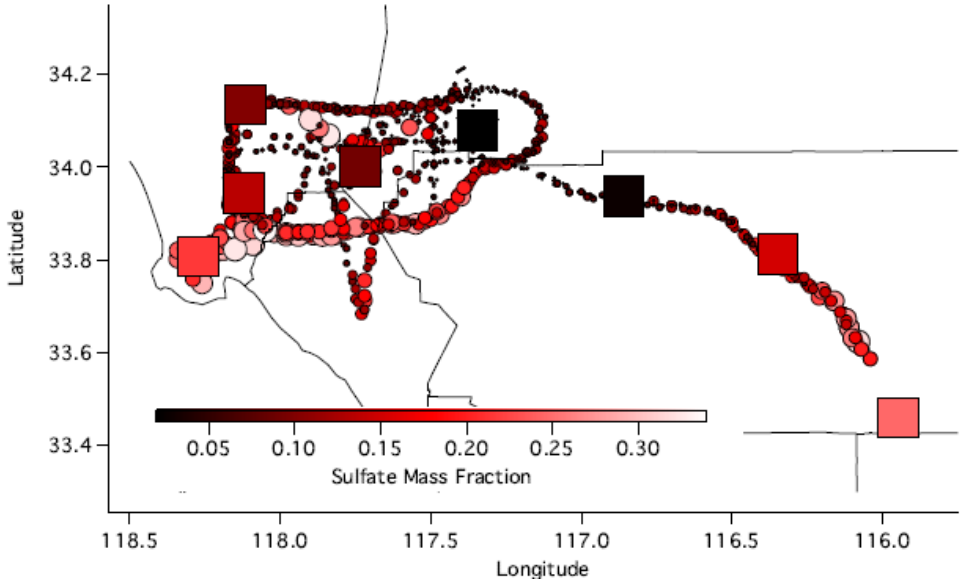

Figure 2. (continued)

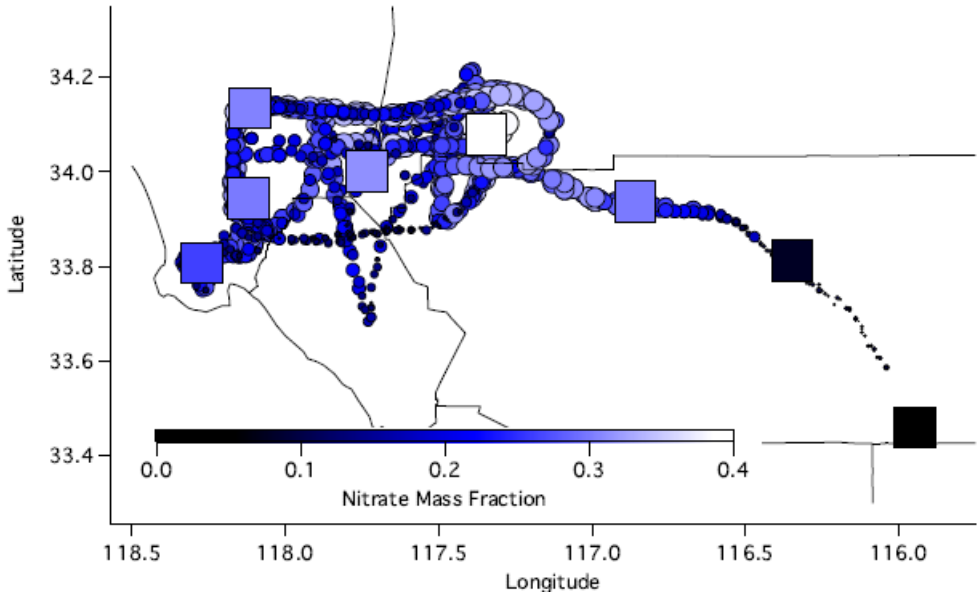

Figure 2. (continued)

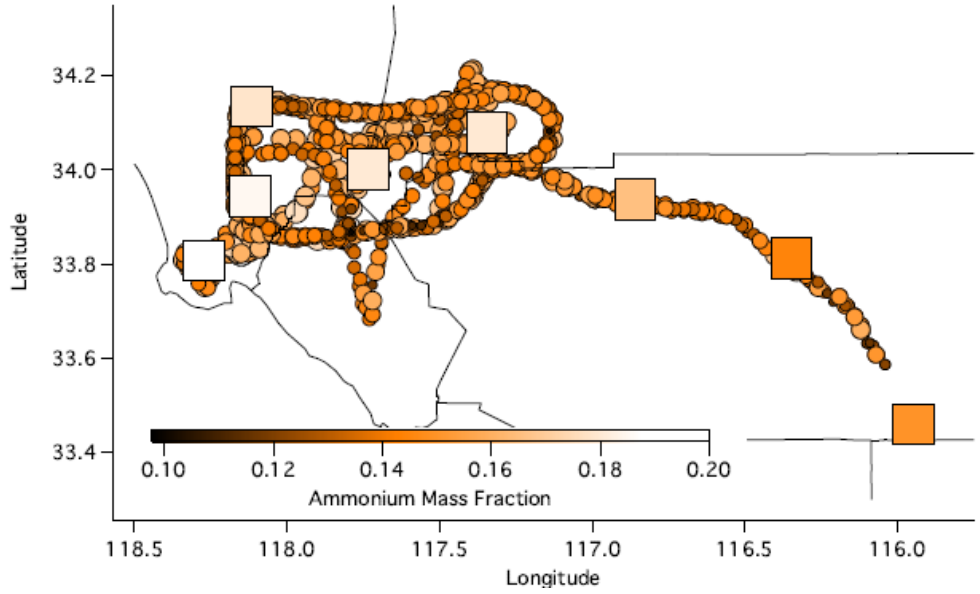

Figure 2. (continued)

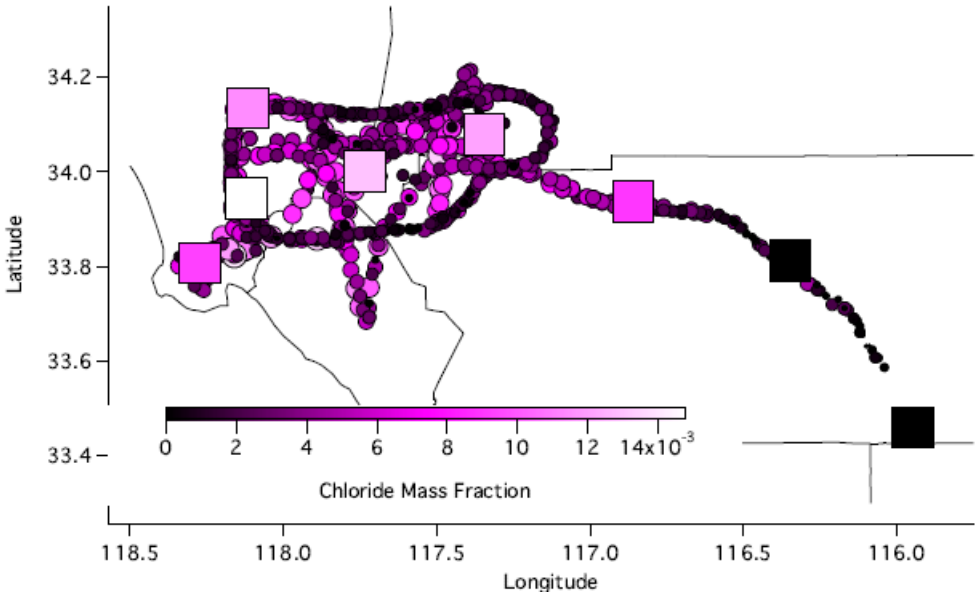

Figure 2. (continued)

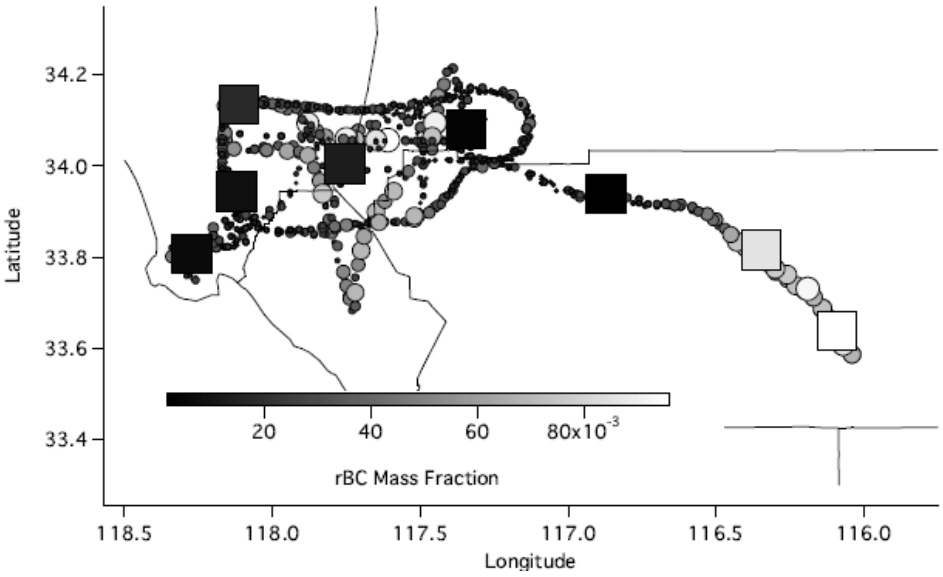

Figure 2. (continued)

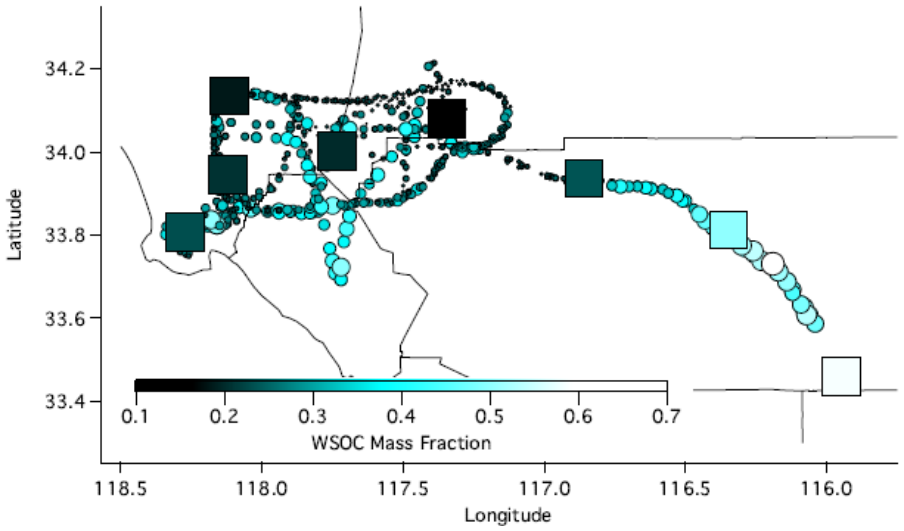

Figure 2. (continued)

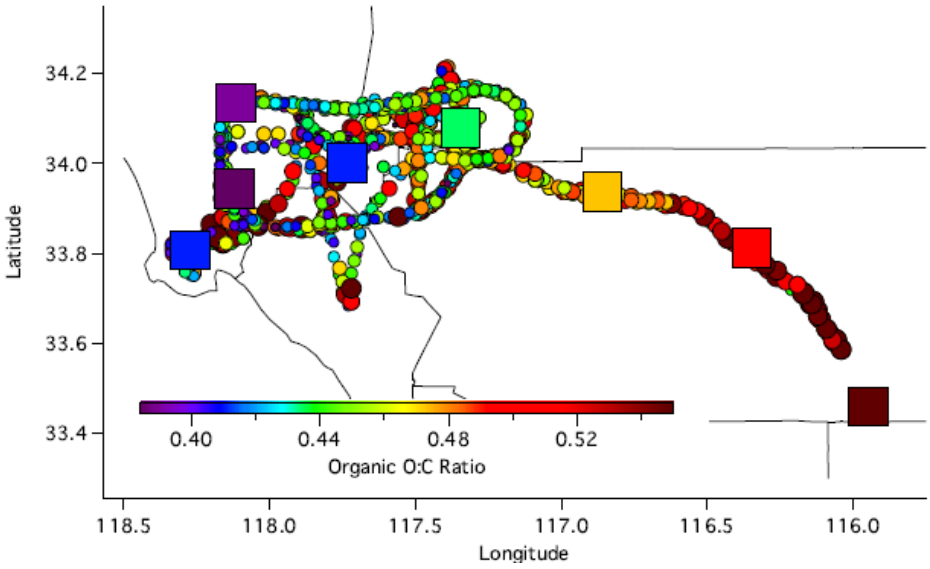

Figure 2. (continued)

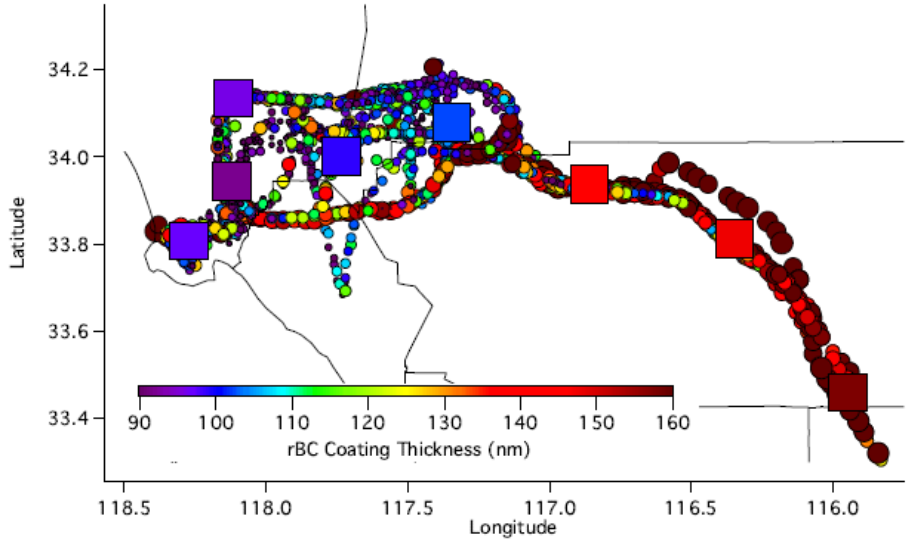

Figure 2. (continued)

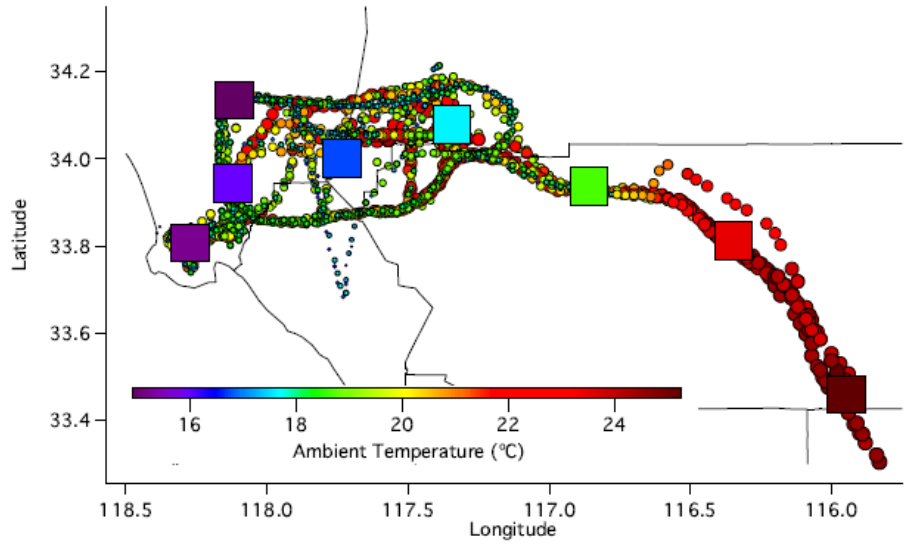

Figure 2. (continued)

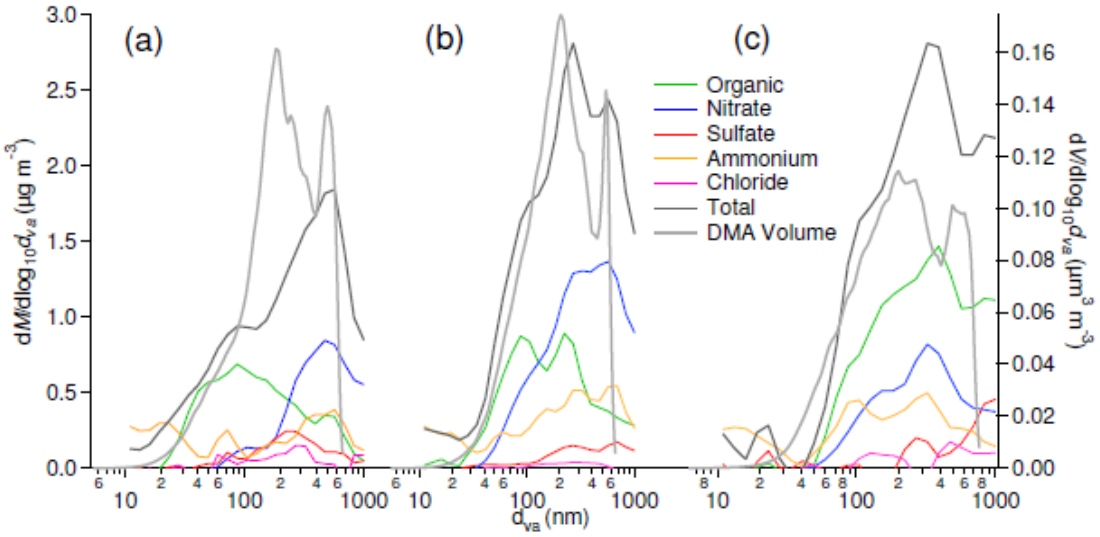

Figure 3: Size-resolved AMS composition and DMA volume, comparing the (a) western Basin, (b) eastern Basin, and (c) outflows, averaged over 5 flights (21, 24-25, 27-28 May 2010). Diameter is vacuum aerodynamic (d_{va}).

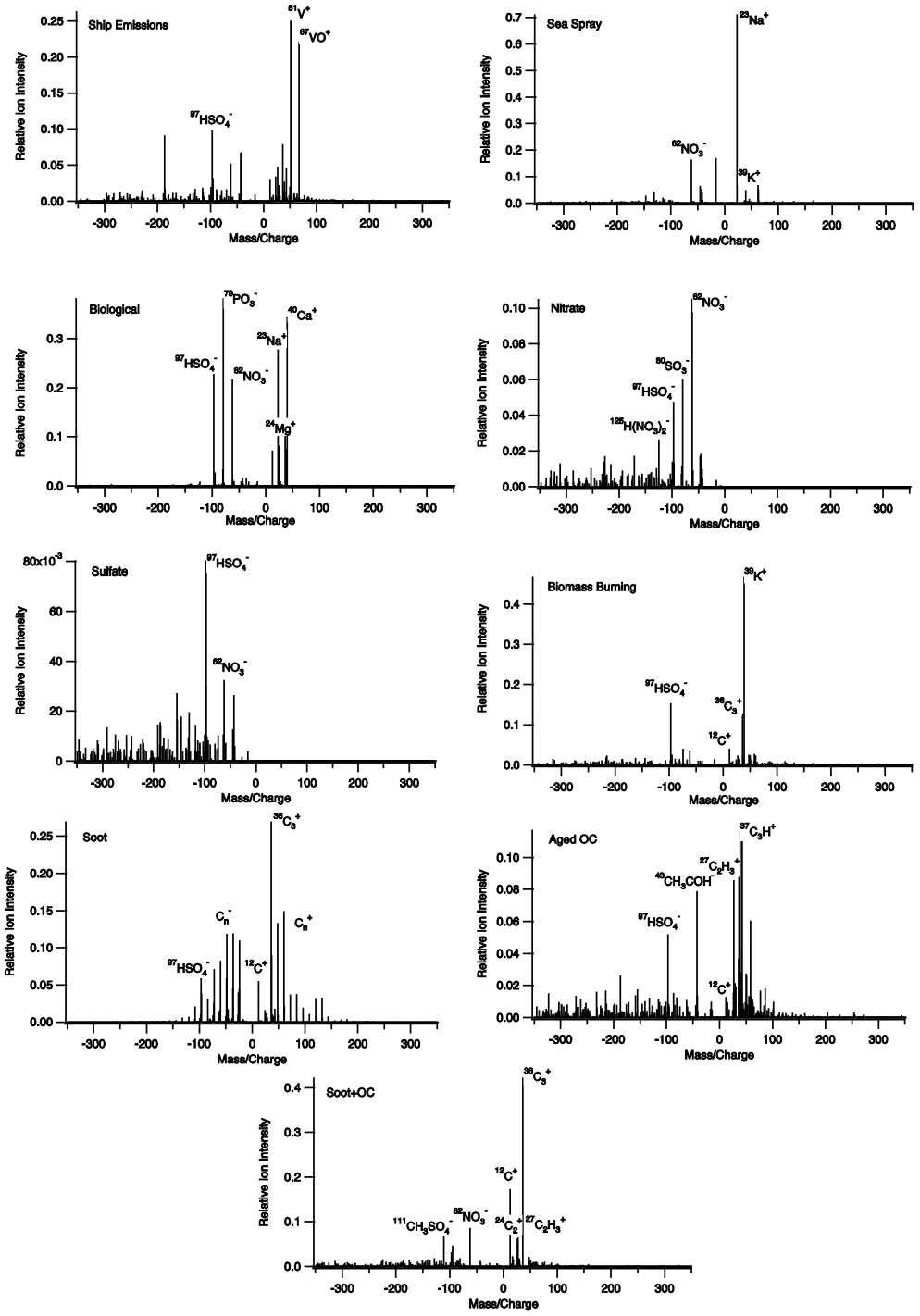

Figure 4: Representative positive and negative mass spectrum for each particle type identified by the ATOFMS.

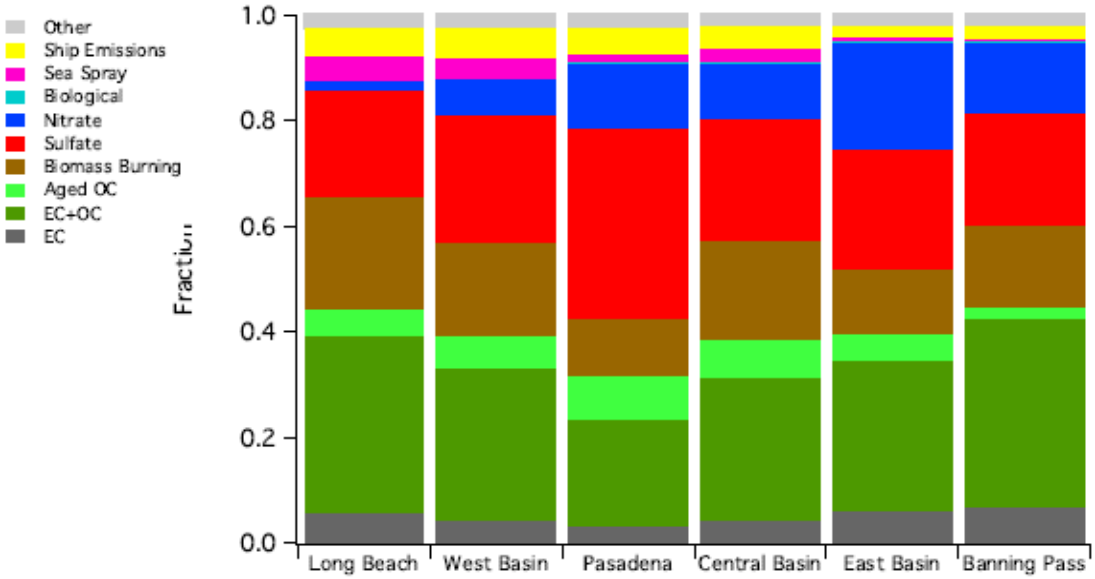

Figure 5: Region-averaged ATOFMS results for 100-300 nm particles, averaged over 5 flights (6-7, 10, 14-15 May 2010). Numbers in parentheses are the total number of particles sampled in each region.

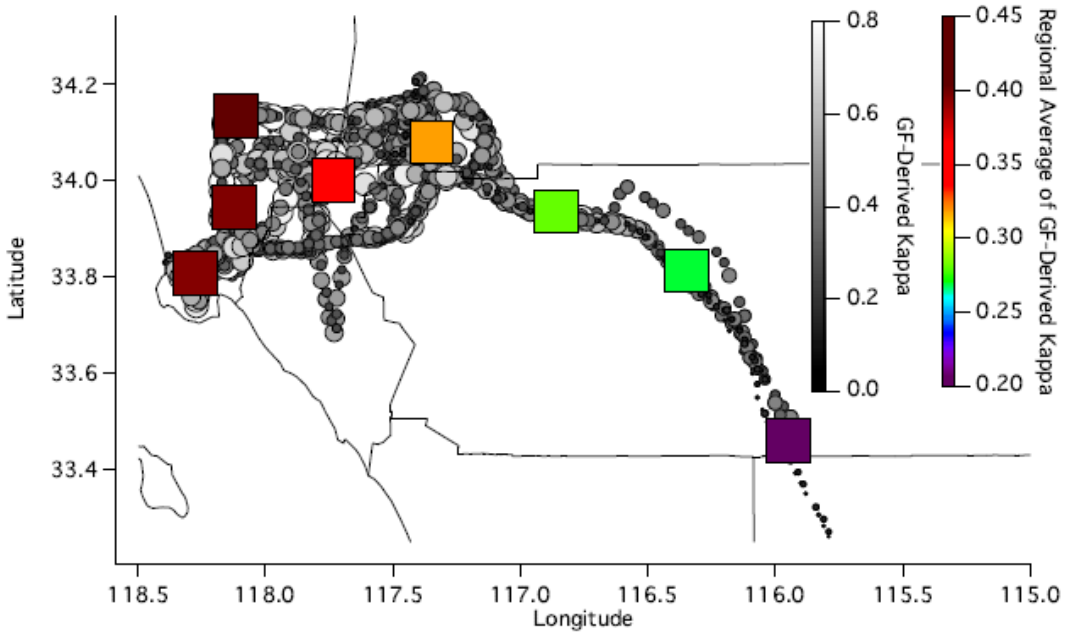

Figure 6: 1 min resolution GF-derived κ (gray circles), and regionally-averaged κ (squares) for 17 flights (4-7, 10, 12, 14-15, 18-22, 24-25, 27-28 May 2010).

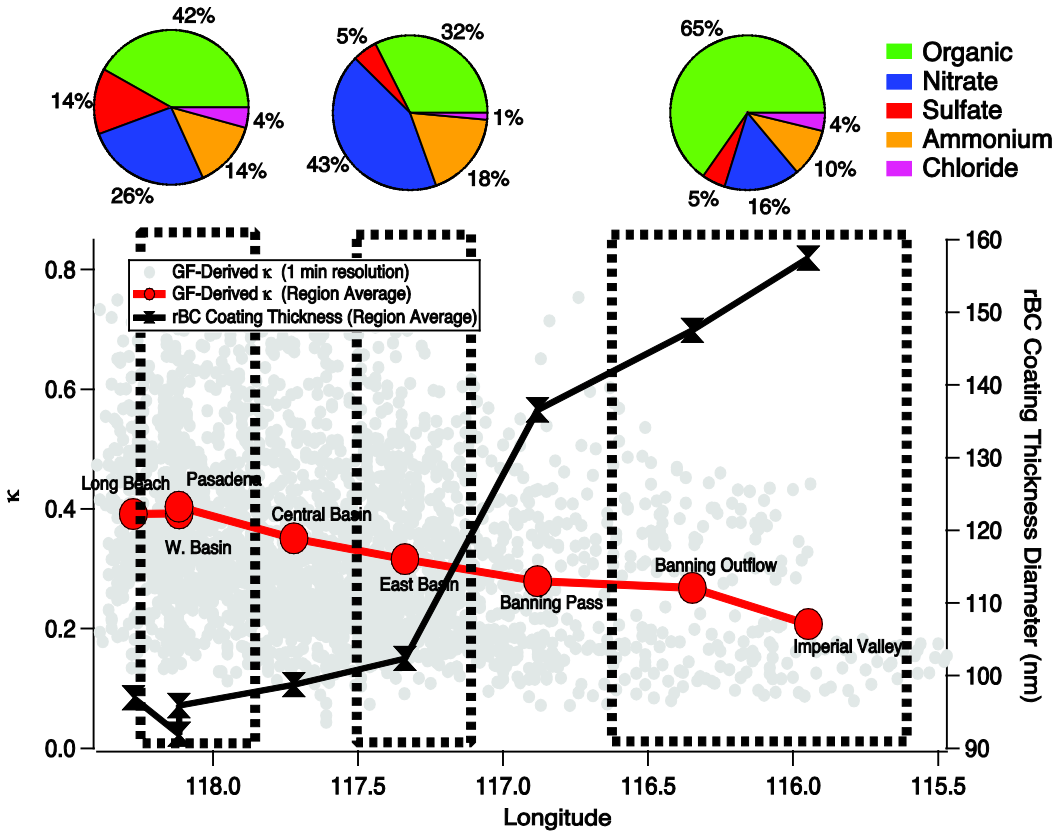

Figure 7: GF-derived hygroscopicity and rBC coating thickness trends with Longitude over 17 flights, from source-rich western Basin to downwind eastern Basin. Pie charts represent size-resolved AMS data for 150-250 nm particles averaged over 5 flights (21, 24-25, 27-28 May 2010).

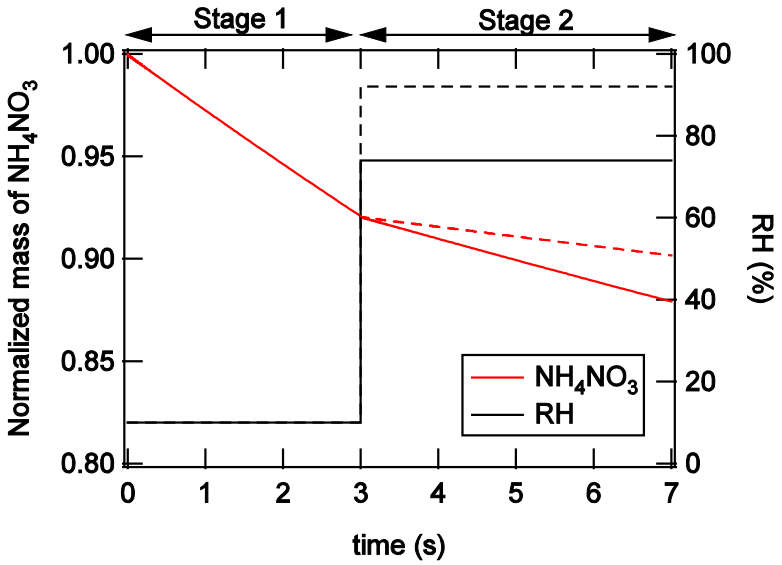

Figure 8. Upper-bound of modeled normalized mass of ammonium nitrate (red lines) in the particle phase as a function of residence time in the DASH instrument operated at 28 ºC. Relative humidity (black lines) is 10 % up to 3 s in stage 1 (drying and DMA) and then increased to either 74 % (solid lines) or 92 % (dashed lines) in the stage 2 (humidification and sizing).

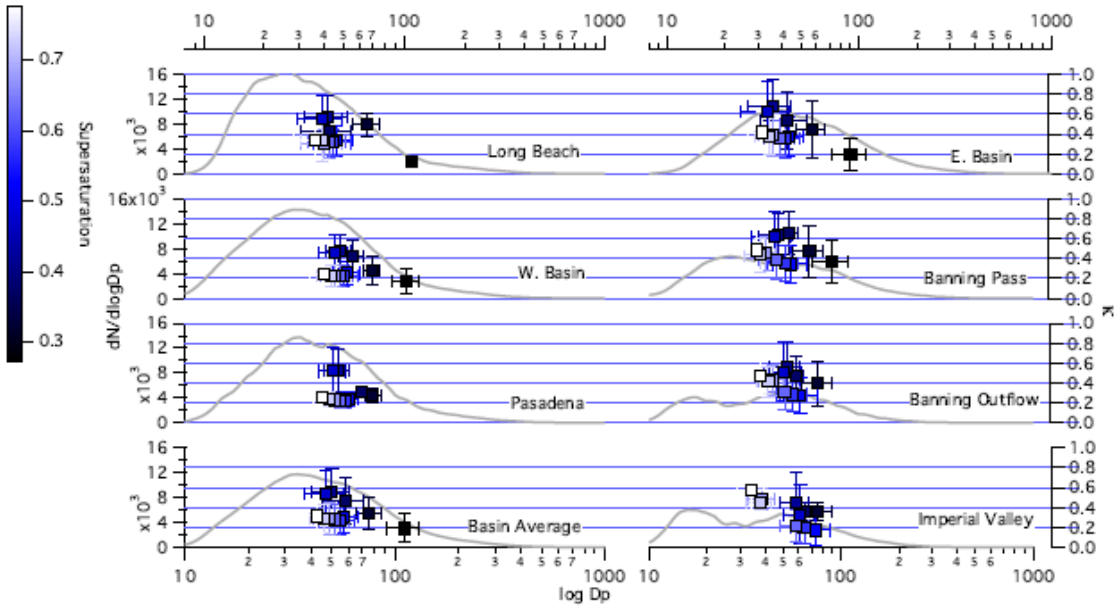

Figure 9: Regional averages over 16 flights (5-7, 10, 12, 14-15, 18-22, 24-25, 27-28 May 2010) of aerosol hygroscopicity, κ, calculated from mean size distributions (gray line) and measured CCN concentrations, plotted against critical diameter (D_{crit}), for supersaturation (SS) ranging from 0.275-0.775%.

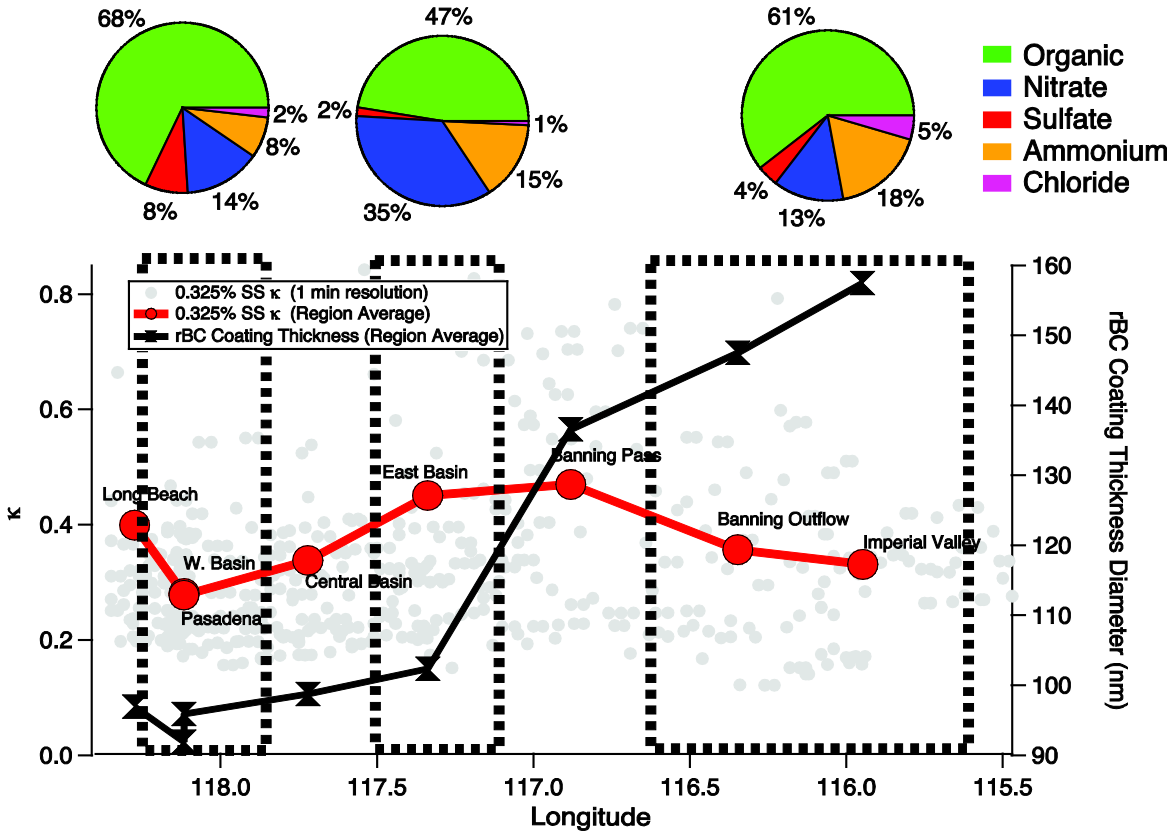

Figure 10: Average over 16 flights of CCN-derived κ (0.325% SS) and rBC coating thickness trends with longitude from source-rich western to downwind eastern areas of the LA Basin. Pie charts represent size-resolved AMS data for 70-120 nm particles averaged over 5 flights (21, 24-25, 27-28 May 2010).

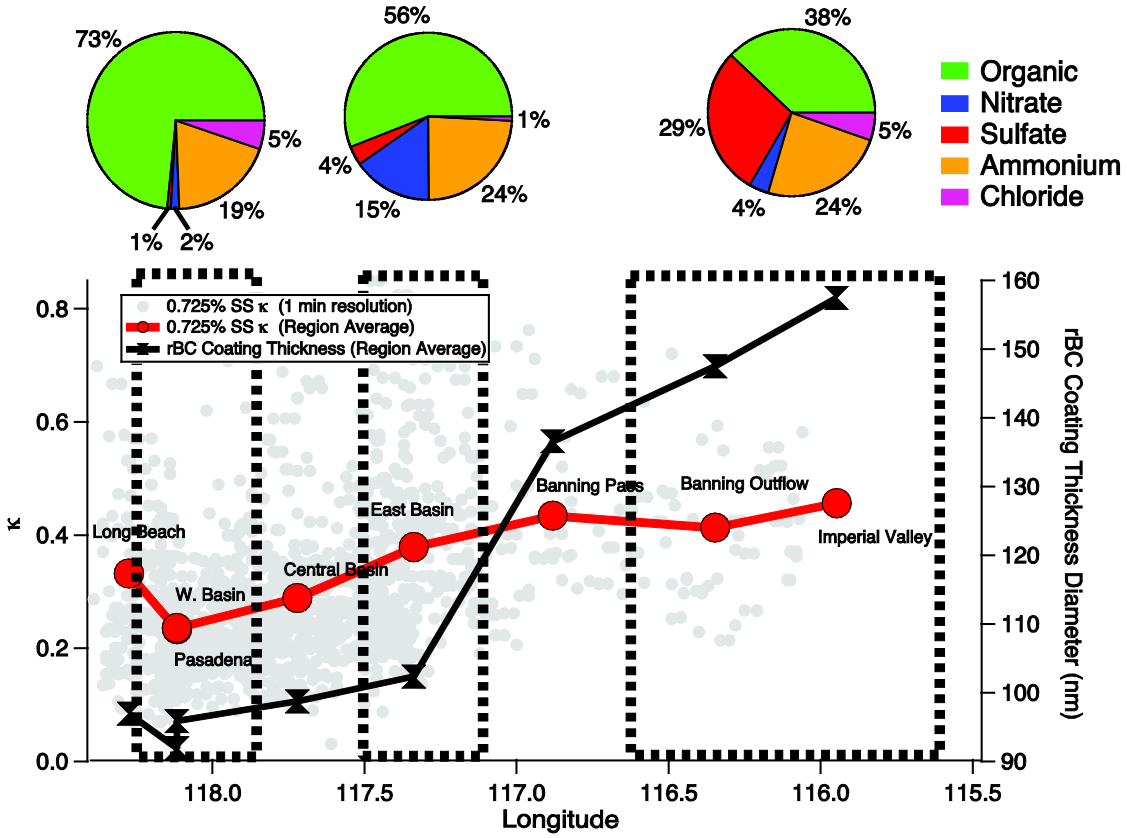

Figure 11: Average over 16 flights of CCN-derived □ (0.725% SS) trends with longitude from source-rich western to downwind eastern areas of the LA Basin. Pie charts represent size-resolved AMS data for 30-60 nm particles averaged over 5 flights (21, 24-25, 27-28 May 2010).

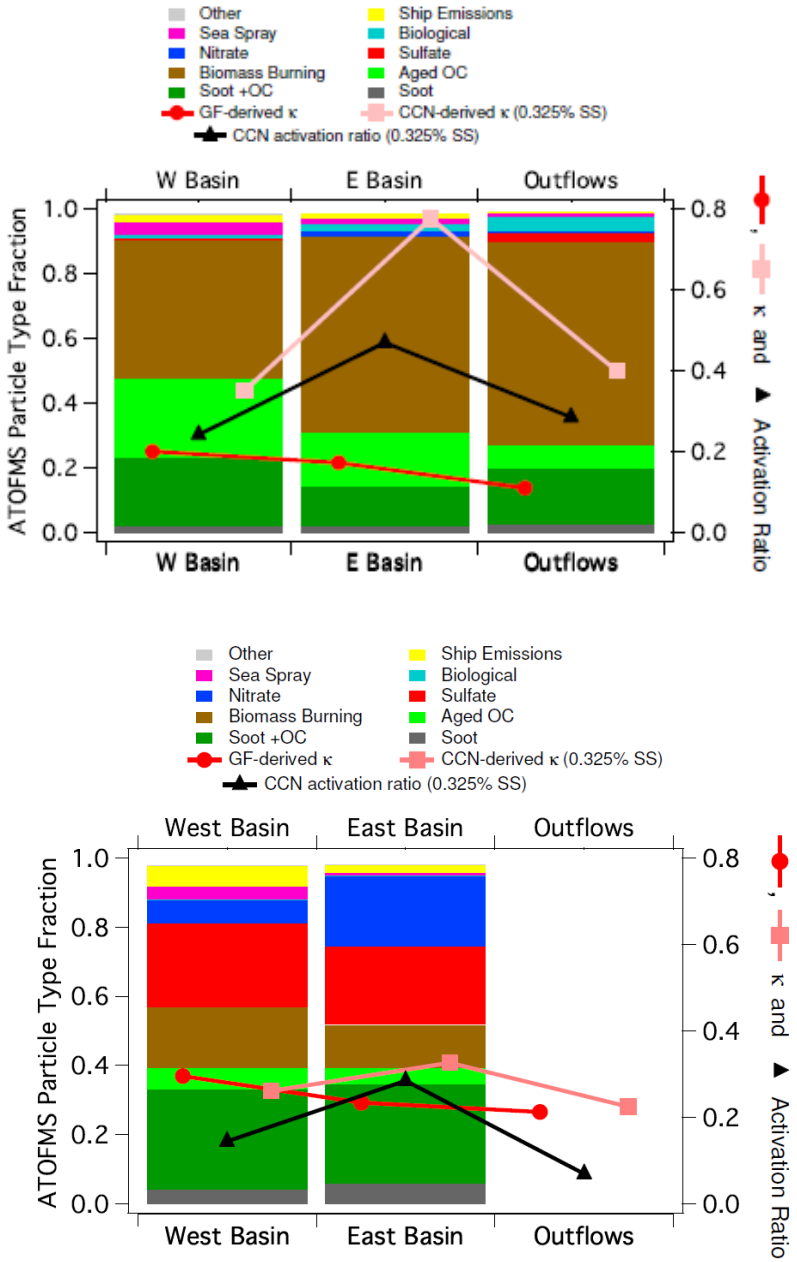

Figure 12: Comparison of ATOFMS particle type fraction, GF-derived κ, CCN-derived κ (0.325% SS), and activation ratio for (a) 13 May2010 and (b) 5 non-biomass-burning-influenced flights (6-7, 10, 14-15 May 2010).

Chapter 9

Los Angeles Basin Airborne Organic Aerosol Characterization During CalNex[1]

[1]This chapter has been submitted to Journal of Geophysical Research: "Los Angeles Basin Airborne Organic Aerosol Characterization During CalNex" by J. S. Craven, A. R. Metcalf, R. Bahreini, A. Middlebrook, P. L. Hayes, H. T. Duong, A. Sorooshian, J. L. Jimenez, R. C. Flagan, and J. H. Seinfeld, Submitted for publication in Journal of Geophysical Research.

JOURNAL OF GEOPHYSICAL RESEARCH, VOL. ???, XXXX, DOI:10.1029/,

Los Angeles Basin Airborne Organic Aerosol Characterization during CalNex

J. S. Craven,[1] A. R. Metcalf,[2,7] R. Bahreini,[3,4] A. Middlebrook,[3,4] P. L. Hayes,[3,5] H. T. Duong,[6] A. Sorooshian,[6] J. L. Jimenez,[3,5] R. C. Flagan,[1,2] and J. H. Seinfeld[1,2]

[1]Division of Chemistry and Chemical Engineering, California Institute of Technology, Pasadena,CA 91125, USA.

[2]Division of Engineering and Applied Science, California Institute of Technology, Pasadena,CA 91125, USA.

[3]Cooperative Institute for Research in Environmental Sciences, University of Colorado at Boulder, Boulder, Colorado, USA.

[4]Earth System Research Laboratory, National Oceanic and Atmospheric Administration, Boulder, Colorado, USA.

Abstract.

We report airborne organic aerosol (OA) measurements over Los Angeles carried out in May 2010 as part of the CalNex field campaign. The principal platform for the airborne data reported here was the CIRPAS Twin Otter (TO); airborne data from NOAA WP-3D aircraft and Pasadena CalNex ground-site data acquired during simultaneous TO fly-bys are also presented. Aerodyne aerosol mass spectrometer (AMS) measurements constitute the main source of data analyzed. The increase in organic aerosol oxidation from west to east in the Basin was sensitive to OA mass loading, with a greater spatial trend in O:C associated with lower mass concentration. Three positive matrix factorization (PMF) components (HOA, SVOOA, and LVOOA) were resolved for the one flight that exhibited the largest variability in es-

[5]Department of Chemistry and Biochemistry, University of Colorado, Boulder, Colorado, USA.

[6]Department of Chemical and Environmental Engineering, University of Arizona, Tucson, Arizona, USA.

[7]Now at the Combustion Research Facility, Sandia National Laboratories, Livermore, CA 94550, USA.

timated O:C ratio. Comparison of the PMF factors with two optical modes of refractory black carbon (rBC)– containing aerosol revealed that the coating of thinly coated rBC–containing aerosol, dominant in the downtown region, is likely composed of HOA, whereas more thickly coated rBC–containing aerosol, dominant in the Banning pass outflow, is composed of SVOOA and LVOOA. The correlation of WSOM to OOA is higher in the outflows than in the Basin, due to the higher mass fraction of OOA/OA in the outflows. By comparison, the average OA concentration over Mexico City MILAGRO campaign was ∼7 times higher than the airborne average during CalNex. The CalNex OA data reflect the effect of decades of air pollution control in Los Angeles.

1. Introduction

Organic matter contributes substantially to the mass of submicron atmospheric aerosols [*Zhang et al.*, 2007; *de Gouw and Jimenez*, 2009]. The lifecycle of atmospheric organic aerosol is complex and continued characterization through laboratory chamber studies, modeling, and field studies is necessary [*Jimenez*, 2009; *Rudich et al.*, 2007]. The 2010 CalNex field campaign (http://www.esrl.noaa.gov/csd/projects/calnex/) was designed to address sources of air pollution and guide air-quality regulation in the state of California, as well as address science questions related to climate change [*Ryerson et al.*, 2012]. The Los Angeles Basin has been a historical site for field studies of air pollution, initially motivated by photochemical smog [*Haagen-Smit et al.*, 1952; *Blumenthal et al.*, 1977]. Air quality in Los Angeles has been steadily improving [*Warneke et al.*, 2012], and the aerosol concentrations measured during CalNex 2010 are among the lowest in the last decade (Figure 1).

The Aerodyne aerosol mass spectrometer (AMS) has emerged as an important analytical tool to characterize the chemical nature of ambient organic aerosol [*Jayne et al.*, 2000; *Drewnick et al.*, 2005; *DeCarlo et al.*, 2006; *Canagaratna et al.*, 2007]. Several recent field campaigns in which organic aerosol (OA) was characterized by the AMS are summarized in Table 1 [*Aiken et al.*, 2009; *DeCarlo et al.*, 2008, 2010; *Morgan et al.*, 2010; *Docherty et al.*, 2008, 2011; *Hersey et al.*, 2011; *Hayes et al.*, submitted]. When combined with measurements of relatively long-lived atmospheric tracers, such as black carbon, and a source apportionment model, such as Positive Matrix Factorization (PMF) [*Paatero and Tapper*, 1994], ground- and aircraft-based AMS data can provide useful constraints on the

composition and transport of the organic aerosol (OA) in a region [*Zhang et al.*, 2011]. Additionally, the quantification of the OA oxidation, with AMS O:C atomic ratio, in the ambient atmosphere has become increasingly important with the advent of recent models that utilize O:C, along with OA mass concentrations and volatility of gas-phase species, to constrain SOA formation [*Dzepina et al.*, 2009, 2011; *Cappa et al.*, 2013].

Receptor modeling of OA using AMS PMF can help identify different sources of aerosol mass. When sources are known, AMS PMF factors can elucidate the extent to which the aerosol has undergone atmospheric processing and can separate OA by chemical characteristics such as water solubility, as shown by *Kondo et al.* [2007] who observed strong correlations between OOA and water soluble organic carbon (WSOC). For the Los Angeles Basin, AMS PMF is helpful in determining the contribution to organic aerosol from freshly emitted primary versus secondary sources, as well as the extent to which the aerosol is locally produced versus transported regionally. The hydrocarbon–like organic aerosol (HOA) fraction is associated with fresh diesel and gasoline emissions; unit mass resolution AMS PMF results alone are not able to separate the contributions from these sources to OA. Other fresh emissions, such as from biomass burning or cooking, have mass spectra that differ from HOA and can often be separated using PMF. As the aerosol ages in the atmosphere, the AMS–derived OA composition appears less variable, as measured by its increased oxidation state and decreased volatility [*Ng et al.*, 2010; *Kroll et al.*, 2011]. Typically, low volatility oxidized organic aerosol (LVOOA) is achieved after primary volatile and/or semi volatile organic compound emissions have undergone several generations of atmospheric oxidation leading to SOA formation, and the aerosol itself has experienced a relatively prolonged period of atmospheric processing.

The focus of the present study is a detailed analysis of the airborne non-refractory submicron organic aerosol composition in the Los Angeles Basin during the 2010 CalNex field campaign. Questions that will be addressed concerning OA in Los Angeles are: (1) How oxidized is Los Angeles OA and is there a spatial trend of OA oxidation? (2) Can OA PMF factors aid in interpretation of the sources of coating for black carbon containing aerosol? (3) Is there a correlation between PMF factors and water soluble organic mass (WSOM)? (4) To what extent is the airborne OA mass concentration and oxidation consistent with that measured in recent ground-based LA area campaigns [*Docherty et al.*, 2011; *Hersey et al.*, 2011; *Hayes et al.*, submitted] as well as in campaigns in Mexico City and Europe [*Aiken et al.*, 2009; *DeCarlo et al.*, 2010; *Morgan et al.*, 2010]?

2. Airborne and Ground-Based Measurements

2.1. Airborne Measurements

Eighteen research flights were carried out in May 2010 using the Center for Interdisciplinary Remotely-Piloted Aircraft Studies (CIRPAS, Naval Postgraduate School, Monterey, CA, USA) Twin Otter (TO). Description of the complete instrument payload and individual flights of the TO and meteorology of the Basin during CalNex appears in *Duong et al.* [2011] and *Metcalf et al.* [2012]. The instruments onboard the TO are in an unpressurized cabin and sample from small individual lines that extend from the main inlet, running through the entire length of the aircraft. The air is sampled with a two stage diffuser inlet designed for the nominal airspeed of the TO (50 m s^{-1}) and has no significant loss for aerosol less than 3.5 μm diameter [*Hegg et al.*, 2005]. Of the two aerosol mass spectrometers deployed onboard the Twin Otter during CalNex, the University of California, San Diego A-ATOFMS [*Cahill et al.*, 2012] and the Caltech Aerodyne AMS,

the AMS was deployed on 9 flights, 6 of which focused on the LA Basin and are the subject of the present study (Table 2). *Duong et al.* [2011], *Metcalf et al.* [2012], and *Hersey et al.* [in press] report the airborne water soluble organic carbon, refractory black carbon (rBC), rBC coating thickness, hygroscopicity, and aerosol composition and size distribution measurements for the TO flights.

The National Oceanic and Atmospheric Administration (NOAA) P-3 aircraft was deployed during CalNex [*Ryerson et al.*, 2012; *Bahreini et al.*, 2012]; the NOAA AMS average mass spectrum from a coordinated flight path on May 19, 2010 is included in the present analysis.

2.1.1. Compact Time-of-Flight Aerosol Mass Spectrometer

Aerodyne compact time-of-flight aerosol mass spectrometers (C-ToF-AMS) [*Drewnick et al.*, 2005; *Canagaratna et al.*, 2007] were deployed to measure submicron aerosol composition onboard both the CIRPAS Twin Otter and NOAA P-3. The C-ToF-AMS sampled at constant pressure (maintained via a pressure-controlled inlet [*Bahreini et al.*, 2008]) through an aerodynamic lens that focuses the aerosols into a beam which is then passed down the particle time-of-flight chamber. Particles ranging 60 – 600 nm in vacuum aerodynamic diameter have a 100 % transmission [*Jayne et al.*, 2000]. The effect of the transmission efficiency on measurement of total inorganic mass for both AMS instruments is estimated and discussed in *Ensberg et al.* [in press]. At the end of the particle time-of-flight chamber, the aerosol is vaporized by a 600 °C heater and ionized with 70 eV electron ionization.

Mass concentrations have been converted to standard temperature and pressure (STP, 273 K and 1 atm) and are reported in units of $\mu g/sm^3$, micro-

grams of aerosol per standard cubic meter of air. The data reported are for altitudes below 400 meters above ground level. Analysis of the mass spectra was carried out in the Squirrel ToF toolkit (http://cires.colorado.edu/jimenez-group/ToFAMSResources/ToFSoftware/index.html) in Igor Pro (WaveMetrics Inc., Lake Oswego, Oregon, USA). Adjustments to the fragmentation table from air interferences were made to the mass spectra based on filter periods taken at the beginning and end of each flight [*Allan et al.*, 2004]. The modifications to the fragmentation table for organic mass at *m/z* 18 and 28 were included [*Aiken et al.*, 2008]. The effect of a change in gas-phase CO_2 on the organic aerosol signal at *m/z* 44 was investigated for the May 19 P3 flight. The variation in gas-phase CO_2 was on the order of 30 ppmv and its contribution to the organic aerosol signal at *m/z* 44 by the AMS was negligible, so a time-dependent gas-phase CO_2 interference correction was not necessary. An aerosol composition-dependent collection efficiency (CE) was applied to all of the data [*Middlebrook et al.*, 2012]. The time resolution of the Twin Otter AMS measurement was either every 10 s in mass spec (MS) mode or 10 s of MS mode and 50 s of particle time-of-flight (PToF) mode every minute. The time resolution of the P-3 AMS was every 5 s in MS mode and 5 s in PToF mode.

Strong correlations of the fraction of organic mass at *m/z* 44 (f_{44}) versus O:C, as measured by HR-ToF-AMS, have been reported for the MILAGRO, SOAR, and CalNex-LA campaigns [*Aiken et al.*, 2008; *Docherty et al.*, 2011; *Hayes et al.*, submitted]. In this work, the O:C reported by the C-ToF-AMS is estimated based on the average of the previously reported regressions of f_{44} versus O:C atomic ratio. The equation used to calculate O:C

for the C-ToF-AMS datasets is:

$$\text{O:C} = 3.74 \times f_{44} - 0.0348 \quad (1)$$

where the organic mass at m/z 44 is assumed to be predominantly the CO_2^+ ion fragment. For example, for the aerosol sampled at the Pasadena ground-site, the average contribution from CO_2^+ to m/z 44 is 95% [*Hayes et al.*, submitted].

The aerosol volume calculated from the AMS data is in good agreement with the volume as calculated by the differential mobility analyzer (DMA) onboard the Twin Otter (see Supplemental Material). A comparison of the AMS measurements and other mass measurements onboard the NOAA-P3 aircraft is discussed in *Bahreini et al.* [2012].

2.1.2. Aerosol Volume Measurement

Aerosol size distribution measurements were made on the Twin Otter by a custom-built, scanning differential mobility analyzer (DMA) system. The data inversion is based on *Collins et al.* [2002]. The electric mobility diameter range for the DMA is 10 to 800 nm. Total aerosol volume is calculated from the inverted size distributions.

2.1.3. Single Particle Soot Photometer

Single-particle refractory black carbon mass and coating thickness measurements were made onboard the Twin Otter [*Metcalf et al.*, 2012] with a Droplet Measurement Technologies Single Particle Soot Photometer (SP2, DMT, Boulder, CO, USA). The size range for the black carbon mass reported, based on lognormal fits of single-particle size distributions, is 1 nm – 1 μm volume equivalent diameter (d_{ve}). The calibration of the rBC mass has been re-analyzed from *Metcalf et al.* [2012] following recommendations of *Laborde et al.* [2012] and *Baumgardner et al.* [2012]. In this work we report the rBC coating thickness diameter, which is derived from the scattering signals in the SP2 by fitting a Mie

scattering model to the data [*Metcalf et al.*, 2012]. The optical diameter detection range, assuming a purely scattering particle with a refractive index of 1.5-0i, is 174 – 420 nm (d_{ve}).

2.1.4. PILS-TOC

Water soluble organic carbon (WSOC) was collected using a particle-into-liquid sampler (PILS; Brechtel Manufacturing Inc.,) coupled to a Total Organic Carbon (TOC) Analyzer (Sievers Model 800) [*Sullivan et al.*, 2006]. Water soluble organic mass (WSOM) was estimated from WSOC using a conversion factor of 1.8 [*Docherty et al.*, 2008].

2.2. Ground-Based Measurements

Meteorology, gas-phase, and aerosol-phase measurements were made as part of the CalNex campaign at a Supersite on the California Institute of Technology campus in Pasadena, California from May 14 through June 16, 2010. The Pasadena ground-site HR-ToF-AMS organic aerosol [*Hayes et al.*, submitted] and planetary boundary layer (PBL) height measurements are utilized here to provide context for the airborne measurements. The PBL height data was acquired using a Vaisala CL31 ceilometer using a method described previously [*Haman et al.*, 2012].

3. Results

3.1. Airborne OA Mass and Composition Measurements

Airborne AMS OA mass concentrations measured on the TO ranged from 0.2 to 12 $\mu g/sm^3$ (Figure 2). Table 2 summarizes the OA average, minimum, and maximum mass loadings for each flight, as well as the limit of detection of OA mass. The greatest variation of OA level is between May 19 and the remaining flights. The May 19 flight observed the

highest average (6.94 μg/sm^3) and maximum (12.0 μg/sm^3) mass concentration of the 6 flights, and did not identify a discernible spatial trend within the Basin. The May 24 and May 25 flights sampled both the Basin and its outflows. The OA mass concentrations in the Basin are similar to that sampled immediately above the Banning pass, after which the mass concentration decreases (in both the Banning and El Cajon passes) due to dilution of a polluted airmass into a cleaner airmass.

The atomic O:C ratio of the OA (Figure 3, shown as the marker color) for May 19, 21, and May 25 is relatively high in the southwestern Basin, near Long Beach. Back trajectory analysis shows that the oxidized aerosol mass in this region of the Basin originates from an aged airmass that was transported up the coast [*Ensberg et al.*, in press]. The relatively high O:C in this region was not observed on May 28. On May 21, 24, and 25, OA in the airborne outflow regions exhibited a higher O:C than in the Basin, indicative of photochemical processing and dilution in the outflows.

To determine the extent to which an increase in O:C exists from west to east in the Basin, O:C is plotted against longitude, to which a linear fit is applied (Figure S7). The results of the fit vary, depending on the flight. The slopes and uncertainties on the slope for each flight's regression line are shown in Figure 4. There was no significant trend in O:C from west to east within the Basin on May 19 (slope of 0.005 ΔO:C/Δ°longitude on Figure 4). The highest average mass loadings were observed on this day, and the lack of spatial variability in O:C could be the result of a relatively well-mixed Basin airmass of fresh and aged emissions. Also, this flight had the latest take-off time, 11:40 local time, which was 40 minutes later than most of the other flights, and had the lowest daily maximum planetary boundary layer height (979 m). Emissions would have had more time

to oxidize, decreasing some of the variability in the fresh emissions measured. On May 21, 24, and 28, the slopes of the O:C versus longitude were ∼0.05 ΔO:C/ Δ°longitude. On May 21, high O:C (0.50 – 0.55) was present in the southwestern Basin, as well as in the outflows, whereas over the downtown LA region and Pasadena ground-site, the O:C was slightly lower (∼0.30). On May 24, the O:C is relatively low again in downtown LA region and Pasadena ground-site (0.25 – 0.3), and then increases slightly to ∼0.35 in the eastern Basin and in the outflows. If only the data in the Basin are considered, the slope for the May 24 flight is much higher (0.17 ΔO:C/ Δ°Longitude, Figure S7). May 24 was preceded by a day with an anomalously high boundary layer in which the Basin was essentially cleaned out (Figure 5A). Thus, the May 24 Basin and outflow trend could reflect the single day O:C trend for SOA formation, rather than from multi-day pollution build-up. On May 28, the OA in the western part of the Basin has a low O:C (close to 0.20), likely due to fresh mobile emissions from the 710 freeway or Port of Long Beach, and then the O:C increases only slightly in the eastern Basin. The May 25 and 27 flights found slopes of ∼0.10 ΔO:C/ Δ°longitude (Figure 4). May 25 exhibited the largest increase in O:C from west to east for an entire flight. This also was the flight with the lowest average mass concentration (1.03 μg/sm^3). Compared to May 24, which had the same flight path as May 25, O:C in the southern part of the Basin, as well as in the outflows, exhibited a higher O:C. The increase in O:C between May 24 and May 25 is likely a result of the fact that the Basin contents and outflow sampled on May 25 represented a combination of aged emissions from May 24 and and fresh emissions from May 25. The difference in slope of increase in O:C from west to east appears to be

anti-correlated with the flight-averaged mass concentration (green markers in Figure 4), making the O:C spatial variability sensitive to organic mass concentration.

3.2. Airborne and Ground-Based AMS OA Mass Loading and Spectrum Comparison

Airborne AMS OA mass loadings, OA/Sulfate ratio, O:C, and altitude are compared with the Pasadena ground-site AMS and PBLH measurements over the duration of the CalNex-LA campaign in Figure 5. The TO AMS sampled on days with relatively high maximum boundary layer heights and relatively low Pasadena ground-site AMS OA mass concentration, as compared to the entire Pasadena ground-site campaign (Figure 5A and D). During the Pasadena ground-site fly-overs (fly-over location given in Figure 5E), the aircraft was sampling within the boundary layer (Figure 5A). AMS measurements on five of the six flights for which the AMS was onboard are compared to the ground-site AMS OA measurements (May 25, 2010 ground-site AMS measurements were not available for comparison). The ground-site OA mass concentrations exceed those measured aloft, except for the May 19, 2010 fly-over. The average ratio of OA airborne : OA ground is 0.61. The ratio between the airborne and ground OA mass concentration is consistent with that reported for Mexico City MILAGRO for which the mid-day airborne OA measurements were approximately 2/3 of those measured at the ground-site [*Aiken et al.*, 2009]. The OA/sulfate ratio is in good-agreement between the airborne and ground samples. The O:C of the airborne samples is slightly lower than the ground measurements, however most data from the fly-overs lie within the uncertainty for O:C based on high-resolution ion analysis, 30% [*Aiken et al.*, 2007], and within the uncertainty for f_{44} (see below).

The TO and NOAA P3 flew a coordinated flight path in the Basin on May 19. The flight map of the locations of the two instruments is shown in Figure S8. The average mass spectrum for each instrument and the difference between the two spectra are shown in Figure 6. The largest difference between the two spectra is in m/z 44. The TO f_{44} is slightly lower, by about 20% of the P3 f_{44}. This provides a measure of uncertainty on the f_{44} measurement. The dominant *m/z*'s are labeled and strongly resemble a mixture of aerosol resulting from hydrocarbon combustion (high *m/z* 27, *m/z* 29, *m/z* 41, *m/z* 43, *m/z* 55, *m/z* 57, *m/z* 69, *m/z* 91) and atmospheric oxidation (high *m/z* 44).

3.3. Deconvolution of Organic Aerosol Mass Spectra

Positive matrix factorization (PMF) has been widely used as a tool to identify the components of organic aerosol [*Lanz et al.*, 2007; *Ulbrich et al.*, 2009; *Aiken et al.*, 2009; *DeCarlo et al.*, 2010; *Morgan et al.*, 2010; *Zhang et al.*, 2011; *Docherty et al.*, 2011; *Hersey et al.*, 2011; *Ng et al.*, 2011; *Brown et al.*, 2012]. In the present work, application of PMF was used to separate the mixture of fresh and aged OA in the Basin and outflows. The results for Twin Otter AMS data were evaluated using the PMF Evaluation Tool (PET) (http://tinyurl.com/PMF-guide) [*Ulbrich et al.*, 2009]. See Supplemental Material for details regarding the solution.

PMF analysis of the data obtained on May 25, during which the largest variation in O:C vs longitude was observed, resolved an HOA, an SVOOA, and an LVOOA factor (Figure 7). The HOA factor is highest in the western Basin, due to proximity to fresh emission sources, such as refineries, the Port of Long Beach, and the concentrated motor vehicle traffic associated with downtown LA (Figure 8A). The average mass fraction of HOA/OA for the entire flight is 0.19. The HOA/OA mass fraction is higher when only the Basin

is considered (0.27) and lower when only the outflows are considered (0.15). Formation of SOA from volatile, semi–volatile and intermediate volatility species is expected to proceed substantially in a few hours at typical summer OH concentrations [*Robinson et al.*, 2007], and can continue even for multiple days [*Dzepina et al.*, 2011]. All of the TO flights considered here occurred mid-day, so the morning rush hour emissions (diesel and gasoline) would have undergone a period of oxidation. Late morning and afternoon traffic emissions would contain substantial fractions of both POA and SOA. The OA in the Basin is dominated by OOA, which has a mass fraction of 0.73, in which SVOOA/OA is 0.55 and LVOOA/OA is 0.18. The amount of OOA, specifically SVOOA, is also high for the ground-site PMF results in the 11:00 – 16:00 (local time) time range [*Hayes et al.*, submitted]. The OOA/OA mass fraction in the outflows, 0.85, is higher than that in the Basin. The SVOOA/OA and LVOOA/OA is 0.43 and 0.42 in the outflows. The flight average OOA/OA, which includes the Basin and outflows is 0.81 (SVOOA/OA flight average is 0.44 and LVOOA/OA flight average is 0.37, Figure 8B and 8C).

In lieu of gas-phase CO, rBC is used as a tracer for fresh emissions. Figure 8D shows the ratio of HOA/rBC, SVOOA/rBC, and LVOOA/rBC from the Basin and the Banning Pass data only. The data have been averaged into 0.5 degree longitude bins to better quantify the trend in oxidation from west to east. Back trajectory analysis confirms that most of the air sampled in the El Cajon and Banning passes originated in the Basin [*Metcalf et al.*, 2012; *Ensberg et al.*, in press]. Only the data east of longitude -116.5 has influence from air masses coming from the south. These data are highlighted in Figure 8D. The trend from west to east for HOA/rBC is flat with perhaps a small decrease, which is expected since this factor represents primary emissions and is likely co-emitted with

black carbon, for which processing in the atmosphere is not especially rapid. The ratio of SVOOA/rBC is higher than HOA/rBC and LVOOA/rBC, indicating most of the OA in the 11:00 – 16:00 time frame is processed, oxidized aerosol. SVOOA/rBC increases in the northeastern part of the Basin and into the outflows by approximately 58% (Table 3). LVOOA/rBC is smallest in the Basin, which means that during mid-day, most of the OOA in the Basin is not the result of long-range transport or lengthy photooxidation. The LVOOA/rBC steadily increases from west to east by 355% (Table 3).

From the PM 2.5 daily averages in Figure 1, May 25 2010 exhibited one of the lowest mass concentrations, not only in May 2010, but also for May in the years 1999 – 2012. These results highlight the potential for SOA formation even from low pollution conditions, perhaps from a single day of megacity emissions.

3.4. Oxygenated Organic Aerosol and Water Soluble Organic Mass in the Basin versus the Outflows

Here we discuss the correlations of the organic aerosol components from PMF with WSOM and compare the results between the data collected in the Basin and in the outflows. Figure 9 summarizes the correlations of the OA components with the WSOM from Basin and outflow separately from the May 25 flight. Also shown is the correlation of HOA vs OOA (SVOOA + LVOOA) ($r = 0.77$ and $r = 0.80$). The high correlation between HOA and OOA can exist because the two components were sampled from a well–mixed airmass, such as in the region downwind of downtown LA, in which high levels of both HOA and SVOOA were observed. In the outflow region, all components are expected to correlate because the plume from LA is diluting and everything decreases with distance from the Basin. Keeping that in mind, a high correlation between one of the components

of OA and WSOM may exist due to mixing. OOA and WSOM have a high correlation in the outflows (r = 0.88 and slope = 1.03± 0.05). This correlation is close to that reported by *Kondo et al.* [2007] for Tokyo, who found that OOA and WSOC were correlated with r^2 values between 0.77 – 0.91. The OA versus WSOM in the outflows has a similar correlation (r = 0.87 and slope = 1.21± 0.05) as that of the OOA, but the slope is higher than 1:1. Also, it is not expected that HOA would contribute substantially to WSOM. The correlation of SVOOA to WSOM (r = 0.86) in the outflows is higher than that of HOA to WSOM (r = 0.73).

The correlation between OOA and WSOM in the Basin is lower than in the outflows (r = 0.69 and slope = 0.41 ± 0.03). When only the correlation of SVOOA versus WSOM in the Basin is considered, r = 0.78 and slope = 0.42 ± 0.02, the r value increases compared to the correlation of OOA with WSOM. The change in slope of the regression between SVOOA and WSOM compared to that of OOA is minor, since the concentration of LVOOA in the Basin is below 0.5 $\mu g/sm^3$. No correlation between LVOOA with WSOM exists in the Basin primarily because the mass concentration is so small. The correlation and slope between HOA and WSOM in the Basin (r = 0.69 and slope = 0.18 ± 0.01) is lower that that between SVOOA and WSOM. The correlation for HOA vs WSOM reported here is higher than the correlation of HOA vs WSOC reported by *Kondo et al.* [2007] (r^2 = 0.22 – 0.23), likely because of the aircraft sampling of well-mixed air masses in polluted regions.

The OOA in the outflows is composed of a significant mass fraction of LVOOA, which could be why the correlation with WSOM is higher [*Duong et al.*, 2011]. The OOA in the basin is composed of mostly SVOOA, and the correlation with WSOM is weaker, which could indicate that some of the freshly formed SOA in the LA Basin is not water soluble.

3.5. Composition of Aerosol Coating Thickness of rBC containing particles

Within the SP2 detection limits, only a small fraction of optically detected particles also contain detectable black carbon. For May 25, the average fraction was 0.08. *Metcalf et al.* [2012] observed two different modes of black carbon aerosol with detectible scattering signals, mode 1, which contained an rBC core diameter of 90 – 125 nm (d_{ve}) with a coating thickness diameter greater than 100 nm, and mode 2, which contained an rBC core diameter of 150 – 200 nm (d_{ve}) and a coating thickness diameter less than 100 nm. These modes were chosen to represent thickly coated particles (mode 1) and thinly coated particles (mode 2). Because of the detection limits on the SP2, it was not possible to choose thickly and thinly coated modes of the same rBC core diameter. Flight maps highlighting mode 1 and mode 2 are shown alongside those for SVOOA, LVOOA and HOA in Figure 10.

On May 25, the two regions with the highest number concentrations of optically active rBC occurred the region downwind of downtown LA and the Banning pass outflow. The number concentration of mode 2 particle was highest near downtown LA, indicating that thinly coated particles dominate in the source-rich region of the Basin. Mode 2 is relatively low in the rest of the Basin. The number concentration of mode 1 is high downwind of downtown (although not as high as mode 2) and then again in the Banning pass outflow region. Mode 1 is the dominant mode in the outflow region. The downtown region contains high amounts of both modes, although the thinly coated rBC particles dominate, whereas in the outflow, the thickly coated rBC particles dominate.

The correlation between mode 2 and HOA is r = 0.73 (Figure 10). The highest mass concentration of HOA occurs downwind of downtown LA, and is low in the remainder of

the Basin, which is similar to mode 2. SVOOA is compared to mode 1 in the top of Figure 10 and has a correlation of r = 0.83. Similar to mode 1, SVOOA is high in both the region downwind of downtown LA and in the Banning outflow. Regions exist where SVOOA is high and mode 1 is not, i.e. the eastern Basin, and this can be explained by aerosol measured by the AMS that did not contain an rBC core, or from particles outside of the SP2 range. LVOOA is high only in the Banning outflow, and although the correlation with mode 1 is low (r = 0.43), LVOOA may contribute to mode 1 in this region. Table 4 shows a summary of the correlations between the number concentration of modes 1 and 2 and the mass concentrations of HOA, SVOOA, and LVOOA for May 25.

The correlation with HOA and SVOOA with mode 2 and 1 respectively, links the mixing state information of the rBC containing aerosol to the sources of organic that coat it. Well characterized coatings may help interpret radiative absorption enhancement of coated black carbon discrepancies found in the lab versus what is measured in the atmosphere [*Cappa et al.*, 2012].

4. Comparison to Other Campaigns

Some of the previous urban characterizations of OA are listed in Table 1. The average O:C of the airborne OA sampled by the TO during the CalNex campaign is 0.31 (± 0.09), which is lower than those of the other LA area and Mexico City ground-based campaigns, SOAR, PACO, CalNex-LA, and MILAGRO. These campaigns reported average mid-day O:C of 0.42 (PACO and SOAR), 0.41 (CalNex-LA), and 0.48 (MILAGRO). The average O:C values during the TO fly-over times only were 0.27 and 0.37 for airborne and ground-site AMS respectively. Given the 30% uncertainty in O:C reported by the high-resolution

AMS [*Aiken et al.*, 2007] and the uncertainty of the f_{44} of the CTOF AMS, these O:C's are not significantly different.

The airborne average OA concentration measured by the TO during CalNex, 2.4 $\mu g/sm^3$, was less than those measured in the three previous LA ground-based campaigns (PACO – 3.2 $\mu g/sm^3$ and SOAR – 19.9 $\mu g/sm^3$). Comparison of CalNex to the PACO campaign is appropriate since sampling for both occurred in the month of May, while SOAR measurements were made later in the summer. The difference between the ground and air OA mass concentrations during CalNex are consistent with measurements in Mexico City. The average OA loading for the airborne and ground-based Mexico City MILAGRO campaign was ∼7 times higher than the airborne average OA on the TO during CalNex. The range of airborne OA reported for the LONGREX and ADIENT Northern Europe campaign is twice that reported for the airborne CalNex. In summary, compared to other airborne and ground-based campaigns, the airborne OA concentrations in Los Angeles are some of the lowest reported. The PM 2.5 measurement taken in at the North Main Street Los Angeles CARB monitoring station confirms that the days sampled during May 2010 were indeed lower for LA (Figure 1).

The final two columns of Table 1 list the average mass fraction for HOA and OOA for the various campaigns. The ground-based LA campaigns yielded average HOA fractions of 12% (Pasadena ground-site), 20% (SOAR), and 23% (PACO). In Mexico City MILAGRO, the HOA fraction was reported to be 20% (airborne) and 29% (ground-based). The HOA fraction for the LONGREX and ADIENT campaigns exhibited a range of 5 - 20%. The HOA fraction reported for the May 25 CalNex flight, 19%, lies within the range of previously reported values. The OOA fraction for the May 25 CalNex flight, 81%, is

consistent with the LONGREX and ADIENT, SOAR, and PACO campaigns that report OOA fractions of 80-95%, 77.8% and 77%, respectively. In the MILAGRO campaigns, and at the CalNex Pasadena ground-site, lower OOA fractions (ranging from 46% - 70%) were found, as compared to the airborne CalNex measurements. Even with low OA mass loadings during May 2010, the fraction of submicron aerosol mass attributed to HOA and OOA based on the airborne measurements is consistent with that of previous LA area campaigns and those in Mexico City and Northern Europe.

In most ambient data sets in the northern hemisphere, the dominant AMS OA mass spectral signals are *m/z* 44 and *m/z* 43. The OA signals at *m/z* 44 and *m/z* 43 are mostly from the CO_2^+ ion (a tracer for carboxylic acid [Alfarra et al. 2004]) and the $C_2H_3O^+$ ion, respectively. Although the gas-phase CO_2 contribution to the organic mass signal at *m/z* 44 can be significant at low OA loadings [*Setyan et al.*, 2012], the gas-phase CO_2 interference during the CalNex campaign was negligible. The f_{44} vs f_{43} space (Figure 11) provides a context for comparing the extent to which OA has undergone atmospheric processing [*Ng et al.*, 2010]. The airborne CalNex HOA factor (black hexagon marker in Figure 11) has a similar f_{44} as the PACO HOA, average HOA from *Ng et al.* [2011], and three of the LONGREX/ADIENT HOA flights, indicating a similarly low level of oxidation in the HOA between cities. The airborne CalNex SVOOA (green hexagon marker) lies near the middle of the range of SVOOA solutions, and is closest to the SVOOA for PACO, CalNex-LA, and one of the LONGREX/ADIENT flights. The airborne CalNex LVOOA (orange hexagon marker) lies in the lower range of f_{44} for the majority of the LVOOA solutions (MILAGRO, SOAR, CalNex Pasadena ground-site) and several of the LONGREX/ADIENT results exhibit a higher f_{44} contribution to the LVOOA solution.

The relatively low f_{44} in the LVOOA airborne CalNex PMF solution is a result of only modest photochemical processing and/or transport from sources before sampling.

5. Conclusions

The May 2010 Los Angeles OA mass concentration measurements from the CIRPAS Twin Otter AMS were made during periods of a relatively deep boundary layer, and are lower than the measurements made during previous LA area campaigns, MILAGRO, and in Northern Europe.

Despite these relatively clean conditions, observations regarding the spatial variability of oxidized mass in the LA Basin can still be made. Higher loadings, perhaps from multi-day build up of pollution, make this spatial pattern difficult to establish, whereas under "clean" conditions in which the PBL height is high, single-day pollution build up and increase of O:C from west to east in the Basin is observed.

The increase in oxidation vs longitude was investigated further with PMF results from the May 25 flight, which exhibited the highest variation in O:C from west to east for 1 flight. The ratio of HOA/rBC remained nearly flat from west to east within the Basin and into the outflows, suggesting that any primary aerosol formed was not evaporating. The ratio of SVOOA/rBC was dominant in the Basin, and both SVOOA/rBC and LVOOA/rBC increased in the outflows, suggesting that SOA is being formed.

The OOA in the Basin has a weaker correlation with WSOM, than with the OOA in the outflows, which could suggest that some of the freshly formed SOA in the LA Basin is not water soluble.

The two optical modes with different coating thickness diameters identified using SP2 data correlate well with the HOA and SVOOA factors, despite the small fraction of rBC

particles with a detectable optical coating. The high correlation of mode 1, particles with coating thickness diameter greater than 100 nm, with SVOOA suggests that the thickly coated particles in the region downwind of downtown LA and in Banning pass are composed of freshly formed SOA. The presence of mode 1 particles and LVOOA in the Banning pass suggest that mode 1 may also be composed of highly oxygenated mass that originated in the Basin. The high correlation of mode 2, particles with coating thickness diameter less than 100 nm, with HOA suggests that the thinly coated particles in the region downwind of downtown LA are composed of HOA, which is co-emitted with rBC.

Acknowledgments.

This work was supported by NOAA grant NA09OAR4310128. The authors would like to acknowledge the Center for Interdisciplinary Remotely-Piloted Aircraft Studies (CIRPAS) crew at the Naval Postgraduate School in Monterey, California for their support during CalNex. The authors would also like to acknowledge B. L. Lefer for use of the PBLH data from the CalNex Pasadena ground-site, and W. T. Morgan for the use of their data on Figure 11. PLH and JLJ thank CARB 08-319/11-305 and DOE (BER/ASR) DE-SC0006035/DE-FG02-11ER65293, as well as a CIRES Visiting Fellowship to PLH.

References

Aiken, A. C., P. F. DeCarlo, and J. L. Jimenez (2007), Elemental Analysis of Organic Species with Electron Ionization High-Resolution Mass Spectrometry, *Analytical Chemistry, 79*, 8350 – 8358.

Aiken, A. C., P. F. DeCarlo, J. H. Kroll, D. R. Worsnop, J. A. Huffman, K. S. Docherty, I. M. Ulbrich, C. Mohr, J. R. Kimmel, D. Sueper, Y. Sun, Q. Zhang, A. Trimborn,

M. Northway, P. J. Ziemann, M. R. Canagaratna, T. B. Onasch, M. R. Alfarra, A. S. H. Prevot, J. Dommen, J. Duplissy, A. Metzger, U. Baltensperger, and J. L. Jimenez (2008), O/C and OM/OC Ratios of Primary, Secondary, and Ambient Organic Aerosols with High-Resolution Time-of-Flight Aerosol Mass Spectrometry, *Environmental Science & Technology, 42(12)*, 4478-4485.

Aiken, A. C., D. Salcedo, M. J. Cubison, J. A. Huffman, P. F. DeCarlo, I. M. Ulbrich, K. S. Docherty, D. Sueper, J. R. Kimmel, D. R. Worsnop, A. Trimborn, M. Northway, E. A. Stone, J. J. Schauer, R. M. Volkamer, E. Fortner, B. de Foy, J. Wang, A. Laskin, V. Shutthanandan, J. Zheng, R. Zhang, J. Gaffney, N. A. Marley, G. Paredes-Miranda, W. P. Arnott, L. T. Molina, G. Sosa, and J. L. Jimenez (2009), Mexico City aerosol analysis during MILAGRO using high resolution aerosol mass spectrometry at the urban supersite (T0) - Part 1: Fine particle composition and organic source apportionment, *Atmospheric Chemistry and Physics, 9 (17)*, 6633-6653.

Allan, J. D., A. E. Delia, H. Coe, K. N. Bower, M. R. Alfarra, J. L. Jimenez, A. M. Middlebrook, F. Drewnick, T. B. Onasch, M. R. Canagaratna, J. T. Jayne, and D. R. Worsnop (2004), A generalised method for the extraction of chemically resolved mass spectra from Aerodyne aerosol mass spectrometer data, *Journal of Aerosol Science, 35(7)*, 909-922.

Allan, J. D., J. L. Jimenez, P. I. Williams, M. R. Alfarra, K. N. Bower, J. T. Jayne, H. Coe, and D. R. Worsnop (2003), Quantitative sampling using an Aerodyne aerosol mass spectrometer 1. Techniques of data interpretation and error analysis, *Journal of Geophysical Research, 108(D3)*, 4090.

Bahreini, R., A. M. Middlebrook, J. A. de Gouw, C. Warneke, M. Trainer, C. A. Brock, H. Stark, S. S. Brown, W. P. Dubé, J. B. Gilman, K. Hall, J. S. Holloway, W. C. Kuster, A. E. Perring, A. S. H. Prévôt, J. P. Schwarz, J. R. Spackman, S. Szidat, N. L. Wagner, R. J. Weber, P. Zotter, and D. D. Parrish (2012), Gasoline emissions dominate over diesel in formation of secondary organic aerosol mass, *Geophysical Research Letters, 39(6)*, L06805.

Bahreini, R., A. M. Middlebrook, C. A. Brock, J. A. de Gouw, S. A. McKeen, L. R. Williams, K. E. Daumit, A. T. Lambe, P. Massoli, M. R. Canagaratna, R. Ahmadov, A. J. Carrasquillo, E. S. Cross, B. Ervens, J. S. Holloway, J. F. Hunter, T. B. Onasch, I. B. Pollack, J. M. Roberts, T. B. Ryerson, C. Warneke, P. Davidovits, D. R. Worsnop, and J. H. Kroll (2012), Mass Spectral Analysis of Organic Aerosol Formed Downwind of the Deepwater Horizon Oil Spill: Field Studies and Laboratory Confirmations, *Environmental Science & Technology, 46(15)*, 8025-8034.

Bahreini, R., E. J. Dunlea, B. M. Matthew, C. Simons, K. S. Docherty, P. F. DeCarlo, J. L. Jimenez, C. A. Brock, and A. M. Middlebrook (2008), Design and Operation of a Pressure-Controlled Inlet for Airborne Sampling with an Aerodynamic Aerosol Lens, *Environmental Science & Technology, 42(6)*, 465-471.

Baumgardner, D., O. Popovicheva, J. Allan, V. Bernardoni, J. Cao, F. Cavalli, J. Cozic, E. Diapouli, K. Eleftheriadis, P. J. Genberg, C. Gonzalez, M. Gysel, A. John, T. W. Kirchstetter, T. A. J. Kuhlbusch, M. Laborde, D. Lack, T. Muller, R. Niessner, A. Petzold, A. Piazzalunga, J. P. Putaud, J. Schwarz, P. Sheridan, R. Subramanian, E. Swietlicki, G. Valli, R. Vecchi, and M. Viana (2012), Soot reference materials for instrument calibration and inter comparisons: a workshop summary with recommendations,

Atmospheric Measurement Techniques, 5, 1869 – 18897.

Blumenthal, D. L., W. H. White, and T. B. Smith (1977), Anatomy of a Los Angeles Smog Episode: Pollutant Transport in the Daytime Sea Breeze Regime, *Atmospheric Environment, 12(4)*, 893-907.

Brock, C. A., D. M. Murphy, R. Bahreini, and A. M. Middlebrook (2011), Formation and growth of organic aerosols downwind of the Deepwater Horizon oil spill, *Geophysical Research Letters 38(17)*, L17805.

Brown, S. G., T. Lee, G. A. Norris, P. T. Roberts, J. L. Collett Jr, P. Paatero, and D. R. Worsnop (2012), Receptor modeling of near-roadway aerosol mass spectrometer data in Las Vegas, Nevada, with EPA PMF, *Atmospheric Chemistry and Physics, 12(1)*, 309-325.

Cahill, J. F., K. Suski, J. H. Seinfeld, R. A. Zaveri, and K. A. Prather (2012), The mixing state of carbonaceous aerosol particles in northern and southern California measured during CARES and CalNex 2010, *Atmos. Chem. Phys., 12*, 10989-11002.

Canagaratna, M. R., J. T. Jayne, J. L. Jimenez, J. D. Allan, M. R. Alfarra, Q. Zhang, T. B. Onasch, F. Drewnick, H. Coe, A. Middlebrook, A. Delia, L. R. Williams, A. M. Trimborn, M. J. Northway, P. F. DeCarlo, C. E. Kolb, P. Davidovits, and D. R. Worsnop (2007), Chemical and microphysical characterization of ambient aerosols with the aerodyne aerosol mass spectrometer, *Mass Spectrometry Reviews, 26(2)*,185-222.

Cappa, C. D., X. Zhang, C. L. Loza, J. S. Craven, L. D. Yee, and J. H. Seinfeld (2013), Application of Statistical Oxidation Model (SOM) to Secondary Organic Aerosol formation from photooxidation of C12 alkanes , *Atmospheric Chemistry and Physics, 13*, 1591 – 1606.

Cappa, C. D., T. B. Onasch, P. Massoli, D. R. Worsnop, T. S. Bates, E. S. Cross, P. Davidovits, J. Hakala, K. L. Hayden, B. T. Jobson, K. R. Kolesar, D. A. Lack, B. M. Lerner, S. Li, D. Mellon, I. Nuaaman, J. S. Olfert, T. Petaja, P.K. Quinn, C. Song, R. Subramanian, E. J. Williams, R. A. Zaveri (2012), Radiative Absorption Enhancements Due to the Mixing State of Atmospheric Black Carbon , *Science, 337*, 1078 – 1081.

Collins, D. R., H. H. Jonsson, H. Liao, R. C. Flagan, J. H. Seinfeld, K. J. Noone, and S. V. Hering (2000), Airborne analysis of the Los Angeles aerosol, *Atmospheric Environment, 34*, 4155-4173.

Collins, D. R., R. C. Flagan, and J. H. Seinfeld (2002), Improved Inversion of Scanning DMA Data, *Aerosol Science and Technology, 36:1*,1-9.

de Gouw, J. A., and J. L. Jimenez (2009), Organic Aerosols in the Earth's Atmosphere, *Environ. Sci. Technol. 43*, 7614–7618.

DeCarlo, P. F., J. R. Kimmel, A. Trimborn, M. J. Northway, J. T. Jayne, A. C. Aiken, M. Gonin, K. Fuhrer, T. Horvath, K. Docherty, D. R. Worsnop, and J. L. Jimenez (2006), Field-Deployable, High-Resolution, Time-of-Flight Aerosol Mass Spectrometer, *Anal. Chem., 78*, 8281-8289.

DeCarlo, P. F., E. J. Dunlea, J. R. Kimmel, A. C. Aiken, D. Sueper, J. Crounse, P. O. Wennberg, L. Emmons, Y. Shinozuka, A. Clarke, J. Zhou, J. Tomlinson, D. R. Collins, D. Knapp, A. J. Weinheimer, D. D. Montzka, T. Campos, and J. L. Jimenez (2008), Fast airborne aerosol size and chemistry measurements above Mexico City and Central Mexico during the MILAGRO campaign, *Atmospheric Chemistry and Physics, 8(14)*, 4027-4048.

DeCarlo, P. F., I. M. Ulbrich, J. Crounse, B. de Foy, E. J. Dunlea, A. C. Aiken, D. Knapp, A. J. Weinheimer, T. Campos, P. O. Wennberg, and J. L. Jimenez (2010), Investigation of the sources and processing of organic aerosol over the Central Mexican Plateau from aircraft measurements during MILAGRO, *Atmospheric Chemistry and Physics, 10 (12)*, 5257-5280.

Docherty, K. S., E. A. Stone, I. M. Ulbrich, P. F. DeCarlo, D. C. Snyder, J. J. Schauer, R. E. Peltier, R. J. Weber, S. M. Murphy, J. H. Seinfeld, B. D. Grover, D. J. Eatough, and J. L. Jimenez (2008), Apportionment of Primary and Secondary organic Aerosols in Southern California during the 2005 Study of Organic Aerosols in Riverside (SOAR-1), *Environ. Sci. Technol., 42*, 7655-7662.

Docherty, K. S., A. C. Aiken, J. A. Huffman, I. M. Ulbrich, P. F. DeCarlo, D. Sueper, D. R. Worsnop, D. C. Snyder, R. E. Peltier, R. J. Weber, B. D. Grover, D. J. Eatough, B. J. Williams, A. H. Goldstein, P. J. Ziemann, J. L. Jimenez (2011), The 2005 Study of Organic Aerosols at Riverside (SOAR-1): instrumental intercomparisons and fine particle composition, *Atmospheric Chemistry and Physics, 11 (23)*, 12387-12420.

Drewnick, F., S. S. Hings, P. F. DeCarlo, J. T. Jayne, M. Gonin, K. Fuhrer, S. Weimer, J. L. Jimenez, K. L. Demerjian, S. Borrmann, and D. R. Worsnop (2005), A New Time-of-Flight Aerosol Mass Spectrometer (TOF-AMS)—Instrument Description and First Field Deployment, *Aerosol Science and Technology, 39(7)*, 637-658.

Duong, H. T., A. Sorooshian, J. S. Craven, S. P. Hersey, A. R. Metcalf, X. Zhang, R. J. Weber, H. Jonsson, R. C. Flagan, and J. H. Seinfeld (2011), Water-soluble organic aerosol in the Los Angeles Basin and outflow regions: Airborne and ground measurements during the 2010 CalNex field campaign, *Journal of Geophysical Research, 116*,

D00V04.

Dzepina, K., R. M. Volkamer, S. Madronich, P. Tulet, I. M. Ulbrich, Q. Zhang, C. D. Cappa, P. J. Ziemann, and J. L. Jimenez (2009), Evaluation of recently-proposed secondary organic aerosol models for a case study in Mexico City , *Atmospheric Chemistry and Physics, 9*, 5681–5709.

Dzepina, K., R. M. Volkamer, C. D. Cappa, , S. Madronich, P. F. Decarlo, R. Z. Zaveri, and J. L. Jimenez (2011), Modeling the Multiday Evolution and Aging of Secondary Organic Aerosol During MILAGRO 2006, *Environmental Science and Technology, 45*, 3496 –3503.

Ensberg, J. J., J. S. Craven, A. R. Metcalf, W. M. Angevine, R. Bahreini, J. Brioude, C. Cai, J. A. de Gouw, R. A. Ellis, J. H. Flynn, C. L. Haman, P. L. Hayes, J. L. Jimenez, B. L. Lefer, A. M. Middlebrook, J. G. Murphy, J. A. Neuman, J. B. Nowak, J. M. Roberts, J. Stutz, P. R. Veres, J. M. Walker, and J. H. Seinfeld (in press), Inorganic and black carbon aerosols in the Los Angeles Basin during CalNex, *Journal of Geophysical Research,X*, XXX-XXX.

Haagen-Smit, A. J. (1952), Chemistry and Physiology of Los Angeles Smog, *Industrial and Engineering Chemistry, 44(6)* 1342-1346.

Haman, C. L., B. Lefer, and G. A. Morris (2012), Seasonal Variability in the Diurnal Evolution of the Boundary Layer in a Near Costal Urban Environment, *Journal of Atmospheric and Oceanic Technology, 29*, 697 – 710.

Hayes, P. L., A. M. Ortega, M. J. Cubison, K. D. Froyd, Y. Zhao, S. S. Cliff, W. W. Hu, D. W. Toohey, J. H. Flynn, B. L. Lefer, N. Grossberg, S. B. Alvarez, B. Rappenglück, J. W. Taylor, J. D. Allan, J. S. Holloway, J. B. Gilman, W. C. Kuster, J. A. de Gouw,

P. Massoli, X. Zhang, J. Liu, R. J. Weber, A. L. Corrigan, L. M. Russell, G. Isaacman, D. R. Worton, N. M. Kreisberg, A. H. Goldstein, R. Thalman, E. M. Waxman, R. Volkamer, Y. H. Lin, J. D. Surrat, T. E. Kleindienst, J. H. Offenberg, S. Dusanter, S. Griffith, P. S. Stevens, J. brioude, W. M. Angevine, and J. L. Jimenez (submitted), Organic Aerosol Composition and Sources in Pasadena, California during the 2010 CalNex Campaign, *Journal of Geophysical Research, XXX*,XXXX-XXXX.

Hegg, D. A., D. S. Covert, H. Jonsson, and P. A. Covert (2005), Determination of the Transmission Efficiency of an Aircrfact Aerosol inlet, *Aerosol Science and Technology, 39(10)*, 966-971.

Hersey, S. P., J. S. Craven, K. A. Schilling, A. R. Metcalf, A. Sorooshian, M. N. Chan, R. C. Flagan, and J. H. Seinfeld (2011), The Pasadena Aerosol Characterization Observatory (PACO): chemical and physical analysis of the Western Los Angeles Basin aerosol, *Atmospheric Chemistry and Physics, 11 (15)*, 7417-7443.

Hersey, S. P., J. S. Craven, A. R. Metcalf, J. Lin, T. Lathem, K. Suski, J. Cahill, H. Duong, A. Sorooshian, H. H. Jonsson, A. Nenes, K. A. Prather, R. C. Flagan, and J. H. Seinfeld (in press),Composition and Hygroscopicity of the Los Angeles Aerosol: CalNex, *Journal of Geophysical Research, XXX* XXX-XXX.

Jayne, J. T., D. C. Leard, X. Zhang, P. Davidovits, K. A. Smith, C. E. Kolb, and D. R. Worsnop (2000), Development of an Aerosol Mass Spectrometer for Size and Composition Analysis of Submicron Particles, *Aerosol Science and Technology, 33*, 49-79.

Jimenez, J. L., M. R. Canagaratna, N. M. Donahue, A. S. H. Prévôt, Q. Zhang, J. H. Kroll, P. F. DeCarlo, J. D. Allan, H. Coe, N. L. Ng, A. C. Aiken, K. S. Docherty, I. M. Ulbrich, A. P. Grieshop, A. L. Robinson, J. Duplissy, J. D. Smith, K. R. Wilson, V.

A. Lanz, C. Hueglin, Y. L. Sun, J. Tian, A. Laaksonen, T. Raatikainen, J. Rautiainen, P. Vaattovaara, M. Ehn, M. Kulmala, J. M. Tomlinson, D. R. Collins, M. J. Cubison, E. J. Dunlea, J. A. Huffman, T. B. Onasch, M. R. Alfarra, P. I. Williams, K. Bower, Y. Kondo, J. Schneider, F. Drewnick, S. Borrmann, S. Weimer, K. Demerjian, D. Salcedo, L. Cottrell, R. Griffin, A. Takami, T. Miyoshi, S. Hatakeyama, A. Shimono, J. Y. Sun, Y. M. Zhang, K. Dzepina, J. R. Kimmel, D. Sueper, J. T. Jayne, S. C. Herndon, A. M. Trimborn, L. R. Williams, E. C. Wood, A. M. Middlebrook, C. E. Kolb, U. Baltensperger, and D. R. Worsnop (2009), Evolution of Organic Aerosols in the Atmosphere, *Science, 326(5959)*, 1525-1529.

Kondo, Y., Y. Miyazaki, N. Takegawa, T. Miyakawa, R. J. Weber, J. L. Jimenez, Q. Zhang, and D. R. Worsnop (2007), Oxygenated and water-soluble organic aerosols in Tokyo, *Journal of Geophysical Research, 112*, D01203.

Kroll, J. H., N. M. Donahue, J. L. Jimenez, S. H. Kessler, M. R. Canagaratna, K. R. Wilson, K. E. Altieri, L. R. Mazzoleni, A. S. Wozniak, H. Bluhm, E. R. Mysak, J. D. Smith, C. E. Kolb, and D. R. Worsnop (2011), Carbon oxidation state as a metric for describing the chemistry of atmospheric organic aerosol, *Nature Chemistry, 3(2)*, 133-139.

Kroll, J. H., J. D. Smith, D. R. Worsnop and K. R. Wilson (2012),Characterization of lightly oxidized organic aerosol formed from the photochemical aging of diesel exhaust particles, *Environmental Chemistry, 9*, 211.

Laborde, M., P. Mertes, P. Zieger, J. Dommen, U. Baltensperger, and M. Gysel (2012),Sensitivity of the Single Particle Soot Photometer to different black carbon types, *Atmospheric Measurement Techniques, 5*, 1031 – 1043.

Lanz, V. A., M. R. Alfarra, U. Baltensperger, B. Buchmann, C. Hueglin, and A. S. H. Prévôt (2007), Source apportionment of submicron organic aerosols at an urban site by factor analytical modelling of aerosol mass spectra, *Atmospheric Chemistry and Physics, 7(6)*, 1503-1522.

Metcalf, A. R., J. S. Craven, J. J. Ensberg, A. Sorooshian, H. T. Duong, H. H. Jonsson, R. C. Flagan, and J. H. Seinfeld (2012), Black Carbon Aerosol over the Los Angeles Basin during CalNex, *Journal of Geophysical Research, 117*, D00V13.

Middlebrook, A. M., R. Bahreini, J. L. Jimenez, and M. R. Canagaratna (2012), Evaluation of Composition-Dependent Collection Efficiencies for the Aerodyne Aerosol Mass Spectrometer using Field Data, *Aerosol Science and Technology, 46 (3)*, 258-271.

Minguillón, M. C., M. Arhami, J. J. Schauer, and C. Sioutas (2008), Seasonal and spatial variations of sources of fine and quasi-ultrafine particulate matter in neighborhoods near the Los Angeles-Long Beach harbor, *Atmospheric Environment, 42*, 7317-7328.

Morgan, W. T., J. D. Allan, K. N. Bower, E. J. Highwood, D. Liu, G. R. McMeeking, M. J. Northway, P. I. Williams, R. Krejci, and H. Coe (2010), Airborne measurements of the spatial distribution of aerosol chemical composition across Europe and evolution of the organic fraction, *Atmospheric Chemistry and Physics, 10(8)*, 4065-4083.

Ng, N. L., M. R. Canagaratna, Q. Zhang, J. L. Jimenez, J. Tian, I. M. Ulbrich, J. H. Kroll, K. S. Docherty, P. S. Chhabra, R. Bahreini, S. M. Murphy, J. H. Seinfeld, L. Hildebrandt, N. M. Donahue, P. F. DeCarlo, V. A. Lanz, A. S. H. Prévôt, E. Dinar, Y. Rudich, and D. R. Worsnop (2010), Organic aerosol components observed in Northern Hemispheric datasets from Aerosol Mass Spectrometry, *Atmospheric Chemistry and Physics, 10 (10)*, 4625-4641.

Ng, N. L., M. R. Canagaratna, J. L. Jimenez, Q. Zhang, I. M. Ulbrich, and D. R. Worsnop (2011), Real-Time Methods for Estimating Organic Component Mass Concentrations from Aerosol Mass Spectrometer Data, *Environmental Science & Technology, 45(3)*, 910-916.

Paatero, P. and U. Tapper (1994), Positive Matrix Factorization - a Nonnegative Factor Model with Optimal Utilization of Error-Estimates of Data Values, *Environmetrics, 5(2)*, 111-126.

Pentti, P. and P. K. Hopke (2003), Discarding or downweighting high-noise variables in factor analytic models, *Journal of Aerosol Science, 490(1-2)*, 277–289.

Seinfeld, J. H. and S. N. Pandis (2006), *Atmospheric Chemistry and Physics: From Air Pollution to Climate Change,* 2nd ed., John Wiley, Hoboken, N. J.

Setyan, A., Q. Zhang, M. Merkel. W. B. Knighton, Y. Sun, C. Song, J. E. Schilling, T. B. Onasch, S. C. Herndon, D. R. Worsnop, J. D. Fast, R. A. Zaveri, L. K. Berg, A. Wiedensohler, B. A. FLowers, M. K. Dubey, and R. Subramanian (2012), Characterization of submicron particles influenced by mixed biogenic and anthropogenic emissions using high-resolution aerosol mass spectrometry: results from CARES, *Atmospheric Chemistry and Physics, 12*, 8131-8156.

Sullivan, A. P., R. E. Peltier, C. A. Brock, J. A. de Gouw, J. S. Halloway, C. Warneke, A. G. Wollny, and R. J. Weber (2006), Airborne measurements of carbonaceous aerosol soluble in water over northeastern United States: Method development and an investigation into water-soluble organic carbon sources, *J. Geophys. Res., 111*, D23S46.

Robinson, A. L., N. M. Donahue, M. K. Shrivastava, E. A. Weitkamp, A. M. Sage, A. P. Grieshop, T. E. Lane, J. R. Pierce, and S. N. Pandis (2007), Rethinking Organic

Aerosols: Semivolatile Emissions and Photochemical Aging, *Science, 315(5816)*, 1259 -1262.

Rudich, Y., N. M. Donahue, and T. F. Mentel (2007), Aging of Organic Aerosol: Bridging the Gap Between Laboratory and Field Studies, *Annu. Rev. Phys. Chem., 58*, 321-352.

Ryerson et al. (in prep), CalNex Overview Manuscript, *Journal of Geophysical Research, XXX* XXX-XXX.

Ulbrich, I. M., M. R. Canagaratna, Q. Zhang, D. R. Worsnop, and J. L. Jimenez (2009), Interpretation of organic components from Positive Matrix Factorization of aerosol mass spectrometric data, *Atmospheric Chemistry and Physics, 9 (9)*, 2891-2918.

Warneke, C., J. A. de Gouw, J. S. Holloway, J. Peischl, T. B. Ryerson, E. Atlas, D. Blake, M. Trainer, and D. D. Parrish (2012), Multiyear trends in volatile organic compounds in Los Angeles, California: Five decades of decreasing emissions, *Journal of Geophysical Research, 117*, D00V17.

Zhang, Q., M. R. Alfarra, D. R. Worsnop, J. D. Allan, H. Coe, M. R. Canagaratna, and J. L. Jimenez (2005), Deconvolution and Quantification of Hydrocarbon-like and Oxygenated Organic Aerosols Based on Aerosol Mass Spectrometry, *Environ. Sci. Technol., 39* 4938 - 4952.

Zhang, Q., J. L. Jimenez, M. R. Canagaratna, J. D. Allan, H. Coe, I. Ulbrich, M. R. Alfarra, A. Takami, A. M. Middlebrook, Y. L. Sun, K. Dzepina, E. Dunlea, K. Docherty, P. F. DeCarlo, D. Salcedo, T. Onasch, J. T. Jayne, T. Miyoshi, A. Shimono, S. Hatakeyama, N. Takegawa, Y. Kondo, J. Schneider, F. Drewnick, S. Borrmann, S. Weimer, K. Demerjian, P. Williams, K. Bower, R. Bahreini, L. Cottrell, R. J. Griffin, J. Rautiainen, J. Y. Sun, Y. M. Zhang, and D. R. Worsnop (2007), Ubiquity and

dominance of oxygenated species in organic aerosols in anthropogenically-influenced Northern Hemisphere midlatitudes, *Geophysical Research Letters, 34(13)*.

Zhang, Q., J. L. Jimenez, M. R. Canagaratna, I. M. Ulbrich, N. L. Ng, D. R. Worsnop, and Y. Sun (2011), Understanding atmospheric organic aerosols via factor analysis of aerosol mass spectrometry: a review, *Analytical and Bioanalytical Chemistry, 401(10)*, 3045-3067.

Table 1. Comparison of Organic Aerosol Data Among Recent Campaigns

Campaign	Location	Type	Date	Reference	Average mid-day OOA/OA (%)	Average mid-day O:C	Average (Range) O:C	Average (Range) OA (μg/m^3)	Average HOA/OA (%)	Average OOA/OA (%)
SOAR	Riverside, CA	ground-based	July 18 - August 14, 2005	Docherty et al. 2008	70-90					
				Docherty et al. 2011		0.42	0.35 (0.19 - 0.53)	19.9 (4.2 - 62.9)	20.7	77.8
MILAGRO	Mexico City	ground-based	March 2006	Aiken et al. 2008		0.48[1]	0.41 (0.15 - 0.75)[1]			
				Aiken et al. 2009	$\geq$ 70			17.3	29	46
PACO	Pasadena, CA	ground-based	Regime I : May - June 2009	Hersey et al. 2011	81	0.42	0.44 (0.14 - 0.52)	3.2 (0.3 - 13.5)	23	77
CalNex-LA	Pasadena, CA	ground-based	May14 - June 16, 2012	Hayes et al. Submitted	70.4	0.41	0.43 (0.1 - 0.84)	7.0 (0.5 - 23.5)	12	66
MILAGRO	Mexico City	airborne	March 2006	DeCarlo et al. 2008			(0.3 - 0.6)[2]	16[3]		
				DeCarlo et al. 2010					20[4]	70[4]
LONGREX and ADIENT	Northern Europe	airborne	May 2008, April, September 2008	Morgan et al. 2010				(1-25)[5]	5-20	80-95
CalNex	Los Angeles, CA	airborne	May 2010	this study			0.31 (0.14-0.64)	2.4 (0.2 - 12.0)	19	81

[1] numbers approximated from Figure 2 in reference

[2]estimated from boxed area (Mexico City urban area) in Figure 8 from reference

[3]approximated from Figure 3 b in reference

[4]estimated from Figure 7 in reference

[5]from Figure 2 in reference

Table 2. Flight Summary Table

Date	Day of Week	Sampling Time (Local)	Region Sampled	OA average (stdev) $\mu g/sm^3$	OA range $\mu g/sm^3$	OA LOD[1] $\mu g/sm^3$	Max BLH[1] (m)
May 19	Wed	11:40 – 15:45	LA Basin	6.94 (1.59)	(3.12 – 12.0)	0.328	979
May 21	Fri	10:57 – 15:05	LA Basin, outflow	2.35 (0.621)	(0.733 – 3.62)	0.150	1209
May 24	Mon	11:01 – 15:03	LA Basin, outflow	1.72 (0.817)	(0.421 – 4.29)	0.141	1749
May 25	Tue	11:27 – 15:31	LA Basin, outflow	1.03 (0.553)	(0.248 – 3.10)	0.152	1519
May 27	Thu	10:59 – 14:45	LA Basin	1.98 (0.630)	(0.630 – 3.79)	0.191	1759
May 28	Fri	10:58 – 15:03	LA Basin	2.27 (0.793)	(0.706 – 4.45)	0.187	1699

[1] LOD = limit of detection = 3 × standard deviation of signal during filter periods

[2] BLH = boundary layer height

Table 3. rBC Normalized Oxidized Factors

Normalized OOA Type	Avg (stdev, std err) for 118.5 - 118.0[1]	Avg (stdev, std err) for 117.0 - 116.5[1]	% Change
SVOOA/rBC	3.84 (0.77, 0.22)	6.07 (1.98, 37)	58.0
LVOOA/rBC	0.67 (0.42, 0.12)	3.08 (1.16, 0.22)	354.7

[1] longitude

Table 4. Pearson's r of SP2 number concentrations of Mode 1 and Mode 2 with mass concentrations of PMF Factors

OA Type	Mode 1	Mode 2
HOA	0.67	0.73
SVOOA	0.83	0.68
LVOOA	0.43	0.16

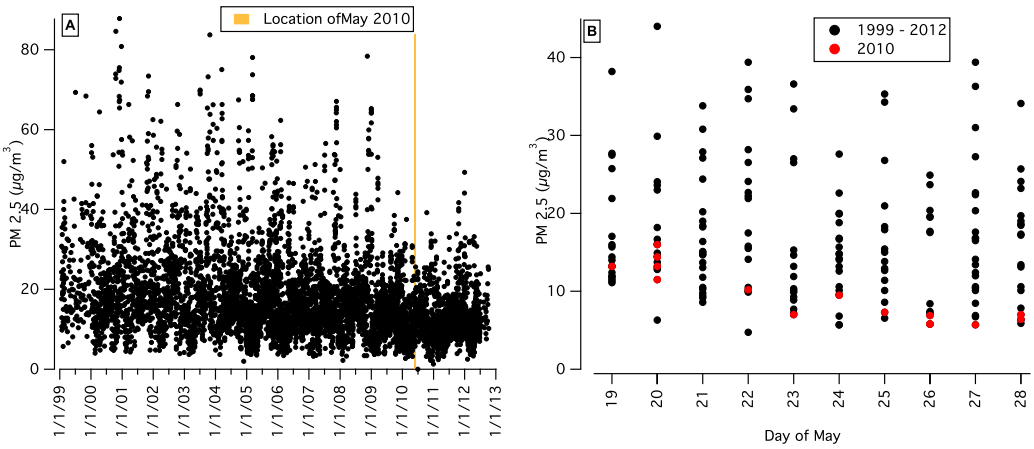

Figure 1. Fourteen years of daily-average PM 2.5 measurements at the Los Angeles - North Main Street (H) CARB monitoring station shown in panel A, and the same data shown for the range of days in May measured by the Twin Otter reported here in panel B.

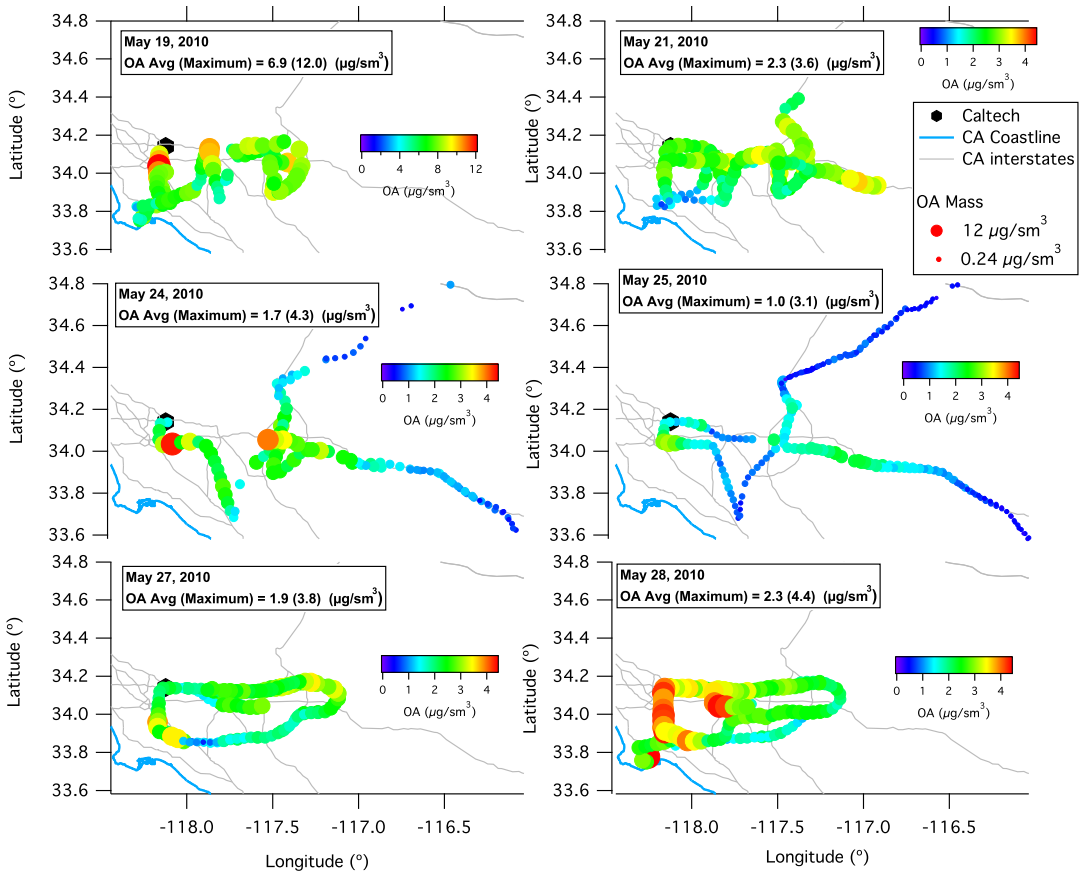

Figure 2. AMS OA mass concentration for each TO flight. Markers are colored and sized according to the mass concentration. The color bar scale are the same except for the May 19 flight, which had higher loadings than the 5 remaining flights.

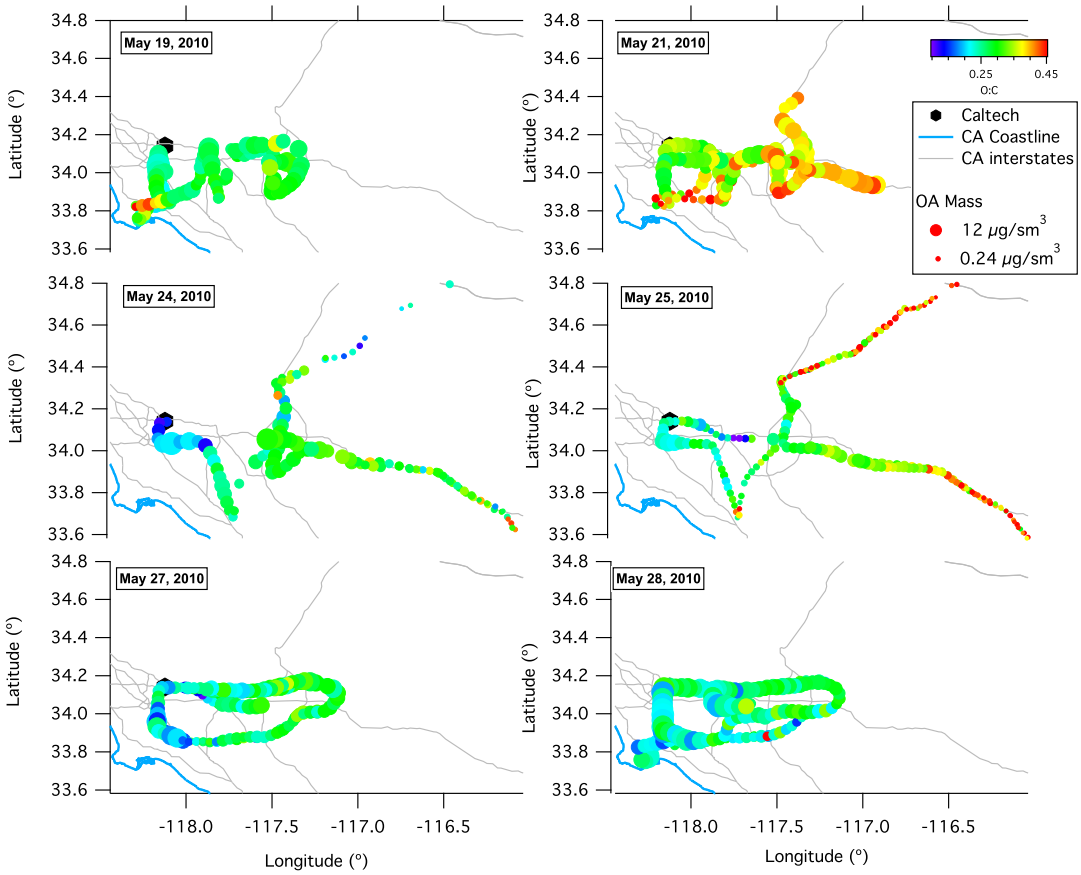

Figure 3. O:C for each TO flight. Markers are colored by O:C and sized according to the mass loading.

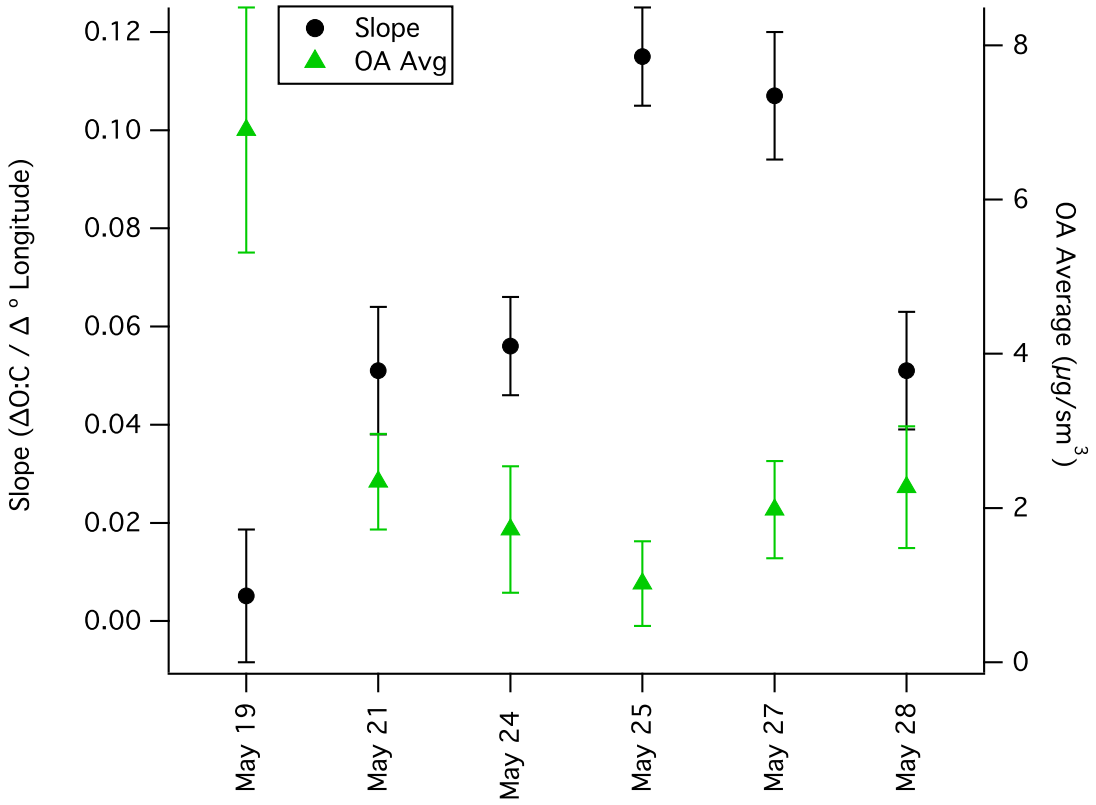

Figure 4. The slope and slope uncertainty from the linear regression of O:C vs longitude are shown in black and the average OA mass concentration is shown in green for each flight.

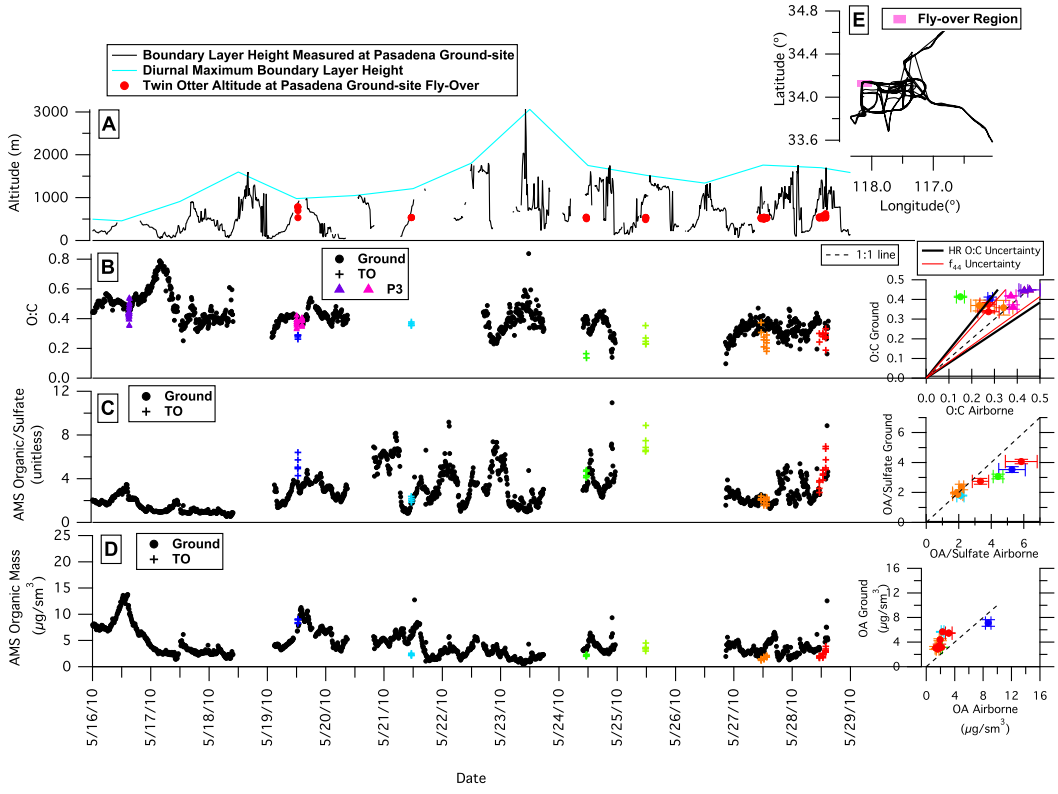

Figure 5. A) PBLH measurements from the Pasadena ground-site and Twin Otter altitude (red markers) during fly-overs versus time. B) Ground (grey line) and airborne fly-over only (black markers) O:C versus time. C) Ground (red line) and airborne fly-over only (black markers) AMS organic/sulfate versus time. D) Ground (green line) and airborne fly-over only (black markers) AMS organic mass concentration versus time. E) Fly-over region is highlighted by pink rectangle.

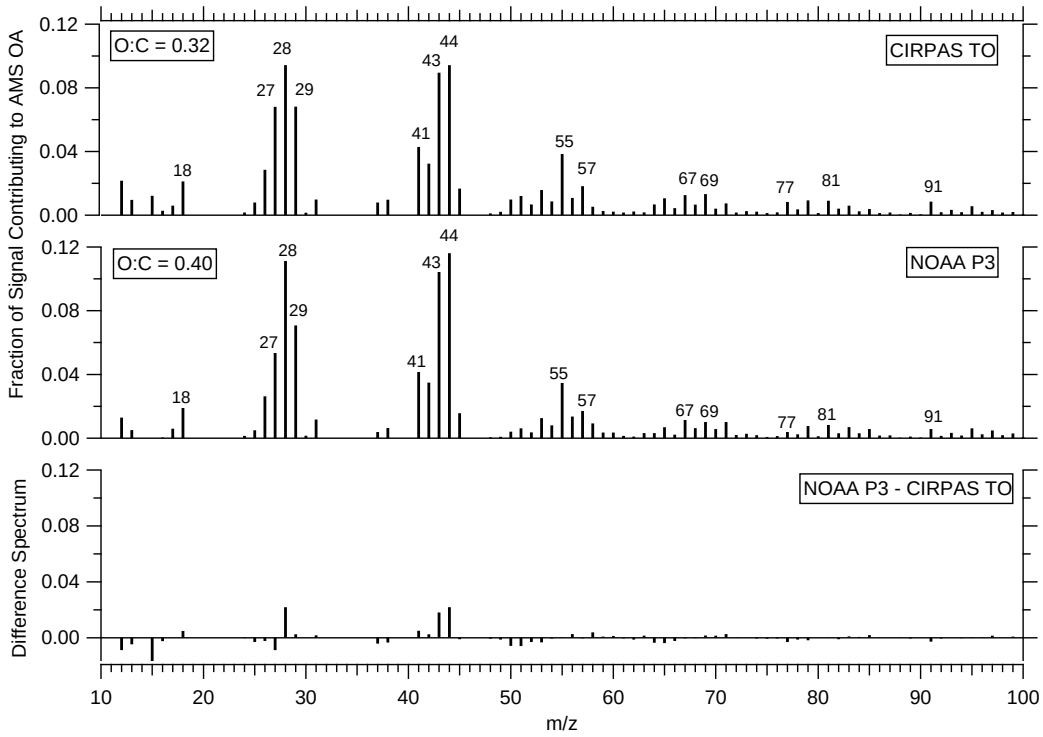

Figure 6. Average AMS mass spectra during the May 19, 2010 intercomparison flight for the CIRPAS TO and NOAA P3. The difference spectrum appears in the bottom panel.

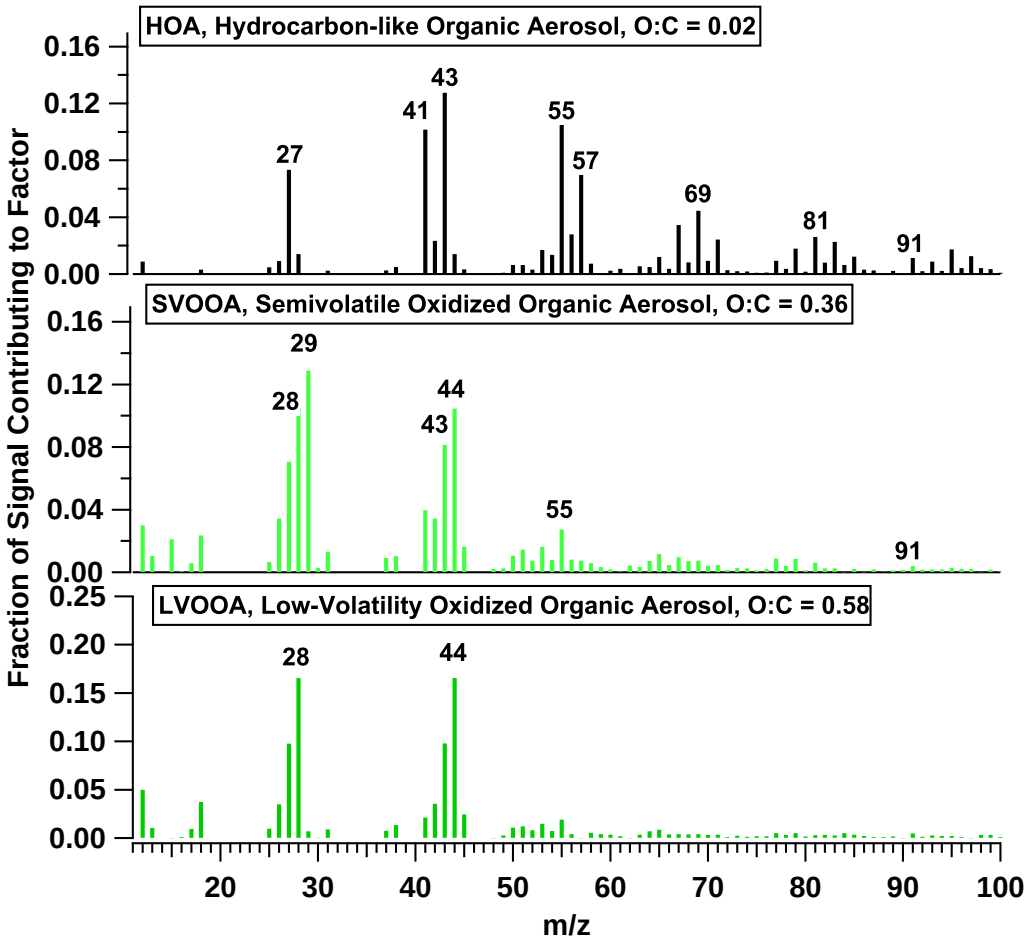

Figure 7. Airborne HOA, SVOOA, and LVOOA factor mass spectral profiles for May 25.

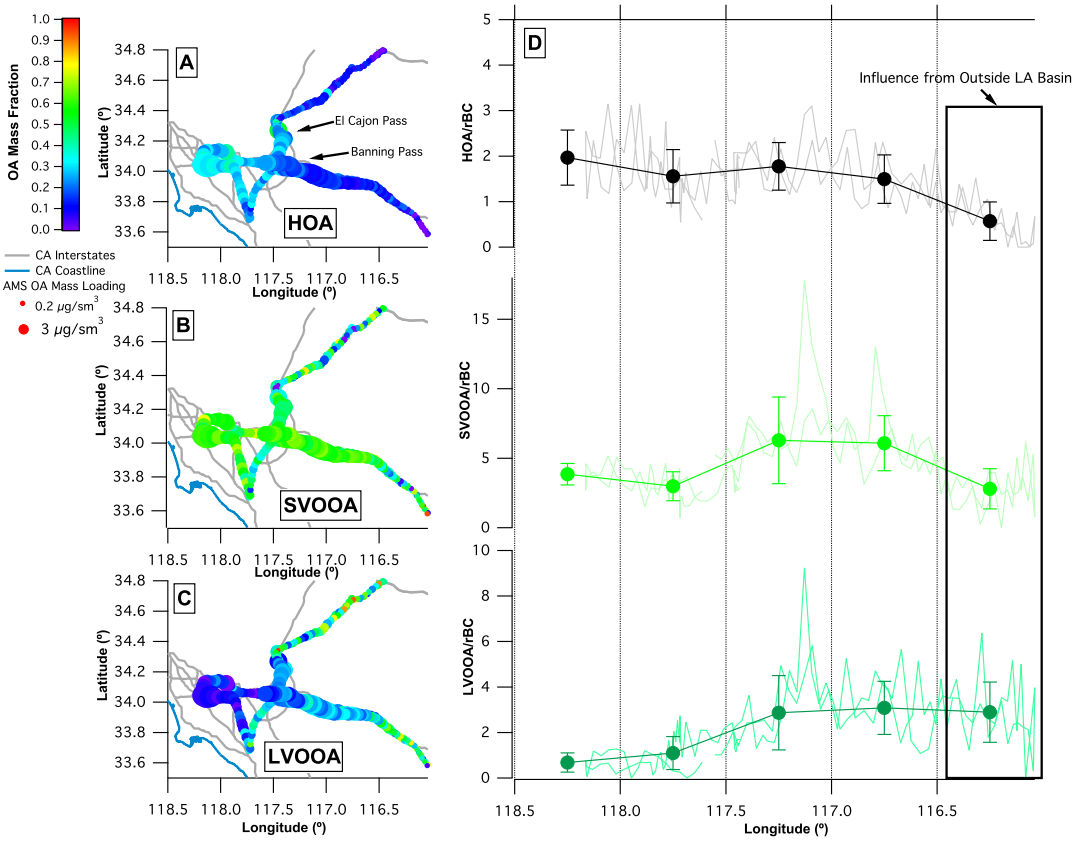

Figure 8. HOA, SVOOA, and LVOOA for May 25. The rBC normalized factors are shown for the Basin and Banning pass data in the right panel. Data to the east of the Banning Pass outflow were influenced by air from the south and are boxed. The data have been averaged into 0.5 ° longitude bins, and both the average and standard deviation (error bars) are shown. The raw data are also displayed to emphasize the variability of the data, especially for the SVOOA and LVOOA normalized factors in the eastern Basin and outflows.

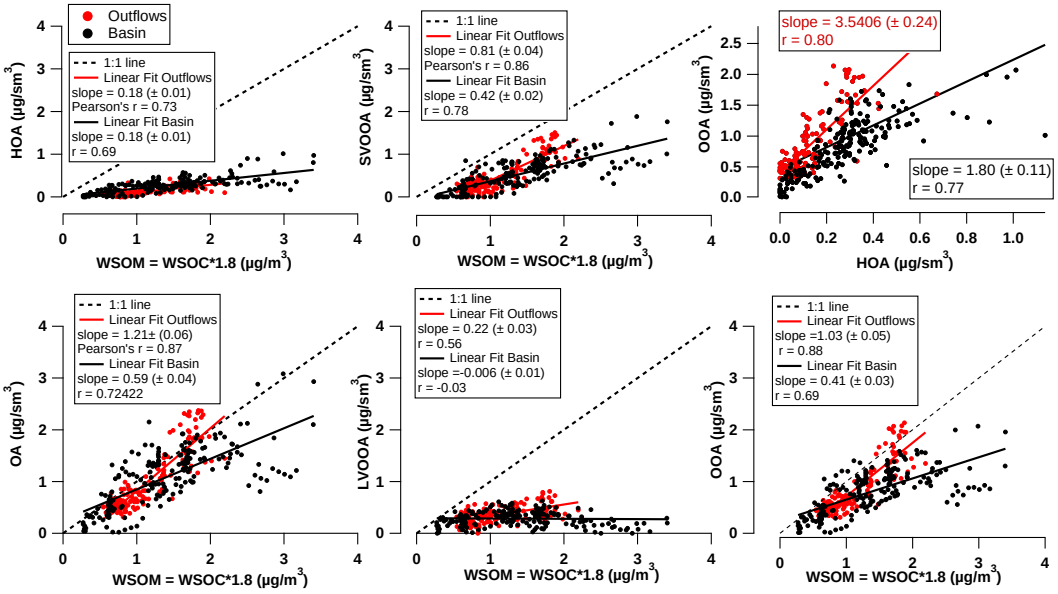

Figure 9. Correlation of OA, HOA, SVOOA, LVOOA, and OOA (SVOOA+LVOOA) vs WSOM and the correlation of HOA with OOA. The best fit line, r, and slope for the Basin (black) outflow (red) are also shown.

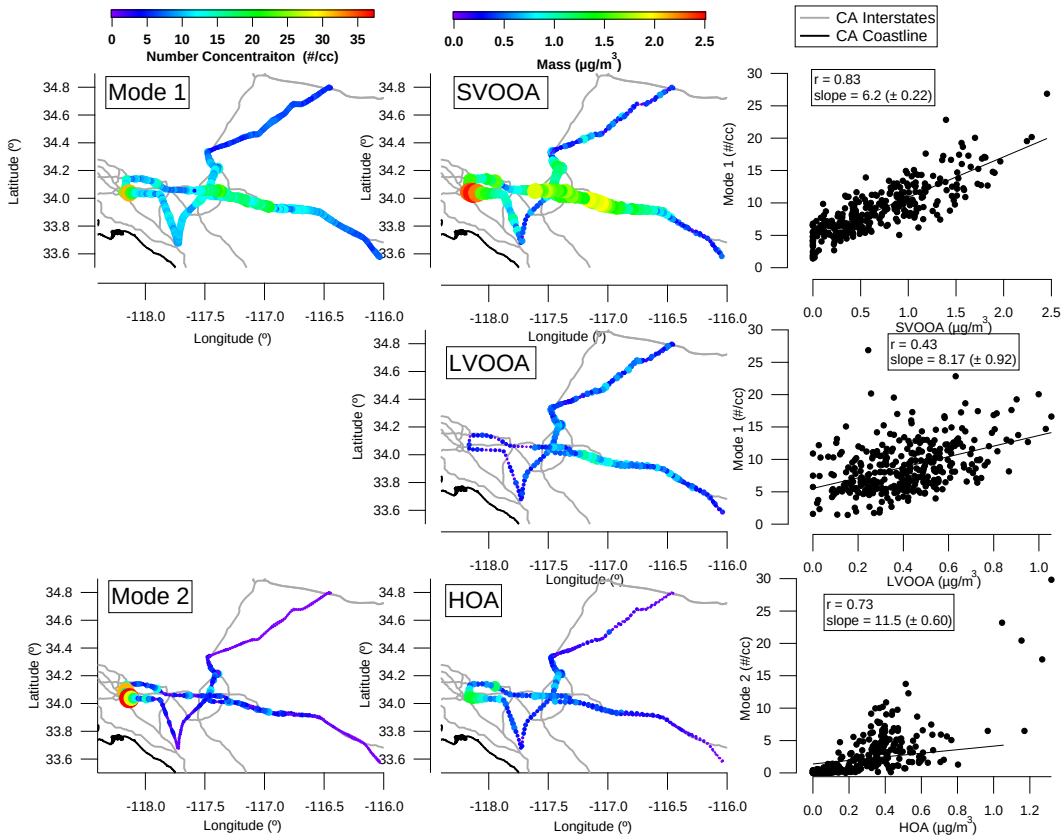

Figure 10. The flight maps of number concentration of mode 1 and mode 2 are plotted with the mass concentration of SVOOA, LVOOA and HOA for May 25. Mode 1 and mode 2 are colored and sized by number concentration, and SVOOA, LVOOA and HOA are colored and sized by mass concentration. The scatter plot of mode 1 vs SVOOA, mode 1 vs LVOOA, and mode 2 vs HOA are also shown with the slope and r value of the best fit line. Note, the PMF factors are colored by organic mass, where as in Figure 8 they are colored by OA mass fraction.

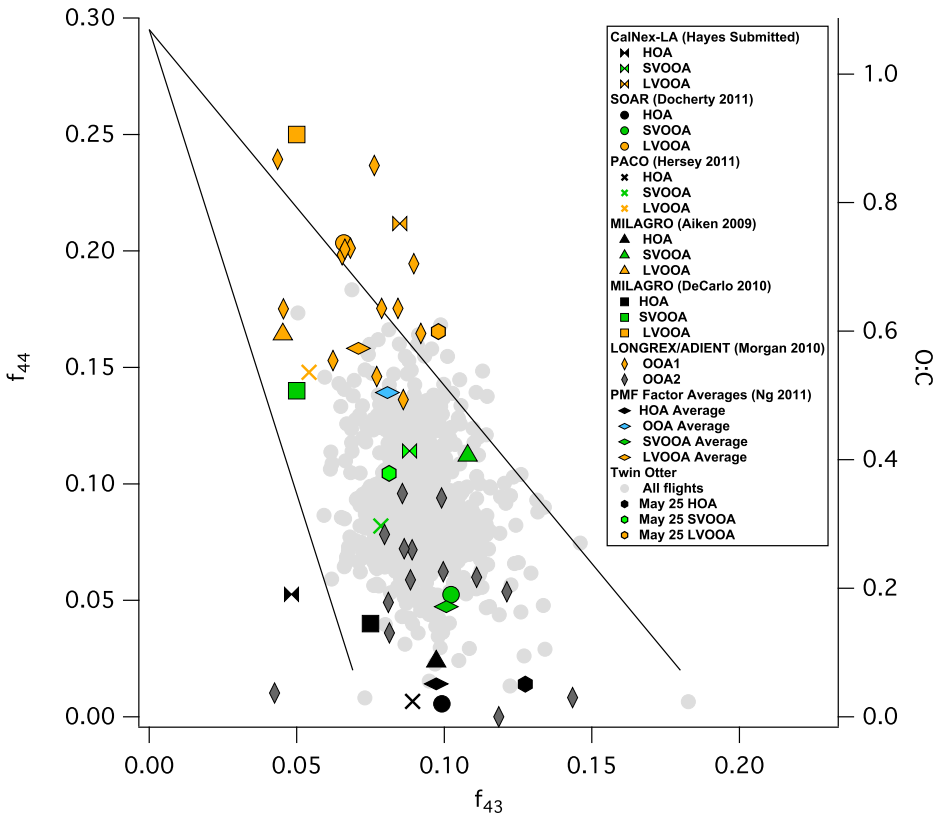

Figure 11. Fraction of OA at *m/z* 44 (f_{44}) versus the fraction of OA at *m/z* 43 (f_{43}) for the Twin Otter data (grey circular points). The three factors from the May 25 flight are shown as hexagon markers. The black, green, and orange markers are the HOA, SVOOA, and LVOOA from the CalNex-LA, SOAR, PACO, and MILAGRO ground-based campaigns, the PMF factor averages from *Ng et al.* [2011], and additionally the MILAGRO and LONGREX/ADIENT aircraft campaigns [*DeCarlo et al.*, 2010; *Morgan et al.*, 2010].

JOURNAL OF GEOPHYSICAL RESEARCH, VOL. ???, XXXX, DOI:10.1029/,

Supplement to "Los Angeles Basin Airborne Organic Aerosol Characterization during CalNex"

J. S. Craven,[1] A. R. Metcalf,[2,7] R. Bahreini,[3,4] A. Middlebrook,[3,4] P. L. Hayes,[3,5] H. T. Duong,[6] A. Sorooshian,[6] J. L. Jimenez,[3,5] R. C. Flagan,[1,2] and J. H. Seinfeld[1,2]

1. AMS and DMA Volume Comparison

he AMS + rBC volume is compared to the DMA volume for the 6 TO flights (Figures S1 and S2. The different colors correspond to different flights. The volume was calculated according to:

$$Volume_{AMS+rBC} = \frac{Mass_{AMS} + Mass_{rBC}}{(1.75)(\chi_{inorganic}) + (1.25)(\chi_{organic}) + (1.8)(\chi_{rBC})} \quad (1)$$

where $\chi_{inorganic}$, $\chi_{organic}$, and χ_{rBC}, are the mass fractions of inorganic, organic and black carbon as measured by the AMS and the SP2. The slope of the AMS + rBC volume to the DMA volume is 0.75, with an r^2 of 0.77. The DMA volume is slightly higher than the volume predicted by the AMS and SP2, however the best fit line is within ± 30% (AMS error) of the 1:1 line. The May 21st flight has the highest offset between the two volumes, and if these data are removed, the remaining data produce a slope of 0.85 with an r^2 of 0.71 (not shown).

2. Positive Matrix Factorization Solution

Signal and error matrices were generated in the Squirrel ToF-AMS Analysis Toolkit (http://cires.colorado.edu/jimenez-group/ToFAMSResources /ToFSoftware/index.html) in IgorPro (WaveMetrics Inc., Lake Oswego, OR, USA), and further matrix preparation was carried out using the PMF evaluation tool (PET) and following recommendations by *Ulbrich et al.* [2009] (http://tinyurl.com/PMF-guide). The size of the matrix for the May 25 PMF was 339 x 73. The columns of the matrix correspond to the signal of organic mass attributed at each m/z according to the UMR fragmentation table [*Allan et al.*, 2004]. The m/z signals with a S/N between 0.2 and 2 were down weighted by a factor or 3, as recommended by *Paatero and Hopke* [2003], and the model error was 0. The m/z 16, 17, 18, 28, and 44 were further down weighted due to m/z 16, 17, 18, and 28 dependence on m/z 44 in the fragmentation table. The time trend in the signals beyond m/z 100 was noisy and removed from PMF analysis.

The PMF was initiated by 50 seeds, and for the p = 1 through p = 4 solutions explored, there was negligible difference between the 50 seeds. The May 25 flight factor profiles for Los Angeles are compared to those from the ground-based CalNex (Pasadena, CA), ground-based and aircraft-based MILAGRO (Mexico City), SOAR (Riverside, CA), and PACO (Pasadena, CA) campaigns [*Hayes et al.*, submitted; *Docherty et al.*, 2011; *Aiken et al.*, 2009; *DeCarlo et al.*, 2010; *Hersey et al.*, 2011], as well as the average PMF factor profiles for 15 urban AMS data sets presented in *Ng et al.* [2011]. The reference mass spectra used in this analysis are available on the Aerosol Mass Spectrometer Database (Unit Mass Resolution) and High Resolution AMS Spectral Database websites (http://cires.colorado.edu/jimenez-group/AMSsd/ and

http://cires.colorado.edu/jimenez-group/HRAMSsd/). The uncentered r correlations for the mass spectral profiles are presented in Table S1. The largest r value for each solution is bolded.

The May 25 flight factor time series are compared to the AMS inorganic mass loadings [*Hersey et al.*, in press], as well as the rBC mass loading [*Metcalf et al.*, 2012]. The person's r for this comparison is listed in Table S2. The largest r value for each solution is bolded.

The $Q/Q_{expected}$ values for the p = 1 though p = 4 solutions are shown in Figure S3. The overall contribution to $Q/Q_{expected}$ versus factor number (p) is shown in the inset (Figure S3). The time trend of $Q/Q_{expected}$ shows that at least 2 factors are needed to describe the variation in the May 25 dataset. The spike just before 11:00 AM and noon is not described well with the p = 1 solution, but is with the p = 2 solution. The change in the time trend of $Q/Q_{expected}$ between p = 2 though p = 4 is minimal. The change in the $Q/Q_{expected}$ for each m/z is significant between the p = 1 and p = 2 solutions. With the additional factor (p = 3 solution) m/z's 29, 30, and m/z 43 are described better. The addition of another factor (p = 4 solution) makes minimal changes in m/z.

The number of factors was chosen to be at least 2 based on the contributions to $Q/Q_{expected}$. The additional factor solution (p= 3) was chosen in part because of the evidence of an HOA factor that was not obvious in the p = 1 and p = 2 solutions. The HOA factor (third factor in the p = 3 solution) had an uncentered r value of 0.98 with the PACO HOA profile (highest r value for all of the solutions), and had consistently higher r values for all reference HOA profiles compared to the remaining OOA reference mass spectra. The correlation in time with rBC had the same r value for the p = 2 and p =

3 solutions. This same factor appeared in the four factor solution (factor 4), indicating that this factor is robust even when the PMF solution is extended to four factors.

The p = 1 solution mass spectral profile has an r value of 0.96 with both the CalNex-Ground SVOOA and the MILAGRO SVOOA mass spectrum, and a high time correlation with nitrate (r=0.84). According to Figure S3, this factor describes most of the variation in the data, and is consistent with ground-based PMF results for the same noon - 4 pm time frame in the LA Basin [*Hayes et al.*, submitted]. However, in the three factor solution, an HOA factor is present (describes the structure in the residual in Figure S3), and an LVOOA factor is resolved in the basin outflows, where O:C is highest and more highly oxidized aerosol is expected from previous analysis [*Duong et al.*, 2011; *Metcalf et al.*, 2012; *Hersey et al.*, in press]. Sulfate and LVOOA have been shown to correlate well when the sulfate represents secondary atmospheric processes [*Lanz et al.*, 2007]. *Ensberg et al.* [in press] estimate that approximately 50% of sulfate on May 25 is attributable to primary and secondary sources within the Basin, and the other 50% is sulfate from boundary conditions. The sulfate contribution from sources within the Basin is likely an upper limit due to potential over estimation of these sources within the Community Multiscale Air Quality (CMAQ version 4.7.1) model. Nevertheless, the contribution of local sources make the correlation between sulfate and LVOOA poor (r = 0.28, Figure S4) . The LVOOA correlates best with nitrate (r = 0.55), but is a weaker correlation than that with the SVOOA and nitrate (r = 0.82). The correlation with LVOOA and nitrate exists likely because of well mixed air masses that the aircraft was sampling.

The 3 factor solution was not uniform across many fpeaks; however, the variation did not change the results and the solution with no rotation was still retained. The mass

spectral profiles and time series for each factor at varying fpeak values is shown in Figures S5 and S6. The different fpeak solutions were correlated to the fpeak = 0 solution, and the time trends in rBC, nitrate, and sulfate as well as the average mass spectral profile solutions for 15 ambient datasets [*Ng et al.*, 2011] in Table S3.

The HOA solution has three fpeak solutions which are essentially the same (fpeak = 0, 0.5 and 1). This is supported by their common mass spectra and correlations in time with rBC (uncentered r and Pearson's r values are on Table S3). The two other solutions for the HOA factor (fpeak = 01 and -0.5) have a worse uncentered r value (r = 0.86 and 0.92) and persons r value (r = 0.74 andr = 0.76) than than with the fpeak = 0 solution.

The LVOOA solution has four fpeak solution which have similar mass spectra (fpeak = -1, -0.5 0, and 0.5), and one that is completely different due to a large increase in m/z 29 (fpeak = 1, see Figure S5, red sticks in second graph.) Pearson's r of LVOOA with sulfate increased with the fpeak = 0.5 and 1 solutions, however since the mass spectral profile is unreasonable, this rules out the fpeak = 1 solution as being feasible. The fpeak = 0.5 solution, which has an improved correlation with sulfate for the LVOOA solution, and has no negative effect on the HOA solution, produces an unreasonable SVOOA mass spectrum and the lowest uncenter r value when compared to the SVOOA average mass spectrum (Table S3 and see Figure S5, yellow sticks in first graph).

The SVOOA solution has an improved uncentered r value for the fpeak = -1 solution, however the Pearson's r with nitrate is decreased, compared to the fpeak = 0 solution. Since there was no consistent improvement across the factors with varying fpeaks, the fpeak = 0 solution was retained.

References

Aiken, A. C., P. F. DeCarlo, and J. L. Jimenez (2007), Elemental Analysis of Organic Species with Electron Ionization High-Resolution Mass Spectrometry, *Analytical Chemistry, 79*, 8350 – 8358.

Aiken, A. C., D. Salcedo, M. J. Cubison, J. A. Huffman, P. F. DeCarlo, I. M. Ulbrich, K. S. Docherty, D. Sueper, J. R. Kimmel, D. R. Worsnop, A. Trimborn, M. Northway, E. A. Stone, J. J. Schauer, R. M. Volkamer, E. Fortner, B. de Foy, J. Wang, A. Laskin, V. Shutthanandan, J. Zheng, R. Zhang, J. Gaffney, N. A. Marley, G. Paredes-Miranda, W. P. Arnott, L. T. Molina, G. Sosa, and J. L. Jimenez (2009), Mexico City aerosol analysis during MILAGRO using high resolution aerosol mass spectrometry at the urban supersite (T0) - Part 1: Fine particle composition and organic source apportionment, *Atmospheric Chemistry and Physics, 9 (17)*, 6633-6653.

Allan, J. D., A. E. Delia, H. Coe, K. N. Bower, M. R. Alfarra, J. L. Jimenez, A. M. Middlebrook, F. Drewnick, T. B. Onasch, M. R. Canagaratna, J. T. Jayne, and D. R. Worsnop (2004), A generalised method for the extraction of chemically resolved mass spectra from Aerodyne aerosol mass spectrometer data, *Journal of Aerosol Science, 35(7)*, 909-922.

DeCarlo, P. F., E. J. Dunlea, J. R. Kimmel, A. C. Aiken, D. Sueper, J. Crounse, P. O. Wennberg, L. Emmons, Y. Shinozuka, A. Clarke, J. Zhou, J. Tomlinson, D. R. Collins, D. Knapp, A. J. Weinheimer, D. D. Montzka, T. Campos, and J. L. Jimenez (2008), Fast airborne aerosol size and chemistry measurements above Mexico City and Central Mexico during the MILAGRO campaign, *Atmospheric Chemistry and Physics, 8(14)*, 4027-4048.

DeCarlo, P. F., I. M. Ulbrich, J. Crounse, B. de Foy, E. J. Dunlea, A. C. Aiken, D. Knapp, A. J. Weinheimer, T. Campos, P. O. Wennberg, and J. L. Jimenez (2010), Investigation of the sources and processing of organic aerosol over the Central Mexican Plateau from aircraft measurements during MILAGRO, *Atmospheric Chemistry and Physics, 10 (12)*, 5257-5280.

Docherty, K. S., A. C. Aiken, J. A. Huffman, I. M. Ulbrich, P. F. DeCarlo, D. Sueper, D. R. Worsnop, D. C. Snyder, R. E. Peltier, R. J. Weber, B. D. Grover, D. J. Eatough, B. J. Williams, A. H. Goldstein, P. J. Ziemann, J. L. Jimenez (2011), The 2005 Study of Organic Aerosols at Riverside (SOAR-1): instrumental intercomparisons and fine particle composition, *Atmospheric Chemistry and Physics, 11 (23)*, 12387-12420.

Duong, H. T., A. Sorooshian, J. S. Craven, S. P. Hersey, A. R. Metcalf, X. Zhang, R. J. Weber, H. Jonsson, R. C. Flagan, and J. H. Seinfeld (2011), Water-soluble organic aerosol in the Los Angeles Basin and outflow regions: Airborne and ground measurements during the 2010 CalNex field campaign, *Journal of Geophysical Research, 116*, D00V04.

Ensberg, J. J., J. S. Craven, A. R. Metcalf, W. M. Angevine, R. Bahreini, J. Brioude, C. Cai, J. A. de Gouw, R. A. Ellis, J. H. Flynn, C. L. Haman, P. L. Hayes, J. L. Jimenez, B. L. Lefer, A. M. Middlebrook, J. G. Murphy, J. A. Neuman, J. B. Nowak, J. M. Roberts, J. Stutz, P. R. Veres, J. M. Walker, and J. H. Seinfeld (in press), Inorganic and black carbon aerosols in the Los Angeles Basin during CalNex, *Journal of Geophysical Research,X*, XXX-XXX.

Hayes, P. L., A. M. Ortega, M. J. Cubison, K. D. Froyd, Y. Zhao, S. S. Cliff, W. W. Hu, D. W. Toohey, J. H. Flynn, B. L. Lefer, N. Grossberg, S. B. Alvarez, B. Rappenglück,

J. W. Taylor, J. D. Allan, J. S. Holloway, J. B. Gilman, W. C. Kuster, J. A. de Gouw, P. Massoli, X. Zhang, J. Liu, R. J. Weber, A. L. Corrigan, L. M. Russell, G. Isaacman, D. R. Worton, N. M. Kreisberg, A. H. Goldstein, R. Thalman, E. M. Waxman, R. Volkamer, Y. H. Lin, J. D. Surrat, T. E. Kleindienst, J. H. Offenberg, S. Dusanter, S. Griffith, P. S. Stevens, J. brioude, W. M. Angevine, and J. L. Jimenez (submitted), Organic Aerosol Composition and Sources in Pasadena, California during the 2010 CalNex Campaign, *Journal of Geophysical Research, XXX*,XXXX-XXXX.

Hersey, S. P., J. S. Craven, K. A. Schilling, A. R. Metcalf, A. Sorooshian, M. N. Chan, R. C. Flagan, and J. H. Seinfeld (2011), The Pasadena Aerosol Characterization Observatory (PACO): chemical and physical analysis of the Western Los Angeles Basin aerosol, *Atmospheric Chemistry and Physics, 11 (15)*, 7417-7443.

Hersey, S. P., J. S. Craven, A. R. Metcalf, J. Lin, T. Lathem, K. Suski, J. Cahill, H. Duong, A. Sorooshian, H. H. Jonsson, A. Nenes, K. A. Prather, R. C. Flagan, and J. H. Seinfeld (in press),Composition and Hygroscopicity of the Los Angeles Aerosol: CalNex, *Journal of Geophysical Research, XXX* XXX-XXX.

Lanz, V. A., M. R. Alfarra, U. Baltensperger, B. Buchmann, C. Hueglin, and A. S. H. Prévôt (2007), Source apportionment of submicron organic aerosols at an urban site by factor analytical modelling of aerosol mass spectra, *Atmospheric Chemistry and Physics, 7(6)*, 1503-1522.

Metcalf, A. R., J. S. Craven, J. J. Ensberg, A. Sorooshian, H. T. Duong, H. H. Jonsson, R. C. Flagan, and J. H. Seinfeld (2012), Black Carbon Aerosol over the Los Angeles Basin during CalNex, *Journal of Geophysical Research, 117*, D00V13.

Ng, N. L., M. R. Canagaratna, J. L. Jimenez, Q. Zhang, I. M. Ulbrich, and D. R. Worsnop (2011), Real-Time Methods for Estimating Organic Component Mass Concentrations from Aerosol Mass Spectrometer Data, *Environmental Science & Technology, 45(3)*, 910-916.

Pentti, P. and P. K. Hopke (2003), Discarding or downweighting high-noise variables in factor analytic models, *Journal of Aerosol Science, 490(1-2)*, 277–289.

Ulbrich, I. M., M. R. Canagaratna, Q. Zhang, D. R. Worsnop, and J. L. Jimenez (2009), Interpretation of organic components from Positive Matrix Factorization of aerosol mass spectrometric data, *Atmospheric Chemistry and Physics, 9 (9)*, 2891-2918.

Table S1. Uncentered r Values for Mass Spectral Profile Comparison of May 25 PMF Solutions

Factor Number (p)	Seed Number	HOA Average (Ng et al. 2011)	HOA CalNex-Ground (Hayes et al. Submitted)	HOA MILAGRO (Aiken et al. 2009)	HOA PACO (Hersey et al. 2011)	HOA SOAR (Docherty et al. 2011)	OOA Average (Ng etl al. 2011)	SVOOA Average (Ng et al. 2011)	SVOOA CalNex-Ground (Hayes et al. Submitted)	SVOOA MILAGRO (Aiken et al. 2009)	SVOOA PACO (Hersey et al. 2011)	SVOOA SOAR (Docherty et al. 2011)	LVOOA Average (Ng et al. 2011)	LVOOA CalNex-Ground (Hayes et al. Submitted)	LVOOA MILAGRO (Aiken et al. 2009)	LVOOA PACO (Hersey et al. 2011)	LVOOA SOAR (Docherty et al. 2011)	May25_w1fact_ms_1_sd_1	May25_w2fact_ms_1_sd_1	May25_w2fact_ms_2_sd_1	May25_w3fact_ms_1_sd_1	May25_w3fact_ms_2_sd_1	May25_w3fact_ms_3_sd_1	May25_w4fact_ms_1_sd_1	May25_w4fact_ms_2_sd_1	May25_w4fact_ms_3_sd_1	May25_w4fact_ms_4_sd_1
1	**1**	0.73	0.86	0.71	0.76	0.57	0.83	0.91	**0.96**	**0.96**	0.92	0.92	0.79	0.84	0.88	0.81	0.86		0.96	0.92	0.96	0.91	0.67	0.90	0.82	0.91	0.63
1	**1**	0.52	0.72	0.51	0.56	0.36	0.86	0.81	**0.94**	0.93	0.86	0.79	0.84	0.92	**0.94**	0.86	0.93	0.96		0.78	0.94	0.97	0.47	0.96	0.75	0.96	0.41
2	**1**	0.91	0.94	0.90	0.92	0.81	0.69	0.93	0.87	0.88	0.89	**0.98**	0.64	0.62	0.67	0.65	0.65	0.92	0.78		0.86	0.71	0.88	0.69	0.80	0.71	0.85
1	**1**	0.60	0.76	0.61	0.62	0.45	0.79	0.86	0.89	**0.92**	0.85	0.86	0.79	0.79	0.89	0.81	0.83	0.96	0.94	0.86		0.84	0.52	0.82	0.93	0.83	0.47
2	**1**	0.47	0.69	0.45	0.51	0.31	0.83	0.74	0.94	0.89	0.82	0.72	0.81	**0.95**	0.91	0.83	0.93	0.91	0.97	0.71	0.84		0.47	1.00	0.57	1.00	0.40
3	**1**	0.96	0.87	0.95	**0.98**	0.94	0.47	0.78	0.65	0.65	0.73	0.84	0.39	0.35	0.34	0.39	0.36	0.67	0.47	0.88	0.52	0.47		0.45	0.45	0.48	1.00
1	**1**	0.46	0.68	0.44	0.49	0.30	0.83	0.73	0.93	0.88	0.81	0.71	0.80	0.96	0.91	0.82	**0.94**	0.90	0.96	0.69	0.82	1.00	0.45		0.54	0.99	0.39
2	**1**	0.56	0.66	0.59	0.57	0.46	0.63	0.76	0.69	0.77	0.72	**0.79**	0.63	0.54	0.71	0.65	0.60	0.82	0.75	0.80	0.93	0.57	0.45	0.54		0.55	0.42
3	**1**	0.48	0.69	0.46	0.52	0.32	0.82	0.74	**0.93**	0.87	0.81	0.73	0.78	**0.93**	0.89	0.81	0.91	0.91	0.96	0.71	0.83	1.00	0.48	0.99	0.55		0.42
4	**1**	0.96	0.85	0.94	**0.97**	0.94	0.43	0.76	0.60	0.60	0.70	0.81	0.36	0.29	0.28	0.35	0.30	0.63	0.41	0.85	0.47	0.40	1.00	0.39	0.42	0.42	

Table S2. Pearson's r Values for Time Series Comparison of May 25 PMF Solutions

Factor Number (p)	Seed Number	AMS Nitrate	AMS Sulfate	AMS Ammonium	AMS Chloride	SP2 rBC mass loading	SP2 Avg Thickness	May25_w1fact_ts_1_sd_1	May25_w2fact_ts_1_sd_1	May25_w2fact_ts_2_sd_1	May25_w3fact_ts_1_sd_1	May25_w3fact_ts_2_sd_1	May25_w3fact_ts_3_sd_1	May25_w4fact_ts_1_sd_1	May25_w4fact_ts_2_sd_1	May25_w4fact_ts_3_sd_1	May25_w4fact_ts_4_sd_1
1	**1**	0.84	0.80	**0.85**	0.78	0.72	-0.72		0.79	0.93	0.94	0.42	0.87	0.62	0.94	0.59	0.87
1	**1**	**0.83**	0.61	**0.83**	0.73	0.38	-0.51	0.79		0.51	0.83	0.70	0.40	0.71	0.85	0.62	0.39
2	**1**	0.68	0.76	0.69	0.65	**0.77**	-0.70	0.93	0.51		0.82	0.17	0.99	0.45	0.81	0.46	0.99
1	**1**	**0.82**	0.77	**0.82**	0.76	0.61	-0.66	0.94	0.83	0.82		0.28	0.73	0.68	0.97	0.48	0.73
2	**1**	**0.55**	0.28	0.54	0.45	0.17	-0.26	0.42	0.70	0.17	0.28		0.14	0.38	0.36	0.67	0.12
3	**1**	0.61	0.71	0.62	0.59	**0.77**	-0.67	0.87	0.40	0.99	0.73	0.14		0.37	0.73	0.44	1.00
1	**1**	**0.66**	0.45	0.65	0.57	0.36	-0.42	0.62	0.71	0.45	0.68	0.38	0.37		0.59	-0.02	0.39
2	**1**	0.82	0.77	**0.83**	0.77	0.59	-0.66	0.94	0.85	0.81	0.97	0.36	0.73	0.59		0.56	0.71
3	**1**	**0.55**	0.48	**0.55**	0.50	0.36	-0.40	0.59	0.62	0.46	0.48	0.67	0.44	-0.02	0.56		0.41
4	**1**	0.60	0.70	0.61	0.58	**0.77**	0.68	0.87	0.39	0.99	0.73	0.12	1.00	0.39	0.71	0.41	

Table S3. Correlations of Factors with varying fpeak values

	n = -1	n = -0.5	n = 0	n = 0.5	n = 1
Mass Spectral Profile Correlation			uncentered r		
Factor 3 (fpeak = 0) with Factor 3 (fpeak= n)	0.82	0.90	1.00	0.99	0.98
Factor 2 (fpeak = 0) with Factor 2 (fpeak= n)	0.99	1.00	1.00	1.00	0.05
Factor 1 (fpeak = 0) with Factor 1 (fpeak= n)	0.98	0.99	1.00	0.63	0.82
HOA (avg Ng 2011) with Factor 3 (fpeak= n)	0.86	0.92	0.96	0.96	0.96
LVOOA (avg Ng 2011) with Factor 2 (fpeak= n)	0.81	0.81	0.81	0.80	0.30
SVOOA (avg, Ng 2011) with Factor 1 (fpeak= n)	0.88	0.87	0.86	0.48	0.73
Time Series Correlation			Pearson's r		
Factor 3 (fpeak = 0) with Factor 3 (fpeak= n)	0.98	1.00	1.00	0.99	0.98
Factor 2 (fpeak = 0) with Factor 2 (fpeak= n)	0.71	0.91	1.00	0.66	0.33
Factor 1 (fpeak = 0) with Factor 1 (fpeak= n)	0.81	0.95	1.00	0.99	0.92
rBC with Factor 3 (fpeak = n)	0.74	0.76	0.77	0.77	0.77
CO with Factor 3 (fpeak = n)	0.70	0.68	0.67	0.65	0.64
NO3 with Factor 1 (fpeak = n)	0.70	0.79	0.82	0.82	0.89
SO4 with Factor 2 (fpeak = n)	-0.05	0.06	0.28	0.73	0.77

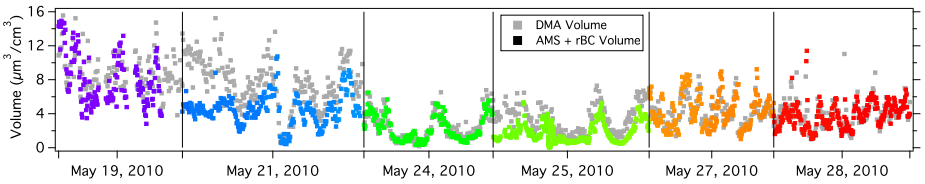

Figure S1. The AMS + rBC and DMA volume for each flight versus time.

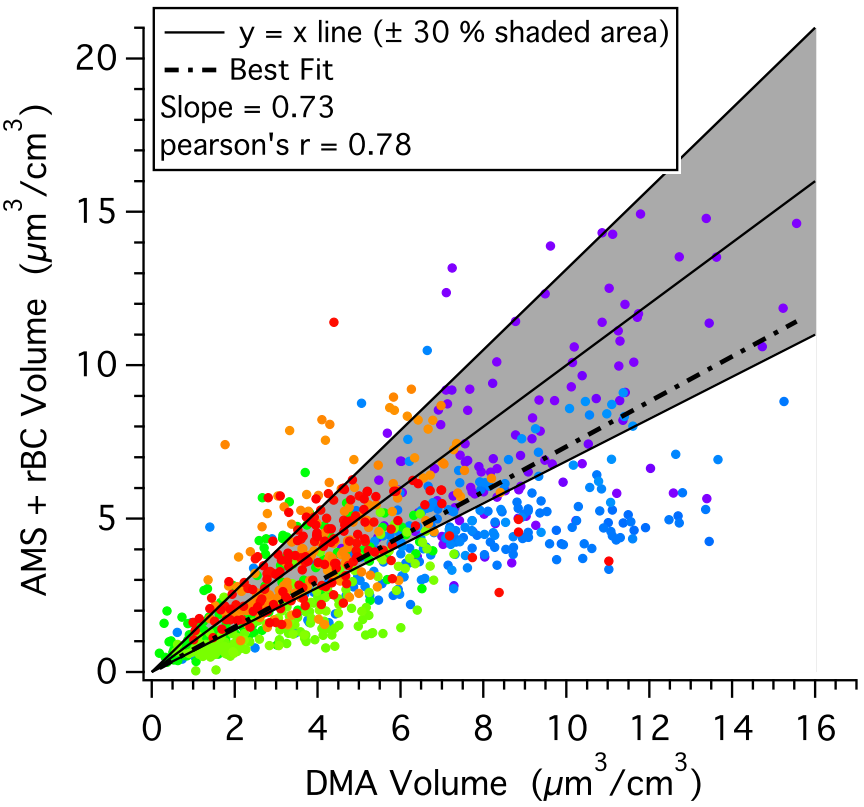

Figure S2. The AMS + rBC volume versus the DMA volume for all 6 flights. The best fit line is shown, in addition to the 1:1 line and the ± 30% shaded area. The blue dots that lie outside of this shaded region are from the May 21, 2010 flight.

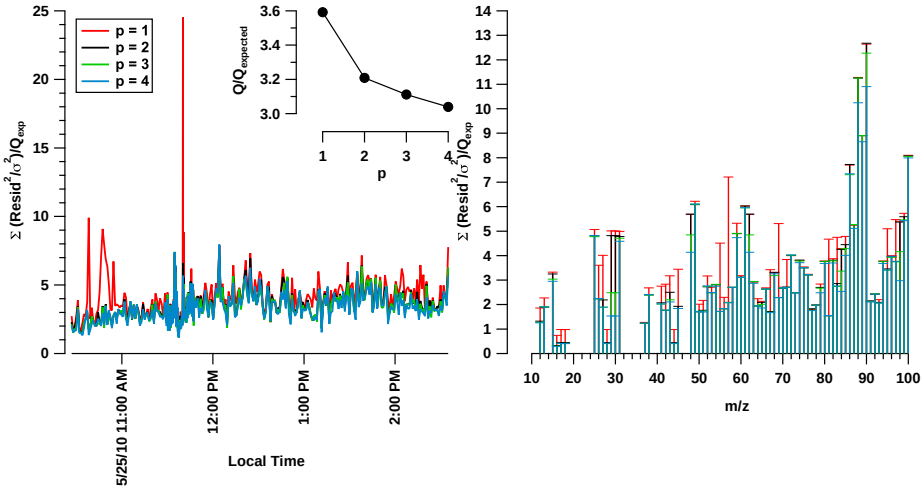

Figure S3. Ratio of $Q/Q_{expected}$ for p = 1, through p = 4 solutions.

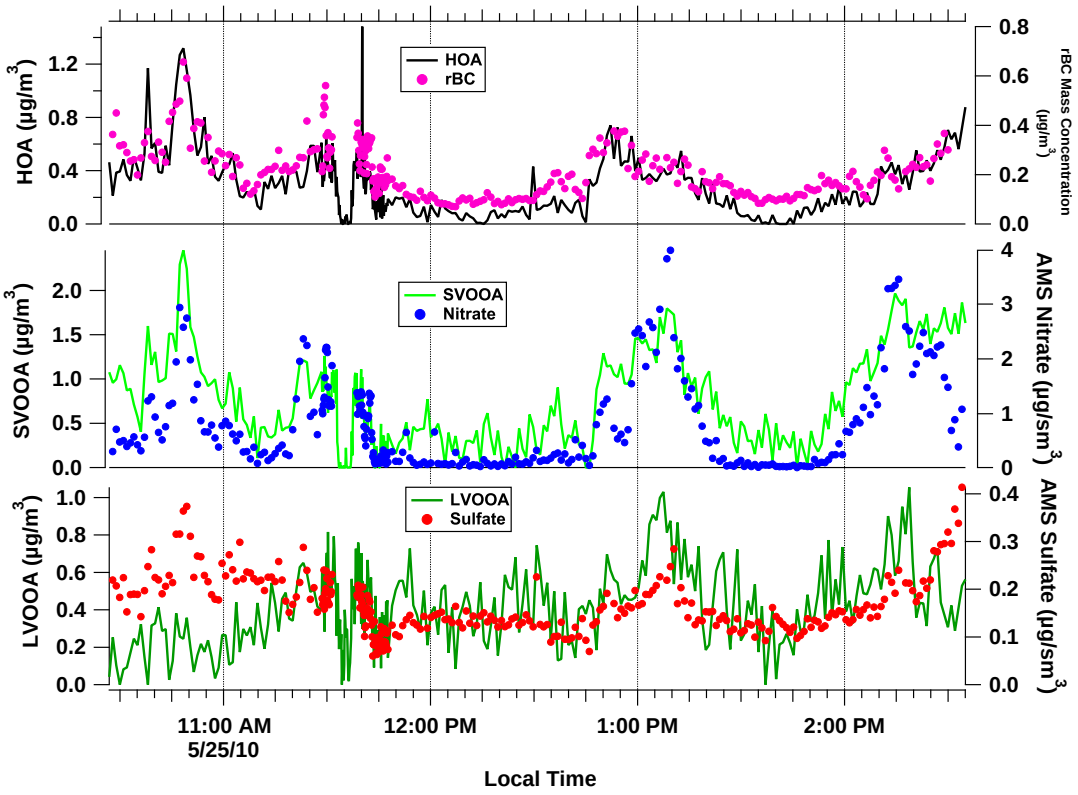

Figure S4. HOA, SVOOA, and LVOOA factors on May 25 with rBC, AMS nitrate, and AMS sulfate.

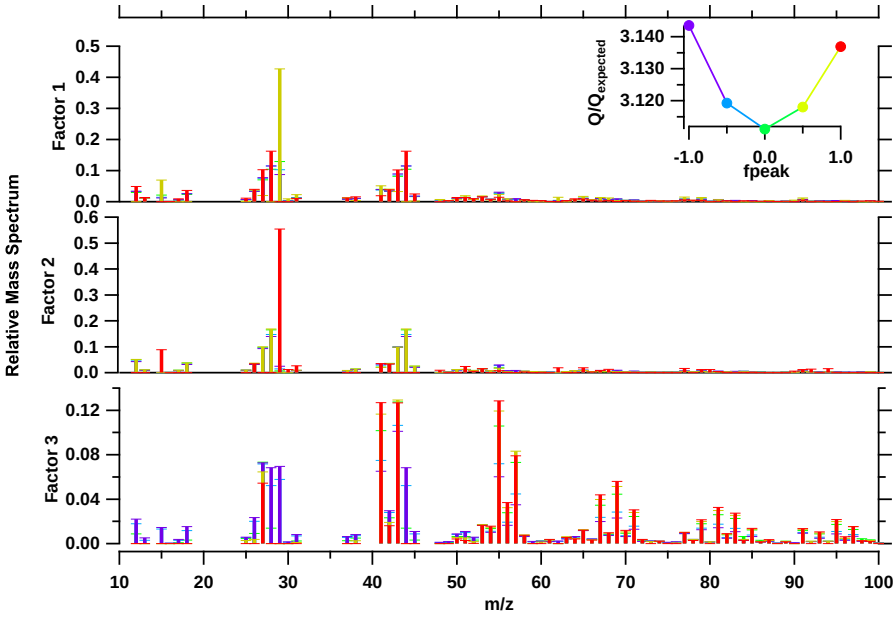

Figure S5. Mass spectrum profile for factors 1, 2, and 3 for varying fpeak values. The contribution to $Q/Q_{expected}$ versus fpeak is also inset. The colors correspond to the different fpeak values.

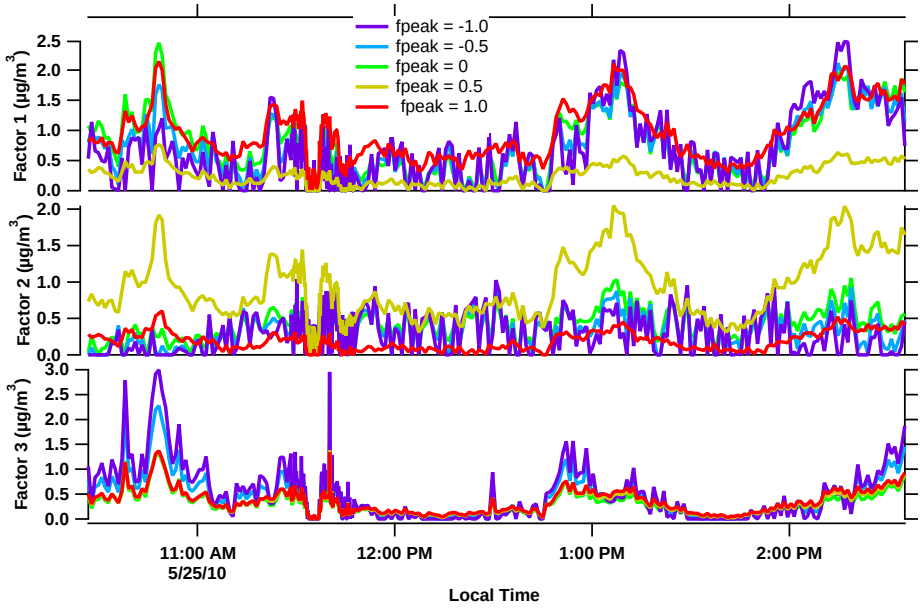

Figure S6. The time series for factors 1, 2, and 3 for varying fpeak values. The colors correspond to the different fpeak values, and match that of figure S5

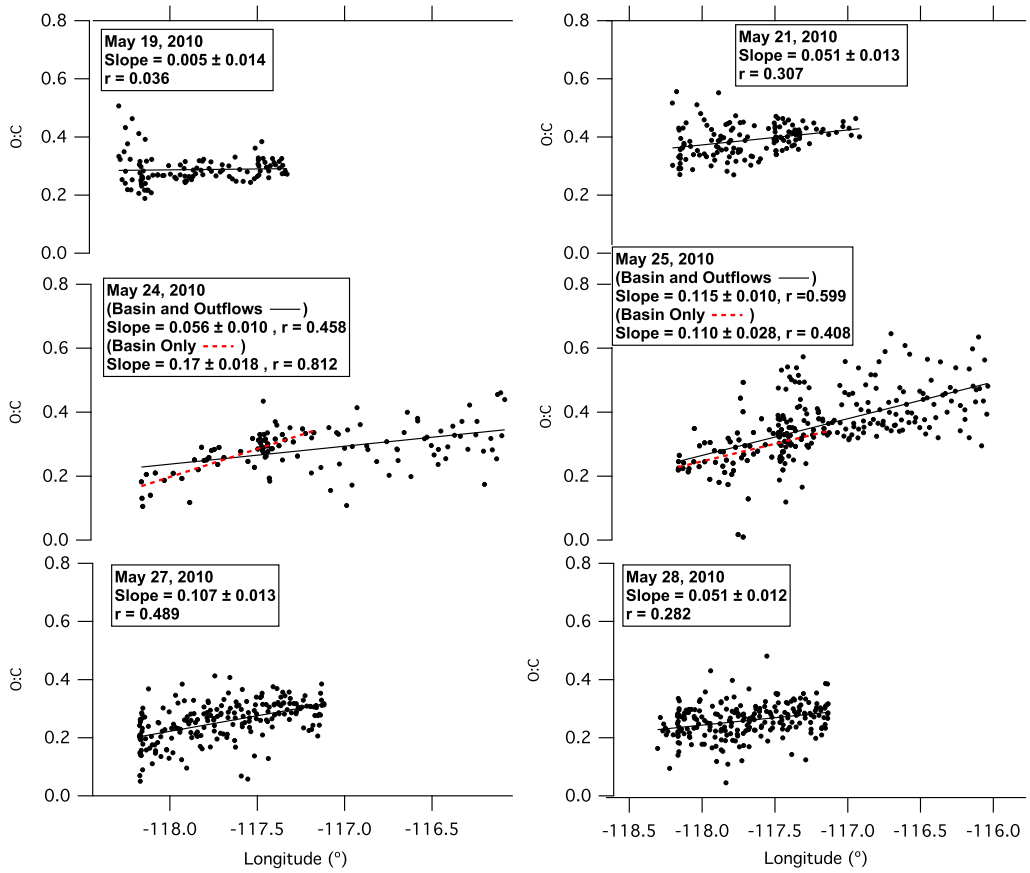

Figure S7. O:C vs longitude for each TO flight.

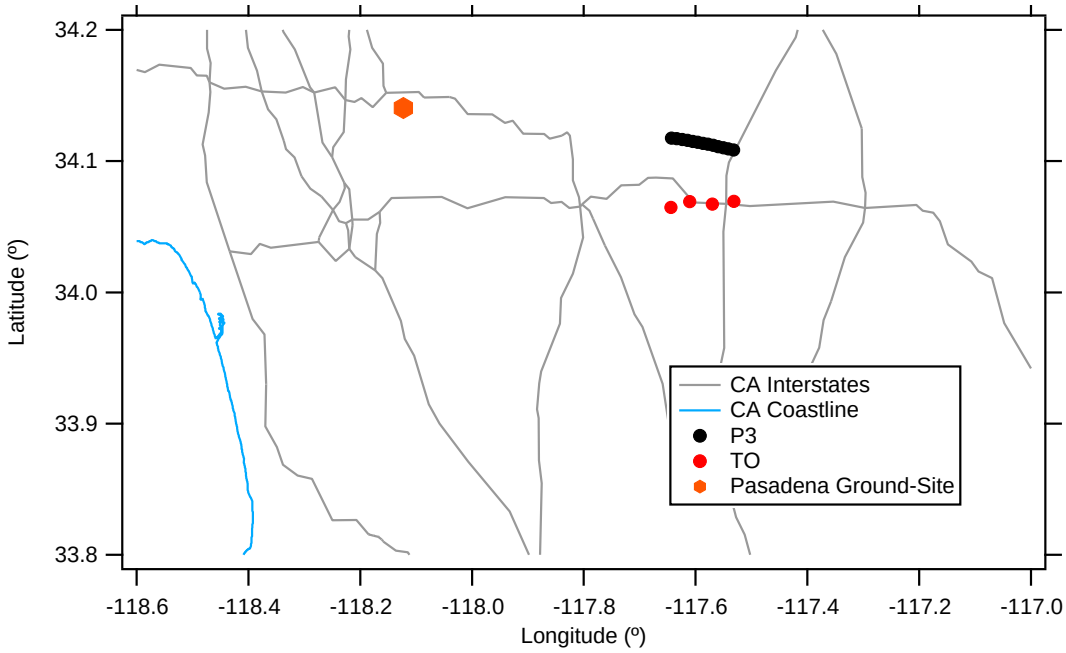

Figure S8. Location of TO and P3 aircraft during airborne mass spectral inter comparison on May 19. The P3 sampled 15 minutes after the TO.

Chapter 10

Conclusions and Future Work

The focus of this thesis is the quantification of submicron aerosol composition using the Aerodyne aerosol mass spectrometer, both in field and chamber studies, in an effort to better understand how atmospheric aerosol are formed and age. The organic mass spectrum is further characterized using the receptor model, positive matrix factorization. Several important scientific questions regarding aerosol formation and aging are answered using the data gathered by the AMS including confirmation of the chemical mechanism of dodecane SOA formation under low NO conditions, proposal of AMS tracer ions for peroxyhemiacetal formation in the aerosol, calculation of organic and inorganic aerosol emission ratios from a wildfire plume, quantification of the amount of freshly produced versus transported organic aerosol in Pasadena and in the greater Los Angeles Area, validation of CMAQ regional model outputs, calculation of rBC coating composition, and calculation of the hygroscopicity parameter, κ_{org}, for atmospheric organic aerosol in Pasadena and greater Los Angeles.

10.1 Dodecane Secondary Organic Aerosol Formation under Low NO Conditions

In chapter 2, the chemical mechanism for dodecane oxidation under RO_2 + HO_2 is discussed. The gas-phase CIMS ions are compared to a photooxidation model and also to high-resolution ions from the AMS, confirming the gas-phase chemistry. The particle-phase composition exhibits many distinct ions greater than m/z 100,

many of which contain 12 carbons, indicating close to molecular level fragments being identified in the AMS. Strong evidence of PHA formation is provided by tracer ions in the particle-phase mass spectra.

While traditionally used to deconvolve the sources of pollution in ambient measurements, PMF is utilized to better understand secondary organic aerosol formation from dodecane under low NO conditions. The PMF results, discussed in chapter 3, exhibit three factors, that correlate with MOVI-CIMS particle-phase molecular ion traces and CIMS gas-phase molecular ion traces, linking the variation in the AMS mass spectra to molecular-level information. Factor 1, 2, and 3 represent the gas-phase partitioning of initial oxidation products with two functional groups, further oxidized tri-functionalized products, and extended oxidation products quadruply functionalized respectively. The three factors also include evidence of oligomerization in the aerosol, perhaps from PHA formation. The PMF results on the Van Krevelen diagram reveal that the slope of -1.78 for dodecane low NO oxidation results from a combination of organic hydroperoxide and ketone/aldehyde functionalization, rather than solely due to carboxylic acid formation with increased oxidation in the chamber.

10.1.1 Future Work: Chemical Conversion in the Condensed-Phase

Condensed-phase chemical conversion is important in the alkane chemical mechanism. Many atmospheric chemistry models do not account for condensed-phase chemistry, because it is so difficult to isolate and unravel in the laboratory. Aerosol phase mechanisms will likely be important to closing the gap between model predictions and observations. There is ongoing work that involves including PHA formation in a kinetic model for SOA formation of dodecane under low NO. The size distributions predicted by the model do not compare well unless the condensed phase chemical reactions, such as PHA formation and oligomerization, are included.

It is difficult to obtain high time-resolution molecular level information from offline analysis techniques, but the high-resolution AMS PMF analysis provides a good

platform for understanding the important variations in the aerosol-phase, something that cannot be learned from the total organic mass trace and O:C and H:C parameters alone. Although the AMS does not provide molecular level information, more chamber studies could be analyzed using the PMF to aid in chemical interpretation and discovery of tracer ions for the AMS mass spectrum.

In the chamber, the initial source of the aerosol is known (the hydrocarbon that was injected), however the subsequent oxidation products may or may not be known. If particle-products are hypothesized, one can use this information and do a mixed chemical mass balance (sources are known) and PMF analysis to help tease out additional information on the products partitioning into the particle. Sampling standards of the known particle-phase products would help constrain the mixed CMB-PMF analysis.

An additional future work involves analyzing gas-phase CIMS measurements in tandem with the aerosol-phase AMS measurements using PMF. In chapters 2 and 3, the particle-phase PMF is compared to single ions from the CIMS, but it would helpful in future work to see if the PMF factors compared.

10.2 Field Studies: San Luis Obispo Biomass Burning Experiment (SLOBB, 2009), Pasadena Aerosol Characterization Observatory (PACO, 2009), and California Nexus: Research at the Nexus of Air Quality and Climate Change (CalNex, 2010)

In Chapter 4 the submicron aerosol composition for an isolated wildfire plume in central California during the San Luis Obispo Biomass Burning Experiment (SLOBB, 2009) is discussed. The smoke plume rose to 1700 m and was clearly visible 4 hours after ignition, which allowed for sampling of both fresh and aged smoke, and study of biomass burning aerosol evolution in the atmosphere. The organic and inorganic

aerosol samples closest to the source of the fire were utilized to calculate initial emission ratios, which are important parameters for constraining atmospheric chemical transport models. In the zero - 1.5 h smoke age the OA/CO_2 ratio decreased and evaporation was dominant, whereas after 2 h, the OA/CO_2 ratio had a slight increase. This is compared to samples from the tropical Yucatan plume [Yokelson et al. 2007], where an increase of OA/CO_2 was observed. These plume samples were, however, already 30 minutes old, had a twice the OH concentration, the RH was higher, and there was higher incident UV radiation. Clearly there are several factors influencing organic aerosol formation in a wildfire plume.

In chapter 5, size-resolved aerosol composition, gas-phase, and meteorology measurements are reported for Pasadena during PACO in Summer 2009 and in chapters 6 - 9 for the greater LA Basin during CalNex in May 2010. The aerosol measurements made during summer 2009 are split into three regimes based on meteorological and chemical characteristics: spring time (May 22 - June 12), Early Summer/Marine influence (Jun 18 - Jul 7), Photochemically active (Jul 10 - August 4), and Station Fire influence (Sept 28 - June 2). The organic aerosol during May 2010 was relatively clean, although spatial patterns of OA oxidation are made within the Basin and into the outflows. In both PACO and CalNex, the organic aerosol is deconvolved into HOA, SVOOA, and LVOOA. Sized resolved aerosol composition measurements are used to calculate the κ_{org} from DASH measurements, which measures the wet and dry diameters at RH values of 74% and 92%. The κ_{org} for Pasadena during the summer of 2009 was higher (0.14) than previously reported values. During CalNex, κ_{org} and found to be 0.1 in the western Basin and 0.0 in the outflows. For the CalNex study, a bimodal rBC-containing aerosol distribution reveal two types of aerosol: one thickly coated, and one thinly coated. The thinly coated aerosol correlats with the HOA, while the thickly coated aerosol correlats with the SVOOA. The correlation of different types of organic links the aerosol composition to its mixing state. Sulfate measurements from the CalNex 2010 study are compared to predicted sulfate measurements in chapter 7. The Twin Otter sulfate is overpredicted by 55% - 268 %. The CMAQ results reveal that long-range transport of sulfate constitutes 22 - 82 %

of the sulfate measured in the basin. Updated emission inventories of sulfate make this fraction even higher.

10.2.1 Future Work Motivated by Field Measurements

During the wildfire plume evolution, the ammonium nitrate increased, but the increase did not fully explain the decrease in HNO_3 and NH_3 in the gas-phase. It is hypothesized that these gases could have condensed on smaller particles to form ammonium nitrate, outside of of the AMS range, that had slow growth due to the low relative humidity (11–26 %). Future work involves design and testing a specialized inlet to improve the transmission of the smaller sizes (in the sub-50 nm d_{va} range) for the AMS. Also, making airborne measurements of number concentrations of small particles in wildfire plumes may help clarify the evaporation versus condensation processes that could be occurring in early wildfire plume evolution.

There are many factors that can contribute to and help explain varying biomass burning OA plume evolution, and these include: smoldering vs flaming condition of the burn, fuel type burned, incident UV light, surrounding relative humidity, and amount of OH generated. The effect of these conditions on biomass burning aerosol formation are being explored in ongoing analysis of data acquired during the 2009 Los Angeles Station Fire. In the AMS there are two wildfire smoke tracers, potassium (K+) and levoglucosan ($C_2H_4O_2$ at m/z 60). A high fraction of potassium in the AMS spectrum has been shown in flaming conditions, whereas a high fraction of levoglucason is consistent with a mixture of flaming and smoldering [Lee et al. 2010]. The future work will be to design a metric where the relative amount of these two aerosol tracers can help explain the amount of biomass burning aerosol produced based on the flaming and/or smoldering conditions of their emission. This will require the design of a technique for better quantification of potassium in the AMS since it is a slowly vaporizing species.

One of the unanswered questions remaining from the CalNex study is if there is a difference in refractive index between fresh versus aged OA, and if this would change

the radiative absorption enhancement of black carbon-containing aerosol. Currently, there is a discrepancy between laboratory and atmospherically observed radiative absorption enhancements [Cappa et al. 2012]. Future work would involve running black carbon seeded experiments in the chamber where the coating composition is aged, analyzed, and categorized into HOA, SVOOA, and LVOOA-like levels of oxidation, and then compared to any changes in absorbance.

Bibliography

[Cappa et al. 2012] Christopher D. Cappa,Timothy B. Onasch, Paola Massoli, Douglas R. Worsnop, Timothy S. Bates, Eben S. Cross, Paul Davidovits, Jani Hakala, Katherine L. Hayden, B. Tom Jobson, Katheryn R. Kolesar, Daniel A. Lack, Brian M. Lerner, Shao-Meng Li, Daniel Mellon, Ibraheem Nuaaman, Jason S. Olfert, Tuukka Petaja, Patricia K. Quinn, Chen Song, R. Subramanian, Eric J. Williams, Rahul A. Zaveri (2012), "Radiative Absorption Enhancements Due to the Mixing State of Atmospheric Black Carbon", *Science,* 337, 1078 – 1081, DOI: 10.1126/science.1223447.

[IPCC 2007] Forster, P., V. Ramaswamy, P. Artaxo, T. Berntsen, R. Betts, D.W. Fahey, J. Haywood, J. Lean, D.C. Lowe, G. Myhre, J. Nganga, R. Prinn, G. Raga, M. Schulz and R. Van Dorland (2007), "Changes in Atmospheric Constituents and in Radiative Forcing. In: Climate Change 2007: The Physical Science Basis. Contribution of Working Group I to the Fourth Assessment Report of the Intergovernmental Panel on Climate Change" [Solomon, S., D. Qin, M. Manning, Z. Chen, M. Marquis, K.B. Averyt, M.Tignor and H.L. Miller (eds.)]., Cambridge University Press, United Kingdom and New York, NY, USA.

[Lee et al. 2010] Taehyoung Lee, Amy P. Sullivan, Laura Mack, Jose L. Jimenez, Sonia M. Kreidenweis, Timothy B. Onasch, Douglas R. Worsnop, William Malm, Cyle E. Wold, Wei Min Hao, and Jeffrey L. Collett, Jr. (2010), "Chemical Smoke Marker Emissions During Flaming and Smoldering Phases of Laboratory Open Burning of Wildland Fuels", *Aerosol Science and Technology,* 44:iÐv, DOI: 10.1080/02786826.2010.499884.

[Yokelson et al. 2007] R. J. Yokelson, T. Karl, P. Artaxo, D. R. Blake, T. J. Christian, D. W. T. Griffith, A. Guenther, and W. M. Hao (2007), "The Tropical Forest and Fire Emissions Experiment: Overview and Airborne Fire Emission Factor Measurements", *Atmospheric Chemistry and Physics,* 7, 5175 – 5196,www.atmos-chem-phys.net/7/5175/2007/.

[Zhang et al. 2007] Q. Zhang, J. L. Jimenez, M. R. Canagaratna, J. D. Allan, H. Coe, I. Ulbrich, M. R. Alfarra, A. Takami, A. M. Middlebrook, Y. L. Sun, K. Dzepina, E. Dunlea, K. Docherty, P. F. DeCarlo, D. Salcedo, T. Onasch, J. T. Jayne, T. Miyoshi, A. Shimono, S. Hatakeyama, N. Takegawa, Y. Kondo, J. Schneider, F. Drewnick, S. Borrmann, S. Weimer, K. Demerjian, P. Williams, K. Bower, R. Bahreini, L. Cottrell, R. J. Griffin, J. Rautiainen, J. Y. Sun, Y. M. Zhang, and D. R. Worsnop (2007), "Ubiquity and Dominance of Oxygenated Species in Organic Aerosols in Anthropogenically-influenced Northern Hemisphere Midlatitudes", *Geophysical Research Letters,* 34, L13801, doi:10.1029/2007GL029979.

Appendix A

Electronic Noise Identification and Removal of AMS Data during CalNex

During the CalNex campaign, the Caltech c-ToF-AMS experienced occasional electronic noise interference. The source of the noise was not identified; however, a common source of electronic noise is cell phone interference. The data are still usable as long as the effect of the noise on the data is identified and the noise is systematically isolated from the data processing. The noisiness was first realized during processing of particle time of flight data (PTOF), and then again during PMF processing. In the PTOF sticks data processing, the electronic noise presents itself as a unusual waveform at every m/z (a sample from one m/z is shown in Figure A.1), and manifests itself in negative or unusual mass distributions (squirrel TOF toolkit functions). In order to get a usable mass distribution, the runs with this type of noise need to be identified and removed.

The electronic noise was an issue again during PMF diagnostics, in which the user has to decipher the structure in the Q time series plot. If there is structure, then another factor may be required to adequately describe the variation in the data. The structure becomes questionable when the Q versus time graph has spikes in it two orders of magnitude higher than expected (Figure A.2C). One tool to systematically remove data that is affected by electronic noise is to plot up the integrated baseline for an m/z with a large signal (m/z 43 in the CalNex dataset) in the open, closed, and difference mass spectra. An elevation in the integrated baseline could indicate a

spike in electronic noise. Figure A.2A shows an illustration example of the integrated baseline at m/z 43 in the closed spectrum. The integrated baseline is not a usual step in AMS mass spectra analysis, but is in the 'Misc.' Tab of the ToF-AMS Analysis Toolkit. Figure A.2 shows that the integrated baseline and the Q versus time plot clearly overlap. Notice that the structure in organic mass loading versus time at m/z 43 does not necessarily reflect this electronic noise (Figure A.2D). The length of time the noise persisted can affect the data. The PMF results with and without the noise show a large difference in the Q diagnostics (Figure A.3). The effect of noise is not obvious from the mass spectra and time series results of each factor (lower portion of Figure A.3), but the factors are different with the noise removed. The effect of noise is clearly seen in the Q versus time series plot (top left part of Figure A.3), and Q versus m/z plot (top right part of Figure A.3).

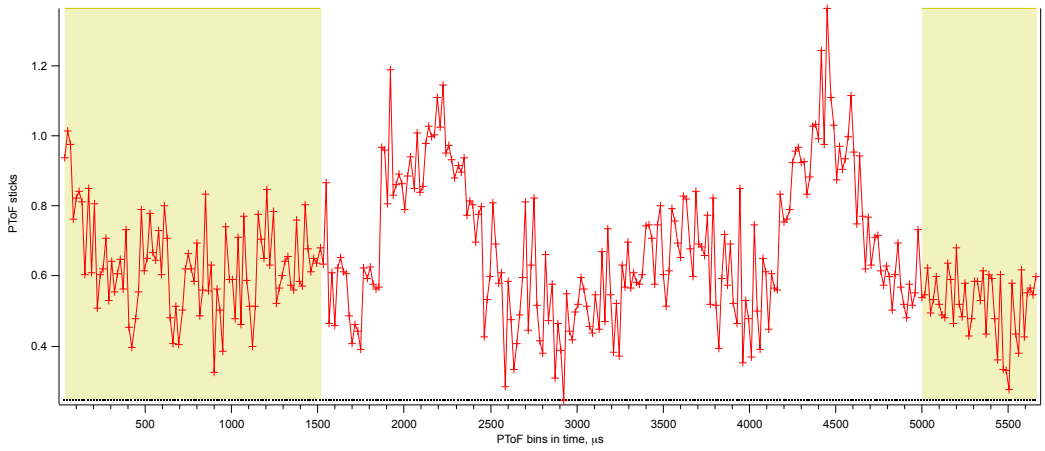

Figure A.1: The PTOF sticks data for one mass is plotted in time (the bottom axis is the particle time-of-flight space). A signal here usually means that either air or aerosol is being detected at this particular mass. This signal however, is indicative of electronic noise interfering with the measurement and means this data needs to be removed from analysis.

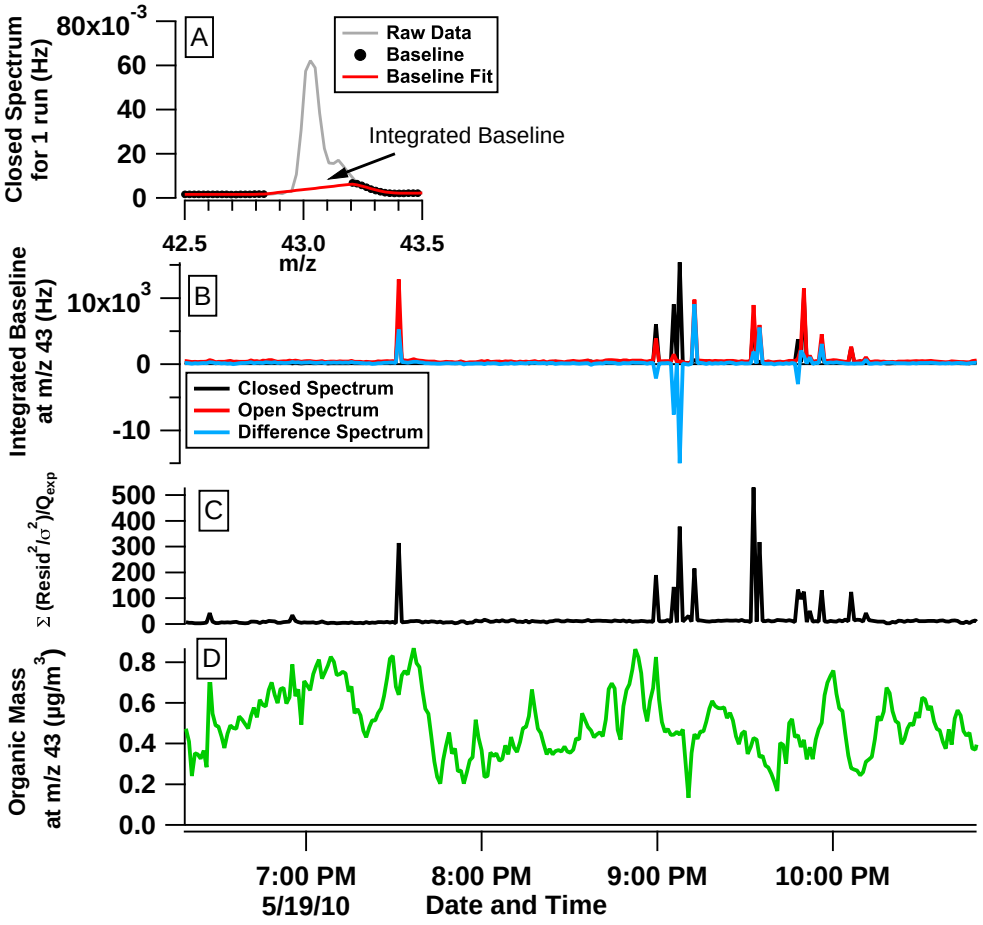

Figure A.2: Integrated baseline for the open, closed, and difference spectrum for m/z 43, organic mass loading at m/z 43 and $Q/Q_{expected}$ versus time for the May 19 flight. The integrated baseline is a diagnostic for identifying electronic noise that can interfere with PMF result interpretation.

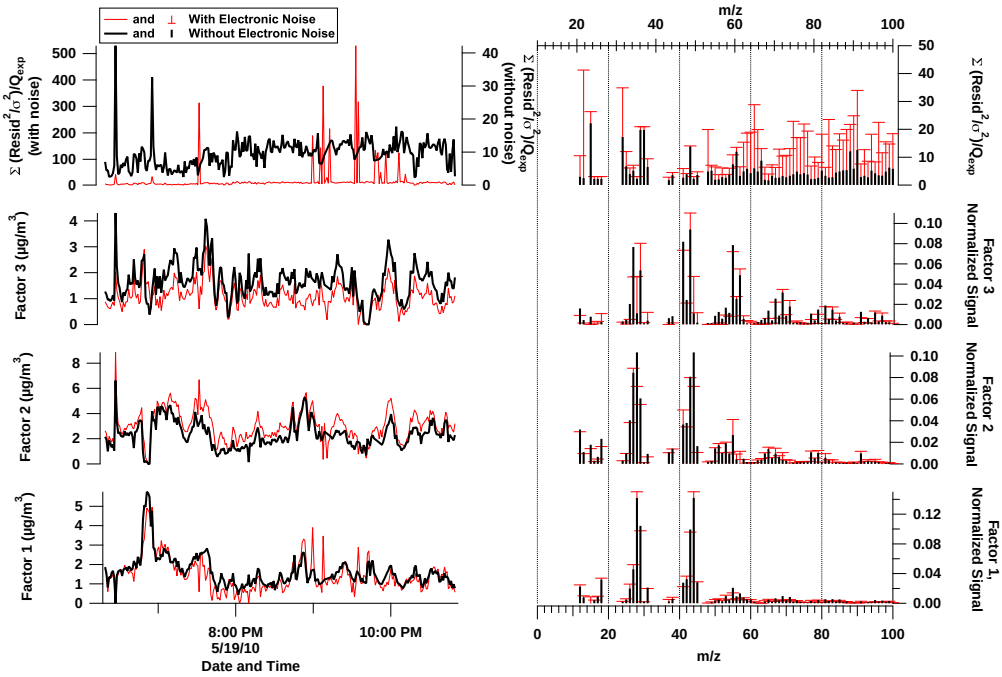

Figure A.3: $Q/Q_{expected}$ and factor profiles versus time (left side) and versus m/z (right side) for the May 19 flight with (red) and without (black) interference from electronic noise.

Appendix B

Application of the Statistical Oxidation Model (SOM) to Secondary Organic Aerosol formation from photooxidation of C12 alkanes[1]

[1]This chapter is reproduced by permission from "Application of the Statistical Oxidation Model (SOM) to Secondary Organic Aerosol formation from photooxidation of C12 alkanes" by C. D. Cappa, X. Zhang, C. L. Loza, J. S. Craven, L. D. Yee, and J. H. Seinfeld, *Atmospheric Chemistry and Physics*, 13, 1591 –1606, doi:10.5194/acp-13-1591-2013, www.atmos-chem-phys.net/13/1591/2013/, 2013.

Atmos. Chem. Phys., 13, 1591–1606, 2013
www.atmos-chem-phys.net/13/1591/2013/
doi:10.5194/acp-13-1591-2013

Atmospheric Chemistry and Physics Open Access

Application of the Statistical Oxidation Model (SOM) to Secondary Organic Aerosol formation from photooxidation of C_{12} alkanes

C. D. Cappa[1], X. Zhang[2], C. L. Loza[3], J. S. Craven[3], L. D. Yee[2], and J. H. Seinfeld[2,3]

[1]Department of Civil and Environmental Engineering, University of California, Davis, CA, 95616, USA
[2]Division of Engineering and Applied Science, California Institute of Technology, Pasadena, CA, 91125, USA
[3]Division of Chemistry and Chemical Engineering, California Institute of Technology, Pasadena, CA, 91125, USA

Correspondence to: C. D. Cappa(cdcappa@ucdavis.edu) and J. H. Seinfeld (seinfeld@caltech.edu)

Received: 14 September 2012 – Published in Atmos. Chem. Phys. Discuss.: 15 October 2012
Revised: 23 January 2013 – Accepted: 25 January 2013 – Published: 8 February 2013

Abstract. Laboratory chamber experiments are the main source of data on the mechanism of oxidation and the secondary organic aerosol (SOA) forming potential of volatile organic compounds. Traditional methods of representing the SOA formation potential of an organic do not fully capture the dynamic, multi-generational nature of the SOA formation process. We apply the Statistical Oxidation Model (SOM) of Cappa and Wilson (2012) to model the formation of SOA from the formation of the four C_{12} alkanes, dodecane, 2-methyl undecane, cyclododecane and hexylcyclohexane, under both high- and low-NO_x conditions, based upon data from the Caltech chambers. In the SOM, the evolution of reaction products is defined by the number of carbon (N_C) and oxygen (N_O) atoms, and the model parameters are (1) the number of oxygen atoms added per reaction, (2) the decrease in volatility upon addition of an oxygen atom and (3) the probability that a given reaction leads to fragmentation of the molecules. Optimal fitting of the model to chamber data is carried out using the measured SOA mass concentration and the aerosol O:C atomic ratio. The use of the kinetic, multi-generational SOM is shown to provide insights into the SOA formation process and to offer promise for application to the extensive library of existing SOA chamber experiments that is available.

1 Introduction

Organic aerosol (OA) comprises a major fraction of the atmospheric sub-micron aerosol burden (Zhang et al., 2007; Jimenez et al., 2009), and the dominant portion of OA is formed from condensation of oxidation products of gas-phase reactions of volatile organic compounds, termed secondary organic aerosol (SOA). The extent to which a given parent organic compound forms SOA depends on a variety of factors, including the carbon chain length, structure and reactivity, as well as external factors such as temperature, the abundance of NO_x ($= NO + NO_2$) and the identity of the oxidant (OH, O_3, NO_3) (Kanakidou et al., 2005). Additionally, the properties of the SOA, e.g. hygroscopicity, volatility and atomic composition, depend on all of the above factors (Jimenez et al., 2009).

Understanding SOA formation via photooxidation (i.e. reactions with OH) presents a unique challenge in that not only is the precursor SOA species (i.e. the parent organic) reactive towards OH, but so are the oxidation products. The extent to which each generation of products contributes directly to SOA formation depends intimately on the details of the atmospheric chemistry for the particular organic. Laboratory chamber experiments are the main source of data on the mechanism of oxidation and the SOA forming potential of a parent organic. Because SOA forms via gas-particle partitioning, the amount of SOA depends on the mass of absorbing material in the aerosol phase, in addition to the unique chemistry. For comparison of SOA formation from different organics, especially in atmospheric models, an SOA model is required. Traditional methods of representing the SOA formation potential, or yield, of an organic do not fully capture the dynamic, multi-generational nature of photooxidation, as they generally treat SOA formation as a one-step process from precursor to products. This includes both the 2-product model (Odum et al., 1996) and static volatility

Table 1. Experimental conditions and results from photooxidation experiments.

Alkane	$[HC]_0$ (ppbv)	[OH][a] (molecules cm^{-3})	C^b_{OA} ($\mu g\,m^{-3}$)	Yield[b] (%)	Yield[c] (%)	O:C max	O:C min
Low NO_x							
dodecane	34.0	2.5×10^6	21.6	10.3	6.1	0.28	0.21
2-methylundecane	28.1	2.4×10^6	18.1	10.8	7.2	0.28	0.20
hexylcyclohexane	15.6	2.95×10^6	28.9	29.6	15.4	0.32	0.22
cyclododecane	9.8	2.7×10^6	15.8	24.4	17.2	0.24	0.15
High NO_x							
dodecane	32.2	4.5×10^7 / 1.85	10.6	6.8	6.2	0.33	0.33
2-methylundecane	72.4	3.3×10^7 / 1.85	23.5	7.8	5.1	0.26	0.26
hexylcyclohexane	22.1	4.1×10^7/1.7	17.5	16.4	12.3	0.32	0.32
cyclododecane	13.8	2.7×10^7/0.92	29.5	41.5	38.3	0.27	0.27

[a] For high-NO_x conditions, [OH] is time dependent and has the form $[OH]_t = [OH]_{t=0}\exp(-kt)$, where t is the time elapsed (in hours) and k is the decay constant. The $[OH]_{t=0}$ and $k$values are reported in the table.
[b] C_{OA} and yield values are reported after 15 h (low-NO_x) and 3 h (high-NO_x) of reaction, respectively.
[c] Yield values are reported for $C_{OA} = 10\,\mu g\,m^{-3}$.

basis-set (Donahue et al., 2006). Recently, methodologies have been developed that represent photooxidation and subsequent SOA formation within more dynamic frameworks (Aumont et al., 2005; Robinson et al., 2007; Lane et al., 2008; Barsanti et al., 2011; Valorso et al., 2011; Cappa and Wilson, 2012; Donahue et al., 2012). Depending on the specific methodology employed, these models allow for reaction of the first (and later) generation oxidation products, fragmentation and tracking of the detailed composition of the particle and gas-phase.

Here, we apply the Statistical Oxidation Model (SOM) of Cappa and Wilson (2012) to model the formation of SOA from the photooxidation of a series of C_{12} alkanes of varying structure, two of which are linear (dodecane and 2-methyl undecane) and two of which have ring structures (cyclododecane and hexylcyclohexane). Experiments were conducted under both high- and low-NO_x conditions to explore the important influence of NO_x on the SOA formation. The best-fit model is found to capture the time-evolution of the observed SOA mass concentration and, to a reasonable extent, the O:C atomic ratio under both high- and low-NO_x conditions. Best-fit SOM parameters are reported, and indicate that, per reaction with OH, photooxidation leads to more rapid oxygen addition under high-NO_x conditions than low-NO_x conditions. Despite the more rapid oxygen addition under high-NO_x conditions, the nature of the functional groups added lead to a smaller decrease in volatility (per oxygen added) than under low-NO_x conditions. The success of fitting the SOM to these alkane SOA formation data offers promise to apply the SOM to the extensive library of existing chamber experiments that is available.

2 Experimental methods

Experiments were conducted in the Caltech dual 28-m^3 Teflon chambers. Details of the facility have been described previously (Cocker et al., 2001). Prior to each experiment, the chambers were flushed with dried, purified air for >24 h, until the particle concentration was $<100\,cm^{-3}$ and the volume concentration was $<0.1\,\mu m^3\,m^{-3}$.

For all experiments, neutral ammonium sulfate seed aerosol was used to provide surface area for condensation of the semi-volatile oxidation products. Particle size distributions were measured using a differential mobility analyser (DMA, TSI, 3081) coupled with a condensation particle counter (CPC, TSI, CNC-3760).

Photooxidation experiments were run under both high and low-NO_x conditions. Low-NO_x (<1 ppb) experiments were conducted using photolysis of H_2O_2 as the OH radical source. High-NO_x experiments were conducted using photolysis of HONO as the OH radical source. The primary NO_x source is direct photolysis of HONO, although some NO and NO_2 formed as part of the HONO preparation. The gas-phase concentration of the SOA precursor was measured throughout the experiments. Initial concentrations are given in Table 1. Four alkanes are considered here, each with 12 carbon atoms: dodecane ($C_{12}H_{26}$), 2-methyl undecane ($C_{12}H_{26}$), hexylcyclohexane ($C_{12}H_{24}$) and cyclododecane ($C_{12}H_{24}$).

Photooxidation was initiated by irradiating the chamber with blacklights. Output from the lights is between 300 and 400 nm, with a maximum at 354 nm. Importantly, HONO photolysis is efficient in this wavelength range, and thus the concentration of HONO (and OH) decays towards zero over a period of ∼3 h once the lights are turned on. H_2O_2 photolysis is comparably much slower, which facilitates operation at

a nearly constant [OH] throughout the low-NO_x experiments. To access long oxidation times (up to 32 h) in the low-NO_x experiments, the methodology set out by Loza et al. (2012) was followed. As a result, the time series of OA mass concentrations (C_{OA}) under low-NO_x conditions have a "gap" of ~6 h (typically from hours 18–24).

Chemically-resolved aerosol mass concentrations were measured using an Aerodyne high-resolution time-of-flight aerosol mass spectrometer (HR-ToF-AMS, henceforth referred to as AMS). Real-time mass spectra of the particles were collected alternating between "V-mode" and "W-mode". The "V-mode" provides higher sensitivity while the "W-mode" provides higher resolution. The "W-mode" data were analysed using the software toolboxes PIKA (DeCarlo et al., 2006) and APES (Aiken et al., 2007; Aiken et al., 2008; Chhabra et al., 2010). Through consideration of ions with specific molecular formulas, as determined from the "W-mode" spectra, the elemental composition of the SOA can be determined (in particular, the O:C and H:C atomic ratios). The estimated uncertainty in the O:C is ±30 % and in the H:C is 10 %.

A correction for wall loss needs to be applied to determine the SOA mass concentration. Two limiting assumptions can be employed to bound the interactions between particles deposited to the wall and vapors in the chamber. Here we use a lower bound, in which particles deposited on the wall are assumed to cease interaction with suspended vapors after deposition (Loza et al., 2012). The total organic mass deposited to the wall was calculated based on the particle number-weighted size distribution. The wall loss rates for particles of different sizes are obtained from separate characterization experiments. The deposited particle number distribution is added to the suspended particle number distribution to give a wall-loss corrected number distribution, which is then converted to a volume concentration and then mass concentration, assuming spherical particles. For the low-NO_x experiments reported on here, wall loss corrections at long times require extrapolation of the C_{OA} across the "gap", which decreases the certainty of the correction and, as a result, the accuracy of the wall-loss corrected C_{OA} values after the gap. Thus, only the pre-gap C_{OA} data are used quantitatively here.

3 Statistical Oxidation Model

The statistical oxidation model (SOM) simulates the oxidation of a parent hydrocarbon and its reaction products in time, and is described in detail in Cappa and Wilson (2012). In the SOM, the evolution of the gas and particle phase composition is followed through a space in which all product species are defined solely by their number of carbon (N_C) and oxygen (N_O) atoms. Equilibrium partitioning between the gas and particle phases is assumed to hold at each time-step of the model (~1–2 min) (Pankow, 1994). It is assumed that the properties of each species (i.e. N_C/N_O pair) can be represented by some mean values that account for the actual distribution of functional groups within the group of molecules that make up an SOM species. There are a few adjustable parameters within the SOM: (1) the number of oxygen atoms added per reaction, which is represented as an array of probabilities of adding 1, 2, 3 or 4 oxygen atoms, termed P_{func}, (2) the decrease in volatility upon addition of an oxygen atom, termed ΔLVP, which is the difference in the log of the saturation concentration, C_{sat}, per oxygen added, or

$$\Delta\mathrm{LVP} = \log\left[\frac{C_{\mathrm{sat},N_O}}{C_{\mathrm{sat},N_O+1}}\right] \quad (1)$$

and (3) the probability that a given reaction leads to fragmentation of the product molecule into two smaller molecules, termed P_{frag}. Note that positive values of ΔLVP correspond to a decrease in vapour pressure upon oxygen addition. These parameters can be adjusted to determine a best fit of the model to the observations. The SOM also includes heterogeneous reactions with OH radicals (Cappa and Wilson, 2012). It is assumed that each heterogeneous OH reaction leads to the addition of one oxygen atom, that the fragmentation probability is assumed equivalent to the gas-phase, and that the reactive uptake coefficient is unity. The model additionally requires as input the initial concentration of the parent hydrocarbon, $[HC]_0$, and the (potentially time-dependent) oxidant concentration. In this study, for the low-NO_x experiments the [OH] was constant (or nearly constant) throughout, while for the high-NO_x experiments the [OH] decayed rapidly. In either case, the model [OH] was specified so that the observed temporal decay of [HC] was reproduced (see Table 1).

It is not yet clear what the most appropriate functional form is for the fragmentation probability, P_{frag}. Therefore, two parameterizations are considered here: $P_{frag}(\mathrm{O{:}C}) = (\mathrm{O{:}C})^{m_{frag}}$ and $P_{frag}(N_O = c_{frag} N_O)$, where m_{frag} and c_{frag} are adjustable parameters, and there is an upper limit of $P_{frag} = 1$. Smaller values of m_{frag} and larger values of c_{frag} indicate more extensive fragmentation, respectively. It is assumed that the generated fragments are randomly distributed in terms of where the carbon bond scission occurs.

Best-fit values for P_{func}, ΔLVP and P_{frag} are determined by simultaneously fitting the time-dependent model predictions to observations of wall-loss corrected organic aerosol mass concentrations (C_{OA}) and O:C for each system (in this case, C_{12} compounds reacting with OH radicals under high- or low-NO_x conditions). Alternatively, the SOM was fit only to the C_{OA} observations. The data fitting was performed using the Levenberg-Marquardt algorithm built into the data analysis program Igor. Uncertainties in the measured C_{OA} were assumed to be the larger of 0.5 μg m^{-3} or 10 %. Uncertainties in the O:C were +/−30 %. An upper limit of ΔLVP = 2.2 was applied. The functional group that contributes most to the decrease of vapour pressure per O atom added is the –OH group. The EVAPORATION model (Compernolle et al., 2011) predicts that ΔLVP upon addition of –OH to primary, secondary and tertiary C is 2.23,

1.70 and 1.16, respectively, whereas the SIMPOL.1 model (Pankow and Asher, 2008) predicts 2.76, 2.10 and 1.49, respectively. Here we take the average between the two vapour pressure models as the upper limit to ΔLVP. For low-NO_x experiments, which have a gap in the C_{OA} data from ∼18–24 h of reaction, the data are fit only prior to this gap. As noted above, the reason for this is that the uncertainty in the wall-loss correction across the gap leads to larger uncertainty in the C_{OA} after the gap.

Variation in the H:C atomic ratio with oxidation is characterized within the SOM by specifying the average number of hydrogen atoms lost per oxygen atom added, which is equal to the negative slope in a Van Krevelen diagram (a graph of H:C vs. O:C) (Heald et al., 2010). Here, the H-loss-per-O-added is specified a priori based on the observed Van Krevelen slope, although it should be noted that the specification of this relationship has a negligible influence on the evolution of either the C_{OA} or O:C.

Condensed phase reactions (besides heterogeneous OH reactions) are not explicitly accounted for in the SOM. Thus, to the extent that condensed phase reactions (e.g. oligomerization, dehydration, cyclization) alter the observed SOA properties, this will be reflected in the best-fit model parameters.

4 Results

4.1 Low-NO_x conditions

The time-evolution of the observed wall-loss corrected SOA mass concentrations (C_{OA}) and the particle-phase O:C atomic ratios are shown in Fig. 1, along with the tuned model results obtained using both P_{frag} parameterizations and after fitting simultaneously to both C_{OA} and O:C. In general, as oxidation proceeds, the observed C_{OA} increases until the parent [HC] decays to around 10 % of its initial value (which occurs around 15–20 h of oxidation). After this point, the C_{OA} starts to level off, or even decrease slightly, even though there is still OH present in the system. The observed SOA O:C atomic ratio at early times tends to decrease slightly until the parent [HC] decays to around 30 % of its initial value (at 5–10 h of oxidation), after which time it begins to slowly increase. Aerosol mass yields for the two ring-containing compounds are larger than for the non-ring containing compounds (Table 1), consistent with previous results from Lim and Ziemann (2009).

The SOM, after fitting, captures the general time-dependent behaviour of the observed C_{OA}, with the model C_{OA} exhibiting a levelling off or slight decrease at long times for many of the simulations (Fig. 1). The exact time-dependence of the model C_{OA} depends somewhat on the assumed fragmentation parameterization and method. In general, the $P_{frag}(N_O)$ parameterization tends to show a more pronounced turnover in the C_{OA} at long times than the P_{frag}(O:C) parameterization. The $P_{frag}(N_O)$ results appear slightly more consistent with the observations, which is an unexpected result given that the more physically intuitive behavior is that the probability of fragmentation for a given molecule should depend on the relative oxygen abundance (i.e. O:C) rather than the absolute oxygen abundance (i.e. N_O). However, the uncertainty in the observed C_{OA} after the data gap limits our ability to definitively make this assessment.

The SOM captures the general shape of the observed O:C time-dependence, with the model O:C typically first decreasing before increasing with time, similar to the experimental results (Fig. 1). Despite the satisfactory shape of the model O:C time-dependence, for all of the hydrocarbons considered the absolute value of the model O:C is somewhat greater than the observed O:C, although typically within the experimental uncertainty. Cyclododecane is the notable exception, with a model O:C that is substantially higher than the observed value (although the shape of the calculated and observed time-dependencies are quite similar). The over-prediction is, in part, a consequence of setting an upper limit for ΔLVP = 2.2 during fitting; allowing for larger values of ΔLVP can lead to better model/measurement agreement for most compounds (although not for cyclododecane) and can still allow for a good fit to the observed C_{OA}. The $P_{frag}(N_O)$ parameterization generally yields somewhat lower absolute O:C values compared to P_{frag}(O:C). An additional reason for the over-prediction of the model O:C relative to the observations could be that the HR-ToF-AMS underestimates the oxygen derived from hyderoperoxides, with these species instead detected with the –OOH removed (Craven et al., 2012). This would lead to a measured O:C that is somewhat lower than the actual O:C, with the extent of this disparity potentially dependent upon the hydroperoxide fraction of the oxygenated functional groups.

When the model is fit to both the C_{OA} and O:C, the best-fit ΔLVP is 2.2 for all compounds, i.e. the imposed upper-limit (Fig. 2 and Table 2). This is not surprising given that the model O:C is particularly sensitive to the ΔLVP parameter (Cappa and Wilson, 2012). When the model is fit to only the C_{OA} data, the best-fit values remain high, with $2 < \Delta LVP < 2.2$. For all compounds considered, the addition of 1 oxygen atom per reaction was most probable, with some smaller fraction of reactions requiring the addition of 2, 3 or 4 oxygen atoms (Fig. 2 and Table 2). The model results indicate that fragmentation is extensive, and the non-ring-containing compounds have larger c_{frag} and smaller m_{frag} values compared to the ring-containing compounds, suggesting more extensive fragmentation of the non-ring containing compounds. For all compounds, the c_{frag} values (for $P_{frag}(N_O)$) were ≥ 0.33, which indicates that any molecule already containing 3 or more oxygen atoms will exclusively fragment upon reaction. Note that this does not preclude formation of species with >3 oxygen atoms because some reactions add more than 1 oxygen atom and because fragmentation also leads to oxygen addition. It does, however, limit the rate and overall extent

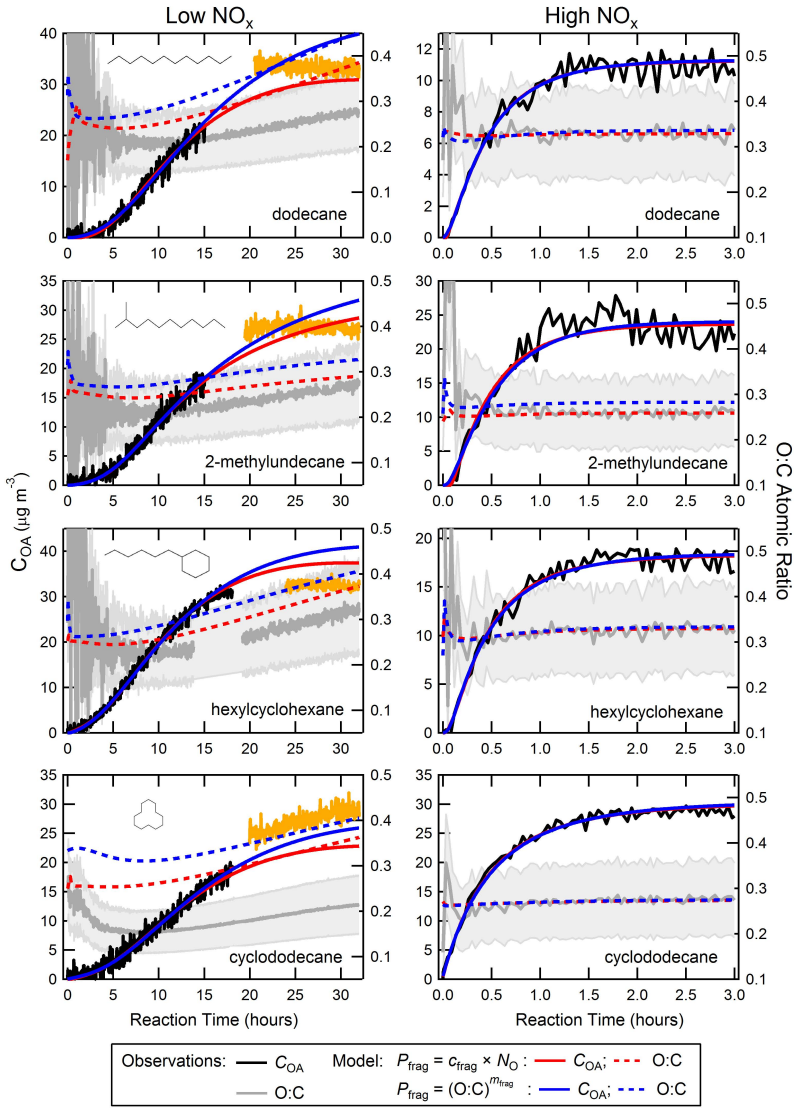

Fig. 1. Evolution of the SOA mass concentration, C_{OA}, (black lines, left axes) and O:C atomic ratio (gray lines, right axes) for low-NO_x (left panels) and high-NO_x (right panels) for dodecane, 2-methylundecane, hexylcyclohexane and cyclododecane (top-to-bottom). The light gray bands on the O:C indicate the estimated uncertainty range (±30 %). The model results using $P_{frag}(N_O)$ and P_{frag}(O:C) are shown as red and blue lines, respectively. Solid lines are model fits for C_{OA} and dashed lines for O:C. The model has been fit simultaneously to the C_{OA} and O:C data for t <15 h (low-NO_x, black lines) or t <3 h (high-NO_x). For the low-NO_x conditions, the orange lines correspond to data collected after a pause in sampling (indicated by a gap in the C_{OA} time series).

to which such highly oxygenated species can form. Similar conclusions are reached if the P_{frag}(O:C) parameterization is instead considered, although the exact details are changed somewhat due to the different functional form of the parameterization.

The observed co-variation of H:C with O:C, shown as a Van Krevelen diagram, indicates that the number of H atoms lost per O atom added, or the negative slope on the graph, ranges from 1.45 to 2.2 (Fig. 3); this parameter is specified within the SOM so as to match the model to the observations. The model aerosol exhibits a continuous evolution of the H:C and O:C throughout the reaction, consistent with the observations, which is indicated by the wide range of values that fall along a line with a constant slope (Fig. 3).

The distribution of molecules in N_C/N_O space at the end of the dodecane + OH reaction is shown for both P_{frag}

Table 2. Statistical oxidation model best-fit parameters when fit to both C_{OA} and O:C.

Alkane	ΔLVP	c_{frag} or m_{frag}	Oxygen Addition Probabilities[a]
Low-NO_x; $P_{frag} = c_{frag} N_O$			
dodecane	2.20[b]	0.423	[0.57,0.12,0.00,0.31]
2-methylundecane	2.20[b]	0.455	[0.79,0.00,0.10,0.11]
hexylcyclohexane	2.20[b]	0.333	[0.80,0.05,0.12,0.03]
cyclododecane	2.20[b]	0.333	[0.86,0.02,0.12,0.0]
Low-NO_x; $P_{frag} = (O:C)^{m\ frag}$			
dodecane	2.20[b]	0.077	[0.79,0.17,0.03,0.0]
2-methylundecane	2.20[b]	0.110	[0.96,0.0,0.04,0.0]
hexylcyclohexane	2.20[b]	0.214	[0.75,0.17,0.08,0.0]
cyclododecane	2.20[b]	0.250	[0.88,0.0,0.0,0.11]
High-NO_x; $P_{frag} = c_{frag} N_O$			
dodecane	1.46	0.279	[0.31,0.41,0.07,0.19]
2-methylundecane	1.68	0.397	[0.24,0.50,0.27,0.0]
hexylcyclohexane	1.54	0.233	[0.0,0.50,0.43,0.06]
cyclododecane	2.01	0.279	[0.0,0.0,0.73,0.26]
High-NO_x; $P_{frag} = (O:C)^{m\ frag}$			
dodecane	1.69	0.105	[0.26,0.38,0.31,0.05]
2-methylundecane	1.80	0.113	[0.30,0.57,0.13,0.0]
hexylcyclohexane	1.67	0.191	[0.18,0.23,0.59,0.0]
cyclododecane	2.06	0.251	[0.0,0.0,0.88,0.12]

[a] The relative probabilities of adding 1, 2, 3 or 4 oxygen atoms per reaction.
[b] Constrained as an upper limit.

parameterizations (Fig. 4a,b). Overall, the OA is dominated by compounds that have $N_C = 12$ (Fig. 4e), although there are interestingly contributions from compounds with as few as 2 carbons at the 0.1 % level. Although the two P_{frag} parameterizations give generally similar results with respect to the temporal variation in the C_{OA} and O:C, the distribution of molecules that make up the OA differ. The P_{frag}(O:C) parameterization allows for a fragmentation probability that asymptotically approaches 1 (at O:C = 1), and thus it is possible to produce molecules with $N_C = 12$ and with a relatively large number of oxygen atoms, although the contribution of species with $N_O > 3$ to the total OA mass is small. For the $P_{frag}(N_O)$ parameterization the probability of fragmentation linearly varies with N_O and, given $c_{frag} = 0.42$ coupled with a P_{func} array dominated by 1 oxygen per reaction, there is similarly not substantial production of $N_C = 12$ species with $N_O > 3$.

4.2 High-NO_x conditions

The observed variations in wall-loss corrected C_{OA} and O:C with reaction time for high-NO_x conditions for each of the alkanes considered are shown in Fig. 1. It is important to note that the OH concentration during these experiments was time dependent and decayed rapidly from $>10^7$ molecules cm^{-3} to zero (by around 3 h). This is in contrast to the low-NO_x experiments, where the OH concentration was constant at around 3×10^6 molecules cm^{-3}. The time-dependence of the [OH] was accounted for in the SOM fit to the observations. The observed C_{OA} in each experiment rapidly increased before reaching a plateau by around 2–3 h. Unlike the low-NO_x experiments, this plateau behaviour results primarily from the loss of OH radicals and the cessation of photochemical reactions and not from an evolution in the distribution of gas-phase photooxidation products. The observed SOA O:C were essentially constant with time. Aerosol mass yields were larger for the ring-containing compounds (Table 1).

The SOM reproduces the observed time-dependent behaviour of the C_{OA} and O:C, both in terms of shape and absolute magnitude. Note that the close match between the observed and predicted O:C is different than for the low-NO_x conditions, where O:C was over-predicted. Fitting to either C_{OA} and O:C simultaneously or only to C_{OA} gave generally similar results. The best-fit ΔLVP values ranged from 1.46 to 2.06 (Fig. 2 and Table 2) and are overall substantially lower compared to the low-NO_x systems, with the exception of cyclododecane. Under high-NO_x conditions the optimal fit of the SOM indicates that the majority of reactions

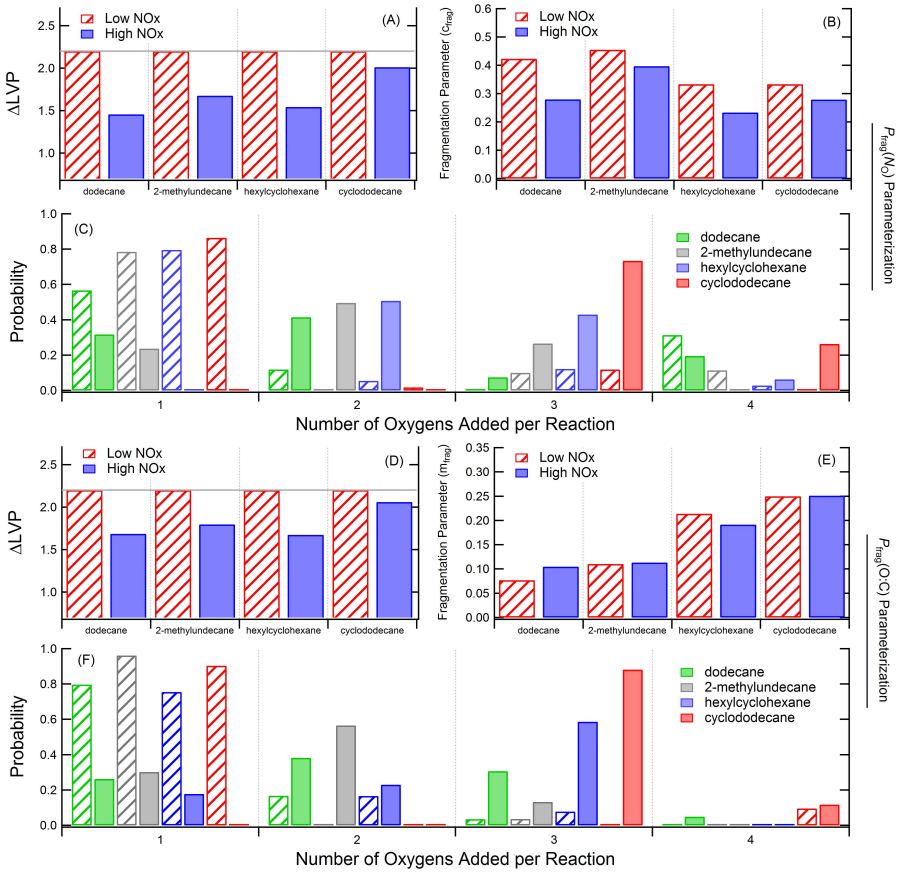

Fig. 2. Best-fit SOM parameters for dodecane, 2-methylundecane, hexylcyclohexane, and cyclodecane under low-NO_x (hashed) and high-NO_x (solid) conditions for different parameterizations for fragmentation: **(A–C)** used $P_{frag}(N_O)$ while **(D–F)** used P_{frag}(O:C). Results are shown for ΔLVP (**A** and **D**), the fragmentation parameter (**B** and **E**) and the oxygen addition array (**C** and **F**). The model was fit simultaneously to the observed C_{OA} and O:C. The two fragmentation parameterizations give generally similar results. Note that for the fragmentation parameter, larger values of c_{frag} correspond to greater fragmentation while smaller values of m_{frag} correspond to greater fragmentation. The grey line in **(A)** and **(D)** indicates the upper-limit constraint on ΔLVP.

added 2 to 4 oxygen atoms per reaction, with the exact probability distribution varying for each alkane considered and some probability of adding 1 oxygen per reaction (with the exception of cyclododecane). This is in distinct contrast to the low-NO_x systems, where predominately only 1 oxygen is predicted to be added per reaction. The P_{func} distributions are generally similar between the two fragmentation parameterizations. In general, the non-ring-containing compounds require larger c_{frag} (or smaller m_{frag}) than the ring-containing compounds, indicating more extensive fragmentation. Additionally, the best-fit c_{frag} values are generally larger (and the m_{frag} smaller) under high-NO_x conditions than under low-NO_x conditions for a given compound, although the extent to which the values differ depends on the specific alkane and whether c_{frag} or m_{frag} is considered; in some cases the differences are slight (Fig. 2 and Table 2).

The observed co-variation of H:C with O:C indicates that the number of H atoms lost per O atom added ranges from 1.25 to 1.83, which is slightly less than for low-NO_x conditions (Fig. 3). The SOM captures the observed behaviour (after specifying the H-per-O relationship), namely that the H:C and O:C are both nearly constant throughout the reaction, unlike the low-NO_x systems (Fig. 3).

The distribution of molecules in N_C/N_O space at the end of the reaction is shown for dodecane (Fig. 4c,d). As in the low-NO_x systems, the overall SOA composition is dominated by compounds with $N_C = 12$ (Fig. 4e), although the fractional contribution of compounds with $N_C < 12$ is less than in the low-NO_x experiments. This is likely the result of a greater number of oxygen atoms being added per reaction for the high- vs. low-NO_x case. This predicts that compounds with $N_C = 12$ more rapidly add oxygen, leading to a volatility

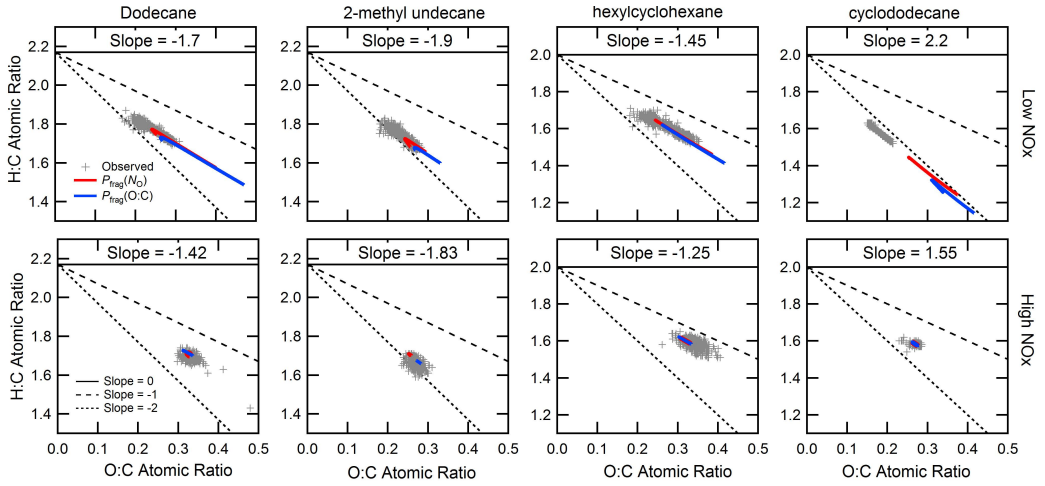

Fig. 3. Van Krevelen diagrams (H:C vs. O:C) for the observed SOA (gray points) and the model SOA using the $P_{frag}(N_O)$ (red lines) and P_{frag}(O:C) (blue lines) fragmentation parameterizations. The top row shows results for low-NO_x conditions and the bottom row for high-NO_x conditions. The Van Krevelen slopes (defined according to the parent hydrocarbon y-intercept) are given in each panel.

sufficiently low that condensation is efficient even though the ΔLVP tends to be smaller for the high-NO_x mechanisms.

5 Discussion

The observations indicate that aerosol mass yields, defined as $C_{OA}/\Delta HC$ (where ΔHC is the amount of precursor reacted), are larger for the ring-containing compounds than for the non-ring-containing compounds for both high- and low-NO_x conditions (Table 1). For equivalent amounts of aerosol formed (specifically, 10 µg m^{-3}), the mass yields for each species under high- and low-NO_x conditions are reasonably similar, with the exception of cyclododecane, for which the high-NO_x yield is greater (Table 1). Low-NO_x conditions typically have greater H-loss per O-added (i.e. more negative Van Krevelen slopes) than high-NO_x conditions and also exhibit a more continuous evolution through the Van Krevelen space as the reactions proceed. Considering the model results, the SOM indicates that the decrease in volatility per oxygen added is substantially larger for low-NO_x vs. high-NO_x conditions. The magnitude of the fragmentation parameter, c_{frag}, is generally larger (and m_{frag} smaller) for low- vs. high-NO_x. Under high-NO_x conditions a greater number and broader distribution of oxygen atoms are added, on average, per reaction. Low-NO_x conditions lead to a slightly broader distribution of compounds with N_C <12 in the particle phase compared to high-NO_x conditions.

To facilitate further comparison between the low-NO_x and high-NO_x experiments, which were conducted using different [OH] temporal profiles and different $[HC]_0$, time-dependent SOA growth simulations were run under the same reaction conditions using the best-fit parameters determined above (Fig. 5). Specific reaction conditions and model inputs were: $[OH] = 2.5 \times 10^6$ molecules cm^{-3}, $[HC]_0 = 33.5$ ppb, the $P_{frag}(N_O)$ parameterization was used and the model was run for 32 h of oxidation. For all except 2-methylundecane, the C_{OA} formed after a given reaction time is initially somewhat greater for the high-NO_x conditions, but with an eventual cross-over to where the C_{OA} becomes larger for the low-NO_x conditions, often substantially so, at long times. For 2-methylundecane the yield under low-NO_x conditions is always greater than under high-NO_x conditions, with the difference growing with time.

For high-NO_x conditions there tends to be a more pronounced turnover in the C_{OA} with time and with the turnover occurring at shorter times compared to low-NO_x conditions. The overall time-dependent evolution of the gas + particle system reflects the combined influence of all of the parameters (P_{frag} and P_{func} and ΔLVP). Thus, the observed NO_x-dependence on the time-dependent aerosol yields can be understood through the influence of NO_x on both the probabilities of fragmentation vs. functionalization reactions and on the nature of the functional groups formed, specifically the decrease in volatility that occurs upon functional group addition.

There are no clear, systematic differences in the evolution of the O:C with oxidation between the low- and high-NO_x cases, although O:C tends to be slightly higher for high-NO_x. In general, for low-NO_x the O:C first decreases then increases, consistent with the experiments (which were conducted under similar conditions as these simulations). For high-NO_x, both 2-methylundecane and hexylcyclohexane exhibit a noticeable increase in the O:C with oxidation, similar to the low-NO_x cases, whereas dodecane and

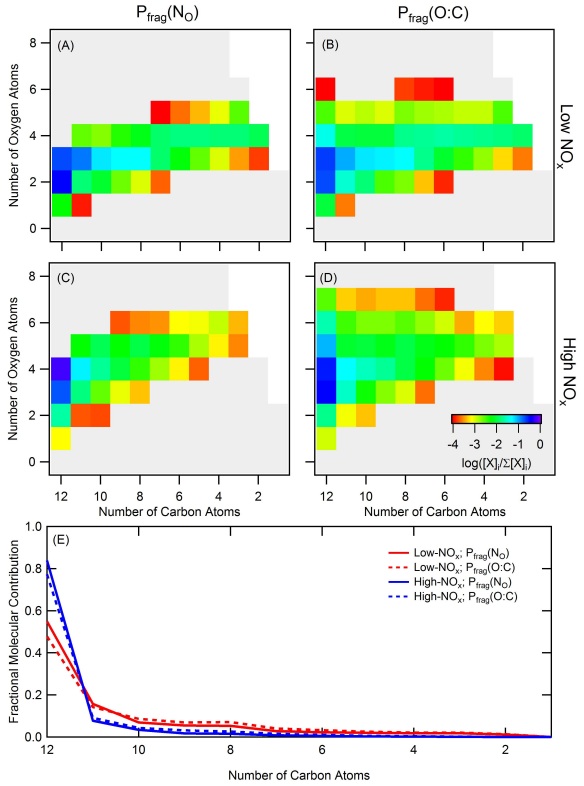

Fig. 4. Distribution of molecules comprising the model dodecane SOA at the end of the experiment for low-NO_x **(A, B)** and high-NO_x **(C, D)** for the $P_{frag}(N_O)$ **(A, C)** and P_{frag}(O:C) **(B, D)** parameterizations. The colors correspond to the log of the fractional molecular abundance, i.e. $\log([X]_j/\Sigma[X]_j)$, with a lower-limit of -4 (= 0.01 %). **(E)** The distributions, binned by N_C, for low-NO_x (red) and high-NO_x (blue).

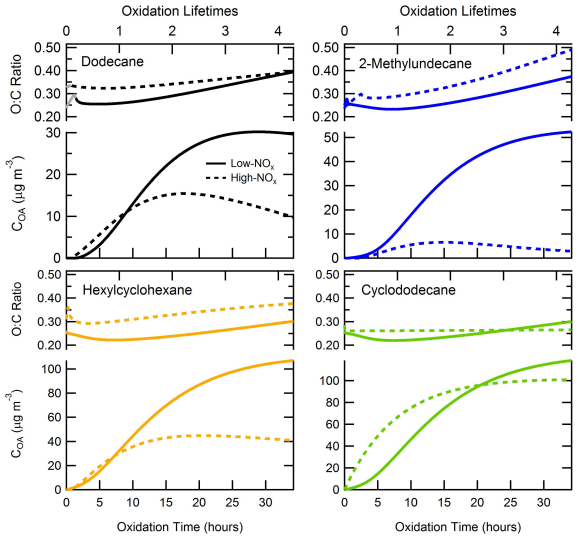

Fig. 5. Simulated time-evolution of C_{OA} and O:C for each of the parent alkanes using the same reaction conditions but with compound-specific best-fit SOM parameters. Results are shown for low-NO_x (solid) and high-NO_x (dashed), assuming $[OH] = 2.5 \times 10^6$ molecules cm^{-3} and $[HC]_0 = 33.5$ ppb.

cyclododecane exhibit comparably small variations in O:C with oxidation.

5.1 Time-evolution of individual SOA species

The SOM can be used to follow the time-evolution of the individual species (i.e. N_C/N_O pairs) that comprise the model SOA. Tracking of each SOM species can help to understand which species contribute most to the SOA mass at any given time during the experiment, and thus how the composition is evolving. An example of such a time-trace is shown for the low-NO_x dodecane system using the $P_{frag}(N_O)$ parameterization, where the individual species have been normalized to their maximum concentration (Fig. 6). It can be seen that there is some clustering of different species with respect to their specific time-evolution, and species that exhibit similar time-dependent behaviour have been colored similarly. The $N_C = 12$ species with 1 and 2 oxygen atoms have unique time-profiles while the $N_C = 8$ to 11 species with 1 or 2 oxygens cluster together into one predominant mode. Similarly, there is a clustering of species with $N_C = 6$–7 and $N_O = 2$–3, and of species with $N_C = 8$–12 with $N_O = 3$. Finally, species with $N_O \geq 4$ cluster together nearly independent of N_C. This type of clustering behaviour is consistent with the identification of unique "factors" associated with the formation and ageing of low-NO_x dodecane SOA (Craven et al., 2012). In general, the concentrations of individual particle-phase species with greater numbers of oxygen atoms and smaller carbon atom numbers peak later in time, consistent with their formation occurring only after many generations of oxidation. (Note that the assumption of random fragmentation and the use of a single SOM "grid" preclude direct, quantitative connections between N_C, N_O and generation number to be made.) The clustering of particular species in terms of their particle-phase concentrations is related to the combined influence of gas-phase formation rates and the volatility of each species.

It is also important to consider the actual time-dependent contributions from each species to the total SOA mass, as the above discussion (which uses normalized traces) might place undue focus on species that contribute negligibly to the SOA mass. Figure 7a shows the actual time-evolution of the particle phase mass concentration for each SOM species, and Fig. 7b–d show snapshots of the concentrations of each species after 5 h, 15 h and 25 h of reaction, normalized to the total particle mass at that time. It is evident that at early times the SOA is dominated by the $N_C = 12$, $N_O = 2$ species and the cluster of $N_C = 8$–12, $N_O = 3$ species. As the

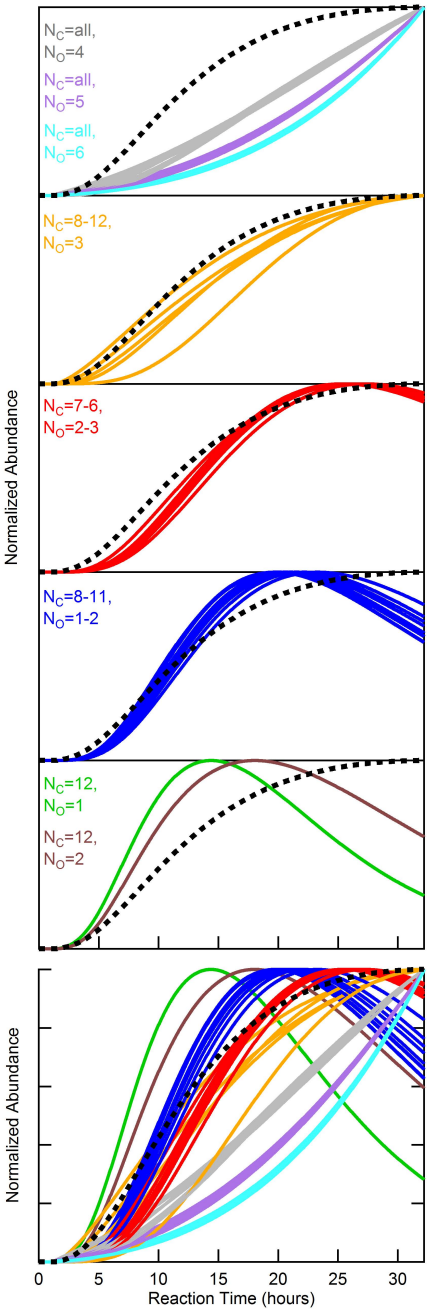

Fig. 6. Simulated time-evolution of each SOM species (i.e. N_C/N_O pair) during the low-NO_x photooxidation of dodecane. Species that exhibit a similar temporal dependence have been grouped into "clusters" and are shown in individual panels with the same color; the N_C and N_O of the species that belong to each "cluster" for each panel are indicated as labels. Each species profile has been normalized to its maximum concentration. For reference, the dashed black trace in each panel shows the time-evolution of the normalized total SOA mass. The bottom panel shows all traces together so that the time-evolution of the various clusters can be compared.

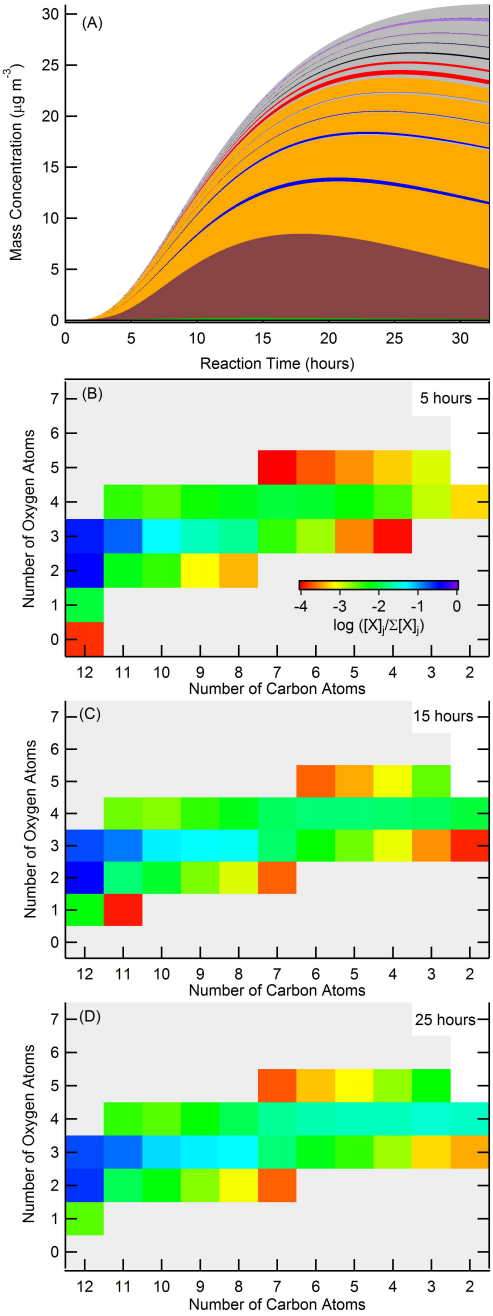

Fig. 7. (A) Simulated mass concentrations of each SOM species, with each species stacked on the previous. The colors correspond to those in Fig. 6 and indicate species of a particular "cluster". **(B)**, **(C)** and **(D)** show snapshots at 5, 15 and 25 hours of reaction, respectively, of the normalized mass concentration of all SOM species on an oxygen/carbon grid, with concentration indicated by the color of each cell in the grid (see legend). For each snapshot, the mass concentration of each species is normalized by the total SOA mass concentration as in Fig. 4; species with a normalized abundance $<10^{-4}$ are shown as gray and species with O:C >2 are shown as white.

reaction progresses, the cluster of $N_O = 4$ species begins to contribute significantly while the abundance of the $N_C = 12$, $N_O = 2$ species decreases as it is converted into more oxidized species. This illustrates the dynamic nature of the SOA composition as it forms and ages.

5.2 Relationship of ΔLVP and oxygen addition

In principle, the addition of different functional groups corresponds to different values for ΔLVP in the SOM. For example, the SIMPOL model of Pankow and Asher (2008) suggests the following: ΔLVP(alcohol) ∼2.23; ΔLVP(ketone) ∼0.94; ΔLVP(aldehyde) ∼1.35; ΔLVP(nitrate) ∼0.74; ΔLVP(hydroperoxide) ∼ 1.24. (Recall that ΔLVP is defined on a per-oxygen basis.)

Under low-NO_x reaction conditions, likely products from gas-phase pathways are hydroperoxides, carbonyl hydroperoxides, hydroxyl hydroperoxides, carboxylic acids, hydroxylcarboxylic acids, hydroxyperacids and hydroxyl carbonyls (Yee et al., 2012). For the low-NO_x systems the best-fit SOM ΔLVP values are all >2, which would suggest the addition of predominately hydroxyl (–OH) functional groups. However, addition only of alcohols seems unlikely, both from a mechanistic perspective (Yee et al., 2012) and from consideration of the observed H-loss per O-added (or Van Krevelen slope). Strict alcohol addition would correspond to a Van Krevelen slope of 0, which can be compared with the addition of a ketone or aldehyde (slope = −2) or hydroperoxide (slope = 0). The observed low-NO_x Van Krevelen slopes ranged from −1.45 to −2.2. Such values are more suggestive of substantial ketone or aldehyde addition, as opposed to addition of alcohols, ketones and hydroperoxides as suggested by Yee et al. (2012). Thus, there appears to be some inconsistency between the model ΔLVP values, the observed Van Krevelen slopes and the expected products.

One potential reconciliation between these differing indications of functional group addition is the presence of condensed phase reactions. The above functional group/ΔLVP relationships do not account for condensed phase reactions that can alter the nature of the functional groups comprising the SOA (and thus the H:C and O:C relationship) and the apparent volatility of the condensed-phase compounds. Importantly, certain condensed phase reactions involve a change in the Van Krevelen slope while others preserve the slope. Dehydration reactions involve loss of water molecules and lead to a change in the observed H:C vs. O:C slope, moving it towards steeper values. For example, ester formation, typically from the reaction of a carboxylic acid and alcohol, involves loss of a water molecule:

$$\mathrm{R(O)OH} + \mathrm{R'OH} \leftrightarrow \mathrm{R(O)OR'} + \mathrm{H_2O} \quad \text{(R1)}$$

Assuming that this water does not influence the SOA O:C measurement, esterification leads to an overall Van Krevelen slope of −2 relative to the unreacted hydrocarbon and, by forming a longer-chain species (i.e. an oligomer), a decrease in vapour pressure despite the loss of functional group (the magnitude of this vapour pressure decrease will depend on the carbon chain length of the molecules involved). Cyclization reactions of hydroxycarbonyl species to form cyclic hemiacetals followed by dehydration to form a dihydrofuran also involve loss of water molecules, again leading to a shift in the Van Krevelen slope towards steeper values. However, such reactions do not lead to oligomerization, and thus the volatility of the dihydrofuran product may be substantially higher than the cyclic hemiacetal. The increased vapour pressure could lead to evaporation of the dihydrofuran, which could undergo further gas-phase processing and, potentially, re-condensation as a more oxidized species. Ultimately, if the dihydrofuran does not remain or end up back in the particle, the Van Krevelen slope of the SOA will be unaffected. It is worth noting that such dehydration reactions will lead to a decrease in the observed SOA O:C, and could provide an explanation for the model over-estimate. Altogether, consideration of the observations and the model results suggest that condensed-phase reactions occur that alter not only the apparent volatility of the SOA species, but also their atomic composition. However, it is possible that a bias against detection of hydroperoxides could also have influenced the observed Van Krevelen slope. Addition of hydroperoxides should yield a slope of 0. Thus, if hydroperoxides are primarily detected following loss of –OOH, the observed slope would be shifted towards more negative values. To the extent that this occurs, the need to invoke condensed phase reactions to explain the differing indications of functional group addition would be lessened.

Under high-NO_x conditions, the model ΔLVP values ranged from 1.46 to 2.06 (or 1.46 to 1.80 if cyclododecane is excluded). Interestingly, these values are significantly larger than that associated with organonitrate addition (ΔLVP = 0.74) even though the best-fit P_{func} array indicates a substantial fraction of reactions add up to 3 or 4 oxygen atoms per reaction, which is consistent with nitrate addition. The mean H-loss-per-O added ranged from 1.25 to 1.83, also significantly larger than expected if nitrate functional group addition dominates (−0.33). Again, these results suggest that condensed phase reactions are altering the observed SOA properties, and thus the interpretation of the SOM best-fit parameters. As with the low-NO_x case, condensed phase reactions that make the Van Krevelen slope more negative (steeper) are suggested to reconcile the observations, expected mechanism and SOM results. In the condensed phase, organonitrates can undergo hydration reactions followed by acid-catalyzed nitrate loss to form alcohols. However, such reactions are unlikely under the very low RH conditions of these experiments, and furthermore would move the slope in the wrong direction (i.e. towards zero). Esterification (dehydration) reactions may also be occurring in the high-NO_x particles, moving the slope towards more negative values and, likely, decreasing the apparent volatility of the condensed species. Taken together, the low and high-NO_x

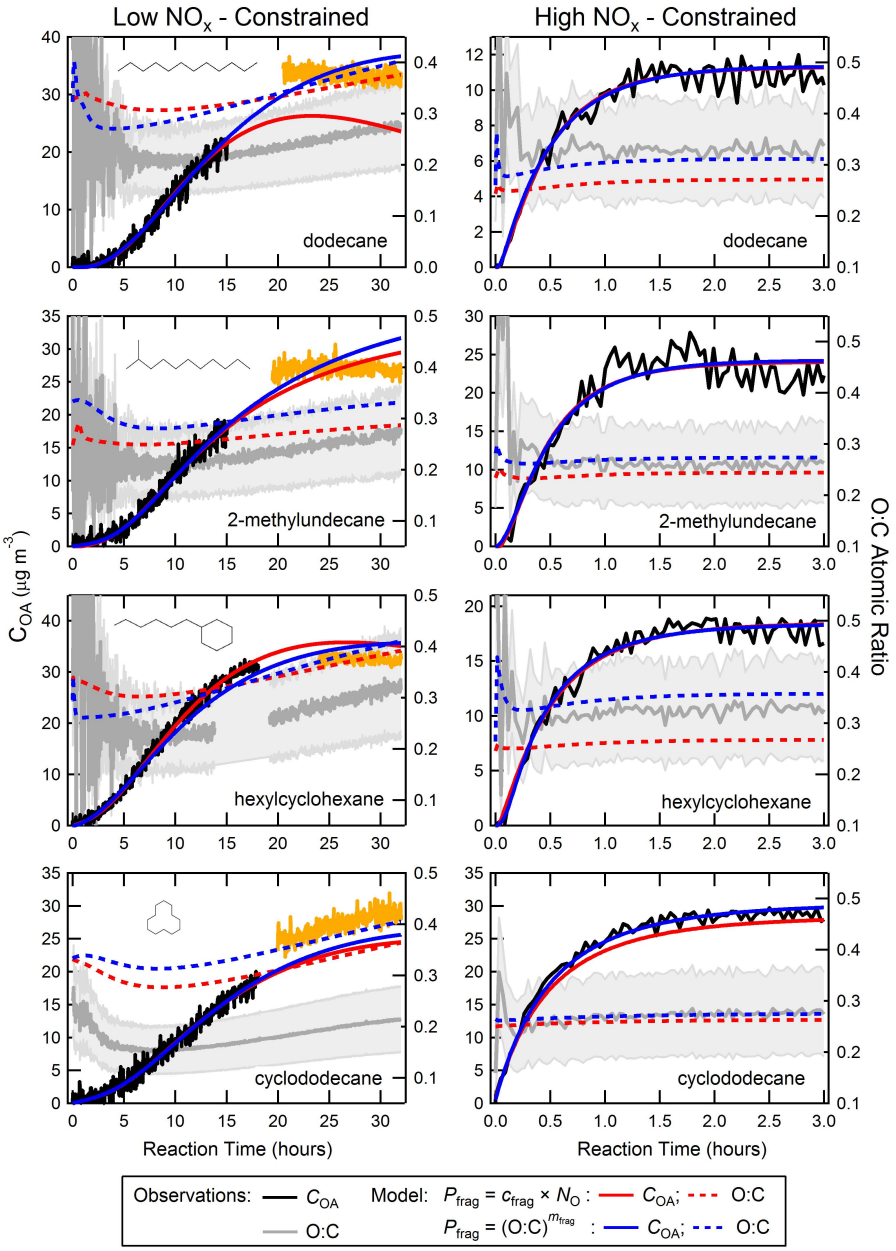

Fig. 8. Same as Fig. 1, but where the high-NO_x and low-NO_x c_{frag} and m_{frag} parameters have been constrained; see text for details.

results illustrate the broader point that interpretation of Van Krevelen diagrams in terms of how the SOA composition relates to the associated gas-phase composition is not necessarily straightforward since the measurements may likely be affected by condensed phase reactions. This conclusion is consistent with the findings of Craven et al. (2012), who determined that movement between the different identified SOA "factors" occurs along multiple Van Krevelen slopes.

When interpreting the best-fit SOM parameters in terms of chemical mechanisms, as above, it is important to consider the robustness of the fit parameters. This is examined here by re-fitting the SOM to observations of C_{OA} only (as opposed to C_{OA} and O:C), but where the P_{frag} parameters (i.e. c_{frag} and m_{frag}) for the high-NO_x reactions are constrained to be equal to the best-fit values from the low-NO_x reactions, and vice versa. The extent to which the constrained c_{frag} and

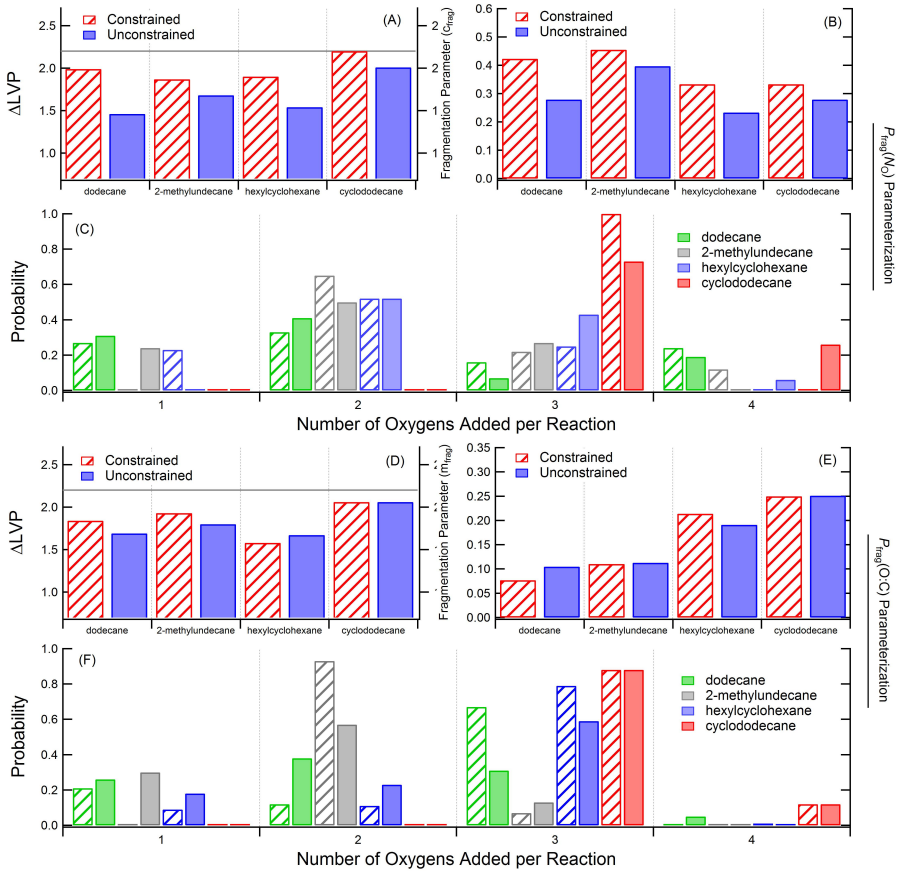

Fig. 9. Best-fit SOM parameters for dodecane, 2-methylundecane, hexylcyclohexane, and cyclodecane under high-NO_x conditions for both the overall best-fit (solid bars, as in Fig. 2) and the best-fit when the c_{frag} and m_{frag} parameters are constrained to be equal to the low-NO_x overall best-fit values (hashed bars). Results are shown for both the $P_{frag}(N_O)$ **(A–C)** and P_{frag}(O:C) **(D–F)** parameterizations and include (**A** and **D**) ΔLVP, (**B** and **E**) the fragmentation parameter, and (**C** and **F**) the oxygen addition array. The constrained model was fit only to the observed C_{OA}. The grey line in **(A)** and **(D)** indicates the upper-limit constraint on ΔLVP.

m_{frag} values differ from the best-fit values differs for each alkane, although in general the constrained high-NO_x c_{frag} is larger (and m_{frag} smaller) compared to the overall best-fit, while for low-NO_x reactions the opposite is true (Table 2). In most cases, it is still possible to fit the SOM to the observed C_{OA} growth, although there are a few exceptions where the C_{OA} is under-predicted after fitting (Fig. 8). In general, the extent to which the best-fit ΔLVP and P_{func} array differ between the constrained and overall fit depends on how different the c_{frag} and m_{frag} parameters are. For the high-NO_x reactions, many of the resulting ΔLVP values for the constrained fits are increased to offset the greater fragmentation, while, importantly, the oxygen distributions are reasonably similar between the constrained and overall best-fit (Fig. 9). The predicted O:C for the constrained fit does not match the observations quite as well as the overall best-fit (although remaining within the ±30 % uncertainty for all cases; Fig. 8). For the low-NO_x reactions, some of the resulting ΔLVP values for the constrained fits are decreased, although for many cases the differences are small, while the oxygen distributions are generally unchanged (Fig. 10). This comparison illustrates that the ΔLVP and P_{frag} parameters can have compensating effects, which indicates that care must be taken in their interpretation. Nonetheless, the results from the constrained and overall best-fits are sufficiently similar that the general conclusions reached above are unchanged.

6 Summary and conclusions

For a comprehensive series of SOA formation experiments from photooxidation of four $N_C = 12$ alkanes, two straight chain and two ring-containing, observations indicate that the SOA yield is larger for these compounds under low- vs. high-NO_x conditions, with the exception of cyclododecane. The

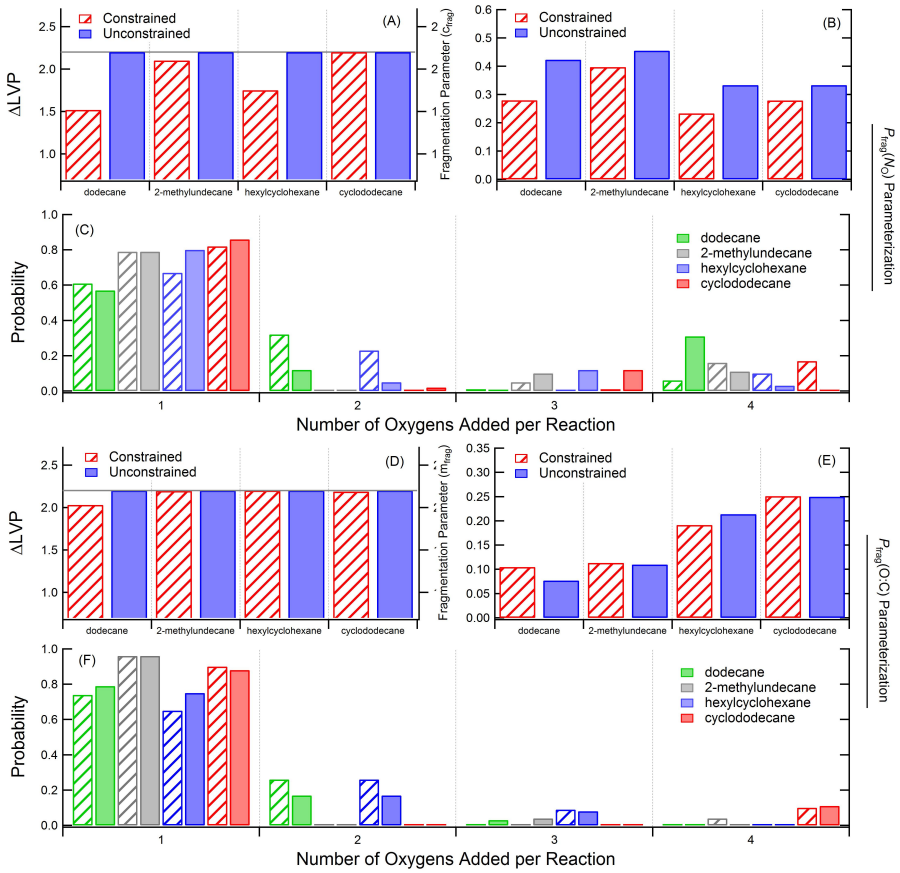

Fig. 10. Best-fit SOM parameters for dodecane, 2-methylundecane, hexylcyclohexane, and cyclodecane under low-NO_x conditions for both the overall best-fit (solid bars, as in Fig. 2) and the best-fit when the c_{frag} and m_{frag} parameters are constrained to be equal to the high-NO_x overall best-fit values (hashed bars). Results are shown for both the $P_{frag}(N_O)$ **(A–C)** and P_{frag}(O:C) **(D–F)** parameterizations and include (**A** and **D**) ΔLVP, (**B** and **E**) the fragmentation parameter, and (**C** and **F**) the oxygen addition array. The constrained model was fit only to the observed C_{OA}. The grey line in **(A)** and **(D)** indicates the upper-limit constraint on ΔLVP.

O:C atomic ratio is generally similar between high- and low-NO_x, although the low-NO_x experiments exhibit a continuous increase in O:C as oxidation proceeds. This difference results primarily from the differing oxidation conditions: the [OH] during low-NO_x experiments was approximately constant around 2×10^6 molecules cm^{-3}, whereas the [OH] during high-NO_x experiments started higher but rapidly decayed due to efficient photolysis of the OH precursor (HONO).

The observed C_{OA} temporal growth curves have been fit to the statistical oxidation model (Cappa and Wilson, 2012) to derive values for the mean decrease in volatility per oxygen added (ΔLVP), the probability of fragmentation and the distribution of oxygens added per reaction. In general, there is excellent model/measurement agreement in terms of the time-evolution of the C_{OA}. This work demonstrates that the use of a kinetic, multi-generation model to represent SOA formation during photooxidation can provide insights into the SOA formation process and facilitate the interpretation of smog chamber observations.

Acknowledgements. This work was supported by the National Science Foundation (ATM-1151062) and the Department of Energy (DE-SC0006626).

Edited by: F. Keutsch

References

Aiken, A. C., DeCarlo, P. F., and Jimenez, J. L.: Elemental analysis of organic species with electron ionization high-resolution mass spectrometry, Anal. Chem., 79, 8350–8358, doi:10.1021/ac071150w, 2007.

Aiken, A. C., Decarlo, P. F., Kroll, J. H., Worsnop, D. R., Huffman, J. A., Docherty, K. S., Ulbrich, I. M., Mohr, C., Kimmel,

J. R., Sueper, D., Sun, Y., Zhang, Q., Trimborn, A., Northway, M., Ziemann, P. J., Canagaratna, M. R., Onasch, T. B., Alfarra, M. R., Prevot, A. S. H., Dommen, J., Duplissy, J., Metzger, A., Baltensperger, U., and Jimenez, J. L.: O/C and OM/OC ratios of primary, secondary, and ambient organic aerosols with high-resolution time-of-flight aerosol mass spectrometry, Environ. Sci. Technol., 42, 4478–4485, doi:10.1021/es703009q, 2008.

Aumont, B., Szopa, S., and Madronich, S.: Modelling the evolution of organic carbon during its gas-phase tropospheric oxidation: development of an explicit model based on a self generating approach, Atmos. Chem. Phys., 5, 2497–2517, doi:10.5194/acp-5-2497-2005, 2005.

Barsanti, K. C., Smith, J. N., and Pankow, J. F.: Application of the np+mP modeling approach for simulating secondary organic particulate matter formation from α-pinene oxidation, Atmos. Environ., 45, 6812-6819, doi:10.1016/j.atmosenv.2011.01.038, 2011.

Cappa, C. D., and Wilson, K. R.: Multi-generation gas-phase oxidation, equilibrium partitioning, and the formation and evolution of secondary organic aerosol, Atmos. Chem. Phys., 12, 9505–9528, doi:10.5194/acp-12-9505-2012, 2012.

Chhabra, P. S., Flagan, R. C., and Seinfeld, J. H.: Elemental analysis of chamber organic aerosol using an aerodyne high-resolution aerosol mass spectrometer, Atmos. Chem. Phys., 10, 4111-4131, doi:10.5194/acp-10-4111-2010, 2010.

Cocker, D. R., Flagan, R. C., and Seinfeld, J. H.: State-of-the-art chamber facility for studying atmospheric aerosol chemistry, Environ. Sci. Technol., 35, 2594–2601, doi:10.1021/es0019169, 2001.

Compernolle, S., Ceulemans, K., and Müller, J. F.: EVAPORATION: a new vapour pressure estimation method for organic molecules including non-additivity and intramolecular interactions, Atmos. Chem. Phys., 11, 9431–9450, doi:10.5194/acp-11-9431-2011, 2011.

Craven, J. S., Yee, L. D., Ng, N. L., Canagaratna, M. R., Loza, C. L., Schilling, K. A., Yatavelli, R. L. N., Thornton, J. A., Ziemann, P. J., Flagan, R. C., and Seinfeld, J. H.: Analysis of secondary organic aerosol formation and aging using positive matrix factorization of high-resolution aerosol mass spectra: application to the dodecane low-NO_x system, Atmos. Chem. Phys., 12, 11795–11817, doi:10.5194/acp-12-11795-2012, 2012.

DeCarlo, P. F., Kimmel, J. R., Trimborn, A., Northway, M. J., Jayne, J. T., Aiken, A. C., Gonin, M., Fuhrer, K., Horvath, T., Docherty, K. S., Worsnop, D. R., and Jimenez, J. L.: Field-deployable, high-resolution, time-of-flight aerosol mass spectrometer, Anal. Chem., 78, 8281–8289, doi:10.1021/ac061249n, 2006.

Donahue, N. M., Robinson, A. L., Stanier, C. O., and Pandis, S. N.: Coupled partitioning, dilution, and chemical aging of semivolatile organics, Environ. Sci. Technol., 40, 2635–2643, doi:10.1021/es052297c, 2006.

Donahue, N. M., Kroll, J. H., Pandis, S. N., and Robinson, A. L.: A two-dimensional volatility basis set – Part 2: Diagnostics of organic-aerosol evolution, Atmos. Chem. Phys., 12, 615–634, doi:10.5194/acp-12-615-2012, 2012.

Heald, C. L., Kroll, J. H., Jimenez, J. L., Docherty, K. S., DeCarlo, P. F., Aiken, A. C., Chen, Q., Martin, S. T., Farmer, D. K., and Artaxo, P.: A simplified description of the evolution of organic aerosol composition in the atmosphere, Geophys. Res. Lett., 37, L08803, doi:10.1029/2010gl042737, 2010.

Jimenez, J. L., Canagaratna, M. R., Donahue, N. M., Prevot, A. S. H., Zhang, Q., Kroll, J. H., DeCarlo, P. F., Allan, J. D., Coe, H., Ng, N. L., Aiken, A. C., Docherty, K. S., Ulbrich, I. M., Grieshop, A. P., Robinson, A. L., Duplissy, J., Smith, J. D., Wilson, K. R., Lanz, V. A., Hueglin, C., Sun, Y. L., Tian, J., Laaksonen, A., Raatikainen, T., Rautiainen, J., Vaattovaara, P., Ehn, M., Kulmala, M., Tomlinson, J. M., Collins, D. R., Cubison, M. J., Dunlea, E. J., Huffman, J. A., Onasch, T. B., Alfarra, M. R., Williams, P. I., Bower, K., Kondo, Y., Schneider, J., Drewnick, F., Borrmann, S., Weimer, S., Demerjian, K., Salcedo, D., Cottrell, L., Griffin, R., Takami, A., Miyoshi, T., Hatakeyama, S., Shimono, A., Sun, J. Y., Zhang, Y. M., Dzepina, K., Kimmel, J. R., Sueper, D., Jayne, J. T., Herndon, S. C., Trimborn, A. M., Williams, L. R., Wood, E. C., Middlebrook, A. M., Kolb, C. E., Baltensperger, U., and Worsnop, D. R.: Evolution of organic aerosols in the atmosphere, Science, 326, 1525–1529, doi:10.1126/science.1180353, 2009.

Kanakidou, M., Seinfeld, J. H., Pandis, S. N., Barnes, I., Dentener, F. J., Facchini, M. C., Van Dingenen, R., Ervens, B., Nenes, A., Nielsen, C. J., Swietlicki, E., Putaud, J. P., Balkanski, Y., Fuzzi, S., Horth, J., Moortgat, G. K., Winterhalter, R., Myhre, C. E. L., Tsigaridis, K., Vignati, E., Stephanou, E. G., and Wilson, J.: Organic aerosol and global climate modelling: a review, Atmos. Chem. Phys., 5, 1053–1123, doi:10.5194/acp-5-1053-2005, 2005.

Lane, T. E., Donahue, N. M., and Pandis, S. N.: Simulating secondary organic aerosol formation using the volatility basis-set approach in a chemical transport model, Atmos. Environ., 42, 7439–7451, doi:10.1016/j.atmosenv.2008.06.026, 2008.

Lim, Y. B. and Ziemann, P. J.: Effects of Molecular Structure on Aerosol Yields from OH Radical-Initiated Reactions of Linear, Branched, and Cyclic Alkanes in the Presence of NO_x, Environ. Sci. Technol., 43, 2328–2334, doi:10.1021/es803389s, 2009.

Loza, C. L., Chhabra, P. S., Yee, L. D., Craven, J. S., Flagan, R. C., and Seinfeld, J. H.: Chemical aging of m-xylene secondary organic aerosol: laboratory chamber study, Atmos. Chem. Phys., 12, 151–167, doi:10.5194/acp-12-151-2012, 2012.

Odum, J. R., Hoffmann, T., Bowman, F., Collins, D., Flagan, R. C., and Seinfeld, J. H.: Gas/particle partitioning and secondary organic aerosol yields, Environ. Sci. Technol., 30, 2580–2585, doi:10.1021/es950943+, 1996.

Pankow, J. F.: An absorption-model of the gas aerosol partitioning involved in the formation of secondary organic aerosol, Atmos. Environ., 28, 189–193, doi:10.1016/1352-2310(94)90094-9, 1994.

Pankow, J. F. and Asher, W. E.: SIMPOL.1: a simple group contribution method for predicting vapor pressures and enthalpies of vaporization of multifunctional organic compounds, Atmos. Chem. Phys., 8, 2773–2796, doi:10.5194/acp-8-2773-2008, 2008.

Robinson, A. L., Donahue, N. M., Shrivastava, M. K., Weitkamp, E. A., Sage, A. M., Grieshop, A. P., Lane, T. E., Pierce, J. R., and Pandis, S. N.: Rethinking organic aerosols: Semivolatile emissions and photochemical aging, Science, 315, 1259–1262, doi:10.1126/science.1133061, 2007.

Valorso, R., Aumont, B., Camredon, M., Raventos-Duran, T., Mouchel-Vallon, C., Ng, N. L., Seinfeld, J. H., Lee-Taylor, J., and Madronich, S.: Explicit modelling of SOA formation from alpha-pinene photooxidation: sensitivity to vapour pressure esti-

mation, Atmos. Chem. Phys., 11, 6895–6910, doi:10.5194/acp-11-6895-2011, 2011.

Yee, L. D., Craven, J. S., Loza, C. L., Schilling, K. A., Ng, N. L., Canagaratna, M. R., Ziemann, P. J., Flagan, R. C., and Seinfeld, J. H.: Secondary organic aerosol formation from Low-NO_x Photooxidation of Dodecane: Evolution of Multigeneration Gas-Phase Chemistry and Aerosol Composition, J. Phys. Chem. A, 116, 6211–6230, doi:10.1021/jp211531h, 2012.

Zhang, Q., Jimenez, J. L., Canagaratna, M. R., Allan, J. D., Coe, H., Ulbrich, I., Alfarra, M. R., Takami, A., Middlebrook, A. M., Sun, Y. L., Dzepina, K., Dunlea, E., Docherty, K., DeCarlo, P. F., Salcedo, D., Onasch, T., Jayne, J. T., Miyoshi, T., Shimono, A., Hatakeyama, S., Takegawa, N., Kondo, Y., Schneider, J., Drewnick, F., Borrmann, S., Weimer, S., Demerjian, K., Williams, P., Bower, K., Bahreini, R., Cottrell, L., Griffin, R. J., Rautiainen, J., Sun, J. Y., Zhang, Y. M., and Worsnop, D. R.: Ubiquity and dominance of oxygenated species in organic aerosols in anthropogenically-influenced Northern Hemisphere midlatitudes, Geophys. Res. Lett., 34, L13801, doi:10.1029/2007GL029979, 2007.

Appendix C

Secondary Organic Aerosol Coating Formation and Evaporation: Chamber Studies Using Black Carbon Seed Aerosol and the Single-Particle Soot Photometer[1]

[1]This chapter is reproduced by permission from "Secondary Organic Aerosol Coating Formation and Evaporation: Chamber Studies Using Black Carbon Seed Aerosol and the Single-Particle Soot Photometer" by Andrew R. Metcalf, Christine L. Loza, Matthew M. Coggon, Jill S. Craven, Haflidi H. Jonsson, Richard C. Flagan, and John H. Seinfeld, *Aerosol Science and Technology*, (47) 326 – 347, ISSN: 0278-6826, 2013, 2013. Copyright 2013

Aerosol Science and Technology, 47:326–347, 2013

ISSN: 0278-6826 print / 1521-7388 online
DOI: 10.1080/02786826.2012.750712

Secondary Organic Aerosol Coating Formation and Evaporation: Chamber Studies Using Black Carbon Seed Aerosol and the Single-Particle Soot Photometer

Andrew R. Metcalf,[1,2] Christine L. Loza,[3] Matthew M. Coggon,[3] Jill S. Craven,[3] Haflidi H. Jonsson,[4] Richard C. Flagan,[1,3] and John H. Seinfeld[1,3]

[1]*Division of Engineering and Applied Science, California Institute of Technology, Pasadena, California, USA*
[2]*Combustion Research Facility, Sandia National Laboratories, Livermore, California, USA*
[3]*Division of Chemistry and Chemical Engineering, California Institute of Technology, Pasadena, California, USA*
[4]*Center for Interdisciplinary Remotely Piloted Aircraft Studies, Naval Postgraduate School, Monterey, California, USA*

We report a protocol for using black carbon (BC) aerosol as the seed for secondary organic aerosol (SOA) formation in an environmental chamber. We employ a single-particle soot photometer (SP2) to probe single-particle SOA coating growth dynamics and find that SOA growth on nonspherical BC aerosol is diffusion-limited. Aerosol composition measurements with an Aerodyne high resolution time-of-flight aerosol mass spectrometer (AMS) confirm that the presence of BC seed does not alter the composition of SOA as compared to self-nucleated SOA or condensed SOA on ammonium sulfate seed. We employ a 3-wavelength photoacoustic soot spectrometer (PASS-3) to measure optical properties of the systems studied, including fullerene soot as the surrogate BC seed, nucleated naphthalene SOA from high-NO_x photooxidation, and nucleated α-pinene SOA from low-NO_x photooxidation. A core-and-shell Mie scattering model of the light absorption enhancement is in good agreement with measured enhancements for both the low- and high-NO_x α-pinene photooxidation systems, reinforcing the assumption of a core-shell morphology for coated BC particles. A discrepancy between measured and modeled absorption enhancement factors in the naphthalene photooxidation system is attributed to the wavelength-dependence of refractive index of the naphthalene SOA. The coating of high-NO_x α-pinene SOA decreases after reaching a peak thickness during irradiation, reflecting a volatility change in the aerosol, as confirmed by the relative magnitudes of f_{43} and f_{44} in the AMS spectra. The protocol described here provides a framework by which future studies of SOA optical properties and single-particle growth dynamics may be explored in environmental chambers.

[Supplementary materials are available for this article. Go to the publisher's online edition of *Aerosol Science and Technology* to view the free supplementary files.]

1. INTRODUCTION

Refractory black carbon (rBC), alternately referred to as elemental carbon, is the dominant component of light-absorbing atmospheric aerosol. While rBC refers to the strongly light-absorbing component of soot, emission sources containing rBC, such as diesel exhaust, may contain other constituents such as polycyclic aromatic hydrocarbons (PAHs), aliphatic hydrocarbons, and other volatile compounds (Schauer et al. 1996; Kleeman et al. 2000; Fruin et al. 2004). These organic compounds co-emitted with rBC evaporate substantially upon dilution from the tailpipe to ambient conditions (Robinson et al. 2007).

The traditional understanding is that fresh, urban-emitted rBC is almost entirely composed of hydrophobic rBC and is unlikely to act as cloud condensation nuclei (CCN) (Weingartner et al. 1997). After emission, rBC particles can become coated by inorganic and organic non-light-absorbing components via coagulation with other particles and condensation of vapors (Abel et al. 2003; Pósfai et al. 2003; Riemer et al. 2004; Moffet and Prather 2009). Recent studies with a single-particle soot photometer (SP2) have revealed that fresh, urban-emitted rBC particles may be thinly coated with light-scattering material, while rBC in aged air masses tends to be more thickly coated (Moteki et al. 2007; Shiraiwa et al. 2007, 2008; Schwarz et al. 2008a; Subramanian et al. 2010; Metcalf et al. 2012). Timescales

Received 23 May 2012; accepted 21 October 2012.
This work was supported by the U.S. Department of Energy grant DE-SC0006626.
Address correspondence to John H. Seinfeld, Division of Chemistry and Chemical Engineering, California Institute of Technology, 1200 E. California Blvd., Mail Code: 210–41, Pasadena, CA 91125, USA. E-mail: seinfeld@caltech.edu

for the transition from a fresh to a more aged state have been estimated to range from 12 h to a day (Johnson et al. 2005; Moteki et al. 2007; Khalizov et al. 2009a; Park et al. 2012). Interactions with gas and aerosol species transform rBC into an internally mixed state, where it may eventually serve as a CCN (Zuberi et al. 2005). Hygroscopic coatings also enhance the wet deposition rate of these particles (Weingartner et al. 1997; Saathoff et al. 2003; Jacobson 2006; Stier et al. 2006). A coating of non-light-absorbing components onto rBC increases the light scattering and absorption cross sections of these particles (Fuller et al. 1999; Saathoff et al. 2003; Schnaiter et al. 2005; Bond et al. 2006; Mikhailov et al. 2006; Stier et al. 2006; Slowik et al. 2007a; Zhang et al. 2008; Wehner et al. 2009; Khalizov et al. 2009b; Cross et al. 2010; Lack and Cappa 2010; Shiraiwa et al. 2010). At least one ambient study, however, found no evidence of an enhancement of light absorption by condensation of secondary material (Chan et al. 2010b). A study of ambient rBC in Toronto showed no detectable change in absorption enhancement between fresh and aged aerosol but attributed this observation to the fact that the fresh rBC had a sufficient coating such that additional coatings did not further enhance absorption (Knox et al. 2009).

While ambient rBC measurements have revealed valuable insights into the aging process, namely coating thicknesses and growth timescales, important questions still remain. What mechanisms govern the transition from externally to internally mixed rBC aerosol? Does rBC, acting as a site for condensation of secondary organic aerosol (SOA), affect the composition of the SOA as compared to SOA condensed onto other aerosol types or nucleated homogeneous aerosol? To what extent are the coatings on rBC sufficiently volatile to evaporate upon dilution? Of what physical structure is the rBC and its "coating" and how might this affect interpretation of absorption enhancements seen (or not seen) in ambient data?

Controlled laboratory experiments of rBC aging can isolate some of the complexities of the aging process. The absorption enhancement that arises from coating nascent soot particles with a variety of non-light-absorbing materials is readily measured (Saathoff et al. 2003; Schnaiter et al. 2003, 2005; Mikhailov et al. 2006; Slowik et al. 2007a; Zhang et al. 2008; Khalizov et al. 2009b; Cross et al. 2010). Initially fractal soot agglomerates tend to compact substantially after a coating has formed (Saathoff et al. 2003; Slowik et al. 2007b; Zhang et al. 2008; Khalizov et al. 2009a,b; Cross et al. 2010; Bueno et al. 2011). In addition, rBC and polystyrene latex spheres (PSL) of the same mobility are observed to acquire sulfuric acid coatings at the same rate, indicating that the coating mechanism is independent of particle composition and shape (Khalizov et al. 2009a).

Limited laboratory chamber studies of SOA growth in the presence of soot seed particles exist. Studies at the University of North Carolina Ambient Air Research Facility have focused on how the presence of soot affects gas-particle partitioning and found that diffusional mass transfer is the limiting control on gas-particle partitioning (Strommen and Kamens 1997, 1999), and that the polarity of the seed particles, including diesel and wood soot, and the gas-phase organic compounds can affect the gas-particle equilibrium partitioning (Leach et al. 1999). These studies have focused on the partitioning between gas and particle phases rather than any unique chemical or physical properties of either the gases or the soot. Studies at the Aerosols, Interactions and Dynamics in the Atmosphere (AIDA) chamber facility report the enhancement of light absorption by soot seed particles coated with α-pinene ozonolysis SOA (Saathoff et al. 2003) and evaluate absorption enhancements by particle coagulation and growth of SOA (Schnaiter et al. 2003, 2005). These studies have focused primarily on the optical and morphological properties of the soot as growth of SOA or coagulation with other particles occurs in the chamber. Studies at the Carnegie Mellon University environmental chamber found that SOA formed by the photooxidation of evaporated diesel exhaust exceeded by a wide margin the SOA mass predicted by a model including the classified hydrocarbons (Weitkamp et al. 2007). A study at the Paul Scherrer Institute (PSI) smog chamber characterized the chemical composition and emission factors of primary and secondary organic aerosol from three diesel vehicles with various engine after-treatment systems (Chirico et al. 2010). These studies have focused on characterizing SOA from the many gas-phase precursors found in diesel exhaust or on the efforts to clean up the exhaust from diesel engines. Most of the studies listed above used fresh diesel or wood soot, which typically has a thin layer of nonrefractory material on the rBC or has soot co-emitted with many gas-phase species, such as PAHs. Uncoated spark-generated soot was also used and has been found to be chemically and optically different than diesel soot and is, therefore, not a good surrogate for atmospheric rBC (Kirchner et al. 2003; Schnaiter et al. 2003). Commercially available fullerene soot is a fractal, hydrophobic particle that most resembles ambient rBC in the SP2 instrument (Moteki and Kondo 2010; Laborde et al. 2012) and is structurally similar to diesel soot (Moteki et al. 2009), although chemical and optical comparisons to ambient soot have yet to be reported.

A principal goal of this study is to demonstrate the utility of chamber experiments that employ fullerene soot as a refractory black carbon seed aerosol in conjunction with the single-particle soot photometer, the photoacoustic soot spectrometer, and the aerosol mass spectrometer to probe the dynamics of secondary aerosol formation. Three SOA systems were studied to demonstrate the utility of this experimental protocol on a variety of chemical and optical properties. To distinguish this study from previous chamber studies with soot, the rBC surrogate used in this study is dry, uncoated fullerene soot to avoid artifacts from coatings and additional hydrocarbons that are present with, for example, diesel soot. Particle-by-particle measurements of the coating thickness of SOA on the rBC seed by the SP2 directly reveal dynamic growth and evaporation processes. Once SOA growth has reached a point at which the coating thickness is no longer changing appreciably, chamber dilution can be used to provide a driving force for SOA evaporation and an assessment of SOA volatility through decrease of coating thickness. Simultaneous particle optical property and coating

composition measurements provide data that can relate growth and evaporation behavior to SOA chemical composition. A fundamental chemical examination of the composition changes during SOA growth is beyond the scope of this study; however, demonstrating that composition changes occur coincidentally with changes in rBC coating thicknesses and aerosol optical properties provide a framework by which future mechanistic studies may be carried out.

2. METHODS

2.1. Experimental Protocols

Experiments (Table 1) were conducted in the Caltech dual 28-m^3 Teflon chambers. Details of the facilities are given elsewhere (Cocker et al. 2001; Keywood et al. 2004). Before each experiment, the chambers were flushed with dried, purified air for >24 h, until the particle number concentration (<10 cm^{-3}), mass concentration (<0.1 $\mu g\ m^{-3}$), and hydrocarbon mixing ratios were below detection limits of the instruments. Seeded experiments were conducted with two types of seeds; fullerene soot (stock #40971, lot #L20W054, Alfa Aesar, Ward Hill, MA, USA) as a fractal, rBC surrogate and ammonium sulfate (AS) as a spherical inorganic particle alternative. Fullerene soot particles were generated by nebulizing a suspension of fullerene soot and milliQ water until the desired particle volume concentration in the chamber was reached. Prior to nebulizing, the fullerene soot suspension was sonicated for ~20 min to facilitate the mixing of the hydrophobic soot particles in water and to break up any large agglomerates. Ammonium sulfate

TABLE 1
Summary of experiments

Experiment number	$[HC]_o$ [ppb]	OH source	Seed	Seed volume[a] [$\mu m^3\ cm^{-3}$]	SOA mass [$\mu g\ m^{-3}$]	Description
Naphthalene						
1	16.6 ± 0.1	CH_3ONO[b]	rBC[c]	10.1 ± 0.7	13.0 ± 0.20	SOA condensation followed by chamber dilution
2	10.7 ± 0.1	CH_3ONO	AS[d] + rBC	34.4 ± 2.8	14.2 ± 0.14	SOA condensation with seed competition followed by chamber dilution
3	21.9 ± 0.1	CH_3ONO	naph[e]	43.6 ± 0.5	–	SOA nucleation with rBC injection and coagulation
4	27.5 ± 0.1	CH_3ONO	naph + rBC	62.3 ± 1.5	22.0 ± 0.34[f]	SOA nucleation followed by rBC injection and SOA growth then chamber dilution
α-pinene						
5	27.0 ± 0.1	CH_3ONO	rBC	14.4 ± 0.5	29.2 ± 0.70[g]	SOA condensation followed by chamber dilution
6	24.1 ± 0.1	CH_3ONO	AS + rBC	28.9 ± 1.1	9.4 ± 0.36	SOA condensation with seed competition followed by chamber dilution
7	10.8 ± 0.2	H_2O_2[h]	rBC	18.2 ± 1.0	23.0 ± 0.12	SOA condensation followed by chamber dilution
8	11.6 ± 0.2	H_2O_2	AS + rBC	32.6 ± 1.5	16.2 ± 0.14	SOA condensation with seed competition followed by chamber dilution
9	18.0 ± 0.1	H_2O_2	α-p[i] + rBC	28.2 ± 1.0	49.8 ± 0.16[f]	SOA nucleation followed by rBC injection and SOA growth then chamber dilution

[a]Calculated from DMA data assuming spherical particles. [b]CH_3ONO was used for high-NO_x experiments, to which extra NO was added prior to irradiation to bring $[NO]_o$ to 369–416 *ppb*. [c]rBC = fullerene soot aerosol. [d]AS = ammonium sulfate aerosol. [e]naph = nucleated SOA from naphthalene-OH photooxidation prior to rBC injection. [f]SOA mass after the second growth period with SOA mass from the first period subtracted. [g]Measurement taken after some evaporation of SOA had occurred. [h]H_2O_2 was used for low-NO_x experiments, to which no extra NO was added prior to irradiation and $[NO]_o$ was 1.5–2.6 *ppb* prior to irradiation. [i]α-p = nucleated SOA from α-pinene-OH photooxidation prior to rBC injection.

(AS), a commonly used seed particle in environmental chambers, was injected into the chamber by atomizing a 0.015 M aqueous ammonium sulfate solution. In the "AS + rBC" experiments denoted in Table 1, ammonium sulfate was injected into the chamber and allowed to mix for ∼30 min while gas-phase species were loaded into the chamber before injection of the fullerene soot. Upon injection of rBC in these dual seed experiments, an attempt was made to match the calculated particle surface areas of the AS and rBC from online scanning mobility particle sizer measurements. The median mobility diameter of the AS seed was ∼90 nm while for the fullerene soot the median mobility diameter was ∼140 nm (Figure S1b).

Experiments were run under both low- and high-NO_x conditions using hydrogen peroxide (H_2O_2) and methyl nitrite (CH_3ONO) as the OH sources, respectively. H_2O_2 was injected into the chamber by evaporating 280 μL of 50% wt aqueous solution into the chamber with 5 L min^{-1} of purified air. CH_3ONO was vaporized into an evacuated 500 mL glass bulb and introduced into the chamber with 5 L min^{-1} of purified air. CH_3ONO was synthesized following the method described by Taylor et al. (1980) and modified by Chan et al. (2010a).

Two SOA precursors were studied: naphthalene and α-pinene. Naphthalene is an important polycyclic aromatic hydrocarbon (PAH) that, like rBC, is a product of incomplete combustion in diesel engines and biomass burning (Schauer et al. 1999, 2001; Ravindra et al. 2008). PAHs, in general, may account for as much as one-half of SOA from diesel emissions (Chan et al. 2009). Napthalene (99%, Sigma-Aldrich, St. Louis, MO, USA) was introduced into the chamber by flowing 1 L min^{-1} purified air through an FEP Teflon tube packed with solid naphthalene (Chan et al. 2009). α-Pinene, the most abundantly emitted monoterpene, is an important biogenic volatile organic compound (VOC), with global emissions of 34–50 Tg C yr^{-1} (Guenther et al. 1995; Chung and Seinfeld 2002; Pye et al. 2010). α-Pinene was introduced into the chamber by injecting a volume of liquid into a glass bulb, and the vapor was carried into the chamber with 5 L min^{-1} of purified air. All naphthalene experiments were conducted in the same chamber, while all but one α-pinene experiment (Experiment 8 in Table 1) were conducted in the other chamber. In all experiments, the chamber contents, seed particles, parent hydrocarbon, and OH source, were allowed to mix for 1 h before beginning irradiation. In most experiments, after maximum particle growth was obtained, the UV lights were turned off and the chamber was diluted ∼12–18 h while sampling continued. After irradiation was stopped and before chamber dilution began, cyclohexane, injected by a method similar to α-pinene injection, was introduced to the chamber to be used as a tracer for dilution.

2.2. Instrumentation

A suite of instruments was used to study the evolution of the gas and particle phases. The parent hydrocarbons and dilution tracer were measured using a gas chromatograph with flame ionization detector (GC/FID, Model 6890N, Agilent Technologies, Inc., Santa Clara, CA, USA), equipped with an HP-5 column (15 m × 0.53 mm ID × 1.5 μm thickness, Agilent). The GC/FID response to naphthalene was calibrated by dissolving a known mass of naphthalene in dichloromethane and vaporizing into a 55 L Teflon chamber. The GC/FID response to α-pinene and cyclohexane was calibrated by vaporizing a small volume of liquid into a 50 L chamber and diluting aliquots of that sample into a 55 L chamber. NO and NO_x were measured with a chemiluminescence NO/NO_x analyzer (Model APNA 360, HORIBA Instruments Incorporated, Irvine, CA, USA). Relative humidity (RH), temperature (T), and O_3 were continuously monitored. RH of the chamber was typically <5% during irradiation periods, rising to ∼10% during the overnight chamber dilution. The initial chamber temperature was typically ∼20–24°C; however, heating from the UV lights caused a rise in temperature of ∼4–6°C during irradiation. Initial O_3 concentration was typically <5 ppb. Varying amounts of NO were added from a gas cylinder (Scott-Marrin, Riverside, CA, USA) to ensure high NO_x conditions at the start of most experiments, except where noted in Table 1. Aerosol size distribution and number concentration were measured continuously using a custom-built scanning mobility particle sizer consisting of a differential mobility analyzer (DMA, Model 3081, TSI Incorporated, Shoreview, MN, USA) coupled to a condensation particle counter (CPC, Model 3010, TSI), henceforth referred to as the DMA.

Refractory black carbon (rBC) mass measurements were made with a Droplet Measurement Technologies (DMT, Boulder, CO, USA) Single Particle Soot Photometer (SP2). The SP2 affords measurements of both the particle-by-particle rBC mass as well as the thickness of non-rBC coating on each particle (Stephens et al. 2003; Baumgardner et al. 2004; Schwarz et al. 2006; Moteki and Kondo 2007; Slowik et al. 2007a). This particular SP2 was used in a previous study (Metcalf et al. 2012) and the only difference in configuration was an increase in the gain setting on the narrowband incandescence channel to increase sensitivity to rBC mass. Calibrations, as detailed by Metcalf et al. (2012), were repeated just prior to this set of chamber experiments. Aquadag (Aqueous Deflocculated Acheson Graphite, Acheson Colloids Company, Port Huron, MI, USA) was mobility-selected by a DMA and sampled by the SP2. Because the SP2 is known to be more sensitive to Aquadag than to other rBC standards (Laborde et al. 2012), a correction factor of 25% is used to relate the SP2 signals to fullerene soot mass (Baumgardner et al. 2012). Estimated uncertainty in single-particle mass determination is ∼40%, based largely on the uncertainty in Aquadag mass during calibration and the relationship to fullerene soot mass. To relate rBC mass to particle size, the volume-equivalent diameter (VED) is calculated assuming the rBC is a void-free sphere with an effective mobility density given by Gysel et al. (2011). Note that there is additional uncertainty in the fullerene mobility density because not all batches of fullerene soot have the same effective density (Laborde et al. 2012); the batch used in this study differs from that measured by Gysel et al. (2011). With propagation of

errors through the calculations, estimated uncertainty in VED is ~12%.

Real-time particle mass spectra were collected continuously by an Aerodyne high resolution time-of-flight aerosol mass spectrometer (AMS) (Jayne et al. 2000; DeCarlo et al. 2006; Canagaratna et al. 2007). The AMS was operated predominantly in the lower resolution, higher sensitivity "V-mode," but was manually switched periodically to the high resolution "W-mode." "V-mode" data were analyzed using a fragmentation table to separate sulfate, ammonium, and organic spectra and to time-trace specific m/z ratios. "W-mode" data were analyzed in IGOR Pro (Wavemetrics, Inc., Lake Oswego, OR, USA) using the PIKA 1.10H module to determine the chemical formulas contributing to distinct m/z ratios (DeCarlo et al. 2006). The AMS ionization efficiency was calibrated at the beginning of the study using dried, 350 nm NH_4NO_3 particles. AMS collection efficiency is assumed to be 0.5 to account for particle bounce off the heater inside the instrument (Huffman et al. 2005; Middlebrook et al. 2012); however, because the collection efficiency could not be explicitly determined for the systems studied, the mass-weighted optical properties calculated in this work use aerosol mass calculated from particle volume concentrations determined by the DMA measurements. Aerosol densities were determined by comparing DMA volume distributions with AMS particle time-of-flight mass distributions following the method described by DeCarlo et al. (2004). AMS mass loadings reported in the figures and in Table 1 have an overall uncertainty of ~30% (Bahreini et al. 2009). AMS bulk masses are averaged over 3 min intervals.

Aerosol absorption and scattering coefficients (b_{abs} and b_{sca}) were measured with a DMT 3-λ photoacoustic soot spectrometer (PASS-3), which is an instrument based on several previous prototypes (Lewis et al. 2008, and references therein). Briefly, submicron aerosol scattering coefficient is determined by an integrating sphere/photodetector at each wavelength, 405 nm, 532 nm, and 781 nm. Aerosol absorption is determined by the photoacoustic method, which uses a microphone to measure sound/pressure waves emanating from heated gas around aerosols absorbing laser light. The PASS-3 scattering signal was calibrated with a concentrated stream of 220 nm polystyrene latex spheres (PSL) and the absorption signal with aerosol from a concentrated Nigrosin dye (product #198285 lot #MKBD9679V, Sigma-Aldrich) solution. Calibrations were performed at particle concentrations much higher than those used in the chamber experiments in order to make use of the laser power meter onboard the instrument and calculate extinction using Beer's Law. The linear response of the PASS-3 is appropriately extrapolated to experiment-relevant values because of the linearity of the detectors (Cross et al. 2010, supplement). During this study, data from the $\lambda = 532$ nm channel were deemed unreliable due to a hardware malfunction and have been omitted from the analysis. Lower detection limit is estimated by three times the standard deviation of signal noise during particle-free sampling. The lower detection limits for b_{abs} are 24.62 ± 0.36 and 3.89 ± 0.65 Mm^{-1} and for b_{sca} are 10.40 ± 1.42 and 8.20 ± 1.64 Mm^{-1} for $\lambda = 405$ and 781 nm, respectively. Absolute accuracy at aerosol levels relevant to this study was not determined; however, other PASS-3 instruments have reported absolute accuracy well within 20% (Flowers et al. 2010, supplement). In this work, measured absorption enhancement, $E^m_{abs,\lambda}$, is defined as

$$E^m_{abs,\lambda}(t) = \frac{b_{abs,\lambda}(t)}{b_{abs,\lambda}(t_0)}, \quad [1]$$

where $b_{abs,\lambda}(t)$ is the measured aerosol absorption coefficient as a function of time, t, and $b_{abs,\lambda}(t_0)$ is the measured absorption coefficient of the (uncoated) fullerene soot seed particles prior to chamber irradiation. Because the mass of rBC in the chamber remains relatively constant during the irradiation periods of the experiments, this formulation is equivalent to defining enhancement using the mass absorption cross section (MAC).

A prototype instrument was used to detect particle sphericity by single-particle laser light scattering (see the online supplemental information). Briefly, single particles are brought into a circularly-polarized laser beam ($\lambda = 532$ nm) and the angular pattern of light scattered off the particle is detected with a photomultiplier tube (PMT) assembly. Eight detectors positioned at a polar angle of 50° in the forward scattering direction measure light scattered onto lenses at one end of fiber optic cables, the other ends of which are mounted in front of a PMT assembly that has a single channel devoted to each cable.

According to Mie theory, homogeneous spherical particles scatter circularly polarized light uniformly around the azimuth of a given polar angle. Particle sphericity, the degree to which a given particle acts like a sphere when scattering light, has been measured and analyzed previously with instruments similar to that used here (Dick et al. 1994, 1998; Sachweh et al. 1995). Our analysis follows the same logic as that of previous authors, although our mathematical formulation of sphericity is different (see the online supplemental information). To determine the degree of sphericity, we quantify the deviation among eight sensors at a fixed polar angle, which we call "nonsphericity" (Φ). Little deviation and smaller nonsphericity values are indicative of a spherical particle, while a large deviation and larger nonsphericity values indicate a nonspherical particle. Because the optical fibers differ in length and in radii of curvature between the lenses and the PMT, these artifacts are accounted for in the nonsphericity calculation by quantifying the extent to which each channel has the same deviation from its respective median signal.

2.3. Mie Scattering Model

For determination of single-particle coating thicknesses from SP2 light-scattering measurements and for comparison to bulk optical properties measured by the PASS-3, the Mie scattering model is used to calculate scattering and absorption cross sections for single particles. The Mie scattering model in this study (used previously by Metcalf et al. 2012) was adapted from

a version of BHMIE (Bohren and Huffman 1998) to compute scattering coefficients for a stratified sphere (Toon and Ackerman 1981). For interpretation of SP2 scattering signals, the scattering function is integrated over the solid angles subtended by the SP2 detectors to compare the measured and modeled signals (scattering cross section) to derive an optical diameter, from which the coating thickness on the rBC core is determined. Note that coating thicknesses reported in this work are in terms of diameter and are, thus, the particle diameter increase as a result of the coating. Mean coating thicknesses are reported as a number-weighted mean over all detected coating thicknesses over all rBC core sizes. The measured peak scattering signal is derived from a leading edge-only (LEO) fit of the scattering signal in order to correct for evaporating coatings as particles traverse the laser in the SP2 (Gao et al. 2007). The rBC refractive index is assumed to be $1.95 + 0.79$i (Bond and Bergstrom 2006), and a coating refractive index of $1.5 + 0.0$i is used, matching previous studies (Schwarz et al. 2008a,b; Metcalf et al. 2012). Uncertainty in retrieved coating thickness from the SP2 scattering signal is ∼40% (Metcalf et al. 2012). The Mie scattering model of SP2 signals is also used to determine the size of purely scattering particles. Again, a refractive index of $1.5 + 0.0$i and the LEO fitting method on the measured scattering signal are used, and the optical size range of detection is 169–600 nm. Estimated uncertainty in retrieved optical diameter is ∼5% for purely scattering particles.

For comparison to the measured absorption enhancement factors, the Mie model is used to calculate a time-dependent absorption enhancement factor from the mean coating thicknesses retrieved from SP2 measurements. Because total scattering and absorption is considered, integration over the SP2 detection angles is not carried out in this calculation. At each time interval, rBC core sizes from SP2 incandescence signals are binned into 36 core size bins spanning 90–265 nm VED and into 37 coating thickness bins of −60–300 nm diameter, based on the detected scattering cross sections. Note that negative coating thicknesses at a given rBC VED represent scattering cross sections smaller than what the core-shell Mie model calculates for a particle with zero coating thickness on those rBC cores. These values are necessary to include due to the uncertainties in assumed refractive index and in SP2 calibration. From these binned number of particles, N, a time- and rBC-core-size-dependent mean coating thickness, $\overline{D}_{\text{coat}}$, is calculated, from which the Mie model is used to calculate the absorption cross sections, $\sigma_{\text{abs},\lambda}$, at $\lambda = 405$ and 781 nm. The rBC core-size-dependent enhancement factors, $\overline{E}^{c}_{\text{abs},\lambda}$, are calculated from these mean coating thicknesses by

$$\overline{E}^{c}_{\text{abs},\lambda}\,(t, \text{VED}) = \frac{\sigma_{\text{abs},\lambda}\left(\text{VED}, \overline{D}_{\text{coat}}\,(t, \text{VED})\right)}{\sigma_{\text{abs},\lambda}\,(\text{VED}, D_{\text{coat}} = 0)}. \quad [2]$$

The fraction, $f_{\sigma_{\text{abs},\lambda}}$, of total absorption cross section present at each rBC core size relative to the total absorption cross section over all sizes is calculated by

$$f_{\sigma_{\text{abs},\lambda}}\,(t, \text{VED}) = \frac{\sum_{D_{\text{coat}}} N\,(t, \text{VED}, D_{\text{coat}}) \times \sigma_{\text{abs},\lambda}\left(\text{VED}, \overline{D}_{\text{coat}}\,(t, \text{VED})\right)}{\sum_{\text{VED}}\sum_{D_{\text{coat}}} N\,(t, \text{VED}, D_{\text{coat}}) \times \sigma_{\text{abs},\lambda}\left(\text{VED}, \overline{D}_{\text{coat}}\,(t, \text{VED})\right)}. \quad [3]$$

Finally, the calculated time-dependent absorption enhancement factor, $E^{c}_{\text{abs},\lambda}$, is calculated by weighting the rBC core-size-dependent enhancement factors by the fraction of absorption cross section at each rBC size bin,

$$E^{c}_{\text{abs},\lambda}\,(t) = \sum_{\text{VED}} f_{\sigma_{\text{abs},\lambda}}\,(t, \text{VED}) \times \overline{E}^{c}_{\text{abs},\lambda}\,(t, \text{VED}). \quad [4]$$

In the final calculation of size-dependent absorption enhancements, only rBC VED of 160–265 nm are considered in the equations above. At rBC VEDs smaller than 160 nm, the scattering cross section of uncoated rBC particles is below the optical detection limit of the SP2, and, therefore, mean coating thicknesses will be biased high at these rBC core sizes. Although the size range of detection of the SP2 is narrower than that of the PASS-3, the weighting done here should give proper importance to the fewer but larger and more optically active coated rBC particles that most influence the PASS-3 signal. Uncertainty in the calculations of absorption enhancements are likely dominated by the uncertainty in rBC VED.

3. RESULTS

3.1. Fullerene Soot Characteristics

3.1.1. Sphericity

Figure 1 presents distributions of nonsphericity values calculated for dry, uncoated fullerene soot (BC), ammonium sulfate (AS), and polystyrene latex spheres (PSL). Lognormal fits to each histogram were calculated to determine the mean nonsphericity values for these populations of particle types (Table 2). PSL exhibits the smallest mean nonsphericity value (0.070), while dry, uncoated rBC has the largest (0.353), indicating nonsphericity. The AS sample in Figure 1 was taken from a chamber wall-deposition experiment in which AS seed was injected into a dry (<10% RH) chamber. AS mean nonsphericity is slightly larger than that for PSL, likely indicating that some AS particles do not retain water in the dry chamber. Calibrations with oxalic acid particles (data not shown in Figure 1, but statistics reported in Table 2) generated with a collision atomizer and sampled directly into the prototype instrument yield a mean nonsphericity similar to that of AS. Dried, cubic salt particles (statistics reported in Table 2), generated by atomizing a solution of NaCl and water and sampling through a nafion dryer directly into the instrument, yield a nonsphericity similar to that for rBC. Like the AS sample, the fullerene

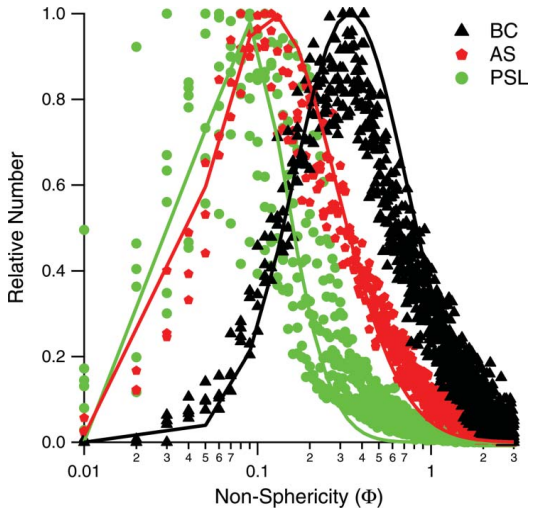

FIG. 1. Distributions of nonsphericity values for ammonium sulfate (AS), fullerene soot (BC) particles, and polystyrene latex spheres (PSL). Each distribution represents ∼10,000 particles sampled at various times throughout the respective experiments. "Relative number" is the number of particles in each bin divided by the maximum number in any bin for the given distribution. Solid lines denote a lognormal fit to a single distribution; only one fit per particle type is shown. Mean nonsphericity values corresponding to lognormal fits to all distributions are given in Table 2. (Color figure available online.)

soot sample was measured during wall-deposition experiments in which only rBC was present in the chamber. These measurements confirm that the fullerene soot, as we have prepared and loaded into the chamber as seed particles, is nonspherical.

3.1.2. *Particle Wall Deposition*

In environmental chamber studies, wall-deposition rates must be known in order to calculate SOA yields from a parent hydrocarbon (Keywood et al. 2004; Ng et al. 2007; Loza et al. 2012). Wall deposition processes have been well-described in the literature (Crump and Seinfeld 1981; McMurry and Rader 1985; Park et al. 2001; Pierce et al. 2008). Particles in the bulk of the chamber can diffuse or settle through a boundary layer near the chamber wall and deposit on the wall. Electrostatic effects can enhance deposition rates, especially for intermediate-sized particles (50–1000 nm diameter) (McMurry and Rader 1985).

TABLE 2
Summary of nonsphericity values

Particle type	Mean nonsphericity ($\pm 1\sigma$)
BC	0.353 ± 0.042
NaCl	0.303 ± 0.057
AS	0.173 ± 0.091
Oxalic acid	0.150 ± 0.030
PSL	0.070 ± 0.029

Typically, wall-deposition rates are determined by atomizing seed aerosol into a clean chamber and measuring the decay of particle concentration over ∼24 h. From these data, size-dependent, first-order loss coefficients, β, are obtained. Measured wall-deposition rates for both AS seed and fullerene soot seed exhibit differences, as shown in Figure 2. The wall-deposition rates presented in Figure 2, calculated from DMA size distribution data, are presented with respect to particle mass rather than mobility diameter in order to better relate the nearly spherical AS with the nonspherical rBC. The different range of masses for the two particle types in Figure 2 is the result

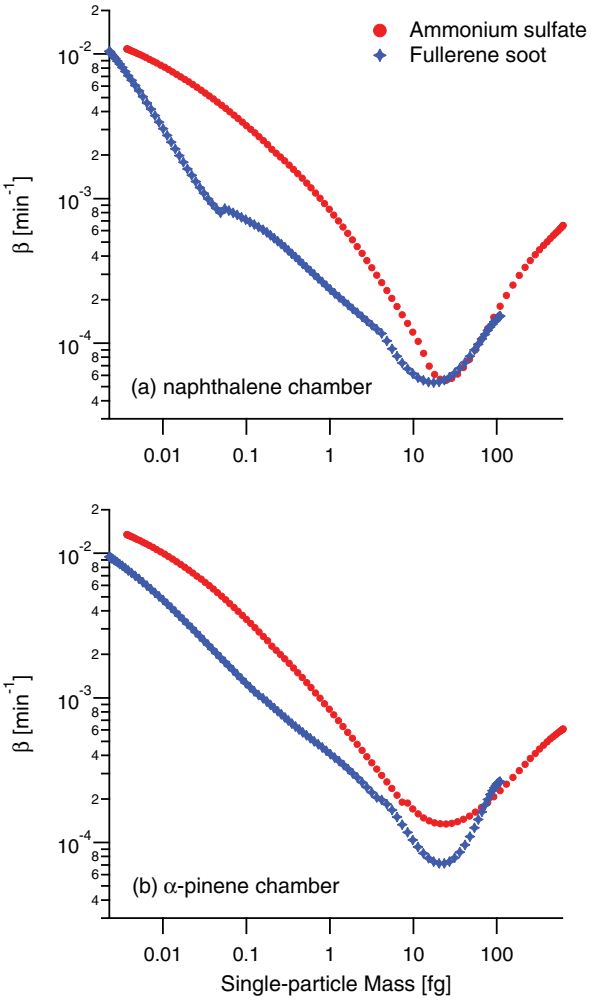

FIG. 2. Particle wall deposition rate coefficients, β, for the two chambers with ammonium sulfate and fullerene soot as the seed particles. Data are displayed by single-particle mass rather than mobility diameter to directly compare AS and BC. Ammonium sulfate mass is calculated from mobility diameter assuming a spherical particle and a density of 1.77 g cm^{-3}. Fullerene soot mass is calculated from mobility diameter using the relation reported by Gysel et al. (2011). (Color figure available online.)

of the smaller effective density (0.6–0.35 g cm^{-3} for mobility diameters 300–800 nm [Gysel et al. 2011]) for fullerene soot than for AS (1.77 g cm^{-3}) over all mobility diameters displayed.

The characteristic "V"-shape of the wall deposition rate curves in Figure 2 arises because of two competing processes: diffusion dominates wall deposition at smaller-size (and mass) particles and gravitational settling dominates wall deposition at larger-size (and mass) particles. The fact that the rBC deposition rate achieves a minimum at nearly the same single-particle mass as that for AS particles indicates a similar balance between these effects. At larger masses, where gravitational settling dominates, AS and rBC have similar values of β, indicating reduced effect of particle shape in this range. At smaller masses, however, the significant difference in β reflects differences in diffusion rates to the chamber walls or an invalid assumption of a first-order wall-deposition rate with unit sticking probability.

Because effective density measurements from a coupled DMA-SP2 system are used (Gysel et al. 2011), any artifacts in the DMA data used to calculated β in these experiments due to particle nonsphericity should be consistent during the entire wall-deposition experiment. Therefore, the differences in wall-deposition rates between AS and fullerene soot are likely not the product of measurement artifacts. The diffusion rate of the fullerene soot could be less than that for AS particles of the same mass owing to the larger size of the fullerene soot particles. Sticking probabilities may also be smaller for the dry fullerene soot than for the AS particles, which likely retain some water, even in a dry chamber. The implication for the current chamber experiments is that the rate of wall deposition can be expected to change over the course of an experiment as initially uncoated rBC particles become coated. For this reason, SOA yields are not calculated in this study.

3.2. General Experimental Results

Figure 3 shows the reaction profile during naphthalene photooxidation, Experiment 1 (Table 1), in the presence of rBC seed particles. The rapidly formed SOA deposits onto the fullerene soot, as indicated by the immediate increase in mean coating thickness. A modest amount (~30% by number in the SP2 detection range) of purely scattering particles, presumably from nucleation, are present after growth initiates, indicated by an increase in total number concentration just after the start of irradiation (Figure 3a). Despite the temperature increase that occurs once the UV lights are turned on (Figure 3b), the coating thickness rapidly increases early in the irradiation. Temperature decreases once the lights are turned off, accompanied by only a small increase in mean coating thickness. Single-particle mean coating thickness does not decrease at any point during Experiment 1, indicating that the decrease of aerosol mass during dilution of the chamber is the result of flushing the particles out of the chamber and wall deposition within the chamber and is not due to evaporation of the aerosol itself. The temperature decrease during dilution favors condensation and could influence mean coating thickness; however, the rate of temperature decrease varies during Experiment 1 while the rate of mean coating thickness increase does not vary in the same manner. Thus, it is unlikely that temperature alone is the dominant control of condensation of SOA in this system.

The evolution of coating thickness as a function of rBC core diameter is presented in Figure 4. About 30 min after the start of irradiation (Figure 4a), rBC particles of all core sizes already have an organic coating growing. As organic growth progresses (Figures 4b and c), the smaller rBC cores have markedly thicker coatings than the larger rBC cores. After ~7.5 h of chamber dilution (Figure 4d), there is no clear, systematic evidence of evaporation of these coatings.

In Figure 4, lines representing a diffusion-controlled growth law (Seinfeld and Pandis 2006) are shown,

$$\frac{dD_p}{dt} = \frac{A}{D_p}, \qquad [5]$$

where D_p is the rBC VED. The parameter A varies with time and was determined by matching the value of $\frac{dD_p}{dt}$ to the coating thickness of 160 nm VED rBC cores (thicknesses of 35, 120, 130, and 150 nm for Figures 4a–d, respectively). The agreement between the model and measurement indicate that the coating thickness diameters follow a diffusion-controlled growth rate. During chamber dilution (Figure 4d), there is some deviation from the diffusion-controlled growth law for particles with rBC core VED <100 nm, but this deviation is likely due to a faster wall deposition rate of larger particles (Figure 2). These rBC size-dependent results are consistent with ambient measurements by Moteki et al. (2007) over the western Pacific who also found that the rate of coating growth onto rBC particles follows a diffusion-controlled growth law. These results also support the findings of a recent modeling study that the aging of rBC by condensation of hygroscopic layers is rBC-size dependent (Park et al. 2012). That this simple, one-hydrocarbon system produces results that resemble ambient rBC aging by condensation of SOA supports this experimental protocol as a viable way to probe rBC aging dynamics in more detail with controlled environmental chambers.

Figure 5 presents results from Experiment 5 (Table 1), high-NO_x α-pinene photooxidation in the presence of fullerene seed particles. Growth of SOA is rapid, indicated by immediate increase of organic mass (Figure 5a), coating thickness (Figure 5b), and change in optical properties (Figure 5c). What differentiates this experiment from the others is that mean coating thickness reaches a peak and then decreases during the irradiation period. Throughout the irradiation period, temperature in the chamber increases, but there is no distinct change in temperature near the peak in coating thickness that would indicate that the aerosol should suddenly start evaporating. Thus, it is likely that the evaporation of coating material is indicative of a chemical change causing particle-phase loss of higher-volatility species. During the irradiation period of Experiment 5, a greater

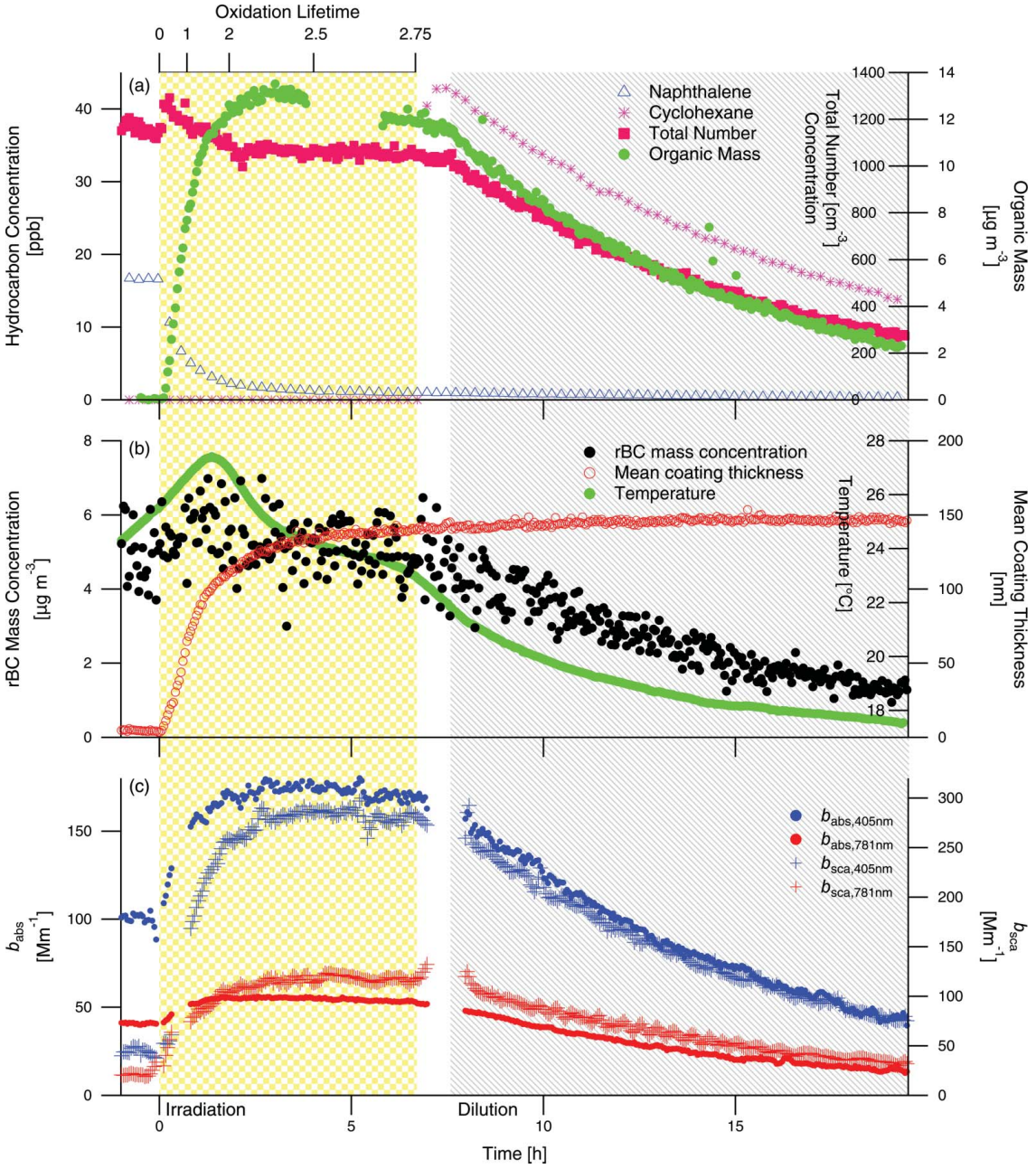

FIG. 3. Experiment 1, naphthalene photooxidation in the presence of rBC seed particles. The shaded regions denote periods of irradiation and dilution of the chamber. (Color figure available online.)

number of oxidation lifetimes (defined in Section 3.4.1) were reached, which may have provided the necessary conditions to allow more chemical aging than the other experiments. The coating evaporation continues after irradiation is stopped, and mean coating thickness does not level off until ∼4.25 h into the dilution period. Examination of the evolution of coating thickness for this system (not shown) reveals that a diffusion-limited growth law continues to be valid, and all rBC core sizes exhibit evaporation of coatings. At the very end of the dilution period, a temperature increase of ∼2°C over the final 2 h of the

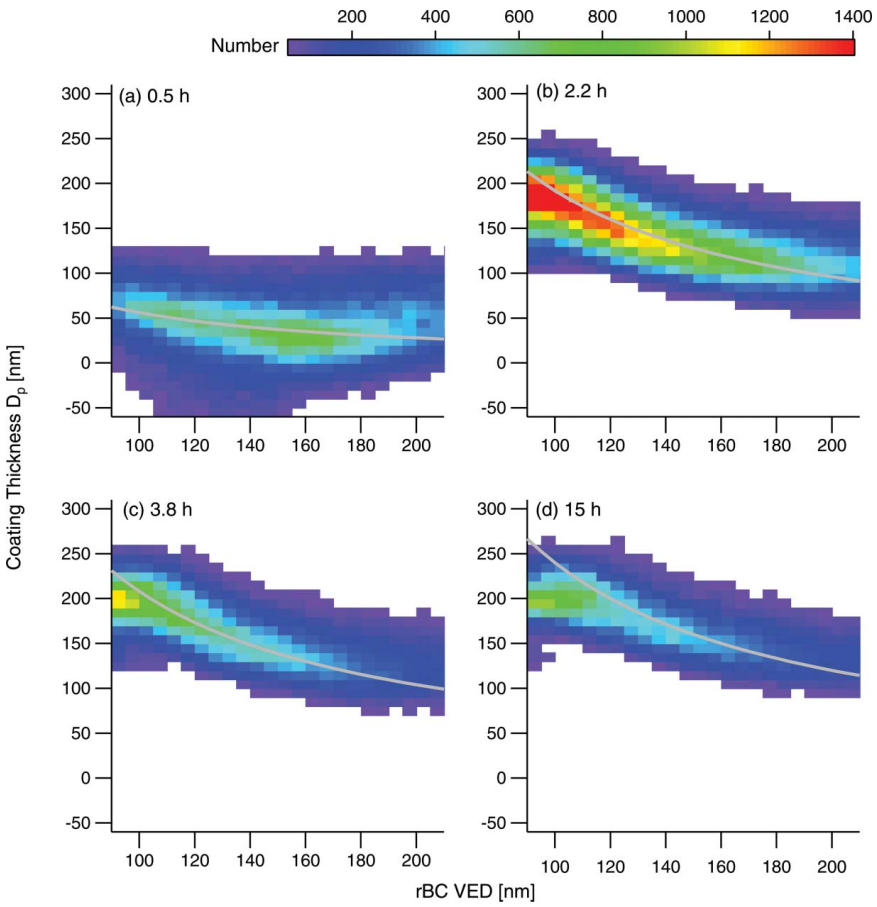

FIG. 4. Evolution of coating thickness in Experiment 1, presented as 2-D histograms of coating thickness determined by fitting the SP2 scattering signal to a core-and-shell Mie model binned versus rBC volume-equivalent diameter. The times are in hours after the onset of irradiation. The gray lines are diffusion-controlled growth laws matched to the coating thickness diameter at an rBC VED of 160 nm. (Color figure available online.)

experiment leads to a coating thickness decrease of ∼5 nm (calculated from 10-min averaged data, not shown), possibly highlighting the role of temperature in SOA volatility. SOA evaporation during chamber irradiation in this system will be further discussed in Section 3.4.2.

Figure 6 presents the results from Experiment 7 (Table 1), low-NO_x α-pinene photooxidation in the presence of fullerene seed particles. In this system, SOA growth proceeds more slowly than in the high-NO_x photooxidation systems as a result of a lower OH concentration produced by H_2O_2 versus CH_3ONO. Total particle number concentration (Figure 6a) gives no evidence of SOA nucleation and shows a steady decline during irradiation, owing to wall-deposition and particle coagulation. Wall- deposition rates are slightly faster in the α-pinene chamber versus the naphthalene chamber (Figure 2) and characteristic time for coagulation is shorter (∼1.8 d versus ∼3.4 d, respectively) (Seinfeld and Pandis 2006) owing to higher initial particle number concentration. Despite a temperature decrease, which favors condensation of SOA (Figure 6b), there is a slight decrease in mean coating thickness during chamber dilution (∼8 nm in ∼10 h). The flushing rate of the chamber does not change during dilution (see cyclohexane curve in Figure 6a), and the rate of decline in mean coating thickness remains constant as well (Figure 6b) despite the change in temperature trend from the first 5 h of flushing (−6.2°C) to the second 5 h of flushing (−0.2°C). A distinguishing feature of this SOA system is the change in SOA growth rate (see organic mass trace in Figure 6a) coincident with a change in optical properties (see the change in slope of the curves in Figure 6c) ∼4 h into the chamber irradiation. The change in particle composition during SOA growth in this system will be discussed in Section 3.4.3.

In this work, we focus on results from these three SOA systems in the presence of rBC seed aerosol. For completeness,

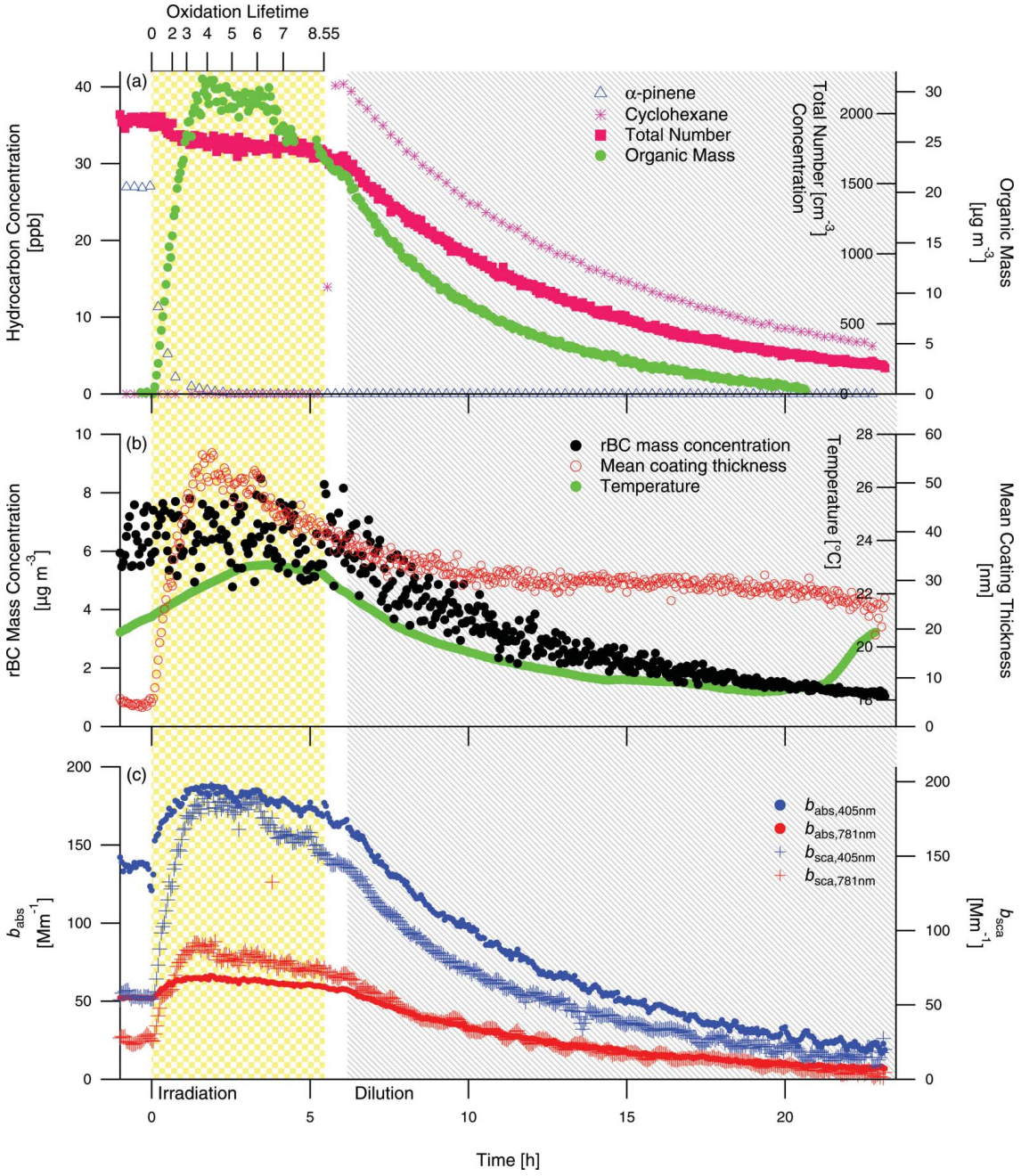

FIG. 5. Experiment 5, high-NO_x α-pinene photooxidation in the presence of rBC seed particles. The shaded regions denote periods of irradiation and dilution of the chamber. (Color figure available online.)

Table 1 lists all experiments performed for this study. Although not shown in this work, each experiment in Table 1 was characterized by growth of organic layers on the rBC aerosol. In Experiment 3, the growth of coating by coagulation is estimated to be small (~20 nm coating diameter in ~16 h), owing to the modest particle number concentration (~11,000 cm^{-3}) and coagulation timescale (~1.3 d). In the dual seed experiments with rBC and AS (Experiments 2, 6, and 8) and with rBC and

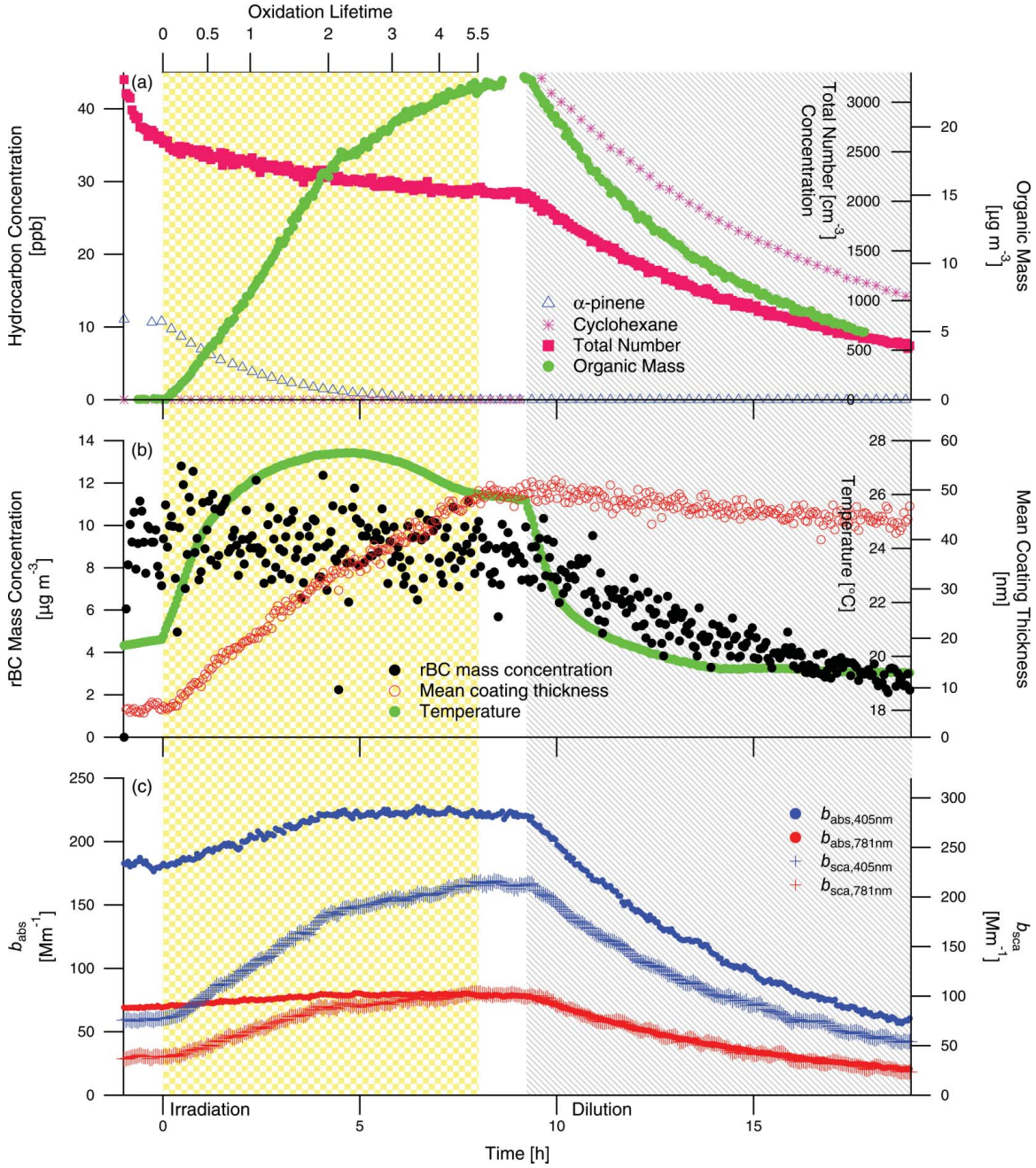

FIG. 6. Experiment 7, low-NO_x α-pinene photooxidation in the presence of rBC seed particles. The shaded regions denote periods of irradiation and dilution of the chamber. (Color figure available online.)

nucleated SOA (Experiments 4 and 9), growth of coatings occurred during irradiation of the chamber at a faster rate than during the period of mixing prior to irradiation, indicative that growth by condensation of SOA was dominant.

3.3. Aerosol Optical Properties

Table 3 presents optical properties of the seed particles and nucleated SOA in this study, including the mass scattering cross section (MSC), mass absorption cross section (MAC),

TABLE 3
Optical properties of particles in this study (mean ± 1σ^a)

	λ	Fullerene soot	Ammonium sulfate	Naphthalene SOA	α-pinene SOA[b]
MSC[c] [m^2 g^{-1}]	405 nm	8.39 ± 0.26	7.74 ± 0.35	10.93 ± 1.58	10.21 ± 0.21
	781 nm	4.28 ± 0.07	3.21 ± 0.20	1.30 ± 0.44	1.14 ± 0.19
MAC[d] [m^2 g^{-1}]	405 nm	20.23 ± 1.08	<0.82[e]	0.81 ± 0.32	<1.90[e]
	781 nm	7.84 ± 0.26	<0.13[e]	<0.08[e]	<0.30[e]
ω_0[f]	405 nm	0.29 ± 0.0041	1.00 ± 0.0065	0.91 ± 0.012	1.00 ± 0.012
	781 nm	0.35 ± 0.0087	0.99 ± 0.0018	0.99 ± 0.0018	0.94 ± 0.026
$Å_{sca}$[g]		1.02	1.34[e]	3.24	3.34[e]
$Å_{abs}$[h]		1.44		>3.53[e]	

[a]Standard deviation during measurement period, not indicative of measurement uncertainty. [b]Low-NO_x experiment only. [c]MSC = mass scattering cross section. [d]MAC = mass absorption cross section. [e]Absorption coefficient (b_{abs}) measurements are at or below detection limit on the PASS-3. [f]ω_0 = single-scatter albedo. [g]$Å_{sca}$ = scattering Ångström exponent. [h]$Å_{abs}$ = absorption Ångström exponent.

single-scatter albedo (ω_0), and scattering and absorption Ångström exponents ($Å_{sca}$ and $Å_{abs}$, respectively), defined as

$$Å_{sca/abs} = -\frac{\ln\frac{b_{sca/abs,405nm}}{b_{sca/abs,781nm}}}{\ln\frac{405}{781}}, \quad [6]$$

where $b_{sca/abs}$ is the observed scattering/absorption coefficient at the specified wavelengths. The fullerene soot and ammonium sulfate values are averages of measurements taken during the hour of chamber mixing prior to the start of irradiation on Experiments 1, 5, and 7 for fullerene soot and Experiments 2, 6, and 8 for ammonium sulfate (before injection of fullerene soot). The nucleated naphthalene and α-pinene SOA values are taken before rBC was injected into the chamber on Experiments 3, 4, and 9. The mass absorption cross sections of uncoated fullerene soot (20.23 ± 1.08 m^2 g^{-1} and 7.84 ± 0.26 m^2 g^{-1} at λ = 405 nm and 781 nm, respectively) are higher than reported ensemble averages for uncoated ambient rBC (7.5 ± 1.2 m^2 g^{-1} at λ = 550 nm; Bond and Bergstrom 2006), but is certainly within the range of ambient measurements (Kirchstetter et al. 2004). In addition, the mass scattering cross section of ammonium sulfate is higher than previously reported ambient values of 2–4 m^2 g^{-1} at λ = 530 nm (Malm et al. 2005a,b). Thus, it is possible that the PASS-3 measurements are biased high due to an offset, perhaps the result of calibrating at much higher aerosol concentrations than those used in the chamber experiments. This bias should not affect the calculations of absorption enhancement presented below.

The value of $Å_{abs}$ for fullerene soot (1.44 ± 0.03) is slightly higher than $Å_{abs}$ = 1 recommended for uncoated rBC (Bond and Bergstrom 2006) but lies within the range of modeled conditions (Lack and Cappa 2010) and ambient measurements of rBC (Gyawali et al. 2009).

Nucleated naphthalene SOA exhibits a small absorption signal at λ = 405 nm; these particles may be classified as "brown carbon," a mildly absorbing carbonaceous aerosol that is distinct from black carbon but has progressively stronger absorption at UV wavelengths as compared to visible wavelengths (Andreae and Gelencsér 2006; Wonaschütz et al. 2012). Nakayama et al. (2010) found a similar value for MAC at λ = 355 nm for SOA from the photooxidation of toluene, also an aromatic hydrocarbon. Some authors have detected absorption from gaseous PAH's (Weiner and Harris 1989; Schoemaecker Moreau et al. 2004), but in the present experiments the initial concentration of naphthalene gave no measurable absorption signal in the PASS-3. The measured value of the MAC of 0.81 m^2 g^{-1} at λ = 405 nm for naphthalene SOA is within range of previously measured MAC values for brown carbon (Kirchstetter et al. 2004; Hoffer et al. 2006; Yang et al. 2009; Nakayama et al. 2010). For naphthalene SOA, $Å_{abs}$ cannot be explicitly determined due to absorption at λ = 781 nm below PASS-3 detection limits, but it is estimated to be >∼3.5, which is indicative of brown carbon (Flowers et al. 2010).

3.3.1. Evolution of Aerosol Optical Properties During SOA Growth on rBC Seed

Figures 3c, 5c, and 6c show the absorption and scattering coefficients of the rBC-coated SOA during Experiments 1, 5, and 7, respectively. For all experiments, after UV lights are turned on, a clear increase in absorption coefficients at all wavelengths occurs, while rBC mass remains constant or slightly decreases due to wall deposition. Figure 7 displays absorption coefficient (b_{abs}), measured absorption enhancement ($E_{abs}{}^m$), and single-scatter albedo (ω_0) as a function of mean coating thickness for Experiments 1, 5, and 7, respectively. Time is shown by marker shading on each figure, generally increasing from left to right because the coating thickness grows during irradiation. For the α-pinene systems (Figures 7b and c), the coating thickness eventually decreases, slightly during dilution of the low-NO_x system (Figure 7c) and more dramatically during irradiation of the high-NO_x system (Figure 7b).

As noted above, there is a small absorption signal from the naphthalene SOA at λ = 405 nm, but not at λ = 781 nm. We

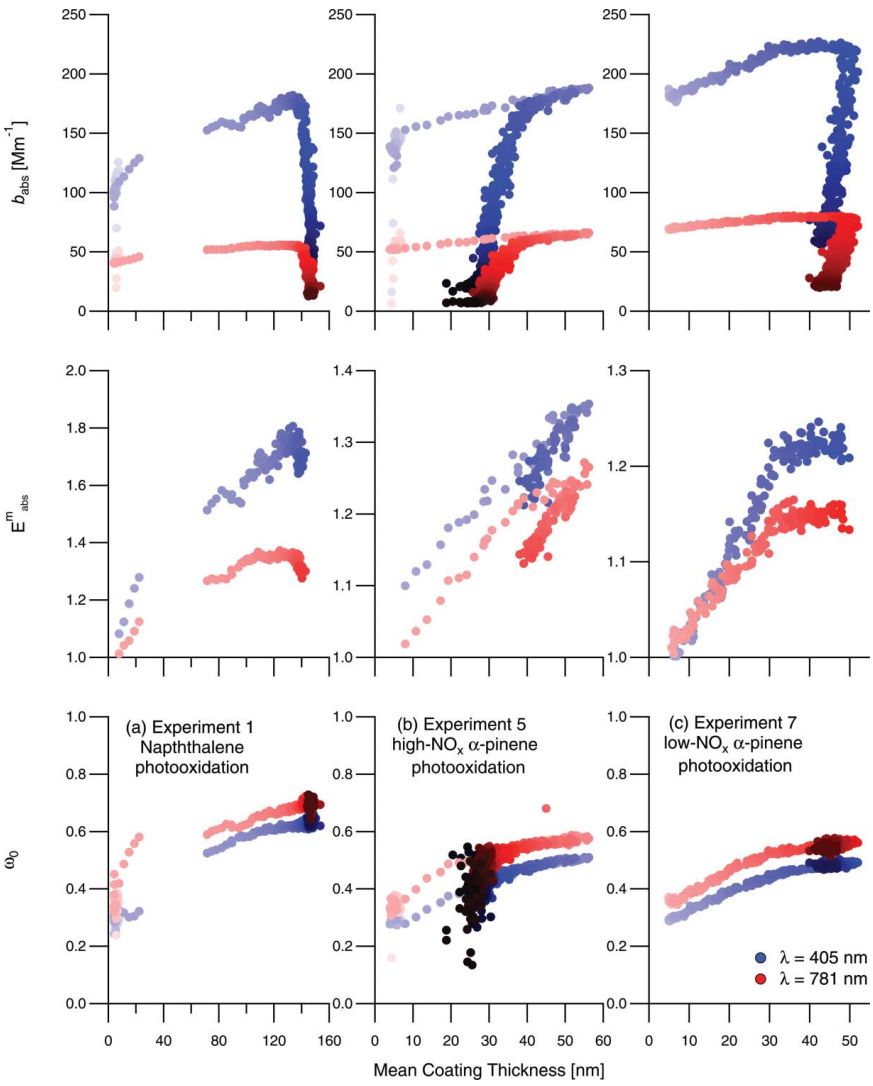

FIG. 7. Aerosol optical properties as a function of mean coating thickness on the fullerene soot seed during Experiment 1, naphthalene photooxidation (a), Experiment 5, high-NO_x α-pinene photooxidation (b), and Experiment 7, low-NO_x α-pinene photooxidation (c). Marker shading is a function of time after onset of irradiation, with later times indicated by darker colors. Measured absorption enhancement, $E_{abs}{}^m$ (middle), is presented for the irradiation time period only. (Color figure available online.)

expect that naphthalene SOA condensed onto seed particles will exhibit optical properties similar to nucleated naphthalene SOA, and, therefore, that the absorption enhancement in Experiment 1 (Figure 7a, middle) at $\lambda = 781$ nm is a result of the lensing effect of the coatings on the rBC seed particles, while at $\lambda =$ 405 nm there is additional absorption from the coating itself (Fuller et al. 1999; Lack and Cappa 2010). In Experiment 1, $Å_{abs}$ increased from 1.37 ± 0.029 to 1.76 ± 0.026 during irradiation, indicating that the aerosol absorption at peak growth is more sensitive to wavelength than the uncoated fullerene soot seed. This is consistent with a small absorption coefficient at $\lambda = 405$ nm of the condensed naphthalene SOA (Table 3) and exceeds the threshold (1.6) for which attribution of brown carbon to observed absorption can be made (Lack and Cappa 2010). The sharp decrease in b_{abs} (Figure 7a, top) occurs simultaneously with the start of chamber dilution. The apparent gap in data between ~25 and 75 nm thickness is a result of the rapid growth of the coatings during irradiation and the timing of an automatic background signal correction on the PASS-3.

In Experiment 5 (high-NO_x α-pinene photooxidation; Figure 5), absorption and scattering coefficients increase rapidly with formation of SOA, then decrease during irradiation as the

SOA evaporates. Figure 7b shows the rather dramatic decrease in coating thicknesses by the end of the experiment. Note that after reaching the peak in coating thicknesses, b_{abs} and ω_0 decrease along the same trajectory as the coatings evaporate. The sharp decreases in b_{abs} that deviate from this trajectory occur when dilution is initiated, because the decrease in total particle concentration has a larger influence on b_{abs} in this experiment than the evaporation of coatings. Single-scatter albedo continues its decline along the same trajectory because ω_0 is an intensive property whereas b_{abs} is an extensive property.

In Experiment 7 (low-NO_x α-pinene photooxidation; Figure 6), absorption and scattering coefficients increase steadily with the slowly forming SOA. During irradiation, there is a clear change in the rate of increase of these properties, coincident with a change in rate of growth of organic mass (Figure 6a). This change in growth is not seen in the mean coating thickness of 160–180 nm VED rBC cores (Figure 6b). In the absorption coefficient and absorption enhancement especially (Figure 7c), this change indicates that additional absorption enhancement has nearly stopped despite continued growth of organic mass and coating thicknesses. Previous studies have speculated that absorption can be no further enhanced after an extremely thick (>300 nm) coating is present on an absorbing core because the shell may actually shield the core from receiving photons (Bond et al. 2006; Knox et al. 2009; Cross et al. 2010; Lack and Cappa 2010). Because the coatings in Experiment 7 are still relatively thin as compared to those in Experiment 1 (Figure 7a), it is unlikely that further absorption enhancement is being thwarted by an exceptionally thick scattering shell in this experiment.

In all experiments presented, coatings on the rBC cores enhance the light absorption of these particles. Single-scatter albedo increased in all systems as the organic coating thicknesses on the fullerene soot grew. In the naphthalene system, there is clear wavelength dependence of the absorption enhancements (Figure 7a, middle), owing to the wavelength dependence of refractive index of naphthalene SOA. In the α-pinene systems, evaporation of the coatings leads to a decline of ω_0 from its peak value, indicating that the changes in optical properties can be considered reversible as the coating material is removed from the rBC cores. The absorption enhancements reported here provide further evidence that the mixing state of rBC in the atmosphere is an important consideration for the radiative forcing by these particles.

3.3.2. *Comparison of Measured and Modeled Absorption Enhancements*

Figure 8 presents a comparison of a core-and-shell Mie model of absorption enhancement, calculated from SP2 measurements as detailed in Section 2.3, to measured absorption enhancement, calculated from PASS-3 measurements, for Experiments 1 (Figure 8a), 5 (Figure 8b), and 7 (Figure 8c).

The rapid increase in absorption enhancement and large enhancement factor (~1.8) at $\lambda = 405$ nm in Experiment 1 (Figure 8a) are represented by the Mie model, despite the known limitation that the refractive index used in the Mie scattering model does not include an absorbing (imaginary) part. Modeled absorption enhancement at $\lambda = 781$ nm does not match the measured enhancement well. This discrepancy indicates a wavelength-dependence of the real part of the refractive index of the naphthalene SOA, which we have not captured with our assumed refractive index. If an absorbing refractive index is considered, then we would expect that the real part of refractive index would need to be smaller than 1.5 in order to keep good agreement at $\lambda = 405$ nm. A further reduction in the real refractive index at $\lambda = 781$ nm is also necessary to bring modeled and measured enhancement factors into better agreement.

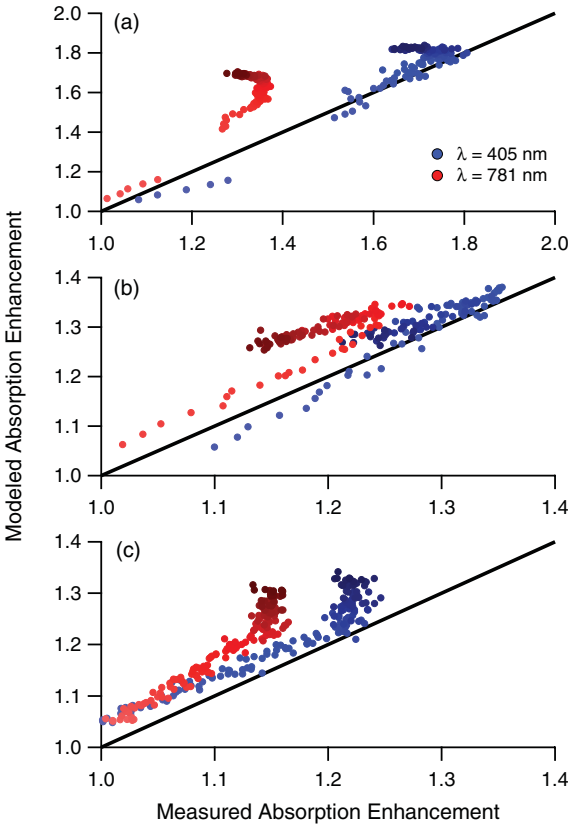

FIG. 8. Comparison of Mie-modeled absorption enhancement to measured absorption enhancement. The measurements are enhancements of b_{abs} at $\lambda = 405$ nm and $\lambda = 781$ nm measured by the PASS-3 relative to the values measured for the fullerene soot seed particles prior to irradiation. The Mie model enhancements are calculated by the increase in absorption cross section from uncoated rBC cores to rBC cores with the mean coating thickness measured by the SP2 (see text for details). Results for (a) Experiment 1, naphthalene photooxidation, (b) Experiment 5, high-NO_x α-pinene photooxidation, and (c) Experiment 7, low-NO_x α-pinene photooxidation are presented. Marker shading is a function of time after onset of irradiation, with later times indicated by darker colors. Data during chamber irradiation only are shown. The solid line is a 1-to-1 line. (Color figure available online.)

The strong wavelength-dependence of the optical properties of naphthalene SOA is supported by the large Å_{abs} in Table 3. In addition, Lack and Cappa (2010) found that coatings on rBC by mildly absorbing material reduces the absorption enhancement relative to rBC coated by non-absorbing material, which further explains why the measured absorption enhancements should be lower than modeled enhancements lacking an absorbing part of refractive index and suggests that any agreement between the model and measurements at $\lambda = 405$ nm is by coincidence.

In Experiment 5 (Figure 8b), the measured increase and decrease in absorption enhancement due to the increase and decrease of coating thickness during irradiation are captured by the model. We expect fairly good agreement using a coating refractive index of 1.5–0.0i based on a recent finding of no significant absorption for α-pinene SOA (Nakayama et al. 2010) and on recent measurements of α-pinene SOA refractive index in the range of 1.42–1.56 for $\lambda = 450$–700 nm (Barkey et al. 2007; Yu et al. 2008). The small wavelength-dependence of refractive index (increasing refractive index with decreasing wavelength) reported by Yu et al. (2008) explains the small difference in the measured enhancement factors in this system.

In Experiment 7 (Figure 8c), there was a change in optical properties during the irradiation period (Figures 6c and 7c). This change, in which the measured absorption enhancement ceases to increase, is not reflected by the Mie model because organic coatings are continuing to grow (Figure 6b). To reconcile the differences between the measurements and model, a change in refractive index of the coating material at the time of this deviation needs to be considered. It is possible that a change in the physical properties of the aerosol is occurring as well; however, it is expected that as coatings deposit, the rBC core will collapse so that the aerosol will become more like a core-shell morphology, which should bring the model and measurements into better agreement rather than worse agreement as is observed.

The results presented here, of a core-and-shell Mie scattering model of absorption enhancement during these single-hydrocarbon SOA systems, suggest that a careful treatment of SOA refractive index is needed to fully model aerosol optical properties. SOA from the photooxidation of naphthalene under dry, high-NO_x conditions has a refractive index with a strong wavelength-dependence which, if not included in the model, will lead to large discrepancies between modeled and measured absorption enhancements. In the α-pinene system, for which measured refractive indices from previous studies exist, a change in optical properties during photooxidation causes discrepancies between the modeled and measured light absorption to arise during growth of coatings on rBC.

3.4. AMS Measurements

3.4.1. Naphthalene SOA

Figure 9 presents normalized (signal at each m/z is divided by the total organic signal) unit-mass resolution AMS organic mass spectra of SOA formed by the photooxidation of naphthalene in the presence of rBC seed particles (Experiment 1; Figure 9a), of nucleated naphthalene SOA (Experiment 3; Figure 9b), and the difference spectrum between the two (Figure 9c). The data are taken at the "peak growth" periods of each experiment, defined as the time after the parent hydrocarbon has either been consumed or has ceased to decrease (presumably due to OH being fully consumed) and when growth of suspended particle volume concentration has leveled off through reaching a balance with wall deposition. The number of oxidation lifetimes is defined as $k_i[\text{OH}]\Delta t$, where k_i is the second-order rate constant of species i reaction with OH, [OH] is the gas-phase concentration of OH, and Δt is the exposure time (Kroll et al. 2009). In Figure 9, the data were taken at an oxidation lifetime of about 2.5 in both cases, and there was about 1.3 (7.8% of initial) and 2.1 ppb (9.6% of initial) naphthalene remaining in the chamber at peak growth for Experiments 1 and 3, respectively.

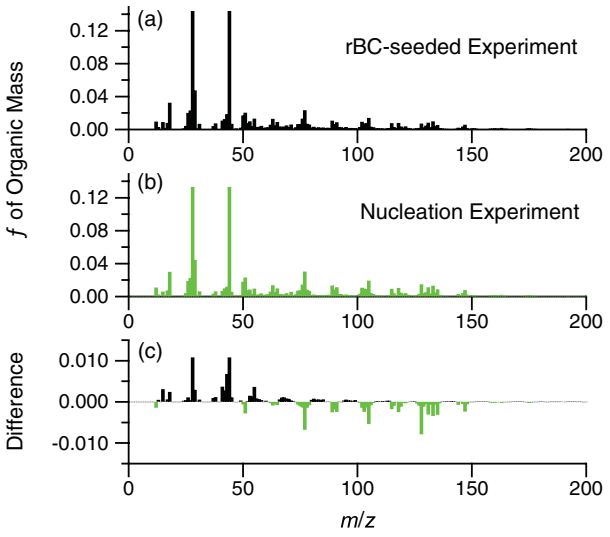

FIG. 9. Normalized unit-mass resolution AMS organic mass spectra at peak growth of (a) naphthalene SOA condensed on rBC seed (Experiment 1), (b) nucleated naphthalene SOA (Experiment 3), and (d) the difference spectrum, calculated relative to the mass spectrum from Experiment 1. On the difference spectrum, positive values denote m/z's enriched in the rBC-seeded experiment and negative values denote m/z's enriched in the nucleation experiment. (Color figure available online.)

Masses larger than about m/z 275 from the nucleation experiment and masses larger than about m/z 200 from the fullerene soot-seeded experiment are generally at or near the detection limit of the AMS for those individual masses. The detection limits at each m/z are calculated as three times the standard deviation of the measured signal during sampling with a particle filter in front of the inlet before the start of the experiment. For Experiment 1, a background spectrum, defined as the average mass spectrum during the hour of chamber mixing prior to irradiation, is subtracted from the raw spectra during the rest of the experiment. Thus, the small signal resulting from the fullerene soot seed is removed from the spectrum in Figure 9a.

There is a small difference between the SOA composition formed by nucleation and condensation onto fullerene soot for this system. The largest change in mass fraction at any given m/z is about ±1% of total organic mass. This difference is most prominent at m/z 44, which is the mass with the largest fraction in the organic spectra (Figures 9a and b). The discrepancies in the particular m/z's between the two experiments may arise owing to a different organic loading at the times of interest (which could force the chemistry through a different pathway); for Experiment 1, organic mass was 6.5 ± 0.08 μgm^{-3}, while for Experiment 3, organic mass was 18.2 ± 0.22 μgm^{-3}. Because the spectra are reported at the same oxidation lifetime, it is expected that these are reported at the most comparable conditions possible. Due to the uncertainty of AMS measurements, a change of ±1% should be viewed as small.

Although not shown in this work, similar AMS mass spectra comparisons were made at peak growth for the AS + rBC seeded experiment (Experiment 2 in Table 1) compared to the two experiments presented above. The largest difference in the mass spectra arises from interferences from sulfate at m/z 48 and 64, which is remedied by properly adjusting the AMS fragmentation table. After adjustment, mass spectral differences are on the order of those shown in Figure 9d. These small differences in mass spectra may mean that the optical properties of the nucleated SOA reported in Table 3 may differ from the condensed SOA onto rBC seed. However, because the mass spectral differences are small among all experiments compared, one concludes that the fullerene soot seed does not affect the composition of the condensed naphthalene SOA more so than condensation on the more conventional AS seed as compared to nucleated SOA.

3.4.2. *High-NO_x α-pinene SOA*

During high-NO_x α-pinene photooxidation (Experiment 5), the mean coating thickness initially increases rapidly, achieves a maximum, then decreases for the remainder of the irradiation period (Figure 5b). Figures 10a and b present normalized AMS mass spectra at two times during irradiation in Experiment 5, at oxidation lifetimes of 9, near the end of the irradiation period, and 1, during the early rapid growth of SOA, respectively. Figure 10c presents the difference between these two mass spectra, relative to the earlier mass spectra, where positive values denote mass fragments enriched at the end of irradiation. Typically, the dominant mass fragments in AMS organic mass spectra of ambient aerosol are at m/z 44, which represents highly oxygenated organic species with low volatility, and at m/z 43, which represents less oxygenated semivolatile species (Ng et al. 2010). The mass fractions of these m/z, $f_{44,}$ and f_{43}, are defined as the mass at m/z 44 and m/z 43, respectively, divided by the total organic mass, which is the sum of masses at all m/z in the AMS organic spectra. f_{43} is initially ∼15% of the total organic mass (Figure 10b) and decreases to ∼13% (Figure 10a) near the end of the irradiation period. Simultaneously, f_{44} increases from ∼8% (Figure 10b) to ∼12% (Figure 10a) of total organic mass during the irradiation period. These results indicate that the aerosol is

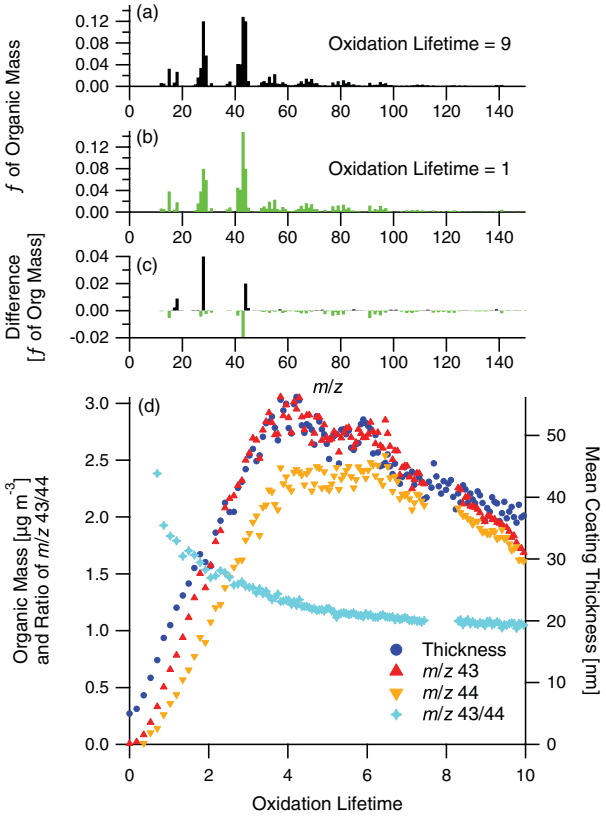

FIG. 10. Normalized unit-mass resolution AMS organic mass spectra from Experiment 5, high-NO_x α-pinene photooxidation in the presence of fullerene soot, at (a) oxidation lifetime = 9 (after peak growth has been reached) and (b) oxidation lifetime = 1 (during rapid growth), (c) the difference spectrum, calculated relative to the earlier mass spectrum, and (d) comparison of AMS m/z 43 and 44 and ratio of m/z 43/44 with mean coating thickness measured by the SP2. On the difference spectrum, positive values denote m/z's enriched in the later condensed SOA and negative values denote m/z's enriched in the earliest condensed SOA. Note that dilution of the chamber began at an oxidation lifetime of approximately 9. (Color figure available online.)

transitioning from a semi-volatile to a lower volatility state, as is commonly observed during chemical aging of aerosol (Ng et al. 2010).

From the time series traces (Figure 10d) of AMS m/z 43 and 44 and mean coating thickness on rBC as measured by the SP2, AMS m/z 43 clearly traces the mean coating thickness (R^2 = 0.97), capturing the decrease in thickness with time quite well, deviating only after chamber dilution has begun. AMS m/z 44 lags behind m/z 43 in formation, and, therefore, does not trace coating thickness as well (R^2 = 0.89). Note that even though m/z 44 decreases during the experiment, f_{44} is continuously increasing, as stated above, meaning that the other mass fragments in the AMS mass spectra are decreasing more rapidly than m/z 44. This is shown in Figure 10d by the signals of m/z 43 and 44 approaching a similar value towards the end of the irradiation

period. After the initial rapid growth, the m/z 43/44 ratio continuously decreases due to f_{44} continuously increasing throughout the experiment. While chemical aging in such a way that converts species yielding high f_{43} to higher f_{44} in the AMS may explain these trends, the combination of single-particle coating thickness measured by the SP2 and the bulk organic mass spectra measured by the AMS suggest that the more semivolatile species are actually evaporating from the aerosol. The SP2 unambiguously shows changes in single particles, whereas AMS measurements of small decreases in organic mass alone may have been attributed to other processes, such as chamber wall deposition.

3.4.3. *Low-NO_x α-pinene SOA*

In the evolution of various measured parameters during the low-NO_x α-pinene photooxidation (Experiment 7), mean coating thickness steadily increased as SOA was formed (Figure 6b). About halfway through the irradiation period, a decrease in the rate of change of the absorption and scattering coefficients occurred (Figure 6c), coincident with a decrease in the growth rate of total organic mass concentration measured by the AMS (Figure 6a). This change during irradiation occurred at an oxidation lifetime of ~2 (~4 h after the onset of irradiation).

Figures 11a and b present normalized AMS mass spectra at oxidation lifetimes of 3 and 1, respectively, on either side of the change in aerosol growth rate. Figure 11c presents the difference spectrum relative to the earlier spectrum and shows a decrease in f_{43}. Figure 11d shows the evolution of various AMS mass fractions with oxidation lifetime in addition to the absorption and scattering coefficients at $\lambda = 405$ nm measured by the PASS-3. A shift in optical properties is evident at an oxidation lifetime of 2, while f_{43} and f_{44} continually change during the experiment and show no clear shift. The other mass fractions presented in Figure 11d also change continually throughout the experiment, although at different rates relative to each other. Some mass fractions, namely $f_{1–50}$ and $f_{50–100}$, change much more rapidly during the early part of irradiation and then begin to approach a relatively constant value after an oxidation lifetime of 2. Throughout the entire period displayed in Figure 11d, organic mass is growing and the raw m/z's are increasing; thus, the changes in mass fractions reflect the fact that different mass fragments are growing at different rates relative to each other, rather than by loss of certain fragments.

While m/z 43 and 44 are important individual mass fragments in the AMS mass spectra, they fail to capture the change in aerosol behavior that occurs at an oxidation lifetime of 2 in this system. Examining a wider range of mass fragments in the AMS mass spectra reveals that the aerosol composition is continually evolving during the irradiation period. This change in composition is likely accompanied by a change in refractive index, explaining the shift in optical properties despite steady growth of rBC coating thicknesses. This experiment demonstrates that measurement of aerosol optical properties can help guide the analysis of data from other instruments, namely the AMS. In

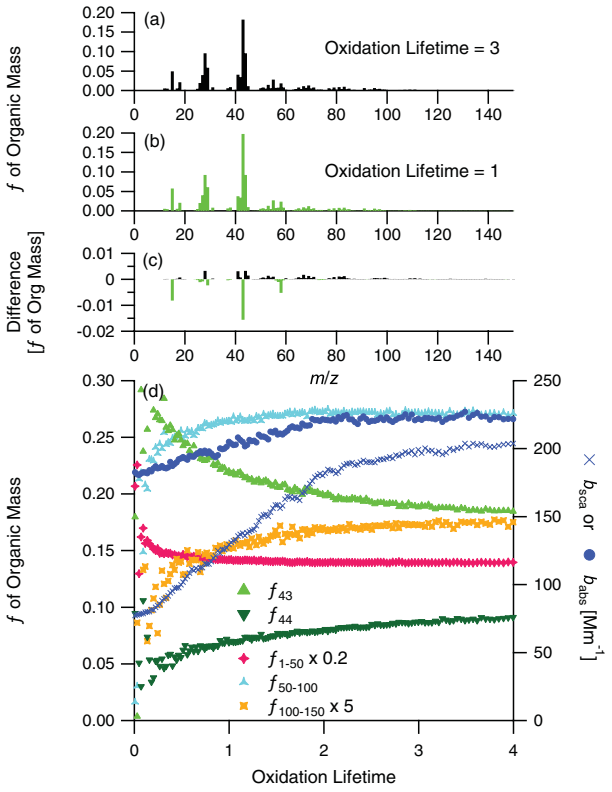

FIG. 11. Normalized unit-mass resolution AMS organic mass spectra from Experiment 7, low-NO_x α-pinene photooxidation in the presence of fullerene soot, at (a) an oxidation lifetime = 3 (during the slower growth rate after the shift in optical properties) and (b) an oxidation lifetime = 1 (during the more rapid growth rate before the change in optical properties), (c) the difference spectrum, calculated relative to the earlier mass spectrum, and (d) comparison of f_{43}, f_{44}, $f_{1–50}$ (scaled by 0.2), $f_{50–100}$, and $f_{100–150}$ (scaled by 5) from the AMS with the scattering and absorption coefficients at $\lambda = 405$ nm measured by the PASS-3. On the difference spectrum, positive values denote m/z's enriched in the later condensed SOA and negative values denote m/z's enriched in the earliest condensed SOA. (Color figure available online.)

the low-NO_x α-pinene photooxidation system, the SOA optical properties change with time, and could be used as a model system to help understand the evolution of atmospheric SOA optical properties.

4. CONCLUSIONS

In this work, we demonstrate the utility of employing fullerene soot, a surrogate for refractory black carbon, as a seed aerosol in chamber studies of secondary organic aerosol formation, when done in conjunction with the single-particle soot photometer. Particle-by-particle measurement of the dynamics of the organic coating thickness on the rBC seed over the course of SOA formation allows evaluation of the rate of growth as a function of particle size. An experimental strategy is implemented in which a period of VOC oxidation and SOA growth is

followed by one in which growth is quenched while the chamber undergoes dilution. The dilution phase is used as a means to assess SOA volatility by measuring the possible evaporation of coatings on the rBC seed. In the experiments presented here, a 3-λ photoacoustic soot spectrometer is used to measure the optical properties of the uncoated rBC seed, initially, and the coated rBC seed during the course of SOA formation. These measurements, coupled with the application of a core-and-shell Mie scattering model, allow one to infer the optical properties of the SOA. Application of a prototype single-particle angularly-resolved light scattering instrument confirms that the uncoated rBC particles are nonspherical. Important to understanding the effect rBC has on SOA formation is whether or not SOA condensed onto rBC seed is chemically and optically similar to nucleated SOA under dry conditions. High-resolution Aerodyne aerosol mass spectrometer measurements for the three systems considered here, naphthalene photooxidation and photooxidation of α-pinene under both high- and low-NO_x conditions, confirm that the composition of SOA coating rBC seed particles differs from homogeneously nucleated SOA by no more than condensing SOA on the more conventional ammonium sulfate seed used in many chamber experiments, so that the use of rBC as a seed is not expected to alter the basic chemistry of SOA formation under dry conditions. Both SP2 and PASS-3 measurements reveal a change in the SOA coating and particle optical properties during SOA growth in the high-NO_x α-pinene system, which is mirrored by a corresponding change in the AMS mass spectra. The combination of SP2 and AMS measurements in this system suggest that semivolatile species are evaporating from the aerosol during chemical aging. A change in optical properties during SOA growth in the low-NO_x α-pinene system is mirrored by a change in organic growth rate and AMS mass spectra, but not in single-particle coating thicknesses. Exploration of a fundamental explanation of the chemistry leading to these changes lies beyond the scope of the present work. We have provided a framework by which future studies of SOA optical properties and single-particle growth dynamics may be explored in environmental chambers.

REFERENCES

Abel, S. J., Haywood, J. M., Highwood, E. J., Li, J., and Buseck, P. R. (2003). Evolution of Biomass Burning Aerosol Properties from an Agricultural Fire in Southern Africa. *Geophys. Res. Lett.*, 30(15):1783, doi:10.1029/2003GL017342.

Andreae, M. O., and Gelencsér, A. (2006). Black Carbon or Brown Carbon? The Nature of Light-Absorbing Carbonaceous Aerosols. *Atmos. Chem. Phys.*, 6:3131–3148, doi:10.5194/acp-6-3131-2006.

Bahreini, R., Ervens, B., Middlebrook, A. M., Warneke, C., de Gouw, J. A., DeCarlo, P. F., Jimenez, J. L., Brock, C. A., Neuman, J. A., Ryerson, T. B., Stark, H., Atlas, E., Brioude, J., Fried, A., Holloway, J. S., Peischl, J., Richter, D., Walega, J., Weibring, P., Wollny, A. G., and Fehsenfeld, F. C. (2009). Organic Aerosol Formation in Urban and Industrial Plumes Near Houston and Dallas, Texas. *J. Geophys. Res.*, 114:D00F16, doi:10.1029/2008JD011493.

Barkey, B., Paulson, S. E., and Chung, A. (2007). Genetic Algorithm Inversion of Dual Polarization Polar Nephelometer Data to Determine Aerosol Refractive Index. *Aerosol Sci. Technol.*, 41(8):751–760, doi:10.1080/02786820701432640.

Baumgardner, D., Kok, G. L., and Raga, G. B. (2004). Warming of the Arctic Lower Stratosphere by Light Absorbing Particles. *Geophys. Res. Lett.*, 31:L06117, doi:10.1029/2003GL018883.

Baumgardner, D., Popovicheva, O., Allan, J., Bernardoni, V., Cao, J., Cavalli, F., Cozic, J., Diapouli, E., Eleftheriadis, K., Genberg, P. J., Gonzalez, C., Gysel, M., John, A. T. W., Kirchstetter, T. A., Kuhlbusch, J., Laborde, M., Lack, D., Müller, T., Niessner, R., Petzold, A., Piazzalunga, A., Putaud, J. P., Schwarz, J., Sheridan, P., Subramanian, R., Swietlicki, E., Valli, G., Vecchi, R., and Viana, M. (2012). Soot Reference Materials for Instrument Calibration and Intercomparisons: A Workshop Summary with Recommendations. *Atmos. Meas. Tech.*, 5:1869–1887, doi:10.5194/amt-5-1869-2012.

Bohren, C. F., and Huffman, D. R. (1998). *Absorption and Scattering of Light by Small Particles*. John Wiley & Sons, Inc., New York.

Bond, T. C., and Bergstrom, R. W. (2006). Light Absorption by Carbonaceous Particles: An Investigative Review. *Aerosol Sci. Technol.*, 40(1):27–67, doi:10.1080/02786820500421521.

Bond, T. C., Habib, G., and Bergstrom, R. W. (2006). Limitations in the Enhancement of Visible Light Absorption Due to Mixing State. *J. Geophys. Res.*, 111:D20211, doi:10.1029/2006JD007315.

Bueno, P. A., Havey, D. K., Mulholland, G. W., Hodges, J. T., Gillis, K. A., Dickerson, R. R., and Zachariah, M. R. (2011). Photoacoustic Measurements of Amplification of the Absorption Cross Section for Coated Soot Aerosols. *Aerosol Sci. Technol.*, 45(10):1217–1230, doi:10.1080/02786826.2011.587477.

Canagaratna, M. R., Jayne, J. T., Jimenez, J. L., Allan, J. D., Alfarra, M. R., Zhang, Q., Onasch, T. B., Drewnick, F., Coe, H., Middlebrook, A., Delia, A., Williams, L.R., Trimborn, A. M., Northway, M. J., DeCarlo, P. F., Kolb, C. E., Davidovits, P., and Worsnop, D. R. (2007). Chemical and Microphysical Characterization of Ambient Aerosols with the Aerodyne Aerosol Mass Spectrometer. *Mass Spectrom. Rev.*, 26(2):185–222, doi:10.1002/mas.20115.

Chan, A. W. H., Kautzman, K. E., Chhabra, P. S., Surratt, J. D., Chan, M. N., Crounse, J. D., Kürten, A., Wennberg, P. O., Flagan, R. C., and Seinfeld, J. H. (2009). Secondary Organic Aerosol Formation from Photooxidation of Naphthalene and Alkylnaphthalenes: Implications for Oxidation of Intermediate Volatility Organic Compounds (IVOCs). *Atmos. Chem. Phys.*, 9:3049–3060, doi:10.5194/acp-9-3049-2009.

Chan, A. W. H., Chan, M. N., Surratt, J. D., Chhabra, P. S., Loza, C. L., Crounse, J. D., Yee, L. D., Flagan, R. C., Wennberg, P. O., and Seinfeld, J. H. (2010a). Role of Aldehyde Chemistry and NO_x Concentrations in Secondary Organic Aerosol Formation. *Atmos. Chem. Phys.*, 10:7169–7188, doi:10.5194/acp-10-7169-2010.

Chan, T. W., et al. (2010b). Observations of OM/OC and Specific Attenuation Coefficients (SAC) in Ambient Fine PM at a Rural Site in Central Ontario, Canada. *Atmos. Chem. Phys.*, 10:2393–2411, doi:10.5194/acp-10-2393-2010.

Chirico, R., DeCarlo, P. F., Heringa, M. F., Tritscher, T., Richter, R., Prévôt, A. S. H., Dommen, J., Weingartner, E., Wehrle, G., Gyse, M., Laborde, M., and Baltensperger, U. (2010). Impact of Aftertreatment Devices on Primary Emissions and Secondary Organic Aerosol Formation Potential from in-use Diesel Vehicles: Results from Smog Chamber Experiments. *Atmos. Chem. Phys.*, 10(11):545–11, 563, doi:10.5194/acp-10-11545-2010.

Chung, S. H., and Seinfeld, J. H. (2002). Global Distribution and Climate Forcing of Carbonaceous Aerosols. *J. Geophys. Res.*, 107(D19):4407, doi:10.1029/2001JD001397.

Cocker, D. R., Flagan, R. C., and Seinfeld, J. H. (2001). State-of-the-art Chamber Facility for Studying Atmospheric Aerosol Chemistry. *Environ. Sci. Technol.*, 35(12):2594–2601, doi:10.1021/es0019169.

Crosso, E. S., Onasch, T. B., Ahern, A., Wrobel, W., Slowik, J. G., Olfert, J., Lack, D. A., Massoli, P., Cappaf, C. D., Schwarz, J. P., Spackman, J. R., Fahey, D. W., Sedlacek, A., Trimborn, A., Jayneb, J. T., Freedman, A., Williams, L. R., Ng, N. L., Mazzoleni, C., Dubey, M., Brem, B., Koki, G., Subramanian, R., Freitag, S., Clarke, A., Thornhill, D., Marrk,

L. C., Kolb, C. E., Worsnop, D. R., and Davidovits, P. (2010). Soot Particle Studies—Instrument Inter-Comparison—Project Overview. *Aerosol Sci. Technol.*, 44(8):592–611, doi:10.1080/02786826.2010.482113.

Crump, J. G., and Seinfeld, J. H. (1981). Turbulent Deposition and Gravitational Sedimentation of an Aerosol in a Vessel of Arbitrary Shape. *J. Aerosol Sci.*, 12(5):405–415, doi:10.1016/0021-8502(81)90036-7.

DeCarlo, P. F., Slowik, J. G., Worsnop, D. R., Davidovits, P., and Jimenez, J. L. (2004). Particle Morphology and Density Characterization by Combined Mobility and Aerodynamic Diameter Measurements. Part 1: Theory. *Aerosol Sci. Technol.*, 38:1185–1205, doi:10.1080/027868290903907.

DeCarlo, P. F., Kimmel, J. R., Trimborn, A., Northway, M. J., Jayne, J. T., Aiken A. C., Gonin, M., Fuhrer, K., Horvath, T., Docherty, K. S., Worsnop, D. R., and Jimenez, J. L. (2006). Field-Deployable, High-Resolution, Time-of-Flight Aerosol Mass Spectrometer. *Anal. Chem.*, 78(24):8281–8289, doi:10.1021/ac061249n.

Dick, W. D., McMurry, P. H., and Bottiger, J. R. (1994). Size- and Composition-Dependent Response of the DAWN-A Multiangle Single-Particle Optical Detector. *Aerosol Sci. Technol.*, 20(4):345–362, doi:10.1080/02786829408959690.

Dick, W. D., Ziemann, P. J., Huang, P.-F., and McMurry, P. H. (1998). Optical Shape Fraction Measurements of Submicrometre Laboratory and Atmospheric Aerosols. *Meas. Sci. Technol.*, 9(2):183–196, doi:10.1088/0957-0233/9/2/006.

Flowers, B. A., Dubey, M. K., Mazzoleni, C., Stone, E. A., Schauer, J. J., Kim, S.-W., et al. (2010). Optical-Chemical-Microphysical Relationships and Closure Studies for Mixed Carbonaceous Aerosols Observed at Jeju Island; 3-Laser Photoacoustic Spectrometer, Particle Sizing, and Filter Analysis. *Atmos. Chem. Phys.*, 10(21):10, 387–10, 398, doi:10.5194/acp-10-10387-2010.

Fruin, S. A., Winer, A. M., and Rodes, C. E. (2004). Black Carbon Concentrations in California Vehicles and Estimation of in-vehicle Diesel Exhaust Particulate Matter Exposures. *Atmos. Environ.*, 38(25):4123–4133, doi:10.1016/j.atmosenv.2004.04.026.

Fuller, K. A., Malm, W. C., and Kreidenweis, S. M. (1999). Effects of Mixing on Extinction by Carbonaceous Particles. *J. Geophys. Res.*, 104(D13):15, 941–15, 954, doi:10.1029/1998JD100069.

Gao, R. S., et al. (2007). A Novel Method for Estimating Light-Scattering Properties of Soot Aerosols Using a Modified Single-Particle Soot Photometer. *Aerosol Sci. Technol.*, 41(2):125–135, doi:10.1080/02786820601118398.

Guenther, A., et al. (1995). A Global Model of Natural Volatile Organic Compound Emissions. *J. Geophys. Res.*, 100(D5):8873–8892.

Gyawali, M., Arnott, W., Lewis, K., and Moosmüller, H. (2009). In Situ Aerosol Optics in Reno, NV, USA During and After the Summer 2008 California Wildfires and the Influence of Absorbing and Non-Absorbing Organic Coatings on Spectral Light Absorption. *Atmos. Chem. Phys.*, 9:8007–8015, doi:10.5194/acp-9-8007-2009.

Gysel, M., Laborde, M., Olfert, J. S., Subramanian, R., and Gröhn, A. J. (2011). Effective Density of Aquadag and Fullerene Soot Black Carbon Reference Materials Used for SP2 Calibration. *Atmos. Meas. Tech.*, 4:2851–2858, doi:10.5194/amt-4-2851-2011.

Hoffer, A., Gelencsér, A., Guyon, P., Kiss, G., Schmid, O., Frank, G. P., et al. (2006). Optical Properties of Humic-Like Substances (HULIS) in Biomass-Burning Aerosols. *Atmos. Chem. Phys.*, 6:3563–3570, doi:10.5194/acp-6-3563-2006.

Huffman, J. A., Jayne, J. T., Drewnick, F., Aiken, A. C., Onasch, T., Worsnop, D. R., et al. (2005). Design, Modeling, Optimization, and Experimental Tests of a Particle Beam Width Probe for the Aerodyne Aerosol Mass Spectrometer. *Aerosol Sci. Technol.*, 39(12):1143–1163, doi:10.1080/02786820500423782.

Jacobson, M. Z. (2006). Effects of Externally-Through-Internally-Mixed Soot Inclusions within Clouds and Precipitation on Global Climate. *J. Phys. Chem. A*, 110(21):6860–6873, doi:10.1021/jp056391r.

Jayne, J. T., Leard, D. C., Zhang, X., Davidovits, P., Smith, K. A., Kolb, C. E., et al. (2000). Development of an Aerosol Mass Spectrometer for Size and Composition Analysis of Submicron Particles. *Aerosol Sci. Technol.*, 33(1–2):49–70, doi:10.1080/027868200410840.

Johnson, K. S., Zuberi, B., Molina, L. T., Molina, M. J., Iedema, M. J., Cowin, J. P., et al. (2005). Processing of Soot in an Urban Environment: Case Study from the Mexico City Metropolitan Area. *Atmos. Chem. Phys.*, 5:3033–3043, doi:10.5194/acp-5-3033-2005.

Keywood, M. D., Varutbangkul, V., Bahreini, R., Flagan, R. C., and Seinfeld, J. H. (2004). Secondary Organic Aerosol Formation from the Ozonolysis of Cycloalkenes and Related Compounds. *Environ. Sci. Technol.*, 38(15):4157–4164, doi:10.1021/es035363o.

Khalizov, A. F., Xue, H., Wang, L., Zheng, J., and Zhang, R. (2009a). Enhanced Light Absorption and Scattering by Carbon Soot Aerosol Internally Mixed with Sulfuric Acid. *J. Phys. Chem. A*, 113(6):1066–1074, doi:10.1021/jp807531n.

Khalizov, A. F., Zhang, R., Zhang, D., Xue, H., Pagels, J., and McMurry, P. H. (2009b). Formation of Highly Hygroscopic Soot Aerosols Upon Internal Mixing with Sulfuric Acid Vapor. *J. Geophys. Res.*, 114:D05208, doi:10.1029/2008JD010595.

Kirchner, U., Vogt, R., Natzeck, C., and Goschnick, J. (2003). Single Particle MS, SNMS, SIMS, XPS, and FTIR Spectroscopic Analysis of Soot Particles During the AIDA Campaign. *J. Aerosol Sci.*, 34(10):1323–1346, doi:10.1016/S0021-8502(03)00362-8.

Kirchstetter, T. W., Novakov, T., and Hobbs, P. V. (2004). Evidence that the Spectral Dependence of Light Absorption by Aerosols is Affected by Organic Carbon. *J. Geophys. Res.*, 109:D21208, doi:10.1029/2004JD004999.

Kleeman, M. J., Schauer, J. J., and Cass, G. R. (2000). Size and Composition Distribution of Fine Particulate Matter Emitted from Motor Vehicles. *Environ. Sci. Technol.*, 34(7):1132–1142, doi: 10.1021/es981276y.

Knox, A., Evans, G. J., Brook, J. R., Yao, X., Jeong, C.-H., Godri, K. J., et al. (2009). Mass Absorption Cross-Section of Ambient Black Carbon Aerosol in Relation to Chemical Age. *Aerosol Sci. Technol.*, 43(6):522–532, doi:10.1080/02786820902777207.

Kroll, J. H., Smith, J. D., Che, D. L., Kessler, S. H., Worsnop, D. R., and Wilson, K. R. (2009). Measurement of Fragmentation and Functionalization Pathways in the Heterogeneous Oxidation of Oxidized Organic Aerosol. *Phys. Chem. Chem. Phys.*, 11(36):8005–8014, doi:10.1039/b905289e.

Laborde, M., Mertes, P., Zieger, P., Dommen, J., Baltensperger, U., and Gysel, M. (2012). Sensitivity of the Single Particle Soot Photometer to Different Black Carbon Types. *Atmos. Meas. Tech.*, 5:1031–1043, doi:10.5194/amt-5-1031-2012.

Lack, D. A., and Cappa, C. D. (2010). Impact of Brown and Clear Carbon on Light Absorption Enhancement, Single Scatter Albedo and Absorption Wavelength Dependence of Black Carbon. *Atmos. Chem. Phys.*, 10:4207–4220, doi:10.5194/acp-10-4207-2010.

Leach, K. B., Kamens, R. M., Strommen, M. R., and Jang, M. (1999). Partitioning of Semivolatile Organic Compounds in the Presence of a Secondary Organic Aerosol in a Controlled Atmosphere. *J. Atmos. Chem.*, 33(3):241–264, doi:10.1023/A:1006108430033.

Lewis, K., Arnott, W. P., Moosmüller, H., and Wold, C. E. (2008). Strong Spectral Variation of Biomass Smoke Light Absorption and Single Scattering Albedo Observed with a Novel Dual-Wavelength Photoacoustic Instrument. *J. Geophys. Res.*, 113:D16203, doi:10.1029/2007JD009699.

Loza, C. L., Chhabra, P. S., Yee, L. D., Craven, J. S., Flagan, R. C., and Seinfeld, J. H. (2012). Chemical Aging of m-xylene Secondary Organic Aerosol: Laboratory Chamber Study. *Atmos. Chem. Phys.*, 12:151–167, doi:10.5194/acp-12-151-2012.

Malm, W. C., Day, D. E., Carrico, C., Kreidenweis, S. M., Collett Jr., J. L., McMeeking, G., Lee, T., Carrillo, J., and Schichtel, B. (2005a). Intercomparison and Closure Calculations Using Measurements of Aerosol Species and Optical Properties During the Yosemite Aerosol Characterization Study. *J. Geophys. Res.*, 110:D14302, doi:10.1029/2004JD005494.

Malm, W. C., Day, D. E., Kreidenweis, S. M., Collett Jr., J. L., Carrico, C., McMeeking, G., and Lee, T. (2005b). Hygroscopic Properties

of an Organic-Laden Aerosol. *Atmos. Environ.*, 39(27):4969–4982, doi:10.1016/j.atmosenv.2005.05.014.

McMurry, P. H., and Rader, D. J. (1985). Aerosol Wall Losses in Electrically Charged Chambers. *Aerosol Sci. Technol.*, 4(3):249–268, doi:10.1080/02786828508959054.

Metcalf, A. R., Craven, J. S., Ensberg, J. J., Brioude, J., Angevine, W., Sorooshian, A., Duong, H. T., Jonsson, H. H., Flagan, R. C., and Seinfeld, J. H. (2012). Black Carbon Aerosol over the Los Angeles Basin During CalNex. *J. Geophys. Res.*, 117:D00V13, doi:10.1029/2011JD017255.

Middlebrook, A. M., Bahreini, R., Jimenez, J. L., and Canagaratna, M. R. (2012). Evaluation of Composition-Dependent Collection Efficiencies for the Aerodyne Aerosol Mass Spectrometer Using Field Data. *Aerosol Sci. Technol.*, 46(3):258–271, doi:10.1080/02786826.2011.620041.

Mikhailov, E. F., Vlasenko, S. S., Podgorny, I. A., Ramanathan, V., and Corrigan, C. E. (2006). Optical Properties of Soot–Water Drop Agglomerates: An Experimental Study. *J. Geophys. Res.*, 111:D07209, doi:10.1029/2005JD006389.

Moffet, R. C., and Prather, K. A. (2009). In-Situ Measurements of the Mixing State and Optical Properties of Soot with Implications for Radiative Forcing Estimates. *Proc. Natl. Acad. Sci. USA*, 106(29):11872–11877, doi:10.1073/pnas.0900040106.

Moteki, N., and Kondo, Y. (2007). Effects of Mixing State on Black Carbon Measurements by Laser-Induced Incandescence. *Aerosol Sci. Technol.*, 41(4):398–417, doi:10.1080/02786820701199728.

Moteki, N., and Kondo, Y. (2010). Dependence of Laser-Induced Incandescence on Physical Properties of Black Carbon Aerosols: Measurements and Theoretical Interpretation. *Aerosol Sci. Technol.*, 44(8):663–675, doi:10.1080/02786826.2010.484450.

Moteki, N., et al. (2007). Evolution of Mixing State of Black Carbon Particles: Aircraft Measurements Over the Western Pacific in March 2004. *Geophys. Res. Lett.*, 34:L11803, doi:10.1029/2006GL028943.

Moteki, N., Kondo, Y., Takegawa, N., and Nakamura, S. (2009). Directional Dependence of Thermal Emission from Nonspherical Carbon Particles. *J. Aerosol Sci.*, 40(9):790–801, doi:10.1016/j.jaerosci.2009.05.003.

Nakayama, T., Matsumi, Y., Sato, K., Imamura, T., Yamazaki, A., and Uchiyama, A. (2010). Laboratory Studies on Optical Properties of Secondary Organic Aerosols Generated During the Photooxidation of Toluene and the Ozonolysis of Alpha-Pinene. *J. Geophys. Res.*, 115:D24203, doi:10.1029/2010JD014387.

Ng, N. L., Kroll, J. H., Chan, A. W. H., Chhabra, P. S., Flagan, R. C., and Seinfeld, J. H. (2007). Secondary Organic Aerosol Formation from m-xylene, Toluene, and Benzene. *Atmos. Chem. Phys.*, 7:3909–3922, doi:10.5194/acp-7-3909-2007.

Ng, N. L., et al. (2010). Organic Aerosol Components Observed in Northern Hemispheric Datasets from Aerosol Mass Spectrometry. *Atmos. Chem. Phys.*, 10:4625–4641, doi:10.5194/acp-10-4625-2010.

Park, S. H., Kim, H. O., Han, Y. T., Kwon, S. B., and Lee, K. W. (2001). Wall Loss Rate of Polydispersed Aerosols. *Aerosol Sci. Technol.*, 35(3):710–717, doi:10.1080/02786820152546752.

Park, Y.-K., Park, S. H., and Bae, G.-N. (2012). Analytical Expression on Characteristic Time Scale of Black Carbon Aging Due to Condensation of Hygroscopic Species. *Aerosol Sci. Technol.*, 46(6):601–609, doi:10.1080/02786826.2011.647119.

Pierce, J. R., Engelhart, G. J., Hildebrandt, L., Weitkamp, E. A., Pathak, R. K., Donahue, N. M., et al. (2008). Constraining Particle Evolution from Wall Losses, Coagulation, and Condensation-Evaporation in Smog-Chamber Experiments: Optimal Estimation Based on Size Distribution Measurements. *Aerosol Sci. Technol.*, 42(12):1001–1015, doi:10.1080/02786820802389251.

Pósfai, M., Simonics, R., Li, J., Hobbs, P. V., and Buseck, P. R. (2003). Individual Aerosol Particles from Biomass Burning in Southern Africa: 1. Compositions and Size Distributions of Carbonaceous Particles. *J. Geophys. Res.*, 108(D13):8483, doi:10.1029/2002JD002291.

Pye, H. O. T., Chan, A. W. H., Barkley, M. P., and Seinfeld, J. H. (2010). Global Modeling of Organic Aerosol: The Importance of Reactive Nitrogen (NO_x and NO_3). *Atmos. Chem. Phys.*, 10(11):261–11, 276, doi:10.5194/acp-10-11261-2010.

Ravindra, K., Sokhi, R., and Van Grieken, R. (2008). Atmospheric Polycyclic Aromatic Hydrocarbons: Source Attribution, Emission Factors and Regulation. *Atmos. Environ.*, 42(13):2895–2921, doi:10.1016/j.atmosenv.2007.12.010.

Riemer, N., Vogel, H., and Vogel, B. (2004). Soot Aging Time Scales in Polluted Regions During Day and Night. *Atmos. Chem. Phys.*, 4:1885–1893, doi:10.5194/acp-4-1885-2004.

Robinson, A. L., Donahue, N. M., Shrivastava, M. K., Weitkamp, E. A., Sage, A. M., Grieshop, A. P., et al. (2007). Rethinking Organic Aerosols: Semivolatile Emissions and Photochemical Aging. *Science*, 315(5816):1259–1262, doi:10.1126/science.1133061.

Saathoff, H., Naumann, K.-H., Schnaiter, M., Schöck, W., Möhler, O., Schurath, U., et al. (2003). Coating of Soot and $(NH_4)_2SO_4$ Particles by Ozonolysis Products of α-pinene. *J. Aerosol Sci.*, 34(10):1297–1321, doi:10.1016/S0021-8502(03)00364-1.

Sachweh, B. A., Dick, W. D., and McMurry, P. H. (1995). Distinguishing between Spherical and Nonspherical Particles by Measuring the Variability in Azimuthal Light Scattering. *Aerosol Sci. Technol.*, 23(3):373–391, doi:10.1080/02786829508965321.

Schauer, J. J., Kleeman, M. J., Cass, G. R., and Simoneit, B. R. T. (1999). Measurement of Emissions from Air Pollution Sources. 2. C1 Through C30 Organic Compounds from Medium Duty Diesel Trucks. *Environ. Sci. Technol.*, 33(10):1578–1587, doi:10.1021/es980081n.

Schauer, J. J., Kleeman, M. J., Cass, G. R., and Simoneit, B. R. T. (2001). Measurement of Emissions from Air Pollution Sources. 3. C1–C29 Organic Compounds from Fireplace Combustion of Wood. *Environ. Sci. Technol.*, 35(9):1716–1728, doi:10.1021/es001331e.

Schauer, J. J., Rogge, W. F., Hildemann, L. M., Mazurek, M. A., Cass, G. R., and Simoneit, B. R.T. (1996). Source Apportionment of Airborne Particulate Matter Using Organic Compounds as Tracers. *Atmos. Environ.*, 30(22):3837–3855, doi:10.1016/1352-2310(96)00085-4.

Schnaiter, M., Horvath, H., Möhler, O., Naumann, K.-H., Saathoff, H., and Schöck, O. W. (2003). UV-VIS-NIR Spectral Optical Properties of Soot and Soot-Containing Aerosols. *J. Aerosol Sci.*, 34(10):1421–1444, doi:10.1016/S0021-8502(03)00361-6.

Schnaiter, M., Linke, C., Möhler, O., Naumann, K.-H., Saathoff, H., Wagner, R., et al. (2005). Absorption Amplification of Black Carbon Internally Mixed with Secondary Organic Aerosol. *J. Geophys. Res.*, 110:D19204, doi:10.1029/2005JD006046.

Schoemaecker Moreau, C., Therssen, E., Mercier, X., Pauwels, J. F., and Desgroux, P. (2004). Two-Color Laser-Induced Incandescence and Cavity Ring-Down Spectroscopy for Sensitive and Quantitative Imaging of Soot and PAHs in Flames. *Appl. Phys. B: Lasers Opt.*, 78(3–4):485–492, doi:10.1007/s00340-003-1370-9.

Schwarz, J. P., Gao, R. S., Fahey, D. W., Thomson, D. S., Watts, L. A., Wilson, J. C., Reeves, J. M., Darbeheshti, M., Baumgardner, D. G., Kok, G. L., Chung, S. H., Schulz, M., Hendricks, J., Lauer, A., Kärcher, B., Slowik, J. G., Rosenlof, K. H., Thompson, T. L., Langford, A. O., Loewenstein, M., and Aikin, K. C. (2006). Single-Particle Measurements of Midlatitude Black Carbon and Light-Scattering Aerosols from the Boundary Layer to the Lower Stratosphere. *J. Geophys. Res.*, 111:D16207, doi:10.1029/2006JD007076.

Schwarz, J. P., R. Gao, S., Spackman, J. R., Watts, L. A., Thomson, D. S., Fahey, D. W., Ryerson, T. B., Peischl, J., Holloway, J. S., Trainer, M., Frost, G. J., Baynard, T., Lack, D. A., de Gouw, J. A., Warneke, C., and Del Negro, L. A. (2008a). Measurement of the Mixing State, Mass, and Optical Size of Individual Black Carbon Particles in Urban and Biomass Burning Emissions. *Geophys. Res. Lett.*, 35:L13810, doi:10.1029/2008GL033968.

Schwarz, J. P., Spackman, J. R., Fahey, D. W., R. Gao, S., Lohmann, U., Stier, P., Watts, L. A., Thomson, D. S., Lack, D. A., Pfister, L., Mahoney,

M. J., Baumgardner, D., Wilson, J. C., and Reeves, J. M. (2008b). Coatings and Their Enhancement of Black Carbon Light Absorption in the Tropical Atmosphere. *J. Geophys. Res.*, 113:D03203, doi:10.1029/2007JD009042.

Seinfeld, J. H., and Pandis, S. N. (2006). *Atmospheric Chemistry and Physics: From Air Pollution to Climate Change,* 2nd ed. John Wiley & Sons, Inc., New York.

Shiraiwa, M., Kondo, Y., Iwamoto, T., and Kita, K. (2010). Amplification of Light Absorption of Black Carbon by Organic Coating. *Aerosol Sci. Technol.*, 44(1):46–54, doi:10.1080/02786820903357686.

Shiraiwa, M., Kondo, Y., Moteki, N., Takegawa, N., Miyazaki, Y., and Blake, D. R. (2007). Evolution of Mixing State of Black Carbon in Polluted Air from Tokyo. *Geophys. Res. Lett.*, 34:L16803, doi:10.1029/2007GL029819.

Shiraiwa, M., Kondo, Y., Moteki, N., Takegawa, N., Sahu, L. K., Takami, A., et al. (2008). Radiative Impact of Mixing State of Black Carbon Aerosol in Asian Outflow. *J. Geophys. Res.*, 113:D24210, doi:10.1029/2008JD010546.

Slowik, J. G., Cross, E. S., Han, J.-H., Davidovits, P., Onasch, T. B., Jayne, J. T., Williams, L. R., Canagaratna, M. R., Worsnop, D. R., Chakrabarty, R. K., Moosmüller, H., Arnott, W. P., Schwarz, J. P., Gao, R.-S., Fahey, D. W., Kok, G. L., and Petzold, A. (2007a). An Inter-Comparison of Instruments Measuring Black Carbon Content of Soot Particles. *Aerosol Sci. Technol.*, 41(3):295–314, doi:10.1080/02786820701197078.

Slowik, J. G., Cross, E. S., Han, J.-H., Kolucki, J., Davidovits, P., Williams, L. R., Onasch, T. B., Jayne, J. T., Kolb, C. E., and Worsnop, D. R. (2007b). Measurements of Morphology Changes of Fractal Soot Particles Using Coating and Denuding Experiments: Implications for Optical Absorption and Atmospheric Lifetime. *Aerosol Sci. Technol.*, 41(8):734–750, doi:10.1080/02786820701432632.

Stephens, M., Turner, N., and Sandberg, J. (2003). Particle Identification by Laser-Induced Incandescence in a Solid-State Laser Cavity. *Appl. Opt.*, 42(19):3726–3736, doi:10.1364/AO.42.003726.

Stier, P., Seinfeld, J. H., Kinne, S., Feichter, J., and Boucher, O. (2006). Impact of Nonabsorbing Anthropogenic Aerosols on Clear-Sky Atmospheric Absorption. *J. Geophys. Res.*, 111:D18201, doi:10.1029/2006JD007147.

Strommen, M. R., and Kamens, R. M. (1997). Development and Application of a Dual-Impedance Radial Diffusion Model to Simulate the Partitioning of Semivolatile Organic Compounds in Combustion Aerosols. *Environ. Sci. Technol.*, 31(10):2983–2990, doi:10.1021/es970079g.

Strommen, M. R., and Kamens, R. M. (1999). Simulation of Semivolatile Organic Compound Microtransport at Different Time Scales in Airborne Diesel Soot Particles. *Environ. Sci. Technol.*, 33(10):1738–1746, doi:10.1021/es981035q.

Subramanian, R., et al. (2010). Black Carbon over Mexico: The Effect of Atmospheric Transport on Mixing State, Mass Absorption Cross-Section, and BC/CO Ratios. *Atmos. Chem. Phys.*, 10:219–237, doi:10.5194/acp-10-219-2010.

Taylor, W. D., Allston, T. D., Moscato, M. J., Fazekas, G. B., Kozlowski, R., and Takacs, G. A. (1980). Atmospheric Photodissociation Lifetimes for Nitromethane, Methyl Nitrite, and Methyl Nitrate. *Int. J. Chem. Kinet.*, 12(4):231–240, doi:10.1002/kin.550120404.

Toon, O. B., and Ackerman, T. P. (1981). Algorithms for the Calculation of Scattering by Stratified Spheres. *Appl. Opt.*, 20(20):3657–3660, doi:10.1364/AO.20.003657.

Wehner, B., et al. (2009). Mixing state of Nonvolatile Aerosol Particle Fractions and Comparison with Light Absorption in the Polluted Beijing Region. *J. Geophys. Res.*, 114:D00G17, doi:10.1029/2008JD010923.

Weiner, A. M., and Harris, S. J. (1989). Optical Detection of Large Soot Precursors. *Combust. Flame*, 77(3–4):261–266, doi:10.1016/0010-2180(89)90133-8.

Weingartner, E., Burtscher, H., and Baltensperger, U. (1997). Hygroscopic Properties of Carbon and Diesel Soot Particles. *Atmos. Environ.*, 31(15):2311–2327, doi:10.1016/S1352-2310(97)00023-X.

Weitkamp, E. A., Sage, A. M., Pierce, J. R., Donahue, N. M., and Robinson, A. L. (2007). Organic Aerosol Formation from Photochemical Oxidation of Diesel Exhaust in a Smog Chamber. *Environ. Sci. Technol.*, 41(20):6969–6975, doi:10.1021/es070193r.

Wonaschütz, A., Hitzenberger, R., Bauer, H., Pouresmaeil, P., Klatzer, B., Caseiro, A., et al. (2012). Application of the Integrating Sphere Method to Separate the Contributions of Brown and Black Carbon in Atmospheric Aerosols. *Environ. Sci. Technol.*, 43(4):1141–1146, doi:doi: 10.1021/es8008503.

Yang, M., Howell, S. G., Zhuang, J., and Huebert, B. J. (2009). Attribution of Aerosol Light Absorption to Black Carbon, Brown Carbon, and Dust in China–Interpretations of Atmospheric Measurements During EAST-AIRE. *Atmos. Chem. Phys.*, 9:2035–2050, doi:10.5194/acp-9-2035-2009.

Yu, Y., Ezella, M. J., Zelenyuk, A., Imre, D., Alexander, L., Ortega, J., D'Anna, B., Harmon, C. W., Johnson, S. N., and Finlayson-Pitts, B. J. (2008). Photooxidation of α-pinene at High Relative Humidity in the Presence of Increasing Concentrations of NO_x. *Atmos. Environ.*, 42(20):5044–5060, doi:10.1016/j.atmosenv.2008.02.026.

Zhang, R., Khalizov, A. F., Pagels, J., Zhang, D., Xue, H., and McMurry, P. H. (2008). Variability in Morphology, Hygroscopicity, and Optical Properties of Soot Aerosols During Atmospheric Processing. *Proc. Natl. Acad. Sci. USA*, 105(30):10291–10296, doi:10.1073/pnas.0804860105.

Zuberi, B., Johnson, K. S., Aleks, G. K., Molina, L. T., and Molina, M. J. (2005). Hydrophilic Properties of Aged Soot. *Geophys. Res. Lett.*, 32:L01807, doi:10.1029/2004GL021496.

Appendix D

Chemical Aging of M–xylene Secondary Organic Aerosol: Laboratory Chamber Study[1]

[1]This chapter is reproduced by permission from "Chemical Aging of M–xylene Secondary Organic Aerosol: Laboratory Chamber Study" by C. L. Loza, P. S. Chhabra, L. D. Yee, J. S. Craven, R. C. Flagan, and J. H. Seinfeld, *Atmospheric Chemistry and Physics*, (12), 151 – 167 , www.atmos-chem-phys.net/12/151/2012/ 2012, doi:10.5194/acp-12-151-2012, 2012.

Atmos. Chem. Phys., 12, 151–167, 2012
www.atmos-chem-phys.net/12/151/2012/
doi:10.5194/acp-12-151-2012

Atmospheric Chemistry and Physics

Chemical aging of *m*-xylene secondary organic aerosol: laboratory chamber study

C. L. Loza[1], P. S. Chhabra[1,*], L. D. Yee[2], J. S. Craven[1], R. C. Flagan[1,2], and J. H. Seinfeld[1,2]

[1]Division of Chemistry and Chemical Engineering, California Institute of Technology, Pasadena, CA, USA
[2]Division of Engineering and Applied Science, California Institute of Technology, Pasadena, CA, USA
[*]now at: Aerodyne Research, Inc., Billerica, MA, USA

Correspondence to: J. H. Seinfeld (seinfeld@caltech.edu)

Received: 20 August 2011 – Published in Atmos. Chem. Phys. Discuss.: 7 September 2011
Revised: 8 December 2011 – Accepted: 20 December 2011 – Published: 3 January 2012

Abstract. Secondary organic aerosol (SOA) can reside in the atmosphere for a week or more. While its initial formation from the gas-phase oxidation of volatile organic compounds tends to take place in the first few hours after emission, SOA can continue to evolve chemically over its atmospheric lifetime. Simulating this chemical aging over an extended time in the laboratory has proven to be challenging. We present here a procedure for studying SOA aging in laboratory chambers that is applied to achieve 36 h of oxidation. The formation and evolution of SOA from the photooxidation of *m*-xylene under low-NO_x conditions and in the presence of either neutral or acidic seed particles is studied. In SOA aging, increasing molecular functionalization leads to less volatile products and an increase in SOA mass, whereas gas- or particle-phase fragmentation chemistry results in more volatile products and a loss of SOA. The challenge is to discern from measured chamber variables the extent to which these processes are important for a given SOA system. In the experiments conducted, *m*-xylene SOA mass, calculated under the assumption of size-invariant particle composition, increased over the initial 12–13 h of photooxidation and decreased beyond that time, suggesting the existence of fragmentation chemistry. The oxidation of the SOA, as manifested in the O:C elemental ratio and fraction of organic ion detected at *m/z* 44 measured by the Aerodyne aerosol mass spectrometer, increased continuously starting after 5 h of irradiation until the 36 h termination. This behavior is consistent with an initial period in which, as the mass of SOA increases, products of higher volatility partition to the aerosol phase, followed by an aging period in which gas- and particle-phase reaction products become increasingly more oxidized. When irradiation is stopped 12.4 h into one experiment, and OH generation ceases, minimal loss of SOA is observed, indicating that the loss of SOA is either light- or OH-induced. Chemical ionization mass spectrometry measurements of low-volatility *m*-xylene oxidation products exhibit behavior indicative of continuous photooxidation chemistry. A condensed chemical mechanism of *m*-xylene oxidation under low-NO_x conditions is capable of reproducing the general behavior of gas-phase evolution observed here. Moreover, order of magnitude analysis of the mechanism suggests that gas-phase OH reaction of low volatility SOA precursors is the dominant pathway of aging in the *m*-xylene system although OH reaction with particle surfaces cannot be ruled out. Finally, the effect of size-dependent particle composition and size-dependent particle wall loss rates on different particle wall loss correction methods is discussed.

1 Introduction

Organic aerosol (OA) constitutes 20–90 % of all submicron particles in the atmosphere, and up to 80 % of this is classified as secondary organic aerosol (SOA) (Zhang et al., 2007; Murphy et al., 2006). Aerosol particles in the atmosphere can have lifetimes of 5–12 days (Balkanski et al., 1993), during which they can undergo continuous physical and chemical processing, commonly called aging (Rudich et al., 2007). Laboratory experiments designed to study SOA formation typically have a duration of up to 1 day, during which all processes that cause ambient particle aging may not be captured. Chemical aging of SOA can affect gas-particle partitioning through processes such as vapor-phase oxidation of semivolatiles, heterogeneous oxidation, and reactions within the particle phase, e.g. oligomerization, that take place on

a fairly long timescale (Kroll and Seinfeld, 2008; Hallquist et al., 2009).

Given the potentially large number of organic species in ambient particles, bulk chemical measurements are useful to describe the extent of oxidative aging of SOA. Using aerosol mass spectrometry, changes in O:C (elemental oxygen to carbon ratio) and H:C (elemental hydrogen to carbon ratio) from high-resolution data and f_{44} (ratio of mass-to-charge (*m/z*) 44 to total signal in the organic component mass spectrum) and f_{43} (ratio of *m/z* 43 to total signal in the organic component mass spectrum) have been reported for ambient and laboratory-generated particles. The dominant organic ion at *m/z* 43 is $C_2H_3O^+$, and the dominant organic ion at *m/z* 44 is CO_2^+. Ng et al. (2010) evaluated a number of aerosol oxidation data sets in the f_{44}–f_{43} space and found that data for ambient OA tend to occupy a triangular region. As the OA becomes more oxidized, it tends to move from a region of lower f_{44} and a wider range of f_{43} at the base of the triangle toward the apex with higher f_{44} and less variable f_{43}. Heald et al. (2010) used the Van Krevelen diagram to show that the H:C and O:C of total ambient OA tend to fall along a line with a slope of -1, suggesting, on average, equal additions of carbonyl and alcohol moieties. More recently, Ng et al. (2011) determined a correlation between f_{43} and H:C and, combined with a correlation between f_{44} and O:C (Aiken et al., 2008), mapped the triangular region in f_{44}–f_{43} space onto the Van Krevelen diagram. They found that for ambient OA classified as oxygenated OA (OOA) and laboratory chamber-generated SOA the H:C and O:C evolution toward the apex of the triangle tends to fall along a line with a slope of -0.5 on a Van Krevelen diagram. This difference in slope between the two studies was attributed to the inclusion of primary OA in the study of Heald et al. The evolution of ambient OA can also be represented in terms of saturation concentration (C^*) and O:C (Jimenez et al., 2009). As the OA becomes more oxidized, C^* decreases and O:C increases. In all three of these frameworks, the oxygen content of the organic aerosol increases upon aging.

Laboratory studies have been conducted to probe the mechanisms of chemical aging of SOA. In flow reactor experiments, which have much shorter residence times than chamber experiments, OH concentrations a few orders of magnitude higher than ambient concentrations are used to attain OH exposure similar to that of multiple days of atmospheric processing. Using a flow reactor, Kroll et al. (2009) found that for oxidation of squalane ($C_{30}H_{36}$) particles, functionalization reactions (addition of polar functional groups) dominated at low OH exposure, and fragmentation reactions (scission of C-C bonds in the carbon skeleton) dominated as OH exposure increased. They observed an O:C ratio of 0.45 after 35.8 squalene OH oxidation lifetimes. Lambe et al. (2011) also used a flow reactor to attain OH exposures equivalent to 1-20 days of atmospheric aging. Using a range of anthropogenic and biogenic SOA and oxidized primary organic aerosol (OPOA) precursors, they found that as OH exposure increased, the SOA and OPOA followed and extended the progression of ambient SOA in f_{44}–f_{43} space, attaining values of f_{44} higher than ambient SOA. The Van Krevelen diagram slope of the SOA and OPOA was indicative of carboxylic acid formation and carbon-carbon bond fragmentation. In chamber experiments of 16 h oxidant exposure, Qi et al. (2010) found that, starting after 2 h of OH exposure, the volatility of SOA generated from *m*-xylene and α-pinene under high-NO_x conditions decreased slowly for the remainder of the experiment. After this initial 2-h period, the O:C ratio for *m*-xylene SOA increased at a rate of $0.007\,h^{-1}$; however, for α-pinene SOA, the O:C ratio decreased at a rate of $0.003\,h^{-1}$. Chhabra et al. (2010) observed increasing O:C for SOA formed from toluene, *m*-xylene, and naphthalene for irradiation times up to 12 h. The most rapid increase in O:C occurred during the first hour of low-NO_x toluene and *m*-xylene experiments and the first 4 h of low-NO_x naphthalene experiments. Similarly to the results of Qi et al. (2010) that SOA from some precursors exhibits minute aging behavior, no change in O:C was observed for SOA from isoprene photooxidation or α-pinene ozonolysis after initial SOA formation. Chhabra et al. (2011) extended the analysis of the SOA formed from the compounds studied in Chhabra et al. (2010) to assess their behavior in both f_{44}–f_{43} space and Van Krevelen diagram representations. Although the SOA formed from the various precursors occupied different regions in each representation, most systems exhibited a progression similar to aging of ambient SOA.

In this work, we develop and apply to *m*-xylene SOA a procedure to extend to 36 h the experimental duration of a laboratory chamber operated as a batch reactor. Aromatic hydrocarbon emissions are an important contribution ($\sim$ 20–30 %) to the total volatile organic compounds in the urban atmosphere (Calvert et al., 2002). *m*-Xylene SOA yields (ratio of mass concentration of SOA formed to mass concentration of parent hydrocarbon reacted) have been measured previously for initial *m*-xylene concentrations of 10 to 180 ppb and experimental durations up to 10 h (Ng et al., 2007; Song et al., 2007). SOA yields for low-NO_x conditions were found to be higher than those for high-NO_x conditions. In addition, Chhabra et al. (2010) and Qi et al. (2010) observed changes in SOA chemical composition for up to 16 h of oxidation, indicating the potential of aging of *m*-xylene SOA over longer timescales. For a long duration experiment, the initial *m*-xylene concentration can be chosen to produce a sufficient amount of SOA to sample for the duration of the experiment yet remaining close to atmospherically relevant loadings, typically 0.1–20 $\mu g\,m^{-3}$ (Shilling et al., 2009). In the present work, the total amount of SOA formed, its chemical composition, and the composition of the gas phase over 36 h of irradiation are evaluated to infer mechanisms of chemical aging of *m*-xylene SOA. For the first time, the effects of size-dependent particle composition on particle wall loss correction methods are discussed.

2 Materials and methods

2.1 Experimental setup

Experiments were conducted in the Caltech dual 28-m^3 Teflon chambers. Details of the facilities are given elsewhere (Cocker et al., 2001; Keywood et al., 2004). Before each experiment, the chambers were flushed with dried, purified air for > 24 h until the particle number concentration $< 50\,cm^{-3}$ and the volume concentration $< 0.1\,\mu m^3\,cm^{-3}$. Experiments were run under low-NO_x conditions using hydrogen peroxide (H_2O_2) as the OH source. With H_2O_2 it is possible to achieve a constant OH concentration for the duration of the experiments. H_2O_2 was injected into the chamber by evaporating 280 µl of 50 % wt aqueous solution into the chamber with $5\,l\,min^{-1}$ of purified air. Seed particles were injected by atomizing a 0.015 M aqueous ammonium sulfate (AS) solution for neutral seed and a 0.03 M aqueous magnesium sulfate with 0.03 M sulfuric acid (MS + SA) solution for acidic seed. *m*-Xylene (Sigma Aldrich, 99+ %) was introduced into the chamber by injecting the volume of the liquid hydrocarbon required to obtain a concentration of 30 ppb into a glass bulb, and the vapor was carried into the chamber with $5\,l\,min^{-1}$ of purified air. The chamber contents were allowed to mix for 1 h before beginning irradiation.

A suite of instruments was used to study the evolution of the gas and particle phases. *m*-Xylene was measured using a gas chromatograph with flame ionization detector (GC/FID, Agilent 6890N), equipped with a HP-5 column (15 m×0.53 mm ID × 1.5 µm thickness, Hewlett Packard). Reactive intermediates and H_2O_2 were continuously monitored using a custom-modified Varian 1200 triple-quadrupole chemical ionization mass spectrometer (CIMS). Details of operation can be found elsewhere (Crounse et al., 2006; Paulot et al., 2009; St. Clair et al., 2010). The CIMS was operated in negative mode in which CF_3O^- is used as the reagent ion. CF_3O^- clusters with the analyte, forming ions at *m/z* MW+85 ($R \cdot CF_3O^-$), or, with more acidic species, at *m/z* MW+19 ($HF \cdot R^-_{-H}$). Relative humidity (RH), temperature, NO, NO_x, and O_3 were continuously monitored. The RH of the chamber was $< 5\%$. The initial chamber temperature was $\sim 19\,^\circ C$; however, heating from the blacklights caused a rise in temperature of approximately $5\,^\circ C$. NO and NO_x concentrations were below the 2 ppb detection limit of the instrument, and initial O_3 concentration was 2 ppb.

Aerosol size distribution and number concentration were measured continuously using a differential mobility analyzer (DMA, TSI, 3081) coupled to a condensation particle counter (CPC, TSI, 3760), henceforth referred to as the DMA. Real-time particle mass spectra were collected continuously by an Aerodyne High Resolution Time-of-Flight Aerosol Mass Spectrometer (DeCarlo et al., 2006; Canagaratna et al., 2007), henceforth referred to as the AMS. The AMS switched once every minute between the high resolution "W-mode' and the lower resolution, higher sensitivity "V-mode". "V-mode" data were analyzed using a fragmentation table to separate sulfate, ammonium, and organic spectra and to time-trace specific *m/z* ratios. "V-mode" and "W-mode" data were analyzed using a separate high-resolution spectra toolbox known as PIKA to determine the chemical formulas contributing to distinct *m/z* ratios (DeCarlo et al., 2006). The signals of organic ions below *m/z* 119 were used to calculate elemental ratios. The ratio of particle-phase CO^+ to CO_2^+ was approximately equal to 1, and the contribution of CO^+ to the organic signal was estimated to equal that of particle-phase CO_2^+. The intensities of water-derived ions (H_2O^+, OH^+, and O^+) were estimated from particle-phase CO_2^+ using the correlation suggested by Aiken et al. (2008). A relative ionization intensity of 1.4 was applied to organic ion signals. AMS data reported in this work are averaged over 10-min intervals.

2.2 Aging experiment protocols

The volume of the reactor limits the duration of experiments in a chamber operated in batch mode; when sampling with all instruments, nearly half of the chamber volume is depleted in 18 h, at which point it is preferable to cease sampling due to deflation of the chamber. To achieve longer OH exposure times with all instruments sampling, sets of experiments were conducted with increasing duration and staggered instrument sampling. Instruments were grouped into two categories based upon their sampling schedule. Group I includes the AMS and a RH and temperature probe. Group II includes the DMA, the CIMS, the GC/FID, the O_3 analyzer, and the NO_x analyzer. All instruments were operated during initial injections before the onset of irradiation. Experimental time began at the onset of irradiation. First, two 18 h experiments were conducted with Group I and II instruments sampling for the entire duration to establish consistency in the gas and particle phases during separate experiments. Subsequent experiments of 24 h, 30 h, and 36 h were conducted to achieve longer OH exposure. The instrument sampling schedule for all experiments is given in Table 1. The entire set of 5 experiments was conducted in the same chamber to avoid any differences between chamber conditions that may arise between the dual chambers. For each of the Group II instruments, the data from all experiments were combined to track the evolution of species for the entire 36 h of OH exposure.

2.3 Total SOA formation

To determine the total SOA mass concentration in the chamber, ΔM_o, particle wall losses must be taken into account. The extent of interactions between particles deposited on the chamber walls and vapors in the chamber has not been determined completely; therefore, two limiting assumptions are used to bound this interaction. These limits have been described and applied to chamber experiments by Weitkamp et al. (2007) and Hildebrandt et al. (2009, 2011). In one

Table 1. Experiment sampling conditions and instrument sampling protocol.

Experiment Type	Duration (h)	Volume Removed (m^3)	Sampling hours Group I[a]	Group II[b]
Wall loss	23	6.14	N/A[c]	N/A
18 h aging	18	7.92	0–18	0–18
24 h aging	24	3.60	0–24	16–24
30 h aging	30	3.63	0–30	22–30
36 h aging	36	3.66	0–36	28–36

[a]Group I instruments: AMS, RH and temperature probe (total volumetric flow rate = 0.084 L min^{-1}).

[b]Group II instruments: DMA, CIMS, GC/FID, O_3 analyzer, NO_x analyzer (total volumetric flow rate = 7.25 L min^{-1}).

[c]Instruments sampling: DMA, O_3 analyzer, NO_x analyzer, RH and temperature probe (total volumetric flow rate = 4.45 L min^{-1}).

limit, particles deposited on the wall are assumed to cease interaction with suspended vapors after deposition. In this case, the amount of organic material in the deposited particles does not change after deposition, and these particles remain at the same size at which they deposited for the remainder of the experiment. In the other limit, particles on the wall are assumed to interact with vapors in the chamber after deposition as if they had remained suspended. Thus, in this case, the amount of organic material in the particles after deposition changes at the same rate as the amount of organic material in the suspended particles, and the deposited particles continue to change size throughout the remainder of the experiment. This limit is analogous in theory to that of a chamber without walls. In either limit, the material on the walls is added to that which remains suspended to obtain the total amount of SOA formed.

During particle growth, the organic mass fraction of the suspended particles increases. In the first limit, the organic mass fraction of deposited particles does not increase after deposition; therefore, this case produces a lower limit for ΔM_o. In the second limit, deposited particles are assumed to continue growing; therefore, this case is an upper limit for ΔM_o. These two limits of wall loss corrected ΔM_o will subsequently be referred to as the lower bound and upper bound, respectively.

The lower bound limit on ΔM_o is calculated from the DMA suspended particle number distribution. For each size bin i at each time step j, the particle number distribution deposited to the wall, $n_{w,ij}$, is calculated using size-dependent wall loss rates, β_i:

$$n_{,w,ij} = n_{s,ij} \exp(\beta_i \Delta t) \quad (1)$$

where $n_{s,ij}$ is the suspended particle number distribution in size bin i at time step j, and Δt is the difference between time step j and time step $j+1$. Wall loss rates were determined from calibration experiments performed prior to the start of the aging experiments (methods detailed in Keywood et al., 2004; Ng et al., 2007). The deposited particle number distribution is added to the suspended particle number distribution to give a wall-loss corrected number distribution, $n_{tot,ij}$, which is then converted to a volume concentration, $V_{tot,j}$, assuming spherical particles:

$$n_{tot,ij} = n_{s,ij} + n_{w,ij} \quad (2)$$

$$V_{tot,j} = \sum_{i=1}^{m} \frac{n_{tot,ij}}{D_{p,i} \ln 10} \times \left(D_{p,i+} - D_{p,i-}\right) \times \frac{\pi}{6} D_{p,i}^3 \quad (3)$$

where m is the total number of size bins, $D_{p,i+}$ is the upper limit diameter for size bin i, and $D_{p,i-}$ is the lower limit diameter for size bin i. A factor of ln10 is necessary to convert from a log normal distribution. The initial seed volume concentration, V_{seed}, is subtracted from the wall-loss corrected volume concentration to give the volume concentration of SOA, $V_{o,j}$. To convert to SOA mass, $\Delta M_{o,j}$, the SOA volume concentration is multiplied by the SOA density, ρ_{org}:

$$\Delta M_{o,j} = \rho_{org}\left(V_{o,j} - V_{seed}\right) \quad (4)$$

For low-NO_x *m*-xylene SOA, $\rho_{org} = 1.33$ g cm^{-3} (Ng et al., 2007). It is possible that ρ_{org} changes as particle age increases, but it was assumed to be constant for the present study, which is consistent with the findings of Qi et al. (2010).

Calculating the lower bound wall-loss corrected mass relies on having continuous number distributions, which were not available for the 24-h, 30-h, and 36-h experiments. To obtain a continuous number distribution, the number distributions for all experiments were combined. The DMA sampling schedule was designed to allow a 2-h overlap period between shorter and longer experiments (i.e. sampling for the 24-h experiment began at 16 h, 2 h prior to the endpoint of the 18-h experiment) to facilitate the comparison of data between shorter and longer experiments. The number distributions from each experiment were combined sequentially. During periods of overlap between two experiments, a weighted average of the number distribution in each size bin was taken giving higher weight to the shorter experiment at the beginning of the overlap period and higher weight to the longer experiment at the end of the overlap period.

Both the number distribution of the seed particles and the initial concentration of *m*-xylene affect the number distribution of the aerosol. In the 24-h experiment, the seed volume was lower than that for the other AS seed experiments (Table 2). Assuming that the SOA produced in this experiment was comparable to that in the other experiments, the suspended particle volume would be lower than that of the other AS seed experiments, and the number distribution would be too small to combine with those of the other AS experiments to obtain a continuous number distribution. Without the data from the 24-h experiment, no number distribution data were available between hours 18 and 22. Number distributions during those 4 h were calculated from the 18- and 30-h experiments by fitting an exponential function to the number

Table 2. Experimental conditions and results.

Seed	Duration (h)	Initial *m*-xylene (ppb)	Seed vol. ($\mu m^3\,cm^{-3}$)	Final *m*-xylene (ppb)	Final ΔM_o[a] ($\mu g\,m^{-3}$)
AS	18	32.2±0.7	11.1±0.3	2.46±0.66	21.9±1.7
AS	18	31.8±0.7	12.3±0.3	0.84±0.66	24.7±1.9
AS	24	29.2±0.7	9.10±0.2	< 0.5	N/A
AS	30	29.1±0.7	12.3±0.4	< 0.5	N/A
AS	36	28.7±0.7	13.1±0.2	< 0.5	N/A
AS	12+8[b]	25.0±0.6	10.5±0.3	2.1±0.6	20.0±1.0
MS + SA	18	32.9±0.7	10.5±0.4	1.94±0.66	22.5±1.8
MS + SA	18	32.4±0.7	10.8±0.4	1.15±0.66	21.7±1.7
MS + SA	24	32.5±0.7	10.6±0.3	< 0.5	N/A
MS + SA	30	29.6±0.7	10.6±0.3	< 0.5	N/A
MS + SA	36	30.0±0.7	10.8±0.4	< 0.5	N/A

[a] Lower bound limit

[b] 12.4 h irradiated + 8 h dark

distribution in each size bin during hours 16–18 of the 18-h experiment and hours 22–24 of the 30-h experiment and using the function to interpolate a number distribution at 4-min increments.

Throughout an experiment, the volume of the chamber decreases due to sampling, but the surface area of the walls remains the same. It is possible that the increasing surface-area-to-volume ratio will increase the particle wall loss rates. The duration of a typical wall loss experiment is 18–24 h, shorter than that of the longest aging experiments. The aging experiments were designed to minimize the amount of air sampled from the chamber. Although more instruments sample from the chamber during an aging experiment than during a wall loss calibration experiment, the volume of air removed during an aging experiment is comparable to that of a wall loss calibration experiment (Table 1).

To confirm that wall loss rates do not vary significantly as chamber volume decreases, an additional wall loss calibration experiment was performed in each chamber. These calibration experiments were conducted following the same protocols as a typical wall loss calibration; however, before AS seed aerosol was injected, approximately 8 m^3 of air was removed from the chambers to simulate conditions found at the end of an 18 h experiment. The wall loss rates determined from these low-volume experiments were within the range of wall loss rates observed in the chambers since they were installed in 2009 (Fig. 1). Therefore, time-dependence of the wall loss rate constants was assumed to be negligible during these aging experiments.

The upper bound limit on ΔM_o is calculated by combining the AMS and DMA data. The experiments in the present work use seed particles containing sulfate, and the only process that decreases sulfate concentration in the suspended phase is wall loss. The initial sulfate concentration is calculated from the DMA seed volume concentration. There

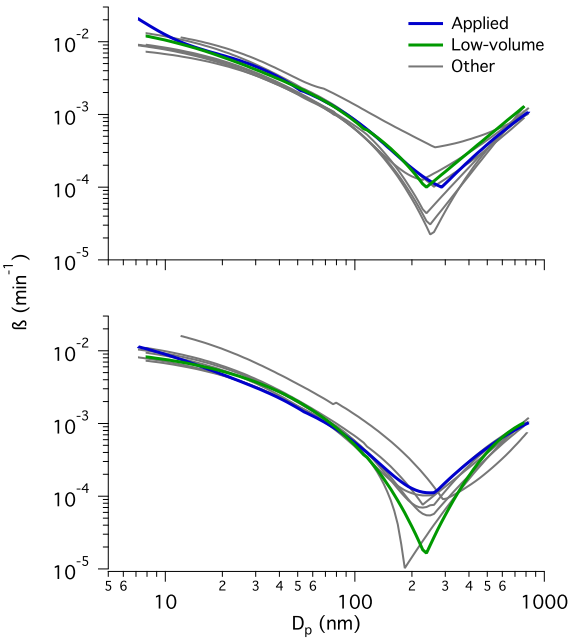

Fig. 1. Particle wall loss rates, β, measured in both chambers from September 2009 to August 2011. The top panel corresponds to near chamber, and the bottom panel corresponds to far chamber. The wall loss rates labeled "applied" were applied to the experiments reported in this manuscript. The wall loss rates labeled "low-volume" were calculated during a wall loss calibration experiment in which the initial chamber volume was decreased by 8 m^3 to simulate conditions achieved after 18 h of sampling. The wall loss rates labeled "other" are those calculated from quarterly calibration experiments.

is more uncertainty for the collection efficiency of seed particles in the AMS than in the DMA. Collection efficiency in the AMS increases as organic content of the particles increases, and because the seed particles do not contain organic material, they are more susceptible to bounce in the instrument and have a collection efficiency that is less than unity (Matthew et al., 2008). To calculate the mass of sulfate in the seed, m_{SO_4}, the following equation is used:

$$m_{SO_4} = V_{seed}\rho_{seed}\frac{MW_{SO_4}}{MW_{seed}} \quad (5)$$

where ρ_{seed} is the density of the seed particles, MW_{SO_4} is the molecular weight of sulfate, and MW_{seed} is the molecular weight of the seed particles. For dry AS seed, ρ_{seed} is $1.77\,g\,cm^{-3}$. In the upper bound limit, both suspended and deposited particles gain or lose organic material at the same rate; therefore, the organic-to-sulfate ratio of all particles of the same size is the same, and this ratio is determined from unit mass resolution AMS data. High-resolution analysis of the dominant sulfate ions, *m/z* 48 and 64, showed less than 1 % contribution of organic signal to the total ion signal; therefore, organic contribution to the unit mass resolution sulfate signal was negligible. Differences in the organic-to-sulfate ratio, r_{OS}, between unit mass resolution and high resolution data are less than 5 %, except during the first 2 h of growth when they are more variable at lower organic loading. To obtain the SOA mass, r_{OS} is multiplied by the initial mass of sulfate in the seed particles:

$$\Delta M_o = m_{SO_4} r_{OS} \quad (6)$$

This equation is valid if the organic-to-sulfate ratio does not vary with particle size or if particle wall loss rates are constant over the particle size range of interest. In the Caltech chambers, particle wall loss rates depend on particle size so the latter assumption is not valid. Depending on the condensation behavior of the SOA, r_{OS} may depend on particle size (Hildebrandt et al., 2009; Riipinen et al., 2011). For the present experiments, data were not available to determine the size dependence of r_{OS} of the particles. For the purpose of calculating the upper bound wall loss corrected organic mass, it is assumed that r_{OS} does not vary with particle size. The implications of this assumption will be discussed in Sect. 3.4.

3 Results and discussion

3.1 SOA formation

Two experiments with the same initial conditions and 18 h of irradiation were performed to assess the reproducibility of initial conditions and SOA production (Table 2). For both AS seed and MS + SA seed, similar concentrations of *m*-xylene reacted and ΔM_o formed after 18 h of irradiation were achieved. Given the consistency between matched experiments, it was not necessary to sample for the entire duration of longer experiments. It was assumed that data collected during previous, shorter experiments are adequate to describe the same time period during longer experiments.

Figure 2 shows decay of *m*-xylene and ΔM_o corrected for wall loss for both the upper and lower bound cases over 36 h of irradiation. The lower bound ΔM_o and *m*-xylene data are a compilation of the 18-, 30-, and 36-h AS seed experiments (the 24-h experiment was omitted as noted earlier due to low seed particle volume), but the upper bound ΔM_o data are from only the 36-h experiment because continuous data were available. The variation in the lower bound wall loss corrected mass concentration after peak growth is likely due to differences in number distributions during the 18-, 30-, and 36-h experiments. The peak in SOA formation occurs before all of the *m*-xylene has been reacted. For the lower bound case, ΔM_o remains relatively stable after its peak, decreasing only slightly over 20 h of irradiation. For the upper bound case, ΔM_o peaks at approximately the same time as in the lower bound case; however, there is a pronounced decay of ΔM_o after the maximum is reached. Wall losses result in 43% of the total volume concentration of particles deposited on the wall for the lower bound case and 56 % of ΔM_o deposited on the wall for the upper bound case after 36 h. The behavior of ΔM_o after peak growth will be discussed in Sect. 3.3.

Throughout each experiment, the OH concentration was approximately 2.5×10^6 molec cm^{-3}, as estimated from the decay of *m*-xylene and simulated by a photochemical model (see Appendix A). After 36 h of irradiation, 40 % of the initial 4 ppm of H_2O_2 injected into the chamber remained unreacted.

3.2 SOA composition

Figure 3 shows the evolution in the elemental oxygen-to-carbon ratio (O:C) of the suspended particles for all 5 of the AS seeded experiments. O:C values overlap for all of the experiments with different irradiation durations. O:C decreases during the first 5 h of irradiation in all but the 36-h experiment. During the 36-h experiment, the sensitivity of the AMS sampling in W-mode was lower than that in the other aging experiments, which hindered the detection of initially-formed SOA. The O:C calculated using V-mode data (not shown) decreasess during the first 5 h of irradiation for all 5 of the aging experiments. The dominant trend in O:C begins after 5 h. After this time, O:C gradually increases at an average rate of 0.0019 h^{-1} for the remainder of the irradiation period. The minimum in O:C occurs before the maximum ΔM_o is reached.

The mass spectral parameter f_{44} is commonly used to characterize SOA chemical composition. Aiken et al. (2008) determined a relationship between O:C and f_{44} for ambient aerosol in Mexico City: $O:C = (3.82 \pm 0.05) \times f_{44} + (0.0794 \pm 0.0070)$ for f_{44} ranging from 0 to 0.25. The SOA in the current set of experiments does not follow the same

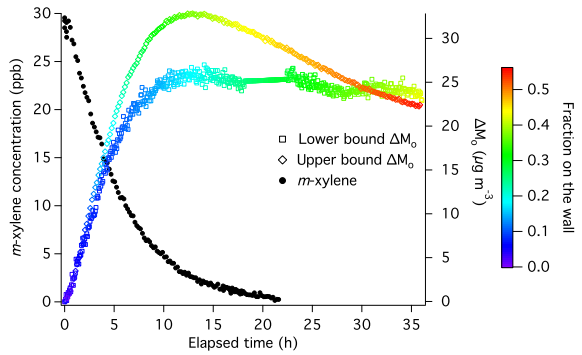

Fig. 2. SOA mass (right axis), corrected for particle wall losses, and *m*-xylene (left axis) for 36 h of OH exposure using AS seed. The lower bound ΔM_o is calculated assuming that, once deposited, particles on the walls do not interact with gases in the chamber. The upper bound ΔM_o assumes that, once deposited, particles continue to exhibit the same gas-particle partitioning behavior as suspended particles. The fraction on the wall for the lower bound is the ratio of particle volume on the wall to total particle volume, both suspended and deposited, and includes seed volume. The fraction on the wall for the upper bound is the ratio of organic mass concentration on the wall to the total organic mass concentration.

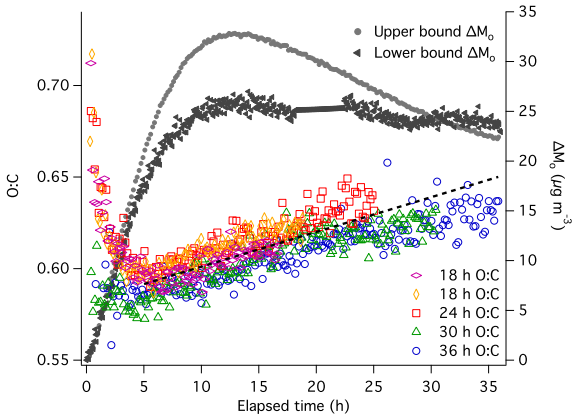

Fig. 3. SOA mass (right axis) and O:C elemental composition (left axis) over 36 h of OH exposure using AS seed. After hour 5, the O:C increases at an average rate of 0.0019 h^{-1} (dashed line).

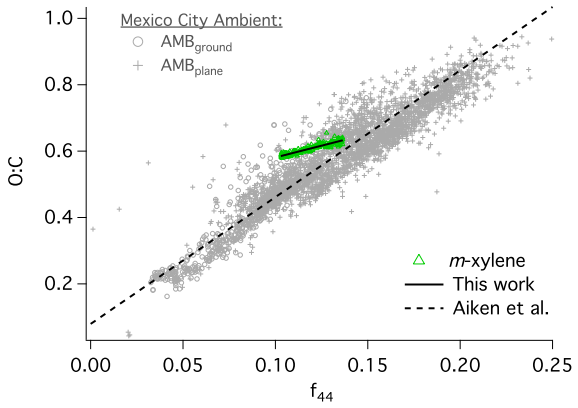

Fig. 4. Correlation of O:C with f_{44} for SOA from *m*-xylene in the present study and Mexico City ambient aerosol from Aiken et al. (2008).

trend as the Mexico City SOA, and exhibits trendline of $O:C = (1.42 \pm 0.04) \times f_{44} + (0.439 \pm 0.005)$ over a range of 0.10 to 0.14 of f_{44}. Although the data for *m*-xylene SOA do not follow the same trendline as the Mexico City data, they lie within the scatter of the Mexico City data (Fig. 4). Using the same AMS instrument as the current study, Chhabra et al. (2010) found that the O:C and f_{44} of SOA from aromatics, isoprene, and glyoxal did not lie along the trendline reported in Aiken et al., but the O:C and f_{44} of SOA from α-pinene and naphthalene did. In general, if CO_2^+ contributed most of the oxygen signal in the spectra, then the O:C and f_{44} of the SOA more closely matched those predicted by the trendline from the Mexico City data. The correlation between O:C and f_{44} for *m*-xylene SOA in the present work differs from that of Lambe et al. (2011), who observed that *m*-xylene SOA follows the same trendline as the Mexico City data. The range of f_{44} values observed by Lambe et al. is much larger than that in the present work, initial hydrocarbon loadings are higher, and OH exposure is 2–3 times greater than the maximum OH exposure achieved in the present work (3.2×10^{11} molec cm^{-3} s). Any of these factors could contribute to the different correlations between O:C and f_{44}. The factor most likely to explain the discrepancy between the correlation in the present work and that in Lambe et al. is the difference in OH exposure. At higher OH exposure, the SOA is likely to be more oxidized, and CO_2^+ is likely to be a major contributor to the oxygen signal in the spectra.

The evolution of *m*-xylene SOA is also represented in f_{44}–f_{43} space (Fig. 5). The change in O:C, derived from the correlation specific to *m*-xylene, is also shown. The marker size is a function of the concentration of suspended organics, normalized to suspended sulfate concentration to account for wall losses. Overall, low-NO_x *m*-xylene SOA exhibits higher f_{43} than the typical range of ambient SOA observed by Ng et al. (2010) and lies to the right of the triangular region derived for ambient SOA. At the beginning of irradiation when the organic mass loading is small, the SOA has a higher f_{44} and a lower f_{43}. As SOA continues to form, f_{44} decreases and f_{43} increases until approximately 5 h of irradiation, at which time the trends reverse. For the remaining duration of irradiation, f_{44} increases and f_{43} decreases, resulting in a progression of the SOA characteristic of the behavior of

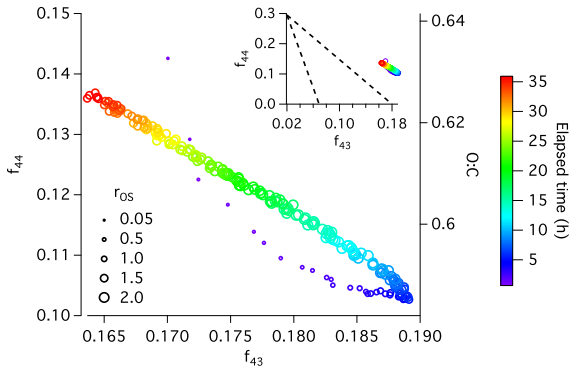

Fig. 5. Evolution of f_{43}, f_{44}, and O:C for 36 h of OH exposure. This system lies to the right of the triangular region in which typical ambient aerosol resides, as shown by the dashed lines in the inset (Ng et al., 2010). Marker size denotes the organic-to-sulfate ratio, r_{OS}, of suspended particles.

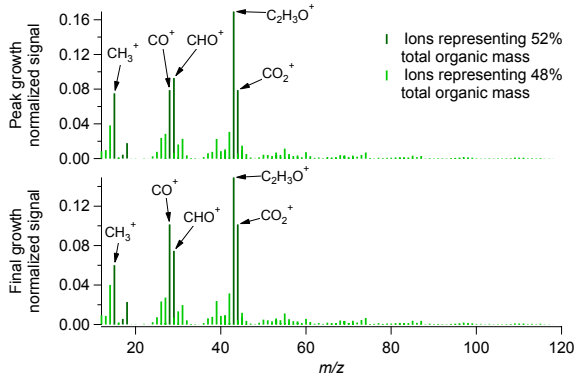

Fig. 6. Average AMS high-resolution organic mass spectra at the time of peak growth and at the end of the experiment (final growth) for the 36-h aging experiment. Prominent peaks are identified. The mass of CO^+ is estimated to equal that of CO_2^+.

more-aged ambient SOA. The time at which the path reversal in f_{44}–f_{43} space occurs is the same as that at which the minimum in O:C occurs. Curvature in f_{44}–f_{43} space has been observed in other studies (Kroll et al., 2009; Ng et al., 2010; Chhabra et al., 2011; Lee et al., 2011; Lambe et al., 2011). Lambe et al. did not observe curvature in f_{44}–f_{43} space for *m*-xylene SOA, and the curvature observed in the present study occurred for lower OH exposures than the lowest value attained by Lambe et al.. It is possible that the OH exposure levels used to form *m*-xylene SOA in Lambe et al. were too large to observe the curvature.

The high-resolution AMS mass spectra provide clues to the trends in O:C, f_{44}, and f_{43}. The average mass spectra at peak organic growth and at the end of the 36-h aging experiment are shown in Fig. 6. Figure 7 shows the time trends

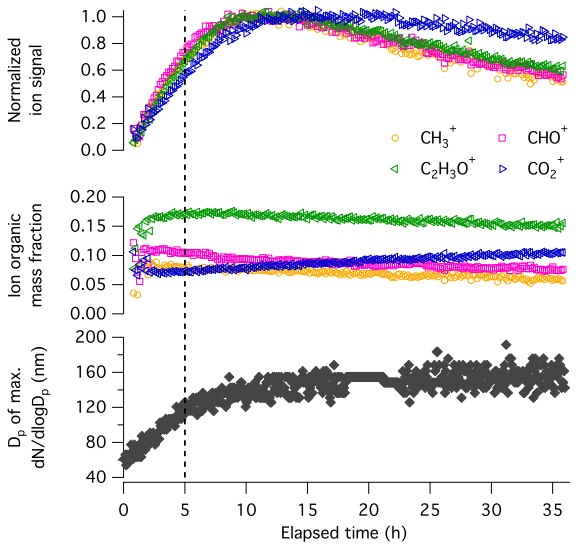

Fig. 7. Evolution of SOA chemical composition from high-resolution AMS measurements and diameter of the maximum number distribution of suspended particles. In the top panel, the ion signal is normalized by sulfate to account for particle wall losses. The sulfate-normalized ion signal is then scaled by the average value at the peak concentration. The middle panel shows the fractional contribution of each ion to the total organic mass signal. A relative ionization efficiency of 1.4 is used when calculating the organic ion concentration. The dashed line at 5 h corresponds to the reversal in trend of O:C.

of the 4 dominant organic ions (CH_3^+, CHO^+, $C_2H_3O^+$, and CO_2^+) in the aerosol mass spectra and the maximum of the suspended particle size distribution throughout 36 h of oxidation. Excluding CO_2^+, these ions account for 30–35 % of the total organic signal throughout the experiment. When organic CO_2^+ and the ions whose organic contributions are assumed to correlate with it (CO^+, H_2O^+, OH^+, and O^+) are included, the mass fraction of the organic signal is approximately 52 %. In the top panel of Fig. 7, the time trends of the normalized, wall-loss corrected ion signals are shown. To obtain this, the ion signal was divided by the sulfate signal to correct for wall losses. The sulfate-normalized ion signal was then scaled by its average value at the peak concentration. In the middle panel, the fractional contribution of each ion to the total organic signal is shown. The bottom panel shows the particle diameter (D_p) of the maximum of the suspended particle size distribution. The most rapid change in D_p occurs during the first 5 h of irradiation. The amount of each of the 4 ions in the particles increases during this time (top panel). After 5 h, D_p changes more slowly, and the contribution of each ion to the spectra begins to peak. CHO^+ reaches a maximum most quickly, followed by CH_3^+ and $C_2H_3O^+$. CO_2^+ peaks later than the other ions. After most of the ions peak, their contribution to the spectra decreases for the remainder

of the experiment; however, the amount of CO_2^+ shows much less of a decrease, suggesting that compounds that contribute to the CO_2^+ signal have a lower tendency to be removed from the particles than those that contribute to the other ion signals.

Shortly after the onset of irradiation, CO_2^+ constitutes the largest fraction of the organic signal, likely from the condensation of low-volatility organics. As irradiation continues, the CO_2^+ fraction of the organic signal decreases as semivolatile material represented by the other ions, especially $C_2H_3O^+$, begins to partition to the particles. Once the rate of particle growth slows, the fraction of CO_2^+ increases because the contribution of CO_2^+ to the mass spectra is still increasing, whereas the amounts of the other ions are beginning to stabilize and then decrease. The increase in the organic fraction of CO_2^+ continues throughout the duration of the experiment caused by a larger decrease in the amounts of the other ions in the particle mass spectra than CO_2^+.

3.3 Fate of SOA after peak growth

After peak growth, a decrease in most of the major organic ions and the total organic mass is observed (Figs. 2 and 7). The magnitude of the decrease in ΔM_o is much greater for the upper bound wall loss correction than that for the lower bound wall loss correction, suggesting that either the process causing the decrease in ΔM_o has a larger effect on the upper bound wall loss case or that an incorrect assumption was made for one of the wall loss corrections. For the upper bound wall loss correction, r_{OS} was assumed to be constant such that the r_{OS} of the suspended particles was equivalent to that of the deposited particles. If this is not the case, the mass lost to the walls may be over- or underestimated. Implications of the size-dependence of r_{OS} on the upper and lower bound wall loss correction and its effects on the conclusions of the present section will be discussed in Sect. 3.4.

If the organic mass lost to the wall was correctly calculated for both upper and lower bound cases, a possible explanation for the decrease in ΔM_o after peak growth is repartitioning of semivolatiles to the gas phase. As irradiation continues, semivolatiles in the gas phase can undergo reaction with OH or photolysis to form higher-volatility products, or they may be lost to the walls. As the concentration of a semivolatile in the gas phase decreases from fragmentation reactions or wall loss, repartitioning can occur to maintain gas-particle equilibrium. OH can also react with the particle surface, forming higher volatility fragmentation products that evaporate and decrease the particle organic mass. These processes are summarized in Fig. 8. Evaporation of semivolatiles is expected to have a greater effect on ΔM_o in the upper bound limit because all particles are assumed to undergo gas-particle partitioning, opposed to only the suspended particles in the lower bound limit, thus a higher decrease in ΔM_o should be expected in the upper bound limit.

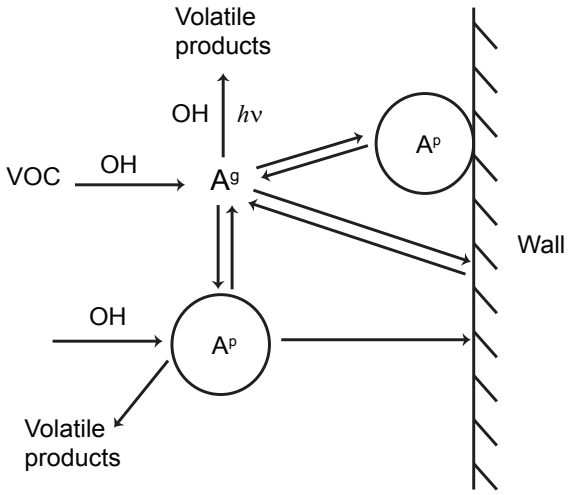

Fig. 8. Sources and sinks of a semivolatile gas-phase species, A^g, and particles containing the condensed semivolatile species, A^p, during SOA aging. We do not explicitly indicate in the sketch processes by which the particle-phase A^p attains a semisolid state, greatly affecting continued exchange with the gas phase (Virtanen et al., 2010; Vaden et al., 2010, 2011; Shiraiwa et al., 2011).

Semivolatile species are expected to repartition from the particle phase more easily than low volatility species. This behavior is observed with the organic ions $C_2H_3O^+$, characteristic of semivolatile oxygenated organic aerosol (SV-OOA), and CO_2^+, characteristic of low volatility oxygenated organic aerosol (LV-OOA). The amount of $C_2H_3O^+$ in the particle mass spectra increases faster than CO_2^+ and shows a much greater decrease than CO_2^+ as the experiment progresses. There is a slight decrease in CO_2^+ at longer irradiation times, and it is possible that the uptake of low volatility species is not completely irreversible, allowing for some evaporation.

Evaporation of particles is characterized by a shift of the D_p at the maximum of the size distribution to smaller size. This shift was not observed in the aging experiments, as shown in the bottom panel of Fig. 7 where D_p increased slightly after the peak organic loading was attained around 12 h. The two main processes affecting the particle size distribution in chamber experiments are gas-particle partitioning and wall loss. In the Caltech chambers, wall loss rates are at a minimum for particles of diameters between 200 and 300 nm (Fig. 1). During the aging experiments, the D_p at the size distribution maximum is below the 200–300 nm minimum in wall loss. If evaporation is occurring, the rate of wall loss will increase as particles get smaller. As a result, the greater loss of small particles will cause size distribution, characterized by the D_p at its maximum, to shift slightly toward the 200–300 nm minimum in wall loss rate. Both the evaporation and wall loss processes are slow; therefore, the

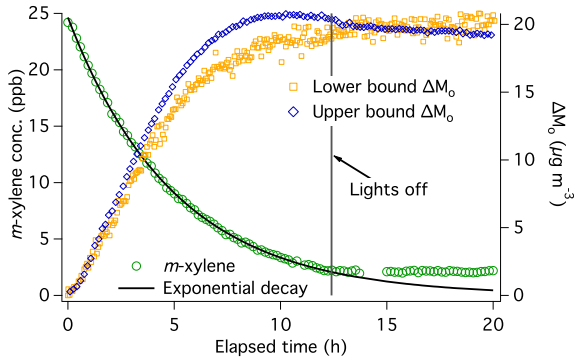

Fig. 9. Trends in *m*-xylene concentration (left axis) and ΔM_o (right axis) when irradiation is stopped once peak ΔM_o is attained.

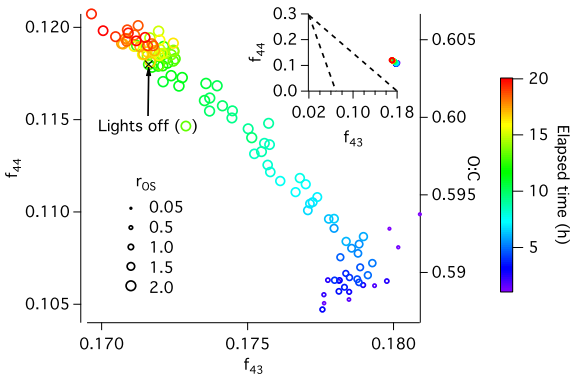

Fig. 10. Evolution of f_{43}, f_{44}, and O:C of *m*-xylene SOA. Irradiation was stopped after 12.4 h, corresponding to the peak of ΔM_o. This point is denoted by the "x". Marker size denotes the organic-to-sulfate ratio, r_{OS}, of suspended particles. After irradiation stops, the chemical composition of the SOA does not change significantly. The inset shows the position of the data with respect to the triangular region characteristic of ambient SOA bounded by the dashed lines, as defined by Ng et al. (2010).

two processes will tend to counteract each other with respect to their effects on the dynamics of the aerosol size distribution, and no change in D_p at the maximum of the size distribution is observed. It is also possible that the upper bound wall loss correction over-predicts the amount of evaporation occurring (see Sect. 3.4). In this case, the D_p at the size distribution maximum would only be expected to increase slightly toward the 200–300 nm minimum in wall loss rate.

To determine the extent to which photochemical processes are affecting the aerosol after peak growth, an experiment was performed in which the lights were turned off after 12.4 h of irradiation (Fig. 9). Production of OH ceases, and shortly thereafter, OH is no longer present in the chambers. The *m*-xylene concentration stabilizes after lights are turned off, and the substantial decrease in the upper bound ΔM_o is not observed with the lights off. The lower bound ΔM_o increases after lights are turned off to result in a 5 % change in mass after 8 h. This increase could be the result of uncertainty induced by the wall loss correction or condensation of vapors as the chamber cooled after irradiation stopped from 24 °C to 19 °C during hours 12.4 to 16. The latter process is not observed in the upper bound ΔM_o, but condensation could be masked by uncertainty in the wall loss correction method, discussed in Sect. 3.4. Despite the potential uncertainties of the wall loss correction and the cooling of the chamber, the decrease observed in the lower bound ΔM_o in the 36-h aging experiment is not observed after irradiation ceases. After the lights are turned off, the chemical composition of the particles also stops changing significantly. This is shown in f_{44}–f_{43} space in Fig. 10. While the aerosol forms, f_{43} decreases and f_{44} increases; however, after the lights are turned off, the rates of change of both f_{43} and f_{44} decrease substantially. In the absence of irradiation, a semivolatile species in the gas phase, A^g, can partition to and from particles or be lost to the walls (Fig. 8). After irradiation stops, the rate of change in the amount and composition of the particles decreases substantially; therefore, no significant repartitioning is occurring. Under these conditions, only vapor phase wall loss is expected to cause repartitioning; therefore, vapor phase wall loss is not significant in this system. If minimal repartitioning is observed without irradiation, and if there are no substantial vapor phase wall losses, then repartitioning must be driven by photochemical processes that affect the chemical composition of the gases and SOA.

It was not possible to distinguish among the photochemical process occurring: reaction of OH with semivolatiles; reaction of OH with particles; and photolysis of semivolatiles. The photochemical model described in Appendix A was used to estimate lifetimes for OH against reaction with particles, OH against reaction with semivolatiles, semivolatiles against reaction with OH, and semivolatiles against photolysis. The lifetime of OH against reaction with gas-phase species A^g, τ_{OH+A} (s), is

$$\tau_{OH+A} = \frac{1}{k_{A+OH} c_A} \quad (7)$$

where k_{A+OH} (cm^3 molec^{-1} s^{-1}) is the reaction rate constant and c_A (molec cm^{-3}) is the gas-phase concentration of A. Using the combined concentrations of species ROOH, ROHOH, ROHOOH, and EPOXOOH and an average rate constant $k_{OH} = 1 \times 10^{-10}$ cm^3 molec^{-1} s^{-1} (Table 3), $\tau_{OH+A} \cong 0.2$ s. The heterogeneous reaction of OH with a particle surface is assumed to be pseudo-first order in terms of OH (Seinfeld and Pandis, 2006). The characteristic time for this process, τ_{OH+P} (s), can be calculated by:

$$\tau_{OH+P} = \frac{1}{\frac{1}{4}\gamma \overline{c_{OH}} A_p} \quad (8)$$

Table 3. Rate constants for the photochemical model.

Rate constant ($cm^3\,molec^{-1}\,s^{-1}$)	Source
$j_{H_2O_2} = 2.9\times10^{-6}$ (s^{-1})	Sander et al. (2011)
$k_1 = 1.8\times10^{-12}$	Sander et al. (2011)
$k_2 = 2.31\times10^{-11}$	Calvert et al. (2002)
$k_3 = 9.8\times10^{-13}$	Birdsall et al. (2010)
$k_4 = 1.96\times10^{-11}$	MCM (Jenkin et al., 2003, Bloss et al., 2005)
$k_5 = 8.02\times10^{-11}$	MCM
$j_{EPOX} = 1.24\times10^{-4}$ (s^{-1})	MCM and Sander et al. (2011)
$k_6 = 9.1\times10^{-11}$	MCM
$k_7 = 1.17\times10^{-10}$	MCM
$j_{ROOH} = 2.1\times10^{-6}$ (s^{-1})	Sander et al. (2011)
$k_8 = 1.96\times10^{-11}$	MCM
$k_9 = 7.41\times10^{-11}$	MCM
$k_{10} = 1.96\times10^{-11}$	MCM
$k_{11} = 1.13\times10^{-10}$	MCM
$k_{12} = 2.05\times10^{-10}$	MCM
$k_{13} = 1.4\times10^{-12}$	Sander et al. (2011)
$k_{14} = 1.1\times10^{-10}$	Sander et al. (2011)

where γ is an uptake coefficient, here assumed to be 1, A_p ($cm^2\,cm^{-3}$) is the surface area concentration of the particles, and $\overline{c_{OH}}$ ($cm\,s^{-1}$) is given by

$$\overline{c_{OH}} = \left(\frac{8RT}{\pi MW_{OH}}\right)^{\frac{1}{2}} \quad (9)$$

where T (K) is temperature and MW_{OH} ($kg\,mol^{-1}$) is the molecular weight of OH. The particle surface area was calculated from measured particle number distributions. Based on the upper and lower bound wall loss corrections, τ_{OH+P} ranges from 6–13.5 s, corresponding to particle surface areas of $(0.47-1.1)\times10^{-5}\,cm^2\,cm^{-3}$.

Some of the semivolatile species used to determine τ_{OH+A} can also photolyze. The lifetimes of these species, ROOH, ROHOOH, and EPOXOOH, against OH reaction and photolysis was also calculated to determine if photolysis is expected to be a large sink of gas-phase species. The lifetime of these species against reaction with OH, τ_{A+OH} (s), is

$$\tau_{A+OH} = \frac{1}{k_{A+OH}c_{OH}} \quad (10)$$

where c_{OH} ($molec\,cm^{-3}$) is the OH concentration, which was estimated to be 2.5×10^6 $molec\,cm^{-3}$ from the measured *m*-xylene decay. Under this condition, $\tau_{A+OH} = 4.0\times10^4$ s. The lifetime of these species against photolysis, $\tau_{A+h\nu}$, is calculated by:

$$\tau_{A+h\nu} = \frac{1}{j_{ROOH}} \quad (11)$$

where j_{ROOH} is the photolysis rate constant of an organic peroxide, as described in Appendix A. The characteristic lifetime against photolysis is estimated as 4.7×10^5 s. Photolysis is an order of magnitude slower than reaction with OH, and photolysis is not expected to be a major sink of gas-phase species. Changes in particle composition are likely driven by continued oxidation of the gas phase, although OH reaction with particle surfaces cannot be categorically dismissed.

The continued oxidation of semivolatile species is apparent upon examination of possible gas-phase *m*-xylene oxidation products using the CIMS (Fig. 11). The top panel shows the time trace of *m/z* 207, which has the same *m/z* as the predicted reagent ion clustering of first-generation oxidation products ROH (MW+85) and ROOH (MW+19) in the model (Table 4). This *m/z* signal increases rapidly and peaks at 3–4 h of irradiation. When lights are turned off during the experiment, the decay slows significantly. The middle panel shows the time trace of *m/z* 223, which has the same *m/z* as the predicted reagent ion clustering of second-generation oxidation products ROHOH (MW+85), ROHOOH (MW+19), and EPOXOOH (MW+19). Again, this *m/z* signal increases rapidly and peaks slightly later at 4–5 h irradiation. When the lights are turned off, the signal stabilizes. The photochemical model predicts the peak of the first generation product concentrations to occur about an hour before that of the second generation product concentrations, and the time difference between the peak of the CIMS signals at *m/z* 207 and *m/z* 223 is consistent with the model output. The bottom panel shows the time trace of *m/z* 271, which has the same *m/z* as the predicted reagent ion clustering of third-generation oxidation product (MW+85) formed by the EPOXOOH + OH reaction ($prod_{EPOXOOH+OH}$ in the model). From model predictions, this compound with predicted reagent ion clustering at *m/z* 271 should form more slowly. The signal at *m/z* 271 peaks at 13–14 h of irradiation and does not decrease after irradiation ceases. The behavior of these signals is consistent with multiple generations of oxidation. The changes are clearly photochemically driven. Vapor-phase wall loss is not a significant sink of compounds contributing to these signals, indicated by the absence of decay after the lights are turned off.

3.4 Role of organic-to-sulfate ratio in particle wall loss corrections

The partitioning behavior of SOA precursors affects how these species condense onto a particle size distribution (Riipinen et al., 2011). If condensation is limited by diffusion, which is typically the case for essentially non-volatile compounds, the rate of condensation depends on the surface area of the particle size distribution (Seinfeld and Pandis, 2006); in that case the organic growth tends to occur on particles with smaller D_p as this is the particle size regime where the surface area is greatest. For organics exhibiting diffusion-limited behavior, organic condensation on AS seed particles

Table 4. Compounds represented in the photochemical model.

Compound	Structure	Formula
RH		C_8H_{12}
RO_2		$C_8H_{11}O_5$
EPOX	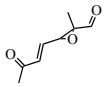	$C_8H_{10}O_3$
ROH		$C_8H_{10}O$
ROOH	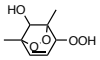	$C_8H_{12}O_5$
$EPOXO_2$	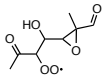	$C_8H_{11}O_6$
$ROHO_2$		$C_8H_{11}O_6$
ROHOH		$C_8H_{10}O_2$
RO		C_8H_9O
EPOXOOH	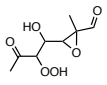	$C_8H_{12}O_6$
ROHOOH		$C_8H_{12}O_6$
$prod_{EPOXOOH+OH}$	e.g. 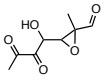	$C_8H_{12}O_5$

tends to form organic and sulfate mass distributions such that mean D_p of the organic mass distribution is smaller than that of the sulfate distribution. If condensation is controlled by gas-particle partitioning equilibrium, which is typically the case for semi-volatile compounds, these species will tend to condense preferentially into the particle size range where the mass concentration is greatest, i.e. a majority of the organic growth will occur on particles with larger D_p (Zhang et al., 2011). In this case, the organic mass distribution will peak at a larger D_p than the sulfate mass distribution. Because information about the organic and sulfate mass distributions was not available for the present experiments, a simulation was performed to assess the effects of different shapes of organic and sulfate mass distributions on the upper bound wall loss correction method.

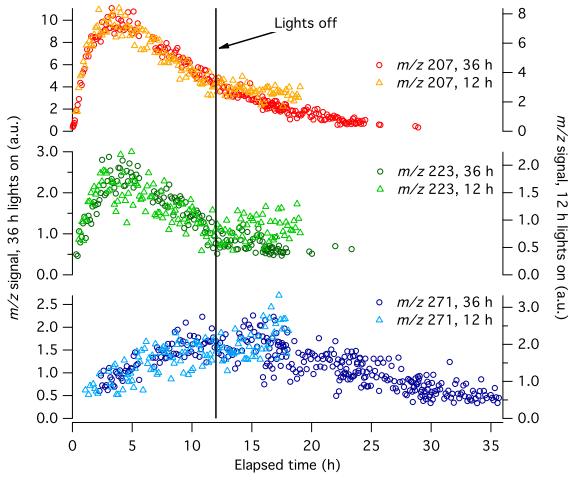

Fig. 11. Time evolution of products formed during *m*-xylene oxidation detected by the CIMS. The signals labeled 36 h were recorded during the set of experiments in which the chamber contents were irradiated for 36 h. The signals labeled 12 h were recorded during the experiment in which the lights were turned off after 12.4 h of irradiation and remained off for the remainder of the experiment.

Three different pairs of organic and sulfate mass distributions consistent with the measured number distribution and r_{OS} were created from the suspended particle number distribution averaged between hours 12 and 12.5 of irradiation from the combined 36 h aging experiment in order to determine the uncertainty in the upper bound wall loss correction induced by size-dependent r_{OS} (Fig. 12). The peak of the measured aerosol number distribution occurs at a D_p smaller than that at which the wall loss rate is at its minimum, and the wall loss rate increases moving from lower D_p to higher D_p across the measured number distribution (not shown). Each of the distributions in Fig. 12 is characterized by the same total particle number distribution, an r_{OS} of 2.00, and an organic mass concentration of 22.7–22.8 $\mu g\,m^{-3}$. Case I represents condensation resulting from equilibrium gas-particle partitioning, and Case III represents condensation resulting from diffusion-limited growth. In Case II all particles have the same r_{OS}.

The aerosol size distribution was subjected to 24 h of wall loss at the rates applied to the experimental number distributions, ignoring condensation (growth and evaporation are assumed to cease) and coagulation. For each of the cases, r_{OS} of the suspended particles and the upper bound wall-loss corrected mass concentration were calculated as a function of time (Fig. 13). In Case I, r_{OS} of suspended particles increased by about 10 % over 24 h as particles with a lower r_{OS} were preferentially lost to the walls. Because r_{OS} of suspended particles is higher than that of deposited particles, using r_{OS} of suspended particles to represent deposited

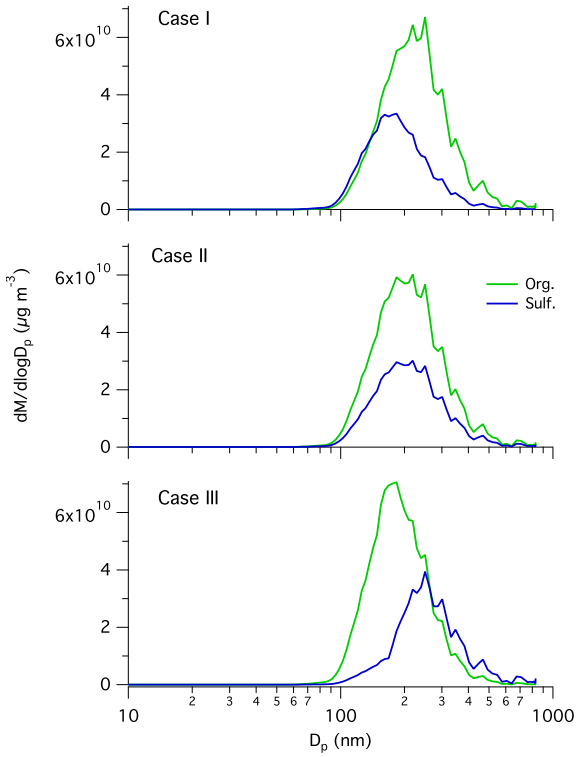

Fig. 12. Organic and sulfate mass distributions used in a simulation to assess the effect of size-dependent r_{OS} on the upper bound organic mass wall loss correction. All mass distributions are derived from the same observed particle number distribution and have r_{OS} of 2.00 and an organic mass concentration of 22.7–22.8 µg m^{-3}. Case I is representative of condensation governed by gas-particle equilibrium partitioning (see text), and Case III is representative of condensation governed by diffusion-limited growth (see text). In Case II, r_{OS} is constant for all D_p.

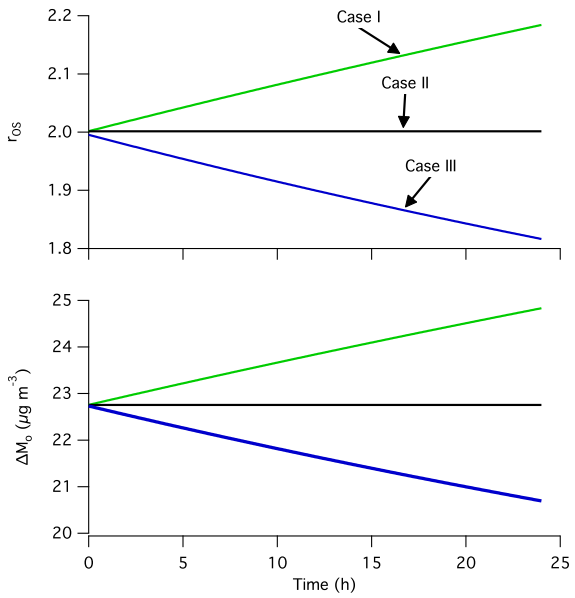

Fig. 13. Effect of 24 h of wall loss on the mass distributions in Fig. 12. The top panel shows the suspended particle organic-to-sulfate ratio, r_{OS}, as a function of time for each case, and the bottom panel shows the upper bound wall-loss corrected organic mass concentration as a function of time for each case.

particles leads to an overestimation of organic mass lost to the walls. The over-prediction of wall-loss corrected organic mass concentration is about 10 %. In Case II, r_{OS} of suspended and deposited particles are the same by definition, and the predicted wall-loss corrected organic mass was estimated properly. In Case III r_{OS} of deposited particles is greater than that of suspended particles, and r_{OS} of suspended particles decreased by about 10 % over 24 h because particles with a higher r_{OS} were preferentially lost to the walls. This resulted in an under-prediction of wall-loss corrected organic mass concentration by about 10 %.

Organic and sulfate mass distributions have been reported for toluene SOA condensed onto AS seed and are indicative of diffusion-limited condensation (Hildebrandt et al., 2009). If *m*-xylene SOA formation occurs by processes similar to those of toluene, the mass distributions during the present experiments will most closely resemble Case III, and increasing under-prediction of the upper bound wall-loss corrected organic mass concentration may occur with time. During the 36 h combined aging experiments, the measured r_{OS} of suspended particles decreased from 2.1 to 1.9 between hours 12.4 and 20 and continued to decrease linearly to 1.4 at 36 h. Between hours 12.4 and 20, the wall-loss corrected organic mass concentration decreased from 32.8 to 30 µg m^{-3}. By hour 36, it had decreased to 22.3 µg m^{-3}. The changes in r_{OS} and mass loss can be compared to those in the experiment in which irradiation ceased after 12 h and in which only particle wall loss occurred after that time. Between hours 12.4 and 20, r_{OS} decreased from 1.50 to 1.42, and the wall-loss corrected mass concentration decreased from 20.5 to 19.2 µg m^{-3}. The decrease in both organic-to-sulfate ratio and wall-loss corrected mass concentration in the 12-h irradiation experiment are indicative of wall loss of an aerosol size distribution characterized by diffusion-limited growth. The experimental conditions of the 36-h experiment were similar to the 12-h irradiation experiment; however, both the initial *m*-xylene concentration and the seed volume concentration in the 12-h irradiation experiment were lower than those in the combined 36-h aging experiments, and r_{OS} is expected to differ as a result. Despite the differences, it is expected that the size distribution of the suspended particles in hours 12.4–20 during 36-h experiment should behave similarly to the size distribution of particles during hours 12.4–20 of the

12-h irradiation experiment if only particle wall loss is occurring. The fractional decrease in r_{OS} during hours 12.4–20 of the 36-h irradiation experiment is approximately double that of the 12-h irradiation experiment, suggesting that an additional process besides particle wall loss, such as gas-particle repartitioning due to evaporation, affected the suspended particle r_{OS}. The magnitude of evaporation, however, may not be as large as originally thought due to uncertainty in the upper bound wall loss correction method.

The lower bound wall loss correction should be unaffected by size-dependent r_{OS} distributions. The number and size of deposited particles is calculated independently of particle composition and is added back to the number distribution of suspended particles to calculate the total volume of particles. In obtaining the total volume of organics, the volume of seed or other background particles is subtracted from the total volume. This calculation assumes that the seed or background particle volume does not change during an experiment.

3.5 Acidic seed effects

Aging experiments were also performed using acidic MS + SA seed to determine the extent to which particle acidity affects chemical aging of *m*-xylene SOA. Figure 14 shows the elemental ratios for both AS and MS + SA seeded experiments. No difference between the acidic and neutral seeds for *m*-xylene-derived SOA is observed. Ng et al. (2007) did not observe a difference in yields for low-NO_x *m*-xylene SOA with neutral and acidic seed particles; therefore, it is plausible that the chemical composition of the aerosol condensed onto the two types of seed particles is similar.

4 Conclusions

Laboratory chamber studies provide fundamental information on the mechanisms of formation of SOA. The duration of chamber experiments is limited by several factors, including wall loss of particles and vapors and depletion of chamber air through instrument sampling. Laboratory experiments attempt to approach durations of OH radical exposure corresponding to those of particles in the atmosphere, on the order of a week, through enhanced OH radical levels. In the present work we extend the duration of chamber experiments by sampling protocols that minimize the amount of chamber air removed over the course of the experiment. The protocol developed here allows experiments up to 36 h duration. Hydroxyl radical levels in the experiments reported here are roughly at atmospheric levels. We address SOA formation from the photooxidation of *m*-xylene, an important anthropogenic precursor to organic aerosol. The extended duration experiments provide a view into the multi-generational chemistry involved in *m*-xylene SOA formation that can be expected to be occurring in the atmosphere. Although the current work studies only low-NO_x chemistry, the *m*-xylene oxidation mechanism leading to SOA formation under high-NO_x conditions is also expected to follow multi-generational chemistry (Kwok et al., 1997; Zhao et al., 2005; Ng et al., 2007; Song et al., 2007; Noda et al., 2009; Birdsall et al., 2010). The generations of oxidation of a precursor volatile organic compound can lead to functionalized products of ever decreasing volatility, characterized by increasing elemental O:C ratio, as well as to products of higher volatility that do not contribute to SOA. Based on CIMS measurements, there is strong evidence of gas-phase loss of higher generation products. That this process involves photooxidation or photolysis is confirmed by the absence of changes in total aerosol amount when irradiation is stopped. Wall loss of vapor can be excluded as the cause of this behavior. Estimates of reaction timescales suggest that gas-phase processes are most likely involved in this latter stage of aging, although direct OH reaction with the surface of the particles cannot be ruled out. Finally, the present work offers a protocol for laboratory chamber experiments to attain times approaching more closely those of atmospheric aerosol residence times.

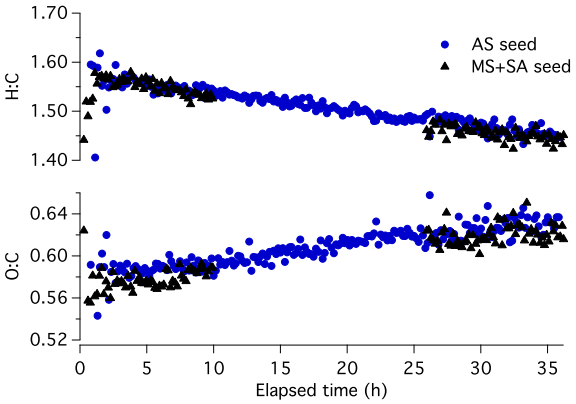

Fig. 14. Elemental ratios of *m*-xylene aerosol condensed onto neutral (AS) and acidic (MS + SA) seed particles.

Appendix A

Photochemical model

To estimate both OH concentration and the importance of OH reaction with later-generation oxidation products, a photochemical model (Reactions R1–R23 below) was constructed. Products through three generations of oxidation are included. Primary oxidation products are those suggested by Birdsall et al. (2010) and Zhao et al. (2005) with product yields and further oxidative pathways as derived from the MCM (Jenkin et al., 2003; Bloss et al., 2005). Values of rate constants are listed in Table 3, and compounds represented in the model are given in Table 4. Photolysis rate constants are calculated using the irradiance spectrum measured for the chamber

lights and absorption cross section values and quantum yields from Sander et al. (2011). The following reactions are included:

$$H_2O_2 + h\nu \xrightarrow{j_{H_2O_2}} 2OH \quad (R1)$$

$$H_2O_2 + OH \xrightarrow{k_1} HO_2 + H_2O \quad (R2)$$

$$RH + OH \xrightarrow{k_2} 0.54RO_2 \quad (R3)$$

$$\xrightarrow{k_2} 0.29EPOX + 0.29HO_2 \quad (R4)$$

$$\xrightarrow{k_2} 0.17ROH + 0.17HO_2 \quad (R5)$$

$$RO_2 + RO_2 \xrightarrow{k_3} prod_{RO_2+RO_2} \quad (R6)$$

$$RO_2 + HO_2 \xrightarrow{k_4} ROOH \quad (R7)$$

$$EPOX + OH \xrightarrow{k_5} EPOXO_2 \quad (R8)$$

$$EPOX + h\nu \xrightarrow{j_{EPOX}} prod_{EPOX+h\nu} \quad (R9)$$

$$ROH + OH \xrightarrow{k_6} 0.51ROHO_2 \quad (R10)$$

$$\xrightarrow{k_6} 0.42ROHOH \quad (R11)$$

$$\xrightarrow{k_6} 0.07RO \quad (R12)$$

$$ROOH + OH \xrightarrow{k_7} prod_{ROOH+OH} + OH \quad (R13)$$

$$ROOH + h\nu \xrightarrow{j_{ROOH}} prod_{ROOH+h\nu} + OH \quad (R14)$$

$$EPOXO_2 + HO_2 \xrightarrow{k_8} EPOXOOH \quad (R15)$$

$$EPOXOOH + OH \xrightarrow{k_9} prod_{EPOXOOH+OH} + OH \quad (R16)$$

$$EPOXOOH + h\nu \xrightarrow{j_{ROOH}} prod_{EPOXOOH+h\nu} + OH \quad (R17)$$

$$ROHO_2 + HO_2 \xrightarrow{k_{10}} ROHOOH \quad (R18)$$

$$ROHOOH + OH \xrightarrow{k_{11}} ROHO_2 \quad (R19)$$

$$ROHOOH + h\nu \xrightarrow{j_{ROOH}} prod_{ROHOOH+h\nu} \quad (R20)$$

$$ROHOH + OH \xrightarrow{k_{12}} prod_{ROHOH+OH} \quad (R21)$$

$$HO_2 + HO_2 \xrightarrow{k_{13}} H_2O_2 + O_2 \quad (R22)$$

$$OH + HO_2 \xrightarrow{k_{14}} H_2O + O_2 \quad (R23)$$

Neither gas-particle partitioning nor vapor-phase wall loss was included in the model because there is not sufficient information about either process to accurately represent it in the model. Vapor-phase wall loss is assumed to be minor (Fig. 11) and should not have a large effect on gas species concentrations.

Acknowledgements. This work was supported by the Office of Science (Biological and Environmental Research), US Department of Energy Grant DE-SC 0006626, and National Science Foundation Grant AGS-1057183. The CIMS instrument was purchased as part of a major research instrumentation grant from the National Science Foundation (Grant ATM-0619783); assembly and testing was supported by the Davidow Discovery Fund. We thank Katherine Schilling and ManNin Chan for experimental assistance and Arthur Chan for helpful discussion. We thank the reviewers for useful feedback on the discussions paper. Christine Loza, Lindsay Yee, and Jill Craven were supported by National Science Foundation Graduate Research Fellowships.

Edited by: N. M. Donahue

References

Aiken, A. C., DeCarlo, P. F., Kroll, J. H., Worsnop, D. R., Huffman, J. A., Docherty, K. S., Ulbrich, I. M., Mohr, C., Kimmel, J. R., Sueper, D., Sun, Y., Zhang, Q., Trimborn, A., Northway, M., Ziemann, P. J., Canagaratna, M. R., Onasch, T. B., Alfarra, M. R., Prevot, A. S. H., Dommen, J., Duplissy, J., Metzger, A., Baltensperger, U., and Jimenez, J. L.: O/C and OM/OC ratios of primary, secondary, and ambient organic aerosols with high-resolution time-of-flight aerosol mass spectrometry, Environ. Sci. Technol., 42, 4478–4485, doi:10.1021/es703009q, 2008.

Balkanski, Y. J., Jacob, D. J., D. J., Gardner, G. M., Graustein, W. C., and Turekian, K. K.: Transport and residence times of tropospheric aerosols inferred from a global 3-dimensional simulation of PB-210, J. Geophys. Res–Atmos., 98, 20573–20586, doi:10.1029/93JD02456, 1993.

Birdsall, A. W., Andreoni, J. F., and Elrod, M. J.: Investigation of the role of bicyclic peroxy radicals in the oxidation mechanism of toluene, J. Phys. Chem. A, 114, 10655–10663, doi:10.1021/jp105467e, 2010.

Bloss, C., Wagner, V., Jenkin, M. E., Volkamer, R., Bloss, W. J., Lee, J. D., Heard, D. E., Wirtz, K., Martin-Reviejo, M., Rea, G., Wenger, J. C., and Pilling, M. J.: Development of a detailed chemical mechanism (MCMv3.1) for the atmospheric oxidation of aromatic hydrocarbons, Atmos. Chem. Phys., 5, 641–664, doi:10.5194/acp-5-641-2005, 2005.

Calvert, J. G., Atkinson, R., H., B. K., Kamens, R. M., Seinfeld, J. H., Wallington, T. J., and Yarwood, G.: The Mechanisms of Atmospheric Oxidation of Aromatic Hydrocarbons, Oxford University Press, New York, 2002.

Canagaratna, M. R., Jayne, J. T., Jimenez, J. L., Allan, J. D., Alfarra, M. R., Zhang, Q., Onasch, T. B., Drewnick, F., Coe, H., Middlebrook, A., Delia, A., Williams, L. R., Trimborn, A. M., Northway, M. J., DeCarlo, P. F., Kolb, C. E., Davidovits, P., and Worsnop, D. R.: Chemical and microphysical characterization of ambient aerosols with the Aerodyne aerosol mass spectrometer, Mass Spectrom. Rev., 26, 185–222, doi:10.1002/mas.20115, 2007.

Chhabra, P. S., Flagan, R. C., and Seinfeld, J. H.: Elemental analysis of chamber organic aerosol using an aerodyne high-resolution aerosol mass spectrometer, Atmos. Chem. Phys., 10, 4111–4131, doi:10.5194/acp-10-4111-2010, 2010.

Chhabra, P. S., Ng, N. L., Canagaratna, M. R., Corrigan, A. L., Russell, L. M., Worsnop, D. R., Flagan, R. C., and Seinfeld, J. H.: Elemental composition and oxidation of chamber organic aerosol, Atmos. Chem. Phys., 11, 8827–8845, doi:10.5194/acp-11-8827-2011, 2011.

Cocker, D. R., Flagan, R. C., and Seinfeld, J. H.: State-of-the-art chamber facility for studying atmospheric aerosol chemistry, Environ. Sci. Technol., 35, 2594–2601, doi:10.1021/es0019169, 2001.

Crounse, J. D., McKinney, K. A., Kwan, A. J., and Wennberg, P. O.: Measurement of gas-phase hydroperoxides by chemical ionization mass spectrometry, Anal. Chem., 78, 6726–6732, doi:10.1021/ac0604235, 2006.

DeCarlo, P. F., Kimmel, J. R., Trimborn, A., Northway, M. J., Jayne, J. T., Aiken, A. C., Gonin, M., Fuhrer, K., Horvath, T., Docherty, K. S., Worsnop, D. R., and Jimenez, J. L.: Field-deployable, high-resolution, time-of-flight aerosol mass spectrometer, Anal. Chem., 78, 8281–8289, doi:10.1021/ac061249n, 2006.

Hallquist, M., Wenger, J. C., Baltensperger, U., Rudich, Y., Simpson, D., Claeys, M., Dommen, J., Donahue, N. M., George, C., Goldstein, A. H., Hamilton, J. F., Herrmann, H., Hoffmann, T., Iinuma, Y., Jang, M., Jenkin, M. E., Jimenez, J. L., Kiendler-Scharr, A., Maenhaut, W., McFiggans, G., Mentel, Th. F., Monod, A., Prévôt, A. S. H., Seinfeld, J. H., Surratt, J. D., Szmigielski, R., and Wildt, J.: The formation, properties and impact of secondary organic aerosol: current and emerging issues, Atmos. Chem. Phys., 9, 5155–5236, doi:10.5194/acp-9-5155-2009, 2009.

Heald, C. L., Kroll, J. H., Jimenez, J. L., Docherty, K. S., DeCarlo, P. F., Aiken, A. C., Chen, Q., Martin, S. T., Farmer, D. K., and Artaxo, P.: A simplified description of the evolution of organic aerosol composition in the atmosphere, Geophys. Res. Lett., 37, L08803, doi:10.1029/2010GL042737, 2010.

Hildebrandt, L., Donahue, N. M., and Pandis, S. N.: High formation of secondary organic aerosol from the photo-oxidation of toluene, Atmos. Chem. Phys., 9, 2973–2986, doi:10.5194/acp-9-2973-2009, 2009.

Hildebrandt, L., Henry, K. M., Kroll, J. H., Worsnop, D. R., Pandis, S. N., and Donahue, N. M.: Evaluating the Mixing of Organic Aerosol Components Using High-Resolution Aerosol Mass Spectrometry, Environ. Sci. Technol., 45, 6329–6335, doi:10.1021/es200825g, 2011.

Jenkin, M. E., Saunders, S. M., Wagner, V., and Pilling, M. J.: Protocol for the development of the Master Chemical Mechanism, MCM v3 (Part B): tropospheric degradation of aromatic volatile organic compounds, Atmos. Chem. Phys., 3, 181–193, doi:10.5194/acp-3-181-2003, 2003.

Jimenez, J. L., Canagaratna, M. R., Donahue, N. M., Prevot, A. S. H., Zhang, Q., Kroll, J. H., DeCarlo, P. F., Allan, J. D., Coe, H., Ng, N. L., Aiken, A. C., Docherty, K. S., Ulbrich, I. M., Grieshop, A. P., Robinson, A. L., Duplissy, J., Smith, J. D., Wilson, K. R., Lanz, V. A., Hueglin, C., Sun, Y. L., Tian, J., Laaksonen, A., Raatikainen, T., Rautiainen, J., Vaattovaara, P., Ehn, M., Kulmala, M., Tomlinson, J. M., Collins, D. R., Cubison, M. J., Dunlea, E. J., Huffman, J. A., Onasch, T. B., Alfarra, M. R., Williams, P. I., Bower, K., Kondo, Y., Schneider, J., Drewnick, F., Borrmann, S., Weimer, S., Demerjian, K., Salcedo, D., Cottrell, L., Griffin, R., Takami, A., Miyoshi, T., Hatakeyama, S., Shimono, A., Sun, J. Y., Zhang, Y. M., Dzepina, K., Kimmel, J. R., Sueper, D., Jayne, J. T., Herndon, S. C., Trimborn, A. M., Williams, L. R., Wood, E. C., Middlebrook, A. M., Kolb, C. E., Baltensperger, U., and Worsnop, D. R.: Evolution of organic aerosols in the atmosphere, Science, 326, 1525–1529, doi:10.1126/science.1180353, 2009.

Keywood, M. D., Varutbangkul, V., Bahreini, R., Flagan, R. C., and Seinfeld, J. H.: Secondary organic aerosol formation from the ozonolysis of cycloalkenes and related compounds, Environ. Sci. Technol., 38, 4157–4164, doi:10.1021/es035363o, 2004.

Kroll, J. and Seinfeld, J.: Chemistry of secondary organic aerosol: Formation and evolution of low-volatility organics in the atmosphere, Atmos. Environ., 42, 3593–3624, doi:10.1016/j.atmosenv.2008.01.003, 2008.

Kroll, J. H., Smith, J. D., Che, D. L., Kessler, S. H., Worsnop, D. R., and Wilson, K. R.: Measurement of fragmentation and functionalization pathways in the heterogeneous oxidation of oxidized organic aerosol, Phys. Chem. Chem. Phys., 11, 8005–8014, doi:10.1039/b905289e, 2009.

Kwok, E., Aschmann, S., Atkinson, R., and Arey, J.: Products of the gas-phase reactions of *o*-, *m*-and *p*-xylene with the OH radical in the presence and absence of NO_x, J. Chem. Soc., Faraday Trans., 93, 2847–2854, 1997.

Lambe, A. T., Onasch, T. B., Massoli, P., Croasdale, D. R., Wright, J. P., Ahern, A. T., Williams, L. R., Worsnop, D. R., Brune, W. H., and Davidovits, P.: Laboratory studies of the chemical composition and cloud condensation nuclei (CCN) activity of secondary organic aerosol (SOA) and oxidized primary organic aerosol (OPOA), Atmos. Chem. Phys., 11, 8913–8928, doi:10.5194/acp-11-8913-2011, 2011.

Lee, A. K. Y., Herckes, P., Leaitch, W. R., Macdonald, A. M., and Abbatt, J. P. D.: Aqueous OH oxidation of ambient organic aerosol and cloud water organics: Formation of highly oxidized products, Geophys. Res. Lett., 38, L11805, doi:10.1029/2011GL047439, 2011.

Matthew, B. M., Middlebrook, A. M., and Onasch, T. B.: Collection efficiencies in an Aerodyne aerosol mass spectrometer as a function of particle phase for laboratory generated aerosols, Aerosol Sci. Tech., 42, 884–898, doi:10.1080/02786820802356797, 2008.

Murphy, D. M., Cziczo, D. J., Froyd, K. D., Hudson, P. K., Matthew, B. M., Middlebrook, A. M., Peltier, R. E., Sullivan, A., Thomson, D. S., and Weber, R. J.: Single-particle mass spectrometry of tropospheric aerosol particles, J. Geophys. Res–Atmos., 111, D23S23, doi:10.1029/2006JD007340, 2006.

Ng, N. L., Kroll, J. H., Chan, A. W. H., Chhabra, P. S., Flagan, R. C., and Seinfeld, J. H.: Secondary organic aerosol formation from m-xylene, toluene, and benzene, Atmos. Chem. Phys., 7, 3909–3922, doi:10.5194/acp-7-3909-2007, 2007.

Ng, N. L., Canagaratna, M. R., Zhang, Q., Jimenez, J. L., Tian, J., Ulbrich, I. M., Kroll, J. H., Docherty, K. S., Chhabra, P. S., Bahreini, R., Murphy, S. M., Seinfeld, J. H., Hildebrandt, L., Donahue, N. M., DeCarlo, P. F., Lanz, V. A., Prévôt, A. S. H., Dinar, E., Rudich, Y., and Worsnop, D. R.: Organic aerosol components observed in Northern Hemispheric datasets from Aerosol Mass Spectrometry, Atmos. Chem. Phys., 10, 4625–4641, doi:10.5194/acp-10-4625-2010, 2010.

Ng, N. L., Canagaratna, M. R., Jimenez, J. L., Chhabra, P. S., Seinfeld, J. H., and Worsnop, D. R.: Changes in organic aerosol composition with aging inferred from aerosol mass spectra, Aerosol Sci. Tech., 11, 6465–6474, doi:10.5194/acp-11-6465-2011, 2011.

Noda, J., Volkamer, R., and Molina, M. J.: Dealkylation of alkylbenzenes: a significant pathway in the toluene, *o*-, *m*-, *p*-xylene + OH reaction, J. Phys. Chem. A, 113, 9658–9666, doi:10.1021/jp901529k, 2009.

Paulot, F., Crounse, J. D., Kjaergaard, H. G., Kurten, A., St Clair, J. M., Seinfeld, J. H., and Wennberg, P. O.: Unexpected epoxide formation in the gas-phase photooxidation of isoprene, Science,

325, 730–733, doi:10.1126/science.1172910, 2009.

Qi, L., Nakao, S., Malloy, Q., Warren, B., and Cocker, D. R.: Can secondary organic aerosol formed in an atmospheric simulation chamber continuously age?, Atmos. Environ., 44, 2990–2996, doi:10.1016/j.atmosenv.2010.05.020, 2010.

Riipinen, I., Pierce, J. R., Yli-Juuti, T., Nieminen, T., Häkkinen, S., Ehn, M., Junninen, H., Lehtipalo, K., Petäjä, T., Slowik, J., Chang, R., Shantz, N. C., Abbatt, J., Leaitch, W. R., Kerminen, V.-M., Worsnop, D. R., Pandis, S. N., Donahue, N. M., and Kulmala, M.: Organic condensation: a vital link connecting aerosol formation to cloud condensation nuclei (CCN) concentrations, Atmos. Chem. Phys., 11, 3865–3878, doi:10.5194/acp-11-3865-2011, 2011.

Rudich, Y., Donahue, N. M., and Mentel, T. F.: Aging of organic aerosol: Bridging the gap between laboratory and field studies, Annu. Rev. Phys. Chem., 58, 321–352, doi:10.1146/annurev.physchem.58.032806.104432, 2007.

Sander, S. P., Abbatt, J., Barker, J. R., Burkholder, J. B., Friedl, R. R., Golden, D. M., Huie, R. E., Kolb, C. E., J., K. M., Moortgat, G. K., Orkin, V. L., and Wine, P. H.: Chemical kinetics and photochemical data for use in atmospheric studies, Evaluation No. 17. JPL Publication 10-6, Jet Propulsion Laboratory, Pasadena, http://jpldataeval.jpl.nasa.gov, 2011.

Seinfeld, J. H. and Pandis, S. N.: Atmospheric Chemistry and Physics, John Wiley and Sons, Inc., Hoboken, NJ, second edn., 2006.

Shilling, J. E., Chen, Q., King, S. M., Rosenoern, T., Kroll, J. H., Worsnop, D. R., DeCarlo, P. F., Aiken, A. C., Sueper, D., Jimenez, J. L., and Martin, S. T.: Loading-dependent elemental composition of α-pinene SOA particles, Atmos. Chem. Phys., 9, 771–782, doi:10.5194/acp-9-771-2009, 2009.

Shiraiwa, M., Ammann, M., Koop, T., and Pöschl, U.: Gas uptake and chemical aging of semisolid organic aerosol particles, Proc. Natl. Acad. Sci. USA, 108, 11003–11008, doi:10.1073/pnas.1103045108, 2011.

Song, C., Na, K., Warren, B., Malloy, Q., and Cocker, D. R.: Secondary organic aerosol formation from *m*-xylene in the absence of NO_x, Environ. Sci. Technol., 41, 7409–7416, doi:10.1021/es070429r, 2007.

St. Clair, J. M., McCabe, D. C., Crounse, J. D., Steiner, U., and Wennberg, P. O.: Chemical ionization tandem mass spectrometer for the in situ measurement of methyl hydrogen peroxide, Rev. Sci. Instrum., 81, 094102, doi:10.1063/1.3480552, 2010.

Vaden, T. D., Song, C., Zaveri, R. A., Imre, D., and Zelenyuk, A.: Morphology of mixed primary and secondary organic particles and the adsorption of spectator organic gases during aerosol formation, P. Natl. Acad. Sci. USA, 107, 6658–6663, doi:10.1073/pnas.0911206107, 2010.

Vaden, T. D., Imre, D., Beránek, J., Shrivastava, M., and Zelenyuk, A.: Evaporation kinetics and phase of laboratory and ambient secondary organic aerosol, P. Natl. Acad. Sci. USA, 108, 2190–2195, doi:10.1073/pnas.1013391108, 2011.

Virtanen, A., Joutsensaari, J., Koop, T., Kannosto, J., Yli-Pirilä, P., Leskinen, J., Mäkelä, J. M., Holopainen, J. K., Pöschl, U., Kulmala, M., Worsnop, D. R., and Laaksonen, A.: An amorphous solid state of biogenic secondary organic aerosol particles, Nature, 467, 824–827, doi:10.1038/nature09455, 2010.

Weitkamp, E. A., Sage, A. M., Pierce, J. R., Donahue, N. M., and Robinson, A. L.: Organic Aerosol Formation from Photochemical Oxidation of Diesel Exhaust in a Smog Chamber, Environ. Sci. Technol., 41, 6969–6975, doi:10.1021/es070193r, 2007.

Zhang, Q., Jimenez, J. L., Canagaratna, M. R., Allan, J. D., Coe, H., Ulbrich, I., Alfarra, M. R., Takami, A., Middlebrook, A. M., Sun, Y. L., Dzepina, K., Dunlea, E., Docherty, K., DeCarlo, P. F., Salcedo, D., Onasch, T., Jayne, J. T., Miyoshi, T., Shimono, A., Hatakeyama, S., Takegawa, N., Kondo, Y., Schneider, J., Drewnick, F., Borrmann, S., Weimer, S., Demerjian, K., Williams, P., Bower, K., Bahreini, R., Cottrell, L., Griffin, R. J., Rautiainen, J., Sun, J. Y., Zhang, Y. M., and Worsnop, D. R.: Ubiquity and dominance of oxygenated species in organic aerosols in anthropogenically-influenced Northern Hemisphere midlatitudes, Geophys. Res. Lett., 34, L13801, doi:10.1029/2007GL029979, 2007.

Zhang, X., Pandis, S. N., and Seinfeld, J. H.: Aerosol condensation: Diffusion limited vs quasi-equilibrium growth, Aerosol Sci. Technol., submitted, 2011.

Zhao, J., Zhang, R., Misawa, K., and Shibuya, K.: Experimental product study of the OH-initiated oxidation of *m*-xylene, J. Photoch. Photobio. A, 176, 199–207, doi:10.1016/j.jphotochem.2005.07.013, 2005.

Appendix E

Ship Impacts on the Marine Atmosphere: Insights into the Contribution of Shipping Emissions to the Properties of Marine Aerosol and Clouds[1]

[1]This chapter is reproduced by permission from "Ship Impacts on the Marine Atmosphere: Insights into the Contribution of Shipping Emissions to the Properties of Marine Aerosol and Clouds" by M. M. Coggon, A. Sorooshian, Z. Wang, A. R. Metcalf, A. A. Frossard, J. J. Lin, J. S. Craven, A. Nenes, H. H. Jonsson, L. M. Russell, R. C. Flagan, and J. H. Seinfeld., *Atmospheric Chemistry and Physics*, (12), 8439 – 8458, www.atmos-chem-phys.net/12/8439/2012/, doi:10.5194/acp-12-8439-2012, 2012.

Atmos. Chem. Phys., 12, 8439–8458, 2012
www.atmos-chem-phys.net/12/8439/2012/
doi:10.5194/acp-12-8439-2012

Atmospheric Chemistry and Physics

Ship impacts on the marine atmosphere: insights into the contribution of shipping emissions to the properties of marine aerosol and clouds

M. M. Coggon[1], A. Sorooshian[2,3], Z. Wang[2], A. R. Metcalf[4], A. A. Frossard[5], J. J. Lin[6], J. S. Craven[1], A. Nenes[6,7], H. H. Jonsson[8], L. M. Russell[5], R. C. Flagan[1,4], and J. H. Seinfeld[1,4]

[1]Department of Chemical Engineering, California Institute of Technology, Pasadena, CA, USA
[2]Department of Chemical and Environmental Engineering, University of Arizona, Tucson, AZ, USA
[3]Department of Atmospheric Sciences, University of Arizona, Tucson, AZ, USA
[4]Department of Environmental Science and Engineering, California Institute of Technology, Pasadena, CA, USA
[5]SCRIPPS Institution of Oceanography, University of California, San Diego, CA, USA
[6]School of Earth and Atmospheric Sciences, Georgia Inst. of Technology, Atlanta, GA, USA
[7]School of Chemical and Biomolecular Engineering, Georgia Institute of Technology, Atlanta, GA, USA
[8]Naval Postgraduate School, Monterey, CA, USA

Correspondence to: J. H. Seinfeld (seinfeld@caltech.edu)

Received: 22 May 2012 – Published in Atmos. Chem. Phys. Discuss.: 7 June 2012
Revised: 1 September 2012 – Accepted: 3 September 2012 – Published: 20 September 2012

Abstract. We report properties of marine aerosol and clouds measured in the shipping lanes between Monterey Bay and San Francisco off the coast of Central California. Using a suite of aerosol instrumentation onboard the CIRPAS Twin Otter aircraft, these measurements represent a unique set of data contrasting the properties of clean and ship-impacted marine air masses in dry aerosol and cloud droplet residuals. Below-cloud aerosol exhibited average mass and number concentrations of $2\,\mu g\,m^{-3}$ and $510\,cm^{-3}$, respectively, which are consistent with previous studies performed off the coast of California. Enhancements in vanadium and cloud droplet number concentrations are observed concurrently with a decrease in cloud water pH, suggesting that periods of high aerosol loading are primarily linked to increased ship influence. Mass spectra from a compact time-of-flight Aerodyne aerosol mass spectrometer reveal an enhancement in the fraction of organic at m/z 42 (f_{42}) and 99 (f_{99}) in ship-impacted clouds. These ions are well correlated to each other ($R^2 > 0.64$) both in and out of cloud and constitute 14 % (f_{44}) and 3 % (f_{99}) of organic mass during periods of enhanced sulfate. High-resolution mass spectral analysis of these masses from ship measurements suggests that the ions responsible for this variation were oxidized, possibly due to cloud processing. We propose that the organic fractions of these ions be used as a metric for determining the extent to which cloud-processed ship emissions impact the marine atmosphere where ($f_{42} > 0.15$; $f_{99} > 0.04$) would imply heavy influence from shipping emissions, ($0.05 < f_{42} < 0.15$; $0.01 < f_{99} < 0.04$) would imply moderate, but persistent, influences from ships, and ($f_{42} < 0.05$; $f_{99} < 0.01$) would imply clean, non-ship-influenced air.

1 Introduction

Ship exhaust is estimated to account for 14 and 16 % of global NO_x and SO_x emissions, respectively (Corbett and Fischbeck, 1997). Models show that ship emissions also contribute $1.67\,Tg\,yr^{-1}$ to global particulate matter, which is nearly equivalent to current estimates of particulate matter emitted by all on-road vehicles (Eyring et al., 2005; Yan et al., 2011). Because many shipping lanes are located along coastal regions where marine stratocumuli persist, ship emissions have the potential to directly affect cloud microphysics. Studies of cargo ship exhaust/cloud interactions have shown distinct cloud responses to these perturbations (e.g., Coakley

et al., 1987; Ackerman et al., 1995; Frick and Hoppel, 2000; Durkee et al., 2000; Hudson et al., 2000; Noone et al., 2000; Lu et al., 2009; Christensen and Stephens, 2011). Satellite imagery shows that ship tracks can exist hours after initial emission (Coakley et al., 1987; Durkee et al., 2000; Christensen and Stephens, 2011) and therefore have the potential to exert a significant effect on local radiative fluxes.

Ship emissions mix with marine aerosol and subsequently with cloud droplets, however the extent of this effect is not well established. Marine aerosol is a complex mixture of natural and anthropogenic sources, and thus the signature from shipping emissions is difficult to detect. Natural marine aerosol comprises particles resulting from sea-spray (e.g., NaCl, KCl, organics), marine biological activity (e.g., dimethylsulfide and subsequent oxidation products), and those from continental origins (e.g., dust, secondary products from biogenic oxidation). Anthropogenic sources include ship emissions, continental pollution, and biomass burning. Sea-salt typically dominates the super micrometer aerosol ($D_p > 1\,\mu m$), whereas organics, sulfate, and ammonium from natural and anthropogenic sources constitute a large portion of mass in the submicrometer regime ($D_p \leq 1\,\mu m$) (Cunningham and Zoller, 1981; McInnes et al., 1996).

With its location along busy shipping lanes and near heavily populated areas, the California coastal zone is an especially advantageous region to evaluate the anthropogenic contribution to marine aerosol and cloud condensation nuclei (CCN). Table 1 summarizes studies conducted in the vicinity of the California coastal zone on marine aerosol and cloud droplets. Important studies by Hegg et al. (2008, 2009, 2010) have utilized source apportionment models to attribute size-resolved hygroscopicity, light scattering coefficient, and CCN activity of marine aerosol to natural and anthropogenic sources. They estimated that 50 % of the measured CCN concentrations and 57 % of the light-scattering coefficient of marine aerosol in the California coastal region originated from anthropogenic sources. Though anthropogenic signatures contribute significantly to measured aerosol properties, the extent to which ship emissions contribute to this signal remains uncertain.

Few studies along the California coast have investigated marine aerosol and cloud properties simultaneously (Table 1). In this study, we utilize state-of-the-art aerosol measurements to build upon the knowledge of marine aerosol and cloud properties, with special attention to the contribution from ship emissions.

2 Methodology

2.1 Field mission description

From July–August 2011, the Eastern Pacific Emitted Aerosol Cloud Experiment 2011 (E-PEACE) was operated out of the Center for Interdisciplinary Remotely-Piloted Aircraft Studies (CIRPAS) in Marina, CA (Russell et al., 2012). The purpose of the field mission was to study the effect of ship emissions, sea-salt and organic aerosol on Eastern Pacific marine stratocumulus commonly found off the coast of Central California. Thirty flights were conducted by the CIRPAS Twin Otter aircraft to probe the emissions of cargo and tanker ships and their effects on marine stratocumulus. The focus of this study is a set of measurements made during twenty-six flights conducted in a sampling region between San Francisco and Monterey Bay (Fig. 1). Four additional flights were performed outside of this sampling region and are analyzed in Sect. 4.1 to compare aerosol properties during cloudy and clear conditions, however a more extensive analysis of these flights will be forthcoming. In addition to sampling direct ship emissions, measurements of aerosol and cloud properties were made below, within, and above cloud during each flight. Simultaneous measurements of marine aerosol properties were conducted onboard the R/V *Point Sur*. Averaged measurements made outside direct ship fumigation were taken to reflect the variation of marine aerosol and cloud properties over the course of the campaign.

2.2 Aerosol and cloud droplet measurement methodology

Cloud and aerosol properties were measured by ship and aircraft using a suite of aerosol instruments (Table 2). A detailed description of the instrumentation used in this study can be found in the Appendix. Cloud droplet residuals were measured downstream of a counterflow virtual impactor (CVI) inlet with a cut size of 11 µm (Shingler et al., 2012).

In the following discussion, we report cloud residual mass concentrations measured behind the CVI inlet. Despite the improved CVI design that can accommodate high sample flow and thus reduce the need for large counterflow and dilution (Shingler et al., 2012), uncertainties remain in total mass and number concentrations that are common among all CVI inlets. Primarily, the transmission efficiency (TE) of the CVI is a function of several parameters, including aircraft speed, sample-flow dilution, and particle diameter. In addition, the instrument is characterized by a cut size that restricts the smallest particle that can be sampled; thus, the cloud residual mass concentrations reported in this study (Table 3) are less than the total cloud residual mass. However, there are relative differences between periods of low and high concentration that suggest a qualitative difference between flights.

An altitude-dependent, zig-zag aircraft sampling pattern was utilized to measure unperturbed and perturbed air masses. Upon locating a ship, the Twin Otter sampled below, within and above cloud in close proximity to the ship's plume. While in cloud, measurements were made behind the CVI, thus sampling only cloud droplet residuals. Measurements made out of cloud were sampled through the main sub-isokinetic aerosol inlet. The main inlet is designed to

Table 1. Previous studies on the properties of marine aerosol over the Northeastern Pacific Ocean. Footnotes define instrument abbreviations.

Author	Research Location	Instruments	Type of Mission	Sources Sampled	CCN Properties	Hygroscopicty	Size Properties	Chemical Properties	Species Analyzed	Summary
Hegg et al. (1996)	Pacific Coast	nephelometer PCASP, SMPS, DNH	Aircraft	Dry Aerosol	–	yes	–	–	–	Authors report the optical and hygroscopic properties of marine aerosol in the vicinity of the California coast. The hygroscopic growth factor was shown to be 1.7 while the ratio of backscatter to total scattering was found to be 0.13.
McInnes et al. (1996)	E. Pacific	Filter Sampling and off-line analytical chemistry	Ground, Ship	Dry Aerosol	–	–	–	yes	sea salt ions, sulfate, ammonium, water	This study investigated the composition of sub-micrometer aerosol. Gravimetric measurements showed that a significant amount of mass (0–76 %) was unaccounted for in filter measurements. Water uptake on the filter samples made up 29 % of the mass and the remaining mass was likely to be organic in nature.
Phinney et al. (2006)	N.E. Pacific	SMPS, PCASP, MOUDI, AMS, GC	Ship	Dry Aerosol	–	–	yes	yes	MSA, sulfate, organics, nitrate, ammonium, sea salt	Marine aerosol off the coast of British Columbia was measured for size and composition. MSA was found to be an order magnitude higher than previously observed in the N.E. Pacific. AMS organic spectra showed that ship emissions may play a role in contributing to the organic signature of marine aerosol.
Straub et al. (2007)	California Coast	Cloud water collector inlet and off-line analytical chemistry, FSSP, PCASP, PVM (LWC)	Aircraft	Cloud Particles	–	–	–	yes	TOC, inorganic ions, sulfate, nitrate, hydrogen peroxide, formaldehyde	Cloud water off the coast of California was analyzed for ionic, TOC, trace ion, soluble organics and formaldehyde concentrations. The measurements represent a unique compilation of remote marine cloud water chemistry.
Sorooshian et al. (2007a)	California Coast	PILS, LWC, CVI	Aircraft	Cloud Particles	–	–	–	yes	oxalate, sulfate	Oxalate: SO_4 measurements tended to increase with altitude, suggesting that cloud processing of below-cloud aerosols generated a higher fraction of oxalate. LES simulations showed that particles above cloud were likely generated due to cloud evaporation; thus, the high fractions of oxalate observed above cloud were partially due to cloud processing.
Hegg et al. (2008)	California Coast	Filter Sampling and off-line analytical chemistry, AHS, Light-scattering humidigraph, PSAP	Aircraft	Dry Aerosol	–	yes	–	yes	organics, inorganic ions, BC, sulfate, lead	Aerosol hygroscopicity was observed to increase with altitude. Given that the MBL is a well mixed system, changes in aerosol properties with altitude plausibly resulted from oxidation of organic films. No evidence for the accumulation of inorganics was observed.
Hegg et al. (2009)	California Coast	Filter Sampling and off-line analytical chemistry, AHS, PSAP, CCN, PCASP	Aircraft	Dry Aerosol	yes	–	yes	yes	organics, inorganic ions, BC, sulfate, lead	CCN measurements off the coast of California are attributed to natural and anthropogenic sources using receptor modeling. Roughly 50 % of the samples measured in the study were anthropogenic in nature.
Hersey et al. (2009)	California Coast	AMS, DASH-SP	Aircraft	Dry Aerosol	–	yes	–	–	organics, sulfate	DASH-SP and AMS measurements are coupled to characterize the chemical dependence of aerosol growth factors. It was found that higher organic fractions yielded lower growth factors at high RH. High organic fractions are correlated with continental sources from back trajectory modeling.
Sorooshian et al. (2009)	California Coast	PILS-IC, LWC, FSSP, SMPS, CCN, DASH-SP	Aircraft, ground, satellite	Aerosol, Clouds	yes	yes	yes	yes	DEA, MSA	The link between chlorophyll *a* concentrations and the fraction of MSA and DEA in aerosol suggests that ocean biota have significant influence over marine aerosol properties including CCN and hygroscopicity. A link between cloud properties and chlorophyll *a* is not shown as cloud properties were heavily influenced by meteorological conditions.
Hegg et al. (2010)	California Coast	Filter Sampling and off-line analytical chemistry, AHS, PSAP, CCN, PCASP	Aircraft	Dry Aerosol	yes	yes	yes	yes	organics, inorganic ions, BC, sulfate, lead	A receptor based model is used to investigate the extent of anthropogenic sources on CCN in the marine environment. The authors report that 63–74 % of the aerosols are anthropogenic in nature.
Langley et al. (2010)	N.E. Pacific	AMS, SMPS, CCN, gas phase SO_2	Ship	Dry Aerosol	yes	–	yes	yes	MSA, SO_2, organics	Ship measurements of marine aerosol showed that periods of high sub-micron CCN activity were consistent with increased concentrations of MSA. CCN and MSA/sulfate were strongly correlated. Organics (primarily anthropogenic) are important as acting as a site for sulfate condensation and subsequent CCN activation.
Moore et al. (2012)	N.E. Pacific	AMS, SMPS, CCN	Aircraft	Dry Aerosol	yes	yes	yes	yes	organic, nitrate, sulfate, ammonium	Detailed characterization of CCN off the coast of California are made and compared to CCN in urban and rural areas. CCN-derived hygroscopicity parameter was highest in marine outflow compared to urban or rural areas.

PCASP – Passive Cavity Aerosol Sizing Probe; FSSP – Forward Scatter Spectrophotometer Probe; PSAP – Particle Soot Absorption Photometer; SMPS – Scanning Mobility Particle Sizer; PVM – Particle Volume Monitor; CCN – Cloud Condensation Nuclei; AMS – Aerosol Mass Spectrometer; LWC – Liquid Water Content; DASH-SP – Differential Aerosol Sizing and Hydroscopicity Spectrometer Probe; DNH – dual-nephelometer humidigraph; CVI – Counter-Flow Virtual Impactor; PILS-IC – Particle Into Liquid Sampler – Ion Chromatography; MOUDI – Micro-Orifice Uniform-Deposit Impactor; AHS – Aerosol Hydration Spectrophotometer

Table 2. Instruments onboard the Twin Otter aircraft and R/V *Point Sur*.

Parameter	Instrument	Time Resolution	Detection Limit	Size Range	Twin Otter	Point Sur
Particle Number Concentration	Condensation Particle Counter (TSI CPC 3010)	1 s	$< 50\,000\ \mathrm{cm}^{-3}$	$\geq$ 10 nm	✓	✓
Aerosol Size Distribution	Scanning Mobility Particle Sizer (SMPS)	110 s	N/A	10–700 nm	✓	✓
Cloud Droplet Residuals	Counterflow Virtual Impactor (CVI)	N/A	N/A	$> 11\ \mu\mathrm{m}$	✓	
Bulk Cloud Water Composition	Modified Mohen Slotted Cloud Water Collector	N/A	N/A	N/A	✓	
Cloud and Aerosol Size Distribution	Cloud and Aerosol Spectrometer Probe (CAS)	1 s	N/A	0.65–55 µm	✓	
Cloud Droplet Liquid Water Content	Light Diffraction (Gerber PVM-100 probe)	1 s	N/A	5–50 µm	✓	
Aerosol Bulk Composition	High Resolution Time-of-Flight Aerosol Mass Spectrometer (HiRes-ToF-AMS)	2 min	$\leq 1\ \mu\mathrm{g\ m}^{-3}$	60–600 nm		✓
Aerosol Bulk Composition	Compact Time-of-Flight Aerosol Mass Spectrometer (C-ToF-AMS)	8–12 s	$\leq 1\ \mu\mathrm{g\ m}^{-3}$	60–600 nm	✓	
Cloud Condensation Nuclei (CCN) Number Concentration	Continuous Flow Streamwise Thermal Gradient CCN chamber	1–20 s	$< 20\,000\ \mathrm{cm}^{-3}$	s.s 0.2–0.7 %	✓	✓

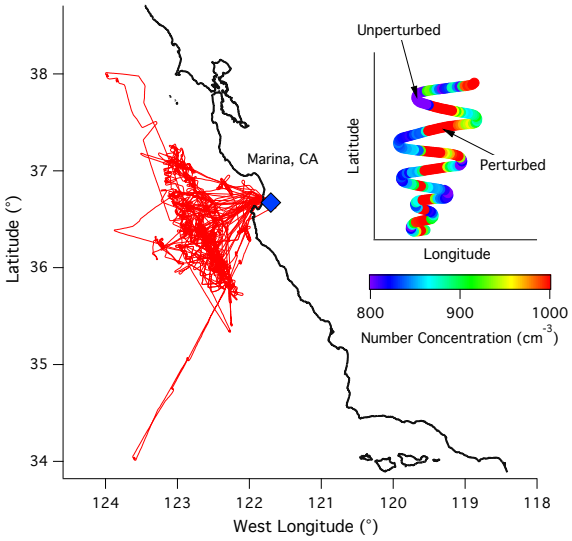

Fig. 1. Twin Otter flight paths for RF 1-26 during the E-PEACE mission. Inset shows a typical sampling pattern when encountering a ship exhaust plume. The color bar indicates the total aerosol number concentration as measured by the Twin Otter CPC.

decelerate airstream velocities outside the cabin ($\sim 50\ \mathrm{m\ s}^{-1}$) to lower velocities that can be effectively sampled by aircraft instruments ($\sim 7\ \mathrm{m\ s}^{-1}$). Under normal airspeed, the inlet on the Twin Otter samples aerosol below 3.5 µm with 100 % efficiency (Hegg et al., 2005). Thus, for the results reported here, there was no appreciable loss of particles due to aircraft sampling.

3 Aerosol and cloud droplet properties

In the following discussion, we use terminology such as "background" and "perturbed" to define aerosol conditions of the marine atmosphere. We acknowledge, however, that the assignment of these terms is not without ambiguity. A solely background signal in the remote marine atmosphere is a condition that occurs only when natural marine processes contribute to the aerosol. Without anthropogenic or continental influences, one might presume that a true baseline marine signal exists. However, even in a total absence of anthropogenic influence, such a signal is likely not unique and constant throughout the remote marine atmosphere. Varying wind speeds that generate sea spray, or biological production of dimethyl sulfide (DMS), which leads to homogeneously nucleated particles, can increase local "background" signal. On the other hand, varying wind speeds can dilute particles and lead to evaporation or ventilate DMS and inhibit new particle formation. Furthermore, particles can be lost due to wet or dry deposition. Even in the absence of non-marine sources, the natural background marine aerosol is dynamic.

Rather than relying on a definition of "background" aerosol, we choose to distinguish between "clean" and "perturbed" conditions based on the extent to which the marine atmosphere is impacted by shipping emissions. We define "perturbed" air masses as being pockets of the marine atmosphere that have been directly impacted by local ship emissions. This would comprise relatively small spatial regions in which the aerosol number concentration has increased, the aerosol number size distribution has shifted in mean diameter, and the aerosol composition has changed relative to the surrounding region. The atmosphere unperturbed by ship emissions, which we take to be synonymous with the term "clean", can be broken into a spectrum of conditions with varying degrees of non-ship related influences. Here, we are interested in comparing properties of the marine aerosol

Table 3. Summary of average aerosol and cloud properties over the course of the E-PEACE campaign. Bottom table summarizes key aerosol properties from previous studies of marine aerosol and cloud droplets off the coast of Central California. Values in brackets represent standard deviations of the average. Values in parenthesis list the range of measurements. Values below detection limit (DL) are noted.

		Below Cloud Aerosol Measurements						Cloud Measurements[g]				Air Equivalent Cloud Water Chemistry					
Research Flight (RF)	Date	Total Mass[a] ($\mu g\,m^{-3}$)	Organic[a] ($\mu g\,m^{-3}$)	Sulfate[a] ($\mu g\,m^{-3}$)	CPC (cm^{-3})	CCN (0.15 %) (cm^{-3})	CCN (0.3 %) (cm^{-3})	Total Mass[a] ($\mu g\,m^{-3}$)	Organic[a] ($\mu g\,m^{-3}$)	Sulfate[a] ($\mu g\,m^{-3}$)	N_d[b] (cm^{-3})	pH	Na (10^4) ($\mu g\,m^{-3}$)	Fe (10^4) ($\mu g\,m^{-3}$)	Mn (10^4) ($\mu g\,m^{-3}$)	V (10^4) ($\mu g\,m^{-3}$)	LWC[b] ($g\,m^{-3}$)
1	8 Jul	0.96	0.65	0.28	665	–	349	1.37	0.76	0.41	208	4.02	87 182	51.41	4.72	0.59	0.10
2	9 Jul	1.32	0.70	0.51	892	–	238	2.06	1.01	0.84	235	4.23	16 956	26.63	2.12	2.12	0.09
4	14 Jul	1.04	0.60	0.45	968	–	131	1.68	0.84	0.69	93	4.32	7757	< (DL)	< (DL)	1.29	0.15
5	15 Jul	0.86	0.75	0.20	364	–	78	0.92	0.49	0.20	23	4.63	688	0.19	0.07	0.31	0.01
6	16 Jul	0.90	0.58	0.31	329	–	–	1.06	0.67	0.22	27	4.50	127	< (DL)	< (DL)	2.02	0.11
7[c]	17 Jul	0.77	0.72	0.18	341	–	–	–	–	–	–	–	–	–	–	–	–
8	19 Jul	0.88	0.44	0.40	323	–	–	1.24	0.68	0.54	145	4.21	3671	11.78	0.52	4.25	0.19
9	21 Jul	1.83	0.70	0.78	578	217	–	1.08	0.63	0.39	127	5.16	17 662	4.85	3.11	1.50	0.23
10	22 Jul	1.80	0.49	1.02	376	213	–	1.81	0.79	0.78	116	4.67	15 212	7.58	1.08	2.46	0.25
11	23 Jul	2.83	0.86	1.56	976	300	400	1.84	0.88	0.81	169	4.30	13 881	17.61	1.55	3.28	0.18
12	24 Jul	2.81	0.92	1.57	736	226	355	1.90	0.87	0.85	170	3.99	5362	15.95	1.36	3.12	0.10
13	26 Jul	0.99	0.60	0.34	221	75	116	1.04	0.56	0.32	87	4.95	11 702	5.13	0.41	4.11	0.23
14[d]	27 Jul	2.99	0.81	1.91	425	207	–	1.53	0.64	0.80	199	3.86	4587	34.05	2.29	16.78	0.22
15	28 Jul	4.74	1.06	3.14	589	101	406	4.98	2.21	2.50	327	2.92	10 772	86.28	4.89	43.08	0.12
16	29 Jul	2.62	0.70	1.59	465	96	304	2.14	0.89	1.13	252	3.84	3664	164.63	17.47	19.99	0.28
17	1 Aug	2.22	0.58	1.44	400	78	352	1.86	0.62	1.10	212	3.77	978	47.07	2.71	7.35	0.10
18	2 Aug	2.55	0.80	1.47	587	184	335	2.34	1.00	1.13	269	4.07	2777	27.67	1.98	8.92	0.21
19	3 Aug	1.41	0.57	0.70	346	167	173	1.11	0.60	0.38	120	4.80	11 406	< (DL)	0.45	3.63	0.19
20[c]	4 Aug	1.08	0.52	0.55	229	44	83	–	–	–	–	–	–	–	–	–	–
21	5 Aug	2.06	0.65	1.17	561	63	254	1.13	0.57	0.48	163	4.65	8376	19.06	1.69	1.03	0.19
22	8 Aug	3.75	1.01	2.24	737	328	333	2.03	0.52	1.30	323	3.66	42 794	26.45	1.31	4.17	0.11
23	9 Aug	2.97	0.92	1.73	428	28	294	1.79	0.75	0.80	226	4.06	34 543	13.77	1.01	1.24	0.11
24	10 Aug	1.57	0.83	0.79	296	49	296	0.99	0.65	0.41	150	4.54	27 015	31.42	1.76	7.64	0.25
25	11 Aug	1.18	0.53	0.46	252	157	91	0.86	0.58	0.21	41	5.07	1538	1.86	0.59	3.97	0.13
26	12 Aug	3.49	1.24	1.94	670	–	459	1.80	0.71	0.97	257	3.90	32 109	17.24	1.07	3.56	0.14
	Min	0.77	0.44	0.18	221	28	78	0.86	0.49	0.20	23	2.92	127	0.19	0.07	0.31	0.01
	Max	4.74	1.24	3.14	976	328	459	4.98	2.21	2.50	327	5.16	87 182	164.63	17.47	43.08	0.28

		Below Cloud Aerosol Measurements						Cloud Measurements[g]				Air Equivalent Cloud Water Chemistry					
Author/ Mission	Date	Total Mass[a] ($\mu g\,m^{-3}$)	Organic[a] ($\mu g\,m^{-3}$)	Sulfate[a] ($\mu g\,m^{-3}$)	CPC (cm^{-3})	CCN (0.15 %) (cm^{-3})	CCN (0.3 %) (cm^{-3})	Total Mass[a] ($\mu g\,m^{-3}$)	Organic[a] ($\mu g\,m^{-3}$)	Sulfate[a] ($\mu g\,m^{-3}$)	N_d[b] (cm^{-3})	pH	Na (10^4) ($\mu g\,m^{-3}$)	Fe (10^4) ($\mu g\,m^{-3}$)	Mn (10^4) ($\mu g\,m^{-3}$)	V (10^4) ($\mu g\,m^{-3}$)	LWC[b] ($g\,m^{-3}$)
E-PEACE Average	Jul–Aug 2011	1.98 [1.07]	0.73 [0.19]	1.07 [0.76]	510 [225]	148 [91]	266 [120]	1.67 [0.85]	0.78 [0.34]	0.75 [0.50]	171 [86]	4.48 [0.72]	13 227 [15 531]	23 [37]	2.3 [4.1]	5.4 [7]	0.16 [0.07]
Hegg et al. (2010)[e]																	
CARMA II	Jul 2004	3.12	–	1.34	–	–	100–825	–	–	–	–	–	–	–	–	–	–
CARMA III	Aug 2005	3.93	–	1.3	–	–	75–1150	–	–	–	–	–	–	–	–	–	–
CARMA IV	Aug 2007	16.3	–	1.04	197–6104	–	50–700	–	–	–	–	–	–	–	–	–	–
Sorooshian et al. (2009) MASE II	Jul 2007	–	–	0.78 [0.59]	307 [239]	–	73 [27]	– –	– –	– –	104 [56]	–	–	–	–	–	0.15 [0.07]
McInnes et al. (1996)[f]	Apr–Jun 1994	2.21 [1.16]	–	–	–	–	–	–	–	–	–	–	–	–	–	–	–
Straub et al. (2007) DYCOMS-II	Jul 2001	–	–	–	–	–	–	–	–	–	174 [79]	3.26–4.82	38 900 (3900–133 900)	71 (0–369)	2.3 (0–11.6)	–	0.33 [0.17]

[a] Measurements from AMS.
[b] Averaged cloud probe data during cloud water sampling period.
[c] No clouds (7/17), few cloud measurements by probes (8/4).
[d] AMS Failure – limited measurements available below cloud (7/27).
[e] Filter samples for aerosol > 0.2 µm in diameter.
[f] Filter samples for aerosol < 1 µm in diameter.
[g] Organics, sulfate and total mass concentrations measured behind the CVI are a fraction of the total loading and may not reflect absolute mass concentrations. See text for details.

during periods of high aerosol mass loading owing to ship emissions (defined here as "perturbed") with properties in adjacent air masses not directly impacted by ship emissions (defined here as "clean"). The nature of non-refractory marine aerosol (i.e., non sea salt components such as organics and sulfate) can be consistently categorized using data from the aerosol mass spectrometer (AMS), which transmits particles with vacuum diameters ranging between 60–600 nm with 100 % transmission efficiency. Initially we will rely on bulk AMS mass concentrations as the basis on which to identify and define "clean" and "perturbed" conditions, but subsequently, we will derive conditions that more concretely define air masses directly impacted by shipping emissions.

Table 3 reports average aerosol properties for each flight compared to measurements reported by other studies conducted in the Eastern Pacific. We note that observations from this study agree broadly with previous findings. Notably, aerosol mass measured by the AMS agrees well with that measured by filter sampling reported in McInnes et al. (1996). Mass loadings from this study reflect submicrometer, non-refractory aerosol, whereas loadings reported by McInnes et al. (1996) reflect total submicrometer mass. The close agreement suggests that the mass measured in the submicrometer regime is dominated by non-sea salt components. This is consistent with McInnes et al. (1997) who show that 87–96 % of the total number concentration of submicrometer particles in the remote marine atmosphere are non-sea salt.

We can use the results from Table 3 to identify flights that were clean and perturbed during the E-PEACE campaign. Figure 2 shows the mass contributions of bulk AMS

species to dry marine aerosol and cloud droplet residuals over the course of the study. As is also shown in Table 3, submicrometer aerosol mass concentrations strongly varied between flights. In the beginning of the study, a continual period of low aerosol loading was observed between 15–19 July (RF 5–8). These measurements yielded aerosol mass concentrations below 1 µg m^{-3} and were among the lowest aerosol concentrations observed during E-PEACE. In the present study, these were likely to have been the least influenced by shipping emissions and are therefore defined as "clean".

Clean conditions have been previously observed in the marine atmosphere and are known to vary greatly (e.g., McInnes et al., 1996; Phinney et al., 2006; Straub et al., 2007; Langley et al., 2010; Ovadnevaite et al., 2011). For example, using an AMS, Phinney et al. (2006) measured submicrometer aerosol mass concentrations of 1.4 µg m^{-3} in the remote sub-arctic Pacific Ocean. The majority of the mass was sulfate (0.74 µg m^{-3}), of which MSA was found to contribute significantly, however organics were also a large fraction of the total signal (0.3 µg m^{-3}). Ammonium and nitrate were present in low amounts, which is consistent with the results from this study (see Fig. 2). In contrast, Ovadnevaite et al. (2011) observed organic aerosol mass concentrations as high as 3.8 µg m^{-3} during high wind events from clean marine air masses. The organic mass spectra and the observation of high biological activity suggested a primary organic source. In Sect. 3.5, we show that the origin of air masses sampled during RF 5–8 was remote marine. Of the previous studies that we have discussed, the clean conditions in this study are most consistent with measurements by Phinney et al. (2006) and McInnes et al. (1996). However, as has been shown, for example, by authors like Ovadnevaite et al. (2011), clean marine environments can exhibit a large range of aerosol mass concentrations.

Of particular interest in the present study are flights with elevated sulfate concentrations. Sulfate in the marine atmosphere is primarily attributed to DMS, continental pollution, and shipping exhaust. Flights conducted between 27 July–2 August (RF 14–18) exhibited enhancements in total aerosol mass concentrations that were nearly double the amount observed during clean conditions. These flights also had some of the highest concentrations of sulfate below cloud and in residual cloud droplets. Though there were other flights in which the total aerosol mass concentration was high, the period during RF 14–18 represents nearly a week of uninterrupted enhancements in aerosol mass. Thus, we focus our attention to these flights and define them as "perturbed".

3.1 Cloud-processed aerosol

Figure 3 shows typical marine aerosol number size distributions as measured by the scanning mobility particle sizer (SMPS). In general, marine aerosol exhibits two modes at approximately 60 and 200 nm, respectively. The peak at

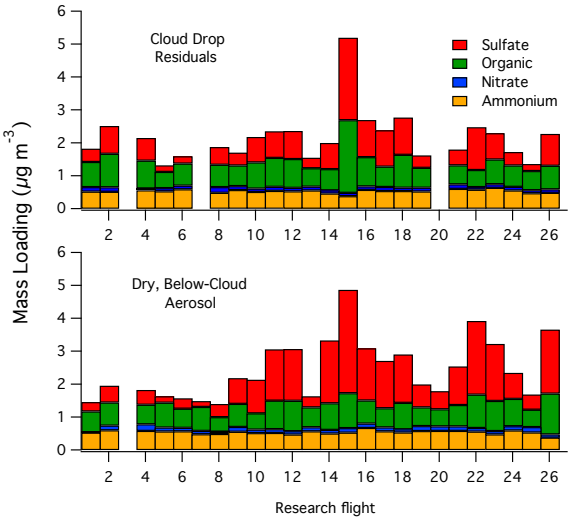

Fig. 2. Bulk AMS species measured in cloud drop residuals (top panel) and dry, below-cloud aerosol (bottom panel) over the course of the study. Only organic and sulfate vary significantly each day (variance of organic = 0.04, sulfate = 0.6 in below-cloud aerosol). Ammonium and nitrate exhibit variances that are at most 0.5 % of the variance of sulfate.

200 nm, which is the accumulation mode commonly observed in regions with marine stratocumulus (Hoppel et al., 1986, 1994; Frick and Hoppel, 2000), may be indicative of cloud processing. We note, however, that other sources can contribute to this mode. For example, Phinney et al. (2006) observed organic mass distributions during periods of direct ship fumigation with modes between 150–200 nm which may enhance number concentrations in this "cloud-processed" mode. However, given that most flights were conducted in the presence of marine stratocumulus, we suspect that cloud processing was a major contributor to aerosol in the accumulation mode.

During perturbed flights, the total aerosol volume concentration is approximately twice as large as that for clean flights. For example, the aerosol volume concentration for flights 16, 26 (perturbed) and 8, 20 (clean) are 2.24, 2.74 µm^3 cm^{-3} and 1.47, 0.47 µm^3 cm^{-3}, respectively. Representative size distributions of fresh ship exhaust from three ships (Fig. 3, bottom panel) exhibit a primary mode between 56–73 nm, which falls in the range of non cloud-processed aerosol. It is possible that ship emissions enhanced the number concentration of small mode aerosol during perturbed flights.

Cloud processing likely affected aerosol composition (Fig. 4), which is consistent with previous studies. Cloud scavenging and subsequent reaction of gaseous sulfur species lead to the accumulation of sulfate (Faloona (2009) and references therein). Under conditions of low acidity, some

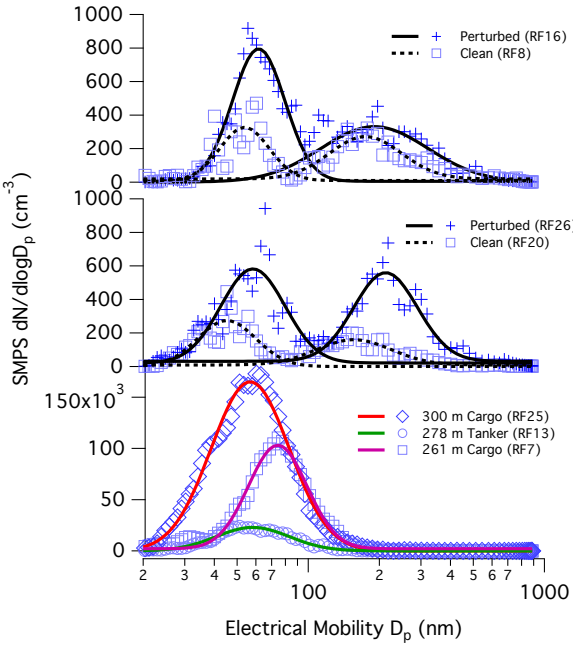

Fig. 3. Marine aerosol number size distributions of below-cloud aerosol measured during clean and perturbed flights (top and middle panels). Aerosol size distributions for the exhaust of three ships (bottom panel). Lines are log-normal fits.

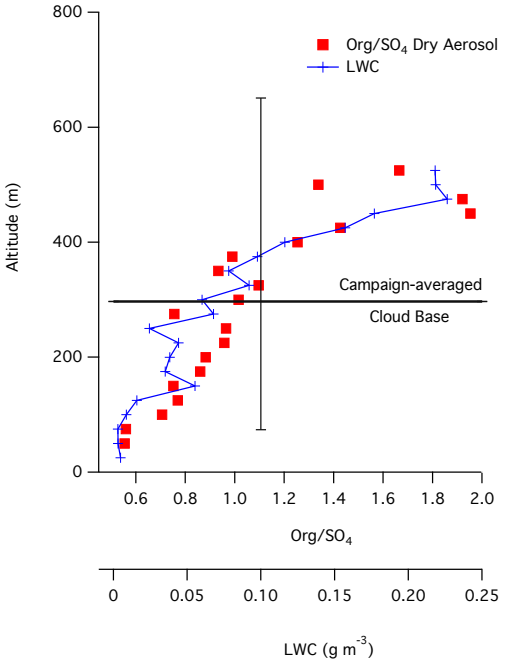

Fig. 4. Average organic:sulfate mass ratio of dry, unperturbed marine aerosol sampled in cloud-free air as a function of altitude. For clarity, standard deviations bars are omitted, however we note that variation increased with altitude. Average LWC is presented to illustrate the study-averaged, below-cloud top liquid water profile and show that cloud processing was prevalent at all altitudes. The campaign-average cloud base is shown with bars depicting the range of cloud bases and tops observed during the campaign. Cloud base altitudes were measured during aircraft soundings.

studies have shown that organics can also be formed from aqueous-phase processing. If the pH is high enough, the uptake and reaction of organic precursors (e.g., glyoxal and acetic acid) may exceed that of SO_2 (Ervens et al., 2003a,b; Sorooshian et al., 2007a) For example, Sorooshian et al. (2007a,b), showed that the ratio of oxalate:sulfate increases in cloud droplets with higher liquid water content (LWC). After the droplet evaporates, low volatility organics that may be formed by aqueous-phase chemistry remain in particle residuals (Sorooshian et al. (2007a) and references therein). Figure 4 shows the average out-of-cloud organic:sulfate ratio as a function of altitude. As observed by Sorooshian et al. (2007a), the ratio of organic:sulfate increases with altitude, a finding that is also coincident with an average increase in LWC. Though we suspect that this may be an indication of aqueous-phase chemistry, there are other processes that could affect the organic : sulfate ratio. During a typical flight, aerosol above cloud top exhibited high concentrations of organic. Previous studies have found that entrainment of air from the free troposphere into the marine boundary layer is a major source of aerosol number (Katoshevski et al., 1999; Kazil et al., 2011). If this aerosol were to be entrained into the cloud, this would elevate organic : sulfate ratios. Furthermore, it is possible that the dry aerosol shown in Fig. 4 did not result from evaporated cloud particles; rather, the aerosol could be the result of incomplete particle activation. Inorganic salts often increase the activation of organic aerosol particles (e.g. Bilde and Svenningsson, 2004). Thus, particles with higher amounts of sulfate may activate to cloud droplets first, therefore leaving behind interstitial aerosol with higher concentrations of organic. Despite these effects, it appears that cloud processing may have played a significant role controlling aerosol composition in the present study, which is consistent with the observation of a cloud-processed mode in the aerosol size distribution data (Fig. 3).

3.2 Cloud water chemistry

Figure 5 summarizes the trends in major cloud water ion and metal concentrations. These data are presented similarly to those reported by Straub et al. (2007) and Benedict et al. (2012), such that the present values can be easily compared. In this study, Cl^-, SO_4^{2-}, and NO_3^- are measured by IC and are therefore representative of soluble ions. Species such as Na, Ca, Mg and K are measured by ICP-MS. This analysis technique strictly gives information about the total metal content. In order to compare the results of the present study

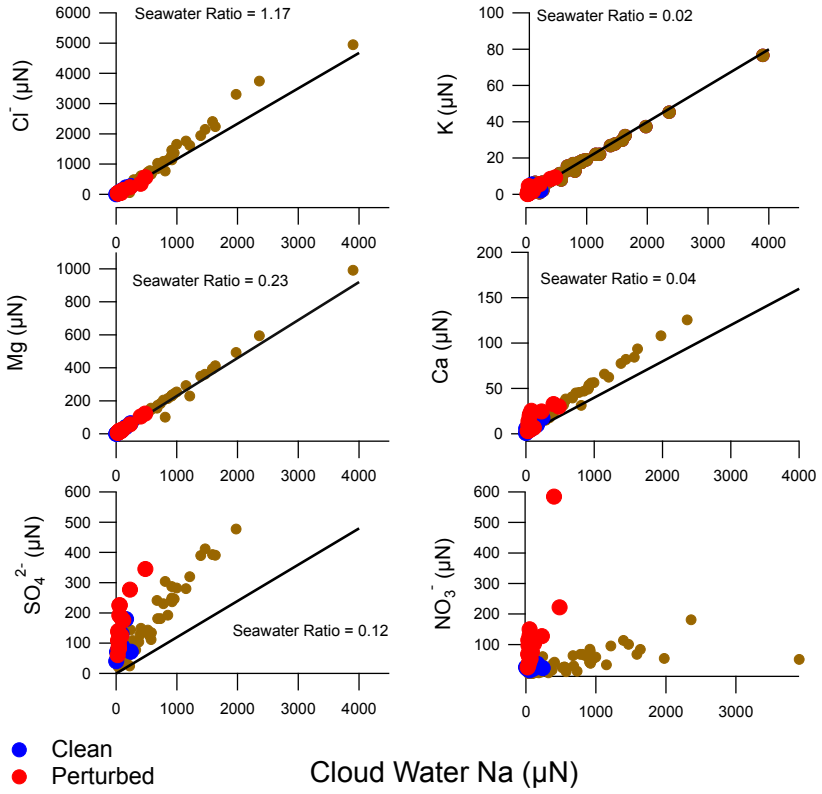

Fig. 5. Summary of major seawater species measured in marine cloud water. Data are presented analogously to those reported by Straub et al. (2007) and Benedict et al. (2012). In the present study, we assume that seawater species measured by ICP-MS (e.g., Na, K, Mg, Ca) reflect aqueous phase ions. The solid lines indicate the ion ratio typically observed in seawater. Each point represents a single cloud water measurement. Clean flights (RF 5–8) are colored in blue while perturbed flights (RF 14–18) are colored in red. The remainder of the flights are shown as brown circles.

to those by Straub et al. (2007) and Benedict et al. (2012), we assume that those species measured by ICP-MS originate from soluble seawater species and represent the ion content of each sample. Furthermore, to calculate concentrations in units of normality (μN), we assume that when present in the aqueous phase, these metals exist in their most stable valence state (for example, we assume that magnesium measured by ICP-MS exists as Mg^{2+}). If we assume that sodium concentrations reported in this study are representative of soluble sodium with +1 valence, then E-PEACE concentrations (0.7–3900 μN) are consistent with those observed by Straub et al. (2007) (36–2784 μN). Of all the common seawater species, Cl^-, Mg, and K exhibit a ratio with respect to Na that is consistent with the global average ratio found in seawater. Calcium is observed at a ratio slightly higher than typical seawater. Similar enhancements in calcium have been observed previously (e.g., Straub et al., 2007; Benedict et al., 2012) and may be the result of dissolved crustal minerals. The strong linear correlation with sodium, however, implies that the variation in calcium was primarily influenced by sea spray.

Of particular interest is the variation of seawater species between flights. Markers in Fig. 5 colored by blue and red indicate flights performed during clean (RF 5–8) and perturbed (RF 14–18) conditions, respectively. In general, the concentration of seawater species in marine cloud water is invariant during clean and perturbed flights. These species also appear to be present at lower concentrations during these flights than compared to all other flights performed during E-PEACE. It is reasonable, therefore, to neglect the mass contribution from seawater to the variation of sulfate observed in Table 3 and Fig. 2, given that clean and perturbed flights show little variation in sea-related species.

Sulfate and nitrate in the present study do not exhibit a strong linear relationship with sodium. These species are also enhanced during perturbed conditions (Fig. 5). In Sect. 3.4, we show that metals associated with shipping emissions (such as vanadium) are also enhanced during perturbed conditions and that their variation is coincident with higher

concentrations of sulfate in dry marine aerosol. It is possible that enhanced sulfate and nitrate in cloud water samples originated from ship-impacted air masses.

3.3 CCN measurements

Marine aerosol CCN measurements are summarized in Fig. 6. In the top panel, CCN activation spectra are compared for perturbed (red, RF 15) and clean (blue, RF 20) flights. In general, the fraction of activated particles at a given supersaturation is enhanced under perturbed conditions. For example, at 0.7 % supersaturation, 90 % of the particles measured during RF 15 activate in the CCN instrument. In contrast, only 60 % of the particles activate in the instrument during RF 20. If we fit a sigmoidal curve of the form $\mathrm{CCN/CN} = a_0/(1+(x/a_1)^{-a_2})$ (where a_0, a_1 and a_2 are fitted parameters) and take the inflection point to reflect the aerosol population ensemble critical supersaturation (Moore et al., 2011), we find that the critical supersaturation is lower for particles measured during RF 15 than those measured during RF 20 (0.23 % vs. 0.27 %). While this does not represent a significant difference in supersaturation, it appears that higher fractions of particles activate to CCN under perturbed conditions relative to clean conditions.

The bottom panel in Fig. 6 shows the fraction of activated particles at 0.15, 0.3, 0.5 and 0.7 % supersaturation for all dry aerosol measurements. Markers are colored by sulfate loading to illustrate the extent to which shipping emissions may have influenced the measurement. In general, a higher fraction of activated particles is coincident with elevated concentrations of sulfate. This is consistent with the averaged spectrum in Fig. 6 (top) which shows that more particles activated during perturbed flight RF 15 compared to clean flight RF 20. From Fig. 3, we see that the aerosol measured during RF 20 exhibited two modes that, when normalized by total aerosol number, have similar peak shape to aerosol measured during a perturbed flight (e.g., RF 16). The only observable difference in normalized number size distributions is that the small mode from RF 20 peaks at a smaller diameter (40 nm) than RF 16 (60 nm). While this may partially explain the increased fraction of CCN during perturbed conditions, the enhancement of activated particles may also result from elevated concentrations of sulfate (as shown in Fig. 6).

Enhanced CCN concentrations in the presence of anthropogenic pollution events has been previously observed in the Eastern Pacific (Hegg et al., 2009, 2010; Langley et al., 2010). Langley et al. (2010) found that anthropogenic pollution acted as condensation sites for sulfur species, resulting in an increase in CCN number concentrations. Hegg et al. (2010) deduced that 67 % of the CCN off the coast of California are anthropogenic in origin. The CCN concentrations reported in the present study are consistent with those results (see Table 3 comparison), suggesting that anthropogenic sources are major contributors to the CCN properties reported in Fig. 6. In Sect. 3.4, we show that increased

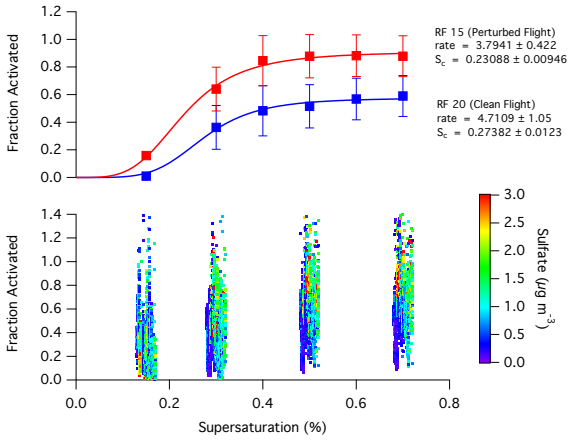

Fig. 6. CCN spectra showing the activation of particles at various supersaturations. The top panel is CCN data from a perturbed flight (red markers, RF 15) and clean flight (blue markers, RF 20) fitted to a sigmoidal curve of the form $\mathrm{CCN/CN} = a_0/(1+(x/a_1)^{-a_2})$ where a_0, a_1 and a_2 are fitted parameters. The error bars represent the measurement standard deviation. The bottom panel shows all CCN measurements made over the course of the campaign at 0.15, 0.3, 0.5 and 0.7 % supersaturation.

sulfate can be primarily linked to shipping emissions; thus, shipping emissions may have exerted a strong control on CCN properties during this study.

3.4 Relationship between marine aerosol and cloud droplet properties

In this study, sulfate is a major constituent of submicrometer marine aerosol (Fig. 2). Sulfate affects cloud water chemistry and cloud droplet number concentrations by lowering cloud water pH (via SO_2 oxidation) and increasing CCN concentrations (e.g., ship emissions, homogeneous nucleation of H_2SO_4 or MSA) (Hegg and Hobbs, 1986; Hoppel et al., 1994; Straub et al., 2007; Hegg et al., 2010; Langley et al., 2010). Sources of sulfate in the marine atmosphere include ship emissions, DMS, and continental pollution. Here, we relate sulfate measured below cloud to properties of cloud water chemistry and present evidence that elevated sulfate measured during perturbed flights was largely influenced by ship emissions. In the present discussion, we only compare trace metals such as iron and vanadium due to their links to shipping. Subsequent work will provide a more complete overview of cloud water chemistry during the E-PEACE campaign.

Figure 7 compares below-cloud sulfate with various cloud properties. Iron and vanadium were measured in cloud water samples using ICP-MS, while hydronium concentrations were calculated from cloud water pH. All data are presented in air equivalent units, which represents the mass of a species per unit volume of air (see Appendix A for details). We

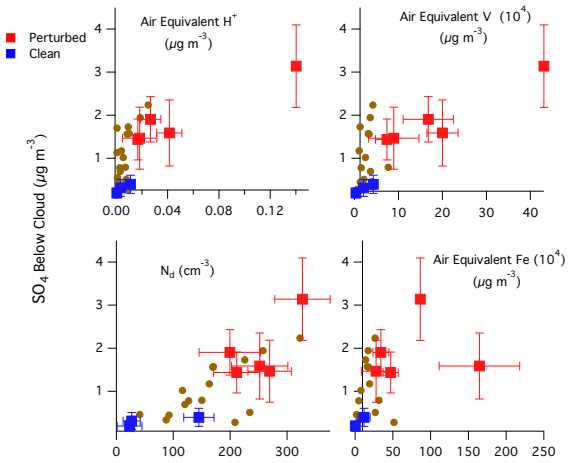

Fig. 7. Trends in below cloud sulfate vs. air equivalent H^+, cloud droplet number concentration (N_d), air equivalent V and air equivalent Fe. Iron and vanadium were measured in cloud water samples using ICP-MS. Hydronium concentrations were calculated based on cloud water sample pH. Air equivalent units are calculated as the product of the concentration of a species in a bulk cloud water sample and the average liquid water content measured during the cloud water collection period. Each point represents a single flight. Clean flights (RF 5–8) are colored blue while perturbed flights (RF 14–18) are colored red. Error bars show the standard deviation of each measurement. The remainder of the flights are shown as brown circles.

observe that sulfate in below-cloud aerosol correlates well with pH (not shown) and cloud droplet number concentration ($R^2 = -0.57$ and 0.64, respectively). This is consistent with observations of enhanced cloud water acidification and CCN in the presence of sulfate (e.g., Hoppel et al., 1994; Straub et al., 2007; Langley et al., 2010). Perturbed flights exhibit greater acidification in cloud water samples and higher concentrations of cloud droplets, vanadium, and iron as compared to clean flights. Of all the flights, the highest concentration of sulfate below cloud occurred during RF 15, which also exhibited the greatest amount of acidification, highest concentration of vanadium, highest concentration of cloud droplets, and second highest concentration of iron in cloud water samples. This enhancement is clearly seen in Table 3, where perturbed flights 14–18 exhibit 5–10 times higher concentrations of iron and vanadium than clean flights.

The hypothesis in the present study is that cloud water acidification results from the oxidation of SO_2 originating from ship emissions. This could occur by several mechanisms. SO_2 could be oxidized in the gas-phase to form sulfuric acid, which could then partition into cloud droplets or aerosol particles. If the aerosol particles were to activate, then this could subsequently lead to cloud droplet acidification. Alternatively, if exhaust were directly emitted into the cloud, then gas-phase SO_2 could partition into the cloud droplet and undergo aqueous-phase processing. The correlation with below-cloud sulfate suggests that enhanced sulfur emissions led to an decrease in pH. Even more suggestive of ship-influenced acidification is the correlation between cloud water vanadium and cloud water acidity ($R^2 = 0.8$, Fig. 8). Studies have shown that shipping emissions are the predominant source of vanadium in the marine atmosphere (Agrawal et al., 2008; Sholkovitz et al., 2009; Furutani et al., 2011). The strong correlation between vanadium and acidity and the enhancement of both during perturbed conditions implies that in the present study, shipping emissions largely contributed to cloud water acidification.

The variation in iron concentrations with below-cloud sulfate (Fig. 7) could result from a number of sources. While iron is often attributed to continental dust, recent studies suggest that iron also has significant sources from ship emissions. Using single particle mass spectrometry, Furutani et al. (2011) found that iron-containing aerosol from Asian outflows could be subdivided into several major iron-containing categories, one of which is iron associated with vanadium. Iron-containing aerosols constituted nearly 40 % of the total number of particles in the ship-associated vanadium category. While it is possible that shipping emissions enhanced iron concentrations during perturbed flights, it appears that elevated iron concentrations in the present study were largely due to continental dust. Figure 8 (bottom) shows the relationship between iron and manganese in cloud water samples. The strong correlation ($R^2 = 0.9$) suggests that the two are linked to a common source.

Manganese is primarily attributed to crustal minerals (Statham and Chester, 1988; Guieu et al., 1994; Ohta et al., 2006; Duvall et al., 2008). Iron and manganese concentrations were not strongly correlated to cloud water sulfate ($R^2 = 0.27$ and 0.29 for iron and manganese, respectively); therefore, the elevation of iron and manganese in cloud water during perturbed flights is likely indicative of air transported from continental sources. The contribution of below-cloud sulfate from continental sources is difficult to quantify given that iron and manganese are related to the transport of dust and are not directly linked to anthropogenic sources. We note, however, that iron and manganese are not strongly correlated with cloud water acidification (not shown, $R^2 = 0.36$) which we hypothesize resulted from SO_2 oxidation. Furthermore, we show in Sect. 3.5 that perturbed flights were largely affected by air masses that were transported through major shipping lanes and not by air masses that were transported directly over land. Though we cannot rule out continental sources as contributors to below-cloud sulfate, we presume that shipping emissions exerted a stronger impact on properties of marine aerosol over continental sources given that metals associated with shipping emissions, such as vanadium, are strongly correlated to other properties of cloud water chemistry such as acidification.

DMS as a major source of sulfate during perturbed flights can be ruled out in the measurements here based on the small variation of methanesulfonic acid (MSA, DMS oxidation

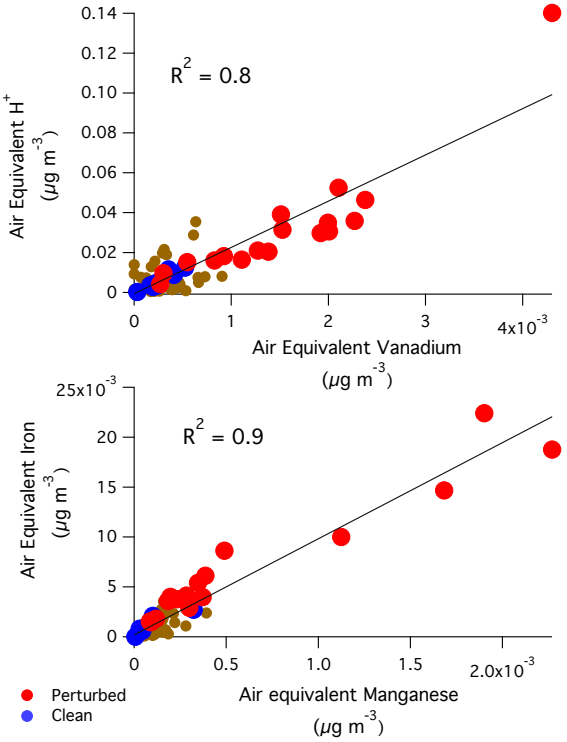

Fig. 8. Top – variation in air equivalent vanadium with respect to air equivalent hydronium concentrations for cloud water samples. Hydronium concentrations were calculated based on cloud water sample pH. Bottom – trend in manganese and iron concentrations in cloud water for measurements made during clean (blue) and perturbed (red) days, respectively.

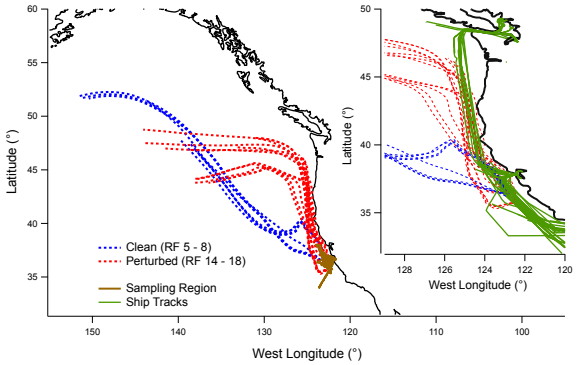

Fig. 9. Back-trajectories (72 h) of cloud water samples collected during clean (blue) and perturbed (red) flights. Back-trajectories were calculated using the NOAA HYSPLIT model (available at: http://www.arl.noaa.gov/ready/hysplit4.html). Simulations were initialized with trajectories ending at the time, location and altitude of cloud water sampling. Inset shows a closer perspective of the California coast. The green traces are the ship tracks of 15 cargo and tanker ships probed during the campaign and illustrate the general location of the shipping lanes north of Long Beach, CA.

product). Appendix Fig. A1 shows the variation of cloud water MSA and sulfate as measured by ion chromatography. The amount of MSA in cloud water was no different during perturbed flights when compared to clean or intermediate flights. We infer from these results and those from Figs. 7 and 8 that the primary source of below-cloud sulfate during perturbed flights originated from ship exhaust.

3.5 Back-trajectory comparisons

As discussed in Sect. 3.4, the variation of manganese and iron in cloud water samples is likely indicative of crustal minerals transported from continental sources. Based on these results, we presume that the enhancement in sulfate during perturbed flights was at least partly due to changes in meteorology. These inferences are supported by the 72 h (NOAA HYSPLIT) back-trajectories corresponding to cloud water samples collected during clean and perturbed flights (Fig. 9).

During clean flights, air was primarily transported across the remote ocean, which may explain the observation of low mass loadings in sulfate, organics, iron, and manganese (Table 3, Fig. 2). During flights in which there is strong evidence of anthropogenic influence, air was primarily transported along the coast and through some of the most heavily transited shipping lanes. This is consistent with the observation of enhanced vanadium (shipping influences), iron, and manganese (continental influence) in cloud water samples during perturbed flights (Figs. 7 and 8). We infer from Fig. 9 that changes in meteorology likely influenced the variation in aerosol and cloud properties and that the enhancement of sulfate below cloud during perturbed conditions is partly due to the transport of air masses through shipping lanes.

4 Ship impacts on marine aerosol and clouds

4.1 Organic aerosol mass spectra

In the following discussion, we compare organic aerosol spectra during clean and perturbed flights to investigate possible influences of ship emissions on the composition of cloud droplet residuals and dry, below-cloud marine aerosol (Fig. 10). Flight 9 (RF 9) was used as a basis for clean conditions, despite exhibiting slightly higher sulfate than most other flights categorized as clean, because in this flight, distinct ship tracks were observed next to unperturbed cloud. As shown in the column of spectra to the right of the dotted line in Fig. 10, we compare perturbed and unperturbed organic spectra of cloud droplet residuals to provide a reference to how the organic composition of cloud particles changes in the presence of ship emissions. These spectra can be compared to those from flight 15 (RF 15), which was found to have the highest concentrations of vanadium and sulfate

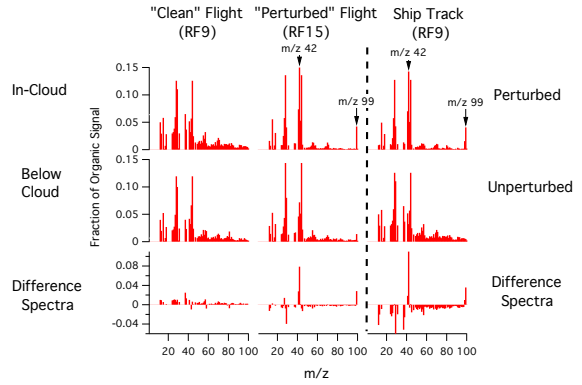

Fig. 10. Aerosol mass spectra comparing the organic signature of aerosol below and within cloud for a clean flight (RF 9) and perturbed flight (RF 15). To the right of the dotted line is a comparison of a ship track in cloud observed during RF 9 to the unperturbed, in-cloud background organics. The bottom row illustrates normalized difference spectra, which are the differences in the normalized (m/z mass/total mass) mass spectra of measurements presented in the top and middle rows. Positive values indicate a relative enhancement in masses observed in the top row spectra whereas negative values indicate a relative enhancement in masses observed in the middle row spectra.

within cloud and was the most likely to have been influenced by ship exhaust.

The top and middle rows in Fig. 10 are normalized organic mass spectra of cloud droplet residuals and dry, below-cloud aerosol, respectively. In general, aerosol and cloud residuals are highly oxidized, exhibiting strong signals at m/z 44 (CO_2^+). These spectra are consistent with marine aerosol measured by Murphy et al. (2009) and Phinney et al. (2006) and cloud droplet residuals measured by Lee et al. (2012). Jimenez et al. (2009) classified aerosol with similar mass spectra as low volatility, highly oxidized secondary organic aerosol (LV-OOA).

Many studies have shown that primary organic aerosol from ship and diesel exhaust exhibit reduced ions consistent with hydrocarbon-like organic aerosol (HOA) (e.g., Canagaratna et al., 2004; Murphy et al., 2009; Phinney et al., 2006). The prominent HOA peaks in fresh ship exhaust (m/z 55, 57, 69, 71, etc.) constitute less than 2 % of the mass in dry aerosol during perturbed flights. Murphy et al. (2009) attributed similar observations to dilution processes by comparing AMS measurements of fresh ship emissions to the organic spectrum of exhaust aged for 60 min. The authors showed that the organic fraction evolved to resemble the surrounding low volatility, unperturbed aerosol – the fraction of m/z 44 increased, while prominent HOA masses decreased. The authors note that this aging process could be explained primarily by dilution with unperturbed aerosol, however accumulation of low volatility organics may have also increased the fraction of oxidized mass.

The lack of prominent HOA masses in aged ship exhaust precludes the use of these peaks as tracers for ship emissions. Figure 10, however, provides evidence for a distinctive mass spectrum of ship emissions in perturbed cloud residuals. During RF 9, little difference existed between the organic signatures of cloud residuals and below-cloud aerosol (Fig. 10, bottom). In contrast, during RF 15, cloud residuals exhibited 8 and 3 % enhancements in masses at m/z 42 and 99 over dry, below-cloud aerosol. This enhancement in m/z 42 and 99 is also observed between the mass spectra of perturbed and unperturbed clouds (Fig. 10, third column), suggesting that m/z 42 and 99 may be linked to cloud-processed ship emissions.

The source of m/z 42 and 99 can be further investigated when considering the time series trend of m/z 99 across multiple flights. Figure 11 illustrates the variation of m/z 99, LWC, and bulk AMS traces for (1) RF 9 – moderately clean, cloudy (2) RF 16 – perturbed, cloudy (3) RF 27 – moderately clean, no clouds and (4) RF 28 – moderately clean, clouds. Flights RF 27 and RF 28 were additional experiments that were conducted outside the sampling area shown in Fig. 1. These flights were performed along the coastline starting in Monterey Bay and ending near the California/Oregon border. Figure 12 shows the flight paths of RF 27 and RF 28 in relationship to the sampling area shown in Fig. 1. Back-trajectories of samples measured in the middle of each flight show that air was transported from the same direction on both days.

Inspection of Fig. 11 reveals multiple trends consistent with the inferences drawn from Fig. 10. First, we note that the time series of m/z 99 varies with bulk AMS traces and is most prominent when measuring ship tracks and perturbed air masses. The time series of m/z 99 shows an enhancement in mass when ship tracks are detected (marked, Fig. 11), which is not observed in nearby unperturbed clouds. Also, we see that m/z 99 is highly variable both in and out of cloud and is coincident with variations of sulfate during a perturbed flight (RF 16). From these results, we infer that the source of m/z 99 is shipping exhaust.

The trends in Fig. 11 also imply that m/z 99 is linked to cloud processing. Among the flights presented, RF 27 was the only one performed under clear meteorological conditions. This is evident by the negligible LWC during vertical soundings. In addition, the larger mode in the aerosol size distribution (Fig. 11, top row) peaks at a lower diameter (77 nm) during clear conditions than during cloudy conditions (180–250 nm). This, along with the low LWC, possibly implies that cloud processing contributed less mass to below-cloud aerosol during RF 27 than other flights. The time series of m/z 99 during RF 27 shows little variation over the course of the flight. If we contrast this to RF 28, which was performed during a cloudy day and along a similar flight path (as illustrated in Fig. 12), we see that the variation of m/z 99

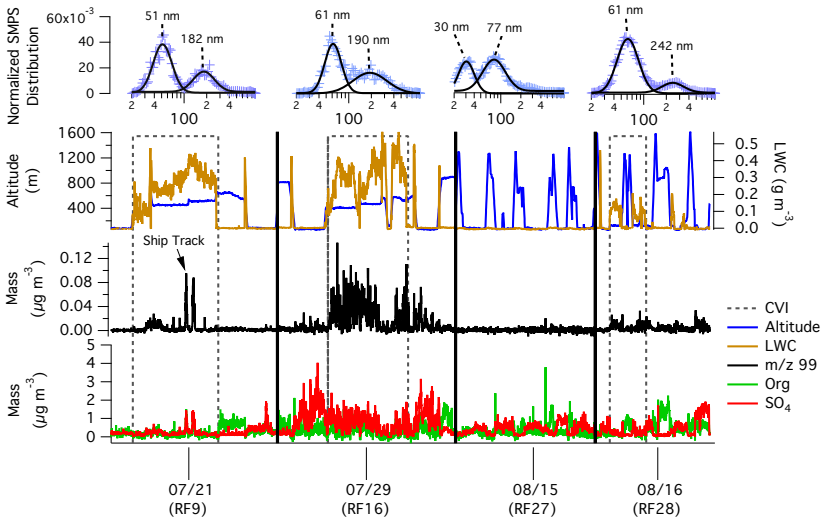

Fig. 11. Time series of organic, sulfate, organic m/z 99, LWC and altitude for research flights RF 9 (moderately clean, clouds), RF 16 (perturbed, clouds), and two additional flights that were performed outside the sampling region defined in Fig. 1, RF 27 (moderately clean, no clouds) and RF 28 (moderately clean, clouds). The top row of normalized aerosol number distributions ($dN/d\log D_p$/(integrated loading)) show the distribution of marine aerosol below cloud for each flight. The dotted boxes show periods when samples were collected through the CVI inlet.

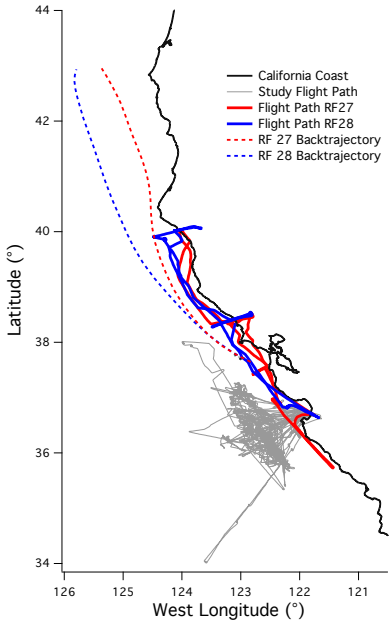

Fig. 12. Path of additional flights RF 27 (red) and RF 28 (blue) compared to the path of all other flights in the present study (grey). Dotted lines are back-trajectories (24 h) for air masses measured during the middle of each flight. RF 27 and RF 28 were coastal gradient flights conducted on clear (RF 27) and cloudy (RF 28) days.

is enhanced in and out of cloud. This evidence, along with the variation of m/z 99 in ship-impacted air masses, leads us to conclude that the variation of m/z 99 likely results from cloud processing of ship emissions.

4.2 Application of m/z 42 and 99 in evaluating ship-impacted airspace

Given the unit mass resolution of the C-ToF AMS, a number of masses could be responsible for the signals observed at m/z 42 and 99. The species $C_2H_2O^+$, $C_3H_6^+$, $C_2H_4N^+$ and $CHOCl_2^+$ are the non-isotopic ions present at m/z 42 while $C_8H_3^+$, $C_6H_{11}O^+$, $C_5H_7O_2^+$ and $C_7H_{15}^+$ are the non-isotopic ions present at m/z 99. Thus, the variation of m/z 42 and 99 in ship-impacted clouds could result from the fragmentation of aqueous-phase oxidation products ($C_2H_2O^+$, $C_5H_7O_2^+$, and $C_6H_{11}O^+$), alkane species ($C_7H_{15}^+$) or unsaturated carbon chains ($C_3H_6^+$, $C_8H_3^+$). High-resolution AMS measurements of marine aerosol performed onboard the R/V *Point Sur* suggests that the enhancements in masses at m/z 42 and 99 result from the increase in signal from $C_2H_2O^+$ and $C_5H_7O_2^+$ (see Sect. 4.3). This supports the presumption that the enhancement of m/z 42 and 99 in perturbed air masses result from aqueous-phase oxidation of ship emissions. We note that other masses, such as m/z 44, are prominent in the mass spectra of ship emissions measured in-cloud (see Fig. 10). We suspect that these masses also result from cloud-processed ship emissions. However, given that these masses also dominate surrounding unperturbed air masses,

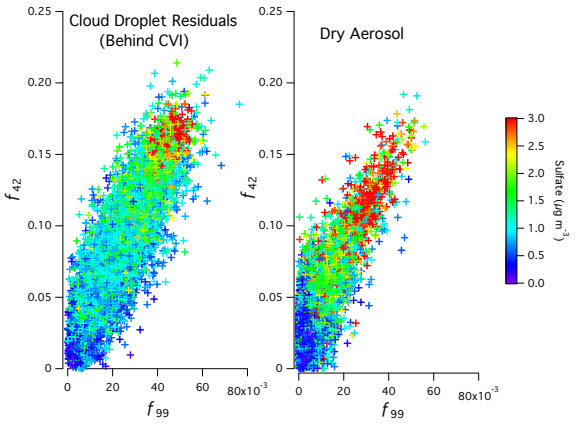

Fig. 13. Variation of the organic fraction of m/z 42 and m/z 99 (f_{42}, f_{99}) in the organic spectra of cloud water droplet residuals and dry aerosol. Markers are colored by sulfate loading to illustrate the potential impact of ships on each measurement.

we believe that using m/z 42 and 99 as tracers for cloud-processed ship emissions will help to delineate the source of subsequent marine aerosol measurements.

Given the large fraction of m/z 42 and 99 in perturbed air relative to clean air, we propose using these masses to indicate the degree to which shipping emissions affect marine aerosol. Figure 13 shows the relationship between the fractions of m/z 42 and 99 in the present study. Markers are colored by sulfate mass concentrations to illustrate the extent to which ships may have impacted each measurement. These plots show that the fraction of m/z 42 in the organic spectra strongly correlates with the fraction of m/z 99, with $R^2 = 0.72$ and 0.67 for measurements of cloud droplet residuals and dry aerosol, respectively. Also, higher fractions of m/z 42 and 99 are coincident with higher loadings of sulfate. Appendix Fig. A2 shows the Pearson R correlation spectrum relating the fraction of m/z 42 and 99 with sulfate loading (top) and the fraction of all other organic masses (middle, bottom). Of all the masses in the organic spectrum, m/z 42 and 99 have the strongest correlation with sulfate ($R = 0.58$ and 0.53, respectively). This correlation could result from simultaneous aqueous phase sulfur oxidation or from the presence of sulfate in shipping emissions. Similarly, these two ions appear to correlate only with each other and not with typical aerosol tracers (e.g., m/z 57 for HOA spectra and m/z 44 for OOA). The relationship between m/z 42 and 99 appears to be unique and strongly linked to ship emissions.

If we take the fraction of m/z 42 and m/z 99 to reflect the degree of cloud-processed ship emissions (as suggested by Figs. 10 and 11) and that ship emissions are coincident with elevated sulfate concentrations (as suggested by Fig. 7 and the observation of high sulfate during the heaviest ship-influenced flights), then we see that Fig. 13 illustrates the extent to which ship emissions influence marine aerosol. Therefore, we propose a metric by which one can evaluate the extent of ship-impacted air masses in the presence of clouds. Measurements of the organic fractions of m/z 42 (f_{42}) and 99 (f_{99}) scattering about the red markers in Fig. 13 ($f_{42} > 0.15$; $f_{99} > 0.04$) would imply heavy influence from shipping emissions. Measurements of m/z 42 and 99 scattering about the green markers ($0.05 < f_{42} < 0.15$; $0.01 < f_{99} < 0.04$) would imply moderate, but persistent, ship influences. Finally, measurements of m/z 42 and 99 scattering about the blue markers ($f_{42} < 0.05$; $f_{99} < 0.01$) would imply clean, non-ship-influenced air. If we apply these metrics to the data in the present study, this would imply that 72 % of the measurements made behind the CVI and 12 % of measurements of dry aerosol were at least moderately impacted by ship emissions.

Despite observing similar spectra from cloud-processed organics originating from many different ships during the E-PEACE campaign, we note that shipping emissions are highly variable. Thus, one cannot assume that all cloud-processed shipping emissions will exhibit the same mass spectra as those presented here. Furthermore, we were unable to determine an exact chemical source for the masses at m/z 42 and 99. Therefore, this proposed metric is subject to future identification of the exact source of these masses. We note that further investigations into the chemical origin of m/z 42 and 99 might also help to elucidate chemical processes not yet identified in current literature.

4.3 High resolution AMS analysis of ions at m/z 42 and 99

Additional aerosol properties were measured below cloud onboard the R/V *Point Sur* from 13–23 July. The R/V *Point Sur* was primarily deployed to generate controlled ship tracks for aerosol/cloud interaction studies (Russell et al., 2012); however, the high-resolution AMS onboard the R/V *Point Sur* continuously sampled marine aerosol. As shown in Table 3 and Fig. 2, the first half of the cruise (14–19 July) was coincident with the cleanest period of the study, whereas the latter half of the cruise (20–23 July) corresponded to periods of elevated sulfate. Investigating the variation of ions at m/z 42 and 99 during the latter half of the cruise is likely to provide information relevant to ship-impacted air masses.

Table 4 summarizes the fraction of the non-isotopic ions at m/z 42 and 99 during the R/V *Point Sur* cruise. Over the entire cruise (top), ions $C_2H_2O^+$ (m/z 42) and $C_5H_7O_2^+$ (m/z 99) constitute the majority (> 50 %) of the mass at their respective m/z. The contribution of these ions to the total signal increased during the latter half of the cruise. The fraction of other ions either decreased or increased little (< 3 %) during the period of elevated sulfate (bottom), implying that ions at m/z 42 and 99 other than $C_2H_2O^+$ and $C_5H_7O_2^+$ are not strongly associated with ship emissions.

Table 4. Fraction of each ion at m/z 42 and m/z 99 over the entire R/V *Point Sur* cruise (top) and during periods of high sulfate loading (bottom). Values in parenthesis are the variance in the measurement.

m/z 42 Average over entire cruise			m/z 99 Average over entire cruise		
Ion	Fraction of total organic signal	Fraction of signal at m/z 42	Ion	Fraction of total organic signal	Fraction of signal at m/z 99
$C_2H_2O^+$	0.014 (5.11×10^{-5})	0.57 (0.030)	$C_5H_7O_2^+$	4.22×10^{-4} (1.26×10^{-7})	0.51 (0.044)
$C_3H_6^+$	0.008 (2.43×10^{-5})	0.33 (0.037)	$C_7H_{15}^+$	2.42×10^{-4} (5.48×10^{-8})	0.21 (0.036)
$C_2H_4N^+$	0.002 (2.36×10^{-6})	0.08 (0.005)	$C_6H_{11}O^+$	1.84×10^{-4} (2.40×10^{-8})	0.19 (0.020)
$CHOCl_2^+$	4.01×10^{-4} (1.26×10^{-7})	0.02 (0.0004)	$C_8H_3^+$	7.81×10^{-5} (9.21×10^{-9})	0.09 (0.008)
Average during period of elevated sulfate (19–23 Jul)			Average during period of elevated sulfate (19–23 Jul)		
Ion	Fraction of total organic signal	Fraction of signal at m/z 42	Ion	Fraction of total organic signal	Fraction of signal at m/z 99
$C_2H_2O^+$	0.020 (5.07×10^{-5})	0.72 (0.013)	$C_5H_7O_2^+$	6.72×10^{-4} (1.25×10^{-7})	0.58 (0.030)
$C_3H_6^+$	0.004 (8.27×10^{-6})	0.15 (0.009)	$C_7H_{15}^+$	2.23×10^{-4} (5.11×10^{-8})	0.15 (0.023)
$C_2H_4N^+$	0.003 (2.51×10^{-6})	0.11 (0.006)	$C_6H_{11}O^+$	2.23×10^{-4} (2.78×10^{-8})	0.18 (0.013)
$CHOCl_2^+$	2.92×10^{-4} (1.21×10^{-7})	0.01 (0.0004)	$C_8H_3^+$	1.08×10^{-4} (1.17×10^{-8})	0.10 (0.007)

Based on Table 4, we presume that $C_2H_2O^+$ and $C_5H_7O_2^+$ are the major ions responsible for the variation in m/z 42 and 99 observed in Fig. 9. Even though the alkane ion at m/z 99 ($C_7H_{15}^+$) constituted approximately 20 % of the signal, this ion can be ruled out as a major contributor to the variation in m/z 99 because other major HOA-type ions (m/z 55, 57, 69, 71, etc.) were not observed to vary significantly with m/z 42 or 99 (see Appendix Fig. A2). $C_3H_6^+$ was also variable and constituted a significant fraction of the signal at m/z 42. Though the contribution of this ion decreased when averaged during the perturbed period, $C_3H_6^+$ is an unsaturated, reduced ion of the series $C_nH_{2n}^+$, which is likely alkene in nature (McLafferty, 1980), that could have originated from an HOA or aged organic source.

Appendix Fig. A3 shows the variation in the organic fraction of $C_2H_2O^+$ and $C_3H_6^+$ at m/z 42 versus the organic fraction of $C_5H_7O_2^+$ at m/z 99. Over the entire cruise, $C_2H_2O^+$ is better correlated with $C_5H_7O_2^+$ than with the reduced ion ($R^2 = 0.49$ versus $R^2 = -0.09$, respectively). The two oxidized ions also exhibit a positive correlation that is consistent with the variation of m/z 42 and m/z 99 observed in Fig. 13. The variation appears to be coincident with increasing sulfate, which is also similar to the trend observed in Fig. 13. Appendix Fig. A3 also shows the time series trends of each ion at m/z 42 and 99 during the clean and perturbed periods. During the clean period, there is little variation in the ions at their respective masses. In contrast, during the periods of inceased sulfate, the variations at m/z 42 and 99 are enhanced and are mostly attributable to $C_2H_2O^+$ and $C_5H_7O_2^+$. In conjunction with Table 5, Fig. A3 suggests that the variations in m/z 42 and 99 observed in C-ToF AMS measurements result from the enhancement of the oxidized ions $C_2H_2O^+$ and $C_5H_7O_2^+$, respectively.

5 Conclusions

A major finding of the present work is the identification of aerosol mass spectral peaks at m/z 42 and 99 as markers for cloud-processed ship emissions. The co-variation of m/z 42 and 99 in dry marine aerosol is unique and likely due to ship emissions that were processed by clouds and subsequently dried. Based on high-resolution AMS measurements, it appears that these masses were primarily due to variations in oxidized ions. In the present study, we are unable to link the variation of these ions to a specific chemical source. Therefore, until future studies can identify a specific compound that is linked to m/z 42 and 99, we must caution that not all cloud-processed shipping emissions may

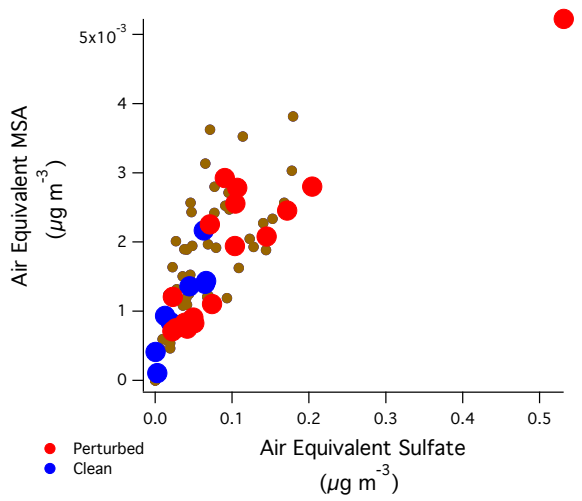

Fig. A1. Variation of air equivalent MSA and sulfate in cloud water droplets. Red markers represent measurements made during perturbed flights (RF 14–18), blue markers represent measurements made during clean flights (RF 5–8). Brown markers are all other measurements.

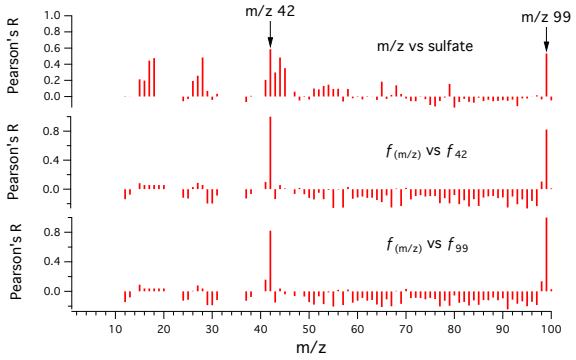

Fig. A2. Pearson R spectrum showing the variation of m/z concentrations vs. the concentration of sulfate (top), the variation of the fraction of m/z 42 (f_{42}) against the fraction of all other organic masses (middle), and the variation of the fraction of m/z 99 (f_{99}) against the fraction of all other organic masses (bottom). These correlations were calculated for measurements made outside of cloud.

exhibit enhancements in these ions. Further investigations into the source of these ions may provide information about the chemical transformations of shipping emissions in the marine atmosphere.

Though the exact chemical source remains uncertain, one can use the fractions of m/z 42 and m/z 99 as a proxy for determining the extent of ship influences on cloud and aerosol properties in the marine environment. Measurements of the organic fractions of m/z 42 (f_{42}) and 99 (f_{99}) falling within the range $f_{42} > 0.15$; $f_{99} > 0.04$ would imply heavy influence from shipping emissions. Measurements of m/z 42 and 99 in the range $0.05 < f_{42} < 0.15$; $0.01 < f_{99} < 0.04$ would imply moderate, but persistent influences from ships. Finally, measurements of m/z 42 and 99 in the range $f_{42} < 0.05$; $f_{99} < 0.01$ would imply clean, non-ship-influenced air. These proxies apply under the condition in which clouds have been impacted by ship emissions. The results from this study also suggest that shipping exhaust is a major contributor to marine aerosol in regions of heavy shipping. If we apply the proposed conditions for moderate shipping influences, we find that 72 % of the measurements illustrated in Fig. 13 are (at least) moderately perturbed cloud particles, while 12 % of the measurements are moderately perturbed evaporated cloud droplets. The marine atmosphere off the coast of Central California is likely seldom free from shipping influences and exhibits a persistent shipping signature on marine particles in the region defined between latitude 35.5–37.5° N and longitude 122–123.25° W.

Appendix A

Additional instrument information

A1 Physical properties of aerosol and cloud droplets

Cloud and aerosol properties were measured onboard the Twin Otter using a suite of wing-mounted probes and cabin-based size classifiers. Aerosol size and number concentrations were measured outside the aircraft using a passive cavity aerosol spectrometer probe (PCASP) (Particle Measuring Systems, Boulder, CO). Simultaneous measurements were performed behind the main aerosol inlet/CVI using a custom-built scanning mobility particle sizer (SMPS) consisting of a differential mobility analyzer (DMA, model 3081, TSI) coupled to a condensation particle counter (CPC 3010, TSI, Shoreview, MN). PCASP and SMPS were calibrated using polystyrene latex spheres.

Cloud droplet distributions were measured using a cloud, aerosol and precipitation spectrometer (CAS) (Droplet Measurement Technologies, Boulder, CO) and was calibrated using glass beads. Cloud droplet number concentrations presented in this study reflect integrated CAS distributions for particles with diameters 2–50 µm.

Cloud condensation nuclei (CCN) number concentrations were measured using a streamwise thermal-graident cloud condensation nuclei counter (CCNC, Droplet Measurement Technologies) (Lance et al., 2006; Roberts and Nenes, 2005). A flow orifice and active control system was used to maintain instrument pressure at 700 mb independent of ambient pressure. The instrument was mostly run in scanning flow CCN analysis (SCFA) mode (Moore and Nenes, 2009). SFCA produced CCN spectra over the range 0.15–0.85 % supersaturation every forty seconds. During zig-zag ship intercepts,

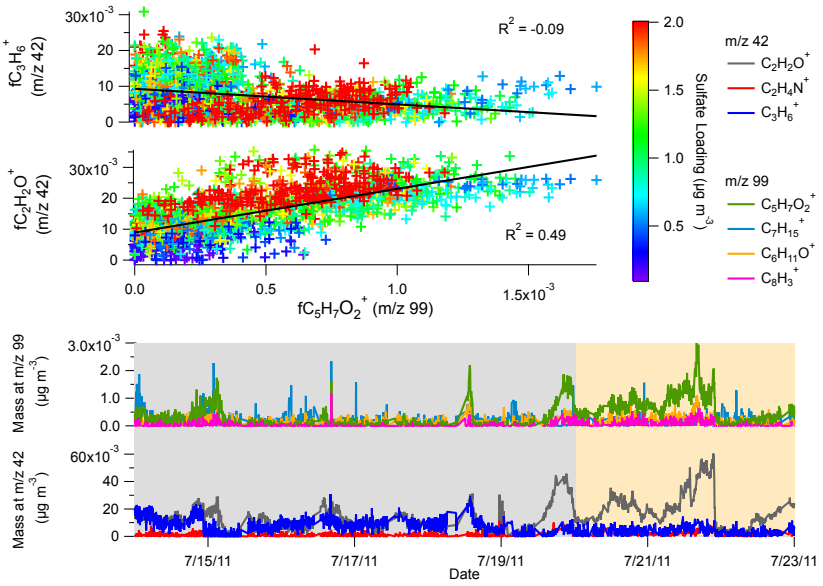

Fig. A3. Top – variation of $C_2H_2O^+$ and $C_3H_6^+$ at m/z 42 with $C_5H_7O_2^+$ at m/z 99. Markers are colored by sulfate loading. Bottom – time series trend showing the variation of the ions at m/z 42 and 99. Region shaded grey corresponds to the clean period of the cruise, region shaded light brown corresponds to the perturbed period of cruise.

CCNC operation was switched to conventional operation, maintaining a constant flow rate and constant 0.15 % supersaturation.

A2 Composition measurements by aerosol mass spectrometry

A compact time-of-flight (CToF) aerosol mass spectrometer (AMS, Aerodyne Research Inc., Billerica, MA) was used onboard the Twin Otter to measure bulk aerosol chemistry. A high-resolution time-of-flight AMS (HR-ToF-AMS) was used onboard the R/V *Point Sur* to characterize detailed aerosol chemistry. The AMS has been described elsewhere and only a brief description is given here (Jayne et al., 2000; Allan et al., 2004; Drewnick et al., 2005). The AMS measures the ensemble average mass spectra and chemically resolved size distribution of non-refractory particle phase organic and inorganic species. Spectra were analyzed in IGOR Pro (WaveMetrics, Inc., Lake Oswego, Oregon, USA) using the SQUIRREL v 1.51H and PIKA v 1.10H modules. Gas phase interferences were corrected using the fragmentation table developed by Allan et al. (2004) and Aiken et al. (2008).

Onboard the Twin Otter, MS mode was run for 8 s per saved run. A pressure-controlled inlet was used to maintain a flow rate of 1.4 $cm^{-3}\,s^{-1}$ to the AMS vacuum chamber. Prior to each flight, the AMS ionization efficiency (the ratio of the number of molecules ionized to the total number of molecules that enter the instrument) was calibrated using dried 350 nm NH_4NO_3 particles. Detection limits were taken to be twice the standard deviation of organic, sulfate, nitrate, ammonium and total mass measured during the filter period.

Composition dependent collection efficiencies (CE) were calculated based on the method by Middlebrook et al. (2012). Figure A4 compares aerosol mass concentrations measured by AMS to calculated aerosol mass concentrations from SMPS data before (left) and after (right) applying the CE correction factor. Volume concentrations measured by the SMPS were calculated by integrating SMPS data from 60–1000 nm. Volume concentrations were then converted to mass concentrations assuming a density of 1.6 g cm^{-3}, which is representative of a mixture of 60 % sulfuric acid ($\rho = 1.84$ g cm^{-3}) and 40 % organics ($\rho = 1.2$ g cm^{-3}) (Phinney et al., 2006). Before applying the CE correction, AMS and SMPS data scatter below the 1 : 1 line with a slope of 0.45. After applying the CE correction, AMS and SMPS data scatter close to the 1 : 1 line with a slope of 0.85. The bias towards higher aerosol mass concentrations calculated from SMPS data may result from a number of unknowns including overestimation of aerosol density, uncertainty of particle losses in the SMPS instrument and uncertainty in the amount of non-refractory material present in the aerosol. In general, however, the good agreement warrants use of the method developed by Middlebrook et al. (2012) in estimating the CE correction factor.

A3 Cloud water chemistry

Cloud water samples were collected using a modified Mohen slotted cloudwater collector (Hegg and Hobbs, 1986).

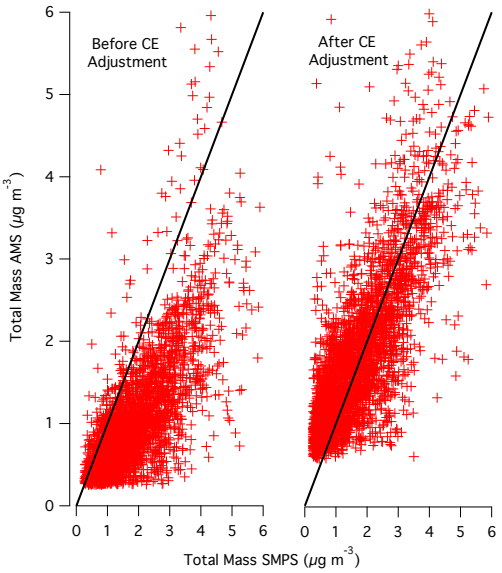

Fig. A4. Comparison of collection efficiency (CE) corrected AMS mass measurements to calculated total mass measured by SMPS. The plot on the left is the trend before CE correction (slope = 0.45), the plot on the right is the trend after CE correction (slope = 0.85). Volume concentration measured by SMPS was converted to mass concentration assuming a density of 1.6 g cm^{-3}, which is representative of a mixture of 60 % sulfuric acid ($\rho = 1.84$ g cm^{-3}) and 40 % organics ($\rho = 1.2$ g cm^{-3}) (Phinney et al., 2006).

Samples were collected at various altitudes and stored at 4 °C until chemical analysis could be performed. Trace metals were measured using inductively coupled plasma mass spectrometry (ICP-MS) and major ions were measured using ion chromatography (IC).

To compare cloud water chemistry measured by off-line analysis to below-cloud aerosol loading measured by AMS, cloud water sample concentrations (ppb) were converted to air equivalent concentrations (μg m^{-3}) as prescribed by (Straub et al., 2007). To achieve this conversion, the ion concentrations measured by ICP-MS and IC were multiplied by the average LWC recorded during sample collection. Measurements reported in air equivalent units reflect the total amount of material present per volume of air.

Acknowledgements. This work was funded by ONR grants N00014-11-1-0783, N00014-10-1-0200, and N00014-10-1-0811, and NSF grants AGS-1013381 and AGS-1008848. We acknowledge Dean Hegg for providing the cloud water collector.

Edited by: R. Krejci

References

Ackerman, A. S., Toon, O. B., and Hobbs, P. V.: Numerical modeling of ship tracks produced by injections of cloud condensation nuclei into marine stratiform clouds, J. Geophys. Res., 100, 7121–7133, 1995.

Agrawal, H., Malloy, Q. G. J., Welch, W. A., Wayne Miller, J., and Cocker III, D. R.: In-use gaseous and particulate matter emissions from a modern ocean going container vessel, Atmos. Environ., 42, 5504–5510, 2008.

Aiken, A. C., DeCarlo, P. F., Kroll, J. H., Worsnop, D. R., Huffman, J. A., Docherty, K. S., Ulbrich, I. M., Mohr, C., Kimmel, J. R., Sueper, D., Sun, Y., Zhang, Q., Trimborn, A., Northway, M., Ziemann, P. J., Canagaratna, M. R., Onasch, T. B., Alfarra, M. R., Prevot, A. S. H., Dommen, J., Duplissy, J., Metzger, A., Baltensperger, U., and Jimenez, J. L.: O/C and OM/OC ratios of primary, secondary, and ambient organic aerosols with high-resolution time-of-flight aerosol mass spectrometry, Environ. Sci. Technol., 42, 4478–4485, 2008.

Allan, J., Delia, A., Coe, H., Bower, K., Alfarra, M., Jimenez, J., Middlebrook, A., Drewnick, F., Onasch, T., and Canagaratna, M.: A generalised method for the extraction of chemically resolved mass spectra from aerodyne aerosol mass spectrometer data, J. Aerosol Sci., 35, 909–922, 2004.

Benedict, K. B., Lee, T., and Collett Jr., J. L.: Cloud water composition over the Southeastern Pacific Ocean during the VOCALS regional experiment, Atmos. Environ., 46, 104–114, 2012.

Bilde, M. and Svenningsson, B.:CCN activation of slightly soluble organics: the importance of small amounts of inorganic salt and particle phase, Tellus, 56B, 128–134, 2004.

Canagaratna, M. R., Jayne, J. T., Ghertner, D. A., Herndon, S., Shi, Q., Jimenez, J. L., Silva, P. J., Williams, P., Lanni, T., Drewnick, F., Demerjian, K. L., Kolb, C. E., and Worsnop, D. R.: Chase studies of particulate emissions from in-use New York City vehicles, Aerosol Sci. Tech., 38, 555–573, 2004.

Christensen, M. W. and Stephens, G. L.: Microphysical and macrophysical responses of marine stratocumulus polluted by underlying ships: Evidence of cloud deepening, J. Geophys. Res., 116, D03201, doi:10.1029/2010JD014638, 2011.

Coakley, J., Bernstein, R., and Durkee, P.: Effect of ship-stack effluents on cloud reflectivity, Science, 237, 1020–1022, 1987.

Corbett, J. J. and Fischbeck, P.: Emissions from ships, Science, 278, 823–824, 1997.

Cunningham, W. C. and Zoller, W. H.: The chemical composition of remote aerosols, J. Aerosol Sci., 12, 367–384, 1981.

Drewnick, F., Hings, S., DeCarlo, P., Jayne, J., Gonin, M., Fuhrer, K., Weimer, S., Jimenez, J., Demerjian, K., Borrmann, S., and Worsnop, D.: A new Time-Of-Flight Aerosol Mass Spectrometer (TOF-AMS) – instrument description and first field deployment, Aerosol Sci. Tech., 39, 637–658, 2005.

Durkee, P. A., Noone, K. J., and Bluth, R. T.: The Monterey area ship track experiment, J. Atmos. Sci., 57, 2523–2541, 2000.

Duvall, R. M., Majestic, B. J., Shafer, M. M., Chuang, P. Y., Simoneit, B. R. T., and Schauer, J. J.: The water-soluble fraction of carbon, sulfur, and crustal elements in Asian aerosols and Asian soils, Atmos. Environ., 42, 5872–5884, 2008.

Eyring, V., Kohler, H., van Aardenne, J., and Lauer, A.: Emissions from international shipping: 1. The last 50 years, J. Geophys. Res., 110, D17305, doi:10.1029/2004JD005619, 2005.

Ervens, B., Gligorovski, S. and Herrmann, H.:Temperature-dependent rate constants for hydroxyl radical reactions with organic compounds in aqueous solutions, Phys. Chem. Chem. Phys., 5, 1811–1824, 2003a.

Ervens, B., George, C., Williams, J.E., Buxton, G.V., Salmon, G.A., Bydder, M., Wilkinson, F., Dentener, F., Mirabel, P., Wolke, R., Herrmann, H.:CAPRAM 2.4 (MODAC mechanism): An extended and condensed tropospheric aqueous phase mechanism and its application, J. Geophys. Res., 108, 4426, doi:10.1029/2002JD002202, 2003b.

Faloona, I.: Sulfur processing in the marine atmospheric boundary layer: A review and critical assessment of modeling uncertainties, Atmos. Environ., 43, 2841–2854, 2009.

Frick, G. and Hoppel, W.: Airship measurements of ship's exhaust plumes and their effect on marine boundary layer clouds, J. Atmos. Sci., 57, 2625–2648, 2000.

Furutani, H., Jung, J., Miura, K., Takami, A., Kato, S., Kajii, Y., and Uematsu, M.: Single-particle chemical characterization and source apportionment of iron-containing atmospheric aerosols in Asian outflow, J. Geophys. Res., 116, D18204, doi:10.1029/2011JD015867, 2011.

Guieu, C., Duce, R., and Arimoto, R.: Dissolved input of manganese to the ocean: Aerosol source, J. Geophys. Res., 99, 18789–18800, 1994.

Hegg, D. A. and Hobbs, P. V.: Sulfate and nitrate chemistry in cumuliform clouds, Atmos. Environ., 20, 901–909, 1986.

Hegg, D. A., Covert, D. S., Rood, M. J., and Hobbs, P. V.: Measurements of aerosol optical properties in marine air, J. Geophys. Res., 101, 12893–12903, 1996.

Hegg, D.A., Covert, D.S., Jonsson, H., Covert, P.A.: Determination of the Transmission Efficiency of an Aircraft Aerosol Inlet, Aerosol Sci. Technol., 39, 966–971, 2005.

Hegg, D. A., Covert, D. S., and Jonsson, H. H.: Measurements of size-resolved hygroscopicity in the California coastal zone, Atmos. Chem. Phys., 8, 7193–7203, doi:10.5194/acp-8-7193-2008, 2008.

Hegg, D. A., Covert, D., Jonsson, H., and Woods, R.: Differentiating natural and anthropogenic cloud condensation nuclei in the California coastal zone, Tellus B, 61, 669–676, 2009.

Hegg, D. A., Covert, D. S., Jonsson, H. H., and Woods, R. K.: The contribution of anthropogenic aerosols to aerosol light-scattering and CCN activity in the California coastal zone, Atmos. Chem. Phys., 10, 7341–7351, doi:10.5194/acp-10-7341-2010, 2010.

Hersey, S. P., Sorooshian, A., Murphy, S. M., Flagan, R. C., and Seinfeld, J. H.: Aerosol hygroscopicity in the marine atmosphere: a closure study using high-time-resolution, multiple-RH DASH-SP and size-resolved C-ToF-AMS data, Atmos. Chem. Phys., 9, 2543–2554, doi:10.5194/acp-9-2543-2009, 2009.

Hoppel, W., Frick, G., and Larson, R.: Effect of nonprecipitating clouds on the aerosol size distribution in the marine boundary layer, Geophys. Res. Lett., 13, 125–128, 1986.

Hoppel, W., Frick, G., and Fitzgerald, J.: Marine boundary layer measurements of new particle formation and the effects nonprecipitating clouds have on aerosol size distribution, J. Geophys. Res., 99, 14443–14459, 1994.

Hudson, J. G., Garrett, T. J., Hobbs, P. V., Strader, S. R., Xie, Y., and Yum, S. S.: Cloud Condensation Nuclei and Ship Tracks, J. Atmos. Sci., 57, 2696–2706, 2000.

Jayne, J. T., Leard, D. C., Zhang, X., Davidovits, P., Smith, K. A., Kolb, C. E., and Worsnop, D. R.: Development of an aerosol mass spectrometer for size and composition analysis of submicron particles, Aerosol Sci. Tech., 33, 49–70, 2000.

Jimenez, J. L.,Canagaratna, M. R., Donahue, N. M.,Prévôt, A. S. H., Zhang, Q., Kroll, J. H., DeCarlo, P. F., Allan, J. D., Coe, H., Ng, N. L., Aiken, A. C., Docherty, K. S., Ulbrich, I. M., Grieshop, A. P., Robinson, A. L., Duplissy, J., Smith, J. D., Wilson, K. R., Lanz, V. A., Hueglin, C., Sun, Y. L., Tian, J., Laaksonen, A., Raatikainen, T., Rautiainen, J., Vaattovaara, P., Ehn, M., Kulmala, M., Tomlinson, J. M., Collins, D. R., Cubison, M. J., Dunlea, J., Huffman, J. A., Onasch, T. B., Alfarra, M. R., Williams, P. I., Bower, K., Kondo, Y., Schneider, J., Drewnick, F., Borrmann, S., Weimer, S., Demerjian, K., Salcedo, D., Cottrell, L., Griffin, R., Takami, A., Miyoshi, T., Hatakeyama, S., Shimono, A., Sun, J. Y., Zhang, Y. M., Dzepina, K., Kimmel, J. R., Sueper, D., Jayne, J. T., Herndon, S. C., Trimborn, A. M., Williams, L. R., Wood, E. C., Middlebrook, A. M., Kolb, C. E., Baltensperger, U., and Worsnop, D. R.:Evolution of Organic Aerosols in the Atmosphere, Science, 326, 1525–1529, 2009.

Katoshevski, D., Nenes, A., and Seinfeld, J. H.:A study of processes that govern the maintenance of aerosols in the marine boundary layer, J. Aerosol Sci., 30, 503–532, 1999.

Kazil, J., Wang, H., Feingold, G., Clarke, A. D., Snider, J. R., and Bandy, A. R.: Modeling chemical and aerosol processes in the transition from closed to open cells during VOCALS-REx, Atmos. Chem. Phys., 11, 7491–7514, doi:10.5194/acp-11-7491-2011, 2011.

Lance, S., Nenes, A., Medina, J., and Smith, J. N.: Mapping the operation of the DMT continuous flow CCN counter, Aerosol Sci. Techol., 40, 242–254, 2006.

Langley, L., Leaitch, W. R., Lohmann, U., Shantz, N. C., and Worsnop, D. R.: Contributions from DMS and ship emissions to CCN observed over the summertime North Pacific, Atmos. Chem. Phys., 10, 1287–1314, doi:10.5194/acp-10-1287-2010, 2010.

Lee, A. K. Y., Hayden, K. L., Herckes, P., Leaitch, W. R., Liggio, J., Macdonald, A. M., and Abbatt, J. P. D.: Characterization of aerosol and cloud water at a mountain site during WACS 2010: secondary organic aerosol formation through oxidative cloud processing, Atmos. Chem. Phys. Discuss., 12, 6019–6047, doi:10.5194/acpd-12-6019-2012, 2012.

Lu, M.-L., Sorooshian, A., Jonsson, H. H., Feingold, G., Flagan, R. C., and Seinfeld, J. H.: Marine stratocumulus aerosol-cloud relationships in the MASE-II experiment: Precipitation susceptibility in Eastern Pacific marine stratocumulus, J. Geophys. Res., 114, D24203, doi:10.1029/2009JD012774, 2009.

McInnes, L., Quinn, P., Covert, D., and Anderson, T.: Gravimetric analysis, ionic composition, and associated water mass of the marine aerosol, Atmos. Environ., 30, 869–884, 1996.

McInnes, L., Covert, D., and Baker, B.: The number of sea-salt, sulfate, and carbonaceous particles in the marine atmosphere, Tellus, 49, 300–313, 1997.

McLafferty, F.: Interpretation of Mass Spectra, University Science Books, 3rd Edn., 1980.

Middlebrook, A. M., Bahreini, R., Jimenez, J. L., and Canagaratna, M. R.: Evaluation of composition-dependent collection efficiencies for the aerodyne aerosol mass spectrometer using

field data, Aerosol Sci. Tech., 46, 258–271, 2012.

Moore, R. H. and Nenes, A.: Scanning flow CCN analysis – a method for fast measurements of CCN spectra, Aerosol Sci. Techol., 43, 1192–1207, 2009.

Moore, R. H., Bahreini, R., Brock, C. A., Froyd, K. D., Cozic, J., Holloway, J. S., Middlebrook, A. M., Murphy, D. M., and Nenes, A.: Hygroscopicity and composition of Alaskan Arctic CCN during April 2008, Atmos. Chem. Phys., 11, 11807–11825, doi:10.5194/acp-11-11807-2011, 2011.

Moore, R. H., Cerully, K., Bahreini, R., Brock, C. A., Middlebrook, A. M., and Nenes, A.: Hygroscopicity and composition of California CCN during summer 2010, J. Geophys. Res., 117, D00V12, doi:10.1029/2011JD017352, 2012.

Murphy, S. M., Agrawal, H., Sorooshian, A., Padró, L. T., Gates, H., Hersey, S., Welch, W. A., Jung, H., Miller, J. W., Cocker III, D. R., Nenes, A., Jonsson, H. H., Flagan, R. C., and Seinfeld, J. H.: Comprehensive simultaneous shipboard and airborne characterization of exhaust from a modern container ship at sea, Environ. Sci. Technol., 43, 4626–4640, 2009.

Noone, K., Ostrom, E., Ferek, R., Garrett, T., Hobbs, P., Johnson, D., Taylor, J., Russell, L., Flagan, R., Seinfeld, J. H., O'Dowd, C., Smith, M., Durkee, P., Nielsen, K., Hudson, J., Pockalny, R., De Bock, L., Van Grieken, R., Gasparovic, R., and Brooks, I.: A case study of ships forming and not forming tracks in moderately polluted clouds, Am. Meterol. Soc., 57, 2729–2747, 2000.

Ohta, A., Tsuno, H., Kagi, H., Kanai, Y., Nomura, M., Zhang, R., and Terashima, S.: Chemical compositions and XANES speciations of Fe, Mn and Zn from aerosols collected in China and Japan during dust events, Geochem. J., 40, 363–376, 2006.

Ovadnevaite, J., O'Dowd, C., Dall'Osto, M., Ceburnis, D., Worsnop, D.R., and Berresheim, H.: Detecting high contributions of primary organic matter to marine aerosol: A case study, Geophys. Res. Lett., 38, L02807, doi:10.1029/2010GL046083, 2011.

Phinney, L., Richard Leaitch, W., Lohmann, U., Boudries, H., Worsnop, D. R., Jayne, J. T., Toom-Sauntry, D., Wadleigh, M., Sharma, S., and Shantz, N.: Characterization of the aerosol over the sub-arctic North East Pacific Ocean, Deep-Sea Res. Pt. II, 53, 2410–2433, 2006.

Roberts, G. C. and Nenes, A.: A continuous-flow streamwise thermal-gradient CCN chamber for atmospheric measurements, Aerosol Sci. Techol., 39, 206–221, 2005.

Russell, L. M., Sorooshian, A., Seinfeld, J. H., Albrecht, B. A., Nenes, A., Ahlm, L., Chen, Y.-C., Coggon, M. M., Craven, J. S., Flagan, R. C., Frossard, A. A., Jonsson, H., Jung, E., Lin, J. J., Metcalf, A. R., Modini, R., Mulmenstadt, J., Roberts, G. C., Shingler, T., Song, S., Wang, Z., and Wonaschutz, A.: Eastern Pacific Emitted Aerosol Cloud Experiment (E-PEACE), B. Am. Meteorol. Soc., in press, 2012.

Shingler, T., Dey, S., Sorooshian, A., Brechtel, F. J., Wang, Z., Metcalf, A., Coggon, M., Mülmenstädt, J., Russell, L. M., Jonsson, H. H., and Seinfeld, J. H.: Characterisation and airborne deployment of a new counterflow virtual impactor inlet, Atmos. Meas. Tech., 5, 1259–1269, doi:10.5194/amt-5-1259-2012, 2012.

Sholkovitz, E. R., Sedwick, P. N., and Church, T. M.: Influence of anthropogenic combustion emissions on the deposition of soluble aerosol iron to the ocean: Empirical estimates for island sites in the North Atlantic, Geochim. Cosmochim. Ac., 73, 3981–4003, 2009.

Sorooshian, A., Lu, M.-L., Brechtel, F. J., Jonsson, H., Feingold, G., Flagan, R. C., and Seinfeld, J. H.: On the Source of Organic Acid Aerosol Layers above Clouds, Environ. Sci. Technol., 41, 4647–4654, 2007a.

Sorooshian, A., Ng, N. L., Chan, A. W. H., Feingold, G., Flagan, R. C., and Seinfeld, J. H.: Particulate organic acids and overall water-soluble aerosol composition measurements from the 2006 Gulf of Mexico Atmospheric Composition and Climate Study (GoMACCS), J. Geophys. Res., 112, D13201, doi:10.1029/2007JD008537, 2007b.

Sorooshian, A., Padró, L. T., Nenes, A., Feingold, G., McComiskey, A., Hersey, S. P., Gates, H., Jonsson, H. H., Miller, S. D., Stephens, G. L., Flagan, R. C., and Seinfeld, J. H.: On the link between ocean biota emissions, aerosol, and maritime clouds: Airborne, ground, and satellite measurements off the coast of California, Global Biogeochem. Cy., 23, GB4007, doi:10.1029/2009GB003464, 2009.

Statham, P. and Chester, R.: Dissolution of manganese from marine atmospheric particulates into seawater and rainwater, Geochim. Cosmochim. Ac., 52, 2433–2437, 1988.

Straub, D. J., Lee, T., and Collett Jr., J. L.: Chemical composition of marine stratocumulus clouds over the Eastern Pacific Ocean, J. Geophys. Res., 112, D04307, doi:10.1029/2006JD007439, 2007.

Ulbrich, I. M., Canagaratna, M. R., Zhang, Q., Worsnop, D. R., and Jimenez, J. L.: Interpretation of organic components from Positive Matrix Factorization of aerosol mass spectrometric data, Atmos. Chem. Phys., 9, 2891–2918, doi:10.5194/acp-9-2891-2009, 2009.

Yan, F., Winijkul, E., Jung, S., Bond, T. C., and Streets, D. G.: Global emission projections of particulate matter (PM): I. Exhaust emissions from on-road vehicles, Atmos. Environ., 45, 4830–4844, 2011.

Appendix F

Eastern Pacific Emitted Aerosol Cloud Experiment (E-PEACE)[1]

[1]This chapter is reproduced by permission from "Eastern Pacific Emitted Aerosol Cloud Experiment (E-PEACE)" by Lynn M Russell, Armin Sorooshian, John H. Seinfeld, Bruce A. Albrecht, Athanasios Nenes, Lars Ahlm, Yi-Chun Chen, Matthew Coggon, Jill S. Craven, Richard C. Flagan, Amanda A. Frossard, Haidi Jonsson, Eunsil Jung, Jack J. Lin, Andrew R. Metcalf, Robin Modini, Johannes Mlmenstdt, Greg C. Roberts, Taylor Shingler, Siwon Song, Zhen Wang, Anna Wonaschtz., *Bulletin of the American Meteorological Society*, DOI:10.1175/BAMS-D-12-00015.1, 2012.

Au: in regard to your supplemental material, our technical editors noticed that the video with the original name "IMG_0762ofPtSurOpsWithSmoke Trail.MOV" is upside down. Please be sure that all of your supplemental video files are properly oriented, and please reupload any videos that need correction. Thank you.

EASTERN PACIFIC EMITTED AEROSOL CLOUD EXPERIMENT

BY LYNN M. RUSSELL, ARMIN SOROOSHIAN, JOHN H. SEINFELD, BRUCE A. ALBRECHT, ATHANASIOS NENES, LARS AHLM, YI-CHUN CHEN, MATTHEW COGGON, JILL S. CRAVEN, RICHARD C. FLAGAN, AMANDA A. FROSSARD, HAFLIDI JONSSON, EUNSIL JUNG, JACK J. LIN, ANDREW R. METCALF, ROBIN MODINI, JOHANNES MÜLMENSTÄDT, GREG C. ROBERTS, TAYLOR SHINGLER, SIWON SONG, ZHEN WANG, AND ANNA WONASCHÜTZ

E-PEACE analyzed aircraft and satellite measurements to separate the aerosol cloud effects of three synthetic particle sources from dynamical variability.

Gaps in our fundamental understanding of cloud processes are the central underlying cause of uncertainty in aerosol radiative forcing, even in widespread and well-defined systems such as those for marine stratocumulus cloud formation. Atmospheric aerosol levels have increased markedly since the Industrial Revolution. We do not fully understand the extent to which this increase has affected the cycles of radiant energy and water in the climate system. It has been well established that clouds forming in a polluted environment tend to have more numerous, smaller droplets, which may lead to a cloud of higher cloud optical depth and albedo. Once cloud droplet size and number concentration are perturbed, the dynamics of both the cloud itself and the atmospheric layer in which it is embedded change in a nonlinear manner. Many important questions arise: What is the relationship between cloud microstructure and the aerosol on which the cloud forms? How can the understanding of cloud responses to increased aerosol levels be represented in theories and models of the climate system? Is it possible to

AFFILIATIONS: RUSSELL, AHLM, FROSSARD, MODINI, AND MÜLMENSTÄDT—Scripps Institution of Oceanography, University of California, San Diego, La Jolla, California; SOROOSHIAN—Department of Chemical and Environmental Engineering, and Department of Atmospheric Sciences, University of Arizona, Tucson, Arizona; SEINFELD, CHEN, COGGON, CRAVEN, FLAGAN, AND METCALF*—California Institute of Technology, Pasadena, California; ALBRECHT, JUNG, AND SONG—Rosenstiel School of Marine and Atmospheric Sciences, University of Miami, Miami, Florida; NENES AND LIN—School of Earth and Atmospheric Sciences, Georgia Institute of Technology, Atlanta, Georgia; JONSSON—Center for Interdisciplinary Remotely-Piloted Aerosol Studies, Marina, California; ROBERTS—Scripps Institution of Oceanography, University of California, San Diego, La Jolla, California, and Groupe d'études de l'Atmosphère Météorologique, Centre National de la Recherche Scientifique, Toulouse, France; SHINGLER AND WANG—Department of Chemical and Environmental Engineering, University of Arizona, Tucson, Arizona; WONASCHÜTZ—Department of Atmospheric Sciences, University of Arizona, Tucson, Arizona
***CURRENT AFFILIATION:** Combustion Research Facility, Sandia National Laboratories, Livermore, California
CORRESPONDING AUTHOR: Lynn M. Russell, Scripps Institution of Oceanography, University of California, San Diego, 9500 Gilman Dr., Mail Code 0221, La Jolla, CA 92093-0221
E-mail: lmrussell@ucsd.edu

The abstract for this article can be found in this issue, following the table of contents.

DOI:10.1175/BAMS-D-12-00015.1

A supplement to this article is available online (10.1175/BAMS-D-12-00015.2)

In final form 9 August 2012

extract observationally the cloud response to aerosols from that of the changing ambient meteorology? Our understanding, especially of warm-phase cloud microphysics, has advanced significantly in the last decade as a result of satellite observations, computational modeling, and field studies. Still, the challenge of untangling the effects of aerosol perturbations on clouds from those of meteorological variability itself and generalizing the findings from such studies to the scales that affect climate remains daunting. Aerosol properties tend to be highly variable, both spatially and temporally, in terms of size and chemical composition. While limited attempts have been made to employ particles of known size and composition in cloud perturbation studies, and thereby alleviate uncertainties associated with cloud activation, such attempts have proved difficult to implement. Here we describe a coordinated field experiment, the Eastern Pacific Emitted Aerosol Cloud Experiment (E-PEACE) campaign, in which the effects of well-defined aerosol perturbations on marine stratocumulus clouds were probed via in situ aircraft and satellite observations.

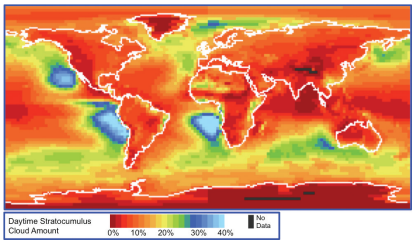

Fig. 1. Daytime annual average stratocumulus cloud amount (%) over the 1983–2009 period. Data obtained from International Satellite Cloud Climatology Project (ISCCP) D2 monthly means (http://isccp.giss.nasa.gov/products/browsed2.html).

Key issues addressed in E-PEACE that have prevented accurate depiction of aerosol effects on clouds in large-scale models include:

1) What observations can constrain the overall effect of particles and the clouds that form on them on Earth's climate?
2) What is the specific effect of the distribution of particles by size on cloud droplet activation and cloud microphysics?
3) Can the effects of chemical makeup of particles be isolated from other cloud responses by seeding experiments?

MARINE STRATOCUMULUS AND CLIMATE. Stratocumulus clouds are characterized by their large spatial extent and are organized into distinctive patterns, often with rolling, linear structures. They are primarily formed over the oceans and are a semipersistent feature in many regions adjacent to continents. The dynamical conditions that lead to their formation involve generation of convective currents below drier, stable air that prevents continued vertical development. Based on this, stratocumulus clouds are typically classified into three categories (Klein and Hartmann 1993). The first and most common category involves clouds forming over oceans with relatively cold sea surface temperatures with a boundary layer that is capped by a strong temperature inversion (maintained by large-scale subsidence). These systems are typically formed in regions near western continental boundaries, where trade winds blow from midlatitudes toward the intertropical convergence zone and generate cold sea surface temperatures. The convection that maintains the stratocumulus is driven by radiative cooling at the top of the boundary layer (Lilly 1968), while precipitation and entrainment are thought to represent key forcings that control the structure and stability of the boundary layer. While this study focuses on this first type of stratocumulus cloud because of their important role in radiative forcing on the global scale, another type of stratocumulus cloud is formed in winter over oceanic western boundary currents, where cold continental air flows over warm waters, and develops convection. Unlike the first category, convection is driven by strong surface heat fluxes (Schubert et al. 1979b,a). Finally, Arctic stratus is formed mostly in the summer and results from radiative cooling of subpolar moist air entrained into the Arctic (Curry et al. 1988).

Considerable areas of subtropical and polar oceans are extensively covered with stratocumuli (Fig. 1). In the midlatitude oceans (40°–60°N, 50°–65°S) maximum cloud cover occurs during the summer months and averages between 62% and 82%; minimum cloud cover occurs in the winter and averages around 50% (Klein and Hartmann 1993). In the subtropics, cloud cover is more variable (but still considerable), ranging from 35% to 72% during peak months and 17%–42% during minimum activity (Klein and Hartmann 1993). The shortwave cloud albedo forcing of stratocumulus is larger than its longwave cloud greenhouse forcing, resulting in a net cooling over the regions they cover. According to the Earth Radiation Budget Experiment (ERBE; Barkstrom 1984), the longwave cloud forcing of midlatitude stratocumulus is about 40 W m^{-2}, while the shortwave forcing reaches a minimum of –150 W m^{-2} in the Pacific and –120 W m^{-2} in the Atlantic. The strong net forcing of approximately –100 W m^{-2} is a cooling effect with considerable impacts on local and global climate (see "Ship tracks" for more information).

RESPONSE OF MARINE STRATOCUMULUS TO AEROSOL PERTURBATIONS. There have been several important measurement campaigns (Table 1) as well as a number of modeling studies (Table 2) aimed at characterizing the response of marine stratocumulus to aerosol perturbations, which we summarize here. The Monterey Area Ship Track (MAST) experiment in 1994 (Durkee et al. 2000c) was one of the first aircraft-based studies that included detailed characterization of aerosol and cloud droplet size distributions down to 20 nm and above 20 μm. This study tracked particle emissions from ships in stratocumulus cloud conditions, allowing identification of the effects of aerosol perturbations on cloud radiative signatures (Noone et al. 2000b,a). The Second Dynamics and Chemistry of the Marine Stratocumulus field study (DYCOMS II) consisted of nine nighttime flights west of San Diego, California, in July 2001 for testing large-eddy simulations of nocturnal stratocumulus (Stevens et al. 2003). A linear relationship between cloud condensation nuclei (CCN) and cloud droplet number emerged (Twohy et al. 2005), together with the drizzle-induced change in cloud structure (Van Zanten and Stevens 2005). A series of Cloud–Aerosol Research in the Marine Atmosphere (CARMA; Hegg et al. 2009) studies helped explain the source attribution of CCN and aerosol light scattering in the northeastern Pacific marine boundary layer. The Cloud Indirect Forcing Experiment (CIFEX) showed that aerosols over the northeastern Pacific Ocean (primarily from North American emissions) enhance the cloud drop number concentration and reduce the drop size for marine stratocumulus and cumulus clouds, resulting in satellite-measured increases in cloud brightness (Wilcox et al. 2006).

SHIP TRACKS

In 1966, Conover (1966) reported "anomalous cloud lines" present in visible-wavelength satellite images from Television and Infrared Observation Satellites (TIROSs). He noted that these lines, as much as 500 km long and up to 25 km in width, were likely due to liquid particles from the exhaust of oceangoing vessels. Twomey et al. (1968) remarked that the observations by Conover were consistent with the impact of additional CCN in a very clean marine boundary layer. Subsequent studies have strengthened the connection between ship exhaust and so-called ship tracks (e.g., Scorer 1987). Observations using near-infrared wavelengths from Advanced Very High Resolution Radiometer (AVHRR) exhibit more extensive features of ship effects on clouds (Coakley et al. 1987). Twomey (1991) showed that marine stratiform clouds may be particularly sensitive to additional CCN, leading to higher cloud droplet number concentration and increased cloud reflectivity (albedo).

In situ airborne measurements of ship tracks during the First ISCCP Regional Experiment (FIRE) in 1987 showed that droplet sizes in two ship tracks decreased significantly, accompanied by a higher liquid water content in the ship track than in the background (Radke et al. 1989); however, other satellite- and simulation-based studies have shown decreases in liquid water content (Coakley and Walsh 2002; Lu et al. 2009; Segrin et al. 2007). Albrecht (1989) proposed that the increase in liquid water content resulted from drizzle suppression in the ship tracks due to smaller droplet sizes and consequent retarded coalescence. Later, aircraft measurements off the Washington coast also noted the reduction of drizzle droplet numbers in the ship tracks (Ferek et al. 1998). The MAST experiment, which took place off the California coast in June 1994 (Durkee et al. 2000b), was designed to examine a series of hypotheses focused on links between the ship-emitted aerosol, mixing of the effluent through the boundary layer, and response in cloud droplets.

Remote sensing data from advanced satellite instrumentation has been applied in a number of studies on ship tracks (e.g., Schreier et al. 2007; Segrin et al. 2007). Recent satellite studies using MODIS imagery (Christensen and Stephens 2011) have observed ship tracks embedded in different cloud structures. Cloud-Aerosol Lidar with Orthogonal Polarization (CALIOP) was used to determine the extent to which ship-emitted aerosols alter the important microphysical and macrophysical properties of marine stratocumulus across the North Pacific Ocean and off the coasts of South America and South Africa. The results show that aerosols change the microphysical and macrophysical responses of marine stratocumulus depending on mesoscale stratocumulus convective regimes.

The Marine Stratus/Stratocumulus Experiment (MASE) was carried out in two phases over the eastern Pacific Ocean off the coast of Monterey, California. The first phase (MASE-I) was undertaken in July 2005 (Lu et al. 2007), and the second phase (MASE-II) was conducted in July 2007 (Lu et al. 2009), each to evaluate aerosol–cloud–drizzle relationships in regions of uniform meteorology with localized aerosol enhancements in ship tracks. The ship-track regions exhibited a smaller cloud drop effective radius, higher cloud droplet number concentration, reduced drizzle drop number concentration, and higher liquid water content (LWC) than the adjacent clean regions; however, trends were obscured by spatial–temporal variability. Results from both individual case studies and ensembles of simulations in both MASE studies are in accord with those from other field campaigns (e.g., Brenguier et al. 2000; Feingold et al. 2006; Roberts et al. 2008; Wilcox et al. 2006), in that increased cloud drop number (CDN) concentration and decreased cloud-top effective radius are associated with increased subcloud aerosol concentration [at fixed liquid water path (LWP)]. The ship-track regions exhibited a smaller cloud drop spectral width and relative dispersion in MASE-I, in accord with large-eddy simulations (Lu and Seinfeld 2006). More polluted clouds were observed to have a smaller cloud-base drizzle rate; however, this did not equate to a larger amount of liquid water in that column of the atmosphere (LWP) when compared with clean clouds. Dynamic adjustment of the cloud in response to drizzle, in-cloud latent heating, subcloud evaporative cooling, and cloud-top entrainment would need to be taken into consideration (Ackerman et al. 2004; Lu and Seinfeld 2005). A new framework of precipitation susceptibility (Feingold and Siebert 2009; Sorooshian et al. 2009b), which quantifies the change in precipitation rate in response to aerosol perturbations, was applied in MASE-II.

The Variability of American Monsoon Systems (VAMOS) Ocean–Cloud–Atmosphere–Land Study Regional Experiment (VOCALS-REx) was conducted in the southeast Pacific off the coast of northern Chile during October and November 2008 to make observations of poorly understood but important components of the coupled climate system of the southeast Pacific (Allen et al. 2011; Bretherton et al. 2010; Wood et al. 2011a,b). VOCALS investigated links between aerosol, clouds, and precipitation and their impacts on stratocumulus radiative properties. Transition and feedbacks of mesoscale cellular convection were addressed (Wood et al. 2011a), as well as the modeling of microphysical and meteorological controls on precipitation and cloud cellular structure (Wang et al. 2010).

Of critical importance to the aerosol–cloud system is how the clouds themselves modify aerosol physicochemical properties, which consequently affects their ability to interact with radiation outside of clouds in addition to serving as CCN the next time the particles are entrained into cloud. Most particles in the marine boundary layer likely have at some point in their lifetime been inside a cloud. Simulations of typical parcel trajectories in the marine atmosphere have shown the impacts of cycling in and out of clouds on particle composition (Feingold et al. 1998). Of the limited studies that have examined cloud effects on aerosol in the northeastern Pacific region, there is evidence that clouds alter both the inorganic and organic fractions of aerosol (Crahan et al. 2004; Sorooshian et al. 2007), which can lead to different hygroscopic properties (Hegg et al. 2008; Hersey et al. 2009). These differing impacts of clouds on aerosol particles motivated the need for designing an experiment that would better constrain the influence of clouds on aerosol size, composition, and water-uptake properties.

E-PEACE. E-PEACE combined a targeted aircraft campaign off the coast of Monterey in July and August 2011 with embedded ship and satellite observations (Fig. 2) and modeling studies. Atmospheric conditions in the northeastern Pacific during July are ideal for the formation of homogeneous layers of persistent stratocumulus clouds. The layers observed have consistent diurnal characteristics, cloud thicknesses of 100–300 m, and cloud-top heights typically below 500 m. The susceptibility of cloud albedo to particle perturbations is well documented for the eastern Pacific near 36°N (Coakley et al. 1987, 2000; Platnick et al. 2000).

We employed the research vessel (R/V) *Point Sur* to measure the aerosol below cloud and as a platform for well-characterized smoke emissions to produce a uniquely identifiable cloud signature. The Center for Interdisciplinary Remotely-Piloted Aircraft Studies (CIRPAS) Twin Otter aircraft was used with a full payload of instruments (Table 3) to measure particle and cloud number, mass, and composition. E-PEACE combined 1) controlled release of smoke from the deck of the *Point Sur*, salt aerosol from the Twin Otter, and exhaust from container ships transiting across the study region; 2) flight plans designed to investigate results from large-eddy simulations (LES) and to provide constraints for aerosol–cloud parcel (ACP) modeling studies, to test our ability to quantitatively predict the cloud dynamical response to increases in particle concentrations in the natural atmosphere; and 3) satellite analyses of marine stratocumulus to constrain the radiative properties of the natural, perturbed, and regional cloud systems.

Table 1. Previous relevant publications from aerosol–cloud interaction experiments on marine stratocumulus. POC is pocket of open cells. CN is condensation nuclei. DECS is the Drizzle and Entrainment Cloud Study.

Experiment	Publications	Key findings (for aerosol–cloud interactions)
MAST (northeast Pacific)	Russell et al. (1999) Hobbs et al. (2000) Frick and Hoppel (2000) Durkee et al. (2000b) Noone et al. (2000b,a) Ferek et al. (2000)	Observed changes in drop distributions and LWC profile. Ship emission characterization and size distributions. Case studies of four ship emissions that produce ship tracks. Test of aerosol-induced ship-track hypothesis. Case studies illustrating background pollution effects on albedo sensitivity. Drizzle and LWC changes in ship tracks relative to unperturbed clouds.
DECS (northeast Pacific)	Stevens et al. (2005) Sharon et al. (2006)	Rift POC study; variability in cloud drizzle characteristics due to natural processes and emissions.
DYCOMS II (nocturnal) (northeast Pacific)	Stevens et al. (2003) Twohy et al. (2005) Petters et al. (2006) Hawkins et al. (2008) Faloona et al. (2005) Van Zanten and Stevens (2005)	Characterization of POCs in nocturnal marine boundary layers. CN/CCN/CDN relationships are linear. CCN closure for marine boundary layer particles. Composition independence of particle activation in the aged boundary layer. Entrainment rates and variability in the nocturnal marine boundary layer. Drizzle in nocturnal boundary layer in intense precipitation pockets.
CIFEX	Wilcox et al. (2006)	CCN increases correlated to CDN and reflected radiation for constant LWP.
MASE-I/II (northeast Pacific)	Lu et al. (2007, 2009) Sorooshian et al. (2007) Hersey et al. (2009) Sorooshian et al. (2009b,a)	Ship tracks had smaller cloud drop effective radius, higher number concentration N_d, reduced drizzle drop number, and larger cloud LWC than adjacent clean regions; however, trends were obscured by spatial–temporal variability. Aerosols above cloud tops are enriched with water-soluble organic species, have higher organic volume fractions, and are less hygroscopic relative to subcloud aerosol.
CARMA	Hegg et al. (2009)	Source attribution of CCN and aerosol light scattering.
VOCALS-REx (southeast Pacific)	Bretherton et al. (2010) Feingold et al. (2010) Wood et al. (2011a)	Offshore drizzle not explained by CCN decrease. Oscillations in aerosol concentrations correspond to precipitation cycles. POC regions had enhanced drizzle and LWC.

Au: please provide expansion for MBL

Table 2. Recent model results on MBL cloud responses to aerosol perturbations.

Model type	Publications	Key findings (for aerosol–cloud interactions)
ACP using observations	Russell et al. (1999)	Feedback effects of particles on supersaturation and LWC profile.
ACP with LES trajectories	Feingold et al. (1998)	Sensitivity of cloud properties to variability in trajectories.
ACP with supersaturation or updraft distributions	Meskhidze et al. (2005) Hsieh et al. (2009)	Effectiveness of parameterization for accurate droplet activation. Importance of maximum supersaturation rather than distribution.
LES—nocturnal (northeast Pacific)	Hill et al. (2009)	Inhomogeneous mixing less important than particles.
LES (Pacific/Atlantic)	Ackerman et al. (2003, 2004)	LWP is reduced as CDN increases. Nighttime CDN increases will suppress drizzle.
LES—diurnal (Pacific/Atlantic)	Lu and Seinfeld (2005, 2006)	Giant CCN increase drizzle in some conditions. Relative dispersion increases apparent indirect effect.
LES—nocturnal (northeast Pacific)	Savic-Jovcic and Stevens (2008)	Reduction in cloud albedo associated with drizzle.
LES (southeast Pacific)	Caldwell and Bretherton (2009)	Diurnal cycle controls drizzle and LWP.
Mixed layer	Wood et al. (2009)	Drizzle decreases cloud height and entrainment and CDN increases.
LES	Sandu et al. (2009)	Vertical stratification affects LWP; diurnal transition effects on LWP.

With 12 days of ship time on the R/V *Point Sur* and 30 flights (each ~4.5 h long) on the CIRPAS Twin Otter (Tables 4 and 5), we could take full advantage of the persistence of stratocumulus clouds to probe the effect of particle sources on marine stratocumulus properties. Since the particles would be emitted in high concentrations over small areas in crosswind directions, their effects on clouds could be separated from those of meteorology. And in terms of number concentration and duration, the impacts of these particle emissions would be large enough to be distinguished from natural cloud variability.

As noted above, three types of particles were involved in E-PEACE: 1) combustion exhaust particles from cargo ships of opportunity, which are the emissions responsible for ship tracks; 2) shipboard smoke-generated particles; and 3) aircraft-based milled salt particles (Fig. 3). Type 1 is the exhaust that consists of 50–100-nm dry-diameter particles emitted at rates of 10^{26}–10^{28} s^{-1} from the engines of large (2,000 ton) cargo ships, in this instance on trans-Pacific, Los Angeles to San Francisco, or other commercial routes. Such emissions were responsible for the first observed ship tracks (Conover 1969). At a fuel cost of about $100,000 (U.S. dollars) per day, operations

Au: addition of "(U.S. dollars)" okay here?

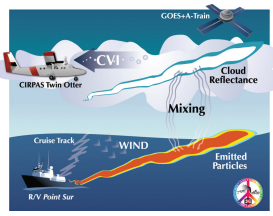

Fig. 2. Illustration of E-PEACE design and observations of emitted particles in marine stratocumulus in Jul and Aug 2011 west of central California. The diagram shows the three platforms used in making observations of particle and cloud chemical and physical properties, namely, the R/V *Point Sur*, the CIRPAS Twin Otter, and the A-Train satellites and GOES. The design included using smoke generated on board the R/V *Point Sur* that was measured after emission by the CIRPAS Twin Otter in clouds. The satellite was used to measure the changes in reflectance of sunlight due to the effects of the emitted particles on the clouds. The CVI was used as an inlet for evaporating droplets as they were brought into the aircraft, allowing sampling of droplet chemical composition.

of such vessels dedicated solely to research are not feasible. However, real-time tracking of commercial vessels (www.marinetraffic.com) was used to identify fast-moving (>30 km h^{-1}) cargo or container ships in the region within the aircraft operating area (as illustrated in Fig. 4). Type 2 involves smoke particles produced at an estimated rate of 10^{11}–10^{13} s^{-1} on the stern deck of the R/V *Point Sur* (described in "Tailor-made particles with a battlefield smoke generator"), with dry diameters that ranged from 50 nm up to 1 μm and very low hygroscopicity. Type 3 particles were dispersed from the Twin Otter aircraft in cloud. An adjustable auger fed a fluidized bed that dispensed NaCl particles, which had been milled to diameters of 3–5μm and mixed with SiO_2 to prevent particles from sticking together (Drofa et al. 2010).

CLOUD ALBEDO EFFECTS. In situ observations provide measurements of aerosol and cloud microphysics on spatial scales relevant to individual clouds and therefore are a critical element in understanding aerosol–cloud effects. To extrapolate from individual clouds to obtain a statistically robust assessment of aerosol effects on clouds and precipitation requires corresponding satellite observations. We used visible and infrared imagery in near–real time from Geostationary Operational Environmental Satellites (GOESs; ~30-min delay at www.nrlmry.navy.mil/sat-bin/epac_westcoast.cgi) and higher-resolution images from the A-Train constellation of satellites (Stephens et al. 2002) for postexperiment analyses (illustrated in the top right of Fig. 2). The relevant satellite-based platforms in the eastern Pacific region include *Terra* and *Aqua*, which collectively provide retrievals of aerosol parameters (e.g., aerosol index) and cloud microphysical properties (e.g., drop effective radius, cloud optical depth). In this project we isolated aerosol-induced changes in these properties by creating tracks with unique geometry in different cloud regimes.

We used the zigzag pattern of the R/V *Point Sur* to create a track in cloud that was easily distinguishable from natural cloud characteristics and was broader than the constant-heading tracks made by ships in transit. These characteristics allowed us to track the plume with the CIRPAS aircraft and to isolate the effects from the smoke generated on the R/V *Point Sur.* Note the satellite image on 16 July 2011 during the 1430 local time (LT) overpass of *Aqua* (Fig. 5), in which the part of cloud affected by the smoke is whiter (i.e., more reflective at 2.2 μm) than the surrounding clouds. To confirm this identification, we calculated and plotted the expected location of the smoke (given the average

Table 3. Instruments on CIRPAS Twin Otter and R/V *Point Sur*. PM10 = particulate matter ≤10 μm.

Instruments	R/V *Point Sur*	CIRPAS Twin Otter
Particle and droplet inlets	PM10	PM1 and CVI[a]
Particle size distributions	CPC3010[b] for diameters > 10 nm Scanning DMA[c] OPS APS	CPC3010[b] for diameters > 10 nm CPC3025[d] for diameters > 3 nm Scanning DMA[e] PCASP
Particle chemical composition	High-resolution (HR) ToF-AMS[f] SP2 FTIR functional group composition XRF elemental composition PILS-TOC for water-soluble organic carbon[k]	Compact (C) ToF-AMS[g] SP2
Particle properties	Tandem scanning and humidified DMAs[i] CCN spectrometer[k]	CCN spectrometer[l] Particle soot absorption photometer (PSAP) Photoacoustic soot spectrometer, three wavelengths (PASS-3)
Droplet and drizzle distributions		Phase Doppler interferometer (PDI) CAS CIP Cloud droplet probe (CDP)[j] Forward Scattering Spectrometer Probe (FSSP) CIP-2D Gerber light diffraction for LWC (particulate volume monitor model PVM-100)
Droplet residual properties (by CVI)		CPC3010[b] for diameters > 10 nm CPC3025[d] for diameters > 3 nm Scanning DMA[e] CCN spectrometer[k] C ToF-AMS SP2 PASS-3
Cloud water composition		Slotted cloud water collector[m]
Meteorological variables	Temperature Relative humidity Pressure Wind speed and direction Altitude and GPS location	Temperature Relative humidity Pressure Wind speed and direction, gust velocity Altitude and GPS location
Cloud structure	Ceilometer (cloud-base height)	Upward-facing Doppler radar[n]
Seawater properties	Sea surface temperature Chlorophyll-A	
Particle generators	Oil smoke generator	Giant salt dispenser

[a] CVI (Shingler et al. 2012).
[b] Condensation particle counter (CPC) model 3010 (TSI, Inc.).
[c] Scanning DMA (Brechtel Manufacturing, Inc.).
[d] CPC model 3025 (TSI, Inc.).
[e] Scanning DMA models 3081 and 3010 (TSI, Inc.).
[f] High-resolution time-of-flight aerosol mass spectrometer (Aerodyne Research, Inc.).
[g] Compact time-of-flight aerosol mass spectrometer (Aerodyne Research, Inc.).
[k] Particle-into-liquid sampler (Brechtel Manufacturing, Inc.) coupled to a total organic carbon analyzer (Sievers model 800; Sullivan et al. 2006).
[i] Scanning and humidified scanning DMA (Brechtel Manufacturing, Inc.; Sorooshian et al. 2012).
[l] CCN spectrometer (Moore and Nenes 2009).
[k] CCN spectrometer [miniaturized from the design of Roberts and Nenes (2005)].
[j] Cloud droplet probe (Droplet Measurement Technology; Lance et al. 2010).
[m] Modified Mohen design (based on Hegg and Hobbs 1986).
[n] 94-GHz frequency-modulated continuous wave cloud radar.

Au: AMS style is to follow Chicago Manual of Style paragraph 8.115: Names of specific ships and other vessels are both capitalized and italicized. Note that when such abbreviations as USS (United States ship) or HMS (Her [or His] Majesty's ship) precede a name, the word ship or other vessel type should not be used. The abbreviations themselves are not italicized. Please confirm vessel names are now okay as set.

Au: please include units for cloud level, either in column head or as a footnote.

Table 4. Summary of CIRPAS Twin Otter flights during E-PEACE 2011.

Flight	Date	Description of clouds and particle sources sampled	Cloud level	Background LWC*	Track LWC*
1	8 Jul	Thin cloud layer; salt seeding	257–362	0.15	—
2	9 Jul	Thick, wet cloud layer, drizzling; salt seeding	283–570	0.28	—
3	13 Jul	Broken clouds; smoke sampling.**	—	—	—
4	14 Jul	High, thick cloud layer; smoke sampling	651–934	0.15	0.22
5	15 Jul	Two broken cloud layers; cargo ships (*Ice Blizzard*); smoke sampling	266, 550–794	0.14	0.12
6	16 Jul	Two broken cloud layers; smoke sampling	142, 550–774	0.12	0.12
7	17 Jul	No clouds; cargo ships (*Hanjin Montevideo*); smoke sampling	—	0.19	—
8	19 Jul	Thick, wet cloud layer, no drizzle; cargo ships (*Cap Preston*); smoke sampling	258–533	0.21	0.25
9	21 Jul	Thick cloud layer, drizzling; cargo ship; smoke sampling	212–533	0.27	0.30
10	22 Jul	Thick cloud layer, intermittent drizzling; smoke sampling	235–551	0.30	0.35
11	23 Jul	Thick cloud layer; smoke sampling; cargo ships (*Pos Yantian*)	308–630	0.28	0.26
12	24 Jul	Mostly clear air, high clouds; cargo ships (*Ken Ryu*)	492–779	0.17	0.18
13	26 Jul	Thick cloud layer; cargo ships (SCF *Samotlor, Vinalines Galaxy, Gluecksburg*); salt seeding	253–560	0.26	0.31
14	27 Jul	Low, thick cloud layer; cargo ship (*Mol Earnest*)	131–441	0.24	0.32
15	28 Jul	Thin cloud layer; cargo ship (*Hanjin Hamburg, Ever Develop, Cap Preston*)	267–413	0.17	0.15
16	29 Jul	High, wet clouds, no drizzle; cargo ship (MSC *Fabienne*); salt seeding	265–534	0.30	0.33
17	1 Aug	Thin, high cloud layer; cargo ship (*Astro Phoenix*)	641–784	0.15	0.13
18	2 Aug	Thick, wet cloud layer, drizzling; cargo ships (*Riga, Australia Express*); salt seeding	310–613	0.27	0.44
19	3 Aug	Thick cloud layer, some drizzle; cargo ships (*Xin Ya Zhou*); salt seeding	309–628	0.23	0.31
20	4 Aug	Cumulus-like broken clouds, drizzling; cargo ships (YM *Cypress*)	294–633	0.17	0.18
21	5 Aug	Low cloud layer, intermittent drizzle; cargo ships (*Nelvana*)	169–501	0.28	0.27
22	8 Aug	Thin cloud layer	281–448	0.22	—
23	9 Aug	Thin cloud layer	324–485	0.21	—
24	10 Aug	Low clouds, intermittent drizzle; cargo ships (*Tian Shang He*); salt seeding	286–553	0.29	0.31
25	11 Aug	Two broken cloud layers; cargo ships (NYK *Artemis*)	216, 440–600	0.16	0.24
26	12 Aug	Thick cloud layer; shipping lane; polluted layer above clouds	278–578	0.24	—
27a,b,c	15 Aug	No clouds; north/south survey	—	—	—
28a,b,c	16 Aug	Low cloud layer; north/south changes in cloud amount	136–379	0.13	—
29a,b	17 Aug	Low cloud layer; north/south survey	156–366	0.21	—
30a,b	18 Aug	Low cloud layer; north/south survey	142–352	0.23	—

*LWC (g kg^{-1}) calculated as a flight average for all LWC > 0.1 g kg^{-1} (using measurements from the Gerber probe). Background and track concentrations were separated for each flight using the PCASP concentration thresholds set for each day: 80 cm^{-3} for 14 Jul; 100 cm^{-3} for 22 Jul; 120 cm^{-3} for 15, 16, 19, 21 Jul; 130 cm^{-3} for 24 Jul; 150 cm^{-3} for 26 Jul and 1, 3, 4, 5, 10, 11 Aug; 200 cm^{-3} for 23, 27, 28, 29 Jul and 2 Aug.

**Some datastreams were corrupted on flight 3, so it is not shown in Fig. 6.

Table 5. Summary of R/V *Point Sur* cruise during E-PEACE 2011.

Date	Description of clouds and smoke generation operations	Cloud bases[a]	SST[b]	Surface wind[c]
12 Jul	Multiple cloud layers; testing smoke generators	70, 160, 430	12.8	8 at 270°
13 Jul	Multiple cloud layers, light winds; intermittent smoke generation	100, 190, 360	13.1	5–20 at 270°
14 Jul	High clouds; smoke generation (6 h)	420, 660	13.9	15–20 at 310°
15 Jul	Broken low and high clouds; smoke generation (6 h)	250, 570	14.7	15 at 330°
16 Jul	Multiple cloud layers; smoke generation (6 h); plume sampling	70, 160,[d] 310	13.7	<5 at 330°
17 Jul	Multiple broken cloud layers; smoke generation (5 h); plume sampling	50, 150, 810, 930	14.6	5–10 at 330°
18 Jul	Multiple broken cloud layers; smoke generation (1 h); plume sampling	60, 160	15.7	8–10 at 250°
19 Jul	Scattered low and high clouds; smoke generation (6 h)	50, 140, 340	14.6	15–20 at 340°
20 Jul	Scattered clouds; smoke generation (1 h)	280[d]	14.5	15–20 at 330°
21 Jul	Low, uniform clouds; smoke generation (5 h)	210[d]	14.1	15–20 at 330°
22 Jul	Low, uniform clouds; smoke generation (5 h)	250,[d] 340	13.9	18–22 at 330°
23 Jul	Low, uniform clouds; smoke generation (6 h)	290, 420	14.4	4–8 at 300°

[a] Altitudes (m MSL) of bases of cloud layers detected by ceilometer measured on R/V *Point Sur*.

[b] Sea surface temperatures (°C) measured on R/V *Point Sur*.

[c] Wind speed (1 kt = 0.5144 m s^{-1}) and direction measured on R/V *Point Sur*.

[d] Clouds in which ship tracks were observed in the region.

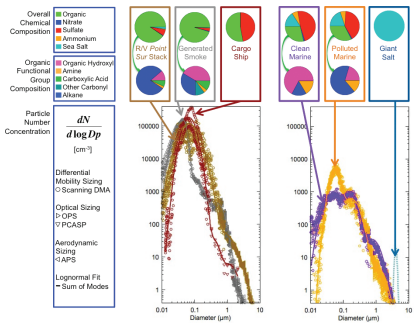

Fig. 3. Distribution by size of the number and submicron composition of particles emitted for E-PEACE, with comparison to both clean and polluted marine background particles measured during the experiment. Composition illustrates the overall mass-based chemical composition, based on AMS and X-ray fluorescence (XRF; where we have calculated sea salt mass from 1.47 × Na + Cl, which was equal to summed components Na + Mg + Cl + Ca + K + non-sea-salt sulfate), and the organic functional group composition, based on Fourier transform infrared (FTIR), with the box colors and arrows indicating the size distribution to which each composition corresponds. Organic functional group composition was not available for the giant generated salt (since there was none) and the cargo ship (since sufficient sampling time was not available). The concentration of giant generated salt has been scaled by 10^4, so that the particle size can be shown on the same graph. Measurements collected on the R/V *Point Sur* [0.01 < scanning differential mobility analyzer (DMA) < 0.9 μm, 0.4 < optical particle sizer (OPS) < 10 μm, 0.5 < aerodynamic particle sizer (APS) < 15 μm] included the smoke generator (1210–1225 LT 17 Jul), the R/V *Point Sur*'s stack emissions (2000–2200 LT 22 Jul), and background aerosol for clean (1100–1135 LT 20 Jul) and polluted (0220–0400 LT 19 Jul) marine conditions. Measurements of cargo ship emissions (0.01 < scanning DMA < 0.9 μm, 0.1 < PCASP < 2 μm) were collected on the Twin Otter (1200–1315 LT 10 Aug).

Au: please confirm you mean time is local time. If it isn't, is it UTC?

wind speed near the sea surface) at the time of the satellite overpass. Even without this simple calculation, the resemblance between the patterns of the ship path and the reflected track in cloud is evident.

We also identified tracks of cargo ships in satellite images similar to historical and recent work (Coakley et al. 1987; Durkee et al. 2000c; Segrin et al. 2007). At least three examples of these tracks from cargo or container ships are visible in the bottom left of Fig. 5. The increase in the reflectance of the cloud tracks from cargo ships (15% mean increase at 545–565 nm for all tracks identified in the E-PEACE region in July and August 2011) was similar to the cloud tracks formed from smoke emitted from the R/V *Point Sur* (14% increase at 545–565 nm). These increases are well within the range reported by Durkee et al. (2000a). For comparison, many ship tracks in the E-PEACE region had lower increases, and Chen et al. (2012) found that 30% of ship tracks during E-PEACE resulted in reduced reflectance.

PARTICLE AND DROPLET NUMBER AND COMPOSITION. The Twin Otter aircraft flew into the same clouds shown in the satellite image (Fig. 5) to measure both the chemical composition of and number of cloud droplets that caused the increased shortwave reflectance. Figure 6 shows the number of particles below cloud and droplets in cloud, and the pie graphs show that these droplets were almost entirely organic components with trace amounts of sulfate. The measured ship and marine characteristics of the organic components during E-PEACE were used to quantify the widespread contributions of ship emissions to the marine boundary layer aerosol (Coggon et al. 2012). The large organic fraction in Fig. 6a is characteristic of smoke emitted from the generators on the R/V *Point Sur* (see "Giant CCN stratocumulus cloud seeding") and contrasts with the composition of droplets in the cloud not affected by the smoke (Fig. 6c), which are made up of three-quarters sulfate and very little organic components.

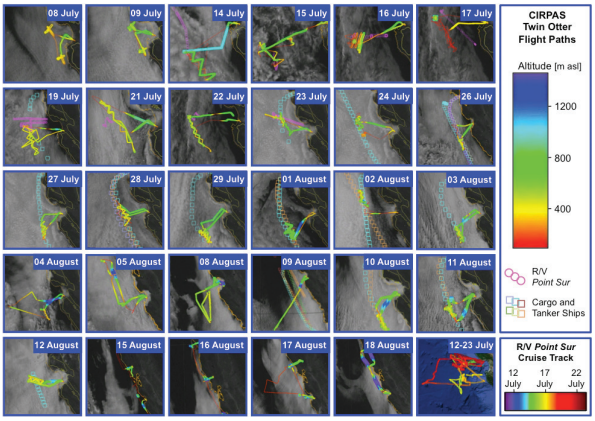

Fig. 4. Summary of the CIRPAS Twin Otter research flight paths and the R/V *Point Sur* cruise track. The first 29 panels show the CIRPAS Twin Otter flight path, colored by altitude MSL, overlaid on a GOES image of the cloud cover from that day. The tracks of the R/V *Point Sur* as well as cargo and tanker ships that were targeted for sampling that day are also shown. The last panel shows the 12-day cruise track of the R/V *Point Sur*, colored by date, overlaid on a Google Earth image of the topography.

Interestingly, the particles that activated to form cloud droplets were sufficiently large (>1.1 μm; see Table 6) to make activation possible even in the near absence of soluble ions (approaching the so-called kelvins limit).

The chemical composition of the cloud droplets was measured using a specialized inlet that separates the droplets from smaller interstitial aerosol particles (i.e., the particles that did not activate into droplets). This kind of inlet is called a counterflow virtual impactor (CVI) because it uses airstreams forced to flow in different directions to separate larger momentum droplets from smaller particles. The isolated droplets are then evaporated and the chemical composition

TAILOR-MADE PARTICLES WITH A BATTLEFIELD SMOKE GENERATOR

Smoke emissions were generated on the stern of the R/V *Point Sur* by two U.S. Army–issued smoke generators (Fig. SB1) that were manufactured in approximately 1980 for use as battlefield obscurants, purchased in 2005, and refurbished. The pulse jet engines employ standard gasoline in a fuel injector head that was ignited by manually pumping the air pressure to 60 psi before generating a spark with a grating device. The engine was used to pump and heat paraffin-type oil so that it vaporizes (but does not ignite) at approximately 150°C (the flash point). The oil pumps were modified at sea using pressurized air to force the pistons, likely required to offset the effects of rusting over time. Maintenance was required hourly to clean the fuel injectors and adjust the fuel and oil delivery rates to optimize the fuel-to-air ratio and temperature in the engine.

The vaporized oil was released through three nozzles into the atmosphere, where it condensed as droplets that range from 200 nm to 8 μm in diameter (Fig. 3). Some oil was emitted as vapor, producing a second smaller mode of particles from oxidized organic components about 100 nm in diameter. The generators ran close to their design values, consuming approximately 5 gal of gasoline and one barrel (55 gal) of oil every hour. Paraffin-type oil is used in similar amounts by skywriting activities, where each three-word message takes about one hour of flight time and consumes one barrel of oil. At 10,000 ft, the lifetime of oil particles is likely seven days, 2–3 times longer than that of surface-emitted particles. The Library of Congress describes the use of this oil in skywriting as "environmentally safe" (www.loc.gov/rr/scitech/mysteries/skywriting.html).

We operated the smoke generators from 12 to 23 July from approximately dawn until noon, following a zigzag pattern similar to that shown in Fig. 2. (Videos of smoke-generating operations are available as supplemental material at the Journals Online website at http://dx.doi.org/10.1175/BAMS-D-12-00015.s1.) We were restricted to headings into the wind by a net 5 kt or more to prevent eddies generated by the ship superstructure from carrying smoke backward into the cabins. This meant that in lower wind conditions, the smoke trail became more concentrated. In winds slower than the ship speed (10 kt), we were able to reverse course and measure the composition and number of particles in the smoke. These particles were 97% organic components, lacking both the ~50% sulfate typically found in cargo ships burning bunker fuel and the ~5% sulfate found in the R/V *Point Sur* emissions from marine diesel (Fig. 3). This unique, almost purely organic composition provided a fingerprint for tracking the smoke in cloud, as well as a surrogate for tracking particle properties in clouds.

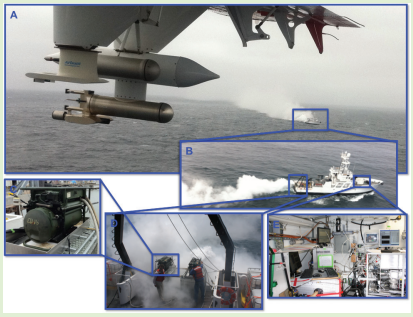

Fig. SB1. Photographs of the R/V *Point Sur* from the CIRPAS Twin Otter, showing (a) the persistence of the plume of smoke from the ship in the atmosphere and some of the aircraft instruments for measuring particles and clouds, (b) the production of smoke, (c) one of the two smoke generators used for producing smoke, (d) the operation of the smoke generators on the stern of the R/V *Point Sur*, and (e) the aerosol instrumentation on the bow of the R/V *Point Sur*.

of the droplet residual particles is measured using an Aerodyne aerosol mass spectrometer (AMS) and other instruments on board the aircraft (see Table 3). Note that the CVI used in E-PEACE is a new design that exhibits a well-characterized 50% lower cutoff diameter (11 μm) corresponding to the specific aircraft speed and CVI flow rate conditions experienced (Shingler et al. 2012). Periods with extensive drizzle, as identified with a cloud imaging probe (CIP) were omitted from this analysis owing to potential artifacts associated with the breakup of large drops.

We also measured cloud droplets in tracks produced by cargo ships (Fig. 6b) and compared them to the surrounding clouds (Fig. 6d). The droplets in clouds affected by the cargo ship emissions contained slightly less than 50% organic components, consistent with particle measurements in cargo ship emissions (Fig. 3). Roughly 5 times as many droplets are in the track from the cargo ship than in the cloud perturbed by the organic smoke generated on the R/V *Point Sur*, although each is about twice the background droplet number concentration for that day. Droplets in both tracks are smaller than those in the background, with the cargo ship droplets being the smallest, having the peak in the CDN concentration near 11.8 μm compared to 18.6 μm from the smoke. But the difference in the background cloud droplet diameter is quite striking between the two days (14.3 μm on 10 August and 26.5 μm on 16 July). The larger drop diameter on 16 July likely results from both the lower supersaturation (0.09%) and the lower particle concentrations (159 cm^{-3}) on 16 July (see Table 6). While there is uncertainty in using the maximum supersaturation calculated from the measured average CDN and the CCN spectra, the calculated updraft velocities were consistent with the measured mean and maximum updraft velocities (in cloud) of 0.12 and 0.94 m s^{-1} on 16 July and 0.32 and 1.2 m s^{-1} on 10 August, respectively. It is interesting to note that the number of below cloud accumulation particles measured by the passive cavity aerosol spectrometer probe (PCASP; 148 cm^{-3}) is very close to the droplet number (156 cm^{-3}) on 10 August, similar to a broad range of marine stratocumulus observations (Hegg et al. 2012), but not on 16 July—perhaps suggesting that the weak updrafts and 0.09% supersaturation are not frequently present.

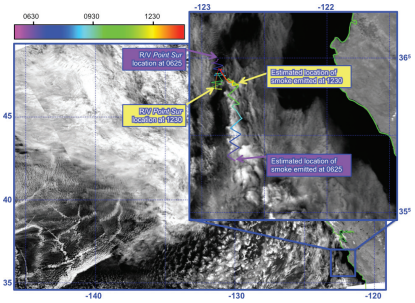

Fig. 5. Cloud tracks from cargo ships and the smoke produced on the R/V *Point Sur*. The larger image shows a composite of *Aqua* and *Terra* Moderate Resolution Imaging Spectroradiometer (MODIS) satellite images in the 2.2-μm channel. The *Terra* overpass (southwestern section of the composite image) occurred at 1250 LT and the *Aqua* overpass occurred at 1430 LT 16 Jul 2011. The smaller inset image at top right shows an enlargement of the smoke track from the region indicated. The colored lines indicate the time at which the R/V *Point Sur* was at the location, indicated by the color bar (thin line) and the estimated location of particles emitted at the time of the color bar (thick line) at the time of the satellite overpass (1430 LT). The location of emitted particles was estimated using the time between the emission and the satellite overpass, scaled by the average wind speed and direction in the boundary layer.

Several interesting questions arise: Why did the cargo ship droplets not grow as large as those from the smoke? Was it simply because they started out smaller and did not catch up, despite the presence of soluble sulfate ions? Also, why were the background droplet concentrations so different on these two days? Was it because of their lower particle concentrations, differences in meteorology, or both?

We can address these questions with an ACP model, which is designed for tracking the detailed microphysical interactions of particles with different chemical composition in clouds under specified thermodynamic conditions (Russell and Seinfeld 1998). Here, we can use the model to track the interactions of chemically different particle populations to isolate the increases in cloud drop number concentration to specific sources, such as ship tracks. For example, Russell et al. (1999) showed that droplet number is predicted to be strongly dependent on the concentration and composition of submicron aerosol particles. More recently, this model was used to analyze the role of organic particles in producing drop distributions in fog (Ming and Russell 2004), making it well suited for looking at smoke particles. The model's key computational features are a two-moment method for aerosol dynamics (both number and mass are tracked separately) and an adjustable framework for incorporating chemical properties (we choose how many different particle types to include). By simulating the step-by-step process of particle activation to droplets and growth beyond that, the model lets us address important questions, such as the role of supersaturation fluctuations from turbulence (e.g., Feingold et al. 1998) and kinetic inhibitions from reduced accommodation of water vapor onto growing droplets in marine stratocumulus in this region (e.g., Ruehl et al. 2009). It is also important to acknowledge that numerous studies have used similar models to understand some of the complex interactions of other types of cloud systems, such as pyroconvective clouds (Reutter et al. 2009).

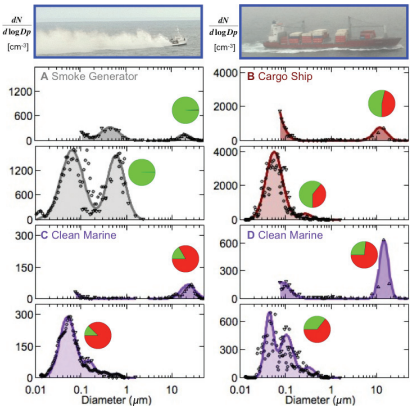

Fig. 6. Examples of particle and droplet number distributions and mass-based nonrefractory chemical composition, from measurements (bottom) below and (top) in cloud, for the (a) smoke generator on the R/V *Point Sur* on 16 Jul (gray) and for the (b) stack emissions of a cargo ship on 10 Aug (maroon). The background particle and droplet concentrations are shown for (c) 16 Jul and (d) 10 Aug (purple). The size distributions are plotted at the measured relative humidity and wet for supermicron droplets in cloud [△: 3 < CDP < 50 μm for 16 Jul and 1 < cloud aerosol spectrometer (CAS) < 50 μm for 10 Aug], with passive heating for submicron particles in (interstitial) and below cloud (▽: 0.1 < PCASP < 2 μm), and dried below cloud (○: 0.01 < scanning DMA < 0.9 μm). The pies show composition of the droplets in cloud measured by AMS for (bottom) submicron particles below cloud and for (top) the residuals of cloud droplets that are left after drying in a CVI (11 μm < CVI), with colors the same as for Fig. 3 (green—organic components; red—sulfate). Refractory chemical components (such as sea salt) were not measured behind the CVI and are not included in the pie graphs. The measurements were collected on the CIRPAS Twin Otter on 10 Aug for the cargo ship (1651–1831 LT) and 16 Jul for the smoke generators (1704–1801 LT).

Au: please confirm you mean time is local time. If it isn't, is it UTC?

The novel aspect of using E-PEACE observations for ACP studies is that we can constrain the starting point with the particle number, size, and composition of emitted particles, predict their activation in cloud by constraining them to a maximum supersaturation calculated from the measured CCN spectra (Table 6), and then compare the extent to which the prediction of the initial cloud droplet growth in the first updraft matches in-cloud observations. The differences in the cloud properties for the two days and different particle types also show that our question of why the background cloud droplets on the two days are so

different has several answers—it is both the larger number and larger size of aerosol particles (148 cm^{-3} in the accumulation mode) on 10 August and the higher updraft velocities needed to give supersaturations of 0.19% rather than 0.09% on 16 July. Exploring the reasons behind these differences with ACP simulations is the topic of a forthcoming paper.

CLOUD DEEPENING BY PARTICLES. In addition to microphysical ACP modeling studies, parallel progress has been made by investigating the complexities of the convective structure of marine boundary layers using LES models constrained by observations, as summarized in Table 2. Investigations from recent LES studies have tackled numerical issues, such as spatial resolution (Hill et al. 2009) and complex feedbacks between cloud droplet distributions and LWP (Ackerman et al. 2003), between relative dispersion and albedo changes (Lu and Seinfeld 2006), between vertical stratification and LWP (Sandu et al. 2009), and between drizzle and LWP (Caldwell and Bretherton 2009; Jiang et al. 2010). These basic feedbacks can be captured in some cases by simpler mixed-layer models (Wood et al. 2009). While many of these studies focus on the changes in boundary layers that occur during the course of a day, Savic-Jovcic and Stevens (2008) have also explored the nighttime marine boundary layer.

We have used large-eddy simulations to represent microphysics and dynamics of marine stratocumulus. A detailed bin-resolved microphysical scheme is employed in the Weather Research and Forecasting (WRF) model running in the LES mode (Chen et al. 2011). In the bin microphysical scheme, aerosol number, cloud drop mass, and cloud drop number are computed over a size-resolved spectrum, predicting both cloud drop mass and number concentration following the moment-conserving technique (Reisin et al. 1996; Tzivion et al. 1987, 1989). The microphysical processes include aerosol activation, drop condensation/evaporation, collision–coalescence, collisional breakup, and sedimentation. The impacts of ship plume and giant sea salt injection enable us to understand how different aerosol sizes, chemical compositions, and emitted locations affect the cloud dynamics.

Measurements on the CIRPAS aircraft show that cloud depth is an important feature of clouds that is affected by particles. As an example, on 4 and 10 August we conducted spiral soundings in an area influenced by large tanker ship emissions immediately adjacent to areas of background marine air. We used a cutoff of 0.05 g m^{-3} of liquid water to identify the top and bottom of the cloud. On 4 August, the cloud region was thicker in the track from the cargo ship, consistent with the hypothesis of Ackerman et al. (2004). However, on 10 August, almost no difference was seen in the clean and polluted areas; in fact, the cloud in the track may have actually been somewhat thinner, contrary to what we expect for indirect effects. GOES images (Fig. 4) taken during the times when the Twin Otter was present show some differences in cloud structure, which may offer clues about these different results.

PRECIPITATION EFFECTS OF GIANT PARTICLES. The pioneering work on the effects of giant particles on precipitation is summarized in "Giant CCN stratocumulus cloud seeding." Recently, L'Ecuyer et al. (2009) showed that injection of sea salt and sulfate aerosols led to nearly opposite cloud responses. Addition of large sea salt particles enhances precipitation and leads to less vertically developed clouds. However, addition of the considerably smaller sulfate particles suppresses precipitation in clouds and results in the onset of light precipitation at higher LWPs. Also, air masses from different source regions may produce different effects on clouds (Su et al. 2010), as those originating above polluted continental areas will have a different physicochemical signature than those from remote ocean regions (Hersey et al. 2009; Sorooshian et al. 2009a).

To study the effects of giant CCN (GCCN) on precipitation (see "Giant CCN stratocumulus cloud seeding"), we released the third type of emitted particle (3–5-μm-diameter milled salt particles) from the aircraft while flying just above cloud base. Nine flights included GCCN seeding, within which three cases (9 July, and 3 and 11 August) revealed enhanced precipitation after seeding (others were characterized by insufficient data, inadequate sampling, or a similar drizzle rate after seeding). In these three seeding cases, GCCN were released crosswind at a constant altitude (below cloud top, or midcloud) in unbroken clouds. The air mass seeded was then sampled downstream, where signatures of enhanced drizzle were observed by the optical probes and the upward-facing radar mounted on the Twin Otter. However, it was found to be challenging to confirm the sampled air mass was the same as that into which the salt was injected. To confirm that the downwind sampling occurred within the seeded region, during the research flight on 11 August, black carbon particles were mixed with the salt to serve as a tracer. Though enhanced precipitation was observed after seeding, the black carbon concentration detected by the single-particle soot photometer (SP2) within the sampling region was similar to its background concentration, and thus it did not provide unequivocal evidence of sampling of the region into which GCCN was injected.

In these three cases, the seeded clouds were clean (with low cloud droplet number concentration)

GIANT CCN STRATOCUMULUS CLOUD SEEDING

The role of GCCN in stimulating precipitation production in stratocumulus clouds suggested by Woodcock (1950) has been studied recently using LES and parcel models (e.g., Feingold et al. 1999; Jensen and Lee 2008). These studies indicate that GCCN introduced into nonprecipitating stratocumulus clouds can promote the growth of droplets to drizzle by acting as collector drops with higher rates of collision and coalescence. Nevertheless, observing the effects of GCCN in real clouds is challenging. First, GCCN concentrations in nature (10^{-4}–10^{-2} cm^{-3}) are many orders of magnitude less than CCN (10^{2} cm^{-3}) and thus difficult to measure from an aircraft. Second, since factors other than GCCN injection can affect and modulate drizzle production, it is difficult to establish cause and effect. In principle, marine stratocumulus clouds present laboratory-like conditions for directly evaluating how added GCCN can modify the cloud properties. By introducing GCCN directly into an unbroken and well-developed cloud, the properties of the seeded cloud region can be compared with the unperturbed background cloud conditions.

Techniques for artificially seeding clouds with GCCN have been developed for the deliberate enhancement of precipitation in warm cumulus clouds. One technique that has been reported for cloud perturbation is airborne flares that produce a wide spectrum of hygroscopic particles with a tail of larger particles that serve as GCCN (Ghate et al. 2007). To artificially introduce GCCN without increasing the smaller CCN, we employ a technique developed by Rosenfeld et al. (2010) that uses milled salt particles (in the range of 3–5-μm diameter) that are mixed with SiO_2 to prevent sticking and clumping of the particles. In E-PEACE we injected salt powder (provided by D. Rosenfeld) from the CIRPAS Twin Otter into the cloud. To deliver these particles, we designed and fabricated an apparatus that used an auger to feed the salt powder into a fluidized bed of grit maintained by air pumped into the grit chamber that then ejects the powder into the aircraft's airflow, where it is dispersed. The injection rate of salt mass from the aircraft is designed to produce GCCN concentrations in the environment of the order of 10^{-3} cm^{-3}. After the GCCN are dispersed into the cloud, the aircraft returns to sample the moving cloudy air mass into which the particles were injected. Airborne frequency-modulated continuous wave cloud radar is especially advantageous in measuring the response of the seeded region in the cloud. Since the radar has a very shallow dead zone (less than 50 m), the reflectivity from the radar returns closest to the aircraft can be compared directly with the in situ aircraft probe observations.

Table 6. Particle and droplet characteristics for below and in-cloud measurements shown in Fig. 7.

Date of measurement	16 Jul		10 Aug	
Description of particles	Background	Generator smoke	Background	Cargo ship
Cloud-base height (m)	145	145	338	338
Cloud-top height (m)	370	370	670	670
Below cloud particles (CPC) (cm^{-3})	159	1,786	361	1,938
Below cloud accumulation particles (PCASP) (cm^{-3})	46	659	148	644
Calculated maximum supersaturation[a] (CCN) (%)	0.09	0.09	0.25	0.25
Calculated activation diameter[b] (μm)	0.13	1.1	0.06	0.09
In-cloud mean/max positive updraft velocity[c] (m s^{-1})	0.12/0.94		0.32/1.2	
In-cloud mean/std dev of all updraft velocity[c] (m s^{-1})	−0.09/0.22		+0.13/0.39	
In-cloud accumulation particles (PCASP) (cm^{-3})	3	188	49	214
In-cloud droplet number (CAS, CDP) (cm^{-3})	25	49	156	277
In-cloud droplet diameter[d] (CAS, CDP) (μm)	26.5	18.6	14.3	11.8

[a] The supersaturation is calculated from the CCN spectrum as the supersaturation at which the measured CDN is equal to the CCN, interpolated between measured supersaturation using sigmoidal fit (±0.04%).

[b] The activation diameter is calculated as the size of the smallest particle needed to activate to produce the measured CDN, assuming all larger particles activated.

[c] The in-cloud updraft velocity is calculated from 1-Hz measurements during 30-min sampling legs in cloud at 220 m for 16 Jul and 480 m for 10 Aug; the same value is used for both background and track, since sampling was insufficient to identify updraft rates in tracks.

[d] Cloud droplet diameters are reported at the peak concentration of the droplet mode.

and already drizzling prior to seeding. Previous modeling studies (e.g., Feingold et al. 1999) suggest that injection of GCCN has the greatest potential for altering cloud behavior when CCN concentrations are already relatively high, so that conditions during these three cases were not optimal for generating a strong precipitation signal. Based on the analysis of these three cases, robust evidence of precipitation enhancement from GCCN seeding was lacking. The difficulty in tracking the moving cloudy air mass within which GCCN were injected by an aircraft underscores the challenge associated with such in situ cloud perturbation experiments.

SUMMARY AND OUTLOOK. The campaign of the Eastern Pacific Emitted Aerosol Cloud Experiment (E-PEACE) was designed to take advantage of recent advances in both instruments and models used to collect detailed, quantitative observations of the effects of particles on clouds. Using an innovative new particle emission and measurement technology, three kinds of particles were emitted and controlled, each as a single variable in the highly complex, natural system governing marine stratocumulus clouds. Since the emitted particles span 100 nm to several micrometers in diameter, the E-PEACE observations cover a wide range of cloud droplet sizes and number concentrations. The outcome of these studies revealed that both incidental smoke and ship emissions are effective at modifying cloud albedo, as well as that giant salt nuclei can increase drizzle rates. The multiple particle sizes provide constraints for both ACP and LES models, allowing us to carry out future modeling simulations to place the observations in a theoretical framework that can be extended to global models. When considering these results in the context of Earth's solar radiation balance and the relative amounts of cooling and warming produced by different particle emissions (see "Cooling efficiency of cargo ships and smoke"), we suggest that the effective carbon offsets from cloud tracks from cargo ships should be considered. Clearly such considerations would need to extend beyond the local aerosol–cloud–radiation interactions assessed here to the effects of tracks on neighboring clouds as well as ecosystem impacts.

ACKNOWLEDGMENTS. The E-PEACE field campaign and modeling studies were funded by the National Science Foundation (Grants AGS-1013423, AGS-1008848, AGS-1013381, AGS-1013319; ATM-0744636, AGS-0821599, and ATM-0349015) and the Office of Naval Research (Grants N00014-11-1-0783, N00014-10-1-0811, N00014-10-1-0200, and N00014-08-1-0465). Sea Spray Research, Inc. provided oil for the operation of the smoke generators. The authors gratefully acknowledge the crews of the CIRPAS Twin Otter and the R/V *Point Sur* for their assistance during the field campaign; Tom Maggard, who revived and tirelessly maintained the smoke generators during the cruise; David Malmberg and the crew of the R/V *Sproul*, for their assistance in testing the smoke generators prior to the campaign; Spyros Pandis, for providing the CCN spectrometer; and Daniel Rosenfeld, for providing the powdered salt. We also thank Richard Leaitch and two anonymous reviewers for providing helpful comments on the submitted manuscript.

Au: correct to note that the funding sources are grants? If they are not grants, are they awards, cooperative agreements, or program elements?

COOLING EFFICIENCY OF CARGO SHIPS AND SMOKE

Smoke emissions from smoke generators were employed in the present study, along with the incidental emissions of transoceanic cargo ships (Conover 1969; Durkee et al. 2000c). Here we consider the extent to which each of these two types of oceangoing particle emissions provides a net cooling effect (based only on fuel consumed, not emissions from ship construction).

Take into consideration a single day for both smoke and cargo ship emissions in clouds that form tracks, an average summertime lifetime of the track in the cloud of 6 h (normalized to a 100-yr time horizon), and an average daily fuel consumption at typical transit speeds. We calculate the asymptotic CO_2-caused temperature increase from 3 K per 280 ppmv (Solomon et al. 2007) and find 1 nK (10^{-9} K) from the 100,000-gal bunker fuel burned by the cargo ship and 0.008 nK for the 500-gal marine diesel burned by the R/V *Point Sur*. The cargo ship typically transits 5 times faster than the R/V *Point Sur*, so the area covered by the track (assuming the same wind speed in the lateral direction) is taken to be 5 times larger, providing 2,500 km^2 for the cargo ship and 500 km^2 for the smoke. We use the 15% cloud brightening measured for the smoke on 16 July (Fig. 5) for both tracks to find 2-nK cooling for the cargo ship and 0.4-nK cooling for the smoke—that gives us ratios of cooling to warming (i.e., a cooling efficiency) of ~2 for the cargo ship and ~50 for the smoke generator.

Although this is a very simplified calculation, we find that, if half of the open-ocean transit days of a cargo ship result in tracks that are on average 15% brighter than the surrounding clouds and cover 2,500 km^2, then cargo ship transit (for consumables only) could be considered "carbon neutral" (in the sense of having no net warming effect) transportation. Further, we find that smoke generators on board smaller ships (that require less than 2% of the fuel per transit mile) could provide a net cooling effect, which could be used to offset some of the warming caused by ship CO_2 emissions.

Au: changed IPCC (2007) to Solomon et al. (2007) throughout per AMS style.

REFERENCES

Ackerman, A. S., O. B. Toon, D. E. Stevens, and J. A. Coakley Jr., 2003: Enhancement of cloud cover and suppression of nocturnal drizzle in stratocumulus polluted by haze. *Geophys. Res. Lett.*, **30,** 1381, doi:10.1029/2002gl016634.

——, M. P. Kirkpatrick, D. E. Stevens, and O. B. Toon, 2004: The impact of humidity above stratiform clouds on indirect aerosol climate forcing. *Nature,* **432,** 1014–1017, doi:10.1038/nature03174.

Albrecht, B. A., 1989: Aerosols, cloud microphysics, and fractional cloudiness. *Science,* **245,** 1227–1230.

Allen, G., and Coauthors, 2011: South east Pacific atmospheric composition and variability sampled along 20° S during VOCALS-REx. *Atmos. Chem. Phys.,* **11,** 5237–5262, doi:10.5194/acp-11-5237-2011.

Barkstrom, B. R., 1984: The Earth Radiation Budget Experiment (ERBE). *Bull. Amer. Meteor. Soc.,* **65,** 1170–1185.

Brenguier, J. L., H. Pawlowska, L. Schuller, R. Preusker, J. Fischer, and Y. Fouquart, 2000: Radiative properties of boundary layer clouds: Droplet effective radius versus number concentration. *J. Atmos. Sci.,* **57,** 803–821.

Bretherton, C. S., R. Wood, R. C. George, D. Leon, G. Allen, and X. Zheng, 2010: Southeast Pacific stratocumulus clouds, precipitation and boundary layer structure sampled along 20° S during VOCALS-REx. *Atmos. Chem. Phys.,* **10,** 10 639–10 654, doi:10.5194/acp-10-10639-2010.

Caldwell, P., and C. S. Bretherton, 2009: Response of a subtropical stratocumulus-capped mixed layer to climate and aerosol changes. *J. Climate,* **22,** 20–38.

Chen, Y.-C., L. Xue, Z. J. Lebo, H. Wang, R. M. Rasmussen, and J. H. Seinfeld, 2011: A comprehensive numerical study of aerosol-cloud-precipitation interactions in marine stratocumulus. *Atmos. Chem. Phys.,* **11,** 9749–9769, doi:10.5194/acp-11-9749-2011.

——, M. W. Christensen, L. Xue, A. Sorooshian, G. L. Stephens, R. M. Rasmussen, and J. H. Seinfeld, 2012: Occurrence of lower cloud albedo in ship tracks. *Atmos. Chem. Phys. Discuss.,* **12,** 13 553–13 580, doi: 10.5194/acpd-12-13553-2012.

Christensen, M. W., and G. L. Stephens, 2011: Microphysical and macrophysical responses of marine stratocumulus polluted by underlying ships: Evidence of cloud deepening. *J. Geophys. Res.,* **116,** D03201, doi:10.1029/2010jd014638.

Coakley, J. A., and C. D. Walsh, 2002: Limits to the aerosol indirect radiative effect derived from observations of ship tracks. *J. Atmos. Sci.,* **59,** 668–680.

——, R. L. Bernstein, and P. A. Durkee, 1987: Effect of ship-stack effluents on cloud reflectivity. *Science,* **237,** 1020–1022.

——, and Coauthors, 2000: The appearance and disappearance of ship tracks on large spatial scales. *J. Atmos. Sci.,* **57,** 2765–2778.

Coggon, M. M., and Coauthors, 2012: Ship impacts on the marine atmosphere: Insights into the contribution of shipping emissions to the properties of marine aerosol and clouds. *Atmos. Chem. Phys. Discuss.,* **12,** 14 393–14 445, doi:10.5194/acpd-12-14393-2012.

Conover, J. H., 1966: Anomalous cloud lines. *J. Atmos. Sci.,* **23,** 778–785.

——, 1969: New observations of anomalous cloud lines. *J. Atmos. Sci.,* **26,** 1153–1154.

Crahan, K. K., D. A. Hegg, D. S. Covert, H. Jonsson, J. S. Reid, D. Khelif, and B. J. Brooks, 2004: Speciation of organic aerosols in the tropical mid-Pacific and their relationship to light scattering. *J. Atmos. Sci.,* **61,** 2544–2558.

Curry, J. A., E. E. Ebert, and G. F. Herman, 1988: Mean and turbulence structure of the summertime Arctic cloudy boundary layer. *Quart. J. Roy. Meteor. Soc.,* **114,** 715–746.

Drofa, A. S., V. N. Ivanov, D. Rosenfeld, and A. G. Shilin, 2010: Studying an effect of salt powder seeding used for precipitation enhancement from convective clouds. *Atmos. Chem. Phys.,* **10,** 8011–8023, doi:10.5194/acp-10-8011-2010.

Durkee, P. A., and Coauthors, 2000a: Composite ship track characteristics. *J. Atmos. Sci.,* **57,** 2542–2553.

——, and Coauthors, 2000b: The impact of ship-produced aerosols on the microstructure and albedo of warm marine stratocumulus clouds: A test of MAST hypotheses 1i and 1ii. *J. Atmos. Sci.,* **57,** 2554–2569.

——, K. J. Noone, and R. T. Bluth, 2000c: The Monterey Area Ship Track Experiment. *J. Atmos. Sci.,* **57,** 2523–2541.

Faloona, I., and Coauthors, 2005: Observations of entrainment in eastern Pacific marine stratocumulus using three conserved scalars. *J. Atmos. Sci.,* **62,** 3268–3285.

Feingold, G., and H. Siebert, 2009: Cloud-aerosol interactions from the micro to the cloud scale. *Clouds in the Perturbed Climate System: Their Relationship to Energy Balance, Atmospheric Dynamics, and Precipitation,* J. Heintzenberg and R. J. Charlson, Eds., MIT Press, 319–338.

——, S. M. Kreidenweis, and Y. Zhang, 1998: Stratocumulus processing of gases and cloud condensation nuclei: 1. Trajectory ensemble model. *J. Geophys. Res.,* **103** (D16), 19 527–19 542.

——, W. R. Cotton, S. M. Kreidenweis, and J. T. Davis, 1999: The impact of giant cloud condensation nuclei on drizzle formation in stratocumulus: Implications for cloud radiative properties. *J. Atmos. Sci.,* **56,** 4100–4117.

——, R. Furrer, P. Pilewskie, L. A. Remer, Q. L. Min, and H. Jonsson, 2006: Aerosol indirect effect studies at Southern Great Plains during the May 2003 intensive operations period. *J. Geophys. Res.,* **111,** D05S14, doi:10.1029/2004jd005648.

——, I. Koren, H. L. Wang, H. W. Xue, and W. A. Brewer, 2010: Precipitation-generated oscillations in open cellular cloud fields. *Nature,* **466,** 849–852, doi:10.1038/nature09314.

Ferek, R. J., D. A. Hegg, P. V. Hobbs, P. Durkee, and K. Nielsen, 1998: Measurements of ship-induced tracks in clouds off the Washington coast. *J. Geophys. Res.,* **103** (D18), 23 199–23 206.

——, and Coauthors, 2000: Drizzle suppression in ship tracks. *J. Atmos. Sci.,* **57,** 2707–2728.

Frick, G. M., and W. A. Hoppel, 2000: Airship measurements of ship's exhaust plumes and their effect on marine boundary layer clouds. *J. Atmos. Sci.,* **57,** 2625–2648.

Ghate, V. P., B. A. Albrecht, P. Kollias, H. H. Jonsson, and D. W. Breed, 2007: Cloud seeding as a technique for studying aerosol-cloud interactions in marine stratocumulus. *Geophys. Res. Lett.,* **34,** L14807, doi:10.1029/2007gl029748.

Hawkins, L. N., L. M. Russell, C. H. Twohy, and J. R. Anderson, 2008: Uniform particle-droplet partitioning of 18 organic and elemental components measured in and below DYCOMS-II stratocumulus clouds. *J. Geophys. Res.,* **113,** D14201, doi:10.1029/2007jd009150.

Hegg, D. A., and P. V. Hobbs, 1986: Sulfate and nitrate chemistry in cumuliform clouds. *Atmos. Environ.,* **20,** 901–909.

——, D. S. Covert, and H. H. Jonsson, 2008: Measurements of size-resolved hygroscopicity in the California coastal zone. *Atmos. Chem. Phys.,* **8,** 7193–7203.

——, ——, ——, and R. Woods, 2009: Differentiating natural and anthropogenic cloud condensation nuclei in the California coastal zone. *Tellus,* **61B,** 669–676, doi:10.1111/j.1600-0889.2009.00435.x.

——, ——, ——, and ——, 2012: A simple relationship between cloud drop number concentration and precursor aerosol concentration for the regions of Earth's large marine stratocumulus decks. *Atmos. Chem. Phys.,* **12,** 1229–1238, doi:10.5194/acp-12-1229-2012.

Hersey, S. P., A. Sorooshian, S. M. Murphy, R. C. Flagan, and J. H. Seinfeld, 2009: Aerosol hygroscopicity in the marine atmosphere: A closure study using high-time-resolution, multiple-RH DASH-SP and size-resolved C-ToF-AMS data. *Atmos. Chem. Phys.,* **9,** 2543–2554.

Hill, A. A., G. Feingold, and H. L. Jiang, 2009: The influence of entrainment and mixing assumption on aerosol–cloud interactions in marine stratocumulus. *J. Atmos. Sci.,* **66,** 1450–1464.

Hobbs, P. V., and Coauthors, 2000: Emissions from ships with respect to their effects on clouds. *J. Atmos. Sci.,* **57,** 2570–2590.

Hsieh, W. C., A. Nenes, R. C. Flagan, J. H. Seinfeld, G. Buzorius, and H. Jonsson, 2009: Parameterization of cloud droplet size distributions: Comparison with parcel models and observations. *J. Geophys. Res.,* **114,** D11205, doi:10.1029/2008jd011387.

Jensen, J. B., and S. Lee, 2008: Giant sea-salt aerosols and warm rain formation in marine stratocumulus. *J. Atmos. Sci.,* **65,** 3678–3694.

Jiang, H. L., G. Feingold, and A. Sorooshian, 2010: Effect of aerosol on the susceptibility and efficiency of precipitation in warm trade cumulus clouds. *J. Atmos. Sci.,* **67,** 3525–3540.

Klein, S. A., and D. L. Hartmann, 1993: The seasonal cycle of low stratiform clouds. *J. Climate,* **6,** 1587–1606.

L'Ecuyer, T. S., W. Berg, J. Haynes, M. Lebsock, and T. Takemura, 2009: Global observations of aerosol impacts on precipitation occurrence in warm maritime clouds. *J. Geophys. Res.,* **114,** D09211, doi:10.1029/2008jd011273.

Lance, S., C. A. Brock, D. Rogers, and J. A. Gordon, 2010: Water droplet calibration of the cloud droplet probe (CDP) and in-flight performance in liquid, ice and mixed-phase clouds during ARCPAC. *Atmos. Meas. Tech.,* **3,** 1683–1706, doi:10.5194/amt-3-1683-2010.

Lilly, D. K., 1968: Models of cloud-topped mixed layers under a strong inversion. *Quart. J. Roy. Meteor. Soc.,* **94,** 292–309.

Lu, M.-L., and J. H. Seinfeld, 2005: Study of the aerosol indirect effect by large-eddy simulation of marine stratocumulus. *J. Atmos. Sci.,* **62,** 3909–3932.

——, and ——, 2006: Effect of aerosol number concentration on cloud droplet dispersion: A large-eddy simulation study and implications for aerosol indirect forcing. *J. Geophys. Res.,* **111,** D02207, doi:10.1029/2005jd006419.

——, W. C. Conant, H. H. Jonsson, V. Varutbangkul, R. C. Flagan, and J. H. Seinfeld, 2007: The Marine Stratus/Stratocumulus Experiment (MASE): Aerosol-cloud relationships in marine stratocumulus. *J. Geophys. Res.,* **112,** D10209, doi:10.1029/2006jd007985.

——, A. Sorooshian, H. H. Jonsson, G. Feingold, R. C. Flagan, and J. H. Seinfeld, 2009: Marine stratocumulus aerosol-cloud relationships in the MASE-II experiment: Precipitation susceptibility in eastern Pacific marine stratocumulus. *J. Geophys. Res.,* **114,** D24203, doi:10.1029/2009jd012774.

Meskhidze, N., A. Nenes, W. C. Conant, and J. H. Seinfeld, 2005: Evaluation of a new cloud droplet activation parameterization with in situ data from CRYSTAL-FACE and CSTRIPE. *J. Geophys. Res.,* **110,** D16202, doi:10.1029/2004jd005703.

Ming, Y., and L. M. Russell, 2004: Organic aerosol effects on fog droplet spectra. *J. Geophys. Res.,* **109,** D10206, doi:10.1029/2003jd004427.

Moore, R. H., and A. Nenes, 2009: Scanning flow CCN analysis—A method for fast measurements of CCN spectra. *Aerosol Sci. Technol.,* **43,** 1192–1207, doi:10.1080/02786820903289780.

Noone, K. J., and Coauthors, 2000a: A case study of ship track formation in a polluted marine boundary layer. *J. Atmos. Sci.,* **57,** 2748–2764.

——, and Coauthors, 2000b: A case study of ships forming and not forming tracks in moderately polluted clouds. *J. Atmos. Sci.,* **57,** 2729–2747.

Petters, M. D., J. R. Snider, B. Stevens, G. Vali, I. Faloona, and L. M. Russell, 2006: Accumulation mode aerosol, pockets of open cells, and particle nucleation in the remote subtropical Pacific marine boundary layer. *J. Geophys. Res.,* **111,** D02206, doi:10.1029/2004jd005694.

Platnick, S., and Coauthors, 2000: The role of background cloud microphysics in the radiative formation of ship tracks. *J. Atmos. Sci.,* **57,** 2607–2624.

Radke, L. F., J. A. Coakley Jr., and M. D. King, 1989: Direct and remote sensing observations of the effects of ships on clouds. *Science,* **246,** 1146–1149.

Reisin, T., Z. Levin, and S. Tzivion, 1996: Rain production in convective clouds as simulated in an axisymmetric model with detailed microphysics. Part I: Description of the model. *J. Atmos. Sci.,* **53,** 497–519.

Reutter, P., and Coauthors, 2009: Aerosol- and updraft-limited regimes of cloud droplet formation: Influence of particle number, size and hygroscopicity on the activation of cloud condensation nuclei (CCN). *Atmos. Chem. Phys.,* **9,** 7067–7080.

Roberts, G. C., and A. Nenes, 2005: A continuous-flow streamwise thermal-gradient CCN chamber for atmospheric measurements. *Aerosol Sci. Technol.,* **39,** 206–221, doi:10.1080/027868290913988.

——, M. V. Ramana, C. Corrigan, D. Kim, and V. Ramanathan, 2008: Simultaneous observations of aerosol–cloud–albedo interactions with three stacked unmanned aerial vehicles. *Proc. Natl. Acad. Sci. USA,* **105,** 7370–7375, doi:10.1073/pnas.0710308105.

Rosenfeld, D., D. Axisa, W. L. Woodley, and R. Lahav, 2010: A quest for effective hygroscopic cloud seeding. *J. Appl. Meteor. Climatol.,* **49,** 1548–1562.

Ruehl, C. R., P. Y. Chuang, and A. Nenes, 2009: Distinct CCN activation kinetics above the marine boundary layer along the California coast. *Geophys. Res. Lett.,* **36,** L15814, doi:10.1029/2009gl038839.

Russell, L. M., and J. H. Seinfeld, 1998: Size- and composition-resolved externally mixed aerosol model. *Aerosol Sci. Technol.,* **28,** 403–416.

——, and Coauthors, 1999: Aerosol dynamics in ship tracks. *J. Geophys. Res.,* **104** (D24), 31 077–31 095.

Sandu, I., J. L. Brenguier, O. Thouron, and B. Stevens, 2009: How important is the vertical structure for the representation of aerosol impacts on the diurnal cycle of marine stratocumulus? *Atmos. Chem. Phys.,* **9,** 4039–4052.

Savic-Jovcic, V., and B. Stevens, 2008: The structure and mesoscale organization of precipitating stratocumulus. *J. Atmos Sci.,* **65,** 1587–1605.

Schreier, M., H. Mannstein, V. Eyring, and H. Bovensmann, 2007: Global ship track distribution and radiative forcing from 1 year of AATSR data. *Geophys. Res. Lett.,* **34,** L17814, doi:10.1029/2007gl030664.

Schubert, W. H., J. S. Wakefield, E. J. Steiner, and S. K. Cox, 1979a: Marine stratocumulus convection. Part I: Governing equations and horizontally homogeneous solutions. *J. Atmos. Sci.,* **36,** 1286–1307.

——, ——, ——, and ——, 1979b: Marine stratocumulus convection. Part II: Horizontally inhomogeneous solutions. *J. Atmos. Sci.,* **36,** 1308–1324.

Scorer, R. S., 1987: Ship trails. *Atmos. Environ.,* **21,** 1417–1425.

Segrin, M. S., J. A. Coakley, and W. R. Tahnk, 2007: MODIS observations of ship tracks in summertime stratus off the West Coast of the United States. *J. Atmos. Sci.,* **64,** 4330–4345.

Sharon, T. M., B. A. Albrecht, H. H. Jonsson, P. Minnis, M. M. Khaiyer, T. M. van Reken, J. Seinfeld, and R. Flagan, 2006: Aerosol and cloud microphysical characteristics of rifts and gradients in maritime stratocumulus clouds. *J. Atmos. Sci.,* **63,** 983–997.

Shingler, T., and Coauthors, 2012: Characterisation and airborne deployment of a new counterflow virtual impactor inlet. *Atmos. Meas. Tech.,* **5,** 1259–1269, doi:10.5194/amt-5-1259-2012.

Solomon, S., D. Qin, M. Manning, M. Marquis, K. Averyt, M. M. B. Tignor, H. L. Miller Jr., and Z. Chen, Eds., 2007: *Climate Change 2007: The Physical Science Basis.* Cambridge University Press, 996 pp.

Sorooshian, A., M. L. Lu, F. J. Brechtel, H. Jonsson, G. Feingold, R. C. Flagan, and J. H. Seinfeld, 2007: On the source of organic acid aerosol layers above clouds.

Au: changed IPCC (2007) to Solomon et al. (2007) throughout per AMS style.

Environ. Sci. Technol., **41,** 4647–4654, doi:10.1021/es0630442.

——, and Coauthors, 2009a: On the link between ocean biota emissions, aerosol, and maritime clouds: Airborne, ground, and satellite measurements off the coast of California. *Global Biogeochem. Cycles,* **23,** GB4007, doi:10.1029/2009gb003464.

——, G. Feingold, M. D. Lebsock, H. L. Jiang, and G. L. Stephens, 2009b: On the precipitation susceptibility of clouds to aerosol perturbations. *Geophys. Res. Lett.,* **36,** L13803, doi:10.1029/2009gl038993.

——, J. Csavina, T. Shingler, S. Dey, F. Brechtel, E. Sáez, and E. Betterton, 2012: Hygroscopic and chemical properties of aerosols collected near a copper smelter: Implications for public and environmental health. *Environ. Sci. Technol.*, **46,** 9473–9480, doi:10.1021/es302275k.

Stephens, G. L., and Coauthors, 2002: The CloudSat mission and the A-Train: A new dimension of space-based observations of clouds and precipitation. *Bull. Amer. Meteor. Soc.,* **83,** 1771–1790.

Stevens, B., and Coauthors, 2003: Dynamics and chemistry of marine stratocumulus— DYCOMS-II. *Bull. Amer. Meteor. Soc.,* **84,** 579–593.

——, G. Vali, K. Comstock, R. Wood, M. C. Van Zanten, P. H. Austin, C. S. Bretherton, and D. H. Lenschow, 2005: Pockets of open cells and drizzle in marine stratocumulus. *Bull. Amer. Meteor. Soc.,* **86,** 51–57.

Su, W. Y., N. G. Loeb, K.-M. Xu, G. L. Schuster, and Z. A. Eitzen, 2010: An estimate of aerosol indirect effect from satellite measurements with concurrent meteorological analysis. *J. Geophys. Res.,* **115,** D18219, doi:10.1029/2010jd013948.

Sullivan, A. P., R. E. Peltier, C. A. Brock, J. A. de Gouw, J. S. Holloway, C. Warneke, A. G. Wollny, and R. J. Weber, 2006: Airborne measurements of carbonaceous aerosol soluble in water over northeastern United States: Method development and an investigation into water-soluble organic carbon sources. *J. Geophys. Res.,* **111,** D23S46, doi:10.1029/2006jd007072.

Twohy, C. H., M. D. Petters, J. R. Snider, B. Stevens, W. Tahnk, M. Wetzel, L. Russell, and F. Burnet, 2005: Evaluation of the aerosol indirect effect in marine stratocumulus clouds: Droplet number, size, liquid water path, and radiative impact. *J. Geophys. Res.,* **110,** D08203, doi:10.1029/2004jd005116.

Twomey, S., 1991: Aerosols, clouds and radiation. *Atmos. Environ.*, **25A,** 2435–2442.

——, H. B. Howell, and T. A. Wojciech, 1968: Comments on anomalous cloud lines. *J. Atmos. Sci.*, **25,** 333–334.

Tzivion, S., G. Feingold, and Z. Levin, 1987: An efficient numerical solution to the stochastic collection equation. *J. Atmos. Sci.,* **44,** 3139–3149.

——, ——, and Z. Levin, 1989: The evolution of raindrop spectra. Part II: Collisional collection/breakup and evaporation in a rainshaft. *J. Atmos. Sci.,* **46,** 3312–3327.

Van Zanten, M. C., and B. Stevens, 2005: Observations of the structure of heavily precipitating marine stratocumulus. *J. Atmos. Sci.,* **62,** 4327–4342.

Wang, H., G. Feingold, R. Wood, and J. Kazil, 2010: Modelling microphysical and meteorological controls on precipitation and cloud cellular structures in southeast Pacific stratocumulus. *Atmos. Chem. Phys.,* **10,** 6347–6362, doi:10.5194/acp-10-6347-2010.

Wilcox, E. M., G. Roberts, and V. Ramanathan, 2006: Influence of aerosols on the shortwave cloud radiative forcing from North Pacific oceanic clouds: Results from the Cloud Indirect Forcing Experiment (CIFEX). *Geophys. Res. Lett.,* **33,** L21804, doi:10.1029/2006gl027150.

Wood, R., T. L. Kubar, and D. L. Hartmann, 2009: Understanding the importance of microphysics and macrophysics for warm rain in marine low clouds. Part II: Heuristic models of rain formation. *J. Atmos. Sci.,* **66,** 2973–2990.

——, C. S. Bretherton, D. Leon, A. D. Clarke, P. Zuidema, G. Allen, and H. Coe, 2011a: An aircraft case study of the spatial transition from closed to open mesoscale cellular convection over the southeast Pacific. *Atmos. Chem. Phys.,* **11,** 2341–2370, doi:10.5194/acp-11-2341-2011.

——, and Coauthors, 2011b: The VAMOS Ocean-Cloud-Atmosphere-Land Study Regional Experiment (VOCALS-REx): Goals, platforms, and field operations. *Atmos. Chem. Phys.,* **11,** 627–654, doi:10.5194/acp-11-627-2011.

Woodcock, A. H., 1950: Condensation nuclei and precipitation. *J Meteor.,* **7,** 161–162.

Au edited the reference Twomey et al. (1968) to match our files. Please confirm you meant to cite this article.

ABSTRACT

Aerosol–cloud–radiation interactions are widely held to be the largest single source of uncertainty in climate model projections of future radiative forcing due to increasing anthropogenic emissions. The underlying causes of this uncertainty among modeled predictions of climate are the gaps in our fundamental understanding of cloud processes. There has been significant progress with both observations and models in addressing these important questions but quantifying them correctly is nontrivial, thus limiting our ability to represent them in global climate models. The Eastern Pacific Emitted Aerosol Cloud Experiment (E-PEACE) 2011 was a targeted aircraft campaign with embedded modeling studies, using the Center for Interdisciplinary Remotely-Piloted Aircraft Studies (CIRPAS) Twin Otter aircraft and the research vessel *Point Sur* in July and August 2011 off the central coast of California, with a full payload of instruments to measure particle and cloud number, mass, composition, and water uptake distributions. E-PEACE used three emitted particle sources to separate particle-induced feedbacks from dynamical variability, namely 1) shipboard smoke-generated particles with 0.05–1-μm diameters (which produced tracks measured by satellite and had drop composition characteristic of organic smoke), 2) combustion particles from container ships with 0.05–0.2-μm diameters (which were measured in a variety of conditions with droplets containing both organic and sulfate components), and 3) aircraft-based milled salt particles with 3–5-μm diameters (which showed enhanced drizzle rates in some clouds). The aircraft observations were consistent with past large-eddy simulations of deeper clouds in ship tracks and aerosol–cloud parcel modeling of cloud drop number and composition, providing quantitative constraints on aerosol effects on warm-cloud microphysics.

Appendix G

Water–soluble Organic Aerosol in the Los Angeles Basin and Outflow Regions: Airborne and Ground Measurements during the 2010 CalNex Field Campaign[1]

[1]This chapter is reproduced by permission from "Water–soluble Organic Aerosol in the Los Angeles Basin and Outflow Regions: Airborne and Ground Measurements during the 2010 CalNex Field Campaign" by Hanh T. Duong, Armin Sorooshian, Jill S. Craven, Scott P. Hersey, Andrew R. Metcalf, Xiaolu Zhang, Rodney J. Weber, Haflidi Jonsson, Richard C. Flagan, and John H. Seinfeld, *Journal of Geophysical Research*, (116), D00V04, doi:10.1029/2011JD016674, 2011. An edited version of this paper was published by AGU.

JOURNAL OF GEOPHYSICAL RESEARCH, VOL. 116, D00V04, doi:10.1029/2011JD016674, 2011

Water-soluble organic aerosol in the Los Angeles Basin and outflow regions: Airborne and ground measurements during the 2010 CalNex field campaign

Hanh T. Duong,[1] Armin Sorooshian,[1,2] Jill S. Craven,[3] Scott P. Hersey,[3] Andrew R. Metcalf,[3] Xiaolu Zhang,[4] Rodney J. Weber,[4] Haflidi Jonsson,[5] Richard C. Flagan,[3] and John H. Seinfeld[3]

Received 3 August 2011; revised 21 September 2011; accepted 25 September 2011; published 18 November 2011.

[1] A particle-into-liquid sampler coupled to a total organic carbon analyzer (PILS-TOC) quantified particulate water-soluble organic carbon (WSOC) mass concentrations during the May 2010 deployment of the Center for Interdisciplinary Remotely Piloted Aircraft Studies (CIRPAS) Twin Otter in the CalNex field study. WSOC data collected during 16 flights provide the first spatiotemporal maps of WSOC in the San Joaquin Valley, Los Angeles Basin, and outflow regions of the Basin. WSOC was consistently higher in concentration within the Los Angeles Basin, where sea breeze transport and Basin topography strongly influence the spatial distribution of WSOC. The highest WSOC levels were associated with fire plumes, highlighting the importance of both primary and secondary sources for WSOC in the region. Residual pollution layers enriched with WSOC are observed aloft up to an altitude of 3.2 km and the highest WSOC levels for each flight were typically observed above 500 m. Simultaneous ground WSOC measurements during aircraft overpasses in Pasadena and Riverside typically exhibit lower levels, especially when relative humidity (RH) was higher aloft suggestive of the influence of aerosol-phase water. This points to the underestimation of the radiative effects of WSOC when using only surface measurements. Reduced aerosol-phase water in the eastern desert outflow region likely promotes the re-partitioning of WSOC to the gas phase and suppression of processes to produce these species (partitioning, multiphase chemistry, photolytic production); as a result, WSOC is reduced relative to sulfate (but not as much as nitrate) as aerosol is advected from the Basin to the outflows.

Citation: Duong, H. T., A. Sorooshian, J. S. Craven, S. P. Hersey, A. R. Metcalf, X. Zhang, R. J. Weber, H. Jonsson, R. C. Flagan, and J. H. Seinfeld (2011), Water-soluble organic aerosol in the Los Angeles Basin and outflow regions: Airborne and ground measurements during the 2010 CalNex field campaign, *J. Geophys. Res.*, *116*, D00V04, doi:10.1029/2011JD016674.

1. Introduction

[2] The spatiotemporal distribution of aerosol chemical composition is influential in aerosol interactions with water vapor and radiation. Organics are of major importance in this regard as they typically represent between 20 and 90% of fine aerosol mass [*Kanakidou et al.*, 2005]. As it is virtually impossible to speciate and quantify the entire spectrum of particulate organic compounds, it is useful to examine classes of organic species. A key category of particulate organics is water-soluble organic species, where water-soluble organic carbon (WSOC) has been shown to account for between 40 and 85% of the global organic carbon (OC) budget [*Ruellan et al.*, 1999; *Graham et al.*, 2002; *Mayol-Bracero et al.*, 2002; *Jaffrezo et al.*, 2005; *Decesari et al.*, 2006]. In the absence of biomass burning, WSOC is often considered a proxy for secondary organic aerosol (SOA) due to the oxidized nature of these species as compared to other organics.

[3] Two widely studied areas in the United States with regard to atmospheric aerosol properties and composition include the Los Angeles Basin [*Hidy et al.*, 1974; *Grosjean and Friedlander*, 1975; *Husar et al.*, 1976, 1977; *Blumenthal et al.*, 1978; *Russell et al.*, 1983; *McElroy and Smith*, 1986; *Russell and Cass*, 1984, 1986; *Kawamura and Kaplan*, 1987; *Wall et al.*, 1988; *Pandis et al.*, 1992a, 1992b; *Zhang et al.*,

[1]Department of Chemical and Environmental Engineering, University of Arizona, Tucson, Arizona, USA.
[2]Department of Atmospheric Sciences, University of Arizona, Tucson, Arizona, USA.
[3]Departments of Environmental Science and Engineering and Chemical Engineering, California Institute of Technology, Pasadena, California, USA.
[4]School of Earth and Atmospheric Sciences, Georgia Institute of Technology, Atlanta, Georgia, USA.
[5]Center for Interdisciplinary Remotely-Piloted Aircraft Studies, Naval Postgraduate School, Monterey, California, USA.

0148-0227/11/2011JD016674

Table 1. Summary of CIRPAS Twin Otter Research Flights (RF)[a]

RF	Flight Date	Day of Week	Flight Time (UTC)	Mission Type
1	5/4/2010	Tuesday	18:01–21:23	LA Basin
2	5/5/2010	Wednesday	18:04–22:10	LA Basin
3	5/6/2010	Thursday	19:06–22:59	LA Basin
4	5/7/2010	Friday	18:02–21:57	LA Basin
5	5/10/2010	Monday	19:00–23:05	LA Basin
6	5/12/2010	Wednesday	17:56–22:08	LA Basin + Salton Sea
7	5/13/2010	Thursday	18:05–21:54	LA Basin + Salton Sea
8	5/14/2010	Friday	17:59–22:01	LA Basin
9	5/15/2010	Saturday	18:13–22:13	LA Basin
10	5/18/2010	Tuesday	18:59–22:53	San Joaquin Valley
11	5/19/2010	Wednesday	18:40–22:45	LA Basin
12	5/20/2010	Thursday	18:53–22:58	San Joaquin Valley + Cajon Pass
13	5/21/2010	Friday	17:57–22:05	LA Basin + Cajon/Banning Passes
14[b]	5/22/2010	Saturday	18:01–22:12	San Joaquin Valley
15[b]	5/24/2010	Monday	18:01–22:03	LA Basin + Cajon Pass + Salton Sea
16	5/25/2010	Tuesday	18:27–22:31	LA Basin + Cajon Pass + Salton Sea
17	5/27/2010	Thursday	17:59–21:45	LA Basin
18	5/28/2010	Friday	17:58–22:03	LA Basin

[a]Local time = UTC – seven hours.
[b]WSOC measurements are not available.

1993; *Chow et al.*, 1994; *Hildemann et al.*, 1994a, 1994b, 1996; *Eldering and Cass*, 1996; *Kleeman et al.*, 1999; *Collins et al.*, 2000; *Hughes et al.*, 2000; *Neuman et al.*, 2003; *Sardar et al.*, 2005; *Vutukuru et al.*, 2006; *Docherty et al.*, 2008; *Hersey et al.*, 2011] and the San Joaquin Valley of California [*Magliano et al.*, 1999; *Schauer and Cass*, 2000; *Chow et al.*, 1992, 1993, 1996, 2006; *Neuman et al.*, 2003; *Sorooshian et al.*, 2008a]. While these studies have provided significant knowledge of regional aerosol characteristics, there remain important uncertainties with regard to organic aerosol composition and properties. There are particularly limited airborne measurements that have attempted to characterize the organic composition of aerosol in the Los Angeles Basin and downwind regions.

[4] Recent ground-based measurements in Pasadena, CA between May and September 2009 indicate that organics account for on average between 40 and 60% of the western Los Angeles Basin sub-micrometer aerosol mass [*Hersey et al.*, 2011]. The oxidation state of the Pasadena organic aerosol, as expressed by the atomic oxygen:carbon ratio (O:C) was relatively stable (~0.5) for periods of weeks with little difference at different times of the day. Water-soluble organics were estimated to account for between ~30–70% of the organic mass [*Wonaschütz et al.*, 2011]. Measurements by *Peltier et al.* [2007a] during the SOAR-1 campaign at Riverside, CA (summer 2005) showed that WSOC accounted for an approximate average of 52% of OC mass. Understanding the main sources and production mechanisms of WSOC in the Los Angeles Basin based on measurements at a fixed site has limitations owing to the meteorology of the Basin and the spatial distribution of the sources that lead to organic aerosol. For example, *Wonaschütz et al.* [2011] showed that the diurnal WSOC profile at Pasadena is governed by a combination of sea breeze winds, boundary layer height, and secondary production along the trajectory of air parcels in the Basin. Constraining the spatiotemporal nature of the amount, composition, and vertical distribution of particulate organic matter is critical as aerosol hygroscopicity in the region is largely governed by the organic mass fraction.

[5] In this work, detailed measurements of the nature and character of WSOC in the Los Angeles Basin and outflow regions were performed using both airborne and ground-based sampling during the California Research at the Nexus of Air Quality and Climate Change (CalNex) study in May 2010. Ground-based measurements of WSOC were carried out at two CalNex ground sites. Aircraft overpasses of the ground sites enabled a simultaneous comparison of WSOC in the same vertical column. We address the temporal and spatial variation of WSOC, with an aim to understand the factors that influence WSOC concentrations such as sources, transport and aging, topography, and meteorology. The structure of this paper is as follows: (i) overview of experimental methods; (ii) cumulative summary of WSOC measurements (e.g., vertical profiles, spatial maps, and relationships with other chemical and meteorological variables); (iii) detailed case studies of specific flights; (iv) conceptual model of the nature of WSOC in the study region; and (v) conclusions.

2. Experimental Methods

[6] A total of 18 flights were carried out with the Center for Interdisciplinary Remotely Piloted Aircraft Studies (CIRPAS) Twin Otter during the 2010 CalNex study between 4 May 2010 and 28 May 2010 (Table 1). WSOC was quantified during 16 flights, using a particle-into-liquid sampler (PILS; Brechtel Manufacturing Inc.) coupled to a Total Organic Carbon (TOC) Analyzer (Sievers Model 800) [*Sullivan et al.*, 2006]. Briefly, particles smaller than 2.5 μm in diameter are sampled by the PILS and passed immediately through an organic carbon denuder (Sunset Laboratory Inc.) to remove organic vapors. Particles are grown into droplets, collected by inertial impaction, and delivered through a 0.5 μm PEEK (polyetheretherketone) liquid filter prior to entering a TOC analyzer for quantification of WSOC every ~4 s. Reported WSOC levels represent the difference between the measured and background concentrations, which were obtained by passing sampled air through a high efficiency particulate air (HEPA) filter. The overall measurement uncertainty is estimated to be approximately 10%, with a minimum detection limit of 0.1 μg C m^{-3}. Synchronization

Table 2. Summary of Measurements in the Vicinity of Banning Pass (33.89°N, 33.98°N; −116.77°W, −116.99°W)[a]

RF	Local Time of Day	WSOC (μg C m^{-3})	PCASP Volume (μm^3 cm^{-3})	PCASP (Number per cm^3)	DMA Volume (μm^3 cm^{-3})	DMA (Number per cm^3)	Alt (m)	T (°C)	RH (%)	Wind Speed (m s^{-1})	Wind Direction (deg)
1	12:20	0.41 (0.12)	3.66 (1.38)	952 (227)	2.51 (0.39)	8031 (941)	1036 (158)	20.8 (1.8)	23.9 (2.4)	5.5 (1.8)	256 (17)
2	12:30	0.94 (0.14)			3.33 (0.73)	6942 (2019)	992 (156)	19.2 (1.6)	36.3 (3.1)	7.5 (2.3)	252 (14)
2	14:30	1.21 (0.17)			4.19 (0.46)	7345 (961)	976 (139)	21.0 (1.5)	30.6 (2.6)	8.2 (1.9)	261 (14)
3	1:30	1.46 (0.15)	8.19 (2.04)	1367 (125)	4.31 (0.60)	5063 (650)	985 (149)	17.6 (1.7)	41.2 (5.7)	6.9 (2.4)	256 (14)
3	3:10	1.15 (0.13)	8.23 (2.70)	1443 (181)	4.72 (1.49)	6469 (99)	1114 (23)	18.3 (0.3)	40.6 (4.6)	7.4 (1.9)	264 (12)
4	12:30	0.37 (0.03)	1.54 (1.04)	269 (39)	1.34 (0.46)	2480 (130)	1065 (24)	21.1 (0.2)	11.4 (0.6)	7.1 (1.2)	94 (13)
4	2:20	0.50 (0.05)			1.49 (0.30)	7720 (1439)	1068 (36)	22.8 (0.3)	14.3 (1.3)	2.8 (1.6)	217 (79)
6	2:20	0.41 (0.07)			3.27 (1.83)	6029 (1194)	1102 (69)	17.6 (0.8)	25.7 (2.5)	5.6 (1.5)	258 (24)
7	1:30	0.48 (0.19)	4.48 (2.70)	1037 (393)	4.38 (2.97)	4967 (1341)	1088 (49)	19.3 (0.8)	25.3 (3.5)	5.1 (2.3)	177(79)
13	2:40	2.12 (0.14)	15.11 (2.83)	2437 (213)	9.38 (1.86)	5416 (352)	1170 (19)	17.2 (0.3)	54.5 (1.8)	8.7 (2.6)	264 (16)
16	2:40	0.89 (0.08)	6.35 (2.04)	1604 (385)	4.38 (0.31)	5186 (396)	1058 (81)	16.0 (1.0)	39.2 (3.1)	7.3 (1.9)	267 (14)

[a]DMA data are reported since PCASP data are not available from Flights 2, 4, and 6.

of WSOC measurements with the other aircraft instrument data described below takes into account well-documented liquid transport delays in the PILS instrument [*Sorooshian et al.*, 2006].

[7] Contemporaneous with the airborne measurements, online $PM_{2.5}$ WSOC measurements were carried out at two ground sites (Pasadena and Riverside) with the same instrument set-up as on the aircraft. The Pasadena CalNex ground site was located on the California Institute of Technology campus (34.1406°N, −118.1225°W). The Riverside site was located on the University of California-Riverside campus (33.9719°N, −117.3227°W). The sample inlet was 7 m above ground level at the Pasadena ground site, and 4.5 m above ground level at Riverside.

[8] Measurements of sub-micrometer inorganic and non-refractory organic mass were obtained with an Aerodyne compact Time of Flight Aerosol Mass Spectrometer (C-ToF-AMS) [*Drewnick et al.*, 2005; *Murphy et al.*, 2009]. AMS data used here include organic markers at specific mass-to-charge ratios (m/z) that serve as proxies for organics with a range of oxidation states: acid-like oxygenated organics (m/z 44 = CO_2^+), aliphatic and non-acid oxygenated organics (m/z 43 = $C_3H_7^+$ and $C_2H_3O^+$), and aliphatic organics (m/z 57 = $C_4H_9^+$) [*McLafferty and Turecek*, 1993; *Zhang et al.*, 2005; *Aiken et al.*, 2008; *Ng et al.*, 2010]. Owing to the size cutoff of the AMS being smaller than the PILS (1 μm versus 2.5 μm), any mass ratios between WSOC and AMS measurements represent an upper limit.

[9] Particle size distribution measurements (D_p = 10 nm–800 nm) on the aircraft were carried out with a cylindrical scanning differential mobility analyzer (DMA; TSI Model 3081) coupled to a condensation particle counter (CPC; TSI Model 3760), in addition to a passive cavity aerosol spectrometer probe (PCASP; D_p = 100 nm–2.6 μm). WSOC data are usually compared only to PCASP data in this study owing to similar size bins, while DMA data are used only when PCASP data were not available (Table 2). Sub-saturated aerosol hygroscopicity measurements were provided by a differential aerosol sizing and hygroscopicity spectrometer probe at relative humidities of 74% and 92% and for dry diameters ranging between 150–225 nm (DASH-SP; Brechtel Mfg Inc. [*Sorooshian et al.*, 2008b]). Black carbon (BC) measurements were obtained using a single particle soot photometer instrument (SP2; Droplet Measurement Technologies).

[10] Ground-based gas (CO, O_3) and aerosol ($PM_{2.5}$) measurements were obtained from existing monitoring stations throughout the Los Angeles Basin and outflow areas (see Figure 1) (http://www.arb.ca.gov/aqmis2/aqmis2.php; CARB IADAM Air Quality Data Statistics, 2010, http://www.arb.ca.gov/adam). Additional hourly meteorological data were obtained from regional surface sites using the Mesowest Database [http://mesowest.utah.edu/index.html]. Solar radiation data were obtained from a ground site at Tonner Canyon (33.948°N, −117.822°W, ~410 m altitude; Mesowest), which is centrally located within the Basin.

3. Los Angeles Basin and Outflow Area Description

[11] The metropolitan Los Angeles population exceeds 17 million and the Basin contains a complete spectrum of air pollution sources, including vehicular emissions, cooking, biomass burning, industrial activity, agricultural activity, and marine shipping. The Los Angeles Basin is bordered on three sides by mountainous terrain and by the Pacific Ocean on the southwestern side (Figure 1). Transport of pollutants in the Los Angeles Basin is governed largely by sea breeze and mountain flows [*Lu and Turco*, 1995]. Average monthly wind roses are shown in auxiliary material Figure S1 for the month of May across the study region and representative wind directions are shown in Figure 1.[1] The general wind pattern in the region during the period of time that flights occurred was as follows: westerly and southwesterly winds transporting air from the western edge of the Basin toward the eastern edge, where air is funneled out of narrow passes into desert regions. The two main passes are to the north through the Cajon Pass toward Victorville and Barstow and to the east via the Banning Pass.

[12] During CalNex, fine particle number concentrations were typically highest (>10,000 cm^{-3}) at the western side of the Los Angeles Basin (longitude: 118.05°W–118.3°W), especially in the Long Beach area owing to major point sources. Fine particle number concentrations generally decreased as a function of distance eastward, while PCASP particle number and volume concentrations exhibited the opposite behavior and typically reached peak levels near the northern and eastern edges of the Basin. This can be explained by aging processes along the typical sea breeze

[1]Auxiliary materials are available in the HTML. doi:10.1029/2011JD016674.

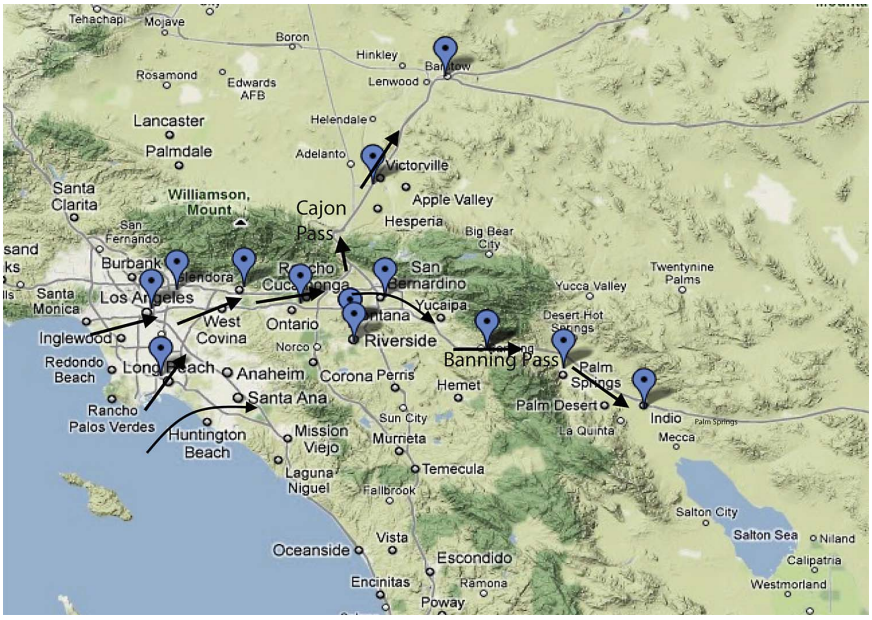

Figure 1. Terrain map of the Los Angeles Basin and outflow regions including Banning Pass, which funnels air out toward areas including Indio and the Salton Sea, and the Cajon Pass, which transports air toward Victorville and Barstow. Blue markers correspond to ground stations (http://www.arb.ca.gov/aqmis2/aqmis2.php) at which gas and $PM_{2.5}$ data were obtained. Black arrows correspond to the typical wind directions during the durations of the flights; specific monthly averaged wind roses across the study region are shown in auxiliary material Figure S1.

trajectory leading to the growth of particles into the size range of the PCASP (D_p > 100 nm).

4. WSOC Distributions

4.1. Spatial WSOC Distribution

[13] Figure 2 shows the cumulative spatial distribution of WSOC concentration measured on the Twin Otter during May 2010. Average levels in specific portions of the region are shown in Figure 3a. WSOC was fairly well-correlated with particle number concentration (r^2 = 0.49; slope = 0.85 ng C m^{-3}/cm^{-3}; n = 34655) and volume concentration (r^2 = 0.53; slope = 0.12 μg C $m^{-3}/(\mu m^3\ cm^{-3})$; n = 33975), as measured by the PCASP. The highest WSOC concentrations were consistently observed in the Los Angeles Basin, as compared to desert outflow regions and the San

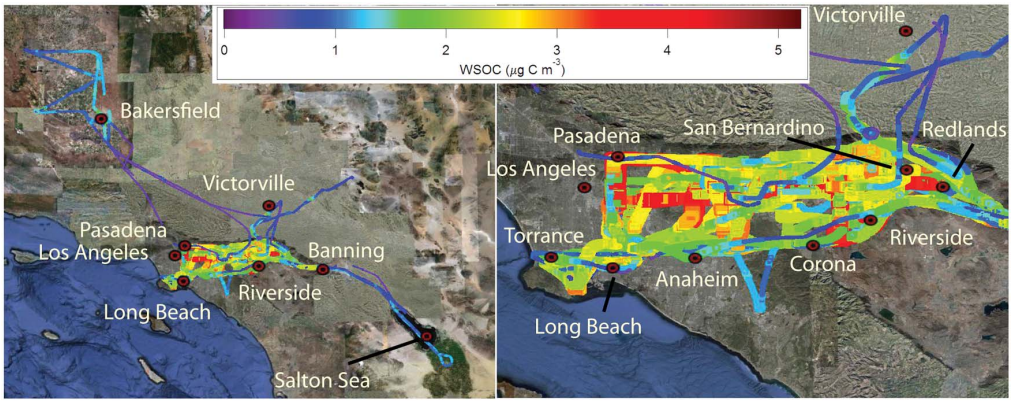

Figure 2. (left) Spatial distribution of WSOC concentrations during the CalNex campaign in the San Joaquin Valley, the Los Angeles Basin, and outflow regions extending north through the Cajon Pass and east through the Banning Pass toward Indio and the Salton Sea. (right) Close-up of WSOC in the Los Angeles Basin.

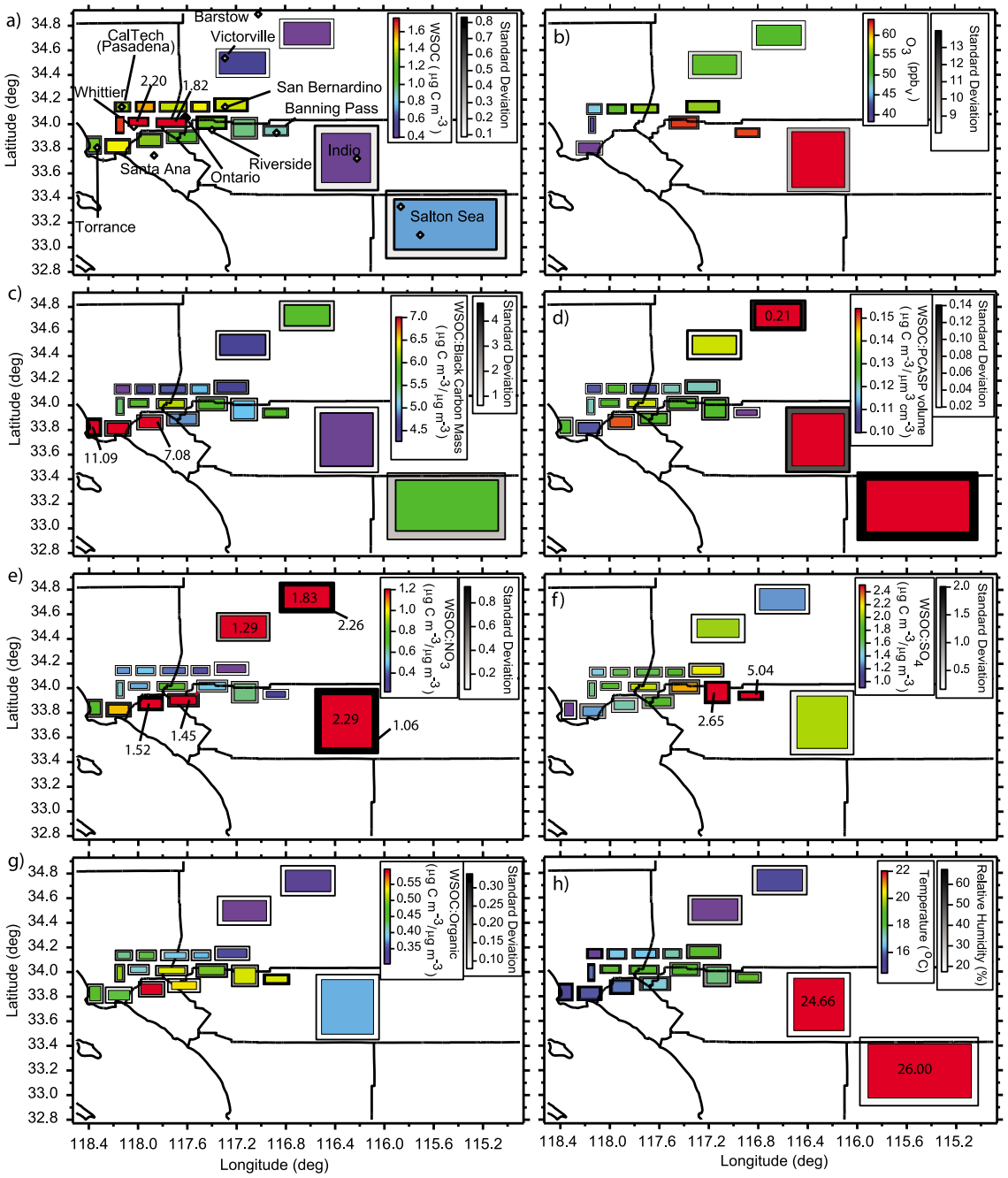

Figure 3. Cumulative spatial averages of (a) WSOC, (b) surface O_3 concentration, (c) WSOC:BC, (d) WSOC:PCASP volume concentration, (e) WSOC:nitrate, (f) WSOC:sulfate, (g) WSOC:organic, and (h) ambient temperature and RH. Numbers in boxes correspond to true values that exceed the range shown in color bars. Sizes of the boxes correspond to the geographic area within which the data were averaged. City labels are included in Figure 3a.

Joaquin Valley, reaching values as high as 5.3 μg C m^{-3}. High concentrations were often observed along the north-south corridor extending between Pasadena and the downtown Los Angeles area, coincident with the highest levels of BC, CO, and *m/z* 57 (>0.3 μg m^{-3}, >0.35 ppm$_v$, >80 ng m^{-3}, respectively). Comparable or higher concentrations were also observed during some flights on the eastern side of the Basin near San Bernardino and Redlands. The lowest concentrations

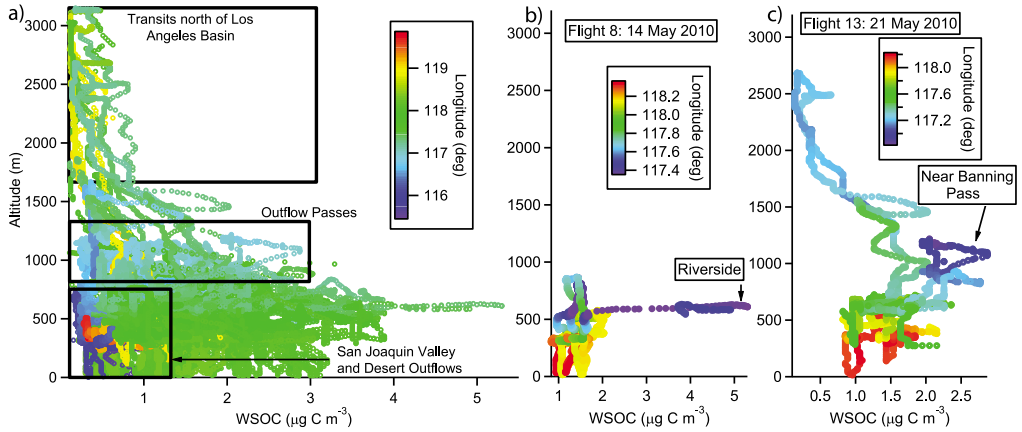

Figure 4. (a) Vertical profile of WSOC mass concentrations during 16 flights over the spatial domain shown in Figure 1. The majority of the data collected below 1 km are from the Los Angeles Basin, with the minority of the yellow-red and blue markers corresponding to San Joaquin Valley and outflow areas to the east of the Basin, respectively. The majority of the markers near 1 km correspond to transits through outflow-passes (i.e., Banning Pass and Cajon Pass), while higher altitudes correspond to transits north of the Los Angeles Basin. (b and c) Examples of vertical profiles during two flights in the Los Angeles Basin showing that the highest WSOC levels were observed above the first few hundred meters. The maximum WSOC level during Flight 8 corresponded to a local fire plume, while the peak WSOC level in Flight 13 was observed over the eastern edge of the Basin near Banning Pass.

of WSOC in the Los Angeles Basin were usually observed near Torrance when the dominant wind direction was westerly from the ocean (i.e., upwind of major emissions sources in Long Beach), and to the southeast/east of the Puente and Chino Hills, which serve as a barrier to the transport of pollution from the western side of the Basin. Outflow regions were characterized by lower WSOC levels than those observed in the Basin mainly owing to dilution during urban plume transport and a lack of significant WSOC sources in the desert. The general west-to-east transect of highest WSOC levels coincided with the average westerly/southwesterly wind patterns during the period of flights, with increases from the western side of the Basin near downtown Los Angeles toward maximum levels near Whittier, then decreasing to the northeast near San Bernardino. Smoke plumes were occasionally intercepted in the Los Angeles Basin, usually near the eastern side in the vicinity of Riverside, owing to small-scale fires. These plumes resulted in the highest WSOC concentrations during the respective flights, with one being the highest of the campaign (maximum levels observed in separate fire plumes: 1.7 μg C m^{-3}, Flight 6; 5.3 μg C m^{-3}, Flight 8; 1.8 μg C m^{-3}, Flight 12; 1.6 μg C m^{-3}, Flight 18). Chemical ratios that can be used to trace secondary production (e.g., WSOC:CO; WSOC:BC) become perturbed in these cases owing to primary production (i.e., direct emission) of WSOC in these fresh plumes.

[14] A number of flights focused on Banning Pass, owing to the role of this area as an exit for the Basin pollution. Table 2 shows a summary of all the WSOC measurements in this area with relevant meteorological information. Out of eleven flight legs through this outflow-pass, nine were characterized by westerly winds and higher WSOC levels than periods with easterly winds. For example, during Flight 4 the first transect was characterized by easterly winds and lower concentrations of WSOC and particle concentration. Approximately two hours later, winds shifted to be westerly resulting in enhancements in WSOC (0.37 to 0.50 μg C m^{-3}) and fine particle number concentration (2480 to 7720 cm^{-3}). Of the other parameters shown in Table 2, WSOC was best correlated with RH and PCASP particle volume concentration (r^2 = 0.79 for both).

4.2. Vertical WSOC Distribution

[15] The airborne measurements were usually conducted below an altitude of 1 km in the Los Angeles Basin and San Joaquin Valley and at higher altitudes through the outflow-passes (Figure 4a). On 11 of the 16 flights, WSOC exhibited its highest concentration above 500 m, usually near the eastern end of the Basin by Riverside, San Bernardino, and Banning Pass. Two representative flights demonstrating this behavior are shown in Figures 4b and 4c, where WSOC peaks between 600 and 1100 m in altitude near Banning Pass and Riverside. The maximum concentration during Flight 8 (5.3 μg C m^{-3}, 14 May 2010) corresponded to a Riverside fire plume and was the highest Twin Otter WSOC measurement of the entire CalNex field study. A cluster of points in Figure 4a (color-coded as blue and yellow-orange) are relatively lower in WSOC concentration than the rest below 1 km as they are from the San Joaquin Valley and outflow areas.

[16] Multiple pollution layers have been observed aloft in this region in past airborne measurements [*Blumenthal et al.*, 1978; *McElroy and Smith*, 1986; *Collins et al.*, 2000]. These layers arise by horizontal and vertical displacement of the morning inversion layer and orographic uplift [*Lu and Turco*, 1995]. It is possible that such layers, which can undergo continued chemical processing while separated from the mixing layer, contribute to surface concentrations through turbulent mixing as the boundary layer deepens [*Husar et al.*,

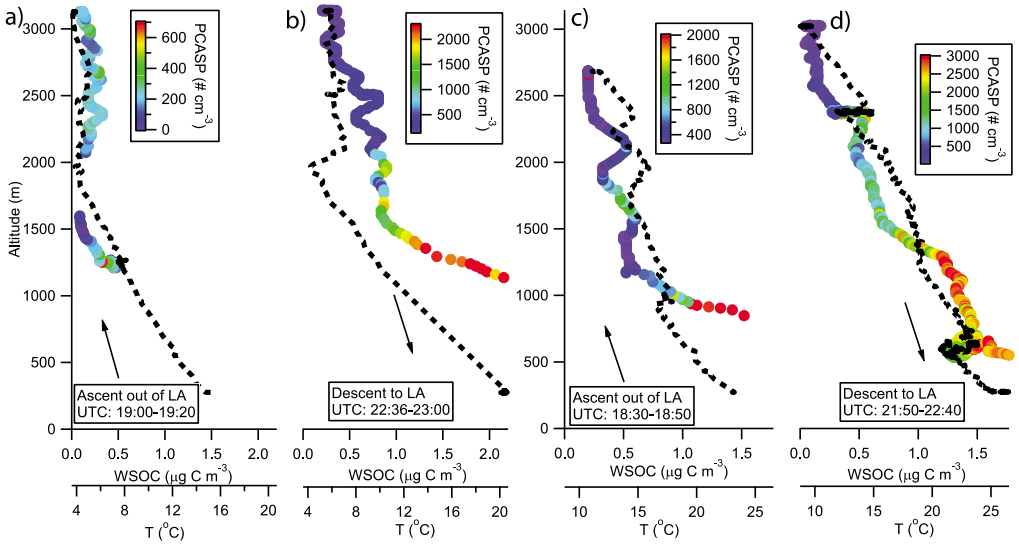

Figure 5. Vertical profiles of WSOC during two flights: (a and b) Flight 10 on 18 May 2010 and (c and d) Flight 12 on 20 May 2010. Colored markers correspond to WSOC and dashed black lines represent ambient temperature. Local time = UTC – seven hours.

1977; *Blumenthal et al.*, 1978]. Vertical profiles of WSOC were obtained during two flights up to an altitude of approximately 3.2 km (Figure 5). The ascents and descents occurred at the northern edge of the Basin. These profiles offer a direct comparison of WSOC separated by 2–4 h of aging time. The ascents out of Los Angeles at the beginning of the flights (Figures 5a and 5c) were characterized by a decrease in WSOC with altitude until a point where a series of vertical layers became evident with enhanced WSOC levels and PCASP particle number concentrations. The descents into the Basin (Figures 5b and 5d) more than two hours later exhibited systematically larger WSOC and PCASP number concentrations in the bottom 1.5 km above the surface with similar layers of WSOC enrichment at higher altitudes. This is likely due to continuous emissions during the daytime and higher photochemical activity occurring to generate more WSOC.

[17] To identify the level of vertical WSOC variation in the mixing layer, simultaneous ground and airborne measurements in the same vertical column are compared at Pasadena (Figure 6a) and Riverside (Figure 6b). A total of 13 and 12 simultaneous measurements were conducted in Pasadena and Riverside, respectively, between 11:00–15:30 (LT). The airborne measurements during the overpasses were conducted within the mixing layer at altitudes between 500–800 m. At both sites, WSOC levels were generally higher aloft, and the difference is more evident in Pasadena. The greatest enhancements aloft relative to ground measurements at both sites were coincident with the highest ratios of RH aloft relative to at the surface, which is most evident at Riverside. The average RHs during the overpasses at Pasadena and Riverside were 67 ± 10% (max = 78%) and 52 ± 9% (max = 65%), respectively. This may be indicative of production of WSOC by processes that are more efficient as a function of increasing aerosol-phase water. High RHs (>70%) have been shown to coincide with enhanced particulate WSOC and organic acid concentrations owing to more effective partitioning of these species to the aerosol phase and multiphase chemistry [e.g., *Hennigan et al.*, 2008b, 2009; *Ervens and Volkamer*, 2010, *Sorooshian et al.*, 2010]. In addition, direct photolytic processing has also been suggested to be an important mechanism to generate SOA in particles residing in humid air [*Bateman et al.*, 2011].

[18] Vertical profiles of ratios of WSOC to PCASP particle volume concentration and AMS organic mass are shown in Figure 7. The range of the average WSOC:particle volume concentration ratio (Figure 7a) was between 0.11 and 0.19 between the surface and 3.2 km, while the WSOC:organic ratio (Figure 7b) ranged widely between 0.26 and 0.63. Both ratios exhibit variable behavior as a function of altitude, with an average reduction from the surface to ~800 m, and with maximum values occurring at altitudes exceeding 1500 m. The large variability in these ratios is largely a result of day-to-day variability; however, the absolute range of the ratios is indicative of WSOC being a significant component of the aerosol from the surface up to 3.2 km.

4.3. WSOC Ratios to Other Aerosol Mass and Volume Measurements

[19] To gain more insight into the relative importance of WSOC to the total aerosol budget and the sources and sinks of WSOC, the ratios of WSOC to other aerosol parameters are examined in Figures 3 and 8. Despite the existence of vertical gradients in aerosol composition and mass, it is useful to constrain airborne-measured WSOC with simultaneous ground-based $PM_{2.5}$ measurements ($PM_{2.5}$ was not quantified on the Twin Otter). For the limited sites at which $PM_{2.5}$ measurements were available within the Basin, WSOC contributed typically between 6 and 11% to $PM_{2.5}$ mass. Note that converting WSOC to an organic mass equivalent concentration requires a conversion factor, which was previously assumed to be ~1.8 for the region [*Docherty*

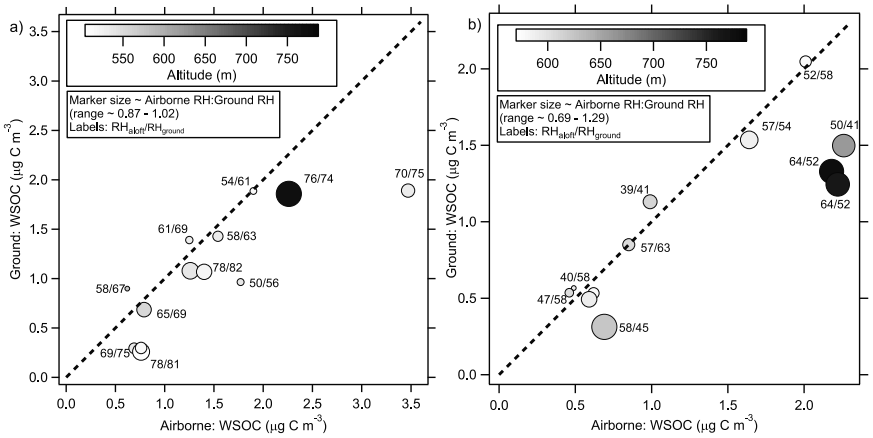

Figure 6. Comparison of simultaneous ground and airborne WSOC measurements in the same vertical column at (a) Pasadena and (b) Riverside.

et al., 2008]. The ratio of WSOC to $PM_{2.5}$ was highest in the western portion of the Los Angeles Basin near Long Beach, downtown Los Angeles, and Glendora (0.10–0.11) and was lowest near Banning Pass (~0.06) owing partly to the major enhancement in ammonium nitrate levels near the eastern side of the Basin. The closest measure of how WSOC contributes to total $PM_{2.5}$ using aircraft measurements is the comparison to PCASP volume concentration, where the PCASP measures particles in a similar size range as the PILS-TOC (<2.5 μm). The WSOC:PCASP volume ratio (Figure 3d) was typically between ~0.1–0.15 μg C m^{-3}/(μm^3 cm^{-3}) in the Los Angeles Basin, while higher average values were observed in the outflow regions. Ratios reached an average of 0.30 ± 0.14 near the Salton Sea to the east of the Basin and 0.21 ± 0.12 near Barstow to the northeast of the Basin. As a basis for comparison, the ratio of WSOC to fine particle volume concentration was 0.12 and 0.10–0.22 μg C m^{-3}/(μm^3 cm^{-3}) in non-biomass and biomass burning plumes, respectively, in the northeastern United States [*Sullivan et al.*, 2006; *Peltier et al.*, 2007b]. An increase in this ratio can be due to a variety of reasons including losses in other aerosol components (e.g., nitrate volatilization), increased production of WSOC during transport, local sources such as fires, or entrained air masses from aloft that are enriched with WSOC relative to other aerosol components.

[20] Examining the variation of relative concentrations of WSOC and other particle and gas-phase constituents along the sea breeze trajectory from west to east provides insight

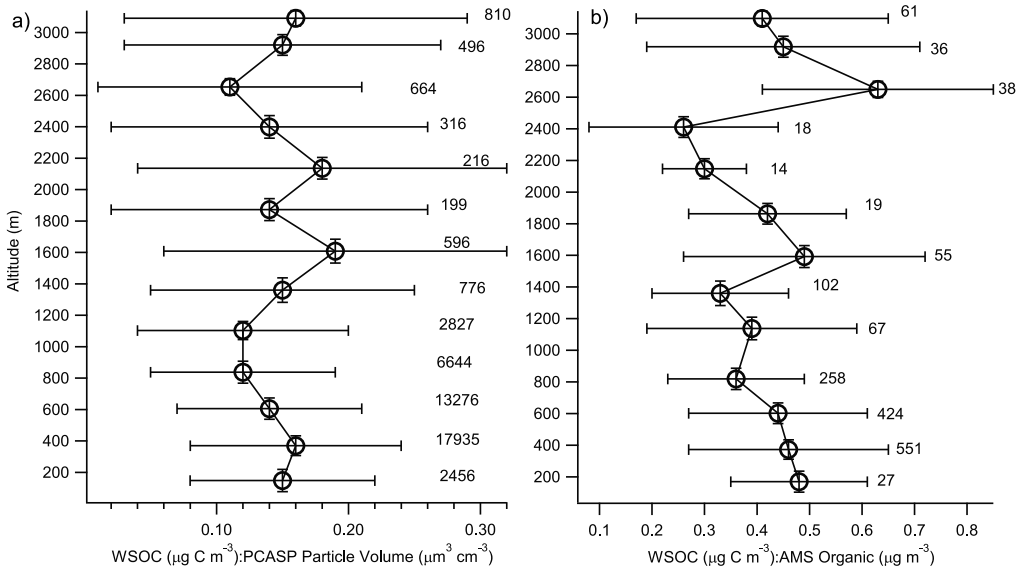

Figure 7. Vertical distribution of (a) the ratio of WSOC to PCASP particle volume concentration (data from all flights) and (b) the ratio of WSOC to total AMS non-refractory organic aerosol mass (Flight 11, 13, 16–18). Numbers beside each point in each panel correspond to the sample size.

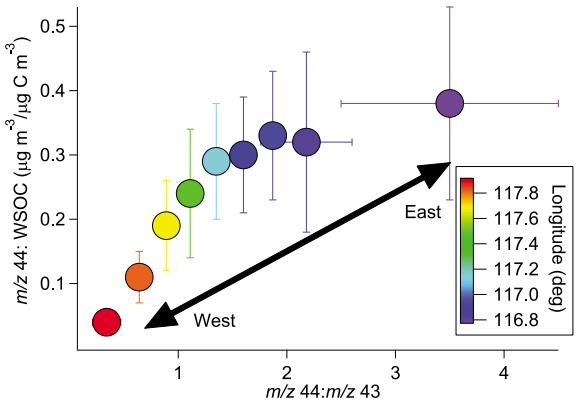

Figure 8. Ratio of *m/z* 44:WSOC as a function of *m/z* 44:43. Markers are color-coded with longitude where red corresponds to western side of the Los Angeles Basin and purple corresponds to outflow desert regions to the east of the Basin.

into the relative importance of volatilization and secondary formation of WSOC (Figure 3). The highest O_3 levels were observed farther inland and were highest in the outflows to the east of the Basin (Figure 3b). This is indicative of increased photochemical processing during sea breeze transport of air masses from the coast to the desert. This would likewise favor secondary production of WSOC. Black carbon is a primary species and thus an increase in the WSOC:BC ratio is a tracer for secondary production. This ratio was highest near the southwestern portion of the study region, presumably owing to the low levels of BC in marine air and upwind of major BC sources in the Basin (Figure 3c). This ratio did not show any clear trend as a function of downwind distance, likely a result of the abundance of BC and organic aerosol sources in the Basin, including the fires observed on the eastern side of the Basin. Unlike the majority of the Basin, there are fewer BC sources along trajectories to the east of the outflow channels; WSOC:BC initially decreases and then increases owing possibly to a combination of WSOC volatilization initially and secondary production afterwards.

[21] The contribution of WSOC to total non-refractory organic mass was highest near the southwestern portion of the Los Angeles Basin (up to ~60% just north of Santa Ana) and lowest in the desert outflow regions (<40%) (Figure 3g). Along the sea breeze trajectory on the northern side of the Basin, the WSOC:Organic ratio tended to increase toward Banning Pass reaching an average value of 53 ± 34%. Recent studies have utilized *m/z* 44 and *m/z* 43 [e.g., *Ng et al.*, 2010] to track the aging of organic aerosol in the atmosphere. The ratio of *m/z* 44:43 provides information about the chemical functionality of oxygenated organic aerosol (OOA), with higher values indicative of a higher state of oxidation. *Wonaschütz et al.* [2011] examined the ratio of *m/z* 44:WSOC as a function of *m/z* 44:43 during the PACO campaign as a way of understanding how the composition of the WSOC fraction of the aerosol changed with photochemical age. Aircraft measurements in Figure 8 show that the ratio of *m/z* 44:WSOC increased as a function of *m/z* 44:43, with increases in both ratios as a function of longitude (higher values to the east). This is consistent with a shift from semi-volatile OOA components to more low-volatility OOA components as a function of photochemical aging. The immediate sharp increase in *m/z* 44:WSOC followed by a plateau is consistent with the findings of *Ng et al.* [2010] and previous measurements during PACO [*Wonaschütz et al.*, 2011]. It is noted that *m/z* 44 levels reached as high as ~1.8 μg m^{-3}, which is roughly similar to peak levels observed in Pittsburgh during September (up to ~1.2 μg m^{-3} [*Zhang et al.*, 2005]), Tokyo in August (up to ~2.29 μg m^{-3} [*Takegawa et al.*, 2007]), but less than that in Tokyo during the summer (up to ~3.5 μg m^{-3}) [*Kondo et al.*, 2007].

[22] More insight into the secondary production of organics arises from the ratio of WSOC:SO_4^{2-} (Figure 3f) as a function of distance eastward from the western end of the Basin where the highest SO_4^{2-} levels were observed, owing to marine shipping sources and other major point sources near the coast. The WSOC:SO_4^{2-} ratio ranged between 0.9 and 5.0 in the study region, which is greater than the cumulative average ratio (~0.55) observed by *Peltier et al.* [2007b] in the northeastern United States. The peak WSOC:SO_4^{2-} ratios between Riverside and Banning are coincident with an area with intense ammonium nitrate production owing largely to the influence of agricultural activity as a source of NH_3, including animal husbandry operations. Ammonium nitrate production results in enhanced aerosol hygroscopicity and aerosol-phase water, which would promote more partitioning of WSOC to the aerosol phase and both multiphase chemistry and photolytic processing to produce WSOC [*Hennigan et al.*, 2008a; *Ervens and Volkamer*, 2010; *Sorooshian et al.*, 2010; *Bateman et al.*, 2011]. In addition, WSOC may have been produced in the emissions from the agricultural activity. The WSOC:SO_4^{2-} ratio decreased immediately downwind of Banning by an average factor of nearly 2.5 and this may be due to volatilization of WSOC (note that SO_4^{2-} is not volatile), which is consistent with the reduction in the WSOC:BC ratio (by an average factor of ~2) in the same area. Production of SO_4^{2-} in this area can likely be ruled out owing to the low RHs, high temperatures, and lack of aqueous-phase chemistry to produce SO_4^{2-} during afternoons (Table 2). The average RH during traverses through Banning Pass ranged between 11 and 55%.

[23] Reductions in aerosol-phase water, such as what happens when air is advected from the Basin to the desert outflows, promotes re-partitioning of WSOC to the gas phase [*Hennigan et al.*, 2008b; 2009]. Lower amounts of the aerosol-phase water are associated with reduced RH and aerosol hygroscopicity. As shown in Figure 3h, the average temperature generally increases from west to east, and vice versa for average RH. The sub-saturated hygroscopicity of the regional aerosol decreased in the outflows, largely owing to ammonium nitrate volatilization. The average hygroscopic growth factor ($D_{p,wet}/D_{p,dry}$) at an RH of 92% for fine aerosol was 1.72 ± 0.25 in the Basin and 1.57 ± 0.19 in the desert outflows. To further examine the likelihood that volatilization is a sink for WSOC downwind of the Los Angeles Basin, the ratio of WSOC:NO_3^- is also examined (Figure 3e), as NO_3^- is vulnerable to evaporation. The range of this ratio was 0.2–2.3, within which are values observed in Mexico City (~0.2–1.0)

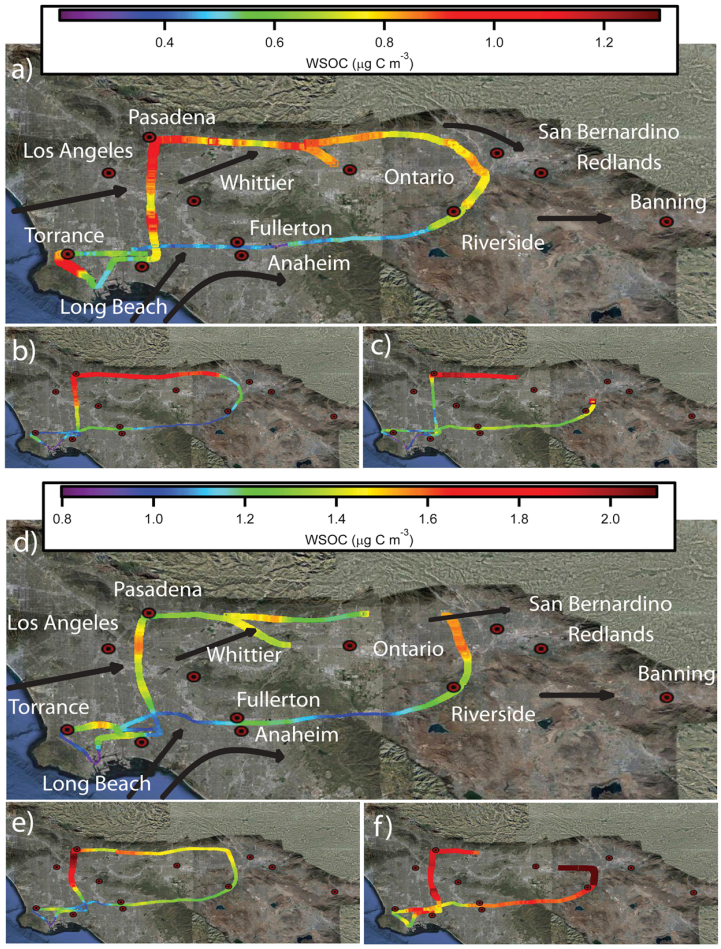

Figure 9. Spatial maps of WSOC during three successive Basin loops in Flight 5 on 10 May 2010 ((a) UTC = 19:00–20:30, (b) 20:30–21:50, and (c) 21:50–23:00) and in Flight 8 on 14 May 2010 ((d) UTC = 18:00–19:30, (e) 19:30–20:50, and (f) 20:50–22:00). Black arrows in Figures 10a and 10d correspond to the typical wind directions during the duration of the two flights as determined by wind roses obtained from the Mesowest Database [http://mesowest.utah.edu/index.html]. Local time = UTC − seven hours.

[*Hennigan et al.*, 2008a] but much less than the cumulative average ratio (>30) observed in the northeastern United States [*Peltier et al.*, 2007b]. AMS NO_3^- mass concentrations are typically highest at San Bernardino (6.08 ± 5.87 μg m^{-3} for the box labeled with this city in Figure 3) and they decrease significantly immediately downwind of the outflow-passes. As a result, the WSOC:NO_3^- ratio increased sharply in the outflows (greater than a factor of six), in contrast to the WSOC:SO_4^{2-} ratio. This indicates that WSOC is less sensitive to volatilization as compared to ammonium nitrate. Such results are consistent with observations in Mexico City [*Hennigan et al.*, 2008a].

[24] The general picture drawn in Figure 3 involves the following: (i) the western Basin is an important anthropogenic source for WSOC and precursors; and (ii) pollutants are transported to the eastern side of the Basin and through outflow-passes with the sea breeze, with aerosol aging processes during this time including dilution, secondary formation of WSOC, and volatilization of some fraction of WSOC. The increasing temperatures (decreasing RH) and reduction of aerosol hygroscopicity and aerosol-phase water in the outflows is likely responsible for the loss of some WSOC mass.

5. Case Studies in the Los Angeles Basin

5.1. Basin Loops

[25] Two weekdays characterized by different meteorological conditions and nearly identical flight paths in the Los Angeles Basin are examined to study the sensitivity of the spatiotemporal distribution of WSOC to meteorology (Figure 9). Flight 5 on 10 May 2010 was characterized by higher wind speeds, higher ambient temperature, and lower incident solar radiation as compared to Flight 8 on 14 May 2010 during the duration of the flights (Table 3). Flight 5 was characterized by cloudy conditions in the Basin during the time span of the flight, unlike Flight 8. The aircraft flew at an altitude of approximately ~300–600 m both

Table 3. Average Values of Meteorological and Aerosol Parameters During Los Angeles Basin Loops During Five Flights[a]

	UTC Time	T (°C)	RH (%)	Wind ($m\ s^{-1}$)	CPC (Number per cm^3)	PCASP (Number per cm^3)	WSOC ($\mu g\ C\ m^{-3}$)	O_3 (ppb)	WSOC:BC ($\mu g\ C\ m^{-3}$/ $\mu g\ m^{-3}$)	Solar Radiation ($W\ m^{-2}$)
Flight 5	Loop 1 (19:00–20:30)	13.3 (1.1)	62.5 (6.5)	4.8 (1.8)	9583 (4649)	754 (312)	0.72 (0.19)	52.3 (8.4)	5.6 (0.8)	896 (173)
	Loop 2 (20:30–21:50)	13.7 (1.1)	61.2 (5.7)	5.8 (1.5)	11025 (4466)	774 (393)	0.66 (0.28)	53.7 (9.7)	6.2 (1.8)	816 (71)
	Loop 3 (21:50–23:00)	13.8 (1.0)	60.3 (6.1)	6.3 (1.8)	10747 (4386)	642 (354)	0.67 (0.25)	53.9 (9.6)	8.8 (5.4)	728 (185)
Flight 8	Loop 1 (18:00–19:30)	14.8 (0.5)	70.4 (3.0)	2.6 (1.0)	9664 (2517)	1372 (264)	1.33 (0.12)	50.8 (11.9)	5.0 (1.1)	1066 (40)
	Loop 2 (19:30–20:50)	16.7 (0.7)	62.8 (4.6)	3.3 (1.0)	12299 (3574)	1575 (294)	1.57 (0.27)	53.3 (11.6)	4.5 (2.4)	1064 (43)
	Loop 3 (20:50–22:00)	17.7 (1.26)	60.8 (6.4)	3.8 (1.0)	14723 (3514)	1641 (301)	1.75 (0.15)	55.8 (11.8)	6.9 (3.9)	985 (85)
Flight 9	Loop 1 (18:20–20:05)	18.1 (2.7)	61.2 (14.5)	3.2 (1.5)	9953 (3706)	1751 (422)	2.61 (0.55)	61.1 (12.2)	9.6 (1.9)	1083 (41)
	Loop 2 (20:05–22:15)	20.2 (3.3)	53.2 (17.1)	5.0 (1.9)	11635 (4155)	1654 (436)	2.89 (0.68)	72.4 (10.1)	10.2 (4.3)	1003 (112)
Flight 11	Loop 1 (18:50–21:05)	17.2 (1.9)	65.6 (10.2)	3.4 (1.5)	10328 (3665)	1580 (1987)	2.11 (0.33)	46.8 (12.8)	6.4 (1.6)	1087 (32)
	Loop 2 (21:05–22:50)	18.4 (2.5)	63.2 (11.2)	5.3 (2.0)	13331 (4383)	1521 (401)	2.23 (0.34)	53.3 (11.6)	8.1 (3.3)	999 (114)
Flight 13	Loop 1 (18:10–20:25)	14.4 (2.0)	65.0 (22.1)	5.0 (3.2)	6815 (2501)	1460 (654)	1.41 (0.53)	56.4 (10.5)	4.7 (1.0)	829 (372)
	Loop 2 (20:25–22:10)	17.7 (1.8)	60.0 (8.8)	4.8 (2.1)	10671 (4535)	1644 (556)	2.27 (0.43)	62.0 (11.3)	6.4 (3.2)	1004 (98)

[a]Refer to Figures 9 and 10. Numbers in parentheses represent standard deviations.

flights. There was no significant difference in wind patterns between these two days. Fine particle concentrations were on average similar, but PCASP particle number concentrations were almost twice as large during Flight 8, indicative of more abundant larger particles.

[26] During Flight 5, three identical loops were carried out as shown in Figures 9a–9c: first loop (19:00–20:30, UTC), second loop (20:30–21:50), and third loop (21:50–23:00). When the sea breeze started to develop around 18:00 UTC, wind speeds gradually increased up to >10 $m\ s^{-1}$ and changed direction to westerly/southwesterly, resulting in the usual transport from west to east. In the southwestern portion of the Basin, WSOC concentrations were highest during the first loop, presumably owing to the influence of residual aged aerosol from the previous day and anthropogenic emissions near Long Beach. In the first loop, the highest WSOC and PCASP particle number concentrations were observed along the north-south axis between Pasadena and downtown Los Angeles. As a result of the westerly/southwesterly flow later during the day, the highest WSOC levels occurred at the base of the San Gabriel Mountains at the northern edge of the Basin. The southern half of the Basin loops extending from Fullerton/Anaheim to San Bernardino were characterized by significantly lower WSOC levels during all three loops, most likely a result of the Basin topography (i.e., Puente and Chino Hills). The data from Flight 5 indicate that the significant factors governing WSOC levels were likely residual aerosol in the Basin from the previous day, pollution near the western edge of the Basin, and the prevailing west-to-east winds with potential production during the transport. These data do not allow one to discern a clear connection between WSOC measurements and the influence of boundary layer deepening and potential entrainment of aerosol aloft.

[27] Flight 8 was conducted almost identically to Flight 5, as shown in Figures 9d–9f. In contrast to Flight 5, the aerosol number concentrations and WSOC increased with each successive loop during Flight 8 (similar to ambient temperature and O_3). The spatial WSOC distribution during the first loop was similar to that of Flight 5, both of which were likely influenced by residual pollutants from the previous day and sources near the western side of the Basin. WSOC increased significantly in concentration over the western side of the Basin during the second and third loops. Unlike Flight 5, the entire north-south axis between Pasadena and downtown Los Angeles exhibited high WSOC levels later in the day owing likely to a combination of secondary WSOC production and lower wind speeds. The third loop of Flight 8 was characterized by systematically higher WSOC levels across the entire Basin. WSOC levels were especially high between Ontario and Riverside owing to a fire that began immediately prior to the third loop.

[28] The data from both flights indicate that, with higher incident solar radiation and relatively low wind speeds, it is likely that secondary production mechanisms contribute to sustained levels of WSOC throughout the daytime periods (especially in Flight 8) even though the mixing layer progressively deepened. While entrainment of polluted air aloft may have contributed to WSOC levels during these flights, this process was not a dominant influence on WSOC in the mixing layer as there were large spatial differences in WSOC across the Basin that are largely controlled by transport and topography.

5.2. Basin North-South Transects

[29] To examine the spatial gradients of WSOC within the regions outlined by the loops in Figure 9, a series of north-south zig zag patterns were flown within the Los Angeles Basin. The paths during Flights 9, 11, and 13 are shown in Figure 10. The flights were conducted approximately during the same time on different days at a similar altitude (~300–700 m). Flight 9 was conducted on a Saturday, whereas the other two are from weekdays (Table 1). Meteorological conditions were relatively similar on these three days (Table 3), with the exception of reduced temperature and incident solar radiation values during the early part of Flight 13 due to cloudy conditions. Particle number concentrations were similar during these flights. WSOC concentrations were enhanced during the second loops, coincident with higher O_3 concentrations, ambient temperatures, and WSOC:BC ratios than the first loop within each flight. This is most evident during Flight 13 presumably due to the shift

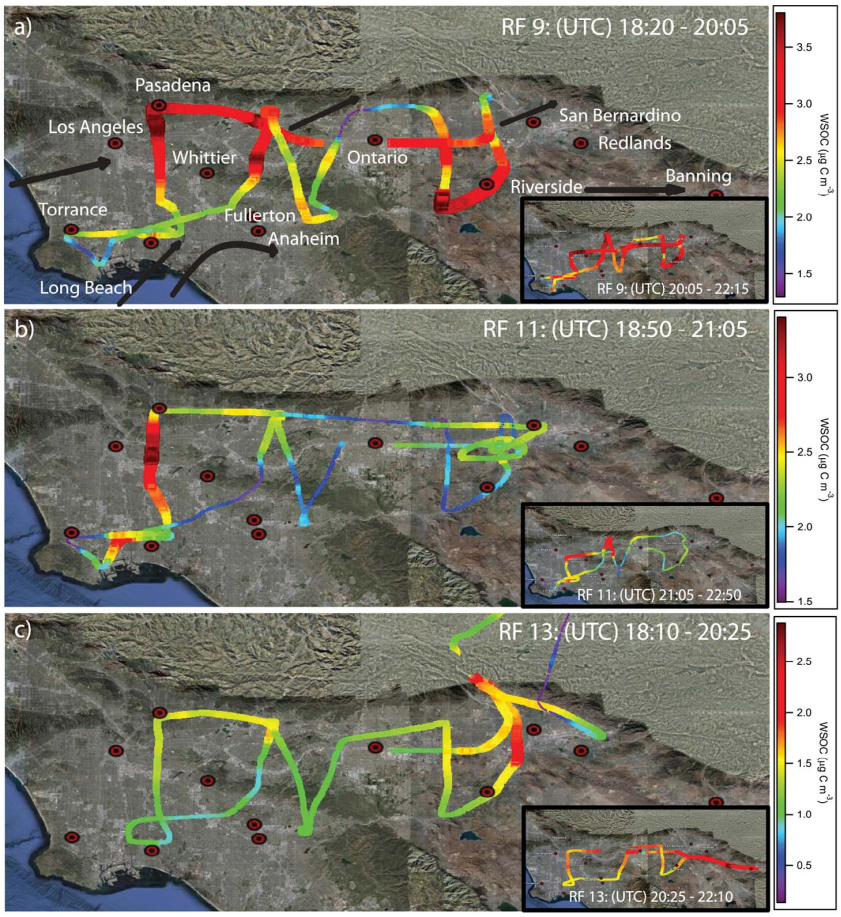

Figure 10. Spatial maps of WSOC during Flights (a) 9 (15 May 2010), (b) 11 (19 May 2010), and (c) 13 (21 May 2010) with black arrows in Figure 10a corresponding to the typical wind directions during the duration of all three flights as determined by wind roses obtained from the Mesowest Database [http://mesowest.utah.edu/index.html]. Local time = UTC – seven hours.

from cloudy to clear conditions (and increase in incident solar radiation) between the two loops. The absolute increases in WSOC later in the daytime most likely were influenced by secondary production.

[30] These three flights demonstrate the influence of the Basin topography on WSOC levels. The Puente and Chino Hills extending from Whittier to the east create a gradient of low WSOC from south of these hills to higher levels on the north side. Sea breeze winds (westerly/southwesterly) near the coast transport air enriched with WSOC to the north side of these hills, which then gets redistributed across a larger area on the eastern end of the Basin extending from San Bernardino down south to Riverside. In addition to the transport of existing WSOC, there is likely production of these species over inland areas that are characterized by enhanced O_3 concentrations (Figure 3b).

6. Conceptual Model of WSOC in the Study Region

[31] Figure 11 shows a conceptual model of the mechanisms describing the sources, transformation, and fate of WSOC during CalNex. Industrial and marine sources of pollution near the western side of the Basin result in enhanced levels of sulfate and carbonaceous components including WSOC. As aerosol is advected with the sea breeze from the west to the east through the outflows, the overall aerosol composition changes owing to numerous point sources, increasing (decreasing) temperature (RH), amount of aerosol-phase water, and secondary formation processes. For example, VOC emissions lead to SOA formation and primary emissions from episodic fires significantly lead to enhanced levels in organics, especially WSOC. The components comprising WSOC become increasingly oxidized as a function of photochemical age from west-to-east. Near the eastern half of the Basin, NH_3 emissions contribute to significant ammonium nitrate formation, leading to more hygroscopic aerosol and increased aerosol-phase water depending on the ambient RH. A number of processes can lead to higher levels of particulate WSOC with increasing aerosol-phase water: partitioning of WSOC to the aerosol phase [*Hennigan et al.*, 2008b, 2009], multiphase chemistry [*Ervens and Volkamer*, 2010; *Sorooshian et al.*, 2010], and

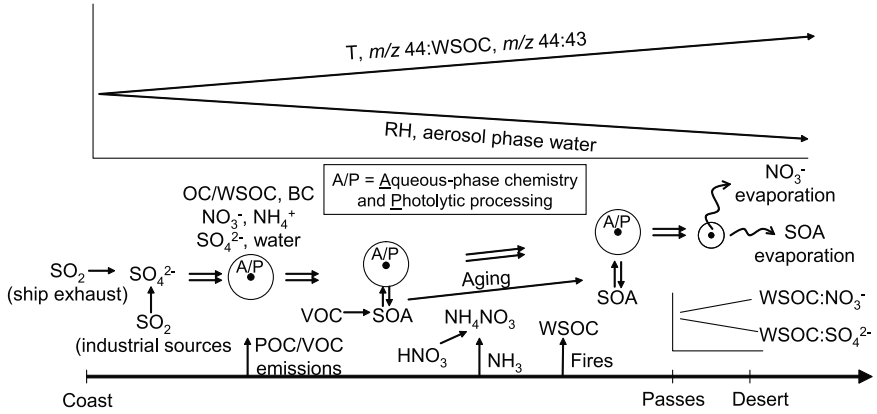

Figure 11. Conceptual model of WSOC in the Los Angeles Basin and desert outflows. The *x* axis represents longitude and extends from the coast to the desert outflows to the east of the Los Angeles Basin.

photolytic processing [*Bateman et al.*, 2011]. As aerosol is transported through the outflows to desert regions, the enhanced temperatures and reduced RH result in NO_3^- evaporation and consequently, reductions in aerosol-phase water. This may promote re-partitioning of WSOC to the gas phase while suppressing humidity-dependent processes that increase particulate WSOC levels.

7. Conclusions

[32] During the May 2010 deployment of the CIRPAS Twin Otter in the CalNex field study, a PILS-TOC instrument was employed to rapidly quantify particulate water-soluble organic carbon (WSOC) during 16 flights covering the Los Angeles Basin, outflow regions, and the San Joaquin Valley. The WSOC measurements were focused on building a spatial map of concentrations across this region in the lateral and vertical directions, on constraining the contribution of these species to the overall aerosol mass budget, and on examining the nature and evolution of this important class of organics due to the prevailing meteorology and daytime air transport patterns.

[33] The highest absolute WSOC concentrations were observed in the Basin (up to 5.3 μg C m^{-3}) and the lowest WSOC levels were in the San Joaquin Valley and in Basin outflow regions owing to plume dilution. The highest WSOC levels during individual flights and for the entire campaign occurred in biomass burning plumes from small-scale fires on the eastern side of the Basin. WSOC contributes approximately 6–11% by mass to $PM_{2.5}$ within the Basin. WSOC was highest relative to both $PM_{2.5}$ near the western Basin sites of Torrance and Long Beach, likely owing to these sites being upwind of major pollution sources and influenced by aged marine aerosol and residual pollutants from the previous day. WSOC levels were typically higher above 500 m in the study region, and layers of enhanced WSOC were identified aloft up to an altitude of 3.2 km. The ratio of WSOC to PCASP particle volume concentration and organic non-refractory mass ranged between 0.11–0.19 and 0.26–0.63, respectively, between the surface and 3.2 km.

[34] Simultaneous ground-based measurements of WSOC during aircraft overpasses in Riverside and Pasadena indicate that higher levels occur more frequently aloft within the mixing layer. This was most evident when the ratio of RH measured on the aircraft versus the surface was also higher, suggestive of an important role for processes that increase particulate WSOC levels as a function of increasing aerosol-phase water such as more efficient partitioning to the aerosol phase. Furthermore, WSOC was highly correlated with RH within the Banning Pass area where pollution is funneled out of the Basin to the east. Since aerosol hygroscopicity and ambient RH generally decreased from the Basin to the eastern desert outflows, there was a reduction in aerosol-phase water that likely influenced WSOC levels; WSOC levels dropped more relative to both BC and SO_4^{2-}, both of which are non-volatile, downwind of the outflows indicative of partitioning of WSOC to the gas phase and suppression of multiphase processes (i.e., partitioning of WSOC to the aerosol phase, multiphase chemistry, photolytic processing) to produce these species. However, WSOC increased relative to NO_3^-, suggesting that although both have a semi-volatile character, NO_3^- was more volatile. Farther downwind in the deserts (e.g., near Salton Sea), WSOC begins to increase relative to BC indicative of secondary production, especially as O_3 levels were enhanced in these areas.

[35] The contribution of acid-like oxygenated organics (*m/z* 44) to WSOC increases from west to east as a result of photochemical aging. Comparisons of nearly identical flight paths on different days show that with higher incident solar radiation and relatively low wind speeds, secondary production mechanisms more clearly contribute to sustained levels of WSOC throughout the daytime periods even though the mixing layer progressively deepens. Entrainment of air aloft may have contributed to WSOC levels within the mixing layer; however, this process was not the key regulator of WSOC in the mixing layer as there were large spatial differences in WSOC across the Basin that are largely controlled by sea breeze transport, topography, secondary production during transport, and presence of fires.

[36] This work adds to the inventory of WSOC data in major mega-cities such as Beijing [*Feng et al.*, 2006], New

Delhi [*Miyazaki et al.*, 2009], and Mexico City [*Hennigan et al.*, 2008a] showing that WSOC contributes significantly to urban aerosol mass concentrations. The aircraft measurements in CalNex highlight the importance of considering the vertical structure of WSOC in the atmosphere. Surface measurements of WSOC are shown to not be entirely representative of the radiative impact of this class of species. This work also emphasizes the importance of considering spatial gradients in aerosol-phase water. For example, the Los Angeles Basin and outflow regions exhibit large variations in RH and have a variety of sources including shipping and agricultural emissions that can create gradients in aerosol hygroscopicity. The resulting spatial variations in aerosol-phase water influence WSOC levels via production processes with efficiencies dependent on this amount of water. Episodic fires and potential volatilization of WSOC point to the use of caution in using ratios of WSOC to other species (e.g., CO and BC) in quantifying the magnitude of SOA production.

[37] **Acknowledgments.** This work was supported by NOAA grant NA 09 OAR 4310128. Surface WSOC measurements were supported by the NSF under grants ATM-0931492 and ATM-0802237.

References

Aiken, A. C., et al. (2008), O/C and OM/OC ratios of primary, secondary, and ambient organic aerosols with high-resolution time-of-flight aerosol mass spectrometry, *Environ. Sci. Technol.*, *42*(12), 4478–4485, doi:10.1021/es703009q.

Bateman, A. P., S. A. Nizkorodov, J. Laskin, and A. Laskin (2011), Photolytic processing of secondary organic aerosols dissolved in cloud droplets, *Phys. Chem. Chem. Phys.*, *13*, 12,199–12,212, doi:10.1039/c1cp20526a.

Blumenthal, D. L., W. H. White, and T. B. Smith (1978), Anatomy of a Los Angeles smog episode: Pollutant transport in daytime sea breeze regime, *Atmos. Environ.*, *12*(4), 893–907, doi:10.1016/0004-6981(78)90028-8.

Chow, J. C., J. G. Watson, D. H. Lowenthal, P. A. Solomon, K. L. Magliano, S. D. Ziman, and L. W. Richards (1992), PM_{10} source apportionment in California San Joaquin Valley, *Atmos. Environ.*, *26*(18), 3335–3354.

Chow, J. C., J. G. Watson, D. H. Lowenthal, P. A. Solomon, K. L. Magliano, S. D. Ziman, and L. W. Richards (1993), PM_{10} and $PM_{2.5}$ compositions in California San Joaquin Valley, *Aerosol Sci. Technol.*, *18*(2), 105–128, doi:10.1080/02786829308959588.

Chow, J. C., J. G. Watson, E. M. Fujita, Z. Q. Lu, D. R. Lawson, and L. L. Ashbaugh (1994), Temporal and spatial variations of $PM_{2.5}$ and PM_{10} aerosol in the Southern California air quality study, *Atmos. Environ.*, *28*(12), 2061–2080, doi:10.1016/1352-2310(94)90474-X.

Chow, J. C., J. G. Watson, Z. Q. Lu, D. H. Lowenthal, C. A. Frazier, P. A. Solomon, R. H. Thuillier, and K. Magliano (1996), Descriptive analysis of $PM_{2.5}$ and PM_{10} at regionally representative locations during SJVAQS/AUSPEX, *Atmos. Environ.*, *30*(12), 2079–2112, doi:10.1016/1352-2310(95)00402-5.

Chow, J. C., L. W. A. Chen, J. G. Watson, D. H. Lowenthal, K. A. Magliano, K. Turkiewicz, and D. E. Lehrman (2006), $PM_{2.5}$ chemical composition and spatiotemporal variability during the California Regional PM_{10}/$PM_{2.5}$ Air Quality Study (CRPAQS), *J. Geophys. Res.*, *111*, D10S04, doi:10.1029/2005JD006457.

Collins, D. R., H. H. Jonsson, H. Liao, R. C. Flagan, J. H. Seinfeld, K. J. Noone, and S. V. Hering (2000), Airborne analysis of the Los Angeles aerosol, *Atmos. Environ.*, *34*(24), 4155–4173, doi:10.1016/S1352-2310(00)00225-9.

Decesari, S., et al. (2006), Characterization of the organic composition of aerosols from Rondonia, Brazil, during the LBA-SMOCC 2002 experiment and its representation through model compounds, *Atmos. Chem. Phys.*, *6*, 375–402, doi:10.5194/acp-6-375-2006.

Docherty, K. S., et al. (2008), Apportionment of primary and secondary organic aerosols in southern California during the 2005 study of organic aerosols in Riverside (SOAR-1), *Environ. Sci. Technol.*, *42*(20), 7655–7662, doi:10.1021/es8008166.

Drewnick, F., et al. (2005), A new time-of-flight aerosol mass spectrometer (TOF-AMS)—Instrument description and first field deployment, *Aerosol Sci. Technol.*, *39*(7), 637–658, doi:10.1080/02786820500182040.

Eldering, A., and G. R. Cass (1996), Source-oriented model for air pollutant effects on visibility, *J. Geophys. Res.*, *101*(D14), 19,343–19,369, doi:10.1029/95JD02928.

Ervens, B., and R. Volkamer (2010), Glyoxal processing by aerosol multiphase chemistry: Towards a kinetic modeling framework of secondary organic aerosol formation in aqueous particles, *Atmos. Chem. Phys.*, *10*(17), 8219–8244, doi:10.5194/acp-10-8219-2010.

Feng, J. L., M. Hu, C. K. Chan, P. S. Lau, L. Y. He, and X. Y. Tang (2006), A comparative study of the organic matter in $PM_{2.5}$ from three Chinese megacities in three different climatic zones, *Atmos. Environ.*, *40*, 3983–3994, doi:10.1016/j.atmosenv.2006.02.017.

Graham, B., O. L. Mayol-Bracero, P. Guyon, G. C. Roberts, S. Decesari, M. C. Facchini, P. Artaxo, W. Maenhaut, P. Koll, and M. O. Andreae (2002), Water-soluble organic compounds in biomass burning aerosols over Amazonia: 1. Characterization by NMR and GC-MS, *J. Geophys. Res.*, *107*(D20), 8047, doi:10.1029/2001JD000336.

Grosjean, D., and S. K. Friedlander (1975), Gas-particle distribution factors for organic and other pollutants in Los Angeles atmosphere, *J. Air Pollut. Control Assoc.*, *25*(10), 1038–1044.

Hennigan, C. J., et al. (2008a), On the volatility and production mechanisms of newly formed nitrate and water soluble organic aerosol in Mexico City, *Atmos. Chem. Phys.*, *8*(14), 3761–3768, doi:10.5194/acp-8-3761-2008.

Hennigan, C. J., M. H. Bergin, J. E. Dibb, and R. J. Weber (2008b), Enhanced secondary organic aerosol formation due to water uptake by fine particles, *Geophys. Res. Lett.*, *35*, L18801, doi:10.1029/2008GL035046.

Hennigan, C. J., M. H. Bergin, A. G. Russell, A. Nenes, and R. J. Weber (2009), Gas/particle partitioning of water-soluble organic aerosol in Atlanta, *Atmos. Chem. Phys.*, *9*(11), 3613–3628, doi:10.5194/acp-9-3613-2009.

Hersey, S. P., J. S. Craven, K. A. Schilling, A. R. Metcalf, A. Sorooshian, M. N. Chan, R. C. Flagan, and J. H. Seinfeld (2011), The Pasadena aerosol characterization observatory (PACO): Chemical and physical analysis of the western Los Angeles Basin aerosol, *Atmos. Chem. Phys.*, *11*, 7417–7443, doi:10.5194/acp-11-7417-2011.

Hidy, G. M., et al. (1974), Characterization of aerosols in California (ACHEX): Final report, *NTIS PB 247*, 947 pp., Calif. Air Resour. Board, Sacramento, Calif.

Hildemann, L. M., D. B. Klinedinst, G. A. Klouda, L. A. Currie, and G. R. Cass (1994a), Sources of urban contemporary carbon aerosol, *Environ. Sci. Technol.*, *28*(9), 1565–1576, doi:10.1021/es00058a006.

Hildemann, L. M., M. A. Mazurek, G. R. Cass, and B. R. T. Simoneit (1994b), Seasonal trends in Los Angeles ambient organic aerosol observed by high-resolution gas chromatography, *Aerosol Sci. Technol.*, *20*(4), 303–317, doi:10.1080/02786829408959687.

Hildemann, L. M., W. F. Rogge, G. R. Cass, M. A. Mazurek, and B. R. T. Simoneit (1996), Contribution of primary aerosol emissions from vegetation-derived sources to fine particle concentrations in Los Angeles, *J. Geophys. Res.*, *101*(D14), 19,541–19,549, doi:10.1029/95JD02136.

Hughes, L. S., J. O. Allen, P. Bhave, M. J. Kleeman, G. R. Cass, D. Y. Liu, D. F. Fergenson, B. D. Morrical, and K. A. Prather (2000), Evolution of atmospheric particles along trajectories crossing the Los Angeles Basin, *Environ. Sci. Technol.*, *34*(15), 3058–3068, doi:10.1021/es9908671.

Husar, R. B., W. H. White, and D. L. Blumenthal (1976), Direct evidence of heterogeneous aerosol formation in Los Angeles smog, *Environ. Sci. Technol.*, *10*(5), 490–491, doi:10.1021/es60116a008.

Husar, R. B., D. E. Patterson, D. L. Blumenthal, W. H. White, and T. B. Smith (1977), 3-dimensional distribution of air-pollutants in Los Angeles Basin, *J. Appl. Meteorol.*, *16*(10), 1089–1096, doi:10.1175/1520-0450-16.10.1089.

Jaffrezo, J. L., G. Aymoz, C. Delaval, and J. Cozic (2005), Seasonal variations of the water soluble organic carbon mass fraction of aerosol in two valleys of the French Alps, *Atmos. Chem. Phys.*, *5*, 2809–2821, doi:10.5194/acp-5-2809-2005.

Kanakidou, M., et al. (2005), Organic aerosol and global climate modelling: A review, *Atmos. Chem. Phys.*, *5*, 1053–1123, doi:10.5194/acp-5-1053-2005.

Kawamura, K., and I. R. Kaplan (1987), Motor exhaust emissions as a primary source for dicarboxylic acids in Los Angeles ambient air, *Environ. Sci. Technol.*, *21*(1), 105–110, doi:10.1021/es00155a014.

Kleeman, M. J., L. S. Hughes, J. O. Allen, and G. R. Cass (1999), Source contributions to the size and composition distribution of atmospheric particles: Southern California in September 1996, *Environ. Sci. Technol.*, *33*(23), 4331–4341, doi:10.1021/es990632p.

Kondo, Y., Y. Miyazaki, N. Takegawa, T. Miyakawa, R. J. Weber, J. L. Jimenez, Q. Zhang, and D. R. Worsnop (2007), Oxygenated and

water-soluble organic aerosols in Tokyo, *J. Geophys. Res.*, *112*, D01203, doi:10.1029/2006JD007056.

Lu, R., and R. P. Turco (1995), Air pollutant transport in a coastal environment—II. Three-dimensional simulations over Los Angeles Basin, *Atmos. Environ.*, *29*(13), 1499–1518, doi:10.1016/1352-2310(95)00015-Q.

Magliano, K. L., V. M. Hughes, L. R. Chinkin, D. L. Coe, T. L. Haste, N. Kumar, and F. W. Lurmann (1999), Spatial and temporal variations in PM_{10} and $PM_{2.5}$ source contributions and comparison to emissions during the 1995 integrated monitoring study, *Atmos. Environ.*, *33*(29), 4757–4773, doi:10.1016/S1352-2310(99)00265-4.

Mayol-Bracero, O. L., P. Guyon, B. Graham, G. Roberts, M. O. Andreae, S. Decesari, M. C. Facchini, S. Fuzzi, and P. Artaxo (2002), Water-soluble organic compounds in biomass burning aerosols over Amazonia: 2. Apportionment of the chemical composition and importance of the polyacidic fraction, *J. Geophys. Res.*, *107*(D20), 8091, doi:10.1029/2001JD000522.

McElroy, J. L., and T. B. Smith (1986), Vertical pollutant distributions and boundary layer structure observed by airborne lidar near the complex southern California coastline, *Atmos. Environ.*, *20*(8), 1555–1566, doi:10.1016/0004-6981(86)90244-1.

McLafferty, F. W., and F. Turecek (1993), *Interpretation of Mass Spectra*, 4th ed., Univ. Sci., Mill Valley, Calif.

Miyazaki, Y., S. G. Aggarwal, K. Singh, P. K. Gupta, and K. Kawamura (2009), Dicarboxylic acids and water-soluble organic carbon in aerosols in New Delhi, India, in winter: Characteristics and formation processes, *J. Geophys. Res.*, *114*, D19206, doi:10.1029/2009JD011790.

Murphy, S. M., et al. (2009), Comprehensive simultaneous shipboard and airborne characterization of exhaust from a modern container ship at sea, *Environ. Sci. Technol.*, *43*(13), 4626–4640, doi:10.1021/es802413j.

Neuman, J. A., et al. (2003), Variability in ammonium nitrate formation and nitric acid depletion with altitude and location over California, *J. Geophys. Res.*, *108*(D17), 4557, doi:10.1029/2003JD003616.

Ng, N. L., et al. (2010), Organic aerosol components observed in Northern Hemispheric datasets from aerosol mass spectrometry, *Atmos. Chem. Phys.*, *10*, 4625–4641, doi:10.5194/acp-10-4625-2010.

Pandis, S. N., J. H. Seinfeld, and C. Pilinis (1992a), Heterogeneous sulfate production in an urban fog, *Atmos. Environ.*, *26*(14), 2509–2522.

Pandis, S. N., R. A. Harley, G. R. Cass, and J. H. Seinfeld (1992b), Secondary organic aerosol formation and transport, *Atmos. Environ.*, *26*(13), 2269–2282.

Peltier, R. E., R. J. Weber, and A. P. Sullivan (2007a), Investigating a liquid-based method for online organic carbon detection in atmospheric particles, *Aerosol Sci. Technol.*, *41*(12), 1117–1127, doi:10.1080/02786820701777465.

Peltier, R. E., A. P. Sullivan, R. J. Weber, C. A. Brock, A. G. Wollny, J. S. Holloway, J. A. de Gouw, and C. Warneke (2007b), Fine aerosol bulk composition measured on WP-3D research aircraft in vicinity of the Northeastern United States—Results from NEAQS, *Atmos. Chem. Phys.*, *7*, 3231–3247, doi:10.5194/acp-7-3231-2007.

Ruellan, S., H. Cachier, A. Gaudichet, P. Masclet, and J. P. Lacaux (1999), Airborne aerosols over central Africa during the experiment for regional sources and sinks of oxidants (EXPRESSO), *J. Geophys. Res.*, *104*(D23), 30,673–30,690, doi:10.1029/1999JD900804.

Russell, A. G., and G. R. Cass (1984), Acquisition of regional air quality model validation data for nitrate, sulfate, ammonium ion and their precursors, *Atmos. Environ.*, *18*(9), 1815–1827, doi:10.1016/0004-6981(84)90357-3.

Russell, A. G., and G. R. Cass (1986), Verification of a mathematical model for aerosol nitrate and nitric acid formation and its use for control measure evaluation, *Atmos. Environ.*, *20*(10), 2011–2025, doi:10.1016/0004-6981(86)90342-2.

Russell, A. G., G. J. McRae, and G. R. Cass (1983), Mathematical modeling of the formation and transport of ammonium-nitrate aerosol, *Atmos. Environ.*, *17*(5), 949–964, doi:10.1016/0004-6981(83)90247-0.

Sardar, S. B., P. M. Fine, and C. Sioutas (2005), Seasonal and spatial variability of the size-resolved chemical composition of particulate matter (PM_{10}) in the Los Angeles Basin, *J. Geophys. Res.*, *110*, D07S08, doi:10.1029/2004JD004627.

Schauer, J. J., and G. R. Cass (2000), Source apportionment of wintertime gas-phase and particle-phase air pollutants using organic compounds as tracers, *Environ. Sci. Technol.*, *34*(9), 1821–1832, doi:10.1021/es981312t.

Sorooshian, A., F. J. Brechtel, Y. L. Ma, R. J. Weber, A. Corless, R. C. Flagan, and J. H. Seinfeld (2006), Modeling and characterization of a particle-into-liquid sampler (PILS), *Aerosol Sci. Technol.*, *40*(6), 396–409, doi:10.1080/02786820600632282.

Sorooshian, A., S. N. Murphy, S. Hersey, H. Gates, L. T. Padro, A. Nenes, F. J. Brechtel, H. Jonsson, R. C. Flagan, and J. H. Seinfeld (2008a), Comprehensive airborne characterization of aerosol from a major bovine source, *Atmos. Chem. Phys.*, *8*(17), 5489–5520, doi:10.5194/acp-8-5489-2008.

Sorooshian, A., S. Hersey, F. J. Brechtel, A. Corless, R. C. Flagan, and J. H. Seinfeld (2008b), Rapid, size-resolved aerosol hygroscopic growth measurements: Differential aerosol sizing and hygroscopicity spectrometer probe (DASH-SP), *Aerosol Sci. Technol.*, *42*(6), 445–464, doi:10.1080/02786820802178506.

Sorooshian, A., S. M. Murphy, S. Hersey, R. Bahreini, H. Jonsson, R. C. Flagan, and J. H. Seinfeld (2010), Constraining the contribution of organic acids and AMS m/z 44 to the organic aerosol budget: On the importance of meteorology, aerosol hygroscopicity, and region, *Geophys. Res. Lett.*, *37*, L21807, doi:10.1029/2010GL044951.

Sullivan, A. P., R. E. Peltier, C. A. Brock, J. A. de Gouw, J. S. Holloway, C. Warneke, A. G. Wollny, and R. J. Weber (2006), Airborne measurements of carbonaceous aerosol soluble in water over northeastern United States: Method development and an investigation into water-soluble organic carbon sources, *J. Geophys. Res.*, *111*, D23S46, doi:10.1029/2006JD007072.

Takegawa, N., T. Miyakawa, K. Kawamura, and Y. Kondo (2007), Contribution of selected dicarboxylic and ω-oxocarboxylic acids in ambient aerosol to the m/z 44 signal of an Aerodyne aerosol mass spectrometer, *Aerosol Sci. Technol.*, *41*, 418–437, doi:10.1080/02786820701203215.

Vutukuru, S., R. J. Griffin, and D. Dabdub (2006), Simulation and analysis of secondary organic aerosol dynamics in the South Coast Air Basin of California, *J. Geophys. Res.*, *111*, D10S12, doi:10.1029/2005JD006139.

Wall, S. M., W. John, and J. L. Ondo (1988), Measurement of aerosol size distributions for nitrate and major ionic species, *Atmos. Environ.*, *22*(8), 1649–1656, doi:10.1016/0004-6981(88)90392-7.

Wonaschütz, A., S. Hersey, A. Sorooshian, J. Craven, A. R. Metcalf, R. C. Flagan, and J. H. Seinfeld (2011), Impact of a large wildfire on water-soluble organic aerosol in a major urban setting: The 2009 station fire in Los Angeles County, *Atmos. Chem. Phys.*, *11*, 8257–8270, doi:10.5194/acp-11-8257-2011.

Zhang, Q., M. R. Alfarra, D. R. Worsnop, J. D. Allan, H. Coe, M. R. Canagaratna, and J. L. Jimenez (2005), Deconvolution and quantification of hydrocarbon-like and oxygenated organic aerosols based on aerosol mass spectrometry, *Environ. Sci. Technol.*, *39*(13), 4938–4952, doi:10.1021/es048568l.

Zhang, X. Q., P. H. McMurry, S. V. Hering, and G. S. Casuccio (1993), Mixing characteristics and water-content of submicron aerosols measured in Los Angeles and at the Grand Canyon, *Atmos. Environ.*, *27*(10), 1593–1607.

J. S. Craven, R. C. Flagan, S. P. Hersey, A. R. Metcalf, and J. H. Seinfeld, Department of Environmental Science and Engineering, California Institute of Technology, 1200 E. California Blvd., Pasadena, CA 91125, USA.

H. T. Duong and A. Sorooshian, Department of Chemical and Environmental Engineering, University of Arizona, PO Box 210011, Tucson, AZ 85721, USA. (armin@email.arizona.edu)

H. Jonsson, Center for Interdisciplinary Remotely-Piloted Aircraft Studies, Naval Postgraduate School, Monterey, CA 93943, USA.

R. J. Weber and X. Zhang, School of Earth and Atmospheric Sciences, Georgia Institute of Technology, Atlanta, GA 30332, USA.

Appendix H

Impact of a Large Wildfire on Water–soluble Organic Aerosol in a Major Urban Area: the 2009 Station Fire in Los Angeles County[1]

[1]This chapter is reproduced by permission from "Impact of a Large Wildfire on Water–soluble Organic Aerosol in a Major Urban Area: the 2009 Station Fire in Los Angeles County" by A. Wonaschutz, S. P. Hersey, A. Sorooshian, J. S. Craven, A. R. Metcalf, R. C. Flagan, and J. H. Seinfeld, *Atmospheric Chemistry and Physics*, (11), 8257–8270, www.atmos-chem-phys.net/11/8257/2011/, doi:10.5194/acp-11-8257-2011, 2011.

Atmos. Chem. Phys., 11, 8257–8270, 2011
www.atmos-chem-phys.net/11/8257/2011/
doi:10.5194/acp-11-8257-2011

Atmospheric Chemistry and Physics

Impact of a large wildfire on water-soluble organic aerosol in a major urban area: the 2009 Station Fire in Los Angeles County

A. Wonaschütz[1], **S. P. Hersey**[2], **A. Sorooshian**[1,3], **J. S. Craven**[2], **A. R. Metcalf**[2], **R. C. Flagan**[2], **and J. H. Seinfeld**[2]

[1]Department of Atmospheric Sciences, University of Arizona, P.O. Box 210081, Tucson, Arizona, 85721, USA
[2]Departments of Environmental Science and Engineering and Chemical Engineering, California Institute of Technology, 1200 E. California Blvd., Pasadena, California 91125, USA
[3]Department of Chemical and Environmental Engineering, Univ. of Arizona, P.O. Box 210011, Tucson, Arizona, 85721, USA

Received: 13 April 2011 – Published in Atmos. Chem. Phys. Discuss.: 27 April 2011
Revised: 24 June 2011 – Accepted: 2 August 2011 – Published: 15 August 2011

Abstract. This study examines the nature of water-soluble organic aerosol measured in Pasadena, CA, under typical conditions and under the influence of a large wildfire (the 2009 Station Fire). During non-fire periods, water-soluble organic carbon (WSOC) variability was driven by photochemical production processes and sea breeze transport, resulting in an average diurnal cycle with a maximum at 15:00 local time (up to 4.9 µg C m^{-3}). During the Station Fire, primary production was a key formation mechanism for WSOC. High concentrations of WSOC (up to 41 µg C m^{-3}) in smoke plumes advected to the site in the morning hours were tightly correlated with nitrate and chloride, numerous aerosol mass spectrometer (AMS) organic mass spectral markers, and total non-refractory organic mass. Processed residual smoke was transported to the measurement site by the sea breeze later in the day, leading to higher afternoon WSOC levels than on non-fire days. Parameters representing higher degrees of oxidation of organics, including the ratios of the organic metrics *m/z* 44:*m/z* 57 and *m/z* 44:*m/z* 43, were elevated in those air masses. Intercomparisons of relative amounts of WSOC, organics, *m/z* 44, and *m/z* 43 show that the fraction of WSOC comprising acid-oxygenates increased as a function of photochemical aging owing to the conversion of aliphatic and non-acid oxygenated organics to more acid-like organics. The contribution of water-soluble organic species to the organic mass budget (10th–90th percentile values) ranged between 27 %–72 % and 27 %–68 % during fire and non-fire periods, respectively. The seasonal incidence of wildfires in the Los Angeles Basin greatly enhances the importance of water-soluble organics, which has implications for the radiative and hygroscopic properties of the regional aerosol.

Correspondence to: A. Sorooshian
(armin@email.arizona.edu)

1 Introduction

Organic compounds constitute roughly one half of atmospheric aerosol mass globally; this fraction can be even higher in urban areas. Between 40–85 % of organic carbon measured in different locations worldwide has been shown to be water-soluble (Ruellan et al., 1999; Graham et al., 2002; Mayol-Bracero et al., 2002; Gao et al., 2003; Jaffrezo et al., 2005; Decesari et al., 2006). Water-soluble organic carbon (WSOC) species are directly emitted in primary particles, especially during biomass combustion, and produced as a result of reactions in the gas and aqueous phases (Miyazaki et al., 2006; Sullivan et al., 2006; Kondo et al., 2007; Weber et al., 2007; Ervens and Volkamer, 2010; Sorooshian et al., 2010; Timonen et al., 2010). WSOC has been suggested as a marker for secondary organic aerosol (SOA) in the absence of biomass burning (e.g. Docherty et al., 2008).

The Los Angeles Basin has been the subject of many studies examining the transport and chemical evolution of atmospheric aerosols. In Pasadena, the setting of this work, particulate pollutant concentrations are governed by numerous production and transport processes. The meteorology in the basin is characterized by early morning inversions, which, through increasing surface heating over the course of the day, give way to a robust midday-afternoon sea breeze. Elevated pollution layers can form by horizontal and vertical displacement of the morning inversion layer and orographic uplift (Lu and Turco, 1995), allowing for aerosol processing in air masses separated from surface pollution sources during the day. These pollution layers can remain aloft during the night and re-entrain the next day through turbulent mixing in a deepening boundary layer, contributing to surface concentrations of aerosols (Husar et al., 1977; Blumenthal et al., 1978).

Published by Copernicus Publications on behalf of the European Geosciences Union.

Organic compounds are a major constituent of the local pollution and are emitted directly as well as produced via secondary processes. Hughes et al. (2000) found increasing relative contributions of organic compounds to increasing mass concentrations of total suspended particulates and fine particles due to chemical processing along a sea breeze trajectory in the Los Angeles Basin. More recent summertime measurements in the area showed that SOA is a major contributor to organic aerosol (Docherty et al., 2008), of which WSOC is an important component (Peltier et al., 2007). Owing to transport processes and spatial gradients in the oxidative capacity of the atmosphere, SOA is expected to contribute more to organic aerosol concentrations at inland areas than at the pollution source regions near the coast (Lu and Turco, 1995; Vutukuru et al., 2006).

In the late summer to fall months (August–November), following hot and dry summers, smoke from wildfires can be an additional component of the organic aerosol budget in the Los Angeles Basin (Phuleria et al., 2005). The impact of wildfires on urban aerosol physicochemical properties has been examined in other locations (Lee et al., 2008) but aerosol studies examining the superposition of biomass burning emissions and typical Los Angeles atmospheric conditions are limited. The issue is especially of interest as wildfires in the southwestern United States have been shown to occur more frequently and to last longer than only a few decades ago and are thus expected to be a major concern in a future drier and warmer climate (Westerling et al., 2006).

An opportunity to study the nature of WSOC in the Los Angeles Basin in both the presence and absence of a major fire presented itself during the 2009 Pasadena Aerosol Characterization Observatory (PACO) field campaign. The Station Fire, which began on 26 August 2009 in the Angeles National Forest and came as close as 10 km to the PACO field site, was the tenth largest wildfire in modern California history and the largest ever in Los Angeles County, burning an area of more than 600 km^2 (California Department of Forestry and Fire Protection; http://bof.fire.ca.gov/incidents/incidents_archived). The overall PACO campaign is described in detail by Hersey et al. (2011). Here we report an analysis of the nature of particulate WSOC in Pasadena during a three-month period with an aim towards characterizing time-dependent concentrations, relationships with other organic aerosol metrics, sensitivity to meteorology and transport, and the impact of the Station Fire. This work also provides a valuable database for comparison with subsequent field datasets collected from surface and airborne platforms during the 2010 CalNex field campaign (http://www.esrl.noaa.gov/csd/calnex/).

2 Methods

2.1 Data

During the PACO field study (May–September 2009), ground-based aerosol measurements were conducted on the roof of the Keck Building on the campus of the California Institute of Technology (Caltech). The focus of this work is the period from 6 July 2009 to 16 September 2009. WSOC in $PM_{2.5}$ was measured every six minutes with a particle-into-liquid sampler (PILS; Brechtel Mfg. Inc.) coupled to a total organic carbon (TOC) analyzer (Sievers Model 800 Turbo, Boulder, CO). The instrument design and operational details are discussed extensively elsewhere (Sullivan et al., 2004). Briefly, the PILS samples particles smaller than 2.5 µm in diameter and passes them through an organic carbon denuder (Sunset Laboratory Inc.) to remove organic vapors. The particles are grown into droplets, which are collected by inertial impaction. The liquid then passes through a 0.5 µm PEEK (polyetheretherketone) liquid filter and is transported to a TOC analyzer for quantification of WSOC. The reported WSOC levels are the difference between the measured and background concentrations. The overall measurement uncertainty is estimated to be approximately 10 %.

Inorganic and non-refractory organic sub-micrometer aerosol measurements were carried out with an Aerodyne Compact Time of Flight Aerosol Mass Spectrometer (C-ToF-AMS) (Drewnick et al., 2005; Murphy et al., 2009) during the non-fire portion of the study and a High-Resolution AMS (HR-AMS) during the Station Fire. AMS data used here include organic markers at specific mass-to-charge ratios (*m/z*) that serve as proxies for organics with a range of oxidation states: acid-like oxygenated organics (*m/z* 44 = COO^+), aliphatic and non-acid oxygenated organics (*m/z* 43 = $C_3H_7^+$ and $C_2H_3O^+$; *m/z* 55 = $C_3H_3O^+$), aliphatic organics (*m/z* 57 = $C_4H_9^+$), and a biomass burning tracer (*m/z* 60) (McLafferty and Turecek, 1993; Zhang et al., 2005; Aiken et al., 2008; Ng et al., 2010; Alfarra et al., 2007). The PILS and AMS chemical measurements were time synchronized, accounting for sampling time delays in the PILS relative to the AMS (Sorooshian et al., 2006). Since the PILS sampled sub-2.5 µm particles while the AMS measured submicrometer particles, ratios of WSOC to AMS data represent an upper limit.

Particle size distributions were measured with a cylindrical Scanning Differential Mobility Analyzer (DMA; TSI Model 3081) coupled to a Condensation Particle Counter (CPC, TSI Model 3760). Thirty-two days of hourly CO, O_3 and $PM_{2.5}$ measurements from ground sites in Pasadena (South Wilson Avenue), Upland, Burbank, and downtown Los Angeles (North Main Street) (http://www.arb.ca.gov) are used to help interpret the WSOC data. Additionally, hourly meteorological data were obtained from the Mesowest database (http://mesowest.utah.edu/index.html). The stations used include the South Wilson Avenue station on the

Caltech campus, the North Main Street station near downtown Los Angeles (∼12.5 km southwest of measurement site), and the Santa Fe Dam station located ∼15 km east of the measurement site.

2.2 Fire development and influence on the measurement site

The Station Fire burned over several weeks. Its spatial extent and exact location, and thus the influence it exerted on the measurement site, changed over that time period. Figure 1 shows the progression of the fire over several days. The fire perimeter was estimated from Moderate Resolution Imaging Spectroradiometer (MODIS) fire maps (http://firefly.geog.umd.edu/firemap/; Justice et al., 2002; Davies et al., 2009). The fire started on 26 August less than 10 km north of the sampling site and grew in areal extent over the next four days. It split into an eastern and a western part on 31 August. The western part quickly decreased in size while moving northward, was reduced to a relatively small remnant ∼25 km northwest of the site by 2 September, and became unidentifiable by MODIS by 4 September. The eastern part remained sizeable, but moved farther eastward. Notable easterly wind patterns did not occur during the measurement period, making the eastern part of the fire an unlikely direct influence on the measurement site.

The dataset was split into a "fire period" and a "non-fire period" by examining the MODIS fire maps and using the AMS *m/z* 60 concentration as a tracer for biomass burning. The "fire period", consisting of the eight days between 26 August and 2 September, was marked by frequent high spikes in the measured *m/z* 60 concentration, reaching values of up to 1.4 $\mu g\,m^{-3}$. The mean *m/z* 60 concentration during the fire period was $0.065 \pm 0.122\,\mu g\,m^{-3}$. During the remaining measurement days ("non-fire period") the mean *m/z* 60 concentration was $0.013 \pm 0.005\,\mu g\,m^{-3}$. While *m/z* 60 (and levoglucosan) have been shown to decay with exposure to the hydroxyl radical (Hennigan et al., 2010), the systematically higher levels of this mass spectral marker during the Station Fire make it a robust tool to identify periods with fire influence. CO similarly exhibited contrasting behavior during non-fire and fire periods, with mean concentrations of 0.13 ± 0.12 ppmv and 0.45 ± 0.50 ppmv, respectively.

3 Results and discussion

3.1 PACO study background

Hersey et al. (2011) provide a comprehensive summary of the physical and chemical properties of aerosols sampled at the PACO measurement site over the time period between 10 July and 4 August, which overlaps with the beginning of the period examined in this work. We briefly describe results from that study that are relevant to the interpretation of WSOC measurements during non-fire periods. Organic mass accounted for approximately 55 % of the submicrometer AMS aerosol mass. Average organic carbon (OC) concentrations were greater by approximately 4 % in the afternoons (15:00–19:00 LT) than in the mornings (07:00–11:00 LT). Conversely, elemental carbon (EC) decreased by approximately 22 % from the mornings to the afternoons. Both trends lead to an enhanced afternoon OC:EC ratio. It was concluded that production of primary organic carbon was more important in the mornings while secondary production of organic carbon was more dominant in the afternoons. Size-resolved measurements showed that the afternoon submicrometer organic mass distribution was bimodal with one modal vacuum aerodynamic diameter centered around 100–200 nm and another around 500–600 nm. Positive matrix factorization analysis showed that low-volatility and semi-volatile oxidized organic aerosol (LV-OOA and SV-OOA) accounted for 86 % of organic aerosol, suggestive of a large oxidized organic fraction. This work will examine the nature and character of the water-soluble fraction of the organic aerosol.

3.2 Meteorological setting and origin of air masses

Weather conditions were warm and dry during the entire WSOC measurement period (Fig. 2). Ambient temperatures ranged approximately from 15° to 40 °C. Relative humidity (RH) usually dropped below 40 % during the day but reached 100 % in the early morning hours of many days. Temperatures averaged several degrees higher during the Station Fire period, while RH was around 20 % lower, helping to sustain the duration and spread of the fire. Air mass back-trajectories calculated with the NOAA HYSPLIT model (Draxler and Rolph, 2003) showed that sampled air masses were generally of marine origin with brief continental exposure prior to reaching the sampling site.

Since the western edge of the Los Angeles Basin is a major source region for pollutants (Lu and Turco, 1995), it is important to identify dominant wind patterns and transport times to Pasadena. Figure 3 shows the local wind characteristics at South Wilson Avenue (next to measurement site) and at several surrounding stations. The most common wind directions at all stations are southerly to westerly, a manifestation of the sea breeze. The diurnal development of wind at South Wilson Avenue starts with very calm air in the early mornings (and late evenings). During the late morning hours the wind tends to turn clockwise from the NE through S to the predominant afternoon sea breeze direction from the SW. Wind speeds increase during the development of the sea breeze. The stagnant air in the early morning is expected to be influenced by local sources and by accumulated residual pollution from the previous day. Over the course of the late morning, air masses from more polluted urban areas are transported to Pasadena and ultimately replaced by air masses of largely

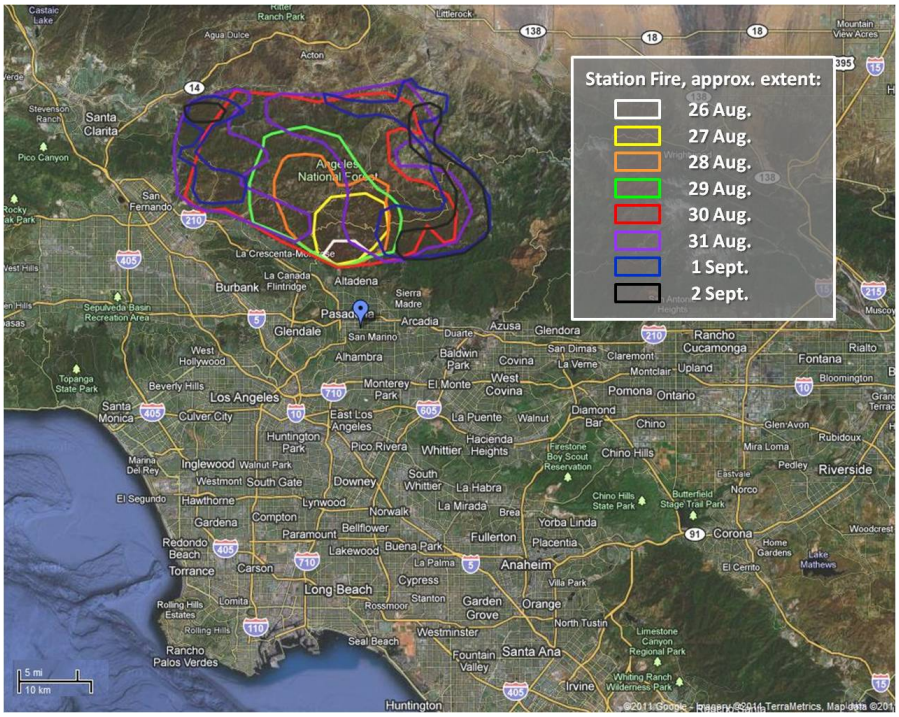

Fig. 1. Approximate spatial extent of the Station Fire by date (bordered areas). The fire area was estimated using fire maps by "Firefly" (University of Maryland; http://firefly.geog.umd.edu/firemap/). The blue marker in Pasadena represents the measurement site.

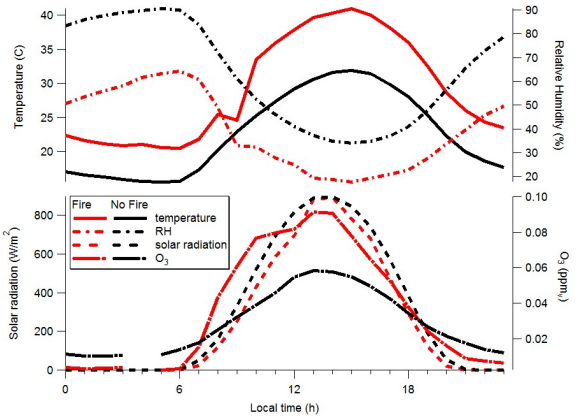

Fig. 2. Diurnal averages of meteorological parameters (Santa Fe Dam station) and O_3 concentrations during the fire- and non-fire periods.

marine origin with anthropogenic influence, carrying particles with a mix of fresh and aged components. The South Wilson Avenue Station measures systematically lower wind speeds than the surrounding stations, which is likely a local effect caused by buildings and trees in the immediate surroundings of the station. Wind speeds measured at that site are therefore assumed to represent a lower limit of the areal wind speed. A statistical analysis of wind speeds and directions between 13:00–18:00 LT showed that the most common wind speeds were 4.5 m s^{-1} at North Main Street and 1.3 m s^{-1} at South Wilson Avenue. The most common wind directions were 270° and 225°, respectively. The afternoon (13:00–18:00 LT) transport time of urban pollution from downtown Los Angeles to Pasadena is thus on the order of 1–2 h, consistent with the estimate by Hersey et al. (2011) for the period between May and August 2009. Based on the most common afternoon wind speed at North Main Street, the transport time of anthropogenically-influenced marine air from the coast to Pasadena from a southwesterly direction is approximately two hours.

3.3 WSOC production pathways and relationship with ozone

Identifying the relative importance of primary and secondary production mechanisms of WSOC is difficult given the large variety of aerosol and precursor sources, the diurnal transport patterns and the dynamic vertical structure of the boundary layer in the basin (Blumenthal et al., 1978; Vutukuru et al., 2006). WSOC concentrations measured on non-fire days

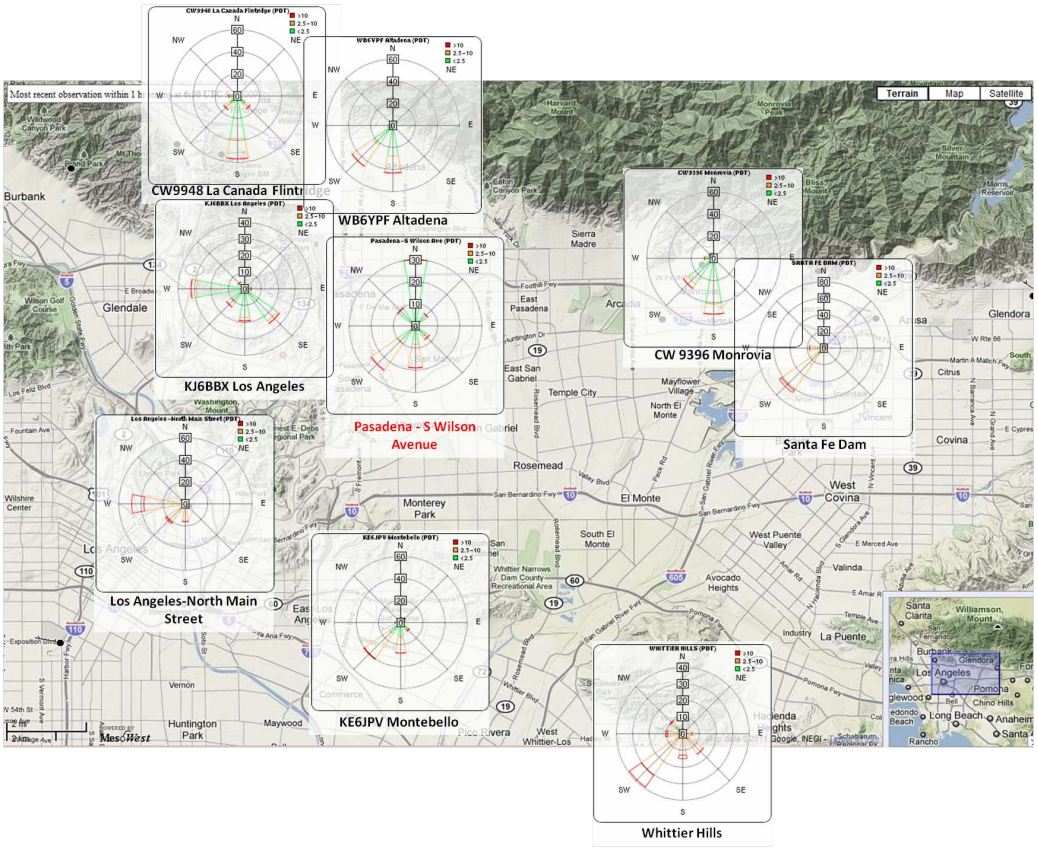

Fig. 3. Wind roses for the month of July for South Wilson Avenue and surrounding stations (data from Mesowest, http://mesowest.utah.edu/index.html).

may be governed by all or a subset of the following mechanisms: (1) local primary production of WSOC; (2) local secondary production; (3) advection of existing WSOC that was either primarily or secondarily produced; (4) advection of precursor volatile organic compounds (VOCs), with WSOC production occurring during transport; (5) volatilization of semivolatile primary organic aerosol (POA) and subsequent oxidation into SOA (Robinson et al., 2007); and (6) re-entrainment of pollution layers aloft. The Station Fire adds another level of complexity by introducing additional sources of WSOC: direct emission and secondary production from precursors emitted in the fire.

Previous work within the PACO campaign has shown that the temporal behavior of organic aerosol is closely related to that of O_3, indicative of photochemical production of SOA (Hersey et al., 2011). In this study, this relationship is explored by examining the relative temporal behavior of O_3 and WSOC on 20 days. WSOC peaked after O_3 on 16 of those days with a typical time lag of 1.5–2.5 h. WSOC peaks occurred simultaneously or slightly before O_3 peaks (0.5 h) on three days, and only on one day did the WSOC peak precede an unusually late O_3 peak by hours. This points to a strong link between overall WSOC concentrations and photochemical processes.

The variability of O_3 concentrations at different ground sites in the Los Angeles Basin provides insight into the spatiotemporal behavior of photochemical processes and the photochemical potential at the Pasadena site. O_3 concentrations measured at ground stations in Pasadena (South Wilson Avenue), Burbank, Upland and downtown Los Angeles (North Main Street) were examined for a period of 24 days in July (Fig. S1, Supplement). In the prevailing sea breeze regime, transport of precursors from downtown Los Angeles (a classic pollutant source location) is expected to influence O_3 concentrations at the measurement site. On 10 out of the examined 24 non-fire days, O_3 peaked in downtown Los Angeles approximately an hour before it did in Pasadena, consistent with the transport times of 1–2 h, given most common mid-afternoon (13:00 to 16:00 LT) wind speeds of 1.3 m s^{-1} in Pasadena and 3.6 m s^{-1} at downtown Los Angeles. Peak O_3 concentrations in Pasadena were consistently higher (22 out of 24 days) than in downtown Los Angeles, owing to

advection of O_3 from upwind locations and additional time for photochemical processing of O_3 precursors during transport. The farther downwind site of Upland is characterized by even higher and more delayed O_3 peaks. This observed spatial O_3 behavior and its implications for SOA production are consistent with the findings of Vutukuru et al. (2006) who showed that SOA levels in the basin are higher at inland sites (e.g. Azusa, Riverside) than at coastal sites. However, on six days O_3 reached peak concentrations in Pasadena before it did in downtown Los Angeles (an average of 1.5 h earlier) and on six other days, it peaked within the same hour as in downtown Los Angeles. These days were not associated with unusual wind directions or increased wind speeds. Local sources, downward mixing of elevated pollution layers from previous days in a deepening mixed layer, and/or unusually vigorous photochemical activity (as described by Hersey et al., 2011) could explain these "early" O_3 peaks. Therefore, on any given day, advection of oxidants from downtown Los Angeles is not necessarily a requirement for photochemical activity in Pasadena.

3.4 Cumulative WSOC statistics

During the non-fire period, the highest WSOC concentration measured was 4.9 µg C m^{-3}. The observed concentration range is consistent with that of independent measurements in other urban areas (Jaffrezo et al., 2005; Sullivan et al., 2004, 2006; Kondo et al., 2007), including those in nearby Riverside during the summer of 2005 (Peltier et al., 2007). WSOC exhibits a weak correlation with solar radiation ($r^2 = 0.28$) and somewhat higher correlations with O_3 ($r^2 = 0.35$) and T ($r^2 = 0.44$) (Table 1). The highest correlations between WSOC and AMS aerosol components were found for the following organic markers: *m/z* 43 ($r^2 = 0.49$), total AMS organic mass ($r^2 = 0.47$), and *m/z* 55 and 60 ($r^2 = 0.45$). The correlation of WSOC with *m/z* 57 ($r^2 = 0.20$) is the lowest among the correlations with AMS organic markers. Although *m/z* 55 and *m/z* 43 are prominent components in traffic emissions, they are more related to oxygenated organics than the primary hydrocarbon-like organic aerosol (HOA) marker *m/z* 57 (e.g. Zhang et al., 2005); for example, they are in general less correlated with NO_x and CO. WSOC exhibits little to no correlation with the inorganic compounds nitrate (NO_3^-), sulfate (SO_4^{2-}), chloride (Cl^-), and ammonium (NH_4^+) ($r^2 \leq 0.08$).

During the fire period, the range of measured WSOC levels (0.8–40.6 µg C m^{-3}) was consistent with that observed in other measurements with major biomass burning influence: 11–46 µg C m^{-3} (Mayol-Bracero et al., 2002), 2.2–39.6 µg C m^{-3} (Graham et al., 2002), 4.4–52.6 µg C m^{-3} (Decesari et al., 2006), and 0.57–18.45 µg C m^{-3} (Sullivan et al., 2006). The highest WSOC concentration, 40.6 µg C m^{-3}, was measured in the morning of 30 August. WSOC correlations (r^2) with most organic metrics (i.e. total AMS organic mass and *m/z* 44, 60, 43, and 55, but not *m/z* 57) ranged between 0.80 and 0.92 (cf. 0.35 and 0.49 during non-fire periods). The systematically higher correlations during the fire period indicate that there was a dominant factor governing the variability of both organic and WSOC levels; since WSOC was highly correlated with *m/z* 60 ($r^2 = 0.90$), the fire emissions were clearly influential. The correlation of WSOC with O_3 is absent during the fire period, even though O_3 concentrations are influenced by the fire (peak concentrations in the diurnal average of 91.5 ppbv during the fire vs. 58.5 ppbv for the non-fire diurnal average; Fig. 2). This suggests that photochemical production is not the dominant process governing the large variability of WSOC concentrations during the fire. A high correlation was observed between WSOC and both NO_3^- ($r^2 = 0.79$) and Cl^- ($r^2 = 0.57$). Correlations with NH_4^+ and SO_4^{2-} ($r^2 \leq 0.18$) were poor. Fresh biomass burning emissions consist mainly of organic carbonaceous components and have been reported to have only minor contributions from inorganic species (Reid et al., 2005; Fuzzi et al., 2007; Grieshop et al., 2009); however, enhanced NO_3^- concentrations have been observed in smoke plumes (Gao et al., 2003; Reid et al., 2005; Peltier et al., 2007). Potassium chloride is also thought to be a common constituent in biomass burning emissions (Posfai et al., 2003; Reid et al., 2005), which can explain the enhanced correlation of WSOC and Cl^- and provides support for a primary WSOC production mechanism. Reid et al. (2005) note that while SO_4^{2-} is a secondary product of biomass burning, its production requires high RH. Enhanced RH also increases WSOC partitioning to the aerosol phase (Hennigan et al., 2008, 2009). However, ambient RH was low during the majority of the PACO study and especially low during the fire (Fig. 2). Liquid-phase production of SO_4^{2-} and organics could conceivably have taken place in pyrocumulus clouds formed by the fire, but given the lack of observed SO_4^{2-} at the sampling site during smoke events and the low RH, it is unlikely that multi-phase processes played a key role in influencing surface WSOC levels.

During the fire period, the ratio of WSOC to organic mass ranged from 0.11 to 0.53 µg C µg^{-1}, with a 10th percentile of 0.15 and a 90th percentile of 0.40 µg C µg^{-1}. After converting the 10th and 90th percentile values to an equivalent organic mass concentration using a factor of 1.8 (Docherty et al., 2008), water soluble organics are estimated to account for between 27 % and 72 % (with an average of 47 % ± 15 %) of the organic mass. The WSOC:organic ratio range during the non-fire period is similar (10th/90th = 0.15/0.38 µg C µg^{-1}).After applying the 1.8 conversion factor to WSOC the 10th–90th percentile range is 27 %–68 % (average of 45 % ± 16 %).

Table 1. Summary of the statistical relationships between WSOC ($\mu g\,C\,m^{-3}$) and other chemical and meteorological parameters (meteorological data from the Santa Fe Dam station).

		Station Fire				No Fire			
		r^2	Slope	Intercept	n	r^2	Slope	Intercept	n
AMS ($\mu g\,m^{-3}$)	Total organic	0.92	−1.05	0.34	1298	0.47	0.14	0.69	1557
	m/z 60	0.90	40.16	1.88	1298	0.45	94.46	0.48	1557
	m/z 44	0.84	3.04	−1.15	1298	0.35	0.95	0.94	1557
	m/z 43	0.84	5.22	−1.45	1298	0.49	2.25	0.51	1557
	m/z 55	0.80	9.47	−1.43	1298	0.45	3.79	0.61	1557
	NO_3^-	0.79	4.30	−1.09	1298	0.00	−0.02	1.75	1557
	Cl^-	0.57	77.39	0.99	1296	0.03	−1.28	1.82	1557
	m/z 57	0.47	1.24	0.60	1298	0.20	6.58	0.96	1557
	NH_4^+	0.18	7.06	0.54	1298	0.00	0.04	1.64	1557
	SO_4^{2-}	0.14	−2.67	7.41	1298	0.08	0.14	1.40	1557
Gas	CO (ppmv)	0.18	3.66	2.78	151	0.00	0.26	1.69	212
	O_3 (ppbv)	0.05	0.03	3.35	151	0.35	0.02	0.83	212
	NO_x (ppbv)	−0.01	−0.01	4.77	151	0.03	−0.01	1.94	212
Meteorology	Wind speed ($m\,s^{-1}$)	0.07	–	–	144	0.11	–	–	210
	Solar radiation ($W\,m^{-2}$)	0.00	–	–	148	0.28	–	–	209
	T (C)	0.01	–	–	144	0.44	–	–	209
	RH (%)	0.00	–	–	147	0.14	–	–	209

3.5 Diurnal WSOC behavior

3.5.1 Non-fire period

During the non-fire period, the daytime diurnal average concentration of WSOC (Fig. 4) exhibits a maximum at 15:00 LT, around the same time as maxima in AMS organic mass, *m/z* 44 and *m/z* 43, but after O_3 (13:00 LT) and solar radiation (14:00 LT) (Fig. 2). Since wind direction has a pronounced diurnal cycle, too, the afternoon peak in WSOC can be explained plausibly by both photochemical production and/or transport from downtown Los Angeles via the afternoon sea breeze (a complication in explaining diurnal variability of pollutants noted specifically for Pasadena by Blumenthal et al., 1978). The behavior of the HOA marker *m/z* 57 provides some insight: while it does show an increase starting at 06:00 and a local peak at 09:00, consistent with local rush hour traffic, its maximum concentration occurs at 13:00, when local primary emissions are expected to be lower than in the morning. Since all other organic metrics and total AMS mass also reach their highest concentrations with high temporal coincidence in the early afternoon, it is likely that transport from more polluted areas, including downtown Los Angeles, plays the dominant role. From the peak at 15:00 until the evening hours, WSOC concentrations decrease, as do other organic metrics and total AMS mass. While dilution as a result of a deepening boundary layer can be a mechanism for daytime concentration decreases, the late onset of the decrease suggests that it is caused by the sea breeze: After initially transporting pollutants from source areas to Pasadena, the continuing onshore winds advect cleaner marine air. This advancing sea breeze front has been shown to produce strong gradients in pollutant concentrations in the Los Angeles Basin (Lu and Turco, 1995).

Transport does not explain all features of diurnal WSOC behavior. Even when it dominates the observed concentration variability at the measurement site, it is possible that the WSOC was secondarily produced upwind or during transport. In the diurnal average, WSOC concentrations (and *m/z* 44) do not show as steep of a decrease as organics and total AMS mass (Fig. 4). The ratio WSOC:organic (Fig. 5) is relatively constant until 14:00, but then begins to increase. A likely scenario for the relative increase of WSOC during the decrease of absolute concentrations of most every organic marker is the superposition of secondary production of WSOC by photochemical processing and transport. Advected marine air may exhibit enhanced WSOC:organic ratios and, in addition, the organic aerosol advected by the sea breeze ages and oxidizes while moving inland.

Examples for these mechanisms governing WSOC concentrations on individual days can be seen in the time series in Fig. 6. On 7 July, sea breeze transport was dominant: there is strong covariance between WSOC, AMS organic mass and numerous *m/z* markers (43, 44, 55, 57, 60). All exhibit a

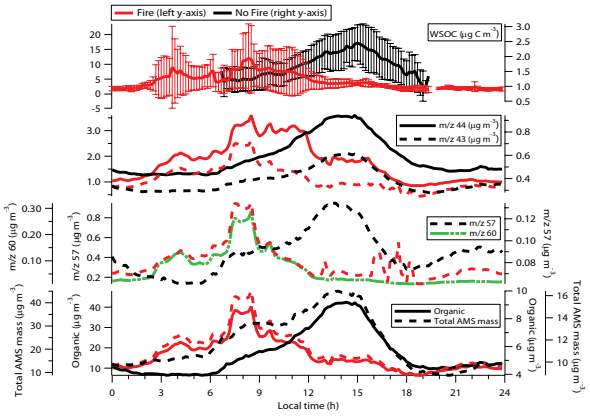

Fig. 4. Diurnal averages of aerosol chemistry (*m/z* 60 shown for the fire period only).

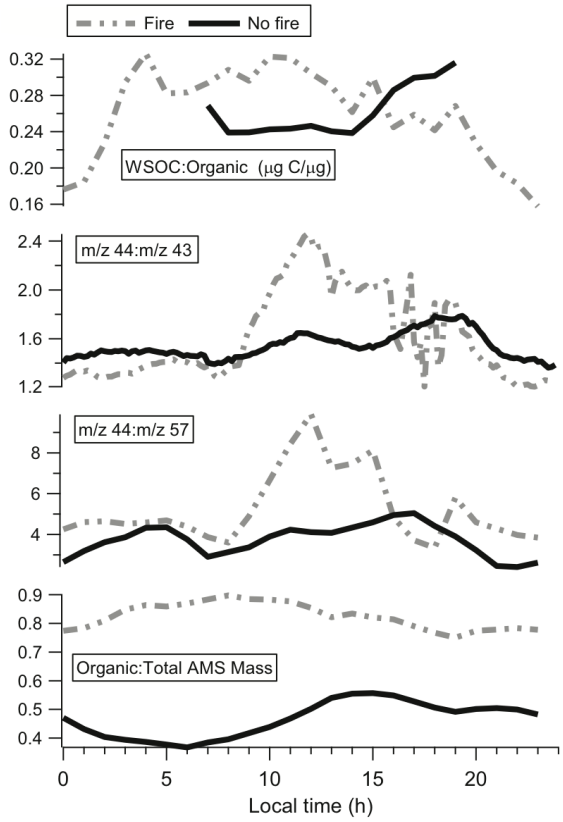

Fig. 5. Diurnally averaged ratios of different organic aerosol measurements during the fire and non-fire periods.

smooth morning increase followed by an equally smooth afternoon decrease which coincides with increasing afternoon wind speeds and southerly to southwesterly wind direction. The ratio of WSOC:total AMS mass shows the same behavior, likely due to photochemical processing of the transported air. The afternoon increase in SO_4^{2-} coupled with the decrease of organics can be attributed to the influx of marine air. On 11 and 15 July, in contrast, WSOC concentrations began to increase before the sea breeze was fully established, indicating that local photochemical production may have played a more important role.

3.5.2 Station Fire period

During the fire period, organic mass fractions (organics:total AMS mass) were substantially higher than in the non-fire period (Fig. 5). The contribution of WSOC to organic mass was systematically elevated from the early morning hours through the late afternoon, with higher WSOC:organic ratios between 04:00–12:00 than at other times. Absolute WSOC concentrations peaked in the mornings. For 08:30 in the morning, the average WSOC concentration (Fig. 4) is higher by a factor of 10 than the non-fire average for the same time of day. The diurnal behavior of the biomass burning tracer *m/z* 60 matches that of WSOC (with the exception of a sharper decrease from 08:00 to 12:00), providing evidence for the presence of biomass burning aerosols at the measurement site when WSOC increased in concentration. Boundary layer deepening over the course of the late morning and the onset of the sea breeze with its southwesterly winds directing smoke plumes away from the measurement site lead to a decrease in measured WSOC concentrations during the rest of the day. The afternoon peak of diurnally-averaged WSOC at 15:00 that was evident during the non-fire period is barely visible given the high WSOC concentrations during earlier parts of the days; nonetheless, the diurnally-averaged WSOC concentration at this time of day exceeds that of the non-fire period by a factor of 1.5. As organic precursors emitted in the fire were likely present in the entire Los Angeles Basin after several days of burning, residual and processed smoke are thought to have played an additional role in the usual transport of pollutants by the afternoon sea breeze.

Day-to-day variability of WSOC concentrations and other aerosol constituents was high during the fire period (Fig. 7). The impact of the fire on the measurement site ranged from large increases of every measured quantity on 28, 30 and 31 August, to much reduced fire influence on 29 August and 1 September. This can be attributed to the dynamic development of the fire itself, as well as effects associated with wind and boundary layer depth. The connection between wind and smoke influence on aerosol composition is clearly visible in Fig. 7: using *m/z* 60 as a tracer for the smoke plume, it is evident that periods with low wind speeds and wind directions with a northerly component feature the highest smoke concentrations. Concentrations are higher in the morning hours than in the evenings (when wind speeds are equally low) because the boundary layer is shallowest in the morning and

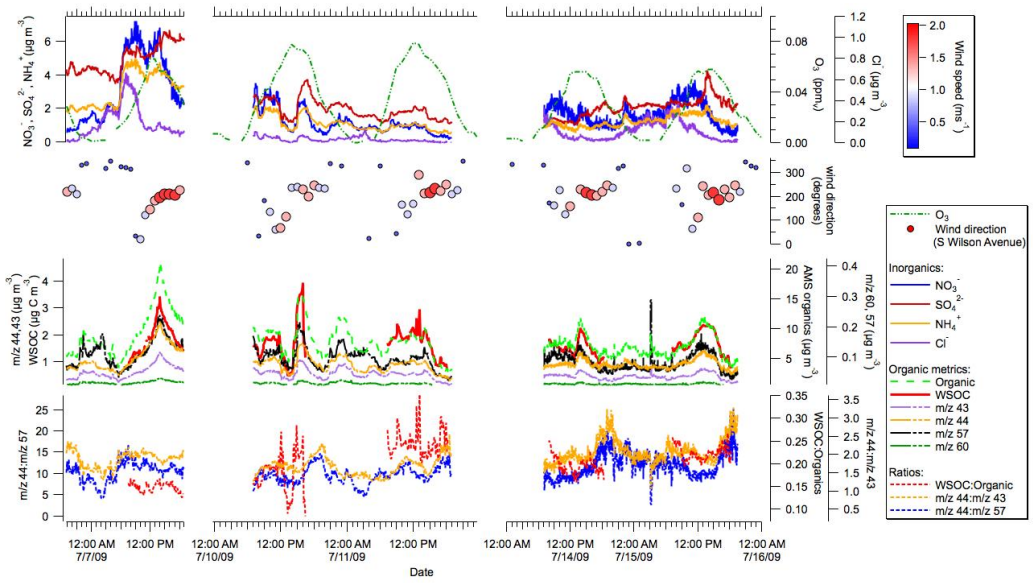

Fig. 6. Time series of various measured and derived parameters during selected days outside the fire period. The symbol size for wind direction is proportional to measured wind speed (South Wilson Avenue station).

the smoke has had time to accumulate in stagnant conditions. Concentrations of *m/z* 60 decrease immediately as the wind direction shifts and the wind speed picks up in the developing sea breeze. During the heavily smoke-impacted mornings of 28, 30 and 31 August, WSOC shows a very tight correlation with *m/z* 60, NO_3^-, and Cl^-, suggestive of primary production of WSOC in the fire. Most other AMS measurements also vary in lockstep with WSOC, with the notable exception of SO_4^{2-}, which exhibited a poor correlation with WSOC and lower levels in the diurnal average than on non-fire days.

In the afternoons of 28, 30 and 31 August, WSOC concentrations were about a factor of two higher than the non-fire average. Concentrations of *m/z* 60, while having dropped since the morning, were still elevated by a factor of two to three above average non-fire concentrations, an indicator that smoke distributed all over the Los Angeles Basin. CO Measurements from ground stations (Fig. S1, Supplement) were used to confirm this wider impact of the fire: on 30 and 31 August, CO levels in downtown Los Angeles exceeded typical rush hour values by a factor of two to three showing that the fire had a direct influence on locations farther south and southwest of Pasadena. Thus, even when the afternoon sea breeze directed the smoke plume away from the site, it still transported residual smoke to the site. This residual smoke was subject to photochemical processing: Fig. 5 shows large systematic increases in the ratios *m/z* 44:43 and *m/z* 44:57 between 09:00–15:00 while the absolute values of all organic measurements decreased (cf. Fig. 4). The larger increases of these ratios during the fire compared to non-fire conditions point to a more vigorous conversion of organics towards a more oxidized state at a relatively stable WSOC:organic ratio. Diurnal average O_3 concentrations (Fig. 2) exhibit an earlier rise and a higher maximum than during the non-fire period, underlining the impact of the fire on the timing and magnitude of photochemical activity. The afternoon increases of *m/z* 44:57 and *m/z* 44:43 and the unusually high O_3 concentrations (176 ppbv at 14:00 on 30 August and 124 ppbv at 10:00 on 31 August) are also clearly visible in the time series for individual days (Fig. 7). Size distribution data (Fig. S2, Supplement) show that the smoke events in the morning hours are associated with larger particles (modal diameter of about 150 nm) than typically observed during that time on non-fire days (modal diameter of 80 nm). In the afternoon, there is a distinct shift to smaller particles (around 40 nm) with a maximum concentration at approximately 15:00, coinciding with an increase in WSOC concentrations owing most likely to photochemical production.

3.6 Relationships between WSOC, AMS organic, *m/z* 44, and *m/z* 43

Primary emission in a fire is a very different source of WSOC than photochemical processing of precursor pollutants. The chemical nature of the WSOC measured in the morning smoke-plumes is therefore expected to differ from that measured in the afternoons. Since WSOC contains both hydrophobic and hydrophilic fractions (e.g. Sullivan and Weber, 2006), it is of interest to investigate the relative behavior

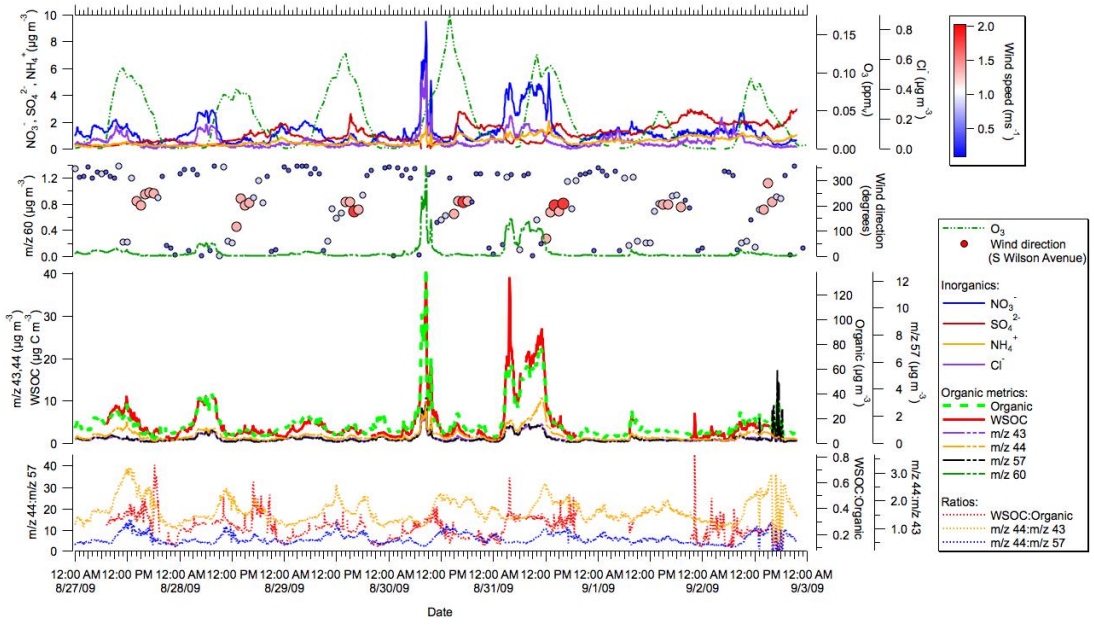

Fig. 7. Time series of various measured and derived parameters during the Station Fire period. The symbol size for wind direction is proportional to measured wind speed (South Wilson Avenue station).

of *m/z* 44, *m/z* 43, total AMS organic, and WSOC. Fire period morning-to-afternoon ratios (i.e. concentrations at 08:00 versus 14:00) of diurnally-averaged *m/z* 44, 43, 60, organic, and WSOC concentrations (shown in Fig. 4) were examined. The smallest morning-to-afternoon ratio for any of these organic metrics was found for *m/z* 44 (1.9), followed by AMS organic (2.4), *m/z* 43 (2.7), and WSOC (3.3). The morning-to-afternoon ratio for *m/z* 60 was 9.6, confirming the much larger direct influence of the fire in the morning. Given the different morning-to-afternoon ratios of *m/z* 44 and 43, it is plausible that the afternoon WSOC contained constituents produced as a result of photochemical processing of smoke, with more of the non-acid oxygenates having been converted to acid-like oxygenates.

Recent studies have utilized *m/z* 44 and *m/z* 43 (Ng et al., 2010; Chhabra et al., 2011) to track the aging of organic aerosols in the atmosphere. For the PACO campaign, Hersey et al. (2011) conducted an analysis of f_{44} (*m/z* 44:total organic signal) versus f_{43} (*m/z* 43:total organic signal), where higher levels of f_{44} relative to f_{43} are thought to indicate a greater degree of organic oxygenation and lower volatility. Over the span of four months, they observed a high level of consistency in the overall degree of oxidation of the aerosol over a span of several months. Ng et al. (2010) conduct a related type of analysis (see their Fig. 5), suitable for incorporating measurements from instruments other than the AMS: plotting f_{44} and the O:C ratio versus *m/z* 44:43, they observed that both f_{44} and the O:C ratio increase sharply at the beginning of oxidation and then plateau at larger *m/z* 44:43 ratios, suggesting the existence of a maximum oxidation state of the aerosol. Following a similar approach, we examine the ratio of *m/z* 44:WSOC as a function of the *m/z* 44:43 ratio for both the fire- and non-fire period (Fig. 8). The *m/z* 44:43 ratios range between 0.6–2.7 (non-fire period) and 1.1–3.1 (fire period). In the mentioned plot in Ng et al. (2010, Fig. 5), this is a range in which the O:C ratio and f_{44} are increasing rapidly prior to reaching a plateau. During both the fire-and the non-fire period, the ratio *m/z* 44:WSOC grows as a function of *m/z* 44:43, indicating that the contribution of acid-like oxygenates to WSOC increases as the chemical functionality of the species contributing to *m/z* 44 and 43 moves towards a more oxidized state. This is most clearly illustrated by the data representing the greatest influence by the fire (larger symbols in Fig. 8). The early morning smoke plumes advected to the measurement site exhibit relatively low values of *m/z* 44:43. The *m/z* 44:WSOC ratio increases gradually as a function of *m/z* 44:43 and time of day, suggesting that conditions associated with transitioning from morning to afternoon hours (higher temperatures, O_3, solar radiation) promoted processing of organics to contain more oxidized species and of WSOC to contain more acid-like oxygenates.

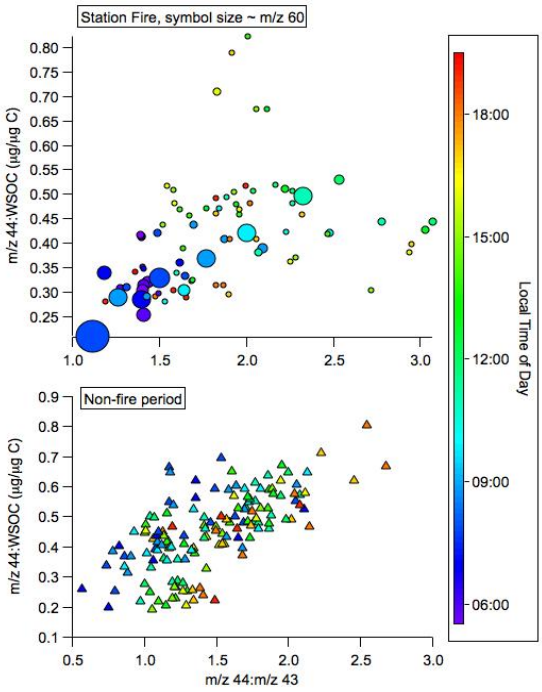

Fig. 8. Summary of the ratio *m/z* 44:WSOC as a function of *m/z* 44:43 during (top panel) and outside (bottom panel) the Station Fire period. Symbols are color-coded by time of day, and in the Station Fire panel the symbol size is proportional to the tracer for biomass burning, *m/z* 60 (range = 0.03–0.9 µg m^{-3}).

4 Conclusions

This work examines a ground-based field dataset of WSOC in conjunction with numerous other aerosol, gas, and meteorological measurements. Two periods governed by the presence and absence of a major wildfire are separately examined with respect to WSOC and the processes governing its temporal variability at a fixed site in Pasadena, California. The PACO study showed that in the absence of biomass burning, changes in WSOC concentrations in Pasadena are largely driven by the diurnal sea breeze circulation and concurrent photooxidation of the transported airmasses. Initially, in the early afternoon, the sea breeze transports pollutants from the direction of the source-rich western Los Angeles area to Pasadena. Chemical processing of those air masses likely occurs while they are on their way and contributes to the temporal WSOC concentration gradient observed at the measurement site, in addition to the influx of WSOC that was already produced at upwind locations. Later in the afternoons, the continuing sea breeze brings in cleaner air masses. These processes cause a marked decrease in WSOC, but enhanced WSOC:organic ratios. Given our observations, photochemical processes are important for overall WSOC formation in the Los Angeles Basin, but cannot be assumed to dominate the observed variability at a single site. That variability is determined by a combination of transport and secondary formation processes, as well as factors we were unable to quantify, such as the magnitude of residual WSOC levels in upwind areas and in layers aloft that may be re-entrained into a deepening boundary layer over the course of the day.

During the Station Fire, WSOC concentrations and their contributions to total organic mass were substantially higher than on typical non-fire days. WSOC was produced via both primary and secondary pathways. Close covariance of WSOC with many other measured species (nitrate, chloride, total AMS organic aerosol mass) in smoke events (defined by unusually high *m/z* 60 concentrations in stagnant/northerly wind conditions) is a good indicator for primary (and potentially sufficiently fast secondary) production of WSOC in the fire emissions. Secondary production of WSOC becomes detectable after the initial morning smoke plumes are directed away from the sampling site and aged smoke from farther upwind makes its way back to the measurement site with the afternoon sea breeze. Increasing *m/z* 44:57 and *m/z* 44:43 ratios show the ongoing oxidation of the smoke-influenced air masses once they arrive back at the measurement site. Unusually high and early O_3 concentration maxima indicate high photochemical activity, which may contribute to the increased WSOC concentrations observed outside of the direct smoke plume. Multiphase processes were not a dominant source of WSOC owing to low relative humidities during the majority of the observation period.

A close examination of the relationship between WSOC, *m/z* 44, and *m/z* 43 provided insight into the contribution of various classes of oxygenated species to WSOC as a result of aerosol aging. The ratio of *m/z* 44:WSOC increased as a function of *m/z* 44:43 both during the fire- and the non-fire period, suggesting that non-acid oxygenates were being converted to more acidic oxygenates, thereby enhancing the contribution of the latter to WSOC.

This work has illustrated the complexity of factors governing WSOC levels at a fixed point in the Los Angeles Basin. A follow-up study using aircraft observations in the same region during the 2010 CalNex field campaign will extend the discussion of the relative importance of various factors (e.g. transport, meteorology, diverse sources) in governing concentrations and spatiotemporal variability in WSOC in this metropolitan center and outflow regions (Duong et al., 2011).

Supplementary material related to this article is available online at: http://www.atmos-chem-phys.net/11/8257/2011/acp-11-8257-2011-supplement.pdf.

Acknowledgements. This work was supported by the Electric Power Research Institute. The authors gratefully acknowledge the NOAA Air Resources Laboratory (ARL) for provision of the HYSPLIT transport and dispersion model. We thank the governmental agencies, commercial firms, and educational institutions participating in MesoWest for providing the meteorological station data and the California EPA Air Resources Board for the access to the measurements of gaseous pollutants. We also acknowledge NASA for the production of the data used in this research effort.

Edited by: A. Nenes

References

Aiken, A. C., Decarlo, P. F., Kroll, J. H., Worsnop, D. R., Huffman, J. A., Docherty, K. S., Ulbrich, I. M., Mohr, C., Kimmel, J. R., Sueper, D., Sun, Y., Zhang, Q., Trimborn, A., Northway, M., Ziemann, P. J., Canagaratna, M. R., Onasch, T. B., Alfarra, M. R., Prevot, A. S. H., Dommen, J., Duplissy, J., Metzger, A., Baltensperger, U., and Jimenez, J. L.: O/C and OM/OC ratios of primary, secondary, and ambient organic aerosols with high-resolution time-of-flight aerosol mass spectrometry, Environ. Sci. Technol., 42, 4478–4485, doi:10.1021/Es703009q, 2008.

Alfarra, M. R., Prevot, A. S. H., Szidat, S., Sandradewi, J., Weimer, S., Lanz, V. A., Schreiber, D., Mohr, M., and Baltensperger, U.: Identification of the mass spectral signature of organic aerosols from wood burning emissions, Environ. Sci. Technol., 41, 5770–5777, doi:10.1021/Es062289b, 2007.

Blumenthal, D. L., White, W. H., and Smith, T. B.: Anatomy of a Los-Angeles Smog Episode - Pollutant Transport in Daytime Sea Breeze Regime, Atmos. Environ., 12, 893–907, 1978.

Chhabra, P. S., Ng, N. L., Canagaratna, M. R., Corrigan, A. L., Russell, L. M., Worsnop, D. R., Flagan, R. C., and Seinfeld, J. H.: Elemental composition and oxidation of chamber organic aerosol, Atmos. Chem. Phys. Discuss., 11, 10305–10342, doi:10.5194/acpd-11-10305-2011, 2011.

Davies, D. K., Ilavajhala, S., Wong, M. M., and Justice, C. O.: Fire information for resource management system: Archiving and distributing MODIS active fire data, IEEE T. Geosci. Remote, 47, 72–79, 2009.

Decesari, S., Fuzzi, S., Facchini, M. C., Mircea, M., Emblico, L., Cavalli, F., Maenhaut, W., Chi, X., Schkolnik, G., Falkovich, A., Rudich, Y., Claeys, M., Pashynska, V., Vas, G., Kourtchev, I., Vermeylen, R., Hoffer, A., Andreae, M. O., Tagliavini, E., Moretti, F., and Artaxo, P.: Characterization of the organic composition of aerosols from Rondnia, Brazil, during the LBA-SMOCC 2002 experiment and its representation through model compounds, Atmos. Chem. Phys., 6, 375–402, doi:10.5194/acp-6-375-2006, 2006.

Docherty, K. S., Stone, E. A., Ulbrich, I. M., DeCarlo, P. F., Snyder, D. C., Schauer, J. J., Peltier, R. E., Weber, R. J., Murphy, S. M., Seinfeld, J. H., Eatough, D. J., Grover, B. D., and Jimenez, J. L.: Apportionment of primary and secondary organic aerosols in Southern California during the 2005 study of organic aerosols in riverside (SOAR), Environ. Sci. Technol., 42, 7655–7662, 2008.

Draxler, R. R. and Rolph, G. D.: HYSPLIT (HYbrid Single-Particle Lagrangian Integrated Trajectory) Model access via NOAA ARL READY Website (http://www.arl.noaa.gov/ready/hysplit4.html), NOAA Air Resources Laboratory, Silver Spring (last access: August 2010), 2003.

Drewnick, F., Hings, S. S., DeCarlo, P., Jayne, J. T., Gonin, M., Fuhrer, K., Weimer, S., Jimenez, J. L., Demerjian, K. L., Borrmann, S., and Worsnop, D. R.: A new time-of-flight aerosol mass spectrometer (TOF-AMS) – Instrument description and first field deployment, Aerosol Sci. Tech., 39, 637–658, doi:10.1080/02786820500182040, 2005.

Duong, H. T., Sorooshian, A., Craven, J. S., Hersey, S. P., Metcalf, A. R., Zhang, X., Weber, R. J., Jonsson, H., Flagan, R. C., and Seinfeld, J. H.: Water-Soluble Organic Aerosol in the Los Angeles Basin and Outflow Regions: Airborne and Ground Measurements During the 2010 CalNex Field Campaign, J. Geophys. Res., in review, 2011.

Ervens, B. and Volkamer, R.: Glyoxal processing by aerosol multiphase chemistry: towards a kinetic modeling framework of secondary organic aerosol formation in aqueous particles, Atmos. Chem. Phys., 10, 8219–8244, doi:10.5194/acp-10-8219-2010, 2010.

Fuzzi, S., Decesari, S., Facchini, M. C., Cavalli, F., Emblico, L., Mircea, M., Andreae, M. O., Trebs, I., Hoffer, A., Guyon, P., Artaxo, P., Rizzo, L. V., Lara, L. L., Pauliquevis, T., Maenhaut, W., Raes, N., Chi, X. G., Mayol-Bracero, O. L., Soto-Garcia, L. L., Claeys, M., Kourtchev, I., Rissler, J., Swietlicki, E., Tagliavini, E., Schkolnik, G., Falkovich, A. H., Rudich, Y., Fisch, G., and Gatti, L. V.: Overview of the inorganic and organic composition of size-segregated aerosol in Rondonia, Brazil, from the biomass-burning period to the onset of the wet season, J. Geophys. Res., 112, D01201, doi:10.1029/2005jd006741, 2007.

Gao, S., Hegg, D. A., Hobbs, P. V., Kirchstetter, T. W., Magi, B. I., and Sadilek, M.: Water-soluble organic components in aerosols associated with savanna fires in southern Africa: Identification, evolution, and distribution, J. Geophys. Res., 108(D13), 8491, doi:10.1029/2002JD002324, 2003.

Graham, B., Mayol-Bracero, O. L., Guyon, P., Roberts, G. C., Decesari, S., Facchini, M. C., Artaxo, P., Maenhaut, W., Koll, P., and Andreae, M. O.: Water-soluble organic compounds in biomass burning aerosols over Amazonia – 1. Characterization by NMR and GC-MS, J. Geophys. Res., 107(D20), 8047, doi:10.1029/2001jd000336, 2002.

Grieshop, A. P., Logue, J. M., Donahue, N. M., and Robinson, A. L.: Laboratory investigation of photochemical oxidation of organic aerosol from wood fires 1: measurement and simulation of organic aerosol evolution, Atmos. Chem. Phys., 9, 1263–1277, doi:10.5194/acp-9-1263-2009, 2009.

Hennigan, C. J., Bergin, M. H., Dibb, J. E., and Weber, R. J.: Enhanced secondary organic aerosol formation due to water uptake by fine particles, Geophys. Res. Lett., 35, L18801, doi:10.1029/2008gl035046, 2008.

Hennigan, C. J., Bergin, M. H., Russell, A. G., Nenes, A., and Weber, R. J.: Gas/particle partitioning of water-soluble organic aerosol in Atlanta, Atmos. Chem. Phys., 9, 3613–3628, doi:10.5194/acp-9-3613-2009, 2009.

Hennigan, C. J., Sullivan, A. P., Collett Jr., J. L., and Robinson, A. L.: Levoglucosan stability in biomass burning particles exposed to hydroxyl radicals, Geophys. Res. Lett., 37, L09806, doi:10.1029/2010GL043088, 2010.

Hersey, S. P., Craven, J. S., Schilling, K. A., Metcalf, A. R., Sorooshian, A., Chan, M. N., Flagan, R. C., and Seinfeld, J. H.:

The Pasadena Aerosol Characterization Observatory (PACO): chemical and physical analysis of the Western Los Angeles basin aerosol, Atmos. Chem. Phys., 11, 7417–7443, doi:10.5194/acp-11-7417-2011, 2011.

Hughes, L. S., Allen, J. O., Bhave, P., Kleeman, M. J., Cass, G. R., Liu, D.-Y., Fergenson, D. P., Morrical, B. D., and Prather, K. A.: Evolution of atmospheric particles along trajectories crossing the Los Angeles Basin, Environ. Sci. Technol., 34, 3058–3068, 2000.

Husar, R. B., Patterson, D. E., Blumenthal, D. L., White, W. H., and Smith, T. B.: 3-dimensional distribution of air-pollutants in Los-Angeles Basin, J. Appl. Meteorol., 16, 1089–1096, 1977.

Jaffrezo, J.-L., Aymoz, G., Delaval, C., and Cozic, J.: Seasonal variations of the water soluble organic carbon mass fraction of aerosol in two valleys of the French Alps, Atmos. Chem. Phys., 5, 2809–2821, doi:10.5194/acp-5-2809-2005, 2005.

Justice, C. O., Giglio, L., Korontzi, S., Owens, J. Morisette, J. T., Roy, D., Descloitres, J., Alleaume, S., Petitcolin, F., and Kaufman, F.: The MODIS fire products, Remote Sens. Environ., 83, 244–262, 2002.

Kondo, Y., Miyazaki, Y., Takegawa, N., Miyakawa, T., Weber, R. J., Jimenez, J. L., Zhang, Q., and Worsnop, D. R.: Oxygenated and water-soluble organic aerosols in Tokyo, J. Geophys. Res., 112, D01203, doi:10.1029/2006jd007056, 2007.

Lee, S., Kim, H. K., Yan, B., Cobb, C. E., Hennigan, C., Nichols, S., Chamber, M., Edgerton, E. S., Jansen, J. J., Hu, Y. T., Zheng, M., Weber, R. J., and Russell, A. G.: Diagnosis of aged prescribed burning plumes impacting an urban area, Environ. Sci. Technol., 42, 1438–1444, doi:10.1021/Es7023059, 2008.

Lu, R. and Turco, R. P.: Air Pollutant Transport in a Coastal Environment .2. 3-Dimensional Simulations over Los-Angeles Basin, Atmos. Environ., 29, 1499–1518, 1995.

Mayol-Bracero, O. L., Guyon, P., Graham, B., Roberts, G., Andreae, M. O., Decesari, S., Facchini, M. C., Fuzzi, S., and Artaxo, P.: Water-soluble organic compounds in biomass burning aerosols over Amazonia – 2. Apportionment of the chemical composition and importance of the polyacidic fraction, J. Geophys. Res., 107(D20), 8091, doi:10.1029/2001jd000522, 2002.

McLafferty, F. W. and Turecek, F.: Interpretation of Mass Spectra, Fourth Edition, University Science Books, Mill Valley, California, 1993.

Miyazaki, Y., Kondo, Y., Takegawa, N., Komazaki, Y., Fukuda, M., Kawamura, K., Mochida, M., Okuzawa, K., and Weber, R. J.: Time-resolved measurements of water-soluble organic carbon in Tokyo, J. Geophys. Res., 111, D23206, doi:10.1029/2006jd007125, 2006.

Murphy, S. M., Agrawal, H., Sorooshian, A., Padro, L. T., Gates, H., Hersey, S., Welch, W. A., Jung, H., Miller, J. W., Cocker, D. R., Nenes, A., Jonsson, H. H., Flagan, R. C., and Seinfeld, J. H.: Comprehensive Simultaneous Shipboard and Airborne Characterization of Exhaust from a Modern Container Ship at Sea, Environ. Sci. Technol., 43, 4626–4640, doi:10.1021/Es802413j, 2009.

Ng, N. L., Canagaratna, M. R., Zhang, Q., Jimenez, J. L., Tian, J., Ulbrich, I. M., Kroll, J. H., Docherty, K. S., Chhabra, P. S., Bahreini, R., Murphy, S. M., Seinfeld, J. H., Hildebrandt, L., Donahue, N. M., DeCarlo, P. F., Lanz, V. A., Prévôt, A. S. H., Dinar, E., Rudich, Y., and Worsnop, D. R.: Organic aerosol components observed in Northern Hemispheric datasets from Aerosol Mass Spectrometry, Atmos. Chem. Phys., 10, 4625–4641, doi:10.5194/acp-10-4625-2010, 2010.

Peltier, R. E., Weber, R. J., and Sullivan, A. P.: Investigating a liquid-based method for online organic carbon detection in atmospheric particles, Aerosol Sci. Tech., 41, 1117–1127, doi:10.1080/02786820701777465, 2007.

Phuleria, H. C., Fine, P. M., Zhu, Y. F., and Sioutas, C.: Air quality impacts of the October 2003 Southern California wildfires, J. Geophys. Res., 110, D07S20, doi:10.1029/2004jd004626, 2005.

Posfai, M., Simonics, R., Li, J., Hobbs, P. V., and Buseck, P. R.: Individual aerosol particles from biomass burning in southern Africa: 1. Composition and size distributions of carbonaceous particles, J. Geophys. Res., 108(D13), 8483, doi:10.1029/2002JD002291, 2003.

Reid, J. S., Koppmann, R., Eck, T. F., and Eleuterio, D. P.: A review of biomass burning emissions part II: intensive physical properties of biomass burning particles, Atmos. Chem. Phys., 5, 799–825, doi:10.5194/acp-5-799-2005, 2005.

Robinson, A. L., Donahue, N. M., Shrivastava, M. K., Weitkamp, E. A., Sage, A. M., Grieshop, A. P., Lane, T. E., Pierce, J. R., and Pandis, S. N.: Rethinking organic aerosols: Semivolatile emissions and photochemical aging, Science, 315, 1259–1262, doi:10.1126/science.1133061, 2007.

Ruellan, S., Cachier, H., Gaudichet, A., Masclet, P., and Lacaux, J. P.: Airborne aerosols over central Africa during the experiment for regional sources and sinks of oxidants (EXPRESSO), J. Geophys. Res., 104, 30673–30690, 1999.

Sorooshian, A., Brechtel, F. J., Ma, Y. L., Weber, R. J., Corless, A., Flagan, R. C., and Seinfeld, J. H.: Modeling and characterization of a particle-into-liquid sampler (PILS), Aerosol Sci. Tech., 40, 396–409, doi:10.1080/02786820600632282, 2006.

Sorooshian, A., Murphy, S. M., Hersey, S., Bahreini, R., Jonsson, H., Flagan, R. C., and Seinfeld, J. H.: Constraining the contribution of organic acids and AMS *m/z*44 to the organic aerosol budget: on the importance of meteorology, aerosol hygroscopicity, and region, Geophys. Res. Lett., 37, L21807, doi:10.1029/2010GL044951, 2010.

Sullivan, A. P. and Weber, R. J.: Chemical characterization of the ambient organic aerosol soluble in water: 1. Isolation of hydrophobic and hydrophilic fractions with a XAD-8 resin, J. Geophys. Res., 111, D05314, doi:10.1029/2005jd006485, 2006.

Sullivan, A. P., Weber, R. J., Clements, A. L., Turner, J. R., Bae, M. S., and Schauer, J. J.: A method for on-line measurement of water-soluble organic carbon in ambient aerosol particles: Results from an urban site, Geophys. Res. Lett., 31, L13105, doi:10.1029/2004gl019681, 2004.

Sullivan, A. P., Peltier, R. E., Brock, C. A., de Gouw, J. A., Holloway, J. S., Warneke, C., Wollny, A. G., and Weber, R. J.: Airborne measurements of carbonaceous aerosol soluble in water over northeastern United States: Method development and an investigation into water-soluble organic carbon sources, J. Geophys. Res., 111, D23S46, doi:10.1029/2006jd007072, 2006.

Timonen, H., Aurela, M., Carbone, S., Saarnio, K., Saarikoski, S., Mäkelä, T., Kulmala, M., Kerminen, V.-M., Worsnop, D. R., and Hillamo, R.: High time-resolution chemical characterization of the water-soluble fraction of ambient aerosols with PILS-TOC-IC and AMS, Atmos. Meas. Tech., 3, 1063–1074, doi:10.5194/amt-3-1063-2010, 2010.

Vutukuru, S., Griffin, R. J., and Dabdub, D.: Simulation and

analysis of secondary organic aerosol dynamics in the South Coast Air Basin of California, J. Geophys. Res., 111, D10S12, doi:10.1029/2005jd006139, 2006.

Weber, R. J., Sullivan, A. P., Peltier, R. E., Russell, A., Yan, B., Zheng, M., de Gouw, J., Warneke, C., Brock, C., Holloway, J. S., Atlas, E. L., and Edgerton, E.: A study of secondary organic aerosol formation in the anthropogenic-influenced southeastern United States, J. Geophys. Res., 112, D13302, doi:10.1029/2007jd008408, 2007.

Westerling, A. L., Hidalgo, H. G., Cayan, D. R., and Swetnam, T. W.: Warming and earlier spring increase western US forest wildfire activity, Science, 313, 940–943, doi:10.1126/science.1128834, 2006.

Zhang, Q., Alfarra, M. R., Worsnop, D. R., Allan, J. D., Coe, H., Canagaratna, M. R., and Jimenez, J. L.: Deconvolution and quantification of hydrocarbon-like and oxygenated organic aerosols based on aerosol mass spectrometry, Environ. Sci. Technol., 39, 4938–4952, doi:10.1021/Es048568l, 2005.